Proceedings of the

15th International Workshop on Deep-Inelastic Scattering and Related Subjects

DIS 2007

April 16-20, 2007
Munich, Germany

Editors:
Günter Grindhammer, Kirsten Sachs

Verlag Deutsches Elektronen-Synchrotron

Impressum

Proceedings of the 15$^{\text{th}}$ International Workshop on Deep-Inelastic Scattering and Related Subjects DIS 2007

This document is also available online at ATLANTIS Press
http://www.sciencewisepublishing.com/publications/DIS07

Conference homepage
http://www.mppmu.mpg.de/dis2007/

Slides at
http://indico.cern.ch/conferenceTimeTable.py?confId=9499

Editors: Günter Grindhammer, Kirsten Sachs
Cover Photo: ©iStockphoto.com/Björn Kindler
Photo of Participants: Daniel Greenwald (MPI for Physics, Munich)
September 2007
DESY-PROC-2007-01
ISSN 1435-8077
ISBN 978-3-935702-23-2

Published by
Deutsches Elektronen-Synchrotron, DESY
Notkestraße 85
22607 Hamburg
Germany

Preface

The 15^{th} International Workshop on Deep-Inelastic Scattering and Related Subjects continued the very successful series which began with a workshop on "HERA Physics" in Durham in 1993. Held at Munich from April 16-20, the workshop united more than 300 physicists engaged in experimental and theoretical work from around the world, including an encouraging number of students. The program contained reviews of progress in the field of deep-inelastic scattering (DIS) and QCD, as well as presentations on the latest results from HERA, the Tevatron, Jefferson Lab, RHIC, and fixed target experiments. It also covered related theoretical topics and future experimental opportunities in the field.

Exceptionally beautiful weather and the surroundings of Munich's Holiday Inn City Centre Hotel and the Gasteig, a modern cultural center, combined to provide a pleasant and stimulating atmosphere at DIS 2007. With two full days of plenary sessions, on the first day to "set the scene" and on the last day to summarize, and with six streams of parallel sessions during the three days in between, the meeting followed the traditional style of DIS workshops. The parallel sessions covered the areas of structure functions and low-x physics, electroweak measurements and physics beyond the Standard Model, heavy flavors, hadronic final states, diffraction and vector mesons, and spin physics. A special session that looked to the future of DIS was particularly topical in view of the shut down of HERA, DESY's electron-proton collider, by the end of June of this year.

For the coming years, much careful analysis remains to be done with the data from HERA in order to achieve the best possible precision. This is expected to yield valuable information for the understanding of QCD and of the data to be produced at the LHC. HERA's final legacy will be an important asset to high-energy physics.

The 2007 workshop was hosted by the Max-Planck-Institute for Physics in Munich, with support from DESY and from the high energy physics groups at Hamburg University and the Ludwig-Maximilians-University and the Technical University, both in Munich. Previous workshops took place in Durham, Eilat, Paris, Rome, Chicago, Brussels, Zeuthen, Liverpool, Bologna, Cracow, St. Petersburg, Strbske Pleso and Tsukuba.

We wish to thank all who contributed to the success of this workshop: the international advisory and local organizing committees, the plenary speakers, the conveners of the working groups for their efforts in assembling an excellent program and the parallel session speakers for making it come true, and finally the secretarial, computing, and scientific staff and students from our institute for their enormous support in running everything very smoothly.

The organizers gratefully acknowledge the financial support of the workshop by the Deutsche Elektronen-Synchrotron, the Deutsche Forschungsgemeinschaft, and by Brookhaven National Laboratory, CERN, Fermilab, Jefferson Laboratory and by our sponsors Dallmayr, IBM and Lufthansa, which made this workshop possible.

Allen Caldwell (Chair), Günter Grindhammer and Christian Kiesling
MPI Munich

Organization

Local Organzing Committee

MPI for Physics, Munich	Iris Abt Juraj Braciník Allen Caldwell (Chair) Vladimir Chekelian Günter Grindhammer Christian Kiesling Daniel Kollár Wolfgang Ochs Franziska Rudert
TU Munich	Stephan Paul
LMU Munich	Dorothee Schaile
University of Hamburg	Bernd Kniehl

International Advisory Committee

Giulio d'Agostini	Roma
Guido Altarelli	CERN
Violette Brisson	Orsay
Dušan Bruncko	Slovak Acad.
John Dainton	Liverpool
Andrzej Eskreys	Krakow
Joel Feltesse	Saclay
Rolf-Dieter Heuer	DESY
Robert Klanner	DESY
Max Klein	Zeuthen
Aharon Levy	Tel Aviv (Chair)
Lev Lipatov	St Petersburg
Pierre Marage	Brussels
Rosario Nania	Bologna
Jose Repond	Argonne
Wesley Smith	Wisconsin
Frank Sciulli	Columbia
James Stirling	Durham
Katsuo Tokushuku	KEK
Albrecht Wagner	DESY
Günter Wolf	DESY

Content

Volume I

Summary Talks

Structure Functions and Low-x

Convenors: Alexandre Glazov, Kunihiro Nagano, Sven Moch

Structure Functions and Low-x / Electroweak Measurements (Including Top) and Beyond the Standard Model

Structure Functions and Low-x / Diffraction and Vector Mesons

Electroweak Measurements (Including Top) and Beyond the Standard Model

Convenors: Martin Wessels, James Ferrando, Thomas Nunnemann, Michael Spira

Spin Physics

Convenors: Delia Hasch, Gerhard Mallot, Daniël Boer

Volume II

Diffraction and Vector Mesons

Convenors: Laurent Favart, Uta Klein, Rolf Ent, Leszek Motyka

Diffraction and Vector Mesons / Spin Physics

Heavy Flavors

Convenors: Stephanie Menzemer, Rainer Mankel, Benno List, Michael Klasen

Heavy Flavors / Diffraction and Vector Mesons

Hadronic Final States and QCD

Convenors: Daniel Traynor, Alexandre Savin, Duncan Brown, Giulia Zanderighi

Special Session on α_s

Future of DIS

Convenors: Abhay L. Deshpande, Paul Newman, Christian Weiss

Plenary Talks

QCD Parton Dynamics, 30 Years later

Yu.L. Dokshitzer

LPTHE, Universities of Paris VI–VII and CNRS, Paris, France;
St. Petersburg Nuclear Physics Institute, Gatchina, Russia

To translate poetry is impossible. But the original is "impossible" too. Then the purpose of a translation is to discover the impossibility of the original. This maxim, belonging to a contemporary poet and philosopher, applies to theoretical physics which attempts to penetrate into the sense of beauty that Einshtein's God indisputably possesses.

1 Introduction

Physical formulae have reasons. Some are simple and lie on a surface, some may be profound and not even visible at a first examination. Obviously, a formula may not contain a sum of the electric tension and the current, $V + I$. For less obvious (though not less general) reasons, a scattering amplitude may not contain a step-function θ (causality), or there can be no strong Wan der Waals force between hadrons (relativistic invariance, cross-channel unitarity).

Physical formulae also know to smile. (Recall an ironic $\pi^2 - 9$ factor in the positronium decay width.) A repetitive smile turns into a laughter: the combination $(\frac{67}{18} - \frac{\pi^2}{6})N_c - \frac{5}{9}n_f$ that persistently appeared in second loop corrections to DIS structure functions, to jet shape distributions and jet cross sections, in Regge trajectories of quarks and gluon, etc., etc., for a good many year laughs at theorists who got stuck with the MS-bar QCD coupling.

At some point formulae smile no more: they cry for help. This is the case of a body of the third loop corrections to various key QCD quantities that has recently become available as a result of the completion of a breakthrough programme of high order QCD calculations carried out by Moch, Vermaseren and Vogt.

The matrix of the leading order (one loop) anomalous dimensions fitted onto two lines; the second loop result occupied about one page; the volume of the third loop formulae is more natural to measure in (tens of) kilobytes rather than in the number of pages.

Is such a monstrous complexity inevitable? Could it be reasonably reduced? The answer I believe is *no*, and *yes* (in this order). I would like to discuss with you two ideas that in my opinion deserve to be explored.

The first idea which I will refer to as "innovative bookkeeping" exploits a hidden symmetry between space- and time-like parton evolution known under the name of the *Gribov–Lipatov reciprocity* (GLR). It constitutes a reformulation of the parton dynamics in terms of a new evolution equation whose *evolution kernel* respects GLR in all orders. In this alternative scheme for organising the perturbative expansion, the anomalous dimension is related to the evolution kernel by a non-linear equation. Within this scheme a significant (if not dominant) part of the higher loop corrections to the anomalous dimension turns out to be *inherited* from the lower orders, thus reducing the complexity of the answer.

The second part of the project is more ambitious. The aim is to understand the major part of the evolution kernel exactly, in all orders of the perturbation theory. It is based on two observations, one physical and another technical. The physical observation is that an essential part of the gluon dynamics is actually *classical*, according to the well known (but often under-appreciated) Low theorem. "Classical" does not mean "simple". However, it

has a good chance to be *solvable*. This belief is based on the second (technical) observation that the QCD shares gluons with super-symmetric Yang–Mills theories and, in particular, with the maximally supersymmetric $\mathcal{N}=4$ SYM quantum field theory which is likely to be *fully integrable*, that is, solvable.

2 Innovative bookkeeping

In the standard approach, the anomalous dimensions $\gamma(N)$ are equated with the (Mellin transformed, $x \to N$) parton splitting functions $P(x)$; they are different for the space-like (DIS) and time-like evolution (e^+e^-); the "clever evolution variables" are different too.

In the new approach, one disconnects the splitting functions from the anomalous dimensions. By organising the parton evolution picture in both channels on the base of the common evolution variable (parton fluctuation time), the new "Hamiltonian" describing the dynamics of partons — the *evolution kernel* — turns out to be identical for space- and time-like cascades (the Gribov–Lipatov reciprocity relation holds in all orders).

2.1 QCD partons and perturbation theory

The universal nature of the parton dynamics goes under the name of *factorisation* of collinear ("mass") singularities. Physically, it is due to the fact that quark–gluon multiplication processes happen at *much larger* space–time distances than the hard interaction itself. It is this separation that makes possible the description of quark–gluon cascades in terms of independent classical *parton splitting processes*. They succeed one another in a cleverly chosen *evolution time*, $t \sim \ln Q^2$, whose flow "counts" basic parton splittings that occur at well separated, strongly ordered space–time scales. The perturbative structure of the cross section of a given process i characterised by the hardness scale Q^2 can be cast, symbolically, as a product (convolution) of three factors:

$$\sigma_h^{(p)}(\ln Q^2) \;\propto\; C^{(p)}[\alpha_s(t)] \otimes \exp\left(\int_{t_0}^{t} d\tau\, P[\alpha_s(\tau)]\right) \otimes w_h(t_0), \qquad t \sim \ln Q^2. \tag{1}$$

Here the functions $C[\alpha_s]$ (hard cross section; coefficient function) and $P[\alpha_s]$ (parton evolution; anomalous dimension matrix) are perturbative objets analysed in terms of the α_s expansion. The last factor w_h embeds non-perturbative information about parton structure of the participating hadron(s) h, be it a target hadron in the initial state (parton distribution) or a hadron triggered in the final state (fragmentation function).

A borderline between perturbative and non-perturbative ingredients in (1) is fictitious; it is set arbitrarily by choosing the launching hardness scale $t_0 \sim \ln Q_0^2$. This is however not the only arbitrariness present in the representation (1). Namely, beyond the leading approximation (one loop; $P = \mathcal{O}(\alpha_s)$), the separation between the C and $\exp(P)$ factors becomes "scheme" dependent. Here one talks about *factorisation scheme* dependence. Another negotiable object is the expansion parameter α_s itself whose definition depends on the ultraviolet renormalisation procedure (*renormalisation scheme* dependence). The so-called MS-bar scheme based on the precisely prescribed procedure of eliminating ultraviolet divergences, based on the dimensional regularisation won the day as the best suited scheme for carrying out laborious high order calculations. It is the MS-bar scheme in which the parton "Hamiltonian" P was recently calculated in the next-to-next-to-leading accuracy, α_s^3 [2, 3].

Formally speaking, the physical answer does not depend on which schemes (factorisation, renormalisation) one chooses to construct the expansion. There is a big "if" however which renders this motto meaningless. It would have been the case, and consolation, if we had hold of the *full* perturbative expansion of the answer. But this goal is not only technically unachievable. More importantly, it is actually useless. The perturbative QFT expansions are *asymptotic series*. This means that starting from some order, $n > n_{\rm crit} = {\rm const}_{(p)}/\alpha_s$, the series for any observable (p) inevitably goes haywire and ceases to represent the answer. For QED where $n_{\rm crit} \sim 100$ this was an academic problem. In QCD on the contrary the best hope the perturbative expansion may offer is a reasonable numerical *estimate* based on the first few orders of the perturbation theory (whose intrinsic uncertainty can often be linked with genuine non-perturbative effects). This being understood, it becomes legitimate, and mandatory, to play with perturbative series trying to recast a formal α_s expansion in the most relevant way, the closest to the physics of the problem.

2.2 Relating DIS and e^+e^-

No surprise, the space- and time-like parton cascades are intimately related. In the DIS case the large virtual momentum q transferred from the incident lepton to the target nucleon with momentum P is *space-like*, $q^2 < 0$. The *inelasticity* of the process is conveniently characterised by the *Bjorken* variable $x_B = -q^2/2(Pq)$. On the other side, inclusive fragmentation of an e^+e^- pair with the total momentum q (large *positive* invariant mass squared q^2) into a final state hadron with momentum P is characterised by the *Feynman* variable $x_F = 2(Pq)/q^2$ (hadron energy fraction in the e^+e^- cms.). The fact that Bjorken and Feynman variables are indicated by the same letter is certainly not accidental. In both channels $0 \le x \le 1$ though these variables are actually reciprocal, $x_F \iff 1/x_B$, rather than identical:

$$x_B \;=\; \frac{-q^2}{2(Pq)}, \qquad x_F \;=\; \frac{2(Pq)}{q^2}. \tag{2}$$

One x becomes the inverse of the other after the crossing operation $P_\mu \to -P_\mu$. Apart from the difference in the hadron momentum P belonging to the initial state in the DIS and final state in the e^+e^- case, the Feynman diagrams for the two processes are just the same. In particular, *mass singularities* that emerge when some parton momentum become collinear to P are therefore also the same. That is why, for the two processes a similar parton interpretation emerges in terms of QCD evolution equations, and the space- and time-like evolution anomalous dimensions turn out to be related.

Drell–Levy–Yan relation [4] follows directly from the comparison of the structure of Feynman diagrams in space- and time-like channels. It states that the e^+e^- splitting functions can be obtained from those of DIS by replacing $x_B \to 1/x_F$ (modulo a kinematical factor):

$$P^{(T)}_{BA}(x) = (-1)^{2(J_A-J_B)+1}\, x \cdot P^{(S)}_{AB}(x^{-1}) \tag{3}$$

(with J_A the spin of the parton A). Beyond the leading logarithmic approximation (LLA) [5, 6, 7], the DLY relation (3) was being used to actually *determine* the time-like splitting functions from their space-like counterparts. True in any QFT,[a] it reflects the crossing and allows one to link the cross sections in the two channels by *analytic continuation* from $x < 1$

[a] when applied to *physical cross sections*, not necessarily to scheme dependent anomalous dimensions [8]

to $x > 1$. So doing, one obtains the time-like splitting function, $P^{(T)}(x)$, by analytically continuing the function $P^{(S)}(x)$ into the unphysical region $x > 1$, and then replacing $x \to 1/x < 1$. The continuation path crosses the singular point $x = 1$ which needs a special care to be taken in defining certain complex logarithms in "arithmetic" sense, $\ln(1-x) \implies |\ln(1-x)|$, see [9, 7]; beyond the first loop, see [10, 8] and references therein.

Gribov–Lipatov relation [5] applies in the physical regions of both channels, $x \leq 1$, and states simply that the splitting functions are *identical*, although their arguments are actually given by the *different* expressions (2):

$$P^{(T)}_{BA}(x_{\text{ Feynman }}) \;=\; P^{(S)}_{BA}(x_{\text{ Bjorken }})\,; \qquad x_B = \frac{-q^2}{2pq}\,, \quad x_F = \frac{2pq}{q^2}.$$

Combined with the DLY relation (3), it becomes the *Gribov–Lipatov reciprocity* (GLR):

$$P_{BA}(x) = \mp\, x \cdot P_{AB}(x^{-1}). \tag{4}$$

True in the leading logarithmic approximation, the Gribov–Lipatov reciprocity (4) was found to be broken beyond the first loop [11]. But why?

2.3 Long live parton fluctuation time!

It is instructive to look more carefully into the origin of logarithmically enhanced contributions to the DIS cross section. Introducing two light-like vectors p_1^μ and p_2^μ one can write down the Sudakov (light-cone) decomposition of momenta:

$$k^\mu = \beta p_1^\mu + \alpha p_2^\mu + k_\perp^\mu\,, \qquad k^2 = \alpha\beta s - \mathbf{k}_\perp^2 \qquad \left(s = 2Pq\,,\ (k_\perp^\mu)^2 = -\mathbf{k}_\perp^2\right).$$

Then, for $k_1^\mu + k_2^\mu + k_3^\mu = 0$ it is straightforward to derive the identity

$$\frac{k_1^2}{\beta_1} + \frac{k_2^2}{\beta_2} + \frac{k_3^2}{\beta_3} \;=\; \frac{\beta_1\beta_2}{\beta_3}\left(\frac{\mathbf{k}_{\perp 1}}{\beta_1} - \frac{\mathbf{k}_{\perp 2}}{\beta_2}\right)^2. \tag{5}$$

Let us now apply this general relation to the parton splitting that involves a space-like parton A decaying into B+C. Choosing for the sake of simplicity the direction of p_1 such

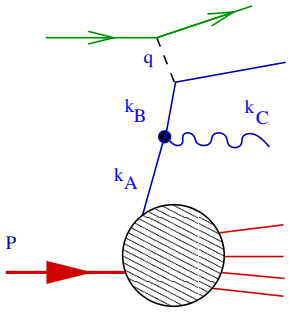

that $\mathbf{k}_{\perp A} = 0$ (so that $\mathbf{k}_{\perp B} = -\mathbf{k}_{\perp C} \equiv \mathbf{k}_\perp$ is the *relative transverse momentum* in the splitting) the relation (5) applied to our basic space-like splitting $A \to B[z] + C[1-z]$ gives

$$\frac{-k_B^2}{z} \;=\; \frac{-k_A^2}{1} + \frac{k_C^2}{1-z} + \frac{\mathbf{k}_\perp^2}{z(1-z)}\,, \tag{6}$$

where z is the longitudinal momentum fraction — the ratio of the Sudakov light-cone variables β. Since the 4-momenta of A and B are space-like, all terms in (6) are positive.

B being an intermediate virtual state, k_B^2 enters in the Feynman denominators in the matrix element. The collinear-log contribution arises upon the $k_\perp^2$ integration over the region where the last term dominates in the r.h.s. of (6), that is from the region

$$\frac{|k_B^2|}{z} \;\simeq\; \frac{\mathbf{k}_\perp^2}{z(1-z)} \;\gg\; \frac{|k_A^2|}{1},\ \frac{k_C^2}{1-z}\,.$$

The physical origin of this strong inequality becomes transparent in terms of lifetimes of virtual states ($p_1^\mu \simeq P^\mu$, $p_2^\mu = q^\mu + xP^\mu$)

$$\frac{\beta_i P}{|k_i^2|} \simeq \frac{k_i^0}{|k_i^2|} \;=\; \tau_i, \tag{7}$$

namely $\tau_B \ll \tau_A\,,\, \tau_C$. This shows that the LLA contributions originate from the sequence of branchings well separated in the *fluctuation time* (7). Invoking the local-scattering analogy (recall $A \to C$ on the "external field" B), we can say that the classical picture naturally implies "fast scattering": probing time τ_B much smaller than the proper lifetimes of the "target" before (τ_A) and after the scattering occurs (τ_C).

In the DIS kinematics the evolution goes from the proton side and, on the way towards the virtual probe Q^2, parton fluctuations become successively shorter-lived (the "probe" is faster than the fluctuation time of the "target"). Assembling a "ladder" of successive parton splittings we get the $n^{\rm th}$-order LLA contribution $(\alpha_s \ln Q^2)^n$ to come from time-ordered kinematics

$$\frac{P}{\mu^2} \gg \tau_1 \gg \tau_2 \gg \;\ldots\; \gg \tau_n \gg \frac{xP}{-q^2}\,; \qquad x = x_{\rm Bjorken} \;\equiv\; \frac{-q^2}{2Pq}. \tag{8a}$$

In the case of a time-like evolution of a jet produced, e.g., In the crossing channel, $e^+e^- \to q\bar q \to h(x) + X$, the process starts from a large scale q^2 (cms annihilation energy) and results in triggering a final particle h with momentum P. Here the order of events is opposite: a parton of the generation $(i+1)$ lives *longer* than its parent (i):

$$\frac{P}{xq^2} \ll \tau_1 \ll \tau_2 \ll \;\ldots\; \ll \tau_n \ll \frac{P}{\mu^2}\,; \qquad x = x_{\rm Feynman} \;\equiv\; \frac{2Pq}{q^2}, \tag{8b}$$

where we have used that the energy of the initial quark stemming form the $\gamma^* \to q\bar q$ vertex is $q_0/2 = P/x_F$. Comparing the two sequences (8) we see that the reciprocity $x \to x^{-1}$ is present in the ordering of successive fluctuation lifetimes. So, why does the Gribov–Lipatov relation break up in higher orders? The answer is quite simple: it is because we *never followed* the fluctuation time ordering[b] for constructing the anomalous dimensions. And for a good reason it seemed.

2.4 Coherence

Beyond the first loop it starts to matter how one orders successive parton splittings, that is, what one chooses for the *parton evolution time* $t \sim \ln Q^2$.

At the LLA level, it does not make sense to argue which of possible "evolution times", $\ln(k^2/\beta)$, $\ln k^2$, $\ln \mathbf{k}_\perp^2$ or alike, does a better job: the options differ by *subleading* terms $\mathcal{O}(\alpha_s)$, negligible as compared to $\alpha_s \ln Q \sim 1$. However, when one studies the kinematical region of numerically small x, the *next-to*-LLA mismatch contributions amount to

$$\alpha_s \ln^2 \frac{\beta_{i+1}}{\beta_i} = \alpha_s \ln^2 z \quad \Longrightarrow \quad (\alpha_s \ln^2 x)^n \tag{9}$$

[b] markedly, with an exception of the study of QCD coherent states within the asymptotic dynamics framework, [12] and references therein

and may become significant. If $\alpha_s \ln^2 x \sim 1$, they must be taken into account in *all orders*. In this situation the *soft gluon radiation* comes onto stage. And here we better be careful: the catch is, for a relatively soft gluon with $z \ll 1$, to be emitted *later* does not guarantee to be emitted *independently*. Interfering diagrams with the gluon radiation off harder partons of different generations enter the game, thus endangering the probabilistic parton picture. It was realised quite some time ago that the probabilistic interpretation can be rescued by simply cutting off a definite part of the logarithmic phase space that is formally allowed by the "kinematical" fluctuation time ordering.

In the DIS environment, the *transverse momentum* ordering proved to be the one that takes care of potentially disturbing corrections (9) in all orders, and in this sense became a preferable choice for constructing the probabilistic scheme for space-like parton cascades (DIS structure functions). On the other hand, in the case of the time-like cascades it turned out to be the *relative angle* between the offspring partons (rather than the transverse momentum) which had to be kept ordered and decreasing along the evolutionary decay chain, from the hard production vertex towards the registered inclusive hadron:

$$dt_- = d\ln k_\perp^2 \quad \text{(space-like)}, \tag{10a}$$

$$dt_+ = d\ln \frac{k_\perp^2}{\beta^2} \quad \text{(time-like)}. \tag{10b}$$

(Since $k_\perp/\beta P = k_\perp/k_+ = 2\tan(\theta/2)$, the variable (10b) corresponds indeed to the *angular ordering*.) What is the difference between the two prescriptions (10) and how do they relate with the fluctuation time ordering discussed above and represented by (8)? For $z \ll 1$ we have $\left|k^2\right| \simeq k_\perp^2$ and the comparison goes as follows

$$\text{DIS} \qquad \begin{cases} \text{time ordering:} & \tau_i = \dfrac{\beta_i P}{k_{\perp i}^2} \;>\; \tau_{i+1} = \dfrac{\beta_{i+1} P}{k_{\perp i+1}^2}, \\ k_\perp \text{ ordering:} & k_{\perp i} \;<\; k_{\perp i+1}; \end{cases}$$

$$\text{mismatch} \Longrightarrow \qquad z \cdot k_{\perp i}^2 < k_{\perp i+1}^2 < k_{\perp i}^2, \tag{11a}$$

while for the time-like cascades

$$e^+e^- \qquad \begin{cases} \text{time ordering:} & \tau_i = \dfrac{\beta_i P}{k_{\perp i}^2} \;<\; \tau_{i+1} = \dfrac{\beta_{i+1} P}{k_{\perp i+1}^2}, \\ \text{angular ordering:} & \theta_i = \dfrac{k_{\perp i}}{\beta_i P} \;>\; \theta_{i+1} = \dfrac{k_{\perp i+1}}{\beta_{i+1} P}; \end{cases}$$

$$\text{mismatch} \Longrightarrow \qquad \theta_i^2 < \theta_{i+1}^2 < \frac{\theta_i^2}{z}. \tag{11b}$$

We conclude that in both cases the fluctuation time ordering turns out to be *more liberal*. The destructive soft gluon interference suppresses the kinematical "mismatch" regions. Physically, the disappearance of the region (11a) in the space-like kinematics is related to the general phenomenon of the vanishing of the forward inelastic diffraction (Gribov, late 1960s); the disappearance of the angular disordered region (11b) can be traced back to the so-called Chudakov effect in the cosmic ray physics.

2.5 Rescuing Gribov–Lipatov reciprocity

Thus, the choice of the variables (10) is a clever dynamical move that takes into full consideration soft gluon coherence and prevents explosively large terms (9) from appearing in higher

loop anomalous dimensions. Not only is the fluctuation time ordering *wrong* both in space- and time-like kinematics, it happens to be *equally*, *symmetrically* wrong: the τ-ordering positions itself just in the middle between the two "clever" ones:

$$k_\perp^2 \quad \Longrightarrow \quad \frac{k_\perp^2}{z} \quad \Longrightarrow \quad \frac{k_\perp^2}{z^2}.$$

What if we decide to play a fool and stubbornly stick to the "wrong" τ-ordering?

Combining (8) and (7) we get the upper limits of virtuality integrals to be

$$\left.\begin{array}{ll} \text{DIS}: & \left|k_i^2\right| \ll \dfrac{\beta_i}{\beta_{i+1}} \left|k_{i+1}^2\right| = z^{-1} \cdot \left|k_{i+1}^2\right| \\ e^+e^-: & k_{i+1}^2 \ll \dfrac{\beta_{i+1}}{\beta_i} \;\; k_i^2 \;\; = \; z \cdot k_i^2 \end{array}\right\} \qquad z = \frac{\beta_{i+1}}{\beta_i} \le 1. \tag{12}$$

Different placing of the z factor causes (beyond the first loop) a violation of the Gribov–Lipatov reciprocity. Moreover, it is likely to be the *one and only* source of this breaking!

Let us probe this idea. Choosing $\kappa^2 = \left|k^2\right|$ as an integration variable and assembling parton evolution sequences, for the probability $D(x,Q^2)$ to find a parton with *virtuality* integrated up to a given Q^2 we obtain (omitting a trivial Born term) [13, 14]

$$D(x,Q^2) = \int_x^1 \frac{dz}{z} \int^{Q^2} \frac{d\kappa^2}{\kappa^2}\, P[z,\alpha_s]\, D\left(\frac{x}{z}, z^\sigma \kappa^2\right); \qquad \sigma = \pm 1 \text{ for the T/S channel.} \tag{13}$$

The second argument of the D function on the r.h.s. of the equation follows from (12). In terms of the Mellin moment representation of parton distributions and splitting functions,

$$D_N(Q^2) \;=\; \int_0^1 \frac{dx}{x}\, x^N\, D(x,Q^2), \qquad \mathcal{P}(N,\alpha_s) \;=\; \int_0^1 dz\, z^{N-1}\, P[z,\alpha_s],$$

by dropping in (13) the z^σ factor, one would obtain

$$\partial_{\ln Q^2} D_N(Q^2) \equiv \gamma(N,\alpha_s)\, D_N(Q^2) \;=\; \int_0^1 \frac{dz}{z}\, z^N\, P[z,\alpha_s]\, D_N\left(Q^2\right) \;=\; \mathcal{P}(N,\alpha_s)\, D_N(Q^2),$$

which equates the anomalous dimension with the Mellin image of the corresponding splitting function: $\gamma_- \equiv \mathcal{P}^{(S)}$ and $\gamma_+ \equiv \mathcal{P}^{(T)}$. The presence of the factor z^σ in the second argument of (13) makes the evolution equation *non-local* in longitudinal (x) and transverse variables (Q^2) and breaks the identification between the splitting functions and anomalous dimensions. What it offers instead is a *link* between the two channels by means of the *universal* reciprocity respecting parton splitting matrix $\mathcal{P}$, the same for T and S evolutions. In spite of the fact that the new *evolution kernel* in (13) does not correspond to any clever choice of the evolution variable (explosive $\alpha_s \ln^2 x$ terms being present in both channels), this universality can be exploited to relate the DIS and e^+e^- anomalous dimensions.

Differentiating (13) and taking Mellin moments of the differential equation

$$\partial_{\ln Q^2} D(x,Q^2) = \int_x^1 \frac{dz}{z}\, P[z,\alpha_s]\, D\left(\frac{x}{z}, z^\sigma Q^2\right),$$

one obtains

$$\gamma_\sigma(N)\, D_N = \int_0^1 \frac{dz}{z}\, z^N\, P[z,\alpha_s]\, z^{\sigma\partial_{\ln Q^2}}\, D_N\,. \tag{14a}$$

This integral can be formally evaluated using the Taylor expansion trick,

$$\gamma_\sigma(N) \;=\; (D_N)^{-1}\, \mathcal{P}(N+\sigma\partial_{\ln Q^2})\, D_N, \tag{14b}$$

expressing the anomalous dimension through the Mellin image of the splitting function that depends on the *differential operator* as an argument, $N \to N + \sigma\partial_{\ln Q^2}$. The derivative acts upon $D_N = D_N(Q^2)$ producing, by definition, $\gamma(N)\cdot D_N$. In high orders it will also act on the *running coupling* the anomalous dimension depends on, $\gamma = \gamma(N,\alpha_s)$. The latter action gives rise to terms proportional to the β-function. Such terms are scheme dependent as they can be reshuffled between the exponent and the coefficient function $C[\alpha_s]$ in (1). Neglecting for the time being these contributions by treating α_s as a constant, (14) reduces to a compact functional equation

$$\gamma_\sigma(N) \;=\; \mathcal{P}\left(N+\sigma\gamma_\sigma(N)\right). \tag{15}$$

Since $\gamma = \mathcal{O}(\alpha_s)$, we can expand the argument of the splitting function perturbatively,

$$\gamma_\sigma \;=\; \mathcal{P} \;+\; \dot{\mathcal{P}}\cdot\sigma\gamma_\sigma \;+\; \tfrac{1}{2}\ddot{\mathcal{P}}\cdot\gamma_\sigma^2 \;+\; \mathcal{O}\left(\beta(\alpha_s)\right) \;+\; \mathcal{O}\left(\alpha_s^4\right), \tag{16a}$$

where each dot marks the derivative over the moment N. Solving (16a) iteratively,

$$\gamma_\sigma \;= \mathcal{P} \;+\; \sigma\mathcal{P}\dot{\mathcal{P}} \;+\; \left[\mathcal{P}\dot{\mathcal{P}}^2 + \tfrac{1}{2}\mathcal{P}^2\ddot{\mathcal{P}}\right] + \;\ldots\,, \tag{16b}$$

and restricting to the first loop, $\mathcal{P} = \alpha_s\, P^{(1)}$ (with $P^{(1)}$ the Mellin image of the good old LLA splitting functions) gives

$$\gamma_\sigma \;=\; \alpha_s P^{(1)} \;+\; \alpha_s^2\,\sigma P^{(1)}\dot{P}^{(1)} \;+\; \ldots \tag{17}$$

Applied to the non-singlet quark evolution, the second term on the r.h.s. of (17) generates the GLR breaking observed by Curci, Furmanski & Petronzio in the second loop [11]. This shows that the GLR violation is not a dynamical higher order effect but is *inherited* from the previous loop(s) via a non-linear relation. In three loops, the GLR breaking predicted by (14) was verified in [15].

The same structure of the GLR violation holds for the gluon→gluon evolution as well. Strictly speaking, this is true only for two colour structures that emerge in the second loop anomalous dimensions $\mathcal{P}_{gg}^{(2)}$ namely, C_A^2 and $C_A C_F$. The third one, $2n_f T_R C_F$, corresponds to the $g \to q(\bar{q}) \to g$ two-step transition that mixes gluon and quark states. This colour factor is also present in the *singlet* quark evolution, $q \to g \to q$, described by the two-loop anomalous dimensions $\mathcal{P}_{qq,s}^{(2)}$. As a result, the structure of the GLR breaking in this specific colour structure turned out to be more involved though natural [13]:

$$\tfrac{1}{2}[\mathcal{P}_{qq,s}^{(2,T)} - \mathcal{P}_{gg}^{(2,S)}] \implies \mathcal{P}_{gq}^{(1)}\dot{\mathcal{P}}_{qg}^{(1)}\,, \qquad \tfrac{1}{2}[\mathcal{P}_{gg}^{(2,T)} - \mathcal{P}_{qq,s}^{(2,S)}] \implies \mathcal{P}_{qg}^{(1)}\dot{\mathcal{P}}_{gq}^{(1)}\,.$$

The analysis of non-diagonal parton transitions is more difficult since here the scheme dependence is more pronounced. Stratmann and Vogelsang have addressed this issue in [10] where a detailed discussion was given of a possibility to rescue GLR in two loops in terms of factorisation scheme transformation. The problem should be further pursued.

2.6 RREE applications

An important aspect of the reciprocity respecting evolution equation (RREE) is the *dual nature* of the expansion (16): it is obviously a series in the coupling ($\mathcal{P} \propto \alpha_s$); at the same time, it is an expansion in N^{-1}. Indeed, the leading behaviour of the evolution kernel is logarithmic, $\mathcal{P}(N) \propto \alpha_s \ln N$, so that each successive term in (16b) acquires a $1/N$ suppression factor: $\dot{\mathcal{P}} \sim N^{-1}$, $\ddot{\mathcal{P}} \sim \dot{\mathcal{P}}^2 \sim N^{-2}$, etc. In the x space, N^{-1} translates into $(1-x)$ — another expansion parameter that becomes small in the quasi-elastic kinematics when the invariant mass of the final state hadron system is much smaller than the hardness scale of the process: $W^2 \simeq Q^2(1-x)/x \ll Q^2$.

In the $x \to 1$ limit (large moments N) the diagonal anomalous dimensions ($q \to q$, $g \to g$) have a general structure

$$\gamma(x) = \frac{A\,x}{(1-x)_+} + B\delta(1-x) + C\ln(1-x) + D + \mathcal{O}\left((1-x)\log^p(1-x)\right), \qquad (18)$$

where A, B, C, D, are series in α known nowadays to three loops. In particular,

$$C_F{}^{-1} \cdot \frac{A_q}{4\pi} = C_A{}^{-1} \cdot \frac{A_g}{4\pi} \equiv \alpha_{\rm phys}$$

is the *physical coupling* (cusp anomalous dimension [16]) which determines the radiation intensity of relatively soft gluons [17, 14]. It universally appears in higher order corrections to observables that are sensitive to soft gluon emission: anomalous dimensions and coefficient functions in the quasi-elastic limit, Sudakov quark and gluon form factors (threshold resummation, the Drell–Yan K-factor, distributions of jet event shapes in the near-to-two-jet kinematics, heavy quark fragmentation functions, etc.), in quark and gluon Regge trajectories, even in power suppressed effects in jet shapes and elsewhere.

Soft radiation has a *classical nature* and is governed by the celebrated Low (Low–Burnett–Kroll; LBK) theorem [18]. LBK taught us that both the singular, $(1-x)^{-1}$, and the constant terms, $(1-x)^0$, in the photon/gluon emission are universal and contained by the first (A) structure in (18), while the quantum contributions vanish in the $x \to 1$ limit as $(1-x)$. The terms C and D fall into the gap between the classical and quantum physics. In the leading order, $C = D = 0$; beyond the leading order, these structures must be therefore *deducible* rather than genuine higher order corrections. Indeed, the RREE answers the call: given the physical coupling $A(\alpha_s)$ and the virtual correction term $B(\alpha_s)$, one obtains the *all-order* relations $C = -\sigma A^2$ [2, 19] and $D = -\sigma A\,B + \mathcal{O}(\beta)$ [19, 20].

Another interesting thing that the RREE offers is a possibility to link together two puzzling perturbative results that were never thought to be of a common origin. These are: the absence of the α_s^2 and α_s^3 terms in the BFKL anomalous dimension in the DIS problem, and, on the other hand, the phenomenon of the *exact angular ordering* that was found to miraculously apply down to the next-to-next-to-leading order in e^+e^- parton cascades.

The deep universal nature of the RREE was elucidated by Basso and Korchemsky who have derived (15) from the *conformal invariance*. In the moment space, the GLR (4) translates into the internal symmetry of the large-N asymptotic series for the anomalous dimensions which relates the terms of even and odd power of $1/N$ ("parity preserving series"). From this perspective, the validity of the RRE was verified in [20] for various anomalous dimensions that had been calculated to higher orders in different quantum field theories.

A special place in this list is occupied by super-symmetric QFTs, and by the maximally super-symmetric $\mathcal{N}=4$ Yang–Mills model in particular.

3 Divide and conquer

The integrability feature manifests itself in certain sectors of QCD, in specific problems like[c]

- the high energy Regge behaviour in the large N_c ('t Hooft) limit [22],
- the spin $\frac{3}{2}$ baryon wave function [23],
- the scale dependence of the maximal helicity multi-gluon operators [24].

In each of these problems (and within the corresponding approximation) one can identify QCD with one or another of its SUSY partner QFTs. The higher the symmetry, the deeper the integrability. From this point of view the $\mathcal{N}=4$ SYM theory is at the top of the pyramid. It is conformally invariant at the quantum level ($\beta(\alpha_s)\equiv 0$) and is likely to be *fully integrable*, via the AdS/CFT correspondence [25].

In $\mathcal{N}=4$ SYM all twist-2 operators belong to one super-multiplet. As a result, all five anomalous dimensions (three for unpolarized distributions of gluons, gauginos and scalars, and two polarized ones) after diagonalization get expresses in terms of the unique function — the "universal anomalous dimension" $\gamma_{\rm uni}(N)$ with shifted arguments. Inspired by the structure of the answer in the first two loops, Kotikov, Lipatov, Onishchenko and Velizhanin (KLOV) have suggested that $\gamma_{\rm uni}^{(n)}$ at n loops is built of Euler–Zagier harmonic sums of transcedentality $\tau=2n-1$. This "maximum transcendentality principle" allowed them to predict $\gamma_{\rm uni}^{(3)}$ by simply picking up from the multi-page three-loop non-singlet QCD anomalous dimension [2] the *most complicated* terms (the maximal transcendentality ones, $\tau=5$) [26].

A half-page long KLOV three-loop anomalous dimension turned out to be generated by a reciprocity respecting evolution kernel that fits on one line [27]. Applied to the *four-loop* anomalous dimension of twist three single trace operators built of three scalar fields that has been recently calculated by solving numerically the Bethe Ansatz equations in [28, 29], the RREE has demonstrated an even more impressive power of "compactification" [30].

The innovative bookkeeping, when properly developed, may perform a fantastic quest of generating $\gamma_{\rm uni}$ of $\mathcal{N}=4$ SYM in *all orders* of the perturbative expansion. Now that we learned that in this theory the physical coupling A can be calculated in all orders [31], such a dream does not look too crazy.

Listening attentively, you may catch the leitmotiv of the $\mathcal{N}=4$ SYM song: its dynamics is devoid of quantum effects and looks essentially classical. The features that speak (or rather sing in unison) to this effect are: the integrability, the all-order Parke–Taylor amplitudes, the zero β-function and, last but not least, the fact that the basic parton Hamiltonian (one-loop $\gamma_{\rm uni}$) contains but *soft classical gluons*, in the LBK meaning of the term.

Recall the structure of the elementary QCD gluon emission probabilities:

$$
\begin{aligned}
P_{q\to q(x)+g} &= \frac{C_F\alpha_s}{\pi}\left[\frac{x}{1-x}+(1-x)\cdot\frac{1}{2}\right],\\
P_{g\to g(x)+g} &= \frac{C_A\alpha_s}{\pi}\left[\frac{x}{1-x}+(1-x)\cdot\left(x+x^{-1}\right)\right].
\end{aligned}
$$

The first term on the r.h.s. is the universal piece due to LBK "classical gluons"; the second terms depend on the nature of the radiator and are due to "quantum gluons" (*clagons* and *quagons*, if you please).

[c] for a review see [21]

Clagons (classical field) and guagons (quantum degrees of freedom) have different nature and play complementary rôles in the QCD play. Radiation of the first is infrared singular, $d\omega/\omega$, and its intensity determines the physical coupling; the second are infrared irrelevant, $\omega d\omega$, but it is them who make the coupling run. Clagons are responsible for the double logarithmic radiative effects (quark and gluon form factors, reggeization); small transverse momentum clagons form the "Lund string" (*gluers*). Quagons are responsible for changing the state of the radiating object (P and C parity, colour) while clagons *do not carry* quantum numbers (sic!). Importantly, it is clagons that determine the major part of the QCD anomalous dimensions.[d]

QCD shares the gluon sector with its SUSY companions, and the $\mathcal{N}=4$ SYM universal anomalous dimension contains but clagons — the contributions of scalars, gauginos and "hard gluons" (quagons) cancel in the anomalous dimension (as they did in the β-function):

$$P(x) \;=\; \frac{C_A\alpha_s}{\pi}\frac{x}{1-x}, \qquad \gamma_{\rm uni}(N) = \int_0^1 \frac{dx}{x}\big[x^N-1\big]P(x) = \psi(N{+}1)+\gamma_E \equiv S_1(N).$$

S_1 is the basic Euler harmonic function — the Mellin image of the classical LBK radiation.

The mystery of the KLOV maximum transcedentality principle may be explained by the fact that the classicality of the $\mathcal{N}=4$ SYM dynamics pertains in higher loops: the generalized Euler–Zagier harmonic sums describe re-interaction of classical gluons higher order, while the truly quantum effects never enter the stage.

4 Conclusions

The notion of the *reciprocity respecting* evolution equation (RREE) emerged in an attempt to combine anomalous dimensions of space-like parton distributions and time-like parton fragmentation functions in a single framework. It showed that the complexity of higher loop contributions is, to a large extent, *inherited* from lower orders. This is especially so for the major part of the QCD anomalous dimensions governed by the "classical" gluon radiation, in the sense of the Low–Burnett–Kroll theorem. I believe there should exist a framework in which the effects of classical gluon fields would be fully generated, in all orders, from the *first loop*, in the spirit of the LBK wisdom. A joy of accomplishing such an ambitious programme would rightfully match that of the creator of the harmonic functions:

> "However sublime are the researches on fluids which we owe to Messrs Bernoulli, Clairaut and d'Alembert, they flow so naturally from my two general formulae that one cannot sufficiently admire this accord of their profound meditations with the simplicity of the principles from which I have drawn my two equations."
>
> Leonard Euler

[d] In a specific example of heavy quark fragmentation functions the innovative bookkeeping was shown to reduce genuine second loop (quantum) corrections to miserable 2% [14].

References

[1] Slides:
http://indico.cern.ch/contributionDisplay.py?contribId=1&sessionId=2&confId=9499

[2] S. Moch, J.A.M. Vermaseren and A. Vogt, Nucl. Phys. **B688** 101 (2004);

[3] A. Vogt, S. Moch and J.A.M. Vermaseren, Nucl. Phys. **B691** 129 (2004).

[4] S.D. Drell, D.J. Levy and T.M. Yan, Phys. Rev. **187** 2159 (1969); *ibid.* **D1**, 1617 (1970).

[5] V.N. Gribov and L.N. Lipatov, Sov. J. Nucl. Phys. **15**, 438 (1972); *ibid* p. 675;
L.N. Lipatov, Sov. J. Nucl. Phys. **20** 94 (1975).

[6] G. Altarelli and G. Parisi, Nucl. Phys. **B126** 298 (1977).

[7] Yu.L. Dokshitzer, Sov. Phys. JETP **46** 641 (1977).

[8] J. Blümlein, V. Ravindran and W.L. van Neerven, Nucl.Phys. **B586** 349 (2000).

[9] A.P. Bukhvostov, L.N. Lipatov and N.P. Popov, Sov. J. Nucl. Phys. **20** 287 (1975).

[10] M. Stratmann and W. Vogelsang, Nucl.Phys. **B496** 41 (1997).

[11] G. Curci, W. Furmanski and R. Petronzio, Nucl. Phys. **B175** 27 (1980);
W. Furmanski and R. Petronzio, Phys. Lett. **97B** 437 (1980).

[12] M. Ciafaloni, Phys. Lett. **B150** 379 (1985);
S. Catani, M. Ciafaloni and G. Marchesini, Nucl. Phys. **B264** 588 (1986).

[13] Yu.L. Dokshitzer, talk at the HERA Workshop, Hamburg, 1993, unpublished.

[14] Yu.L. Dokshitzer, V.A. Khoze and S.I. Troian, Phys. Rev. **D53** 89 (1996).

[15] A. Mitov, S. Moch and A. Vogt, Phys. Lett. **B638** 61 (2006).

[16] G.P. Korchemsky, Mod. Phys. Lett. **A4** 1257 (1989);
G.P. Korchemsky and G. Marchesini, Nucl. Phys. **B406** 225 (1993).

[17] S. Catani, G. Marchesini and B.R. Webber, Nucl. Phys. **B349** 635 (1991).

[18] F.E. Low, Phys.Rev. **110** 974 (1958) ;
T.H. Burnett and N.M. Kroll, Phys. Rev. Lett. **20** 86 (1968).

[19] Yu.L. Dokshitzer, G. Marchesini and G.P. Salam, Phys. Lett. **B634** 504 (2006).

[20] B. Basso and G.P. Korchemsky, Nucl. Phys. **B775** 1 (2007).

[21] A.V. Belitsky, V.M. Braun, A.S. Gorsky and G.P. Korchemsky, Int. J. Mod. Phys. A **19**, 4715 (2004).

[22] L.N. Lipatov, Phys. Lett. **B309** 394 (1993); JETP Lett. **59** 596 (1994);
L.D. Faddeev and G.P. Korchemsky, Phys. Lett. **B342** 311 (1995).

[23] V.M. Braun, S.E. Derkachov, G.P. Korchemsky and A.N. Manashov, Nucl. Phys. B **553**, 355 (1999) ;
A.V. Belitsky, Phys. Lett. **B453** 59 (1999); Nucl. Phys. **B558** 259 (1999).

[24] L.N. Lipatov, Evolution equations in QCD, in Perspectives in Hadronic Physics, eds. S. Boffi, C. Ciofi Degli Atti, M. Giannini, World Scientific (Singapore, 1998) p. 413;
J.A. Minahan and K. Zarembo, J. High Ener. Phys. **0303** 013 (2003); N. Beisert and M. Staudacher, Nucl. Phys. **B670** 439 (2003).

[25] J.M. Maldacena, Adv. Theor. Math. Phys. **2** 231 (1998);
S.S. Gubser, I.R. Klebanov and A.M. Polyakov, Phys. Lett. **B428** 105 (1998);
E. Witten, Adv. Theor. Math. Phys. **2** 253 (1998).

[26] A.V. Kotikov, L.N. Lipatov, A.I. Onishchenko and V.N. Velizhanin, Phys. Lett. **B595** 521 (2004); Erratum *ibid.* **B632** 754 (2006)].

[27] Yu.L. Dokshitzer and G. Marchesini, Phys.Lett. **B646** 189 (2007) .

[28] M. Beccaria, *Anomalous dimensions at twist 3 of the sl*(2) *sector of* $N=4$ *SYM*, hep-th/0704.3570.

[29] A.V. Kotikov, L.N. Lipatov, A. Rej, M. Staudacher and V.N. Velizhanin, *Dressing and Wrapping*, hep-th/0704.3586.

[30] M. Beccaria, Yu.L. Dokshitzer and G. Marchesini, *Twist 3 of the sl*(2) *sector of* $N = 4$ *SYM and reciprocity respecting evolution*, hep-th/0705.2639.

[31] N. Beisert, B. Eden and M. Staudacher, J. Stat. Mech. **0701** 021 (2007).

Recent Results from H1 Experiment at HERA

Cristinel Diaconu *

Centre de Physique des Particules de Marseille
163, Avenue de Luminy, case 902, 13288 Marseille, France

Recent results obtained by the H1 experiment at HERA are presented: searches for new physics using the full luminosity accumulated at high energy, measurements of the proton structure at low and high Q^2 and studies of hadronic final states.

1 Introduction

HERA is a unique electron– or positron–proton collider with a centre–of–mass energy of up to 320 GeV. The data taking extended over 15 years since 1992 and yielded an integrated luminosity of close to 0.5 fb^{-1} for physics analyses. In March 2007 HERA completed data taking at high energy and started collisions at lower centre-of-mass energies of 225 GeV and 275 GeV in order to allow a direct measurement of the longitudinal structure function of the proton. The main physics avenues of the HERA program are illustrated in this paper with recent results obtained by the H1 collaboration in the following areas: searches for new physics proton structure measurements and studies of hadronic final states [1].

2 Searches at the Energy Frontier

2.1 Measurement of events with isolated leptons at HERA

The H1 data sample accumulated at high energy and corresponding to 0.5 fb^{-1} enables the search for rare phenomena, with cross sections around or below 1 pb. One such process is the production of W bosons, for which the total production cross section is around 1.3 pb^{-1}, calculated including NLO-QCD corrections [2]. If the W boson decays leptonically, the corresponding events contain an energetic, isolated lepton and significant missing energy due to the escaping neutrino.

Such events have been observed at HERA by the H1 collaboration [3]. Moreover, an excess of events with large hadronic transverse momentum P_T^X was reported after the first data taking period HERA I (1994–2000, 118 pb^{-1}), where 11 events are observed with $P_T^X > 25$ GeV for a Standard Model (SM) expectation of 3.5 ± 0.6. The ZEUS collaboration also performed a search for this event topology, within an analysis aimed at a search for anomalous top production [4], but did not confirm the excess observed by H1. Here the results from the H1 analysis performed including all available data is presented [5]. A comparison with the most recent ZEUS analysis is also made [6].

Events with a lepton (electron or muon) transverse momentum above 10 GeV in the angular range $5^\circ < \theta_e < 140^\circ$ and with missing transverse momentum $P_T^{miss} > 12$ GeV are selected. Extra background suppression criteria are also applied. A good agreement is observed with the SM predictions in the full phase space of the analysis. The H1 analysis measures 59 events for a SM expectation of 58 ± 8.2. The signal purity (dominated by the W production) is 60–68% in the electron channel and 76–83% in the muon channel. This result therefore provides clear evidence of single W boson production at HERA.

*Support from DESY is kindly acknowledged.

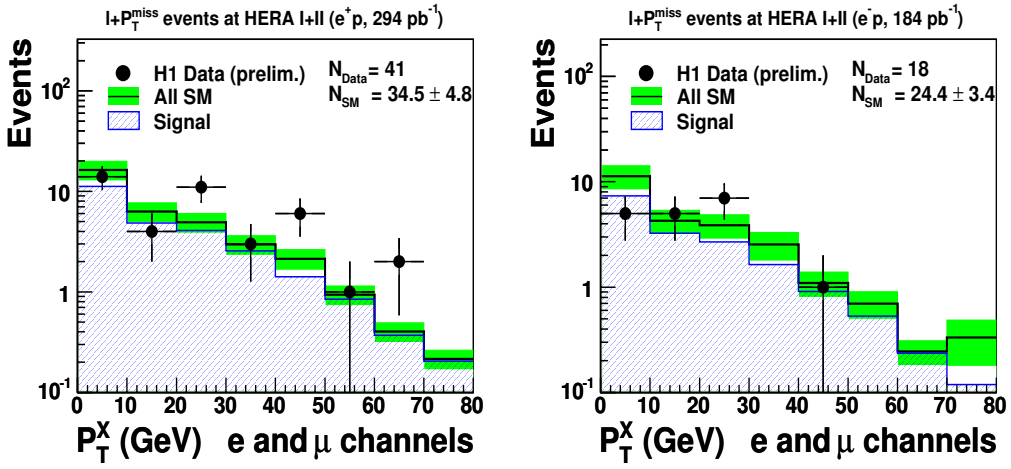

Figure 1: The distributions of the observed events as a function of P_T^X in the H1 analysis in e^+p data (left) and e^-p data (right).

e$^\pm$p **Data Preliminary** $P_T^X > 25$ **GeV**			Electron obs./exp.	Muon obs./exp.	Combined obs./exp.
$\boldsymbol{e^+p}$	H1	294 pb^{-1}	11 / 4.7 ± 0.9	10 / 4.2 ± 0.7	21 / 8.9 ± 1.5
	ZEUS	228 pb^{-1}	1 / 3.2 ± 0.4	3 / 3.1 ± 0.5	4 / 6.3 ± 0.9
$\boldsymbol{e^-p}$	H1	184 pb^{-1}	3 / 3.8 ± 0.6	0 / 3.1 ± 0.5	3 / 6.9 ± 1.1
	ZEUS	204 pb^{-1}	5 / 3.8 ± 0.6	2 / 2.2 ± 0.3	5 / 6.0 ± 0.9

Table 1: The observed and expected numbers of events in the region $P_T^X > 25$ GeV in H1 and ZEUS analyses.

The distribution of events in the H1 analysis as a function of P_T^X is shown separately in e^+p and e^-p data samples in figure 1. This result indicates that the excess of events at large P_T^X originates from the e^+p data sample. The observations of H1 and ZEUS analyses at $P_T^X > 25$ GeV are shown in table 1. The excess observed by H1 in e^+p data has a significance of about 3.0 σ but is not confirmed by the ZEUS analysis. In the e^-p data sample, a good agreement with the SM is observed by both H1 and ZEUS. The different observations of H1 and ZEUS at large P_T^X have been investigated and differences in the acceptance understood [7]. An analysis in a common phase space of H1 and ZEUS would allow the direct comparison and the combination of the data in order to exploit these events for further SM measurements of W production and investigations of new physics models.

2.2 Multi-lepton events at HERA

Within the Standard Model (SM) the production of multilepton events in ep collisions is possible mainly through photon-photon interactions, where quasi-real photons radiated from the incident electron and proton interact for producing a pair of leptons $\gamma\gamma \to \ell^+\ell^-$. The

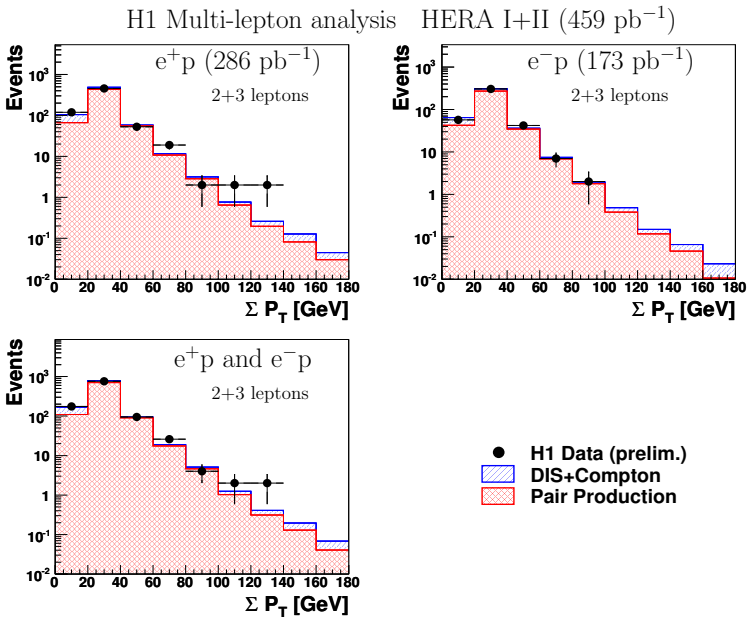

Figure 2: Distributions of the sum of the transverse momenta of the leptons in the H1 multi-lepton analysis.

H1 collaboration uses the full data sample at high energy to seach for events with several leptons (electrons or muons) [8]. Events with at least two leptons in the central region of the detector $20^\circ < \theta_\ell^{1,2} < 140^\circ$ and with high transverse momenta $P_T^{1(2)} > 10(5)$ GeV are selected. All other leptons in the full detector acceptance are identified and the events are classified according to the lepton content. Data events are observed in the configuration ee, eee, $e\mu$, $\mu\mu$ and $e\mu\mu$ in agreement with the predictions from the SM. In order to compare the di-lepton and the tri-lepton events, the scalar sum of the transverse momenta of the leptons in the event $\sum P_T$ is used. The distributions of $\sum P_T$ obtained after combining all channels are shown in figure 2 for e^+p, e^-p and full data samples. Four events are observed with a scalar sum of lepton transverse momenta greater than 100 GeV, compared to a SM expectation of 1.9 ± 0.4. The four events with $\sum P_T > 100$ GeV are observed in e^+p collisions only, where the SM expectation is of 1.2 ± 0.2.

2.3 Searches for leptoquarks at HERA

HERA is an ideal machine for producing new bosons coupling to lepton and quarks. In a minimal model incorporating the SM internal and chiral symetries [9], 14 species of leptoquarks are predicted. In addition to charge, isospin and chirality, these new bosons are characterised by the fermion number F which is an additive quantum number that reflects the particle (+1) and antiparticle (-1) coupling content. The LQs produced in e^-p collisions have predominantly $F = 2$, whereas $F = 0$ leptoquarks are mainly produced in e^+p collisions. The significant increase in luminosity at HERA II, especially in e^-p collisions, opened a new discovery window. The leptoquarks decays are seached for in the electron-jet

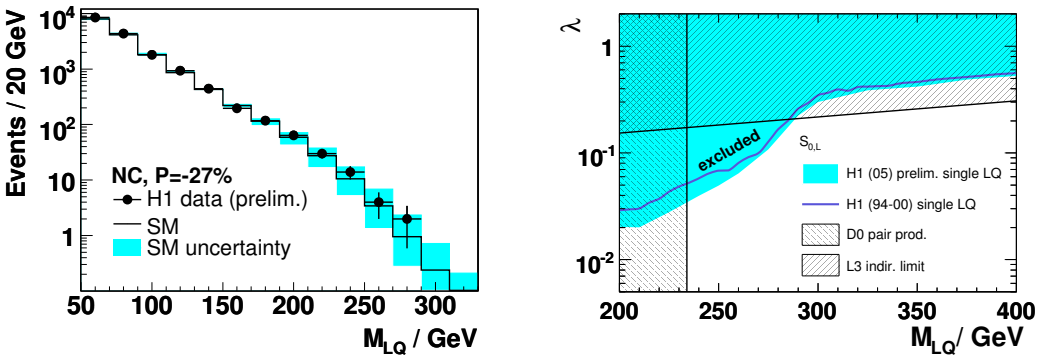

Figure 3: Exclusion domains in the plane of the leptoquark mass and its coupling to fermions λ. Limits from the present H1 analysis, based on e^-p data (92 pb^{-1}), are compared with limits from LEP and Tevatron.

and neutrino-jet final states, corresponding to irreducible backgrounds from neutral and charged current DIS scattering [10]. Due to the chiral nature of LQ's, the e-beam polarisation enhances the sensitivity to certain species. An example of invariant mass spectrum obtained in electron-jet channel for negative e-beam polarisation is shown in figure 3 (left). No LQ signal is detected. Limits on the model parameter are deduced. An example of exclusion domain is shown in figure 3 (right), comparing also with limits obtained at LEP and Tevatron. The new results extend significantly the domains explored at HERA I. The increase in data in both e^+p and e^-p is expected to give rise to new opportunities to search for leptoquarks at HERA.

2.4 Searches for matter substructure

The fermion mass hierarchy is one of the greatest puzzles of the Standard Model (SM). It can naturally be explained if the SM fermions are composite, in which case excited states may exist and be produced at colliders. A minimal extension [11] of the SM that incorporates excited fermions introduces new parameters: the compositness scale Λ (which reflects the range of the new confinement force) and the couplings f and f' (corresponding to the weak SU(2) and electromagnetic U(1) sectors respectively).

Excited electrons and neutrinos can be produced in electron–proton collisions at HERA via the t–channel neutral current $e^\pm p \to e^* X$ or charged current $e^\pm p \to \nu^* X$ reactions.

For the excited neutrinos, the cross section is much larger in e^-p collisions than in e^+p collisions due to the helicity enhancement, specific to CC-like processes. The present search for ν^* uses a data sample corresponding to an integrated luminosity of 184 pb^{-1} data sample, a factor of 12 larger than the previously published analyses at HERA [12]. The full data sample at highest energy ($\sqrt{s}$ = 319 GeV, 435 pb^{-1}) is used for excited electron searches [13].

Excited neutrinos are searched for in the channels $\nu^* \to \nu\gamma, \nu Z, eW$ where the W and Z bosons are reconstructed in the leptonic and hadronic channels. The analysis covers 95% (85%) of the total branching ratio for $f = -f'$ ($f = +f'$). The excited electrons are searched

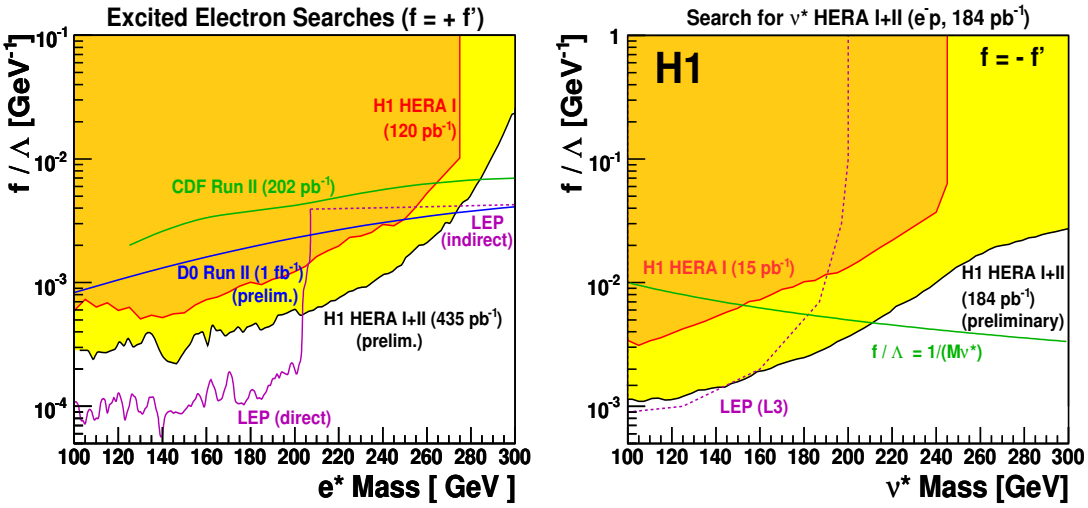

Figure 4: Exclusion domains for f/Λ as a function of the excited state mass obtained for excited electrons (left, $f = +f'$) and excited neutrinos (right, $f = -f'$)

in the channels $e^* \to e\gamma, eZ, \nu W$ where the W and Z bosons are reconstructed in the hadronic decay channel, for a 85% coverage of the e^* decay width, independent of its mass. The signal is searched for as a peak in the invariant mass distributions. No significant deviation from the SM prediction is found and limits on the production of excited leptons are deduced. These limits on the cross section are translated into exclusion domains in the plane (f/Λ, $M_{\nu*,e^*}$). The result obtained for e^* assuming $f = +f'$ is shown in figure 4(left). For this configuration and assuming $f/\Lambda = 1/M_{e*}$, excited electrons with masses below 273 GeV are excluded at 95% CL. The exclusion domain obtained for excited neutrinos for $f = -f'$ (maximal $\gamma\nu\nu*$ coupling) is shown in figure 4(right). Assuming $f/\Lambda = 1/M_{\nu*}$, excited neutrinos with masses below 188 GeV are excluded at 95% CL. The present results greatly extend previous searched domains at HERA and confirm the unique HERA sensitivity for excited electrons and neutrinos with masses beyond the reach of LEP.

3 Proton Structure Measurements with the Highest Precision

3.1 Measurements at high Q^2 and electroweak fits

The increase in luminosity and the use of polarised electron or positron beams at HERA II creates new opportunities for proton structure measurements at high Q^2. The electroweak effects in the inclusive NC cross sections are measured for instance by comparing the e^+p and e^-p data. The difference is proportional to the parity violating structure function xF_3. A measurement of this structure function performed by combining H1 and ZEUS data is shown in figure 5.

The combined QCD–electroweak fit [14] has been performed using HERA II data [15], taking advantage of the electron or positron beam longitudinal polarisation. In this fit, the strategy is to leave free in the fit the EW parameters together with the parameterisation

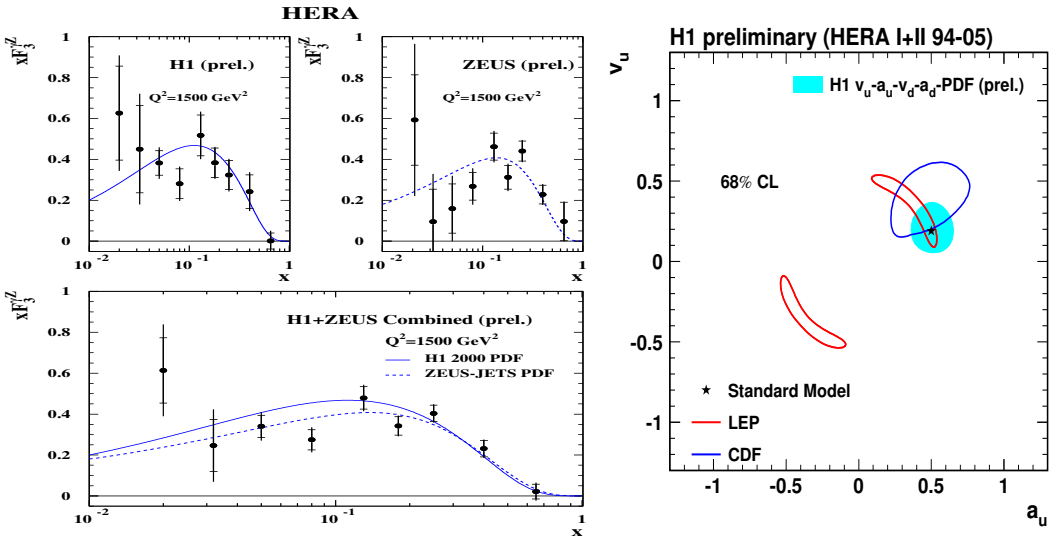

Figure 5: Left: Measurement of the parity violating structure function $xF3$. Right: Axial and vector couplings of the u–quark measured from the combined electroweak–QCD fit at HERA and compared with measurements from LEP and Tevatron.

of the parton distribution functions. Due to the t-channel electron-quark scattering via Z bosons, the DIS cross sections at high Q^2 are sensitive to light quark axial (a_q) and vector (v_q) coupling to the Z. This dependence includes linear terms with significant weight in the cross section which allow the determination of not only the value but also the sign of the couplings. In contrast, the measurements at the Z resonance (LEP1 and SLD) only access av or a^2+v^2 combinations. Therefore there is an ambiguity between axial and vector couplings and only the relative sign can be determined. In addition, since the flavour separation for light quarks cannot be achieved experimentally, flavour universality assumptions have to be made. The Tevatron measurement [16] of the Drell-Yan process allows to access the couplings at an energy beyond the Z mass resonance, where linear contributions are significant. The measurements of the u–quark couplings obtained at HERA, LEP and the Tevatron are shown in figure 5(right). The new H1 measurement has an improved precision compared to previous published values, corresponding for instance to a factor two for v_u. The data to be collected at the Tevatron and HERA as well as the use of polarised $e^{\pm}$ beams at HERA open interesting oportunities for the light quarks couplings measurements in the near future.

3.2 High precision studies at low Q^2

The measurements of deeply inelastic scattering at HERA reach very low values of photon virtuality and extend to domains where perturbative QCD cannot be applied. The transition region from photoproduction ($Q^2 \simeq 0$) to DIS is studied with high precisions using the low angle detectors and special runs with either high trigger rates to improve statistical and systematical errors or shifted collision vertex in order to access lower scattering angles and therefore smaller Q^2 values.

The H1 collaboration has recentlly released the final results of the measurement of DIS in the range $0.2 < Q^2 < 12$ GeV^2 and at very low x from $4 \cdot 10^{-6}$ to 0.02 [17]. A precision of 2% to 4% is achieved and various models of the transition from real to virtual photon–proton interactions are tested. The lowest x region is sensitive to the longitudinal structure function F_L since this region corresponds to the highest y domain, where the contribution of F_L term to the reduced cross section is favoured, according to $\sigma_r = F_2 - (y^2/Y^+)F_L$ where $Y^+ = 1 + (1-y)^2$. The longitudial structure function is a fundamental form factor of the proton, related to the scattering of longitudinally polarised photons of quarks, which can only take place if gluons are radiated during the interaction. As a consequence, F_L give access to the gluon content of the proton $F_L(x, Q^2) \sim \alpha_s x g(x, Q^2)$. The measurement of the high y region is therefore important for the precision measurement of the proton content.

3.3 Measurements at high y and direct determination of F_L

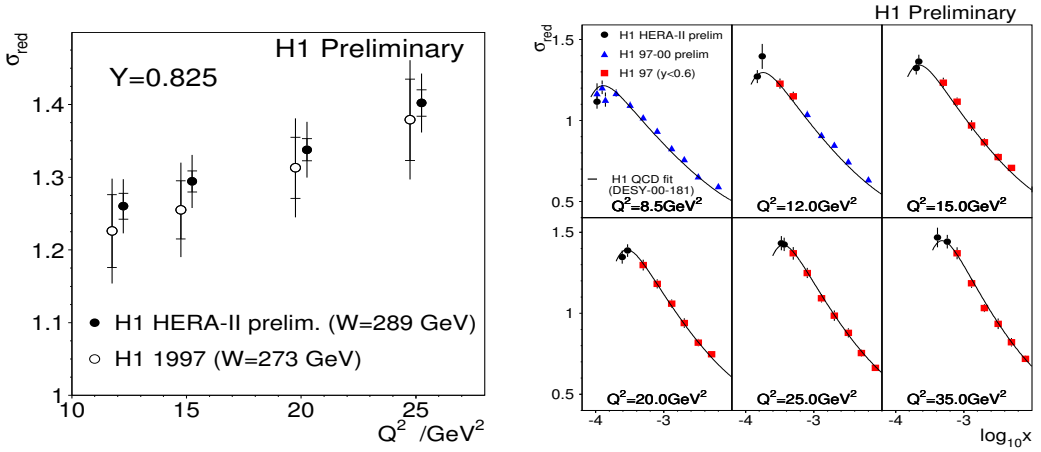

Figure 6: Reduced cross section measurements of DIS process at high y in the range $8 < Q^2 < 35$ GeV^2, for $y = 0.825$ (left) and as a function of x and Q^2 (right).

In the proton rest frame, the inelasticity can be expressed as a function of the energies of the incoming and scattered electrons: $y = (E_e^0 - E_e)/E_e^0$. The high y regime therefore corresponds to events where the final state electron has a low energy. The measurement of this kinematic region implies a special experimental approach since the trigger and the background rejection are difficult. In particular, the background from photoproduction induced by the misidentification of hadrons as electrons has to be subtracted. In a new analysis [18], H1 collaboration uses the electron candidate charge measurement, in order to subtract this background using data. The measurement of the reduced cross section as a function of Q^2 for $y = 0.825$ is shown in figure 6(left) and displays a significant improvement in precision compared with the previous publication. The new cross section measurement as a function of x and Q^2 is shown in figure 6(right). It dramatically improves the precision in the regions at low x where the F_L contribution is expected to be significant.

The F_L structure function can be directly measured if the reduced cross section $\sigma \sim F_2(x, Q^2) + f(y)\ F_L(x, Q^2)$ is measured for different y values at fixed x and Q^2. This can

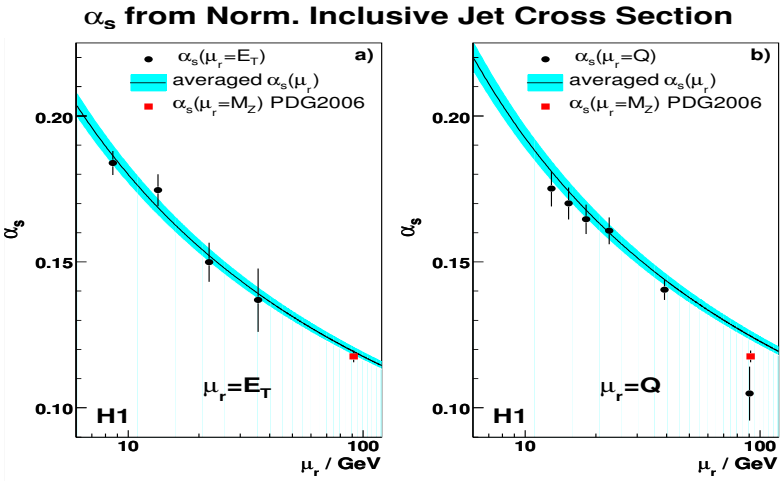

Figure 7: Results for the fitted values of a) $\alpha_s(\mu_r = E_T)$ averaged over all Q^2 regions, and b) $\alpha_s(\mu_r = Q)$ averaged over all E_T regions. The error bars denote the total experimental uncertainty for each data point. The solid curve shows the result of evolving $\alpha_s(M_Z)$ averaged from all Q^2 and E_T regions, with the band denoting the total experimental uncertainty. The world average from PDG is also shown.

be achieved if the beam energies are varied. The last three months of HERA running were dedicated to a run a lower centre-of-mass energy. This data will be used for the first direct measurement of F_L at low x and will provide a new constraint on the gluon density in the proton [19].

4 QCD Studies in a Clean High Energy Laboratory

4.1 Jet Production at high Q^2 and determination of α_S

The measurement of jet production allows to test QCD since it can be related to gluon radiation of to gluon-photon collisions. A new measurement of jet production using HERA I data has been recently published [20].

The inclusive jet cross section is measured in DIS with a $Q^2 > 100$ GeV^2. For NC DIS events in the range $0.2 < y < 0.7$ and in a given Q^2 bin, the normalised inclusive jet cross section is defined as the average number of jets within $-1.0 < \eta^{\rm Lab} < 2.5$ per event. The double differential cross section is measured in six bins of Q^2 and four bins of E_T. The normalised jet cross section is used to extract a precise measurement of the strong coupling. To study the scale dependence of α_s, the six data points with different Q^2 at a given E_T are used together, and four values of $\alpha_s(E_T)$ are extracted. The results are shown in figure 7a, where the running of the strong coupling is also clearly observed. Finally, all 24 measurements are used in a common fit of the strong coupling, which yields

$$\alpha_s(M_Z) = 0.1193 \ \pm 0.0014\,(\text{exp.}) \ ^{+0.0047}_{-0.0030}\,(\text{th.}) \ \pm 0.0016\,(\text{pdf}) \ , \qquad (1)$$

with a fit quality of $\chi^2/\text{ndf} = 28.7/23$. The dominating source of error is the renormalisation scale dependence which is used to estimate the effect of missing higher orders beyond NLO

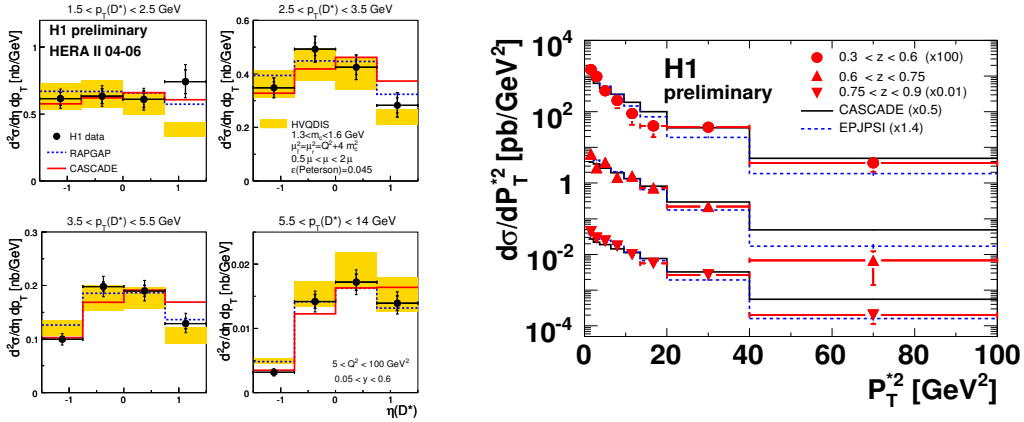

Figure 8: Left: the measured double differential cross section for D^* production as a function of pseudorapidity and transverse momentum. Right: the measurement of the double differential cross section for J/Ψ production as a function of the transverse momentum and the fraction of virtual photon momentum carried by the J/Ψ meson.

in the pQCD prediction. This result shows a level of experimental precision competitive with α_s determinations from other recent jet production measurements at HERA [21] and is in good agreement with the world average 0.1176 ± 0.0020 (PDG 2006) [22].

4.2 Charm production

The measurement of the production of charm particles is particularly important since the theoretical predictions are expected to be robust due to the large scale in the calculation provided by the charm quark mass. Using the HERA II data, the H1 collaboration performed two new measurements which significantly improve the precision in this area.

First, the D^* production cross section is measured using a data sample collected by H1 experiment in the years 2004 to 2006 and corresponding to an intergated luminosity of 226 pb^{-1}. The analysis covers the kinematic region $5 < Q^2 < 100$ GeV^2 and $0.05 < y < 0.6$. The visible range for the D* meson is restricted to $P_T(D^*) > 1.5$ GeV and $|\eta(D^*)| < 1.5$ where more than 10,000 D* mesons are reconstructed. The preliminary measurement of the double differential cross section is shown in figure 8(left). Precise measurements of single and double differential inclusive cross sections of D* meson production are compared to LO predictions and a NLO calculation in the 'massive scheme'.

Second, the electroproduction of J/Ψ mesons is measured with high precision using HERA II data accumulated in the period 2004-2006 and corresponding to 258 pb^{-1}. Charmonium production in DIS is modelled in non-relativistic QCD as a convolution between the short distance effects driven by the Q^2 and long distance matrix elements associated to the J/Ψ emergence. Single and double differential cross sections and angular distributions are measured and compared to predictions from Monte Carlo programs implementing the colour singlet model at leading order. The predictions have to be scaled by large factors and, even after this scaling, they do not describe all aspects of the data, as illustrated in figure 8(right). The increased experimental precision therefore challenges the theoretical

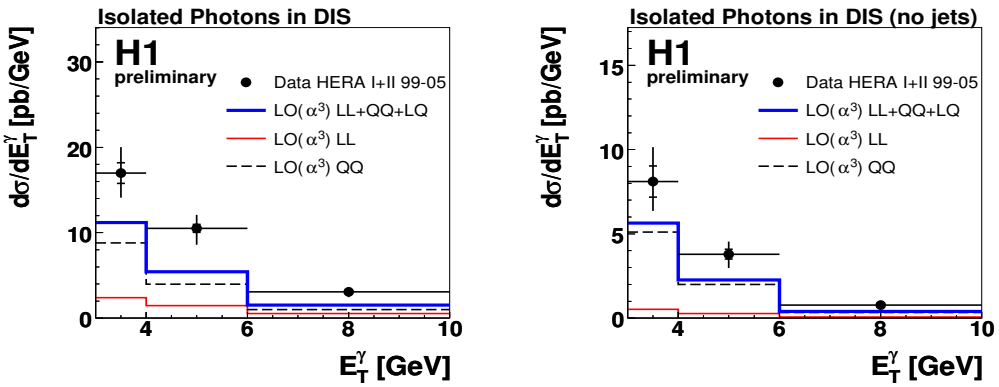

Figure 9: The cross section for isolated photons production in DIS as a function of photon transverse momentum for the inclusive analysis (left) and for events with no extra hadronic jet (right).

predictions in this area.

4.3 Isolated photon production

The production of isolated photons in hadronic collisions can bring important information about the hard scattering since the photons act as a clean probe, unaffected by the hadronisation uncertainties specific to hadrons emerging from the interaction. The production of isolated photons is studied in DIS with a four-momentum transfer squared of $4 < Q^2 < 150$ GeV^2 and a squared mass of the hadronic system $W_X^2 > 2500$ GeV^2 using a total integrated luminosity of 226 ps^{-1} including HERA II data [23]. Photons are identified in the transverse momentum range $3 < E_T^\gamma < 10$ GeV and in the pseudorapidity range $-1.2 < \eta_\gamma < 1.8$ using a multivariate analysis based on the cluster shower shapes in the calorimeter. Measured cross sections are compared with predictions from a LO calculation and MC models including the contribution of radiation from quarks (QQ) and from electrons (LL). The result is shown as a function of the photon transverse momentum in figure 9(left). The QQ contribution is enhanced when no jet is allowed in the events, as seen in figure 9(right). The LO predictions underestimate the measurements by up to a factor of two, in particular at low Q^2. The understanding of this difference may greatly profit from the NLO calculation, which exists at present only for events with an additional jet [24].

4.4 Deeply virtual Compton scattering

Information beyond the longitudinal momentum distributions, including transverse momentum distribtutions and correlations between partons inside the proton can be obtained via processes where the proton remains intact after the interaction though the transverse momentum of the transfer is non–zero. Such a process is the diffractive scattering of a virtual photon $\gamma^* p \to \gamma p$, also called elastic Deeply Virtual Compton Scattering (DVCS). This process is accessed at HERA via the reaction $ep \to ep\gamma$, which also receives an important contribution from the Bethe-Heitler (BH) process, where the photon is radiated off the electron in the final state. The reaction is measured by the H1 collaboration using e^+p

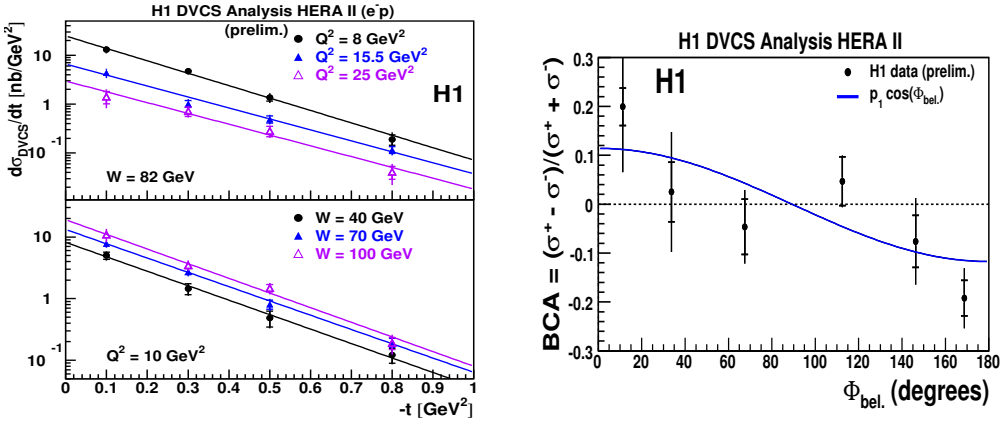

Figure 10: Left: the measurement of the DVCS cross section as a function of t n various Q^2 and W bins. Right: the measured beam charge asymmetry as a function of the angle Φ between the production plane and the scattering plane.

(146 pb^{-1}) and e^-p data (146 pb^{-1}) [25]. Cross sections are measured as a function of the virtuality of the exchanged photon Q^2 and the centre-of-mass energy of the γ^*p system, W, in the kinematic domain $6.5 < Q^2 < 80$ GeV^2, $30 < W < 140$ GeV and $|t| < 1$ GeV, where t denotes the squared momentum transfer at the proton vertex. The cross sections are measured differentially in t for different Q^2 and W values, as shown in figure 10(left). Using an exponential t-dependence parameterisation $d\sigma/dt \sim \exp -bt$, a global exponential t-slope parameter is derived to be $5.45 \pm 0.19 \pm 0.34$. The b parameter is related to the mean impact parameter and can be related to a transverse size of the proton of 0.65 ± 0.02 fm at $x = 1.2 \cdot 10^{-2}$. This is lower than the estimated proton radius $R_p = 0.862(12)$ fm, as expected, since DVCS probes the core of the proton with no account of the peripheral soft structure. The cross sections are compared with NLO calculation based on generalised parton distributions and are found to be in good agreement. The dipole model is also investigated. The data is found to be in good agreement with the geometric scaling predicted by this model. Finally, the beam charge asymmetry (BCA) of the DVCS cross section is measured as a function of the angle Φ between the production plane and the scattering plane. The first measurement of this observable in colision mode is shown in figure 10(right). The BCA is proportional with the interference between the DVCS and BH cross sections and therefore directly accesses the generalised parton distribution functions. A dependence in $\cos\Phi$ is established $BCA = p_1 cos\Phi$ with $p_1 = 0.17 \pm 0.03(stat) \pm 0.05(sys)$ after the experimental deconvolution.

5 Outlook

The end of data taking opened a new, exciting era of final analyses at HERA[a]. The searches for new physics are now performed on the full available statistics corresponding to a luminosity of 0.5 fb^{-1}. The excess of events with isolated electrons or muons, missing transverse

[a]Many other new H1 results, not presented here, can be found as contributions to these proceedings.

momentum and a prominent hadronic jet measured by H1 persists over more than ten years and constitutes one of the remaining puzzles of the HERA program. The precise measurement of the proton structure continues and benefits from the significant increase in statistics. The measurements of DIS at low Q^2 are complemented by a new, dedicated analysis of the high y domain which will constrain the gluon density at low x. The measurements of hadronic final states allow an improved precision in α_s determination. Using the HERA II data, heavy quark measurements enter a precision domain and challenge further the theoretical calculations. The "final touch" of HERA is the run at low energy, which will allow the measurement of the longitudinal structure function and a new constraint on the gluon density at low x.

High precision measurements will be achieved at HERA in the following years using the full data sample and by combining H1 and ZEUS data sets. The physics contained in this data will be revealed in the next years and will constitute the legacy of HERA for the LHC and beyond.

References

[1] Slides: `http://indico.cern.ch/contributionDisplay.py?contribId=2&sessionId=2&confId=9499`

[2] K.-P. O. Diener, C. Schwanenberger, and M. Spira, Eur. Phys. J. C **25** (2002) 405, and references therein.

[3] V. Andreev *et al.* [H1 Collaboration], Phys. Lett. **B561** (2003) 241, [hep-ex/0301030].

[4] S. Chekanov *et al.* [ZEUS Collaboration], Phys. Lett. **B 559** (2003) 153, [hep-ex/0302010].

[5] H1 Collaboration, Conference Note available at `http://www-h1.desy.de/h1/www/publications/htmlsplit/H1prelim-07-063.long.html`

[6] Katherine Korcsak-Gorzo, these proceedings.

[7] Ytsen de Boer, these proceedings.

[8] Gerhard Brandt, these proceedings.

[9] W. Buchmüller, R. Rückl and D. Wyler, Phys. Lett. B **191** (1987) 442; Erratum-ibid. B **448** (1999) 320.

[10] Anna Dubak, these proceedings.

[11] K. Hagiwara, D. Zeppenfeld and S. Komamiya, Z. Phys. C **29** (1985) 115; U. Baur, M. Spira and P. M. Zerwas, Phys. Rev. D **42** (1990) 815; F. Boudjema, A. Djouadi and J. L. Kneur, Z. Phys. C **57** (1993) 425.

[12] C. Adloff *et al.* [H1 Collaboration], Phys. Lett. B **525** (2002) 9.

[13] Nguyet Trihn, these proceedings.

[14] A. Aktas *et al.* [H1 Collaboration], hep-ex/0507080.

[15] Li Gang, these proceedings

[16] D. Acosta *et al.* [CDF Collaboration], Phys. Rev. D **71**, 052002 (2005) [hep-ex/0411059].

[17] Andrea Vargas, these proceedings

[18] Natasa Raicevic, these proceedings

[19] Max Klein, these proceedings

[20] A. Aktas *et al.* [H1 Collaboration], arXiv:0706.3722 [hep-ex], to be published in Phys. Lett. B.

[21] S. Chekanov *et al.* [ZEUS Collaboration], Submitted to Phys. Lett. B [hep-ex/0701039].

[22] W. M. Yao *et al.* [Particle Data Group], J. Phys. G **33** (2006) 1.

[23] Katharina Müller, these proceedings.

[24] A. Gehrmann-De Ridder et al., Nucl. Phys. B **578** (2000) 326 [hep-ph/0003082].

[25] Laurent Schoffel, these proceedings.

Preview of ZEUS Results

Massimo Corradi *

INFN Bologna
Via Irnerio 46, I-40126 Bologna - Italy

Recent results from the ZEUS experiment are reviewed. They provide new constraints on parton densities, limits on new physics and precise tests of QCD.

1 Introduction

The HERA running at high energy ($\sqrt{s}$ = 300–318 GeV) ended on 20$^{\text{th}}$ March. At the time of this conference, HERA was running with reduced proton energy (E_e = 27.5 GeV, E_p = 460 GeV, $\sqrt{s}$ = 225 GeV) with the main purpose of providing a second energy point to measure the longitudinal structure function F_L (see Section 8). The full luminosity collected by ZEUS in high-energy runs and available for physics analysis is about 0.5 fb^{-1}. The breakdown according to the lepton–beam charge and to the lepton beam being unpolarised (HERA-I) or polarised (HERA-II) is given in Table 1.

Period	e^+p	e^-p
HERA-I	115 pb^{-1}	17 pb^{-1}
HERA-II (pol.)	182 pb^{-1}	190 pb^{-1}
Total	297 pb^{-1}	207 pb^{-1}

Table 1: Useful luminosity collected by ZEUS at $\sqrt{s}$ = 300–318GeV^2

Many new physics results have been released by the ZEUS collaboration since DIS2006. They consist of the final publications of HERA-I analyses and preliminary results from the large e^-p data sample collected in the 2005-2006 period, with some analysis of the full data sample including the last e^+p run from 2006-2007. A brief overview of some of the latest results is given here.

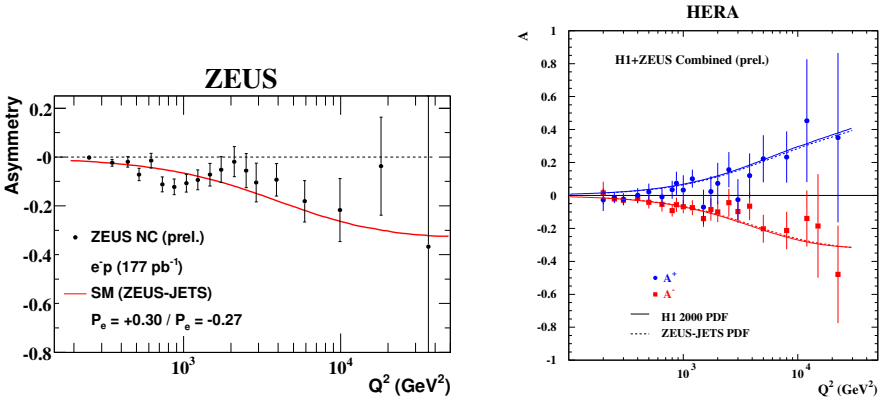

Figure 1: Polarisation asymmetry from ZEUS e^-p DIS (left) and from combined H1 and ZEUS e^+p (A^+) and e^-p (A^-) data (right).

*also Univ. Hamburg I, Von Humboldt Fellow.

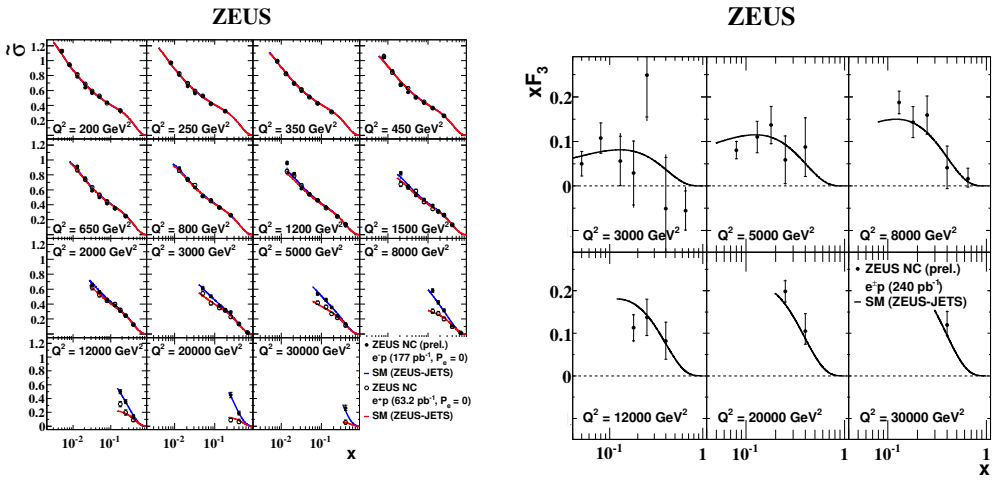

Figure 2: Reduced cross-section for unpolarised e^-p and e^+p DIS (left) and the structure function F_3 (right).

2 Neutral Current DIS at high Q^2

The polarised e^-p data sample, which consists of 72 pb^{-1} of collisions with right-handed polarised electrons (average polarisation $P_R = +0.30$) and 105 pb^{-1} with left-handed polarisation ($P_L = -0.27$), was used to investigate parity violation effects in neutral current (NC) DIS at large Q^2.

The Standard Model (SM) predicts a dependence of the NC DIS cross-section on the lepton beam polarisation, arising mainly from the γ–Z^0 interference term. The polarisation asymmetry, defined from the cross sections of the right– and left–handed samples $\sigma_{R,L}$ as

$$A = \frac{2}{P_R - P_L} \frac{\sigma_R - \sigma_L}{\sigma_R + \sigma_L}$$

is expected to be suppressed by the Z^0 propagator and proportional to the quark vector coupling to the Z^0, v_q. Figure 1(left) shows the polarisation asymmetry measured with the ZEUS e^-p data as a function of Q^2 compared the the SM prediction using the ZEUS-JETS parton density functions (PDFs) [2]. Good agreement is observed. To increase the statistical significance of this measurement, data from the H1 and ZEUS collaborations have been combined. The combined polarisation asymmetries for the e^+p data collected in 2003-2004 and part of e^-p data, for a total luminosity of 478 pb^{-1}, are shown in Fig. 1(right). The asymmetry for e^+p has opposite sign to that for e^-p, in agreement with the SM [3]. The presence of parity violation in high-Q^2 NC DIS is well established from these data.

The two samples with opposite polarisation have been combined to measure the NC cross section for unpolarised e^-p DIS. Figure 2 (left) shows the reduced cross section $\tilde{\sigma} = \frac{d\sigma}{dxdQ^2}\frac{xQ^4}{2\pi\alpha^2 Y_+}$, where $Y_\pm = 1 \pm (1-y^2)$, compared to e^+p data from HERA-I and to SM predictions. At large Q^2 the cross section for e^-p is larger than for e^+p, again due to the

effect of the γ–Z^0 interference, and is proportional to the structure function F_3:

$$\tilde{\sigma}(e^-p) - \tilde{\sigma}(e^+p) = 2\frac{Y^-}{Y+}xF_3 \sim 2\frac{Y^-}{Y+}\sum(q-\bar{q})2e_q a_q a_e \chi_Z,$$

where $\chi_Z = \frac{Q^2}{Q^2+M_Z^2}\frac{1}{\sin^2 2\theta_W}$, e_q is the quark electric charge, and a_q and a_e are the axial couplings to the Z^0 of quarks and electrons, respectively.

The measurement of xF_3 from the lepton-charge dependence provides a direct probe of the valence-quark distributions using a pure proton target. The measured structure function F_3 is presented in Fig. 2 (right). It is in good agreement with the SM prediction based on the ZEUS-JETS PDFs.

3 Search for new physics

NC DIS data at high Q^2 can be used to search for new physics that could contribute to the $eq \to eq$ amplitude when large scales are involved. In an analysis of 274 pb^{-1} of HERA-I and polarised HERA-II data, no significant deviation from the SM was found, providing competitive limits on contact interactions, large extra dimensions and quark substructure [4]. As an example, Fig. 3 shows the ratio of the number of events observed and expected by SM using the CTEQ5D PDFs, as a function of Q^2 for the whole sample. A finite quark size would show up to first order as a deviation of the SM cross section of the form

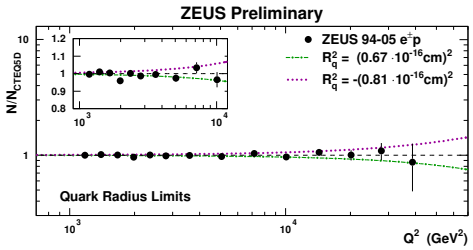

Figure 3: Quark radius

$$\frac{d\sigma}{dQ^2} = \left(\frac{d\sigma}{dQ^2}\right)_{\rm SM}\left(1-\frac{1}{6}R_q^2Q^2\right)^2,$$

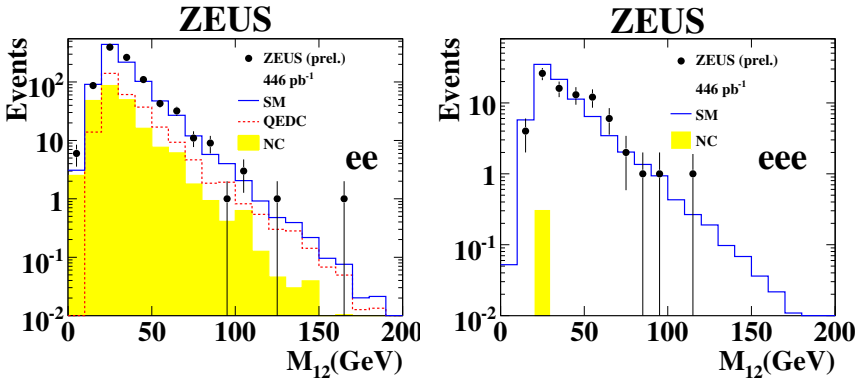

Figure 4: Multielectron mass distributions

where R_q^2 is the RMS radius of the electroweak charge distribution of the quark. The dot–dashed line corresponds to the upper limit $R_q < 0.67 \times 10^{-3}$fm.

New physics could also show up as events with uncommon topologies in the SM, such as multileptons or events with leptons and missing momentum. Figure 4 shows the mass distribution for events with two electrons with $p_T^e > 10,5$ GeV and for events with a third additional electron with energy $E_e > 10$ GeV (5 GeV if rear), updated to almost all the collected luminosity. The data agree with the SM expectation which is dominated by the $\gamma^{(*)}\gamma \to e^+e^-$ process, with some background in the two-electron sample at high mass from QED Compton events in which the photon was misidentified as an electron [5].

The search for events with an high-p_T isolated lepton and large missing momentum was extended to 432 pb^{-1} both in the electron and muon channel. The data are in agreement with the SM prediction which is dominated by W boson production [6]. The H1 collaboration has been reporting a possible excess of events with isolated lepton and missing momentum plus a hadronic system with transverse momentum $p_T^X > 25$ GeV in e^-p collisions. In the ZEUS case, 7 events ($5e + 2\mu$) of this kind have been found in e^-p data, in agreement with the SM expectation of 6 events. Similarly, the 4 events ($1e + 3\mu$) found in the e^+p sample agree with the 6 expected by the SM.

4 Jet physics

Jet production provides a precise means to test QCD and to probe the gluon density in the proton, $g(x, Q^2)$. In particular, the inclusive production of high-E_T jets in DIS, measured with the k_T algorithm in the Breit frame, can be calculated with small theoretical uncertainties in next-to-leading order (NLO) QCD. The analysis of inclusive jets in HERA-I data has been completed recently [7]. Figure 5(left) shows the dependence of the jet cross section on the radius parameter R of the k_T algorithm for $Q^2 > 125$ GeV^2. For $R = 1$, the data have an uncertainty of $\sim 5\%$ dominated by the calorimeter energy scale, while the theoretical uncertainty is about 10%. Both uncertainties decrease with Q^2, to $\sim 3.5\%$ and $\sim 5\%$, respectively, for $Q^2 > 500$ GeV^2. The NLO calculation can reproduce the data well for R between 0.5 and 1, provided that hadronisation correction, which become large at small R, are applied. Comparing the rate of jets with $E_T^{\text{Breit}} > 8$ GeV in events with $Q^2 > 500$ GeV^2 to NLO QCD predictions, one of the most precise measurement of the strong coupling constant α_S has been obtained:

$$\alpha_S(M_Z) = 0.1207 \pm 0.0014(\text{stat.}) \pm 0.0035(\text{syst.}) \pm 0.0023(\text{theo.}).$$

While the measurement of inclusive jets has the smallest experimental and theoretical uncertainties, the study of dijets provides a more direct probe of the gluon density since the two-jet kinematics allows the reconstruction of the parton momentum fraction ξ and to select regions dominated by the boson–gluon fusion process. The analysis of events with two jets with $E_T^{\text{Breit}} > 12,8$ GeV has been extended to part of the HERA-II data for a total of 209 pb^{-1} [8]. The agreement with NLO QCD, shown in Fig. 5(right), is very good. At large ξ and large Q^2, where the uncertainties are still dominated by statistics, the analysis of dijets can add a significant constraint to $g(x)$.

High-E_T jets in NC DIS appear to be well understood. It is anyway important to check that QCD predictions for high-E_T jets also hold in other processes. Charged current (CC) DIS provides an alternative sample in which jet production can be studied. Inclusive, two-

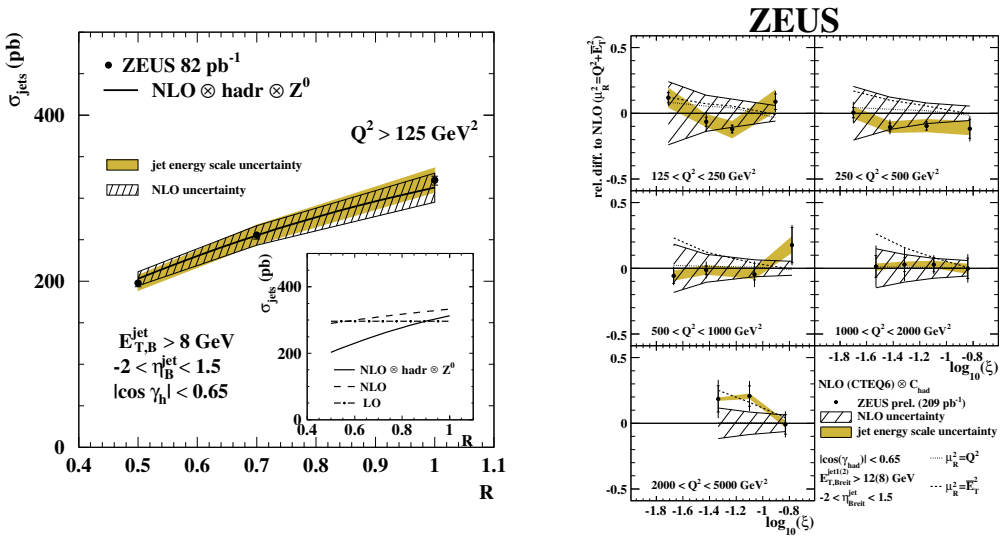

Figure 5: Left: inclusive jet cross section in the Breit frame in NC DIS for different values of the jet radius parameter R of the k_T algorithm. Right: data/theory ratio for dijets in DIS.

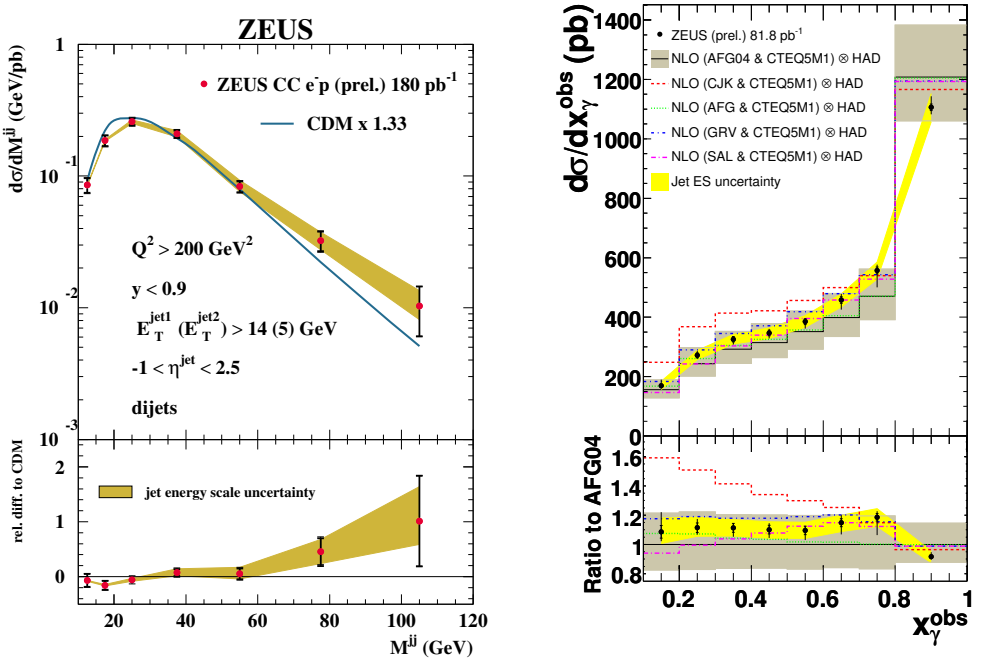

Figure 6: Left: two-jet mass distribution in CC DIS. Right: dijet cross-section in photoproduction as a function of $x_\gamma^{\rm obs}$

and three-jet cross sections have been studied for the first time in a large e^-p CC DIS sample of 209 pb^{-1}. The cross section for two jets in the laboratory frame is shown in Fig. 6(left) as a function of the dijet mass. The agreement with the ARIADNE Monte Carlo is satisfactory [9]. A better insight will be obtained when a comparison with NLO QCD will be available.

High-E_T dijets in photoproduction (i.e. $Q^2 < 1$ GeV^2) are another sensitive tool to constrain the gluon density in the proton at large x. Resolved-photon events, in which the photon behaves as a source of partons, provide also sensitivity to the gluon density inside the photon. Cross sections for events with two jets with $E_T > 20, 15$ GeV and with pseudorapidity $\eta < 3$ for the most forward and $-1 < \eta < 2.5$ for the most backward jet, have been measured and compared to different NLO QCD predictions based on different parton densities. Figure 6(right) shows the cross section as a function of $x_\gamma^{\rm obs}$, the fraction of photon momentum taken by the two–jet system in the proton rest frame, compared to NLO QCD predictions computed with different photon PDFs. At large $x_\gamma^{\rm obs}$, all the curves are in good agreement with the data. In the low $x_\gamma^{\rm obs}$ region, dominated by resolved-photon processes, the theoretical curves can differ by up to a factor two, reflecting the poor knowledge of $g(x)$ of the photon. The dijet data have sufficient precision to distinguish among different parametrisations [10].

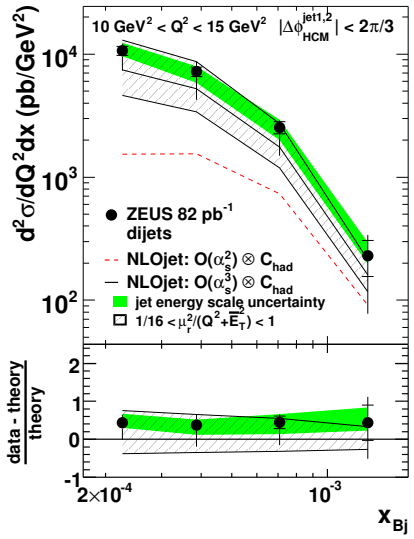

Figure 7: Cross section for unbalanced jets (azimuthal separation $\Delta\Phi < 2\pi/3$) in DIS, compared to $\mathcal{O}(\alpha_S^3)$ and $\mathcal{O}(\alpha_S^2)$ QCD calculations.

The jet analyses described so far aim at a comparison with precise QCD predictions and therfore focus on the high-E_T region where perturbative QCD is expected to be more reliable. It is also interesting to look at regions of the phase space where the standard QCD predictions based on NLO matrix elements and collinear factorisation are expected to break down. This is the case of the low-x regime, where large logarithms of $1/x$ could spoil standard DGLAP evolution and where saturation effects may show up. These effects could be too small to produce a significant deviation from DGLAP evolution in inclusive DIS data but could be revealed by particular jet observables. Effects beyond the standard collinear factorisation are expected to enhance the radiation of high-p_T gluons from the initial state, thus producing an excess of forward jets and/or an excess of multijet events at low x in which the two highest-E_T jets are not balanced in transverse momentum. These effects have been investigated in two recent ZEUS analyses: the measurement of forward jet production, extended up to $\eta = 4$ thanks to the forward plug calorimeter [11], and the measurement of two– and three–jet events at low x [12]. Figure 7 shows the cross section for two jets that are not back–to–back ($\Delta\Phi < 2\pi/3$) for $10 < Q^2 < 15$ GeV^2 as a function of x compared to QCD calculations at the order α_s^2 and α_s^3. The highest–order calculation is compatible with the data within a large theoretical uncertainty which reflects the loss of predictability of standard QCD in this region.

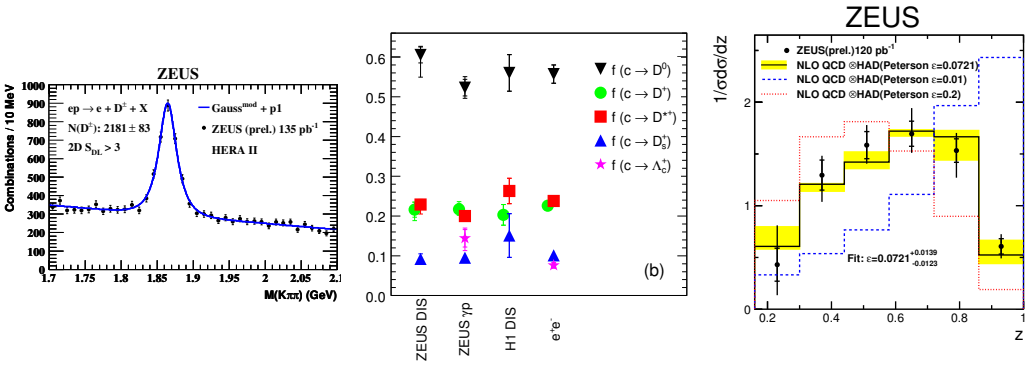

Figure 8: The HERA-II signal for D^+ in DIS (left). Charm fragmentation fractions (centre) and charm fragmentation function (right).

5 Heavy flavours

Heavy flavour production is an alternative probe of the gluon content of the proton and provides another precise tool to test QCD. New measurements of the production of charmed mesons in DIS are now available, including D^{*+}, D^+, D^0, D_s^+(+c.c.) from HERA-I data [13] and D^* [14] and D^+ [15] from HERA-II data. The signal-over-background ratio for the $D^+ \to K^-\pi^+\pi^+$ peak at HERA-II largely improved with respect to HERA-I, thanks to the secondary vertexing capability of the silicon microvertex detector. Fig. 8(left) shows the D^+ mass peak after the cut on the lifetime significance in the transverse plane $L_{xy}/\sigma > 3$. This improvement makes the D^+ channel competitive to the D^* "golden" channel $D^{*+} \to (D^0 \to K^-\pi^+)\pi_S^+$ for charm tagging.

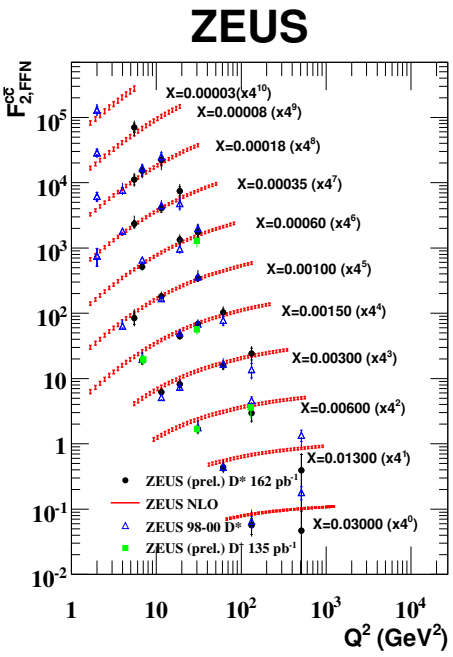

Figure 9: $F_2^{c\bar{c}}$ measured from D^{*+} and D^+, compared with NLO predictions based on the ZEUS PDFs.

To compare the D meson cross sections to the perturbative QCD predictions for charm quarks, some knowledge of the non-perturbative fragmentation of charm quarks into hadrons is needed. The fragmentation fractions of charm into different hadrons have been now directly measured in DIS, as shown in Fig. 8(center) where they are compared to the previous ZEUS measurement in photoproduction and to H1 and e^+e^- data. The ZEUS measurements have similar precision to the combined e^+e^- data and support

the process independence of charm fragmentation [13]. The charm fragmentation function $f(z)$ has been measured in events with a D^{*+} meson associated to a jet [16]. Figure 8(right) shows the measured $f(z)$ compared to NLO predictions implementing different values of the Peterson fragmentation parameter ϵ. Here z is defined as the fraction of the jet $E + P_{||}$ taken by the D^{*+} meson. A relatively large value of ϵ, $\epsilon = 0.072^{+0.014}_{-0.012}$, gives the best fit within fixed-order NLO theory.

Using the fragmentation parameters and with some extrapolation outside the detector acceptance, the D meson cross sections have been transformed into the charm contribution to the proton structure function, $F_2^{c\bar{c}}$. Figure 9 shows $F_2^{c\bar{c}}$ as a function of Q^2 for fixed values of x, as obtained from HERA-I and HERA-II D^{*+} and from HERA-II D^+ mesons. The HERA-II data improve the precision of the measurement at large x and Q^2. The data show clearly a strong scaling violation, in agreement with the QCD predictions based on the ZEUS-JETS PDF fit which includes DIS and jet data but not heavy flavour data, thus providing an independent check of the input PDFs.

In principle beauty production could be an even more precise testing ground for QCD since perturbative calculations should be more reliable thanks to the large b-quark mass. However, beauty tagging is experimentally more difficult, mainly because of its small cross section. Therfore different experimental techniques have been used. The latest ZEUS measurements exploited $D^{*+}\mu$ [17] or $\mu\mu$ [18] correlations to reduce the background and access the low-p_T^b region that dominates the total $b\bar{b}$ cross section and was not accessed by previous analyses based on jets.

Figure 10 shows the b-quark p_T spectrum as reconstructed from different measurements of beauty photoproduction at HERA. The data are in general in agreement with the NLO QCD theory. At low p_T the data tend to cluster somewhat above the theoretical uncertainty band. More precise data would be needed to decide whether it is a real deviation from the theory or a fluctuation.

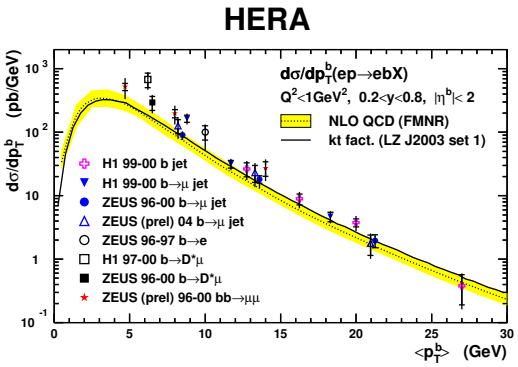

Figure 10: Compilation of ZEUS and H1 measurements of beauty photoproduction shown as a function of the b–quark transverse momentum.

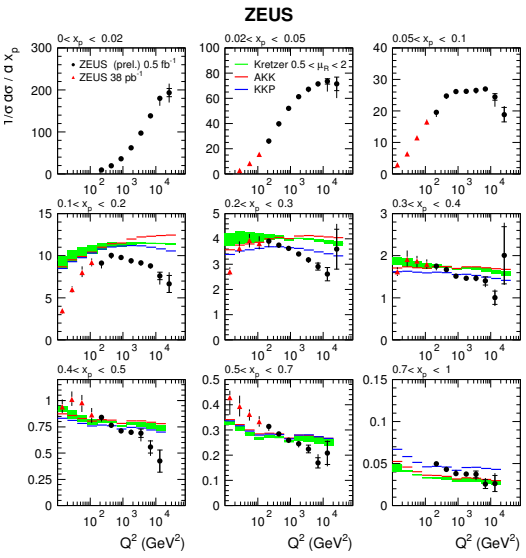

Figure 11: Scaling violation of charged particle fragmentation.

t

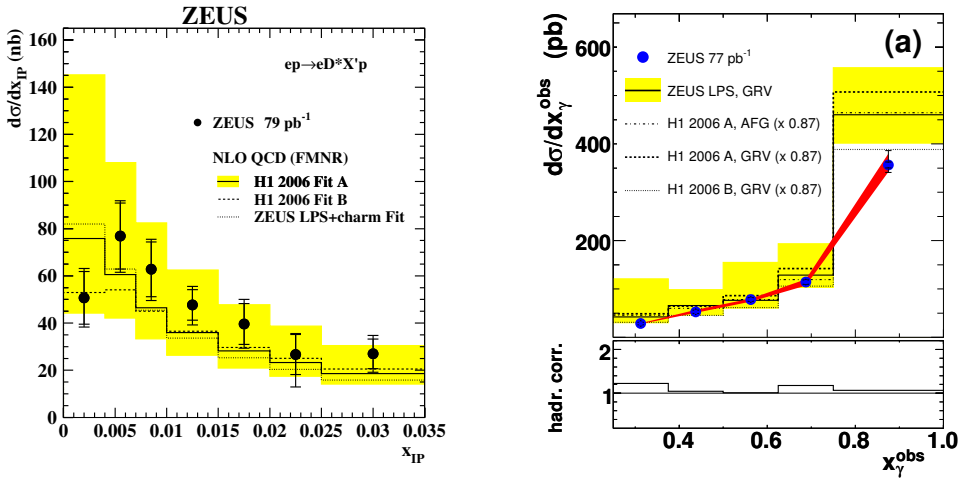

Figure 12: Diffractive D^{*+} (left) and dijet (right) cross sections in photoproduction, compared to NLO QCD predictions using diffractive PDFs

6 Particle production

The light-flavour fragmentation functions (FFs), defined as the probability that a final state parton p produces a hadron h with fractional momentum x_p, are the final-state analogue of the parton densities. Similarly to parton densities, they obey QCD evolution in Q^2. A measurement of inclusive charged particle fragmentation has been performed in NC DIS, using almost the full HERA data sample, which allowed to extend the previous measurements up to $Q^2 = 40000$ GeV^2 [19]. Experimentally x_p has been defined in the current hemisphere of the Breit frame as $x_p = 2p_h^{\rm Breit}/Q$, where $p_h^{\rm Breit}$ is the hadron momentum. Figure 11 shows the measured charged particles rate $\frac{1}{\sigma}\frac{d\sigma}{dx_p}$ in bins of x_p as a function of Q^2. At low x_p and low Q^2 (i.e. where $p_h \sim< 1$ GeV), particle production is suppressed by hadronisation effects. At large x_p, a negative logarithmic scaling violation is observed. NLO predictions, based on FFs measured at LEP, are also shown. They reproduce the behaviour of the data qualitatively but predict a milder Q^2 dependence.

For the new results on the production of heavy stable particle $(p, \bar{p}, d, \bar{d})$ and on Bose-Einstein correlations between identified kaons, the reader can refer to the recent publications [20, 21].

7 Diffraction

Three different characteristics of diffractive events have been used to select diffraction at ZEUS: the presence of a proton carrying a large fraction of the initial proton momentum, which can be tagged by the ZEUS Leading Proton Spectrometer (LPS method); the presence of a large rapidity gap between the hadronic system X observed in the central detector and the forward beam pipe where the proton escapes undetected (LRG method); the small mass of the observed hadronic system X (M_X method). The analysis is in progress and the three

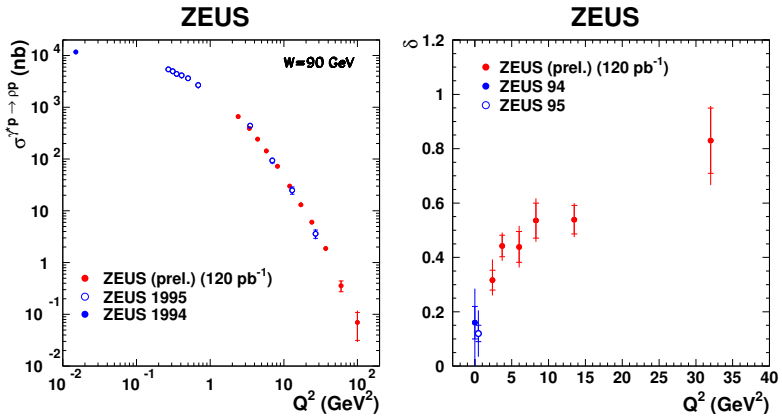

Figure 13: Q^2 dependence of the exclusive ρ cross section (left). The power $\delta(Q^2)$ from a fit of the form $\sigma(\gamma p \to \rho p) \propto W^{\delta(Q^2)}$ is shown on the right.

methods are in reasonable agreement, as reported elsewhere in these proceedings [22].

From the QCD factorisation theorem it is expected that diffractive parton density functions (dPDFs), extracted from diffractive DIS cross sections in analogy to the standard PDFs, can be used to compute diffractive cross sections for other (hard) processes. It is well known that this approach fails when applied to dijet production in $p\bar{p}$ collisions [23], where the diffractive cross section is about a factor 10 lower than what is obtained using dPDFs extracted from HERA data. This failure is generally explained as an effect of the rescattering of the proton remnants which destroys the rapidity gap. A similar suppression of diffractive events due to rescattering could be expected also in photoproduction, in particular in resolved-photon events in which the photon behaves similarly to a hadron. The measurement of diffractive photoproduction of D^* mesons and of dijets has been finalised recently. Figure 12(left) shows the cross section for diffractive D^* production as a function of the fractional energy loss of the proton, $x_{I\!P}$, compared to NLO QCD predictions based on dPDFs from diffractive DIS data [24]. The agreement is good, supporting the validity of QCD factorisation in diffraction. In the right panel, the dijet cross section for $x_{I\!P} < 0.025$ and for jets with $E_T > 7.5, 6.5$ GeV is shown as a function of $x_\gamma^{\rm obs}$ and compared to a preliminary NLO QCD calculation based on dPDFs. The theory agrees with the data and is not compatible with a large suppression in the low-$x_\gamma^{\rm obs}$ region dominated by resolved events. This suggests that indeed photons in high-E_T interactions are not behaving exactly like hadrons. Further investigations are ongoing to understand if these results are compatible with a similar analysis recently published by H1 [26].

The precise measurement of exclusive ρ^0 production has been extended to large Q^2, where perturbative QCD calculations are expected to be reliable. The cross section for $\gamma^* p \to \rho^0 p$ decreases steeply with Q^2, as shown in Fig. 13, and increases with the γp center-of-mass energy W as $W^{\delta(Q^2)}$. The power δ increases from values comparable to those found in "soft" hadron-hadron scattering, at $Q^2 \sim 0$, to values more typical of hard scattering at large Q^2, in qualitative agreement with QCD predictions [27].

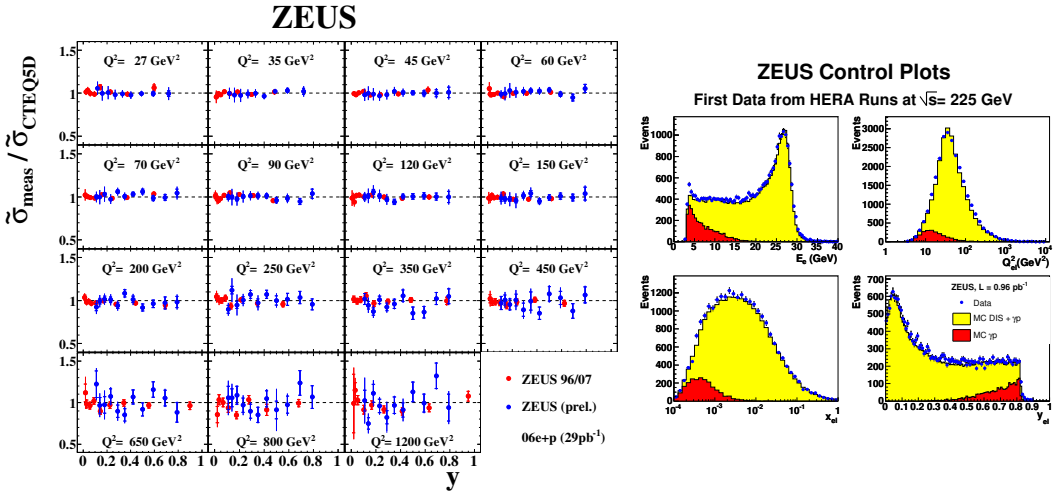

Figure 14: Left: ratio between the measured reduced DIS cross sections and the expectation from CTEQ5D PDFs. The blue points show the new high-y data, the red points are from the standard HERA-I analysis. Right: first data from low energy runs, compared to Monte Carlo

8 High y and F_L

The reduced cross-section at low Q^2 can be written as

$$\tilde{\sigma}(x,Q^2) = F_2(x,Q^2) - \frac{y^2}{Y^+}F_L(x,Q^2).$$

To disentangle F_L from F_2, it is therfore needed to vary the factor $\frac{y^2}{Y^+}$ keeping x and Q^2 fixed. This can be accomplished by varying the ep center of mass energy, since $y = Q^2/(xs)$, which is the main reason for the current runs with reduced proton energy. To maximise the sensitivity to F_L, the DIS measurement has to be extended to the highest possible y. High-y corresponds to low scattered-electron energy and therefore the largest accessible y is limited by the ability to reconstruct and identify low-energy electrons keeping the background under control.

A first extension of the ZEUS DIS kinematic coverage towards higher y has been attempted using 29 pb^{-1} of data taken in 2006 in high-energy runs with a special trigger for low-energy electrons, similar to that being used in the low-energy running. The results are presented as a ratio to the theory (CTEQ5D) and compared to previous ZEUS data in Fig. 14(left). The improvement at large y and low Q^2 is apparent [28].

The HERA running at reduced beam energy has been proceeding smoothly. At the time of this conference ZEUS collected about 3 pb^{-1}. The distribution of the electron energy, Q^2, x and y from these data are shown in Fig. 14(right) where they are compared to Monte Carlo distributions for DIS and for the photoproduction background. The good agreement shows the level of understanding of these low-energy data.

9 Postscript

At the time of writing (July 2007), HERA has been switched off and the dismantling of the ZEUS detector has already started. The low energy running has been more succesfull than expected, with 13 pb^{-1} collected at $\sqrt{s} = 225$ GeV and $7\mathrm{pb}^{-1}$ at an intermediate energy point at $\sqrt{s} = 252$ GeV. Obviously this is not the end of ZEUS, since the final and most precise physics results, based on the full luminosity and on the low-energy data, are still to come.

References

[1] Slides:
http://indico.cern.ch/contributionDisplay.py?contribId=3&sessionId=2&confId=9499

[2] S. Bhadra, these proceedings.

[3] H1 and ZEUS collaborations, contributed paper to the ICHEP06 conference,
http://www-h1.desy.de/h1/www/publications/htmlsplit/H1prelim-06-142.long.html.

[4] ZEUS collaboration, contributed paper to ICHEP06
http://www-zeus.desy.de/physics/phch/conf/ichep06/hiq2/8/ZEUS-prel-06-018.pdf.

[5] O. Ota, these proceedings.

[6] K. Korcsak-Gorzo, these proceedings.

[7] ZEUS Collaboration; S. Chekanov *et al.*, Phys. Lett. **B 649** 12 (2007);
ZEUS Collaboration; S. Chekanov *et al.*,Nucl. Phys. **B 765** 1 (2007).

[8] T. Schoerner-Sadenius, these proceedings.

[9] H. Wolfe, these proceedings.

[10] ZEUS Collaboration, S. Chekanov *et al.*, DESY-07-092, arXiv:0706.3809 [hep-ex], submitted to Phys. Rev. **D**.

[11] ZEUS Collaboration, S. Chekanov et al., DESY-07-100, submitted to Eur. Phys. J. **C**.

[12] ZEUS Collaboration, S. Chekanov et al., DESY-07-062, arXiv:0705.1931 [hep-ex], published online by Nuc. Phys. **B**.

[13] ZEUS Collaboration, S. Chekanov et al., DESY-07-052, arXiv:0704.3562 [hep-ex], accepted by JHEP.

[14] H. Stadie, these proceedings.

[15] D. Nicholass, these proceedings.

[16] S. Fang, these proceedings.

[17] ZEUS collaboration, S. Chekanov *et al.*, Eur. Phys. J. **C 50** 299 (2007).

[18] ZEUS collaboration, contributed paper to ICHEP06,
http://www-zeus.desy.de/physics/phch/conf/ichep06/hfl/6/ZEUS-prel-05-008-updated.ps

[19] B. Brzozowska, these proceedings.

[20] ZEUS Collaboration; S. Chekanov *et al.* DESY-07-070, arXiv:0705.3770 [hep-ex], published online in Nucl. Phys. **B**.

[21] ZEUS Collaboration; S. Chekanov *et al.*, DESY-07-069, arXiv:0706.2538 [hep-ex], published online in Phys. Lett.**B**.

[22] J. Lukasik, these proceedings;
B. Loehr, these proceedings.

[23] CDF Collaboration, T. Affolder *et al.*, Phys. Rev. Lett. 84, 5043 (2000).

[24] ZEUS Collaboration; S. Chekanov *et al.*, Eur.Phys.J. **C 51** 301 (2007).

[25] Y. Yamazaki, these proceedings.

[26] H1 Collaboration, A. Aktas *et al.*, DESY-07-018 , hep-ex/0703022, submitted to Eur. Phys. J.**C**.

[27] A. Levy, these proceedings.

[28] S. Shimizu, these proceedings.

Parton Distributions: Progress and Challenges

Andreas Vogt

Department of Mathematical Sciences, University of Liverpool
Liverpool L69 3BX, United Kingdom

We briefly discuss recent research on the spin-averaged parton densities of the proton, focusing on some aspects relevant to hard processes at the LHC. Specifically, after recalling the basic framework and the need for higher-order calculations, we address the evolution equations governing the scale dependence of the parton distributions and their solution, schemes for initial conditions and the inclusion of heavy quarks, recent progress on fits to data, and future high-precision constraints from LHC measurements.

1 Introduction: partons for the LHC

For at least the next ten years, proton–(anti-) proton colliders will continue to form the high-energy frontier in particle physics. At such machines, many quantitative studies of hard (high mass/scale) standard-model and new-physics processes require a precise understanding of the parton structure of the proton. The present talk [1] briefly discusses some recent developments in this field.

We start by recalling the description of hard proton processes using the simplest case, inclusive lepton-proton deep-inelastic scattering (DIS), the process providing the major part of the present constraints on the parton densities. Here the hard scale is the virtuality $Q^2 = -q^2$ of the exchanged gauge boson, a photon in Fig. 1, and the Bjorken variable $x = Q^2/(2Pq)$, with P the proton momentum, is usually chosen as the second independent variable. At zeroth order in the strong coupling constant α_s the hard coefficient functions $c_{a,i}$ are trivial, and the momentum fraction ξ carried by the struck quark i is equal to Bjorken-x if mass effects are neglected.

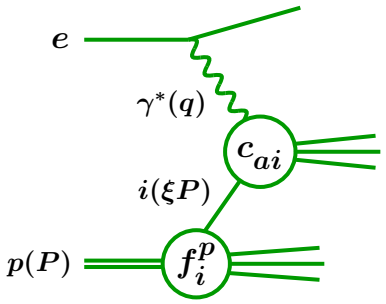

Figure 1: Kinematics of photon-exchange DIS in the QCD-improved parton model. Particle momenta are given in brackets.

In general, the structure functions $F^p_{2,L}$ for the process of Fig. 1 are given by

$$x^{-1} F^p_a(x,Q^2) \;=\; \sum_{i\,=\,q,g} \int_x^1 \frac{d\xi}{\xi}\, c_{a,i}\!\left(\frac{x}{\xi}, \alpha_s(\mu^2), \frac{\mu^2}{Q^2}\right) f^p_i(\xi,\mu^2) \tag{1}$$

plus terms of order $1/Q^2$ which, for the purpose of high-scale predictions, are best suppressed by sufficiently stringent cuts on the fitted experimental data. Besides on the factorization scheme used to define the parton densities f^p_i – in this talk $\overline{\rm MS}$ unless stated otherwise – the coefficient functions depend on the renormalization and factorization scale μ (identified here for notational simplicity) which ought to be chosen as $\mu^2 = \mathcal{O}(Q^2)$ in order to avoid large logarithms. The parton distributions depend on this scale via the evolution equations

$$\frac{d}{d\ln\mu^2}\, f_i(\xi,\mu^2) \;=\; \sum_k \left[P_{ik}(\alpha_s(\mu^2)) \otimes f_k(\mu^2)\right](\xi) \;. \tag{2}$$

Here $\otimes$ is a short-hand for the Mellin convolution written out in Eq. (1) above. The initial conditions for Eq. (2) are, of course, not calculable in perturbative QCD. As lattice results are restricted to very few Mellin moments (with, at present, still rather limited accuracy), predictions for collider cross sections are obtained via fits to suitable sets of reference observables, including structure functions in DIS, and the universality of the parton densities.

The splitting functions P and the process-dependent hard coefficient functions c_a admit expansions in powers of α_s,

$$\begin{aligned} P &= \alpha_s P^{(0)} + \alpha_s^2 P^{(1)} + \alpha_s^3 P^{(2)} + \dots \\ c_a &= \alpha_s^{n_a} \left[c_a^{(0)} + \alpha_s c_a^{(1)} + \alpha_s^2 c_a^{(2)} + \dots \right] \end{aligned} \tag{3}$$

with, for example, $n_a = 0$ for F_2 and $n_a = 1$ for F_L. For a consistent approximation the same number of terms has to be kept in the two lines of Eq. (3). The first $n+1$ terms define the $\mathrm{N^nLO}$ approximation. As the normalization of the LO prediction is rather arbitrary, the next-to-leading order (NLO) provides the first real prediction of the cross sections and, consequently, the NNLO the first serious error estimate of the perturbative expansions.

The successive approximations of perturbative QCD are illustrated in Fig. 2 for an LHC process of utmost importance, the production of the standard-model Higgs boson dominated by gluon-gluon fusion via a top-quark loop. Obviously the NLO approximation [2] is insufficient for a quantitative prediction in this case, and even at NNLO [3, 4] higher-order uncertainties of about 15% remain for the total cross section. A perturbative accuracy of 5% is only reached at $\mathrm{N^3LO}$, known to a sufficient approximation from Ref. [5] (for an extension to the rapidity distribution see Ref. [6]). Note that these uncertainties do not include those of the coupling α_s and the parton densities, taken for Fig. 2 from Ref. [7] where at NNLO previous (but sufficiently accurate) approximations [8] were used for $P^{(2)}$ in Eq. (3).

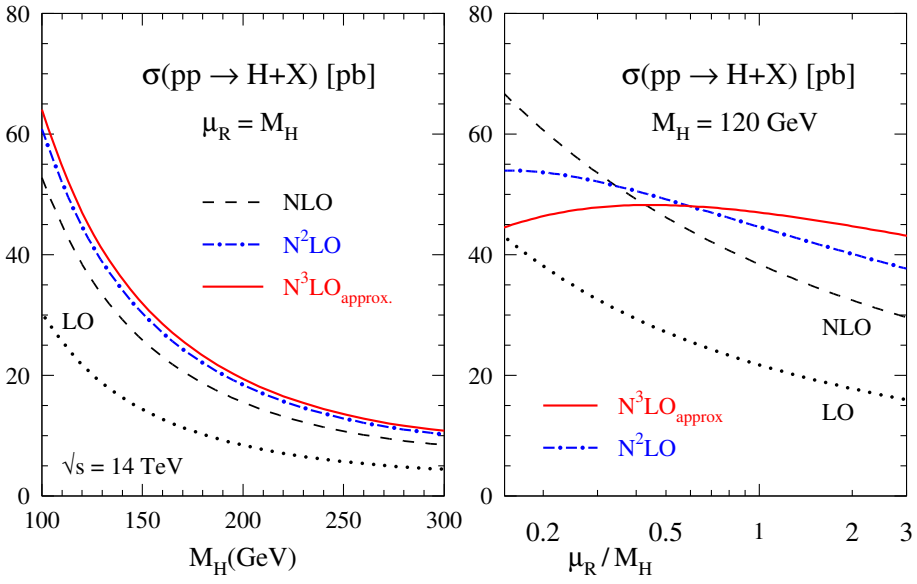

Figure 2: Perturbative expansion of the total cross section for Higgs production at the LHC. Shown are the dependence on the mass M_H and the renormalization scale μ_r (from Ref. [5]).

The minimal momentum fractions ξ_- of partons contributing to the production of a particle of mass M at the LHC are shown in Fig. 3, together with the kinematic reach of HERA and fixed-target DIS experiments at the corresponding scales Q^2. Taking into account also the limited rapidity coverage of the LHC detectors, one reads off $\xi_- \gtrsim 10^{-4}$ for the most important processes, including the production of the W, Z and Higgs bosons and the top quark, and the search for new particles. Thus the HERA data can be fitted with a cut of $Q^2 \approx 10$ GeV^2 which should be sufficient to suppress low-scale instabilities (as, e.g., in F_L to NNLO [9]) and power corrections to Eq. (1).

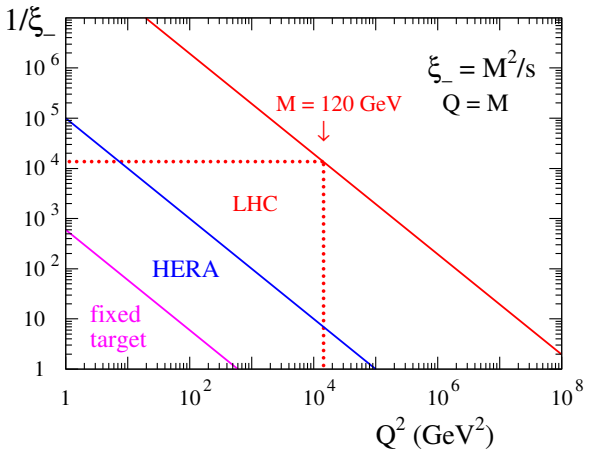

Figure 3: Minimal parton momenta ξ_- probed at the LHC, compared with the DIS coverage of HERA and previous fixed-target experiments.

2 Higher orders in the parton evolution

The complete NNLO splitting functions $P^{(2)}(x)$ – from now on we, as usual, denote also the parton momentum fractions by x – in Eq. (3) have been computed three years ago in Refs. [10, 11]. We first consider the flavour non-singlet evolution of quark-distribution differences such as the combination $q_{\rm ns}^+ = u+\bar{u}-(d+\bar{d})$ probed by $F_2^p - F_2^n$. Figure 4 illustrates the perturbative expansion of the Mellin moments of the corresponding splitting function and the resulting approximations for the scale dependence of $q_{\rm ns}^+$ at large x.

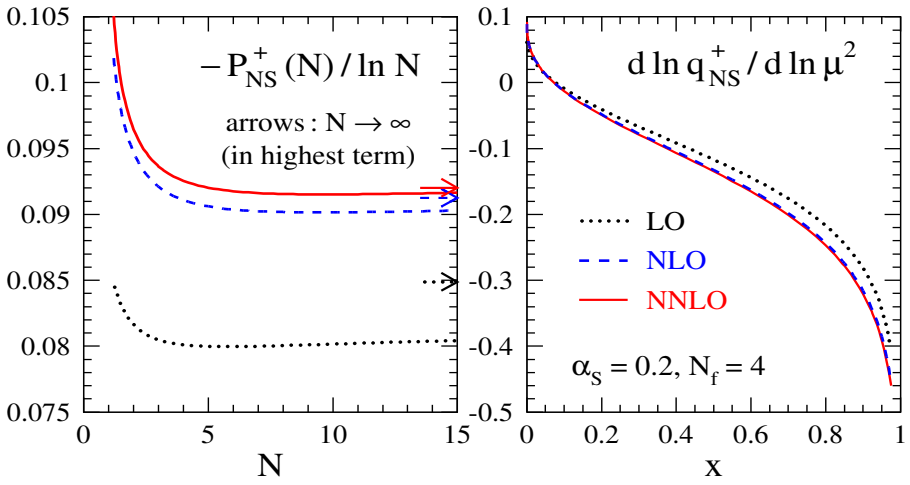

Figure 4: The LO, NLO and NNLO approximations to the splitting-function moments $P_{\rm ns}^+(N)$ for four flavours at $\alpha_{\rm s} = 0.2$, and the resulting logarithmic scale derivatives for $xq_{\rm ns}^+ = x^{0.5}(1-x)^3$, a schematic but characteristic model distribution (from Ref. [10]).

The first fourth-order result for this splitting function has been presented last year [12]: the second moment of $P_{\rm ns}^+(x)$ is now known to N^{3}LO for three flavours, numerically reading

$$P_{\rm ns}^+(N\!=\!2,n_f\!=\!3) \;=\; -0.283\,\alpha_{\rm s}\,[\,1\,+\,0.869\,\alpha_{\rm s}\,+\,0.798\,\alpha_{\rm s}^2\,+\,0.926\,\alpha_{\rm s}^3\,+\,\ldots\,]\;. \qquad (4)$$

Taking into account the weak N-dependence of $P_{\rm ns}^+$ at $N>2$ demonstrated in Fig. 4, this result sets the scale for the N^{3}LO contributions for the whole large-x region. According to the general pattern, the corresponding corrections for $n_f = 4\ldots6$ will be even smaller.

The low-x behaviour of the non-singlet splitting functions and coefficient functions is not too relevant in practice, but provides an interesting lab for the study of small-x logarithms: unlike in the singlet case, two additional powers of $\ln x$ enter per order in $\alpha_{\rm s}$, e.g., terms up to $\ln^4 x$ and $\ln^5 x$ occur in $P_{\rm ns}$ and $c_{2,\rm ns}$ already at order $\alpha_{\rm s}^3$. Successive approximations of these functions including the leading, next-to-leading, ... small-x terms are shown in Fig. 5. Obviously, a 'low-order' approximation of this type is not appropriate at any x-values relevant to colliders. Consequently leading- and next-to-leading-log resummations can, at best, provide only very rough indications of the maximal size of the higher-order corrections. In the present case the all-order leading-logarithmic contributions [13] are small enough to exclude small-x instabilities, e.g., for $xq_{\rm ns}^+ \sim x^{0.5}$, down to extremely low values of x [14].

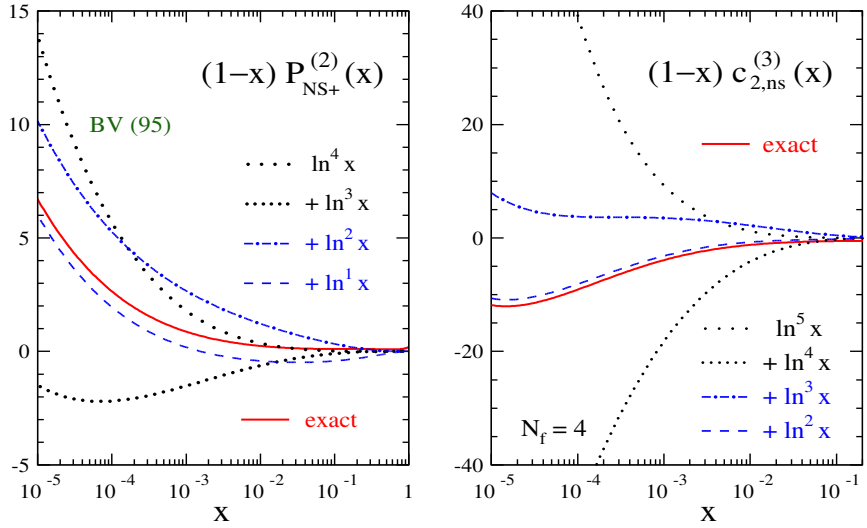

Figure 5: The exact $\alpha_{\rm s}^3$ contributions to the non-singlet splitting function and coefficient function for F_2, compared to approximations obtained from the small-x logarithms (from Refs. [10, 15]). The leading small-x term of $P_{\rm ns+}^{(2)}$ was derived before in Ref. [13].

The flavour-singlet splitting functions are vital for transferring small-x information from HERA to LHC scales across up to three orders of magnitude in Q^2, recall Fig. 3. The corresponding NNLO contribution [11] to Eq. (2) is shown in Fig. 6 for the gluon-gluon case. Also here the leading small-x term, obtained before in Ref. [16] (and transformed to $\overline{\rm MS}$ in Ref. [17]), does not provide a good approximation for any practically relevant values of x. Moreover, the splitting functions enter physical quantities only via the Mellin convolutions of Eqs. (1) and (2). Hence a locally accurate low-x approximation, as provided for $P_{\rm gg}^{(2)}$ by the $x^{-1}\ln x$ plus the x^{-1} terms at $x \lesssim 10^{-3}$, is insufficient for $dg/d\ln\mu^2$ even at small x.

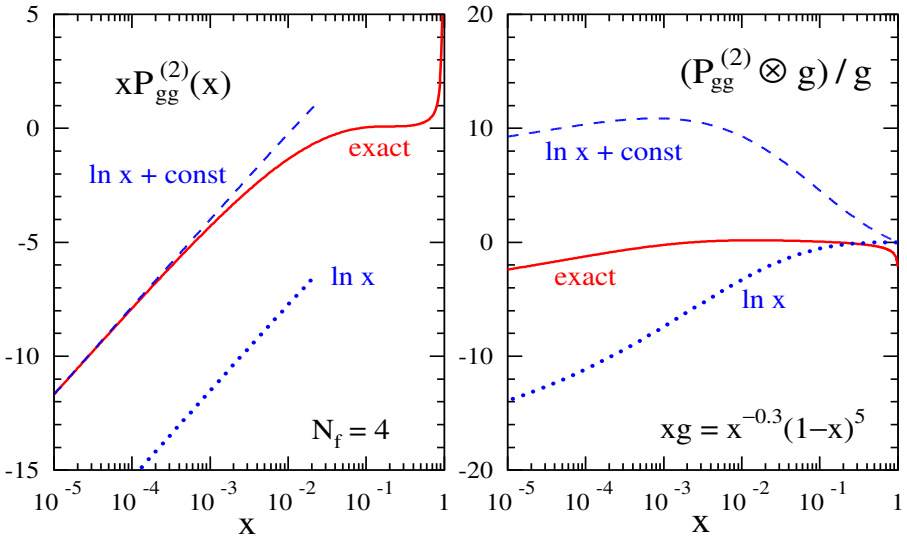

Figure 6: Left: the α_s^3 contribution $P_{gg}^{(2)}$ to the gluon-gluon splitting function, compared to its leading [16, 17] and next-to-leading small-x approximations. Right: the convolution of these three functions with a schematic but typical gluon distribution (from Ref. [11]).

Consequently, reliable estimates of the post-NNLO corrections to the small-x evolution will become possible, via approximations analogous to those of Ref. [17], only once a few singlet moments have been computed to order α_s^4. Fortunately, as illustrated in Fig. 7, the expansion of the quark and gluon evolution to NNLO appears to be very stable, at least for the main HERA-to-LHC region $x \gtrsim 10^{-4}$ at $Q^2 \gtrsim 10$ GeV^2 (see above).

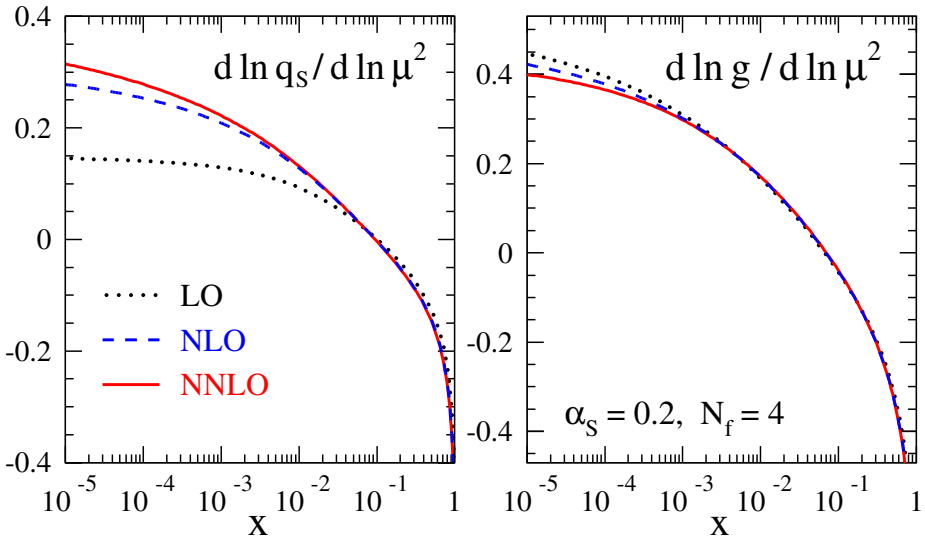

Figure 7: Perturbative expansion of the scale derivatives of typical quark and gluon distributions at $\mu^2 \approx 30$ GeV^2 (from Ref. [11], where the initial conditions are specified).

3 Solutions of the evolution equations

The most direct manner to solve the system (2) of coupled integro-differential equations is by a discretization in both x and μ^2. Recently written or updated public codes including the NNLO evolution are HOPPET [18] and the new version 17 (beta-released at the time of this talk) of QCDNUM [19]. Alternatively, Eqs. (2) can be transformed to ordinary differential equations in (complex) Mellin-N space. These are then treated analytically and the solutions transformed back by quadratures. This approach has been employed in QCD-PEGASUS [20]. The left part of Fig. 8 shows a sample comparison of the programs [18] and [20], using the Les Houches initial conditions discussed below. The right part of the figure, taken from the QCDNUM manual, illustrates the greatly improved numerical accuracy of the new version.

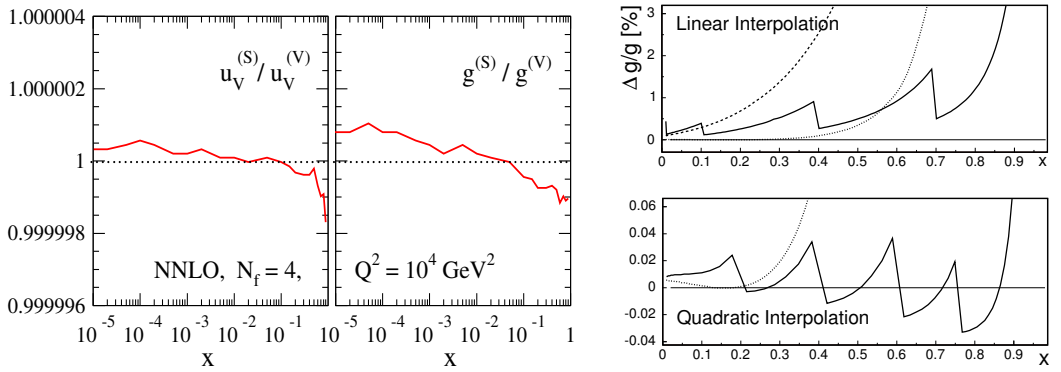

Figure 8: Left: ratios of high-scale NNLO up-valence and gluon distributions after evolution with the codes [18] (S) and [20] (V). Right: the accuracy improvement of QCDNUM due to the new quadratic x-interpolation with actually fewer points (for details see Ref. [19]).

Obviously it is very useful, e.g., for validating newly written or ported codes, to have at one's disposal a set of benchmark evolution results. A reference input was set up for this at the 2001 Les Houches collider-physics workshop (see Ref. [21] for the complete expressions),

$$x u_{\rm v}(x,\mu^2_{\rm f,0}) \;=\; 5.1072\; x^{0.8}\;(1-x)^3\;,\;\ldots,\; xg(x,\mu^2_{\rm f,0}) \;=\; 1.7000\, x^{-0.1}\,(1-x)^5 \qquad (5)$$

for the initial factorization scale $\mu^2_{\rm f,0} = 2$ GeV^2 and the coupling $\alpha_{\rm s}(\mu^2_{\rm r} = 2\ {\rm GeV}^2) = 0.35$. As illustrated in Fig. 8, the results of the programs [18] and [20] agree to five significant digits over a wide range in x and $\mu^2_{\rm f}$, a level of agreement not reached before between x-space and N-space programs. The results at the important scale $\mu^2_{\rm f} = 10^4$ GeV^2 have therefore been cast into reference tables for the evolution at LO, NLO – including, for different initial conditions, the spin-dependent case – and NNLO for the scales ratios $\mu_{\rm r}/\mu_{\rm f} = 0.5$, 1 and 2, using both a fixed and a variable number of flavours n_f (see below). For example, the (iterated, see Ref. [20]) four-flavour NNLO evolution of Eq. (5) for $\mu_{\rm f} = 2\mu_{\rm r}$ yields

$$\begin{aligned} x &= 10^{-5}\,, \quad xu_v = 2.9032\cdot 10^{-3}\,, \quad \ldots\,, \quad xg = 2.2307\cdot 10^{2} \\ &\ldots \\ x &= 0.9 \quad , \quad xu_v = 3.6527\cdot 10^{-4}\,, \quad \ldots\,, \quad xg = 1.2489\cdot 10^{-6} \end{aligned} \qquad (6)$$

at this scale. The complete tables can be found in Refs. [21]. It would be very reasonable to employ only programs which have been checked against these benchmarks.

4 Input shapes, factorization schemes and heavy quarks

The $\overline{\rm MS}$ scheme adopted so far is calculationally convenient and leads to a perturbatively stable parton evolution – recall Eq. (4), Figs. 4 and 7. However, the NLO, NNLO, ... parton distributions are not physical in this scheme. Therefore $\overline{\rm MS}$ may not be the scheme in which the initial distributions retain their physically motivated shapes (as long known for the photon structure [22]), e.g., for the proton's gluon density at large x, see Ref. [23]. Moreover, it seems unclear which positivity bound in particular $g(x,\mu^2)$ has to obey in this scheme, and which NLO partons (if any) are best suited for obtaining estimates from leading-order Monte-Carlo programs [24].

The traditional alternative to $\overline{\rm MS}$ has been the DIS scheme [25], in which the quark distributions are rendered physical via the structure function F_2. For the singlet sector the transformation to this scheme is given by

$$\begin{aligned} q_S^{\rm DIS} &= q_S + \alpha_{\rm s}\big[\, c_{2,q}^{(1)} \otimes q_S + c_{2,g}^{(1)} \otimes g \,\big] + \ldots \\ g^{\rm DIS} &= g - \alpha_{\rm s}\big[\, c_{2,q}^{(1)} \otimes q_S + c_{2,g}^{(1)} \otimes g \,\big] + \ldots \ . \end{aligned} \tag{7}$$

Its large drawback is that the second row of Eq. (7) is arbitrary except for the moment $N = 2$ fixed by the momentum sum rule. Thus there is nothing physical about the DIS-scheme gluon density especially where constraints are needed most, for very large and for small x.

This shortcoming is absent in an interesting old suggestion, the DIS$_\phi$ scheme going back (at least) to Ref. [26]. Here also the shape of the gluon distribution is rendered physical via the structure function F_ϕ of a scalar directly coupling to gluons (such as the Higgs boson in the large-$m_{\rm top}$ effective theory). The transformation to DIS$_\phi$ at N$^{\rm n}$LO requires the corresponding coefficient functions $c_{\phi,q}^{(n)}$ and $c_{\phi,g}^{(n)}$. Scalar-exchange DIS had to be considered anyway in Ref. [11], and the determination of these coefficient function to order $\alpha_{\rm s}^3$ requires only a minor extension of the published calculations. These functions and possible constraints arising, for example, from the positivity of F_ϕ will be presented elsewhere.

Now we turn to heavy quarks. For processes at a sufficiently high scale, charm and bottom become effectively light flavours which have to be included in the parton structure of the proton. For most values of x one can disregard a possible non-perturbative 'intrinsic charm' (or bottom) component (which, however, can be relevant at large x for some specific LHC processes [27]). The $\overline{\rm MS}$ evolution of $\alpha_{\rm s}$ [28] and the parton densities with a variable number of flavours then proceed via a matching of effective theories for different n_f. The matching conditions for the parton distributions are especially simple at the heavy-quark mass, $\mu_{\rm f} = m_h$. Denoting the light-quark distributions by l_i, they up to N$^{m=2}$LO read [29]

$$\begin{aligned} l_i^{\,(N_{\rm f}+1)} &= l_i^{\,(N_{\rm f})} + \delta_{m2}\, a_{\rm s}^2\, A_{qq,h}^{{\rm NS},(2)} \otimes l_i^{\,(N_{\rm f})} \\ g^{\,(N_{\rm f}+1)} &= g^{\,(N_{\rm f})} + \delta_{m2}\, a_{\rm s}^2 \left[A_{\rm gq,h}^{{\rm S},(2)} \otimes q_S^{\,(N_{\rm f})} + A_{\rm gg,h}^{{\rm S},(2)} \otimes g^{\,(N_{\rm f})} \right] \\ (h+\bar h)^{\,(N_{\rm f}+1)} &= \delta_{m2}\, a_{\rm s}^2 \left[A_{\rm hq}^{{\rm S},(2)} \otimes q_S^{\,(N_{\rm f})} + A_{\rm hg}^{{\rm S},(2)} \otimes g^{\,(N_{\rm f})} \right] . \end{aligned} \tag{8}$$

The results [30] underlying the qq, hq and hg coefficients have been confirmed recently [31].

The matching conditions (8) are included in the above evolution codes and benchmarks. Note that the $\alpha_{\rm s}^2$ NNLO discontinuities were so far ignored in the (published) MRST parton densities. However, they have now been implemented and found to significantly affect the

cross sections for W/Z production at the LHC [32]. Forthcoming updates of also the NLO distributions will include further significant improvements, e.g., the use of fastNLO [33] for jet cross sections instead of pre-calculated K-factor tables.

In general, the calculation of heavy-quark effects on observables is far more involved. We briefly summarize this issue for charm production at HERA, a process which affects the vital extraction of the small-x quark and gluon densities from F_2^p. There are three regimes: For $Q \not\gg m_c$ only u, d, s and g act as partons, and charm production can be calculated using the fixed-order massive coefficient functions, presently known to NLO [34]. This framework is usually referred to as the fixed-flavour number scheme (FFNS). At $Q \ggg m_c$ all terms with m_c/Q are negligible, and $n_f = 4$ partons – obtained via the matching conditions (8) – can be used with massless four-flavour coefficient functions, a procedure often called the zero-mass variable flavour-number scheme (ZM-VFNS). Finally there is, in general, an intermediate region $Q \gg m_c$, where terms with m_c/Q are not negligible, but large quasi-collinear logarithms require a resummation via Eqs. (2). Then the $n_f = 4$ partons have to be used with 'interpolating' coefficient functions for which several prescriptions have been suggested, see refs. [29, 35–37]. This is the genuine (or general-mass, GM-) VFNS.

The transition regions between these regimes are process-dependent and tend to lie at higher scales than one might at first expect, something to be kept in mind when using bottom distributions with massless coefficient functions at the LHC. For example, there are strong experimental (see Fig. 9) and theoretical (recall, e.g., Ref. [38]) indications that the FFNS is applicable for the small-x HERA data on F_2^c at least up to $Q^2 \gtrsim 100$ GeV^2.

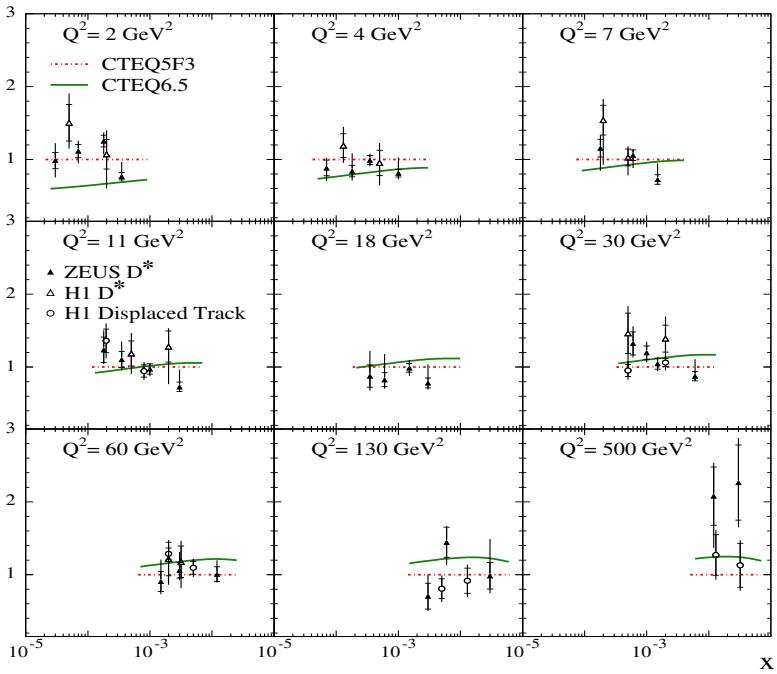

Figure 9: HERA measurements of the charm structure function F_2^c, compared to NLO CTEQ calculations in the fixed [39] and variable flavour-number [37] schemes. All results have been normalized to the former calculation (adapted from Ref. [40]).

5 Recent parton analyses and future LHC constraints

Recently the CTEQ collaboration has published a major update, CTEQ 6.5, of their NLO global fits [37]. A salient improvement is that the mass suppression of the charm contribution to F_2^p at HERA has finally been included – before the inadequate ZM-VFNS (see above) had been used. The reduced charm component is compensated by larger u and d distributions at small x as illustrated in Fig. 10. This increase leads to larger predictions for the W- and Z-production cross sections at the LHC, by about 8%, a shift well outside the uncertainty bands obtained from the previous CTEQ 6.1 sets [41]. It should be noted, however, that both this shift and the similar NNLO result of Ref. [32] mentioned above do not invalidate the widths of the previous error bands. Rather the previous central values should be considered unreliable, as they resulted from fits disregarding well-known theoretical information.

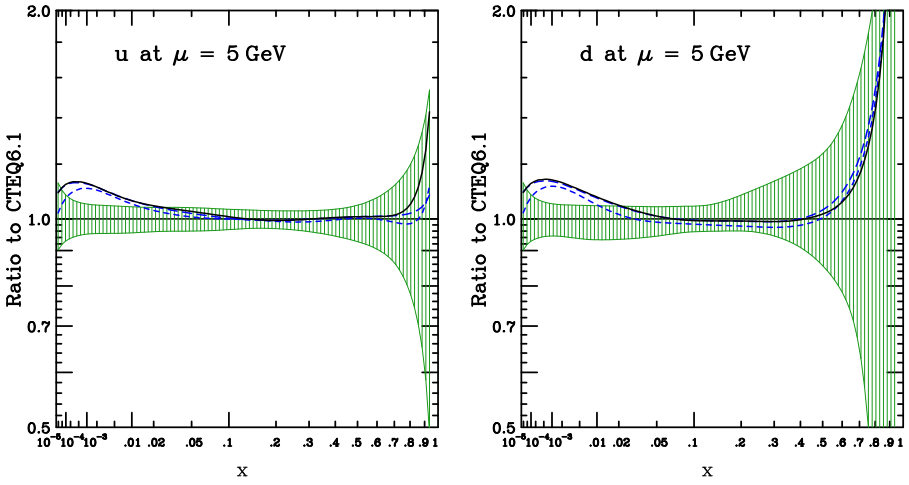

Figure 10: Central u and d distributions of the CTEQ 6.5 fit, normalized to previous results from the same group [41]. Also shown are the estimated error bands resulting from the experimental uncertainties of the data included in the analysis (from Ref. [37]).

In any case, it is important to have at one's disposal several independent sets of parton distributions at each order of perturbative QCD. Until recently, the only NNLO analysis besides those of MRST (now MSTW) was that of Ref. [42], based only on data from deep-inelastic scattering. Last year this analysis has been expanded in Ref. [43]: a consistent subset has been included of the available data on Drell-Yan lepton-pair production – note the difference in approach to CTEQ, who are working on their treatment of inconsistent data sets. The NNLO corrections to these cross sections [44, 45] are found to be crucial for the fits and, interestingly, as before a rather low value of $\alpha_s(M_Z)$ is preferred, in marked contrast to the recent NNLO fits of MSTW [32].

Usually the initial conditions for Eq. (2) are written in terms of an ansatz, as in Eq. (5) but with more free parameters. The resulting bias is monitored by varying this functional forms as, e.g., in the two dashed curves in Fig. 10. An alternative approach is pursued by the NNPDF collaboration, using neural networks to avoid any such bias. A first analysis of non-singlet structure functions has been performed in Ref. [46], using a new hybrid evolution method combining advantages of the x-space and Mellin-N techniques mentioned above.

Four uncertainty bands for the combination $u+\bar{u}-(d+\bar{d})$ of NLO quark distributions are displayed in Fig. 11. There are many differences between the chosen analyses of Refs. [7, 41, 42, 46], thus it seems difficult to isolate the possible impact of the parametrization bias. It would be interesting to see fits of a reference data set using different approaches to the initial conditions but otherwise identical conditions. In any case, given the precision of the data on the proton structure function F_2^p and the neutron-proton ratio, for example at $x \approx 0.2$, it seems rather unlikely that the very wide NNPDF band reflects the true uncertainty.

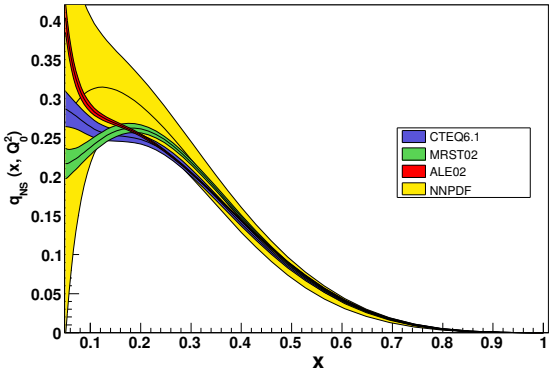

Figure 11: Experimental error bands for the NLO non-singlet combination $q_{\rm ns}^+ = u+\bar{u}-(d+\bar{d})$, according to the older fits in Refs. [7, 41, 42] and the recent NNPDF analysis (from Ref. [46]).

Finally a non-singlet analysis of electromagnetic DIS has been performed in Ref. [47], besides the quark distributions focusing on determinations of $\alpha_{\rm s}$ up to the N^{3}LO of Eq. 3. This order is accessible outside the small-x region since, as confirmed by Ref. [12], the N^{3}LO corrections to the structure function evolution are dominated by the known coefficient functions, see Fig. 20 of Ref. [15]. The results of Ref. [47] for the strong coupling constant read $\alpha_{\rm s}(M_Z) = 0.1134, 41 \pm 0.002$ at N^{2,3}LO, consistent with Ref. [43] but not with Ref. [32]. Obviously more research is required before firm conclusions can be drawn on the uncertainties of the parton densities (as in Fig. 11) and the determination of $\alpha_{\rm s}$.

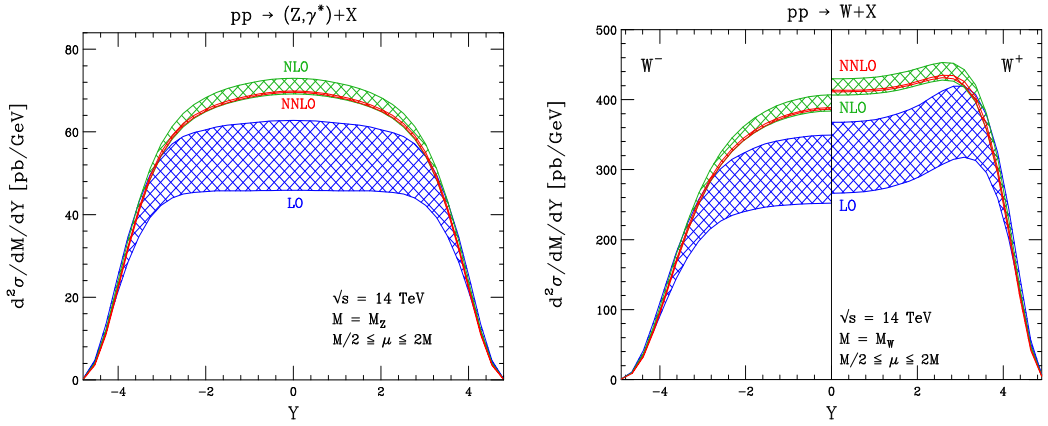

Figure 12: Rapidity-dependent cross sections for gauge-boson production at the LHC, using the partons of Ref. [7]. Shown are the theoretical uncertainty estimates obtained by varying the scale μ by the arbitrary but conventional factor of two around $M_{W,Z}$ (from Ref. [44]).

The pre-LHC determinations of the parton densities will be improved upon by including reference cross sections measured at the LHC. The 'gold-plated' process of gauge-boson production is illustrated in Fig. 12; see Ref. [48] for a more detailed discussion including

experimental aspects. The results shown demonstrate the importance of NNLO results even for processes with a far more benign perturbative expansion than the Higgs-production cross section of Fig. 2: It would clearly be impossible to make precision predictions, or perform precision analyses, based on the rough (and non-overlapping) LO and NLO error estimates obtained by varying the renormalization and factorization scale(s). Thanks to the NNLO calculations [44, 45], on the other hand, the perturbative uncertainty has been reduced to a level of about 1%, an accuracy unprecedented for hadron-collider cross sections.

6 Outlook: HERA results for the LHC era

Precision parton densities and QCD cross sections are required to fully realize the potential of the LHC. For example, a very precise W-mass determination with $\delta M_W \lesssim 10$ MeV seems experimentally feasible, see Ref. [49]. Combined with $\delta m_{\rm top} \simeq 1$ GeV such a result could help to discriminate between, e.g., the standard model and its minimal supersymmetric extension – see the figure (updated from Refs. [50]) shown at the end of the talk [1]. While great progress has been made during the past years, considerable challenges remain.

At the time of this write-up 15 years of data-taking at HERA have ended. Its results will remain indispensable throughout the LHC era, and it is important that also the high-luminosity results of the last phase are fully exploited – despite the obvious temptation to move on to, say, LHC Higgs hunting as soon as possible. Moreover, it is highly desirable to preserve important data, e.g., on heavy quarks and jet production, in a manner facilitating detailed re-analyses (as performed for PETRA data in Ref. [51]) a decade from now.

Acknowledgements

It is a pleasure to thank M. Botje and S. Heinemeyer for providing figures used here and in Ref. [1], and S. Moch and R. Thorne for critically reading parts of the manuscript.

References

[1] Slides: `http://indico.cern.ch/contributionDisplay.py?contribId=4&sessionId=2&confId=9499`

[2] M. Spira, A. Djouadi, D. Graudenz and P.M. Zerwas, Nucl. Phys. B453 (1995) 17, hep-ph/9504378; R. Harlander and P. Kant, JHEP **0512** (2005) 015, hep-ph/0509189

[3] R.V. Harlander and W.B. Kilgore, Phys. Rev. Lett. 88 (2002) 201801, hep-ph/0201206; C. Anastasiou and K. Melnikov, Nucl. Phys. B646 (2002) 220, hep-ph/0207004; V. Ravindran, J. Smith and W.L. van Neerven, Nucl. Phys. B665 (2003) 325, hep-ph/0302135

[4] C. Anastasiou, K. Melnikov and F. Petriello, Nucl. Phys. B724 (2005) 197, hep-ph/0501130

[5] S. Moch and A. Vogt, Phys. Lett. B631 (2005) 48, hep-ph/0508265

[6] V. Ravindran, J. Smith and W.L. van Neerven, Nucl. Phys. B767 (2007) 100, hep-ph/0608308

[7] A.D. Martin, R.G. Roberts, W.J. Stirling and R.S. Thorne, Eur. Phys. J. C23 (2002) 73, hep-ph/0110215; Phys. Lett. B531 (2002) 216 hep-ph/0201127

[8] W.L. van Neerven and A. Vogt, Phys. Lett. B490 (2000) 111, hep-ph/0007362

[9] S. Moch, J.A.M. Vermaseren and A. Vogt, Phys. Lett. B606 (2005) 123, hep-ph/0411112

[10] S. Moch, J.A.M. Vermaseren and A. Vogt, Nucl. Phys. B688 (2004) 101, hep-ph/0403192

[11] A. Vogt, S. Moch and J.A.M. Vermaseren, Nucl. Phys. B691 (2004) 129, hep-ph/0404111

[12] P.A. Baikov and K.G. Chetyrkin, Nucl. Phys. (Proc. Suppl.) 160 (2006) 76

[13] J. Blümlein and A. Vogt, Phys. Lett. B370 (1996) 149, hep-ph/9510410

[14] J. Blumlein and A. Vogt, Acta Phys. Polon. B27 (1996) 1309, hep-ph/9603450

[15] J.A.M. Vermaseren, A. Vogt and S. Moch, Nucl. Phys. B724 (2005) 3, hep-ph/0504242
[16] V.S. Fadin and L.N. Lipatov, Phys. Lett. B429 (1998) 127, hep-ph/9802290;
M. Ciafaloni and G. Camici, Phys. Lett. B430 (1998) 349, hep-ph/9803389
[17] W.L. van Neerven and A. Vogt, Nucl. Phys. B588 (2000) 345, hep-ph/0006154
[18] G. Salam, `http://projects.hepforge.org/hoppet/`
[19] M. Botje, `http://www.nikhef.nl/~h24/qcdnum/`
[20] A. Vogt, CPC 170 (2005) 65, hep-ph/0408244; `http://www.liv.ac.uk/~avogt/pegasus.html`
[21] W. Giele *et al.*, hep-ph/0204316 (pages 13 – 22); M. Dittmar *et al.*, hep-ph/0511119 (pages 93 – 102)
[22] M. Glück, E. Reya and A. Vogt, Phys. Rev. D45 (1992) 3986.
[23] A.D. Martin, R.G. Roberts, W.J. Stirling and R.S. Thorne, Phys. Lett. B604 (2004) 61, hep-ph/0410230
[24] J.M. Campbell, J.W. Huston and W.J. Stirling, Rept. Prog. Phys. 70 (2007) 89, hep-ph/0611148;
R.S. Thorne, A. Sherstnev and C. Gwenlan, arXiv:0706.2131 [hep-ph] (these proceedings)
[25] G. Altarelli, R.K. Ellis and G. Martinelli, Nucl. Phys. B157 (1979) 461
[26] W. Furmanski and R. Petronzio, Z. Phys. C11 (1982) 293
[27] J. Pumplin, H.L. Lai and W.K. Tung, Phys. Rev. D75 (2007) 054029, hep-ph/0701220;
H.L. Lai *et al.*, JHEP 0704 (2007) 089, hep-ph/0702268
[28] K.G. Chetyrkin, B.A. Kniehl and M. Steinhauser, Phys. Rev. Lett. 79 (1997) 2184, hep-ph/9706430
[29] M. Buza, Y. Matiounine, J. Smith and W. L. van Neerven, Eur. Phys. J. C1 (1998) 301, hep-ph/9612398
[30] M. Buza *et al.*, Nucl. Phys. B472 (1996) 611, hep-ph/9601302.
[31] I. Bierenbaum, J. Blümlein and S. Klein, hep-ph/0703285 (Nucl. Phys. B, in press)
[32] A.D. Martin, W.J. Stirling, R.S. Thorne and G. Watt, arXiv:0706.0459 [hep-ph].
[33] T. Kluge, K. Rabbertz and M. Wobisch, hep-ph/0609285 (proceedings of DIS 2006)
[34] E. Laenen, S. Riemersma, J. Smith and W.L. van Neerven, Nucl. Phys. B392 (1993) 162;
B.W. Harris and J. Smith, Phys. Rev. D57 (1998) 2806, hep-ph/9706334
[35] A. Chuvakin, J. Smith and W.L. van Neerven, Phys. Rev. D61 (2000) 096004, hep-ph/9910250
[36] R.S. Thorne and R.G. Roberts, Phys. Rev. D57 (1998) 6871, hep-ph/9709442;
R.S. Thorne, Phys. Rev. D73 (2006) 054019, hep-ph/0601245
[37] W.K. Tung *et al.*, JHEP 0702 (2007) 053, hep-ph/0611254
[38] A. Vogt, hep-ph/9601352 (proceedings of DIS 96)
[39] H. L. Lai *et al.*, Eur. Phys. J. C12 (2000) 375, hep-ph/9903282
[40] P.D. Thompson, J. Phys. G34 (2007) N177, hep-ph/0703103
[41] J. Pumplin *et al.*, JHEP 0207 (2002) 012, hep-ph/0201195
[42] S. Alekhin, Phys. Rev. D68 (2003) 014002, hep-ph/0211096
[43] S. Alekhin, K. Melnikov and F. Petriello, Phys. Rev. D74 (2006) 054033, hep-ph/0606237
[44] C. Anastasiou, L. Dixon, K. Melnikov and F. Petriello, Phys. Rev. D69 (2004) 094008, hep-ph/0312266
[45] K. Melnikov and F. Petriello, Phys. Rev. Lett. 96 (2006) 231803, hep-ph/0603182
[46] L. Del Debbio *et al.*, JHEP 0703 (2007) 039, hep-ph/0701127
[47] J. Blümlein, H. Böttcher and A. Guffanti, Nucl. Phys. B774 (2007) 182, hep-ph/0607200
[48] A.M. Cooper-Sarkar, hep-ph/0512228 (2005 Les Houches collider-physics workshop)
[49] M. Boonekamp, Acta Phys. Polon. B38 (2007) 2229
[50] S. Heinemeyer *et al.*, Phys. Rept. 425 (2006) 265; JHEP 0608 (2006) 052, hep-ph/0604147
[51] P. Pfeifenschneider *et al.* [JADE collaboration], Eur. Phys. J. C17 (2000) 19, hep-ex/0001055

The Spin Structure of the Nucleon

Jörg Pretz[1]

Physikalisches Institut, Universität Bonn,
Nußallee 12, D-53115 Bonn

This article reviews recent results on the spin structure of the nucleon from polarized deep inelastic lepton-nucleon scattering and polarized proton-proton scattering.

For a description of the nucleon in terms of parton distribution functions (pdf) the knowledge of three basic distributions is needed: The relatively well known unpolarized pdfs, the helicity distributions and the transversity distributions. The latter two play an essential role in understanding the spin structure of the nucleon. New results on the gluon helicity distribution $\Delta G(x)$ and the helicity distributions for strange and valence quarks are discussed. A first determination of the up to now unknown transversity distributions $\Delta_T q(x)$ is presented. Finally results from deep virtual Compton scattering, giving access to the orbital angular momentum contribution of quarks to the nucleon spin, are discussed.

1 Introduction

1.1 A short review of the nucleon spin puzzle

The spin 1/2 of the nucleon can be decomposed in the helicity contribution of quarks ($\Delta\Sigma$) and gluons (ΔG) as well as orbital angular momentum contributions of quarks (L_q) and gluons (L_g). This leads to the following sumrule:

$$\frac{1}{2} \overset{(1)}{=} \frac{1}{2}\Delta\Sigma + \Delta G + L_q + L_g \; .$$

In the static quark model the nucleon is described by an $\mathrm{SU}_{\mathrm{flavor}}(3) \times \mathrm{SU}_{\mathrm{spin}}(2)$ wave function and one can easily calculate the helicity contributions of u and d quarks to the nucleon spin:

$$\begin{array}{rcr} \Delta u & = & \frac{4}{3} \\ \Delta d & = & -\frac{1}{3} \\ \hline \Delta\Sigma = \Delta u + \Delta d & = & 1 \end{array}$$

In this model the spin of the nucleon is entirely given by the helicity contribution of the u and d quarks. The last three terms in eq. (1) are 0.

Experimental information on the quark helicity contribution can be obtained from axial matrix elements of baryon decays. These matrix elements, a_3 and a_8, are related to the first moments of the quark helicity distributions: $\Delta q = \int_0^1 \Delta q(x)\,\mathrm{dx}$ by the following relations:

$$\begin{aligned} a_3 &= \Delta u + \Delta\bar{u} - \Delta d - \Delta\bar{d} = 1.2670 \pm 0.0035 \quad \text{and} \\ a_8 &= \Delta u + \Delta\bar{u} + \Delta d + \Delta\bar{d} - 2(\Delta s + \Delta\bar{s}) = 0.585 \pm 0.025 \; . \end{aligned}$$

Assuming a vanishing contribution of the strange quarks ($\Delta s + \Delta\bar{s} = 0$) one arrives at

$$\Delta\Sigma = 0.585 \pm 0.025 \; , \tag{1}$$

i.e. the quark helicity contribution is of the order of 60%.

The static quark model predicts for the weak coupling constant $g_A \equiv a_3 = 4/3 + 1/3 = 5/3$, a value 30% above the measured value. In relativistic quark models, quarks acquire orbital angular momentum and the helicity contribution of quarks is reduced in order to find the correct value for g_A, such that one typically finds $\Delta\Sigma \approx 0.7$, i.e. of the same order as the value obtained from the analysis of the baryon decays.

To be able to drop the assumption $\Delta s(x) + \Delta\bar{s}(x) = 0$ and to determine the contribution of all three flavors, a third independent quantity is needed. It is provided by polarized deep inelastic lepton-nucleon scattering. This allows then to determine the matrix element a_0 which is in leading order QCD identical to the quark helicity contribution $\Delta\Sigma$:

$$a_0 \overset{LO\ QCD}{\equiv} \Delta\Sigma = \Delta u + \Delta\bar{u} + \Delta d - \Delta\bar{d} + \Delta s - \Delta\bar{s}\ .$$

A recent leading order (LO) analysis [2] of polarized deep inelastic data arrives at the following values

$$\begin{aligned} \Delta\Sigma &= 0.18 \pm 0.04\,, \\ \Delta s + \Delta\bar{s} &= -0.14 \pm 0.01\,, \end{aligned}$$

The difference between this small value for $\Delta\Sigma$ in deep inelastic scattering and the value of about 60%–70% coming from the weak baryon decays and quark models is called the nucleon spin puzzle.

At next-to-leading (NLO) QCD the relation of the experimentally measured matrix element a_0 and $\Delta\Sigma$ is more difficult due to the axial anomaly. It depends on the renormalization and factorization scheme used. In the Adler-Bardeen (AB) scheme the relation is

$$a_0(Q^2) = \Delta\Sigma - 3\frac{\alpha_s}{2\pi}\Delta G(Q^2)\,.$$

In this scheme $\Delta\Sigma$ does not depend on Q^2. It allows thus a comparison with values obtained in quark models. One scenario proposed is that the small measured value of a_0 is due to a value of $\Delta\Sigma = 0.6 - 0.7$ and a large contribution $\Delta G = 2 - 3$. Such large values of ΔG would reconcile results from polarized deep inelastic scattering and baryon decays.

In section 2 recent results on ΔG will be discussed. Section 3 presents measurements of the quark helicity contributions for different flavors. Generalized Parton Distributions are discussed in Section 5. They provide a tool to learn something about the role of angular orbital momentum in the spin sumrule (1).

1.2 Description of the nucleon in terms of parton distribution functions

At leading twist and after integration over the quark transverse momentum the nucleon can be described by three types of parton distribution functions:

- The relatively well known unpolarized distributions $q(x)$ and $G(x)$,
- the helicity distribution $\Delta q(x)$ and $\Delta G(x)$ discussed in the previous section
- and the transversity distribution $\Delta_T q(x)$.

The importance of the helicity distributions was discussed in the previous subsection. A first determination of the transversity distribution will be discussed in Section 5. Note that there is, due to helicity conservation, no transverse gluon distribution, $\Delta_T G(x)$, on a spin 1/2 target.

2 The gluon helicity contribution ΔG

The gluon helicity distribution can be accessed through

- Next-to-leading order analysis of the structure function g_1
- semi-inclusive double spin asymmetries in polarized deep inelastic scattering
- double spin asymmetries in polarized proton-proton scattering

This section starts with discussing various analyses of inclusive data on the structure functions g_1 to extract ΔG. Then the recent results from semi-inclusive deep inelastic scattering are presented and finally the determination of ΔG from polarized proton-proton scattering is discussed.

2.1 Next-to-leading order analysis of the structure function g_1

At NLO QCD the structure function $g_1(x, Q^2)$ depends on the polarized gluon distribution ΔG which allows in principle a determination of $\Delta G(x)$. Fits to the world data on g_1^p, g_1^d and g_1^n were performed by different groups [3, 4, 5]. Ref. [3] includes higher twist corrections in their fits. Ref. [5] includes as well data from π^0 double spin asymmetries from PHENIX.

In refs. [3, 4] two solutions with different signs are found for $\Delta G(x)$. Both solutions have similar acceptable χ^2 values. Figure 1 shows data on g_1^d as a function of the Bjorken variable x. The curves correspond to the two solutions with positive and negative ΔG of ref. [4].

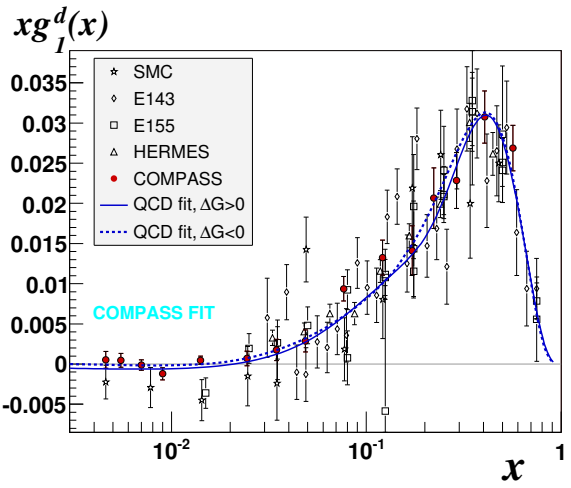

Figure 1: The structure function g_1^d vs. x. The two curves correspond to the two solutions with positive and negative ΔG of ref. [4].

The corresponding results for $\Delta G(x)$ are shown in Fig. 3. The grey error bands only show the statistical error. The first moments of the two solutions are $\Delta G = 0.34$ and $\Delta G = -0.31$ with an statistical error of approximately 0.1. The absolute values are similar but the shape is different. Note that the systematic uncertainties coming from the choice of the factorization and renormalization scale and other theoretical uncertainties can be much larger than the statistical error shown. This shows that with presented available data it is difficult to determine ΔG and underlines the necessity for a direct measurement. For a more detailed discussion see [6, 7].

2.2 Semi-inclusive double spin asymmetries in polarized deep inelastic scattering

A more direct information on $\Delta G/G$ comes from double spin asymmetries in semi-inclusive deep inelastic scattering. The selection of specific hadronic final states signals the participation of a gluon in the underlying partonic subprocess. For example, the presence of a

hadron with large transverse momentum (typically $p_T > 0.7$ GeV) with respect to the virtual photon axis tags events where the photon interacts with a gluon inside the proton via the photon-gluon fusion process. Unfortunately, other processes, like the QCD-Compton process, have the same signature leading to background contributions. A much cleaner tag of the photon-gluon fusion process is the observation of charmed particles in the final state. Because of the small intrinsic charm contribution in the proton and the low probability to produce charm quarks in the fragmentation process, charm quarks are almost exclusively produced via the photon-gluon fusion process. Experimentally, one detects D^0 and D^{*+} mesons and their anti-particles via their respective decays in $K^- + \pi^+$ and $K^- + \pi^+ + \pi^+_{slow}$.

In both methods (high p_T and open charm) one has to measure a double spin asymmetry with longitudinally polarized beam and target. To extract $\Delta G/G$ from this asymmetry one important quantity is the fraction of signal events R. For the high p_T method it has to be estimated from Monte Carlo generators (PHYTIA for $Q^2 < 1\text{GeV}^2$ and LEPTO for $Q^2 > 1\text{GeV}^2$), whereas in the open charm method it can be measured from the background in the invariant mass spectrum of the reconstructed D mesons which reduces the model dependence of the result. This is illustrated in Fig. 2. The left figure shows the contribution of various subprocesses contributing to the cross section obtained by a PYTHIA MC simulation for the COMPASS analysis for events with $Q^2 < 1\text{GeV}^2$. After optimizing the cuts a contribution of $R \approx 30\%$ is obtained for the photon-gluon-fusion process. Figure 2 right shows the invariant mass spectra for the two decay channels used in the open charm analysis. Here the signal fraction can be directly determined from the data. At the maximum it is approximately 50% (10%) for the D^* (D^0) channel. In the new HERMES analysis single hadrons with large p_T were considered. The signal fraction R, obtained by a PYTHIA MC, ranges from 10–20% depending on p_T. Note that in the case of HERMES, p_T is calculated with respect to the beam axis which coincides approximately with the virtual photon axis. The direction of the virtual photon is not known because the scattered electron is not reconstructed.

Figure 3 shows the results for $\Delta G/G$ obtained by different experiments. The three solid curves are parameterizations corresponding to three different first moments [8]. The two dotted curves with error bands are the two results from the inclusive analysis discussed above. The direct measurements presented here clearly favor small values of $\Delta G/G$ at $x_g \approx 0.1$. Tab. 1 summarizes the results of the direct measurements of $\Delta G/G$. It gives as well the scale at which $\Delta G/G$ is probed. A discussion of these results can also be found in [9, 10].

Experiment	Method	$\Delta G/G \pm$ stat. err. $\pm$ sys. err.	scale μ [GeV^2]	$< x_g >$	ref.
COMPASS	had. pairs,$Q^2 < 1$ GeV^2	$0.016 \pm 0.058 \pm 0.055$	3	0.085	[11], prelim.
COMPASS	had. pairs,$Q^2 > 1$ GeV^2	$0.06 \pm 0.31 \pm 0.06$	2.4	0.13	prelim.
COMPASS	open charm	$-0.57 \pm 0.41 \pm 0.17$	13	0.15	prelim.
HERMES	hadron pairs	$0.41 \pm 0.18 \pm 0.03$[1)]	2	0.17	[12]
HERMES	single hadrons	$0.071 \pm 0.034^{+0.105}_{-0.127}$	1.35	0.22	[9],prelim.
SMC	had. pairs,$Q^2 > 1$ GeV^2	$-0.20 \pm 0.28 \pm 0.10$	3	0.07	[13]

Table 1: Results on $\frac{\Delta G}{G}$ from various experiments. [1)] Only the experimental systematic error is given.

High p_T

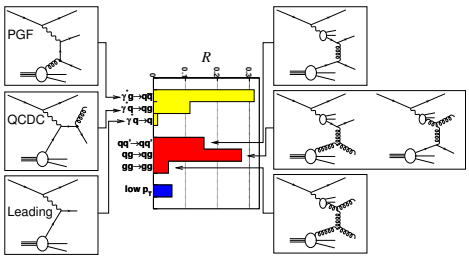

$$R = \frac{\sigma_{PGF}}{\sigma_{PGF}+\sigma_{bgd}} \approx 0.3$$
from PYTHIA MC

Open Charm

$D^{*+} \to D^0\pi^+ \to K^-\pi^+\pi^+$

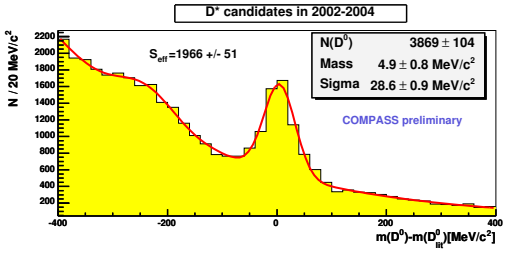

$D^0 \to K^-\pi^+$

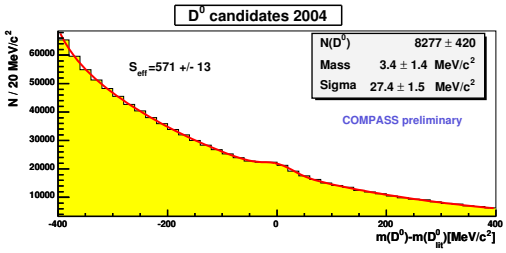

$$R = \frac{\sigma_{PGF}}{\sigma_{PGF}+\sigma_{bgd}} \approx 0.5(0.1)$$
from data

Figure 2: Left: Contribution of various subprocesses to the cross section obtained from a PYTHIA MC simulation for the COMPASS high p_T analysis, $Q^2 < 1\text{GeV}^2$. Right: Invariant mass spectra of $K\pi$ pairs for the two decay channels.

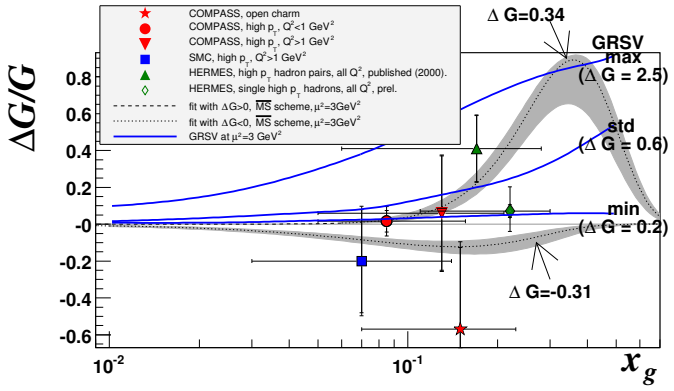

Figure 3: Results on $\Delta G/G$ from different experiments. The two dotted curves are results from the COMPASS NLO fits to inclusive asymmetries [4]. The three solid curves labeled max, std and min are parameterizations from GRSV [8]. They correspond to first moments at $\mu = 3\text{GeV}^2$ of 2.5, 0.6, 0.2 respectively.

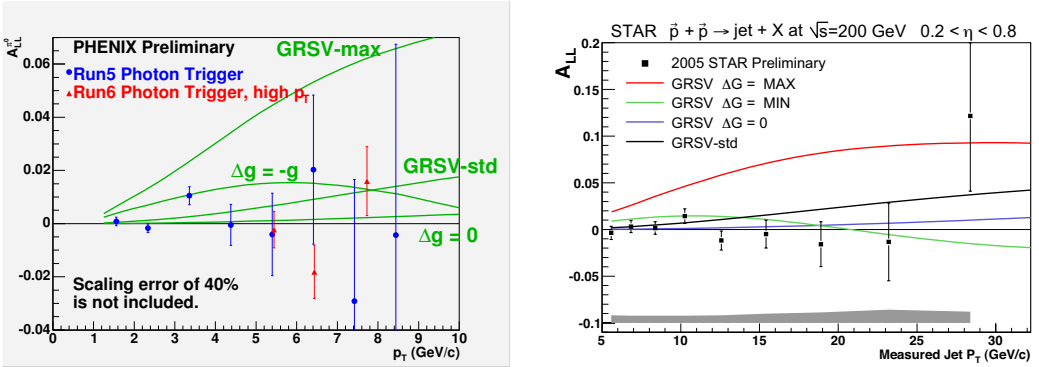

Figure 4: A_{LL} as a function of p_T. Left: For π^0 production from PHENIX. Right: for inclusive jet production at STAR

2.3 Double spin asymmetries in polarized proton-proton scattering

Another possibility to determine the gluon polarization, pursued by the PHENIX and STAR collaborations at the Relativistic Heavy Ion Collider (RHIC) are polarized proton-proton collisions. The experimentally determined quantity is a double spin asymmetry, A_{LL}, as a function of the transverse momentum of various final states. These asymmetries are then compared with theoretical predictions, including all partonic subprocesses like qq, qg and gg scattering, using different parameterizations of $\Delta G(x)$. Figure 4 shows A_{LL} as a function of p_T for π^0 production from PHENIX and Jet production from STAR. A comparison with the theoretical curves clearly indicates that the data prefer parameterizations with small ΔG. This becomes clearer in the quantitative analysis shown in Fig. 5. The left plot shows the χ^2 of a comparison of the PHENIX data with parameterizations of $\Delta G(x)$ as a function of the integral $\int_{0.02}^{0.3} \Delta G(x)\mathrm{dx}$. The right plot shows a similar plot for the STAR data. In both cases values of $\Delta G \gtrsim 0.5$ are excluded by the data. Details about the RHIC measurements including asymmetries of other final state can be found in [14, 15, 16].

One advantage of these measurements with respect to deep inelastic scattering is the higher available center of mass energy (up to $\sqrt{s} = 200$ GeV at the moment) compared to $\sqrt{s} = \sqrt{2ME} = \sqrt{2 \cdot 0.938 \cdot 160}\,\mathrm{GeV} = 17$ GeV for the COMPASS muon beam. This makes the perturbative QCD analysis of the data more reliable. On the other hand, the presence of two hadrons in the initial state makes the interpretation of the data more difficult compared to deep inelastic scattering where the nucleon is probed with a point-like particle.

2.4 Summary of Results on $\Delta G/G$

Although a combined analysis of all available data is still missing the following conclusion can be drawn. All measurements favor small first moments of the gluon helicity distribution $\Delta G = \int_0^1 \Delta G(x)\mathrm{dx}$ of the order $|\Delta G| \lesssim 1$. Scenarios with large value of ΔG of $2-3$ needed to reconcile results from deep inelastic scattering and quark models are excluded. Note that with the present precession a contribution of the gluon spin to the nucleon spin ranging from -100% to $+100\%$ is still possible and that the shape of $\Delta G(x)$ is not at all constrained.

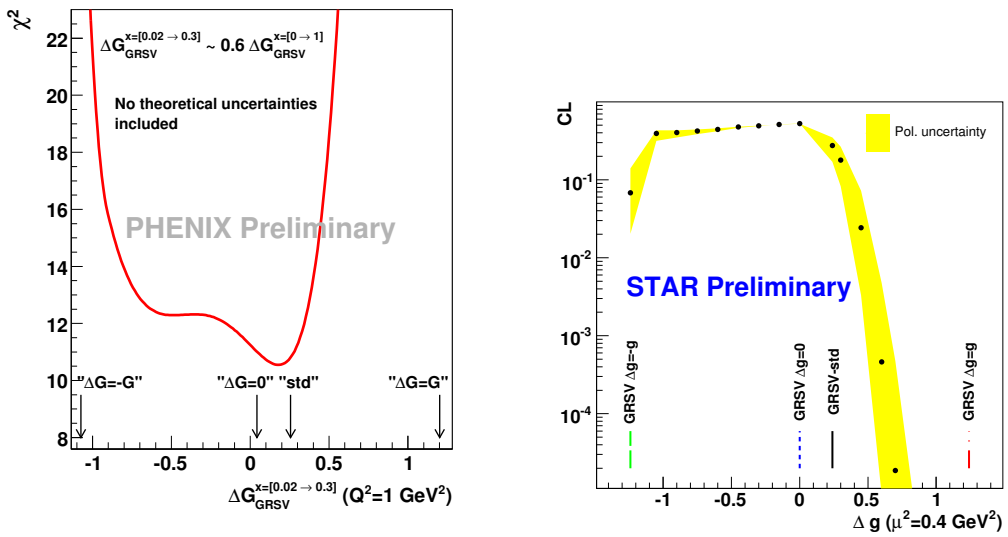

Figure 5: Left: χ^2 of a comparison of the PHENIX data with parameterization of $\Delta G(x)$ as a function of the integral $\int_{0.02}^{0.3} \Delta G(x_g) \mathrm{dx_g}$. Right: χ^2 confidence limits of a comparison of the STAR data with a parameterization of $\Delta G(x)$ as a function of the first moment ΔG.

3 The quark helicity contribution $\Delta q(x)$

Quark helicity distributions can be measured in semi-inclusive polarized deep inelastic scattering parallel to the measurement of ΔG, thus not requiring additional beam time. Here I will focus on two recent measurements by HERMES on the strange quark helicity distribution and by COMPASS on the helicity distribution of the valence quarks.

In general, at LO QCD a double spin asymmetry for a given hadron species is given by

$$A^h(x,z) = \frac{\Sigma_{q=u,d,s} e_q^2 (\Delta q(x) D_q^h(z) + \Delta\bar{q}(x) D_{\bar{q}}^h(z))}{\Sigma_{q=u,d,s} e_q^2 (q(x) D_q^h(z) + \bar{q}(x) D_{\bar{q}}^h(z))}$$

where the D_q^h are fragmentation functions. One advantage as compared to inclusive asymmetries is the possibility to disentangle the contribution of quarks and anti-quarks, because in general $D_q^h(z) \neq D_{\bar{q}}^h(z)$. Selecting different hadrons h allows to determine the contribution of the various quark flavors.

3.1 Strange Quark Helicity Distribution

HERMES has determined the strange quark helicity distribution from K^+ and K^- asymmetries and their inclusive asymmetry A_1^d [17]. The result is shown in Fig. 6. The contribution in the measured region is consistent with 0:

$$\int_{0.02}^{1} \Delta s(x)+\Delta\bar{s}(x)\mathrm{dx} = 0.006\pm0.029\pm0.007\,.$$

The NLO analysis of inclusive DIS data [4] yields a negative result for the first moment:

$$\int_{0}^{1} \Delta s(x)+\Delta\bar{s}(x)\mathrm{dx} = -0.08\pm0.01\pm0.02.$$

To find agreement between the HERMES result and the result from NLO QCD analysis a negative contribution of the $\Delta s(x) + \Delta\bar{s}(x)$ in the low x region, which will be covered by COMPASS data down to $x = 0.004$, is needed.

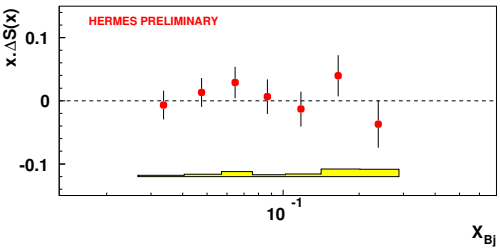

Figure 6: $x(\Delta s(x)+x\Delta\bar{s}(x))$ vs. x as obtained from HERMES inclusive and $K^{\pm}$ asymmetries on a deuteron target.

3.2 Valence Quark Helicity Distribution

The double spin asymmetry of the difference of positive and negative hadrons on a deuteron target gives directly the polarization of valence quarks in the nucleon:

$$A_d^{h^+-h^-} = \frac{(\sigma_{\uparrow\downarrow}^{h+} - \sigma_{\uparrow\downarrow}^{h-}) - (\sigma_{\uparrow\uparrow}^{h+} - \sigma_{\uparrow\uparrow}^{h-})}{(\sigma_{\uparrow\downarrow}^{h+} - \sigma_{\uparrow\downarrow}^{h-}) + (\sigma_{\uparrow\uparrow}^{h+} - \sigma_{\uparrow\uparrow}^{h-})} = \frac{\Delta u_V + \Delta d_V}{u_V + d_V}\,.$$

The contribution of the fragmentation functions drop out in this expression. Figure 7 left shows the difference asymmetry as a function of Bjorken x as measured by COMPASS.

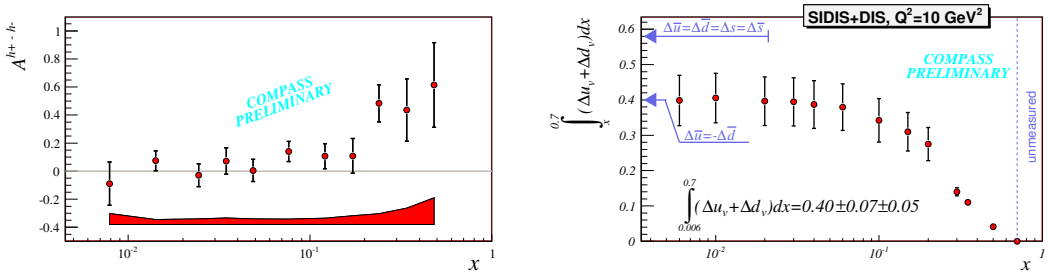

Figure 7: Left: The difference asymmetry $A_d^{h^+-h^-}$ vs. x from COMPASS data on a deuteron target. Right: The integral $\int_x^{0.7} \Delta u_v(x') + \Delta_d(x')\mathrm{dx}'$ vs. x.

Figure 7 right shows the integral $\int_x^{0.7} \Delta u_v(x') + \Delta_d(x')\mathrm{dx}'$ vs. x. In the unmeasured region $x > 0.7$ the unpolarized distribution $u_V + d_V$ is small which means that $\Delta u_V + \Delta d_V$

gives a negligible contribution. At low x the integral $\int_x^{0.7} \Delta u_v(x') + \Delta_d(x')\mathrm{dx}'$ saturates, such that the low x contribution can be assumed to be small as well. This means that the integral over the measured region and the first moment is practically the same. For the first moment one finds:

$$\Delta u_V + \Delta d_V = 0.40 \pm 0.07 \pm 0.05 \; .$$

A value below expectations from quark models. Note that the valence distribution does not receive corrections due to the axial anomaly like $\Delta\Sigma$ does.

From this data together with inclusive data, one can also deduce information about the polarization of the non-strange sea quarks. $A_d^{h^+-h^-}$ measures the valence quark polarization, the inclusive asymmetry A_1^d measures valence plus sea quark polarization. Thus the difference is sensitive to the sea:

$$\Delta\bar{u} + \Delta\bar{d} \approx 3\int_0^1 g_1^d \,\mathrm{dx} - \frac{1}{2}(\Delta \mathrm{u_V} + \Delta \mathrm{d_V}) + \frac{1}{12}\mathrm{a_8}$$

From the COMPASS data one finds

$$\Delta\bar{u} + \Delta\bar{d} = 0.00 \pm 0.04 \pm 0.03 \; .$$

This result is smaller than the contribution of the strange quarks extracted from the analysis of inclusive data and weak baryon decays and thus favors a non-SU(3) symmetric sea contribution. Details about this analysis can be found in [18].

4 The transversity distribution $\Delta q_T(x)$

Deep inelastic scattering on a transversally polarized target gives access to a number of new parton distribution functions. The most prominent ones are the so called Sivers function and the transversity distribution function $\Delta_T q(x)$. The Sivers function describes the correlation between the quark transverse momentum and the nucleon spin. The transversity distribution $\Delta_T q(x)$ has the same probabilistic interpretation in a transversally polarized nucleon as the helicity distribution in a longitudinally polarized nucleon.

Here I will focus on the transversity distribution. In semi-inclusive deep inelastic scattering various processes are proposed to measure $\Delta_T q(x)$: The Collins asymmetry, two hadron interference asymmetry and Λ polarization. In general:

Asymmetry (or Polarization) $\propto \Delta_T q \times$analyzing power .

The analyzing power, i.e. the measurement of the quark's final state polarization is different for the different processes and sometimes even not well known, underlining the importance to study several independent ways to determine $\Delta_T q(x)$.

In case of the Collins asymmetry one has

$$A_T^h \overset{(2)}{=} \frac{\sigma^\uparrow - \sigma^\downarrow}{\sigma^\uparrow + \sigma^\downarrow} \propto \frac{\Sigma_q e_q^2 \Delta_T q(x) \Delta_T^0 D_q^h(z)}{\Sigma_q e_q^2 q(x) D_q^h(z)} \; \sin(\Phi_S + \Phi) \; .$$

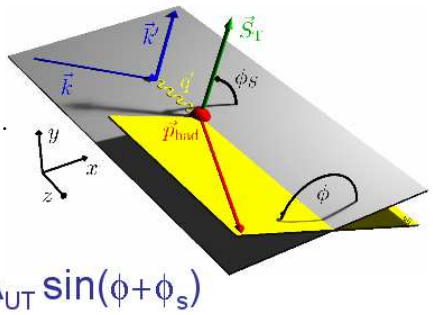

Figure 8: Definition of the angles used in eq. (2)

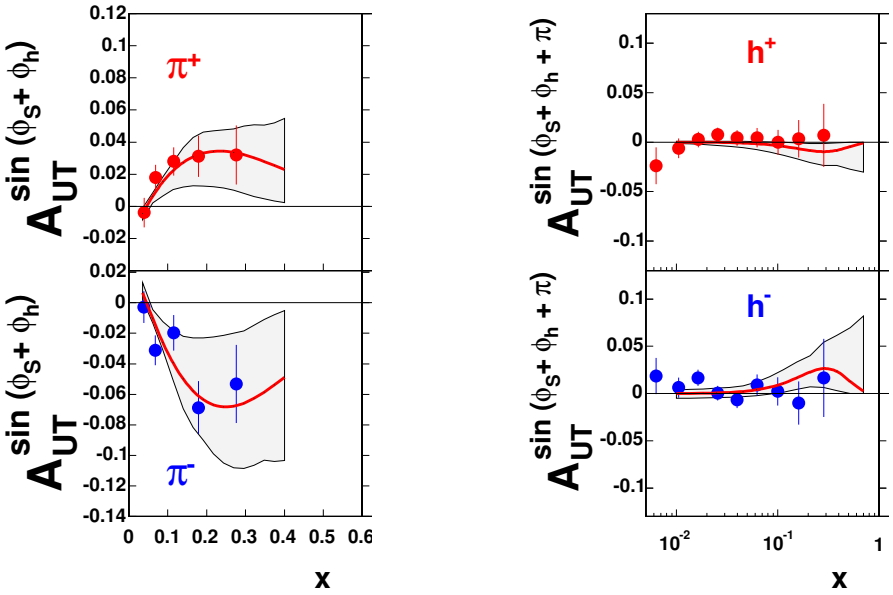

Figure 9: Collins asymmetries vs. x as used in the analysis of ref. [21]. Left: HERMES results for $\pi^{\pm}$ on a proton target. Right: COMPASS results for positive and negative hadrons on a deuteron target.

The angles appearing in eq.(2) are explained in Fig. 8. In this case the analyzing power is given by the Collins fragmentation function $\Delta_T^0 D_q^h(z)$. It describes the correlation between the spin of the quark q and the azimuthal angle of the hadron h.

Collins asymmetries were measured by HERMES on a proton target (Fig. 9, left), where non-zero asymmetries were observed and on a deuteron target by COMPASS (Fig. 9, right), where all asymmetries are consistent with 0 which can be explained by a cancellation between u and d quark contributions. The Collins fragmentation function was recently measured by BELLE [19, 20]. Figure 10 shows the favored and unfavored Collins fragmentation function normalized to the unpolarized fragmentation function D_q^h as a function of z extracted from the BELLE data in [21].

Combining the data on the Collins asymmetry and the fragmentation functions it was possible for the first time to extract $\Delta_T u(x)$ and $\Delta_T d(x)$ neglecting sea quark contributions [21, 22]. The resulting transverse quark distributions are shown in Fig. 11. The u-quark distributions, $\Delta_T u(x)$, is positive, $\Delta_T d(x)$ is negative, similar to the corresponding helicity distributions. The upper and lower blue lines show the Soffer bound $\Delta_T q(x) \leq 1/2|q(x) + \Delta q(x)|$.

At this conference more data were shown on transverse asymmetries [23, 24, 25, 26, 27, 28, 29] also from proton-proton scattering. In the future data on identified hadrons will also allow to extract the sea quark distributions.

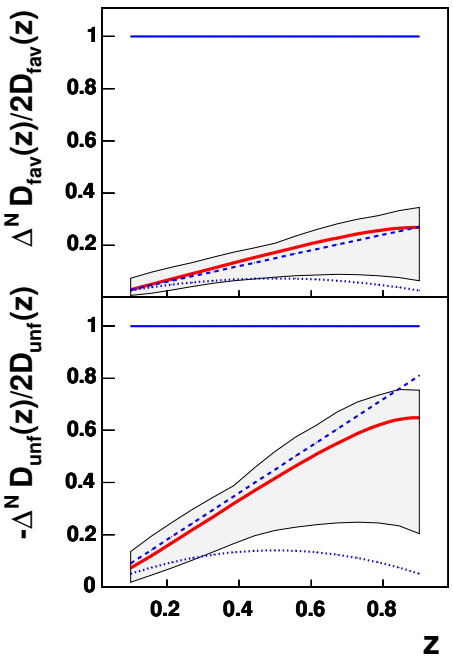

Figure 10: The Collins fragmentation function (black lines with error bands) normalized to the unpolarized fragmentation function from BELLE data[19, 21].

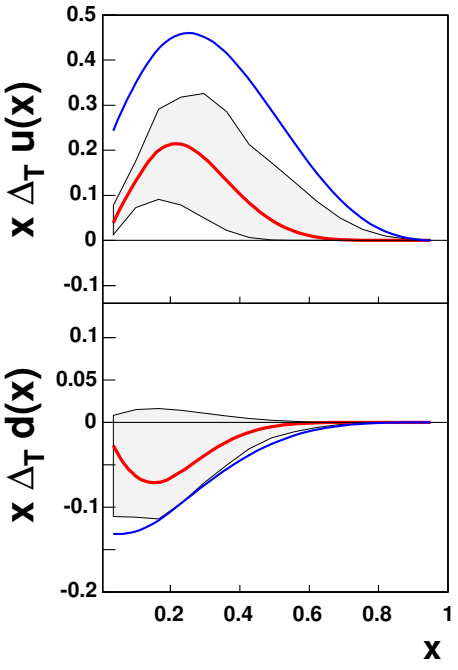

Figure 11: Transverse quark distributions $\Delta_T u(x)$ and $\Delta_T d(x)$ vs. x with error bands [21]. The upper and lower blue lines indicate the Soffer bound $\Delta_T q(x) \leq 1/2|q(x) + \Delta q(x)|$ [21].

5 Generalized Parton Distributions

Generalized parton distributions (GPD) are hybrids between form factors and parton distribution functions. They can be measured in deep virtual Compton scattering or deep virtual exclusive meson production. At leading twist 4 generalized parton distributions are defined: H ,E, $\tilde{H}$ and $\tilde{E}$.

Of particular interest in studying the spin structure of the nucleon is Ji's sum rule [30]:

$$\frac{1}{2}\int x(H_q + E_q)(x,\xi,0)dx = J_q = \frac{1}{2}\Delta\Sigma + L_q$$

which relates moments of the quark GPDs H_q and E_q to the the total angular momentum contribution J_q of a quark.

Figures 12 and 13 show results from HERMES [31] of a transverse target spin asymmetry on a proton target sensitive to J_u and from the JLab HALL A experiment [32] on

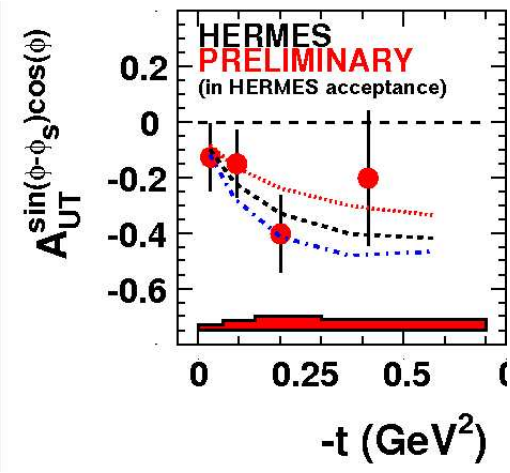

Figure 12: HERMES transverse target spin asymmetry on a proton target vs. proton momentum transfer t. The three curves are calculated using a model with $J_d = 0$ and correspond to $J_u = 0.4, 0.2, 0$ from top to bottom.[33]

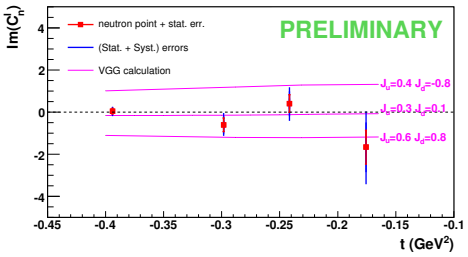

Figure 13: Difference of cross sections for a longitudinally polarized beam for the neutron vs. t from the JLab Hall A experiment. The three curves are from a model developed by Vanderhaeghen, Guichon and Guidal.

the difference between cross sections for a longitudinally polarized beam for the neutron sensitive to J_d. A combined analysis of these data will provide a measurement of J_u and J_d. Measurements on generalized parton distributions are planned at JLab, COMPASS and FAIR(GSI).

6 Summary and Outlook

Recent results from polarized deep inelastic lepton-nucleon scattering and polarized proton-proton scattering show that a large contribution of the gluon helicity to the nucleon spin to explain the nucleon spin puzzle is excluded. Nevertheless the data still leave room for gluon contribution to the nucleon spin ranging from -100% to $+100\%$. Further data, expected from COMPASS and RHIC, are needed to better determine shape and size of the gluon helicity contribution.

Collins asymmetries together with a recent measurement of the Collins fragmentation function allowed for the first time to determine the third basic parton distribution function $\Delta_T q(x)$. In this first analysis only the contribution of u and d quark were considered. In future more precise data will allow to determine also the contributions of other flavors.

In future, measurements of generalized parton distributions will give access to the orbital angular momentum contribution to the nucleon spin and hopefully allow to verify one day the spin sumrule in eq. (1).

References

[1] Slides:
http://indico.cern.ch/contributionDisplay.py?contribId=5&sessionId=2&confId=9499
[2] E. Leader, A. V. Sidorov and D. B. Stamenov, Phys. Rev. D **73** (2006) 034023
[3] E. Leader, A. V. Sidorov and D. B. Stamenov, Phys. Rev. D **75** (2007) 074027
[4] V. Y. Alexakhin *et al.* [COMPASS Collaboration], Phys. Lett. B **647** (2007) 8
[5] M. Hirai, S. Kumano and N. Saito, arXiv:hep-ph/0612037.
[6] D. Stamenov, these proceedings
[7] K. Kurek, these proceedings
[8] M. Glück, E. Reya, M. Stratmann and W. Vogelsang, Phys. Rev. D **63**, 094005 (2001)
[9] P. Liebing, these proceedings
[10] S. Koblitz, these proceedings
[11] E. S. Ageev *et al.* [COMPASS Collaboration], Phys. Lett. B **633** (2006) 25
[12] A. Airapetian *et al.* [HERMES Collaboration], Phys. Rev. Lett. **84** (2000) 2584
[13] B. Adeva *et al.* [Spin Muon Collaboration (SMC)], Phys. Rev. D **70**, 012002 (2004)
[14] F. Simon, these proceedings
[15] K. Okada, these proceedings
[16] R. Fatemi, these proceedings
[17] H.E. Jackson, SPIN 06 proceedings
[18] A. Korzenev, these proceedings
[19] K. Abe *et al.* [Belle Collaboration], Phys. Rev. Lett. **96** (2006) 232002
[20] R. Seidel, these proceedings
[21] M. Anselmino, M. Boglione, U. D'Alesio, A. Kotzinian, F. Murgia, A. Prokudin and C. Turk, Phys. Rev. D **75** (2007) 054032
[22] U. d'Alesio, these proceedings
[23] M. Diefenthaler, these proceedings
[24] A. Bresan, these proceedings
[25] C. Schill, these proceedings
[26] A. Kotzinian, these proceedings
[27] K. Eyser, these proceedings
[28] S. Heppelmann, these proceedings
[29] JH. Lee, these proceedings
[30] X. D. Ji, Phys. Rev. D **55** (1997) 7114
[31] A. Mussgiller, these proceedings
[32] E. Voutiert, these proceedings
[33] F. Ellinghaus, W. D. Nowak, A. V. Vinnikov and Z. Ye, Eur. Phys. J. C **46** (2006) 729

QCD and Monte Carlo generators

Zoltán Nagy

Theory Division, CERN CH-1211 Geneva 23, Switzerland
E-mail: Zoltan.Nagy@cern.ch

In this talk I gave a brief summary of leading order, next-to-leading order and shower calculations. I discussed the main ideas and approximations of the shower algorithms and the related matching schemes. I tried to focus on QCD issues and open questions instead of making a inventory of the existing programs.

1 Fix order calculations

1.1 Born level calculations

The simplest calculation what one can do is the Born level fix order calculation. This calculation involves the phase space integral of the tree level matrix element square and the jet measurement function. The structure of the cross section is

$$\sigma[F_J] = \int_m d\Gamma^{(m)}(\{p\}_m)|\mathcal{M}(\{p\}_m)|^2 F_J(\{p\}_m) \ , \tag{1}$$

where $d\Gamma^{(m)}(\{p\}_m)$ is the phase space integral measure, $\mathcal{M}(\{p\}_m)$ represents the m-paraton tree level matrix element and $F_J(\{p\}_m)$ is the jet measurement function that defines the physical observable.

This calculation is relatively simple. The integral free from the infrared and ultraviolet singularities. The matrix element is basically a complicated expression but it can be generated in a automated way. Several implementations can be found in the literature, Alpgen, Grace, Helac, Madgraph and Sherpa[2].

We can say that the tree level cross sections can predict the shape of the cross sections but in general they have several defects: i) Since it is the leading order term in the strong coupling expansion the result strongly depends on the unphysical renormalization and factorization scheme. ii) The exclusive physical quantities suffer on large logarithms. In the phase space regions where these logarithms are dominant the predictions are unreliable. iii) In the Born level calculations every jet is represented by a single parton, thus we don't have any information about the jet inner structure. iv) On the other hand in a real measurement, in the detector we can see hadrons and every jet consists many of them. We are not able to consider hadroniziation effects in the Born level calculations.

1.2 Next-to-leading order calculations

We can increase the precision of our theory (QCD) prediction by calculating the next term in the perturbative expansion, the next-to-leading order correction (NLO). However this is just one order higher to the Born cross section but the complexity of the calculations increases enormously. We have to face to algebraic and analytic complexity.

The naive structure of the NLO calculation is

$$\sigma_{\rm NLO} = \int_N d\sigma^B + \int_{N+1} d\sigma^R + \int_N d\sigma^V \ . \tag{2}$$

Here σ^B, σ^R and σ^V correspond to the Born, real and virtual contributions, respectively. This expression is well defined only in $d = 4-2\epsilon$ dimension because both the real and virtual terms are singular separately in $d = 4$ dimension, but their sum is finite. Thus we cannot calculate them separately, first we have to regularize this integral. In the real part the singularities comes from the phase space integral from the regions where a gluon becomes soft of two partons become collinear and the integral over these degenerated phase space regions leads to contributions those are proportional to $1/\epsilon$ and $1/\epsilon^2$. The infrared singularity structure of the virtual contributions is exactly the same but with opposite sign, thus they cancel each other. To achieve this cancellation we have to reorganize our calculation in such a way that can be carried out in $d = 4$ dimension

$$\sigma_{\mathrm{NLO}} = \int_N d\sigma^B + \int_{N+1} \left[d\sigma^R - d\sigma^A\right]_{\epsilon=0} + \int_N \left[d\sigma^V + \int_1 d\sigma^A\right]_{\epsilon=0} \ . \tag{3}$$

Here we subtracted the approximated version of real contribution and added it back in different form. In the second term $d\sigma^A$ cancels the singularities of $d\sigma^R$ and it is safe to perform the integral in $d = 4$ dimension while in the third term the explicit singularities of $d\sigma^V$ are cancelled by $\int_1 d\sigma^A$, where we performed the integral over the unresolved phase space analytically. It is important that the approximated real contribution has universal structure. This term is based on the soft and collinear factorization property of the QCD matrix elements. A general subtraction scheme was defined by Catani and Seymour [3] and the extenion of this method for massive fermions is also available [4].

The NLO calculation can be carried out but it hasn't been automated like the Born level calculations. The most complicated processes what we can calculate are $2 \to 3$ type [5]. To go beyond this limit we have to find an efficient way to compute the virtual correction. Recently we have had some very promising developement on this area [6].

With the NLO corrections we can significantly reduce the dependence on the renormalization and factorization scales but in some cases it is not enough and the NNLO is also required. In these calculations one of the jet is represented by two partons. This can give some minimal information about the inner jet structure but is still very poor. The exclusive quantities are still suffers on large logarithms and we are still not able to consider hadronization effects.

1.3 Next-to-next-to-leading order calculation

For some processes and/or jet observables it is important to know the cross sections at next-to-next-toleading order level. In this cases the NLO K-factor usually large even larger than 2 which means that the NLO correction doesn't reduce the scale dependences. Recently some simple but important processes have been calculated using sector decomposition method [7] and there are some ongoing developments on defining a general scheme for NNLO calculations [8].

2 Leading order parton shower

The fix order calculations are systematically defined order by order and usually give good description well the data over the phase space where the large p_T event are the dominant. In any order we still have to deal with the presence of the large logarithms and we cannot consider hadronization effect.

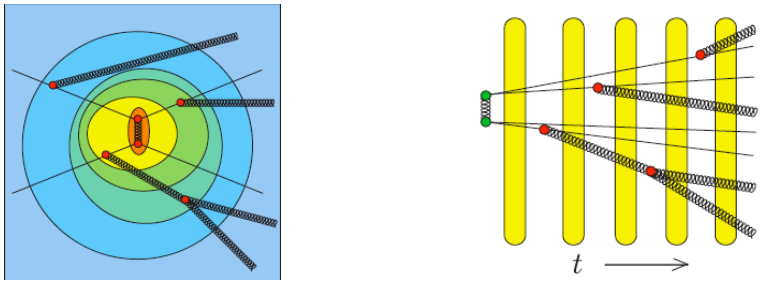

Real time picture Shower time picture

Figure 1: The left-hand picture depicts quark-quark scattering, with time proceeding from left to right. The hardest interactions are those toward the center of the picture. These are treated first in a parton shower Monte Carlo program. Thus in Monte Carlo time t, we start with the hard process and work toward softer interactions (with some of the particles moving backwards in real physical time), as depicted in the right hand picture. The rounded rectangles represent intervals of Monte Carlo time in which nothing happens.

There is an other way to calculate crass section in the perturbative framework, the parton shower calculations. Consider the parton shower picture of hadron-hadron scattering in which there is some sort of hard event, say jet production. The parton shower description starts form hard scattering and proceeds forward to the softer scattering. In the final state the shower proceed forward in real time but for initial state parton the sowers proceeds backward in real time. This is depicted in Figure 1.

2.1 Shower evolution

The parton shower evolution can be represented by an evolution equation and it is the solution of the following integral equation

$$\mathcal{U}(t_{\rm f},t_2)\big|\mathcal{M}_2\big) = \mathcal{N}(t_{\rm f},t_2)\big|\mathcal{M}_2\big) + \int_{t_2}^{t_{\rm f}} dt_3\, \mathcal{U}(t_{\rm f},t_3)\mathcal{H}(t_3)\mathcal{N}(t_3,t_2)\big|\mathcal{M}_2\big) \quad . \tag{4}$$

The shower evolution starts form the hard scattering and it is represented by the function $\big|\mathcal{M}_2\big)$ that is a probability of a given partonic state in shower time t_2. Then $\mathcal{U}(t_{\rm f},t_2)$ is the probability function of having a particular partonic state in a later evolution time $t_{\rm f}$. The evolution operator is sum of two terms. The first term in Eq. (4) represents parton evolution without splitting. The non splitting operator $\mathcal{N}(t_{\rm f},t_2)$ that inserts Sudakov factors giving the probability that nothing happens between time t_2 and $t_{\rm f}$. The Sudakov is the exponentiated inclusive (summed over spin and color and integrated over the momenta of unresolved partons) splitting kernel. The second term in Eq. (4) represent the splitting. The partonic state is evolved without splitting to an intermediate time t_3 and splitting happens given by the splitting operator $\mathcal{H}(t_3)$ and the system is evolved with possible splitting from t_3 to $t_{\rm f}$. The splitting operator is based on the universal soft and collinear factorization property of the QCD matrix element. This evolution equation is depicted in Figure 2.

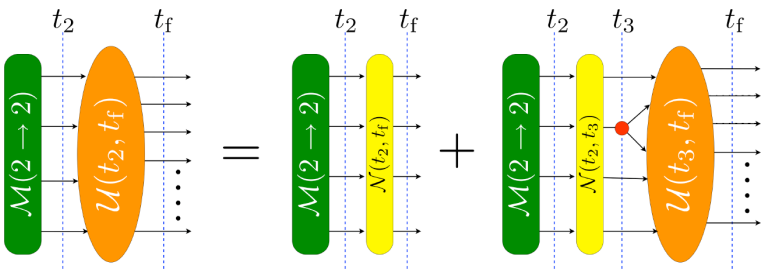

Figure 2: Evolution equation. The shower (*orange rectangle*) starts from the hard matrix elements (*green rounded rectangle*) and the partons are evolved to the final scale without splitting (*yellow rounded rectengle*) or with splitting at an intermediate time (*red circle*) and evolved to the finial scale with possible splittings.

2.2 Splitting operator

The splitting operator of the leading order (LO) shower is derived from the factorization property of the QCD matrix elements in the soft and collinear limits. This factorization property is universal. Let us start with collinear factorization.

When two parton become collinear the $m+1$ tree level matrix element (and the matrix element square) can be written as a convolution of m parton hard matrix element and a universal singular factor in the spin space. This factorization is depicted in Figure 3 at matrix element level.

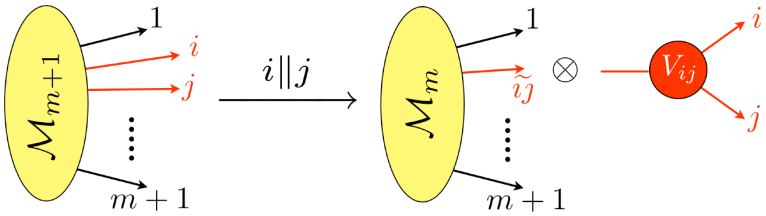

Figure 3: Collinear limit. The universal singular part is represented by the red circle and it is based on the $1 \to 2$ matrix element at LO level and the yellow ovals represent the corresponding m and $m+1$ parton matrix elements.

The collinear limit has some nice features. In the squared matrix element the singularity doesn't make color connection, it is completely factorized out. There are some spin correlation in the gluon splitting but this spin correlation is rather trivial. On the other hand one can always use spin averaged splitting functions but this is an additional approximation. Considering only the collinear emission our first "candidate" for the splitting kernel[a] would be

$$\overline{\mathcal{H}}(t) = \sum_{l=1}^{m} \boldsymbol{T}_l^2 \, V_{lm+1}(\hat{p}_l, \hat{p}_{m+1}) \big[V_{lm+1}(\hat{p}_l, \hat{p}_{m+1}) \big]^* \quad . \tag{5}$$

[a]For the shake of the simplicity I give a formal definition for the spin and color averaged splitting function which actually appears in the Sudakov exponent.

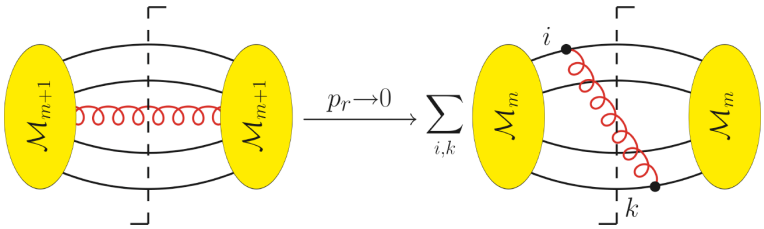

Figure 4: Soft factorization. The soft gluon is represented by the red wiggle line and the tree level matrix elements by the yellow ovals. The soft gluon can be emitted from any hard parton thus it makes color connections all possible way.

Here $\boldsymbol{T}_l$ is the color charge operator of the mother parton and V_{lm+1} is the vertex function. Every parton can split and after the splitting the daughter partons are labeled by l and $m+1$. The momenta of the daughter partons are $\hat{p}_l$ and $\hat{p}_{m+1}$. With collinear splitting operator one can sum up the leading (double) logarithmic contributions properly.

The matrix element has universal factorization property in the soft limit, when the energy of a final state gluon becomes zero. We cannot neglect soft gluon contributions since they produce next-to-leading logarithms when we integrate the matrix elements over the phase space. The structure of the soft gluon radiation is depicted in Figure 4. In this case we have non-trivial color structure because the soft gluon makes color connections all the possible way between the hard partons. Combining the soft factorization formulae with collinear one our splitting kernel is given by

$$\overline{\mathcal{H}}(t) = \sum_{l=1}^{m} \sum_{\substack{k=1 \\ k \neq l}}^{m} \boldsymbol{T}_l \cdot \boldsymbol{T}_k \, V_{lm+1}(\hat{p}_l, \hat{p}_{m+1}) \left[V_{km+1}(\hat{p}_k, \hat{p}_{m+1}) - V_{lm+1}(\hat{p}_l, \hat{p}_{m+1}) \right]^* \quad . \tag{6}$$

Here we used the color conservation, that is $\boldsymbol{T}_l^2 = -\boldsymbol{T}_l \cdot \sum_{k \neq l} \boldsymbol{T}_k$. One can show that the expression under the square brackets vanishes in large angle limit when $\vartheta_{lk} \ll \vartheta_{lm+1}, \vartheta_{km+1}$ (The ϑ_{ij} denotes the angle between momenta p_i and p_j.). This effect is know as *color coherence*. Note, the color coherence breaks down with massive hard partons (quarks, SUSY particles). In this case we have wide angle soft radiations.

This is it, we defined a splitting kernel based on the soft and collinear approximation. With this we are able to sum up the leading and next-to-leading logarithms. We still have some freedom, for example the definition of splitting kernel away from the limits or the momentum mapping. The evolution (ordering) parameter can be basically any infrared sensitive variable such as the virtuality or the transverse momentum of the daughter partons. Note, if we want to consider spin and color correlations properly in the parton shower we *cannot* avoid negative weights. So far there is only one algorithm has been defined along this ideas [9] but it hasn't been implemented yet. From the point of the implementation, the color interferences make some complications but one can impose some further approximations to simplify it.

HERWING[10] and OLD PYTHIA[11] implement direct angular ordering[12]. Inserting the

conditions for the emission angles into Eq. (6) then we have

$$\overline{\mathcal{H}}(t) = -\frac{1}{2}\sum_{l=1}^{m}\sum_{\substack{k=1\\k\neq l}}^{m} \boldsymbol{T}_l\cdot\boldsymbol{T}_k \left\{|V_{lm+1}|^2\theta(\vartheta_{lm+1}<\vartheta_{lk}) + |V_{km+1}|^2\theta(\vartheta_{km+1}<\vartheta_{lk})\right\} + \cdots \quad , \quad (7)$$

where the dots stand for the neglected terms those are finite in both soft and collinear limits. Note, these contributions are finite only after we perform the integral over the azimuthal angle of $\hat{p}_{m+1}$ about the direction p_l and p_k. If we consider only those phase space regions where emissions are ordered in angle then $\theta(\vartheta_{lm+1} < \vartheta_{lk}) = \theta(\vartheta_{km+1} < \vartheta_{lk}) = 1$ and the color part of Eq. (7) becomes trivial and the approximated splitting kernel is identical to the collinear splitting kernel which is given in Eq. (5).

The other way to simplify the color structure is to expand the splitting kernel in powers of $1/N_c^2$, where N_c is the number of the color states in fundamental representation. The gluon is a color $\mathbf{8}$, but in leading color approximation the gluon can be considered to be a $\mathbf{3}\otimes\bar{\mathbf{3}}$. The partons makes $\mathbf{3}\bar{\mathbf{3}}$ color dipoles with other partons but at leading color level the gluon never makes a color dipole with itself. The color connection operator $\boldsymbol{T}_l\cdot\boldsymbol{T}_k$ becomes simple, it is non-zero if the partons l and k makes a $\mathbf{3}\bar{\mathbf{3}}$ color dipole and the approximated splitting operator is identical to the collinear splitting kernel given in Eq. (5). In this approximation it is important that the momentum mapping must be exact or based on dipole kinematics; if parton l radiates a gluon then the recoiled parton must be the color connected one. ARIADNE[13] and the NEW PYTHIA[11] implement this approximation. There are some new developments [14] based on the leading color approximation and they implement this color dipole shower model.

The parton shower algorithms have been derived from perturbative QCD but we cannot consider them as theory predictions because they use rather nonsystematic approximations. The original idea was to consider and simulate higher order matrix element by using only soft and collinear factorization of the QCD matrix elements. This is a systematical approximation since the factorization properties of the matrix elements are held all order. At the end of this section it is worthwhile to highlight the addition approximations and the limitation of the available parton shower implementations:

1. The current parton shower programs are still leading order calculations however they consider higher order contributions in an approximated way. Dependence on the unphysical scales is still strong.
2. The phase space is usually treated approximately. The angular ordered showers don't cover the phase space properly ("dead cone") and some special treatment is required to to fill these regions.
3. The direct angular ordering or the leading color approximation neglect the color correlations. The color interferences could be significant in the case of non-global observables [15]. Usually the spin correlations are also neglected. HERWIG considers spin correlations.
4. They are not defined systematically. The direct angular ordering is not defined or hard to define at higher order. Even the kinematics of the dipole shower model is inconsistent with the higher order. We have some freedom to define the splitting kernel and momentum mapping but the core algorithm should independent of the level of the calculation.

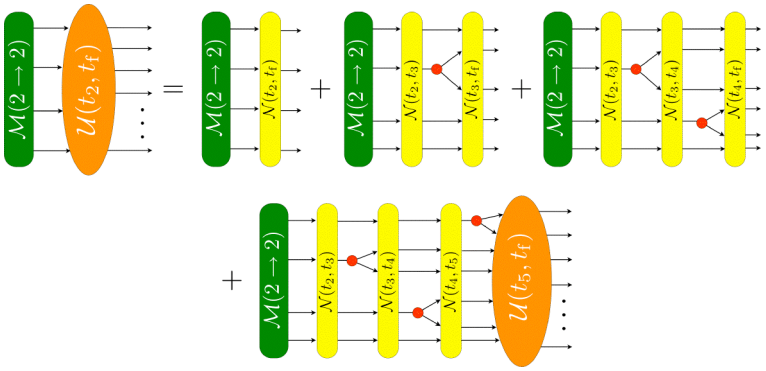

Figure 5: Calculation of a shower starting with a $2 \to 2$ hard cross section (green rounded rectangle). The shower evolution operator has been iterated twice, so that the first term represents no splitting, the second term has one splitting, the third term has two splittings, and the final term contains contributions with three or more splittings.

5. The only exact matrix element in the calculations is $2 \to 2$ like. If we want to calculate say $3, 4, 5, ...$-jet cross section we should use $2 \to 3, 4, 5, ...$ LO or NLO matrix elements. In the next section I discuss the matching of shower to exact matrix elements.
6. More questions on non-perturbative effects: What is underlying event? How can we model it? How to consider quantum interferences in hadronization models?

3 Matching parton showers to fix order calculations

3.1 Born level matching

The standard shower depicted in Figure 5 has a deficiency, which is illustrated in Figure 6. The left-hand picture depicts a term contributing to the standard shower. In this term, there are Sudakov factors and $1 \to 2$ parton splitting functions. If we omit the Sudakov factors, we have the $1 \to 2$ parton splittings as depicted in the middle picture. These splittings are approximations based on the splitting angles being small or one of the daughter partons having small momentum. Thus the shower splitting probability with two splittings approximates the exact squared matrix element for $2 \to 4$ scattering. The approximation is good in parts of the final state phase space, but not in all of it. Thus one might want to replace the approximate squared matrix element of the middle picture with the exact squared matrix element of the right-hand picture. However, if we use the exact squared matrix element, we lack the Sudakov factors.

One can improve the approximation as illustrated in Figure 7. We reweight the exact squared matrix element by the ratio of the shower approximation with Sudakov factors to the shower approximation without Sudakov factors. The idea is to insert the Sudakov factors into the exact squared matrix element. This is the essential idea in the paper of Catani, Krauss, Kuhn, and Webber [16]. They use the k_T jet algorithm to define the ratio needed to calculate the Sudakov reweighting factor.

There is another way to improve shower as illustrated in Figure 8. First we generate the event according to the shower and then rewieght it by the ratio of the exact and approximated

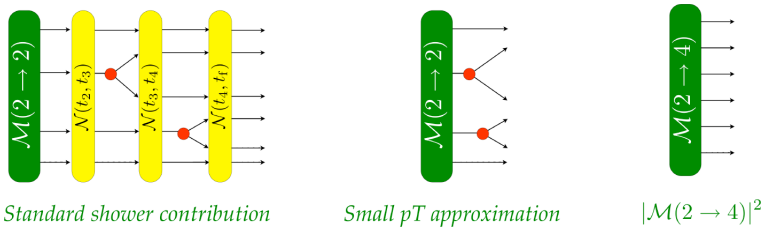

Figure 6: The left-hand picture is the $2 \to 4$ cross section in shower approximation. The center picture is the shower approximation omitting the Sudakov factors. The right hand picture is the exact tree level $2 \to 4$ cross section. The cross section based on splitting functions (middle picture) is a collinear/soft approximation to this.

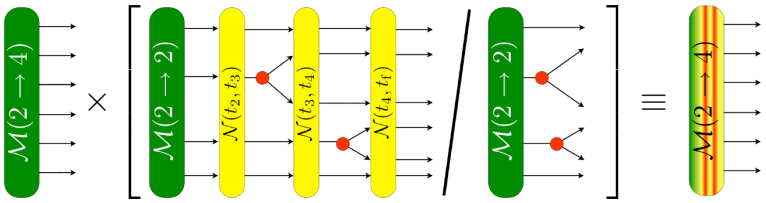

Figure 7: An improved version of the $2 \to 4$ cross section. First we generate the 4-parton configuration according to the exact matrix element and take the shower approximation (with sudakov factors), divide by the approximate collinear squared matrix element, and multiply by the exact tree level squared matrix element. The graphical symbol on the right hand side represents this Sudakov reweighted cross section.

matrix element. The approximated matrix element is calculated over a unique emission history that is determined by a jet algorithm. The original MLM algorithm [17] uses the cone algorithm. The advantage of this method over the CKKW method is that the algorithm use the native Sudakov factors of the underlying parton shower.

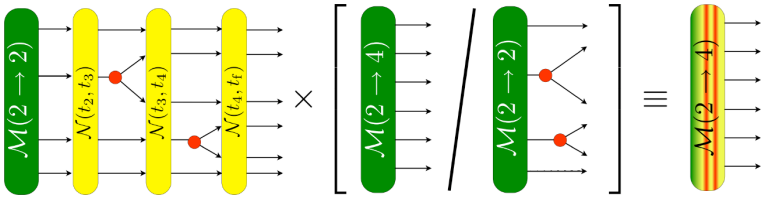

Figure 8: An improved version of the $2 \to 4$ cross section with matrix element reweighting factor.

There is a further step in implementing this idea. CKKW divide the shower evolution into two stages, $0 < t < t_{\rm ini}$ and $t_{\rm ini} < t < t_{\rm f}$, where $t_{\rm ini}$ is a parameter that represents a moderate P_T scale and $t_{\rm f}$ represents the very small P_T scale at which showers stop and hadronization is simulated.

With this division, the Sudakov reweighting can be performed for the part of the shower

at scale harder than $t_{\rm ini}$, as depicted in Figure 9. The first term has no splittings at scale harder than $t_{\rm ini}$. In the second term there is one splitting, generated via the exact matrix element with a Sudakov correction as discussed above. In the next term there are two splittings. If we suppose that we do not have exact matrix elements for more than $2 \to 4$ partons, states at scale $t_{\rm ini}$ with more partons are generated with the ordinary parton shower. However, this contribution is suppressed by factors of α_s. Evolution from $t_{\rm ini}$ to $t_{\rm f}$ is done via the ordinary shower algorithm.

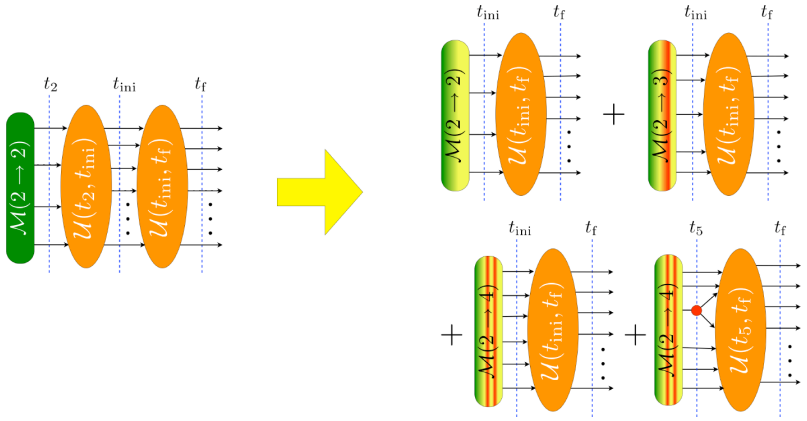

Figure 9: Shower with CKKW jet number matching. The calculation for n jets at scale $t_{\rm ini}$ is based on the Sudakov reweighted tree level cross section for the production of n partons.

To state the main idea of this jet number matching in a little different language, we can consider the cross section for an observable F. In the CKKW method, we break $\sigma[F]$ into a sum of contributions $\sigma_m[F]$ from final states with m jets at resolution scale $t_{\rm ini}$. Then $\sigma_m[F]$ is evaluated using the exact tree level matrix element for $2 \to m$ parton scattering, supplemented by Sudakov reweighting and further supplemented by showering of the $m+2$ partons at scales softer than $t_{\rm ini}$. If F is an infrared safe observable, this method gets $\sigma_m[F]$ correct to the leading perturbative order, α_s^m. The method can be extended. The present authors have shown (at least for the case of electron-positron annihilation) how to get $\sigma_m[F]$ for an infrared safe observable correct to next-to-leading order, α_s^{m+1} [18]. The required NLO adjustments are a little complicated, so I do not discuss them here.

3.2 Next-to-leading order matching

Matching parton shower with NLO fix order calculation is a very active field of parton shower developments. There are two basic approaches. First one is the MC@NLO project [19]. The main idea here is to avoid the double counting by introducing extra counterterm which is extracted out from the underlying shower algorithm. This method has been applied for several $2 \to 0+X$ where no colored object in the final state and some $2 \to 1+X$, $2 \to 2+X$ processes, where the QCD particles in the final state are heavy [19].

The other approach was originally proposed by Krämer and Soper [20] and they implemented it for $e^+e^- \to$ 3-jets. The idea is to include the first step of the shower in the NLO calculation and then start the parton shower from this configuration. Based on this concept some matching algorithm have been proposed but they are haven't been implemented

[14, 18, 21]. In the next I discuss in detail only the MC@NLO approach because only this scheme has been implemented for LHC processes so far.

Let us start with the NLO cross section. After applying a subtraction scheme to remove the infrared singularities, we have

$$\sigma_{\rm NLO} = \int_m \left[d\sigma^B + d\sigma^V + d\sigma^C + \int_1 d\sigma^A\right] F_{\rm J}^{(m)} + \int_{m+1} \left[d\sigma^{\rm R} F_{\rm J}^{(m+1)} - d\sigma^{\rm A} F_{\rm J}^{(m)}\right] \quad , \tag{8}$$

where $d\sigma^B$, $d\sigma^{\rm R}$, $d\sigma^V$, $d\sigma^C$ and $d\sigma^A$ are the Born, real, virtual contributions, collinear counterterm and subtraction term of the NLO scheme, respectively. The physical quantity is defined by the functions $F_{\rm J}^{(m)}$ and $F_{\rm J}^{(m+1)}$.

The naive way to add parton shower corrections is to replace the jet functions with the shower interface function. This approach is not good because it leads to double counting. It is easy to see, the shower that starts from the Born term generates higher order contributions those are already considered by NLO terms.

To avoid double counting Frixione and Webber [19] organized the calculation in the following way:

$$\begin{aligned}\sigma_{\rm MC} = & \int_m \left[d\sigma^B + d\sigma^V + d\sigma^C + \int_1 d\sigma^A\right] I_{\rm MC}^{(2\to m)} \\ & + \int_{m+1} \left[d\sigma_{m+1}^{\rm R} - d\sigma_{m+1}^{\rm MC}\right] I_{\rm MC}^{(2\to m+1)} + \int_{m+1} \left[d\sigma_{m+1}^{\rm MC} - d\sigma_{m+1}^{\rm A}\right] I_{\rm MC}^{(2\to m)} \quad .\end{aligned} \tag{9}$$

Here the contribution $d\sigma_{m+1}^{\rm MC}$ is extracted from the underlying parton shower algorithm. The functions $I_{\rm MC}^{(2\to m)}$ and $I_{\rm MC}^{(2\to m+1)}$ are the interface functions to the shower. We have different choices for the m and $m+1$ parton interface functions, thus we have

$$I_{\rm MC}^{(2\to m)} \sim \mathcal{U}(t_{\rm f}, t_m) \qquad \text{and} \qquad I_{\rm MC}^{(2\to m+1)} \sim \mathcal{U}(t_{\rm f}, t_{m+1})\mathcal{N}(t_{m+1}, t_m) \ . \tag{10}$$

In the m-parton case we simply start the shower from the m-parton configuration while in the $m+1$ parton case first we insert some Sudakov factor representing the probability of nothing happens between the m-parton and $m+1$ parton states and starts the shower from the $m+1$ parton configuration.

There are some limitation of the MC@NLO approach: i) It is worked out for HERWIG. One has to redo the Monte Carlo subtraction scheme if we want to match say PYTHIA to NLO computations. ii) Matching procedure is defined only for simple processes like $2 \to 0 + X, 1 + X, 2$. iii) The double counting problem is not fully solved but it is probably numerically invisible because of the strong Sudakov suppression. The problem related to the soft singularities and it appears only in the $2 \to 2$ like processes where the color structure is not trivial.

4 Conclusions

Parton shower event generators have proved to be an essential tool for particle physics. These computer programs perform calculations of cross sections according to an approximation to the standard model or some of its possible extensions. Because of the great success of these programs, it is worthwhile to investigate possible improvements.

In a typical parton shower event generator, the physics is modeled as a process in classical statistical mechanics. Some number of partons are produced in a hard interaction. Then each parton has a chance to split into two partons, with the probability to split determined from an approximation to the theory. Parton splitting continues in this probabilistic style until a complete parton shower has developed.

The underlying approximation is the factorization of amplitudes in the soft or collinear limits. However, further approximations are usually added: i) The interference between a diagram in which a soft gluon is emitted from one hard parton and a diagram in which the same soft gluon is emitted from another hard parton is treated in an approximate way, with the "angular ordering" approximation. ii) Color is treated in an approximate way, valid when $1/N_c^2 \to 0$ where $N_c = 3$ is the number of colors. iii) Parton spin is treated in an approximate way. According to the full quantum amplitudes, when a parton splits, the angular distribution of the daughter partons depends on the mother parton spin and even on the interference between different mother-parton spin states. This dependence is typically ignored. With the use of these further approximations, one can get to a formalism in which the shower develops according to classical statistical mechanics with a certain evolution operator.

I think the way to improve the parton showers is to formulate it based on the factorization of amplitudes in the soft or collinear limits in which one does not make the additional approximations enumerated above. For this, one would have to use quantum statistical mechanics instead of classical statistical mechanics.

On the other hand the parton shower algorithm should cooperate with exact LO and NLO matrix elements. Currently we have some very promising tools such as CKKW, MLM and MC@NLO matching schemes. The CKKW and MLM matching procedures patch the "hole" between the Born level fix order and the shower calculations while the MC@NLO and other NLO matching schemes do the same between the shower and fix order NLO calculations. If we want more precise tools we need more advanced framework. We need a general LO shower framework that naturally includes the LO and NLO calculation. Or phrase it differently, we should reformulate the LO and NLO calculation to make the shower part of them.

5 Acknowledgment

I am greatful to the organizers of the DIS 2007 workshop for their invitation as well as for providing a pleasant atmosphere during the meeting. This work was supported by the Hungarian Scientific Research Fund grants OTKA T-60432.

References

[1] Slides:
`http://indico.cern.ch/contributionDisplay.py?contribId=6&sessionId=2&confId=9499`

[2] M. L. Mangano, M. Moretti, F. Piccinini, R. Pittau and A. D. Polosa, JHEP **0307** (2003) 001 [arXiv:hep-ph/0206293]; G. Belanger, F. Boudjema, J. Fujimoto, T. Ishikawa, T. Kaneko, K. Kato and Y. Shimizu, Phys. Rept. **430** (2006) 117 [arXiv:hep-ph/0308080]; A. Kanaki and C. G. Papadopoulos, Comput. Phys. Commun. **132** (2000) 306 [arXiv:hep-ph/0002082]; F. Maltoni and T. Stelzer, JHEP **0302** (2003) 027 [arXiv:hep-ph/0208156]; T. Gleisberg, S. Hoche, F. Krauss, A. Schalicke, S. Schumann and J. C. Winter, JHEP **0402** (2004) 056 [arXiv:hep-ph/0311263].

[3] S. Catani and M. H. Seymour, Nucl. Phys. B **485** (1997) 291 [Erratum-ibid. B **510** (1998) 503] [arXiv:hep-ph/9605323].

[4] S. Catani, S. Dittmaier, M. H. Seymour and Z. Trocsanyi, Nucl. Phys. B **627** (2002) 189 [arXiv:hep-ph/0201036].

[5] Z. Nagy, Phys. Rev. D **68** (2003) 094002 [arXiv:hep-ph/0307268]; Z. Nagy and Z. Trocsanyi, Phys. Lett. B **634** (2006) 498 [arXiv:hep-ph/0511328]; J. M. Campbell, R. Keith Ellis and G. Zanderighi, JHEP **0610** (2006) 028 [arXiv:hep-ph/0608194]; J. Campbell, R. K. Ellis and D. L. Rainwater, Phys. Rev. D **68** (2003) 094021 [arXiv:hep-ph/0308195].

[6] G. Ossola, C. G. Papadopoulos and R. Pittau, Nucl. Phys. B **763** (2007) 147 [arXiv:hep-ph/0609007]; T. Binoth, J. P. Guillet and G. Heinrich, JHEP **0702** (2007) 013 [arXiv:hep-ph/0609054]; Z. Nagy and D. E. Soper, JHEP **0309** (2003) 055 [arXiv:hep-ph/0308127]; C. F. Berger, Z. Bern, L. J. Dixon, D. Forde and D. A. Kosower, Phys. Rev. D **74** (2006) 036009 [arXiv:hep-ph/0604195]; Z. Bern, L. J. Dixon and D. A. Kosower, Phys. Rev. D **71** (2005) 105013 [arXiv:hep-th/0501240]; C. Anastasiou, R. Britto, B. Feng, Z. Kunszt and P. Mastrolia, JHEP **0703** (2007) 111 [arXiv:hep-ph/0612277]; R. Britto, B. Feng and P. Mastrolia, Phys. Rev. D **73** (2006) 105004 [arXiv:hep-ph/0602178]; T. Binoth, G. Heinrich, T. Gehrmann and P. Mastrolia, Phys. Lett. B **649** (2007) 422 [arXiv:hep-ph/0703311]

[7] G. Heinrich, Nucl. Phys. Proc. Suppl. **116** (2003) 368 [arXiv:hep-ph/0211144]; T. Binoth and G. Heinrich, Nucl. Phys. B **693** (2004) 134 [arXiv:hep-ph/0402265]; C. Anastasiou, K. Melnikov and F. Petriello, Phys. Rev. Lett. **93** (2004) 262002 [arXiv:hep-ph/0409088].

[8] A. Gehrmann-De Ridder, T. Gehrmann, E. W. N. Glover and G. Heinrich, Nucl. Phys. Proc. Suppl. **160** (2006) 190 [arXiv:hep-ph/0607042]; A. Gehrmann-De Ridder, T. Gehrmann and E. W. N. Glover, JHEP **0509** (2005) 056 [arXiv:hep-ph/0505111]; G. Somogyi, Z. Trocsanyi and V. Del Duca, JHEP **0701** (2007) 070 [arXiv:hep-ph/0609042]; G. Somogyi and Z. Trocsanyi, JHEP **0701** (2007) 052 [arXiv:hep-ph/0609043]; S. Catani and M. Grazzini, arXiv:hep-ph/0703012; S. Weinzierl, Phys. Rev. D **74** (2006) 014020 [arXiv:hep-ph/0606008].

[9] Z. Nagy and D. E. Soper, arXiv:0706.0017 [hep-ph] and these proceedings
`http://indico.cern.ch/contributionDisplay.py?contribId=205&sessionId=6&confId=9499`

[10] G. Marchesini, B. R. Webber, G. Abbiendi, I. G. Knowles, M. H. Seymour and L. Stanco, Comput. Phys. Commun. **67** (1992) 465 ; S. Gieseke *et al.*, [arXiv:hep-ph/0609306].

[11] T. Sjöstrand, Comput. Phys. Commun. **82** (1994) 74; T. Sjöstrand, S. Mrenna and P. Skands, JHEP **0605** (2006) 026 [arXiv:hep-ph/0603175].

[12] G. Marchesini and B. R. Webber, Nucl. Phys. B **238** (1984) 1; R. K. Ellis, G. Marchesini and B. R. Webber, Nucl. Phys. B **286** (1987) 643 [Erratum-ibid. B **294** (1987) 1180].

[13] L. Lönnblad, Comput. Phys. Commun. **71** (1992) 15.

[14] Z. Nagy and D. E. Soper, arXiv:hep-ph/0601021.

[15] J. R. Forshaw, A. Kyrieleis and M. H. Seymour, JHEP **0608** (2006) 059 [arXiv:hep-ph/0604094]; M. Dasgupta and G. P. Salam, Phys. Lett. B **512** (2001) 323 [arXiv:hep-ph/0104277].

[16] S. Catani, F. Krauss, R. Kuhn and B. R. Webber, JHEP **0111** (2001) 063 [arXiv:hep-ph/0109231]; L. Lönnblad, JHEP **0205** (2002) 046 [arXiv:hep-ph/0112284]; N. Lavesson and L. Lönnblad, JHEP **0507** (2005) 054 [arXiv:hep-ph/0503293];

[17] M. L. Mangano, M. Moretti, F. Piccinini and M. Treccani, JHEP **0701** (2007) 013 [arXiv:hep-ph/0611129].

[18] Z. Nagy and D. E. Soper, JHEP **0510** (2005) 024 [arXiv:hep-ph/0503053].

[19] S. Frixione and B. R. Webber, JHEP **0206** (2002) 029 [arXiv:hep-ph/0204244]; S. Frixione, P. Nason and B. R. Webber, JHEP **0308** (2003) 007 [arXiv:hep-ph/0305252]; S. Frixione and B. R. Webber, arXiv:hep-ph/0612272.

[20] M. Krämer and D. E. Soper, Phys. Rev. D **69** (2004) 054019 [arXiv:hep-ph/0306222]; D. E. Soper, Phys. Rev. D **69** (2004) 054020 [arXiv:hep-ph/0306268]; M. Krämer, S. Mrenna and D. E. Soper, Phys. Rev. D **73** (2006) 014022 [arXiv:hep-ph/0509127].

[21] P. Nason, JHEP **0411** (2004) 040 [arXiv:hep-ph/0409146].

Jefferson Lab Physics Overview: Recent Results

Z.-E. Meziani *

Temple University - Department of Physics
1900 N. 13th St., Philadelphia, PA 19122-6082 - USA

I review highlights of the Jefferson Lab nucleon structure program. I shall emphasize recent results from experiments exploring the spin structure of the nucleon and from dedicated experiments aimed at accessing the generalized parton distributions (GPDs) [1].

1 Introduction

A very rich experimental program on the structure of the nucleon has been carried out at Jefferson Laboratory using the continuous electron beam with a maximum energy of 6 GeV and about 80 % polarization. A series of polarized targets, ^{3}He in Hall A and NH_3 and ND_3 in hall B and C, combined with a variety of detection schemes, using high resolutions or large acceptance spectrometers, provided for the needed luminosity critical to precision measurements of asymmetries and polarized cross sections in deep inelastic scattering or deep virtual Compton scattering (DVCS) . There is now a large body of spin structure data on the proton, deuteron and neutron that allows us to study quantum chromodynamics (QCD) in the non-perturbative regime, that is at a scale of about Λ_{QCD}. Sum rules are used to test our understanding of the theory as we decrease the probe resolution from the size of current quarks to that of the nucleon passing by the size of constituent quarks. Furthermore, a new series of dedicated DVCS experiments have been performed to provide precision data necessary to constrain the generalized parton distributions (GPDs), required for a three-dimensional mapping of the internal nucleon structure.

2 Sum rules Q^2 evolution

Sum rules involving the spin structure of the nucleon offer an important opportunity to study QCD. Among the examples are the Bjorken sum rule[2] at infinite four-momentum transfer ($Q^2 = \infty$) and the Gerasimov, Drell and Hearn (GDH) sum rule[3] at the real photon point ($Q^2 = 0$). These sum rules relate the first moments of the spin structure functions (or, equivalently, the spin-dependent total photoabsorption cross sections) to the nucleon's static properties. The above sum rules are based on "unsubtracted" dispersion relations and the optical theorem[4]. Furthermore, another general assumption, such as a low energy theorem[5] for the GDH sum rule and operator production expansion (OPE)[6] for the Bjorken sum rule, is needed to relate the Compton amplitude to a static property. In the case of the GDH sum rule it is the anomalous magnetic moment $\kappa_{p,n}$ while for the Bjorken sum rule it is the nucleon axial coupling constant g_A. The large set of new spin structure of the nucleon data allows us to address the convergence of the expansion, as Q^2 decreases form very large values to values of the order of Λ_{QCD}, and to evaluate the higher twists contributions.

One example is the study of the evolution to low Q^2 values of the Bjorken sum in order to extract the higher twists contributions. These contributions contain information about

*This work is supported in part by DOE grant contract DE-FG02-94ER40844 .

quark-quark and quark-gluon correlations. The Bjorken sum rule is evaluated at finite Q^2 using the following expression:

$$\Gamma_1^{p-n} = \int_0^1 (g_1^p - g_1^n)dx = \frac{g_A}{6}\left[1 - \frac{\alpha_s}{\pi} - 3.58\left(\frac{\alpha_s}{\pi}\right)^2 - 20.21\left(\frac{\alpha_s}{\pi}\right)^3 + ...\right] + O\left(\frac{1}{Q^2}\right). \quad (1)$$

Deviations from the above expression are due to higher twists contributions which can be extracted by direct comparison with the data over a wide range of Q^2.

Figure 1 shows the evolution of the Bjorken integral when the contribution of elastic scattering is not included. The Bjorken sum rule sets the absolute scale for $\overline{\Gamma}_1^{p-n}$ at large Q^2 and the difference between the leading twist contribution shown by the grey band in Figure 1 and the data gives an estimate of higher twists as Q^2 decreases to about 1 GeV^2. An overall suppression of higher twist effects is observed to surprisingly low Q^2. An analysis of the data, which includes the elastic contribution, down to $Q^2 = 0.8$ GeV^2 allowed the extraction of the non-singlet twist-4 matrix element f_2^{p-n} [7]. The singlet pieces corresponding to the proton and the neutron were determined in References [8] and [9] respectively. The combination of the twist-4 f_2^{p-n} matrix element with the twist-3 matrix element d_2^{p-n} extracted from these measurements of g_1 and g_2 gave access to "color polarizabilities" for the first time with limited precision. More data from the Eg1b experiment in Hall B with much higher statistical precision will be available soon for publication.

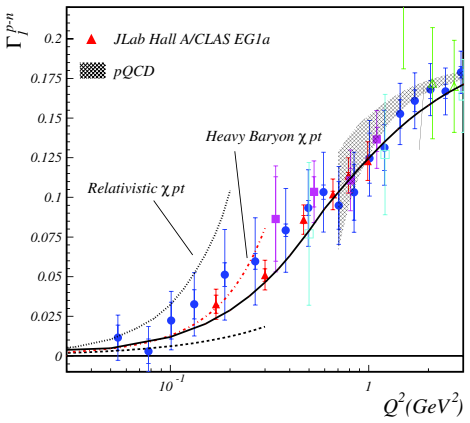

Figure 1: Data on the evolution of the Bjorken integral excluding the elastic contribution which is negligible at large Q^2 but becomes significant below $Q^2 = 1$ GeV^2. The leading twist pQCD evolution is shown by the grey band. Close to the photon point ($Q^2 = 0$) the covariant chiral perturbation and the heavy baryon chiral perturbation calculations are shown.

3 Helicity Dependent Parton Distributions

The virtual photon-neutron asymmetry A_1^n and spin structure function g_1^n are poorly known in the valence quark region ($x > 0.3$). This shortcoming is due to the small scattering cross sections at large x and Q^2 combined with a lack of high polarized luminosity facilities. This region, however, is clean and unambiguous since it is not polluted by sea quarks and gluons offering thus a unique opportunity to test predictions that are difficult if not impossible at low x.

The set of predictions of A_1^n in the valence quark region fall into two categories, those of relativistic constituent quark models (RCQM) which break SU(6) symmetry in the ground state wave function by hyperfine interaction [10, 11, 22] and include orbital angular momentum implicitly, and those of perturbative quantum chromodynamics (pQCD) with a hadron

helicity conservation (HHC) constraint [12, 13] as $x \to 1$ which break SU(6) symmetry dynamically.

The difference between these approaches is dramatic when the constituents flavor-spin decomposition is performed. For a proton and in the case of pQCD with HHC, we have $\Delta u(x)/u(x) \to 1$ and $\Delta d(x)/d(x) \to 1$, while for the case of RCQM's $\Delta u/u \to 1$, $\Delta d/d \to -1/3$. We note that in leading order pQCD with HHC $\Delta d/d$ changes sign from negative at low x to positive starting at around $x = 0.3$.

Using Jefferson Lab unparalleled polarized luminosity, data of the asymmetries of the neutron A_1^n [16] and the proton A_1^p [17] were obtained . The quark parton model interpretation of g_1 and F_1 was used to perform a flavor decomposition of the spin dependent quark distributions assuming a negligible strange quark contribution above $x = 0.3$. The up-quark and down-quark distributions obtained along with results from HERMES semi-inclusive measurements [18] are shown in Fig. 2.

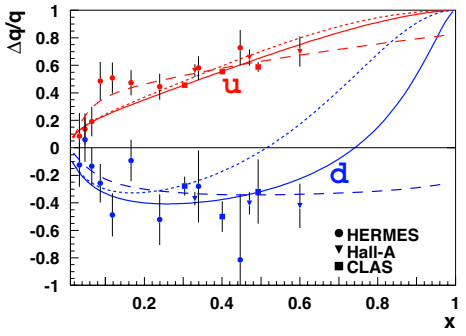

Figure 2: Spin-flavor dependent up-quark and down-quark distributions for a proton extracted from this experiment and the world data using the quark-parton model. The curves describe a pQCD leading order calculation [14] without (short dashed line) and with orbital angular momentum (solid line). The long dashed line is a quark-diquark calculation from Ref. [22] described in the text.

The solid line is a pQCD leading order fit to the world data using the HHC constraint as $x \to 1$. The long dashed line correspond to an RCQM prediction [22]. It is clear that up to $x = 0.6$ the data favor the RCQM rather than the HHC pQCD based calculations. While in the former some OAM is included through the small components of the nucleon wave function in the latter no orbital angular momentum (OAM) until recently [14]. The result of including the OAM is shown in Fig. 2 with the solid line, where the agreement with the data is fair up to $x = 0.6$. Of course this gives a strong motivation to test the role of OAM at even larger x than 0.6, where the difference between pQCD and the RQCM still remains large.

These results point to the importance of considering the orbital momentum of quarks in the nucleon wave function and in the extraction of the nucleon universal quark-helicity distributions.

3.1 Quark-hadron duality in the spin structure of the nucleon

One of the fascinating aspects of nucleon structure, known as "quark-hadron duality", is an observation made in the early 70's by Bloom and Gilman[19] while investigating the spin-independent nucleon response in deep inelastic lepton scattering (DIS). These authors found that, in the scaling regime at large momentum transfers, this response is well described by an average over the resonances structure at lower momentum transfers. Subsequently, in an attempt to explain this observation within the framework of QCD, De Rújula, Georgi and Politzer [20] used the OPE method to suggest a possible link between the average over the resonances response and the DIS scaling response. While many studies were performed

on the spin-independent response functions of the nucleon [57, 21], a renewed interest has emerged in testing this "duality" behavior in the spin-dependent response functions [22, 23]. In principle with a deeper understanding of QCD and its confinement properties one should be able to predict the observed behavior in either case. With the OPE method one has the opportunity to test the validity of our expansion at low momentum transfers by extracting the higher twist contributions and investigating the convergence and breakdown of such an expansion. Compared to the spin-independent response of the nucleon, the study the spin-dependent response offers a new variety of matrix elements of operators which describe quark-quark and quark-gluon interactions beyond the naive quark-parton model.

We show in Fig. 3 new preliminary results of JLab experiment E01-012 [28] where the virtual photon-nucleus asymmetry A_1 of ^{3}He was measured at several momentum transfers with excitation energies spanning the nucleon resonance region. For the lowest Q^2 data points, the prominent feature is the Δ resonance with a noticeable negative asymmetry. As Q^2 increases we notice that the asymmetry crosses over to positive values and becomes Q^2 independent similar to the DIS case. This is suggestive to a behavior of the resonance region similar to that of the DIS region and thus to a duality phenomenon. This behavior is comparable to what was observed in the proton case [23]. This duality has been studied quantitatively using the new data and it is shown that "global duality" of the neutron and ^{3}He polarized structure function g_1 holds well above $Q^2 = 1.8$ GeV^2.

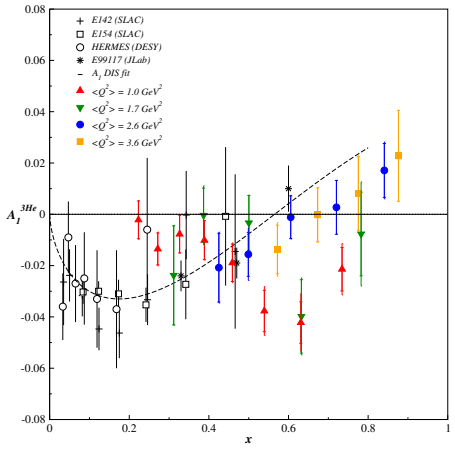

Figure 3: Preliminary result of the asymmetry A_1 for ^{3}He in the resonance region along the world ^{3}He DIS data [25, 26, 27, 16]. The outer error bars are total uncertainties while the inner bars represent the statistical part only. The resonance data of the JLab experiment are represented by the filled symbols. The curve is a fit of the $A_1^{^3\mathrm{He}}$

4 Color Polarizabilities

While g_1 discussed earlier can be understood in terms of the Feynman's parton model which describes the scattering in terms of *incoherent* parton scattering, g_2 cannot. Using the operator product expansion (OPE) [29, 30], it is possible to interpret the g_2 spin structure function beyond the simple quark-parton model. In fact g_2 provides a unique opportunity to study the quark-gluon correlations in the nucleon which are otherwise inaccessible. According to the optical theorem, g_2 is the imaginary part of the spin-dependent doubly virtual Compton amplitude which involves the t-channel helicity exchange +1. When it is factorized in terms of parton sub-processes, the intermediate partons must carry this helicity exchange. Because of chirality conservation in vector coupling, massless quarks in perturbative processes cannot produce a helicity flip. Nevertheless, in QCD this helicity exchange may occur in the following two ways: first, single quark scattering in which the quark carries one unit of orbital angular momentum through its transverse mo-

mentum wave function; second, quark scattering with an additional transversely-polarized gluon from the nucleon target. The two mechanisms are combined in such a way to yield a gauge-invariant result. Consequently, g_2 provides a direct probe of the quark-gluon correlations in the nucleon wave function. In particular the piece of interesting physics is contained in the second moment in x of a linear combination of g_1 and g_2,

$$d_2(Q^2) = \int_0^1 x^2[2g_1(x,Q^2) + 3g_2(x,Q^2)]dx \tag{2}$$

This specific combination of g_1 and g_2 filters out the free quark scattering interaction exposing the higher twist or quark-gluon interaction. The quantity $d_2(Q^2)$ is a twist-three matrix element which is related to a certain quark-gluon correlation, and describes how the gluon field inside the nucleon responds when this latter is polarized. Due to parity conservation, a color magnetic field $\vec{B}$ can be induced along the nucleon polarization (spin direction) while a color electric field $\vec{E}$ in the plane perpendicular to the polarization". In fact d_2 can be written as [31, 32]

$$d_2 = (2\chi_B + \chi_E)/3 \ . \tag{3}$$

where χ_B and χ_E are the gluon-field polarizabilities defined in the rest frame of the nucleon using the color-singlet operators $O_B = \psi^\dagger g\vec{B}\psi$ and $O_E = \psi^\dagger\vec{\alpha}\times g\vec{E}\psi$:

$$\chi_{B,E}2M^2\vec{S} = \langle PS|O_{B,E}|PS\rangle \ . \tag{4}$$

where M is the nucleon mass and $\vec{S}$ its spin.

Presently d_2^p and d_2^n have been evaluated using state of the art computers in the framework of lattice QCD. The proton d_2 world data have a precision equivalent to that of the present lattice QCD calculation. This situation might change soon with the rapid increase in computers processing speed. The neutron data lack the precision required for a meaningful comparison. The present results are very encouraging but much experimental progress needs to be achieved for a definitive comparison with the data.

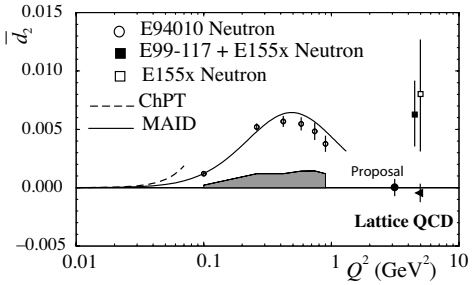

Figure 4: The quantity $\bar{d}_2(Q^2)$ is shown at several values of Q^2. The results of JLab E94-010[39] without the nucleon elastic contribution are the solid circles . The grey band represents their corresponding systematic uncertainty. The SLAC E155 [33] neutron result is the open square. The solid line is the MAID calculation[34] while the dashed line is a HBχPT calculation[35] valid only at very low Q^2. The lattice prediction [36] at $Q^2 = 5$ GeV^2 for the neutron d_2 reduced matrix element is negative but close to zero. We note that many nucleon models not shown in this figure predict a negative or zero value at large Q^2 where the elastic contribution is negligible. The SLAC datum shows a positive value of d_2^n but with a rather large error bar. The projected errors of this proposal are the filled circles

4.1 Precision measurement of the neutron d_2

Measurements of the helicity dependent cross sections in the large x (valence) region are essential for the determination of higher moments of g_1^p and g_2^p. These moments are the

natural connection between experiment and observables calculable in lattice QCD. Lattice QCD calculations do not directly determine spin observables but rather moments of the various polarized and unpolarized structure functions. Lattice QCD collaborations hope to calculate the moments of these structure functions without the quenching approximation and with near-physical pion masses in the next few years employing Teraflop·Year computing resources. Results available today still require extrapolations to the chiral limit[36].

Figure 4 shows how the approved experiment, JLab E06-114 [38], will impact the neutron present comparison between theory and experiment if one uses 20 days of the 6 GeV polarized electron beam on the polarized ^{3}He target and the Bigbite spectrometer to detect the scattered electrons at large angle (40°). The improvement is rather impressive and will prove to be powerful as both the calculations and the experiment reach new precision levels. This experiment is planned to run in the spring of 2008..

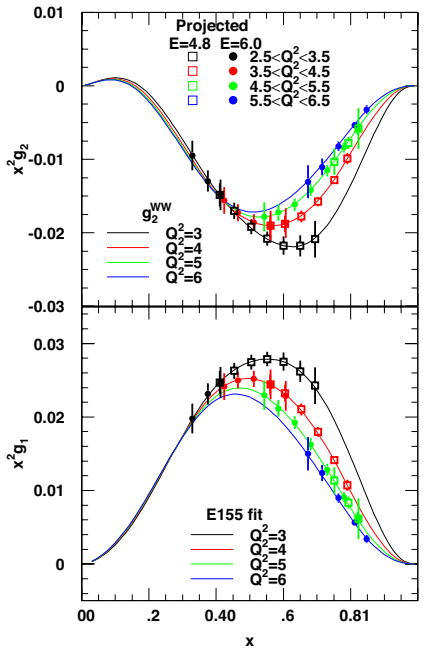

Figure 5: Statistical uncertainties in $x^2 g_2^p$ and $x^2 g_1^p$ in $\Delta Q^2 = 1$ GeV^2 bins as a function of x. The E155 fit [37] to g_1/F_1 was used to calculate g_1 and g_2^{WW} for the solid lines. The projected uncertainties for 6.0 GeV are shown as solid circles and for 4.8 GeV as hollow squares.

4.2 Spin Asymmetries on the Nucleon Experiment (SANE)

Although there is a large world data set for A_1^p, the trend of the data in the limit $x \to 1$ is not clear, and is completely inadequate for estimating all but the first moment of g_1^p. Our goal is to obtain precision A_1^p and A_2^p results at the largest possible x. A new experiment with a significant increase in Figure of Merit for making high x spin structure function measurements was proposed and approved. The experiment is called SANE (**S**pin **A**symmetries on the **N**ucleon **E**xperiment) [40], and is based on a 194 msr electron detector viewing the UVa polarized NH_3 target operating at 8.5×10^{34} proton-luminosity.

The proposed measurements of g_1^p and g_2^p (Fig. 5 shows the projected uncertainties of the proposed measurement) will allow us to determine d_2^p with unprecedented precision at several values of $Q^2 < 6$ (GeV/c)^2 for a significantly improved determination of this fundamental quantity.

The SANE experiment is planned to be carried during the summer 2008 in Hall C using an NH_3 polarized target. The scattered electrons will be detected in a newly built Big Electron Telescope Array ($BETA$) detector. The goal is to perform the measurement of two asymmetries for two different orientations of the target magnetic field relative to the beam direction. And to extract in the proton A_1^p only limited by systematic errors and a

simultaneous statistics limited measurement of g_2^p in the range $0.3 \leq x \leq 0.8$ at an average Q^2=4.5 GeV^2. The measured A_1 and g_2 will be used to study their Q^2 dependence at fixed x in both the DIS and resonance region, probe the approach of A_1 to $x = 1$ at constant Q^2 in order to test quark models and pQCD.

Finally, in both the neutron or proton case the sea contribution (or disconnected diagrams) is neglected in the present Lattice QCD calculations. However since d_2 is a higher moment of spin structure functions those contributions to the total integral are likely to be small. The non-singlet combination $d_2^p - d_2^n$ will be used as a true benchmark test of Lattice QCD calculations since this quantity is free from the "disconnected diagrams" (sea contributions) which are less likely to be evaluated in the next few years.

5 Generalized Parton Distributions

A comprehensive framework has been developed in the last ten years to unravel the structure of the nucleon [41, 42, 43] (see also reviews and references therein [44, 45, 46, 47]). In this framework it is shown that the nucleon structure is encoded in the so-called generalized parton distributions (GPDs). For the nucleon, which is a spin 1/2 composite particle, four universal functions for quarks denoted by H_f E_f, $\tilde{H}_f$ and $\tilde{E}_f$ describe the helicity-conserving and the helicity-flip nucleon matrix elements of the vector and axial-vector current for quark flavor q. Similarly four gluon GPDs describe the gluon structure of the nucleon. Each quark GPD corresponds to the amplitude of probability for removing a quark of momentum fraction $x + \xi$ and restoring it in the nucleon with a momentum fraction of $x - \xi$. The overall momentum transfer received by the nucleon is denoted by the Mandelstam variable $t = \Delta^2$ and in an impact parameter space, defined by the Fourier transform of the transverse momentum $\Delta_\perp$, the GPDs represent distributions of partons of longitudinal momentum x in the transverse plane [48, 49, 50, 51]. These functions can be identified, in specific limits of their variables, as the elastic form factors of the nucleon measured in electron elastic scattering or parton distributions measured in inclusive deep inelastic lepton scattering. Within this new framework it was shown that one way to access the GPDs is through deep exclusive processes. However an important aspect of the interpretation of the measured cross section of a given deep exclusive process in terms of GPDs is its factorization into a hard-part that is calculable and a soft-part that embeds the structure, namely the GPDs.

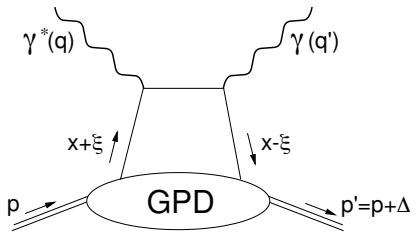

Figure 6: Lowest order amplitude for the virtual Compton scattering process. Shown are the initial four-momentum vectors of the incident virtual photon q and the real scattered photon q' as well as the initial p and final p' four-momentum of the nucleon. x is the Bjorken scaling variable and $\xi = x/(2 - x)$ called skewedness.

5.1 Deep Virtual Compton Scattering

It was recognized early that Deep Virtual Compton Scattering (DVCS) would be an ideal process to study because factorization might be possible at fixed x and $|t| \ll Q^2$ but relatively low Q^2 ($\sim$ few GeV^2). This range of Q^2 is accessible at the present maximum electron beam energy of Jefferson Lab namely 6 GeV. The DVCS amplitude is typically expressed in terms of integrals over x of GPDs and has the following form

$$T^{DVCS} \sim \int_{-1}^{+1} \frac{H(x,\xi,t)}{x \pm \xi - i\epsilon} dx + ... \sim \mathcal{P} \int_{-1}^{+1} \frac{H(x,\xi,t)}{x \pm \xi} dx - i\pi H(\pm\xi,\xi,t) \qquad (5)$$

Clearly observables like the cross section of the DVCS process is usually expressed in terms of integrals of GPDs. However, the use of a polarized beam or a polarized target gives access to the imaginary part of the GPDs and thus allows a direct access to the GPDS at specific values of x namely $x = \pm\xi$. This unique situation arises because of the interference between the DVCS and the Bethe-Heitler process through polarization observables.

Up to now most of the existing data showing the DVCS signals originated from non dedicated experiments [54, 55, 56]. Taking advantage of the interference between the DVCS and the Bethe-Heitler process a series of dedicated experiments have been recently performed at Jefferson Lab to determine the DVCS amplitude. In Hall A a dedicated experiment [52] using a highly longitudinally polarized electron beam was scattered of a hydrogen target. The scattered electrons were detected in the standard High Resolution Spectrometer, the outgoing photons and protons were detected in a lead fluoride calorimeter with fast digitizing electronics and and plastic scintillator annular array respectively. This setup allowed for unprecedented luminosities, of about 10^{37}, even with the calorimeter in direct view of the hydrogen target. Helicity dependent cross sections differences ($d^4\Sigma_{LU}$ were measured at three kinematical points where $x = 0.36$ was fixed but Q^2 increased from 1.5 GeV^2 to 2.3 GeV^2. Due to the high resolution and well matched acceptance of the spectrometer and the calorimeter $ep \to ep\gamma$ events were clearly identified and $ep \to e\gamma X$ background shape was calibrated using the proton array and subtracted when necessary.

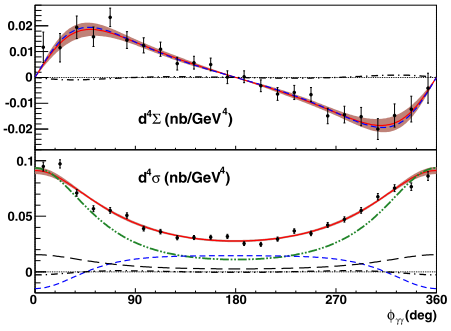

Figure 7: Hall A results for helicity dependent and helicity-independent cross sections as a function of the azimuthal angle $\phi_{\gamma\gamma}$ at $x = 0.35$, $Q^2 = 2.3$ GeV^2 and $t = -0.28$ GeV^2.

Fig. 7 shows the result of the azimuthal distribution of the helicity dependent and independent DVCS cross section. Although the Q^2 range scanned is small, no Q^2 dependence of the extracted amplitudes is observed pointing to scaling and the validity of the dominance of the leading order contribution represented by the diagram of Fig. 6

In a subsequent experiment a deuterium target was used with a slightly different setup to determine the quasi-free DVCS on the neutron. In this case there is direct sensitivity to the GPD E which is needed to evaluate Ji's spin sum rule [57]. Preliminary results can be

seen in reference [53]

In Hall B another dedicated experiment [58] was performed with full exclusivity of the $ep \to ep\gamma$ process thanks to the detection of all three final states particles. This was achieved by adding a new inner calorimeter to the standard CLAS configuration and a super-conducting solenoid surrounding the hydrogen target to eliminate the intense Möller scattering background, in the range of 5° to 15°, which otherwise would swamp the calorimeter at the required luminosity. The calorimeter was made out of lead-tungstate crystals read by state of the art technology developed at the LHC, namely by avalanche photodiode stabilized in temperature. This was the first experiment were this technology has been used successfully. The large acceptance of the spectrometer allowed for a wide kinematic coverage in x, t and Q^2. The preliminary results of asymmetries were shown at this conference but are not ready for public release.

6 Conclusion

A strong and diverse program of nucleon spin structure and of three-dimensional mapping of nucleon internal structure through the determination of GPDs is being carried at Jefferson Lab using the maximum beam energy of 6 GeV. This program has a natural extension as the laboratory is preparing for the energy upgrade to 12 GeV incident beam energy. Specific experimental proposals are being submitted to the 12 GeV program advisory committee and some have already been approved . The reader can obtain more information on 12 GeV proposals at the following urls [59].

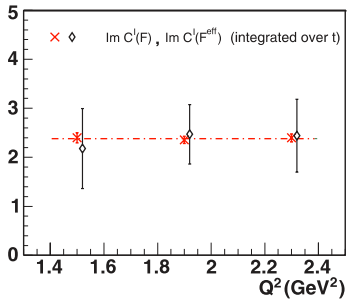

Figure 8: Q^2 dependence of the imaginary parts of (twist-2) $\mathcal{C}^{\mathcal{I}}(\mathcal{F})$ and (twist-3) $\mathcal{C}^{\mathcal{I}}(\mathcal{F}^{\rm eff})$ angular harmonics averaged over t. See Ref. [52] for more details

7 Acknowledgment

I would like to first thank the organizers, in particular, A. Caldwell and C. Weiss for the opportunity to present part of the Jefferson Lab exciting program on nucleon structure. I also would like to thank some of my colleagues and collaborators who helped me gather the results presented in this talk, among them J.-P. Chen, M. Garcon, C. Munoz-Camacho, E. Voutier, N. Liyanage, A. Deur, and P. Solvignon. This work was supported by DOE contract DE-AC05-84ER40150 under which the Southeastern Universities Research Association (SURA) operates the Thomas Jefferson National Accelerator Facility.

References

[1] Slides:
`http://indico.cern.ch/contributionDisplay.py?contribId=7&sessionId=2&confId=9499`

[2] J. D. Bjorken, Phys. Rev. **148**, 1467 (1966); Phys. Rev. D **1**, 465 (1970); Phys. Rev. D **1**, 1376 (1970).

[3] S. B. Gerasimov, Sov. J. Nucl. Phys. **2**, 598 (1965); S. D. Drell and A. C. Hearn, Phys. Rev. Lett. **16**, 908 (1966).

[4] see, J. D. Bjorken and S. D. Drell, "Relativistic Quantum Fields", McGraw Hill, New York (1965).

[5] F. E. Low, Phys. Rev. **96**, 1428 (1954).
[6] K. Wilson, Phys. Rev. **179**, 1499 (1969).
[7] A. Deur *et al.*, Phys. Rev. Lett. **93**, 212001 (2004).
[8] M. Osipenko *et al.*, Phys. Rev. D **71**, 054007 (2005), hep-ph/0503018.
[9] Z. E. Meziani *et al.*, Phys. Lett. B **613**, 148 (2005), hep-ph/0404066.
[10] F. Close and A. W. Thomas, Phys. Lett. B **212**, 227 (1988).
[11] N. Isgur, Phys. Rev. D **59**, 034013 (1999).
[12] G. R. Farrar and A. D. Jackson, Phys. Rev. Lett. **35**, 1416 (1975).
[13] S. J. Brodsky, M. Burkhardt and I. Schmidt, Nucl. Phys. B **441**, 197 (1995).
[14] H. Avakian, S. J. Brodsky, A. Deur and F. Yuan, hep-ph/0705.1553.
[15] I. C. Cloet, W. Bentz and A. W. Thomas, Phys. Lett. B **621**, 246 (2005), hep-ph/0504229.
[16] X. Zheng *et al.* [Jefferson Lab Hall A Collaboration], Phys. Rev. Lett. **92**, 012004 (2004) and Phys. Rev. C **70**, 065207 (2004)
[17] K. V. Dharmawardane *et al.* [CLAS Collaboration], Phys. Lett. B **641**, 11 (2006), nucl-ex/0605028.
[18] A. Airapetian *et al.* [HERMES Collaboration], Phys. Rev. Lett. **94**, 012002 (2005)
[19] E. D. Bloom and F. J. Gilman, Phys. Rev. Lett. **25**, 1140 (1970) and Phys. Rev. D **4**, 2901 (1971).
[20] A. De Rújula, H. Georgi and H. D. Politzer, Annals Phys. (N.Y.) **103**, 315 (1977).
[21] W. Melnitchouk, R. Ent and C. Keppel, Phys. Rept. **406**, 127 (2005), hep-ph/0501217.
[22] F. Close and W. Melnitchouk, Phys. Rev. C **68**, 035210 (2003), hep-ph/0302013.
[23] A. Airapetian *et al.* [HERMES Collaboration], Phys. Rev. Lett. **90**, 092002 (2003), hep-ex/0209018.
[24] X. Ji and W. Melnitchouk, Phys. Rev. D **56**, 1 (1997).
[25] P. L. Anthony *et al.* [SLAC E142 Collaboration], Phys. Rev. D **54**, 6620 (1996), hep-ex/9610007.
[26] K. Abe *et al.* [SLAC E154 Collaboration], Phys. Rev. Lett. **79**, 26 (1997), hep-ex/9705012.
[27] K. Ackerstaff *et al.* [HERMES Collaboration], Phys. Lett. B **464**, 123 (1999), hep-ex/9906035.
[28] JLab experiment E01-012, N. Liyanage, S. Choi and J.-P. Chen, spokespersons and P. Solvignon, Ph.D. thesis, Temple University (2006).
[29] E. Shuryak and A. Vainshtein, Nuc. Phys. B **201**, 141 (1982).
[30] R. L. Jaffe and X. Ji, Phys. Rev. D **43**, 724 (1991).
[31] E. Stein *et al.*, Phys. Lett. B **353**, 107 (1995).
[32] B. W. Filippone and X. Ji, Adv. Nucl. Phys. **26**, 1 (2001).
[33] SLAC E155: P. L. Anthony *et al.*, Phys. Lett. B **553**, 18 (2003).
[34] D. Drechsel, S. Kamalov and L. Tiator, Phys. Rev. **D63**, 114010 (2001).
[35] C. W. Kao, T. Spitzenberg and M. Vanderhaeghen, Phys. Rev. D **67**, 016001 (2003).
[36] M. Gockeler *et al.*, Phys. Rev. D **72**, 054507 (2005), hep-lat/0506017.
[37] P L. Anthony *et al.*, Phys. Lett. B **493**, 19 (2000).
[38] Jefferson Lab experiment E06-114, S. Choi, X. Jiang, Z.-E. Meziani and B. Sawatzky spokespersons.
[39] M. Amarian *et al.* [Jefferson Lab E94-010 Collaboration], Phys. Rev. Lett. **92**, 022301 (2004).
[40] Jefferson Lab experiment E03-110, O. Rondon, S. Choi and Z.-E. Meziani spokespersons.
[41] D. Muller, D. Robaschik, B. Geyer, F. M Dittes and J. Horejsi, Fortsch. Phys. **42**, 101 (1994).
[42] A. V. Radyushkin, Phys. Rev. D **56**, 5524 (1997).
[43] X. Ji, Phys. Rev. Lett. **78**, 610 (1997).
[44] M. Diehl, Phys. Rep. **388**, 41 (2003).
[45] X. Ji, Ann. Rev. Nucl. Part. Sci. **54**, 413 (2004).
[46] P. Kroll, Prog. Part. Nucl. Phys. **55**, 281 (2005).
[47] A. V. Belitskyand and A. V. Radyushki, Phys. Rep. **418**, 1 (2005).
[48] M. Burkardt, Phys. Rev. D **62**, 071503 (2000).
[49] J. P. Ralston and B. Pire, Phys. Rev. D **66**, 111501 (2002).
[50] M. Diehl, Eur. Phys. J. C **25**, 223 (2002).
[51] A. V. Belitsky and D. Mueller, Nucl. Phys. A **711**, 118 (2002).

[52] C. Munoz Camacho *et al.* [Jefferson Lab Hall A Collaboration], Phys. Rev. Lett. **97**, 262002 (2006), nucl-ex/0607029.

[53] M. Mazouz, Nucl. Phys. A **782**, 41 (2007).

[54] A. Airapetian *et al.* [HERMES collaboration], Phys. Rev. Lett. **87**, 182001 2001 and Phys. Rev. D **75**, 011103 (2007).

[55] S. Stepanyan *et al.* [CLAS collaboration], Phys. Rev. Lett. **87**, 182002 (2001).

[56] S. Chen *et al.* [CLAS Collaboration], Phys. Rev. Lett. **97**, 072002 (2006), hep-ex/0605012.

[57] X. Ji, Phys. Rev. Lett. **78**, 610 (1997).

[58] M. Garçon, AIP Conf. Proc. **870**, 93 (2006).

[59] `http://www.jlab.org/Hall-B/clas12/Physics/`
`http://www.jlab.org/Hall-C/upgrade/index.html`

News from Lattice QCD

Peter Weisz

Max-Planck-Institut für Physik
Föhringer Ring 6, 80805 Munich - Germany

In this short talk I will present some recent developments from lattice QCD. The presentation is prepared for non-experts with emphasis on general information which will hopefully act as a guide on how to assess phenomenological results presented from various lattice simulations.

1 Introduction

Quantum chromodynamics is the commonly accepted candidate theory of the strong interactions. Its action, describing the interactions of quarks and gluons:

$$S = \int \mathrm{d}^4x \left\{ \frac{1}{2}\mathrm{tr}F_{\mu\nu}F^{\mu\nu} + \sum_f \bar{q}_f[i\gamma D + m_f]q_f \right\}, \tag{1}$$

is rather esthetic, apart from the quark mass terms. Various high energy processes can be reliably computed using renormalized perturbation theory because of the property of asymptotic freedom. The results thereby obtained are in all cases certainly consistent with experiment. However we should also compute low energy properties of the bound states (hadrons) from first principles. If such QCD computations agreed with experiment to a satisfactorily good precision, then we could really accept QCD as the theory of strong interactions. It is often underestimated what a great achievement this would be!

For example to obtain the pion mass we would like to compute the (Euclidean) two-point function of local fields with pion quantum numbers for large time separations:

$$\langle \pi(t)\pi(0)\rangle \propto \int [\mathrm{d}A\mathrm{d}\bar{q}\mathrm{d}q]\mathrm{e}^{-S[A,\bar{q},q]}\pi(t)\pi(0) \sim \mathrm{e}^{-m_\pi t}. \tag{2}$$

The expression above is however formal because we don't know how to define the measure in the continuum, outside the framework of perturbation theory. The only known way how to approach this difficulty and to obtain a non-perturbative definition of the theory is to employ lattice regularization where the continuum space–time is replaced by a (hyper–cubic) lattice. Euclidean invariance is broken but gauge invariance is maintained. QCD should however be obtained in the limit of taking the lattice spacing a to zero.

In such a short review it is impossible to present many details of the theoretical framework. Here we only recall that instead of the local gauge field A_μ we now deal with variables $U_\mu(x) \in \mathrm{SU}(3)$ associated with the links joining a point x to a neighboring point $x + a\hat{\mu}$ on the lattice, which correspond to parallel transporters:

$$U_\mu(x) \sim P\exp\int_0^1 \mathrm{d}t\, A_\mu(x + ta\hat{\mu}). \tag{3}$$

Quark fields $q(x)$ and antiquark fields $\bar{q}(x)$ are defined at points x on the lattice Λ. The formal measure in (2) is then replaced by

$$\int [\mathrm{d}A \mathrm{d}\bar{q}\mathrm{d}q] \to \int \prod_{x\in\Lambda} \left[\mathrm{d}\bar{q}(x)\mathrm{d}q(x) \prod_{\mu} \mathrm{d}U_\mu(x) \right] , \tag{4}$$

where $\mathrm{d}U$ is the SU(3) Haar measure. If the lattice has a finite number of points the resulting functional integral is well defined without the necessity of fixing a gauge, and we have a solid non-perturbative definition of the theory.

One simple feature of the QCD action is that it is bilinear in the quark fields, and so we can "integrate" them exactly using the rules of Grassmannian integration. An expectation value then reduces to

$$\langle \mathcal{O}[U,\bar{q},q] \rangle \propto \int [\mathrm{d}U] \exp(-S[U]) \mathcal{O}[U, D[U]] , \tag{5}$$

where the action above includes the contribution from the internal quark loops which is encoded in the determinant of the Dirac operator:

$$S[U] = S_{\mathrm{gauge}}[U] - \ln\det(i\gamma D[U] + m) . \tag{6}$$

The problem thus reduces to the evaluation of an enormous integral over the lattice gauge fields only, which is done by sophisticated Monte Carlo methods which we shall not describe here. There is a huge saving in computation if one neglects the fermion determinant in (6). This procedure called the "Quenched approximation", which has been widely employed in the past in order to make the simulations feasible (and also to gain valuable experience in numerical methods), is completely ad hoc and hence introduces uncontrolled systematic errors. Serious unquenched simulations (keeping the fermion determinant) have only been performed in recent years.

1.1 Systematic errors

Although the starting point of a lattice computation is completely well defined there are unfortunately various sources of systematic errors in obtaining physical quantities. The three main ones are: 1) finite ultraviolet cutoff (finite lattice spacing): here the effects are assumed to be dominantly power-like in a and quantitatively described by Symanzik's effective langrangian [2, 3]. 2) Since we work with a finite number of points the volume is also finite. For large volumes the nature of the effects on various quantities have been analyzed by Lüscher [4]. 3) Finally, since the computational time depends quite strongly on the quark mass (see below), we are presently still working with quark masses larger than the accepted physical values (corresponding now to pion masses $m_\pi >\sim 300$ MeV), and here the extrapolations are made using Chiral Perturbation Theory (χPT) [5].

Many lattice projects invest a big effort in reducing and controlling these effects. In particular this involves establishing at which scales the theoretically expected behaviors set in for various observables. This activity is of utmost importance because it is our goal to obtain results from first principles with a sufficient accuracy, so that any deviation of theory from experiment could not be simply explained by saying that some systematic errors have been underestimated.

When attempting to assess results of a lattice simulation for phenomenological applications, one should check whether and how the authors have taken into account the systematic errors mentioned above. At this point let me also draw attention to the fact that since lattice gauge theory computations only produce dimensionless numbers, only values for ratios of physical dimensionful quantities are determined. To quote numbers in MeV for masses (or decay constants etc) some scales have to be fixed by identifying some chosen subset with their experimental values. This is obviously a rather ad hoc procedure if one is not working with the physical number of degrees of freedom (e.g. in the quenched approximation or with a small number of flavors $N_{\rm f} = 2$). The subsets chosen sometimes differ from one collaboration to another which often explains the apparent discrepancy in their quoted results.

1.2 Lattice actions

The plausible but yet unproven principle of universality leads to a great freedom in choosing an admissible QCD lattice action. Many different gauge and fermion actions, all maintaining locality, are presently in use by various collaborations. This rather confusing state of affairs has its advantages and disadvantages. One disadvantage is that raw data are often not cross-checked. On the other hand obtaining the same physical result (i.e. in the continuum limit) by various independent methods increases its credibility.

The fermion actions employed differ mainly on how chiral symmetry is treated. The original Wilson action [6], or its O(a) improved version [7], explicitly breaks chiral symmetry for zero bare quark mass, and the bare quark mass has to be tuned to regain the chiral Ward identities. It has the advantage of being conceptually simple. Staggered or Kogut–Susskind fermions [8], which break flavor symmetry at finite cutoff but have too much symmetry flavor symmetry in the continuum limit (see Subsection. 1.3), have the advantage that they are relatively cheap to simulate. Neuberger's overlap fermions [9], for which the Dirac operator obeys the Ginsparg–Wilson [10, 12], relation has an exact chiral symmetry [13] [a], but they are very expensive. Kaplan's domain wall quarks [15] have an approximate chiral symmetry, and so too the implementation of the fixed-point action by Hasenfratz and Niedermayer [11, 12]. Finally twisted mass QCD [16, 17] and chirally improved quarks [18, 19] are sorts of a compromises.

1.3 Fourth root trick

There have recently been strong claims of lattice phenomenological successes using staggered quarks [20, 21]. But this formulation has problems when $N_{\rm f}/4 \neq$ integer and to treat non-degenerate quarks (e.g. the strange quark) the so-called "rooting trick" was employed in which $\mathrm{Det}(iD + m)$ is replaced by its fourth root $\mathrm{Det}(iD + m)^{1/4}$ by hand! The validity of such a manipulation is at first sight highly suspect since one would expect that it would cause violations of unitarity and locality. One outspoken opponent to its use is Creutz [22], but his critiques are not yet sufficiently strong, and indeed no one has yet been able to find a proof that the formulation is actually wrong. The topic is hotly debated in lattice workshops, as it will be again this year. The verdict of Sharpe in his plenary talk last year [23] with the catchy title "Rooted staggered fermions, good, bad or ugly?", was that

[a] differing from the continuum transformations by lattice artifacts and hence overcoming the Ninomiya–Nielsen theorem [14]

they were "at least ugly". In any case it is important to appreciate that with our present level of understanding the formulation may be wrong, and hence any hence results obtained using it [b]!

1.4 Sofware advances; "breaking down the Berlin wall"

A very good news in the past year was that Wilson quarks are not as expensive as previously thought, thereby eliminating the motivation of working with staggered quarks and invoking uncertain procedures. At the lattice workshop in Berlin in 2001 Ukawa [25] proposed the following formula for dependence of the number of operations in Teraflop years required to produce an ensemble of (statistically independent) field configurations N on the spatial extent L, the lattice spacing a and quark mass m:

$$N_{\rm Ukawa} = 5.00 \left[\frac{20{\rm MeV}}{m}\right]^3 \left[\frac{0.1{\rm fm}}{a}\right]^7 \left[\frac{L}{3{\rm fm}}\right]^5 . \quad (7)$$

This at the time discouraging formula [c] was not obtained by rigorous arguments but based on the experience gained by the CP-PACS and JLQCD simulations. At last year's lattice workshop Giusti [24] presented the following estimate for the same physical parameters but now based on the simulations of Ref. [26]:

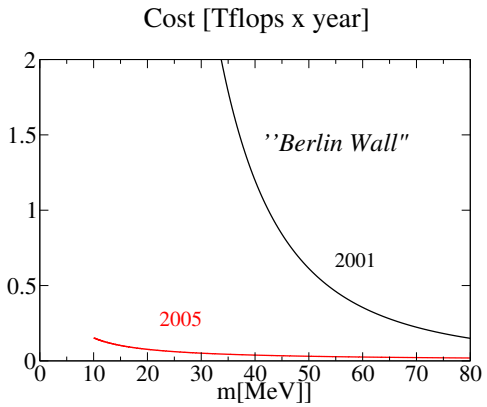

Figure 1: The cost formulae (7) (black) and (8) (red) versus m for the case $a \simeq 0.08$fm and $L = 32a \simeq 2.5$fm.

$$N_{\rm Giusti} = 0.05 \left[\frac{20{\rm MeV}}{m}\right]^1 \left[\frac{0.1{\rm fm}}{a}\right]^6 \left[\frac{L}{3{\rm fm}}\right]^5 . \quad (8)$$

What is striking is the reduction of the amplitude by a factor 100, the significant reduction on the dependence on the quark mass, and also a reduction on the dependence on the lattice spacing! The enormous gain is more easily appreciated by inspecting Fig. 1. Similar performances to (8) were reported by other groups using various simulation techniques e.g. [27, 28]. The impressive acceleration is mainly due to the progress in algorithms [28]–[31] and the inclusion of features to improve program efficiency (see e.g. [32]).

1.5 Hardware

The huge acceleration gained by the software has also been supplemented by the availability of powerful computer resources. Table 1 gives an incomplete list of the facilities used by the lattice community. It is to be noted that the peak performance has

[b] (unless one could argue that the wrong procedure effects the physical quantities under consideration only weakly)

[c] (given here explicitly for $N_{\rm f} = 2$ flavors of O(a)-improved Wilson quarks in a volume $V = 2L \times L^3$ and with degenerate quarks of mass $m = m_{\overline{\rm MS}}(2{\rm GeV})$)

been entered; typical programs perform at $\sim$ 50% of the peak [d]. Finally the upcoming International Lattice Data Grid [33] organizing the storing of gauge configurations generated in the time consuming dynamical simulations, will be a big asset which will aid the extraction of physical observables and further promote international cooperation.

Type	Facility	Peak
Custom computers	Blue GeneL, Jülich	46
	Blue GeneL, KEK	57
PC clusters	Altix, LRZ	26
	PACS-CS, Tsukuba	14
Self-built	QCDOC, BNL	20
	APE-next, Rome	8

Table 1: Computing facilities, with peak performance in TFlops.

2 Observables

In lattice simulations one measures Euclidean lattice correlation functions of the type $\langle \mathcal{O}_1 \mathcal{O}_2 \dots \rangle$ where $\mathcal{O}_1$ are gauge invariant observables. For example $\langle \mathcal{O}(0)\mathcal{P}(t) \rangle$ for large t gives information on the matrix element $\langle 0|\mathcal{O}(0)|P\rangle$ where $|P\rangle$ is the lowest state with quantum numbers of the local operator $\mathcal{P}$. One is usually interested in the connected parts of such correlation functions and thus the computation tends to become very difficult if the number of operators in the product is large because of severe statistical fluctuations.

Nevertheless one can obtain information on many quantities of phenomenological relevance to hadron structure including spectra, resonance properties and phase shifts, hadronic contributions to $g-2$, running couplings, meson distribution amplitudes, elastic and transition form factors and moments of (generalized) structure functions. Because of lack of space I will in this section restrict myself to the last three topics, and finally in Sect. 3 briefly report on running couplings. For a thorough review of lattice results on hadron structure I recommend the article by Orginos [34].

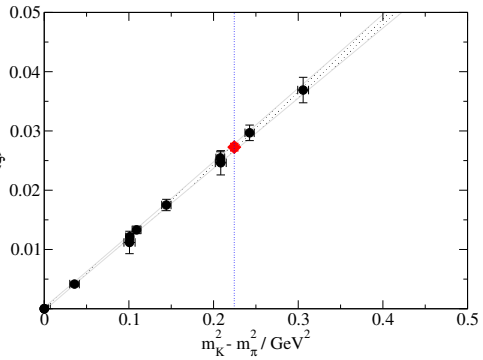

Figure 2: QCDSF [37] $N_f = 2$ results for the first moment of the kaon distribution function.

2.1 Meson distribution amplitudes

Meson distribution amplitudes are defined (in Minkowski space) by matrix elements of bilocal operators e.g. the kaon distribution amplitude $\phi_K(\xi,\mu)$ is given by:

$$f_K i p_\rho \int_{-1}^{1} \mathrm{d}\xi \, \mathrm{e}^{i\xi p\cdot z} \phi_K(\xi,\mu) = \langle 0|\bar{q}(z)\gamma_\rho\gamma_5 P \exp\left[i\int_{-z}^{z} A(x)\cdot \mathrm{d}x\right] s(-z)|K(p)\rangle_{z^2=0} \,. \quad (9)$$

[d] Note also that some of the facilities are shared with groups working on other topics.

The distribution is not directly measurable on the lattice however its (low) moments

$$\langle \xi^n \rangle_K(\mu) = \int_{-1}^{1} \mathrm{d}\xi \, \xi^n \phi_K(\xi, \mu) \tag{10}$$

are, since they are expressed as matrix elements of local operators:

$$\langle \xi \rangle_K(\mu) f_K p_\rho p_\nu = \langle 0 | \bar{q}(0) \gamma_\rho \gamma_5 \overleftrightarrow{D}_\nu s(0) | K(p) \rangle \, . \tag{11}$$

These were one of the first quantities to be measured in (quenched) lattice simulations [35, 36]. Fig. 2 shows recent measurements by QCDSF [37] with $N_\mathrm{f} = 2$ of the first moment $\langle \xi \rangle_K$ as a function of the meson (squared) mass difference. A nice feature is that it approaches zero in the degenerate case as expected. Interpolating to the physical value of $m_K^2 - m_\pi^2$ yields $\langle \xi \rangle_K^{\overline{\mathrm{MS}}}(2\mathrm{GeV}) = 0.027(02)$. This is consistent with the central value 0.030(12) of the computation using QCD sum rules [38, 39, 40]; the quoted errors of the lattice computation are smaller but these do not include some systematic errors e.g. those due to lattice artifacts. Another computation [41] using (RBC/UKQCD) configurations from simulating $N_\mathrm{f} = 2 + 1$ dynamical flavors of domain wall quarks, yields a similar number 0.032(03). QCDSF also quote a result for the second moment of the kaon DF $\langle \xi^2 \rangle_K^{\overline{\mathrm{MS}}}(2\mathrm{GeV}) = 0.26(2)$, and furthermore for the corresponding value for the pion $\langle \xi^2 \rangle_\pi^{\overline{\mathrm{MS}}}(2\mathrm{GeV}) = 0.27(4)$ which turns out to be practically the same.

2.2 Nucleon axial coupling

The nucleon axial coupling has been computed by many groups [42]–[46] with encouragingly consistent results. These are summarized in Fig. 3 which also shows that dependence of g_A on m_π is surprisingly weak.

Note however that for this quantity there are rather significant finite volume effects which must be taken into account. At LAT06 Orginos [34] quoted a value $g_A(m_\pi = 140\mathrm{MeV}) = 1.23(8)$ consistent with the experimental value of 1.2695(29) but much more inaccurate. In any case to compare with experiment in more detail isospin breaking effects would have to be included. To enable a better comparison with χPT [47] measurements with $N_\mathrm{f} = 2 + 1$ dynamical quarks at smaller m_π are under way.

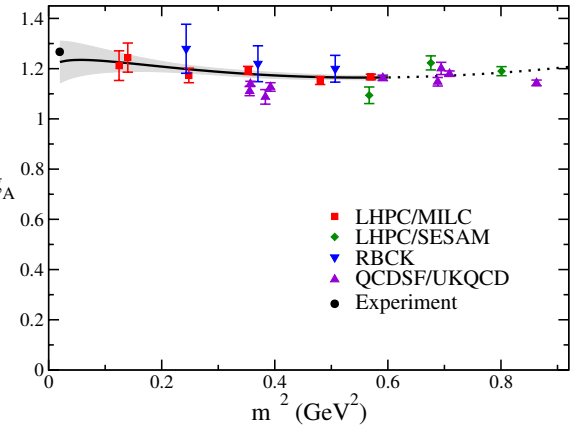

Figure 3: Dependence of lattice values for g_A on the pion mass.

2.3 Nucleon form factors

Figure 4 shows some recent measurements of the isovector F_1 form factor. Note that the values of m_π there are still large, but the form factor seems to approach the experimental measurements as m_π decreases.

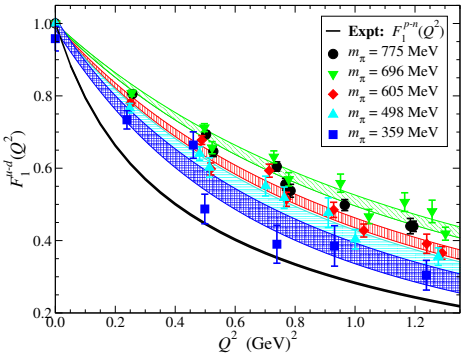

Figure 4: LHPC '06 measurement of the nucleon isovector F_1 form factor

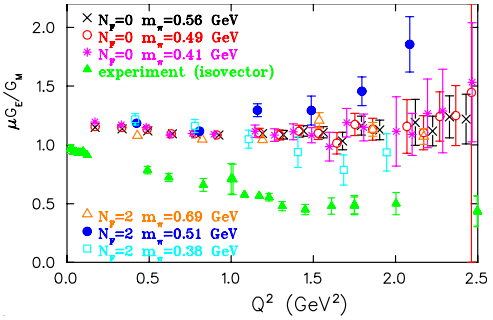

Figure 5: Ratio of electric and magnetic isovector form factors

One general point to appreciate is that if periodic boundary conditions (pbc) are used, then momentum components are quantized in units $2\pi/L$ where L is the spatial extent of the lattice. For example a lattice of size $L = 24a$ with $a = 0.1$fm gives $2\pi/L \sim 0.52$GeV. Hence typically only quite widely separated points on the curves are obtained. In addition one has the problem that lattice artifacts become larger at the higher momenta. An idea to improve this situation proposed by Bedaque [48], and applied e.g. in [49], is to use twisted pbc where the allowed momentum coefficients have the form $p_i = (2\pi n + \theta_i)/L$. This yields more points on the curves at the price that each different set of values for the twists θ_i requires a separate simulation.

An illustration that not everything is so rosy yet is Fig. 5 from Alexandrou et al [50] showing a measurement of the ratio of electric and magnetic isovector form factors. As one can see there is presently an apparent disagreement of this measurement with with that obtained by the preferred JLab polarization transfer experiments [51]. In fact the result resembles more the older experimental findings using the Rosenbluth separation technique [52]. But the authors of Ref. [50] caution that there may be strong lattice artifacts which still need to be examined.

2.4 Moments of structure function

Figure 6 shows some data for the average value for the isovector first moment $\langle x \rangle_{u-d}$. The squares are points from a quenched simulation (QCDSF) with the overlap operator, which are quite far from the accepted experimental value. The circles are data from the LHPC group [53] for $N_f = 2+1$ dynamical (staggered) quarks (at one lattice spacing $a \sim 0.125$fm). This data does not yet show the expected chiral logarithm [54]

$$\langle x \rangle_{u-d} = C \left[1 - r^2 (A \ln r^2 + B) + \dots \right] , \tag{12}$$

where $r = m_\pi/(4\pi f_\pi)$ with a computed large amplitude $A = 6g_A^2 + 2 \sim 11$. But if one extrapolates the present data using the formula above one indeed obtains a value consistent with experiment.

The situation for the ratios of moments is much the same; i.e. fitting to χPT one obtains good agreement with experiment for a wide range of moments as illustrated in Fig. 7.

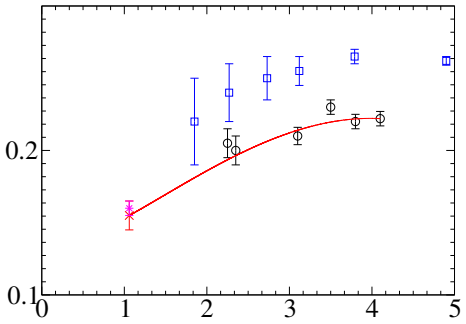

Figure 6: Isovector first moment $\langle x \rangle_{u-d}$. The curve is an extrapolation using χPT.

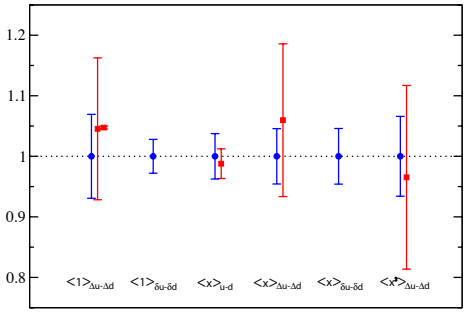

Figure 7: Ratios of Moments: Lattice/DIS

3 Running couplings

Various physical processes measured can be computed at high energies within the framework of perturbation theory. If the perturbative expression for a given process $P(s)$ at scale s starts with $c\alpha^n$ (for some perturbative renormalized coupling α) then we can define a non-perturbative running coupling by $\alpha[P](s) = [P(s)/c]^{1/n}$. Such running couplings are often defined down to low energies where perturbation theory is surely no longer valid.

What is usually done is to match the measurement of $P(s)$ with its perturbative expression in order to obtain values of the coupling in the $\overline{\rm MS}$–scheme $\alpha_{\overline{\rm MS}}(s)$ in the energy range of the experiment. A collection of the values obtained from various experiments is then compared to the *function* $\alpha_{\overline{\rm MS}}(s)$ which is the solution of a renormalization group equation with the β-function computed to a certain order. If good agreement is observed it is often said that "running of the coupling has been observed". This is a mild misuse of words since we are patching together various experiments and also the function $\alpha_{\overline{\rm MS}}(s)$ certainly runs! We should rather just say we observe satisfactory agreement with the perturbative prediction (which entails asymptotic freedom).

To actually observe running of a given physical coupling we should measure it over a wide range of energies and check at which energy perturbative behavior seems to sets in (to a given accuracy). At that stage we can estimate the associated Λ–parameter and convert to the $\overline{\rm MS}$ scheme if desired.

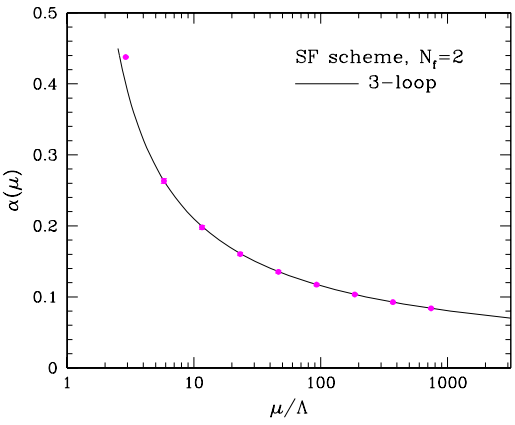

Figure 8: Running coupling in the SF scheme for $N_{\rm f} = 2$.

There are unfortunately few experiments which cover a sufficiently wide energy range. Indeed some experiments cover only a short range at relatively low energies. In this case one has to resort to the mere hope that perturbative behavior has already set in. This can certainly lead to uncontrolled errors. In the lattice literature there are analogous procedures. An example is the much publicized work [20] who quote a value for $\alpha_{\overline{\rm MS}}(m_Z)$ with small error bars. In an admittedly over-simplified presentation, their result is basically obtained by measuring various quantities e.g. charmonium splittings at a given value of the bare coupling g_0, thereby extracting a value of the lattice spacing $a(g_0)$ in physical units. Subsequently an estimate of $\alpha_{\overline{\rm MS}}(a(g_0))$ is obtained in terms of a (modified) perturbative relation to g_0. Finally they use the RG equation to evolve from the charm scale up to the Z mass. No actual running is measured; moreover the non-perturbative measurements used the questionable fourth-root trick discussed in Subsect. 1.3. Its theoretical status should certainly be taken into account when making comparisons with experimental results, which albeit often also have their own sources of uncontrolled systematic errors [55, 56].

A more satisfactory job, in my opinion, is that what has been done by the Alpha Collaboration [57]. They indeed measure a special non-perturbatively defined running coupling[e] over a wide range of energies, including careful extrapolations to the continuum limit. They first check that perturbation theory indeed seems to set in, as seen in Fig. 8. Amusingly this coupling runs according to 3-loop PT right down to relatively low energies, but this must certainly not be misunderstood as a universal property of running couplings. Unfortunately their computations are so far only for the unphysical case of $N_{\rm f} = 2$ flavors. Converting to the $\overline{\rm MS}$–scheme at their highest measured energy they obtain the result $[\Lambda_{\overline{\rm MS}} r_0]^{(2)} = 0.62(6)$; if one sets the Sommer scale [58] to its phenomenological value $r_0 = 0.5$fm one obtains $\Lambda^{(2)}_{\overline{\rm MS}} = 245(23)$MeV, but as discussed in Subsect. 1.1 the choice of scale introduces an additional systematic error if one wishes to compare with experiment.

In Fig. 9 they plot the extracted non-perturbative beta function for $N_{\rm f} = 0, 2$. One first clearly sees the expected contribution from the fermions. Furthermore one observes the onset of a deviation from perturbative behavior at the lowest energies.

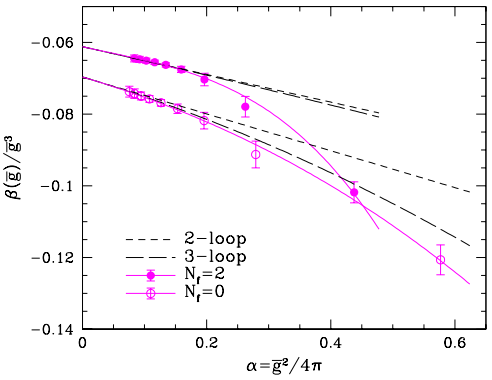

Figure 9: Comparison of non-perturbative to perturbative β–functions.

4 Summary

Much algorithmic progress in lattice QCD has been achieved in the last 5 years. Serious dynamical quark simulations of QCD with larger physical volumes and relatively small

[e] which depends on the physical volume, and defined through the Schroedinger functional

lattice spacings are now under way. However a big effort is still needed to simulate with the physical value of the pion $m_\pi \sim 140$MeV. Chiral logarithms have not yet been clearly seen, but lattice simulations combined with extrapolations using χPT gives reasonable agreement with experiment for many observables describing hadronic structure. Finally there is a huge effort to control the various systematic errors which is as essential for the quality of a lattice computation as it is for any real experiment.

5 Acknowledgments

I would like to thank Kostas Orginos for sending me the figures which appeared in his lattice proceedings, some of which are reproduced here. I also thank Meinulf Goeckeler for his suggestions concerning the selection of topics covered in Sect. 2.

References

[1] Slides:
`http://indico.cern.ch/contributionDisplay.py?contribId=8&sessionId=2&confId=9499`

[2] K. Symanzik, Nucl. Phys. **B226** 187 (1983).

[3] M. Lüscher, In Les Houches 1984 Proceedings, *Critical Phenomena, Random Systems, Gauge Theories*, 359.

[4] M. Lüscher, Commun. Math. Phys. **104** 177 (1986); ibid **105** 153 (1986); Nucl. Phys. **B354** 531 (1991); ibid **B364** 237 (1991).

[5] J. Gasser, H. Leutwyler, Ann. Phys. **158** 142 (1984).

[6] K. Wilson, Phys. Rev. **D10** 2445 (1974).

[7] B. Sheikholeslami, R. Wohlert, Nucl. Phys. **B259** 572 (1985).

[8] L .Susskind, Phys. Rev. **D16** 3031 (1977).

[9] H. Neuberger, Phys. Lett. **B427** 353 (1998);ibid **B414** 341 (1998).

[10] P.H. Ginsparg, K.G. Wilson, Phys. Rev. **D25** 2649 (1982).

[11] P. Hasenfratz, Nucl. Phys. Proc. Suppl. **63** 53 (1998).

[12] F. Niedermayer, Nucl. Phys. Proc. Suppl. **73** 105 (1999).

[13] M. Lüscher, Phys. Lett. **B428** 342 (1998).

[14] N. Nielsen,M. Nimomiya, Phys. Lett. **B105** 219 (1981).

[15] D. Kaplan, Phys. Lett. **B288** 342 (1992).

[16] R. Frezzotti, P.A. Grassi, S. Sint, P. Weisz, JHEP **0108**:058 (2001).

[17] R. Frezzotti, G.C, Rossi, JHEP **0408**:007 (2004).

[18] C. Gattringer, Phys. Rev. **D63** 114501 (2001).

[19] C.B. Lang, P. Majumdar, W. Ortner, Phys. Rev. **D73** 034507 (2006).

[20] Q. Mason *et al.* (HPQCD), Phys. Rev. Lett. **95** 052002 (2005).

[21] C.T.H. Davies *et al.* Phys. Rev. Lett. **92** 022001 (2004);Q. Mason *et al.* (HPQCD), Phys. Rev. **D73** 114501 (2006).

[22] M. Creutz, hep-lat/0701018v2.

[23] S. Sharpe, PoS LAT2006:022 (2006).

[24] L. Giusti, PoS LAT2006:009 (2006).

[25] A. Ukawa *et al.* (CPPACS and JLQCD), Nucl. Phys. Proc. Suppl. **106** 195 (2002).

[26] L. Del Debbio, L. Giusti, M. Lüscher, R. Petronzio, N. Tantalo, JHEP 0702:056 (2007); JHEP **0702**:082 (2007).

[27] M.A Clark, A.D. Kennedy, Phys. Rev. Lett. **98** 051601 (2007).

[28] C. Urbach, K. Jansen, A. Shindler, U. Wenger, Comput. Phys. Commun. **174** 87 (2006).

[29] M. Hasenbusch, Phys. Lett. **B519** 177 (2001).

[30] M. Lüscher, JHEP **0305**:052 (2003).

[31] M.A Clark, A.D. Kennedy, Nucl. Phys. Proc. Suppl. **129** 850 (2004).
[32] M. Lüscher, Nucl. Phys. Proc. Suppl. **106** 21 (2002).
[33] K. Jansen, hep-lat 0609012.
[34] K. Orginos, Pos (LATT2006) 018.
[35] A.S. kronfeld, A.M. Photiadis, Phys. Rev. **D31** 2939 (1985).
[36] G. Martinelli, C.T. Sachrajda, Phys. Lett. **B190** 152 (1987).
[37] V.M. Braun *et al.*, Phys. Rev. **D74** 074501 (2006).
[38] A. Khodjamirian, T. Mannel, M. Melcher, Phys. Rev. **D70** 094002 (2004).
[39] V.M. Braun, A. Lenz, Phys. Rev. **D70** 074020 (2004).
[40] P. Ball, R. Zwicky, Phys. Lett. **B633** 289 (2006); JHEP **02** 034 (2006).
[41] P.A. Boyle *et al.*, Phys. Lett. **B641** 67 (2006).
[42] S.R. Beane, M.J.Savage, Phys. Rev. **D70** 074029 (2004).
[43] S. Ohta, K. Orginos (RBCK), Nucl. Phys. Proc. Suppl. **140** 396 (2005).
[44] H.W. Lin, S. Ohta, hep-lat/0610028.
[45] A. Ali Khan *et al.* (HPQCD and UKQCD), Nucl. Phys. Proc. Suppl. **153** 128 (2006).
[46] D. Dolgov *et al.*, Phys. Rev. **D66** 034506 (2006).
[47] V. Bernard, U.G. Meissner, Phys. Lett. **B639** 278 (2006).
[48] P.F. Bedaque, Phys. Lett. **B593** 82 (2004).
[49] J.M. Flynn, A. Juttner, C.T. Sachrajda [UKQCD], Phys. Lett. **B632** 313 (2006).
[50] C. Alexandrou, G. Koutsou, J.W. Negele, A. Tsapalis, Phys. Rev. **D74** 034508 (2006).
[51] V. Punjabi *et al.*, Phys. Rev. **C71** 055202 (2005).
[52] L. Andivahis *et al.*, Phys. Rev. **D50** 5491 (1994);
M.E. Christy *et al.* (E94110), Phys. Rev. **C70** 015206 (2004).
[53] R.G. Edwards *et al.* (LHPC), Proc. Sci. LAT2006 (2006).
[54] D. Arndt, M.J. Savage, Nucl. Phys. **A697** 429 (2002).
[55] S. Bethke, Prog. Part. Nucl. Phys. **58** 351 (2007).
[56] S. Kluth, hep-ex/0609010.
[57] M. Della Morte *et al.* [ALPHA Collab.], Nucl. Phys. **B713** 378 (2005).
[58] R. Sommer, Nucl. Phys. **B411** 839 (1994).

A Review of Recent Results from the Tevatron

Giorgio Chiarelli [1] *

INFN Sezione di Pisa
Largo B.Pontecorvo 3, I-56127, Pisa - Italy

The D0 and CDF experiments have been taking data at the Run 2 of the Tevatron Collider since 2001. We present a selection of recent results, most of them obtained with an integrated luminosity of $\simeq 1$ fb^{-1}. I will describe the most important facets of the physics programme and detail some results. Recent direct limits on standard model Higgs obtained at the Tevatron, and their their prospects will be also reviewed.

1 Introduction

The D0 and CDF experiments are two 4π multi-purpose detectors taking data at the Tevatron Collider. Run 2 (started in 2001) is designed to provide each detector with $4-8$ fb^{-1} of $p\bar{p}$ collisions by the end of 2009. With respect to Tevatron Run I, the accelerator complex underwent a large upgrade which radically changed the way it operates. The interbunch distance was reduced from $3.5\mu s$ to 392 ns, the whole $\bar{p}$ production, cooling and stacking was revised. As a result, after a relatively long startup, the accelerator is now performing very well. The peak luminosity reached 2.92 10^{32}cm^{-2}s^{-1} and is now delivering about 40 pb^{-1}/week with a record of 45 pb^{-1} in a single week. Based on the current performances, the integrated luminosity per experiment extrapolates to $6-8$ fb^{-1}/experiment by the end of 2009.

The CDF and D0 detectors were upgraded fully to exploit the physics opportunities provided by the Tevatron. CDF completely rebuilt its tracking system (both the outer chamber and the silicon tracker), the forward calorimeter, its trigger and front end electronics and extended the muon coverage. It also added the capability to trigger on tracks at Level1 (i.e. syncronous with the bunch crossing) and to identify and trigger on tracks displaced with respect to the primary vertex at Level 2. The silicon tracker is an important asset of its physics programme with a precision single sided layer located right on the beam pipe, five layers of double sided silicon sensors at various radii between 2.5 and 10 cm and two layers located at $\simeq 20$ and $\simeq 28$ cm covering $|\eta| < 2$ and $1 < |\eta| < 2$ respectively.

D0 changed its philosophy by becoming a full magnetic spectrometer with the addition of a 2 Tesla superconducting solenoid. It also replaced its old tracker with a new 8-layer fiber tracker which -combined with a microvertex silicon detector- provides a powerful instrument to reconstruct tracks coming from the primary vertex and offline to identify vertices due to long-lived particles. D0 also improved its acceptance for muons and upgraded the trigger system. Recently, in the shutdown of 2006, the collaboration added an extra layer of silicon sensors located right outside the beam pipe.

The detectors collect data with an efficiency of $\simeq 90$ %. The small inefficiency is partly due to a deadtime coming from the trigger and Data Acquisition and partly to operational constraints. As we write $\simeq 2.5$ fb^{-1} were written to tape by each experiment. However, in the following, unless otherwise indicated, I will present results obtained with $\simeq 1$ fb^{-1}, less than half of the data on tape.

*for the CDF and D0 Collaborations

2 Flavour Physics

Despite the large production cross section, processes involving HF remain largely buried under a large background. CDF Run 1 pioneered the identification of heavy flavour at hadron colliders by detection of secondary vertices, a powerful tool complementary to other tagging techniques. In Run 2 the experiment increased its B-physics reach by adding the capability to trigger on tracks not coming from the primary vertex (SVT). A number of b and c -related physics processes, otherwise completely buried by a large background, can theferore be selected online for further analyses. Thanks to its microvertex detector and to its large muon coverage D0 is also able to perform a number of measurements. Details can be found in [2], here I only mention a few, very interesting results.

In Spring 2005 D0 presented a limit on B_s oscillations using 0.9 fb^{-1} of $14.9 < \Delta m_s < 21$ ps^{-1} at 90% C.L. With 1 fb^{-1} CDF presented (Fall 2005) a 5 σ observation of B_s oscillations (Fig. 1) and a measurement of $\Delta m_s = 17.77 \pm 0.10(stat) \pm 0.07(syst)$ ps^{-1}. D0 exploits a combination of its measurement of the $B_s \to J/\Psi\phi$ channel and of the B_s semileptonic decays together with results from the B factories and CDF Δm_s to obtain a measurement of $\phi_s = 0.70^{+0.47}_{-0.39}$ [2].

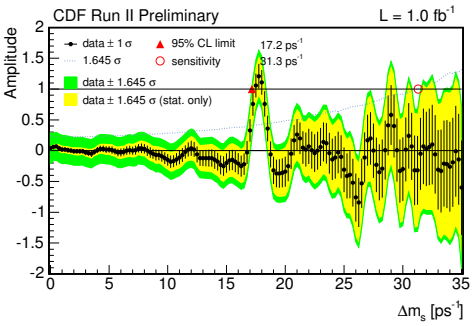

Figure 1: Amplitude scan for Δm_s at CDF.

CDF and D0 search for rare B decays. Thanks to SVT, CDF directly measures $B \to hh$ decays and their A_{CP}. B_d,B_s decays to $\mu\mu$ have tiny SM branching fractions (O(10^{-9}) which are enhanced (by powers of $\tan\beta$) in several SUSY models, therefore both Collaborations search for new physics through this channel. CDF has not yet updated its measurement performed with 0.8 fb^{-1}, while D0 just presented its result with the full dataset of 2 fb^{-1}. Combining the 2a (without the silicon layer on the beampipe) and 2b data they find 3 candidate events with a background of 2.3± 0.7 and set a limit for $B_s \to \mu\mu < 9.3(7.5) \cdot 10^{-8}$ at 95(90) % C.L. and $B_d \to \mu\mu < 2.3(2.0) \cdot 10^{-8}$ at 95(90) % C.L. This result (which will soon be improved by adding the CDF search), sets interesting limits on many SUSY models by excluding zones in the $\tan\beta - M_A$ plane [4]. We expect that by 2009, with 8 fb^{-1}, the Tevatron will be able to set a limit of $\approx 2 \cdot 10^{-8}$ on the B_s decay.

state	Mass value ± stat. ± syst.
Σ_B^+	$5808^{+2.0}_{-2.3} \pm 1.7$
Σ_B^-	$5816^{+1.0}_{-1.0} \pm 1.7$
Σ_B^{*+}	$5829^{+1.6}_{-1.8} \pm 1.7$
Σ_B^{*-}	$5379^{+2.1}_{-1.9} \pm 1.7$

Table 1: Σ_B and σ_B^* masses (in MeV/c^2).

Searches for rare decays of known states are complemented by the search for new states, and CDF recently presented the observation of two new B baryons: Σ_B and Σ_B^* with masses shown in table 1. Last but not least, new measurements of Λ_B lifetime are presented. CDF measures (exclusive states) $1.5 \pm 0.077 \pm 0.012$ ps while D0 reports $1.28 \pm 0.11 \pm 0.09$ ps in semileptonic decays and $1.3 \pm 0.14 \pm 0.05$ ps in exclusive channels [2].

3 QCD and jet physics

Tests of the strong interaction and measurements of jet distributions have been the bread and butter physics at the Tevatron for more than 20 years. Besides testing theoretical prediction those processes are often used to test algorithms but they also play an important role to estimate the background in rare processes and searches for new physics. This dual aspect is present in many analyses. Details can be found in the many Tevatron contributions to this Conference [3]. In the following I will only refer to a small subset.

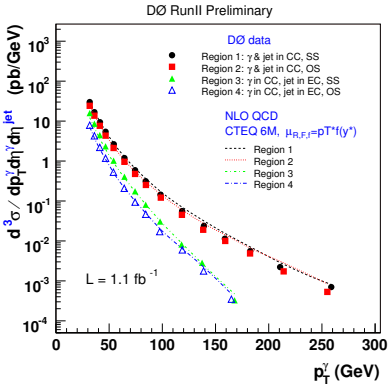

Figure 2: D0 triple differential $\gamma - j$ cross section.

Thanks to the large statistics available it is now possible to make precisios measurements of associated production of jets and vector bosons (W, Z, γ). D0 measures the triple differential cross section in the $\gamma - jet$ process (Fig. 2) where finds a good agreement with available NLO QCD calculations. CDF finds a good agreement between its inclusive jet distribution and theoretical prediction. The difference between theory and CDF data of Run 1, has now disappeared. The large statistics, combined with the exploitation of the SVT trigger. allows CDF to study $b\bar{b}$ correlations in a small dataset ($\simeq 260$ pb^{-1}). Existing MC do not fully describe the data, as you can see from Figure 3 where several MC are used for the comparison. The region in which the two bs are close in φ exhibits a clear deviation of data with respect to calculations. Even the improvement obtained by using Jimmy (a Monte Carlo describing multiple parton interactions) does not fully account for this difference, which happens in the region where gluon splitting is expected to provide a sizeable contribution to the process.

4 Electroweak Physics Measurements

Electroweak (EWK) processes can be used to understand better the capabilities of the detectors and to develop new tools (from trigger to analysis technique). They also often represent background for searches. With its large dataset, the Tevatron became a place where precision EWK measurements can be performed to test the SM at its boundaries.

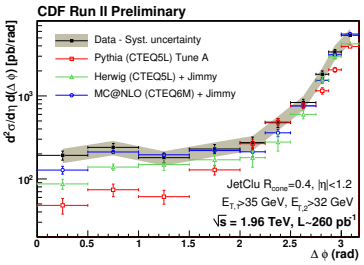

Figure 3: $\Delta\varphi$ between two identified bs

Among the many results, I chose a few which are significant for their implications. The W and Z integral and differential cross sections provide an excellent testing ground for PDFs. NLO and NNLO calculations of the inclusive processes have been available for

quite some time and recently a full differential calculation at NNLO became available [7]. The large statistics collected allows CDF to present a $d\sigma/dy$ for $Z \rightarrow ll$ events (Figure 4). While the agreement with theory is good, this measurement -with increasing statistics- can be used to costrain PDFs. Recently CDF measured the ratio of central-to-forward cross section for $p\bar{p} \rightarrow W + X$ with the $W \rightarrow e\nu$ and demonstrated a sensitivity of this quantity to PDFs. This can be a promising way to study PDFs at the LHC where the W asymmetry measurement will play a less prominent role [6].

Tevatron experiments recently obtained significant results in the diboson sector. The tiny cross sections (of the order of a few pb, less than the top cross section) challenged the experimentalists' determination and ingenuity. Diboson production represents also a test bed for the detection of Higgs and indeed represents a background in several channels.

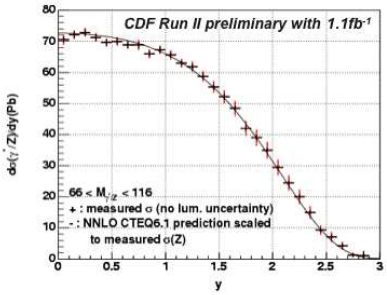

Figure 4: $d\sigma/dy$ for $Z\gamma* \rightarrow ee$ CDF events.

In Summer 2006 D0 presented its evidence of WZ production, with $WZ \rightarrow l\nu l\nu$ signal at 3.3 σ level and a cross section of $3.98^{+1.91}_{-1.53}$ pb (statistical and systematic uncertainty combined), consistent with SM expectation of 3.7 ± 0.1 pb. In Winter 2007 CDF confirmed its previous evidence observing a signal of 16 events with a background of $2.7 \pm 0.28 \pm 0.33 \pm 0.09$. The probability of a null signal is $< 1.5 \times 10^{-7}$ equivalent to a $\simeq 6\sigma$ effect. The measured cross section is $5.0^{+1.8}_{-1.6}$ pb (statistical and systematic uncertainty combined). In this case the improvement did not come from a larger dataset but rather from improved analysis technique and a larger lepton acceptance.

Another challenging process is $ZZ \rightarrow llll$. CDF shows a 3σ evidence (Figure 5) and measures a cross section of $0.75^{+0.71}_{-0.54}$ pb, compatible with the NLO prediction of 1.4 ± 0.1 pb. At present the case in which one of the two bosons decays hadronically still remains unobserved.

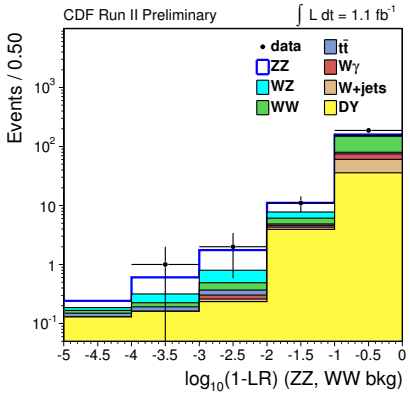

Figure 5: Log-Likelihood ratio for ZZ candidates superimposed to background.

The gauge structure of the SM finds a crucial test in the associated production of $W\gamma$. The destructive interference at tree level of the relevant diagrams creates a zero in the $dN/d\cos\theta^*$ distribution at $cos\theta^* = \pm\frac{1}{3}$, where θ^* is the c.o.m. angle between the W and the incoming quarks. In our detectors we measure the charged lepton from the W decay and the sensitive variable is $Q \cdot \Delta\eta_{l,\gamma}$ where Q is charge of the lepton. The distribution of this quantuty still shows a dip at ≈ -0.3. As the photon does not directly couples to the Z the interference is not present in the $Z\gamma$ process. Both experiments measure the inclusive $W\gamma$ and $Z\gamma$

production cross section. CDF finds $\sigma(W\gamma) = 19.1 \pm 2.8$ pb and $\sigma(Z\gamma) = 4.9 \pm 0.5$ pb. D0 applies a cut to the photon E_T (>7 GeV) and to the transverse mass M(γ,l,ν) > 90 GeV and quotes $\sigma(W\gamma) = 3.2 \pm 0.5 \pm 0.2$(lum) and $\sigma(Z\gamma)$ of $4.51 \pm 0.4 \pm 0.3$ pb. D0 measures the $Q \cdot \Delta\eta$ distribution in 900 pb^{-1} and in its data there is evidence of a dip related to the destructive intereference predicted by the SM (Figure 6).

In the single boson realm, the most significant contribution came from CDF which directly measured the W mass and width. The traditional way is to study the transverse mass ($M_T = \sqrt{2 \cdot E_T^{\nu} \cdot E_T^{l} \cdot (1 - cos\theta_{l,\nu})}$) distribution where $l = e,\mu$ and neutrino transverse momentum is estimated from the transverse missing energy size and direction. The peak provides information about the W mass where the non-Gaussian tail (due to the Lorentz distribution) about the W width. In its M_W measurement CDF also fits the transverse momentum distributions of the leptons. The result is $M_W = 80413 \pm 48$ MeV/c^2 where statistical and systematic uncertainties contribute evenly (34 MeV/c^2 each). This is the best measurement obtained by a single experiment. As it was performed on 200 pb^{-1}, while the current sample on tape exceeds it by a factor 12, it is reasonable to expect a large reduction of the statistical error. The systematics can also be addressed with a larger statistics and a precision of $\simeq$ 25 MeV/c^2 seems achievable. The measurement of $\Gamma_W = 2032 \pm 71$ MeV/c^2 (with 350 pb^{-1}) (Fig. 7), combined with Run 1 measurements, now dominates the world average.

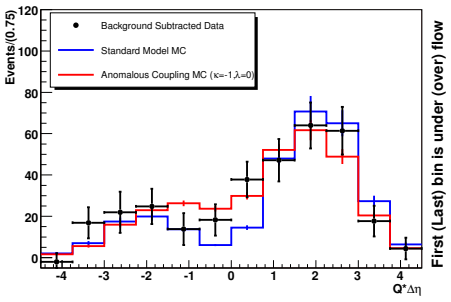

Figure 6: Signed $\Delta\eta_{l,\gamma}$ distribution at D0.

5 Top Physics

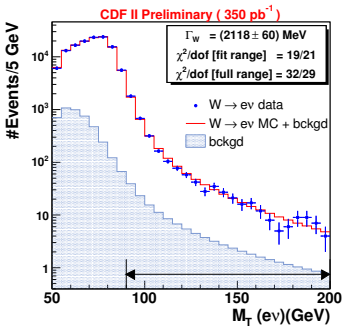

Figure 7: Fit to M_T in the $W \to e\nu$ channel.

Top quark production was first discovered at the Tevatron Collider in 1994-1995. Until the LHC starts it is still the only place where it can be studied and several new results are presented [9].

As the $t \to bW$ $\simeq$100 % of the times, one can classify the various decay channels according to the way the W boson decays. In this way one can measure *dilepton* channel (both Ws decay into $l\nu$), *lepton+jets* channel where only one of the two Ws decays leptonically and finally the *all-hadronic* channel in which both Ws decay hadronically. The final states contain, accordingly, one, two or no high P_T lepton. The structure of

the Wtb vertex can be directly studied in top-pair decays. Anomalous couplings (FCNC) and new physics might appear as deviation from SM expectations. The Top cross section has been measured in essentially all decay channels. A compilation of the $t\bar{t}$ production cross section measured by CDF can be found in Fig. 8.

Some comments are in order. The dilepton channel, by far the one with least background has a BF of only $\simeq 4.9$ % summing together the ee,$\mu\mu$,$e\mu$ channels. In order to improve statistics CDF selects events with one fully identified high-P_T lepton and an isolated high P_T track. Its recent result with 1.1 fb^{-1} is $\sigma_{dil} = 9.0 \pm 1.3(stat) \pm 0.5(sys) \pm 0.5(lum)$ pb. D0 has a comparable result with a similar data sample: $\sigma_{dil} = 6.8^{+1.2}_{-1.1}(stat)^{+0.9}_{-0.8}(sys) \pm 0.4(lum)$ pb.

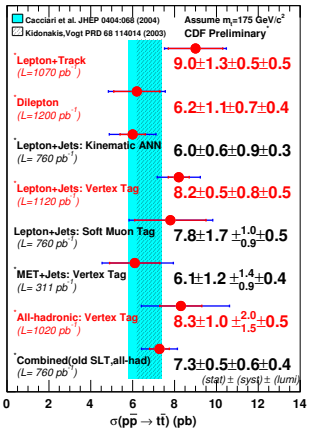

Figure 8: $t\bar{t}$ production cross section at CDF.

The $l + jets$ channel has worst signal-to background ratio, therefore, since the beginning of top physics, it has been customary to exploit the presence of two jets containing b quark. The characteristic signature due to the presence of long-lived particles is used to improve S/B. One can require one or two b tags (i.e. jets identified as containing b debris) with an efficiency that, for $t\bar{t}$ events reaches $\simeq$ 55 %. While both CDF and D0 are trying to improve their b tagging algorithms to increase efficiency, the overall acceptance and S/B ratio are already good enough to ensure that this channel is the most important in many top quark physics measurements. As for the cross section, the most recent result comes from D0 (1 fb^{-1}) and is $\sigma_{l+j} = 8.3^{+0.6}_{-0.5}(stat)^{+0.9}_{-1.0}(sys) \pm 0.5(lum)$ pb.

In the fully hadronic channel the final state (6 jets) has a large multi-jet background to compete with. Therefore, after triggering the S/B is $\simeq 1/1300$. A combined neural-net based kinematic analysis and b tagging improve this ratio to $\simeq 1/16$. Thanks to this selection the result for the cross section is comparable to the other two channels. In $\simeq 1$ fb^{-1} CDF measures: $\sigma_{all-had} = 8.3 \pm 1.0(stat)^{+2.0}_{-1.5}(sys) \pm 0.5(lum)$ pb

With less than 50% of the dataset analyzed, the cross section measurements are reaching the level of the theoretical NLO calculations. $\sigma_{t\bar{t}} = 6.7^{+0.7}_{-0.9}$ pb [10], $\sigma_{t\bar{t}} = 6.8 \pm 0.6$ pb [11]. A NNLO calculation might become quite interesting, even more when the LHC comes into operation although at the moment it appears too challenging to be addressed with standard calculation procedures.

Top decays before hadronizing, therefore there are no bound states, unlike the other quarks. Therefore its mass, a fundamental quantity that combined with the W mass, provides us on insight on the Higgs sector, can be accurately measured. CDF and D0 measure M_{top} in each decay channel using several techniques. The original *template* method, where distributions from data were compared with expectations from (combined) top MC and background, is now complemented by Matrix Element (ME) and Dynamic Likelihood Method (DLM) where the intrinsic structure of the decay enters directly and helps to improve the measurement.

In table 2 we summarize the most recent results obtained with $\approx$ 1 fb^{-1}.

All-hadronic (CDF, 943 pb^{-1})	171.1 ± 4.3
Dilepton (CDF, 1030 pb^{-1})	164.5 ± 5.6
Dilepton (D0, 1000 pb^{-1})	172.5 ± 8.0
Lepton+jets (CDF, 940 pb^{-1})	170.9 ± 2.5
Lepton+jets (D0, 900 pb^{-1})	170.5 ± 2.7
World Average	170.9 ± 1.8

Table 2: Best M_{top}results (in GeV/c^2).

The new world average is $M_{top} = 170.9 \pm 1.8$ GeV/c^2. While this measurement is largely dominated (about 70 %) by the results in the $l + jets$ channel, the all-hadronic channel is acquiring a more prominent role. The systematic uncertainty in this measurement is already 2.1 GeV/c^2 close to the 1.4 GeV/c^2 of the lepton+jets channel.

In previous measurements the dominant systematic effect came from the Jet Energy Scale (JES). JES indicates all the effects that -for a given measured jet energy- provide us with the information about the energy of the original parton. Both experiments are now calibrating *in situ* the JES by exploiting the constraint provided by the jets coming from the hadronic W decay. In this way the JES is included in the statistical uncertainty of the measurements and will improve with larger data sets. For example the statistical uncertainty of the CDF $l + jets$ measurement (166 events) includes two contributions: 1.6 GeV/c^2 from statistics and the remaining from JES.

With more than 2 fb^{-1} on tape, the future of top quark measurements looks bright. The top mass will improve with the larger dataset, as the JES will be better constrained. Also, both experiments isolated a sample of $Z \rightarrow b\bar{b}$ events that can be used to set the b specific jet energy scale. In figure 9 we show the prediction for the top mass measurement at CDF. While, for example CDF is already doing better than predicted in the TDR [12], it is difficult to establish what the asymptotic limit will be, but a precision < 1 % can be reached and the Tevatron can aim for a combined accuracy of ≤ 1 GeV/c^2, making this measurement a long lasting Tevatron legacy. Such an accuracy is, however, inducing both Collaborations to start addressing a number of effects that, too small to have an impact in the first measurements, can now become relevant. Moreover, a more general discussion of the meaning of the quantity measured is in order. CDF and D0, use Pythia Monte Carlo to generate top templates to which they compare data. With such an accuracy, of the order of the top natural width, one should be careful in interpreting the meaning of the measurement, in particular as we make larger use of DLM and ME methods.

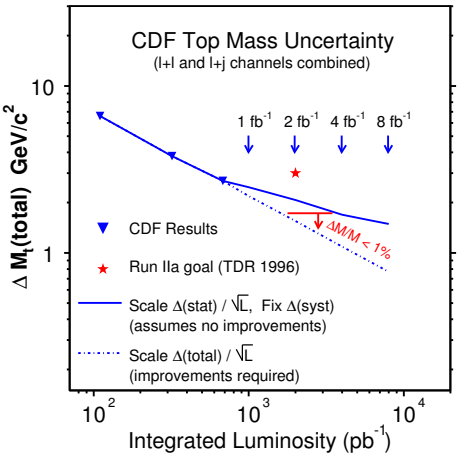

Figure 9: Prediction for M_{top} accuracy as a function of integrated luminosity.

The most significant recent result in terms of *top* production came from D0 which, for the first time, presented evidence for *single top* production. This purely EWK process proceeds through two (s and t) channels, which have SM cross section of 0.88 and 1.98 pb respectively. While CDF sets a combined upper limit of 2.6 pb at 95 % C.L., D0 finds a

3.4 σ signal combining three analyses and advanced statistical techniques. The measured production cross section is 4.9 ± 1.4pb (Figure 10), as it is direcly proportional to $|V_{tb}|^2$, D0 is able to set a direct limit $0.68 < |V_{tb}| < 1$ at 95 % C.L.

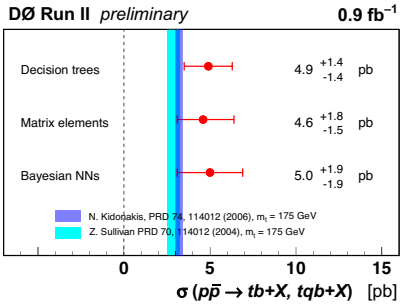

Figure 10: Evidence for single top.

6 Higgs Searches

In the SM the Higgs mass is directly connected to the W and top mass, therefore precision measurements of the W and top mass mentioned above translate into a limit $M_H < 144$ GeV/c^2 at 95 % C.L. which rises to 182 GeV/c^2 if one takes into account the (direct) LEP 2 limit of $M_H > 114$ GeV/c^2. This result might imply some tension between the SM prediction and the observation, however it only appears at 1 σ level. Figure 11 shows the 95 % C.L. contour which demonstrates how only by the end of Run 2 one might really gather (indirect) information on the Higgs SUSY sector from the M_{top} and M_W measurements.

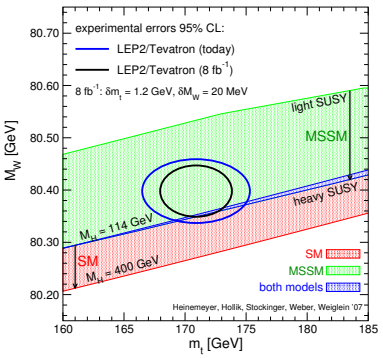

Figure 11: Constraints on SM and non-SM Higgs from indirect measurements

While the indirect measurement was always seen as the major contribution of the Tevatron to Higgs hunting, in recent years the increased luminosity delivered by the accelerator pushed the two Collaborations aggressively to pursue direct Higgs searches. The experimental situation at the Tevatron has two bounds. One is the cross section. For low mass Higgs ($<$ 120 GeV/c^2) direct production from gluon fusion is still $\leq$ 1 pb, while associated production of Higgs with W or Z boson is about an order of magnitude smaller. In this region Higgs decay $\approx 80\%$ of the time directly into $b\bar{b}$ pairs. The huge background due to heavy flavour jets prevents us from searching in the $b\bar{b}$ channel while the low cross section prevents us from searching for this production mode through its rare -but almost background free- decays (like $\gamma\gamma$). Therefore in this region we concentrate on the search in the WH and ZH channel where the W and Z provides a clean signature and (most) of the triggering opportunities. The Higgs decay into two bs can be exploited further to reduce the background by exploiting the b-tagging technique, as already done in *top* events.

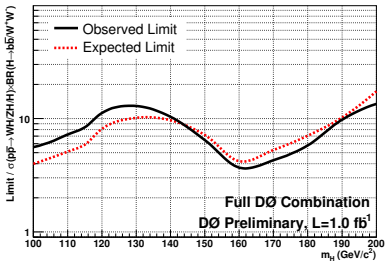

Figure 12: D0 direct Higgs limits($\simeq$ 1 fb^{-1}).

Recently the large data sample available opened up the opportunity to look for high mass Higgs ($\simeq$ 160 GeV/c^2) directly produced by gg fusion and decaying into W pairs. By exploiting the leptonic decays of the W the background is very low and mostly due to SM processes. By increasing the acceptance as much as possible Tevatron experiments have become quite competitive.

Both D0 and CDF present results with 1 fb^{-1} in several channels. Figure 12 shows the combination of D0 results from many channels across the whole mass range of searches. The ratio 95% CL/SM is 8.4 for $M_H = 115$ GeV/c^2 and 3.7 for $M_H = 160$ GeV/c^2. With respect to Summer 2006 more analyses were performed and new techniques were used.

CDF has not yet provided a full combination of its searches. The most recent results, all with $\simeq$ 1 fb^{-1} are in the ZH,$Z \to ll$, $Z \to \nu\nu$ channels and in the $H \to WW^*$ channel. In the first two searches the ratio with respect to the SM cross section is 16 (for $M_H = 115$ GeV/c^2) while for the third is 5.6 for $M_H = 160$ GeV/c^2 (equivalent to a cross section limit of 2.2 pb).

Unfortunately no official Tevatron combined limit is yet available and, indeed, for example, the D0 combined limit alone is already better than the previous (Summer 06) Tevatron combined. Despite that, it is clear that, even before the end of Run 2, the search for the Higgs at the Tevatron will provide useful input to the LHC experiments.

7 Searches for New Physics

The Tevatron is not only performing precision measurements of the SM, but is testing its frontier to check a number of theories which have been proposed as well as for any unknown possibility. It is not possible to fully present the whole set of analyses, ranging from SUSY to Extra Dimensions, Leptoquarks and more, which are, however, discussed in other contributions to this Conference [13]. Therefore I will only present a sample of recent results.

The SUSY paradigm is intensively tested, as already discussed in the flavour sector. First of all both CDF and D0 search for non-SM Higgs. As the SUSY Higgs has a large decay rate in τ pairs, and its production can be enhanced for large $\tan\beta$ both experiments developed a number of τ-ID algorithms to exploit the good S/B ratio of the $H \to \tau\tau$ channel.

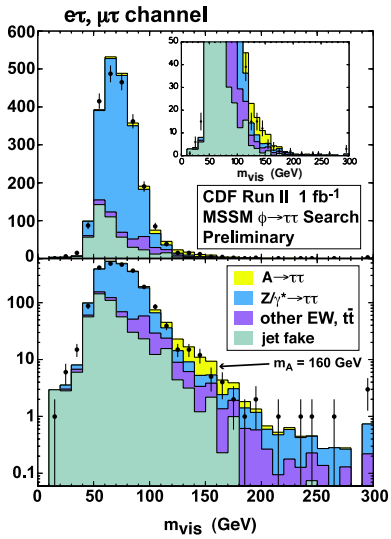

Figure 13: CDF Search for $H \to \tau\tau$.

Dedicated triggers and extensive improvement of algorithms brought up the efficiency for this channel. τ are identified through the detection of their debris in the $\tau \rightarrow l + \nu\nu$ and the $\tau \rightarrow$ hadronic decay. CDF searched for a discrepancy from SM expectations in the visible mass (m_{vis}) distribution, where by m_{vis} we mean the invariant mass of the visible τ decays and the missing E_T. In the region $\simeq 150$ GeV/c^2 a small excess of $\simeq 2\sigma$ is visible in the channel where one of the two taus decays hadronically. Figure 13 shows a hypothetical Higgs with mass $M_A = 150$ GeV/c^2 superimposed on data. In the corresponding channel in which both τs decay leptonically the search does not have enough statistics to see a possible signal. D0 result does not exhibit a similar enhancement.

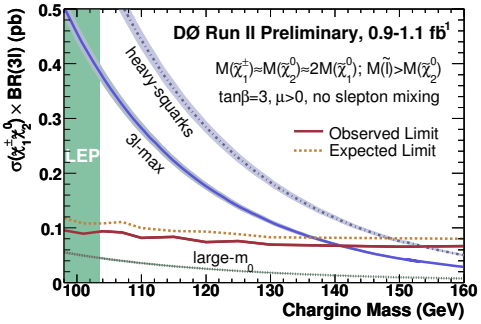

Figure 14: D0 limit for chargino production.

Another SUSY sector being tested is through the direct search for chargino and neutralino which are produced with sizeable cross sections. No signal is observed and therefore limits are set for $M_{\chi^{\pm}}$ (figure 14).

Despite the large background and the small cross section, CDF performed a search for direct squark and gluino production in a sample of events containing large missing transverse energy and three jets. The negative result is converted in a limit in the $M_{squark} - M_{gluino}$ plane (Fig. 15).

8 Conclusion

With more than 2 fb^{-1} already on tape, and the prospects of integrating between 6 and 8 fb^{-1}, the Tevatron experiments are now testing the standard model at its boundaries. The detectors are well understood and the analyses are now mature, therefore the precision study of known processes can be used to measure structure functions, test theoretical calculations and challenge measurements performed elsewhere. The measurement of M_W and M_{top} can represent an enduring legacy of the Tevatron well after the LHC starts taking data. The large datasets allow to search for new physics and for the yet undetected Higgs particle which now appears -for some mass ranges- within reach.

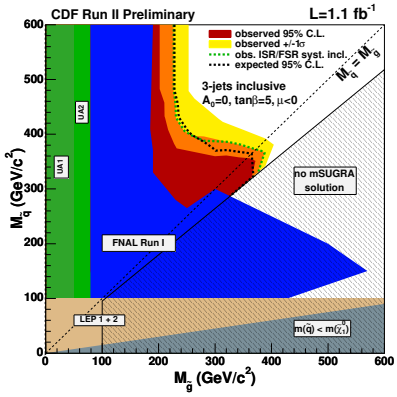

Figure 15: CDF limits in the $M_{Squark} - M_{gluino}$ plane.

Acknowdledgments

I would like to thank many CDF and D0 colleagues who helped me in preparing my contribution to this Conference. In particular my thanks to O. Atramentov, P. Bussey, J. Cammin, M. Corcoran, M. D'Onofrio, R. Erbacher, S. Jabeen, R. Kehoe, M. Heck, J. Hobbs, S. Leone, C. Mesropian, M. Neubauer, L. Pinera, B. Reisert, A. Robson, P. Strohemer, D. Stuart, S. Vallecorsa. R. Van Kooten, R. Vilar, J. Wagner. All mistakes are, of course, mine.

References

[1] Slides:
`http://indico.cern.ch/contributionDisplay.py?contribId=9&sessionId=2&confId=9499`

[2] For B Physics see contribution to these Proceedings by M. Corcoran, R. Kehoe, M. Heck, B. Reisert.

[3] For Tevatron results on strong interactions, diffraction and jet studies, see contribution to these Proceedings by O. Atramentov, J. Cammin, D. D'Onofrio, L. Pinera, C. Mesropian, S. Vallecorsa.

[4] M. Carena, A. Menon,C. E.M. Wagner arXiv:hep-ph/07041143

[5] For recent Tevatron results on EWK physics see contributions to these Proceedings by S. Malik, Y. Maravin, A. Robson.

[6] A. Abulencia et al., Phys. Rev. Lett. **98**, 251801(2007).

[7] K. Melnikov, F. Petriello, Phys. Rev. D **74**, 114017(2006).

[8] Tevatron results for direct Higgs searches were presented in this conference by R. Vilar.

[9] Top phyiscs results are detailed in the contributions to this Conference by C. Gerber, S. Jabeen, J. Wagner.

[10] M. Cacciari, S. Frixione, G. Ridolfi, M. Mangano and P. Nason, J. High Energy Phys. 04(2004) 068.

[11] N. Kidonakis and R. Vogt, Phys. Rev. D **68** 114014 (2003).

[12] CDF Collaboration, Technical Design Report, Fermilab-Pub-96-390-E, Nov. 1996.

[13] Many searches for physics beyond the standard model are discussed in the contributions to these Proceedings by P. Strohemer and D. Stuart,

RECENT DEVELOPMENTS IN HEAVY FLAVOUR PRODUCTION

G. KRAMER

Universität Hamburg - II. Institut für Theoretische Physik
Luruper Chaussee 149 - 22761 Hamburg - Germany

We review one-particle inclusive production of heavy-flavoured hadrons in a framework which resums the large collinear logarithms through the evolution of the FFs and PDFs and retains the full dependence on the heavy-quark mass without additional theoretical assumptions. We focus on presenting results for the inclusive cross section for the production of charmed mesons in $p\bar{p}$ collisions and the comparison with CDF data from the Tevatron as well as on inclusive B-meson production and comparison with recent CDF data. The third topic is the production of $D^\star$ mesons in photoproduction and comparison with recent H1 data from HERA.

1 Introduction

One-particle inclusive production processes provide extensive tests of perturbative quantum chromodynamics (pQCD). In contrast to fully inclusive processes, it is possible to study distributions in the momentum of the final-state particle and to apply kinematical cuts close to the experimental situation. On the other hand, contrary to even more exclusive cases, QCD factorisation theorems [2, 3] still hold stating that this class of observables can be computed as convolutions of *universal* parton distribution functions (PDFs) and fragmentation functions (FFs) with perturbatively calculable hard scattering cross sections. As is well-known, it is due to the factorisation property that the parton model of QCD has predictive power. Hence, tests of the universality of the PDFs and FFs are of crucial importance for validating this QCD framework. At the same time, lowest-order expressions for the hard scattering cross sections are often not sufficient for meaningful tests and the use of higher order computations is needed.

The perturbative analysis is becoming more involved and interesting if the observed final state hadron contains a heavy (charm or bottom) quark. In this case, the heavy-quark mass m enters as an additional scale. Clearly, the conventional massless formalism, also known as zero-mass variable-flavour-number scheme (ZM-VFNS), can also be applied to this case, provided the hard scale Q of the process is much bigger than the heavy-quark mass so that terms m/Q are negligible. However, at present collider energies, most of the experimental data lie in the kinematic region $Q \gtrsim m$ and it is necessary to take the power-like mass terms into account in a consistent framework.

The conventional calculational scheme is the so-called massive scheme or fixed-flavour-number scheme (FFNS) [4], in which the number of active flavours in the initial state is limited to $n_f = 3$ ($n_f = 4$) in the case of massive charm (bottom) production, and the c (b) quark appears only in the final state. In this case, the c (b) quark is always treated as a heavy particle, not as a parton. The actual mass parameter m is explicitly taken into account along with p_T. In this scheme, m acts as a cutoff for the initial- and final sate collinear singularities and sets the scale for the perturbative calculations. A factorisation of these would-be initial- and final state collinear singularities is not necessary, neither is the introduction of a FF for the transition $b \to B$. However at NLO, terms proportional to

$\alpha_s \ln(p_T^2/m^2)$, where α_s is the strong coupling constant, arise from collinear gluon emissions by c (b) quarks or from branchings of gluons into collinear $c\bar{c}$ ($b\bar{b}$) pairs. These terms are of order $O(1)$ for large p_T and spoil the convergence of the perturbation series. The FFNS with $n_f = 3$ ($n_f = 4$) should be limited to a rather limited range of p_T, from $p_T = 0$ to $p_T \gtrsim m$. The advantage of this scheme, however, is that the m^2/p_T^2 power terms are fully taken into account.

The ZM-VFNS and FFNS are valid in complementary regions of p_T, and it is desirable to combine them in a unified approach that incorporates the advantages of both schemes, i.e. to resum the large logarithms, retain the full finite-m effects, and preserve the universality of the FFs. An earlier approach to implement such an interpolation is the so-called fixed-order-next-to-leading logarithm (FONLL) scheme, in which the conventional cross section in the FFNS is linearly combined wit a suitably modified cross section in the ZM-VFNS with perturbative FFs, using a p_T-dependent weight function [5]. Then the FONLL cross section is convoluted with a non-pertubative FF for the $b \to B$ transition.

The subject of this review is the theoretical description of one-particle inclusive production of heavy-flavoured hadrons $X_h = D, B, \Lambda_c, \ldots$ in a massive variable-flavour-number scheme (GM-VFNS). In such a scheme the large collinear logarithms of the heavy-quark mass $\ln \mu/m$ are subtracted from the hard scattering cross sections and resummed through the evolution of the FFs and PDFs. At the same time, finite non-logarithmic mass terms m/Q are retained in the hard part and fully taken into account.

In order to test the pQCD formalism, in particular the universality of the FFs, it is important to provide a description of all relevant processes in a coherent framework. Therefore, it is important to work out the GM-VFNS at next-to-leading order (NLO) of QCD for all the relevant processes. Previously, the GM-VFNS has been applied to the following processes: $\gamma + \gamma \to D^{\star +} + X$ (direct part) [6], $\gamma + \gamma \to D^{\star +} + X$ (single resolved part) [7], $\gamma + p \to D^{\star +} + X$ (direct part) [8], $p + \bar{p} \to (D^0, D^{\star +}, D^+, D_s^+) + X$ [9, 10, 11], where the latter results for hadron–hadron collisions also constitute the resolved contribution to the photoproduction process $\gamma + p \to X_h + X$.

In this contribution, I will review the progress achieved in describing the production of heavy-flavoured hadrons X_h in hadron–hadron and photon–proton collisions in the GM-VFN scheme as it has been worked out recently. The main focus will be on the comparison with experimental data from CDF at the Tevatron for $p + \bar{p} \to (D^0, D^{*+}, D^+, D_s^+) + X$ and $p + \bar{p} \to B^+ + X$ and from H1 at HERA for $\gamma + p \to D^{*+} + X$.

2 Theoretical Framework

2.1 GM-VFNS

The differential cross sections for inclusive heavy-flavoured hadron production can be computed in the GM-VFNS according to the familiar factorisation formulae, however, with heavy-quark mass terms included in the hard scattering cross sections [12]. Generically, the physical cross sections are expressed as convolutions of PDFs for the incoming hadron(s), hard scattering cross sections, and FFs for the fragmentation of the outgoing partons into the observed hadron. All possible partonic subprocesses are taken into account. The massive hard scattering cross sections are constructed in a way that in the limit $m \to 0$ the conventional ZM-VFNS is recovered. A more detailed discussion of the GM-VFNS and the construction of the massive hard scattering cross sections can be found in Refs. [9, 10] and

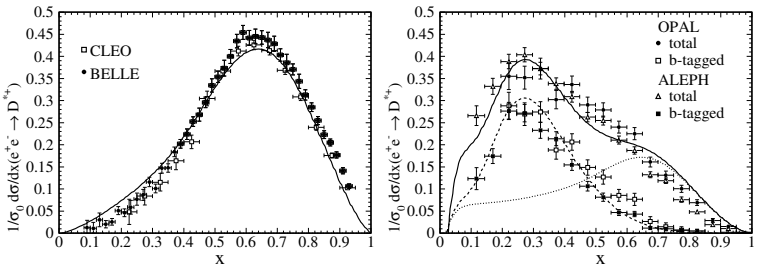

Figure 1: The cross section for inclusive $D^{*\pm}$ production in e^+e^- annihilation evaluated in NLO is compared with from CLEO [23] and BELLE [24] (left) as well as from the ALEPH [18] and OPAL [19] data (right). The three curves in the right figure correspond to the $Z \to c\bar{c}$, $Z \to b\bar{b}$ and full samples.

the conference proceedings [13, 14, 15, 16].

2.2 Fragmentation Functions

A crucial ingredient entering these calculation are the non-perturbative FFs for the transition of the final state parton into the observed hadron X_h. For charm-flavoured mesons, X_c, such sets of FFs have been constructed quite some time ago. For $X_c = D^{*+}$, FFs were extracted at LO and NLO in the $\overline{\rm MS}$ factorisation scheme with $n_f = 5$ massless quark flavours [17] from the scaled-energy (x) distribution $d\sigma/dx$ of the cross section of $e^+e^- \to D^{*+} + X$ measured by the ALEPH [18] and OPAL [19] collaborations at CERN LEP1. Recently, this analysis was extended [20] to include $X_c = D^0, D^+, D_s^+, \Lambda_c^+$ by exploiting appropriate OPAL data [21]. In Refs. [17, 20], the starting scales μ_0 for the DGLAP evolution of the $a \to X_c$ FFs in the factorisation scale μ'_F have been taken to be $\mu_0 = 2m_c$ for $a = g, u, \overline{u}, d, \overline{d}, s, \overline{s}, c, \overline{c}$ and $\mu_0 = 2m_b$ for $a = b, \overline{b}$. The FFs for $a = g, u, \overline{u}, d, \overline{d}, s, \overline{s}$ were assumed to be zero at $\mu'_F = \mu_0$ and were generated through the DGLAP evolution to larger values of μ'_F. For consistency with the $\overline{\rm MS}$ prescription for PDFs, we repeated the fits of the X_c FFs for the choice $\mu_0 = m_c, m_b$ [22]. This changes the c-quark FFs only marginally, but has an appreciable effect on the gluon FF, which is important at Tevatron energies, as was found for D^{*+} production in Ref. [9]. In the meantime much more accurate data for the inclusive production of D^0, D^+ and D^{*+} mesons in e^+e^- annihilation have been published by the CLEO [23] and the BELLE [24] collaborations. With these data new FFs have been constructed. These fits were done in the framework of the GM-VFNS, where the finite charm- and bottom-quark masses were kept in the hard scattering cross sections. A global fit with the data from CLEO and BELLE at 10.52 GeV together with the ALEPH [18] and OPAL [19] data at the Z-resonance are shown in Fig. 1 [25].

Already many years ago we made an analysis towards FFs for bottom-flavoured mesons $B^{\pm}$ [26] by using data from the OPAL collaboration at LEP1 [27]. In the last years much more accurate measurements of the inclusive B meson production at the Z-resonance have been done by the ALEPH [28], SLD [29] and the OPAL [30] collaborations. With the data in these references combined we have performed a new fit to obtain the FFs for $q, g, b \to B$,

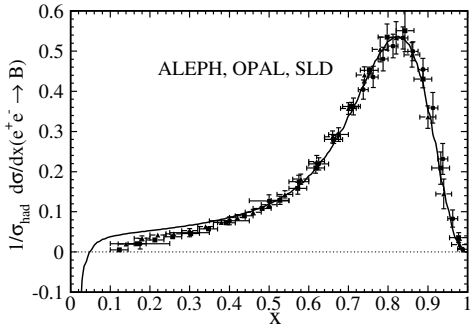

Figure 2: Comparison of the ALEPH [28] (circles), SLD [29] (triangles) and OPAL [30] (squares) data with the NLO fits using the power ansatz. The initial factorisation scale for all partons is μ_0=4.5 GeV.

where, in this case, q are the light quarks including c. To be consistent with the starting scale of the PDFs the FFs of these light partons are assumed to vanish at the starting scale $\mu_0 = m_b = 4.5$ GeV and only the $b \to B$ FF is parametrised by the usual power ansatz at the starting scale μ_0. The FFs of the light quarks and the gluon are generated via DGLAP evolution at higher scales. The result of the combined fit is seen in Fig. 2. All three data sets are consistent with each other and the fit describes the data quite well in the whole x range, except possibly at rather small x [31].

2.3 Input Parameters

For the numerical results presented below we have chosen the following input. For the proton PDFs we have employed the CTEQ6.1M PDFs from the CTEQ collaboration [32, 33] and for the charmed meson fragmentation functions the sets from [22]. We have set $m_c = 1.5$ GeV, $m_b = 5$ GeV (in the case of charmed meson production), $m_b = 4.5$ GeV (in the case of B-meson production) and have used the two-loop formula for $\alpha_s^{(n_f)}(\mu_R)$ in the $\overline{\rm MS}$ scheme with $\alpha_s^{(5)}(m_Z) = 0.118$. The theoretical predictions depend on three scales, the renormalisation scale μ_R, and the initial- and final-state factorisation scales μ_F and μ'_F, respectively. Our default choice for hadro- and photoproduction has been $\mu_R = \mu_F = \mu'_F = m_T$, where $m_T = \sqrt{p_T^2 + m^2}$ is the transverse mass. Scale changes are controlled by ξ_R and ξ_F, where $\xi_R = \mu_R/m_T$, $\xi_F = \mu_F/m_T$ and $\xi'_F = \mu'_F/m_T$.

3 Hadroproduction

A few years ago the CDF collaboration has published first cross section data for the inclusive production of D^0, D^+, D^{*+}, and D_s^+ mesons in $p\bar{p}$ collisions [34] obtained in Run II at the Tevatron at center-of-mass energies of $\sqrt{S} = 1.96$ TeV. The data come as distributions $d\sigma/dp_T$ with y integrated over the range $|y| \leq 1$ and the particle and antiparticle contributions are averaged.

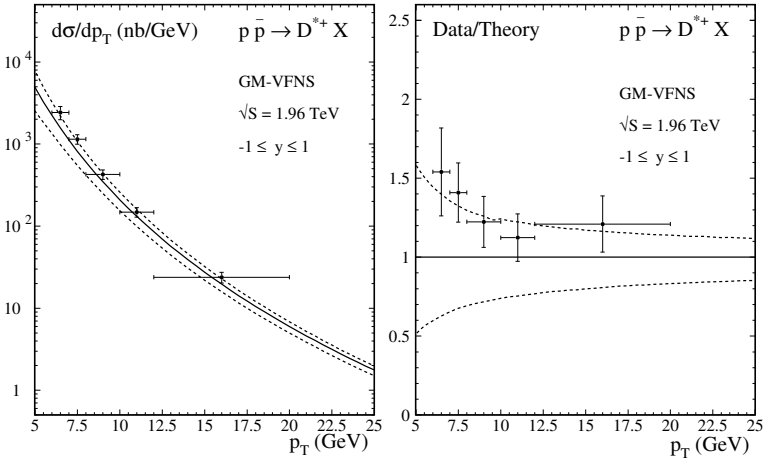

Figure 3: Comparison of the CDF data [34] with our NLO predictions for D^{*+}. The solid line represents our default prediction obtained with $\mu_R = \mu_F = \mu'_F = m_T$, while the dashed lines indicate the scale uncertainty estimated by varying μ_R, μ_F, and μ'_F independently within a factor of 2 up and down relative to the central values. The right figure shows the data-over-theory representation with respect to our default prediction.

Our theoretical predictions in the GM-VFNS are compared with the CDF data for $D^\star$ mesons on an absolute scale in Fig. 3 (left) and in the data-over-theory representation with respect to our default results in Fig. 3 (right). We find good agreement in the sense that the theoretical and experimental errors overlap, where the experimental results are gathered on the upper side of the theoretical error band, corresponding to a small value of μ_R and large values of μ_F and μ'_F, the μ_R dependence being dominant in the upper p_T range. As is evident from Fig. 3 (right), the central data points tend to overshoot the central QCD prediction by a factor of about 1.5 at the lower end of the considered p_T range, where the errors are largest, however. This factor is rapidly approaching unity as the value of p_T is increased. The tendency of measurements of inclusive hadroproduction in Tevatron run II to prefer smaller renormalisation scales is familiar from single jets, which actually favour $\mu_R = p_T/2$ [35]. It will be interesting to compare these data with predictions using the most recently constructed fragmentation functions based on the BELLE and CLEO data shown above. For more details and a comparison with the data for the D^0, D^+, and D_s^+ mesons we refer to Ref. [11].

In the GM-VFNS framework we have also calculated the cross section distribution $d\sigma/dp_T$ of B-meson hadroproduction. The calculations proceed analogously to the case of D mesons outlined in Ref. [9]. Now the heavy quark mass m is the b quark mass m_b. The c quark belongs to the group of light quarks q, whose mass is put to zero.

The NLO cross section consists of three classes of contributions.
Class (i) contains all the partonic subprocesses with a $b, \bar{b} \to B$ transition in the final state that have only light partons $(g, q, \bar{q})$ in the initial state, the possible pairings being gg, gq,

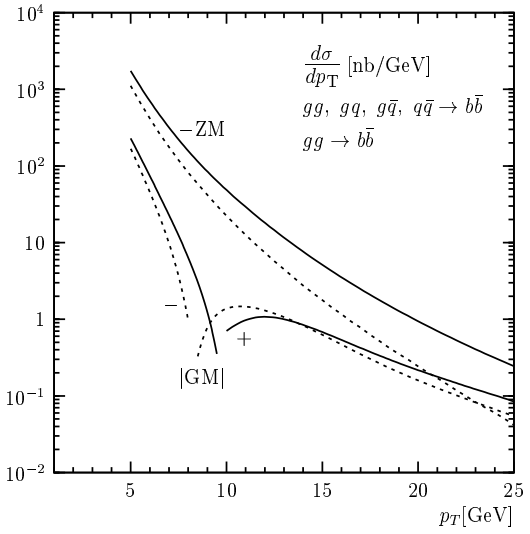

Figure 4: Transverse-momentum distribution $d\sigma/dp_T$ of $p\bar{p} \to B+X$ at c.m. energy $\sqrt{S} = 1.96$ TeV integrated over the rapidity range $|y| < 1$. The contributions of class (i) (solid lines) and their gg-initiated parts (dashed lines) evaluated at NLO in the ZM-VFNS (upper lines) and the GM-VFNS (lower lines) are compared.

$g\bar{q}$, and $q\bar{q}$.
Class (ii) contains all the partonic subprocesses with $b, \bar{b} \to B$ transitions in the final state that also have b or $\bar{b}$ quarks in the initial state, the possible pairings being gb, $g\bar{b}$, qb, $q\bar{b}$, $\bar{q}b$, $\bar{q}\bar{b}$ and $b\bar{b}$.
Class (iii) contains all the partonic subprocesses with a $g, q, \bar{q} \to B$ transition in the final state.
In the FFNS only the contributions of class (i) are included, but the full m dependence is retained. On the other hand, in the ZM-VFNS, the contributions of all the three classes are taken into account, but they are evaluated for $m = 0$. In the GM-VFNS, the class-(i) contribution of the FFNS is matched to the $\overline{\rm MS}$ scheme through appropriate subtractions of would-be collinear singularities, and is then combined with the class-(ii) and class-(iii) contributions of the ZM-VFNS. Thus only the hard scattering cross sections of class (i) carry explicit m dependence. Specifically, the subtractions affect initial states involving $g \to b\bar{b}$ splittings and final states involving $g \to b\bar{b}$, $b \to gb$ and $\bar{b} \to g\bar{b}$ splittings, and they introduce logarithmic dependences on the initial- and final-state factorisation scales in the hard-scattering cross sections of class (i), which are compensated through NLO by the respective factorisation scale dependences by the b-quark PDF and the $b \to B$ FF, respectively. It turns out that the q-quark fragmentation contribution is negligible. However, the gluon fragmentation reaches approximately 50% at small values of p_T, and somewhat less towards larger values of p_T.

The explicit contributions to the hard scattering cross sections of class (i) as they contribute to the final result, after all the subtractions are made, are shown in Fig. 4. The results for $m = 0$ and finite m are shown in this figure as the upper and lower solid lines,

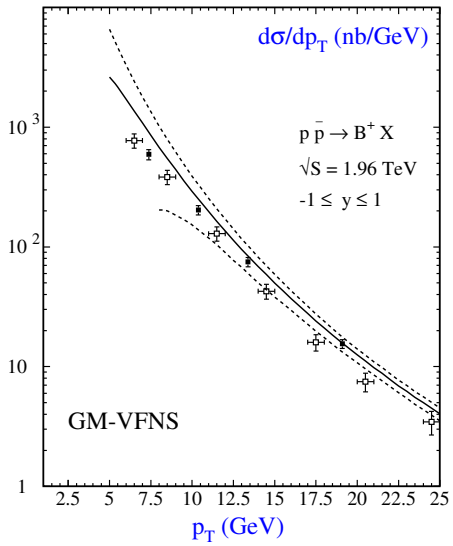

Figure 5: Transverse-momentum distribution $d\sigma/dp_T$ of $p\bar{p} \to B+X$ at c.m. energy $\sqrt{S} = 1.96$ TeV integrated over the rapidity range $|y| < 1$. The central NLO prediction with $\xi_R = \xi_F = 1$ (solid line) of the GM-VFNS is compared with CDF data from Refs. [36] (open squares) and [37] (solid squares). The maximum and minimum values obtained by independently varying ξ_R and ξ_F in the range $1/2 \leq \xi_R, \xi_F \leq 2$ with the constraint that $1/2 \leq \xi_R/\xi_F \leq 2$ are also indicated (dashed lines).

respectively. They constitute parts of the final ZM-VFNS and GM-VFNS results. In both cases, the contributions of classes (ii) and (iii) for $m = 0$ still must be added to obtain the full predictions to be compared with experimental data. The class-(i) contributions in the ZM-VFNS and GM-VFNS schemes are, therefore, entitled to be negative and they indeed are, for $p_T \lesssim 76$ GeV and $p_T \lesssim 10$ GeV, respectively, as may be seen from Fig. 4. Comparing the ZM-VFNS and GM-VFNS results, we notice that the finite-m effects are significant for $p_T \lesssim 10$ GeV and even cause a sign change for 10 GeV $\lesssim p_T \lesssim 76$ GeV. However, as will become apparent below, the contributions of class (i) are overwhelmed by those of classes (ii) and (iii), so that the finite-m effects are washed out in the final predictions, except for very small values of p_T. It is instructive to study the relative importance of the gg-initiated contributions. They are also included in Fig. 4 for $m = 0$ and finite m as the upper and lower dashed lines, respectively. They exhibit a similar pattern as the full class-(i) contributions and dominate the latter in the small-p_T range. Comparing Fig. 4 with Fig. 2(c) in Ref. [9], we observe that the relative influence of the finite-m effects is much smaller in the c-quark case, as expected because the c quark is much lighter than the b quark. One can also see from Fig. 4 that the difference of the class (i) contributions in the GM-VFNS and ZM-VFNS decrease with increasing p_T.

In Fig. 5 we show the comparison of the final prediction, in which all contributions of classes (i), (ii) and (iii) are combined [31] with recent Tevatron data. We compare our

prediction to the more recent CDF data from run II in Refs. [36] (open squares) and [37] (solid squares). In this figure the solid line presents the central prediction for $\xi_R = \xi_F = 1$ and the dashed lines indicate the maximum and minimum values obtained by independently varying ξ_R and $\xi_F = \xi'_F$ in the range $1/2 \leq \xi_R, \xi_F \leq 2$ with the constraint $1/2 \leq \xi_R/\xi_F \leq 2$. The maximum and minimum values correspond to $\xi_F = 2$ and $\xi_F = 1/2$, respectively. The variation with ξ_R is milder than the one with ξ_F. For $\xi_F < 1$, μ_F reaches the starting scale $\mu_0 = m$ for the DGLAP evolution of the FFs and the b-quark PDF at $p_T = m_b\sqrt{1/\xi_F^2 - 1}$. For smaller values of p_T, there is no prediction because the FFs and the b-quark PDF are put to zero for $\mu_F < \mu_0$. This explains why the p_T distribution for $\xi_F = 1/2$ only starts at $p_T = \sqrt{3}m_b \approx 7.8$ GeV. The most recent data [37] nicely agree with the GM-VFNS result. They lie close to the central prediction, with a tendency to fall below it in the lower p_T range, and they are comfortably contained within the theoretical error band. We conclude from this, that the notorious Tevatron B-meson anomaly with data-to-theory ratios of typically 2-3, that has been in the literature for more than a decade, is actually not present thanks to both experimental and theoretical progress. The previous CDF data [36] based on the measurement of $J/\psi + X$ final states are compatible with the latest ones for $p_T < 12$ GeV, but are systematically below them for the larger values of p_T. This inconsistency becomes even more apparent by noticing that Fig. 4 only contains 4 out of the 13 data points for $p_T > 12$ GeV quoted in Ref. [36] and that the omitted data points line up with the selected ones. This suggests that the systematical errors in Ref. [36] and perhaps also in ref. [37], might be underestimated and that the overall normalisation might need some adjustment.

The measured p_T distributions of Ref. [36] reaches down to almost $p_T = 0$ and exhibits a maximum at $p_T \approx 2.5$ GeV. This small-p_T behaviour is correctly reproduced in the FFNS without DGLAP-evolved FFs, which receive only contributions of class (i) without any subtractions. It is clear that our present implementation of the GM-VFNS is not suitable for cross sections in the small-p_T region. Although the GM-VFNS is designed to approach the FFNS in its region of validity without introducing additional matching factors, to implement this numerically is not easy due to necessary cancellations between different terms in the calculation. The problem to achieve such cancellations is complicated by the extra factorisation scale; to obtain a smooth transition from the GM-VFNS to the FFNS, one has to carefully match terms that are taken into account at fixed order with terms that are resummed to higher orders in the PDFs and FFs. In addition, it remains to be investigated whether a proper scale choice in the small-p_T range is required and helpful to ensure that the FFs and b-quark PDF are sufficiently suppressed already at $p_T = \mathcal{O}(m)$.

We extend our numerical analysis to include the NLO prediction in the FFNS with $n_f = 4$ massless quark flavours in the initial state, which allows us to also compare with the small-p_T data from Ref. [36]. We evaluate $\alpha_s^{(n_f)}(\mu_R)$ with $n_f = 4$ and $\Lambda^{(4)} = 326$ MeV [32], while we continue using the CTEQ6.1M proton PDFs [32], in want of a rigorous FFNS set with $n_f = 4$. In the FFNS, there is no room for DGLAP-evolved FFs, and only $b, \bar{b} \to B$ transitions are included. For simplicity, we identify b (anti)quarks with B mesons and account for non-perturbative effects by including the branching fraction $B(b \to B) = 39.8\%$ [38] as an overall normalisation factor, *i.e.* we use a $b \to B$ FF of the form $D(x) = B(b \to B)\delta(1-x)$, while the $g, q, \bar{q} \to B$ FFs are put to zero. In Fig. 6, the central FFNS (dot-dashed line), ZM-VFNS (dashed line), and GM-VFNS (solid line) predictions, for $\xi_R = \xi_F = 1$, are compared with the CDF data from Refs. [36, 37]. As in Fig. 4, some of the data points with $p_T > 7$ GeV from Ref. [36] are omitted for clarity. Since the ZM-VFNS and our present

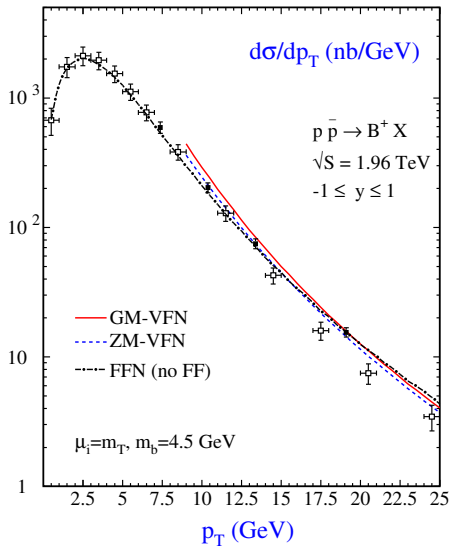

Figure 6: Transverse-momentum distribution $d\sigma/dp_T$ of $p\bar{p} \to B+X$ at c.m. energy $\sqrt{S} = 1.96$ TeV integrated over the rapidity range $|y| < 1$. The central NLO predictions in the FFNS with $n_f = 4$ and without FFs (dot-dashed line), the ZM-VFNS (dashed line), and the GM-VFNS (solid line) are compared with CDF data from Refs. [36] (open squares) and [37] (solid squares).

implementation of the GM-VFNS are not applicable to the small-p_T range, we show the respective predictions only for $p_T > 2m = 9$ GeV. The GM-VFNS prediction shown in Fig. 6 is identical with the central one in Fig. 5. By construction, it merges with the ZM-VFNS prediction with increasing value of p_T. In accordance with the expectation expressed in the discussion of Fig. 4, the difference between the GM-VFNS and ZM-VFNS results is rather modest also at $p_T \gtrsim 2m$, since the m-dependent contribution, of class (i), is numerically small and overwhelmed by the m-independent ones, of classes (ii) and (iii). The FFNS prediction faithfully describes the peak structure exhibited by the next-to-latest CDF data [36] in the small-p_T range and it also nicely agrees with the latest CDF data [37] way out to the largest p_T values. In fact, for $p_T > 4m$, where its perturbative stability is jeopardised by unresummed logarithms of the form $\ln(m_T^2/m^2) \gtrsim 3$, the FFNS prediction almost coincides with the GM-VFNS one, where such large logarithms are resummed. This might be a pure coincidence, which becomes even more apparent if we also recall that the implementation of the $b, \bar{b} \to B$ transition in the FFNS is not based on a factorisation theorem and quite inappropriate for such large values of p_T.

4 Photoproduction

Inclusive photoproduction of $D^\star$ mesons, $\gamma + p \to D^\star + X$, has been studied in Ref. [8] where the direct part has been computed in the GM-VFNS whereas the resolved part has been included in the ZM-VFNS. In this analysis the FFs of Ref. [17] and, for the resolved

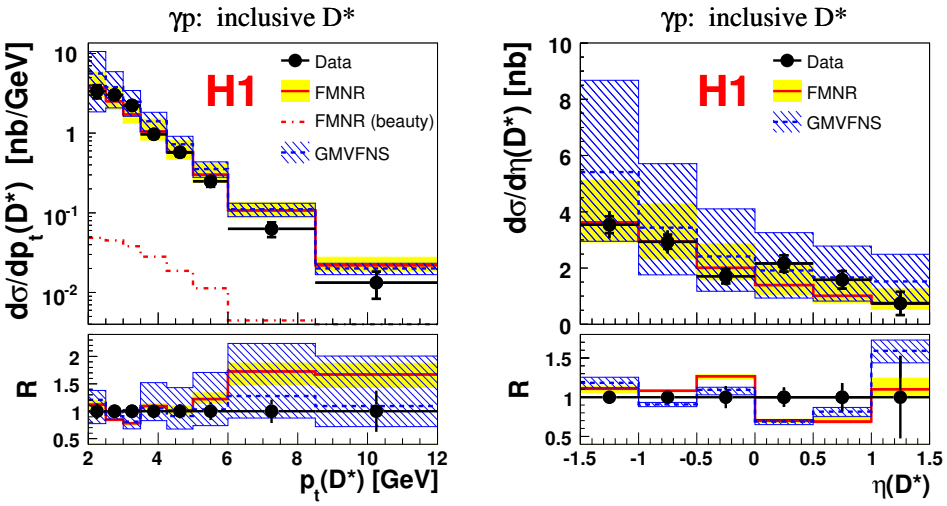

Figure 7: Inclusive D^* cross sections as a function of $p_t(D^*)$ (left) and $\eta(D^*)$ (right) compared to NLO QCD calculations of FMNR [43] in the FFNS and GM-VFNS for photoproduction in the laboratory frame. The FMNR bottom contribution is shown separately for the $p_t(D^*)$ distribution.

contribution, the GRV92 photon PDFs [39] have been utilized. The other parameters have been chosen as specified in Sec. 2.3. In Fig. 6 of Ref. [8], the central numerical predictions for the p_T distributions of the $D^\star$ meson have been compared with preliminary ZEUS data [40]. There exist similar data by the H1 collaboration [41] which have not been used in this analysis. As can be seen in this figure, the agreement of the p_T-distributions with the data is quite good down to $p_T \simeq 2m_c$ and the mass effects turn out to be small. In order to extend the range of applicability of the GM-VFNS into the region $p_T < 3$ GeV more work on the matching to the 3-fixed flavour theory would be needed. Figs. 7 – 9 of Ref. [8], showing results for the rapidity (y), invariant mass (W) and inelasticity ($z(D^\star)$) distributions, have to be taken with a grain of salt since they receive large contributions from the transverse momentum region $1.9 < p_T < 3$ GeV which is outside the range of validity of the present theory. With the work in Ref. [9], it was possible to include also the resolved part in the GM-VFNS. This has been done and the predictions in the complete GM-VFNS framework at NLO, combined with updated FFs [22], have been compared with recent H1 photoproduction data [42]. The results of the calculation and the comparison with the data is shown in Fig. 7. In this figure also the predictions in the FFNS based on the FMNR program [43] are shown. The experimental cross section as a function of p_T falls steeply with increasing p_T as predicted by both calculations. FMNR predicts a distribution which decreases less steeply at large p_T than the data as is seen more clearly from the plot of the ratio of the theoretical over the measured cross section. Also in Fig. 7 the differential cross section as a function of the pseudorapidity $\eta(D^*)$ is shown. This cross section decreases with increasing η. Both calculations predict a similar shape and agree nicely with the data. The GM-VFNS prediction shows a larger scale dependence. Otherwise the two calculations

give rather similar results, which is remarkable, considering the very different ingredients of the two approaches.

5 Summary

We have discussed one-particle inclusive production of heavy-flavoured hadrons in hadron–hadron and photon–proton collisions in a massive variable-flavour-number scheme (GM-VFNS). The importance of a unified treatment of all these processes, based on QCD factorisation theorems, has been emphasised, in order to provide meaningful tests of the universality of the FFs and hence of QCD. At the same time, it is necessary to incorporate heavy-quark mass effects in the formalism since many of the present experimental data points lie in a kinematical region where the hard scale of the process is not much larger than the heavy-quark mass. This is achieved in the GM-VFNS, which includes heavy-quark mass effects and still relies on QCD factorization. We have discussed numerical results for two reactions. In general, the description of the transverse momentum spectra is quite good down to transverse momenta $p_T \simeq 2m$. Extending the range of applicability of our scheme to smaller p_T would require more work on the matching to the corresponding theories in the fixed flavor number scheme.

Acknowledgments

The author would like to thank the organisers of the DIS 2007 workshop for the kind invitation, B. A. Kniehl, I. Schienbein and H. Spiesberger for their collaboration.

References

[1] Slides:
`http://indico.cern.ch/contributionDisplay.py?contribId=10&sessionId=2&confId=9499`

[2] J. C. Collins, D. E. Soper, and G. Sterman, in *Perturbative Quantum Chromodynamics*, edited by A. H. Mueller (World Scientific, 1989).

[3] J. C. Collins and D. E. Soper, Ann. Rev. Nucl. Part. Sci. **37**, 383 (1987).

[4] P. Nason, S. Dawson, and R.K. Ellis, Nucl. Phys. **B303**, 607 (1988); **B327**, 49 (1989); **B335**, 260(E) (1989); W. Beenakker, H. Kuijf, W.L. van Neerven, and J. Smith, Phys. Rev. **D40**, 54 (1989); W. Beenakker, W.L. van Neerven, R. Meng, G.A. Schuler, and J. Smith, Nucl. Phys. **B351**, 507 (1991); I. Bojak and M. Stratmann, Phys. Rev. **D67**, 034010 (2003).

[5] M. Cacciari, M. Greco and P. Nason, JHEP **05** 007 (1998); M. Cacciari and P. Nason, Phys. Rev. Lett. **89** 122003 (2002).

[6] G. Kramer and H. Spiesberger, Eur. Phys. J. **C22**, 289 (2001).

[7] G. Kramer and H. Spiesberger, Eur. Phys. J. **C28**, 495 (2003).

[8] G. Kramer and H. Spiesberger, Eur. Phys. J. **C38**, 309 (2004).

[9] B. A. Kniehl, G. Kramer, I. Schienbein, and H. Spiesberger, Phys. Rev. **D71**, 014018 (2005).

[10] B. A. Kniehl, G. Kramer, I. Schienbein, and H. Spiesberger, Eur. Phys. J. **C41**, 199 (2005).

[11] B. A. Kniehl, G. Kramer, I. Schienbein, and H. Spiesberger, Phys. Rev. Lett. **96**, 012001 (2006).

[12] J. C. Collins, Phys. Rev. **D58**, 094002 (1998).

[13] I. Schienbein, *Open heavy-flavour photoproduction at NLO*, Proceedings of the Ringberg Workshop, *New Trends in HERA Physics 2003*, edited by G. Grindhammer, B. A. Kniehl, G. Kramer and W. Ochs, World Scientific, 2004, p. 197;

[14] I. Schienbein, Proceedings of the 12th International Workshop on Deep Inelastic Scattering (DIS 2004), Strbske Pleso, Slovakia, 14-18 Apr 2004, hep-ph/0408036;

[15] B. A. Kniehl, G. Kramer, I. Schienbein, and H. Spiesberger, Proceedings of the 13th International Workshop on Deep Inelastic Scattering (DIS 2005), Madison, Wisconsin, USA, April 27 - May 1,2005, hep-ph/0507068.

[16] J. Baines et al, Summary report of the heavy-flavour working group of the HERA-LHC Workshop, hep-ph/0601164.

[17] J. Binnewies, B. A. Kniehl, and G. Kramer, Phys. Rev. **D58**, 014014 (1998).

[18] R. Barate *et al.*, [ALEPH Collaboration], Eur. Phys. J. **C16**, 597 (2000).

[19] K. Ackerstaff *et al.*, [OPAL Collaboration], Eur. Phys. J. **C1**, 439 (1998).

[20] B. A. Kniehl and G. Kramer, Phys. Rev. **D71**, 094013 (2005).

[21] G. Alexander *et al.*, [OPAL Collaboration], Z. Phys. **C72**, 1 (1996).

[22] B. A. Kniehl and G. Kramer, Phys. Rev. **D74** 037502 (2006).

[23] M. Artuso *et al.* [CLEO Collaboration], Phys. Rev. **D70** 112001 (2004)

[24] R. Seuster *et al.* [Belle Collaboration], Phys. Rev. **D73** 032002 (2006)

[25] T. Kneesch, B. A. Kniehl, G. Kramer and I. Schienbein, in preparation

[26] J. Binnewies, B. A. Kniehl and G. Kramer, Phys. Rev. **D58** 034016 (1998)

[27] G. Alexander *et al.* [OPAL Collaboration], Phys. Lett. **B364** 93 (1995).

[28] A. Heister *et al.* [ALEPH Collaboration], Phys. Lett. **B512** 30 (2001).

[29] K. Abe *et al.* [SLD Collaboration], Phys. Rev. **D65** 092006 (2002), [Erratum-ibid. **D66** 079905 (2002)].

[30] G. Abbiendi *et al.* [OPAL Collaboration], Eur. Phys. J. **C29** 463 (2003).

[31] B. A. Kniehl, G. Kramer, I. Schienbein, and H. Spiesberger, arXiv:0705.4392 [hep-ph] (2007).

[32] J. Pumplin *et al.*, JHEP **07**, 012 (2002)

[33] D. Stump *et al.*, JHEP **10**, 046 (2003).

[34] D. Acosta *et al.*, [CDF Collaboration], Phys. Rev. Lett. **91**, 241804 (2003).

[35] R. Field, for the CDF Collaboration, in Proceedings of the XIII$^{\rm th}$ International Workshop on Deep Inelastic Scattering (DIS05), Madison, Wisconsin, 2005 (American Institute of Physics, Melville, to be published); B. Davies, for the D0 Collaboration, *ibid.*

[36] D. Acosta *et al.* [CDF Collaboration], Phys. Rev. **D71** 032001 (2005).

[37] A. Abulencia *et al.* [CDF Collaboration], Phys. Rev. **D75** 012010 (2007).

[38] W.M. Yao *et al.* (Particle Data Group), J. Phys. **G33**, 1 (2006).

[39] M. Glück, E. Reya, and A. Vogt, Phys. Rev. **D46**, 1973 (1992).

[40] ZEUS Collaboration, S. Chekanov et al., 31st International Conference on High Energy Physics, ICHEP02, July 24–31 2002, Amsterdam, Abstract 786; see also: ZEUS Collaboration, `http://www-zeus.de/public-plots`, Measurement of $D^\star$ photoproduction at HERA, 2003.

[41] H1 Collaboration, International Europhysics Conference on High Energy Physics, EPS03, July 17–23 2003, Aachen, Abstract 097, DESY-H1prelim-03-071 and earlier H1 papers given in this reference.

[42] A. Aktas *et al.* [H1 Collaboration], Eur. Phys. J. **C50** 251 (2007).

[43] S. Frixione, P. Nason and G. Ridolfi, Nucl. Phys. **B454** 3 (1995); S. Frixione, M. L. Mangano, P. Nason and G. Ridolfi, Phys. Lett. **B348** 633 (1995).

The Fluid Nature of the Quark-Gluon Plasma

William A. Zajc

Columbia University
Department of Physics, New York, NY 10027, USA

Experimental observations on identified particle yields, particle flows, jet "quenching", Mach cones and transverse momentum correlations by the BRAHMS, PHENIX, PHOBOS and STAR experiments, making use of the unprecedented capabilities of RHIC, are highlighted. Their theoretical interpretation in terms of the production of a nearly perfect and highly viscous quark-gluon fluid is discussed.

References

[1] Slides:
http://indico.cern.ch/contributionDisplay.py?contribId=11&sessionId=2&confId=9499

Universal Features of QCD Dynamics in Hadrons and Nuclei at High Energies

Raju Venugopalan *

Physics Department, Brookhaven National Laboratory
Upton, NY 11973, USA

We discuss the empirical evidence for a universal Color Glass Condensate and outline prospects for further studies at future colliders. Some ramifications for initial conditions in heavy ion collisions are pointed out.

1 Introduction

QCD has been called the perfect theory [2]; as a renormalizable field theory whose validity could extend up to the grand unification scale, it provides the mechanism for generating nearly all the mass of the visible universe. The current quark masses are the only external parameters in the theory. Quenched QCD, without dynamical quarks, explains the hadron spectrum to an accuracy [a] of 10%. These lattice results suggest that gluons play a central role in the structure of matter.

The role of glue in QCD is best understood in the asymptotic weak coupling regimes of the theory where analytical computations are feasible. Much of the discussion in perturbative QCD (pQCD) has been in the Bjorken-Feynman asymptotics where $Q^2 \longrightarrow \infty$, $s \longrightarrow \infty$ and $x_{\rm Bj} \equiv Q^2/s =$ fixed. The machinery of precision physics in QCD such as the operator product expansion and factorization theorems are derived in this limit of the theory. The progress in this direction has been truly remarkable [4]. In DIS for instance, both coefficient functions and splitting functions have been derived to next-to-next-to leading order (NNLO).

What does the hadron look like in the Bjorken-Feynman asymptotics? The DGLAP evolution equations tell us that the gluon distribution grows rapidly with increasing Q^2 at small $x_{\rm Bj}$. However, the phase space density (in a particular gauge and frame), decreases rapidly with increasing Q^2. The proton become more "dilute" even though the number of partons increases; the typical size of resolved partons decreases as $1/Q^2$, faster than the increase in the number through QCD evolution. The more dilute the hadron, the cleaner will be the QCD background for new physics beyond the standard model.

Much of the current focus in QCD is in quantifying this background. It would be unfortunate however if this were the only focus in QCD studies because the theory, even in the weak coupling domain, contains rich and non-trivial dynamics. We speak here of the Regge-Gribov asymptotics where $x_{\rm Bj} \longrightarrow 0$, $s \longrightarrow \infty$ and $Q^2 =$ fixed. This regime of strong color fields is responsible for the bulk of multiparticle production in QCD. What does the hadron look like in the Regge-Gribov asymptotics ? The BFKL equation, which resums the leading logarithms in x, indicates that the gluon distributions grow even more rapidly in this asymptotics. Unlike the Bjorken-Feynman case, the phase space density in the hadron grows rapidly as well. The stability of the theory requires that the phase space densities (or more generally, the field strengths squared) be no larger than $\sim 1/\alpha_S$. In the pQCD

*This work is supported by DOE Contract No. DE-AC02-98CH10886.

[a]Some lattice QCD computations with dynamical quarks claim improved agreement to within a few percent [3].

framework, mechanisms for the saturation of the growth in the phase space density are provided by "higher twist" recombination and screening contributions [5]. These counter the bremsstrahlung growth of soft gluons described by the DGLAP and BFKL equations. The saturation scale $Q_s(x)$ generated by the dynamics demarcates the separation between the linear and non-linear regimes of the theory: for momenta $Q^2 \ll Q_s^2$, non-linear QCD dynamics is dominant, for momenta $Q^2 \gg Q_s^2$, weak coupling physics is governed by the DGLAP/BFKL evolution equations.

The universal properties of gluons in the non-linear regime are described by a classical effective field theory of dynamical gluon fields coupled to static, stochastic sources. This is the Color Glass Condensate (CGC) [6]. The evolution of multi-parton correlators with energy is described by the Wilsonian JIMWLK renormalization group (RG) equations [7]. In the limit of large nuclei and large N_c, one recovers the Balitsky-Kovchegov equation for the forward dipole cross-section [8]. A universal saturation scale arises naturally in the theory and its energy dependence is given by the JIMWLK/BK equations. The typical momentum of gluons $\sim Q_s \gg \Lambda_{\rm QCD}$; the bulk of the contributions to high energy cross-sections may be therefore described in a weak coupling framework.

The saturation scale also grows with the nuclear size. A fast compact probe of size $1/Q_s < R_p$, where R_p is the proton size, will interact coherently at high energies with partons localized in nucleons all along the nuclear diameter. The field strength squared experienced by the probe is therefore enhanced parametrically by a factor proportional to the nuclear diameter $\sim A^{1/3}$. As clearly illustrated in the CGC effective theory, the dynamics of partons at small x is universal regardless of one speaks of hadrons or nuclei; the latter, as we will discuss further, are therefore an efficient (and cheaper) amplifier of the non-linear dynamics of these gluons.

This talk is organized as follows. We will outline our current (limited!) understanding of the different dynamical regimes in high energy QCD from experiments at HERA and RHIC. We will then discuss how experiments at the LHC and future DIS experiments on nuclei can help further quantify our understanding. Finally, to illustrate the scope of these studies, we will discuss how the strong color field dynamics of partons in nuclear wavefunctions contributes to a quantitative understanding of the formation and subsequent thermalization of a strongly interacting "glasma" in heavy ion collisions.

2 The evidence for the CGC from e+p DIS

A strong hint that semi-hard scales may play a role in small x dynamics at HERA came from "geometrical scaling" of the HERA data [9]. The inclusive virtual photon+proton cross-section for $x \leq 0.01$ and all available Q^2 scales [b] as a function of $\tau \equiv Q^2/Q_s^2$, where $Q_s^2(x) = \exp(\lambda Y)$ in GeV^2, with $Y = \ln(x_0/x)$, $x_0 = 3 \cdot 10^{-4}$ and $\lambda = 0.288$ as fit parameters [9, 10]. Further, the inclusive diffractive, vector meson and DVCS cross-sections at HERA, with a slight modification [c] in the definition of τ, also appear to show geometrical scaling [10]. Geometrical scaling of the e+p data is shown in Fig. 1. A recent "quality factor" statistical analysis [11] indicates that this scaling is robust; it is however unable to distinguish between the above fixed coupling energy dependence of Q_s and the running coupling $Q_s(x) \propto \exp(\sqrt{Y})$ dependence of the saturation scale. Geometrical scaling is only

[b] The E665 data are a notable exception.

[c] $\tau_{D,VM} = (Q^2 + M^2)/Q_s^2$, where M denotes the mass of the diffractive/vector meson final state.

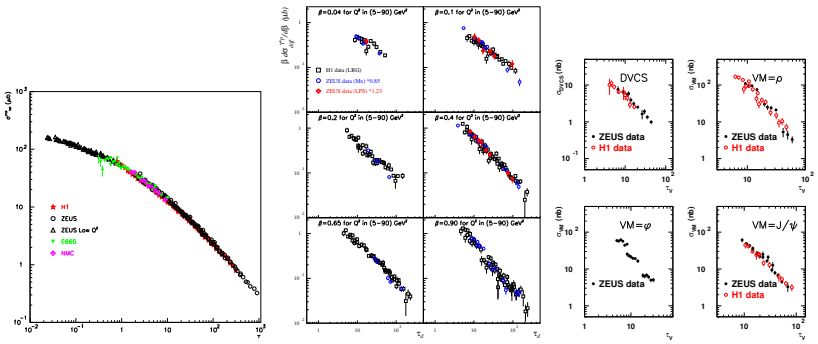

Figure 1: Geometrical scaling fully inclusive, diffractive and exclusive vector meson cross-sections. From [10].

asymptotic in both fixed and running coupling evolution equations [d]. Pre-asymptotic corrections have been computed previously, to good approximation, in both fixed and running coupling cases for the BK equation [12]. A recent NLO BK analysis [13] suggests that the onset of the scaling asymptotics may be precocious, thereby providing a possible explanation for its manifestation in the HERA data. A caveat that has been raised is that there is a strong correlation between x and Q^2 in the HERA data [14]. The scaling however persists even where there is a significant lever arm in Q^2 for small x. Nevertheless, geometrical scaling alone is not sufficient evidence of saturation effects and it is important to look at the data in greater detail in saturation/CGC models.

All saturation models [15] express the inclusive virtual photon+proton cross-section as

$$\sigma_{L,T}^{\gamma^* p} = \int \mathrm{d}^2\mathbf{r}_\perp \int_0^1 \mathrm{d}z \left|\Psi_{L,T}^{\gamma^*}\right|^2 \int \mathrm{d}^2\mathbf{b}_\perp \frac{\mathrm{d}\sigma_{\mathrm{dip}}^{\mathrm{p}}}{\mathrm{d}^2\mathbf{b}_\perp}. \tag{1}$$

Here $\left|\Psi_{L,T}^{\gamma^*}(\mathbf{r}_\perp, z, Q)\right|^2$ represents the probability for a virtual photon to produce a quark–anti-quark pair of size $r = |\mathbf{r}_\perp|$ and $\frac{\mathrm{d}\sigma_{\mathrm{dip}}^{\mathrm{p}}}{\mathrm{d}^2\mathbf{b}_\perp}(\mathbf{r}_\perp, x, \mathbf{b}_\perp)$ denotes the *dipole cross section* for this pair to scatter off the target at an impact parameter $\mathbf{b}_\perp$. The former is well known from QED, while the latter represents the dynamics of QCD scattering at small x. A simple saturation model (known as the GBW model [16]) of the dipole cross section, parametrized as $\frac{\mathrm{d}\sigma_{\mathrm{dip}}^{\mathrm{p}}}{\mathrm{d}^2\mathbf{b}_\perp} = 2(1 - e^{-r^2 Q_{\mathrm{s,p}}^2(x)/4})$ where $Q_{\mathrm{s,p}}^2(x) = (x_0/x)^\lambda$ GeV^2, gives a good qualitative fit to the HERA inclusive cross section data for $x_0 = 3 \cdot 10^{-4}$ and $\lambda = 0.288$. Though this model captures the qualitative features of saturation, it does not contain the bremsstrahlung limit of perturbative QCD (pQCD) that applies to small dipoles of size $r \ll 1/Q_{\mathrm{s}}(x)$.

In the classical effective theory of the CGC, one can derive, to leading logarithmic accuracy, the dipole cross section [17] containing the right small r limit. This dipole cross section can be represented as [18]

$$\frac{\mathrm{d}\sigma_{\mathrm{dip}}^{\mathrm{p}}}{\mathrm{d}^2\mathbf{b}_\perp} = 2\left[1 - \exp\left(-r^2 F(x,r) T_p(\mathbf{b}_\perp)\right)\right], \tag{2}$$

[d] The effect of "pomeron loops" on this scaling will be discussed later.

where $T_p(\mathbf{b}_\perp)$ is the impact parameter profile function in the proton, normalized as $\int d^2\mathbf{b}_\perp\, T_p(\mathbf{b}_\perp) = 1$ and F is proportional to the gluon distribution [19]

$$F(x, r^2) = \pi^2 \alpha_s \left(\mu_0^2 + 4/r^2\right) xg\left(x, \mu_0^2 + 4/r^2\right) / (2N_c)\,, \tag{3}$$

evolved from the initial scale μ_0 by the DGLAP equations. The dipole cross section in Eq. (2) was implemented in the impact parameter saturation model (IPsat) [18] where the parameters are fit to reproduce the HERA data on the inclusive structure function F_2. Here Q_s is defined as the solution of $\frac{d\sigma_{dip}}{d^2\mathbf{b}_\perp}(x, r^2 = 1/Q_s^2(x, \mathbf{b}_\perp)) = 2(1 - e^{-1/4})$ [e].

The IPsat dipole cross section in Eq. (2) is valid when leading logarithms in x in pQCD are not dominant over leading logs in Q^2. At very small x, where logs in x dominate, quantum evolution in the CGC describes both the BFKL limit of linear small x evolution as well as nonlinear JIMWLK/BK evolution at high parton densities [7, 8]. These asymptotics are combined with a more realistic b-dependence in the b-CGC model [20, 21]. Both the IPsat model and the b-CGC model provide excellent fits to HERA data for $x \leq 0.01$ [21, 22]. An important caveat [23] to the success of the saturation models is that the saturation scale,

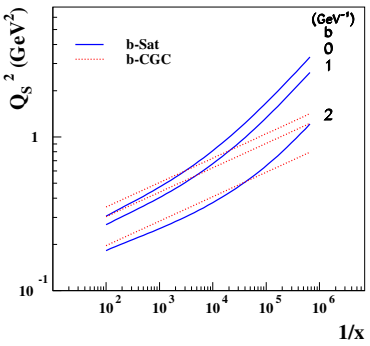

Figure 2: The saturation scale vs $1/x$ in the IPsat and b-CGC models [21].

at median impact parameters, extracted from these fits is ≤ 1 GeV^2 even at the lowest x values at HERA [21, 24]. The saturation scale extracted from the fit in the IPsat model is shown in Fig. 2. We should note however that the uncertainty in the magnitude of the saturation scale is significant and is a factor of 2 larger in recent CGC fits [25]. NLO computations in the small x dipole framework are now becoming available [26]; these will provide theoretical guidance into precisely how the coupling runs as a function of Q_s at small x. Finally, from Fig. 2, it is clear that the energy dependence of the extracted Q_s is significantly stronger than those predicted in non-perturbative models [27].

[e] This choice of is equivalent to the saturation scale in the GBW model for the case of a Gaussian dipole cross section.

3 The evidence for the CGC from e+A DIS and d+A and A+A collisions

The strong field dynamics of small x partons is universal and should be manifest in large nuclei at lower energies than in the proton. In Fig. 3 (left), we show the well known shadowing of F_2^A in the fixed target e+A E665 and NMC experiments. Expressed in terms of $\tau \equiv Q^2/Q_s^2$ (Fig. 3 (right)), the data show geometrical scaling [28]. In Ref. [28], the A dependence of Q_s is determined to be $A^{1/4}$ and not $A^{1/3}$ as suggested in a simple random walk picture. However, as we shall discuss shortly, this conclusion is a little misleading. A study of nuclear

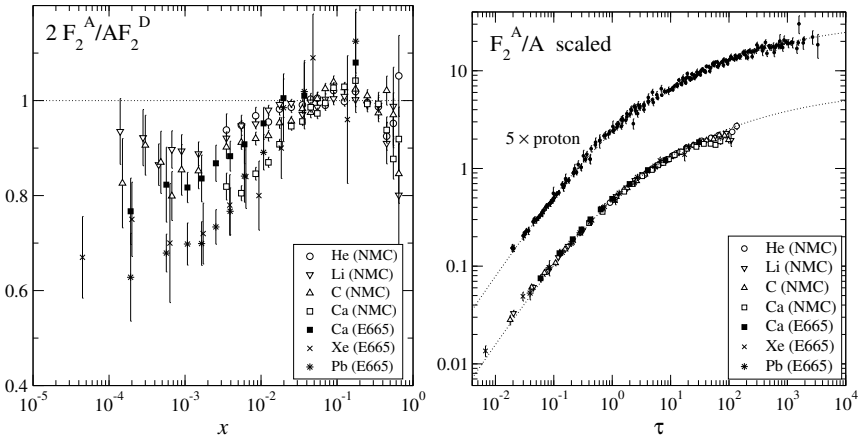

Figure 3: Left: Shadowing of F_2 from the NMC and E665 fixed target experiments. Right: The data scaled as a function of $\tau \equiv Q^2/Q_s^2$ [28].

DIS in the IPsat CGC framework was performed in Ref. [18, 29]. The average differential dipole cross section is well approximated by $\left\langle \frac{\mathrm{d}\sigma^A_{\mathrm{dip}}}{\mathrm{d}^2\mathbf{b}_\perp} \right\rangle_{\mathrm{N}} \approx 2\left[1-\left(1-\frac{T_A(\mathbf{b}_\perp)}{2}\sigma^{\mathrm{p}}_{\mathrm{dip}}\right)^A\right]$, where $T_A(\mathbf{b}_\perp)$ is the well known Woods Saxon distribution. Here $\sigma^{\mathrm{p}}_{\mathrm{dip}}$ is determined from the IPsat fits to the e+p data; no additional parameters are introduced for eA collisions. In Fig. 4 (left), the model is compared to NMC data on Carbon and Calcium nuclei-the agreement is quite good. In Fig. 4 (right), we show the extracted saturation scale in nuclei for both central and median impact parameters. To a good approximation [f], the saturation scale in nuclei scales as $Q^2_{\mathrm{s,A}}(x, b_{\mathrm{med.}}) \approx Q^2_{\mathrm{s,p}}(x, b_{\mathrm{med.}}) \cdot (A/x)^{1/3}$. The factor of $200^{1/3} \approx 6$ gives a huge "oomph" in the parton density of a nucleus relative to that of a proton at the same x. *Indeed, one would require a center of mass energy* ~ 14 *times larger* [g] *in an e+p collider relative to an e+Au collider to obtain the same* $Q^2_{\mathrm{s,A}}(b_{med.})$. The reasons for the additional enhancement are two fold. Firstly, because the density profile in a nucleus is more uniform than that of the proton, $Q^2_{\mathrm{s,p}}(b_{\mathrm{med.}})$ is only $\sim 35\%$ of the value at $b = 0$; in contrast, in

[f] This is considerably larger than the simplest estimate of a θ-function impact parameter in the GBW model, which yields $Q^2_{\mathrm{s,A}} \approx A^{1/3}\frac{R_p^2 A^{2/3}}{R_A^2} Q^2_{\mathrm{s,p}} \approx 0.26 A^{1/3} Q^2_{\mathrm{s,p}}$ for $2\pi R_p^2 \approx 20$ mb and $R_A \approx 1.1\, A^{1/3}$ fm.

[g] At extremely high energies, this statement must be qualified to account for the effects of QCD evolution [30].

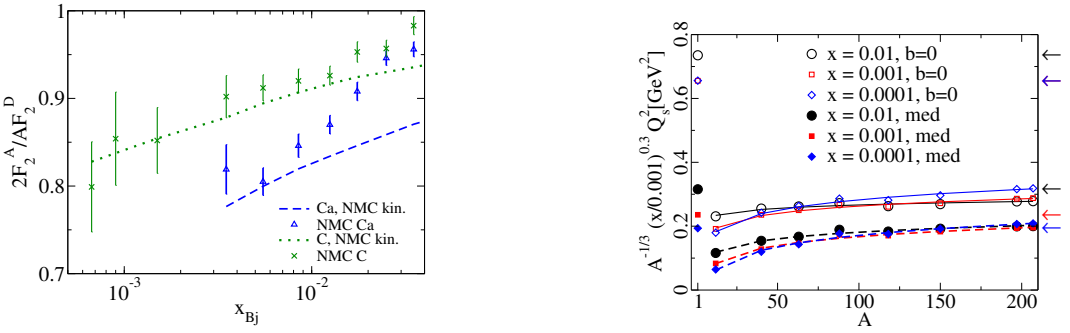

Figure 4: Left: Comparison of the IPsat model (with no adjustable parameters) to the NMC data. Right: The A and x dependence of the saturation scale in the IPsat model [29].

gold nuclei it is 70%. Because the median impact parameter dominates inclusive scattering, this effect gives a significant enhancement to the effective Q_s. The second reason for the enhancement is the DGLAP-like growth of the gluon distribution in the IPsat nuclear dipole cross section. For two nuclei, A and B (with $A > B$), in a "smooth nucleus" approximation ($\sum_{i=1}^{A} T_p(\mathbf{b}_\perp - \mathbf{b}_{\perp i}) \longrightarrow A\,T_A(\mathbf{b}_\perp)$), $\frac{Q^2_{\rm s,A}}{Q^2_{\rm s,B}} \approx \frac{A^{1/3}}{B^{1/3}} \frac{F(x,Q^2_{\rm s,A})}{F(x,Q^2_{\rm s,B})}$, where F was defined in eq. 3. The scaling violations in F imply that, as observed in Refs. [18, 31], the growth of $Q_{\rm s}$ is faster than $A^{1/3}$. Also, because the increase of F with Q^2 is faster for smaller x, the A-dependence of $Q_{\rm s}$ is stronger for higher energies. In contrast, the dipole cross section in the b-CGC model depends only on the combination $rQ_{\rm s}(x)$ without DGLAP scaling violations. It therefore does not have this particular nuclear enhancement. Another interesting possibility, following from running coupling corrections to the leading logs in x, is that QCD evolution actually depletes the nuclear enhancement of $Q_{\rm s}$ at very small x [30]. *Precise extraction of the A dependence of $Q_{\rm s}$ can therefore help distinguish between "classical" and "quantum" RG evolution at small x.*

We now turn to a discussion of CGC effects in hadronic collisions. A systematic treatment of the scattering of two strong color sources (such as two high energy nuclei) is discussed in Section 5. To leading order, the problem reduces to the solution of the classical Yang-Mills (CYM) equations averaged over color sources for each nucleus [32, 33]; the variance of this distribution of sources is proportional to $Q^2_{\rm s,A}$. Besides the nuclear radius, $Q^2_{\rm s,A}$ is the only scale in the problem, and the $Q^2_{\rm s,A} \sim Q^2_{\rm s,p} \cdot (A/x)^{0.3}$ expression for the saturation scale was used in CGC models of nuclear collisions to successfully predict the multiplicity [33] and centrality [34] dependence in gold+gold collisions at RHIC. The universality of the saturation scale also has a bearing on the hydrodynamics of the Quark Gluon Plasma (QGP); the universal form leads to a lower eccentricity [37] (and therefore lower viscosity) than a non-universal form that generates a larger eccentricity [38] (leaving room for a larger viscosity) of the QGP.

For asymmetric (off-central rapidity) nuclear collisions, or proton/deuteron+heavy nucleus collisions, $k_\perp$-factorization can be derived systematically for gluon production, at leading order, in the CGC framework [39]. The simplicity of $k_\perp$ factorization is convenient for phenomenology; predictions based on this formalism describe the rapidity distributions in

$A + A$ collisions [35] and the phenomenon of "limiting fragmentation" [40]. The latter, and deviations thereoff, are described by solutions of the BK-equation. Predictions for the multiplicity distribution in A+A collisions at the LHC [41] for both GBW and classical CGC (MV) initial conditions [h] give a charged particle multiplicity of 1000-1400 in central lead+lead collisions at the LHC. The results are shown in Fig. 5. In deuteron+gold collisions

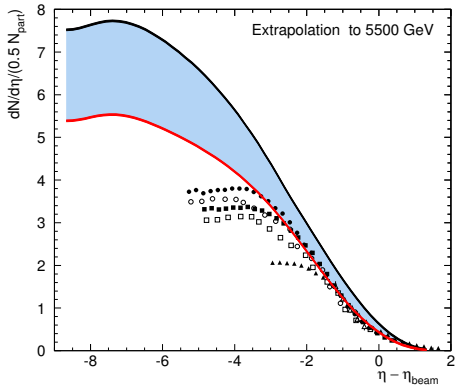

Figure 5: Prediction for limiting fragmentation and deviations away from it at LHC energies. The bands denote the range in the predictions for GBW and MV models. From [41].

at RHIC, the normalized ratio R_{pA} of the inclusive hadron spectrum relative to the same in proton+proton collisions shows a mild "Cronin" peak at mid-rapidities corresponding to multiple scattering in the classical CGC; at forward rapidities, however, R_{pA} decreases systematically below unity. In the CGC, this reflects quantum evolution of the dipole cross-section in a large nucleus and has the same origin as the extension of the geometrical scaling regime [42] to $Q \gg Q_s$. This effect [i], should also exist in hadronic collisions [43]; specifically, it was predicted this would occur in deuteron+gold collisions [44]. In general, R_{pA} while suggestive, is not an ideal variable because it is not clear the same formalism applies to p+p collisions at the same rapidity. Data on the inclusive hadron spectrum in deuteron+gold collisions can be directly compared to model predictions [45] [j]. The result is shown in Fig. 6. For a comprehensive review of applications of CGC picture to RHIC phenomenology, we refer the reader to Ref. [47]. There are a couple of caveats to this picture. Firstly, $k_\perp$ factorization is very fragile. It does not hold for quark production even at leading order in the parton density [48], albeit it may be a good approximation for large masses and transverse momenta [49]. For gluon production, it does not hold beyond leading order in the parton density [50, 33]. Secondly, a combined comprehensive analysis of HERA and RHIC data is still lacking though there have been first attempts in this direction [51].

[h] The McLerran-Venugopalan (MV) initial condition has the same form as the IPsat dipole cross-section discussed earlier.

[i] Quantum evolution here corresponds to the BK anomalous dimension of $\gamma = 0.63$ in the dipole cross-section, as opposed to $\gamma = 1$ (DGLAP) and $\gamma = 0.5$ (BFKL).

[j] The same analysis also gives good agreement for the forward p+p spectrum at RHIC [46].

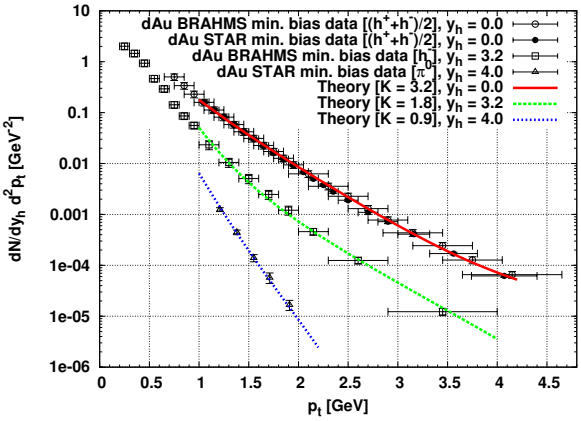

Figure 6: The inclusive $k_\perp$ distributions in deuteron+gold collisions compared to theory curves for different rapidities. From [45].

4 The future of small x physics at hadron colliders and DIS

The LHC is the ultimate small x machine in terms of reach in x for large Q^2. A plot from Ref. [52] illustrating this reach is shown in Fig. 7 (left). For a recent review of the small x opportunities at the LHC, see Ref. [53]. The LHC will provide further, more extensive tests of the hints for the CGC seen at RHIC. At very high energies, a novel "diffusive scaling" regime has been proposed, which incorporates the physics of Pomeron loops. The physics of this regime was discussed at DIS06 by Iancu and at DIS07 by Shoshi [54]; possible signatures at the LHC have been proposed [55]. Very recent computations including running coupling effects however suggest that this regime is unlikely to be accessed realistic collider energies [56].

The universality of parton distributions is often taken for granted but factorization theorems proving this universality have been proven only for a limited number of inclusive final states. However, as we have discussed, small x is the domain of rich multi-parton correlations. These are more sensitive to more exclusive final states for which universality is not proven [57]. Therefore, while the LHC will have unprecedented reach in x, precision studies of high energy QCD and clean theoretical interpretations of these motivate future DIS projects. Two such projects discussed at this conference are the EIC project in the United States [58] and the LHeC project in Europe [59].

As we discussed previously, strong color fields may be more easily accessible in DIS off nuclei relative to the proton due to the "oomph" factor. In Fig. 7 (right), we show the saturation scale $Q^2_{\rm s,A}(x)$ overlaid on the x-Q^2 kinematic domain spanned by the EIC. It is interesting that there is a significant kinematic domain where $Q^2_{\rm s,A} > Q^2$, including in particular $Q^2_{\rm s,A} > 1$ GeV^2. In the weak field regime where $Q^2 \gg Q^2_{\rm s,A}$, we are accustomed to thinking of $\alpha_S \equiv \alpha_S(Q^2)$. In the strong field regime, where $Q^2_{\rm s,A} \gg Q^2$, is $\alpha_S \equiv \alpha_S(Q^2_{\rm s,A})$? As suggested by the figure, the EIC (and clearly the LHeC) will cleanly probe the cross-over regime from linear to non-linear dynamics in QCD. A particularly striking feature of e+A DIS will be diffractive scattering [60, 29]; it is anticipated that $\sim 30\%$ of the cross-

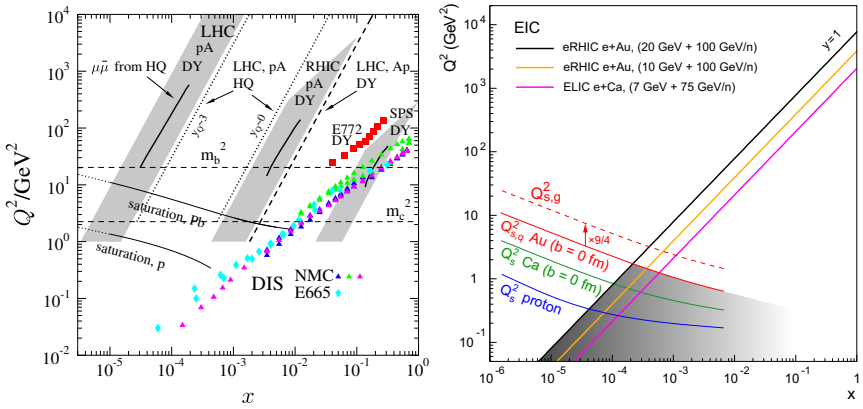

Figure 7: Left: Kinematic x-Q^2 reach of different final states at the LHC compared to other experiments with nuclei . From [52]. Right: The saturation scale in the proton, calcium and gold in the kinematic acceptance of the EIC.

section corresponds to hard diffractive final states. For further discussion of the physics of an Electron Ion collider, see Ref. [61].

5 From CGC to QGP: how classical fields decay in the exploding Glasma

The word "Glasma" describes the strongly interacting matter in heavy ion collisions from the time when particles are produced in the shattering of two CGCs to the time when a thermalized QGP is formed [63]. We will discuss here a systematic approach to computing particle production in heavy ion collisions to NLO. This approach suggests a deep connection between quantum evolution effects in the nuclear wavefunction and instabilities that may be responsible for fast thermalization of the Glasma.

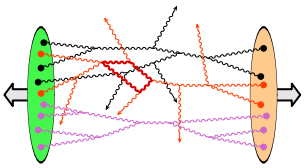

Figure 8: Cartoon of gluon production in the collision of two sheets of Colored Glass. The dots denote large x color sources.

A cartoon of multi-particle production in a heavy ion collision is shown in Fig. 8. The probability of producing n particles, in field theories (such as the CGC) with strong external

sources can be expressed as [62]

$$P_n = \exp\left(-\frac{1}{g^2}\sum_r b_r\right)\sum_{p=1}^{n}\frac{1}{p!}\sum_{\alpha_1+\cdots\alpha_p=n}\frac{b_{\alpha_1}\cdots b_{\alpha_p}}{g^{2p}}\,. \tag{4}$$

where b_r denotes the sum of vacuum-to-vacuum graphs with r cuts. This formula has remarkable features: a) P_n is non-perturbative in g even for $g \ll 1$-no simple power expansion in terms of g exists. b) P_n, for any n, gets contributions from cut tree vacuum graphs-this would not apply for field theories in the vacuum. c) Even at tree level, P_n is *not* a Poisson distribution which is counter to presumptions that classical field theories have only "trivial" Poissonian correlations. The simple formula in Eq. 4 contains many features of the well known AGK calculus [65] of multi-particle production.

Computing the probabilities in Eq. 4 is hopeless even for $g \ll 1$. Fortunately, a systematic expansion in powers of g exists for moments of the multiplicity. Both the LO and NLO multiplicity can be represented in terms of solutions of equations of motion with retarded boundary conditions. At leading order, these are solutions $A^{a,\mu}_{\rm cl.}$ to the Yang-Mills equations; these equations, with *boost invariant* CGC initial conditions, were solved numerically in Ref. [33, 36] to compute the gauge fields at late times.

A next-to-leading order (NLO) computation is important to understand the renormalization and factorization issues that are fundamental to any quantum field theory. As we shall discuss shortly, it is also important to understand the quantum fluctuations that generate the plasma instabilities which may speed up thermalization. Remarkably, the NLO contributions can be computed by solving the initial value problem of small fluctuation equations of motion with retarded boundary conditions. A similar algorithm has been constructed and implemented to study quark pair production in the classical CGC background field [64].

In the Glasma, the classical LO *boost invariant* fields are purely longitudinal. The corresponding momentum distributions are very unstable–indeed, they lead to an instability analogous to the Weibel instability in electromagnetic plasmas. For a review and relevant references, see Ref. [66]. 3+1-D numerical simulations demonstrate that small rapidity dependent quantum fluctuations grow exponentially and generate longitudinal pressure [67]. The initial "seed for the simulations corresponded to "white noise" Gaussian random fluctuations. The maximally unstable modes of the longitudinal pressure grow as $\exp\left(C\sqrt{\Lambda_s\tau}\right)$ with $C \approx 0.425$; this form of the growth was previously predicted for Weibel instabilities in expanding plasmas. Albeit the solutions of the Yang-Mills equations display similar features to the HTL studies, a deeper understanding of this connection is elusive.

First (WKB) quantum corrections to the classical background field of two nuclei at $\tau = 0$ give initial conditions that are quite different from those in Ref. [67]. Simulations are underway to determine whether these initial conditions speed up thermalization. A full treatment of quantum fluctuations requires that we understand how some NLO contributions are absorbed in the evolution of the nuclear wavefunctions with energy while the rest contribute to gluon production. A proof of this high energy "factorization" is in progress [69]. To fully understand fast thermalization in the presence of instabilities, one also needs a kinetic theory of the Glasma that describes the decay of classical fields into particles. A first step has been made in this direction [70].

References

[1] Slides:
http://indico.cern.ch/contributionDisplay.py?contribId=12&sessionId=2&confId=9499

[2] F. Wilczek, hep-ph/9907340.

[3] P. Weisz, *these proceedings*.

[4] A. Vogt, *these proceedings*.

[5] L. V. Gribov, E. M. Levin and M. G. Ryskin, Phys. Rept. **100**, 1 (1983); A. H. Mueller and J.-W. Qiu, Nucl. Phys. **B268**, 427 (1986).

[6] L.D. McLerran, R. Venugopalan, Phys. Rev. **D 49**, 2233 (1994); *ibid.*, **D 49**, 3352 (1994); *ibid.* **D 50**, 2225 (1994); Yu.V. Kovchegov, Phys. Rev. **D 54**, 5463 (1996); J. Jalilian-Marian, A. Kovner, L.D. McLerran, H. Weigert, Phys. Rev. **D 55**, 5414 (1997); E. Iancu, A. Leonidov and L. D. McLerran, Nucl. Phys. A **692**, 583 (2001).

[7] J. Jalilian-Marian, A. Kovner, L.D. McLerran, H. Weigert, Phys. Rev. **D 55**, 5414 (1997); J. Jalilian-Marian, A. Kovner, A. Leonidov, H. Weigert, Nucl. Phys. **B 504**, 415 (1997); *ibid.*,Phys. Rev. **D 59**, 034007 (1999); E. Iancu, A. Leonidov and L. D. McLerran, Nucl. Phys. A **692**, 583 (2001); E. Ferreiro, E. Iancu, A. Leonidov and L. McLerran, Nucl. Phys. A **703**, 489 (2002).

[8] I. Balitsky, Nucl. Phys. **B 463**, 99 (1996); Yu.V. Kovchegov, Phys. Rev. **D 61**, 074018 (2000).

[9] A. M. Stasto, K. Golec-Biernat and J. Kwiecinski, Phys. Rev. Lett. **86**, 596 (2001).

[10] C. Marquet and L. Schoeffel, Phys. Lett. B **639**, 471 (2006).

[11] F. Gelis, R. Peschanski, G. Soyez and L. Schoeffel, Phys. Lett. B **647**, 376 (2007).

[12] S. Munier and R. Peschanski, Phys. Rev. Lett. **91**, 232001 (2003); Phys. Rev. D **69**, 034008 (2004); *ibid.*,**70**, 077503 (2004).

[13] J. L. Albacete and Y. V. Kovchegov, Phys. Rev. D **75**, 125021 (2007).

[14] E. Avsar and G. Gustafson, JHEP **0704**, 067 (2007).

[15] A. H. Mueller, Nucl. Phys. **B335**, 115 (1990); N. N. Nikolaev and B. G. Zakharov, Phys. Lett. **B260**, 414 (1991); Z. Phys. **C49**, 607 (1991). Z. Phys. **C53**, 331 (1992).

[16] K. Golec-Biernat and M. Wusthoff, Phys. Rev. **D59**, 014017 (1999); Phys. Rev. **D60**, 114023 (1999).

[17] L. D. McLerran and R. Venugopalan, Phys. Rev. **D59**, 094002 (1999); R. Venugopalan, Acta Phys. Polon. **B30**, 3731 (1999).

[18] H. Kowalski and D. Teaney, Phys. Rev. **D68**, 114005 (2003).

[19] J. Bartels, K. Golec-Biernat and H. Kowalski, Phys. Rev. **D66**, 014001 (2002).

[20] E. Iancu, K. Itakura and S. Munier, Phys. Lett. **B590**, 199 (2004).

[21] H. Kowalski, L. Motyka and G. Watt, Phys. Rev. **D74**, 074016 (2006).

[22] J. R. Forshaw, R. Sandapen and G. Shaw, JHEP **11**, 025 (2006).

[23] R. S. Thorne, Phys. Rev. D **71**, 054024 (2005); C. Ewerz and O. Nachtmann, Annals Phys. **322**, 1635 (2007).

[24] K. Golec-Biernat and S. Sapeta, Phys. Rev. D **74**, 054032 (2006).

[25] G. Soyez, arXiv:0705.3672 [hep-ph]; C. Marquet, arXiv:0706.2682 [hep-ph].

[26] V. S. Fadin, R. Fiore, A. V. Grabovsky and A. Papa, arXiv:0705.1885 [hep-ph]; V. S. Fadin, R. Fiore and A. Papa, Phys. Lett. B **647**, 179 (2007); Nucl. Phys. B **769**, 108 (2007); I. Balitsky, Phys. Rev. D **75**, 014001 (2007); Y. V. Kovchegov and H. Weigert, Nucl. Phys. A **789**, 260 (2007); *ibid.*, Nucl. Phys. A **784**, 188 (2007); E. Gardi, J. Kuokkanen, K. Rummukainen and H. Weigert, Nucl. Phys. A **784**, 282 (2007).

[27] A. Donnachie and P. V. Landshoff, Phys. Lett. B **437**, 408 (1998).

[28] A. Freund, K. Rummukainen, H. Weigert and A. Schafer, Phys. Rev. Lett. **90**, 222002 (2003).

[29] H. Kowalski, T. Lappi and R. Venugopalan, arXiv:0705.3047 [hep-ph].

[30] A. H. Mueller, Nucl. Phys. **A724**, 223 (2003).

[31] N. Armesto, C. A. Salgado and U. A. Wiedemann, Phys. Rev. Lett. **94**, 022002 (2005).

[32] A. Kovner, L.D. McLerran, H. Weigert, Phys. Rev. **D 52**, 3809 (1995); **D 52**, 6231 (1995); Yu.V. Kovchegov, D.H. Rischke, Phys. Rev. **C 56**, 1084 (1997).

[33] A. Krasnitz, R. Venugopalan, Nucl. Phys. **B 557**, 237 (1999); Phys. Rev. Lett. **84**, 4309 (2000); **86**, 1717 (2001).

[34] D. Kharzeev, M. Nardi, Phys. Lett. **B 507**, 121 (2001).
[35] D. Kharzeev, E. Levin, Phys. Lett. **B 523**, 79 (2001).
[36] A. Krasnitz, Y. Nara and R. Venugopalan, Phys. Rev. Lett. **87**, 192302 (2001); Nucl. Phys. A **717**, 268 (2003); *ibid.*, **727**, 427 (2003); T. Lappi, Phys. Rev. C **67**, 054903 (2003); Phys. Lett. B **643**, 11 (2006); K. Fukushima, arXiv:0704.3625 [hep-ph].
[37] T. Lappi and R. Venugopalan, Phys. Rev. C **74**, 054905 (2006).
[38] T. Hirano, U.W. Heinz, D. Kharzeev, R. Lacey, Y. Nara, Phys. Lett. **B 636**, 299 (2006); H.-J. Drescher, A. Dumitru, A. Hayashigaki, Y. Nara, Phys. Rev. **C 74**, 044905 (2006).
[39] Y. V. Kovchegov and A. H. Mueller, Nucl. Phys. B **529**, 451 (1998); A. Dumitru and L. D. McLerran, Nucl. Phys. A **700**, 492 (2002); J. P. Blaizot, F. Gelis and R. Venugopalan, Nucl. Phys. A **743**, 13 (2004); F. Gelis and Y. Mehtar-Tani, Phys. Rev. D **73**, 034019 (2006).
[40] J. Jalilian-Marian, Phys. Rev. **C 70**, 027902 (2004).
[41] F. Gelis, A. M. Stasto and R. Venugopalan, Eur. Phys. J. C **48**, 489 (2006).
[42] E. Iancu, K. Itakura and L. McLerran, Nucl. Phys. A **721**, 293 (2003).
[43] D. Kharzeev, E. Levin and L. McLerran, Phys. Lett. B **561**, 93 (2003).
[44] D. Kharzeev, Yu. Kovchegov, K. Tuchin, Phys. Rev. **D 68**, 094013 (2003).
[45] A. Dumitru, A. Hayashigaki and J. Jalilian-Marian, Nucl. Phys. A **770**, 57 (2006).
[46] D. Boer, A. Dumitru and A. Hayashigaki, Phys. Rev. D **74**, 074018 (2006).
[47] J. Jalilian-Marian, Y. Kovchegov, Prog. Part. Nucl. Phys. **56**, 104 (2006).
[48] J.P. Blaizot, F. Gelis, R. Venugopalan, Nucl. Phys. **A 743**, 57 (2004); H. Fujii, F. Gelis, R. Venugopalan, Phys. Rev. Lett. **95**, 162002 (2005); Nucl. Phys. A **780**, 146 (2006); K. Tuchin, Phys. Lett. B **593**, 66 (2004); N.N. Nikolaev, W. Schafer, Phys. Rev. **D 71**, 014023 (2005); N.N. Nikolaev, W. Schafer, B.G. Zakharov, Phys. Rev. Lett. **95**, 221803 (2005).
[49] F. Gelis, R. Venugopalan, Phys. Rev. **D 69**, 014019 (2004).
[50] I. Balitsky, Phys. Rev. D **72**, 074027 (2005); J. Jalilian-Marian and Y. V. Kovchegov, Phys. Rev. D **70**, 114017 (2004) [Erratum-ibid. D **71**, 079901 (2005)].
[51] V. P. Goncalves, M. S. Kugeratski, M. V. T. Machado and F. S. Navarra, Phys. Lett. **B643**, 273 (2006).
[52] D. d'Enterria, Eur. Phys. J. A **31**, 816 (2007).
[53] L. Frankfurt, M. Strikman and C. Weiss, Ann. Rev. Nucl. Part. Sci. **55**, 403 (2005).
[54] E. Iancu, arXiv:hep-ph/0608086; A. I. Shoshi, arXiv:0706.1866 [hep-ph].
[55] E. Iancu, C. Marquet and G. Soyez, Nucl. Phys. A **780**, 52 (2006); M. Kozlov, A. I. Shoshi and B. W. Xiao, arXiv:hep-ph/0612053.
[56] A. Dumitru, E. Iancu, L. Portugal, G. Soyez and D. N. Triantafyllopoulos, arXiv:0706.2540 [hep-ph].
[57] J. Collins and J. W. Qiu, Phys. Rev. D **75**, 114014 (2007).
[58] B. Surrow, *these proceedings*.
[59] P. Newman, *these proceedings*.
[60] N. N. Nikolaev, B. G. Zakharov and V. R. Zoller, Z. Phys. A **351**, 435 (1995); L. Frankfurt, V. Guzey and M. Strikman, Phys. Lett. B **586**, 41 (2004); E. Levin and M. Lublinsky, Nucl. Phys. A **712**, 95 (2002); M. S. Kugeratski, V. P. Goncalves and F. S. Navarra, Eur. Phys. J. C **46**, 413 (2006).
[61] A. Deshpande, R. Milner, R. Venugopalan and W. Vogelsang, Ann. Rev. Nucl. Part. Sci. **55**, 165 (2005).
[62] F. Gelis and R. Venugopalan, Nucl. Phys. A **776**, 135 (2006); *ibid.* **779**, 177 (2006); arXiv:hep-ph/0611157; F. Gelis, arXiv:hep-ph/0701225.
[63] T. Lappi and L. McLerran, Nucl. Phys. A **772**, 200 (2006); D. Kharzeev, A. Krasnitz and R. Venugopalan, Phys. Lett. B **545**, 298 (2002).
[64] F. Gelis, K. Kajantie and T. Lappi, Phys. Rev. C **71**, 024904 (2005); Phys. Rev. Lett. **96**, 032304 (2006).
[65] V.A. Abramovsky, V.N. Gribov, O.V. Kancheli, Sov. J. Nucl. Phys. **18**, 308 (1974).
[66] S. Mrowczynski and M. H. Thoma, arXiv:nucl-th/0701002; M. Strickland, arXiv:hep-ph/0701238.
[67] P. Romatschke and R. Venugopalan, Phys. Rev. Lett. **96**, 062302 (2006); Eur. Phys. J. A **29**, 71 (2006); Phys. Rev. D **74**, 045011 (2006).
[68] K. Fukushima, F. Gelis and L. McLerran, Nucl. Phys. A **786**, 107 (2007).
[69] F. Gelis, T. Lappi and R. Venugopalan, in preparation.
[70] F. Gelis, S. Jeon and R. Venugopalan, arXiv:0706.3775 [hep-ph].

QCD and String Theory

Johanna Erdmenger

Max-Planck-Institut für Physik (Werner-Heisenberg-Institut)
Föhringer Ring 6, 80805 München, Germany

We review recent new relations between string theory and QCD based on the AdS/CFT correspondence and its extensions. We give a brief overview over AdS/CFT and discuss generalizations to field theories with running gauge coupling, partially or fully broken supersymmetry and with added flavor degrees of freedom. Moreover we discuss applications such as chiral symmetry breaking and meson spectra, as well as finite temperature field theories and transport phenomena.

1 Introduction

String theory originated as a theory of hadrons in the 1960's, when it was noticed that hadron spectra coincide with excited states of a rotating string. String theory as a theory of strong interactions was abandoned however since four-dimensional string theory contains tachyonic modes. From the beginning of the 1970's, Quantum Chromodynamics (QCD) has established itself as a very successful quantum field theory of strong interactions, which is by now very well tested experimentally.

String theory took a rather different route due to the fact that it contains a graviton in its spectrum and is by now a very promising candidate for a unified quantum theory of all four fundamental interactions.

Within the last ten years, following the paper by Maldacena [1] introducing the AdS/CFT correspondence, a wealth of interesting new relations between modern string theory and quantum field theory have been found. In this review we discuss a series of examples for these new relations. The slides for this talk may be found at [2].

2 Gauge/gravity duality

2.1 AdS/CFT correspondence

The AdS/CFT correspondence is a *duality* which – in its simplest form – maps a quantum field theory at strong coupling to a gravity theory at weak coupling. The best known example is the map between $\mathcal{N} = 4$ supersymmetric $U(N)$ Yang-Mills theory, which is mapped to type IIB supergravity on the space $AdS_5 \times S^5$. Here AdS_5 denotes five-dimensional Anti-de Sitter space and S^5 denotes the five-sphere. Anti-de Sitter space is a space of constant negative curvature which has a boundary. The metric of $AdS_5 \times S^5$ may be written in the form

$$ds^2 = L^2 \left(\frac{1}{u^2} \eta_{ij} dx^i dx^j + \frac{du^2}{u^2} + d\Omega_5{}^2 \right) , \tag{1}$$

where L is the AdS radius and η_{ij} is the standard $3+1$-dimensional Minkowski metric. There is a boundary of AdS_5 at $u = 0$. It is sometimes convenient to perform a coordinate transformation and to write the metric of AdS_5 in the form

$$ds^2 = e^{2r/L} \eta_{ij} dx^i dx^j + dr^2 , \tag{2}$$

The boundary is then located at $r \to \infty$.

The AdS/CFT correspondence arises from string theory in a particular low-energy limit in which the 't Hooft coupling is large and fixed, while $N \to \infty$, such that the planar limit of the gauge theory is considered. $\mathcal{N} = 4$ Super Yang-Mills theory is a conformal field theory in which the beta function vanishes to all orders in perturbation theory. Therefore it has a $SO(4,2)$ conformal symmetry, which coincides exactly with the isometry of AdS_5. Similarly, the $SU(4) \simeq SO(6)$ R symmetry of the field theory coincides with the isometry of the five-sphere S^5.

The AdS/CFT correspondence has been developed further in [3, 4] where a *field-operator map* has been established: There is a one-to-one correspondence between gauge-invariant operators in the field theory and supergravity fields on AdS_5. This maps gauge invariant operators of $\mathcal{N} = 4$ Yang-Mills theory in a particular irreducible representation of $SU(4)$ to supergravity fields in the same representation. These five-dimensional supergravity fields are obtained by Kaluza-Klein reduction of the original ten-dimensional supergravity fields on the five-sphere S^5. There is a precise relation between the Kaluza-Klein mass m_{sugra} of the supergravity fields and the dimension Δ of the dual operator. For scalars this relation is $m^2_{\text{sugra}} = \Delta(\Delta - d)$, with d the dimension of the AdS boundary. For our purposes, $d = 4$. The asymptotic behaviour of the supergravity fields at the AdS boundary is of central importance. For a given supergravity field ϕ of Kaluza-Klein mass m it is given by

$$\phi(u) \sim u^{d-\Delta}\phi_0 \; + \; u^{\Delta}\langle \mathcal{O} \rangle \tag{3}$$

for $u \to 0$. As discussed in [4], the boundary value ϕ_0 may be identified with the source of the gauge theory-operator $\mathcal{O}$, and $\langle \mathcal{O} \rangle$ is the VEV of $\mathcal{O}$. – The AdS/CFT correspondence has been tested in numerous examples, among which the calculation of correlation functions [5, 6] and of the conformal anomaly [7].

The string-theoretical origin of the AdS/CFT correspondence arises from the two different interpretations of D3 branes, i. e. 3+1-dimensional hyperplanes within 9+1-dimensional space. On the one hand, D3 branes are hyperplanes on which open strings can end. In the low-energy limit where only massless string excitations are taken into account, the degrees of freedom on a stack of N D3 branes correspond to $\mathcal{N} = 4$ $U(N)$ Super Yang-Mills theory in four-dimensional Minkowski space. On the other hand, D3 branes are a solitonic solution of ten-dimensional IIB supergravity. As such they are massive extended objects which curve the space around them. In the *near-horizon* limit, which is also a low-energy limit, this curved space is just $AdS_5 \times S^5$. The excitations in this curved-space background are closed strings whose massless mode corresponds to gravitons. In the *Maldacena limit* in which the 't Hooft coupling is large and fixed, while $N \to \infty$, the string modes decouple, such that only supergravity, i.e. pointlike particles, survive.

2.2 Generalizations of AdS/CFT

It is an appealing idea to generalize this gauge/gravity duality to less symmetric quantum field theories which at least in some respects are similar to QCD. A number of avenues have been pursued over the last few years. These are listed in the following:

- **Holographic RG flows:** By considering more involved metrics than $AdS_5 \times S^5$ with a reduced degree of symmetry, it is possible to construct gravity duals of field theories with running gauge coupling. Important examples are [8, 9]. In many cases

these correspond to $\mathcal{N} = 4$ theory perturbed by relevant operators, for instance in [10, 11]. The fifth dimension – perpendicular to the boundary on which the field theory lives – may be interpreted as an energy scale. Some of these holographic renormalization group flows flow to confining field theories in the infrared, as may be shown by calculating the Wilson loop within the dual gravity theory, which follows an area law in this case.

- **Adding flavor:** In $\mathcal{N} = 4$ theory, all fields are in the adjoint representation of the gauge group, since all fields are in the same supermultiplet as the gauge field. Matter in the fundamental representation of the gauge group, i.e. quarks, may be added by adding further D-branes to the original stack of N D3 branes. The prototype example is the addition of D7 brane probes. This corresponds to adding $\mathcal{N} = 2$ hypermultiplets in the fundamental representation of the gauge group. By combining the addition of brane probes with the deformation of the gravity background, a gravity dual description of spontaneous chiral symmetry breaking by a quark condensate is obtained, as well as meson spectra involving Goldstone bosons. An alternative approach which provides a gravity dual realization of $U(N_f) \times U(N_f) \to U(N_f)$ chiral symmetry breaking uses D4, D8 and $\overline{\text{D8}}$ branes.
- **Quark-gluon plasma:** By considering the field-theory dual of the AdS black hole background, a strongly coupled field theory at finite temperature is obtained. By virtue of relevant Kubo formulae, this allows to calculate hydrodynamic quantities for a strongly coupled field theory. This may be of relevance for describing the quark-gluon plasma. A particular virtue is the natural formulation in Minkowski space which allows for the description of non-equilibrium transport processes. A central result is the ratio of shear viscosity and entropy density, which provides a very small lower bound.
- **Integrability:** Another avenue of generalizing AdS/CFT in a different direction is to go beyond the Maldacena supergravity limit discussed in section 2.1, and to consider classical string configurations in $AdS_5 \times S^5$. The energy levels of these string modes are mapped to anomalous scaling dimensions of local operators in $\mathcal{N} = 4$ super Yang-Mills theory. Due to their integrability properties these operators may be described with the Bethe ansatz [12, 13]. Similar integrability methods have been used in QCD for some time [14]. Using classical string configurations, it is possible to test the AdS/CFT correspondence at higher loop order in a perturbative expansion on the field theory side. Relevant calculations on the field theory side have been performed for instance in [15].
- **Hard scattering:** In a similar approach, hard scattering of glueballs is mapped to string amplitudes in $AdS_5 \times S^5$. This provides in particular a unified description of the soft and hard pomeron [16]. Recently, a classical string configuration was proposed for gluon scattering itself [17].
- **AdS/QCD:** Whereas this review is devoted to the 'top-down' approach where string-theory models are developed fo describing field theory features, it should also be mentioned that there are important efforts in a 'bottom-up' approach of constructing phenomenological five-dimensional models for describing QCD phenomenology, for instance [18, 19]. These models are quite successful in describing QCD masses and decay constants. It remains an open question though about how to realize these models

within string theory.

3 Flavor and Chiral symmetry breaking

3.1 Adding Flavor

The original AdS/CFT correspondence only involves fields in the adjoint representation of the gauge group. For generalising the correspondence to quark degrees of freedom, which are in the fundamental representation of the gauge group, additional ingredients are necessary. The simplest way to obtain quark bilinear operators within gauge/gravity duality is to add a D7 brane probe [20]. This is done in such a way that the D7 brane probe extends in space-time as given in Table 1, where 0 is the time direction.

	0	1	2	3	4	5	6	7	8	9
D3	X	X	X	X						
D7	X	X	X	X	X	X	X	X		

Table 1: Embedding of the D7 brane probe into 9+1 dimensional space relatively to the D3 branes.

The term 'brane probe' refers to the fact that only a very small number of D7 branes is added, while the number of D3 branes, N, which also determines the rank of the gauge group $U(N)$, goes to infinity. In this limit we neglect the backreaction of the D7 branes on the geometry.

The field theory corresponding to this brane set-up is a $\mathcal{N} = 2$ supersymmetric $U(N)$ gauge theory, which in addition to the degrees of freedom of $\mathcal{N} = 4$ Super Yang-Mills contains N_f hypermultiplets in the fundamental representation of the gauge group, where N_f is given by the number of D7 branes. N_f must be small in the probe limit.

On the supergravity side of the duality, the $\mathcal{N} = 4$ degrees of freedom are described by supergravity on $AdS_5 \times S^5$ as before. However in addition, there are new degrees of freedom corresponding to the D7 brane probe within the ten-dimensional curved space. The low-energy degrees of freedom of this brane are described by the Dirac-Born-Infeld action. These correspond to open string fluctuations on the D7 probe. It turns out that the minimum action configuration for the D7 brane probe corresponds to the probe wrapping an $AdS_5 \times S^3$ subspace of $AdS_5 \times S^5$.

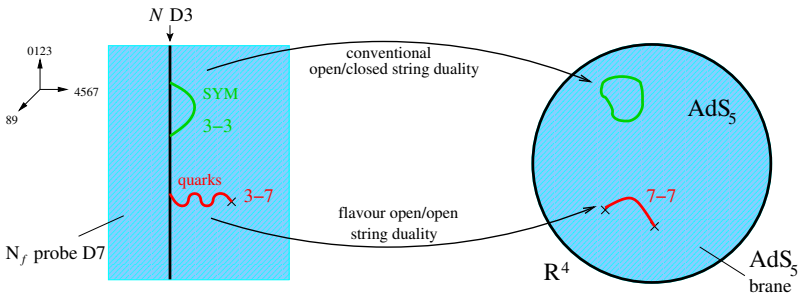

Figure 1: Schematic representation of the AdS/CFT duality with added flavour. In addition to the original AdS/CFT duality, open string degrees of freedom representing quarks are mapped to open strings beginning and ending on the D7 probe wrapping $AdS_5 \times S^3$ inside $AdS_5 \times S^5$. For simplicity, the five-sphere is not drawn in this picture.

The new duality conjectured in [20] is an open-open string duality, as opposed to the

original AdS/CFT correspondence which is an open-closed string duality. The duality states that in addition to the original AdS/CFT duality, gauge invariant field theory operators involving fundamental fields are mapped to fluctuations of the D7 brane probe on $AdS_5 \times S^3$ within $AdS_5 \times S^5$. This is shown in Figure 1.

A particularly interesting feature arises if the $D7$ brane probe is separated from the stack of D3 branes in either the x_8 or x_9 directions, where the indices refer to the coordinates given in Table 1. This corresponds to giving a mass to the fundamental hypermultiplet. In this case the radius of the S^3 becomes a function of the radial coordinate r in AdS_5. At a radial distance from the deep interior of the AdS space given by the hypermultiplet mass, the radius of the S^3 shrinks to zero. From a five-dimensional AdS point of view, the D7 brane probe seems to 'end' at this value of the AdS radial coordinate.

The scalar mode of the D7 brane probe embedding with dimension $\Delta = 3$ (i.e. supergravity mass $m^2_{\rm sugra} = -3$) maps to the fermion bilinear $\tilde{\psi}\psi$ in the dual field theory. This mode corresponds to a imaginary AdS mass. However this mass is above the Breitenlohner-Freedman bound [21] for AdS_5 ($m^2_{\rm BF} = -4$) and thus guarantees stability. For this is important that the D7 branes do not carry any net charge from the five-dimensional point of view, since they wrap a topologically trivial cycle with zero flux.

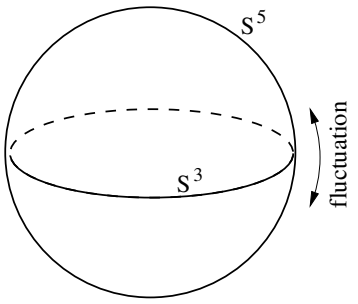

Figure 2: Fluctuations of the S^3 wrapped by the D7 probe inside S^5. These modes give rise to the meson masses.

Fluctuations of the D7 brane give rise to meson masses [22]. This is similar to previously studied supergravity fluctuations which give rise to glueball masses [23]. For this, fluctuations of the D7 brane probe of the form $\delta w(\rho, x) = f(\rho) sin(k \cdot x)$ are considered. Here ρ is the radial direction in the four-dimensional space spanned by the cartesian $4, 5, 6, 7$ directions (see Table 1), and x denote the coordinates on $3 + 1$-dimensional Minkowski space at the boundary of the five-dimensional Anti-de Sitter space. The meson masses are defined by $M^2 = -k^2$ for the wavevector k.

3.2 Chiral symmetry breaking

To obtain a gravity dual of spontaneous chiral symmetry breaking by a quark condensate [24], the addition of a D7 brane probe is combined with an appropriate deformation of the $AdS_5 \times S^5$ space. A suitable background is the one introduced by Constable-Myers [25]. This background has a single deformation parameter b, which may be related to $\Lambda_{\rm QCD}$ on the field theory side, and a singularity at $r = b$. On the field theory side, the $\mathcal{N} = 4$ Super-Yang-Mills theory is deformed to a non-supersymmetric, confining field theory, as can be seen by a Wilson loop analysis.

By adding a D7 brane probe to this background, we obtain a gravity dual of a confining $U(N)$ gauge theory with one flavor [24]. This theory has an $U(1)_{\rm A}$ axial symmetry. In the $N \to \infty$ limit, this symmetry is non-anomalous. It can thus be spontaneously broken by the quark condensate $\langle \bar{\psi}\psi \rangle$.

The $U(1)$ rotational invariance in the two space directions perpendicular to the D7 brane (see Table 1) corresponds to the field theory' s $U(1)_A$. The fluctuations in the two directions transverse to the probe are associated to the quark bilinear operator. The UV asymptotic behaviour of the embedding scalars is of the form $|w| \propto m\, e^{-r} + c\, e^{-3r}$. m and c fix the boundary conditions for the second order supergravity equations of motion.

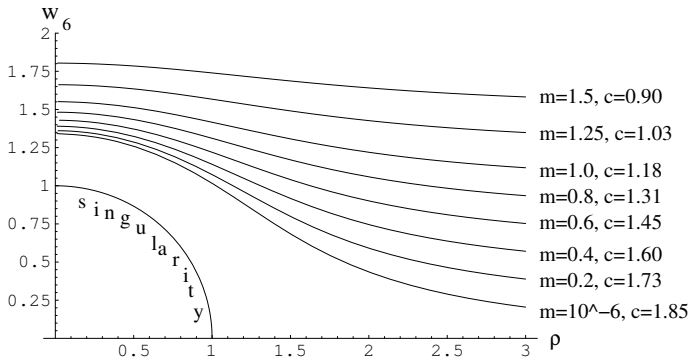

Figure 3: Regular solutions for D7 embeddings in the Constable-Myers background (Scale $b = 1$, $b \sim \Lambda_{\rm QCD}$). w_6 denotes one of the coordinates perpendicular to the D7 probe, ρ given by $r^2 = \rho^2 + {w_6}^2$ is related to the radial coordinate r which corresponds to an energy scale: In the IR r is small and in the UV r is large. The fact that the D7 branes bend corresponds to a geometric realization of spontaneous $U(1)$ symmetry breaking. From [24].

Following the standard AdS/CFT prescription (see Section 2.1 above), we associate the coefficient m with the quark mass and c with the quark condensate $\langle\bar{\psi}\psi\rangle$. Solutions with $m \neq 0$ explicitly breaks the $U(1)_A$ symmetry. The solution with $m = 0$, but $c \neq 0$ realizes spontaneous breaking of chiral symmetry.

Imposing the regularity of the solution in the IR selects a condensate c for each given quark mass m. Figure 3 shows regular solutions of the D7-brane equation of motion for different values of m. There are three important features of the solutions. The first is the presence of a screening effect: All regular solutions end before reaching the singularity. The presence of a condensate ($c \neq 0$) is essential for this behavior. Moreover we see a geometrical realization of the $U(1)_A$ spontaneous breaking, since for $m \to 0$ we still have $c \neq 0$. Finally, at large m we have $c \sim 1/m$, as expected from field theory.

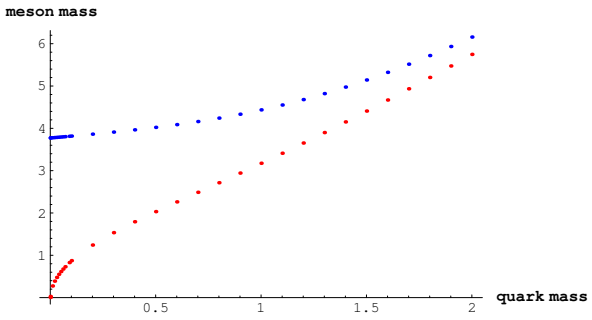

Figure 4: Meson mass versus quark mass as obtained from D7 probe brane fluctuations. The upper curve corresponds to the radial fluctuation, the bottom one to the $U(1)$ symmetric fluctuation. In units of $\Lambda_{\rm QCD}$. From [24].

Since there is spontaneous symmetry breaking for $m \to 0$, we expect a Goldstone boson in the meson spectrum. Solving the supergravity equation of motion for D7 probe brane fluctuations in the two directions transverse to probe, ($\delta w_5 = f(r)\sin(k{\cdot}x)\,, \quad \delta w_6 = h(r)\sin(k{\cdot}x)$) around the D7 brane probe embedding shown in Figure 3, the meson masses are given by $M^2 = -k^2$. There are indeed two distinct mesons (see Figure 4): One is massive for every m,

and corresponds to fluctuations in the radial transverse direction, the other, corresponding to the $U(1)$ symmetric fluctuation, is massless for $m = 0$ and is thus a Goldstone boson. It may be identified with the η', which becomes a $U(1)_A$ Goldstone boson for $N \to \infty$. At finite N, pure stringy corrections will give the η' a non-zero mass in the gravity picture, similarly to instantons in the field theory dual [26].

Another important property of the model of [24] is the small quark mass behaviour of the meson mass, proportional to the square root of m, thus satisfying the Gell-Mann–Oakes–Renner relation [27] of chiral QCD. Also the linear asymptotics for large m correctly reproduce the field theory results.

The model has many remarkable QCD-like features. For instance heavy light mesons, involving a heavy and a light quark, have been studied in [28, 29]. Note however that in the UV, it flows again to strongly coupled $\mathcal{N} = 2$ theory with the degrees of freedom of $\mathcal{N} = 4$ theory plus one additional fundamental hypermultiplet, and thus is not asymptotically free.

A similar model based on a $D4$ brane background in which one of the space directions wrapped by the D4 branes is compacitified on a circle was studied in [30]. There the flavor degrees of freedom are provided by D6 and $\bar{\text{D}}6$ brane probes. Chiral symmetry breaking is seen in this model too. It has the advantage of not displaying a singularity in the interior of the curved space. On the hand, the dual gauge theory becomes five-dimensional in the UV.

3.3 $D4/D8/\bar{\text{D}}8$ brane model

In a further development of the model of [30], Sakai and Sugimoto [31] have considered a model of D4 branes with D8 and $\bar{\text{D}}8$ probes, distributed as shown in Table 2, with the 4-direction again compactified on a circle.

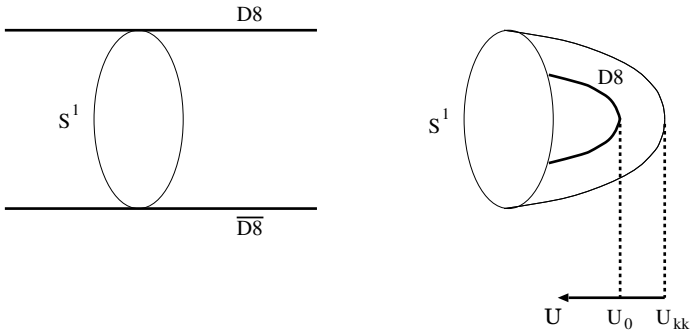

Figure 5: Brane configuration in the Sakai-Sugimoto model. From [31].

The brane configuration in the probe limit is given by N_c D4-branes compactified on a supersymmetry-breaking S^1 and N_f D8-$\bar{\text{D}}8$ pairs transverse to this S^1. Anti-periodic boundary conditions are imposed for the fermions on the D4-branes in order to break SUSY and to cause unwanted fields to become massive. The $U(N_f)_L \times U(N_f)_R$ chiral symmetry in QCD is realized as the gauge symmetry of the N_f D8-$\bar{\text{D}}8$ pairs. The existence of the compact direction plays a crucial role in obtaining a holographic picture of chiral symmetry breaking. The radial coordinate U transverse to the D4-branes is known to be bounded from below due to the existence of a horizon $U \geq U_{\rm KK}$ in the supergravity background. As $U \to U_{\rm KK}$, the radius of the S^1 shrinks to zero. It is found through the study of the D8 and $\bar{\text{D}}8$ probe brane action that the D8 and $\bar{\text{D}}8$ branes merge at some point $U = U_0$ to form a single component of the D8-branes, yielding, in general, a one-parameter family of solutions (See Fig. 5). On the resultant D8-brane, only a single

factor of $U(N_f)$ survives. This mechanism is interpreted as the gravity dual of spontaneous breaking of $U(N_f)_L \times U(N_f)_R$ chiral symmetry.

	0	1	2	3	(4)	5	6	7	8	9
D4	X	X	X	X	X					
D8 - $\bar{\text{D}}$8	X	X	X	X		X	X	X	X	X

Table 2: Embedding of the D8 and $\bar{\text{D}}$8 brane probes into 9+1 dimensional space relatively to the D4 branes.

This construction provides a model of $U(N)$ QCD with N_f massless flavors. It allows for the calculation of a number of observables, such as meson masses, which may be compared with experiment. A striking example is the ratio of the ρ and a_1 meson masses, for which Sakai and Sugimoto find

$$\frac{{M_\rho}^2}{{M_{a_1}}^2} = 2.4\,. \tag{4}$$

The experimental value according to the Review of Particle Physics [32] is 2.51. The theoretical result is strikingly close, though of course it has to be stressed that it is hard to estimate the error of the prediction.

4 Quark-gluon plasma

A particular feature of gauge/gravity dualities is that they are naturally formulated for field theories in Minkowski space. They are thus useful for describing non-equilibrium processes. In particular, the kinetic coefficients of hydrodynamics may be calculated for strongly coupled thermal field theory.

This is potentially of use for describing the quark-gluon plasma. Significant evidence for the presence of the quark-gluon plasma at the Relativistic Heavy Ion Collider (RHIC) at Brookhaven was accumulated [a]. The quark-gluon plasma created at RHIC is not described by a weakly coupled gas of quarks and hadrons. Its temperature is approximately 170 MeV, which is close to the confinement scale of QCD, i.e. in the non-perturbative regime of QCD. A review of the relation between generalizations of AdS/CFT and hydrodynamics is found in [33].

It was noted already in [34] that $\mathcal{N} = 4$ Super Yang-Mills theory at finite temperature (where supersymmetry is broken) may be viewed as being dual to the AdS-Schwarzschild black hole background., A notable result in this context is the calculation of the ratio between shear viscosity η and entropy density s [35]. This gives

$$\frac{\eta}{s} = \frac{\hbar}{4\pi}\,, \tag{5}$$

which provides a lower bound. The calculation is performed using the Kubo formula

$$\eta \;=\; \lim_{\omega\to 0}\frac{1}{2\omega}\int dt d^3x\, e^{i\omega t}\,\langle[T_{xy}(t,\mathbf{x})T_{xy}(0,0)]\rangle\,. \tag{6}$$

The stress tensor correlator is obtained according to the standard AdS/CFT procedure from graviton propagation in AdS-Schwarzschild space.

[a] See talk by B. Zajc at DIS 2007.

Jet quenching, i.e. medium-induced modification of high-p_T parton fragmentation, may also be described within the gauge/gravity approach. There are several ansätze for calculating the jet quenching parameter, for instance one using a Wilson loop [36], and another one using the drag force on a heavy quark. This drag force is described by the force necessary to pull a string moving through the AdS-Schwarzschild background. The string begins on a D7 brane probe and extends to the black hole horizon. From this calculation, a jet quenching of

$$\frac{d}{dt}\langle(\vec{p}_\perp)^2\rangle = 2\pi\sqrt{\lambda}T^3 \tag{7}$$

is obtained, where the jet quenching parameter $\hat{q}$ is given by $d/dt\,\langle(\vec{p}_\perp)^2\rangle$ divided by the velocity v of the quark. – Recently, also the sonic boom expected to be present in the quark-gluon plasma has been explored using gauge/gravity duality [38].

The description of finite temperature field theories using gauge/gravity duality may be combined with the addition of flavor via brane probes. The embedding of a D7 brane probe into the AdS Schwarzschild black hole background gives rise to an interesting first order phase transition of geometrical nature, where the two phases are distinguished by whether or not the D7 brane probe reaches the black hole horizon [24, 39, 40]. If they do, the meson masses associated with the fluctuations of the brane probe become unstable. This may be interpreted as meson melting [41]. – Moreover, the presence of flavor branes give rise to an additional contribution to the shear viscosity relation (5) of the form [40] $\eta_{\text{fund}} \propto \lambda N N_f T^3$.

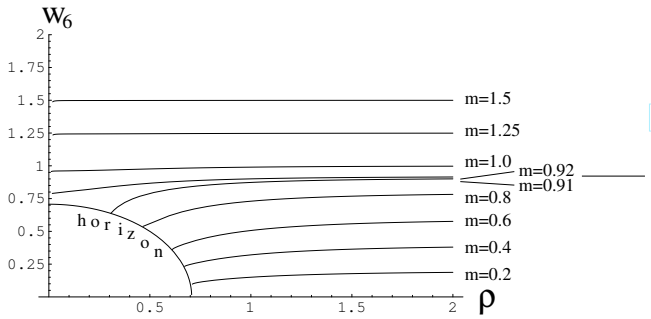

Figure 6: D7 brane probe embeddings in the AdS-Schwarzschild black hole background. There are two phases distinguished by whether or not the brane probes end on the black hole horizon. The phase transition is first order. w_6 is one of the two coordinates perpendicular to the D7 probe. ρ, given by $r^2 = \rho^2 + {w_6}^2$, is related to the the radial (energy) coordinate r and runs from IR (left) to UV (right). All dimensionful quantities are normalized to the temperature. From [24].

Transport processes in the presence of D7 brane probes have also been studied. Here, a chemical potential is introduced by giving a VEV to the time component of the gauge field on the D7 brane probe. In [42], an isospin chemical potential is introduced by considering the $SU(2)$ gauge field on two coincident D7 brane probes. This gives rise to a memory function and frequency-dependent diffusion. Transport processes in presence of a baryon chemical potential for the $U(1)$ symmetry on a single brane probe have been studied in detail in [43].

5 Hard scattering

In the context of hard scattering, the AdS/CFT has been used to give a unified description of the soft and hard pomeron. The pomeron is the coherent excitation that dominates hadronic elastic scattering in a large N gauge theory at large s and small t. At large N, the pomeron contributes the leading singularity in the angular momentum plane. In [16], the calculation of the field theory glueball scattering amplitude is calculated from the ten-dimensional string amplitude in $AdS_5 \times S^5$ with a cut-off in the AdS radial direction. Four-dimensional scattering is obtained from a coherent sum over the six transverse directions.

The holographic encoding of the gauge theory physics is central to this calculation, the AdS radial direction r corresponding to an energy scale. Low-energy states are mapped to states at small r, i.e. in the interior of AdS space. High-energy states are mapped to states at large r, ie. near the boundary. For the momenta there is the relation

$$p_\mu = \frac{r}{L}\,\tilde{p}_\mu\,, \qquad (8)$$

where the conserved four-momentum p_μ corresponds to the invariance under translation of the boundary coordinates x^μ. $\tilde{p}_\mu$ is the momentum in local inertial coordinates for momenta localized at r. L is the AdS radius. The amplitudes depend on r,

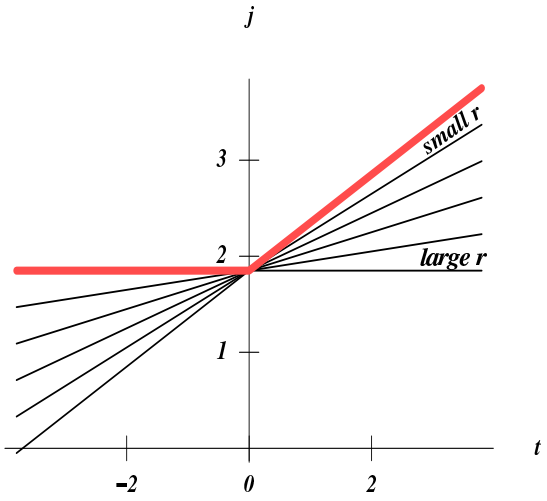

Figure 7: Unified description of soft and hard pomeron from [16].

$$\mathcal{A}(s,t) \propto s^{\alpha(t,r)}\,, \quad \alpha(t,r) = 2 + \alpha' L^2 \frac{t}{2r^2}. \qquad (9)$$

This gives a unified description of soft and hard pomeron, as shown in Figure 7: At large s, highest trajectory dominates. For t positive, this is the case for r small. Thus there is a soft (Regge) pomeron, whose properties are determined by confining dynamics. This corresponds to a glueball. On the other hand, for t negative, the r large case gives the highest trajectory: There is a hard (BFKL) pomeron, i.e. a two-gluon perturbative small object.

6 Conclusion

The examples given show that the AdS/CFT correspondence and its gauge/gravity duality generalizations are useful tools for describing strongly-coupled gauge theories. They give

remarkable agreement with QCD for instance as far as meson masses are concerned. Moreover they are particularly successful in making predictions for non-equilibrium processes in strongly coupled field theories.

The challenge which remains of course is to explain why the gauge/gravity dual description works so well, and to investigate whether it is possible to make progress towards understanding the microscopic dynamics in the field theory. A further important challenge is to use the recent results in gauge/gravity duality for gaining further insight into the structure of string theory itself.

References

[1] Maldacena AdS/CFT J. M. Maldacena, Adv. Theor. Math. Phys. **2** (1998) 231 [Int. J. Theor. Phys. **38** (1999) 1113] [arXiv:hep-th/9711200].

[2] Slides:
`http://indico.cern.ch/contributionDisplay.py?contribId=13&sessionId=2&confId=9499`

[3] E. Witten, Adv. Theor. Math. Phys. **2** (1998) 253 [arXiv:hep-th/9802150].

[4] S. S. Gubser, I. R. Klebanov and A. M. Polyakov, Phys. Lett. B **428** (1998) 105 [arXiv:hep-th/9802109].

[5] D. Z. Freedman, S. D. Mathur, A. Matusis and L. Rastelli, Nucl. Phys. B **546** (1999) 96 [arXiv:hep-th/9804058].

[6] S. Lee, S. Minwalla, M. Rangamani and N. Seiberg, Adv. Theor. Math. Phys. **2** (1998) 697 [arXiv:hep-th/9806074].

[7] JHEP **9807** (1998) 023 [arXiv:hep-th/9806087].

[8] I. R. Klebanov and M. J. Strassler, JHEP **0008** (2000) 052 [arXiv:hep-th/0007191].

[9] J. M. Maldacena and C. Nuñez, Phys. Rev. Lett. **86** (2001) 588 [arXiv:hep-th/0008001].

[10] J. Polchinski and M. J. Strassler, arXiv:hep-th/0003136.

[11] D. Z. Freedman, S. S. Gubser, K. Pilch and N. P. Warner, Adv. Theor. Math. Phys. **3** (1999) 363 [arXiv:hep-th/9904017].

[12] J. A. Minahan and K. Zarembo, JHEP **0303** (2003) 013 [arXiv:hep-th/0212208].

[13] N. Beisert, C. Kristjansen and M. Staudacher, Nucl. Phys. B **664** (2003) 131 [arXiv:hep-th/0303060].

[14] G. P. Korchemsky, Nucl. Phys. B **443** (1995) 255 [arXiv:hep-ph/9501232].

[15] A. V. Kotikov, L. N. Lipatov, A. I. Onishchenko and V. N. Velizhanin, Phys. Lett. B **595** (2004) 521 [Erratum-ibid. B **632** (2006) 754] [arXiv:hep-th/0404092].

[16] R. C. Brower, J. Polchinski, M. J. Strassler and C. I. Tan, arXiv:hep-th/0603115.

[17] L. F. Alday and J. Maldacena, JHEP **0706** (2007) 064 [arXiv:0705.0303 [hep-th]].

[18] S. J. Brodsky and G. F. de Teramond, Phys. Rev. Lett. **96** (2006) 201601 [arXiv:hep-ph/0602252].

[19] J. Erlich, E. Katz, D. T. Son and M. A. Stephanov, Phys. Rev. Lett. **95** (2005) 261602 [arXiv:hep-ph/0501128].

[20] A. Karch and E. Katz, JHEP **0206** (2002) 043 [arXiv:hep-th/0205236].

[21] P. Breitenlohner and D. Z. Freedman, Phys. Lett. B **115** (1982) 197.

[22] M. Kruczenski, D. Mateos, R. C. Myers and D. J. Winters, JHEP **0307** (2003) 049 [arXiv:hep-th/0304032].

[23] C. Csaki, H. Ooguri, Y. Oz and J. Terning, JHEP **9901** (1999) 017 [arXiv:hep-th/9806021].

[24] J. Babington, J. Erdmenger, N. J. Evans, Z. Guralnik and I. Kirsch, Phys. Rev. D **69** (2004) 066007 [arXiv:hep-th/0306018].

[25] N. R. Constable and R. C. Myers, JHEP **9911** (1999) 020 [arXiv:hep-th/9905081].

[26] J. L. F. Barbon, C. Hoyos, D. Mateos and R. C. Myers, JHEP **0410** (2004) 029 [arXiv:hep-th/0404260].

[27] M. Gell-Mann, R. J. Oakes and B. Renner, Phys. Rev. **175** (1968) 2195.

[28] J. Erdmenger, N. Evans and J. Grosse, JHEP **0701** (2007) 098 [arXiv:hep-th/0605241].

[29] J. Erdmenger, K. Ghoroku and I. Kirsch, arXiv:0706.3978 [hep-th].

[30] M. Kruczenski, D. Mateos, R. C. Myers and D. J. Winters, JHEP **0405** (2004) 041 [arXiv:hep-th/0311270].

[31] T. Sakai and S. Sugimoto, Prog. Theor. Phys. **113** (2005) 843 [arXiv:hep-th/0412141].
[32] W.-M. Yao et al., Journal of Physics G **33** (2006) 1.
[33] D. T. Son and A. O. Starinets, arXiv:0704.0240 [hep-th].
[34] E. Witten, Adv. Theor. Math. Phys. **2** (1998) 505 [arXiv:hep-th/9803131].
[35] G. Policastro, D. T. Son and A. O. Starinets, Phys. Rev. Lett. **87** (2001) 081601 [arXiv:hep-th/0104066].
[36] H. Liu, K. Rajagopal and U. A. Wiedemann, Phys. Rev. Lett. **97** (2006) 182301 [arXiv:hep-ph/0605178].
[37] C. P. Herzog, A. Karch, P. Kovtun, C. Kozcaz and L. G. Yaffe, JHEP **0607** (2006) 013 [arXiv:hep-th/0605158].
[38] S. S. Gubser, S. S. Pufu and A. Yarom, arXiv:0706.4307 [hep-th].
[39] I. Kirsch, Fortsch. Phys. **52** (2004) 727 [arXiv:hep-th/0406274].
[40] D. Mateos, R. C. Myers and R. M. Thomson, Phys. Rev. Lett. **98** (2007) 101601 [arXiv:hep-th/0610184].
[41] C. Hoyos, K. Landsteiner and S. Montero, JHEP **0704** (2007) 031 [arXiv:hep-th/0612169].
[42] J. Erdmenger, M. Kaminski and F. Rust, arXiv:0704.1290 [hep-th].
[43] R. C. Myers, A. O. Starinets and R. M. Thomson, arXiv:0706.0162 [hep-th].

Open Questions

G.G. Ross
Rudolf Peierls Centre for Theoretical Physics,
Department of Physics,
University of Oxford,
1Keble Road,
Oxford,
England

As we enter the LHC era the open questions in hard processes shift to the prospects for discovery of physics beyond the Standard Model. In this talk I discuss the main phenomenological questions that will need to be answered if we are to be able to distinguish between the various suggestions for the nature of the new physics that may be visible at the LHC.

1 Introduction.

In thinking about an appropriate choice for a talk on "Open Questions" I was influenced by the fact that the LHC era is almost upon us and that it is time to think seriously about the questions that will need to be answered if the LHC is to reveal the nature of the physics "Beyond the Standard Model" that many think must be present if we are to answer the questions left unanswered by the Standard Model (SM).

The LHC will open a new energy frontier and should reveal significant information about what lies Beyond the Standard Model. The fact that the electroweak breaking scale is well within the reach of the LHC means that we will be able to probe the origin of mass. In particular we should be able to answer the first open question whether the spontaneous symmetry breaking responsible for the masses of the weak gauge bosons and the quark and lepton current masses is due to an elementary Higgs boson, as in the Standard Model, or involves a composite Higgs bound by a new strong interaction alternatives as in technicolour. The need to solve the hierarchy problem which arises because radiative corrections tend to drive up the electroweak breaking to the scale of new physics strongly suggests that signals for new physics will appear at an energy scale less than $1Tev$ and within the reach of the LHC.

A second open question is whether the fundamental forces are unified, possible at a very high scale. The precision with which the gauge couplings unify is remarkable, accurate to better than 1%, and provides the best quantitative indication we have for such a unification. However this precision only applies if the effective theory at a scale of $1Tev$ is supersymmetric, consistent with the constraint following from the supersymmetric solution to the hierarchy problem. The new supersymmetric partners of the Standard Model states should be within the reach of the LHC but, even if found, it will require considerable effort to establish their supersymmetric origin.

In seeking a unified theory it is natural to include gravity and the fact that the gauge coupling unification scale is close to the Planck scale is some indication of this unification. The best candidate for a quantum theory of gravity is the superstring and a further open question is whether there will be evidence for strings at the LHC. If the string states are at the Planck scale such indications will necessarily be indirect, leaving relations amongst the parameters of the effective low energy theory such as the relations between the gauge

couplings. For the case of low energy supersymmetry the superstring unification may give relations between the soft supersymmetry breaking parameters, such as the squark and slepton masses. Another possibility, which has been suggested as an alternative solution to the hierarchy problem, is that new states associated with the additional space dimensions required by the string, or indeed the string states themselves, are associated with a low scale of $O(1TeV)$ and are accessible to discovery by the LHC. If such states are present it will require much work to distinguish them from other possibilities such as a supersymmetric origin.

Another important open question is the origin of dark matter. Many of the suggestions for solving the hierarchy problem involve dark matter candidates; for example the lightest supersymmetric particle (LSP) or the lightest KK mode associated with a new space dimension. To prove that any of these candidates is the source of dark matter will require that its detailed interactions are determined in order to reliably compute the annihilation cross sections and hence the relic abundance.

Given these questions what are the likely LHC answers? The search for new states largely relies on missing momentum signals putting the questions firmly in the area of expertise covered by this meeting and I will discuss some of the suggestions that have been made for ways to determine the underlying physics origin of any new states found at the LHC. In this talk I will start by considering the (pessimistic) possibility that the electroweak breaking is associated with a Higgless model or a very heavy Higgs model. Such possibilities occur in models with large extra dimensions or in technicolour models and can be very difficult to test at the LHC. The second half of the talk will concentrate on the new physics associated with a light Higgs boson, for example in supersymmetric theories or in little Higgs models.

2 Higgless (or very heavy Higgs) at the LHC.

The most pessimistic possibility for LHC physics is that the Standard Model is all there is up to the limit of the LHC reach with a very heavy Higgs scalar or even no Higgs scalar at all. Precision measurements at LEP argue against this possibility because they favour the radiative corrections corresponding to a light Higgs[2]. However new physics at the TeV scale could affect these corrections so a heavy Higgs is still a possibility. In perturbation theory one may show that a Standard Model Higgs cannot be very heavy without violating perturbative unitarity. The effect is strongest in processes involving the longitudinal component of the W and Z bosons. For example in the Standard Model the graphs (a) to (d) of Fig 1 are the tree level contributions to $W_L + Z_L$ elastic scattering. If the Higgs is very heavy the graph (d) is suppressed. In this case the remaining graphs will violate the unitarity bound at a scale $\Lambda \simeq 1.8TeV$. Of course this does not mean that unitarity is violated but it does require that higher order graphs restore unitarity, i.e. the interaction becomes strong. Recently an alternative class of "Higgsless" models have been constructed which postpone the scale at which the interactions become strong[4]. They are based on models with additional space dimensions and in the four dimensional effective field theory there are the additional contributions of graphs (e) and (f) involving the exchange of massive vector bosons, Kaluza Klein excitations of the W. The effect of these contributions is to raise the scale at which the unitarity bound is reached to $\Lambda \simeq 5 - 10TeV$, out of the reach of the LHC. What are the prospects for measuring at the LHC the strong coupling behaviour in the heavy Higgs case or the presence of the additional heavy vector bosons in the Higgsless case? From Fig 1 one may see that in the SM case there is no s-channel resonance while in the Higgsless case there

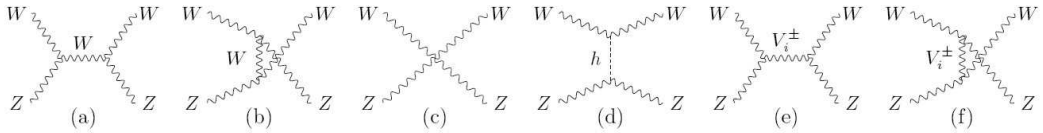

Figure 1: Feynman graphs contributing to $W_L + Z_L$ elastic scattering.

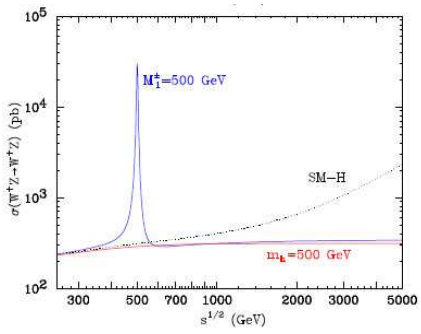

Figure 2: $W_L + Z_L$ elastic scattering (i) in the Standard Model without a Higgs boson (ii) in the Standard Model with a $500GeV$ Higgs and (iii) in the Higgsless model with a $500GeV$ heavy vector boson.

is a characteristic narrow resonance. In the SM case when the weak interactions become strong there may be a s-channel resonance due to strong binding effects but it is expected to be very wide and heavy, approximately $2TeV$ if the strong interaction is QCD-like. For this reason the $W_L + Z_L$ elastic scattering case provides a very good discriminator for the Higgsless models.

The production of the initial W and Z is via bremsstrahlung off quarks, and the signal is two forward jets plus a gauge boson pair giving a gold plated final state of two jets plus 3 leptons plus missing transverse momentum. The various cross sections are shown in Fig 2.

Figure 3 shows the number of events at the LHC to be expected in the SM with a $500GeV$ Higgs and in the Higgsless model for a heavy vector of mass $700GeV$ for an integrated luminosity of $300fb^{-1}$[15]. In addition are shown two estimates for the cross section for the case the Higgs mass is well above the perturbative limit corresponding to the case the weak interactions become strong at high energies. In this case it is necessary to include higher order radiative corrections to preserve unitarity and this has been done in two ways, the first using the $K-$matrix approach [5] and the second using Pade approximants [6]. The most obvious feature of these graphs is that in all cases the signal is very small for the SM with a Higgs of $500GeV$ or above. Given this small SM background the discovery reach for the Higgsless model requires only of the order of 10 events corresponding to $10fb^{-1}$ of data. By looking at various channels it is in principle possible to check this identification. In the SM the Higgs can appear as a resonance in the $WW \to WW, ZZ$ channels but not as we

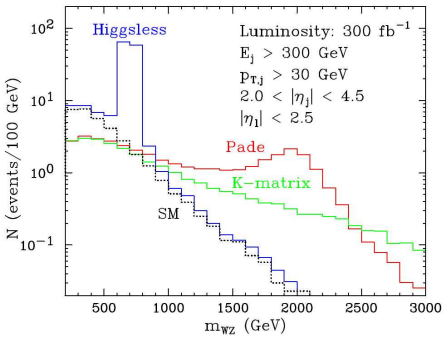

Figure 3: The number of events at the LHC for an integrated luminosity of 300fb^{-1} with the cuts indicated.

have seen in the $WZ \to WZ$ channel. For the case of the Higgsless models the resonance appears in the $WW \to WW$ and $WZ \to WZ$ channels but not in the $WW \to ZZ$ channel.

For the very heavy Higgs case it is necessary to establish the corresponding existence of strong interactions. However this requires the measurement of the excess of events of the curves labeled K-matrix and Pade over the SM case. The total number of such events for $300 fb^{-1}$ is only 6 so the LHC will not be able to probe this possibility and it will be necessary to wait for the SLHC upgrade with a luminosity increase of a factor of 10 before one can measure the effect of a strongly interacting weak sector in the very heavy Higgs limit. This will still be very difficult and will require a detailed understanding of the initial parton distributions.

3 Light Higgs and the hierarchy problem.

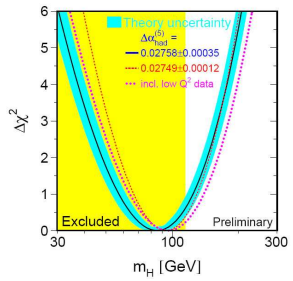

Figure 4: The value of $\Delta\chi^2$ as a function of the Higgs mass for a fit to precision observables in the Standard Model[2]

However there is already evidence that just the SM with a very heavy Higgs is unlikely. The evidence comes from the need to have a light Higgs to fit the precision electroweak data from LEP. In Fig 4 the χ squared dependence of the precision electroweak fit to the Higgs

mass is shown [2] and corresponds to a bound on the Higgs mass given by $m_H < 200GeV$. Given this I turn now to a discussion of the important questions that will need to be answered in the light Higgs case. The driving force in constructing extensions of the Standard model has been the requirement that it should solve the hierarchy problem, that is the need to control radiative corrections to the Higgs boson mass that would normally drive it to the scale of new physics such as the Grand Unified (GUT) scale or the Planck scale. As illustrated in Fig 5 there are two options - the Higgs could be composite or elementary.

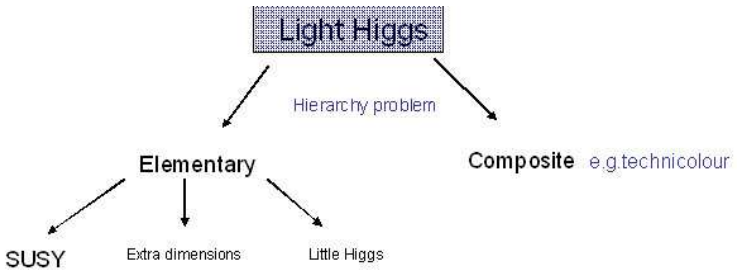

Figure 5: Competing explanations for the existence of a light Higgs scalar and the solution of the herarchy problem.

In the former case the hierarchy problem is evaded if the scale of compositeness is low, of $O(1TeV)$, because the radiative corrections are cut-off at virtual momenta of order the composite scale. The achetypical example of a composite theory is technicolour. The need to suppress flavour changing neutral currents and the need to be consistent with precision electroweak tests have imposed strong constraints on technicolour showing that the strong binding force must be quite different from QCD. The difficulty associated with calculating strong interaction effects in such a theory makes it difficult to extract definite predictions but there should be a zoo of composite bound states including many familon states, pseudo Goldstone modes associated with the breaking of approximate family symmetries of the extended technicolour model. Given the difficulty in making definite predictions I will not discuss this possibility further here but refer the reader to a study of the signals to be expected in some particular models and references therein[8].

For the case the Higgs is elementary perturbative calculations may be applicable, making it possible to make more definite predictions for the signals to be expected at the LHC. This is the case if supersymmetry is responsible for protecting the Higgs against large radiative corrections to its mass[9]. Moreover the new supersymmetric states must be light, accessible to production and detection at the LHC, if the hierarchy problem is to be avoided. While many of the properties of the supersymmetric states are determined, being related to the properties of their Standard Model partners, the spectrum results from supersymmetry breaking and consequently is less well understood. In Fig 6 I show a variety of supersymmetric spectra for various possible supersymmetry breaking mechanisms[10]. It is clear that there are a wide variety of possibilities and one of the important tasks we need to address is to identify the best ways to measure the mass spectra at the LHC. This will require the development of techniques to measure both the masses and spins of the new states for the case that the signals always involve missing momentum. This need for spin measurement is particularly important because alternative explanations of the hierarchy problem can give

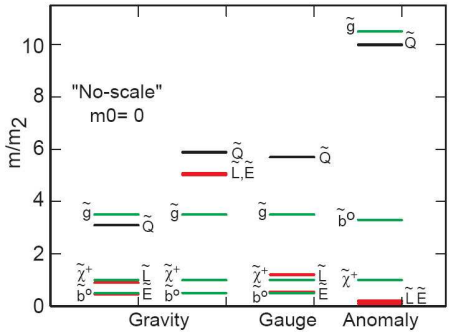

Figure 6: The supersymmetric spectrum for various choices of supersymmetry breaking-mechanisms [10].

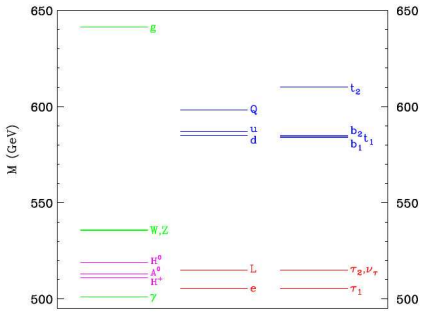

Figure 7: One loop corrected mass spectrum of the first KK level in MUED for a characteristic choice of parameters[11].

similar spectra. This is illustrated in Fig 7 [11] where one can see significant similarities in the mass spectrum coming from an extra dimensional theory with Universal Extra Dimensions (UED)[12]. The reason for this is that the radiative corrections responsible for splitting the states are similar simply because the gauge interactions responsible for much of the splitting are the same. In the UED case the new states are the KK excitations of the SM states while in the SUSY case the new states are the SUSY partners of the SM states; in both cases they belong to the same representations of the SM gauge group as their SM partners. Of course in the case of UED there will be a tower of KK excitations but the splitting may be such tat only the first excitations are accessible to the LHC. However the spins of the states differ in the SUSY and UED cases so the spin determination is crucial to the identification of the nature of the new physics. There are more reasons why measuring the spectrum in detail is important. In the case of supersymmetry the mass spectrum offers a window on the high energy theory and on the possible unification of the fundamental forces. This illustrated in Fig 8 where one may see that, like the gauge couplings, the soft SUSY masses have radiative corrections that split them even if they are universal at a high

scale[a]. As may be seen in the first panel the gauge couplings unify very precisely at a scale of $2.10^6 GeV$[13] due to the inclusion of the supersymmetric states in the calculation of the corrections. It is largely for this reason that so much attention has been paid to the supersymmetric solution of the hierarchy problem. However given that the value of the unification coupling at the unification scale is unknown as is the unification scale itself there is only one prediction being tested by the gauge coupling unification and it would be very important if further evidence of unification is found. Such evidence could be provided by the unification of soft SUSY breaking masses as is illustrated in the second panel of Figure 8. The evidence for unification will be overwhelming if the masses as measured at low scales should follow the pattern shown which follows if the masses unify at the same scale as is found for the gauge coupling unification. In fact there is already some evidence for soft mass unification because the Higgs scalars are also expected to unify. Due to the large top Yukawa coupling radiative corrections systematically drive the mass squared of the Higgs negative, triggering electroweak breaking[14]. The top squarks, which are the other scalar states to feel the effects of the top Yukawa coupling, are coloured and hence have stabilising QCD radiative corrections which drive the mass squared positive and dominate over the Yukawa contribution. Thus mass unification leads to a natural explanation of why the Standard Model gauge group breaks to $SU(3) \times U(1)$.

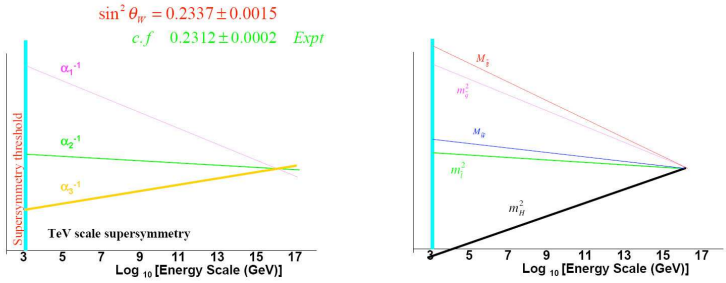

Figure 8: Renormalisation group flow of a) gauge couplings and b) scalar masses, with unification at a high scale.

Another very important reason for measuring the spectrum and spin structure of the new supersymmetric states is that only with this information will it be possible to determine whether the lightest of such states (LSP) provides the answer to the dark matter problem[9]. The dark matter abundance is very sensitive to the LSP mass and the states to which it couples, usually the sleptons, so it is particularly important to be able to measure them.

Given this motivation what are the prospects for being able to measure the masses of any new states, given that identification of such states requires large missing momentum? As a good example let us consider the possibility for slepton mass measurement. Direct slepton production has large SM corrections due to WW and $\bar{t}t$ production. For this reason a more promising channel is production of neutralinos, χ_2, followed by cascade decay to the LSP,

[a]It has recently been pointed out [?] that radiative corrections involving the hidden supersymmetry breaking sector can significantly change the evolution of the soft scalar masses and obscure the unification of masses. In many of the favoured SUSY breaking schemes these corrections are small and in any case the unification of gaugino masses is unaffected by such corrections.

χ_1, which is sensitive to the slepton mass. The relevant Feynman diagrams are shown in Fig 9. For the case that the decay occurs through a real Z this contribution dominates

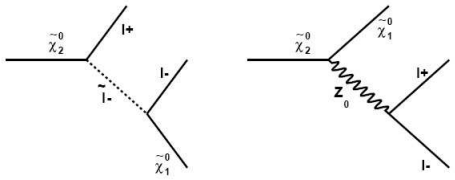

Figure 9: Feynman diagrams contributing to neutraino decay.

and there is no mass information. For the case the decay is through a virtual intermediate state the dilepton invariant mass distribution endpoint is given by

$$m_{ll} = m_{\chi_2} - m_{\chi_1}$$

If the decay is through a real slepton the end point is

$$m_{ll} = \sqrt{\frac{(m_{\chi_2}^2 - m_l^2)(m_l^2 - m_{\chi_1}^2)}{m_l^2}}$$

Thus endpoint measurement can give one constraint on the SUSY mass spectrum. The full invariant mass distribution gives some further information which can establish reasonable upper and lower bounds on light slepton masses. A detailed study including detector effects demonstrated that the signal can be distinguished from the background at the LHC with $10 fb^{-1}$[?]. While the information thus obtained is important, it falls short of a complete determination of the light neutralino and slepton spectrum. To obtain more information requires studying additional processes, for example cascade decays involving longer chains and additional final states. This gives more information because there are now several invariant masses that can be measured and used to determine the masses of the particles involved in the chain. However to access this information it will be necessary to fold in the detector and background effects together with the ambiguities associated with misidentification of the particle in the cascade chain that necessarily will be present in the multiparticle final states that abound at the LHC. Doing this and identifying the most sensitive processes for determining the mass spectrum remains one of the pressing open questions. Clearly, since all such processes necessarily involves high transverse missing momenta in order to avoid SM backgrounds, the expertise of calculating DIS processes will be crucial in this task.

An even more difficult task will be the development of efficient methods capable of measuring the spin of the new particles; as emphasised above this is crucial to the identification of the nature of the physics beyond the Standard Model. One promising method again involves studying the invariant mass distributions associated with long cascade chains. Consider the decay chain of Fig 10 which leads to a quark jet and a dilepton plus missing energy signal. The lower state assignments correspond to the states involved in UED in the decay of a KK quark excitation. The upper state assignments correspond to the states involved in SUSY in the decay of a squark. The spins of the states in the decay chain for the UED case are 1/2, 1,

1/2 and 1 while for the SUSY case they are 0,1/2,0.1/2. The question is can one distinguish these two possibilities? In general there are in fact six possible spin assignments giving rise

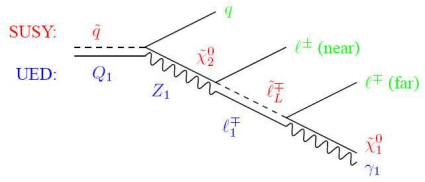

Figure 10: Cascade decays for a KK quark excitation in a UED model and for a squark decay in a SUSY model.

to the same visible final state which can arise in SUSY and UED models. These are shown in Fig 11. A discriminant that can differentiate between these cases is given by[16, 17]

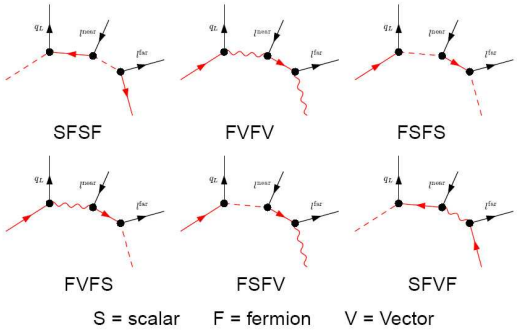

Figure 11: Six possible spin assignments giving rise to a quark jet plus a charged lepton antilepton pair.

$$\frac{dP}{dm} = \frac{1}{\Gamma}\frac{d\Gamma}{dm}$$

where Γ is the total decay rate of the chain and $m_{ab}^2 = (p_a + p_b)^2$ is the invariant mass squared of particles a and b. For example, consider the invariant mass distribution of the lepton pair. Consider also a choice of masses given by the benchmark SPS1a for the SUSY case and by inverse radius $R^{-1} = 800GeV$ and higher dimension Planck mass Λ given by $\Lambda R = 20$ for the UED case. For these choices the distribution for the two possibilities given in Fig 11 are shown in Figure 12[17]. One may see that the distributions do distinguish between several of the possible spin chains. To quantify this the authors of [17] determined the number of events that are needed if the SUSY decay chain of Fig 11 is true to establish that it is 1000 times more likely than each of the other possibilities. This is shown by the light gray entry in Fig 13. While the numbers are encouragingly small for this case some caveats are in order. In particular in a multiparticle final state there will be ambiguities

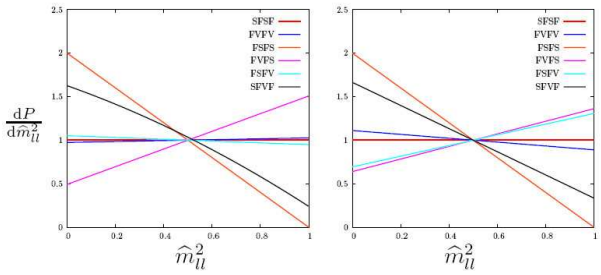

Figure 12: The m_{ll}^2 distribution for SUSY and UED spin chains.

T↓ S→	SFSF	FVFV	FSFS	FVFS	FSFV	SFVF
SFSF	∞	60486	23	148	15608	66
FVFV	60622	∞	22	164	6866	62
FSFS	36	34	∞	16	39	266
FVFS	156	173	11	∞	130	24
FSFV	15600	6864	25	122	∞	76
SFVF	78	73	187	27	90	∞

Figure 13: The number events needed to establish that a given spin chain assignment is 1000 tme more likely than the other possibilities. The light entry corresponds to the case that the SUSY case of Fig 11 is true.

in identifying the relevant lepton momenta when forming the invariant mass. Furthermore the discriminant is dependent on the masses within the cascade and these masses may be poorly determined (the examples above assumed definite, but not identical, mass spectra for the SUSY and UED cases). Indeed, as emphasised by [18], one may adjust the parameters of the UED model so that the mass spectra actually coincides with the SUSY case and then the lepton mass squared distribution are so similar for the SUSY and UED cases that they are not be distinguishable once the background, radiative corrections and the detector simulation are taken into account. The authors of reference [18] studied in some detail the jet-lepton invariant mass distribution as a way to resolve this ambiguity. The spin information comes from the asymmetry between the positive and negative charged lepton pairings with the quark jet. The result is shown in Fig 16. The errors are calculated assuming $10fb^{-1}$ luminosity and a 10% jet energy resolution. One may see that it is possible to distinguish the SUSY chain from the UED chain. However no account has been taken yet of the uncertainty associated with misidentifying the jets. Furthermore it relies on a charge asymmetry which may be very small if the initial production mechanism is dominated by gluons.

In summary, the LHC will probe the energy regime relevant to electroweak breaking and should shed light on the origin of mass. Many possibilities have been identified for the

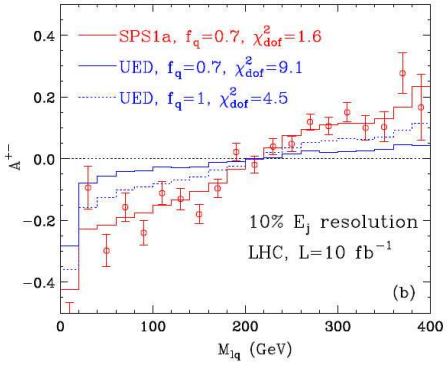

Figure 14: The lepton-jet charge asymmetry plotted versus the lepton-jet invariant mass for the case of SUSY and UED disucssed in the text. The quantity f_q gives the proportion of squarks or KK quarks compared to the antiparticles.

physics Beyond the Standard Model relevant to the LHC, mostly motivated by the need to avoid the hierarchy problem. What has become clear is that it will need detailed information on the masses, spins and interactions to distinguish between these possibilities. Searches for new states rely on missing momentum signals to separate them from Standard Model backgrounds and so the expertise developed for studying perturbative processes in Deep Inelastic Scattering will be invaluable in the analysis of these signals. Obviously the parton distribution functions at the LHC will be an essential input to the calculation of these signals. So too will be the calculation of higher order radiative corrections for processes involving massive states preliminary studies as we know these can significantly modify the cross sections. In addition it is very important to develop precise methods to determine the mass and spin of new states. preliminary work has been carried out studying the possibility of measuring masses and spins in cascade decay chains. The results suggest that while mass and spin discriminants based on invariant mass distributions are viable they are going to be very difficult to achieve due to the many uncertainties associated with the overall rate, the backgrounds, the particle identification and the detector simulations. Alternative methods are being developed which may offer complementary information based on studying the dependence of the cross section on angular variables[19]. Clearly much work remains to be done in establishing the optimum methods and in doing a complete Monte Carlo simulation of the events.

References

[1] Slides:
`http://indico.cern.ch/contributionDisplay.py?contribId=21&sessionId=2&confId=9499`

[2] J. Alcaraz *et al.* [ALEPH Collaboration], arXiv:hep-ex/0612034.

[3] See M. S. Chanowitz, "The no-Higgs signal: Strong W W scattering at the LHC," and references therein, Czech. J. Phys. **55** (2005) B45 [arXiv:hep-ph/0412203].

[4] R. Sekhar Chivukula, D. A. Dicus and H. J. He, Phys. Lett. B **525** (2002) 175 [arXiv:hep-ph/0111016].

[5] A. Dobado, M. J. Herrero and J. Terron, Z. Phys. C **50**, 205 (1991).

[6] A. Dobado, M. J. Herrero and J. Terron, Z. Phys. C **50**, 465 (1991).

[7] A.Birkedal, K.Matchev and M. Perelstein "Phenomenology of Higgsless models at the LHC" in "Tevatron-for-LHC report: Preparations for discoveries," eds. V. Buescher, M. Carena, B. Dobrescu, S. Mrenna, D. Rainwater and M. Schmitt, arXiv:hep-ph/0608322.

[8] K.Lane, "Search for low scale Technicolor at the Tevatron" in "Tevatron-for-LHC report: Preparations for discoveries," eds. V. Buescher, M. Carena, B. Dobrescu, S. Mrenna, D. Rainwater and M. Schmitt, arXiv:hep-ph/0608322.

[9] For extensive reviews of SUSY see: H. P. Nilles, Phys. Rept. **110**, 1 (1984); J. A. Bagger, arXiv:hep-ph/9604232; S. P. Martin, arXiv:hep-ph/9709356. ; D. Bailin and A. Love, "Supersymmetric gauge field theory and string theory," Institute of Physics publishing 1994; M. Drees, R. Godbole and P. Roy, "Theory and phenomenology of sparticles: An account of four-dimensional N=1 supersymmetry in high energy physics,"Cambridge University Press 2007; H. Baer and X. Tata, "Weak scale supersymmetry: From superfields to scattering events," Cambridge University Press 2006; P.Binetruy, "Supersymmetry, Theory, Experiment and Cosmology", Oxford University Press 2006.

[10] M. E. Peskin, arXiv:hep-ph/0002041.

[11] H. C. Cheng, K. T. Matchev and M. Schmaltz, Phys. Rev. D **66** (2002) 056006 [arXiv:hep-ph/0205314].

[12] T. Appelquist, H. C. Cheng and B. A. Dobrescu, Phys. Rev. D **64** (2001) 035002 [arXiv:hep-ph/0012100].

[13] See D. M. Ghilencea and G. G. Ross, Nucl. Phys. B **606** (2001) 101 and references therein [arXiv:hep-ph/0102306].

[14] For a recent review see: L. E. Ibanez and G. G. Ross, arXiv:hep-ph/0702046.

[15] A.Birkedal, C.Group and K.Matchev, "Slepton mass measurements at the LHC" in "Tevatron-for-LHC report: Preparations for discoveries," eds. V. Buescher, M. Carena, B. Dobrescu, S. Mrenna, D. Rainwater and M. Schmitt, arXiv:hep-ph/0608322.

[16] A. J. Barr, Phys. Lett. B **596** (2004) 205 [arXiv:hep-ph/0405052].

[17] C. Athanasiou, C. G. Lester, J. M. Smillie and B. R. Webber, JHEP **0608** (2006) 055 [arXiv:hep-ph/0605286].

[18] AK.Datta, K.Kong and K.Matchev, "Spin determination at the LHC" in "Tevatron-for-LHC report: Preparations for discoveries," eds. V. Buescher, M. Carena, B. Dobrescu, S. Mrenna, D. Rainwater and M. Schmitt, arXiv:hep-ph/0608322.

[19] A. J. Barr, JHEP **0602** (2006) 042 [arXiv:hep-ph/0511115].

Summary Talks

Structure Functions and Low-x

A. Glazov[1], S. Moch[2] and K. Nagano[3]

1- Deutsches Elektronensynchrotron DESY
Notkestraße 85, D–22607 Hamburg - Germany

2- Deutsches Elektronensynchrotron DESY
Platanenallee 6, D–15738 Zeuthen - Germany

3- High Energy Accelerator Research Organization KEK
1-1 Oho, Tsukuba, Ibaraki 305-0801 - Japan

We summarize recent experimental and theoretical results, which were reported in the working group on Structure Functions and Low-x at the DIS 2007 workshop.

1 Introduction

Nucleon structure functions and their scale evolution are closely related to the origins of Quantum Chromodynamics (QCD) as the gauge theory of the strong interaction. With high-precision data from HERA and the TEVATRON available and in view of the outstanding importance of hard scattering processes at the forthcoming LHC, a quantitative understanding of the nucleon's structure in terms of parton distributions is indispensable. In this respect, highlights of the workshop were new HERA measurements at low-Q^2 and large-y, and news on global analyses of parton density functions. The kinematical region of low-x is of particular interest here, because of the rapidly growing gluon density at very small momentum fractions. Consequences of effective theoretical descriptions can for instance be tested on results for measurements of forward jets.

In this summary we give a concise overview of recent experimental and theoretical efforts in this direction, which were presented at our working group [1].

2 Inclusive Structure Function Measurements

The measurement of the inclusive structure functions in deep-inelastic scattering (DIS) is one of the primary tasks of the HERA collider. For the neutral current (NC) process the HERA experiments have reported so far on the measurements of the dominant structure function F_2 and of the structure function xF_3. The scientific program of structure function measurements however is incomplete without measuring the longitudinal structure function F_L and the HERA collider provides a unique opportunity to do so.

2.1 H1 low-Q^2 DIS cross section measurement

A measurement of the DIS cross section by the H1 collaboration in the kinematical domain $0.2 < Q^2 < 12$ GeV^2 was presented by Vargas. The measurement is based on a dedicated "shifted vertex" run which improved the detector acceptance for low Q^2 and a "minimum bias" run with open triggers for low-Q^2 inclusive data. Both runs were done during the HERA-I period in 1999 and 2000. The new preliminary data are combined with the published

H1 results [2] using an averaging procedure which takes into account correlated systematic uncertainties.

As shown in Figure 1, the data are in good agreement with the publications of the ZEUS collaboration at even lower Q^2 [3] and at $Q^2 > 2$ GeV [4]. Moreover, the new data fills the gap in Q^2 between the previous measurements and also extends to high values of the inelasticity, $y = 0.8$, where the cross section is sensitive to the longitudinal structure function F_L although limited to a precision of $\sim 5\%$. For lower values of y, the precision of the new result reaches 1.5% for $Q^2 > 5$ GeV^2, which is an initial step to the ultimate goal of achieving a 1% precision.

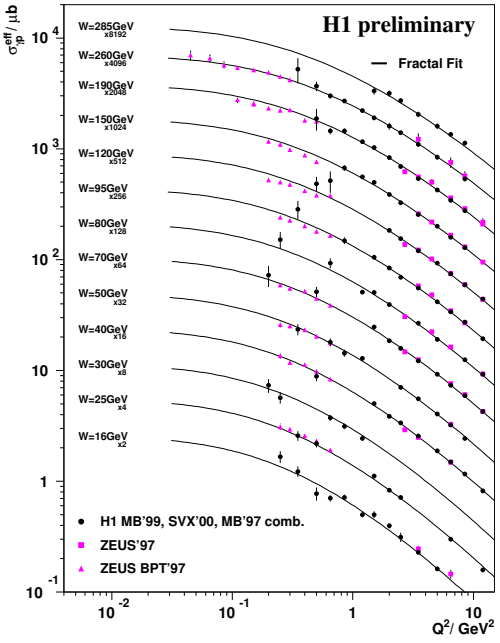

Figure 1: Effective $\gamma^* p$ cross sections at HERA measured by H1, shown as a function of Q^2 at various fixed values of W.

2.2 High-y DIS cross section measurement at low Q^2

A measurement of the longitudinal structure function F_L is the next challenge for the HERA experiments. For this measurement two conditions must be satisfied:

(i) The experiments must measure the DIS cross section for high inelasticity $y > 0.5$ with an accuracy of a few percent.

(ii) HERA must run with different center of mass energies such that the DIS cross section can be determined for the same values of x, Q^2 but at different y.

Results at high-y were presented by Raicevic and Shimizu for the H1 and ZEUS collaborations, respectively. The measurement at high-y is especially difficult at lower Q^2, because of the high level of photoproduction background. High values of y in this kinematical domain correspond to a low energy of the scattered electron which complicates the electron identification.

To that end, H1 has developed a measurement technique in which the background contribution is estimated by using electron candidates with a measured charge opposite to the lepton beam charge. Here, the e^+p data is used to estimate the background for the e^-p data and vice versa. A new preliminary H1 result based on the entire HERA-II sample collected with dedicated low energy triggers utilizes the large e^-p sample, which has not been available during the HERA-I period. The new cross section measurement is based on 96 pb^{-1} of data where 51 pb^{-1} is from e^+p and 45 pb^{-1} from e^-p interactions. This corresponds to more than a ten-fold increase of the total luminosity compared to the previously published result [2]. The measurement covers the range $12 \leq Q^2 \leq 25$ GeV^2 for the inelasticity

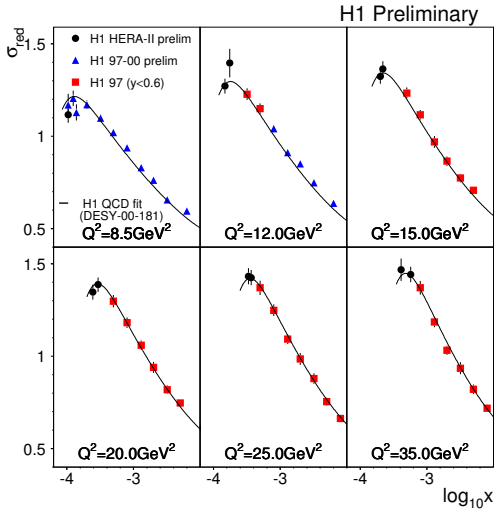

Figure 2: Reduced cross section at low Q^2 and high y at HERA, measured by H1 shown as a function of x at several values of Q^2.

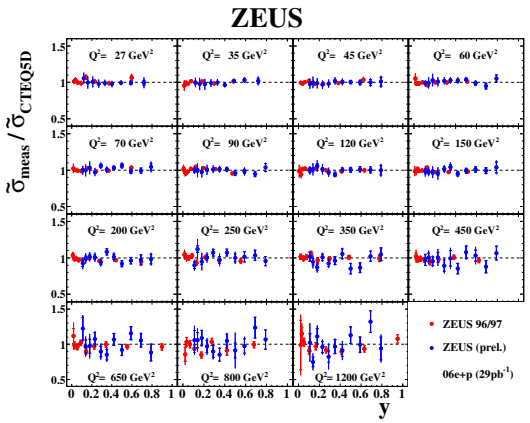

Figure 3: Reduced cross section at high y at HERA as measured by ZEUS and shown in a ratio to the theory prediction as a function of x at several values of Q^2.

$y = 0.825$. Figure 2 shows the measured cross sections together with the previous results. The new preliminary measurement has total uncertainties reduced by factor of two and the total errors are at $2-3\%$ level. Further improvements are possible with a better understanding of the tracking efficiency. The large statistics of the sample is very important for detailed studies of the experimental condition at high-y, as needed for the direct measurement of the structure function F_L.

ZEUS has also performed a cross section measurement optimized for the high-y kinematic range, based on 29.5 pb^{-1} of e^+p collision data collected during year 2006 [5]. In the ZEUS analysis, the photoproduction background is controlled by using a small calorimeter installed close to the beam pipe. It tags electrons which have escaped down the beam pipe in photoproduction events, thus providing a direct measure of the photoproduction background. Compared to the previous measurement [4], the new measurement extends to high values of y up until $y = 0.8$, providing also more data points at $0.1 < y \lesssim 0.8$ and $25 < Q^2 < 1300$ GeV^2, as shown in Figure 3. It serves also as a good demonstration of the feasibility of performing measurements with low energy electrons, which is a necessary prerequisite for future F_L measurements.

2.3 Measurement of xF_3 from ZEUS

Bhadra has reported on a ZEUS measurement of the NC cross sections at large values of Q^2, aiming at pinning down the proton with smallest spatial resolution. The measurement makes use of the full luminosity of e^-p collision data at HERA-II, which amounts to 177 pb^{-1}. The measured cross section showed a good agreement with the Standard Model prediction up to a very large value of $Q^2 \approx 30000$ GeV^2, i.e. down to distances of about 10^{-18} m.

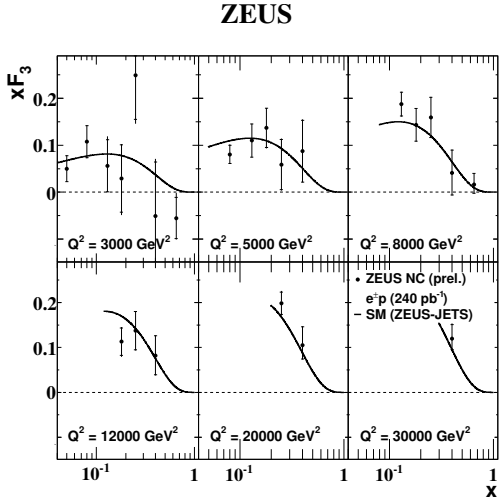

Figure 4: xF_3 measured by ZEUS and shown as a function of x at various values of Q^2.

From this measurement together with the previous e^+p measurement from HERA-I, the structure function xF_3, which is sensitive to the valence quarks, was extracted as shown in Figure 4. The ZEUS measurement will provide important information at smaller x in the region of $10^{-2} \lesssim x \lesssim 10^{-1}$. This is in contrast to fixed target DIS experiments which provide data on xF_3 at large x in the region of $x \gtrsim 0.1$. It was also pointed out that the ZEUS data is collected on a pure proton-target at high Q^2, so that the theoretical uncertainties is significantly less compared to fixed target DIS.

2.4 HERA low energy run

The last three months of HERA operation were dedicated to the measurement of the longitudinal proton structure function F_L using beams with a reduced proton energy. A first look at the machine performance and the data quality collected by the two experiments was presented by Klein. In general the HERA performance exceeded the initial expectations. Instead of the planned data sample of 10 pb^{-1} at a proton energy of $E_p = 460$ GeV, each of the two experiments collected about 13 pb^{-1} at 460 GeV and additionally, about 7 pb^{-1} at 575 GeV. The intermediate proton energy data at 575 GeV should allow for an important cross check of the measurements since the systematic uncertainties, in particular the photoproduction background, are different for the same bins of x, Q^2 but different values of E_p. The online checks of the data show a good quality and near to optimal performance of the detectors. Based on this, Klein concluded that the data for the measurement of the longitudinal structure function F_L were taken successfully, with the next step being a rigorous analysis of these data. Eventually, the measurements will have to be confronted to perturbative QCD predictions [6] and will provide additional information on the gluon distribution at low scales and small x. The latter is in fact poorly known so far, and has led some analyses in the past [7, 8] to prefer a rather small gluon density in this region, to the extend that at NLO in QCD F_L can become almost zero at $Q^2 \lesssim 2$ GeV^2 and very small x.

3 News on Parton density functions

Parton density functions (PDFs) were a central topic of many presentations. This is motivated by the need to have a consistent description of the nucleon's parton content starting from lower scales, were new data sets e.g. from fixed target neutrino-nucleon scattering have become available and theoretical concepts like higher twist are important. Evolution up to high scales by means of perturbative QCD then provides precision predictions for parton luminosities in hard scattering processes at the energy frontier.

3.1 Updates of global PDF analyses

To start with the latter, Thorne has presented a parameterization of PDFs based on a consistent evolution through next-to-next-to-leading order (NNLO) in perturbative QCD. As a new result a PDF set with errors at NNLO is now available [9], where the best fit is supplemented by 30 additional sets representing the uncertainties of the partons (in the Hessian approach). The benefits of NNLO QCD predictions are generally improved stability with respect to scale variations and a consistently better fit than in NLO perturbation theory. Furthermore, higher orders resolve more features of theory, as e.g. the different quark flavor combinations of the PDFs (q_s, q_v, q_-) are all governed by different kernels [10, 11].

Based on this work, Thorne has also reported on a preliminary set of updated NLO PDFs now called MSTW [12] for use at LHC. Main emphasis here besides an improved gluon extraction with the help of jet data from HERA and TEVATRON was on the separation of flavors in the proton. Most importantly, the down quark valence distribution $d_v(x)$ was constrained by lepton asymmetry data from CDF run II. Also, with new results for neutrino-structure functions from CHORUS and NuTeV [13,14] and the CCFR/NuTeV dimuon cross sections [15] a quantitative extraction of the strange quark and antiquark distributions and their uncertainties has become feasible. Upon relaxing previous assumptions on the parameterization,

$$s(x, Q_0^2) = \bar{s}(x, Q_0^2) = \frac{\kappa}{2}[\bar{u}(x, Q_0^2) + \bar{d}(x, Q_0^2)] \qquad (\kappa \approx 0.5), \tag{1}$$

at the input scale of $Q_0^2 = 1\,\mathrm{GeV}^2$, a direct fit of $s(x)$ and $\bar{s}(x)$ to the CCFR/NuTeV dimuon cross sections now becomes possible.

This point of view has been shared by Tung [16] who presented updates on PDF determinations from global QCD analyses for CTEQ. In particular, CTEQ also determined the strangeness on the proton [17] along with the consequences for the strange asymmetry. The latter are of interest, because a non-zero $s(x) - \bar{s}(x)$ has long been identified as a potential explanation for the "NuTeV anomaly" in the measurement of the weak mixing angle $\sin^2\theta_W$. Current global analyses do not require a non-zero $s(x) - \bar{s}(x)$, but they are consistent with one and the integrated momentum asymmetry for the best fit is small and (mostly) positive.

New measurements of the double differential CC neutrino/anti-neutrino scattering cross section by the NuTeV experiment were reported by Radescu. The new data show agreement with the other neutrino-iron scattering experiments CCFR [18] and CDHSW [19] at lower $x < 0.4$ while for $x > 0.4$ the CCFR result is consistently below NuTeV. For $x = 0.65$ the difference between NuTeV and CCFR is about 18%. The high-x kinematic range is challenging for both experiments and part of the difference can be explained by improvements of the experimental techniques. NuTeV extracts the structure functions F_2 and xF_3 and performs a NLO QCD fit with the charm quark contribution accounted for by using the ACOT scheme [20] to obtain a rather large value $\alpha_S = 0.1247 \pm 0.0020\ \exp^{+0.0030}_{-0.0047}$ th. The controversy surrounding the new NuTeV structure functions measurements is further enhanced if the new results are compared to the predictions of MSTW and CTEQ which agree better with CCFR than with NuTeV. The fits for PDF predictions are based on lepton scattering data. Thus the difference between NuTeV and the former predictions may be explained by the difference of the lepton-iron versus neutrino-iron nuclear screening corrections.

To improve the theoretical treatment of the neutrino scattering data, Rogal reported on the calculation of three-loop QCD corrections to the coefficient functions in Paschos-

Wolfenstein relation [21], i.e. the observable measured by NuTeV to extract $\sin^2\theta_W$. Based on the calculation of first five integer Mellin moments for the charged current structure functions F_2, F_L and F_3 [22] the convergence of the perturbative series could be studied, which is well under control for this observable.

On the theory side, CTEQ has improved the treatment of the charm-threshold in their global analysis by implementing now a general-mass formalism, which is consistent with QCD factorization. The improved description of the (anti-)strange quark distributions leads to interesting implications for collider phenomenology. For instance the production of a charged Higgs boson H^+ via the partonic process $c + \bar{s} \to H^+$, provides an example of a beyond Standard Model (BSM) process that is sensitive to the strange PDF in models with two or more Higgs doublets. The cross section also depends on a possible intrinsic charm component of the proton and the recent PDF set CTEQ6.5c provides various models for such a component [23].

Overall, directly fitting the s and $\bar{s}$ distributions affects the correlated uncertainties on the light sea quarks. An independent uncertainty on s and $\bar{s}$ feeds into that on the $\bar{u}$ and $\bar{d}$ quarks, because the neutral current DIS data on $F_2(x, Q^2)$ constrains the combination $4/9(u + \bar{u}) + 1/9(d + \bar{d} + s + \bar{s})$. As an upshot, the size of the uncertainty on the sea quarks for values $x \sim 10^{-3} - 10^{-2}$ at hard scales $Q^2 \sim M_W^2$ roughly doubles from $\sim 1.5\%$ to $\sim 3\%$ for MSTW. Also CTEQ has reported on significant changes in the light quark PDFs between the new CTEQ6.5 and the older CTEQ6.1 sets. Thorne also reminded that currently in the absence of measurements the error on the gluon density at low-x, say $x = 10^{-5}$ is largely due to the parameterization bias. In summary, the inclusion of new data and the changes in the analysis have had a significant impact on the NLO parton distributions.

3.2 PDF constraints from CDF and DØ

New results from the Tevatron experiments were presented by Robson and Toole. The Tevatron $p\bar{p}$ data provides important constraints for d_v and u_v valence quarks via a measurement of the $W^\pm$ charge asymmetry and, of the gluon PDF at high-x by measuring the inclusive jet cross section. Recently, the experiments were focused on the extension of their measurement range to larger rapidities η thus probing the low-x domain. This is of special interest for Standard Model processes at Lhc, because kinematically central rapidities $\eta = 0$ at Lhc correspond to $\eta = 2$ at Tevatron.

Robson presented for the CDF collaboration new measurements of the Z rapidity distribution based on 1.1 fb^{-1} of data from run II. The data extends in rapidity to $|\eta| \sim 2.5$ and shows agreement with NNLO QCD predictions. For $|\eta| \sim 2$ the experimental precision is currently about 8%, which should be improved with larger statistics. For the DØ collaboration the measurement of the Z rapidity distribution based on 0.4 fb^{-1} of data was presented by Toole. This data has already a precision of $\sim 6\%$ for $|\eta| = 2$ and is also in good agreement with NNLO QCD predictions as shown in Figure 5. CDF also extended the $W^\pm$ cross section measurements to the forward region of $1.2 < |\eta| < 2.8$. For that purpose they used the forward silicon detectors for lepton identification. They reported on a measurement of the cross section ratio in $|\eta| < 1$ to $1.2 < |\eta| < 2.8$, which provides additional constraints on the PDFs at small x.

Both experiments, CDF and DØ, reported $W^\pm$ charge asymmetry measurement based on their run II data. CDF showed results using the standard approach which relies on the lepton rapidity and a new method which reconstructs $W^\pm$ rapidity with up to two-fold

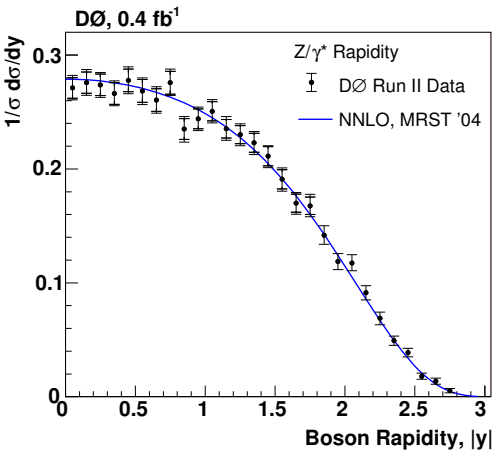

Figure 5: Rapidity distribution of Z produced at TEVATRON measured by DØ in comparison to perturbative QCD predictions at NNLO.

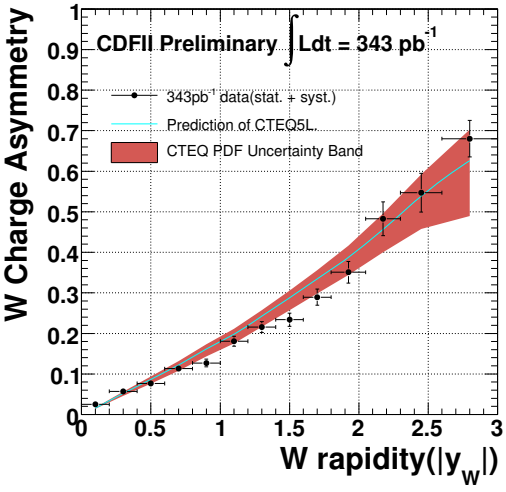

Figure 6: $W^{\pm}$ charge asymmetry at TEVATRON, measured by CDF shown as a function of rapidity of the W.

ambiguity based on the W mass as a constraint. Better forward tracking allows to extend the measurement to higher rapidities. For $|\eta| \sim 2.5$ the precision of the measurement is comparable to the current PDF uncertainties. Figure 6 shows the measured $W^{\pm}$ charge asymmetry with the new method. DØ showed the $W^{\pm}$ asymmetry measurement using $W^{\pm} \rightarrow \mu^{\pm}\nu$ decays. This measurement has a small systematic uncertainty dominated by differences in the efficiencies for positive and negative muons, with the errors being comparable to the present PDF accuracy.

Finally, CDF has shown inclusive jet cross section results using the k_t and the midpoint jet clustering algorithms based on run II data. Figure 7 shows the cross sections in a ratio to QCD theory at NLO as a function of p_t^{jet}. The new results are consistent with the PDF predictions, which in turn are based on run I data. DØ presented a new measurement of the γ-jet differential cross sections for different γ-system topologies. They observed disagreement between the data and theory prediction for the p_t^{γ} distribution, similar to previous observations by UA2 and CDF, as shown in Figure 8.

3.3 Parton luminosity at LHC

The imminent question of how these improvements in the parameterizations of PDFs affect predictions for physical cross sections at LHC was addressed by Cooper-Sarkar [24]. For instance, it was pointed out by her that the predictions for $W^{\pm}$- and Z-production cross sections at LHC (which are sensitive to PDFs in the $x \sim 10^{-3}$ range) shift by 8% between the PDF sets CTEQ6.5 and CTEQ6.1 – a fact that had also been discussed by Tung. Previously, theory predictions for these processes were thought to be known well enough to be used as a parton luminosity monitor [25]. Therefore, Cooper-Sarkar explored which LHC measurements may crucially depend on our knowledge of PDFs and, in turn, which might

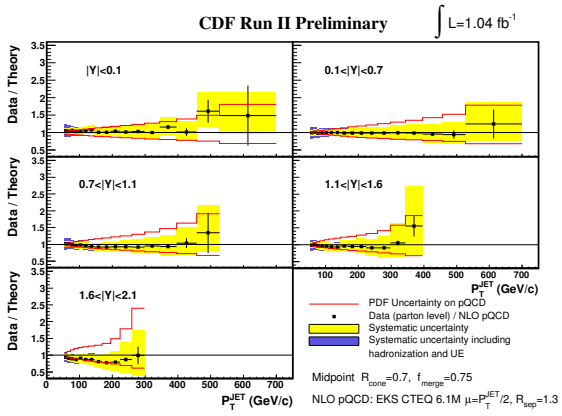

Figure 7: Inclusive jet cross section at TEVATRON, measured by CDF shown in a ratio to QCD theory predictions at NLO.

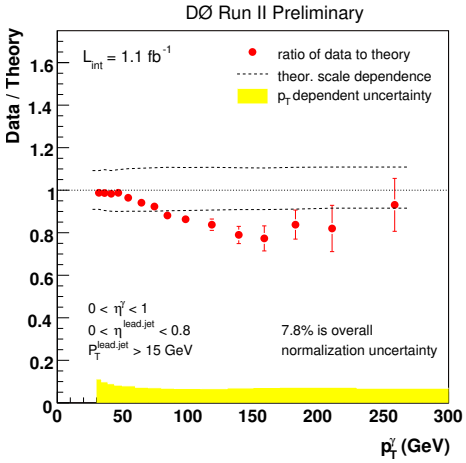

Figure 8: Photon plus jet cross section at TEVATRON, measured by DØ shown in a ratio to QCD theory prediction.

be used to improve it.

In summary, she stated that PDF uncertainties will have a significant impact on the precision of $W^{\pm}$- and Z-cross-sections, although the $W^{\pm}/Z$-ratio would still be a golden calibration measurement. High-E_t jet cross-sections, hence the discovery of new physics parameterized in terms of contact interactions would also depend on uncertainty of the gluon PDF especially at low-x. On the other hand, PDF uncertainties would not affect the discovery potential of a Higgs in the mass range $100 - 1000$ GeV or a high mass Z' in the mass range $150 - 2500$ GeV. Promising measurements to be conducted at LHC itself include hadronic di-jets and direct photon production to constrain the gluon PDF at low-x or the $W^{\pm}$-asymmetry to pin down the low-x valence PDFs.

Another study by Thorne addressed the issue of combining leading-order (LO) partonic matrix elements with different orders of parton distributions [26]. Different prescription for those combinations were compared to the default standard defined by using NLO in QCD for both matrix elements of the hard scattering process and parton distributions. This investigation aims at determining which parton distributions are most appropriate to use in those cases where only LO matrix elements are available, as e.g. in many Monte Carlo generators. It turned out, that the prescriptions are largely depended on the observable under consideration, but this is an important question to be investigated further in the future.

3.4 Resummations improve global analyses

Further improvements of global PDF analyses rely on the possibility to resum perturbation theory in kinematical regions, where large logarithms occur. Yuan advocated to include transverse momentum (p_t) dependent distributions and he reported on successfully combining the traditional fixed-order global PDF fits with p_t resummation calculations [27].

This stabilizes perturbative predictions in regions of large transverse momentum where the logarithms in p_t require an additional resummation. Combinations of conventional and p_t-resummed global fits can potentially improve the determination of parton degrees of freedom entering for instance in precision W-mass measurements and Higgs phenomenology.

In a different kinematical regime at low-x, White has conducted a global fit to scattering data with Balitsky-Fadin-Kuraev-Lipatov (BFKL) resummations to NLL accuracy [28]. In this approach, logarithms $\ln(1/x)$ in the higher order coefficient and splitting functions are resummed and improved descriptions of DIS data for F_2 and F_L presently available in the kinematical region of low-x (and, simultaneously, of low scales Q^2) are achieved. It was shown that the resummed fit improves over a standard fixed order NLO fit and predicts the turnover of the reduced cross section at high-y consistent with the HERA data. However, the question whether the small-x logarithms are indeed the numerically dominant contribution of the higher order perturbative QCD corrections in the kinematical region considered still needs further studies.

3.5 The low Q^2 region in PDF analyses

Different aspects become important in the determination of PDFs and the analysis of DIS data when switching to the kinematical domain of low-Q^2 scales. The presentation of Alekhin has been particularly devoted to the study low-Q^2 DIS data in the global fit of PDFs. The reasons for doing so are obvious. First of all, the DIS cross section with momentum transferred Q decreases as $1/Q^4$ thus a large part of the experimental data is collected at low-Q^2 and also the perturbative QCD corrections are sizable in this region due to the large value of the strong coupling constant at low scales. Moreover, modeling the low-Q^2 region is important for low energy neutrino experiments and also for spin asymmetries analysis. Phenomenological studies of the data can give important constraints on the value of power corrections (higher twist) and thereby define the region of validity for the parton model. Writing for F_2,

$$F_2^{\rm data}(x,Q^2) = F_2^{\rm twist-2}(x,Q^2) + \frac{H_2^{\rm twist-4}(x,Q^2)}{Q^2[{\rm GeV}^2]}\,,$$

one can attempt to parameterize the effect of higher twist. $F_2^{\rm twist-2}$ on the other hand is subject to description within perturbative QCD although target mass corrections still need to be accounted for. In conclusion, Alekhin stated that the existing DIS data at $x \gtrsim 0.001$ can well be described within perturbative QCD in the NNLO approximation down to $Q^2 = 1{\rm GeV}^2$, with the low-Q^2 data providing valuable constraints on the d_v-quark distribution. The contribution of the twist-4 terms was found to be less than 10% in this kinematical region and the higher twist terms in the ratio $R = \sigma_L/\sigma_T$ of the longitudinal over the transverse cross section are generally small.

The fact, that the high-Q^2 region of lepton-nucleon scattering is typically well understood in terms of PDFs and more detailed studies at low-Q^2 are still being conducted, have led Yang to propose a unified approach to the electron- and neutrino-nucleon DIS cross sections at all values of Q^2. Improvements here would for example be very important for many neutrino oscillation experiments. The model presented by him tries to incorporate higher twist and target mass corrections at low scales. This is done through an effective LO QCD evolution with PDFs based on the set GRV98 [29] although with a modified scaling variable to absorb all these effects as well as missing higher orders. The predictions are

in good agreement with the DIS world data as well as photo-production and high-energy neutrino data. Eventually, the model should also describe low energy neutrino cross sections reasonably well and would be useful for Monte-Carlo simulations in experiments like e.g. MINOS, MiniBooNE or K2K.

With a similar motivation, the ALLM parameterization [30] of the total cross section $\sigma_{\rm tot}(\gamma^* p)$ has been updated by Gabbert using new F_2 data to determine its parameters. As an upshot a fit of the world data for inclusive proton DIS cross sections is available which is useful for all extractions requiring F_2 as input and relevant for Monte Carlo simulations at low-Q^2.

3.6 New theory developments

As an alternative to the standard methods of PDF global analyses Rojo presented a general introduction to the neural network approach to parton distributions [31]. The use of neural networks provides a solution to the problem of constructing a faithful and unbiased probability distribution of PDFs based on available experimental information [32]. The talk emphasized the necessary techniques in order to construct a Monte Carlo representation of the data, to construct and evolve neural parton distributions, and to train neural networks in such a way that the correct statistical features of the data are reproduced. As a first application, a determination of the non-singlet quark distribution up to NNLO from available DIS data was presented and compared with those obtained using other approaches. The obvious next step is a complete singlet analysis and the release of the first neural PDF set was announced for summer 2008. In a similar spirit, Liuti reported on first attempts to perform PDF fits with self-organizing maps, and presented LO fits as a proof of principle.

A possible test of the validity of perturbative QCD evolution in a global fit to the proton structure function $F_2^p(x,Q^2)$ was discussed by Pisano [33]. The idea is to probe the range of validity of the NLO and NNLO QCD evolutions of parton distributions in particular in the small-x region using the curvature of F_2^p as a criterion [34]. The characteristic feature to be exploited here is a positive curvature of F_2^p which increases as x decreases. This is a perturbatively stable prediction and turns out to be rather insensitive to the specific choice of the factorization scheme ($\overline{\rm MS}$ or DIS) as well. Therefore, Pisano argued that the curvature of F_2^p does indeed provide a sensitive test of the range of validity of perturbative QCD evolution.

The talk by Zotov discussed the concept of un-integrated PDFs in the k_t-factorization approach, in particular its uses to obtain an un-integrated gluon distribution with k_t-dependence from a fit to measured structure functions F_2 and $F_2^{\rm charm}$ at HERA [35]. As a critical test he then applied the results of his fit to the experimental data for observables like $F_2^{\rm bottom}$ and F_L, all of which are dominated by the gluon PDF.

Finally, the discussions on PDFs were nicely complemented by presentations of Gousset, who reported on research to quantify nuclear modifications of PDFs. For the gluon distribution, they can amount up to 30% and prompt-photon production in p-A collisions offer the chance to study the effects. Detmold contributed from the side of lattice QCD, where moments of PDFs at low scales can be computed in an entirely non-perturbative way.

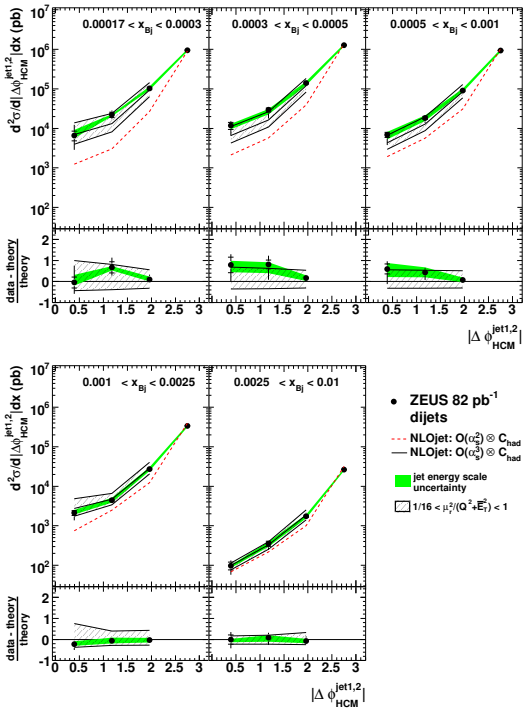

Figure 9: Di-jet cross sections at HERA, measured by ZEUS as a function of the angular separation of the two jets.

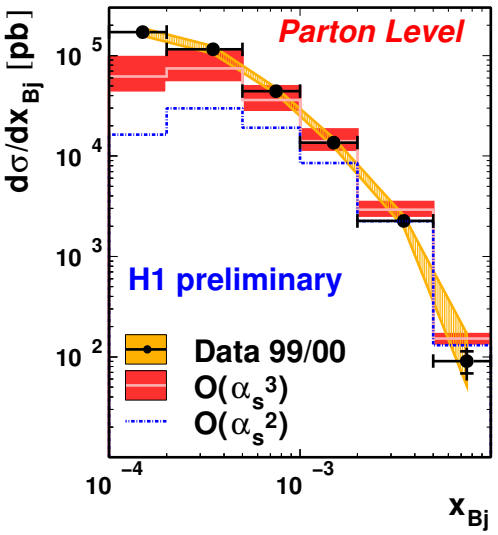

Figure 10: Differential cross section in x for two forward jet at HERA, measured by H1.

4 Forward jets and low-x

4.1 Parton dynamics with DIS multi-jets at HERA

Studies of multiple jet production in DIS have been performed by H1 as reported by Novak and by ZEUS as reported by Danielson. The main goal is to investigate a possible enhancement of gluon radiation, which is expected to become important at low x. ZEUS studied di-jet and tri-jet production in DIS at low-x based on 82 pb^{-1} of data collected during 1998 and 2000 [36]. The kinematic range is $10 < Q^2 < 100$ GeV^2 and $10^{-4} < x < 10^{-2}$. The correlations in angles and p_t between the two highest E_t jets were examined to search for effects of higher orders or from the underlying hard scattering beyond the conventional (i.e. NLO in QCD) Dokshitzer-Gribov-Lipatov-Altarelli-Parisi (DGLAP) evolution. The data were found to be well described by the NLOJET calculations at $O(\alpha_s^3)$, while calculations at $O(\alpha_s^2)$ do not describe data in particular at low x. It was shown that these measurements are very sensitive to QCD higher order effects which can be enhanced by up to a factor ten at the lowest x.

The H1 study is based on 44 pb^{-1} of data collected in 1999 and 2000. The kinematic range of the measurement is focused on the low-x domain, $x < 10^{-2}$ with $5 < Q^2 < 80$ GeV^2. A comparison of the inclusive ≥ 3 jet sample shows that leading order calculations

undershoot the data while NLO predictions are marginally consistent, although within a large scale uncertainty. Yet the data tends to be higher compared to the NLO prediction for the smallest x and the largest η. To investigate this kinematic domain in more detail, the 3-jet sample was split in sub-samples with one or two jets in the forward direction. A significant discrepancy was observed for the sample with two forward jets for $x \sim 10^{-4}$. This discrepancy may indicate an enhancement of gluon radiation compared to NLO QCD evolution, but also higher order QCD calculations for the hard scattering may improve the data description.

4.2 Forward jet production at HERA

Khein presented a new ZEUS measurement on forward jet production in DIS with a significant extension in forward region up to rapidities of $\eta^{jet} < 4.3$ [37]. This measurement is expected to highlight the differences between predictions of the BFKL and DGLAP formalism with BFKL resulting in a larger fraction of small-x events with forward-jets than typically present in DGLAP evolution to NLO in QCD.

The measurements were presented for inclusive forward jets as well as for a forward jet accompanied by a di-jet system. As shown in Figure 11, NLO QCD calculations were found to be below the data, in certain regions by as much as a factor of two. Amongst the Monte Carlo models, the color-dipole model (CDM) of ARIANDE was capable of describing the data over the whole phase space. The CASCADE Monte Carlo with the J2003 set-1 and set-2 un-integrated gluon densities however failed to describe the data. Therefore, these measurements can be used for further improvements by adjusting the input parameters of the CASCADE model.

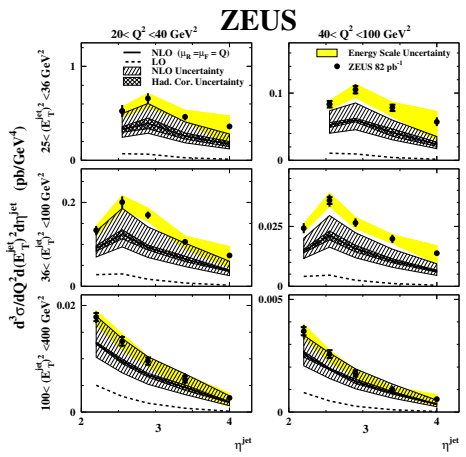

Figure 11: Differential jet cross sections at HERA, measured by ZEUS shown as a function of η^{jet} in different bins of Q^2 and $(E_t^{jet})^2$.

4.3 Theory progress in multiple gluon scattering

On the theory side a number of presentations were concerned with improved predictions and models for the production of forward jets at HERA and multiple gluons in the low-x kinematical region.

Avsar reported on efforts to further improve dipole phenomenology. Starting from the Mueller dipole picture, where the dipoles are assumed to interact independently, he modeled multiple scattering effects typically attributed to Pomeron loops. Putting particular emphasis on a Monte Carlo approach and adding as a new feature color-suppressed effects, he described saturation both in the evolution of dipoles and in the interactions of dipoles with a target by means of an effectively unitary formula for the amplitude. Applications of the formalism for the $\gamma^* p$ total cross sections as measured by HERA and $p\bar{p}$ cross sections at TEVATRON were shown.

On the analytical side, Shoshi discussed the Balitsky-Kovchegov (BK) equation as basis for the high-energy scattering of a dipole off a nucleus/hadron in the mean field approximation [38]. Although the BK-equation results in a geometric scaling behavior of the scattering amplitude and a roughly power-like energy dependence of the saturation scale, it is known that it needs improvements, as it misses for instance Pomeron loops. Shoshi reviewed recent progress in understanding the small-x dynamics beyond the mean field approximation, guided by the natural requirements of unitarity and Lorentz invariance. He pointed out relations between high-energy QCD and statistical physics inspired by dynamics of reaction-diffusion processes. As an upshot, fluctuations in gluon number from one scattering event to another lead to corrections to the geometric scaling which will be modified to diffusive scaling at large energies. He concluded that Pomeron loops and fluctuations in the gluon number will strongly influence predictions for instance for diffractive scattering or the forward gluon production cross section, although it is too early to make the phenomenological consequences quantitative.

Lublinsky on the other hand pointed out that multi-gluon production via high energy evolution can also be modeled by improvements within the JIMWLK high energy evolution. He presented results for the multi-gluon cross section in terms of a generating functional for arbitrary numbers of gluons n, which extends the dipole approximation (and the previously known results for single and double gluon inclusive cross sections) and which generalizes for an arbitrary multi-gluon amplitude in terms of Feynman diagrams of Pomeron-like objects coupled to an external rapidity dependent field. He discussed some general properties of the expressions and suggested a line of argument to simplify the approach further.

The presentations of the theory framework were nicely complemented by Royon and Sabio Vera. The contribution by Royon was concerned with the phenomenology of forward jets at HERA and Mueller-Navelet jets at hadron colliders (TEVATRON, LHC) [39], both being sensitive to low-x physics and, potentially, well described within the BFKL formalism. In particular Mueller-Navelet jets are ideal processes to study BFKL resummation effects with two jets having similar tranverse momenta and being separated by a large interval in rapidity. There, a typical observable to look for BFKL effects is the measurement of the azimuthal correlations between both jets. Fixed order perturbative (i.e. NLO) QCD predictions based on DGLAP predict a distribution peaked towards π as it is typical for back-to-back jets. On the other hand, multiple gluon emissions at small-x in the BFKL formalism smoothen this distribution. Fits to H1 data from HERA were presented and suggestions for measurements by CDF at TEVATRON were made.

Also Sabio Vera [40] looked at the azimuthal angle correlation of Mueller-Navelet jets. In particular, he highlighted the need of collinear improvements in the BFKL kernel to obtain stable theory results, and better fits to the TEVATRON data of D$\emptyset$ which has analyzed data for Mueller-Navelet jets at $\sqrt{s} = 630$ and 1800 GeV many years ago. He estimated several uncertainties and suggested improvements depending on the conformal spins. For LHC where larger rapidity differences will occur the Mueller-Navelet jets will be a very useful tool to investigate the importance of BFKL effects in multi-jet production in particular for the azimuthal dependence which is driven by the BFKL kernel with increasing rapidity.

5 Theory outlook

A lot of the success of QCD in the theoretical description of DIS structure functions relies on the possibility to predict the scale dependence, which is governed by anomalous dimensions

of composite Wilson operators that arise in the operator product expansion of conserved currents. The anomalous dimensions reflect the symmetries of the underlying gauge theory and depend on the quantum numbers of the Wilson operators such as Lorentz spin.

For operators with large Lorentz spin the anomalous dimensions scale logarithmically with the spin. Recent higher order QCD calculations of twist-two anomalous dimensions [10, 11] revealed the existence of intriguing underlying structures in the large spin expansion. In his presentation Basso discussed this structure of inheritance across orders in perturbation theory for terms suppressed by powers of the Lorentz spin [41]. He argued that it relates to the properties of a conformal field theory (CFT) where the corresponding anomalous dimensions are functions of their conformal spin only and supplemented with well determined modifications in higher loops [42].

For a more symmetric relative of QCD, the $\mathcal{N} = 4$ supersymmetric Yang-Mills (SYM) theory, the corresponding anomalous dimensions display very interesting integrability properties, which have been reviewed in the presentation of Lipatov. Using an inspired observation, he had earlier been able to obtain the $\mathcal{N} = 4$ SYM results from the "leading-transcendentality" contributions of QCD [43] up to three loops. In the planar limit the $\mathcal{N} = 4$ SYM theory is believed to be dual to weakly-coupled gravity in five-dimensional anti-de Sitter (AdS) space. Based on the AdS/CFT correspondence, Lipatov related the Pomeron at low-x in the strong coupling limit of the gauge theory to the graviton in the weakly-coupled gravity. These investigations based on integrability and strong-weak duality offer not only great chances to improve our understanding of $\mathcal{N} = 4$ SYM theory by providing us with conjectures for the exact four-loop anomalous dimension of twist-two operators [44], but in the future they will hopefully also lead to new insights into QCD.

6 Summary

Many new results on nucleon structure functions and subjects related to low-x physics were presented at this workshop, which covered both, theory and experiment. On the latter side, the experimental contributions came not only from DIS experiments (e.g. H1, ZEUS) but also from hadron-collider experiments (e.g. CDF, D$\emptyset$), which we believe is a clear demonstration of the importance of our field and of the presence of lively activities. In view of the forthcoming LHC, particular attention was paid to a further precise understanding of the QCD dynamics. This includes the gluon density at low-x in particular, and also a more precise and robust determination of parton distribution functions in general. Clearly, the progress reported here was remarkable. The first F_L measurement at HERA is foreseen in near future. It becomes possible with the newly developed experimental techniques reported at this workshop and is expected to give new insight into low-x physics and the gluon density. In summary, the various efforts made, many of them being based on new and unique ideas, are likely to improve our understanding of structure functions in near future. We believe that the field continues to contribute to fruitful research in the LHC era.

The authors would like to thank all the participants of our working group for their contributions as well as for the lively and useful discussions, and the organizers for the excellent organization of the workshop.

References

[1] Slides:
http://indico.cern.ch/contributionDisplay.py?contribId=14&sessionId=2&confId=9499
[2] H1, C. Adloff et al., Eur. Phys. J. C21 (2001) 33, hep-ex/0012053
[3] ZEUS, J. Breitweg et al., Phys. Lett. B 487 (2000) 53, hep-ex/0005018
[4] ZEUS, S. Chekanov et al., Eur. Phys. J. C 21 (2001) 443, hep-ex/0105090
[5] ZEUS, abstract #78, contribution paper to The 2007 Europhysics Conference on High Energy Physics.
[6] S. Moch, J.A.M. Vermaseren and A. Vogt, Phys. Lett. B606 (2005) 123, hep-ph/0411112
[7] A.D. Martin et al., Phys. Lett. B531 (2002) 216, hep-ph/0201127
[8] S. Alekhin, Phys. Rev. D68 (2003) 014002, hep-ph/0211096
[9] A.D. Martin et al., (2007), arXiv:0706.0459 [hep-ph]
[10] S. Moch, J.A.M. Vermaseren and A. Vogt, Nucl. Phys. B688 (2004) 101, hep-ph/0403192
[11] A. Vogt, S. Moch and J.A.M. Vermaseren, Nucl. Phys. B691 (2004) 129, hep-ph/0404111
[12] R.S. Thorne et al., (2007), arXiv:0706.0456 [hep-ph]
[13] CHORUS, G. Onengut et al., Phys. Lett. B632 (2006) 65
[14] NuTeV, M. Tzanov et al., Phys. Rev. D74 (2006) 012008, hep-ex/0509010
[15] NuTeV, M. Goncharov et al., Phys. Rev. D64 (2001) 112006, hep-ex/0102049
[16] W.K. Tung et al., (2007), arXiv:0707.0275 [hep-ph]
[17] H.L. Lai et al., JHEP 04 (2007) 089, hep-ph/0702268
[18] W.G. Seligman, FERMILAB-THESIS-1997-21.
[19] J.P. Berge et al., Z. Phys. C49 (1991) 187
[20] M.A.G. Aivazis et al., Phys. Rev. D50 (1994) 3102, hep-ph/9312319
[21] M. Rogal and S. Moch, (2007), arXiv:0706.3297 [hep-ph]
[22] S. Moch and M. Rogal, Nucl. Phys. B in press, arXiv:0704.1740 [hep-ph]
[23] J. Pumplin, H.L. Lai and W.K. Tung, Phys. Rev. D75 (2007) 054029, hep-ph/0701220
[24] A.M. Cooper-Sarkar, (2007), arXiv:0707.1593 [hep-ph]
[25] M. Dittmar et al., (2005), hep-ph/0511119
[26] R.S. Thorne, A. Sherstnev and C. Gwenlan, (2007), arXiv:0706.2131 [hep-ph]
[27] J.C. Collins, D.E. Soper and G. Sterman, Nucl. Phys. B250 (1985) 199
[28] C.D. White and R.S. Thorne, (2007), arXiv:0706.2609 [hep-ph]
[29] M. Glück, E. Reya and A. Vogt, Eur. Phys. J. C5 (1998) 461, hep-ph/9806404
[30] H. Abramowicz et al., Phys. Lett. B269 (1991) 465
[31] NNPDF, J. Rojo et al., (2007), arXiv:0706.2130 [hep-ph]
[32] NNPDF, L. Del Debbio et al., JHEP 03 (2007) 039, hep-ph/0701127
[33] C. Pisano, (2007), arXiv:0706.1902 [hep-ph]
[34] M. Glück, C. Pisano and E. Reya, Eur. Phys. J. C50 (2007) 29, hep-ph/0610060
[35] H. Jung et al., (2007), arXiv:0706.3793 [hep-ph]
[36] ZEUS, S. Chekanov et al., Nucl. Phys. B in press, arXiv:0705.1931 [hep-ex]
[37] ZEUS, S. Chekanov et al., Eur. Phys. J. C subm., arXiv:0707.3093 [hep-ex]
[38] A.I. Shoshi, (2007), arXiv:0706.1866 [hep-ph]
[39] C. Royon, (2007), arXiv:0706.1799 [hep-ph]
[40] A. Sabio Vera and F. Schwennsen, (0700), arXiv:0707.0256 [hep-ph]
[41] Y.L. Dokshitzer, G. Marchesini and G.P. Salam, Phys. Lett. B634 (2006) 504, hep-ph/0511302
[42] B. Basso and G.P. Korchemsky, Nucl. Phys. B775 (2007) 1, hep-th/0612247
[43] A.V. Kotikov et al., Phys. Lett. B595 (2004) 521, hep-th/0404092
[44] A.V. Kotikov et al., (2007), arXiv:0704.3586 [hep-th]

Diffraction and Vector Mesons: Summary

Uta Klein[1] and Leszek Motyka[2,3]

1- University of Liverpool, Oliver Lodge Laboratory, L69 7ZE, England, U.K.

2- II. Institute for Theoretical Physics, Hamburg University,
Luruper Chaussee 149, 22761 Hamburg, Germany

3- Institute of Physics, Jagellonian University,
Reymonta 4, 30-059 Kraków, Poland

We summarize recent experimental results and theoretical developments related to the topics of diffraction and vector mesons discussed at the DIS2007 Workshop.

1 Preface

For nearly two decades, diffractive phenomena studied at the high energy frontier in $p\bar{p}$ collisions at the Tevatron and in ep collisions at HERA are shaping and challenging our understanding of the underlying dynamical quantum processes. Experimentally, diffractive processes are characterized by large 'rapidity gaps', regions of (pseudo-)rapidity in which no hadrons are produced, and/or by a beam particle ($p/\bar{p}$) which remains intact after the scatter. Large gaps in the final state may occur by the exchange of a color singlet object with vacuum quantum numbers, historically referred to as the Pomeron. The spectacular phenomenon of hard diffraction provides a unique way to probe QCD dynamics at low-x and to interpret diffractive reactions by the exchange of partons, mainly gluons, of the interacting nucleon. A particularly *exciting feature* of diffractive Deep Inelastic Scattering (dDIS) is its relation to unitarity effects in hard QCD scattering amplitudes such as are implemented in modern QCD inspired saturation models and within the k_T factorization framework in perturbative QCD (pQCD). An important merit of the k_T factorization approach and the saturation model is a unified picture of inclusive and diffractive DIS that they provide. Complementary, in the collinear framework of pQCD, the Operator Product Expansion, inclusive hard diffraction is encoded in diffractive parton densities evolving according to the DGLAP evolution equations. Both frameworks are successfully used to describe data, however, the collinear approach doesn't connect inclusive and diffractive cross sections provided by the S-matrix unitarity.

Exclusive diffractive processes are excellent tools to probe the proton structure beyond the reach of inclusive DIS. Exclusive production of mesons, vector mesons and real photons in ep scattering contains combined information about longitudinal momentum distributions of partons and their position on the transverse plane as encoded in Generalized Parton Distribution functions (GPDs). In the high energy and/or very small Bjorken-x regime, exclusive processes can be intimately linked to inclusive DIS in the light-cone color dipole picture. This regime is dominated by the exchange of a hard pQCD Pomeron while data at lower energies are strongly affected by non-vacuum exchanges. A wealth of HERA data established the gross features of the pQCD based description of diffractive vector meson production as for example $(Q^2 + M^2)$ as the hard scale for small-t diffraction. The s-channel helicity non-conservation in high energy small-t diffractive scattering may be regarded as one of the important observations at HERA.

Recently, efforts are made to understand exclusive processes in the collinear factorization beyond leading order. Systematic studies of NLO corrections clearly show that the perturbative expansion is stable at low and moderate collision energies but at large energies (that is at small Bjorken-x) the NLO are enhanced by $\log(1/x)$ and become large. This calls for further developments of the NLO k_T-factorization formalism at small x as performed in the Balitsky-Fadin-Kuraev-Lipatov (BFKL) frame.

Diffractive reactions constitute a significant fraction of the hadronic and electroproduction cross sections. With increasing statistics, improved instrumentation and better detector understanding, many important observations could be made and further established, e.g. regarding the diffractive structure function of the Pomeron and the breakdown of QCD factorization in hard diffraction between ep at HERA and $p\bar{p}$ at Tevatron. The applicability of the hard diffractive factorization to semi-inclusive processes, e.g. to the diffractive dijet or diffractive charm photoproduction is not proven and recent, more precise HERA data are challenging the validity of factorization in hard diffractive dijet photoproduction.

The information extracted from diffraction in ep collisions, mainly the dPDFs, may be used to calculate the hard diffractive subprocess in pp and $p\bar{p}$ scattering. Due to non-perturbative effects, like proton remnant rescattering, diffractive factorization does not hold in hadronic collisions and the pattern of factorization breaking could be probed. In particular it is interesting to test the hypothesis of universal soft proton remnant rescattering that may be factorized out from the hard diffractive amplitude. Recent, precise HERA data on leading neutron production in DIS and in photoproduction give further insight into rescattering models which are necessary to understand gap-survival probabilities in high energy diffractive hadronic collisions. The hard hadronic diffraction is interesting not only because it is sensitive to the dynamics of QCD at large parton densities but also because new physics may be probed in a unique way in diffractive scattering at the LHC. The most important example is central exclusive diffractive Higgs boson production, a measurement that may provide a clean signal and facilitate a precise determination of the Higgs boson quantum numbers, its mass and width. In order to perform such measurements, vivid activities are ongoing on designing new forward and very forward detectors at the LHC.

In the following, we report on selected topics on latest experimental and theoretical developments as were presented to the session 'Diffraction and Vector Mesons' of this Workshop. The slides and more plots can be found in [1].

2 Hard diffraction in ep scattering

At HERA, individual proton constituents may be resolved with a hard (that is small) probe provided by a virtual photon mediating $e^{\pm}p$ scattering. Virtual photons carrying large negative momentum transfer, say $Q^2 = -q^2 = 10$ GeV^2, to a single parton are expected to destroy the proton with a probability very close to unity while final-state particles are uniformly emitted between the struck quark and the proton remnant. However, it is now a well-established fact that the proton emerges intact in a sizable fraction of DIS events: between 30% and 5% when the photon virtuality increases from $Q^2 \simeq 0$ to $Q^2 \simeq 190$ GeV^2. The signature of hard diffraction at HERA is depicted in Fig. 1, characterized by a large separation in rapidity between the proton remnant (p') and any other hadronic activity (X) in the event. Diffractive scattering shows up as a peak at large fractions of the outgoing to the incoming proton momentum, $x_L \sim 1$, and small fractions of the proton momentum carried by the Pomeron, $x_{I\!P} = 1 - x_L \lesssim 0.01$. Diffractive production

in the t channel, where $t = (p - p')^2$ is the four-momentum transfer at the proton vertex, leads to an approximately constant $\ln M_X^2$ distribution for the particles of the system X observed in the detector, in strong contrast to the exponential fall-off as seen for non-peripheral DIS events. The fraction of the Pomeron momentum carried by the struck quark, β, is related to the Bjorken-x, x_{Bj}, via $\beta = x_{\mathrm{Bj}}/x_{I\!P}$. The fractional energy transferred to the proton in its rest system is y, the c.m. energy of the $\gamma^* p$ system is given with W.

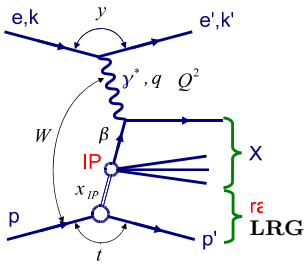

Figure 1: Schematic illustration of the diffractive contribution in neutral current DIS; plot from [2].

The described signatures are used by both H1 and ZEUS collaborations for the measurements of hard diffraction in ep collisons: either via event selections based on the detection of the outgoing proton with forward (leading) proton spectrometers (H1 FPS, ZEUS LPS methods) and on the detection of a large rapidity gap (LRG method) or via the determination of the mass distribution $\ln M_X^2$ of the diffractively produced hadronic system where background and non-diffractive DIS contributions are subtracted statistically (M_X method).

At the workshop latest results of the HERA collaborations H1 and ZEUS were lively discussed, now with emphasis on results based on finalized HERA I data statistics. Using such larger data samples, a more detailed exploration of hard diffractive phenomena at HERA beyond the scope of the 'flagship' inclusive channel could be done. Those are studies of diffractive dijets in DIS and of diffractive dijets and open charm in photoproduction.

ZEUS reported [2] new results on the inclusive diffractive dissociation of virtual photons in events with a large rapidity gap and in events with a measured leading proton using integrated luminosities of 45.4 pb^{-1} and of 32.6 pb^{-1}, respectively. The LRG (LPS) data cover photon virtualities $2 < Q^2 < 305$ (120) GeV^2 and $2 < M_X < 25$ (40) GeV. LRG events were selected with $x_{I\!P} < 0.02$, LPS events were required to have a proton detected in the leading proton spectrometer carrying at least 90% of the incoming proton energy. The t integrated, reduced cross sections $\sigma_r^{D(3)}$ show good agreement between the results extracted with the LPS method and the LRG method. The agreement between ZEUS LPS and recently published H1 FPS results is fair keeping in mind a 10% normalization uncertainty of each of the data sets. There is also good agreement between both ZEUS LRG and recently published H1 LRG $\sigma_r^{D(3)}$ data after correcting for the different p dissociation contribution per experiment; here the ZEUS data have been normalized to the H1 data. The ratio of the diffractive structure functions $F_2^{D(3)}$ from LPS/FPS and LRG is about 80%. It thus allows an experimental estimate of the p dissociation contribution with a precision limited by the 10% normalization uncertainties of the LPS/FPS methods.

Using the proton tag methods the exponential t dependence of the cross section could be measured with a b slope of 7 ± 0.3 GeV^{-2} (ZEUS) without any observed dependence on Q^2, M_X and $x_{I\!P}$ in the measured region, $x_{I\!P} < 0.01$. Within Regge phenomenology the exchange can be described by an effective Pomeron trajectory. From the $x_{I\!P}$ dependence of the diffractive structure function $F_2^{D(4)}$ and $F_2^{D(3)}$ a Pomeron intercept of 1.1 ± 0.04 in good agreement with H1 was measured. The Pomeron slope was found to be consistent with zero within a total uncertainty of about 0.1 GeV^{-2} but significantly smaller than the value of 0.25 GeV^{-2}

found in soft hadronic interactions. The LPS data could be well described by a Regge fit in terms of Pomeron and Reggeon contributions with $x_{I\!P}$ and t dependent flux factors and and β and Q^2 dependent structure functions.

Furthermore ZEUS reported [3] new studies on inclusive and diffractive DIS based on the M_X method for masses $1.2 < M_X < 30$ GeV in an extended kinematic range of $25 < Q^2 < 35$ GeV^2 and of $45 < Q^2 < 220$ GeV^2 with an integrated luminosity of 11 pb^{-1} and 52.4 pb^{-1}, respectively. Using a Forward Plug Calorimeter at HERA I, ZEUS diffractive analyzes profit from the measurement of the energy of particles in the pseudorapidity range $\eta \approx 4.0 - 5.0$ limiting the mass of the diffractively produced nucleonic system to $M_N \leq 2.3$ GeV; H1 quotes $M_N < 1.6$ GeV for the proton-dissociation system. A comparison for two values of proton momentum fractions of the Pomeron between the (Q^2, β) dependence of $x_{I\!P} F_2^{D(3)}$ obtained with the LRG method (H1) and the M_X method is shown in Fig. 2. The diffractive structure function values extracted with the different methods and different detectors show fair agreement for the Q^2 dependence except for a few bins. Observed differences at higher $x_{I\!P} > 0.01$ (not shown here) may be affected by Reggeon contributions which could enter differently in the M_X and LRG methods. In any case, the comparison and the consistency of these measurements is an important step forward in our understanding of an overall picture of hard diffraction at HERA. A next step could be a

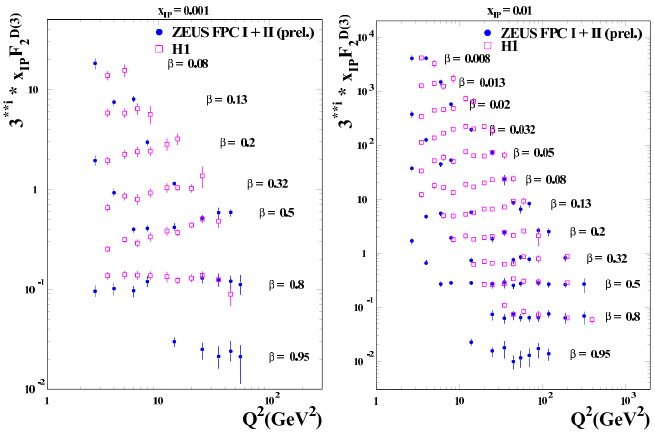

Figure 2: Comparison of the (Q^2, β) dependence of $x_{I\!P} F_2^{D(3)}$ obtained with the LRG method (H1) and the M_X method (ZEUS, shifted to centers of H1 bins) for $x_{I\!P} = 0.001$ (left) and $x_{I\!P} = 0.01$ (right); plot from [3].

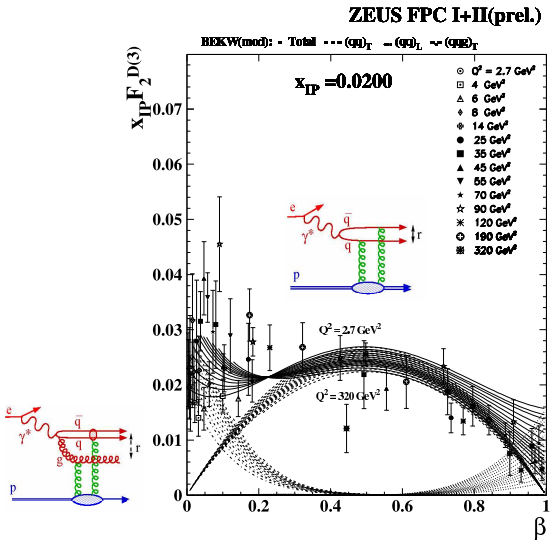

Figure 3: Compilation of the β dependence of $x_{I\!P} F_2^{D(3)}$ for various Q^2 values but fixed $x_{I\!P} = 0.02$. The curves are resulting from a BEKW fit (full) including the contributions from $q\bar{q}$ (depicted with an insert) for transverse (dashed) and longitudinal (dotted) photons as well as from $q\bar{q}g$ (depicted with an insert) for transverse photons (dashed-dotted); plot from [3].

comparison within a QCD NLO fit although this requires the assumption that the diffractive structure function factorizes in a term depending only on $x_{I\!P}$ and another term depending only on β and Q^2. The LRG method results are consistent with this assumption but the M_X method results indicate a breaking of the Regge (or proton vertex) factorization.

A good description of the M_X method values of $x_{I\!P} F_2^{D(3)}$ could be obtained with a 5 parameter fit according to a modified BEKW model [3], see Fig. 3, which gives an intuitive picture in terms of contributions from the fluctuations of the incoming photon into dipoles: transverse photons to $q\bar{q}$, longitudinal photons to $q\bar{q}$, and transverse photons to $q\bar{q}g$. The dipole interacts with the target proton via two-gluon exchange. As expected from the model, the $q\bar{q}$ contributions from transverse photons dominate for $0.2 < \beta < 0.9$ while contributions from $q\bar{q}g$ dipoles become important at smaller $\beta \leq 0.15$. Only in the region close to β near 1 contributions from longitudinal photons may become important.

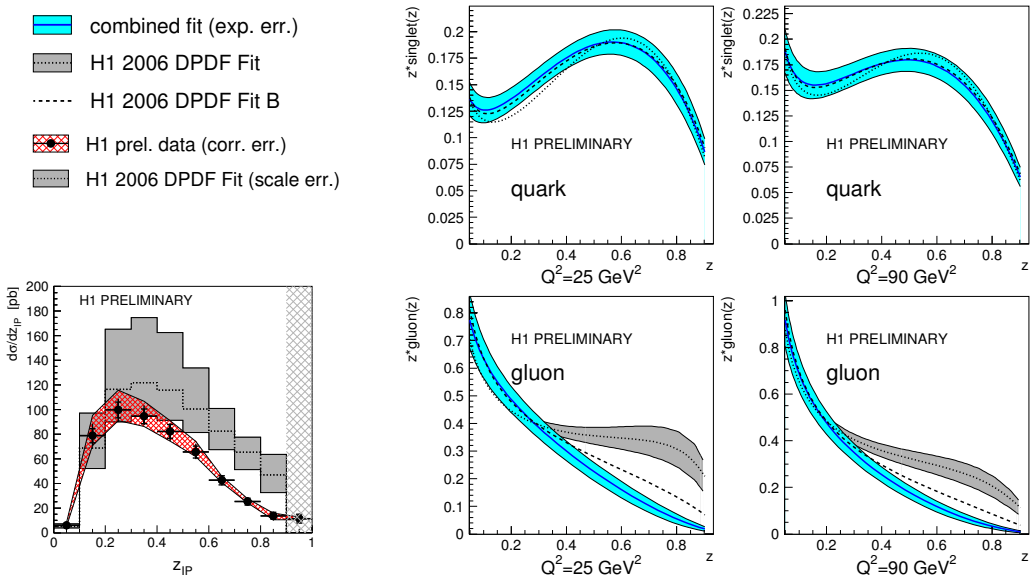

Figure 4: Left: Cross section $d\sigma/dz_{I\!P}$ of diffractive dijets in DIS with hatched band of correlated systematic uncertainties compared to NLO QCD predictions based on H1 2006 dPDFs with grey band indicating the scale uncertainty. Right: NLO QCD fit results for diffractive singlet (top) and gluon (bottom) distributions for two Q^2 scales, plots from [4].

At the workshop preliminary dijet cross sections in diffractive DIS were presented by H1 [4] selecting jets with transverse momenta, $p_{T_1} > 5.5$ GeV and $p_{T_2} > 4.0$ GeV. The data span a broad kinematic range of $4 < Q^2 < 80$ GeV^2, $0.1 < y < 0.7$ and $x_{I\!P} < 0.03$. The data are in good agreement with a similar analysis performed by ZEUS ZEUS [5]. The p_T and $x_{I\!P}$ dependencies are well described by the recently published H1 NLO QCD fits 2006 A and B. However, the $z_{I\!P}$ ($z_{I\!P} = \beta$) dependence, see Fig. 4 left, allows to further constrain the diffractive gluon distribution at $\beta > 0.4$, a region where inclusive diffractive data have little sensitivity and the systematic uncertainties are high. A simultaneous NLO QCD fit of diffractive inclusive and dijet DIS cross sections result in a very good description of both data sets thus supporting QCD factorization. The extracted dPDFs are shown in Fig. 4 right.

The diffractive singlet distribution is basically unchanged. However the diffractive gluon distribution of the combined fit is closer to the H1 2006 fit B but with reduced experimental uncertainty at large $z_{I\!P}$ due to the inclusion of the diffractive dijet data in DIS.

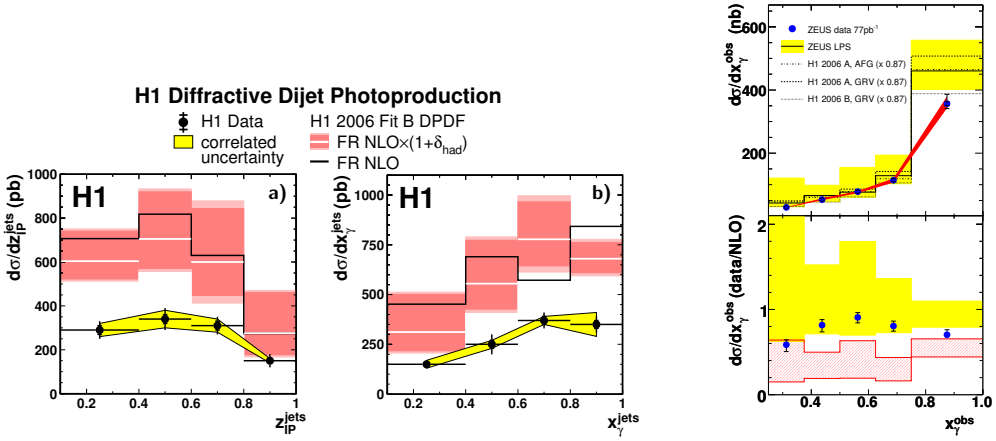

Figure 5: Left: Cross sections $d\sigma/dz_{IP}$ (a) and $d\sigma/dx_\gamma^{obs}$ (b) of diffractive dijets in photoproduction with yellow band of correlated systematic uncertainties. The H1 data are compared to NLO QCD prediction based on H1 2006 dPDFs fit B with a band indicating the scale uncertainty, plots from [4]. Right: ZEUS results on the cross section $d\sigma/dx_\gamma^{obs}$ compared to NLO QCD predictions based on different dPDF inputs, plot from [5].

QCD factorization, broken at Tevatron, can be tested within HERA investigating diffractive dijet photoproduction ($Q^2 \sim 0$), where the hard scale is provided by the E_T of the jets. At LO QCD there are two processes contributing to dijet photoproduction: direct photon reactions proceeding via a point-like photon (photon-gluon fusion) and resolved processes where the photon fluctuates into partons. Further interactions from the partons of the photon and of the proton may fill the rapidity gap via rescattering effects discussed also in chapter 4. In principle, factorization is not expected to hold in photoproduction events. However, the suppression of the diffractive cross section could be different for direct and resolved processes. ZEUS [5] and H1 [4] presented precise HERA I data on diffractive dijet photoproduction, see Figs. 5 left and right, using an integrated luminosity of 77 pb^{-1} and 18 pb^{-1}, respectively. H1 observed a suppression factor of 2 both needed for the direct and the resolved contributions w.r.t. a NLO QCD calculation. ZEUS reported that no suppression is needed to describe the data over the full x_γ^{obs} range and the data are well described by a NLO QCD prediction using the H1 2006 B dPDFs. However it has to be noted that the selection criteria differ, in particular in the minimum transverse momentum required for the highest E_T jet which is 5 GeV for H1 and 7.5 GeV for ZEUS. In addition, the covered $x_{I\!P}$ range is somewhat different with $x_{I\!P} < 0.025$ (0.03) for ZEUS (H1). Following discussions at the workshop, several questions were raised: Do events at lower E_T require larger suppressions w.r.t. NLO QCD and the different suppression factors are due to the different E_T cuts? Are the two different NLO QCD programs used for the predictions in agreement? How is the charm contribution treated in the NLO calculations? These interesting points are under further careful evaluation by the collaborations and theorists.

Recently published measurements of diffractive open charm production in DIS and in photoproduction were reported by H1 [6] and by ZEUS [7] using integrated luminosities of about 48 pb^{-1} and 79 pb^{-1}, respectively. Here, the diffractively produced system X should contain at least one charmed hadron which is usually tagged by the reconstruction of a $D^{*\pm}(2010)$ meson. With this method ZEUS determined the ratio of diffractive to inclusive charm cross section to $5.7^{+0.9}_{-0.7}$% for $x_{I\!P} < 0.035$ in very good agreement with NLO QCD calculations [7]. Using a second analysis technique based on the displacement of tracks from the primary vertex, H1 measured the diffractive cross section of a charm enriched sample in photoproduction. The measurements are found to be in good agreement between the two methods and with ZEUS results and are well described by NLO QCD prediction, see Fig. 6 confirming the validity of QCD factorization for open charm production in diffractive DIS and photoproduction.

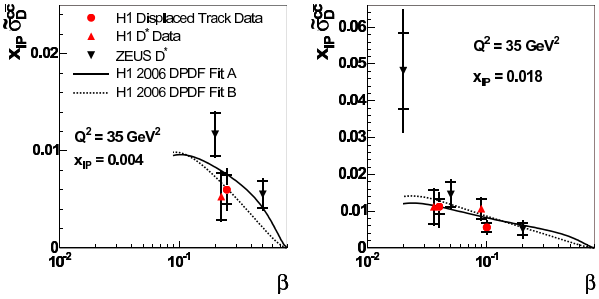

Figure 6: The reduced cross section $x_{I\!P}\tilde{\sigma}^{c\bar{c}}$, integrated over $|t| < 1$ GeV^2, as a function of β for two $x_{I\!P}$ values. The ZEUS and H1 data are compared to recent NLO QCD calculations using H1 2006 dPDFs A and B; plot from [6].

At HERA II, H1 collected with a newly installed Very Forward Proton Spectrometer (VFPS) [8] an integrated luminosity of around 140 pb^{-1} since 2005. The fiber detectors in the Roman pots, located at 218 and 222m downstream from the H1 interaction point, tag and measure diffractively scattered protons with a high acceptance in the range $0.01 < x_{I\!P} < 0.025$. It was reported that the VFPS acceptance is well suited for dijet studies both in DIS and photoproduction regimes and more precise data in extended kinematic ranges are anticipated to be confronted with theory.

3 Exclusive diffraction

The study of hard exclusive reactions, $ep \to eXp$, where the hadronic system X is a vector meson (VM) like $\rho, \omega, J/\Psi, ...$ or a photon (DVCS), provides a very interesting laboratory to test the mechanism of diffraction in dependence of various scales. At HERA, the large accessible range in terms of vector meson masses, of Q^2 and of t allows the investigation of the transition from the soft, non-perturbative regime described within the Regge phenomenology to the hard regime described by perturbative QCD.

ZEUS presented [9] final results on exclusive ρ^0 meson production using an integrated luminosity of 120 pb^{-1} in the kinematic range of $2 < Q^2 < 160$ GeV^2 and $32 < W < 180$ GeV. The $\gamma^* p \to \rho^0 p$ cross section falls steeply with increasing Q^2 but can not be described by a simple propagator term like $\sigma \propto (Q^2 + M^2)^{-n}$, where M is the vector meson mass. The cross section is rising with increasing $\gamma^* p$ c.m. energy, $\sigma \propto W^\delta$. The δ parameter increases with the scale $Q^2 + M^2$ as expected for a transition from a soft to a hard regime. The values of δ obtained for cross sections of exclusive $\rho, \phi, J/\Psi$ as a function of $Q^2 + M^2$ show an universal behaviour, see Fig. 7 left. The t dependence of the cross section can be parametrized via a fit $d\sigma/d|t| \propto e^{-b|t|}$. The exponential slope of the t distribution decreases with increasing $Q^2 + M^2$ and levels off with a value of $b \sim 5$ GeV^{-2} at about 40 GeV^2. A

compilation of the Q^2+M^2 dependence of b parameters shows the same trend for HERA VM and DVCS measurements, see Fig. 7 right. The helicity analysis of the decay-matrix elements of the ρ^0 indicates s-channel helicity breaking. was used to extract the ratio of longitudinal to transverse $\gamma^* p$ cross section as a function of Q^2 and W. The ratio of the cross sections induced by longitudinally and transversely polarized virtual photons is found to increase as a function of Q^2 but is independent of W. This is a somehow surprising observation since it suggests a similar transverse size of the $q\bar{q}$ configurations in the wave functions of γ^*_L and γ^*_T. Finally, an effective Pomeron trajectory was extracted with a larger intercept but smaller slope than those found in soft hadron-hadron interactions. The presented extensive studies of the properties of the ρ^0 meson are qualitatively in agreement with expectations from pQCD. However, none of the models considered could describe all the observed features of the excellent precision data.

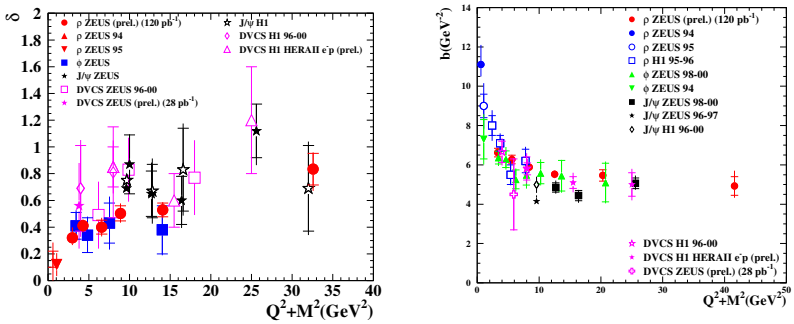

Figure 7: Dependence on the $Q^2 + M^2$ scale of the parameter δ (left) and b (right) for HERA VM and DVCS data; plot from [9].

Deeply Virtual Compton Scattering (DVCS), $\gamma^* p \to \gamma p$, consists of the hard diffractive scattering of a virtual photon off a proton. The interest of the DVCS process resides in its clear experimental signature and in the particular insight it gives to the applicability of pQCD in the field of diffractive interactions and to the nucleon partonic structure as described in terms of GPDs.

A new DVCS measurement was presented [10] based on data taken by the H1 detector during the HERA II period using e^+ and e^- lepton beam data with an integrated luminosity of 145 pb^{-1} each. At the present small values of $|t|$ the reaction $ep \to e\gamma p$ used to extract

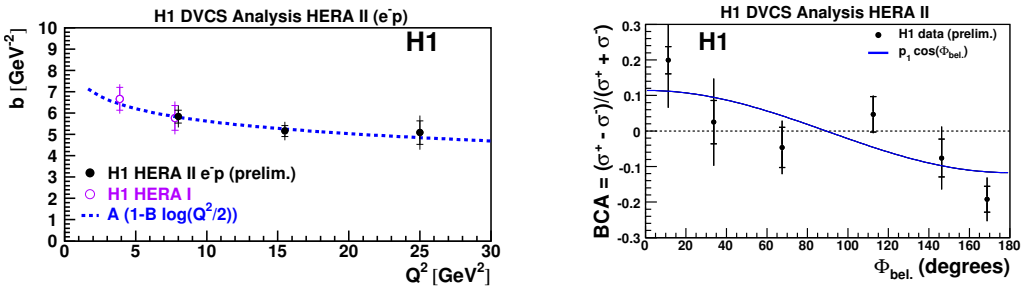

Figure 8: Left: The t slope parameter b as a function of Q^2. Right: Beam charge asymmetry as a function of azimuthal angle ϕ; plots from [10].

the DVCS signal is dominated by the purely electromagnetic Bethe-Heitler (BH) process whose cross section, depending only on QED calculations and proton elastic form factors, is precisely known and therefore can be subtracted. To enhance the ratio of selected DVCS events to BH events the outgoing photon is selected in the forward, or outgoing proton, region with transverse momentum larger than 2 GeV. The $\gamma^* p$ cross sections as a function of Q^2 and W are well described by QCD based calculations, in particular showing a typical Q^2 evolution of GPDs. The t dependence is measured and fitting an exponential dependence, $e^{-b|t|}$, the parameter b is found to depend on Q^2, see Fig. 8 left, and not on W. For the first time, a beam charge asymmetry is observed at an ep collider, as shown in Fig. 8 right, combining the e^+p and e^-p data samples. A significant non zero value is measured, for $|t| > 0.05$ GeV^2, related to the interference of the DVCS and Bethe-Heitler processes.

At RHIC, the Phenix experiment uses hadronic and leptonic decays of Φ mesons as a probe sensitive to media effects induced by an extremely hot and dense matter produced in Au+Au collisions at $\sqrt{s_{NN}} = 200$ GeV [11]. The integrated yields of the Φ meson productions by e^+e^- and K^+K^- decays were found to be consistent with each other and also independent of the centrality of the collision and so far no media modification could be detected within the present uncertainties. Phenix reported [12] also results on multi-particle decay of K^0_S, η, and ω mesons at high p_T in p+p, p+d and Au+Au collisions. No suppression of the meson yields were observed in p+d collisions but a strong suppression of η and ω production in 0-20% most central Au+Au events at the same energy.

4 Leading baryon production at HERA

The production of leading baryons belongs to one of the most interesting semi-inclusive reactions which may be explored with an electromagnetic probe at the HERA collider. While hard interactions are well understood in the QCD improved parton model, predictions for semi-inclusive processes are not so reliable yet. The applicability of pQCD, if at all, is restricted to the range of events with high p_T. The production mechanisms at low p_T is reasonably described by so-called exchange models: in the $\gamma^* p$ reaction the incoming photon is considered as a $q\bar{q}$ state which scatters on a virtual particle emitted from the proton. The outgoing, leading baryon carries a significant fraction of the incoming protons energy, x_L. From this picture it becomes obvious that in such a process long range properties of the baryon could be analyzed: at which length breaks the proton into two colorless objects, a meson and a nucleon which could be a pion and a neutron in the simplest picture for leading neutron production? For nuclear physics this question is interesting for a further understanding of the role of meson exchange forces in nucleon-nucleon interactions. Regarding high energy physics the factorization hypothesis could be tested: can this process be separated into the interaction and an universal target fragmentation, i.e. is it independent of the probe which initiates the fragmentation? There are predictions that this simple factorization picture is only valid for a well separated nucleon-meson system in the target proton at peripheral collisions where the nucleon acts as a spectator. In more central collisions, larger projectiles like a proton or a real photon (a large sized $q\bar{q}$ pair) can destroy the nucleon through rescattering effects and break the factorization.

At HERA around 10% of the inclusive DIS events contain a leading baryon. Now the ZEUS collaboration presented its final, high precision HERA I results on the production of energetic neutrons in ep collisions using a lead-scintillator calorimeter and a scintillator hodoscope as a forward neutron detector [13]. The neutron energy and p_T^2

distributions were measured in a broad kinematic range, $0.2 < x_L < 1$ and $p_T^2 < 0.476 x_L^2$ GeV^2, in a 40 pb^{-1} sample of inclusive DIS data ($\sigma_{\rm inc}$) and a 6 pb^{-1} sample of photoproduction data. The normalized neutron production rate rises due to the increase in p_T^2 space from lowest x_L towards its maximum at around $x_L \sim 0.7$, and falls to zero at $x_L = 1$, but the neutron yield in photoproduction is suppressed relative to DIS for the lower neutron energies, see Fig. 9 left. Screening effects lower the neutron yield mainly at lower neutron energies (lower x_L) depending on the transverse size of the $q\bar{q}$ pair: absorptive corrections are expected to be smaller for highly virtual photons (larger Q^2) due to less rescattering of small size color dipoles on the target fragment neutron. The observed Q^2 dependence of the neutron yields violates the factorization hypothesis. The p_T^2 distributions are steeper for events in photoproduction, i.e. there are fewer neutrons at higher p_T. The (x_L, p_T^2) distribution of the normalized neutron yields can be fully parametrized by an exponential fit with a slope parameter $b(x_L)$ and an intercept $a(x_L)$. The b slopes for photoproduction are larger for the range $0.6 < x_L < 0.9$, see Fig. 9b, indicating the breakdown of vertex factorization. As shown in Fig. 9a, the precision of the data allows to distinguish between the various models: pure one-pion exchange with neutron absorption predicts too large b values, but the addition of subleading (ρ, a_2) Reggeons gives a fair description of both parameters. The model also accounts for migration of neutrons in (x_L, p_T^2) after rescattering and estimates the loss of neutrons through absorption to about 50%.

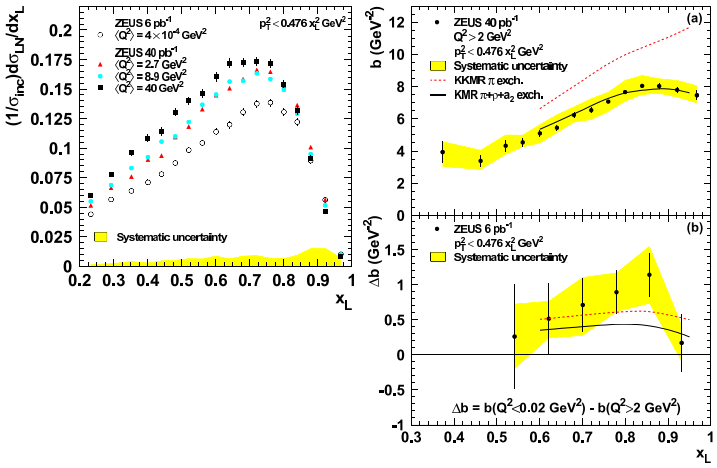

Figure 9: Left: Normalized leading neutron production rate versus x_L for three DIS samples and for photoproduction. Systematics common to all samples is shown as a shaded band. Right: (a) Slopes b from an exponential fit to the p_T^2 distribution for DIS and (b) difference of photoproduction and DIS b slopes. The shaded band shows the systematic uncertainty. The dashed curves come from a prediction based on pion exchange with enhanced neutron absorption and migration, the solid curves include also ρ and a_2 exchanges in the calculation; plot from [13].

None of the Monte Carlo models commonly used for simulating DIS and photoproduction events describe the leading neutron data. Adding to the implemented standard proton fragmentation also diffraction and pion exchanges gives a good description of the shapes of the slopes, although with too large absolute values.

The present data can be used to further constrain exchange models and thus to improve the calculations of diffractive productions at the LHC.

5 Diffraction in hadronic collisions

New diffraction results obtained in proton-antiproton collisions at the Fermilab Tevatron collider at c.m.s. energy of $\sqrt{s} = 1.96$ TeV (Run II) confirm and extend important observations made at lower c.m.s. energies of 0.63 TeV and 1.8 TeV (Run I). For the diffractive program at Run II, the CDF collaboration instrumented the detector with special forward components [14] : a Roman Pot spectrometer (RPS) to detect leading antiprotons (improved acceptance for small $|t|$ in comparison to Run Ic), Mini Plug calorimeters to cover the region of about $3.5 < |\eta| < 5.2$, and beam shower counters positioned along the p and $\bar{p}$ beam directions to tag gaps within $5.5 < |\eta| < 7.5$.

In hard single diffraction, CDF obtained preliminary Run II results for the Bjorken-x and Q^2 dependence of the diffractive structure function from the ratio of two dijet samples: single diffractive (SD) dijets triggered by an intact antiproton in the RPS and non-diffractive (ND) dijet events. This ratio is in LO QCD approximately equivalent to the ratio of the corresponding structure functions. The diffractive structure function versus Bjorken-x, the momentum fraction of a parton in the antiproton, confirms the factorization breakdown by about factor of 10. In Run II, higher E_T^{jet} energies up to 100 GeV could be recoreded thus allowing decent tests of the Q^2 dependence, where Q^2 is here given by the value of $< E_T^* >^2$. In the range of $100 < Q^2 < 10000$ GeV^2, no significant dependence on the Q^2 scale could be observed for the SD/ND dijet ratio, although in this range the inclusive E_T distribution falls by a factor of 10000. This result suggests that the Q^2 evolution of diffractive and non-diffractive interactions is similar. The t dependence of the diffractive cross section was explored by a double exponential fit, no diffraction dips were observed for the range $|t| < 1$ GeV^2 and no strong Q^2 dependence of the slope parameter $b(Q^2)|_{t=0}$.

With the advent of the luminosity upgrade of Tevatron, the diffraction program of CDF could be extended to the study of central exclusive production in $p\bar{p}$ collisions. This process is not only of interest for testing QCD inspired models of hard diffraction but also due to its discovery potential. Exclusive Higgs production, $p + p \rightarrow p + H + p$, is expected to provide clean events with suppressed QCD background and a precise measurement of the Higgs mass based on the momentum measurements of the two outgoing protons. However, those advantages are hampered by the low production rates predicted. The rate calculations suffer from considerable model dependencies due to the unknown non-perturbative suppression factors. While exclusive Higgs boson production is not in the reach at Tevatron energies, exclusive dijet production, $\bar{p} + p \rightarrow \bar{p} + Jet + Jet + p$, could be considered as a rather high rate process which proceeds through

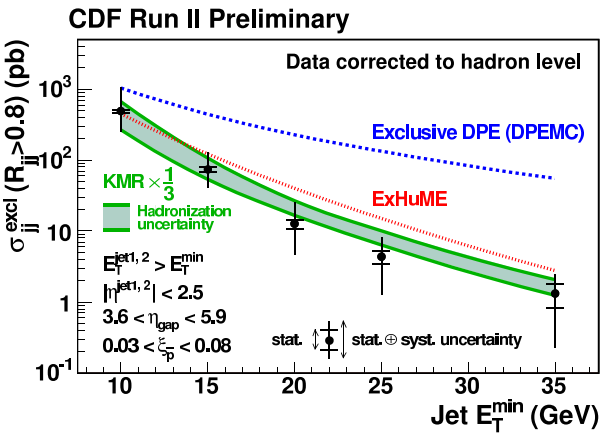

Figure 10: Exclusive dijet cross section measured from data as a function of minimum second jet E_T. The dotted (dashed) lines show the ExHuMe (exclusive DPE in DPEMC) Monte Carlo predictions.

the same mechanism and could allow the determination of the suppression factor experimentally.

CDF presented first results on central exclusive dijet cross sections, see Fig. 10, produced in Double Pomeron Exchange (DPE) based on a data sample of about 310 pb^{-1} collected with a dedicated diffractive trigger in Run II [14]. Exclusive dijet searches use a measurement of the dijet mass fraction, R_{jj}, defined as the ratio of the mass of the two leading jets in an event, M_{jj}, to the total mass, M_X. Exclusively produced dijet events could be observed as a significant excess of data at large R_{jj} by comparing the Rjj distribution shapes between the data and inclusive DPE dijet Monte Carlo predictions. Also shown in Fig. 10 is a LO calculation for exclusive Higgs boson production at the LHC downscaled by factor of three. The agreement between calculation and data is encouraging keeping in mind experimental and theoretical uncertainties.

Like exclusive dijet production, exclusive $\gamma\gamma$ production could be used for calibrating diffractive Higgs boson production models. Based on three events, CDF reported for the first time a 95% C.L. upper limit of 410 fb on the cross section, $\bar{p}+p \to \bar{p}+\gamma+\gamma+p$, [14]. The robustness of the exclusive event selection was checked by a measurement of the purely QED process, $\bar{p}+p \to \bar{p}+e^+e^-+p$, which was found to be in good agreement with the expectation.

At the workshop comprehensive reports on the forward and very forward physics projects and the status of the relevant detectors for the LHC experiments CMS [15] and ATLAS [16] were presented. Within both collaborations the installation of Roman Pot stations at 420 m, as investigated by the FP420 R&D Collaboration [17], is under discussion. New studies were presented [18] showing that additional roman pot stations at 220 m nicely complement the FP420 project. Combined 220m/420m detectors could achieve acceptances of at least 30% for a large missing mass range of 100 until 800 GeV which is important for a discovery of the Higgs boson in exclusive reactions. Lively discussed were questions regarding the trigger, the technology for the pots, the position and the timing detectors, e.g. requirements of 5 to 10 ps resolutions are discussed for a fast timing needed to reject background from pile-up events.

6 New theoretical developments

The standard QCD description of the inclusive hard diffraction is based on the Operator Product Expansion and DGLAP evolution of collinear diffractive parton densities. Limits of validity of this framework were investigated [19] when the proton mass M_P and momentum transfer t cannot be neglected. The twist 2 contributions to the structure functions were studied. In the limit of $M_P \to 0$ and $t \to 0$ the expected results were found: there exist two structure functions in the unpolarized case connected at leading order by a modified Callan-Gross relation. In the polarized case, four structure functions appear, that are connected by an all order Wilczek-Wandzura relation. All these structure functions may be expressed in terms of diffractive parton densities. This picture changes at low Q^2 and the large β where it is necessary to extend the analysis beyond the $M_P \to 0$ and $t \to 0$ limit. Then, the number of structure functions grows to four (eight) in the unpolarized (polarized) scattering case. Moreover, the connection of those structure functions to the diffractive parton densities is lost.

The region of low Q^2 and large β is interesting also because large higher twist corrections to the dDIS cross section should appear there. One of the reasons is, that the twist 2 contri-

butions vanish as $\beta \to 1$, while it is not the case for twist 4. In particular, the contribution to the diffractive cross section coming from longitudinally polarized virtual photons is known to be important at large β. This contribution may be evaluated perturbatively within the k_T-factorization framework. Thus, it was proposed to fit the dDIS data within a modified DGLAP approach, in which the twist 4 contribution is subtracted from the data [20, 21]. The modified fits give values of χ^2 only slightly worse than the conventional twist 2 DGLAP fit. The diffractive quark densities emerging from the modified fit are slightly lower w.r.t. the twist 2 case while the gluon density is enhanced at large β, and the effect is particularly pronounced at lower Q^2. It turns out, that inclusion of the twist 4 contribution increases dramatically the predictions for F_L^D at $\beta > 0.5$ and typical values of Q^2. Thus, it should be very interesting to measure F_L^D at large β.

The diffractive scattering may be viewed as a manifestation of unitarity corrections to a single (cut) Pomeron exchange contribution to the total cross-section. In addition, in contrast to the inclusive DIS the diffractive deep inelastic scattering amplitude is dominated by hadronic fluctuation of large sizes, even though the photon virtuality is large. Thus, the dDIS is intimately connected to the effects of parton saturation and it probes unitarity corrections to the QCD evolution of parton densities. This connection was exploited in the very successful saturation model, proposed by Golec-Biernat and Wüsthoff (GBW). Since then the simple saturation model was extended to incorporate effects of QCD evolution and of the proton shape; it was also used to describe a broader spectrum of observables. In particular, it was shown that saturation models provide a rather good description of exclusive diffractive processes: exclusive vector meson photo- and electroproduction and DVCS at small x, including the t-dependence [22, 23].

This complementary approach to the hard diffraction is based on the k_T-factorization. The theoretical framework is rooted in the Balitsky-Fadin-Kuraev-Lipatov formalism for rapidity evolution of high energy scattering amplitudes into which some unitarity corrections are incorporated (e.g. multiple scattering or gluon recombination). In this approach the issues of unitarity corrections and diffractive scattering at high energies may be conveniently addressed in the transverse position space. Along this line an interesting generalization of the GBW approach to the hard diffraction was developed [24]. The hadronic multi-parton state that scatters diffractively was constructed using Mueller's color dipole model of BFKL dynamics. In the large N_c limit the hadronic state may be decomposed into color dipoles. The coherent ensemble of QCD dipoles scatters multiply and the scattering amplitude obeys unitarity constraints. Thus, the projectile evolution and the scattering process are factorized at the rapidity corresponding to the rapidity gap size. The multi-dipole scattering amplitudes should follow from small-x evolution equations obtained within the so called Color Glass Condensate (CGC) framework. The main merit of this approach is a possibility to incorporate an arbitrary number of (soft) gluons in the scattering state. Unfortunately, exact solutions to the CGC evolution equations at full accuracy (that is including the Pomeron loops) are not yet known. Thus these amplitudes still have to be modeled. The problem of diffractive scattering beyond the large N_c limit was addressed in terms of the JIMWLK evolution equation [25]. The structure of this equation is similar to the Balitsky-Kovchegov (BK) equation, that is the Pomeron loops are not well represented. In contrast to the BK equation, however, the JIMWLK evolution may generate multi-gap diffractive final states. It turns out that the difference originates from subleading effects in the $1/N_c$ expansion which lead to color reconnection and formation of additional rapidity gaps.

Recently, new extensions of saturation models to exclusive processes were put forward. A new model of the color dipole scattering amplitude was constructed, based on an analysis of the non-forward BK equation in full momentum space [23]. An interesting feature of this model is the presence of a saturation scale that depends on the momentum transfer and not on the transverse position. The model provides a very good description of the light vector meson data at small x. Another approach is based on the Glauber-Mueller formula assuming multiple independent scatterings [22]. The model is constructed using spatial coordinates: the dipole size r and transverse position b. The LO DGLAP effects of the gluon evolution are incorporated and the b-dependence of the single scattering amplitude $T\Omega(r,b)$ is assumed to take a factorized form: $\Omega(r,b) \sim xg(x,\mu_0^2 + C/r^2)\, S(b)$, where μ_0 provides a freeze-down scale for the DGLAP evolution, and $S(b)$ describes the proton shape. Within this model a reasonably good unified description of the inclusive observables (including shadowing effects in DIS on nuclei) and most of exclusive diffractive observables was obtained. It was found that a Gaussian proton shape $S(b) \sim \exp(-b^2/R^2)$ is strongly preferred to a box-like shape $S(b) \sim \Theta(R-b)$. The radius of the gluon distribution in the proton was determined to be $R = 0.69$ fm, a value smaller than the electromagnetic Hofstadter proton radius $R_H = 0.870 \pm 0.008$ fm. Saturation effects were found to be moderate, at HERA: for $x > 10^{-4}$ one obtains $Q_s^2(b) < 1$ GeV^2 for $b = 0$ fm and $Q_s^2(b) < 0.4$ GeV^2 for $b = 0.4$ fm. Another version of the saturation model was successfully applied also for heavy quark production at HERA [26]. The flavored structure functions F_2^c and F_2^b were described together with F_2 and $F_2^{D(3)}$ within a saturation model with DGLAP evolution, but without the impact parameter dependence. The best fit to F_2 with $\chi^2/\text{d.o.f.} = 1.16$ is significantly improved with respect to the GBW fit without QCD evolution. The best fit required, however, a surprisingly large freeze-down scale $\mu_0^2 = 1.6$ GeV^2. It is interesting to note that the fits based on the saturation model with the QCD evolution and heavy flavors imply an almost flat x dependence of the gluon density $xg(x,\mu_0^2)$ at the low scale.

An important feature of the GBW saturation model is the geometric scaling property: the total $\gamma^*(Q^2)p$ cross section depends only on one variable $\xi = Q^2/Q_s^2(x)$ where $\log Q_s(x) \sim \log(1/x)$. The geometric scaling was actually found in the HERA data and, interestingly enough, it is also a universal property of the solutions of the Balitsky-Kovchegov equation at large rapidities. In fact, the geometric scaling emerges in a wider class of non-linear evolution equations incorporating phenomena of growth and saturation. Inclusion of the QCD running coupling into the BK equation leads to a modified form of geometric scaling, $\log Q_s(x) \sim \sqrt{\log(1/x)}$. It was verified [27] that: (i) the asymptotic solution to the BK equation with the running coupling and non-leading BFKL kernel, is universal and does not depend on details of the treatment of the non-leading QCD effects beyond the running of α_s, and (ii) the HERA F_2 data agree well with the modified geometric scaling. It should be remembered, however, that the HERA data probe the gluon density evolution in a rather limited range of rapidities. In this range, some violations of geometric scaling should be still visible due to pre-asymptotic effects. It was also pointed out that some models used in the literature, of the dipole cross section that incorporate geometric scaling violations differ significantly from solutions to the BK equation [28].

In most of the applications of the color dipole model developed so far one assumes that the dipole cross section $\sigma_d(x,r)$ depends only on the x variable and the dipole size r. This assumption is not obvious at all — it was argued [29, 30] that an alternative choice of $\sigma_d(W^2,r)$ which depends on r and on the photon-proton collision energy, W, could be more

natural. The choice of W as the relevant variable imposes strong constraints on the ratio of DIS cross sections with longitudinal and transverse photons $R = \sigma_L/\sigma_T < 0.37$ [30]. It was noticed [29], however, that this bound is completely removed if one improves the treatment of the photon wave function by limiting the allowed invariant masses of the $q\bar{q}$ fluctuations of the virtual photon.

Exclusive vector meson production data provide a lot of insight into proton structure and QCD dynamics. For instance, J/ψ photo- and electroproduction is a direct and sensitive probe of the gluon density. It was proposed to use the data for the exclusive photoproduction of J/ψ at HERA to constrain the gluon density beyond the leading logarithmic approximation [31]. The dependence of the hard matrix element to the gluon momentum was taken into account within the k_T factorization framework, and the unintegrated gluon density was obtained from the collinear gluon density using the Kimber-Martin-Ryskin prescription. This construction aims at accounting important non-leading corrections to the collinear LO formula, that are predominantly of kinematic origin. The gluon densities that emerge from the fit are flatter functions of gluon x than the LO MRST and CTEQ parameterizations, getting close to the NLO and NNLO gluon densities. A good description of the light vector meson electroproduction data that range from the fixed target kinematics down to small x was obtained [32] within a collinear factorization approach with GPDs at the LL accuracy. It was necessary, however, to use a model of the meson wave function which incorporates the quark transverse momentum — with the leading twist distribution amplitude the data are badly underestimated. This result is interpreted as a manifestation of large power corrections to the exclusive ρ^0 production amplitude.

Meson impact factors at NLO accuracy that were calculated in recent years are now used in estimates of the NLO effects in meson production amplitudes. A detailed analysis of the NLO effects in the longitudinally polarized ρ^0 meson photoproduction was performed [33]. It follows from this analysis that the perturbative expansion is rather stable at large and moderate Bjorken x, corresponding to the kinematics of fixed target experiments. At small x, however, the NLO corrections are enhanced by $\log(1/x)$, and they are comparable to the leading amplitudes, even at pretty large values of the photon virtuality Q^2. For instance, at $x = 2 \cdot 10^{-3}$ ($x = 2 \cdot 10^{-4}$) the NLO correction is still dangerously large at $Q^2 = 16$ GeV^2 (at $Q^2 = 49$ GeV^2). This questions both the reliability of the LL calculations and the stability of the fixed order perturbative calculations in the small x domain and at moderate Q^2.

The generalized parton densities of the nucleon emerge partially from non-perturbative QCD dynamics. Thus, within perturbative QCD it necessary to determine them from fits to experimental data. An interesting attempt was made [34] to improve this situation and to use QCD simulations on the lattice to constrain the nucleon GPDs the flavor non-singlet sector. As a result new parameterizations of those GPDs were obtained in which the model dependence is expected to be reduced w.r.t. the conventional parameterizations.

An excellent probe of the BFKL effects is given by an exclusive production of two vector mesons in two virtual photon collisions. Such measurements should be possible at future e^+e^- colliders. The process of $\gamma^*\gamma^* \to \rho^0_L\rho^0_L$ in the high energy limit was studied [35] in the framework of the NLL BFKL, including the impact factors at the NLL accuracy. The sensitivity of the amplitude to the scheme choice, the factorization scale and the energy scale was systematically analyzed. The NLL predictions are found to be stable against variations of the scheme and of the scales. A rather surprising result was obtained that the NLL BFKL cross section at moderate energies is much lower than its lower order approximation of a two-gluon exchange. A complementary study of the double ρ^0 meson production in two

photon collisions was carried out for moderate collision energies, where a quark exchange dominates over the BFKL amplitude. An interesting pattern of QCD factorization(s) was found there [36]. Namely, the QCD factorization of the amplitude for $\gamma^*(Q_1^2)\gamma^*(Q_2^2) \to \rho_L^0\rho_L^0$ at a moderate c.m.s. energy squared W^2 may be performed using usual *Brodsky-Lepage distribution amplitudes*. For $\gamma_T^*(Q_1^2)\gamma_T^*(Q_2^2) \to \rho_L^0\rho_L^0$ at $W^2 \ll Q_i^2$ the factorization into the hard matrix element and a *generalized distribution amplitude* works. Finally, when the photon virtualities are strongly ordered, $Q_1^2 \gg Q_2^2$ a hard factorization is possible with a suitable *transition distribution amplitude*. Thus, in the exclusive double ρ^0 photoproduction (with virtual photons) one may probe in detail various features of QCD dynamics and the meson structure.

Exclusive C-even meson photoproduction is driven by the C-odd gluonic exchange i.e. the QCD Odderon instead of the Pomeron, Therefore, an exclusive π^0 photoproduction off the proton was expected to be a sensitive probe of the Odderon. In the measurement performed at HERA, however, no signal was found: the upper limit for the exclusive cross section was found to be 49 nb, much below theory expectations of about 300 nb. It was suggested that this puzzling discrepancy may be removed when the theoretical estimates properly take into account the chiral symmetry of QCD [37]. In the preceding theoretical estimate of the cross section the constraints imposed by the chiral symmetry were neglected and the cross section was overestimated.

Shortly before the LHC is going to start, hard exclusive diffractive processes in pp collisions receive a lot of attention. The highlight here are possible studies of the Higgs boson in the exclusive channel, using forward proton detectors e.g. in the FP420. The main merit of the exclusive Higgs boson production process is a strong background suppression and potential precision of the measurements of the Higgs boson properties, including the quantum numbers, the mass and the width. On the other hand, the price to be paid is a reduction of the signal by four orders of magnitude with respect to the inclusive case. Nevertheless, there are chances that the signal is visible, especially if a supersymmetric scenario with large $\tan\beta$ is realized.

From the theory side, the QCD approach elaborated by the Durham group (the KMR model) remains the reference calculational framework. It is assumed that the exclusive diffractive amplitude may be factorized into a hard production amplitude calculable in perturbative QCD, and soft rescattering of spectator partons. The soft part represented by a gap survival factor, S^2, is estimated from models of the unitary S matrix fitted to data on pp / $p\bar{p}$ scattering. An independent theoretical analysis of this framework foundations confirmed its validity [38]. It was argued that independence of the hard production and the soft rescattering follows from essential difference in space-time scales characteristic for these subprocesses. Also, the obtained value of $\hat{S}^2$ agreed well with the value determined by the Durham group. A still open problem remains, however, of the relevance of hard rescattering corrections both of the spectators and within the hard Higgs boson production amplitude. It is therefore encouraging that the data from Tevatron on exclusive diphoton and dijet production are reasonably well described within the KMR model [14]. An analysis using a Monte-Carlo code DPEMC clearly shows that a model of hard exclusive production based on a non-perturbative approach (originally proposed by Białas and Landshoff for diffractive Higgs boson production) is not able to describe the invariant mass dependence of the exclusive dijet production [21], see Fig. 10. Another model for diffractive scattering, the Soft Color Interaction model (SCI), is based on random color reconnections between the hard partons in the final state. The model has been also implemented in the DPEMC. The

exclusive jet production cross section from SCI was shown to underestimate the Tevatron data.

A key problem in the Higgs boson searches in the exclusive production process at the LHC is a good background control. The $b\bar{b}$ decay channel favored for low Higgs boson masses $M_H < 130$ GeV has an irreducible background from central exclusive production of $b\bar{b}$ dijets. In addition, a reducible background comes from multiple events in a single bunch crossing — the overlap events. Detailed simulations based on Monte-Carlo implementations of diffractive physics, ExHuME, POMWIG and HERWIG+JIMMY, showed that it should be possible to perform a significant (3–4 σ) measurement of the exclusive Higgs boson events provided that a supersymmetric scenario with large $\tan\beta$ is realized [17]. A precise time-of-flight analysis is necessary to suppress the background from overlap events. For instance, with suitably tuned cuts on the dijet kinematics and the underlying event, the supersymmetric Higgs boson with $\tan\beta = 40$ and $M_H = 119.5$ GeV can be measured in the exclusive channel with the cross-section (after cuts) of about 0.5 fb with a signal to background ratio of about one. The reducible background from overlap events is negligible in a low luminosity mode $\mathcal{L} \simeq 10^{33}\ \mathrm{cm}^{-2}\,\mathrm{s}^{-1}$ but it is as large as the signal at high luminosities. As a result the significance of the exclusive Higgs boson measurement does not grow with the LHC luminosity beyond $\mathcal{L} \simeq 2 \times 10^{33}\ \mathrm{cm}^{-2}\,\mathrm{s}^{-1}$.

Acknowledgments

We would like to thank warmly all session participants and contributors for making the session lively and interesting. We are grateful to the organizers for hospitality and assistance. We thank our co-covenors Rolf Ent and Laurent Favart for organizing the session, and Laurent Favart for his help in preparing the write-up.

References

[1] Slides: http://indico.cern.ch/contributionDisplay.py?contribId=15&sessionId=2&confId=9499
[2] J. Lukasik, these Proceedings.
[3] B. Löhr, these Proceedings.
[4] M. Mozer, these Proceedings.
[5] Y. Yamazaki, these Proceedings.
[6] P. Thompson, these Proceedings.
[7] I. Melzer-Pellmann, these Proceedings.
[8] L. Favart, these Proceedings.
[9] A. Levy, these Proceedings.
[10] L. Schoeffel, these Proceedings.
[11] S. Huang, these Proceedings.
[12] A. Milov, these Proceedings.
[13] W. Schmidke, these Proceedings.
[14] C. Mesropian, these Proceedings.
[15] K. Borras, these Proceedings.
[16] S. Ask, these Proceedings.
[17] A. Pilkington, these Proceedings.
[18] C. Royon, these Proceedings.
[19] J. Blümlein, B. Geyer and D. Robaschik, these Proceedings; Nucl. Phys. B **755** (2006) 112.
[20] K. Golec-Biernat and A. Łuszczak, arXiv:hep-ph/0704.1608.

[21] O. Kepka and C. Royon, these Proceedings; C. Royon et. al., arXiv:hep-ph/0609291.
[22] H. Kowalski, these Proceedings; H. Kowalski, L. Motyka and G. Watt, Phys. Rev. D **74** (2006) 074016.
[23] R. Peschanski, C. Marquet and G. Soyez, these Proceedings; arXiv:hep-ph/0702171.
[24] C. Marquet, these Proceedings; Y. Hatta et. al., Nucl. Phys. A **773** (2006) 95.
[25] M. Lublinsky, these Proceedings; A. Kovner, M. Lublinsky and H. Weigert, Phys. Rev. D **74** (2006) 114023.
[26] S. Sapeta, these Proceedings; K. Golec-Biernat and S. Sapeta, Phys. Rev. D **74** (2006) 054032.
[27] G. Beuf, R. Peschanski and S. Sapeta, these Proceedings; G. Beuf and R. Peschanski, Phys. Rev. D **75** (2007) 114001.
[28] D. Boer, A. Utermann and E. Wessels, these Proceedings; Phys. Rev. D **75** (2007) 094022.
[29] D. Schildknecht, these Proceedings.
[30] C. Ewerz and O. Nachtmann, Phys. Lett. B **648** (2007) 279.
[31] T. Teubner, these Proceedings.
[32] P. Kroll, these Proceedings; S. V. Goloskokov and P. Kroll, Eur. Phys. J. C **50** (2007) 829.
[33] M. Diehl and W. Kugler, these Proceedings; arXiv:0708.1121 [hep-ph].
[34] S. Liuti, these Proceedings; S. Ahmad et. al., arXiv:0708.0268 [hep-ph].
[35] D. Ivanov, A. Papa, these Proceedings; Eur. Phys. J. C **49** (2007) 947.
[36] M. Segond, these Proceedings; B. Pire et. al., Phys. Lett. B **639** (2006) 642.
[37] C. Ewerz and O. Nachtmann, these Proceedings; Eur. Phys. J. C **49** (2007) 685.
[38] C. Weiss, these Proceedings; L. Frankfurt et. al., Phys. Rev. D **75** (2007) 054009.

Summary of the Electroweak and Beyond the Standard Model Working Group

J. Ferrando[1], T. Nunnemann[2], M. Spira[3], M. Wessels[4]

1- Department of Physics, University of Oxford
Keble Road, Oxford, OX1 3RH, UK.

2- Department für Physik, Ludwig-Maximillians Universität München
Am Coulomwall 1, D-85748 Garching, Germany.

3- Paul Scherrer Institut
CH-5232 Villigen, Switzerland.

4- Deutsches Elektronen-Synchrotron DESY
Notkestr. 85, D-22607 Hamburg, Germany.

We present an overview of the Electroweak and Beyond the Standard Model Physics working group at the DIS2007 conference.

1 Introduction

For more than a century, high energy collisions of particles have been the golden method of investigating the ultimate structure of matter. Along with precision studies of heavy meson decays, primarily at lower energy colliders, these experiments have led to consolidation of the Standard Model (SM) as the theory of particle physics at energy scales up to $\mathcal{O}(10^2)$ GeV. Recent results from high energy colliders HERA and the TeVatron, complemented by the extraordinary precision measurements from the b-factories, display no significant deviations from SM predictions.

2 The status of the Standard Model

2.1 Electroweak physics

2.1.1 Weak boson measurements at the TeVatron

The mass of the W boson is an important parameter of the Standard Model. Precise knowledge of the W mass in combination with knowledge of the top quark mass results in a significant constraint on the mass of the Higgs boson. CDF have recently performed a new measurement of the W mass using Run II data [2]. The W mass is measured in the $W \to e\nu$ and $W \to \mu\nu$ decay channels by performing a binned maximum-likelihood fit to various kinematic distributions: lepton and neutrino p_T and transverse mass (M_T). The fit regions used are $65 < M_T < 90$ GeV and $p_T > 32$ GeV, $\not\!\!E_T < 48$ GeV. The combination of all six fits gives $M_W = 80413 \pm 34$ (stat) ± 34 (syst) MeV.

The width of the W boson has also been extracted by modelling the transverse mass distribution over the range 50-200 GeV. The data in the region 50-90 GeV is used for normalisation. A fit for the width in the high transverse mass region 90-200 GeV is then performed. This tail region, separated from the bulk of the resolution effects that determine the shape of the transverse mass distribution close to M_W, is sensitive to the width of the Breit-Wigner line-shape. The final measurement is $\Gamma_W = 2032 \pm 71$ MeV.

Both of these measurements are the most precise single direct determinations of their kind, the M_W measurement is compared to other measurements in Fig. 1.

The M_W and Γ_W results were obtained using approx 200 pb^{-1} and 350 pb^{-1} data. With over 2 fb^{-1} data already delivered in Run II, prospects for improvement are good. The additional data are likely to yield not only an improvement of the statistical errors but also smaller systematic uncertainty due to the possibility of improving the precision to which, for example, the momentum scale is determined.

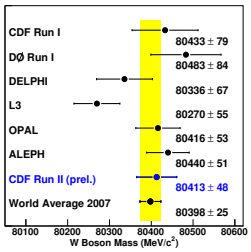

Figure 1: Summary of measurements of M_W including the current world average.

Diboson production measurements at the TeVatron also provide fertile ground for electroweak (EW) studies. The diboson cross-sections are sensitive to triple and quartic electroweak gauge-boson vertices predicted by the non-Abelian structure of the EW theory. Hence measurements of diboson production at the TeVatron are an important test of this part of the SM and provide a sensitive probe to any low energy remnants of new physics at a higher scale. Various limits had been set on such processes in Run I, new studies of WW, WZ, $W\gamma$, $Z\gamma$ and ZZ production have been performed by the CDF and D0 collaborations using Run II data [3].

The D0 collaboration has reported evidence for associated WZ production, whilst the CDF collaboration were able to declare the first observation (at the 5.9 σ level) for the process. The CDF observation comes from 1.1 fb^{-1} of Run II data, 16 data candidates are observed compared to an expected background of 2.7 ± 0.28 (stat) ± 0.33 (syst) ± 0.09 (lumi) events. The measured cross-section agrees well with the SM theoretical prediction.

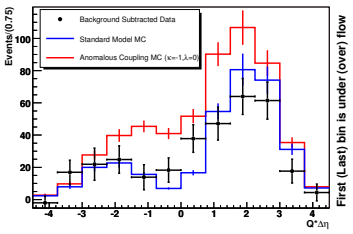

Figure 2: Comparison of the SM distribution and an anomalous $WW\gamma$ coupling distribution to the background subtracted charge-sign rapidity difference in the D0 $W\gamma$ analysis.

Both D0 and CDF have performed measurements of $W\gamma$ production using samples of approximately 1 fb^{-1}. CDF only use the $W \to \mu\nu$ decay channel whilst D0 also use the $W \to e\nu$ decay channel. In both cases the production cross-section shows good agreement with the SM predictions. In addition (see Figure 2) D0 see the first hint of the "amplitude zero" effect [4], where interference among tree-level diagrams creates zero amplitude in the centre-of-mass distribution of the angle between the W and the incoming quarks. Anomalous $WW\gamma$ couplings would wash out this zero amplitude.

Measurements of the $Z\gamma$ production cross-section have been performed by both CDF and D0 using 1 fb^{-1} of Run II data . Good agreement with the SM predictions is observed. D0 also sets the worlds tightest limits on anomalous $ZZ\gamma$ and $ZZ\gamma$ couplings which would arise in the case of some new physics scenarios.

The CDF collaboration has reported the first evidence for ZZ production from a search performed on 1.5 fb^{-1} of Run II data. The search was performed using a combination of the four charged-lepton and two charged-lepton two neutrino final states. A 3.0 σ signal was extracted from a likelihood ratio fit. The measured cross-section $\sigma(p\bar{p} \to ZZ) = 0.75^{+0.71}_{-0.54}$ pb is consistent with the NLO calculation of the SM expectation.

2.1.2 *Electroweak measurements at HERA*

The ZEUS collaboration has performed a measurement of Neutral Current (NC) *ep* Deep Inelastic Scattering (DIS) at HERA using polarised electron beams [5]. Figure 3 shows the asymmetry parameter $A^{\pm} \propto a_e v_q$ where a_e is the axial vector coupling to the electron and v_q the vector coupling to the quark for this $e^- p$ data and previously published [6] ZEUS $e^+ p$ data. The results are in good agreement with the SM and the asymmetry between the cross-section in left- and right-handed polarisations clearly shows the effect of parity violation as expected in the SM. In addition an H1-ZEUS working group has been set up to combine ZEUS and H1 data to produce the best possible precision HERA measurements of structure functions and electroweak parameters.

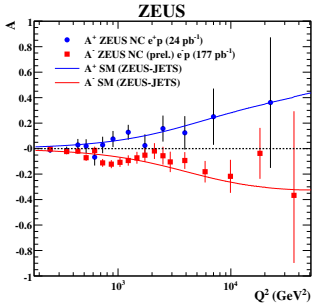

Figure 3: Measurement of the polarisation asymmetries $A^{\pm}$ by the ZEUS collaboration.

The H1 experiment, exploiting polarised electron and positron beams, performed a combined QCD and electroweak fit to their NC and Charged Current (CC) DIS data from the 1994-2005 running period [7]. This fit makes it possible to extract the electroweak NC vector (v_u, v_d) and axial vector (a_u, a_d) couplings of the Z boson to the light quarks. Figure 4 shows the H1 constraints in the a_u-v_u plane. Results are in agreement with SM expectations and generally more precise than existing TeVatron constraints. Ambiguities from LEP constraints on the signs of the couplings are resolved.

2.2 Top quark physics

Until recently little was known about the top quark, what information we had came from statistically limited direct measurements at the TeVatron (Run I data) and indirect constraints from low energy data. Tops will be copiously produced at the LHC, but currently the only running accelerator with access to real top production is the TeVatron. With an order of magnitude more luminosity available in Run II than in Run I, it is now possible to perform top measurements that are no longer statistically limited. Many new measurements of top quark production and properties have recently been made [8, 9, 10].

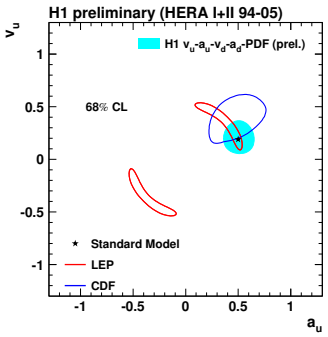

Figure 4: Results of the H1 combined QCD and Electroweak fit in the a_u-v_u plane.

2.2.1 *Top production cross-section at the TeVatron*

At TeVatron top quarks are mainly produced in pairs via the strong interaction, approximately 85% of the production cross-section arises from $q\bar{q}$ annihilation whilst the remaining 15% comes from gluon-gluon fusion. Theoretical calculations [11, 12] yield a total pair-production cross-section at TeVatron of order 7pb. Higher cross-sections could be observed in the case of resonance or other non-SM production. The most recent measurements of the total pair production cross-section from CDF and D0 have made use of different $t\bar{t}$ decay channels in order to obtain independent results.

The CDF collaboration has performed a measurement of the $t\bar{t}$-pair production cross-section in the dilepton final state using a lepton plus isolated track selection [8]. Although the choice of requiring an isolated track rather than a fully identified lepton candidate results in worse background, acceptance is significantly increased. Under the assumptions $M_t = 175$ GeV and BR$(W \to l\nu) = 10.8\%$ the measurement in this channel is translated to a measurement of the total cross-section of $\sigma(p\bar{p} \to t\bar{t}) = 9.0 \pm 1.3(\text{stat}) \pm 0.5(\text{sys}) \pm 0.5(\text{lumi})$ pb. This measurement is in good agreement with the SM prediction.

The D0 collaboration has recently performed measurements of $p\bar{p} \to t\bar{t}$ in lepton plus jets final states using a neural network b-tagging algorithm and in dilepton final states [8]. The cross-section measured in the dilepton channel $\sigma(p\bar{p} \to t\bar{t}) = 6.8^{+1.2}_{-1.1}(\text{stat})^{+0.9}_{-0.8}(\text{sys}) \pm 0.4(\text{lumi})$ pb is the most precise measurement in this decay channel. A higher precision is obtained in the ℓ+ jets channel yielding $\sigma(p\bar{p} \to t\bar{t}) = 8.3^{+0.6}_{-0.5}(\text{stat})^{+0.9}_{-1.0}(\text{sys}) \pm 0.5(\text{lumi})$ pb. The precision of the CDF and D0 measurements is now approaching that of the theoretical predictions.

Top quarks may also be singly produced via electroweak processes at the TeVatron. The predicted NLO SM cross-section in the s-channel is $\sigma(p\bar{p} \to tb + X) = 0.88 \pm 0.11$ pb and in the t-channel $\sigma(p\bar{p} \to tqb + X) = 1.98 \pm 0.25$ pb [13]. More recent calculations including higher order soft gluon corrections are discussed in section 4.1. Single top quark events can be used to study the Wtb coupling [14] and to measure the magnitude of the quark-mixing matrix [15, 16] without assuming only three generations of quarks [17]. Although the single top production cross-section is of a similar order to the top pair production cross-section, the signal suffers from larger backgrounds (from W + jet, $t\bar{t}$ and QCD multi-jet production). As a result of this, sophisticated analysis techniques must be employed to extract a signal.

The D0 collaboration has recently reported evidence for single top production at the 3.4 σ level [10]. Three different multivariate techniques were applied to 0.9 fb^{-1} of Run II data. The techniques used were 'boosted' decision trees, the 'matrix-element' method and Bayesian neural networks. The cross-section itself was extracted using a Bayesian approach based on a binned likelihood over all bins and channels of the discriminant variable from each multivariate technique, separately for $tb + tqb$, tqb and tb analyses. All three multivariate techniques yield a non-zero cross-section, however the decision tree measurement is chosen for the main result since it is able to rule out the background-only hypothesis with greatest significance. The expected SM and measured posterior probabilities for $tb + tqb$ are shown in Figure 5. The total measured cross-section is $\sigma(p\bar{p} \to tb + X, tqb + X) = 4.9 \pm 1.4$ pb. This measurement is used to extract $0.68 < |V_{tb}| \leq 1$ at 95% confidence level, without assuming CKM matrix unitarity.

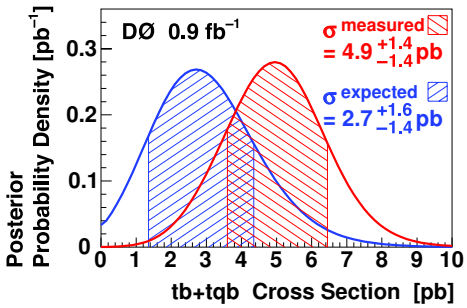

Figure 5: Expected SM and measured Bayesian posterior probability densities for the $tb + tqb$ cross-section obtained by the D0 collaboration. The shaded regions indicate one standard deviation above and below the peak positions.

The CDF collaboration has also performed a search for single top production using three different multivariate techniques. The techniques used by CDF were likelihood discrimi-

nants, Bayesian neural networks and the 'matrix element' method. The largest signal that can be extracted comes from the matrix element technique and corresponds to a significance of 2.6 σ. Figure 6 shows constraints on the Higgs arising from the most recent M_t and M_W measurements from TeVatron and results from LEP and SLD.

2.2.2 Top quark properties

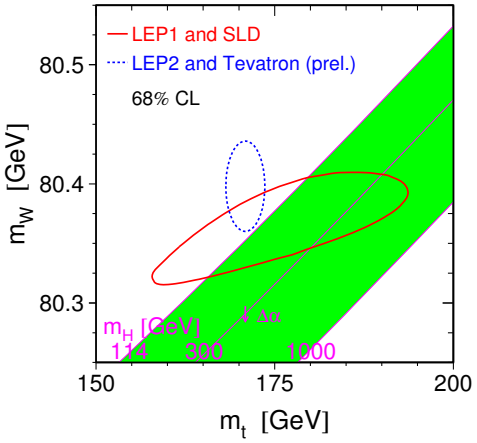

Figure 6: Constraints on the Higgs from measurements of M_W and M_t.

Measurements of the top quark mass together with the W mass provide constraints on the mass of the SM Higgs boson. Several measurements of the top mass have been performed recently at the TeVatron [9], using samples of $p\bar{p} \rightarrow t\bar{t}$ events. Template methods, where an observable strongly correlated to M_t is compared to simulated signals for different values of M_t, are commonly used. In addition matrix element analyses based on calculating the per event probability density as a function of the measurement given M_t and the multiplying the likelihoods from all measurements are used.

The most precise measurements of M_t from CDF and D0 have both been obtained using the matrix element method in the l + jets channel. A relative uncertainty of approximately 1.5% is achieved, with CDF obtaining 170.9 ± 2.5 GeV and D0 obtaining 170.5 ± 2.7 GeV. The present TeVatron combined result which also includes fully hadronic $t\bar{t}$ decay channel results and dilepton channel results is $M_t = 170.9 \pm 1.8$ GeV.

The top quark charge has not yet been directly determined. One possible scenario is that the discovered top quark is an exotic quark of charge $4e/3$ while the top quark with charge $2e/3$ has mass 270 GeV and has not yet been observed (XM) [18]. The CDF and D0 collaborations have both attempted to measure the charge of tops in $t\bar{t}$ production using $t \rightarrow bW$, $(W \rightarrow l\nu)$ decays. In this case the charge of the W-decay lepton is measured directly and the charge of the $b-$jet is measured using the momentum-weighted sum of the charges of the tracks in the jet. The charge of the lepton and jet are multiplied together and this distribution is compared to predictions from the SM and the XM. Using differing statistical methods both D0 and CDF obtain results strongly favouring the SM.

Measurements have also been made of the W-helicity in top decays and of the top branching fraction $R = \mathrm{Br}(t \rightarrow bW)/\mathrm{Br}(t \rightarrow qW)$ [9]. In both cases measurements from CDF and D0 are consistent with the SM prediction.

2.3 Standard Model Higgs searches

The experimental search for the SM Higgs boson has been ongoing since the 1970s. Direct limits from LEP suggest that the Higgs mass M_H is greater than 114.4 GeV at 95% confi-

dence level. Indirect measurements from EW fits to measurements of M_t and M_W suggest $M_H = 76^{+33}_{-24}$ GeV. Combining the LEP direct search data with the EW fits derive an upper limit of $M_H < 182$ GeV. New searches for the Higgs have been performed at the TeVatron [19].

The dominant decay modes for the SM Higgs boson are $H \to b\bar{b}$ for $M_H < 135$ GeV and $H \to WW^{(*)}$ for $M_H > 135$ GeV. This leads to a twofold search strategy at the TeVatron. For $M_H < 135$ GeV associated WH and ZH production with subsequent $H \to b\bar{b}$ are the processes of choice. For $M_H > 135$ GeV, $gg \to H$ production with subsequent $WW^{(*)}$ decay is the process searched for. The cross-section for ZH (WH) production at the TeVatron is expected to be between 0.1 (0.2) pb and 0.01 (0.03) pb, while for $gg \to H$ it is expected to be between 0.8 and 0.2 pb depending on the Higgs mass. In all channels discovery of the Higgs remains immensely challenging; a considerable amount of effort has been invested in making sure to cover as many Higgs decay channels as possible over a wide phase space. New triggers and trigger algorithms have been developed by D0 and CDF, a large amount of effort has been devoted to improving b-tagging in order to reduce backgrounds, and jet energy corrections have been significantly improved yielding final results that have improved by more than just the factor expected by scaling luminosity.

A variety of analyses have been applied to CDF and D0 data [19]. Cut-based analyses have been employed as well as more sophisticated matrix-element- and neural-network-based searches. No evidence for Higgs production has been observed and limits on the production cross-section compared to the SM have been set. The best individual limits have come from $H \to WW \to l\nu l\nu$ searches where the CDF and D0 limits extend down to $3-4$ times the SM prediction. The combined D0 limits are presented in Figure 7, showing that the strongest limits are set on Higgs masses around 160 GeV. With about 8 fb^{-1} of data expected to be taken by each experiment by the end of TeVatron running, improved statistical precision alone may not be sufficient to discover the Higgs, however considerable work is still being done to improve the reach of the TeVatron experiments. Improvements currently being studied include increasing lepton acceptance, further improving jet resolution and b-tagging as well as making more use of advanced analysis techniques such as those used in the TeVatron single top production searches.

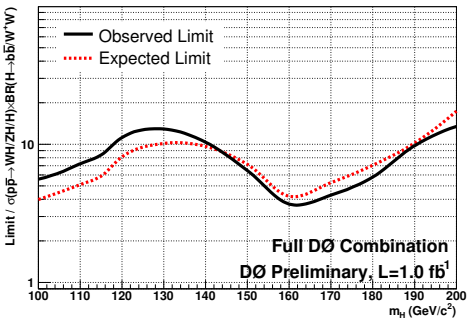

Figure 7: The D0 combined observed and expected cross-section limits on Higgs production, normalised to the SM prediction.

2.4 Flavour physics at the B-Factories

The B-factories at SLAC and KEK continue to perform strongly accumulating very high statistics. Over 384 million BB events have been collected by the Babar experiment at SLAC and over 535 million BB events by the Belle experiment at KEK. Both experiments have made significant progress in studies of CP violation and rare decays.

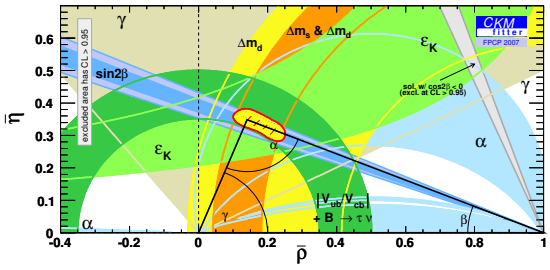

Figure 8: Constraints in the ρ-η plane from recent measurements at B-factories

Recent measurements of the angles [20] and sides of the unitarity triangle [21] have improved constraints in the $\rho - \eta$ plane (see Fig. 8). Not only has $\beta(\phi_1)$ been measured to a precision close to 1° and $\alpha(\phi_2)$ to around 10° but also $\gamma(\phi_3)$ angle, previously thought to be beyond the reach of the B factories is already known to around 30°. By the end of running the B factories may be able to provide a useful constraint on $\gamma(\phi_3)$.

Both Babar and Belle have studied a large number of rare B-decays as well as lepton flavour violating and rare decays of the τ lepton [22], observing no deviations from the SM and setting strong limits on new physics. Studies of $\tau \to \pi^-\pi^0\nu_\tau$ indicate a difference between the spectral function of the $\pi\pi$ system arising from tau decay compared to that arising from $e^+e^- \to \pi\pi$. This is very interesting in the context of $\frac{g_\mu - 2}{2}$ measurements where it is expected to be possible to evaluate the dominant part of hadronic vacuum polarisation term in the theoretical calculation from the $\pi\pi$ spectral function in either e^+e^- or τ data.

On the theoretical side a new development has emerged by linking B and K physics calculations with high-energy collider data. Particular examples are strong constraints on Z-penguin dominated flavour-changing K and B decays, since the generic coupling $Zd^i\bar{d}^j$ of the Z boson to any kind of down-type quarks is related to the $Zb\bar{b}$ coupling. The latter mediates the $Z \to b\bar{b}$ decay so that severe limits can be derived from the LEP and SLC data leading to significant suppressions of Z-penguin contributions [23].

3 Beyond the Standard Model

3.1 Model-independent searches

3.1.1 Events with isolated leptons and missing transverse momentum at HERA

Events with isolated leptons (electrons, muons and taus) and missing transverse momentum were observed in the HERA I data (1994–2000) [24, 25, 26, 27]. The only SM process which yields those events in ep collisions at HERA is single production of W bosons. Events with large P_T^X, the transverse momentum of the hadronic final state, are of particular interest. Although no significant deviation from the SM was found, some atypical events with prominent jets have been observed in the electron and muon channels by the H1 collaboration and in the tau channel by the ZEUS collaboration.

The H1 search for isolated leptons has been updated to include data from the whole HERA I+II high-energy running 1994-2007 [28]. The overall yield of isolated leptons is in agreement with the SM predictions, however at large values of $P_T^X > 25$ GeV, the region sensitive to new physics, 21 electron or muon candidate events are observed in e^+p data where 8.9 ± 1.5 events are expected from the SM. No excess is observed in e^-p data. In the case of isolated tau leptons good agreement with the SM expectation is observed in all data sets, however the sensitivity to new physics is less than in the muon and electron channel due to the lower efficiency and purity.

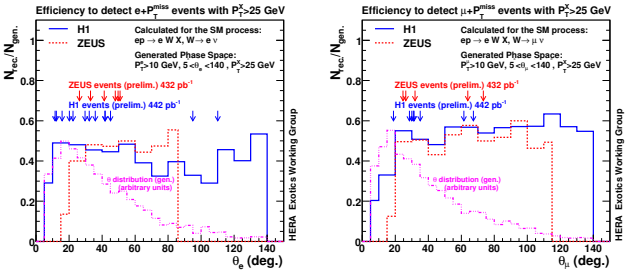

Figure 9: The efficiency of the H1 and ZEUS isolated lepton searches for $ep \to eWX$ (left $W \to e\nu_e$, right $W \to \mu\nu_\mu$) events with $P_T^X > 25$ GeV as a function of the lepton polar angle ($\theta_{e,\mu}$). The arrows in the figures denote the H1 and ZEUS candidate events. The generated spectrum for $ep \to eWX$ Monte Carlo is also shown.

The ZEUS collaboration has performed a similar search to H1 in the electron and muon channels on 432 pb^{-1} data from the 1996-2007 running period [29]. Overall the ZEUS data are in good agreement with the SM predictions. For $P_T^X > 25$ GeV no significant excess is observed in either e^+p or e^-p data, a total of 6 (5) candidate electron (muon) events are observed compared to a SM expectation of 7.0 ± 0.7 (5.3 ± 0.6).

In order to understand the differences between the ZEUS and H1 searches a common H1-ZEUS working group has been formed. Comparisons of the efficiencies of H1 and ZEUS searches as a function of P_T^X and as a function of the lepton polar angle θ_l have been made. The comparisons of the efficiencies of the two searches as a function of P_T^X show that the ZEUS and H1 have similar efficiency for selecting $e^\pm p \to e^\pm WX$ events at high values of P_T^X. The more restricted phase space of the ZEUS search leads to a slightly lower efficiency than the H1 search. Figure 9 shows that in regions of the lepton polar angle $\theta_{e,\mu}$ common to both analyses the efficiencies of the two searches are similar. The majority of the H1 candidates lie within the ZEUS search acceptance, indicating that the ZEUS search is also sensitive to physics which could be responsible for the H1 excess, such as $\mathcal{R}$-Parity violating supersymmetry [30].

3.1.2 Multi-lepton production at HERA

The main multi-lepton production mechanism at HERA is photon-photon collision. H1 has performed a search for high transverse momentum ee, eee, $\mu\mu$ and $e\mu\mu$ topologies on the full HERA I+II set of 456 pb^{-1} $e^\pm p$ data [31]. The invariant mass and summed scalar transverse momentum distributions (ΣP_T), sensitive to new physics, for these classes of events are observed to be overall in agreement with the SM. In the e^+p data only, four interesting events are observed with $\Sigma P_T > 100$ GeV.

The ZEUS collaboration has performed a search for ee and eee topologies on 446 pb^{-1} $e^\pm p$ HERA I+II data [32]. The ZEUS search suffers from a higher background, mainly arising from QED Compton events, than the H1 search. In both the ee and eee channels the ZEUS data are in agreement with the SM expectation.

3.1.3 General BSM search at HERA

A model-independent search for deviations from the SM was previously performed by H1 [33], using HERA I data. This search has been updated to the full HERA II data set [34], corresponding to 178 pb^{-1} (159 pb^{-1}) e^+p (e^-p) data. High P_T final state configurations involving electrons (e), muons (μ), jets (j), photons (γ) or neutrinos (ν) are considered.

All final state configurations containing at least two such objects with $P_T > 20$ GeV in the central region of the detector are investigated and classified into exclusive event classes.

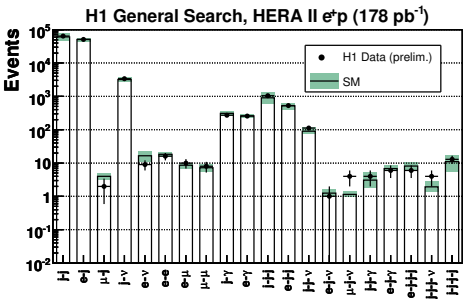

Figure 10: The yields for the different event classes in the H1 general search, on e^+p, data compared to the SM predictions.

The yields for the different classes for the e^+p data are shown in Figure 10. Data events are found in 21 event classes each for e^+p and e^-p data and good agreement is observed between data and the SM expectations in most event classes. The largest disagreement in yield is in the $\mu-j-\nu$ topology for the e^+p data, corresponding to the excess discussed in section 3.1.1. A non-biased statistical method is used to search for deviations of the data with respect to the SM in the summed scalar transverse momentum ($\sum P_T$) and total invariant mass ($M_{\rm all}$) distributions, sensitive to new physics, and to quantify their significance. Good agreement is observed in all event classes.

The data from the H1 general search has been added to QUAERO [35], providing a public interface to H1 and D0 data. With this interface, it is possible to quickly test any new physics models to data. The fact that the H1 general search covers all final states at HERA makes it ideal for this purpose. The performance of QUAERO on H1 and D0 data has been tested with example models such as leptoquark production and $\mathcal{R}$ parity violating SUSY. New data from H1 can now be easily added.

3.1.4 Model-independent searches at the TeVatron

Several model independent searches have been performed at the TeVatron [36]. The CDF collaboration has searched for Z bosons with high P_T in 0.94 fb^{-1} of data. New physics models to which the search is sensitive include right-handed heavy quarks, technicolor particles, gauginos, squarks and excited states resulting from large extra dimensions. High P_T Z bosons are searched for inclusively and in $Z + X$ or $Z + Y + X$ final states, where X and Y can be leptons, photons, missing energy or large total transverse energy (H_T). For each signature the observed $P_T(Z)$ spectrum and other distributions are compared with the SM expectations. No significant variation from the SM is observed.

The CDF collaboration has also searched for heavy objects decaying into high P_T dileptons using 929 pb^{-1} of Run II data. Acceptance is maximised by including all three generations of leptons, loosening fiducial requirements and using loose P_T requirements. b-tagging is required in order to distinguish new physics involving the third generation quark. Dileptons are searched for in association with X, where X may be large H_T, high E_T jets, b tags, third leptons or large missing E_T. The results show good agreement with the SM. To test the reach of the search a cross-section limit on a 300 GeV right handed down type quark [37] is set using the electron and muon channels only. The limit is 1.4 σ_Q where $\sigma_Q = 0.289$ pb is the expected SM cross-section.

3.2 SUSY searches

Supersymmetry (SUSY) is a popular extension of the SM. SUSY associates supersymmetric partners (*s*particles) with the known particles and unifies internal symmetries with Lorentz invariance. Supersymmetric models provide solutions to many problems of the SM, such as fine-tuning, unification and hierarchy, and predict spectacular final states in high-energy particle collisions. Despite extensive studies at colliders and elsewhere, no trace of SUSY has yet been found. Many new searches for signatures of SUSY have been performed at the TeVatron [38]. Two of the most popular scenarios for searches are the minimal supersymmetric extension of the SM (MSSM) and minimal Supergravity (mSUGRA).

MSSM is the simplest realistic SUSY theory. It requires two Higgs doublets resulting in a Higgs sector with two charged and three neutral scalar bosons. Assuming CP-invariance, one of the neutral bosons (A) is CP-odd, and the other two (h, H) are CP-even. The Yukawa couplings of A to down-type particles (e.g. τ lepton or b quark) are enhanced by a factor $\tan\beta$ relative to the SM. The leading decay modes of A and the corresponding degenerate CP-even Higgs boson are $\phi \to b\bar{b}$ ($\sim 90\%$) and $\phi \to \tau\tau$ ($\sim 10\%$). Both CDF and D0 have searched in the $\tau\tau$ decay channel, where the QCD background is lower. The results of the CDF search in the $\tau_e\tau_{\rm had}$ and $\tau_\mu\tau_{\rm had}$ channels combined are shown in Fig. 11. No evidence for $M_A = 90 - 250$ GeV is observed, a small excess of events exists with a significance less than $2\,\sigma$ when the entire mass range is considered. No excess above the expected backgrounds is observed in the D0 search. The two experiments have set limits within the framework of the MSSM for Higgs masses in the range 90 to 250 GeV.

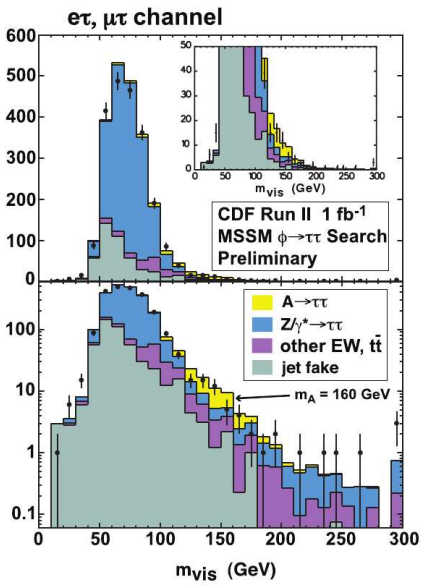

Figure 11: Partially reconstructed di-tau mass in the $A \to \tau\tau$ CDF search. The normalisation of backgrounds and signal ($M_A = 160$ GeV) correspond to fit results for the signal exclusion.

Associated $\tilde{\chi}_1^\pm\tilde{\chi}_2^0$ production can lead to clean multi-lepton final states when $p\bar{p} \to \tilde{\chi}_1^\pm\tilde{\chi}_2^0$ is followed by $\tilde{\chi}_2^0 \to ll\tilde{\chi}_1^0$ and $\tilde{\chi}_1^\pm \to l\nu\tilde{\chi}_1^0$. The CDF (D0) collaboration has performed 14 (6) searches respectively for such final states each using up to 1.0 (1.1) fb^{-1} of Run II data. No evidence for SUSY is observed and limits have been set on the production cross-section multiplied by the branching ratio to three leptons of 0.2 (0.08) pb for $M(\tilde{\chi}) = 140$ GeV, compared to expected limits of the order of 0.1 pb.

The D0 collaboration has also updated their search for scalar quark, $\tilde{q}$, and gluino, $\tilde{g}$, production using their 1 fb^{-1} data set. An exclusion region as function of $M_{\tilde{q}}$ and $M_{\tilde{g}}$ was derived, yielding lower mass limits of $M_{\tilde{q}} > 375$ GeV and $M_{\tilde{g}} > 289$ GeV, respectively.

3.3 Leptoquarks

Leptoquarks (LQs) are hypothetical bosons which couple to a lepton and a quark via a Yukawa coupling (denoted λ). In the SM, both quarks and leptons occur in left-handed

$SU(2)$ doublets and right-handed $SU(2)$ singlets. The symmetry between quarks and leptons leads to the cancellation of triangle anomalies which make the SM renormalizable. Leptoquarks appear in theories in which this symmetry is more fundamental.

Leptoquarks are colour triplets which would be pair-produced in either $q\bar{q}$ or gg interactions at $p\bar{p}$ or pp colliders. Since LQs carry electroweak charge, they would also be produced in e^+e^- collisions. Only SM gauge couplings are involved in pair-production of scalar LQs. Therefore the cross-sections depend neither on the quark-lepton-LQ Yukawa coupling nor on the quark and lepton generations to which the leptoquark couples. In contrast, leptoquarks would be singly produced via the Yukawa coupling in lepton-quark collisions. Searches at ep colliders are sensitive only to LQs which couple to electrons and the sensitivity to LQs which couple to the second and third generation quarks is far below that of first-generation LQs. Leptoquarks are usually (but not always) assumed to be *generation diagonal*. Models in which LQs couple to more than one generation of quarks or leptons would induce flavour-changing neutral currents or lepton flavour violation (LFV), respectively.

LQs can be classified into 14 types with respect to the quantum numbers spin, isospin and chirality within the framework of the Buchmüller-Rückl-Wyler (BRW) model [39]. Leptoquarks carry both lepton (L) and baryon (B) quantum numbers. The fermion number $F = L + 3B$ is assumed to be conserved.

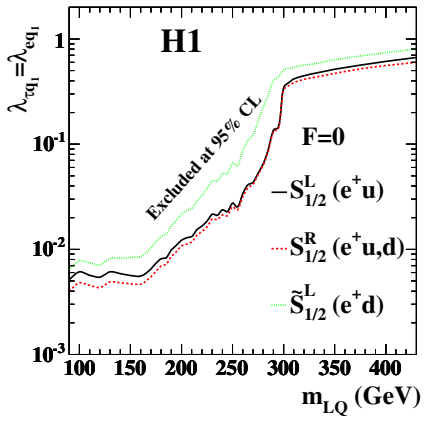

Figure 12: Limits on the coupling constants $\lambda_{\tau q_1} = \lambda_{eq_1}$ as a function of the LQ mass M_{LQ} for F=0 scalar LQs. Regions above the lines are excluded at 95% CL. The notation q_1 indicates that only processes involving first generation quarks are considered.

A search for pair-production of second generation leptoquarks has been performed by the D0 collaboration in the $\mu\nu qq$ final state using 1 fb^{-1} of Run II data [36]. No evidence for leptoquark production is observed, and a lower limit on the leptoquark mass, $M_{\rm LQ} > 214$ GeV is set at 95% confidence level for the scenario where β, the branching fraction of the LQ to μq, is set to 0.5.

The H1 and ZEUS collaborations have previously searched for production of first generation LQs [40, 41] in HERA I data, dominated by e^+p collision data. A new H1 search has been performed on 92 pb^{-1} of e^-p data from the 2004-05 running period [42]. No evidence for LQs is observed, and limits have been set in the $\lambda - M_{\rm LQ}$ plane. For $\lambda = (4\pi\alpha)^2 = 0.3$ lower limits on $M_{\rm LQ}$ ranging from $276 - 304$ GeV have been set for $F = 2$ LQs.

The H1 collaboration has searched for LFV in ep collisions at HERA [43]. The LFV processes $ep \to \mu X$ and $ep \to \tau X$ can be attributed to LQs produced predominantly by electron-quark fusion. The fermion number takes values of $F = 2$ for e^-q processes and $F = 0$ for e^+q processes. For M_{LQ} well below the ep centre-of-mass energy, the s channel production dominates. For M_{LQ} greater than the centre-of-mass energy the s and u channel processes become of equal importance. The BRW model assumes lepton flavour conservation such that the LQs produced in ep collisions decay only to eX or $\nu_e X$ final states. A general extension of the BRW model allows for the decay of LQs to final states containing a lepton of different flavour (μ or τ) and a jet. Non-zero couplings to

an eq pair and to a μq or τq pair are assumed.

In the H1 analysis, high P_T muon and tau signatures are searched for and no evidence for LFV is found. Limits on couplings to 14 different LQs as a function of M_{LQ} are derived. An example of the limits under the assumption that the tau- and electron-first generation quark couplings are equal is shown in Figure 12. The H1 results are directly comparable to previous limits set by ZEUS [44] and are found to be similar. Lower mass limits on the first and second generation leptoquarks from hadron-hadron collisions extend up to about 250 GeV [45, 46], lower mass bounds from e^+e^- annihilation reach values of 100 GeV [47].

3.4 Other non-SUSY BSM models

The proliferation of fermions can naturally be explained if the SM fermions are composite, in which case excited states may exist. A minimal extension [48, 49, 50] of the SM can incorporate excited fermions such as excited leptons (l^*). Considering only EW gauge mediated interactions (GMI), the excitation part of the Lagrangian is:

$$\mathcal{L}_{F^*F} = \frac{1}{2\Lambda}\overline{F_R^*}\sigma^{\mu\nu}\left[gf\frac{\overrightarrow{\tau}}{2}\overrightarrow{W_{\mu\nu}} + g'f'\frac{Y}{2}B_{\mu\nu}\right]F_L + \text{h.c.},$$

where the new weights f and f' multiply the SM coupling constants g and g' corresponding to the weak $SU(2)$ and electromagnetic $U(1)$ sectors respectively. The corresponding gauge boson fields are denoted by W and B, the matrix $\sigma_{\mu\nu} = (i/2)[\gamma^\mu, \gamma^\nu]$, τ are the Pauli matrices and Y is the hypercharge. The compositeness scale Λ reflects the range of the new confinement force and, together with f and f', determines the production cross-section.

The H1 collaboration has recently performed a search for excited leptons at HERA using 434 pb^{-1} $e^\pm p$ data [51]. Both excited neutrinos (ν^*) and excited electrons (e^*) have been searched for. Sensitivity to ν^*s is much higher in e^-p collisions due to helicity enhancement specific to CC like processes and only the e^-p data was used to search for ν^*s. The search was performed for the decay channels $\nu^* \to \nu\gamma$, $\nu^* \to \nu Z$ and $\nu^* \to We$, using six subsequent decay channels, covering approximately 90% of the total branching fraction. No evidence for ν^*s is observed and limits on the cross-section are set and translated to limits in the f/Λ–M_{ν^*} plane, with M_{ν^*} the mass of the excited neutrino. The limits are set for two scenarios: $f = f'$ (no $\gamma\nu^*\nu$ coupling) and $f = -f'$ (maximal $\gamma\nu^*\nu$ coupling). For $f = -f'$ and $f/\Lambda = 1/M_{\nu^*}$, a lower limit of $M_{\nu^*} > 211$ GeV is obtained. These limits explore new domains and significantly improve on previous LEP limits.

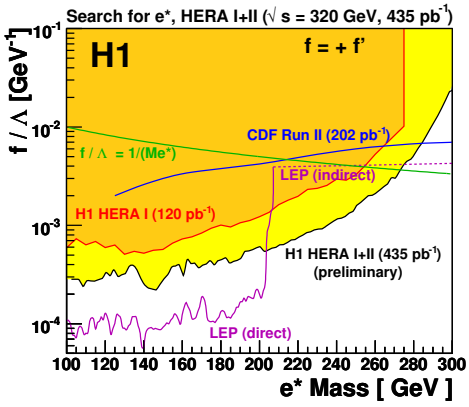

Figure 13: H1 limits on the coupling as function of excited electron mass.

The full HERA I+II 434 pb^{-1} $e^\pm p$ data set was used in the e^* search. The decay channels $e^* \to e\gamma$, $e \to eZ$ and $e \to \nu W$ with subsequent hadronic decay of the weak bosons were studied. In the case of $f = -f'$ (no $\gamma e^* e$ coupling) the production cross-section is

suppressed, therefore only the maximal $\gamma e^* e$ coupling case ($f = f'$) was considered. No excess over the SM is observed in the data and limits are set in the f/Λ-M_{e^*} plane. For $f/\Lambda = 1/M_{e^*}$ a lower bound of $M_{e^*} > 273$ GeV is set. Figure 13 shows these results in comparison with limits obtained at the TeVatron assuming that the excited electrons are only produced via GMI.

At the TeVatron production of excited leptons is dominated by contact interactions rather than GMI. A search for $e^* \to e\gamma$ has been performed by the D0 collaboration [36] using 1.0 fb^{-1} of Run II data. Limits have been set in the Λ-M_{e^*} plane, yielding a lower mass limit of $M_{e^*} > 756$ GeV for a compositeness scale of $\Lambda = 1$ TeV.

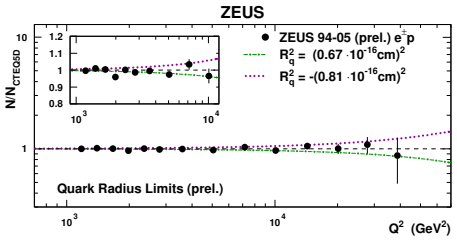

Figure 14: ZEUS limits on the quark radius obtained using the CI search. The points show the ratio of the data to the SM predictions in bins of Q^2. The expected deviation for the derived quark radius limits are also shown.

The ZEUS collaboration has exploited the precision of their high Q^2 NC DIS measurements to search for new physics within the framework of four-fermion contact interactions (CIs) [52]. The addition of CIs adds new terms to the NC SM Lagrangian. By comparing the deviations of the data from the SM predictions and parametrising possible effects using the CI formalism limits are set on contact interactions themselves and various other specific models, such as heavy leptoquarks, large extra dimensions and finite-radius quarks. An example of the limits expressed in terms of the quark radius is shown in Figure 14, an upper limit of 0.67×10^{-4} fm is set.

A host of other BSM searches too numerous to cover in detail here has been performed at the TeVatron [36]. Models such as fourth generation quarks, extra gauge bosons (W' and Z') and extra dimensions have all been tested and no evidence for new physics has been found.

4 A theoretical perspective

4.1 Single top production and top decay

Recent calculations for single top production at the LHC and TeVatron [53] have applied NNNLO soft-gluon corrections, leading to corrections of the order of $3 - 3.5\%$ relative to NNLO calculations. For all channels at TeVatron the cross-sections for single top and single anti-top production are identical, whereas at the LHC the cross-section in the s and t channels is larger for single top production than for anti-top production.

Single top production and top decay including spin correlations have been recently implemented in the event generator MC@NLO [54]. For this implementation the NLO single top production had to be computed using the FKS subtraction method [55] and MC counter terms had to be calculated. Studies of spin correlations in (single) top decay can determine the handedness of the electroweak coupling of the top. The top-spin is very strongly correlated to the decay lepton production making it possible to measure the coupling. Angular correlations in top decay were implemented in MC@NLO precise to NLO for real (hard) emissions and LO for soft or collinear emissions. The effect of the spin correlations on the

lepton decay angle relative to the hardest jet which does not contain a stable b hadron is shown in Figure 15.

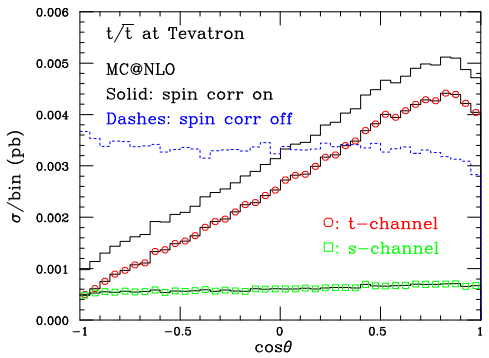

Figure 15: Effect of spin correlations on the lepton decay angle θ relative to the hardest jet which does not contain a stable b hadron for single $t/\bar{t}$ production at the TeVatron.

Single top studies have also been preformed using the Monte Carlo code MCFM [56]. MCFM has been extended to include the three single top channels and correctly deal with the full spin correlation of the leptonic decay of the top. Soft and collinear divergences were treated according to the subtraction method of Catani, Dittmaier, Seymour and Trócsányi [57].

5 Future colliders

5.1 LHC physics prospects

With the LHC-era fast approaching, many studies have been performed on the physics-reach of the LHC experiments using the first two years of data [58]. It is reasonable to expect data sets of approximately 5 fb^{-1} providing machine schedules are adhered to. Although the initial emphasis of LHC physics will be on understanding detector performance and SM processes there will be sensitivity to new physics. In the case of high mass di-lepton resonances, $Z'(W')$, where the background is low the prospects of an early discovery are good for new physics in the TeV mass region. Both ATLAS and CMS could start to probe SUSY at $1-2$ TeV and there would be high potential for BSM physics discoveries such as Majorana neutrinos and technicolor. It is possible that the $H \rightarrow WW$ channel will allow evidence of a SM Higgs boson at $M_H \sim 165$ GeV with 1 fb^{-1} luminosity, while the $H \rightarrow ZZ$ channel will allow discovery in the mass range $190-450$ GeV with 4 fb^{-1}. At least 10 fb^{-1} would be required for a MSSM Higgs 5 σ discovery.

The sensitivity of the LHC searches are affected by the precision to which the proton parton distribution functions (PDFs) are known [59]. Uncertainties on the PDFs lead directly to uncertainties on both SM processes such as W, Z, t and H production and BSM processes such as hH^+ and aH^+ production in the MSSM. The new CTEQ6.5M PDF shifts the total cross-section, $\sigma_{\rm tot}$ relative to CTEQ6.1M by similar magnitudes to the PDF uncertainties, cross-sections for specific new physics processes are also modified by up to 20%. With this in mind it is clear that further precision measurements of the PDFs will be of significant value to searches at the LHC.

Electroweak and top quark measurements will be amongst the first studied by both ATLAS [60] and CMS [61]. Large W and Z boson samples should be accrued in early running offering valuable tools for the understanding of the performance of the detectors. With sufficiently precise PDFs the W and Z production processes could be used to check luminosity measurements. $t\bar{t}$ production will provide useful samples for jet energy scale and b-tagging efficiency. Early and basic W, Z and top measurements could be made using 100 pb^{-1} to 1 fb^{-1} of data. Indeed with only 1 fb^{-1} of data, CMS expect their precision to

already be dominated by systematics in their measurements of W and Z production.

5.2 ILC physics prospects

A future high energy linear e^+e^- collider such as the ILC could complement results from the LHC [62]. If one considers a scenario where EW symmetry breaking is realised through the Higgs mechanism and where low energy SUSY exists, then the prospective measurements from the ILC would greatly enhance knowledge obtained from LHC measurements. In such a scenario the LHC experiments would likely discover the Higgs and explore the strongly-interacting SUSY sector (squarks and gluinos) and make measurements of moderate precision that many of which will be model-dependent. The ILC would then be able to make high precision measurements of the Higgs sector and a detailed exploration of the electroweakly interacting SUSY sector (sleptons and gauginos). In addition there would be possible discoveries in regions of parameter space to which the LHC would not be sensitive.

There are several examples of possible measurements at ILC which will not be possible at the LHC. The ILC can detect the Higgs boson independent of the decay mode even if it decays into invisible particles, using the recoil mass spectrum in $ZH \to (ee, \mu\mu)X$. The ILC can also establish the spin of the Higgs. The sensitivity to the electroweakly interacting SUSY sector with clean signatures and low backgrounds makes precise SUSY spectroscopy possible at the ILC. The physical observables within the LHC and ILC reach would make it possible to constrain the SUSY Lagrangian. With many other possible physics topics to be searched for at the ILC, it is clear that the ILC is likely to greatly increase our knowledge of the electroweak sector and possible BSM scenarios.

6 Conclusion and outlook

This is an exciting time for EW and BSM physics. With high energy HERA running finished the H1 and ZEUS collaborations are beginning to produce their final statements on many searches for new physics, so far the SM is holding up well. The polarised running of HERA II has been a success, resulting in increasingly precise constraints from the HERA experiments on EW parameters. The performance of the TeVatron in Run II has been excellent and this has been reflected in a clutch of impressive results. The high precision measurement of M_W together with improving M_t determination is reflected in stronger constraints on the SM Higgs boson mass. Direct searches for the SM Higgs boson an new physics are showing ever improving sensitivity. With an order of magnitude more data statistics expected by the end of Run II, TeVatron data could yet yield the discovery of the Higgs. We await the imminent start of the LHC-era. Though early work will focus on detector-commissioning and calibration using standard candles, it will be possible to search previously unexplored regions of phase-space for new physics with the first two years of LHC data.

7 Acknowledgements

We thank all participants in the parallel session for interesting talks and lively discussion.

References

[1] Slides:
http://indico.cern.ch/contributionDisplay.py?contribId=16&sessionId=2&confId=9499

[2] CDF, S. Malik, These proceedings.
[3] CDF/D0, Y. Maravin, These proceedings.
[4] U. Baur, S. Errede and G. L. Landsberg, Phys. Rev. **D50**, 1917 (1994), [hep-ph/9402282].
[5] ZEUS, S. Bhadra, These proceedings.
[6] ZEUS, S. Chekanov *et al.*, Phys. Lett. **B637**, 210 (2006), [hep-ex/0602026].
[7] H1, G. Li, These proceedings.
[8] CDF/D0, C. Gerber, These proceedings.
[9] CDF/D0, J. Wagner, These proceedings.
[10] CDF/D0, S. Jabeen, These proceedings.
[11] N. Kidonakis and R. Vogt, Phys. Rev. **D68**, 114014 (2003), [hep-ph/0308222].
[12] M. Cacciari, S. Frixione, M. L. Mangano, P. Nason and G. Ridolfi, JHEP **04**, 068 (2004), [hep-ph/0303085].
[13] Z. Sullivan, Phys. Rev. **D70**, 114012 (2004), [hep-ph/0408049].
[14] A. P. Heinson, A. S. Belyaev and E. E. Boos, Phys. Rev. **D56**, 3114 (1997), [hep-ph/9612424].
[15] N. Cabibbo, Phys. Rev. Lett. **10**, 531 (1963).
[16] M. Kobayashi and T. Maskawa, Prog. Theor. Phys. **49**, 652 (1973).
[17] G. V. Jikia and S. R. Slabospitsky, Sov. J. Nucl. Phys. **55**, 1387 (1992).
[18] D. Chang, W.-F. Chang and E. Ma, Phys. Rev. **D59**, 091503 (1999), [hep-ph/9810531].
[19] CDF/D0, R. Vilar, These proceedings.
[20] Babar, N. Barlow, These proceedings.
[21] Belle, I. Nakamura, These proceedings.
[22] Belle, H. Hayashii, These proceedings.
[23] U. Haisch, These proceedings.
[24] H1, V. Andreev *et al.*, Phys. Lett. **B561**, 241 (2003), [hep-ex/0301030].
[25] ZEUS, S. Chekanov *et al.*, Phys. Lett. **B559**, 153 (2003), [hep-ex/0302010].
[26] ZEUS, S. Chekanov *et al.*, Phys. Lett. **B583**, 41 (2004), [hep-ex/0311028].
[27] H1, A. Aktas *et al.*, Eur. Phys. J. **C48**, 699 (2006), [hep-ex/0604022].
[28] H1, Y. De Boer, These proceedings.
[29] ZEUS, K. Korcsak-Gorzo, These proceedings.
[30] S. Y. Choi *et al.*, arXiv:hep-ph/0612302.
[31] H1, G. Brandt, These proceedings.
[32] ZEUS, O. Ota, These proceedings.
[33] H1, A. Aktas *et al.*, Phys. Lett. **B602**, 14 (2004), [hep-ex/0408044].
[34] ZEUS, E. Sauvan, These proceedings.
[35] S. Caron, These proceedings.
[36] CDF/D0, D. Stuart, These proceedings.
[37] J. D. Bjorken, S. Pakvasa and S. F. Tuan, Phys. Rev. **D66**, 053008 (2002), [hep-ph/0206116].
[38] CDF/D0, R. Ströhmer, These proceedings.
[39] W. Buchmuller, R. Ruckl and D. Wyler, Phys. Lett. **B191**, 442 (1987).
[40] H1, A. Aktas *et al.*, Phys. Lett. **B629**, 9 (2005), [hep-ex/0506044].
[41] ZEUS, S. Chekanov *et al.*, Phys. Rev. **D68**, 052004 (2003), [hep-ex/0304008].
[42] H1, A. Dubak, These proceedings.
[43] H1, A. Aktas *et al.*, hep-ex/0703004.
[44] ZEUS, S. Chekanov *et al.*, Eur. Phys. J. **C44**, 463 (2005), [hep-ex/0501070].
[45] D0, V. M. Abazov *et al.*, Phys. Lett. **B636**, 183 (2006), [hep-ex/0601047].
[46] CDF, A. Abulencia *et al.*, Phys. Rev. **D73**, 051102 (2006), [hep-ex/0512055].
[47] OPAL, G. Abbiendi *et al.*, Eur. Phys. J. **C31**, 281 (2003), [hep-ex/0305053].
[48] K. Hagiwara, D. Zeppenfeld and S. Komamiya, Z. Phys. **C29**, 115 (1985).
[49] U. Baur, M. Spira and P. M. Zerwas, Phys. Rev. **D42**, 815 (1990).
[50] F. Boudjema, A. Djouadi and J. L. Kneur, Z. Phys. **C57**, 425 (1993).

[51] H1, N. Trinh, These proceedings.
[52] ZEUS, S. Schlenstedt, These proceedings.
[53] N. Kidonakis, These proceedings.
[54] P. Motylinski, These proceedings.
[55] S. Frixione, Z. Kunszt and A. Signer, Nucl. Phys. **B467**, 399 (1996), [hep-ph/9512328].
[56] F. Tramontano, These proceedings.
[57] S. Catani, S. Dittmaier, M. H. Seymour and Z. Trocsanyi, Nucl. Phys. **B627**, 189 (2002), [hep-ph/0201036].
[58] ATLAS/CMS, D. Rebuzzi, These proceedings.
[59] C. Yuan, These proceedings.
[60] ATLAS, A.-C. Le Bihan, These proceedings.
[61] CMS, F.-P. Schilling, These proceedings.
[62] ILC, A. Raspereza, These proceedings.

Future Opportunities in DIS

Joël Feltesse *

CEA, DSM/DAPNIA
CE-Saclay, Gif-sur-Yvette, France

The talk presents a personal view on future prospects in DIS. The open questions which have not been fully answered in lepton-nucleon Deep Inelastic Scattering by the past and present facilities are sketched. The proposals of future facilities are briefly reviewed and discussed.

1 Introduction

The year 2007 is a turning point of high energy physics. Data taking at HERA in the e-p collider experiments H1 and ZEUS as well as in the fixed target experiment HERMES should come to an end on 30th June. The new proton-proton collider LHC should start to be commissioned at CERN by the end of 2007. It is timely to ask ourselves whether this new era is the end of Deep Inelastic lepton-nucleon Physics (DIS), a bit more than 50 years after the pioneering work of R. Hoftater at SLAC [2] on elastic electron scattering off hydrogen, deuterium and helium. This talk gives a personal view on the perspective in DIS rather than a summary of the very rich parallel session on Future of DIS. Section 2 presents what I see as the most important issues in DIS in 2007. Section 3 gives an overview of the new DIS projects which have been proposed or are under consideration. Section 4 reminds how complementary are the e-p, p-p,e-A, A-A facilities to get more insight into DIS physics. Finally a tentative conclusion is given in section 5.

2 Open questions

After decades of effort in fixed target and collider experiments the momentum distribution of quark and gluon in the proton is known at a fair level of accuracy which is further commented below. However even in the kinematic domain reached so far there are still a lot to explore.

- How does the proton's spin 1/2 originate from the dynamics of quarks and gluons? In the domain where a quark carries almost the whole momentum of the proton ($x \to 1$), what is the d/u ratio ?
- How well do we know the quark and gluon distributions in nuleons imbedded in nuclei?
- As the LHC is about to start running we should ask ourselves if the Parton Distribution Functions (PDF), mainly extracted from deep inelastic scattering experiments, have the necessary precision for predicting cross sections at a 14 TeV pp collider.
- HERA has open up the small x and the hard diffraction domains. Are these domains well understood within QCD ?
- At last, but not the least, is it hopeless to find a new interaction between the quark and lepton sectors beyond the standard electroweak interaction (and the gravitation)?

A few examples to illustrate these important questions follow.

*Also at DESY and University Hamburg, Helmoltz Humboldt Research Award.

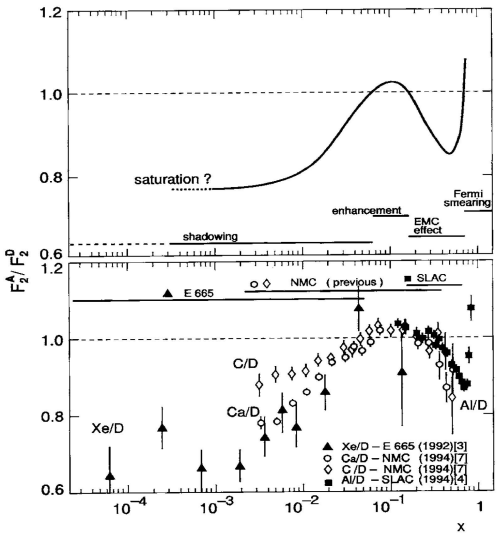

Figure 1: Upper: an idealized depiction of the ratio of the structure function of a nucleus $F_2^A(x, Q^2)$ per nucleon to $F_2^D(x, Q^2)$ of Deuterium from [5]. Lower: measured structure functions relative to Deuterium from [6].

2.1 Proton structure

The proton spin sum-rule :

$$\frac{1}{2} = \Delta\Sigma + \Delta G + L_q + L_g \tag{1}$$

states that the proton spin is the sum of the quark ($\Delta\Sigma$) and gluon intrinsic spins (ΔG) and orbital angular momentum (L_q, L_g contributions). If the quarks $\Delta\Sigma$ term is at present rather well known $\Delta\Sigma \approx 0.25$ the other terms are practically unknown. Precise masurements of scaling violation and measuement of photon-gluon processes with polarised beams and polarised targets would give access to ΔG . The only hope to have some hint on the orbital angular momentum would be through the JI Sum rule [3]:

$$J^q = \frac{1}{2}\int_{-1}^{+1} x dx[H^q(x,\xi,t\to 0)E^q(x,\xi,t\to 0)] = \frac{1}{2}\Delta\Sigma + L_q \tag{2}$$

where H^q and E^q are two General Parton Distributions (GPD) which are related to the correlation between the momentum and the spatial distributions of partons in the nucleon. Measurement of GPDs is a new field which has started recently. A model independent extraction of the GPDs is out of reach of the present and proposed future facilities. However precise measurements in the accessible range should bring some insight into this fully unknown domain of the structure of the proton.

2.2 Quarks and gluons in Nuclei

After the pioneering experiments at SLAC, the experiments of DIS off proton and neutron have been extended to scattering of muons off heavy nuclei at CERN. In 1982, it came as a

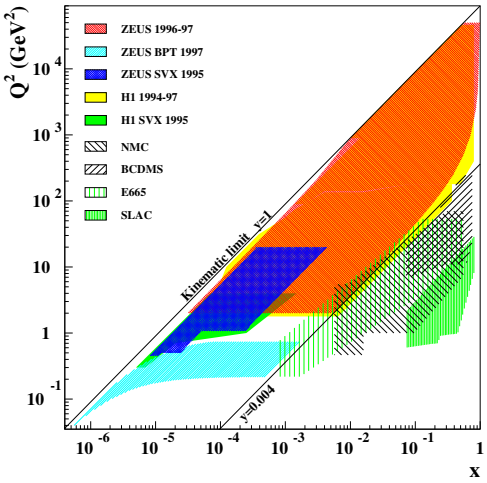

Figure 2: Kinematic regions in x and Q^2 covered by fixed target experiments and the H1 and ZEUS experiments at HERA.

surprise when the EMC experiment observed a nuclear dependence to the nuclear structure $F_2(x, Q^2)$ in iron relative to that for Deuterium : a rise at $x \sim 0.05$ and a strong drop at $x \sim 0.5$ [4]. Several dedicated fixed target experiments [6] confirm the effect at large x and extended the measurement down to about $x \sim 10^{-3}$ where a strong drop , called the nuclear shadowing effect, was observed (Figure 1). It is striking that about the same time a group of theoreticians from Saint-Petersburg predicted that the gluon distribution in the proton should rise with decreasing x and eventually saturate at a dynamical Q_s^2 value [7]. Simple considerations predict a significant dependence of the saturation scale on the atomic number A [8]:

$$Q_s^2 \sim (\frac{A}{x})^{\frac{1}{3}} \tag{3}$$

The nucleus is expected to be an amplifier of the saturation scale. It is tempting to connect these two phenomena : shadowing i.e. $xg_A(x, Q^2) < xg(x, Q^2)$ and saturation i.e. $xg(x, Q^2) < xg_{sat}(x, Q^2)$), although it is not yet proved that saturation can explain the shadowing.

At HERA, the gluonic structure of the proton has been measured down to $x \sim 10^{-4}$. In contrast, the gluon in nuclei is completely unknown. Extrapolation of the gluon distribution in Pb nuclei to x values $\sim 10^{-3}$ differ by a factor of three pending on the model of shadowing [9]. The measurement of the gluon density in nuclei at this very low x values may turn out to be vital [10] to understand the formation and the thermalization of the strongly interacting Quark Gluon Pasma (QGP) at RHIC and LHC.

2.3 Understanding and Exploring QCD

The H1 and ZEUS at HERA discovered surprising behaviour in previously unexplored regions. Principle among these was the discovery that the proton contains a substantial

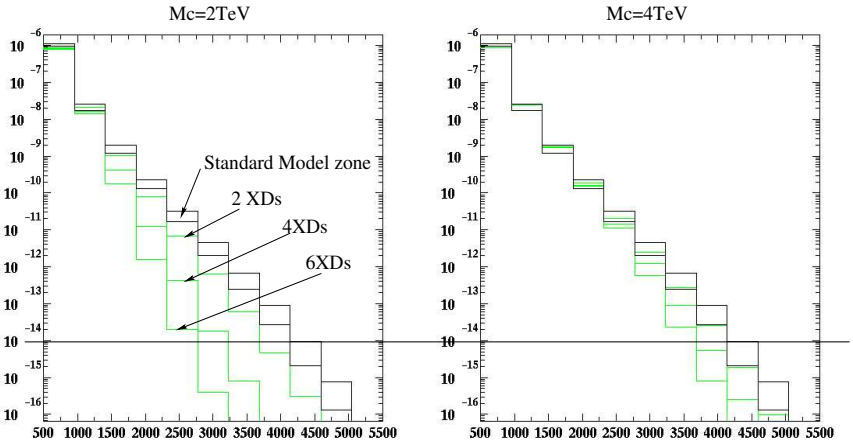

Figure 3: Di-jets cross section (mb) predictions at LHC versus P_t (GeV)with two compactification scales. At $M_c = 4\ TeV$ (right) the predictions fall into the Standard Model band bounded by the present uncertainties on the PDFs [15]. The horizontal line corresponds to an integrated luminosity of 100 fb^{-1}.

quantity of quarks and gluons at very low x values. There is a steep rise of the structure function F_2 and of the gluon density with x decreasing [11]. Although this feature had been anticipated qualitatively, the distribution of quark and gluon momenta at low x had not been predicted and its quantitative understanding represents still today a significant theoretical challenge which needs to be guided by data at lower x values. Also, the possibility that the gluon component might saturate remains an unanswered question. The inclusive HERA data can be fully described by the DGLAP equations [12] and there is no evidence that the saturation domain has been reached. The (x, Q^2) position of the saturation limit requires further experimental guidance. In addition, diffractive processes contributing to deep inelastic processes were found to be more substantial than expected [13]; another feature which still lacks a theoretical understanding and requires further experimental explorations.

2.4 Precision of PDFs

The study of the structure of the proton is not only a fascinating topic in its own right but also a perequisit to predict the cross sections of production of the Higgs Boson or other Standard Model phenomena at the LHC. As has been shown at this conference [14] there is still an uncertainty of about 10% on the cross sections of W bosons at LHC, pending on the data set which are used to extract the gluon density and the method to take into account the heavy quark mass threshold. The uncertainty on PDFs could be a severe limitation to the discovery of new phenomena at LHC. A typical example is the discovery of extra-dimensions which would be restricted to a compactification scale of 2 TeV [15] (Figure 3).

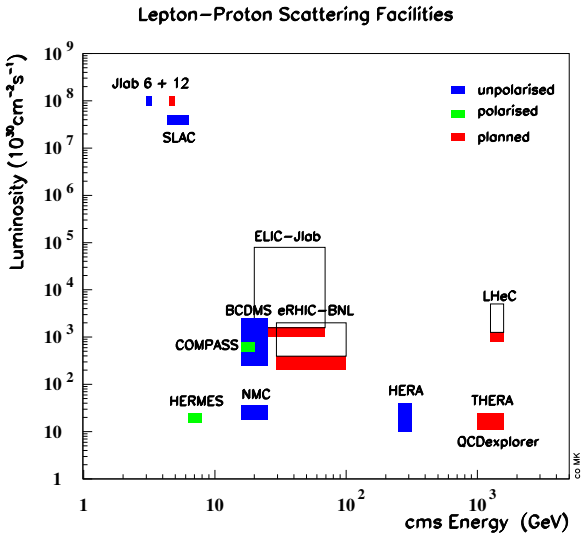

Figure 4: Energy and luminosity for existing (dark, blue boxes) and prospects for new (grey, red boxes) facilities in lepton-proton DIS. For the polarised facilities (green boxes) no dilution factor has been taken into account.

2.5 Relation between quark and lepton sector

Despite intensive searches with the full HERA statistics of 1 fb^{-1} (0.5 fb^{-1} per experiment) no clear evidence for new physics has been found. The hope to find a relation between the quark and the lepton sectors beyond the standard Electroweak interaction has not been fulfilled. But the new physics which is expected at the TeV level may generate new motivations for futher study of the electron parton interaction.

3 Proposed projects

3.1 JLAB 12 GeV

Amongst the future facilities which are under consideration to extend the study of the lepton nucleon deep inelastic scattering, the most advanced is the 12 GeV Upgrade of the electron beam at Jefferson Lab (lower part of Figure 7). Scope of the project includes doubling the accelerator beam energy by adding new cryomodules and upgrading magnets, a new experimental Hall and upgrades to the existing three experimental Halls [16]. The preliminary baseline range has been approved in February 2006, Critical Decision 1 by the DOE (CD-1). The construction and performance baseline (CD-2) is expected to be approved in September 2007. The construction could start in 2008 and the commissioning of the accelerator by 2013. Although the 5 GeV energy in the center-of-mass is rather modest, the huge luminosity, up to 10^7 higher than at HERMES when no dilution nor average polarisation factor are applied (Figure 4), gives access to the valence quark region in the perturbative QCD domain up to $Q^2 = 8\ GeV^2$. It is expected to allow for a precise measurement of the spin and flavour dependence of the valence quark region, both in nucleons

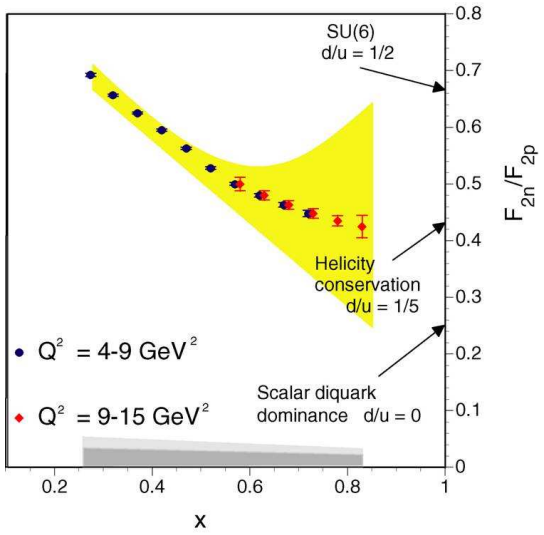

Figure 5: Predicted precision on F_2^n/F_2^p at JLab 12 GeV compared to the present uncertainty (yellow band) and to various theoretical predictions as $x \to 1$.

and nuclei. It gives access to the unique domain where the proton momentum is carried by one parton. A beautiful example would be to solve a long standing issue : the d/u ratio as $x \to 1$ (Figure 5) .

3.2 EIC

A new high energy electron-ion collider (EIC) has been identified [17] as an optimal experimental approach to address essential questions on quark gluon structure of the proton and of the nuclei and to explore QCD dynamics at high density of quark-gluon matter. The goals for the electron-ion collider include:

- A center-of-mass range from 20 GeV (to overlap with muon fixed target experiments at CERN) to 100 GeV to access the low x domain and explore saturation phenomena in nuclei.
- A high luminosity electron/positron ion collider of at least $10^{33}/cm^2/s$.
- Polarized ($\sim 70\%$) electron, positron, proton and neutron effective beams.
- Nuclear beams from Deuterium to Uranium.

There are at present two concepts to realize EIC:

1. To construct an electron beam (either ring or linac) to collide with the existing RHIC ion complex. This is known as eRHIC
2. To construct an ion complex to collide with upgraded CEBAF accelerator. This is known as Electron-Light-Ion-Collider or ELIC.

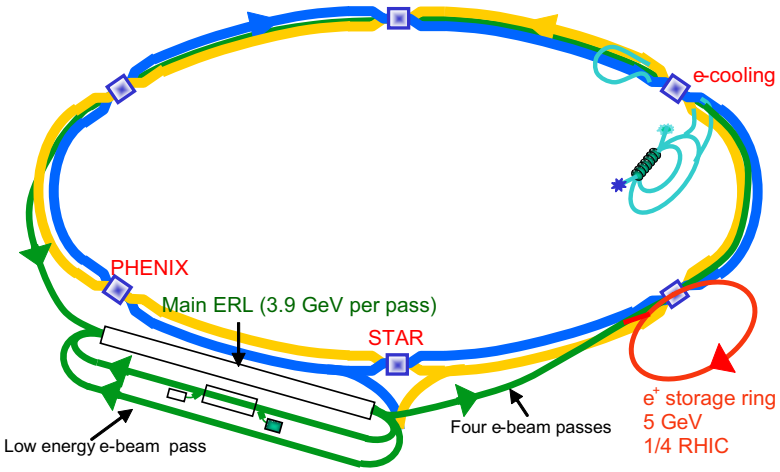

Figure 6: Design layout of the eRHIC collider based on the Energy Recovery Linac.

3.2.1 eRHIC

The existing RHIC complex allows polarised protons to be stored for collisions from 30 to 250 GeV/c. It should be soon (by 2010) possible to accelerate all nuclei up to Uranium to 100 GeV/c per nucleon (approved project EBIS) and to have a 10-fold increase of luminosity. This is the project RHIC-II which is not yet approved but expected to be ready by 2014. On longer term there are still two design options to realize eRHIC:

1. An eRHIC Linac-ring design, which involves construction of a 10 GeV/c Energy Recovery Linac (ERL)(Figure 6). It is presently the most promising design [18]. As many as four electron-ion interaction points are possible.The peak luminosity is 2.6 $10^{33}/cm^2/s$ with potential for upgrade (Figure 4). The high intensity polarized electron current source and the energy recovery capability require extensive R&D effort.
2. An eRHIC ring-ring (RR) design , which involves construction of a ring of 10 GeV/c electrons or positrons along side the RHIC. The storage ring design is more mature than the ERL-based design. It is based on existing technology but the luminosity would be 5 to 10 times smaller than in the ERL option. Today, both designs have similar cost and could be operational at BNL by 2019 [18].

3.2.2 ELIC

An ambitious design is pursued at Jefferson Lab [16]. It uses the 12 GeV upgraded CEBAF linear accelerator and requires the construction of a 30 to 225 GeV ion storage ring in its vicinity (Figure 7). A peak luminosity of up to about $10^{35}/cm^2/s$ looks achievable for electron-light ion collisions at a center-of-mass energy between 20 and 90 GeV (Figure 4). It requires a vigorous R&D but could start at $10^{33}/cm^2/s$ with state-of-the art technology except for electron cooling. Four interaction regions for detectors are possible. It could be operational by 2024.

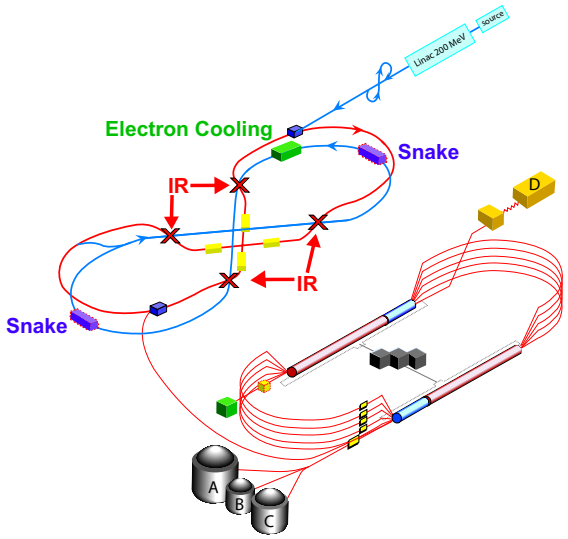

Figure 7: ELIC lay out. Upper part : ion complex. Lower part : the 12 geV upgrade of CEBAF.

3.2.3 Highlights of EIC Physics

The scientific case for EIC addresses questions central to the study and the exploration of QCD. Here a very small selection of the highlights is given as an illustration of the rich physics programme of EIC.

The spin structure of the nucleon A very spectacular improvement on the precision of the contribution of gluons to the spin of the proton is expected [19] from measurement of scaling violations of the $g_1(x, Q^2)$ spin structure functions down to $x \sim 10^{-4}$ or (and) of the measurement of the photon gluon process from charm production (Figure 8). The huge luminosity gives also a reasonable hope that it would be possible to quantify at some level how the orbital motion of quarks in the nucleon contributes to the nucleon spin from the measurement of the General Parton Distributions in hard exclusive processes [17].

Nuclear matter The low x domain ($x < 0.01$) at Q^2 values in the perturbative region (Q^2 of a few GeV^2) is still completely unknown. Measurement of the structure function F_2 and of the longitudinal structure function F_L would give access to the gluon distribution in nuclei at very low x. In Figure 9 , the ratio of gluon distributions extracted from the longitudinal structure function is shown for 10 nucleon fb^{-1} data for DIS and lead nuclei. Only statistical errors are shown. It would provide an impressive discrimination between the various models of shadowing in nuclei. Only statistical errors are shown The effects are so large that systematics should not spoil the physics message in the low x regime which is relevant for formation of hot and dense gluonic matter when nuclei are smashed together at RHIC and the future LHC.

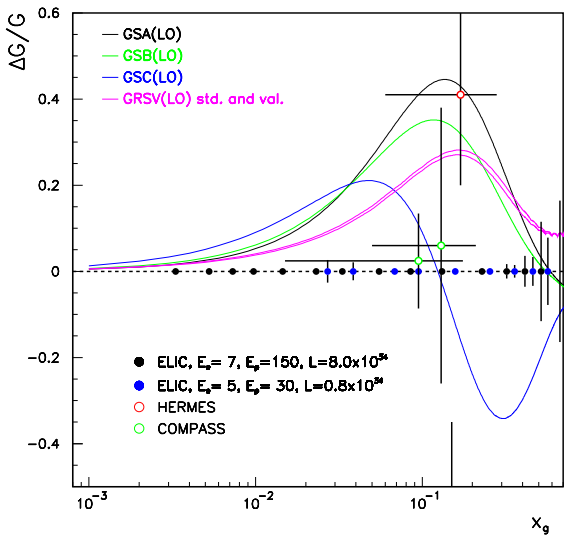

Figure 8: Projected uncertainties in $\Delta G(x)/G(x)$ from the charm production at the EIC. The integrated luminosity is 10 fb^{-1} for the 10 GeV electron on 250 GeV proton measurement, and 2.5 fb^{-1} for 5 GeV electrons on 50 GeV protons. For comparison, COMPASS and HERMES data points are shown.

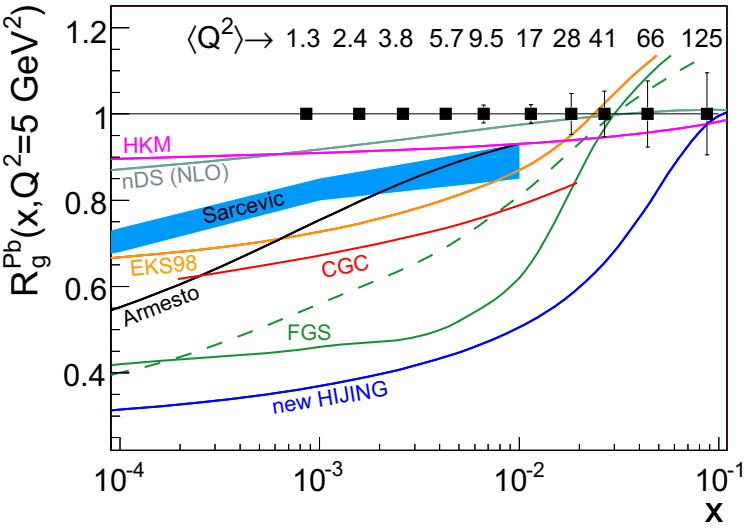

Figure 9: The ratio of gluon distribution in Pb nuclei to those in deuterium. The error bars correspond to statistical uncertainties for $10/A$ fb^{-1} at the EIC. A variety of model predictions which differ widely are shown.

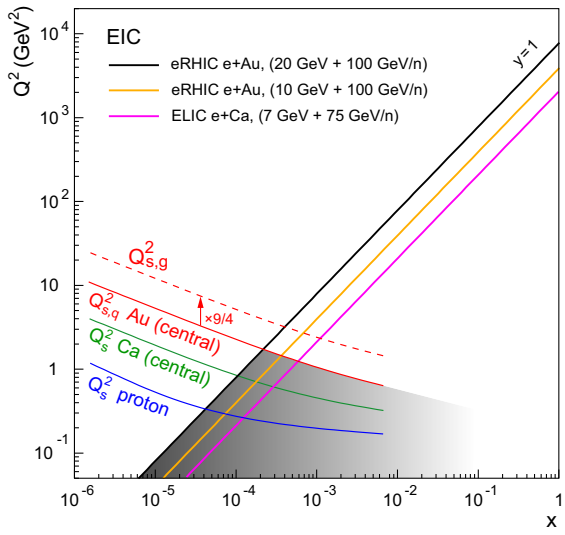

Figure 10: Kinematical acceptance in the (Q^2, x) plane for the two concepts to realize EIC, eRHIC and ELIC. Lines showing the quark $Q^2_{s,q}$ or the gluon $Q^2_{s,g}$ saturation scale are superimposed.

QCD at low x The strong rise of the gluon distribution as $x \to 0$ observed at HERA suggests that the gluon density in the proton attained its maximum values and saturates at lower x than accessed at HERA in the proton, or at even a bit larger x values in heavy nuclei. The saturation value Q^2_s on gold could be around 2 GeV^2 at $x = 10^{-3}$, a domain fully accessed at EIC (Figure 10).

3.3 LHec

The LHC will explore a new range of mass and energy which goes far beyond the domain of HERA ($\sim$ 300 GeV center-of-mass energy). An attractive proposition for an e-p collider [20] operating in the energy domain of the LHC is to make use of the 7 TeV LHC p beam by colliding it with an intense electron and positron beam stored in a ring mounted above the LHC, a Large Hadron Electron Collider (LHeC). There appears to be sufficient space to place the lepton beam line above the LHC magnets in the arc sections. A feasibility study using an electron ring of 70 GeV energy leads to an estimated luminosity of about $10^{33}/cm^2/s$, at a center-of-mass energy of 1.4 TeV (Figure 4). It is premature to have a time schedule. However a new ring cannot be installed before the LHC has produced physics and has, very likely, been upgraded to higher luminosity.

3.3.1 Highlights of the Physics at LHeC

The physics potential would not only be to increase by more than one order of magnitude the x and Q^2 limits reached at HERA in e-p collisions but also, with heavy ions in the LHC ring, to study the e-A interactions in a completely unknown domain. Today the most attractive physics motivation is probably the 1.4 TeV energy in the center-of-mass of the

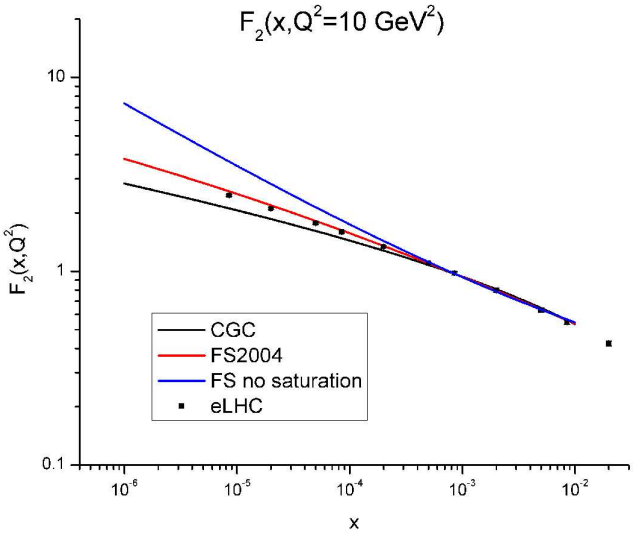

Figure 11: Predicted uncertainty on F_2 at very low x with the LHeC. The integrated luminosity is 1 fb^-1. The statistical precision is below 0.1% and systematics are about $1-3\%$.

electron-parton interaction, a very promising domain for new physics. Workshops for a deeper evaluation of the physics potential and a thorough evalation of the LHeC physics in its relation to the LHC will be organised [21]. A few examples can already give a foretaste of the physics potential thanks to the unprecedented very high luminosity and the very high energy.

Very very low x physics HERA has taught us a lot on low x physics but many questions are not fully answered. Figure 11 shows how precise data at very low x could clearly establish saturation at Q^2 values where perturbative QCD calculations apply [22]. It could distinguish between models of saturation.

Precision QCD The gluon density extracted from the QCD fit of the inclusive cross section at HERA has still an overall error of about 20% at $Q^2 = 4\ GeV^2$. Simulation shows (Figure 12) that the experimental precision of the gluon density at LHeC could be of about 3% at low x, down to $x = 10^{-6}$ [23]. It should also be also possible to extract from the scaling violation of the structure function F_2 the strong coupling constant α_s with a relative precision of three per mil at the Z mass [23].

Low x in protons and nuclei In eA interactions LHeC extends by three orders of magnitude towards lower x the range so far reached in fixed target experiments. In symbiosis with RHIC and ALICE it could help disentangling Quark Gluon Pasma from shadowing or parton saturation effects. In Figure 13 the gluon density has been extrapolated from HERA measurements towards lower x. It shows how the saturation point (also called unitarity limit) could be reached in e-p collisions at $Q_s^2 \sim 5\ GeV^2$ and at much higher Q_s^2 values in e-A interactions when the $A^{1/3}$ increase of the gluon density in nuclei is taken into ac-

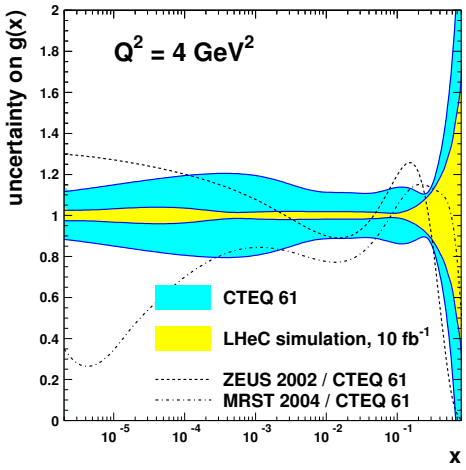

Figure 12: Expected uncertainty on $g(x)$ at the LHeC.

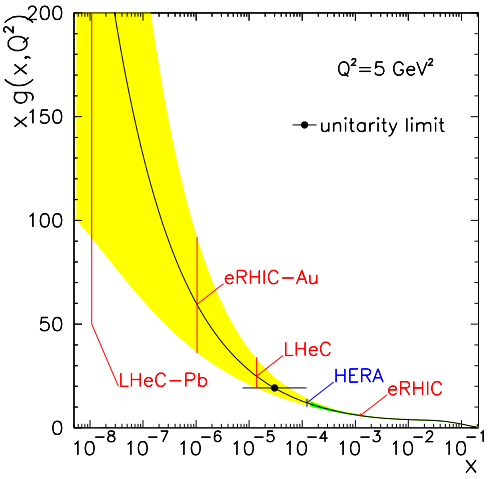

Figure 13: The gluon distribution from a NLO DGLAP QCD analysis of H1 data extrapolated to much lower values of x. The unitarity limit together with the region which can be accessed in e-p, e-Au and e-Pb scattering at the EIC and the LHeC are shown.

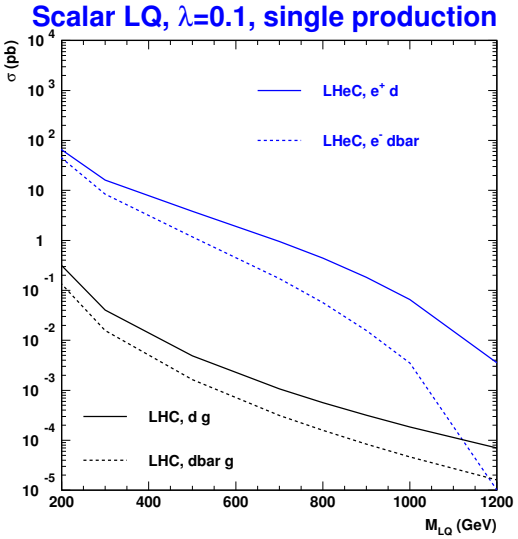

Figure 14: Single LQ production cross section at the LHeC (top) and LHC (bottom) for a scalar LQ coupling to e^+d with a coupling constant $\lambda = 0.1$. The integrated luminosity is 100 fb^{-1} for the LHC and 10 fb^{-1} for the LHeC.

count [22]. The saturation point is likely to be observed in e-p scattering at the LHeC and its effects in e-A scattering should be very large.

Physics Beyond the Standard Model Sensitivity to unknown physics beyond the Standard Model can be quantified within model assumptions. The Leptoquark production is an example. The high energy of the LHeC extends the mass range of single Leptoquark production up to ~ 1 TeV [24], the same limits as in the pair production at LHC. An e-p collider, providing both baryonic and leptonic quantum numbers in the initial state, is unique to study properties of an electron-quark resonance. A measurement of the asymmetry between the e^+p and e^-p cross section would determine the fermion number of the Leptoquark production [24]. The single Leptoquark production at the LHC could as well provide the Fermion number by comparing the signal cross sections with an e^+ and an e^- coming from the decay of the Leptoquark. However, the single Leptoquark production cross section at LHC is two orders of magnitude lower than at the LHeC (Figure 14).

4 Complementarity of lepton-hadron and hadron-hadron facilities

We have seen in the example of the leptoquark how the LHeC would provide complementary information to the LHC : discovery at LHC and measurement of quantum numbers at LHeC.

More generally, the physics adressed in DIS facilities provides complementary information to hadron hadron collision or can be complemented by information from hadron hadron collisions, in particular in PDFs determinations, study of nuclear matter or spin structure of the nucleon.

4.1 Complementarity of p-p and e-p on PDFs

When extracting the PDFs, the main source of informations on quark densities comes from DIS experiments on fixed target at HERA. Complementary information has been provided by Drell Yan pair, prompt photons and di-jets in p-p scattering. At this workshop it has been shown [25] how measurements from LHC may improve knowledge of gluon density at low x from the W rapidity distribution and at high x from the high transverse momentum jets. The W asymmetry should provide an additional constraint on low x quark distributions. However, the present contribution of the Tevatron to PDFs shows that we should not expect miracles. It is not a substitute to lepton-nucleon DIS.

4.2 Complementarity of polarized $\vec{e}-\vec{N}$ and $\vec{p}-\vec{p}$ facilities

So far information on spin structure of the nucleon comes from polarised lepton-nucleon fixed target experiments at SLAC, CERN (muon beams) and DESY down to $x \sim 0.01$. Further data on the densities $\Delta u, \Delta \bar{u}, \Delta d, \Delta \bar{d}$ at relatively large x in the nucleon will come from RHIC through its W-physics program, and from the 12 GeV upgrade at JLAB. Only an e-p collider, as the EIC, with polarised electron and protons (deuterons) can give access to the low x domain which is crucial for the determination of the integral of spin distributions and to test the very fundamental Bjorken Sum Rule [26].

4.3 Complementarities of p-A and e-A studies

The complementarity between lepton-nucleus, proton-nucleus and nucleus nucleus studies can be shown in two different types of study of nuclear matter :

Saturation at low x Saturation models predict that the saturation limit will be well inside the (Q^2, x) range probed at RHIC and LHC in pA collisions [27] . However factorization is uncertain in the strong gluon field regime even for inclusive observables [28]. It may turn out that e-A data in the same $(Q2, x)$ region are vital to understand the dynamics of saturation.

Hot and dense matter To further explore and quantify the properties of the new collective behaviour observed at RHIC in ion-ion collisions, upgrades at RHIC are planned. At the LHC, p-p, p-A and A-A collisions will provide substantially higher energies. To fully understand the dynamics of a Quark Gluon Plasma, a precise knowledge of the initial parton distribution in nuclei, would be an important asset which can be independently extracted from e-A collisions in the same kinematic range at the EIC [29].

5 Conclusion

To conclude I would like to express a few personnal comments:

- The physics of DIS will not stop with the end of data taking at HERA.

- The final data of HERA will be an important asset to high energy physics. Precision of most results is still dominated by experimental and theoretical systematic uncertainties. All efforts should be made to achieve the highest possible precision. It will be a safe and cheap investment in the future.
- The 12 GeV upgrade of the electron beam at Jefferson Lab is on the right track to be finally approved and to get new and precise insights into the valence quark region at Q^2 of a few GeV^2.
- The proposed Electron Ion Collider (EIC) at Brookhaven or Jefferson lab would be a real break through in nucleon spin and nuclear matter physics. It's urgent to establish a process to choose the best design. It should be a trade-off between luminosity, energy, time schedule and cost.
- The project of a Large Hadron Electron Collider is a very attractive complement to the proton-proton and ion programmes at CERN. But in Europe it would be in competition to all other future facilities beyond the fist phase of the LHC. Today it is quite uncertain to be supported by the high energy physics community and the european funding agencies, unless new developments at LHC indicate the physics case becomes even more desirable.

6 Acknowledgments

I thank all the speakers of the Future of DIS session for their enthusiastic talks, and Abbay Deshpande, Max Klein, Naomi Makins and Alexei Petrukhin for valuable help.

References

[1] Slides:
`http://indico.cern.ch/contributionDisplay.py?contribId=17&sessionId=2&confId=9499`

[2] R. Hofstadter, Phys. Rev. **98** 217 (1955).

[3] X. Ji, Phys. Rev. Lett. **78** 610 (1997).

[4] JJ. Aubert *et al.* EMC Collaboration, Phys. Lett. **B123** 275 (1983).

[5] A. Deshpande *et al.*, Ann. Rev. Nucl. Part. Sci. **55** 165 (2005).

[6] M. Arneodo, Phys. Rep. **240** 301 (1994).

[7] L.V. Gribov, E.M. Levin and. M.G. Ryskin, Phys. Rep. **100** 1 (1983).

[8] H. Kowalski, T. Lappi and R. Venugopalan, *Nuclear enhancements of universal dynamics of high parton densities*, arXiv:hep-ph/07053047 (2007).

[9] N. Armesto, J. Phys. **G32** R367 (2006).

[10] EIC Collaboration,*Physics Opportunities with e+A Collisions at an Electron Ion Collider*, White paper final, April 4 (2007).

[11] I. Abt *et al.* H1 Collaboration, Nucl. Phys. **B407** 515 (1993); M. Derrick*et al.* ZEUS Collaboration, Phys. Lett. **B316** 412 (1993).

[12] G. Altarelli and G. Parisi, Nucl. Phys. **126** 298 (1977);
Y.L. Dokshitzer, Sov. Phys. JETP **46** 641 (1977);
L.N. Lipatov, Yad. Fiz. **20** 181 (1974);
V. Gribov and L. Lipatov, Sov. J. Nucl. Phys. **15** 438 (1972).

[13] M. Derrick*et al.* ZEUS Collaboration, Phys. Lett. **B315** 481 (1993); T. Ahmed*et al.* H1 Collaboration, Nucl. Phys. **B429** 477 (1994).

[14] W.K. Tung, *Update on CTEQ global analyses*, these proceedings.

[15] S. Ferrag, arXiv:hep-ph/0407303 (2004), proceedings of 39th Rencontres de Moriond on QCD and High-Energy Hadronic Interactions, La Thuile, Italy (2004).

[16] A. Lung, *Future plans at Jefferson Lab: 12 GeV Upgrade and ELIC*, these proceedings.

[17] EIC Collaboration,*A High Luminosity, High Energy Electron-Ion-Collider*, White paper final, April 24 (2007).

[18] S. Aronson, *Future plans at BNL: RHIC-II and eRHIC*, these proceedings.

[19] A. Bruell, ΔG*, spin/flavour and GPDs at EIC*, these proceedings.

[20] J.B. Dainton *et al.*, *Deep Inelastic Electron-Nucleon Scattering at the LHC*, arXiv:hep-ex/0603016 (2006).

[21] J.B. Dainton, *LHeC*, these proceedings.

[22] P. Newman, *Low x physics at the LHeC*, these proceedings.

[23] M. Klein, *Parton Distributions from the LHeC*, these proceedings.

[24] E. Perez, *LHeC and Physics Beyond the Standard Model*, these proceedings.

[25] A.M. Cooper-Sarkar, *Impacts and constraints on PDFS at ATLAS*, these proceedings.

[26] J.D. Bjorken, Phys. Rev. **148** 1467 (1966);
Phys. Rev. **D1** 1376 (1970).

[27] D Kharzeev and M. Nardi, Phys. Lett. **B 507** 121 (2001);
D Kharzeev, E. Levin and M. Nardi, Nucl. Phys.**A 747** 609 (2005).

[28] J.W. Qiu and G. Sterman, Nucl. Phys.**B353** 137 (1990).

[29] A. Accardi *et al.*, in CERN Yellow report, *Hard Probes in Heavy Ion collisions at the LHC*, arXiv:hep-ph/0308248 (2003).

Hadronic Final States

Duncan Brown[1], Daniel Traynor[2], Alexander Savin[3] and Giulia Zanderighi[4]

1- University of Virginia - Dept. of Physics
382 McCormick Rd, P.O.Box 400714, Charlottesville, VA 22904-4714, USA

2- Queen Mary, University of London
Mile End, London, E1 4NS

3- University of Wisconsin-Madison,
1150 University Ave., Madison, WI 5370-1390, USA

4- CERN - Theory Division, Geneve 23, CH-1211.

In this summary we give a concise overview of the experimental and theoretical results, which were presented during the QCD and Hadronic Final State Working Group sessions at the DIS 2007 workshop.

1 Introduction

Final states provide a unique source of information to study elementary particle interactions. They make it possible to test our general understanding of QCD, explore QCD evolution in limiting regimes and also provide a solid reference for new physics searches. It is beyond question that precise input from the Standard Model (SM) is needed for many new physics searches that could be carried out at the upcoming LHC, most notably precise values of α_s and of the parton density functions (PDF) are needed. The role of HERA and the Tevatron in this respect is indisputable. In this document we summarize the current experimental and theoretical efforts in this direction presented at our Working Group [1].

2 Theoretical progress

2.1 Higher orders and formal developments

One of the highlights of our Working Group was the presentation of the full NNLO calculation of $e^+e^- \to 3$ jets by Aude Gehrmann [2]. The main motivation for this calculation is that the current error on $\alpha_s(M_Z) = 0.121 \pm 0.001(\text{exp}) \pm 0.005(\text{th})$ is dominated by theory and that this uncertainty largely comes from missing higher orders. A reduction of this error can be achieved by computing NNLO 3-jet event shapes and jet rates. This means computing 2-loop matrix elements with 3 partons in the final state, one-loop matrix elements with 4 partons and tree-level five parton final states. Additionally one needs to develop a formalism to cancel divergences before clustering partons into jets, this is done with a NNLO antenna subtraction [3]. After implementing results in an extended version of the program EERAD2, one can obtain a thrust distribution at NNLO for all possible color structures. The results presented show that large cancellations between the various color configurations occur, high precision results are therefore needed. This work is currently in progress, together with an implementation of other event shapes and 3-jet rates. This will allow a first NNLO determination of α_s from event shape data.

An essential ingredient in performing fixed order calculations within any quantum field theory is a method to regulate the ultraviolet (UV) divergences appearing in perturbative

calculations. One of the most widely used schemes is dimensional regularization (DREG), where one extends the number of dimensions to $D = 4-2\epsilon$. It has long been known however that dimensional regularization breaks supersymmetry (SUSY), one of the promising new physics scenarios which might be discovered at the LHC, because the number of degrees of freedom for fermions and bosons is different. Precision calculations within SUSY are most conveniently done in a scheme which preserves the boson-fermion symmetry. An alternative to DREG is provided by dimensional reduction (DRED), where one splits the four-dimensional gluon field in a D-dimensional component and a so called ϵ-scalar, a scalar whose coupling to fermions vanishes in four dimensions (*evanescent coupling*).

One attractive feature of SUSY is the unification of couplings close to the grand unification (GUT) scale. If one wants to test unification within SUSY one needs to relate a five-flavour $\overline{\rm MS}$ coupling at the electroweak scale, $\alpha_s^{(5),\overline{\rm MS}}(M_Z)$, where all heavy degrees have been integrated out (decoupled), to a full $\overline{\rm DR}$ coupling at the GUT scale, $\alpha_s^{({\rm full}),\overline{\rm DR}}(M_{\rm GUT})$. To obtain a next-to-next-to-leading logarithmic (NNLL) result one needs three-loop QCD running of the $\overline{\rm MS}$ coupling from M_Z up to $M_{\rm SUSY}$, the typical mass scale of SUSY particles, two-loop decoupling and three-loop running in SUSY from $M_{\rm SUSY}$ up to $M_{\rm GUT}$. Robert Harlander reported on this involved calculation [4]. The result turns out to be almost independent of the decoupling scale. Such a feature was also present in the Supersymmetry Parameter Analysis (SPA 05) prescription which was however based only on one-loop decoupling and one-loop running.[a] The difference between the two results is larger than the experimental uncertainty by almost a factor of four. A peculiar feature of the presented results is that the $\overline{\rm MS}$–$\overline{\rm DR}$ conversion and the $\overline{\rm DR}$ running both depend on the unphysical coupling of the ϵ-scalars to quarks.

Higher order calculations are crucial in a variety of different contexts. However, at higher orders one has to deal with highly complex structures. Johannes Bluemlein reported on a method to simplify considerably physical quantities appearing in Quantum Field Theories (QFT) which depend on a single scale [5]. Single scale problems in massless or massive perturbative calculations in QFT can be expressed in terms of finite harmonic sums. These sums occur in the ϵ expansion of the integrals for higher order corrections to QCD spitting functions and Wilson coefficients for space-like and time-like processes and high-energy scattering processes such as Bhabba scattering and many others.

The idea is to perform a Mellin transform and exploit the symmetry of Feynman parameter integrals in Mellin space to perform simplifications. One derives algebraic and structural relations between multiple harmonic sums, and uses those relations to compactify considerably the result of higher order corrections. Applications of the method include the representation of $\mathcal{O}(\alpha_s^2)$ Drell-Yan and Higgs-Boson production cross-sections, anomalous dimensions and Wilson coefficients at $\mathcal{O}(\alpha_s^3)$, asymptotic heavy flavor Wilson coefficients up to $\mathcal{O}(\alpha_s^3)$, and soft and virtual corrections to Bhabba scattering. Whether the method can be extended to multi-scale problems is something to explore in the future.

At partonic level, a typical final state in small-x deep inelastic scattering off nuclei and hard proton-nucleus collisions can be characterized by the multiplicity of color-excited nucleons. Within the Reggeon field theory, each color-exited nucleon is associated with

[a] This is not consistent, one-loop matching needs a two-loop running.

the unitarity cut of the pomeron exchanged between projectile and nucleus. The pre-QCD Abramovsky, Gribov and Kancheli unitarity cutting rules formulated in the 1970s relate precisely these multi-pomeron exchange contributions to total, diffractive and inelastic cross sections.

Koyla Nikolaev explained how, starting with an exact k_t-factorization for hard pQCD in nuclear environment, a dramatic revision of the AGK rules within QCD is found [6]. Two kinds of unitarity cut pomerons emerge which describe the color excitation and color rotation inelastic interactions. The departure of the unitarity cutting rules from the ones suggested by AGK stems from the coupled-channel features of non-Abelian intranuclear pQCD. In the Reggeon field theory language, the results entail a large variety of multi-pomeron couplings which vary from one universality class for hard pQCD processes to another.

2.2 Jets, event shapes and unintegrated PDFs

Jets enter a variety of measurements at colliders. What a jet roughly is is quite intuitive: a bunch of particles created in a hard interaction moving around a common direction and depositing energy on their way. Theoretically, jets are tools to create a link between the hadrons measured in detectors and perturbative calculations. Given a set of four-vectors, they are fully specified by the choice of a jet-clustering algorithm, its parameters and a recombination scheme. A variety of algorithms exist (the most simple classifications are cone types and sequential recombination type algorithms), some better than others as far as infrared safety, sensitivity to higher order or to hadronization effects are concerned. Once jets are defined, a number of observables can be studied.

One interesting variable is the azimuthal correlation between two jets in QCD hard processes, $\Delta\phi \equiv |\phi_{j1} - \phi_{j2}|$. In the presence of only two hard partons, without additional radiation, the two jets are back-to-back, $\Delta\phi = \pi$, the non-zero azimuthal correlation provides therefore a measurement of the additional QCD radiation. The azimuthal correlation is sensitive to a variety of physical effects: it depends on the jet algorithm and recombination scheme; it is sensitive to soft/collinear gluon radiation and non-perturbative effects; according to the recombination procedure in the clustering it can be affected by so-called non-global logarithms [7] and it is one of the observables commonly used for Monte Carlo (MC) tunings. Non-global logarithms have been the subject of many studies recently. The current status is that they can be resummed numerically in the large N_c limit with single-log accuracy. Some time ago, it has been shown that the use of a jet-algorithm reduces the presence of undesired non-global logs [8], however recently it has been shown that additional logs can originate from using a jet-clustering [9]. For the azimuthal correlation the recombination scheme turns out be to decisive to establish the presence of non-global logs: if one uses a recombination scheme which adds four-momenta, as is done at the Tevatron, the observable is non-global, if on the contrary one uses an E_t weighted average azimuth, as was done at HERA, then the observable is continuously global.

At last year's DIS workshop experimental results were presented by Magnus Hansson which did not agree with NLO 3-jet predictions [10]. Triggered by this lack of agreement between data and theory theoretical work started to improve on the theoretical accuracy. The disagreement between fixed order perturbative calculations and data is to be expected in the back-to-back region since in this region multiple soft-collinear effects become important. Yazid Delenda reported on the resummation of soft-collinear logarithms in the azimuthal

correlation distribution in the region $\pi - \Delta\phi \sim 0$ [11]. Work in progress is now the matching with fixed NLO predictions, the inclusion of power corrections and the extension of this study to the Tevatron for which similar measurements exist.

Event-shapes provide a continuous measure of energy and momentum of the final state. Usually, they are computed perturbatively at NLO and they have large soft-collinear logarithms which can be resummed at next-to-leading logarithmic (NLL) accuracy. Additionally, they have large hadronization corrections which give rise to $1/Q$ corrections, where Q is the hard scale of the process. These corrections can be modeled in terms of one universal parameter α_0. Universality implies that if one performs a combined fit of α_s and α_0 then the values obtained should be independent of the event-shape used in the fit. This picture proved to work well both in e^+e^- and DIS. However, it has been tested only in three-jet event shapes, those, like the thrust, whose first non zero contribution comes from events with three hard partons (one incoming and two outgoing in DIS).

Andrea Banfi presented results for four-jet event shapes, whose first non-zero contribution is due to configurations with at least four partons in the event [12]. Specifically he considered $K_{\rm out}$, roughly the radiation out of the plane spanned by the three hardest partons and the D-parameter, proportional to the determinant of the energy-momentum tensor, $\theta^{\alpha,\beta} \equiv \sum_h p_h^\alpha p_h^\beta/(Q|\vec{p}_h|)$. Andrea presented fits of α_s and α_0 from distributions of the D-parameter for various values of $y_{\rm cut}$, the cut used to select events containing three hard jets. It turns out that fits from the D-parameter give values of α_s and α_0 which are compatible with other three-jet event-shapes, where the fit region is limited to the region to the right of the peak of the distribution. For $K_{\rm out}$ on the other hand the shape of the distribution did not allow to perform a consistent fit. A possible explanation is that the $K_{\rm out}$ distribution is sensitive to power corrections from the four-jet region currently not included.

Final state predictions depend critically on which initial state partons enter the hard interaction and on the energy distribution of those partons. This is described by parton density functions. Standard PDFs depend on the factorization scale μ and on the longitudinal momentum fraction x, but they are integrated over the transverse $k_\perp$ component. Unintegrated parton densities (uPDFs) $\mathcal{A}(x, k_\perp^2, \mu)$ keep the information over the transverse component during the perturbative evolution. Cross sections are then given by the convolution of uPDFs with off-shell partonic cross-sections $\hat{\sigma}(x_i, k_\perp^2)$. If one considers e.g. the cross section for a single heavy flavoured parton as a function of p_t, because of momentum conservation at LO $p_t = 0$, and non zero contributions appear first at NLO. If one instead uses uPDFs, the first non-zero contribution opens up already at LO. The advantage of uPDFs is therefore that by having the correct kinematics at LO one reduces considerably the size of the NLO corrections. At high energies the gluon density is dominant, therefore, as a first approximation, one can consider the contribution from gluons uPDFs only.

The uPDF is determined by a convolution of a non-perturbative starting distribution $\mathcal{A}_0(x, \mu_0)$ and the CCFM evolution [13] $\tilde{\mathcal{A}}(x, k_\perp, \bar{q})$

$$x\mathcal{A}(x, k_\perp, \bar{q}) = \int dx' \mathcal{A}_0(x') \frac{x}{x'} \tilde{\mathcal{A}}(x, k_\perp, \bar{q}) \,, \tag{1}$$

where the distribution $\mathcal{A}_0$ is parametrized at a starting scale μ_0 by

$$x\mathcal{A}_0(x, \mu_0) = N x^{-B_g} (1 - x)^4 \,. \tag{2}$$

Hannes Jung presented results of fits of B_g from inclusive F_2 and from semi-inclusive F_2^c, giving values of $B_g = 0.028 \pm 0.003$ and $B_g = 0.286 \pm 0.002$ respectively (for $\mu_0 = 1.2$GeV) [14]. The different value of B_g from F_c^c changes the uPDF significantly, since the discrepancy is not covered by the experimental uncertainty. To resolve the discrepancy one can perform a fit to DIS dijet cross sections. The result for B_g turns out to be very similar to the one obtained from F_2. Regarding the residual discrepancy with the determination of the x component of $\mathcal{A}_0$ from F_2^c one can observe that the rise of the gluon distribution from F_2^c comes from lowest x points. If one considers only $x > 2 \cdot 10^{-4}$ and uses the F_2 value of B_g in the F_2^c distribution one obtains a χ^2/d.o.f. ~ 1.1. Finally, Hannes presented the first measurement of the intrinsic k_t component of $x\mathcal{A}(x, \mu_0)$ assuming a Gaussian distribution $\sim \exp(-(k_{t0} - \mu)^2/\sigma^2)$. The fit to the intrinsic k_t distribution, presented at this workshop for the first time, gives $\sigma \sim 1.5$ and $\mu \sim 1.5$ and is consistent with a Gaussian distribution, although other distributions are not excluded. One additional remark about uPDFs is that one can describe the $\Delta\Phi$ distribution between jets with Cascade using the new fit for the uPDFs.

While NLO predictions for inclusive jet spectra typically have errors $\sim 10 - 20\%$, NLO predictions for heavy jets[b] fare much worse, the uncertainty being around $\sim 40 - 60\%$. The NLO prediction for heavy-jets is thus a poorly constrained NLO calculation. Additionally, the experimental errors of the measurement at the Tevatron are smaller than the corresponding theoretical uncertainty. To understand the reason for the large theoretical uncertainty it is useful to examine the flavour production mechanisms. At LO the only production mechanism for heavy flavour is flavour creation (FC), $ll \to hh$, where l is a generic light flavour and h denotes the heavy flavour under study. At NLO on the other hand two other processes enter, flavour excitation (FEX), $lh \to lh$, where the incoming heavy quark stems from a collinear splitting of an incoming gluon, and gluon splitting (GSP) $ll \to l(l \to hh)$. Since the NLO processes are enhanced by collinear and soft logarithms, $\ln(p_{\mathrm{t,jet}}/m_Q)$ (where m_Q denotes the mass of the heavy quark), they turn out to be more important that the LO contribution. This means that a NLO calculation, which treats FC at NLO, but where FEX and GSP enter only at LO has very large K-factors (~ 5 at the Tevatron and ~ 8 at the LHC, for accessible p_t values) and therefore also very large scale dependencies.

Giulia Zanderighi showed that if one instead clusters events using an infrared-safe, flavour algorithm, which takes into account the difference between quark and gluon QCD production, then flavour becomes an infrared safe quantity. This implies that no logarithms $\ln(p_{\mathrm{t,jet}}/m_Q)$ are present and one can accordingly perform a light-quark calculation e.g. with NLOJET++ [15]. This gains roughly a factor 3 in accuracy: K factors become ~ 1.3 and scale variation uncertainties are around $10 - 20\%$, as is to be expected from a true NLO calculation [16]. The method however requires a good understanding of single and double b-tagging efficiencies, and further experimental investigation in this direction is needed.

2.3 Parton showers and matrix element event generators

QCD Monte Carlo (MC) generators and simulations are vital for physics at the LHC. It is therefore crucial to examine critically different MC components, including perturbative aspects (parton showers, matrix element corrections, matching), non-perturbative aspects

[b] Experimentaly a heavy-jet is any jet containing at least one heavy tagged object.

(hadronization, underlying event) and tuning of the event generators. Parton showers (PS) reflect our understanding of pQCD to all-orders. They are commonly believed to capture at least the leading logarithmic structure. Observables sensitive to radiation in a limited phase space region (energy flow distributions, event shapes, ...) are sensitive to non-global logarithms even at leading order. Is it therefore important to re-examine the accuracy of showers in these instances in order to establish if for example leading non-global logarithms are erroneously tuned in the MC parameters.

The starting point of the study presented by Mrinal Dasgupta is the fact that angular ordering (AO) catches the relevant part of these non-global logarithmic corrections. HERWIG, therefore, which is based on angular ordering is expected to be close to the full resummation of the non-global logarithms (known only in the large N_c limit). PYTHIA (before v.6.4) uses as an ordering variable, the virtuality m^2 and rejects a posteriori configurations which do not respect AO, and is expected to do worse. PYTHIA v.6.4 on the other hand, like ARIADNE, is based on dipole phase space, and should have the full leading logarithmic behaviour. In the study presented by Mrinal Dasgupta these expectations are tested by comparing full resummed results matched to NLO with predictions for parton showers for the radiation in a slice in rapidity $\Delta\eta$ as a function of E_t, the total transverse energy of hadrons in the rapidity slice [17]. It turns out that the above expectations are confirmed unless one takes a quite large region of pseudorapidity, e.g. $\Delta\eta = 3$. For large rapidity slices a large discrepancy is found between the new PYTHIA (v.6.4) and the resummed result. Further studies are needed to clarify this discrepancy and to generally understand the various parton showers in a quantitative fashion. In general, it has been stressed that whenever possible one should compare results from HERWIG and PYTHIA, and when possible of other Monte Carlos.

As stressed above, Monte Carlos today are indispensable tools for many experimental studies. One of their very conventional application is to estimate non-perturbative (NP) effects. NP effects at hadron colliders include both final state hadronization effects and effects due to the underlying event (UE). Single jet inclusive distributions, parametrized in terms of a jet-radius $R \equiv \sqrt{(\Delta y)^2 + (\Delta\phi)^2}$ have $1/p_{t,\mathrm{jet}}$ power corrections due to the hadronization and UE.

Lorenzo Magnea [18] explained that it is possible to show analytically that hadronization corrections are distinguishable from UE because they exhibit a singular dependence on R, while UE effects are proportional to the radiation they collect in a given region and so scale as $\sim \pi R^2$. Lorenzo then presented a MC study where one runs a MC at parton level (p), hadron level without UE (h) and with UE (u). One then selects events with two hard jets with the hardest jet in a chosen p_t range and one defines for each hadron level a measure of the size of the power correction

$$\Delta p_T^{(h/u)} \equiv \frac{1}{2}\left(p_{T,1}^{(h/u)} + p_{T,2}^{(h/u)} - p_{T,1}^{(p)} - p_{T,2}^{(p)}\right), \qquad \Delta p_T^{(u-h)} \equiv \Delta p_T^{(u)} - \Delta p_T^{(h)}. \tag{3}$$

One can examine $\Delta p_t^{(h/u)}$ divided by the leading behaviour in R ($1/R$ for hadronization effects and R^2 for UE) for two different partonic channels, e.g. a quark dominated channel, $qq \to qq$, and a gluon dominated one, $gg \to gg$, both for HERWIG and PYTHIA. With HERWIG the result of this operation is a flat distribution as a function of R, signaling that the leading R dependence has been correctly extracted. Additionally, one can see that

the size of the UE is independent on the hard partonic scattering channel. With PYTHIA on the contrary the UE seems to "know about the hard scattering" i.e. instead of a flat distribution one has a leftover $1/R$ dependence. This is perhaps surprising. Additionally the UE is sensitive to the hard channel (increases when going from quarks to gluons). A correct modeling of the UE is the basis for precision phenomenology at the LHC, since for example this input enters into the determination of the jet energy scale. These types of discrepancies should therefore be addressed soon. The work presented here is based on disentangling hadronization from UE effects by exploiting their different R dependences. It was therefore recommended that, whenever possible, measurements for different values of the jet-radius R should be provided.

In a more general context parton showers rely on the universal soft and collinear (SC) factorization of the QCD matrix elements. This is a universal property and is true to all perturbative orders. In an ideal world this should be the only approximation made in MCs. However, practically all current MCs are subject to many other approximations, e.g. interference diagrams are treated only approximately with angular ordering, the color algebra is valid only in the large N_c limit, spin treatment is usually inexact, other first approximations are carried in order to simplify phase space and further arbitrary techniques are often employed.

Zoltan Nagy reported on ongoing work to formulate a parton shower which removes all the above approximations [19]. The method is based on recursive equations that can be used to generate a lowest order parton shower for hard scattering in hadron-hadron collisions. The formalism is based on the factorization of soft and collinear interactions from harder interactions. It incorporates quantum interference between different amplitudes in cases where the interference diagrams have leading soft or collinear singularities. It incorporates the color and spin information for the hard partons. One of the motivations for this more formal development of a parton shower is to have a method that can be merged to NLO calculations in a natural way.

While parton showers are crucial for many studies, it is also well-known that in many cases parton showers fail dramatically. This is for instance the case in events with many hard jets: a parton shower has the full matrix element only for the primary hard scattering involving few partons, while all other emissions are treated in the soft-collinear approximation.[c] Therefore, any study which looks at properties of events with many hard well-separated particles in the final state should be based on tools which go beyond the soft/collinear approximation of parton showers. Today tree level matrix element generators (ALPGEN, Helac, MadGraph/MadEvent, Amegic++, ...) exist which can treat according to the process up to around 5-8 particles in the final state including full spin correlations/interference. Simon Visscher reported on progress in Madgraph/MadEvent (MG/ME) [20]. Specifically, MG/ME have now two different matching schemes, an MLM type based on event rejection after the PS and a CKKW type based on Sudakov reweighting and vetoing on showers. This work set a basis for a systematic comparison between different generators, matching techniques and shower algorithms. [21]

[c] Traditionally, using the soft/collinear approximation means that there is a deficit of radiation in the large angle region. This is however not always the case, one can enhance the shower arbitrarily so as to fill, even overfill, those regions, but this is artificial and ad-hoc.

As an example Simon presented results obtained with MG/ME for $t\bar{t} + 0, 1, 2, 3 \ldots$ jet events. These processes are important for a variety of reasons. In addition to their interest *per se*, they are a background to $t\bar{t}H$ production and in two-Higgs Doublet Models (2HDM) $pp \to W^+W^-b\bar{b}b\bar{b}$ could be the most interesting channel to discover the charged Higgs. In this case one needs a reliable $t\bar{t} + 0, 1, 2, 3 \ldots$ jet event sample. If one looks at the rapidity distribution of the hardest jet, predictions obtained with Pythia are depleted of radiation in the central rapidity region. Full matrix element based predictions are not, showing the need to go beyond SC approximation of parton showers for this type of analysis.

Despite the fact that QCD and EW corrections are nothing but higher order corrections dictated by the same SM Lagrangian, traditionally the two corrections have mostly been treated separately. Alessandro Vicini reported on a calculation of combined QCD ($\mathcal{O}(\alpha_s)$ + PS)) and EW ($\mathcal{O}(\alpha_{\rm ew})$ + PS) corrections to charged current Drell-Yan (DY) processes at hadron colliders [22]. DY processes are unique at hadron colliders. The presence of high p_t leptons, together with the large cross section makes their detection very easy. DY processes are useful for validating pdfs, as luminosity monitors or to obtain precision measurement of EW observables (M_W, Γ_W...). W/Z production in association with jets is an important background to SM and beyond Standard Model (BSM) signals, especially to new gauge bosons. In pure QCD the state-of-the-art are fully differential NNLO predictions exist [23].

Alessandro Vicini presented results obtained with the HORACE event generator, which includes state of the art EW radiative corrections to DY processes including exact $\mathcal{O}(\alpha_{\rm ew})$ radiative corrections matched to multiple photon radiation via PS. It's a fully exclusive event generator, which can be easily interfaced to QCD showering programs like HERWIG, events are saved in a Les Houches compliant form and it can be interfaced to the LHAPDF package. The QCD and EW corrections are matched with an approximate additive procedure, which works to $\mathcal{O}(\alpha_s\alpha_{\rm ew})$ as long as hard non-collinear radiation effects are not important. Beyond the additive approximation a full two-loop $\mathcal{O}(\alpha_s\alpha_{\rm ew})$ calculation is needed. Results presented for M_T^W and $p_\perp^l$ show that around the jacobian peak positive QCD corrections compensate negative EW corrections and that EW effects are mandatory in order to extract M_W, only QCD PS are not sufficient. Another interesting QCD-EW interplay effect lies in the fact the convolution with QCD PS modifies the relative size and shape of the EW corrections. Due to the presence of EW logarithms, EW effects become important in the tails of distributions ($M_T^W \sim 2$TeV, $p_\perp^\mu \sim 1$TeV) they can amount to up to $\sim \mathcal{O}(30)\%$ corrections, however cross-sections are very tiny in those regions.

3 Particle production in ee, ep, $p\bar{p}$ and pp collisions

3.1 Pentaquark searches

In 2004 a comprehensive program to search for pentaquarks (PQ) in high statistic, high resolution experiments was started by the CLAS collaboration at Jefferson Lab. P. Rossi (CLAS) presented recent results for the four photoproduction channels studied so far [24]. No evidence for a PQ signal was observed. From these results CLAS set an upper limit on the PQ production cross section on protons and neutrons.

M. Del Degan (H1) presented the invariant mass spectrum of the $\Xi\pi$ system, studied using deep inelastic scattering (DIS) data collected with the H1 detector at HERA [25]. A clear signal for the well established unexotic $\Xi(1530)^0$ baryon is observed. Despite having

similar statistics as NA49, the $\Xi^{--/0}$ PQ signal could not be confirmed. Upper limits for $\Xi^{--/0}$ PQ production from H1 are in agreement with those published by the ZEUS collaboration.

3.2 Deuteron and antideuteron production

A first measurement of the production of deuterons and antideuterons in DIS was presented by S. Chekanov (ZEUS) [26]. It is interesting to mention that this is the first measurement of deuteron production in elementary particles collisions. Production rates of (anti)deuterons are significantly reduced relative to the production of (anti)protons, consistent with other world measurements. The production rate of deuterons was measured to be approximately three times larger than for antideuterons. The production rates were also studied in terms of the coalescence model.

3.3 Exclusive final states in e^+e^-

BaBar has now taken over $400fb^{-1}$ of data and has used this data in a variety of tests of QCD using different production channels. The first observation of $e^+e^- \rightarrow \rho^0\rho^0$ and $e^+e^- \rightarrow \phi\rho^0$ was reported by S. Saremi (BaBar) [27]. The final states for these channels are even under charge conjugation. Such processes can be understood in terms the Two-Virtual-Photon Annihilation model. Other results presented were a new test of factorization in the $\overline{B}0 \rightarrow D^* + \omega\pi^-$ channel, for which there is good agreement, and a measurement of the η and η' transition form factors, were the ratio of the form factors is inconsistent with theoretical predictions.

3.4 Identified particle measurements in *ep* and *pp*

Recent results on strange particle production ($K^{\pm}, K^0_S, \Lambda's$) and Bose-Einstein correlation's (BEC) between kaons were presented in a talk given by B. Levchenko (ZEUS) [28]. The parameters for the BEC agree well for different kaons and are consistent with H1 and e^+e^- results. No sizeable barion-antibarion asymmetry was observed. The ratio of baryons to mesons in the resolved photoproduction regime is much larger than in e^+e^- and is not described by Pythia predictions.

This observation agrees well with similar results from *pp*, presented by M. Heinz (STAR) [29]. STAR also presented the p_T spectra for different particles, which for the first time can be described by the NLO pQCD predictions due to improved fragmentation functions (FF) for baryons and strange particles using the light-flavour separated measurements in e^+e^- collisions from OPAL.

3.5 Fragmentation functions at HERA

The scaled momentum spectra in the current region of the Breit frame in DIS *ep* scattering at HERA was measured by ZEUS, presented by B. Brzozowska, with high precision data covering a large range of energy scale (5 to 170 GeV) [30]. The NLO pQCD theoretical predictions cannot reproduce the data in the entire phase space and cannot describe the Q^2 evolution of the x_P distribution. Differences between predictions using different FF were found to be small.

3.6 Particle production in jets

The relative roles of perturbative and non-perturbative QCD in the development of jets have been studied by CDF. In his talk L. Pinera presented the momentum distributions and multiplicity of charged particles in jets, momentum correlations of particles and their k_T distribution [31]. The energy scale range covered in this analysis goes from 20 to 160 GeV. The data are generally well described by pQCD within MLLA approach, but at large k_T the theory predictions significantly deviates from data.

4 Particle production in collisions with heavy-ions

4.1 Property of the Quark-Gluon Plasma

Hadronic final states and their correlations were used by the PHENIX collaboration (talk presented by C. Ogilvie) to investigate properties of the Quark-Gluon Plasma (QGP) and it's impact on particles passing through it [32]. Energy loss and meson suppression deliver information on the density of QPG while direct photons are insensitive to the QPG. These properties can aid the comparison of collisions of protons with that of heavy-ions. The broadening of jets can be explained in terms of induced gluon radiation in the QGP. High p_T jet production is biased towards being produced on the surface of the QGP, the second jet in these types of events has to then travel through the QGP to the far side. Studies of the far side reveal that the second jet is suppressed and takes on the properties of the medium it travels through. Studies show that the medium also responds to the passage of the second jet and heavy quarks are seen to lose less energy than light quarks.

4.2 Colour transparency

A study of colour transparency (CT) was presented by M. Holtrop (CLAS) [33]. The CT was studied in terms of nuclear transparency $T(A, Q^2)$ and is clearly observed in ρ^0 electroproduction, where $T(A, Q^2)$ was measured to increase with increasing Q^2, in a good agreement with predictions of the theoretical model by Kopelovich et al.

4.3 Hadronisation in nuclear environment

Recent results from HERMES were presented by Z. Akopov and Y. van Haarlem [34, 35]. Detailed studies of hadronisation on many nuclear targets were performed. Substantial nuclear attenuation was observed as a function of different kinematic variables. For the first time these studies were done using double-differential distributions. For the first time the formation length of the nuclear attenuation was studied. Absolute measurement of the p_T-broadening has been performed using different targets and hadron types for different kinematic variables.

5 Jet production

5.1 Prompt photons

S. Chekanov (ZEUS) presented recent results on prompt photons with an associated jet in photoproduction at HERA [36]. Prompt photon identification was based on conversion probabilities measured by a dedicated detector - Barrel Pre-sampler. Both PYTHIA and

HERWIG fail to describe the shape and normalization of the cross sections. Best agreement is achieved using the k_T-factorization approach. An improved agreement with other NLO pQCD calculations was achieved by hardening the cut on the transverse momentum of the photon.

The H1 collaboration (talk by K. Müller) has performed prompt photon studies in DIS [37]. The Prompt photon signal was extracted using a log-likelihood approach based on a shower shape analysis. The measurements were done both for isolated photons and photons with jets. The LO MC models underestimate the data but the shapes are generally described. NLO pQCD calculations were not yet available.

O. Atramentov (DØ) presented inclusive photon+jet results in $p\bar{p}$ collisions [38]. Triple differential cross sections were measured as well as the ratios of these cross sections, significantly reducing the effect of experimental and theoretical correlated uncertainties. Four different photon+jet topologies were studied to explore different kinematic regions of the gluon distribution functions. For some kinematic regions quantitative deviations from current QCD predictions are observed.

5.2 Jets photoproduction at HERA

High-E_T jets in photoproduction (PHP) measured by ZEUS and presented by H. Perrey show sensitivity to the gluon PDF and have the potential to further constrain the parton densities of the proton and photon [39]. None of the compared photon PDFs provided an adequate description of the ZEUS resolved data, although the direct enriched cross sections, which are less sensitive to the photon PDF, are in good agreement with NLO pQCD calculations.

The photoproduction of dijet events with a large rapidity gap between the jets was used by ZEUS to estimate the colour-singlet exchange contribution, as reported by A. Savin (ZEUS) [40]. Multi-jet photoproduction was used to study the properties of Multi-Parton Interactions (MPI) at HERA. The low-invariant-jet-mass region can only be described by adding the MPI to the MC simulation, thus providing a good testing ground for different MPI models. This information is very important for understanding the structure of underlying events at the LHC.

5.3 Study of underlying events in DIS

Further studies on underlying events at HERA were performed by H1 using the DIS data by measuring jets with low transverse momenta. S. Osman (H1) demonstrated in his talk, that the standard QCD MC models fail to describe the data in different azimuthal regions with respect to the leading jet [41]. Adding the MPI significantly improves the description at low Q^2 where resolved photon processes are expected to contribute, but still fails at high Q^2. Due to lack of NLO pQCD calculation suitable for this analysis no conclusion from high-order contribution was drawn.

5.4 Charge current jets at HERA

The first charge current (CC) *ep* jet analysis of the HERAII data was presented by H. Wolfe (ZEUS) [42]. For the first time the three- and four-jet events in CC DIS are analyzed. Inclusive jets and multi-jet cross sections were measured. Total polarized inclusive jet cross sections agree with predictions of the Standard Model.

5.5 Jets in ee

An investigation of high momentum hadron and jet production by the OPAL collaboration was presented by A. Krasznahorkay [43]. Previously measured exclusive jet cross sections by L3 was not well reproduced by the pQCD NLO predictions. The new measurement by OPAL is well described by the theory. When compared in the same kinematic regime as L3, the OPAL and L3 measurement do not agree well and this difference has to be understood. The p_T spectrum of hadrons is well described by the calculation except in the very high p_T bin.

5.6 Jets in $p\bar{p}$ and pp

A preliminary measurement of the $b\bar{b}$ dijet production cross section and the angular correlation of the jets was presented by S. Vallecorsa (CDF) [44]. The NLO calculations describe the data well. The $b\bar{b}$ angular correlation shows that events are mainly produced by the flavour creation mechanism. The low $\Delta\phi$ tail suggests non-negligible contribution from other processes. It was demonstrated that the inclusion of the underlying event in the simulation significantly improves the description of the data.

M. D'Onofrio (CDF) reported on measurements of W+jets and Z+jets production cross sections at CDF [45]. Boson+jet production channels are fundamental to test pQCD, underlying events and new theoretical calculations. Comparisons to different calculations were shown. The size of non-perturbative corrections was also estimated. The measurement is important since it gives an estimate of background for new physics like top, Higgs and SUSY searches.

Jet production measurements was also reported by J. Cammin (DØ) [46]. Good agreement with NLO pQCD predictions over a large p_T range was demonstrated. Systematic uncertainties are dominated by the jet energy scale. Measurements of jets with a μ tag, used to identify Heavy Flavor jets, and Z+jet production were also presented.

Prospects for inclusive jet cross section measurements with early data at ATLAS were presented by D. Clements [47]. Experimental errors are expected to be dominated by the jet energy scale. Theoretical errors at high p_T are dominated by the uncertainty on the high-x gluon PDF.

5.7 Inclusive jet production and jet correlations in DIS

Recent results on angular correlations in three-jet events and jet substructure were presented by E. Ron (ZEUS) [48]. Fixed-order calculations, separated according to the colour configurations, were used to study the sensitivity of the angular distributions to the underlying gauge structure. Using different variables one can distinguish between contributions from triple-gluon vertexes in quark-induced and gluon-induced processes. The measurements are consistent with the admixture of colour configurations as predicted by $SU(3)$ and disfavour some other combinations. Subjet structure is reasonably described by the fixed-order QCD calculations and are consistent with the dominance of quark-induced processes.

Inclusive jet production in DIS at high Q^2 is a well established measurement and is well reproduced by different pQCD calculations. This is why this regime is used for precise QCD measurements and extraction of α_S. An updated H1 analysis with improved precision was presented by T. Kluge (H1) [49]. The α_S fit was performed minimising the experimental uncertainty. A first extraction of α_S using the ratio of inclusive jet to the inclusive DIS

cross sections was made which provides a more precise measurement. The ZEUS measurements were presented by T. Schoerner-Sadenius [50]. Together with inclusive cross sections ZEUS measured dependence of inclusive jet cross section on jet radius and used this measurement to extract the α_s value. The inclusive dijet sample was analyzed using combined HERAI and HERAII data, correspondent to integrated luminosity of 210 pb$^-$1. For all these measurements the theoretical uncertainties still dominate.

Inclusive jet production cross section in the low Q^2 region, $5 < Q^2 < 100$ GeV^2, was presented by A.Baghdasaryan (H1) [51]. The analysis extends to lower Q the similar analysis performed by H1 at high Q^2. Good agreement with NLO pQCD calculation was observed for Q^2 above 10 GeV^2. For further talks on jet production in the low-x regime see forward jet production and HERA multi-jet production at low-x and low-Q^2 presented during a special Structure Function WG session.

6 Summary

In addition to several formal theoretical developments, further experimental and theoretical contributions demonstrated great progress towards a more precise understanding of QCD final state production. Enormous progress in the theoretical calculations triggered by more precise data included a first resummation for QCD 3-jet production at Next-to-Leading Order which should provide a better description of dijet azimuthal correlation measurements both at HERA and the Tevatron. An additional dedicated session was held to discuss α_S, where theoretical uncertainties dominate experimental measurements at HERA. NNLO calculations for 3-jet production in e^+e^- were presented and are expected to lead to new fits for α_s with reduced theoretical uncertainties.

Future new physics searches at the LHC will rely on the most precise determinations of the parton density functions. HERA and Tevatron photon + jet production measurements, highlight regions where continuing improvements to theoretical models and inputs are still required and measurements of high E_T forward dijet production at HERA and inclusive jet production at the Tevatron should also help further constrain these inputs. Progress towards a precision determination of unintegrated PDFs and a first determination of their intrinsic k_T component was also presented at the meeting.

Tests of power corrections arising from hadronization effects have been extended to 3-jet event shape distributions. Progress in perturbative evolution and hadronization issues, the role of the underlying event implementation in Monte Carlos, reducing model approximations for parton showers and issues that arise when Monte Carlos are tuned to non-global parameters were highlighted. The importance of multiple interaction modeling was demonstrated by HERA γp multijet production measurements and $b\bar{b}$ jet azimuthal correlations at the Tevatron. Improvements using a new flavor jet algorithm to theoretical uncertainties for heavy flavor jet production were demonstrated.

Recent exclusive final state measurements include an observation of two virtual photon annihilation final states at BaBar. Work in progress to resolve pentaquark issues currently show no further evidence for pentaquark states. A first measurement of the ratio of deuteron and antideuteron production rates in DIS at HERA is smaller than expected in the coalescence model. NLO pQCD predictions using improved fragmentation functions are found to describe the measured particle p_t spectra at RHIC, however the effect of fragmentation functions is small and unable to account for observed differences to NLO pQCD predictions in scaled momentum spectra measurements in DIS at HERA. In collisions with heavy ions

recent measurements at RHIC on the impact of Quark-Gluon plasma properties to particles passing through it were presented, together with first double differential nuclear attenuation measurements on a series of different nuclear targets at HERMES and color transparency effects which were reported in ρ^0 electroproduction measurements at CLAS. Further details for each individually presented topic can be found in the dedicated contributions to these proceedings.

References

[1] `http://indico.cern.ch/contributionDisplay.py?contribId=18&sessionId=2&confId=9499`

[2] A. Gehrmann, these proceedings; see also A. Gehrmann-De Ridder, T. Gehrmann, E. W. N. Glover and G. Heinrich, Nucl. Phys. Proc. Suppl. **160** (2006) 190 [arXiv:hep-ph/0607042].

[3] A. Gehrmann-De Ridder, T. Gehrmann and E. W. N. Glover, JHEP **0509** (2005) 056 [arXiv:hep-ph/0505111].

[4] R. Harlander, P. Kant, L.Mihaila, M. Steinhauser, these proceedings, arXiv:0706.2982 [hep-ph]; see also R. Harlander, P. Kant, L. Mihaila and M. Steinhauser, JHEP **0609** (2006) 053 [arXiv:hep-ph/0607240]; R. V. Harlander, D. R. T. Jones, P. Kant, L. Mihaila and M. Steinhauser, JHEP **0612** (2006) 024 [arXiv:hep-ph/0610206].

[5] J. Bluemleinand S. Klein, these proceedings, arXiv:0706.2426 [hep-ph]; see also J. Blumlein, Comput. Phys. Commun. **159** (2004) 19 [arXiv:hep-ph/0311046].

[6] N. Nikolaev, these proceedings; N. N. Nikolaev and W. Schafer, Phys. Rev. D **74** (2006) 074021 [arXiv:hep-ph/0607307].

[7] M. Dasgupta and G. P. Salam, Phys. Lett. B **512** (2001) 323 [arXiv:hep-ph/0104277].

[8] R. B. Appleby and M. H. Seymour, JHEP **0212** (2002) 063 [arXiv:hep-ph/0211426].

[9] Y. Delenda, R. Appleby, M. Dasgupta and A. Banfi, JHEP **0612** (2006) 044 [arXiv:hep-ph/0610242]. A. Banfi and M. Dasgupta, Phys. Lett. B **628** (2005) 49 [arXiv:hep-ph/0508159].

[10] M. Hansson [H1 Collaboration], *Prepared for 14th International Workshop on Deep Inelastic Scattering (DIS 2006), Tsukuba, Japan, 20-24 Apr 2006.*

[11] Y. Delenda, these proceedings, arXiv:0706.2172 [hep-ph].

[12] A. Banfi, these proceedings arXiv:0706.2722 [hep-ph]; see also A. Banfi, *In the Proceedings of FRIF workshop on first principles non-perturbative QCD of hadron jets, LPTHE, Paris, France, 12-14 Jan 2006, pp B001* [arXiv:hep-ph/0605125].

[13] H. Jung and G. P. Salam, Eur. Phys. J. C **19** (2001) 351 [arXiv:hep-ph/0012143].

[14] H. Jung, these proceedings; see also H. Jung, A. V. Kotikov, A. V. Lipatov and N. P. Zotov, arXiv:hep-ph/0611093.

[15] Z. Nagy, Phys. Rev. Lett. **88**, 122003 (2002) [arXiv:hep-ph/0110315]; Phys. Rev. D **68**, 094002 (2003) [arXiv:hep-ph/0307268].

[16] G. Zanderighi, these proceedings, arXiv:0705.1937 [hep-ph]; see also A. Banfi, G. P. Salam and G. Zanderighi, arXiv:0704.2999 [hep-ph].

[17] M. Dasgupta, these proceedings, arXiv:0706.2630 [hep-ph]; see also A. Banfi, G. Corcella and M. Dasgupta, JHEP **0703** (2007) 050 [arXiv:hep-ph/0612282].

[18] L. Magnea, these proceedings.

[19] Z. Nagy, these proceedings; see also Z. Nagy and D. E. Soper, arXiv:0706.0017 [hep-ph].

[20] S. Visscher, these proceedings; see also J. Alwall *et al.*, arXiv:0706.2334 [hep-ph].

[21] F. Maltoni, T. McElmurry, R. Putman and S. Willenbrock, arXiv:hep-ph/0703156.

[22] A. Vicini, these proceedings; see also C. M. Carloni Calame, G. Montagna, O. Nicrosini and A. Vicini, JHEP **0612** (2006) 016 [arXiv:hep-ph/0609170].

[23] K. Melnikov and F. Petriello, Phys. Rev. D **74** (2006) 114017 [arXiv:hep-ph/0609070];
C. Anastasiou, L. J. Dixon, K. Melnikov and F. Petriello, Phys. Rev. D **69** (2004) 094008 [arXiv:hep-ph/0312266].

[24] P. Rossi, these proceedings and references therein.

[25] M. Del Degan, these proceedings and references therein.

[26] S. Chekanov, these proceedings and references therein.
[27] S. Saremi, these proceedings and references therein.
[28] B. Levchenko, these proceedings and references therein.
[29] M. Heinz, these proceedings and references therein.
[30] B. Brzozowska, these proceedings and references therein.
[31] L. Pinera, these proceedings and references therein.
[32] C. Ogilvie, these proceedings and references therein.
[33] M. Holtrop, these proceedings and references therein.
[34] Z. Akopov, these proceedings and references therein.
[35] Y. Van Haarlem, these proceedings and references therein.
[36] S. Chekanov, these proceedings and references therein.
[37] K. Müller, these proceedings and references therein.
[38] O. Atramentov, these proceedings and references therein.
[39] H. Perrey, these proceedings and references therein.
[40] A. Savin, these proceedings and references therein.
[41] S. Osman, these proceedings and references therein.
[42] H. Wolfe, these proceedings and references therein.
[43] A. Krasznahorkay, these proceedings and references therein.
[44] S. Vallecorsa, these proceedings and references therein.
[45] M. D'Onofrio, these proceedings and references therein.
[46] J. Cammin, these proceedings and references therein.
[47] D. Clements, these proceedings and references therein.
[48] E. Ron, these proceedings and references therein.
[49] T. Kluge, these proceedings and references therein.
[50] T. Schoerner-Sadenius, these proceedings and references therein.
[51] A. Baghdasaryan, these proceedings and references therein.

Summary of the Heavy Flavor Working Group

Michael Klasen[1], Benno List[2], Stephanie Hansmann-Menzemer[3], and Rainer Mankel[4]

1- Université Grenoble I - Laboratoire de Physique Subatomique et de Cosmologie
53 Avenue des Martyrs - 38026 Grenoble - France

2- Universität Hamburg - Institut für Experimentalphysik
Luruper Chaussee 149 - 22761 Hamburg - Germany

3- Universität Heidelberg - Physikalisches Institut
Philosophenweg 12 - 69120 Heidelberg - Germany

4- Deutsches Elektronen-Synchrotron DESY - F1
Notkestr. 85 - 22603 Hamburg - Hamburg

During the last year many important results have been achieved in heavy flavour physics: New measurements of charm and beauty production have been performed at HERA and the Tevatron. A wealth of new spectroscopy data with several new, unexpected states in the charmonium and the D_s systems has been collected and $b \to d\gamma$ transitions have been established. The oscillation frequency in the $B_s\bar{B}_s$ is now measured, and mixing in the $D^0\bar{D}^0$ system has been observed. Theoretical progress in the areas of open heavy flavour production, quarkonium production and decays, and multiquark spectroscopy has been presented at this workshop.

1 Experimental Summary

In this section we summarize the experimental results from the heavy flavour working group [1]. The presentations covered a wide range of topics, from charm, beauty and charmonium production in ep and $p\bar{p}$ collisions, heavy ion results on charm suppression, spectroscopy and rare decays, over oscillations in the $B_s\bar{B}_s$ and $D^0\bar{D}^0$ systems to the outlook for heavy flavour physics at future experiments at the LHC and the ILC.

1.1 Charm and Beauty Production

1.1.1 Charm Production

Charm Production in ep collisions has been studied extensively over the last years at HERA, and a wealth of data exist in photoproduction (where the exchanged photon is quasi-real, with a virtuality $Q^2 \approx 0$) and deep-inelastic scattering (DIS). The HERA collider experiments, H1 and ZEUS, have presented new preliminary results on charm production from the HERA-II running period [2, 3, 4]. The ZEUS Collaboration reported on two charm measurements in DIS with HERA-II data (Fig. 1): One analysis [2] uses D^* mesons to identify charm production, and utilizes $162\,\mathrm{pb}^{-1}$ of new data to achieve improved statistical accuracy compared to previous analyses. The second analysis [3] uses $D^{\pm}$ mesons instead and is one of the first measurements to utilize the new silicon strip Micro Vertex Detector (MVD) of ZEUS. Based on $135\,\mathrm{pb}^{-1}$, this analysis achieves similar accuracies as previous ZEUS measurements of the inclusive charm cross section in DIS.

The ZEUS collaboration has recently also finalized two analyses of charm production from older HERA-I data [2]. One analysis [5] covers the region of very low momentum transfer ($0.05 < Q^2 < 0.7\,\mathrm{GeV}^2$) at the transition between photoproduction and DIS. The data provide a good test of perturbative QCD calculations, which are available in NLO, and are

well described by massive calculations in the fixed flavour number scheme, as implemented in the HVQDIS program [6]. In the second analysis [7], the pseudoscalar states D^0, D^+, and D_s^+ are reconstructed, rather than the vector state D^{*+}, which allows a measurement of the fragmentation fractions, which turn out to be compatible with those measured in e^+e^- annihilation and in photoproduction [8, 9]. The inclusive charm cross section derived from this measurement is consistent with previous results. Also a new, preliminary measurement of charm fragmentation was presented by the ZEUS collaboration [8], which shows broad agreement with other measurements from H1 [4], and also with measurements from e^+e^- experiments.

Another new measurement of D^* production in DIS, based on $222\,\mathrm{pb}^{-1}$ of HERA-II data, was presented by the H1 collaboration [4]. Here, differential and double differential visible cross sections for D^* production were measured and compared to the QCD calculations. Overall, these quantities are well described by the NLO predictions of HVQDIS; in fact, the data uncertainties are in many cases smaller than the theory uncertainties from the variation of the charm mass and the variation of the renormalization and factorization scales. However, in some quantities, most notably the $\eta(D^*)$ distribution, even in spite of the relatively large theory uncertainties the NLO predictions deviate significantly from the trend observed in data.

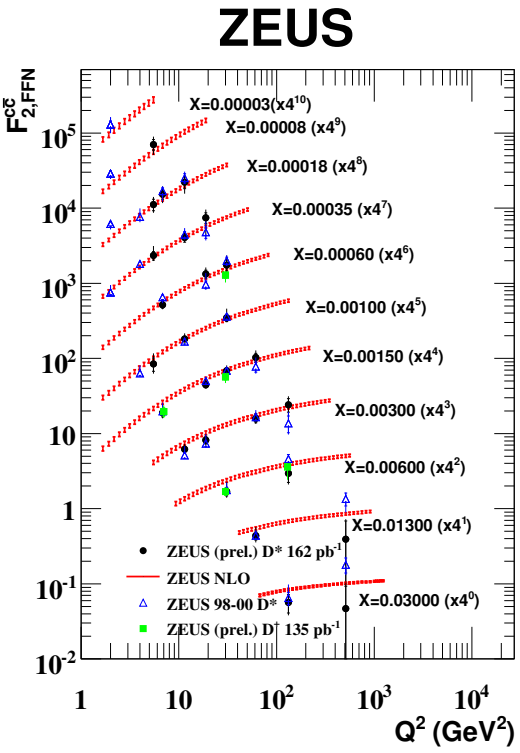

Figure 1: Compilation of F_2^c measurements from ZEUS.

This confirms, with higher statistics, the observation made in a recently published analysis from the H1 collaboration [10, 11]. However, that analysis goes one step further and investigates D^* production in DIS in conjunction with jets. As heavy flavour production is dominated by boson gluon fusion, a two-jet structure is expected for most of the events. In the DIS analysis, one jet in addition to the D^* meson is required. Again, HVQDIS describes the data satisfactorily, with the notable exception of the azimuthal angle difference $\Delta\phi$ between the D^* and the jet, a quantity which would be almost exactly equal to 180° in leading order, where the two charm jets must be back-to-back; hard gluon emission, which enters only in NLO, leads to an enhancement at lower values of $\Delta\phi$, which is underestimated by HVQDIS, whereas Monte Carlo models such as CASCADE [12], which include parton showers as approximation for higher-order gluon radiation, work significantly better. In another recent publication [10, 13], the H1 collaboration has investigated charm photoproduction with two jets, with very similar findings.

The results show that charm measurements have now reached a level of accuracy where

more precise QCD predictions would be desirable. On one hand a full NLO Monte Carlo with matched parton showers is needed, as opposed to HVQDIS, which produces only parton four-vectors and has been augmented with relatively simple independent fragmentation routines to make the extraction of visible cross sections possible. A second way to reduce theory uncertainties would be to reduce the variation of input parameters such as the charm mass or fragmentation parameters by detailed comparisons between MC predictions and data of (double) differential visible cross sections in terms of relevant quantities such as $p_{\mathrm{t}}\,(D^*)$ and $\eta\,(D^*)$. On the other hand, NNLO calculations would provide the most reliable way to reduce theory uncertainties, in particular for inclusive quantities such as $F_2^{c\bar{c}}$.

1.1.2 Beauty Production

Beauty production at HERA and the Tevatron has generated a lot of interest in recent years, not least because at both colliders inclusive cross sections for beauty production were observed that are considerably higher than the expectation from perturbative QCD calculations in next-to-leading order.

Achim Geiser gave an overview over the existing experimental results from HERA, with additional glimpses at Tevatron and UA1 data [14]. He discussed in detail the issue of scale dependence of QCD calculations, where he presented a survey of QCD calculations in different orders of α_{s} for a number of processes and argued that a good choice for the factorisation and renormalisation scales $\mu_{\mathrm{r,f}}$ would be a scale at which higher order calculations give a result that coincides with the calculations at lower order. He observed that this is achieved in most of the cases at a scale between $1/4\mu_0$ and $1\mu_0$, where μ_0 is the "natural" choice of scale such as E_{T}^2, $Q^2+m_{\mathrm{Q}}^2$, or $p_{\mathrm{t}}^2+m_{\mathrm{Q}}^2$. Based on this observation he argued that the factorisation and renormalisation scales should be varied in the range $1/4\mu_0 < \mu_{\mathrm{r,f}} < 1\mu_0$, with a choice of $\mu_{\mathrm{r,f}} = 1/2\mu_0$ for the central value, rather than using a variation of $1/2\mu_0 < \mu_{\mathrm{r,f}} < 2\mu_0$, as is customary in most HERA publications. He also pointed out that this prescription has already been adopted silently by the Tevatron experiments in recent preliminary results. This proposal was received well by the audience, as the discussion after the presentation showed.

New, preliminary results on beauty production were presented by the D0 and CDF collaborations [15]. D0 has performed a new measurement of muon tagged jet cross sections based on $300\,\mathrm{pb}^{-1}$ of data that extends up to $p_{\mathrm{t}} = 420\,\mathrm{GeV}$. Again, the data lie above the theory prediction. In a new measurement of inclusive B cross sections, the CDF collaboration utilizes the decays $B \to \ell D^0, D^{*+}X$ in addition to the previously used channel and $B \to J/\psi X$, with consistent results. These measurements are also consistent with a fixed order calculation at next to leading log.

The first, preliminary HERA-II result on beauty production, based on $39\,\mathrm{pb}^{-1}$ of data, was presented by the ZEUS collaboration [16]. The results are somewhat higher, but still consistent with previous measurements from H1 [17].

1.2 Charmonium Production

The inclusive production of charmonium and bottomium states in ep and $p\bar{p}$ collisions remains an intersting testing ground for perturbative QCD, as was shown in a review by Katja Krüger [18]. The working horse for these investigations are J/ψ mesons, where the largest data sets are available. While leading order calculations in the colour singlet model [19] fail

to describe the production rates of J/ψ mesons at the Tevatron [20], NRQCD models [21] models have been successfully applied there. In these models the production of $c\bar{c}$ states with different colour and spin/parity configuration is calculated perturbatively, and the transition to bound states is described by non-perturbative long distance matrix elements (LDME), which have to be determined from data. This allows the production of J/ψ mesons by gluon splitting into a $c\bar{c}$ pair, followed by a transition to a J/ψ meson, which is predicted to be transversely polarized. The observation of such a polarization is therefore considered the "smoking gun" for (large) colour octet (CO) contributions.

However, new data from CDF that were presented at this conference [15] show a clear evidence for longitudinal J/ψ polarization, which is in contrast to NRQCD expectations. New data on ψ' polarisation are still not precise enough for firm conclusions.

A second test of NRQCD predictions is the measurement of the production rates of χ_{c2} versus χ_{c1} states, which in NRQCD models is expected to follow the spin counting prediction of 5/3. New measurements from CDF [22, 15] give a significantly smaller result for the ratio of prompt χ_c production: $\sigma(\chi_{c2})/\sigma(\chi_{c1}) = 0.70 \pm 0.04(stat.) \pm 0.04(syst.) \pm 0.06(BF)$.

After the initial success of the NRQCD model indications for the necessity of large CO contributions where also searched for in inelastic J/ψ production at HERA. The H1 collaboration has presented new, preliminary data from HERA-II on inelastic J/ψ production in deep inelastic ep scattering [23]. Production rates were measured double differentially in the transverse momentum p_t and the momentum fraction z of the J/ψ meson, and compared to Monte Carlo predictions by programs which implement the colour singlet model in leading order. These models describe the shape of the measurements quite well, whereas the CO contributions in NRQCD models tend to have different p_t and z shapes than the CS contributions. Therefore, the new H1 data do not show any clear need for large CO contributions to inelastic J/ψ production. In the discussion of the results the need was stressed for NLO calculations of this process, in the CS as well as in NRQCD models. NLO calculations are currently only available in the CS model for photoproduction of J/ψ mesons [24], where they describe the data from HERA [25] quite well.

A different issue in charmonium production is adressed by the new data from HERA-B [26]: HERA-B has collected large samples of J/ψ and ψ' mesons decaying to $\mu^+\mu^-$ and e^+e^- pairs, which made it possible to investigate the dependence of charmonium production on the atomic weight A in a new range of Feynman-x_F, extending the range covered by the experiments down to $x_F = -0.35$, which is a region where theoretical models make widely different predictions.

1.3 Heavy Ion Results

The new results from heavy ion experiments at RHIC have been reviewed in this conference by William Zajc [27]. Therefore we only briefly highlight some of the new results presented in the heavy flavour session.

New results on heavy quark production in Au+Au collisions were presented by the PHENIX [28] and the STAR [29] collaborations. Due to their larger mass and the dead cone effect, charm quarks are expected to lose energy at a smaller rate than light quarks. The observation of supression of electrons from charm decays in central Au+Au collisions [28, 30, 29, 31] therefore comes as a surprise. It appears that charm quarks participate in the flow of the opaque hadronic medium just as much as light quarks, which means that they thermalize more quickly than expected in many theoretical models.

The PHENIX collaboration has also presented new measurements of J/ψ suppression in Au+Au collisions [32, 33]. These measurements, which are performed in two rapidity ranges $|y| < 0.35$ and $1.2 < y < 2.2$, show a significant suppression of J/ψ production in Au+Au collisions, which is stronger at large rapidities than at central rapidity values. The explanation of this rapidity dependence is a real challenge to theoretical models.

1.4 Spectroscopy and Rare Decays

The large data sets from the B factory experiments BaBar and Belle, from CLEO-c and from the Tevatron experiments CDF and D0 have lead to a renewed interest in the spectroscopy of charm and bottom hadrons with beautyful results, and have opened the possibility to identify extremely rare decays.

1.4.1 The Charmonium System

In the charmonium system, finally all expected charmonium states below the D-meson threshold have now been firmly identified. One of last two missing states, the η_c', has now seen by BaBar, CLEO-c, and Belle [34, 35], at an average mass of $m(\eta_c') = 3638 \pm 4\,\mathrm{MeV}$. This allows a comparison of the hyper fine splitting of the $1S$ and $2S$ states in the charmonium system, which are $\Delta m_{\mathrm{hf}}\,(1S) = 117 \pm 1\,MeV$ and $\Delta m_{\mathrm{hf}}\,(2S) = 48 \pm 4\,MeV$; the large difference of these values poses a challenge to theory [34].

The long elusive h_c state has observed by CLEO-c [34, 36] in the decay chain $\psi(2S) \to \pi^0 h_c$, $h_c \to \gamma\eta_c$, with a mass of $m(h_c) = 3524.4 \pm 0.6 \pm 0.4\mathrm{MeV}$, which corresponds to a hyper fine splitting between the h_c and the center of gravity of the $\chi_{c0,1,2}$ states of $m_{\mathrm{hf}}(1P) = +1.0 \pm 0.6 \pm 0.4\mathrm{MeV}$, consistent with the expected value of zero. Meanwhile, CLEO-c has increased its $\psi(2S)$ sample eightfold, which yield the promise of further, improved results.

In addition to these expected charmonium states, recent years have seen the discovery of several unexpected charmonium-like resonances:

New results were obtained on the $X(3872)$, which is already considered firmly established by the PDG [37], and on the $Y(3940)$ and $Y(4260)$. Results were also presented on two additional states, the $X(3940)$ and the $Z(3930)$.

For the $X(3872)$, one explanation that has been put forward is the interpretation as a $D^0\bar{D^{0*}}$ molecule. CLEO has performed a new measurement of the D^0 mass [34]: $m(D^0) = 1864.847 \pm 0.150(stat.) \pm 0.095(syst.)\mathrm{MeV}$ [38]. The total uncertainty of this measurement of 0.178 MeV is a factor of 2.2 better than the uncertainty of 0.4 MeV of the 2006 world average [37]. Combinig this result with the PDG06 value of the $X(3872)$ mass of $3871.2 \pm 0.5\,\mathrm{MeV}$ results in a very small binding energy of $E_b = 0.6 \pm 0.6\mathrm{MeV}$ for a $D^0\bar{D^{0*}}$ molecule [34]. Meanwhile, Belle and BaBar have also found indications for the $X(3872)$ in the decays $B \to \bar{D}^0 D^0 \pi^0 K$ (Belle) and $B \to \bar{D}^0 D^{0*} K$ (BaBar) [39]. In these channels, the observed mass values for the $X(3872)$ of $m = 3875.4 \pm 0.7^{+1.2}_{-2.0}\,\mathrm{MeV}$ (Belle) [40] and $m = 3875.6 \pm 0.7^{+1.4}_{-1.5}\,\mathrm{MeV}$ (BaBar) are $2.5\,\sigma$ higher than the current world average. Belle also concludes that the quantum numbers $J^{PC} = 1^{++}$ are favoured if the observed enhancement is indeed the $X(3872)$. All in all, the interpretation of this state remains unclear.

New data were also presented on the $Y(4260)$ [39], which was first observed in initial state radiation events at BaBar. BaBar sets a limit [41] of $BR(Y(4260) \to D\bar{D})/BR(Y(4260) \to J/\psi\,\pi^+\pi^-) < 7.6$, which is a further indication that the $Y(4260)$ is not a conventional charmonium state. CLEO has also confirmed the $Y(4260)$ [34, 42], and finds [43] its mass to be

$m = 4284^{+17}_{-16}(stat) \pm 4(syst.)$MeV, in poor agreement with the original BaBar measurement [44] of $m = 4259 \pm 8^{+2}_{-6}$ MeV. The latest Belle [39, 45] result $m = 4295 \pm 10^{+10}_{-3}$ MeV is consistent with the CLEO measurement.

The discovery of new, unexpected charmonium-like states has also triggered new investigations of $R = \sigma(e^+e^- \to hadrons)/\sigma(e^+e^- \to \mu^+\mu^-)$ at Belle and CLEO [46, 42, 43, 45]. These scans show a marked dip around the $Y(4260)$. Belle, BaBar and CLEO have also looked [46, 41, 47, 48] into the more exclusive channels $e^+e^- \to D^{(*)}D^{(*)}$. A weak signal for the $Y(4260)$ is seen in the $D\bar{D}^*$ channel, no signal in the DD channel, and a dip, similar to the one observed in the inclusive R measurement, is observed in the D^*D^* channel around the $Y(4260)$ resonance.

Meanwhile, BaBar observes yet another state [39, 49] in initial state production of $e^+e^- \to \psi(2S)\pi^+\pi^-$ at a mass of $m = 4324 \pm 24$ MeV and a width of $\Gamma = 172 \pm 33$ MeV, which is incompatible with the $Y(4260)$ or other known states such as the $\psi(4415)$.

Three more states observed by Belle [39, 50], termed $X(3940)$, $Y(3940)$, and $Z(3930)$, may have an interpretation as conventional charmonium states, namely the $\eta_c(3S)[3\,^1S_0]$, the $\chi'_{c1}[2\,^3P_1]$ and the $\chi'_{c2}[2\,^3P_2]$.

1.4.2 Charmed, Strange Mesons

In the sector of charmed, strange mesons new measurements were presented by BaBar and Belle [39]. In addition to new measurements of the properties of the $D^*_{s0}(2317)$ and $D_{s1}(2460)$, another new state, termed $D^*_{sJ}(2860)$, has been identified by BaBar [51] with a mass $m = 2856.6 \pm 1.5 \pm 5.0$MeV and a spin parity assignment $J^P = 0^+, 1^-, 2^+, ...$ In addition, a hint for another state with $m = 2688 \pm 4 \pm 3$MeV has also been observed. Furthermore, Belle, in a Dalitz analysis of the decay $B^+ \to \bar{D}^0 D^0 K^+$, sees indications for a state $D_{sJ}(2700)$ with $m = 2715 \pm 11^{+11}_{-14}$ MeV, with quantum numbers $J^P = 1^-$ favoured. The theoretical interpretation of these states is not yet clear. While the $D^*_{s0}(2317)$ and $D_{s1}(2460)$ states can be explained as 0^+ and 1^+ P-wave $c\bar{s}$ states, their masses are substantially lower than expected from potential models. The interpretation of the other states is still less clear.

1.4.3 Charmed Baryons

Coming to charmed baryons, BaBar and Belle have reported discoveries of several new states [46]. Both observe the new state $\Lambda_c(2940)^+$ in the channels D^0p (BaBar) and $\Lambda_c^+\pi^+\pi^-$ (Belle) [52]. The Belle discovery of the new charmed, strange baryons $\Xi_c(2980)^+$ and $\Xi_c(3077)^+$ has been confirmed by BaBar [53], and Belle sees also some evidence for the isospin partners $\Xi_c(2980)^0$ and $\Xi_c(3077)^0$. BaBar has also reported the first observation of the Ω_c^*, an excited css state [54].

1.4.4 Bottom Mesons

In the B meson sector, the progress comes from the Tevatron experiments CDF and D0 [55]. The B_c^+ has already been observed by both experiments, now CDF reports the first direct observation of the B_c^+ in the exclusive decay channel $B_c^+ \to J/\psi\,\pi^+$, which allows a very precise mass measurement with the preliminary result of $m(B_c^+) = 6276.5 \pm 4.0 \pm 2.7$ MeV, while the uncertainty on the old world average was 400 MeV. The η_b is last spin singlet ground state in the bottomium sector that has not been unambiguously discovered yet. CDF

has performed a new search for the decay $\eta_b \to J/\psi\, J/\psi$, without indications for a signal. Both, D0 and CDF, report first direct observations on orbitally excited B mesons with $L = 1$ by looking for decays $B^{**} \to B^{(*)+}\pi^-$. Both see clear evidence for B_1 and B_2 states. With a similar analysis of the channels $B_s^{**} \to B^{(*)} + K^-$ both experiments observe also the B_{s2}^* state, in addition CDF reports evidence for the B_{s1} state.

1.4.5 Bottom Baryons

In the bottom baryon sector, where up to now the Λ_b^0 is the only well established particle, CDF performed a blind analysis of the decay channel $\Lambda_b^0\pi^\pm$; after unblinding, four resonances were found with significances greater than $5\,\sigma$, which constitute the first direct observation of $\Sigma_b^{(*)}$ baryons. The resonances are identified as the $\Sigma_b^\pm$ and the $\Sigma_b^{*\pm}$.

1.4.6 Rare Decays

In the field of rare decays, the large data sets of altogether more than 1 billion $B\bar{B}$ events obtained at the B factory experiments allow more and more precise measurements of $b \to s\gamma$ decay modes [56], which are interesting because in the Standard Model they are forbidden at tree level and proceed through loop diagrams. In extensions of the Standard Model, additional particles contribute to the loops, which may lead to observable deviations of the transition rates from the expected SM values. While the $b \to s\gamma$ decay channels are investigated with higher and higher precision, the large statistics now allows even the measurement of $b \to d\gamma$ transitions, which were first observed by Belle in 2005 [57]. The latest compilation from the Heavy Flavour Averaging Group [58] contains 20 measured $b \to s/d\gamma$ decay channels, with branching fractions as small as $4.6 \cdot 10^{-7}$ for $B^0 \to \omega\gamma$ and precisions down to 6.5 % for $B^+ \to K^+\pi^+\pi^-\gamma$. The 2006 average for $b \to s\gamma$ decays [59] is now $BR(B \to X_s\gamma) = (3.55 \pm 0.26) \cdot 10^{-4}$, which is on the high side of recent NNLO predictions [56, 60]. The latest measurements from BaBar and Belle of $B \to \rho/\omega\gamma$ [61] are particularly impressive, measuring branching fractions around 10^{-6}, in some cases with more than $5\,\sigma$ significance. From a combination of the $b \to d/s\gamma$ measurements from Belle and BaBar, a constraint of $|V_{td}/V_{ts}| = 0.202^{+0.017}_{-0.016}(exp.) \pm 0.015(theor.)$ has been derived.

A very difficult, but interesting decay channel is $B^+ \to \tau^+\bar{\nu}$ [56, 62], which has been observed by Belle at $3.5\,\sigma$ significance with a branching ratio of $BR(B^+ \to \tau^+\bar{\nu}) = (1.79^{+0.56\ +0.39}_{-0.49\ -0.46}) \cdot 10^{-4}$, while BaBar measures $(0.88^{+0.68}_{-0.67} \pm 0.11) \cdot 10^{-4}$, or, translated into a 90 % CL limit, $BR(B^+ \to \tau^+\bar{\nu}) < 1.8 \cdot 10^{-4}$. The combination of both results yields $(1.31 \pm 0.48) \cdot 10^{-4}$, corresponding to a $2.5\,\sigma$ evidence. This result can be used to derive limits on the $H^\pm$ mass in SUSY models.

After the observation of B_s oscillations, the search for the decays $B_{s,d} \to \mu^+\mu^-$ might be considered the next race in B physics. The Standard Model expectations for these decays are extremely small, and probably out of reach for current experiments: $BR(B_s \to \mu^+\mu^-) = (3.42 \pm 0.54) \cdot 10^{-9}$ and $BR(B_d \to \mu^+\mu^-) = (1.0 \pm 0.14) \cdot 10^{-10}$. Again, these decays can only proceed through loop diagrams in the SM, and contributions from new particles may increase the rate by orders of magnitude [63]. Both Tevatron experiments have searched for the $B_s \to \mu^+\mu^-$ decay and have reported new, preliminary results based on new Run-II data. The limits are $BR(B_s \to \mu^+\mu^-) < 10 \cdot 10^{-8}(9.3 \cdot 10^{-8})$ from CDF (D0); these limits correspond to branching ratios that are 29 (27) times larger than the SM expectation. CDF has also reported a preliminary limit for B_d decays: $BR(B_d \to \mu^+\mu^-) < 2.3 \cdot 10^{-8}$, which

is 230 times greater than the SM expectation.

1.5 Mixing and Oscillations

While oscillations have long been established and thoroughly investigated in the $K^0\bar{K}^0$ and $B^0\bar{B}^0$ systems, until recently the frequency of the $B_s\bar{B}_s$ oscillations had not been measured, and no firm signal for mixing in the $D^0\bar{D}^0$ system had been observed. During the last year, both these gaps in our knowledge of neutral meson mixing have been filled.

The B_s oscillation frequency has now been measured by the Tevatron experiments [64]. After the first report on a double sided limit for the B_s oscillation frequency of $17 < \Delta m_s < 21\,\mathrm{ps}^{-1}$ at 90 % CL from the D0 collaboration [65], CDF has for the first time observed a nonzero oscillation amplitude with more than $3\,\sigma$ significance [66], at a frequency $\Delta m_s = 17.77 \pm 0.10 \pm 0.07\,\mathrm{ps}^{-1}$, consistent with the D0 result.

Meanwhile, the D0 collaboration has gone several steps further.

Based on a sample of $1.1\,\mathrm{fb}^{-1}$ of decays $B_s \to J/\psi\,\phi$, D0 has made a new measurement [67] of the difference between the lifetimes of the long and short lived B_s eigenstates. Both states can decay to the $J/\psi\,\phi$ final state, and by fitting the decay angle distributions their respective contributions to the sample at different eigentimes can be determined, with the result $\Delta\Gamma_s = 0.17 \pm 0.09 \pm 0.02\,\mathrm{ps}^{-1}$. For the first time, the D0 collaboration has used this data also to extract the CP violating phase ϕ_s, which is the relative phase of the off-diagonal elements of the mass and decay matrices in the $B_s\bar{B}_s$ basis, from this data: $\phi_s = -0.79 \pm 0.56(stat.)^{+0.14}_{-0.01}(syst.)$. The SM prediction for ϕ_s is very small, namely $\phi_s = (4.2 \pm 1.4) \cdot 10^{-3}$ [68].

D0 has also reported on a new measurement [69] of the branching ratio $BR\,(B_s \to D_s^{(*)} D_s^{(*)}) = 0.039^{+0.019}_{-0.017}(stat.)\,^{+0.016}_{-0.017}(syst.)$, which is lower than the only pre-existing measurement from ALEPH. This branching ratio is linked theoretically to the width difference $\Delta\Gamma_s^{CP}$ between the CP-even and odd B_s eigenstates. The resulting constraint is $\Delta\Gamma_s^{CP}/\Gamma_s = 0.079^{+0.038}_{-0.035}(stat.)\,^{+0.031}_{-0.030}(syst.)$.

While the difficulty in B_s mixing lies in the fact that the mixing is almost perfect because the oscillations occur much faster than the decay, the situation is reversed in the $D^0\bar{D}^0$ system. Here, the Standard Model prediction for the mixing parameters $x = \Delta m/\Gamma$ and $y = \Delta\Gamma/2\Gamma$ are very small [46], of the order $10^{-6\cdots-2}$, which means that the D^0 decays much faster than one oscillation period lasts. Again, additional particles in the loop may increase the mixing, which could indicate new physics. In particular, new physics processes such as Flavour-Changing Neutral Currents, SUSY particles etc. would increase x (i.e., the oscillation frequency), but not y (the lifetime difference).

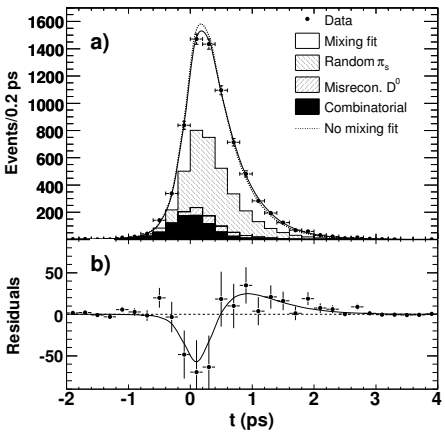

Figure 2: Proper time distribution of the $D^0 \to K^+\pi^-$ (wrong-sign WS) decays from BaBar

Until march of this year, the no-mixing case had been disfavoured with a significance of

2.1 (2.3) σ by Belle (BaBar) analyses [70]. Then both collaborations published two papers titled "Evidence for $D^0\bar{D}^0$ mixing" side by side in Physics Review Letters [71], both reporting more than $3\,\sigma$ evidence for $D^0\bar{D}^0$ oscillations.

The Belle analysis is based on $540\,\mathrm{fb}^{-1}$ of data and measures the difference in apparent lifetime for the CP even decays $D^0 \to K^+K^-, \pi^+\pi^-$ to the lifetime of the decay $D^0 \to K^-\pi^+$. The data show indications for mixing with $3.2\,\sigma$ significance. In addition, the Belle collaboration has performed a Dalitz analysis of the decay $D^0 \to K^0_S\pi^-\pi^+$, which provides the most sensitive result on x to date: $x = (0.80\pm0.29\pm0.17)\,\%$ and disfavours the no-mixing solution with $2.7\,\sigma$ significance [46, 72].

The BaBar analysis uses $384\,\mathrm{fb}^{-1}$ of data and analyses the decays $D^0 \to K^-\pi^+, K^+\pi^-$. The dominant decay mode is the right-sign (RS) decay mode to $K^-\pi^+$, while the wrong-sign (WS) decay mode to $K^+\pi^-$ may occur as doubly Cabibbo-suppressed (DCS) decay or through mixing. These two mechanisms are separated by the analysis of the time dependence of the decay, see Fig 2. From this data, BaBar can exclude the no-mixing hypothesis with $3.9\,\sigma$.

1.6 Future Experiments

Looking ahead into the future, first beams at the LHC are now expected in early 2008. Heavy flavour physics will be of interest at the experiments ATLAS, CMS [73] and LHCb [74].

In ATLAS and CMS, the expected rates for beauty production are high: at a luminosity of $\mathcal{L} = 10^{33}\,\mathrm{cm}^{-2}\,\mathrm{s}^{-1}$, around 10^5 $b\bar{b}$ pairs will be produced per second, which should allow high precision measurements despite the difficult environment. The big challenge here is to set up a reasonably efficient trigger, because bottom quarks are predominantly produced at relatively low transverse momenta, while the detectors are optimized for high-p_t discovery physics.

In the initial, "low" luminosity phase with expected luminosities around $\mathcal{L} = 10^{33}\,\mathrm{cm}^{-2}\,\mathrm{s}^{-1}$, the ATLAS experiment envisages to use single particle triggers at Level 1, which will be refined by searches for more complex signatures in the High Level Trigger (HLT) [73]. Channels that have been studied include e.g. $B_\mathrm{s} \to D_\mathrm{s}\pi$ with subsequent decays $D_\mathrm{s} \to \phi\pi$, states involving a electromagnetic signature such as $J/\psi \to ee, K^*\gamma, \phi\gamma$, and final states with two muons. In the high luminosity mode at $\mathcal{L} = 10^{34}\,\mathrm{cm}^{-2}\,\mathrm{s}^{-1}$, Level 1 will predominantly use the dimuon channel to identify J/ψ or B_s decays to $\mu\mu$. CMS will also use muon triggers at Level 1, and plans to identify decay vertices from heavy flavour decays in the High Level trigger. A number of topics have been studied by both collaborations, such as the measurement of inclusive beauty cross sections (CMS), the measurement of sin 2β in the golden mode $B^0 \to J/\psi\,K^0_S$ (ATLAS), analysis of $B_\mathrm{s} \to J/\psi\,\phi$ decays (ATLAS and CMS), and searches for rare decays such as $\Lambda_\mathrm{b} \to \Lambda\mu\mu$, $B^0 \to K^*\mu\mu$ or $B_\mathrm{s} \to \phi\mu\mu$ (ATLAS). The ATLAS collaboration has also studied the prospects to measure B_s oscillations. They conclude that they could measure Δm_s with $5\,\sigma$ significance at the current CDF value with the data from one year, i.e. $10\,\mathrm{fb}^{-1}$.

CMS has also studied the prospects to measure the B_c mass from decays to $J/\psi\,\pi$; the expected resolution from $1\,\mathrm{fb}^{-1}$ of data is 22 MeV statistical and 15 MeV systematical uncertainty, which can be compared to the preliminary CDF result reported in this conference [55], based on $1.1\,\mathrm{fb}^{-1}$, with statistical and systematic errors of 4.0 and 2.7 MeV, respectively.

The LHCb experiment [74], is an experiment dedicated to the study of B physics at LHC. The detector is a single arm spectrometer, optimized to detect b hadrons at pseudo rapidities $1.9 < \eta < 4.9$, and will run at an interaction zone with a relatively low luminosity to reduce backgrounds, where one year of running at nominal luminosity will provide $2\,\mathrm{fb}^{-1}$ of data. The LHCb collaboration has studied the prospects to measure the angles of the unitarity triangle; for $\sin 2\beta$ they hope to achieve a statistical precision of 0.02 from one year of data taking in the golden channel $B^0 \to J/\psi\, K^0_S$. For the least well determined angle γ, the most promising method seems to be the analysis of decays $B^{0,+} \to D^0 K^{0,+}$ with D^0 decays to $K\pi, K3\pi, \pi\pi$ and KK, with a comparison of the rates of Cabibbo Favoured and Doubly Cabibbo Suppressed decays. The estimated sensitivities are in the range $\sigma(\gamma) \approx 5^\circ - 15^\circ$, depending on the actual value of γ.

An interesting benchmark is provided by the sensitivity of $B_{\mathrm{d,s}} \to \mu\mu$, which has been studied by ATLAS, CMS [73], and LHCb [74]. Recall that currently CDF and D0 have reported upper limits of $100 \cdot 10^{-9}$ for the branching ratio [63] based on samples of $2\,\mathrm{fb}^{-1}$ (D0) and $0.78\,\mathrm{fb}^{-1}$ (CDF); these limits lie about 30 times above the SM expectation of $3.4 \cdot 10^{-9}$. A recent ATLAS study concludes that with an integrated luminosity of $30\,\mathrm{fb}^{-1}$, corresponding to about three year's running in the low luminosity mode, an upper limit of $6.6 \cdot 10^{-9}$ at 90 % CL is achieveable, which is about a factor of two above the SM expectation. CMS concludes that it could provide a limit of $14 \cdot 10^{-9}$ (four times the SM expectation) with $10\,\mathrm{fb}^{-1}$, i.e. one year's worth of data. LHCb on the other hand, which will operate at lower luminosities, claims a sensitivity that would allow a $3\,\sigma$ observation of the decay $B_s \to \mu\mu$ at the Standard Model branching ratio of $3.4 \cdot 10^{-9}$ with $2\,\mathrm{fb}^{-1}$, corresponding to one year's worth of data [74] at nominal luminosity.

Looking even farther into the future, Tim Greenshaw reported on the applications of heavy flavour at the planned Innternational Linear Collider (ILC) [75], an e^+e^- collider with a centre-of-mass energy between 500 and 1000 GeV. The detector designs for this machine forsee a very good flavour separation power, which calls for vertex detectors with spectacular performance. Several groups are currently investigating various technologies that could fulfill the requirements for the inner pixel detector of an ILC detector. One important application of the heavy flavour identification capabilities of such a detector would be the measurement of the various branching fractions of a Higgs boson. Even if only one neutral Higgs boson were found at the LHC, this would allow to check wether these fractions are consistent with the predictions from the Standard Model, where only one Higgs doublet is assumed and therefore all branching fractions depend only on the mass of the single physical Higgs boson, or whether for instance up- and down-type fermions have different couplings to the Higgs, as expected for instance in Supersymmetric models, which have at least two Higgs doublets.

1.7 Conclusions for the Experimental Part

Heavy flavour production at HERA and Tevatron remains an interesting field of research, both from the experimental and the theory side. The experimental results become more and more precise, which makes it interesting to include them in the determination of parton densities, provided that the theoretical obstacles can be overcome and uncertainties arising from charm mass and fragmentation functions are treated consistently between experiment and theory. The beauty production data have taught us that the calculation of production cross sections do not always become more accurate for heavier quarks if there is sufficient

phase space for QCD dynamics, which is something to keep in mind for LHC, where also the top will fall into this category.

During the last years we have seen a veritable renaissance of hadron spectroscopy. As the particle data book fills up, we see more and more results that indicate how incomplete our understanding of hadron structure still is, as illustrated by unexpected differences in hyperfine splittings in the charmonium sector [34], by unexpected states and masses in the $c\bar{s}$ system [39], and by the appearance of charmonium-like resonances for which we have no ready explanation [34, 39, 46]. While resonances that do not fit into the conventional $q\bar{q}$ picture have been known for a long time in the light meson sector, we now learn that also in the heavy quark sector there is more than is written in our philosophy. On the other hand, the investigation of rare decays such as $B^+ \to \tau\nu$ or $B \to \mu\mu$ and other rare processes such as $D^0\bar{D}^0$ mixing, where we wait for results that would point to physics beyond the Standard Model, has once again failed to turn up anything unexpected.

2 Theory

In this section, we summarize the six theory contributions to the heavy-flavor working group, emphasizing computations that have been performed during the years 2006 and 2007 and have therefore not yet been presented at previous DIS workshops [76]. We start with new perturbative results for inclusive final states, i.e. heavy-quark structure functions and their relation to parton densities, and then move on to less inclusive final states, in particular quarkonium production and decay and heavy-quark spectroscopy. For the latter we emphasize new results from lattice QCD and QCD sum rules. Note that a series of new calculations on open heavy-quark production at various colliders in the general-mass variable-flavor number scheme (GM-VFNS) has been presented at this workshop in an introductory plenary talk by G. Kramer [77].

The heavy-quark coefficient functions for deep-inelastic lepton-hadron scattering (DIS) in the kinematic regime $Q^2 \gg m^2$ have been calculated more than ten years ago in next-to-leading order (NLO) of QCD by M. Buza et al., using operator product expansion techniques [78]. Here Q^2 and m^2 stand for the masses squared of the virtual photon and heavy quark respectively. The analytical results had been expressed in terms of 48 independent functions and had been used to check earlier, general calculations, which were, however, only accessible via large computer programs. J. Blümlein has now presented a re-calculation of the $\mathcal{O}(\alpha_s^2)$ massive operator matrix elements for the twist-2 operators, which contribute to the heavy flavor Wilson coefficients in unpolarized DIS in the region $Q^2 \gg m^2$, using light-cone expansion techniques and confirming the above-cited calculation [79]. The application of the integration-by-parts method and harmonic sums in Mellin space allowed for a significant compactification of the results, which can now be expressed in terms of the basis $\{S_1,\ S_2,\ S_3,\ S_{-2},\ S_{-3}\}$ and $S_{-2,1}$, i.e. of only two independent functions.

While the proton is just a simple $|uud\rangle$ Fock state in the quark model, the possibility of an intrinsic-charm, i.e. a $|uudc\bar{c}\rangle$, component has repeatedly been put forward in the context of light-cone [80] or meson-cloud models [81, 82]. W.K. Tung et al. have performed global fits of parton density functions (PDFs), assuming that the charm-density is not only generated radiatively at $\mu = m_c$ and then evolved to Q, but allowing for the possibility of light-cone, meson-cloud, or sea-quark like intrinsic charm density [83]. The quality of each fit is measured by a global χ^2, shown in Fig. 3 as a function of the momentum fraction $\langle x\rangle_{c+\bar{c}}$ carried by the charm quark at the starting scale $\mu = m_c = 1.3$ GeV. For $\langle x\rangle_{c+\bar{c}} \leq$

0.01, the quality of the fit varies very little, i.e. the global analysis of hard-scattering data provides no evidence either for or against intrinsic charm. Above this point, all three curves in Fig. 3 rise steeply with $\langle x \rangle_{c+\bar{c}}$, so that global fits do place useful upper bounds on intrinsic charm. There is no data set that is particularly sensitive to intrinsic charm, but the global QCD analysis rules out the possibility of an intrinsic charm component much larger than 0.02 in momentum fraction. A variation of the charm quark mass m_c shows that the data prefer lower masses around 1.3 GeV with respect to higher masses of 1.5 GeV. The difference in χ^2 is in this case almost entirely due to the charm contribution to the proton structure function F^2, which has been precisely measured at HERA.

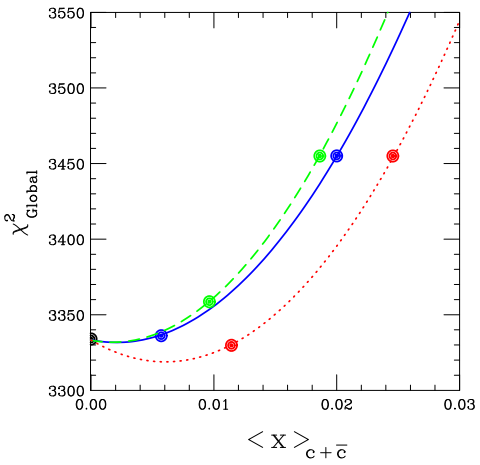

Figure 3: Goodness-of-fit vs. momentum fraction of intrinsic charm at the starting scale $\mu = 1.3$ GeV for the light-cone (solid curve), meson-cloud (dashed curve), and sea-like model (dotted curve).

Turning to less inclusive quantities, the production and decay of heavy quark-antiquark bound states (quarkonia $\mathcal{Q}$) is still far from understood. While the effective field theory of non-relativistic QCD (NRQCD) has long been believed to be phenomenologically successful and is still believed to be theoretically more consistent than the color-singlet model (CSM), recent Tevatron Run II data on the polarization of large-p_T J/Ψ- and Υ-mesons do not support the idea that their production is dominated by color-octet fragmentation processes as predicted in NRQCD. Since higher-order QCD corrections are largely unknown (except for color-singlet photoproduction [84], color-singlet and color-octet production in photon-photon collisions [85, 86] and a very recent calculation for direct color-singlet hadroproduction [87]), other theoretical frameworks continue to be investigated. One example is the k_T-factorization formalism, where the production cross section

$$\begin{aligned} \mathrm{d}\sigma(p\bar{p} \to \mathcal{Q} + X) \;=\; & \int \frac{\mathrm{d}x_1}{x_1} \int \mathrm{d}k_{1T}^2 \int \frac{\mathrm{d}\phi_1}{2\pi} \Phi(x_1, k_{1T}^2, \mu^2) \\ & \times \int \frac{\mathrm{d}x_2}{x_2} \int \mathrm{d}k_{2T}^2 \int \frac{\mathrm{d}\phi_2}{2\pi} \Phi(x_2, k_{2T}^2, \mu^2)\; \mathrm{d}\hat{\sigma}(RR \to \mathcal{Q} + X) \end{aligned} \tag{1}$$

is computed by a double convolution of unintegrated parton densities Φ and partonic cross section $\hat{\sigma}$ over longitudinal momentum fractions $x_{1,2}$ and intrinsic transverse momenta $k_{1T,2T}$ of the reggeized partons R in the (anti-)proton p ($\bar{p}$). This method has been applied by Kniehl et al. to charmonium production at different colliders [88] and now, as V.A. Saleev reported, also to bottomonium hadroproduction at the Tevatron [89]. The long-distance operator matrix elements (OMEs) of NRQCD have been refitted to the p_T-spectra of prompt Υ mesons at the Tevatron. Since the intrinsic k_T leads to a harder p_T-spectrum already for the color-singlet contributions, the color-octet OMEs turn out to be considerably smaller and in many cases even consistent with zero, as their values are not sufficiently constrained by the data. In addition, the results depend strongly on the assumed unintegrated parton

densities, which are poorly known and only constrained to agree with the integrated ones,

$$xf(x_{1,2},\mu^2) \;=\; \int_0^{\mu^2} \mathrm{d}k_{1T,2T}^2\, \Phi(x_{1,2},k_{1T,2T}^2,\mu^2). \qquad (2)$$

As can be seen from Tab. 1, the quality of the fit, measured by χ^2 per degree of freedom,

Table 1: OMEs of the $\Upsilon(1S,2S,3S)$ and $\chi_{b0}(1P,2P)$ mesons from fits to CDF data from Runs I and II in the Regge-kinematics approach using unintegrated gluon distributions by J. Blümlein (JB), Jung and Salam (JS), and Kimber, Martin and Ryskin (KMR).

NME	Fit JB	Fit JS	Fit KMR
$\langle\mathcal{O}^{\Upsilon(1S)}[^3S_1^{(1)}]\rangle/\mathrm{GeV}^3$	10.9 ± 1.6	10.9 ± 1.6	10.9 ± 1.6
$\langle\mathcal{O}^{\Upsilon(1S)}[^3S_1^{(8)}]\rangle/\mathrm{GeV}^3$	$(5.3 \pm 0.5) \times 10^{-3}$	$(0.0 \pm 1.8) \times 10^{-4}$	$(0.0 \pm 3.1) \times 10^{-3}$
$\langle\mathcal{O}^{\Upsilon(1S)}[^1S_0^{(8)}]\rangle/\mathrm{GeV}^3$	$(0.0 \pm 4.7) \times 10^{-4}$	$(0.0 \pm 5.2) \times 10^{-5}$	$(0.0 \pm 4.3) \times 10^{-3}$
$\langle\mathcal{O}^{\Upsilon(1S)}[^3P_0^{(8)}]\rangle/\mathrm{GeV}^5$	$(0.0 \pm 1.3) \times 10^{-3}$	$(0.0 \pm 1.6) \times 10^{-4}$	$(9.5 \pm 2.0) \times 10^{-2}$
$M_5^{\Upsilon(1S)}/\mathrm{GeV}^3$	$(0.0 \pm 7.6) \times 10^{-4}$	$(0.0 \pm 8.7) \times 10^{-5}$	$(2.1 \pm 0.9) \times 10^{-2}$
$\langle\mathcal{O}^{\chi_{b0}(1P)}[^3P_0^{(1)}]\rangle/\mathrm{GeV}^5$	2.4 ± 0.4	2.4 ± 0.4	2.4 ± 0.4
$\langle\mathcal{O}^{\chi_{b0}(1P)}[^3S_1^{(8)}]\rangle/\mathrm{GeV}^3$	$(0.0 \pm 2.1) \times 10^{-3}$	$(0.0 \pm 8.4) \times 10^{-5}$	$(0.0 \pm 1.4) \times 10^{-3}$
$\langle\mathcal{O}^{\Upsilon(2S)}[^3S_1^{(1)}]\rangle/\mathrm{GeV}^3$	4.5 ± 0.7	4.5 ± 0.7	4.5 ± 0.7
$\langle\mathcal{O}^{\Upsilon(2S)}[^3S_1^{(8)}]\rangle/\mathrm{GeV}^3$	$(0.0 \pm 5.9) \times 10^{-3}$	$(0.0 \pm 4.1) \times 10^{-4}$	$(3.3 \pm 0.8) \times 10^{-2}$
$\langle\mathcal{O}^{\Upsilon(2S)}[^1S_0^{(8)}]\rangle/\mathrm{GeV}^3$	$(0.0 \pm 9.2) \times 10^{-4}$	$(0.0 \pm 8.3) \times 10^{-5}$	$(0.0 \pm 3.7) \times 10^{-3}$
$\langle\mathcal{O}^{\Upsilon(2S)}[^3P_0^{(8)}]\rangle/\mathrm{GeV}^5$	$(0.0 \pm 2.6) \times 10^{-3}$	$(0.0 \pm 2.8) \times 10^{-4}$	$(0.0 \pm 1.6) \times 10^{-2}$
$M_5^{\Upsilon(2S)}/\mathrm{GeV}^3$	$(0.0 \pm 1.5) \times 10^{-3}$	$(0.0 \pm 1.4) \times 10^{-4}$	$(0.0 \pm 7.2) \times 10^{-3}$
$\langle\mathcal{O}^{\chi_{b0}(2P)}[^3P_0^{(1)}]\rangle/\mathrm{GeV}^5$	2.6 ± 0.5	2.6 ± 0.5	2.6 ± 0.5
$\langle\mathcal{O}^{\chi_{b0}(2P)}[^3S_1^{(8)}]\rangle/\mathrm{GeV}^3$	$(1.1 \pm 0.4) \times 10^{-2}$	$(0.0 \pm 2.8) \times 10^{-4}$	$(0.0 \pm 5.7) \times 10^{-3}$
$\langle\mathcal{O}^{\Upsilon(3S)}[^3S_1^{(1)}]\rangle/\mathrm{GeV}^3$	4.3 ± 0.9	4.3 ± 0.9	4.3 ± 0.9
$\langle\mathcal{O}^{\Upsilon(3S)}[^3S_1^{(8)}]\rangle/\mathrm{GeV}^3$	$(1.4 \pm 0.3) \times 10^{-2}$	$(5.9 \pm 4.2) \times 10^{-3}$	$(1.1 \pm 0.4) \times 10^{-2}$
$\langle\mathcal{O}^{\Upsilon(3S)}[^1S_0^{(8)}]\rangle/\mathrm{GeV}^3$	$(0.0 \pm 2.6) \times 10^{-3}$	$(0.0 \pm 8.1) \times 10^{-4}$	$(0.0 \pm 2.7) \times 10^{-3}$
$\langle\mathcal{O}^{\Upsilon(3S)}[^3P_0^{(8)}]\rangle/\mathrm{GeV}^5$	$(2.4 \pm 0.8) \times 10^{-2}$	$(3.4 \pm 4.2) \times 10^{-3}$	$(5.2 \pm 1.1) \times 10^{-2}$
$M_5^{\Upsilon(3S)}/\mathrm{GeV}^3$	$(5.2 \pm 4.4) \times 10^{-3}$	$(7.4 \pm 10.2) \times 10^{-4}$	$(1.1 \pm 0.5) \times 10^{-2}$
$\langle\mathcal{O}^{\chi_{b0}(3P)}[^3P_0^{(1)}]\rangle/\mathrm{GeV}^5$	2.7 ± 0.7	2.7 ± 0.7	2.7 ± 0.7
χ^2/d.o.f.	2.9	27	0.5

varies widely with the PDFs from 0.5 to 27.

Quarkonium decay OMEs can be computed from first principles using lattice QCD, so that their determination becomes independent of fits to experimental data or potential model assumptions. A. Hart reported about a recent result that matches the electromagnetic vector-annihilation current in lattice NRQCD to the one in continuum QCD, which should allow for a prediction of the leptonic decay widths of S-wave bottomonia with ten percent accuracy and of the ratio of the 2S and 1S Υ-states with one percent accuracy [90]. Numerical results should be available soon.

Charmonium (η_c and χ_{c0}) decays into two photons have been calculated for the first time by Dudek and Edwards, albeit only in the quenched approximation, using relativistic

valence quarks and a perturbative expansion of the photon-quark coupling, which allows to replace the photon by a superposition of QCD states [91]. While the width obtained for the χ_{c0} ($2.41 \pm 0.58 \pm 0.72 \pm 0.48$ keV) is in rather good agreement with the experimental value (2.84 ± 0.40 keV), the one for the η_c ($2.65 \pm 0.26 \pm 0.80 \pm 0.53$ keV) is smaller by a factor of three (7.14 ± 2.49 keV). This might be due to an incorrect running of the strong coupling constant and a depleted wave function at the origin in this calculation. In addition, the discretization error might not be reliable, as only one lattice spacing has been used.

Lansberg and Pham have computed the two-photon widths of ground-state and radially excited η_c [92] and η_b mesons [93] with an effective Lagrangian in the static approximation, taking into account binding energy effects for the radial excitations. Using heavy-quark spin symmetry, they assume equality of the f_{η_c} ($f_{\eta_{c'}}$) and $f_{J/\Psi}$ ($f_{\Psi'}$) decay constants and relate the two-photon width of the η_c to the leptonic decay width of the J/Ψ. While good agreement with the experimental value is found for the η_c ground state (7.5-10 keV), their result for η_c' (3.5-4.5 keV) is three times larger than the CLEO measurement (1.3 ± 0.6 keV). This may be due to the fact that $f_{\eta_c'}$ is not equal, but three times smaller than $f_{\Psi'}$, according to a recent lattice calculation in the quenched approximation by Dudek and Edwards [94].

Radiative decays of charmonia to light mesons have recently been computed in perturbative QCD [95], albeit keeping only the color-singlet wave function contribution and assuming the light mesons to be also described by non-relativistic color-singlet $q\bar{q}$ bound states with finite constituent quark masses. These have then been used to regularize the one-loop diagrams. The numerical results are given in Tab. 2. Unfortunately a systematic study on the theoretical uncertainties with the chosen masses and scales and with respect to possible

Table 2: Proposed theoretical and measured experimental values for $\mathcal{B}(J/\psi \to f_J\gamma)$.

	$f_0(980)$	$f_1(1285)$	$f_2(1270)$	$f_1'(1420)$	$f_2'(1525)$
$\mathcal{B}_{th} \times 10^4$	1.6	7.0	8.7	1.8	2.0
$\mathcal{B}_{ex} \times 10^4$	-	6.1 ± 0.8	13.8 ± 1.4	7.9 ± 1.3	$4.5^{+0.7}_{-0.4}$

color-octet contributions has not been performed. The calculated J/ψ-decay branching ratios to the P-wave mesons $f_2(1270)$ and $f_1(1285)$ fit the data well, while that of $f_0(980)$ (if treated as an $s\bar{s}$ meson) is predicted to be 1.6×10^{-4}, which implies that $f_0(1710)$ can not be the $s\bar{s}$ or $(u\bar{u} + d\bar{d})/\sqrt{2}$ meson. Decays of P-wave charmonia $\chi_{cJ} \to \rho(\omega, \phi)\gamma$ ($J = 0, 1, 2$) have also been studied. The branching ratio of $\chi_{c1} \to \rho\gamma$ is predicted to be 1.4×10^{-5}, which may be tested by CLEO-c and BESIII with future experiments.

A similar calculation has been performed for the radiative decays of bottomonia into charmonia and light mesons, taking into account in addition the sometimes significant QED contributions [96]. While the results for radiative decays into truly non-relativistic charmonia are likely to be more reliable than those for radiative decays into (in reality relativistic) light mesons, these decays remain to be observed. On the other hand, the calculated branching ratios for $\Upsilon \to f_2(1270)\gamma$ (6.3×10^{-5}) and $\Upsilon \to f_2'(1525)\gamma$ (2.0×10^{-5}) are only barely consistent with recent CLEO data [$(1.0 \pm 0.1) \times 10^{-4}$ and $(3.7 \pm 1.2) \times 10^{-5}$], suggesting that the theoretical approach may still need improvement.

Finally, J.M. Richard reviewed the current status of light and heavy multiquark spectroscopy [97]. While experimental evidence for the $uudd\bar{s}$ pentaquark θ^+ seems to vanish, a single-charm baryon with a mass of 2940 MeV and a width of approximately 17 MeV

has recently been confirmed by BaBar, and a double-charm baryon with a mass of 3520 MeV may have been observed by the Selex collaboration. Potential models have since long predicted the existence of baryons with at least one heavy quark, assuming them to be diquark-quark systems that can be described with hyperspherical coordinates. In the meson sector, the state $X(3940)$ may be a 1^{-+} candidate for a ccg hybrid state, to be described in the Born-Oppenheimer approximation with classical constituent gluons. A second recently confirmed state is the $X(3872)$, which QCD sum rules predict to be a 1^{++} $c\bar{c}q\bar{q}$ bound state, even if the theoretical mass found is slightly larger (3925 ± 127 MeV) [98].

3 Acknowledgments

We thank all the speakers of the heavy-flavor working group for their contributions and the local committee for the perfect organization of the DIS 2007 workshop.

References

[1] B. List, " Heavy flavour WG summary – Experiment," *slides available at* `http://indico.cern.ch/contributionDisplay.py?contribId=19&sessionId=2&confId=9499`

[2] H. Stadie [ZEUS Collab.], "DIS charm cross sections through D^* and D meson tagging by the ZEUS detector," *these proceedings.*

[3] D. Nicholass [ZEUS Collab.], "$D^{\pm}$ cross sections in DIS using the ZEUS Micro Vertex Detector," *these proceedings.*

[4] K. Lipka [H1 Collab.], "Charm production in DIS at H1," *these proceedings.*

[5] S. Chekanov *et al.* [ZEUS Collab.], Phys. Lett. B **649**, 111 (2007).

[6] B. W. Harris and J. Smith, Phys. Rev. D **57**, 2806 (1998).

[7] S. Chekanov *et al.* [ZEUS Collab.], arXiv:0704.3562 [hep-ex].

[8] S. Fang [ZEUS Collab.], "Charm fragmentation function and fragmentation functions of charm mesons at ZEUS," *these proceedings.*

[9] S. Chekanov *et al.* [ZEUS Collab.], Eur. Phys. J. C **44**, 351 (2005).

[10] S. Schmidt [H1 Collab.], "Charm production with jets at H1," *these proceedings.*

[11] A. Aktas *et al.* [H1 Collab.], arXiv:hep-ex/0701023.

[12] H. Jung, Comput. Phys. Commun. **143** (2002) 100.

[13] A. Aktas *et al.* [H1 Collab.], Eur. Phys. J. C **50**, 251 (2007).

[14] A. Geiser, "Review of beauty production at HERA," *these proceedings.*

[15] B. Reisert [CDF and D0 Collab.], "Charm and beauty production at the Tevatron," *these proceedings.*

[16] B. Kahle [ZEUS Collab.], "$F_2^{b\bar{b}}$ from the ZEUS HERA-II data," *these proceedings.*

[17] A. Aktas *et al.* [H1 Collaboration], Eur. Phys. J. C **40** (2005) 349,
A. Aktas *et al.* [H1 Collaboration], Eur. Phys. J. C **45** (2006) 23.

[18] K. Krüger, "Review on charmonium production," *these proceedings.*

[19] E. L. Berger and D. L. Jones, Phys. Rev. D **23**, 1521 (1981),
R. Baier and R. Rückl, Phys. Lett. B **102**, 364 (1981).

[20] F. Abe *et al.* [CDF Collab.], Phys. Rev. Lett. **79**, 572 (1997),
T. Shears [CDF Collab.], Eur. Phys. J. C **33**, S475 (2004).

[21] G. T. Bodwin, E. Braaten and G. P. Lepage, Phys. Rev. D **51**, 1125 (1995) [Erratum-ibid. D **55**, 5853 (1997)].

[22] A. Abulencia *et al.* [CDF Collab.], arXiv:hep-ex/0703028.

[23] M. Steder [H1 Collab.], "Inelastic J/ψ production in DIS at H1," *these proceedings.*

[24] M. Krämer, Nucl. Phys. B **459**, 3 (1996).

[25] C. Adloff *et al.* [H1 Collab.], Eur. Phys. J. C **25**, 25 (2002),
S. Chekanov *et al.* [ZEUS Collab.], Eur. Phys. J. C **27**, 173 (2003).

[26] M. zur Nedden [HERA-B Collab.], "Recent charmonium results from HERA-B," *these proceedings.*

[27] W. A. Zajc, "The fluid nature of quark-gluon-plasma," *these proceedings.*

[28] D. Hornback [PHENIX Collab.], "Measurements of heavy quark production via single leptons in $p+p$ and $Au+Au$ collisions at $\sqrt{s} = 200\,\mathrm{GeV}$," *these proceedings.*

[29] A. Mischke [STAR Collab.], "Recent heavy flavour results from STAR," *these proceedings.*

[30] A. Adare *et al.* [PHENIX Collab.], Phys. Rev. Lett. **98**, 172301 (2007).

[31] B. I. Abelev *et al.* [STAR Collab.], arXiv:nucl-ex/0607012.

[32] E. T. Atomssa [PHENIX Collab.], "J/ψ suppression measurements by the PHENIX experiment at RHIC," *these proceedings.*

[33] A. Adare *et al.* [PHENIX Collab.], arXiv:nucl-ex/0611020.

[34] K. K. Seth [CLEO-c Collab.], "Charm at CLEO-c," *these proceedings.*

[35] S. K. Choi *et al.* [Belle Collab.], Phys. Rev. Lett. **89**, 102001 (2002) [Erratum-ibid. **89**, 129901 (2002)], D. M. Asner *et al.* [CLEO Collab.], Phys. Rev. Lett. **92**, 142001 (2004), K. Abe *et al.* [Belle Collab.], arXiv:hep-ex/0507019.

[36] J. L. Rosner *et al.* [CLEO Collab.], Phys. Rev. Lett. **95**, 102003 (2005).

[37] W. M. Yao *et al.* [Particle Data Group], J. Phys. G **33**, 1 (2006).

[38] C. Cawlfield *et al.* [CLEO Collab.], Phys. Rev. Lett. **98**, 092002 (2007).

[39] V. Poireau [Belle and BaBar Collab.], "New resonances and meson spectroscopy at Belle and BaBar," *these proceedings.*

[40] G. Gokhroo *et al.* [Belle Collab.], Phys. Rev. Lett. **97**, 162002 (2006).

[41] B. Aubert *et al.* [BaBar Collab.], arXiv:hep-ex/0607083.

[42] T. E. Coan *et al.* [CLEO Collab.], Phys. Rev. Lett. **96**, 162003 (2006).

[43] Q. He *et al.* [CLEO Collab.], Phys. Rev. D **74**, 091104 (2006).

[44] B. Aubert *et al.* [BaBar Collab.], Phys. Rev. Lett. **95**, 142001 (2005).

[45] K. Abe *et al.* [Belle Collab.], arXiv:hep-ex/0612006.

[46] G. Pakhlova [Belle and BaBar Collab.], "Charm physics at B factories," *these proceedings.*

[47] K. Abe *et al.* [Belle Collab.], Phys. Rev. Lett. **98**, 092001 (2007).

[48] H. Mendez [CLEO Collab.], arXiv:hep-ex/0702008.

[49] B. Aubert *et al.* [BaBar Collab.], arXiv:hep-ex/0610057.

[50] K. Abe *et al.* [Belle Collab.], arXiv:hep-ex/0507019, K. Abe *et al.* [Belle Collab.], Phys. Rev. Lett. **94**, 182002 (2005), S. Uehara *et al.* [Belle Collab.], Phys. Rev. Lett. **96**, 082003 (2006).

[51] B. Aubert *et al.* [BaBar Collab.], Phys. Rev. Lett. **97**, 222001 (2006).

[52] B. Aubert *et al.* [BaBar Collab.], Phys. Rev. Lett. **98**, 012001 (2007), K. Abe *et al.* [Belle Collab.], arXiv:hep-ex/0608043.

[53] R. Chistov *et al.* [Belle Collab.], Phys. Rev. Lett. **97**, 162001 (2006), B. Aubert *et al.* [BaBar Collab.], arXiv:hep-ex/0607042.

[54] B. Aubert *et al.* [BaBar Collab.], Phys. Rev. Lett. **97**, 232001 (2006).

[55] M. Heck [CDF and D0 Collab.], "Recent results on B spectroscopy at the Tevatron," *these proceedings.*

[56] I. G. Eschrich [BaBar Collab.], "Rare decays at the B Factories," *these proceedings.*

[57] K. Abe *et al.* [Belle Collab.], Phys. Rev. Lett. **96**, 221601 (2006).

[58] E. Barberio *et al.* [Heavy Flavor Averaging Group (HFAG)], arXiv:0704.3575 [hep-ex].

[59] E. Barberio *et al.* [Heavy Flavor Averaging Group (HFAG)], arXiv:hep-ex/0603003.

[60] M. Misiak *et al.*, Phys. Rev. Lett. **98**, 022002 (2007), T. Becher and M. Neubert, Phys. Rev. Lett. **98**, 022003 (2007).

[61] K. Abe *et al.* [Belle Collab.], Phys. Rev. Lett. **96**, 221601 (2006), B. Aubert *et al.* [BaBar Collab.], Phys. Rev. Lett. **98**, 151802 (2007).

[62] K. Ikado *et al.* [Belle Collab.], Phys. Rev. Lett. **97**, 251802 (2006), B. Aubert *et al.* [BaBar Collab.], arXiv:hep-ex/0608019.

[63] M. Corcoran [CDF and D0 Collab.], "B hadron rare decays and lifetimes," *these proceedings.*

[64] R. Kehoe [CDF and D0 Collab.], "B_s mixing and lifetime difference measurements," *these proceedings.*

[65] V. M. Abazov *et al.* [D0 Collab.], Phys. Rev. Lett. **97**, 021802 (2006).
[66] A. Abulencia *et al.* [CDF Collab.], Phys. Rev. Lett. **97**, 062003 (2006).
[67] V. M. Abazov *et al.* [D0 Collab.], Phys. Rev. Lett. **98**, 121801 (2007).
[68] A. Lenz and U. Nierste, arXiv:hep-ph/0612167.
[69] V. M. Abazov *et al.* [D0 Collab.], arXiv:hep-ex/0702049.
[70] L. M. Zhang *et al.* [Belle Collab.], Phys. Rev. Lett. **96**, 151801 (2006), B. Aubert *et al.* [BaBar Collab.], Phys. Rev. Lett. **97**, 221803 (2006).
[71] B. Aubert *et al.* [BaBar Collab.], Phys. Rev. Lett. **98**, 211802 (2007), M. Staric *et al.* [Belle Collab.], Phys. Rev. Lett. **98**, 211803 (2007).
[72] K. Abe *et al.* [Belle Collab.], arXiv:0704.1000 [hep-ex].
[73] A. Krasznahorkay Jr. [ATLAS and CMS Collab.], "Outlook for b and c physics at the LHC in ATLAS and CMS," *these proceedings.*
[74] E. Santovetti [LHCb Collab.], "B physics prospects at LHCb," *these proceedings.*
[75] T. Greenshaw, "Physics with flavour at the International Linear Collider," *these proceedings.*
[76] M. Klasen, "Heavy Flavour WG – Theory summary," *slides available at* `http://indico.cern.ch/contributionDisplay.py?contribId=19&sessionId=2&confId=9499`
[77] G. Kramer, "Recent developments in heavy flavour production," *these proceedings.*
[78] M. Buza, Y. Matiounine, J. Smith, R. Migneron and W. L. van Neerven, Nucl. Phys. B **472**, 611 (1996).
[79] I. Bierenbaum, J. Blümlein and S. Klein, arXiv:hep-ph/0703285 *and these proceedings.*
[80] S. J. Brodsky, P. Hoyer, C. Peterson and N. Sakai, Phys. Lett. B **93**, 451 (1980).
[81] F. S. Navarra, M. Nielsen, C. A. A. Nunes and M. Teixeira, Phys. Rev. D **54**, 842 (1996).
[82] W. Melnitchouk and A. W. Thomas, Phys. Lett. B **414**, 134 (1997).
[83] J. Pumplin, H. L. Lai and W. K. Tung, Phys. Rev. D **75**, 054029 (2007) *and these proceedings.*
[84] M. Krämer, J. Zunft, J. Steegborn and P. M. Zerwas, Phys. Lett. B **348**, 657 (1995).
[85] M. Klasen, B. A. Kniehl, L. N. Mihaila and M. Steinhauser, Nucl. Phys. B **713**, 487 (2005).
[86] M. Klasen, B. A. Kniehl, L. N. Mihaila and M. Steinhauser, Phys. Rev. D **71**, 014016 (2005).
[87] J. Campbell, F. Maltoni and F. Tramontano, arXiv:hep-ph/0703113.
[88] B. A. Kniehl, D. V. Vasin and V. A. Saleev, Phys. Rev. D **73**, 074022 (2006).
[89] B. A. Kniehl, V. A. Saleev and D. V. Vasin, Phys. Rev. D **74**, 014024 (2006) *and these proceedings.*
[90] A. Hart, G. M. von Hippel and R. R. Horgan, Phys. Rev. D **75**, 014008 (2007) *and these proceedings.*
[91] J. J. Dudek and R. G. Edwards, Phys. Rev. Lett. **97**, 172001 (2006).
[92] J. P. Lansberg and T. N. Pham, Phys. Rev. D **74**, 034001 (2006)
[93] J. P. Lansberg and T. N. Pham, Phys. Rev. D **75**, 017501 (2007).
[94] J. J. Dudek, R. G. Edwards and D. G. Richards, Phys. Rev. D **73**, 074507 (2006).
[95] Y. J. Gao, Y. J. Zhang and K. T. Chao, Chin. Phys. Lett. **23**, 2376 (2006).
[96] Y. J. Gao, Y. J. Zhang and K. T. Chao, arXiv:hep-ph/0701009.
[97] J. M. Richard, Nucl. Phys. Proc. Suppl. **164**, 131 (2007) *and these proceedings.*
[98] R. D. Matheus, S. Narison, M. Nielsen and J. M. Richard, Phys. Rev. D **75**, 014005 (2007).

Spin Physics: Session Summary

Daniël Boer[1], Delia Hasch[2] and Gerhard Mallot[3]

1- Vrije Universiteit Amsterdam - Department of Physics and Astronomy
De Boelelaan 1081, NL-1081 HV Amsterdam - The Netherlands

2- INFN Laboratory Nazionali di Frascati
Via Enrico Fermi 40, I-00044 Frascati - Italy

3- CERN, CH-1211 Geneva 23 - Switzerland

We summarize the main results of the spin physics Working Group Session of DIS 2007, the 15th International Workshop on "Deep-Inelastic Scattering and Related Subjects".

1 Introduction

Many spin physics experiments have been performed in recent years and many new exciting results have been reported at DIS 2007 [1], which will be highlighted in this summary. Also on the theory side many new results were reported, especially regarding transverse spin effects which are most challenging. Recent years have seen quite some unexpected developments concerning so-called TMDs, transverse momentum dependent parton distributions, and we can look forward to more such developments over the coming years. Therefore, this summary is very much a snapshot of the current status.

This summary is split into three main parts. We start with longitudinal spin physics, most notably, experimental results on gluon polarization. We proceed with transverse spin, which is mainly focused on transverse spin asymmetries and the possible explanation in terms of TMDs. The third and last part is about exclusive processes and generalized parton distributions, which provide more detailed information about the spatial distribution of partons inside hadrons. This spatial distribution is often probed using spin asymmetries and recent developments have started to point to a connection between GPDs and TMDs. A very interesting development.

2 Longitudinal spin

The discovery by the European Muon Collaboration [2] that the first moment Γ_1^p of the spin-dependent structure function g_1^p of the proton

$$\Gamma_1^{p/n}(Q^2) = \int_0^1 \mathrm{d}x\; g_1^{p/n}(x,Q^2) = \frac{1}{36}\left(4\Delta\Sigma \pm 3\Delta q_3 + \Delta q_8\right)\left(1+\frac{\alpha_s}{\pi}\right) + \mathcal{O}(\alpha_s^2)$$

is much smaller than expected implies that the total contribution of the quark spins to the nucleon spin $\Delta\Sigma \equiv \Delta u + \Delta d + \Delta s$ is small. Here $\Delta q = (q_+ - q_-) + (\bar{q}_+ - \bar{q}_-)$ is the difference of the number of quarks and antiquarks of flavor q with positive and negative helicity and $\Delta q_3 \equiv \Delta u - \Delta d$ and $\Delta q_8 \equiv \Delta u + \Delta d - 2\Delta s$ are known from β decays.

HERMES presented the final analysis of their g_1^p and g_1^d measurements [3] and COMPASS showed new, very precise deuteron data [4] (Fig. 1). Both collaborations evaluated $\Delta\Sigma$ from their deuteron data with $Q^2 > 1$ GeV^2 yielding $\Delta\Sigma = 0.330 \pm 0.025\,(\mathrm{exp.}) \pm 0.028\,(\mathrm{evol.}) \pm 0.011\,(\mathrm{theo.})$ at $Q^2 = 5$ GeV^2 from HERMES and $\Delta\Sigma = 0.35 \pm 0.03\,(\mathrm{stat.}) \pm 0.05\,(\mathrm{syst.})$ at $Q^2 = 3$ GeV^2 from COMPASS. The results are in excellent agreement. The value for

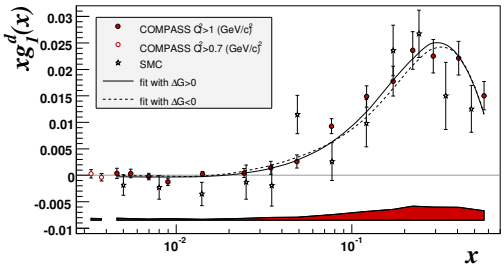

Figure 1: The deuteron structure function xg_1^d as function of x from COMPASS [4]. Also shown are QCD fits with positive and negative ΔG.

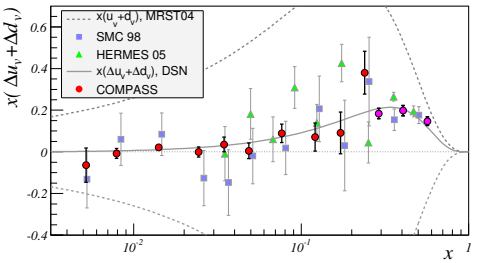

Figure 3: The valence quark distribution $x(\Delta u_v + \Delta d_v)$ as function of x from SIDIS obtained in LO and evolved to $Q^2 = 10$ GeV^2 [7] using the PDFs of Ref. [8].

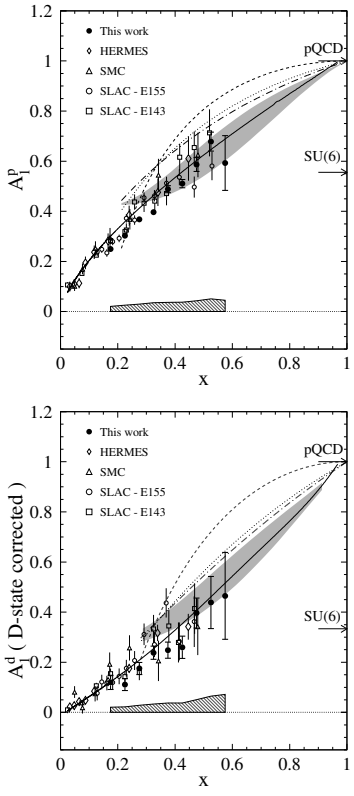

Figure 2: Asymmetry A_1 for the proton (top) and the deuteron (bottom) from CLAS EG1 for $Q^2 > 1$ GeV^2 and $W > 2$ GeV [5].

$\Delta\Sigma$ is somewhat larger than the original EMC result of $\Delta\Sigma = 0.12 \pm 0.17$, which was given at a larger scale $Q^2 = 10.7$ GeV^2. All results are consistent with each other upon taking evolution into account. Therefore, the conclusion that the quark spins contribute little to the nucleon spin remains valid.

CLAS from JLAB showed a wealth of proton and deuteron g_1 data covering the range $0.05 < Q^2 < 5$ GeV^2. For $Q^2 > 1$ GeV^2 the range $0.15 < x < 0.58$ is covered [5] (Fig. 2). The spin structure in the resonance region and the Burkhardt–Cottingham sum rule were explored by the Hall-C experiment E01-006 [6].

Semi-inclusive DIS (SIDIS), in which in addition to the scattered lepton a hadron is observed, can be analyzed in terms of the valence quark helicity distributions Δq_v. New COMPASS deuteron data obtained in leading order (LO) and using a fragmentation-function independent method [7] are shown in Fig. 3 together with previous data. They disfavour a flavor-symmetric quark sea with $\Delta\overline{u} = \Delta\overline{d} = \Delta s = \Delta\overline{s}$.

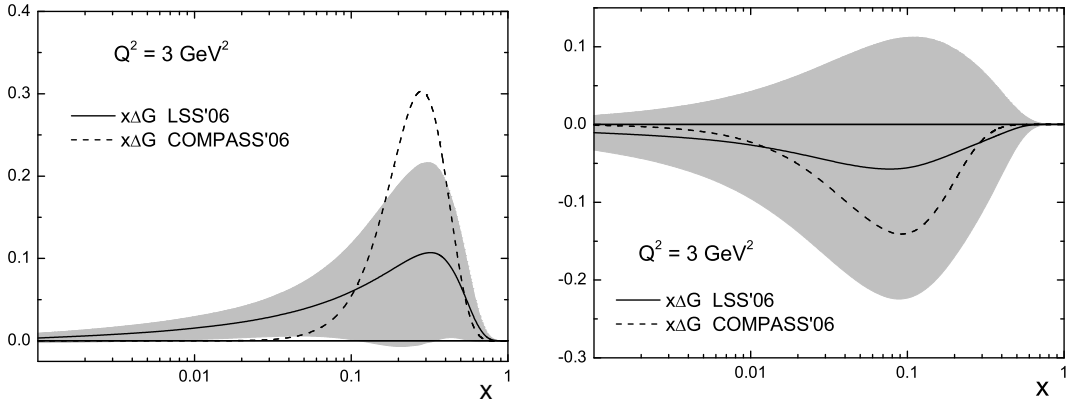

Figure 4: Solutions for positive (left) and negative (right) gluon polarizations $x\Delta G(x)$ as function of x from LSS [10] (solid line) with uncertainties. The dashed line shows the corresponding COMPASS fits [4].

Apart from the contribution of the quark spins $\Delta\Sigma$, the nucleon spin sum rule

$$\frac{1}{2} = \frac{1}{2}\Delta\Sigma + \Delta G + L_z$$

receives contributions from gluon spins $\Delta G = \int \mathrm{d}x\ (G_+ - G_-)$ and from orbital angular momentum L_z, which must compensate for the smallness of $\Delta\Sigma$. Experiments start to obtain information on the gluon polarization ΔG, although uncertainties are still large. The gluon polarization can be studied in polarized DIS and SIDIS and in $\vec{p}\vec{p}$ interactions.

Inclusive DIS is sensitive to $\Delta G(x)$ through the Q^2 evolution of g_1. However, the lack of a polarized lepton–proton collider limits the kinematic range of g_1 to the fixed-target domain at moderate x and Q^2. The status of QCD fits to the world g_1 data from CERN, DESY, JLAB and SLAC were reviewed by J. Blümlein. He also summarized the status of $\alpha_s(M_Z^2)$ as obtained from DIS up to NNNLO for the unpolarized case and NLO for the polarized case [9]. Although the precision of α_s from polarized DIS can not yet reach that from the unpolarized data, the precision is remarkable.

As example for the present status of the QCD analyses we show the recent one by the LSS group [10], which takes into account the latest data from COMPASS [4] and CLAS [5]. They obtain three equally good solutions for positive, negative and sign-changing gluon polarization. The positive and negative solutions are compared in Fig. 4 with the solutions obtained by COMPASS in a similar analysis. At present even the sign of the gluon polarization cannot be determined from DIS data, however all fits yield a small value for the first moment $|\Delta G| \lesssim 0.3$ at $Q^2 = 3$ GeV^2.

At small Q^2 standard DGLAP fits cannot be applied without considering higher-twist effects. The LSS group explicitly included such terms in their fits. The resulting higher-twist contributions are driven by the CLAS data [5]. Ermolaev focused on the small-x aspects of the singlet part of g_1, in particular the resummation of the leading $\ln 1/x$ terms [11]. He suggested to study the dependence on the invariant energy $2P\cdot q$ rather than Q^2 to estimate the impact of the initial gluon density.

More direct information on the gluon polarization can be obtained in SIDIS. Photon–gluon fusion (PGF) $\gamma g \to q\overline{q}$ leading to a quark–antiquark pair gives rise to a double-spin cross-section asymmetry proportional to the gluon polarization

$$A_{\parallel} = R_{\mathsf{pgf}} a_{LL}^{\mathsf{pgf}} \frac{\Delta G}{G} + A_{\mathsf{bgd}},$$

where R_{pgf} is the fraction of PGF events and a_{LL}^{pgf} is the analyzing power of the PGF subprocess. For a particular measurement both, R_{pgf} and the average a_{LL}^{pgf}, have to be estimated using Monte Carlo (MC) simulations. This introduces a model dependence in the determination of $\Delta G/G$. In the light-quark case the QCD-Compton process $\gamma q \to qg$ and the direct process $\gamma q \to q$ limit R_{pgf} to about 30 %, while for charmed quark pairs R_{pgf} is essentially unity. Here the challenges are the low production cross-section and the detection of open charm (D mesons). The most promising decay channel $D \to K\pi$ has a branching ratio of only 3.8 % which implies that only one of the two charmed hadrons can be observed with reasonable statistics. Until now all analyses were performed in leading order.

HERMES determined $\Delta G/G$ from single high-p_T hadron production asymmetries in four bins of transverse hadron momentum p_T in the range 1.05 GeV $< p_T <$ 2.5 GeV using two methods [12]. Method I directly used the above equation for $A_{\parallel}$ with $R_{\mathsf{pgf}}(p_T)$ and $a_{LL}^{\mathsf{pgf}}(p_T)$ determined using a PYTHIA Monte Carlo simulation. In Method II two different parameterizations of $\Delta G/G$ were fitted to the measured asymmetries in the four p_T bins. The gluon polarization is small and probed around $x \simeq 0.22$ at $\mu^2 = 1.35$ GeV^2. The resulting value $\Delta G/G = 0.071 \pm 0.034\,(\text{stat.}) \pm 0.010\,(\text{syst.})^{+0.127}_{-0.105}\,(\text{model})$ is shown together with the fitted parameterizations and other data in Fig. 5.

COMPASS determined $\Delta G/G$ from the cross-section asymmetries for D meson production in [13]. This method relies much less on Monte Carlo simulations but is limited in statistical precision. A neural network was used to estimate a_{LL}^{pgf} from the event kinematics on an event-by-event basis. The result $\Delta G/G = -0.57 \pm 0.41 \pm 0.17\,(\text{syst.})$ is compatible with zero and probes the gluon distribution around $\mu^2 = 13$ GeV^2 and $x = 0.15$. This is also compatible with the most precise COMPASS result from light-quark pairs at $Q^2 < 1$ GeV^2 of $\Delta G/G = 0.016 \pm 0.058 \pm 0.055\,(\text{syst.})$. All results from PGF in DIS are summarized in Fig. 5 and in Ref. [14].

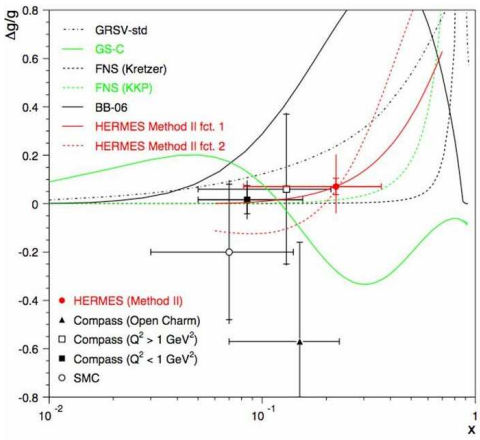

Figure 5: The gluon polarization $\Delta G/G$ as function of x. The new HERMES point lies at $\Delta G/G \simeq 0.07$ and $x \simeq 0.2$, where the two fitted parameterizations intersect.

ΔG can in principle also be obtained from polarized photoproduction of hadron pairs with high transverse momenta $(p_{T,3}, p_{T,4})$. Hendlmeier presented NLO calculations for this process with HERMES and COMPASS kinematics. The scale dependence for the cross-sections and asymmetries at NLO is generally not smaller than at LO. An interesting option is the reduction of the

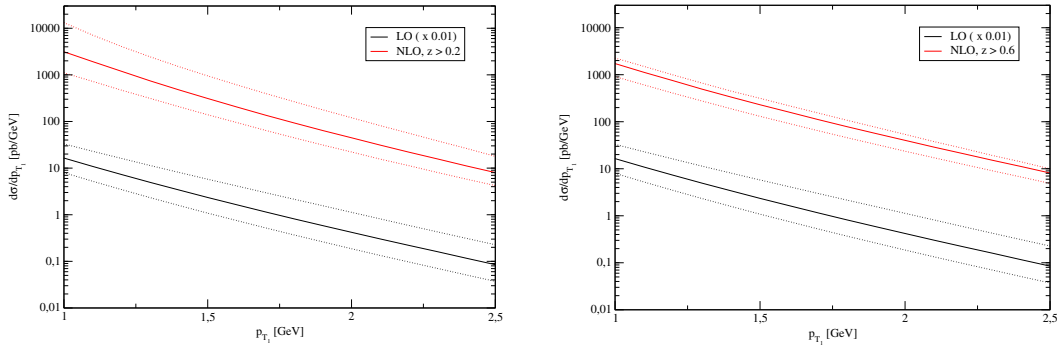

Figure 6: Scale dependence for the pair cross-section as function of the p_T of the first hadron in LO (bottom curves) and NLO (top curves) for $z > 0.2$ (left) and $z > 0.6$ (right) and COMPASS kinematics. The scale μ is varied by a factor two around $\mu = p_{T,3} + p_{T,4}$, see the text for the definition of z.

scale dependence by cutting on a variable defined as $z = -\vec{p}_{T,3} \cdot \vec{p}_{T,4}/\vec{p}^{\,2}_{T,3}$. This only works for the COMPASS kinematics (Fig. 6), while in the HERMES case the cut has little effect.

At RHIC cross-section asymmetries for longitudinally polarized $\vec{p}\vec{p}$ scattering at $\sqrt{s} =$ 200 GeV were analyzed for several channels. PHENIX presented results for π^0 production [15]. The cross-section is well understood over seven orders of magnitude in NLO [16], as can be seen in Fig. 8. Their data favour a small gluon polarization and are compatible with the $\Delta G = 0$ and the standard scenario of GRSV [17] in NLO (Fig. 7). Also a negative gluon polarization cannot be excluded. Future measurements at $\sqrt{s} = 500$ GeV will remove the present ambiguity because of the decreasing relative importance of the quadratic term in ΔG with increasing p_T. Data taken in 2006 at $\sqrt{s} = 62.4$ GeV (see Fig. 8 for the cross section measured by BRAHMS at this energy) will allow to probe higher x_{gluon}.

STAR presented longitudinal spin asymmetries for inclusive jet production [18] (Fig. 9) and pions [19] from the 2005 run. Again the cross-sections are well understood in NLO [20] and the data point to a rather small gluon polarization and negative values cannot be excluded. The precise data taken in 2006 will drastically improve the statistical precision.

All data suggest gluon polarization $|\Delta G| \lesssim 0.3$, where one has to keep in mind that the relevant scales for the various measurements vary. Although this value is by far smaller than the values around 2–3 predicted by some models assuming a restoration of $\Delta\Sigma$ to the Ellis–Jaffe value of 0.6 via the axial anomaly, it does not exclude that the gluon and quark spins make up the entire nucleon spin of 1/2. Therefore, the importance of orbital angular momentum remains to be seen (further discussion on this topic can be found in section 4).

3 Transverse spin

In analogy to the axial charge Δq the tensor charge δq is defined as

$$\langle P, S|\overline{\psi}_q[\gamma^\mu, \gamma^\nu]\gamma_5\psi_q(0)|P, S\rangle \sim \delta q\ [P^\mu S^\nu - P^\nu S^\mu]\,,$$

which arises for a transversely polarized proton. This fundamental charge δq is the first Mellin moment of the so-called transversity distribution $h_1(x)$. It encodes completely new

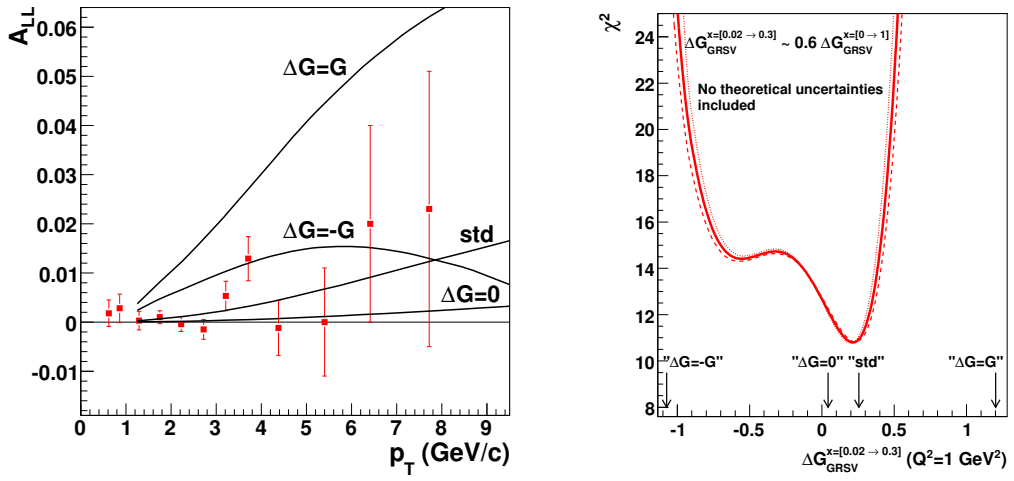

Figure 7: PHENIX π^0 asymmetry data [15]. Left: A_{LL} as function of p_T. A scale uncertainty of 9.4 % is not included. The curves correspond to the NLO predictions for various GRSV parameterizations [17]. Right: χ^2 as function of ΔG_{GRSV}, only statistical errors are taken into account.

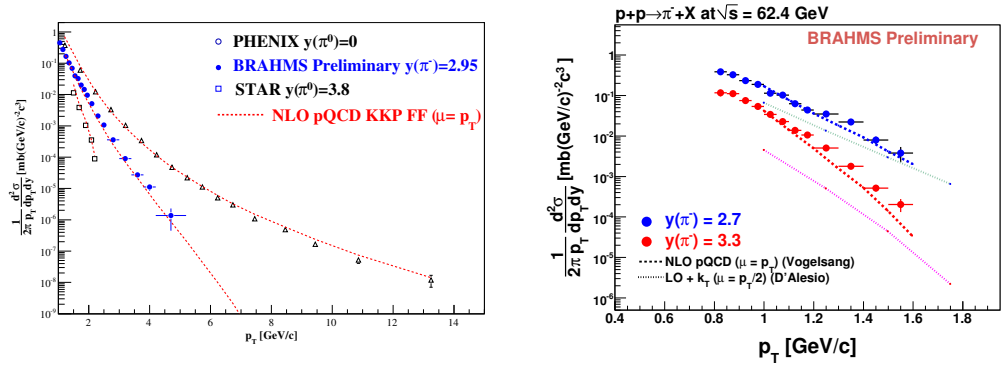

Figure 8: Cross-sections measured at RHIC. Left: Data by the PHENIX, STAR and BRAHMS experiments at $\sqrt{s} = 200$ GeV, compared with NLO pQCD predictions. Right: Similarly for data by the BRAHMS experiment at $\sqrt{s} = 62.4$ GeV.

information on the proton spin structure and is difficult, but not impossible to measure. Theoretically the most safe extractions can come from processes for which collinear factorization can be applied. In this case these are the following single and double transverse-spin asymmetries:

- A_{TT} in $p^\uparrow \bar{p}^\uparrow \to \ell\bar{\ell}\, X$
- A_T in various processes exploiting two-hadron fragmentation functions

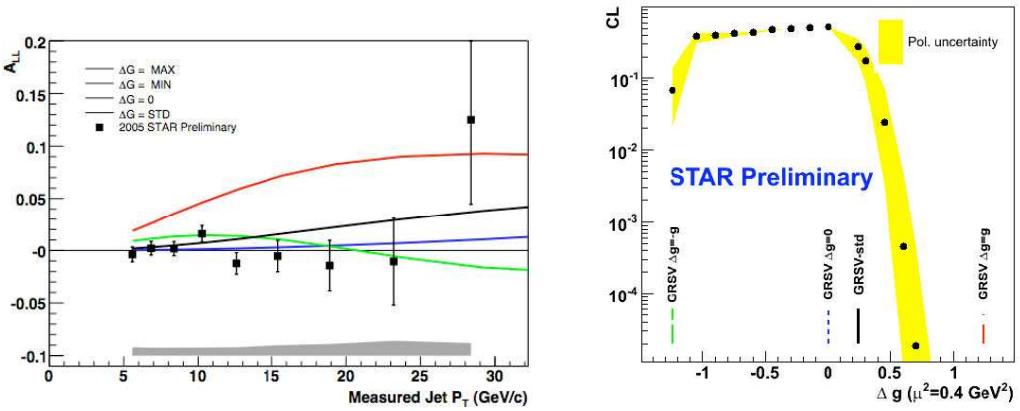

Figure 9: STAR inclusive jet asymmetry data. Left: A_{LL} as function of the measured jet p_T. The scale uncertainty of 25 % is not included in the shaded systematic error band. The curves correspond to the NLO predictions for various GRSV parameterizations [17]. Right: Confidence level as function of ΔG_{GRSV}.

The HERMES experiment has obtained the first non-zero transversity signal from the measurement of A_T in the process $e\,p^\uparrow \to e'\,(\pi^+\pi^-)\,X$ [21]. At DIS 2007 the COMPASS results on A_T in $\mu\,d^\uparrow \to \mu'\,(\pi^+\pi^-)\,X$ were presented: they are consistent with zero [22]. This is in line with the expectation that $h_1^u \approx -h_1^d$ leading to cancellations for a deuteron target. In the near future COMPASS will run with a proton target, allowing a check of the HERMES results. The two-hadron fragmentation functions themselves will be extracted in the future from BELLE data [23], which is crucial for the quantitative extraction of transversity from $e/\mu\,p^\uparrow$ or $p\,p^\uparrow$ processes. On the theory side, Radici discussed evolution equations for two-hadron fragmentation functions [24], which is an important issue when extracting transversity from a combination of two-hadron production observables measured in different experiments. Radici pointed out that the R_T^2 dependence (which is the square of the difference of the transverse momenta of the two hadrons) leads to a homogeneous evolution equation for the two-hadron fragmentation functions.

Hägler discussed the transverse spin structure of hadrons from lattice QCD with dynamical quarks, in particular more precise results on tensor GPDs (generalized parton distributions will be addressed further in section 4) [25], which may also shed light on transverse momentum dependent parton distributions, as will be discussed below.

Kawamura presented results [26] for $A_{TT}(Q_T)$ in the Drell–Yan process, which is proportional to h_1 times h_1. Soft gluon resummation was taken into account. Predictions for $p^\uparrow p^\uparrow$ at RHIC and J-PARC and for $p^\uparrow \bar{p}^\uparrow$ at GSI were given (Fig. 10). The latter observable displays a notably larger dependence on the scale Q^2 than the former.

Not all transverse spin asymmetries are associated with transversity though. Large single-spin asymmetries (A_N) in $p\,p^\uparrow \to \pi\,X$ have been observed by several experiments (E704 Collab. ('91); AGS ('99); STAR ('02); BRAHMS ('05); ...). The observed asymmetries are left-right asymmetries, which means the pion distribution is left-right asymmetric depending on the transverse spin direction and the pion charge.

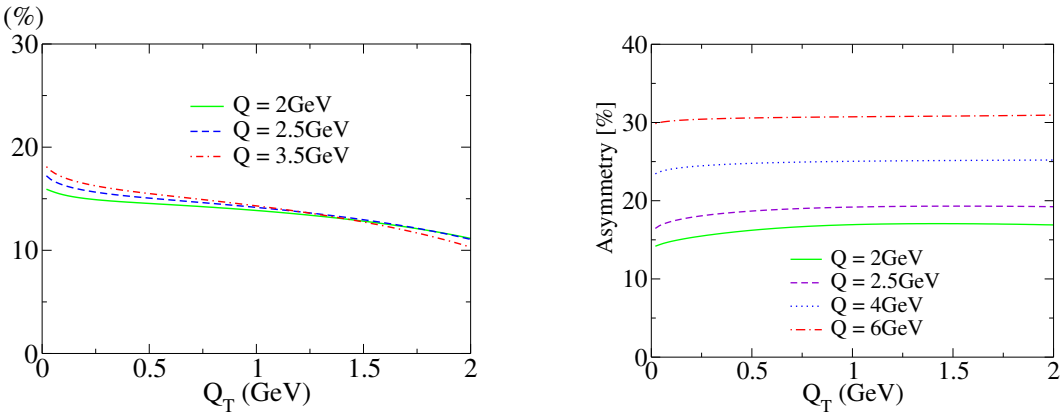

Figure 10: $A_{TT}(Q_T)$ predictions for $p^\uparrow p^\uparrow$ at J-PARC and $p^\uparrow \bar{p}^\uparrow$ at GSI (at $\sqrt{s} = 10$ and 14.5 GeV, resp.) [26].

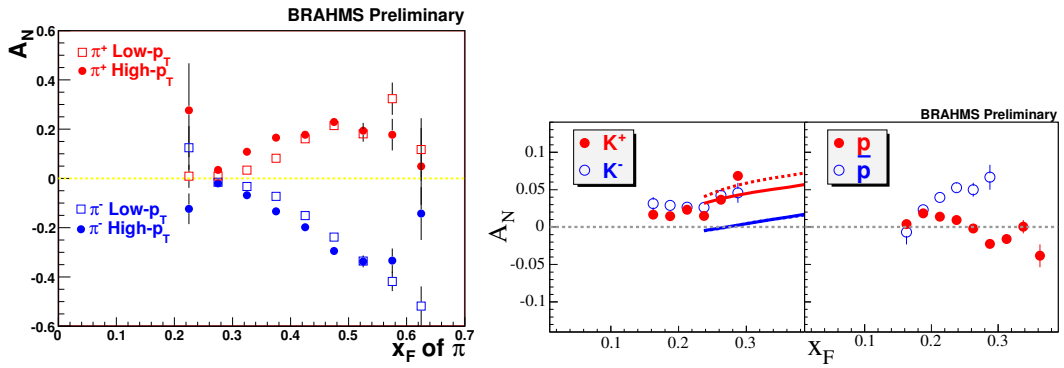

Figure 11: Single spin asymmetries measured by BRAHMS. Left: A_N for $\pi^\pm$ as function of x_F, a high and low p_T data comparison at $\sqrt{s} = 62$ GeV. Right: A_N for $K^\pm$, p and $\bar{p}$ at $\sqrt{s} = 200$ GeV.

New A_N measurements were presented at DIS2007. For example, Fig. 11 shows several single-spin asymmetries measured by BRAHMS [27]. PHENIX presented A_N asymmetries for charged hadrons at mid rapidity as function of p_T and for $J/\psi \to \mu^+\mu^-$ at $x_F \approx \pm 0.1$; all are consistent with zero [28]. STAR presented A_N asymmetries for forward π^0's and for larger x_F (> 0.4) also as a function of p_T, these are shown in Fig. 12 [29].

To understand the origin of these single-spin asymmetries a different explanation at the quark–gluon level is required than simply non-zero transversity.

One suggestion put forward is to describe A_N at the twist-3 level, the so-called Qiu-Sterman effect [30]. It involves a matrix element of the form

$$G_F \sim \langle P, S_T | \, \overline{\psi}(0) \int d\eta^- \; F^{+\alpha}(\eta^-) \, \gamma^+ \, \psi(\xi^-) \, | P, S_T \rangle$$

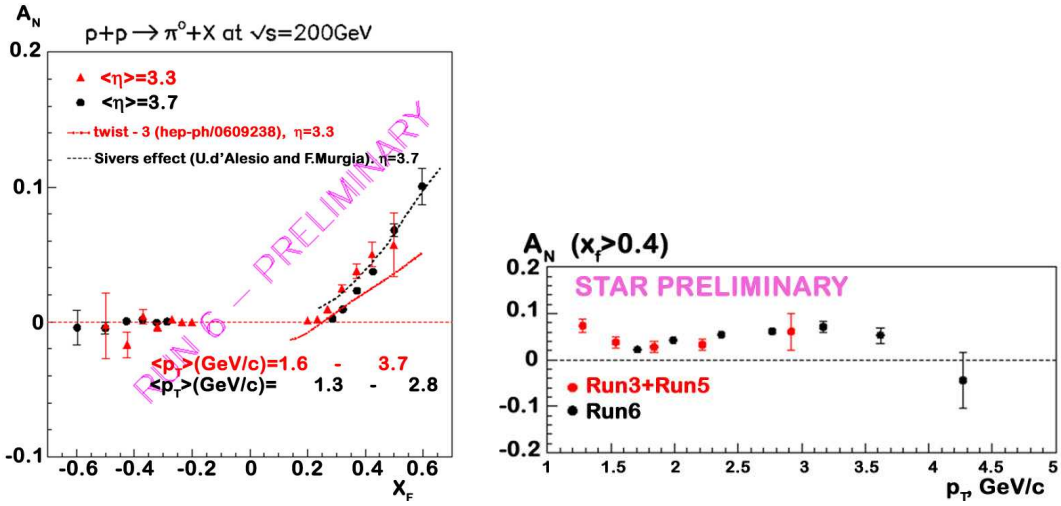

Figure 12: Single spin asymmetries measured by STAR. Left: A_N for forward π^0 as function of x_F at $\sqrt{s} = 200$ GeV. Right: A_N for $x_F > 0.4$ as a function of p_T.

This formalism applies at high transverse momentum of the pion. At DIS 2007 recent progress concerning this formalism was presented. Koike discussed the recent demonstration of twist-3 factorization and gauge invariance of the A_N expression [31]. Tanaka presented a novel master formula for A_N in various processes [32]. He showed that the twist-3 single-spin asymmetry can be obtained from the twist-2 unpolarized cross-section. This provides a significant simplification of the calculation and an understanding of why always the combination $G_F - x\,dG_F/dx$ appears.

Another suggestion is to describe A_N using transverse momentum dependent parton distributions (TMDs). TMDs arise from the natural extension of x dependent functions to x and k_T dependent functions. But allowing for a dependence on k_T also implies the appearance of new functions, such as the Sivers function [33] $f_{1T}^{\perp}$:

$$f_1(x) \Longrightarrow f_1(x, \boldsymbol{k}_T^2) + \frac{\boldsymbol{P}\cdot(\boldsymbol{k}_T \times \boldsymbol{S}_T)}{M}\, f_{1T}^{\perp}(x, \boldsymbol{k}_T^2).$$

Upon integration over transverse momentum the k_T-odd Sivers function $f_{1T}^{\perp}$ drops out. Similarly, a chiral-odd TMD can arise that is also k_T-odd: $h_1^{\perp}$. In addition, the fragmentation function analogues $D_{1T}^{\perp}$ and $H_1^{\perp}$ arise.

The Sivers effect can lead to a non-zero A_N in $p p^{\uparrow} \to \pi X$, but also to azimuthal spin asymmetries in many different processes, such as in semi-inclusive DIS or back-to-back jets in $p p$ scattering. This allows to test the consistency of the many asymmetries described within this formalism.

In semi-inclusive DIS (Fig. 13) the Sivers function leads to a $\sin(\phi_h - \phi_S)$ asymmetry ($\propto f_{1T}^{\perp} D_1$), which can be distinguished from the Collins asymmetry $\sin(\phi_h + \phi_S)$ which arises with the transversity function ($\propto h_1 H_1^{\perp}$) [35]. Bacchetta presented the complete expressions of all 18 possible semi-inclusive DIS structure functions in terms of TMDs [34].

The first azimuthal spin asymmetry measurement was done by the HERMES Collaboration [36]. At DIS 2007 the latest HERMES and COMPASS results on the Sivers and Collins

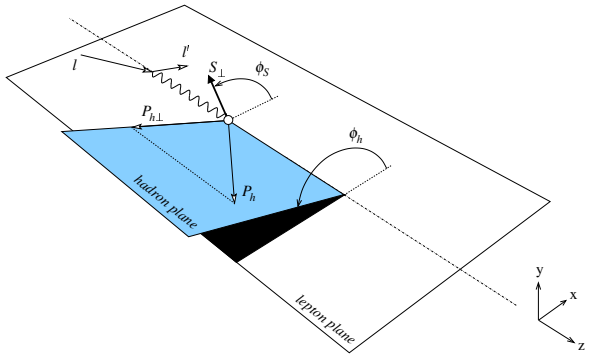

Figure 13: Kinematics of semi-inclusive DIS, with azimuthal angles ϕ_S and ϕ_h indicated [34].

asymmetries were presented. The HERMES data from 2002–2005 show large positive (negative) Collins asymmetries for π^+ (π^-) [37], indicating that the Collins function $H_1^\perp$ for favored fragmentation is approximately equal in magnitude to unfavored fragmentation, but of opposite sign. For the Sivers asymmetry the π^+ data show a significant non-zero asymmetry, but the π^- data are consistent with zero. The neutral pions follow the expectation from isospin symmetry for both types of asymmetry. The $K^\pm$ asymmetries have less statistical accuracy, but are similar to those for $\pi^\pm$, although K^+ shows even larger Sivers asymmetries than π^+. This may indicate that the sea contribution to the Sivers mechanism is of importance. COMPASS results on these and other asymmetries show that for the deuteron these asymmetries are all consistent with zero, indicating cancellations rather than small functions [38, 39].

As mentioned, the Sivers effect can also lead to a non-zero A_N asymmetry for back-to-back jet production in $p\,p^\uparrow$ scattering [40]. In general, the two jets are not exactly back-to-back and an asymmetric distribution of one jet around the other may arise from the Sivers effect. This effect translates into a (generally smaller) left-right asymmetry for the bisector of the two jet directions. STAR results on the bisector left-right asymmetry are consistent with zero [42]. The data are also consistent with a recent prediction presented by Bomhof [41], based on Sivers function input from semi-inclusive DIS which probes mostly the large-x part of the Sivers functions. One concludes that the smaller x part that is probed in the back-to-back jets Sivers asymmetry is likely to be small. However, another aspect that contributes to the suppression of the magnitude of the back-to-back jets Sivers asymmetry is that the color flow of the process makes it less sensitive to the Sivers function. It has been noted several years ago by Collins [43] that TMDs can exhibit a calculable process dependence, leading to the result that the Sivers function that enter the semi-inclusive asymmetry enters the analogous Drell–Yan asymmetry with opposite sign. This is due to the different color flows in the two processes. Bomhof and collaborators have found that the more hadrons are observed in a process, the more complicated the end result. At DIS 2007 Bomhof presented results [41] for $p^\uparrow\, p \to$ jet jet X, included in Fig. 14.

Also the Collins function can lead to asymmetries in other processes besides semi-inclusive DIS. It leads to $\cos 2\phi$ asymmetries in several processes, most notably in $e^+\, e^- \to \pi^+\, \pi^-\, X$, which can be used to extract the Collins function [44]. This has been done using

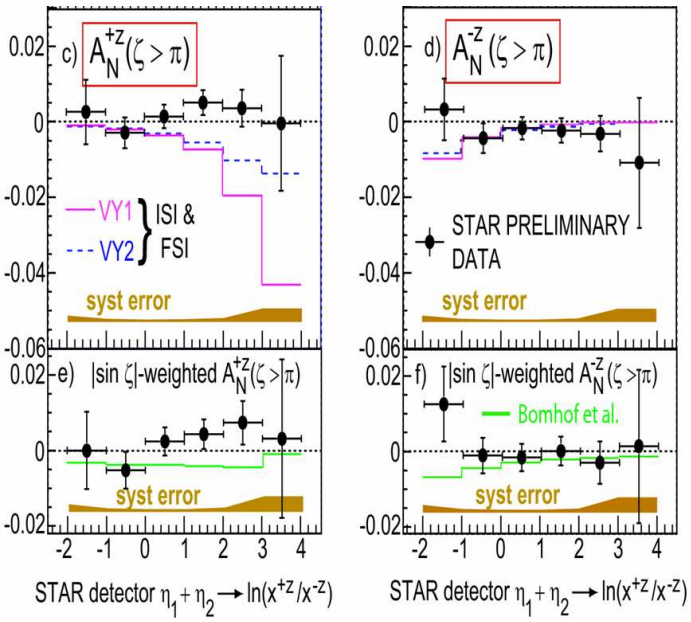

Figure 14: The bisector left-right asymmetry in $p^\uparrow p \rightarrow$ jet jet X measured by STAR [42].

BELLE data. The latest results of this analysis are shown in Fig. 15 [23], with an impressive factor of 19 more statistics compared to the published results [45].

D'Alesio presented a fit of h_1 and the Collins functions $H_1^\perp$ from both the e^+e^- $\cos 2\phi$ asymmetry (the published data [45]) and the semi-inclusive Collins $\sin(\phi_h + \phi_S)$ asymmetry (using both HERMES and COMPASS data) [46]. It is interesting to see that all this data can be simultaneously described within the TMD framework. The result supports the above-mentioned observation that the Collins function for favored fragmentation is approximately equal in magnitude to unfavored fragmentation, but of opposite sign. The extracted transversity functions indicate $|h_1^d(x)| < |h_1^u(x)|$ and opposite sign of h_1^u w.r.t. h_1^d, see Fig. 16. The question of how to evolve the considered TMD-dependent observables was not yet addressed.

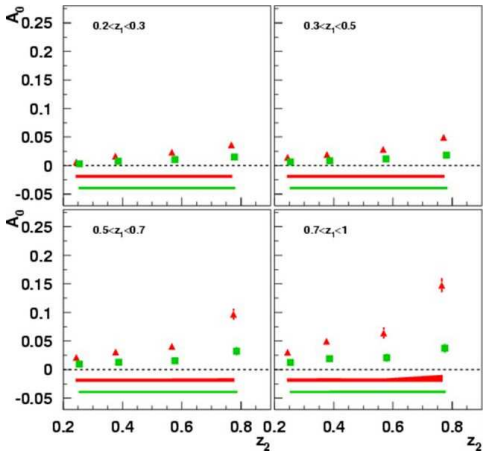

Figure 15: The analyzing power A_0 of the $\cos 2\phi$ asymmetry from 547 fb^{-1} of BELLE data [23].

Gamberg presented a model prediction [47] of the $\cos 2\phi$ asymmetry in unpolarized semi-inclusive DIS ($\propto h_1^\perp H_1^\perp$) for the 12 GeV upgrade at JLab, which should provide access to $h_1^\perp$ (Fig. 17).

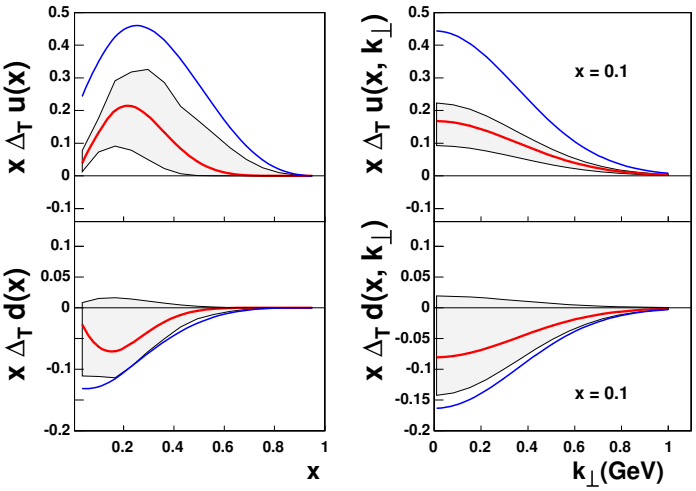

Figure 16: Left panel: the transversity distributions for u and d quarks times x, as obtained from a transversity and Collins function fit to BELLE, COMPASS and HERMES data. Right panel: transverse momentum dependence at $x = 0.1$. For details cf. [46]

TMDs like $f_{1T}^{\perp}$ and $h_1^{\perp}$ that are odd in k_T are spin-orbit coupling quantities, therefore, it is natural to expect a relation with the orbital angular momentum of the quarks, and hence with GPDs. Burkardt [48] pointed out a model-dependent relation between $f_{1T}^{\perp(1)}$ and the GPD E

$$f_{1T}^{\perp(1)}(x) \propto \epsilon_{ij} S_T^i b_\perp^j \int db_\perp^2 \boldsymbol{I}(b_\perp^2) \frac{\partial}{\partial b_\perp^2} E(x, b_\perp^2)$$

The factor $\boldsymbol{I}(b_\perp^2)$ is not analytically calculable, but has to be modeled. Nevertheless, this relation allows to make a qualitative link between the Sivers functions and the anomalous magnetic moment of the u and d quarks. Similarly, Burkardt pointed out a relation between $h_1^{\perp}$ and a particular combination of two tensor GPDs, for which Hägler presented preliminary lattice results from QCDSF/UKQCD [25], Fig. 18. These are the first lattice results that provide some qualitative information on $h_1^{\perp}$ of the pion, indicating that the pion has a surprisingly nontrivial transverse quark spin structure. Metz extended this type of model-dependent, but nontrivial, relations to the other TMDs [49].

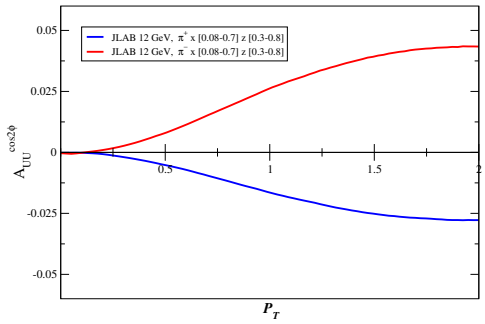

Figure 17: Model prediction of the $\cos 2\phi$ asymmetry in unpolarized semi-inclusive DIS for JLab@12GeV (updated plot by Gamberg).

4 Exclusive processes and GPDs

An outstanding task in solving the 'spin puzzle' of the nucleon is a measurement of the orbital angular momenta of quarks and gluons. For the first time, a possibility to reveal

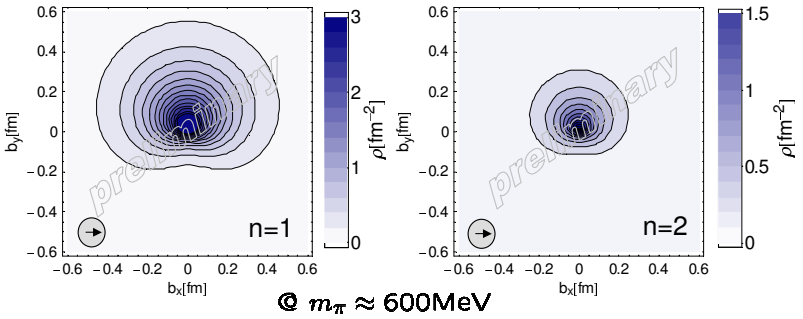

Figure 18: Asymmetric $b_\perp$-space distribution of transversely polarized quarks inside a pion from lattice QCD [25].

the total angular momentum carried by the quarks in the nucleon [50] became available within the formalism of Generalized Parton Distributions (GPDs) (see [51] for recent reviews). These functions are related both to the conventional parton densities and to elastic form factors. GPDs provide a wealth of new information as they simultaneously measure longitudinal momentum distribution and transverse location of partons thereby offering a three-dimensional representation of hadrons at the parton level.

GPDs appear in the scattering amplitude of hard exclusive processes. The DVCS process, i.e. the hard exclusive production of a real photon, provides the theoretically cleanest access to GPDs. DVCS amplitudes can be measured most readily through the interference between the Bethe–Heitler process and the DVCS process. A large number of reaction channels can be accessed in hard exclusive meson production. In all cases, polarization observables (e.g. single-spin azimuthal asymmetries) are a powerful tool to obtain information about GPDs.

From the theoretical side, there has been important technical progress in the description of hard exclusive processes, with full NLO results in α_s available for most relevant channels, partial NNLO results for Compton scattering and a better understanding of the evolution of GPDs. At DIS2007 Diehl presented such NLO calculations for exclusive meson production at HERA collider and at fixed target kinematics [52]. New avenues have been opened for the parameterization of GPDs: Luiti introduced an alternative to the mathematical ansatz of double distributions in that GPDs are generated from direct constraints from experimental data combined with lattice calculations yielding a model independent extraction [53]. Experimental access to GPDs is very difficult as the count rates for hard exclusive reactions typically drop drastically with increase of the hardness of the process. Nevertheless, there is great progress on the experimental side. HERMES has presented an overview about the so far measured DVCS observables which comprises the full set of azimuthal and single-spin asymmetries w.r.t. the charge and helicity of the lepton beam, and w.r.t. to the spin polarization of the target, either longitudinal or transverse w.r.t. the lepton beam [54]. These results are very promising in view of the greatly improved detection capabilities for exclusive processes with the information from the recoil detector installed early 2006. HERMES also presented the DVCS beam-spin asymmetries measured with a variety of nuclear targets ranging from Deuterium to Xenon [55] which may provide information about the nuclear forces as well as on the modification of nucleon properties in the nuclear medium. Fig. 19, left panel, shows the ratio of the nuclear to free proton DVCS beam-spin asymmetries as a

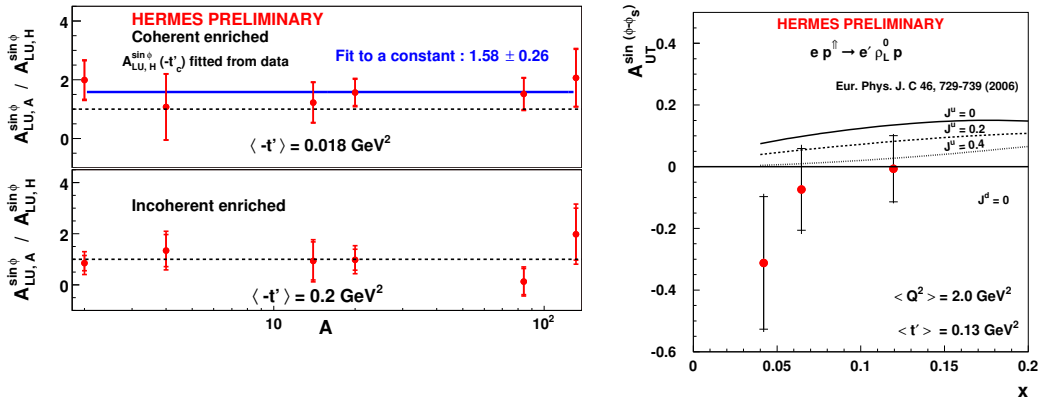

Figure 19: Left panel: The ratio of the nuclear to free proton DVCS beam-spin asymmetries as a function of the atomic mass number A measured by HERMES [55]. Right panel: Transverse target-spin asymmetry for exclusive production of longitudinally-polarized ρ^0 measured by HERMES [56] and compared to model calculations [57].

function of the atomic mass number A. For the coherent region this ratio is predicted [58] to have values ranging from 1.85 to 1.95 for $A = 12$ to $A = 90$.

The Jefferson Laboratory Hall-A experiment presented a measurement of the DVCS cross-section in the valence quark region on proton and neutron targets [59]. The experiment on the proton provides a strong indication of factorization at Q^2 as low as 2 GeV^2, therefore validating a GPD based analysis.

Of particular interest in the context of spin physics is the proton helicity-flip distribution E^q which has connection with two crucial aspects of spin physics: transverse polarization effects and the orbital angular momentum L^q carried by quarks in the nucleon. Key observables for these studies are transverse target-spin asymmetries in DVCS and in exclusive ρ^0 production. HERMES has presented preliminary results for both channels [56, 54] (see Fig. 19 right panel for the ρ^0 asymmetry). Their comparison with a model calculation [60] using the total angular momentum of quarks, J_q, as input parameter in the ansatz for E^q shows that these asymmetries are indeed sensitive to J_u in the HERMES kinematics. The measurement of the DVCS cross-section on the neutron at Jefferson Laboratory Hall-A experiment [59] provide information about J_d using the same GPD model. The complementary constraints on the total angular momenta of up- and down-quarks from both experiments remarkably coincide with recent calculations of J_q from lattice QCD [61].

5 Conclusion and outlook

Exciting new information has been obtained on the nucleon spin structure from polarized lepton–nucleon and proton–proton scattering. However, a detailed measurement of the gluon polarization remains one of the most important issues in spin physics. Running RHIC at higher energy ($\sqrt{s} = 500$ GeV) will shed more light on this issue.

Transverse spin physics turns out to be a very active and quickly developing field. Important results comprise the first extraction of the transversity as well as of transverse momentum dependent distribution and fragmentation functions like the Sivers distribution

and the Collins fragmentation function. These achievements can be considered as milestones in the field. They constitute the first step towards a complete description of the partonic structure of hadrons beyond the collinear parton model.

A rich future is expected for the elegant concept of generalized parton distributions (GPDs). Intensive experimental efforts have demonstrated the feasibility of measurements of hard-exclusive reactions in a large variety of channels. It turned out that polarization observables serve as a very powerful tool to access the different GPDs. The interplay between spin degrees of freedom and parton orbital angular momentum will be a key to understand the spin structure of the nucleon.

We thank the organizers for the kind invitation to be part of this successful workshop and furthermore, all speakers of the spin physics sessions for making it such an exciting Working Group.

References

[1] Slides:
`http://indico.cern.ch/contributionDisplay.py?contribId=20&sessionId=2&confId=9499`
[2] EMC, J. Ashman *et al.*, Nucl. Phys. B **328**, 1 (1989).
[3] HERMES, L. De Nardo, these proceedings; A. Airapetian *et al.*, Phys. Rev. D **75**, 012007 (2007).
[4] COMPASS, K. Kurek, these proceedings; V. Y. Alexakhin *et al.*, Phys. Lett. B **647**, 8 (2007).
[5] K. Griffioen, these proceedings; CLAS, K. V. Dharmawardane *et al.*, Phys. Lett. B **641**, 11 (2006).
[6] K. Slifer, these proceedings.
[7] A. Korzenev these proceedings.
[8] D. de Florian, G. A. Navarro and R. Sassot, Phys. Rev. D **71**, 094018 (2005).
[9] J. Blümlein, these proceedings; J. Blümlein, H. Böttcher and A. Guffanti, arXiv:hep-ph/0607200.
[10] D. B. Stamenov, these proceedings;
E. Leader, A. V. Sidorov and D. B. Stamenov, Phys. Rev. D **75**, 074027 (2007).
[11] B. I. Ermolaev, these proceedings; B. I. Ermolaev, M. Greco and S. I. Troyan, Eur. Phys. J. C **50**, 823 (2007).
[12] P. Liebing, these proceedings.
[13] S. Koblitz, these proceedings.
[14] G. K. Mallot, Proceedings SPIN2006, arXiv:hep-ph/0612055.
[15] K. Okada, these proceedings; PHENIX, A. Adare *et al.*, arXiv:0704.3599 [hep-ex].
[16] B. Jager, A. Schäfer, M. Stratmann and W. Vogelsang, Phys. Rev. D **67**, 054005 (2003).
[17] M. Glück, E. Reya, M. Stratmann and W. Vogelsang, Phys. Rev. D **63**, 094005 (2001).
[18] R. Fatemi, these proceedings.
[19] F. Simon, these proceedings.
[20] B. Jager, M. Stratmann and W. Vogelsang, Phys. Rev. D **70**, 034010 (2004).
[21] P. van der Nat, for the HERMES Collaboration, arXiv:hep-ex/0512019.
[22] C. Schill, these proceedings.
[23] R. Seidl, these proceedings.
[24] M. Radici, these proceedings; F. A. Ceccopieri, M. Radici and A. Bacchetta, arXiv:hep-ph/0703265.
[25] Ph. Hägler, these proceedings.
[26] H. Kawamura, these proceedings; H. Kawamura, J. Kodaira and K. Tanaka, arXiv:hep-ph/0703079.
[27] J. H. Lee, these proceedings.
[28] K. O. Eyser, these proceedings.
[29] S. Heppelmann, these proceedings.

[30] J. Qiu and G. Sterman, Phys. Rev. Lett. **67**, 2264 (1991); Phys. Rev. D **59**, 014004 (1999).
[31] Y. Koike, these proceedings; H. Eguchi, Y. Koike and K. Tanaka, Nucl. Phys. B **752**, 1 (2006); Nucl. Phys. B **763**, 198 (2007).
[32] K. Tanaka, these proceedings; Y. Koike and K. Tanaka, Phys. Lett. B **646**, 232 (2007); arXiv:hep-ph/0703169.
[33] D. W. Sivers, Phys. Rev. D **41**, 83 (1990); Phys. Rev. D **43**, 261 (1991).
[34] A. Bacchetta, these proceedings; A. Bacchetta *et al.*, JHEP **0702**, 093 (2007).
[35] D. Boer and P. J. Mulders, Phys. Rev. D **57**, 5780 (1998).
[36] A. Airapetian *et al.* [HERMES Collaboration], Phys. Rev. Lett. **84**, 4047 (2000).
[37] M. Diefenthaler, these proceedings.
[38] A. Bressan, these proceedings.
[39] A. Kotzinian, these proceedings.
[40] D. Boer and W. Vogelsang, Phys. Rev. D **69**, 094025 (2004).
[41] C. J. Bomhof, these proceedings; C. J. Bomhof, P. J. Mulders, W. Vogelsang and F. Yuan, arXiv:hep-ph/0701277.
[42] J. Balewski, these proceedings.
[43] J. C. Collins, Phys. Lett. B **536**, 43 (2002).
[44] D. Boer, R. Jakob and P. J. Mulders, Nucl. Phys. B **504**, 345 (1997); Phys. Lett. B **424**, 143 (1998).
[45] K. Abe *et al.* [Belle Collaboration], Phys. Rev. Lett. **96**, 232002 (2006).
[46] U. D'Alesio, these proceedings; M. Anselmino *et al.*, Phys. Rev. D **75**, 054032 (2007).
[47] L. Gamberg, these proceedings.
[48] M. Burkardt, Nucl. Phys. A **735**, 185 (2004).
[49] S. Meissner, A. Metz and K. Goeke, arXiv:hep-ph/0703176.
[50] X. Ji, Phys. Rev. Lett. **78**, 610 (1997).
[51] K. Goeke *et al.*, Prog. Part. Nucl. Phys. **47**, 401 (2001); M. Diehl, Phys. Rept. **388**, 41 (2003); A.V. Belitsky and A.V. Radyushkin, Phys. Rept. **418**, 1 (2005).
[52] M. Diehl, these proceedings.
[53] S. Luiti, these proceedings.
[54] A. Mussgiller, these proceedings.
[55] H. Guler, these proceedings.
[56] A. Rostomyan, these proceedings.
[57] F. Ellinghaus *et al.*, EPJC **46**, 729 (2006).
[58] V. Guzey and M. Siddikov, J. Phys. G **32**, 251 (2006).
[59] E. Voutier, these proceedings.
[60] M. Vanderhaegen, P. A. M. Guichon, M. V. Guidal, Phys. Rev. D **60**, 094017 (1999); K. Goeke, M. Polyakov, M. Vanderhaegen, Prog. Part. Nucl. Phys. **47**, 401 (2001).
[61] LHPC and MILC collaboration, arXiv:0705.4295 [hep-lat].

Structure Functions and Low-x

Convenors:
Alexandre Glazov,
Kunihiro Nagano,
Sven Moch

Measurement of the Inclusive ep Scattering Cross Section at low Q^2 and x at HERA

Andrea del Rocio Vargas Treviño
on behalf of the H1 Collaboration

DESY
Notkestrasse 85 - 22607 Hamburg, Germany

Measurements of the inclusive ep scattering cross section in the region of low four-momentum transfer squared, $0.2\,\mathrm{GeV}^2 < Q^2 < 12\,\mathrm{GeV}^2$, and low Bjorken x, $4\times10^{-6} < x < 0.02$ are presented. The results are based on two data sets collected in dedicated runs by the H1 Collaboration at beam energies of 27.6 GeV and 920 GeV for positrons and protons. These new measurements extend the kinematic phase space to lower values of Q^2 by using non tagged radiative ep scattering events. The combination of these new measurements with data previously published by H1 is presented.

1 Introduction

The kinematics of inclusive deep inelastic scattering (DIS) are usually described by the variables Q^2, the negative four-momentum transfer squared, and x, the fraction of the proton's longitudinal momentum carried by the struck quark. The reduced cross section for electron-proton scattering in the one-photon approximation, which is valid in the region of this measurement, is given by the expression:

$$\sigma_r = F_2(x,Q^2) - \frac{y^2}{Y_+}F_L(x,Q^2) \qquad Y_+ = 1+(1-y)^2 \tag{1}$$

where y is the inelasticity, given by $y = Q^2/sx$, and s is the centre of mass energy of the ep collision.

The proton structure function F_2 is the dominant contribution to the inclusive cross section, while F_L contributes only at high values of y. The experiments at the HERA ep collider have shown that the Q^2 evolution of the proton structure F_2 is well described by pQCD over a wide range in x and Q^2 [2, 3]. However, at low $Q^2 < 2\,\mathrm{GeV}^2$, the transition to photoproduction takes place and the data can be only described by phenomenological models. This note presents new cross section measurements of the H1 collaboration in the transition region. A combination of the new measurements with previous H1 data with comparable accuracy is also presented.

2 Cross Section Measurements

Two dedicated runs taken in the years 1999 (MB'99) and 2000 (SVX'00) by the H1 experiment, were used to measure the cross section in the transition region. The MB'99 data sample covers a kinematic phase space from $0.5 \le Q^2 \le 12\,\mathrm{GeV}^2$ while the SVX'00 data sample covers the lowest values $0.2 \le Q^2 \le 3.5\,\mathrm{GeV}^2$. The trigger configuration of the MB'99 data taking allows to measure the cross section towards high $y = 0.75$, into the region of high sensitivity to F_L. During the SVX'00 data sample, the interaction point of the ep collision was shifted in the proton beam direction, such that larger positron scattering angles could

be measured and hence lower values of Q^2 were accessed. In addition, the measurement at even lower values of Q^2 was possible by using initial state radiative (ISR) events. In this analyses the detection of the radiated photon was not required. The energy of the incoming electron is reconstructed from energy and longitudinal momentum conservation, assuming that the photon is radiated collinearly with the electron beam. Using the reduced incoming electron energy, the kinematic variables are reconstructed with the so called Σ method.

In Fig. 1 the cross section measurements are shown for the MB'99 and SVX'00 data samples. A good agreement between the two data sets is observed in the overlap region $0.5 \leq Q^2 \leq 3.5\,\mathrm{GeV}^2$.

The total error of the measurement contains two types of error sources. One error source affects the measurement bin by bin (uncorrelated), while the another source affects the measurement as a whole (correlated). Examples of correlated sources are the uncertainty on the measurement of the energy, angular position of the scattered electron, while uncertainties on efficiencies are examples of uncorrelated sources. The dominant uncertainties of the MB'99 and SVX'00 cross section measurements are the vertex efficiency (2%) and the uncertainty on the luminosity measurement (3%), respectively. The total error of the measurement for the MB'99 sample varies from 10% at low values of Q^2 to 2% for the bulk region $Q^2 > 2\,\mathrm{GeV}^2$. The SVX'00 sample has comparable precision for values of $Q^2 > 2\,\mathrm{GeV}^2$, but is of limited precision for the lowest values of Q^2.

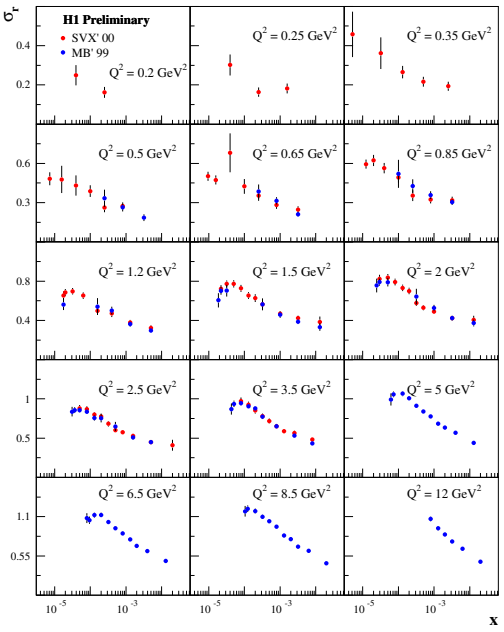

Figure 1: Reduced inclusive *ep* scattering cross sections as measured with the MB'99 and SVX'00 data samples

The MB'99 and SVX'00 measurements are the final H1 DIS cross section measurements in the low Q^2 transition region. These measurements have a comparable precision with the previously published H1 data collected in 1997 (MB'97) [2]. For obtaining a coherent result of minimum uncertainty, the data is combined using the procedure described below. The agreement between the MB'99, SVX'00 and the published MB'97 measurement is good, after a global 3.4% correction of the MB'97 data sample. This correction did result from a detailed luminosity reanalysis of the MB'97 data taking.

3 Combination of Data Sets

The combination of the three data samples is performed using a minimization procedure [4]. The correlated and uncorrelated errors of the different cross section measurements are taken carefully into account.

Let M_i be a set of cross section measurements, the combined cross section measurement M^{comb} can be obtained by minimazing the χ^2 function:

$$\chi^2(M_i^{comb}, \alpha_j) = \sum_i \frac{\left[M_i^{comb} - \left(M_i + \sum_j \frac{\partial M_i}{\partial \alpha_j}\alpha_j\right)\right]^2}{\sigma_i^2} + \sum_j \frac{\alpha_j^2}{\sigma_{\alpha_j^2}^2} \quad (2)$$

where σ_i are the statistical and uncorrelated systematic uncertainties of the measurement. The sensitivity of the measurement to the correlated uncertainties α_j are taken by the term $\partial M_i/\partial \alpha_j$ into account.

The χ^2 function of Eq. 2 has by construction a minimum $\chi^2 = 0$ for $M_i^{comb} = M_i$ and $\alpha_j = 0$. The total uncertainty for M_i^{comb} determined from the formal minimisation of Eq. 2 is equal to the sum in quadrature of the statistical and systematic uncertainties.

The combination of the MB'99, SVX'00 and MB'97 cross section measurements is performed using the prescription of Eq. 2. The published H1 data [2] were taken with a different proton beam energy, $E_p = 820\,\text{GeV}$. Thus a centre of mass energy correction is applied to the published cross section. The correction becomes sizable only for the highest y analysis bins which for the published data is at $y = 0.75$. The combination of the three data sets is shown in Fig. 2. The total error of the combined cross section measurement has a precision varying with Q^2 and x, for the central values of Q^2 and x is about 2% but larger towards the edges of the covered phase space. The behaviour of the cross section data, which extend from photoproduction to the DIS region, can be analysed within phenomenological models. As an example, the data in Fig. 2 is compared to the fractal model [5], in which F_2 is parameterised exploiting self similarity features of proton structure at low x. F_L is expressed via F_2 and the cross section ratio $R = F_L/(F_2 - F_L)$. A good fit is obtained with $R \simeq 0.5$ in the whole Q^2 range covered which corresponds to $F_2 \simeq 3F_L$.

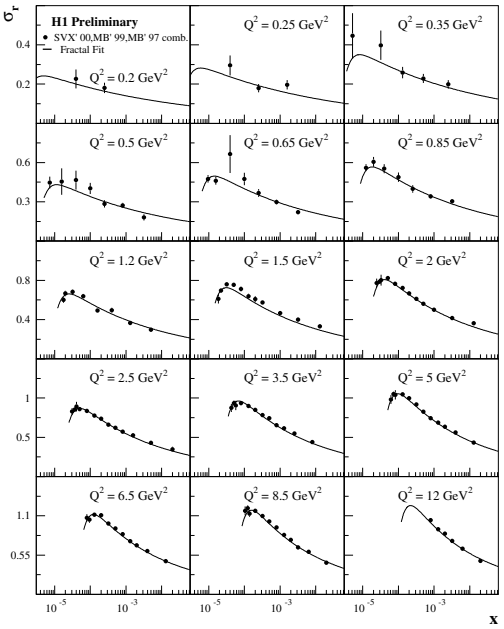

Figure 2: Reduced inclusive ep scattering cross section measurement obtained by combining the MB'99, SVX'00 and the published MB'97 cross sections (see text).

4 λ Extraction

The rise of the structure function F_2 at low values of x can be described by a power law in x, $F_2 \sim x^{-\lambda}$. The coefficient λ increases approximately linearly as a function of $\ln Q^2$ for $Q^2 > 2\,\mathrm{GeV}^2$. The rise of F_2 above $1\,\mathrm{GeV}^2$ increases with $\ln Q^2$. This parametrisation can be used at low x to fit the reduced cross section σ_r, allowing the extraction of λ and F_L simultaneously. Assuming that F_L is constant for a given Q^2, the reduced cross section from Eq. 1 can be written as:

$$\sigma_r(x, Q^2) = c(Q^2)x^{-\lambda(Q^2)} - \frac{y^2}{Y_+}F_L(Q^2) \qquad (3)$$

The global normalisation $c(Q^2)$, the power law exponent $\lambda(Q^2)$ and F_L are three parameters which are obtained by fitting the reduced cross section. The result of these fits are shown in Fig. 3.

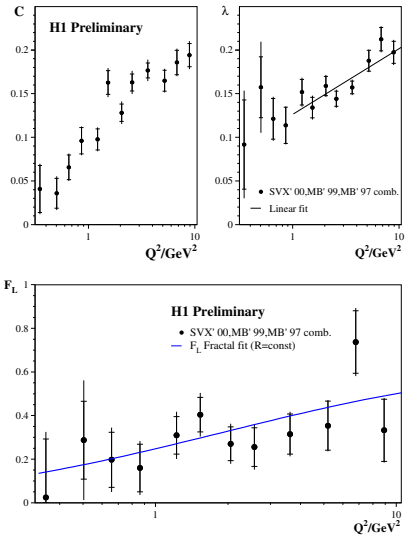

Figure 3: Coefficients c, λ and F_L defined in Eq. 3 determined from a fit to the H1 preliminary data (Fig. 2) as a function of Q^2.

5 Summary

New inclusive cross section measurements of ep collision in the Q^2 transition region from photoproduction to DIS are presented. The data from dedicated runs in 1999 and 2000 are combined here with previously measured data, leading to a coherent result for the low Q^2 cross section data measured by H1 in the HERA-I data taking period. The systematic uncertainty for a large part of the phase space is about 2%.

6 Acknowledgments

I would like to acknowledge the work of all members of the H1 Collaboration, in particular I would like to thank to O. Behrendt, S. Glazov, M. Klein, K. Krueger, V. Lendermann, A. Petrukhin, H. Schultz-Coulon and D. Wegener, for their help and support during the preparation of these results.

References

[1] Slides: `http://indico.cern.ch/contributionDisplay.py?contribId=25&sessionId=8&confId=9499`

[2] C. Adloff *et al.* (H1 Collab.), Eur. Phys. J. C **21** (2001) 33;

[3] S. Aid *et al.* (H1 Collab.), Nucl. Phys. B **470** (1996) 3; M. Derrick *et al.* (ZEUS Collab.), Z. Phys. C **72** (1996) 399; C. Adloff *et al.* (H1 Collab.), Phys. Lett. B **393** (1997) 452.

[4] S. Glazov, in "13th International Workshop on DIS, DIS2005," edited by W. Smith and S. R. Dasu, AIP Conference Proceedings, 2005.

[5] T. Lastovicka, Eur. Phys. J. C **24** (2002) 529.

ZEUS high-y Cross Section Measurement and Preparation for Low Energy Running

Shima Shimizu*
on behalf of the ZEUS collaboration

University of Tokyo
7-3-1 Hongo, Bunkyo-ku, Tokyo 113-0033, JAPAN

HERA is the only place to provide information on F_L in the gluon dominated region of ep interactions. The ZEUS experiment has extended its cross section measurement to the high-y region, where the F_L contribution can be sizable. In this report, details of the measurement and the first look on data from the Low Energy Running, which allows separation of F_2 and F_L, are presented.

1 Introduction

The ep collider HERA has played a crucial role in the investigation of proton structure, especially in the low-x region where gluons are dominant in the proton. The ZEUS experiment performed a precise measurement of Deep Inelastic Scattering (DIS) reduced cross sections using data collected in 1996 and 1997 [2]. The kinematics of lepton-proton DIS is described by x, the Bjorken scaling variable, Q^2, the negative square of the invariant mass of the virtual exchanged boson, and y, the inelasticy. The reduced cross sections can be defined as

$$\tilde{\sigma} \equiv \frac{xQ^4}{2\pi\alpha^2 Y_+}\frac{d^2\sigma}{dxdQ^2} = F_2(x,Q^2) - \frac{y^2}{Y_+}F_L(x,Q^2), \tag{1}$$

where $Y_+ = 1 + (1-y)^2$. Since the contribution of F_L to the cross section is sizable only at high y, the measurement provided information mainly on F_2, which is sensitive to the total number of quarks and anti-quarks in the proton. A measurement of F_2 also allows to determine a gluon distribution indirectly from the scaling violation, $\frac{\partial F_2}{\partial \ln Q^2}$.

The longitudinal structure function of the proton, F_L, is directly sensitive to gluon dynamics in the proton. Since high-y corresponds to the low-x region, F_L with gluon dominance can be investigated at HERA. The ZEUS experiment has performed a new cross section measurement, which is optimized for the high-y region, with data collected in 2006. A special trigger was prepared for this measurement, which takes events in a new kinematic region of high y. The measurement requires a good understanding of the scattered electron energy and a good control of background contamination, since events with higher y have lower energy of the scattered electron[a], which is more difficult to identify. Details and results of the measurement are presented.

For separation of F_2 and F_L, cross sections at the same (x, Q^2) but different y values need to be measured (See Eq. 1). This requires measurements with different center-of-mass (CM) energies because of the relation $s = Q^2/xy$, where s is the ep center-of-mass energy. For that reason, HERA started the operation with lowered proton beam energy, called Low Energy Run (LER), in March 2007. Also shown in this report are the first LER data collected by the ZEUS experiment.

*JSPS (Japan Society for the Promotion of Science) research fellow, DC.
[a]The word *electron* is used for both electron and positron in this paper.

2 High-y cross section measurement

2.1 Details of the analysis

The data were collected with the CM energy of 318 GeV, where proton and positron beam energies were 920 GeV and 27.5 GeV, respectively. The total luminosity was 29.5 pb^{-1}.

For online event selection, two independent trigger-logic were prepared to take events with low scattered electron energy. One required a scattered electron with energy above 4 GeV. The second logic required $\Sigma_{\rm total}(E-p_z)_i > 30$ GeV and $\Sigma_{\theta_i \lesssim 165^\circ}(E-p_z)_i > 20$ GeV, where E_i and p_{zi}[b] are energy and longitudinal momentum of the i-th cell of the calorimeter and each sum runs over all the cells and the cells excluding the ones in the rear, close to the beam pipe, respectively. Events satisfying at least one of the two triggers were selected.

For offline event selection, the following conditions were applied:

- $|{\rm Z_{vtx}}| < 50$ cm, where $\rm Z_{vtx}$ is the z position of an event vertex.
- $\Sigma_{\rm total}(E-p_z)_i > 38$ GeV
- The presence of an electron candidate found in the calorimeter with energy ($E_e > 5$ GeV) and angle ($\theta_e \lesssim 170^\circ$). For $\theta_e \lesssim 151^\circ$, a track was required to be matched to the candidate.

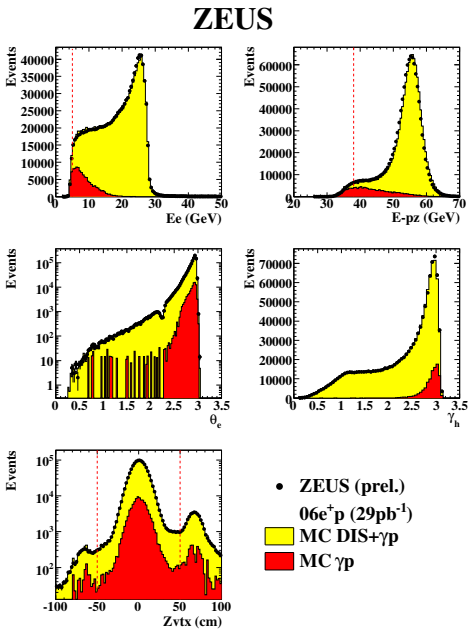

Figure 1: Distributions of measured quantities, E_e, $\Sigma_{\rm total}(E-p_z)_i$, θ_e, hadronic angle (γ_h) and $\rm Z_{vtx}$, compared to MC prediction as described in the figure.

The electron energy scale and the dead material corrections are well understood based on the investigation of three data samples, namely exclusive J/Ψ photoproduction ($E_e \lesssim 5$ GeV), QED Compton (5 GeV $< E_e <$ 25 GeV) and DIS (10 GeV $< E_e <$ 35 GeV). The uncertainty on the electron energy scale is assigned a value of $\pm 2\%$.

The main source of contamination to the DIS sample are photoproduction (γp) events, $\gamma p \to X$, where the electron emits a quasi-real photon and disappears down the beam pipe. The photon interacts with the proton producing in particular π^0 and low energy $\pi^\pm$, which may be misidentified as electron in the calorimeter. The contamination is severe at high-y, where the energy of the scattered electron is small. To understand the γp background, two analyses were performed. The first analysis was done with events tagged by the 6m tagger, which is a detector placed downstream of the electron beam and which can directly detect an escaping electron. The sample is reasonably described by the γp MC except for the

[b] In the ZEUS coordinate, proton beam direction is in the z direction.

overall normalization. The second analysis was done with a γp enriched sample, in which a low quality scattered electron was found, based on its calorimeter shower shape. In this sample, the difference between the data and the DIS MC is described by the scaled γp MC. The normalization factor for the γp MC was extracted for each sample separately and the two values agreed within 5%. Considering the imperfect description of the shape of the considered distributions by the γp MC, an uncertainty of $\pm 10\%$ was conservatively assigned to the normalization factor.

Distributions of measured quantities for selected DIS events are shown in Fig. 1. They are well described by MC prediction in which the normalization factor described above is applied to the γp MC.

2.2 Reduced cross sections

Kinematic variables are reconstructed using the energy and the angle of the scattered electron. Bins are defined in the (y, Q^2) plane for good coverage of the high-y region. In the region where reduced cross sections were extracted, most of the bins had acceptance above 60% and the contamination of γp events was estimated to be less than 40% in each bin.

Reduced cross sections are extracted as,

$$\tilde{\sigma} = \frac{N_{\rm data} - N_{\gamma \rm p\ MC}}{N_{\rm DIS\ MC}} \cdot \tilde{\sigma}^{\rm BORN}_{\rm theory}. \quad (2)$$

The following systematic sources were taken into account:

- electron energy scale ($\pm 2\%$),
- γp MC normalization factor ($\pm 10\%$),
- electron finding inefficiency ($\pm 10\%$),
- $\Sigma_{\rm total}(E - p_z)_i$ threshold (± 2 GeV).

The effect on the cross section measurement was evaluated by varying the value of each systematic source by a factor in brackets. At highest y, for low Q^2 ($Q^2 < 50$ GeV^2), the systematic uncertainty from the γp MC normalizaton factor was largest, giving $\sim 5\%$ uncertainty on the cross section.

The measurement was done for $0.1 < y \lesssim 0.8$ and $25\ \text{GeV}^2 < Q^2 < 1300\ \text{GeV}^2$. The extracted reduced cross sections are shown in Fig. 2, as a function of y for fixed Q^2 values. They are compared with the Standard Model predictions with CTEQ5d PDF [3] and with ZEUS-Jets PDF [4]. The measured reduced cross sections are well described by the predictions.

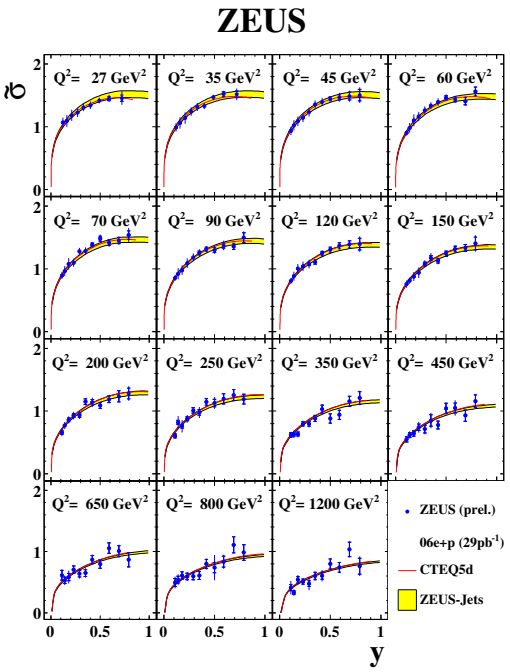

Figure 2: The reduced cross sections as a function of y for fixed Q^2.

The measurement was successfully extended to the high-y region. The measured points are extended to higher y for $Q^2 \lesssim 300$ GeV^2, compared to the previous measurement, and more measured points are provided at mid-y value ($y \gtrsim 0.3$).

3 Low Energy Running (LER)

HERA ended its operation with proton beam energy of 920 GeV in March 2007. Since then, HERA started to operate with lowered proton beam energy, namely 460 GeV, for the DIS cross section measurement with different center of mass energies which will allow the extraction of F_2 and F_L.

The ZEUS experiment has performed a feasibility study for F_L measurement [5]. As can be seen in Eq. 1, larger difference in y between the measurements at different beam energies brings better precision for F_L. It can be achieved by a cross section measurement at higher y in LER data. As presented in this report, the ZEUS experiment has already extended its measurement to higher y compared to the previous measurement. The experiment started to collect LER data, as shown in Fig. 3, with a newly implemented trigger which requires $\Sigma_{\text{total}}(E-p_z)_i > 30$ GeV and has no electron finding requirement online.

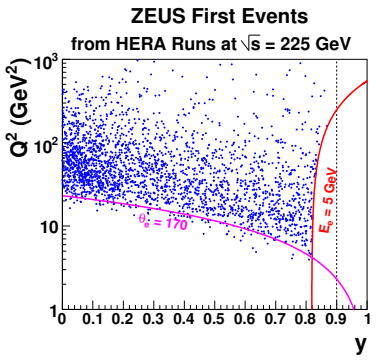

Figure 3: First look on the LER data, in the (y, Q^2) plane.

4 Summary

The ZEUS experiment performed a new cross section measurement which is optimized for the high-y region using data collected in 2006. The measurement extended to higher y in the kinematic region, compared to the previous measurement. The experiment started to collect LER data, aiming for a direct measurement of F_L.

References

[1] Slides:
`http://indico.cern.ch/contributionDisplay.py?contribId=278&sessionId=8&confId=9499`

[2] ZEUS Coll., S. Chekanov *et al.*, Eur. Phys. J. **C21** 443 (2001).

[3] CTEQ Coll., H.L. Lai *et al.*, Eur. Phys. J. **C12** 375 (2000).

[4] ZEUS Coll., S. Chekanov *et al.*, Eur. Phys. J. **C42** 1 (2005).

[5] D. Kollar, *Prospects for a measurement of F_L at HERA with the ZEUS detector*, in proceedings, DIS 2006 (2006).

High y DIS Cross Section Measurement with H1

Nataša Raičević
on behalf of the H1 Collaboration

University of Montenegro - Faculty of Science
Cetinjski put BB, 81000 Podgorica - Montenegro

A new preliminary measurement of the inclusive ep scattering cross section from H1 experiment at HERA is presented in the region of low four-momentum transfer squared, 12 GeV $^2 < Q^2 < 50$ GeV^2 and very high inelasticity, $0.75 < y < 0.9$. The cross section in this kinematic domain is sensitive to the longitudinal structure function F_L and thus provides additional constraints to the DGLAP evolution. The results are based on data collected in 2003-2006 (HERA-II). About equal luminosities obtained for e^+p and e^-p collisions allow for a high precision control of background processes.

1 Introduction

The $e^{\pm}p$ deep-inelastic scattering (DIS) double-differential cross section at low values of squared four momentum transfer, Q^2, in the one-photon exchange approximation, can be expressed as,

$$\frac{d^2\sigma}{dxdQ^2} \cdot \frac{Q^4 x}{2\pi\alpha^2 Y_+} = \sigma_r = F_2(x,Q^2) - \frac{y^2}{Y_+} \cdot F_L(x,Q^2) \ , \tag{1}$$

where x is the Bjorken scaling variable, $y = Q^2/sx$ is the inelasticity which is a fraction of the electron's[a] energy loss, s is the center of mass energy squared of the electron-proton system and $Y_+ = 1 + (1-y)^2$. The two structure functions F_2 and F_L obey the relation $0 \leq F_L \leq F_2$ due to the positivity of the cross sections for transversely and longitudinally polarised photons scattering off protons. Therefore, the longitudinal structure function, F_L, gives a sizable contribution to the cross section only at large values of the inelasticity y. The longitudinal structure function, F_L, is identically zero in lowest order QCD, but due to gluon radiation gets a non-zero value in perturbative QCD. The measurement of F_L can thus provide constraints on the gluon density function which are complementary to those obtained from the scaling violations of F_2 assuming DGLAP evolution[2].

At high y the event kinematics is best determined using the measured energy of the scattered electron, $E_e{}'$, and its polar angle, θ_e, (electron method) according to the relations

$$y = 1 - \frac{E_e{}'}{E_e}\sin^2(\theta_e/2), \qquad Q^2 = \frac{E_e{}'^2 \sin^2\theta_e}{1-y}. \tag{2}$$

Thus, to measure at largest values of y, it is necessary to reach as low as possible $E_e{}'$.

The new high y cross section measurement from H1 is based on HERA-II data with integrated luminosity of 96 pb^{-1} where 51 pb^{-1} is from e^+p and 45 pb^{-1} from e^-p interactions. The kinematic plane covered in this analysis is shown in Figure 1 together with kinematic planes from the analysis of HERA-I data from H1 and fixed target experiments.

[a]The name *electron* in the text is used to denote both electrons and positrons.

2 Principle of the measurement

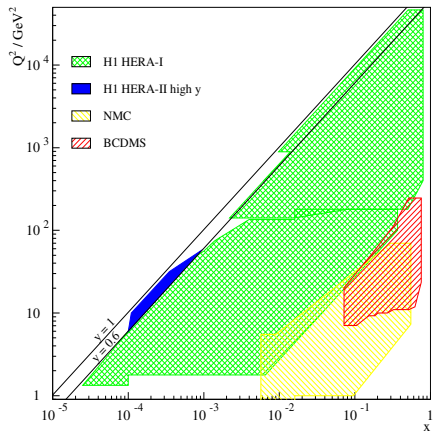

Figure 1: Kinematic plane covered by H1 and fixed target experiments. Dark region, labeled H1 HERA-II high y, corresponds to this analysis.

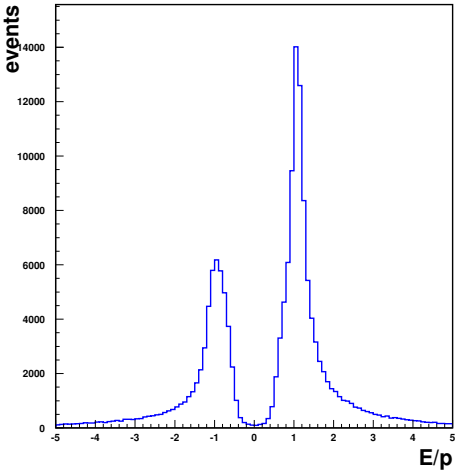

Figure 2: Energy over momentum for tracks from e^+p interactions linked to clusters in SpaCal with energy from 3.4 to 10 GeV.

To select events with low and medium Q^2 with the H1 detector [3], at least one cluster in the backward electromagnetic calorimeter (spaghetti calorimeter - SpaCal) is required. Copious photoproduction processes often lead to electron-like low energy deposits in SpaCal. Thus the high level of the photoproduction background is the main difficulty for a cross section measurement at large values of y. A sizable background of hadrons originates also from deep inelastic scattering because at high y and low Q^2 the hadronic final state is scattered backwards. To suppress hadronic contributions, cuts on the shower shape estimators are performed. An additional suppression of the radiative events and photoproduction background is performed by requiring energy and longitudinal momentum conservation. A well reconstructed vertex is required in the interaction region to further reduce background and contribution from beam background events. The cuts were optimized to avoid efficiency loss as much as possible and to still significantly reduce background.

The high level of the background at large values of y leads directly to an additional uncertainty in the background subtraction procedure. The background also complicates the estimation of the signal selection efficiency in an unbiased way. To achieve an efficient rejection and identification of photoproduction background, this analysis does not rely on the Monte Carlo simulation for the background level estimation, but uses experimental information by employing the charge assignment of central tracks associated with SpaCal energy cluster. The sample of candidates with negative charge is taken to represent the background in the positron data sample and vice versa. This allows the energy range to be extended down to 3.4 GeV corresponding to $y \leq 0.9$.

Figure 2 shows the energy over momentum ratio from e^+p interactions for tracks which pass all the cuts and are linked to clusters with energy from 3.4 GeV to 10 GeV (energy is measured from SpaCal and momentum from the central tracking chambers). The smaller peak corresponds to tracks with negative charge and is almost a pure background with a charge misidentification probability about 0.5 %. These tracks are termed as wrong sign tracks. The higher peak, near E/p = 1, contains signal plus remaining positive background (correct sign tracks) which can be determined from e^-p interactions.

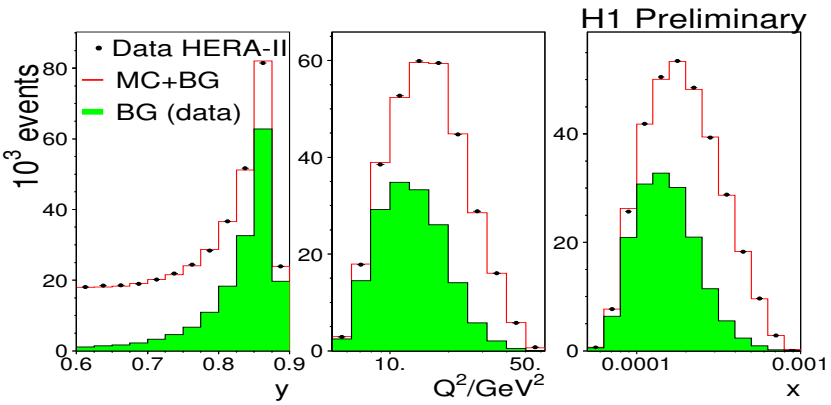

Figure 3: Comparison of the correct sign data (dots) with a sum of background determined from the wrong sign data (shadowed histogram) and DIS Monte Carlo simulation for y, Q^2 and x distributions.

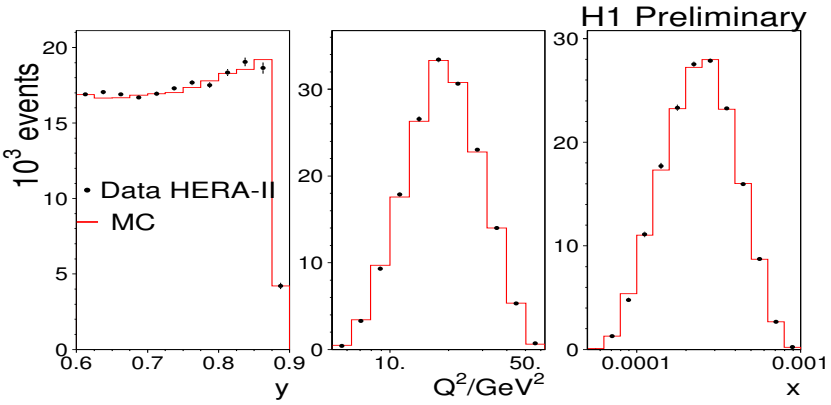

Figure 4: Comparison of the background subtracted data (dots) and DIS Monte Carlo simulation (histogram) for y, Q^2 and x distributions.

The efficiency of the high y first level trigger used in the analysis is uniform in radius and energy in SpaCal and is about 97 % for the total data sample.

3 Results

Figure 3 shows a comparison of the correct sign data (dots) with a sum of background determined from the wrong sign data (shadowed histogram) and DIS Monte Carlo simulation for y, Q^2 and x distributions. The simulation of the DIS cross section uses a QCD parameterisation of the structure functions which in an iterative process has been adjusted to the measured cross section. A comparison for the corresponding background subtracted distributions is shown in Figure 4. As can be seen from these figures, data are well described by Monte Carlo simulation.

The systematic uncertainty of the new measurement is 2-3 % and is dominated by the track link efficiency uncertainty which is estimated to be 1.5 %. Other sources of uncorrelated

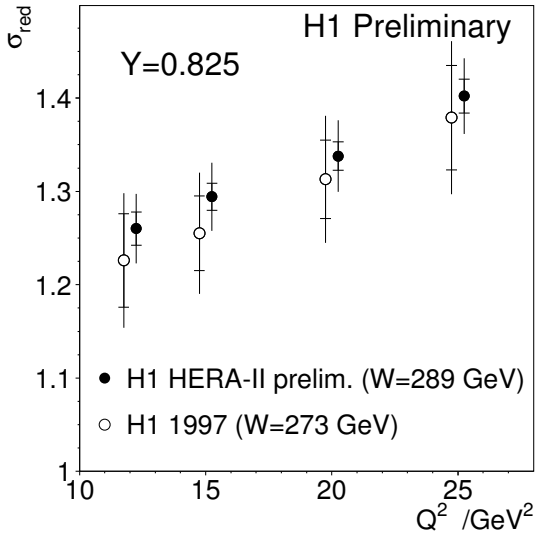

Figure 5: Comparison of Q^2 dependence of preliminary cross section measurement (solid circles) at inelasticity $y = 0.825$ with the published H1 result (open circles). Note that the published data corresponds to a slightly lower center of mass energy.

systematic uncertainties are: trigger efficiency (1.2 %), track charge identification (0.5 %) and electron identification (0.5 %). Concerning correlated errors, the main influence comes from the $E_e{}'$ energy scale uncertainty (1 % at 3 GeV), the θ_e uncertainty (1 mrad) and the calorimeter hadronic energy scale uncertainty ($\pm$ 1 GeV).

Figure 5 compares the new preliminary cross section depending on Q^2 at inelasticity $y = 0.825$ with the published H1 result based on HERA-I data [4, 5]. The new measurement has significantly reduced uncertainties. The total uncertainty is reduced by about factor of two. Unlike for the published H1 result, based on HERA-I data, for this analysis a large sample of data from e^-p interactions is available for cross section measurement and the control of the charge asymmetry which provides much improved understanding of systematics.

This analysis shows that at H1 there are advanced tools to cope with a large background at low energies which is vital for the direct accurate measurement of the longitudinal structure function as is expected to be derived from the HERA low proton energy run data.

References

[1] Slides: `http://indico.cern.ch/contributionDisplay.py?contribId=26&sessionId=8&confId=9499`

[2] V. Gribov and L. Lipatov, Sov. J. Nucl. Phys. **15**, 438 and 675 (1972); L. Lipatov, Sov. J. Nucl. Phys. **20**, 94 (1975); G. Altarelli and G. Parisi, Nucl. Phys. B **126**, 298 (1977); Y. Dokshitzer, Sov. Phys. JETP , 641 (1977).

[3] H1 Collaboration, I. Abt *et al.*, Nucl. Instr. and Meth. **A386** 310 and **A386** 348 (1997).

[4] A.A. Glazov, PhD Thesis, Berlin, Humboldt-University, 1998, DESY-Thesis-1998-005.

[5] H1 Collaboration, C. Adloff *et al.*, Eur. Phys. J. **C19**, 269 (2001).

Constraints on PDFs from CDF

Aidan Robson *

Glasgow University - Department of Physics and Astronomy
Glasgow G12 8QQ - UK

Recent results from CDF that provide PDF-constraining power are presented.

1 Introduction

The Tevatron probes a region of x and Q^2 between that accessible to HERA and that of the LHC, and thus provides important information about the content of the proton. Measurements using high-p_T leptons from W and Z boson decays, and using jets, are sensitive to parton distribution functions (PDFs) and provide PDF-constraining power.

2 CDF

CDF is a general-purpose detector with excellent tracking capability – provided by a drift chamber covering $|\eta| < 1$ and extended forward by silicon detectors – and calorimetry, which extends to $|\eta| < 3$. Together with muon chamber coverage for $|\eta| < 1.5$, these systems allow accurate reconstruction of electrons, muons and jets.

3 High-p_T lepton measurements

Events with a W or Z boson decaying to electrons or muons are distinctive and are clean to reconstruct. Inclusive W and Z cross-sections from CDF were early measurements that, even with a small dataset, had significant systematic uncertainties coming from PDFs [2]. With the higher statistics now collected, related measurements can provide PDF constraints.

3.1 Z boson rapidity

One such measurement is the Z boson rapidity, measured in the electron decay channel. The boson rapidity y_Z is closely related to the momentum fractions x of the interacting partons, and at leading order the relation $x_{1,2} = (m_Z/\sqrt{s})e^{\pm y_Z}$ holds exactly. By measuring the rapidity distribution the proton content is therefore probed directly.

Inclusion of the forward calorimeters allows Z bosons to be reconstructed over almost the full kinematic range, and it is the high-rapidity events, corresponding to one interacting parton having very low x and the other high x, that probe the less well-known parts of the parameter space. For the highest rapidity events, where both electrons are reconstructed in the forward calorimeters, one electron candidate is required to have an associated track in order to reduce backgrounds.

Challenging aspects of the measurement are in understanding the tracking efficiencies far forward in the detector, and in the background determination.

The preliminary result is shown in Figure 1 with a NNLO calculation overlaid, normalised for shape comparison. CTEQ 6.1 PDFs are used and there is good agreement with the data.

*On behalf of the CDF Collaboration

3.2 Forward W bosons

In leptonically-decaying W boson events the neutrino escapes the detector so, unlike in the case of the Z boson, the rapidity of the W cannot be directly reconstructed.

However different regions of rapidity may be probed using the electron decay mode by measuring the cross-section for W boson production separately in the central and forward calorimeters [3]. Figure 2 shows the complementary acceptances for the two sections of the calorimeter. Forward electrons are required to have associated tracks, and silicon-only tracking is heavily relied upon.

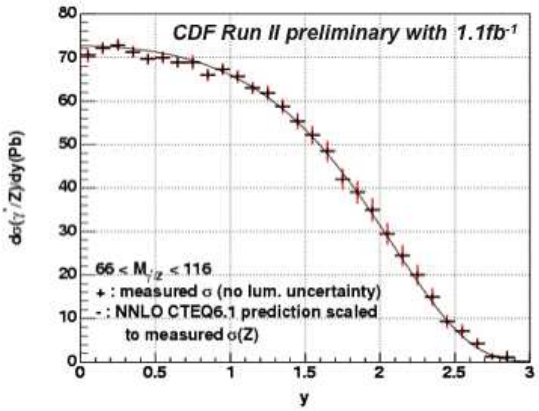

Figure 1: Z boson rapidity from Z→ee

The total cross-section using forward electrons is found to be consistent with the previously-measured total cross-section using central electrons. The 'visible' cross-sections are defined $\sigma_{\rm vis} = \sigma_{\rm tot} \times A$ where A is the detector acceptance for either the central or forward regions. Then the ratio of the visible cross-sections in the two regions can be tested against theoretical predictions:

$$\begin{array}{lcll} R_{exp} & = & \sigma_{\rm vis}^{\rm central}/\sigma_{\rm vis}^{\rm forward} & = \quad 0.925 \pm 0.033 \\ R_{th} & = & A^{\rm central}/A^{\rm forward} & = \quad 0.924 \pm 0.030 \ \ \text{(CTEQ6.1)} \\ & & & = \quad 0.941 \pm 0.012 \ \ \text{(MRST01E)} \end{array}$$

An advantage of taking the ratio is that it removes the luminosity uncertainty. The uncertainty on the measurement is comparable with the CTEQ theoretical uncertainty, and the main contribution to the measured ratio is 2.5% from the electron identification, which tends to decrease with greater statistics. This measurement is therefore promising for PDF constraining.

3.3 W charge asymmetry

More information about the proton content can be found by separating W boson events by charge. Since the proton carries on average more u-quark density than d-quark density and the antiproton more $\overline{u}$-quark density than $\overline{d}$-quark density, W^+ bosons tend to be produced moving in the direction of the proton beam, and W^- in the antiproton direction. At a given rapidity there is therefore a non-zero W charge asymmetry. The asymmetry is directly related to the ratio of d- to u-quark densities, which is otherwise not well-constrained.

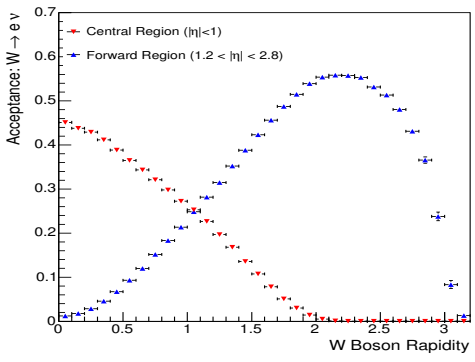

Figure 2: Central and forward W acceptance

Experimentally the observable asymmetry is that of the decay leptons, which is diluted

from the boson production asymmetry by the preferential emission of the charged lepton opposite to the boson direction in a V–A interaction. The first CDF Run 2 W charge asymmetry measurement [4] was made as a function of electron rapidity. A new approach uses all of the event kinematics to unfold directly back to the W boson production asymmetry [5].

By imposing a constraint on the mass of the W boson, two solutions can be found for the unknown longitudinal component of the neutrino momentum. Since the angular distribution of a V–A interaction is known, the two solutions can be weighted so that the ambiguity is resolved statistically. The result is iterated to remove dependence on $d\sigma/dy$, which is an input. One of the most difficult uncertainties is the electron charge misidentification rate.

The result is given in Figure 3 with the CTEQ uncertainty band, and it is clear that the measurement should affect future fits.

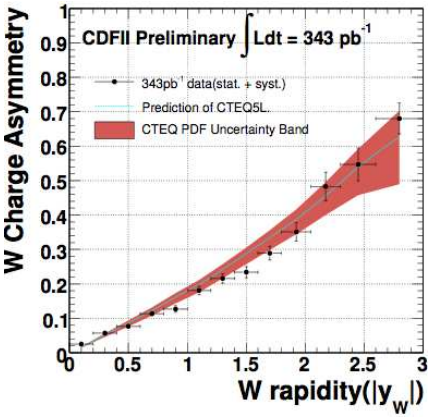

Figure 3: W charge asymmetry

4 Jet measurements

The inclusive jet cross-section directly probes the gluon density – the least well-known of the parton distributions. The increase of the Tevatron's centre-of-mass energy from 1.8 TeV to 1.96 TeV between Run 1 and Run 2 has extended the reach of the inclusive jet cross-section by around 150 GeV in E_T, and increased the cross-section by a factor of around three at $E_T = 500$ GeV.

Two jet clustering algorithms are in use: the cone-based 'midpoint' algorithm, and the k_T algorithm, which combines proto-jets according to their separation in transverse momentum (k_T). The midpoint algorithm is improved over a simple cone algorithm by iterating with additional seeds in between pairs of proto-jets. Overlapping jets are merged if $> 75\%$ of the energy is in the overlap region; otherwise they are split. The extra midpoint seeds provide some infra-red safety but the algorithm is still not collinear-safe. While the k_T algorithm is more theoretically motivated, there are different systematic uncertainties associated with the two approaches and it is valuable to compare the results from each.

An important correction to the jet energy measurements is the effect of multiple proton-antiproton interactions. On average there are 1.5 inelastic p–$\overline{\text{p}}$ interactions per bunch-crossing, but at the highest instantaneous luminosities this increases to 6 interactions per crossing. Energy is subtracted according to the number of vertices reconstructed in an event.

From Monte Carlo simulation, perturbative QCD partons and non-perturbative contributions from the underlying event and from fragmentation are reconstructed into jets. The resulting distributions can then be compared with experiment once the data has been unfolded to hadron-level distributions, using a bin-by-bin energy unfolding determined from the detector simulation.

The cross-section measurement is made in five bins of rapidity [6]. New physics is not expected to appear in the high rapidity bins so these can be used to constrain PDFs while maintaining sensitivity to new physics in the low rapidity bins. However the principal systematic uncertainty, the jet energy scale, is larger in the forward detectors. A ± 2–3% jet

energy scale uncertainty translates to a $\pm 9\%$ cross-section uncertainty at low jet E_T and $^{+60\%}_{-40\%}$ at high jet E_T.

The shapes show excellent agreement over nine orders of magnitude of cross-section. The fractional uncertainties are shown for the highest rapidity bin of each analysis in Figure 4. Since experimental uncertainties are smaller than the band allowed by the current PDF fits, these measurements will improve PDF constraints, particularly on the high-x gluon.

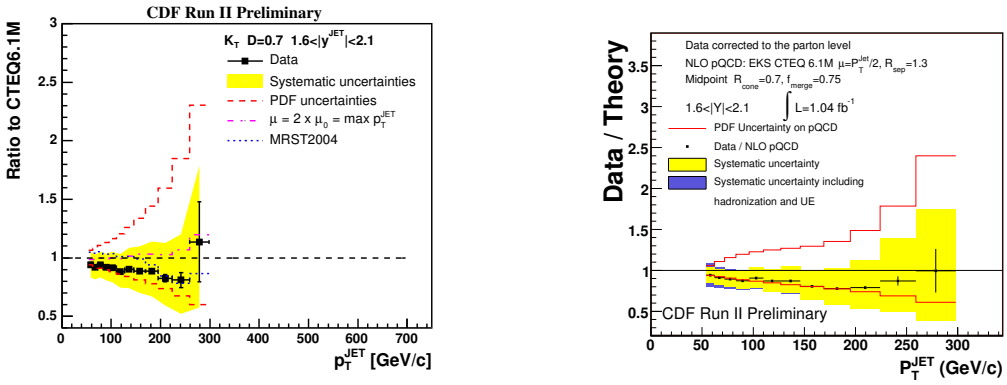

Figure 4: Inclusive jet cross-section fractional uncertainties in the highest jet rapidity bin, $1.6 < |y| < 2.1$: (left) the k_T clustering algorithm and (right) the midpoint algorithm.

5 Conclusions

Measurements of W and Z bosons and of the inclusive jet cross-section all provide PDF constraints that are unique to the Tevatron. All will benefit from higher statistics and will continue to be updated.

6 Acknowledgments

The author thanks the UK Science and Technology Facilities Council for financial support.

References

[1] Slides:
`http://indico.cern.ch/contributionDisplay.py?contribId=244&sessionId=8&confId=9499`
[2] D. Acosta *et al.*, Phys. Rev. Lett. **94** 091803 (2005).
[3] A. Abulencia *et al.*, arXiv:hep-ex/0702037 (2007).
[4] D. Acosta *et al.*, Phys. Rev. D **71** 052002 (2005).
[5] CDF Collaboration, CDF Conference Note 8679 (2007).
[6] CDF Collaboration, CDF Conference Notes 8374, 8388 (2006).

Constraints on PDFs from D0

Terrence Toole for the D0 Collaboration

University of Maryland - Dept of Physics
College Park, MD 20742-4111 - U.S.A.

We present three recent results from the D0 collaboration which are sensitive to Parton Distribution Functions (PDFs). The measurements are made using data collected during Run II at the Fermilab Tevatron.

1 Introduction

There exists an interdependency between the Run II physics program at the Tevatron and PDFs. A good understanding of PDFs is critical to the success of the physics program. Most measurements at the Tevatron use PDFs as an input at some level. With a large data set in hand, the Tevatron experiments can contribute to our understanding of PDFs. Because the Tevatron is colliding $p\bar{p}$ at $\sqrt{s} = 1.96$ TeV, some of these contributions are unique to the Tevatron experiments. For the processes used, a large fraction of the events come from lower order diagrams which are theoretically well understood, and have clean signatures with low backgrounds. The D0 detector has excellent coverage for electrons and muons in both central and forward regions. This enables D0 to measure over much of the x and Q^2 range that is accessible at the Tevatron.

We present three recent D0 analyses which are sensitive to PDFs. The first is the rapidity distribution for Z bosons which uses final state electrons [2]. The W charge asymmetry is described for $W \to \mu\nu$ [3]. The last analysis is a differential cross section measurement for $\gamma+$ jet events [4].

2 Z boson rapidity

The primary source of Z production at the Tevatron is from $q\bar{q}$ annihilation. The Q^2 of the interaction is roughly the Z mass squared (M_Z^2). At leading order, the momentum fraction carried by the incident quarks is related to the boson rapidity by $x_{1,2} = \frac{M_Z}{\sqrt{s}} e^{\pm y}$ where $x_{1,2}$ is the momentum fraction carried by the incident quark and antiquark and y is the boson rapidity. As $|y|$ increases, $\Delta x = |x_1 - x_2|$ increases. At large values of $|y|$, the initial state involves a $q(\bar{q})$ with large x and a $\bar{q}(q)$ with small x. The range of momentum fraction accessible at the Tevatron is roughly $0.003 < x < 0.8$. This measurement overlaps in (x, Q^2) with Tevatron jet measurements. Because electrons are used, systematic uncertainties are different than for jet data. For example, there is no contribution from the jet energy scale.

A measurement of the normalized differential cross section is made using

$$\frac{1}{\sigma}\left(\frac{\mathrm{d}\sigma}{\mathrm{d}y}\right)_i = \frac{(\epsilon \times A)_{\mathrm{avg}}}{N^{\mathrm{obs}}_{\mathrm{total}} - N^{\mathrm{bg}}_{\mathrm{total}}} \frac{N^{\mathrm{obs}}_i - N^{\mathrm{bg}}_i}{\Delta_i \left(\epsilon \times A\right)_i},$$

where i indicates the boson rapidity bin. In the first term on the right hand side, ϵ_{avg} is the average efficiency and A_{avg} is the average acceptance for kinematic and geometric cuts. $N^{\mathrm{obs}}_{\mathrm{total}}$ ($N^{\mathrm{bg}}_{\mathrm{total}}$) is the number of candidate bosons (background events). In the second term,

ϵ_i, A_i, $N_i^{\rm obs}$, and $N_i^{\rm bg}$ are as before, but determined in each bin i. Δ_i is the bin width. Dividing by the cross section cancels some systematic uncertainties, such as the luminosity.

The measurement is made with 0.4 fb^{-1} of data. Isolated electrons are selected from the central (forward) region that have $|\eta| < 0.9$ ($1.5 < |\eta| < 3.2$) [a]. The leading (second) electron has $p_T > 25$ GeV ($p_T > 15$ GeV). The invariant mass must be within $71 < M_{ee} < 111$ GeV. Main backgrounds come from multijet or electron plus jet events where one or more jets is misidentified as an electron. The background fraction ranges from $< 1\%$ to around 5%. Main contributions to the systematic uncertainties, depending on y, are from electron efficiencies, background, and PDFs. The current measurement is statistics limited.

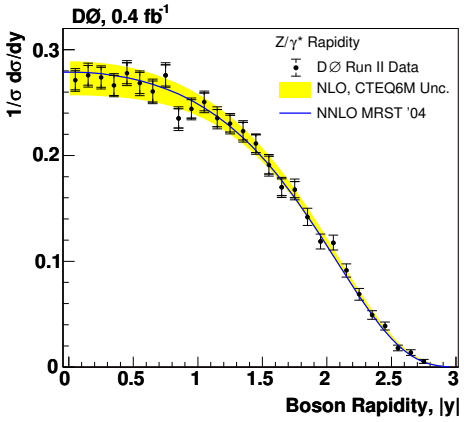

Figure 1: Z boson rapidity measured by D0. Inner (outer) error bars indicate the statistical (total) uncertainty. The spread in a NLO calculation using CTEQ6M error PDFs is shown as a yellow band. A NNLO calculation using MRST 2004 PDFs is shown as a solid line.

The result is presented in Fig. 1 as a function of $|y|$. Also shown is a NNLO curve using code from Ref. [5] and MRST 2004 PDFs [6]. The calculation is in good agreement with our data. The yellow band in Fig. 1 shows the spread when performing NLO calculations with the same code for each of the 40 CTEQ6M error PDFs [7]. At lower $|y|$ values the uncertainties are comparable to or smaller than the spread.

3 $W \to \mu\nu$ charge asymmetry

As with Z bosons, the main production mechanism for W bosons at the Tevatron is $q\bar{q}$ annihilation. A large fraction of the events involve valence-valence or valence-sea interactions. W^+ bosons are created from $u + \bar{d}$ in the initial state, with the u ($\bar{d}$) often coming from the p ($\bar{p}$). On average a u carries more momentum fraction than a d which tends to boost the $W^{+(-)}$ along the p ($\bar{p}$) direction. This produces an asymmetry in the charge separated W rapidity distribution. For leptonically decaying Ws, the ν is not measured directly, making reconstruction of y_W difficult. One approach is to measure the charge asymmetry using the μ rapidity. This contains the W charge asymmetry convoluted with the asymmetry from the (V-A) decay, which is well understood. The μ charge asymmetry is directly proportional to the $u(x)/d(x)$ ratio. The asymmetry is defined as

$$A(y_\mu) = \frac{\frac{d\sigma(\mu^+)}{dy} - \frac{d\sigma(\mu^-)}{dy}}{\frac{d\sigma(\mu^+)}{dy} + \frac{d\sigma(\mu^-)}{dy}} \quad \text{where} \quad \frac{d\sigma(\mu^\pm)}{dy} = \frac{N_i^{\mu^\pm}}{\mathcal{L} A_i \epsilon_i^\pm}.$$

Here $N_i^{\mu^\pm}$ is the number of charge separated μ candidates after background subtraction in a give rapidity bin. $\epsilon_i^\pm$ is rapidity dependent efficiency for $\mu^\pm$. $\mathcal{L}$ is the luminosity and A_i

[a] $\eta = -\ln[\tan(\theta/2)]$. In the relativistic limit $\eta = y$.

is the acceptance for μ. The acceptance and luminosity are the same for μ^+ and μ^-. They cancel in the asymmetry, which helps to minimize the measurement's dependency on PDFs.

This measurement uses 230 pb^{-1} of data. Isolated μ candidates are selected with $p_T > 20$ GeV. Candidate events are in the region $|\eta| < 2$. The events must have $\not\!\!E_T < 20$ GeV and $M_T(W) > 40$ GeV, which cut on the missing transverse energy and transverse mass respectively. Main sources of background come from electroweak processes such as $Z \to \mu\mu$ where a μ goes undetected or from $W \to \tau\mu$ where the τ decays to a μ. These backgrounds are estimated using PYTHIA [8] and are at a level of few percent. Another significant source of background comes from multijet events which can produce a μ. This contribution also is at the few percent level and is measured using data. The main contribution to the systematic uncertainty is from the efficiencies.

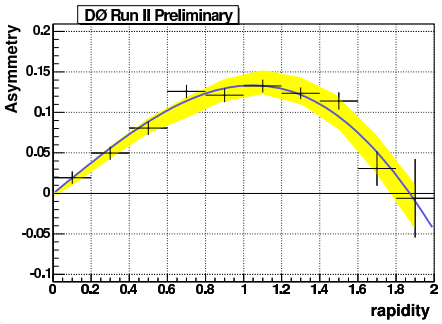

Figure 2: W charge asymmetry in the μ channel as a function of the μ | rapidity |. Error bars show the total uncertainty. In the yellow band is the spread in a NLO calculation when using CTEQ6.1M error PDFs. The solid blue curve uses the same calculation but with MRST 2002 PDFs.

The CP folded result is presented in Fig. 2. Error bars show the total uncertainty. In a yellow band is the spread obtained by following the CTEQ recipe [9] using the RESBOS-A NLO generator [10] with CTEQ6.1M 40 error PDFs. Note that in certain regions the experimental uncertainties are already smaller than the spread. Shown in a solid blue line is the RESBOS-A prediction using MRST 2002 PDF [11]. The current measurement is statistics limited.

4 Photon + jet triple differential cross section

The cross section for $p\bar{p} \to \gamma + jet + X$ is measured as a function of the p_T of the most energetic photon. The data are divided into four kinematic regions based on η^γ and η^{jet}:

Region 1: $0.0 < |\eta^\gamma| < 1.0$ and $0.0 < |\eta^{jet}| < 0.8$ and $\eta^\gamma \times \eta^{jet} > 0$
Region 2: $0.0 < |\eta^\gamma| < 1.0$ and $0.0 < |\eta^{jet}| < 0.8$ and $\eta^\gamma \times \eta^{jet} < 0$
Region 3: $0.0 < |\eta^\gamma| < 1.0$ and $1.5 < |\eta^{jet}| < 2.5$ and $\eta^\gamma \times \eta^{jet} > 0$
Region 4: $0.0 < |\eta^\gamma| < 1.0$ and $1.5 < |\eta^{jet}| < 2.5$ and $\eta^\gamma \times \eta^{jet} < 0$

Here η^{jet} is that of the leading jet. Main contributions to the "$\gamma + jet$" measurement come from the $gq \to q\gamma$ Compton diagram and from $q\bar{q}$ annihilation. The Compton diagram dominates for $p_T(\gamma) < 150$ GeV, making the measurement sensitive to the gluon distribution.

The analysis is made using 1.1 fb^{-1} of data and requires isolated photons in the central region. The leading jet must have $p_T > 15$ GeV and there is a cut on the opening angle between the photon and jet in $\eta - \phi$ space. Main backgrounds come from jet-jet or electron-jet events, where the jet or electron is misidentified as a photon. A Neural Network is used to suppress the background and also to measure the photon purity.

The main systematic uncertainty is from the luminosity (6%). After the luminosity, the main contributions to the systematic uncertainties are from the photon purity and the photon and jet selections. Each of these contributions are around 3-5%.

The result is presented in Fig. 3 along with a NLO QCD calculation using JetPhox[12] with CTEQ6.1M PDFs. Comparing data to the prediction shows some disagreement for all four regions. Similar disagreements were seen earlier by UA2 [13], CDF [14] and D0 [15]. The disagreement cannot be completely accounted for by the overall uncertainty. For more details, see Ref. [4] and O. Atramentov's report at this conference [16].

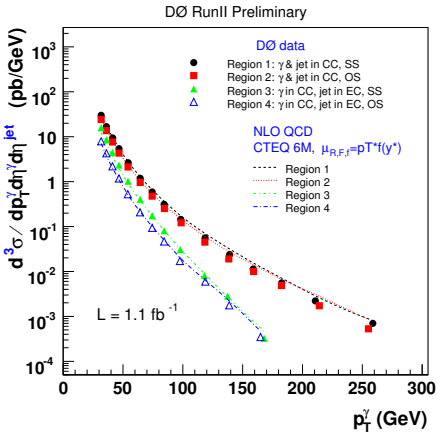

Figure 3: D0 measurement of differential cross sections for "$\gamma + jet$". Also shown are curves from NLO QCD calculation using JetPhox with CTEQ6.1M PDFs.

5 Summary

We demonstrate that even with small statistics, D0 analyses are sensitive to PDFs. We can expect significant improvements for analyses which are currently statistics limited, but are made on a small fraction of the existing data set. At the present time, D0 has more than 2.5 fb^{-1} on tape and the data set is expected to increase significantly by the end of Run II. In addition there are a number of analyses in progress, such as W, Z, or γ with a tagged b or c jet, which will complement the efforts presented here.

References

[1] `http://indico.cern.ch/contributionDisplay.py?contribId=277&sessionId=8&confId=9499`
[2] V. M. Abazov *et al.* [D0 Collaboration], arXiv:hep-ex/0702025.
[3] http://www-d0.fnal.gov/Run2Physics/WWW/results/prelim/EW/E14/E14.pdf
[4] http://www-d0.fnal.gov/Run2Physics/WWW/results/prelim/QCD/Q07/Q07.pdf
[5] C. Anastasiou *et al.*, Phys. Rev. D **69** (2004) 094008 [arXiv:hep-ph/0312266].
[6] R. S. Thorne *et al.*, arXiv:hep-ph/0407311.
[7] D. Stump *et al.*, JHEP **0310** (2003) 046 [arXiv:hep-ph/0303013].
[8] T. Sjostrand *et al.*, Comput. Phys. Commun. **135** (2001) 238 [arXiv:hep-ph/0010017].
[9] J. Pumplin *et al.*, JHEP **0207** (2002) 012 [arXiv:hep-ph/0201195].
[10] Q. H. Cao and C. P. Yuan, Phys. Rev. Lett. **93** (2004) 042001 [arXiv:hep-ph/0401026].
[11] R. S. Thorne *et al.*, Acta Phys. Polon. B **33**, 2927 (2002) [arXiv:hep-ph/0207067].
[12] P. Aurenche, R. Baier, M. Fontannaz and D. Schiff, Nucl. Phys. B **297** (1988) 661;
F. Aversa, P. Chiappetta, M. Greco and J. P. Guillet, Nucl. Phys. B **327** (1989) 105;
S. Catani, M. Fontannaz, J. P. Guillet and E. Pilon, JHEP **0205** (2002) 028 [arXiv:hep-ph/0204023].
[13] J. Alitti *et al.* [UA2 Collaboration], Phys. Lett. B **263** (1991) 544.
[14] D. Acosta *et al.* [CDF Collaboration], Phys. Rev. D **65** (2002) 112003 [arXiv:hep-ex/0201004].
[15] V. M. Abazov *et al.* [D0 Collaboration], Phys. Lett. B **639** (2006) 151 [arXiv:hep-ex/0511054].
[16] `http://indico.cern.ch/contributionDisplay.py?contribId=173&sessionId=6&confId=9499`

Parton Distributions for the LHC

R.S. Thorne[1]*, A.D. Martin[2], W.J. Stirling[2] and G. Watt[1]

1- Department of Physics and Astronomy, University College London, WC1E 6BT, UK

2- Institute for Particle Physics Phenomenology, University of Durham, DH1 3LE, UK

We present a preliminary set of updated NLO parton distributions. For the first time we have a quantitative extraction of the strange quark and antiquark distributions and their uncertainties determined from CCFR and NuTeV dimuon cross sections. Additional jet data from HERA and the Tevatron improve our gluon extraction. Lepton asymmetry data and neutrino structure functions improve the flavour separation, particularly constraining the down quark valence distribution.

There are many reasons why an update [1] to the MRST2004 parton distributions [2] is necessary. The MRST (now MSTW) group have used a general-mass variable flavour number scheme (VFNS) since 1998 [3], but a new scheme [4], although primarily devised for use at NNLO [5], also changes the details of the NLO implementation. We now make use of the `fastNLO` package [6], which provides an efficient combination of NLO partonic cross sections with parton distributions, allowing for a more rigorous inclusion of jet data into global parton fits.

There are also many new data sets available to include: CHORUS and NuTeV neutrino structure functions $F_2^{\nu,\bar{\nu}}(x,Q^2)$ and $F_3^{\nu,\bar{\nu}}(x,Q^2)$ [7], CCFR and NuTeV dimuon cross sections [8] providing a direct constraint on s and $\bar{s}$, CDF Run II lepton asymmetry data [9] in two different E_T bins, HERA jet data [10], and new CDF Run II high-E_T jet data [11]. We also include all recent charm and bottom HERA structure function data [12].

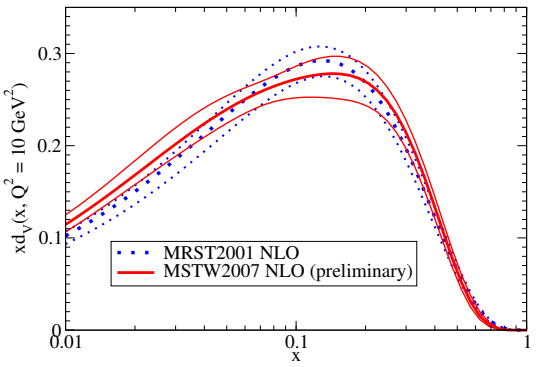

Figure 1: The distribution $xd_V(x, 10\,\mathrm{GeV}^2)$.

Let us consider the effects of some of these new data sets. It has already been noticed that the NuTeV neutrino structure functions are not completely compatible with the older CCFR data, both by the experiment themselves and by groups performing fits [13, 14]. Previous parton distributions were perfectly compatible with the CCFR data when using EMC-inspired Q^2-independent nuclear correction factors, whereas the NuTeV structure function data are difficult to fit at high x. Moreover, recent CHORUS structure function data (which were taken with a lead rather than an iron target) turn out to be fairly consistent with the CCFR data. Thus, there is a problem at high x. However, the partons in this region are already very well determined from charged lepton structure functions. The important information from charged current data is in the region $x < 0.3$, probing the separation into valence quarks and sea quarks, and there is general consistency between data sets here. Hence, we choose to exclude from the fit all neutrino structure function data for $x > 0.5$. In our analysis we now also implement

*Royal Society University Research Fellow

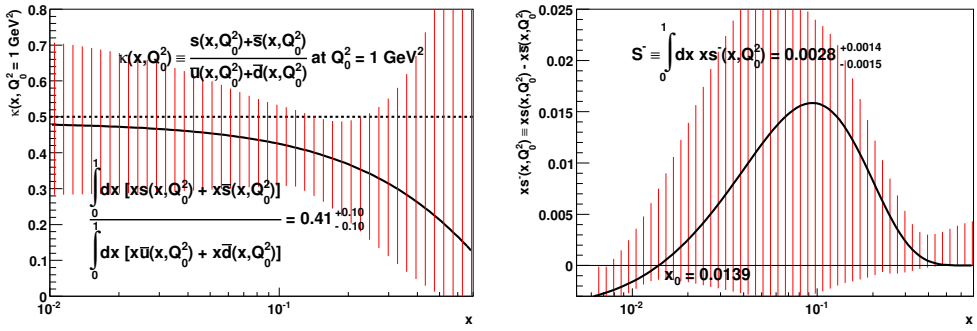

Figure 2: The input distributions $s^+(x,Q_0^2)$ (left) and $s^-(x,Q_0^2)$ (right).

more sophisticated flavour-dependent nuclear correction factors [15] extracted using NLO partons, allowing a $\sim 3\%$ uncertainty on these factors.

The CDF lepton asymmetry data constrain similar partons as the neutrino structure functions. The W asymmetry at the Tevatron is defined by $A_W(y_W) \propto \mathrm{d}\sigma(W^+)/\mathrm{d}y_W - \mathrm{d}\sigma(W^-)/\mathrm{d}y_W \approx u(x_1)d(x_2) - d(x_1)u(x_2)$, where $x_{1,2} = (M_W/\sqrt{s})\exp(\pm y_W)$. In practice it is the final state leptons from the W decay that are detected, so it is really the lepton asymmetry $A(y_l) = [\sigma(l^+) - \sigma(l^-)]/[\sigma(l^+) + \sigma(l^-)]$ which is measured. Defining the emission angle of the lepton relative to the proton beam in the W rest frame by $\cos^2\theta^* = 1 - 4E_T^2/M_W^2$ leads to $y_l = y_W \pm 1/2 \ln[(1+\cos\theta^*)/(1-\cos\theta^*)]$. To a good approximation

$$\sigma(l^+) - \sigma(l^-) \propto u(x_1)d(x_2)(1-\cos\theta^*)^2 + \bar{d}(x_1)\bar{u}(x_2)(1+\cos\theta^*)^2 - d(x_1)u(x_2)(1+\cos\theta^*)^2,$$

where the antiquark term is boosted by the large $(1+\cos\theta^*)^2$ and the asymmetry is fairly sensitive to antiquarks at lower E_T. Hence, it probes the separation into valence and sea quarks, particularly for the less well-constrained down quark. We find that the CDF Run II data influence $d(x,Q^2)$, and that there is some tension with the neutrino structure function data. Our fit gives $\chi^2 = 41$ for the 22 lepton asymmetry data points, although much of this χ^2 comes from only 2 data points. Overall, $d_V(x,Q^2)$ has a slightly different shape to previously [16], seen in Fig. 1. The uncertainty is generally bigger than before, despite more constraints, due to a better parameterisation when determining uncertainty eigenvectors.

The CCFR and NuTeV dimuon cross sections for neutrino (antineutrino) scattering, $\nu_\mu(\bar{\nu}_\mu)N \to \mu^+\mu^- X$, are sensitive to the strange quark (antiquark) distribution through the LO partonic process $\nu_\mu s(\bar{\nu}_\mu \bar{s}) \to c\mu^-(\bar{c}\mu^+)X$. In previous MRST fits, CCFR dimuon data have been indirectly used to justify the input parameterisation assumption of

$$s(x,Q_0^2) = \bar{s}(x,Q_0^2) = \frac{\kappa}{2}[\bar{u}(x,Q_0^2) + \bar{d}(x,Q_0^2)] \qquad (\kappa \approx 0.5),$$

at the input scale of $Q_0^2 = 1\,\mathrm{GeV}^2$. We now relax this assumption and fit the CCFR/NuTeV dimuon cross sections directly. Defining $s^+ \equiv s + \bar{s}$ and $s^- \equiv s - \bar{s}$, then the input forms are taken to be $s^+(x,Q_0^2) = A_+\,(1-x)^{\eta_+}\,S(x,Q_0^2)$ and $s^-(x,Q_0^2) = A_-\,x^{-1+\delta_-}\,(1-x)^{\eta_-}\,(1 - x/x_0)$, where $S(x,Q_0^2)$ is the total sea quark distribution and x_0 is determined by zero strangeness of the proton, i.e. $\int_0^1 \mathrm{d}x\; s^-(x,Q_0^2) = 0$. The preference for extra freedom in both

s^+ and s^- is confirmed by the fit, with the global χ^2 improving by 15 when s^+ is allowed to go free, and by a further 14 when s^- is allowed to go free. There is no improvement with the addition of further free parameters. Indeed, A_- and δ_- are highly correlated so we fix δ_- at 0.2, i.e. a valence-like value.

The input s^+ and s^- distributions from the best fit, with approximately 90% confidence level uncertainty bands, are shown in Fig. 2. There is a reduced ratio of strange to non-strange sea distributions compared to our previous default $\kappa = 0.5$, and a marked suppression at high x, i.e. low W^2, probably due to the effect of the strange quark mass. The integrated momentum asymmetry is positive, $0.0028^{+0.0014}_{-0.0015}$ at $Q_0^2 = 1\,\mathrm{GeV}^2$, decreasing to $0.0021^{+0.0010}_{-0.0011}$ at $Q^2 = 10\,\mathrm{GeV}^2$. The results on both s^+ and s^- are qualitatively consistent with those obtained by the CTEQ group [17]. Directly fitting the s and $\bar{s}$ distributions affects the uncertainties on the light quarks. Until recently all parton fitting groups assumed s^+ to be a fixed proportion of the total sea in the global fit. An independent uncertainty on s and $\bar{s}$ feeds into that on the $\bar{u}$ and $\bar{d}$ quarks, since the neutral current DIS data on $F_2(x, Q^2)$ constrain the combination $4/9(u + \bar{u}) + 1/9(d + \bar{d} + s + \bar{s})$. Consequently, the size of the uncertainty on the sea quarks at $x \sim 0.001 - 0.01$ at hard scales $Q^2 \sim M_W^2$ roughly doubles from $\sim 1.5\%$ to $\sim 3\%$.

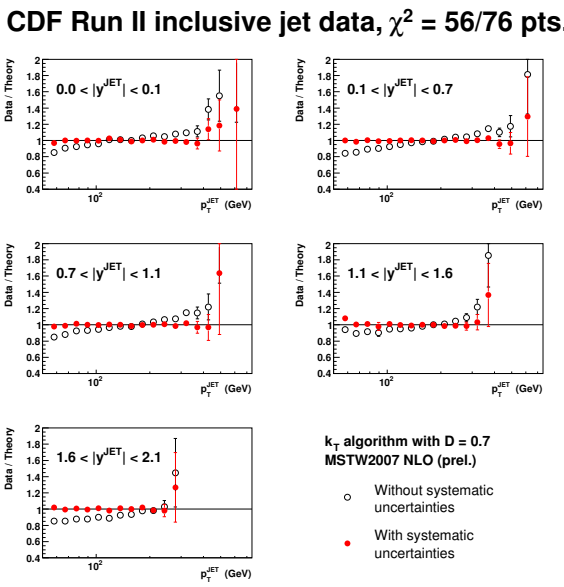

Figure 3: The fit to the CDF Run II jet data.

We now use the `fastNLO` [6] package during the fit to calculate Tevatron and HERA jet cross sections at NLO, improving upon previous approximations for the former and allowing our first analysis of the latter. We find a slight change in the shape of the gluon distribution using only Tevatron Run I data (for which we now include previously absent hadronisation corrections). The fit to the HERA jet data is excellent, although we do not find that they provide a strong constraint within the global fit. We also include CDF Run II inclusive jet data [11] obtained in different rapidity bins using the k_T jet algorithm. We obtain a very good fit, $\chi^2 = 56$ for 76 data points, as seen in Fig. 3, at the expense of a

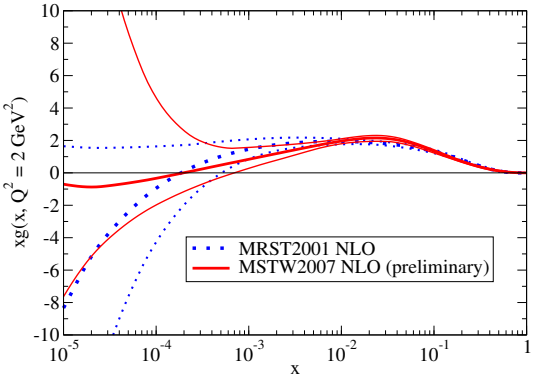

Figure 4: The distribution $xg(x, 2\,\mathrm{GeV}^2)$.

slight deterioration in the fit to the DØ Run I inclusive jet data [18]. The CDF Run II data prefer a smaller gluon distribution at very high x compared to the Run I data included in the MRST2004 fit [2]. The gluon distribution is shown in Fig. 4 compared to MRST2001 [16]. The uncertainty is similar at high x, but is actually larger overall due to allowing an additional parameter to go free when determining the eigenvectors. The uncertainty on the gluon is extremely large at $x = 10^{-5}$ due to our lack of theoretical prejudice on the form taken in this region.

Finally, we investigate the dependence of the fit on m_c, the pole mass of the charm quark. We take the pole mass of the bottom quark to be $m_b = 4.75\,\text{GeV}$. We vary m_c in steps of $0.1\,\text{GeV}$, finding a preference for $m_c = 1.4\,\text{GeV}$ with an uncertainty $\sim 0.2\,\text{GeV}$. The results are shown in Table 1. There is a clear correlation between m_c and $\alpha_S(M_Z^2)$. The value of the (NLO, $\overline{\text{MS}}$) coupling for the best fit is $\alpha_S(M_Z^2) = 0.1206$, very similar to that in MRST2004 [2].

m_c (GeV)	χ^2_{global} 2659 pts.	$\chi^2_{F_2^c}$ 78 pts.	$\alpha_s(M_Z^2)$
1.2	2541	179	0.1183
1.3	2485	129	0.1191
1.4	2472	100	0.1206
1.5	2479	95	0.1213
1.6	2518	101	0.1223
1.7	2576	123	0.1221

Table 1: The dependence of the fit on m_c.

Overall, the inclusion of new data and the changes in the analysis have a significant impact on our NLO parton distributions. Based on the developments in this paper we will soon have fully updated NLO and NNLO partons for the LHC complete with uncertainties.

References

[1] Slides:
`http://indico.cern.ch/contributionDisplay.py?contribId=33&sessionId=8&confId=9499`

[2] A.D. Martin, R.G. Roberts, W.J. Stirling and R.S. Thorne, Phys. Lett. **B604** 61 (2004).

[3] A.D. Martin, R.G. Roberts, W.J. Stirling and R.S. Thorne, Eur. Phys. J. **C4** 463 (1998).

[4] R.S. Thorne, Phys. Rev. **D73** 054019 (2006).

[5] A.D. Martin, W.J. Stirling, R.S. Thorne and G. Watt, `arXiv:0706.0459` [hep-ph].

[6] T. Kluge, K. Rabbertz and M. Wobisch, `hep-ph/0609285`.

[7] CHORUS Collaboration: G. Onengut *et al.*, Phys. Lett. **B632** 65 (2006);
NuTeV Collaboration: M. Tzanov *et al.*, Phys. Rev. **D74** 012008 (2006).

[8] NuTeV Collaboration: M. Goncharov *et al.*, Phys. Rev. **D64** 112006 (2001).

[9] CDF Collaboration: D. Acosta *et al.* Phys. Rev. **D71** 051104 (2005).

[10] H1 Collaboration: C. Adloff *et al.*, Eur. Phys. J. **C19** 289 (2001);
ZEUS Collaboration: S. Chekanov *et al.*, Phys. Lett. **B547** 164 (2002); Nucl. Phys. **B765** 1 (2007).

[11] CDF Collaboration; A. Abulencia *et al.*, `hep-ex/0701051`.

[12] H1 Collaboration: A. Aktas *et al.*, Eur. Phys. J. **C40** 349 (2005); Eur. Phys. J. **C45** 23 (2006);
ZEUS Collaboration: S. Chekanov *et al.*, Phys. Rev. **D69** 012004 (2004).

[13] R.S. Thorne, A.D. Martin, R.G. Roberts and W.J. Stirling, `hep-ph/0606244`.

[14] J.F. Owens *et al.*, Phys. Rev. **D75** 054030 (2007).

[15] D. de Florian and R. Sassot, Phys. Rev. **D69** 074028 (2004).

[16] A.D. Martin, R.G. Roberts, W.J. Stirling and R.S. Thorne, Eur. Phys. J. **C28** 455 (2003).

[17] H.L. Lai *et al.*, JHEP **0704** 089 (2007).

[18] DØ Collaboration: B. Abbott *et al.*, Phys. Rev. Lett. **86** 1707 (2001).

Global QCD Analysis and Collider Phenomenology—CTEQ

Wu-Ki Tung[1,2], H.L. Lai[1,2,3], J. Pumplin[1], P. Nadolsky[4], and C.-P. Yuan[1].

[1] Michigan State University, East Lansing, MI - USA
[2] University of Washington, Seattle, Washington - USA
[3] Taipei Municipal University of Education, Taipei, Taiwan
[4] Argonne National Laboratory, Argonne, IL, USA

An overview is given of recent progress on a variety of fronts in the global QCD analysis of the parton structure of the nucleon and its implication for collider phenomenology, carried out by various subgroups of the CTEQ collaboration.

1 Introduction

Parton distribution functions (PDFs) are essential input to all calculations on high energy cross sections with initial state hadrons. PDFs are extracted from comprehensive *global analysis* of available hard scattering data within the framework of *perturbative QCD.* This report covers recent progress on global QCD analysis made by members of the CTEQ collaboration on a variety of fronts. [1]

The basis of most of the recent progress is a new implementation of the general mass (GM) formulation for perturbative QCD that systematically includes heavy quark mass effects, both in kinematics and in the order-by-order factorization formula. [2] The next section describes the main implications of the new global QCD analysis on collider phenomenology at the Tevatron and the LHC. [3]

This is followed by the first in-depth study of the strangeness sector of the parton parameter space, based on the most up-to-date global analysis. [4] We found that current data imply a symmetric component of the strange parton distribution, $s(x) + \bar{s}(x)$, that has a shape independent of that of the isospin singlet non-strange sea; and a strangeness asymmetry function $s(x) - \bar{s}(x)$ that has a slightly positive first moment.

The same formalism has been applied to investigate the possibility of a non-perturbative (intrinsic) charm component in the nucleon. [5] This study is discussed in a separate talk in this workshop [6]. In a significant expansion of global QCD analysis, we have succeeded in combining the traditional fixed-order global fits with p_t resummation calculations. Combined conventional and p_t-resummed global fits can now be made to pin down parton degrees of freedom that are most pertinent for precision W-mass measurement and Higgs particle phenomenology. [7] Another subgroup of CTEQ has performed a detailed investigation of the role of recent neutrino scattering experiments (NuTeV, Chorus) and fixed-target Drell-Yan cross section measurement (E866) on global analysis, particularly pertaining to the large-x behavior of parton distributions. The results are reported in [8].

Due to space limitation, it is impossible to include in this short written report the figures that illustrate the results discussed in the corresponding talk, as summarized above. However, since the slides for the talk have been made available at the official conference URL [1], we shall make use of these, and refer the reader to the actual figures by the slide numbers where they appear in the posted talk [1]. The same space limitation restricts citations to only the papers and talks on which this report is directly based.

2 New Generation of PDFs and Their Implications for Collider Phenomenology

The base parton distribution set from the new generation of global analysis incorporating the GM formalism for heavy quark mass effects is the CTEQ6.5M PDF set [2]. The main improvements over the previous generation of PDFs—CTEQ6.0 and CTEQ6.1—are the mass treatment and the incorporation of the full HERA Run 1 cross section measurements, with their correlated systematic errors.

The most noticeable change in the output parton distributions is a sizable increase in the u- and d-quark distributions in the region $x \sim 10^{-3}$ for a wide range of Q. The three figures on slides 4/5 of [1] show the ratio of the CTEQ6.1 u, d-quark and the gluon distribution to that of CTEQ6.5 at $Q = 2$ GeV. The differences are moderated by QCD evolution, but still persist to a high energy scale such as the W/Z masses. The origin of these differences can be traced to the treatment of the heavy quark mass, as explained in slide 6. This change has immediate phenomenological consequences. The figure on slide 7 shows ratios of predicted cross sections at the LHC for the standard model (SM) processes $W^{\pm}/Z$ production, Higgs production $gg \to H^0$, and associated production of $W^{\pm}H$; as well as some representative beyond standard model (BSM) processes, e.g. charged Higgs production $\bar{s}c \to H^+ \to \bar{b}t$.

Of immediate interest is the 7% increase in the predicted W and Z production cross sections at LHC (which are sensitive to PDFs in the $x \sim 10^{-3}$ range) compared to previous estimates. The plot on slide 10 shows the predicted Z vs. the W cross sections for several commonly available PDF sets. The predictions seem to fall into two groups, with no obvious pattern. The results on slide 11 represent an attempt to see whether the difference between Zeus and H1 predictions can be reproduced in the CTEQ framework. We do not see a substantial difference between the two experimental inputs, but do see a clear dependence on how mass effects are treated. Further mysteries are (i) why are the Zeus predictions independent of their mass treatment; and (ii) why are their predictions with mass effects so different from that of MRST, even though they use the MRST formalism for mass treatment. The resolution of these apparent puzzles concerning the W and Z cross sections at the LHC is clearly of great importance to its physics program.

To see the impact of the new PDFs on collider phenomenology in general, it is convenient to examine the luminosity curves. These are shown in slides 8-9 over the range 10 GeV $< \hat{s} <$ 5 TeV for LHC (normalized to that of CTEQ6.1), including bands representing the estimated uncertainties due to experimental input to the global analysis. The quark-quark (q-q) luminosity curves show the largest change between the two generations of PDFs; the g-g luminosity is shifted only slightly, and the g-q luminosity shift lies in between.

The cross sections shown in slide 7 also include some typical BSM processes. Notice in particular the very large predicted cross section for the last process due to a new PDF set CTEQ6.5C that permits a non-perturbative (intrinsic) charm component of the nucleon [5].

In the base PDF set CTEQ6.5M, we adopted the conventional assumptions that the strange distributions $s(x)$ and $\bar{s}(x)$ are of the same shape as the isospin symmetric non-strange sea at the initial scale $\mu = Q_0$ for QCD evolution, and that the charm distribution $c(x)$ is zero at the scale $\mu = m_c$. There are of no independent degrees of freedom for strange and charm. The improved theoretical and experimental inputs to the new generation of global analysis now permit us to relax these ad hoc assumptions, and hence to study where the truth lies. The results on strange PDFs obtained by [4] will be summarized in the following section. The subject of charm PDF is covered in [6].

3 Systematic Study of the Strangeness PDFs

Within the global QCD analysis framework, the only currently measurable process that is directly sensitive to the strange distributions $s(x)$ and $\bar{s}(x)$ is dimuon (charm) production in neutrino (and anti-neutrino) scattering off nucleons, via the partonic process $W^+(W^-) + s\,(\bar{s}) \to c\,(\bar{c})$. The final data of the NuTev experiment [9] is thus crucial for this analysis. The constraining power of these data can be realized, however, *only within the framework of a comprehensive global analysis*, since the same final state is produced also by the down quarks, and since the strange sea is intricately coupled to the gluon and the non-strange partons by QCD interactions. Also, because of the presence of the charm particle in the final state of the dimuon signal, a consistent theoretical treatment of heavy quark mass effects for both charged-current and neutral-current DIS processes [2] is essential to obtain reliable results.

For convenience, we define the symmetric strange sea $s_+(x) \equiv s(x) + \bar{s}(x)$ and the strangeness asymmetry $s_-(x) \equiv s(x) - \bar{s}(x)$. All these functions refer to the initial distributions at $\mu = Q_0$; QCD evolution then dictates their μ dependence at higher energy scales. We address the following three issues in turn.

Is the shape of the symmetric strange sea independent of that of the non-strange sea? The answer appears to be yes, according to the up-to-date global analysis [4]. The evidence is shown on slide 14. The table gives the changes in the goodness-of-fit for the full set of 3542 data points used in the global analysis, as well as the subset of 149 points for neutrino dimuon data sets, that we found in performing a series of global analysis, using 2/3/4 independent strangeness shape parameters, compared to the CTEQ6.5M reference fit that tied the shape of $s(x)$ and $\bar{s}(x)$ to that of the non-strange sea. We see that there is a substantial improvement in the quality of the fit to the dimuon data with $s_+(x)$ different from that of the non-strange sea. We also see that current data cannot discriminate between 2-, 3-, or 4-parameter forms for $s_+(x)$. Thus, a 2-parameter form will serve as a practical working hypothesis.

What is the size of the symmetric strange sea, and what are the allowed ranges for its size and shape? Slide 15 presents results of our study on these issues. The upper figure shows the goodness-of-fit in terms of χ^2/point for the dimuon data (deep parabola) and for the global data (shallow parabola) as a function of the momentum fraction carried by the strange sea, $\langle x \rangle_{s+} = \int x s_+(x) dx$. The dimuon data clearly favor a central value of $\langle x \rangle_s \sim 0.027$. The range of allowed size is obtained by adopting a 90% confidence level criterion. In terms of the ratio of the first moments (fractional momentum) of the strange to non-strange sea, this range corresponds to (0.27, 0.67), as indicated on the slide. The range of possible shape of $s_+(x)$ is a little more elusive to quantify. The lower figure presents a range of possible candidates, within the 90% C.L. criterion, when both the size and shape parameters are allowed to vary. These representative PDF sets are labeled CTEQ6.5Sn, $n = 0, 1, ..., 4$, with $n = 0$ being the central fit.

Current status of the strangeness asymmetry: Non-perturbative models of nucleon structure suggest a possible non-vanishing strangeness asymmetry. Within the PQCD framework, QCD evolution beyond the first two leading orders causes a non-vanishing $s_-(x, \mu)$, even if one starts with a symmetric strange sea. Historically, $s_-(x)$ was first studied phenomenologically in 2003 as a possible explanation for the "NuTeV anomaly" associated with the Weinberg angle measurement. Therefore, it is natural to ask: what can we say about $s_-(x)$ currently, now that both the theory and experimental situation have improved? The

results of our study, [4], are summarized in slide 17: (i) current global analysis still does not require a non-zero $s_-(x)$, although it is consistent with one; (ii) the best fit corresponds to a positive asymmetry $\langle x \rangle_{s-} = \int x s_-(x) dx \sim 0.002$; and (iii) the 90% C.L. range for $\langle x \rangle_{s-}$ is $(-0.001,\ 0.005)$. These results are consistent with both the 2003 CTEQ study and the most recent NuTeV analysis [9]. The figures on slide 17 show the shape of $s_-(x)$ and the momentum distribution $x s_-(x)$ for a variety of possible candidate PDFs within the 90% C.L. criterion.

4 New neutrino DIS and Drell-Yan data and large-x PDFs

It has been known for some time that the relatively recent NuTeV total cross section and E866 Drell-Yan cross section data sets pose puzzling dilemmas for quantitative global QCD analysis of PDFs, as indicated in slides 20 and 21. Attempts to incorporate these data in global analysis by Owens *et.al.* [8] led to the following key observations: (i) the NuTeV data set pulls against several of the other data sets, notably the E-866 and the BCDMS and NMC data. Nuclear corrections (heavy target) do not improve the situation. (In fact, assuming no nuclear correction lessens, but does not remove, the problem.); (ii) the conflicts are most pronounced when one examines the d/u ratio. Adding NuTeV and E-866 simultaneously in the global analysis causes the d/u ratio to flatten out substantially, resulting in worsened fits to other precision DIS data; and (iii) the E866 *pp* data is more comparable with precision DIS data sets than the *pd* data. Slides 23 - 26 show the figures that support these observations.

Conclusion: Results presented here, in conjunction with those covered in [3, 6, 7], represent significant evolutionary advancement of global QCD analysis, as well as some groundbreaking development (such as the incorporation of p_t resummation [7]). There are, however, also open problems that require further study and resolution [8]. Much remains to be done.

References

[1] Slides for this talk:
`http://indico.cern.ch/contributionDisplay.py?contribId=189&sessionId=8&confId=9499`.

[2] W. K. Tung, H. L. Lai, A. Belyaev, J. Pumplin, D. Stump and C. P. Yuan, JHEP **0702**, 053 (2007).

[3] See also C.-P. Yuan, talk in the Electroweak work group of this Workshop:
`http://indico.cern.ch/contributionDisplay.py?contribId=120&sessionId=9&confId=9499`.

[4] H. L. Lai, P. Nadolsky, J. Pumplin, D. Stump, W. K. Tung and C. P. Yuan, JHEP **0704**, 089 (2007).

[5] J. Pumplin, H. L. Lai and W. K. Tung, Phys. Rev. D **75**, 054029 (2007).

[6] Wu-Ki Tung, talk in the Heavy Flavors work group of this Workshop:
`http://indico.cern.ch/contributionDisplay.py?contribId=276&sessionId=5&confId=9499`.

[7] Cf. C.-P. Yuan, talk in the Structure Function work group of this Workshop:
`http://indico.cern.ch/contributionDisplay.py?contribId=251&sessionId=8&confId=9499`.

[8] J. F. Owens *et al.*, Phys. Rev. D **75**, 054030 (2007).

[9] D. A. Mason, Proceedings of 14th International Workshop on Deep Inelastic Scattering (DIS 2006), Tsukuba, Japan; and FERMILAB-THESIS-2006-01.

The Low-Q Deep-Inelastic Scattering Data in the Global Fit of PDFs

S. Alekhin[1], S. Kulagin[2], R. Petti[3] *

1- Institute for High Energy Physics
142281 Protvino, Moscow region - Russia

2- Institute for Nuclear research
117312 Moscow - Russia

3- South Carolina University - Department of Physics and Astronomy
Columbia SC 29208 - USA

We check impact of the existing deep-inelastic scattering (DIS) data at low momentum transfer Q on the global QCD fit of parton distribution functions (PDFs). We find that DIS data are described well within the NNLO QCD approximation with the target mass and phenomenological high-twist corrections down to $Q \sim 1$ GeV. The twist-4 terms in the DIS structure functions are extracted; for $F_{\rm L}$ its value is comparable to 0 within the errors at $x \gtrsim 0.1$. The updated PDF set with reduced uncertainties and relevant for modeling the low-Q lepton-nucleon scattering is obtained.

The existing DIS data at small momentum transfer Q in principle can put valuable constraints on the parton distribution functions (PDFs) and the strong coupling constant $\alpha_{\rm s}$ due to their very good statistical precision. Besides, the low-Q DIS data are necessary for clarification of the limits at which the parton model is valid. A study of this kinematical region in terms of the perturbative QCD is labored due to significant high-order QCD corrections, however recent progress in the NNLO QCD calculations [2] allows to use the DIS data down to $Q \sim 1$ GeV for a fit of PDFs keeping perturbative stability under control. The power corrections to the perturbative QCD terms should be also taken into account. These corrections appearing in the formalism of operator-product expansion (OPE) spoil factorization therefore one has to consider its impact on the PDFs extracted, particularly in analysis of the low-Q data. In this communication we report our results on using the DIS data down to $Q = 1$ GeV in the global QCD fit of PDFs with the power corrections due to the kinematical target mass effects [3] and the dynamical high-twist (HT) terms included into analysis.

The analyzed data set consist of the world charged-leptons DIS cross section data for the proton and deuteron targets by the SLAC, BCDMS, NMC, FNAL-E-665, H1, and ZEUS experiments supplemented by the fixed-target Drell-Yan data, the latter constrain the sea quark distribution, which is poorly determined by the DIS data alone. Basically the same combination of data was used in the earlier fit of Ref.[4] with the cut $Q^2 > 2.5$ GeV^2 imposed on the DIS data. In the present fit alongside with the softer cut imposed on the SLAC and NMC data, $Q > 1$ GeV, we also add the DIS data by FNAL-E-665 experiment [5] since they give additional constraint on the PDFs at small x provided not too stringent cut on Q is applied. The cut on invariant mass of the hadron system $W > 1.8$ GeV is imposed on the DIS data to avoid resonance region. The total number of data points (NDP) used in the fit is 3076, in the range of $x = 0.0001 \div 0.9$. The analysis is performed in the NNLO QCD approximation with the target mass corrections taken into account, the dynamical twist-4

*This work is partially supported by by the RFBR grant 06-02-16659 and the Russian Ministry of Science and Education grant Nsh 5911.2006.

terms parameterized in the additive form as

$$F_{2,T}(x,Q^2) = F_{2,T}^{\text{twist}-2}(x,Q^2) + \frac{H_{2,T}(x)}{Q^2[\text{GeV}^2]}, \quad (1)$$

and correction for the nuclear effects in the form of model [6] applied to the deuteron data[a].

As a first step of the analysis we checked possible twist-6 contribution to the DIS structure functions (SFs) adding the terms $H^{(6)}(x)/Q^2$ to Eq.(1). Since the twist-6 terms are insensitive to the large-x part of the data used due to the cut on W they were set to 0 at $x \geq 0.5$. Values of the HT terms at $x = 0$ were also set to 0 in view of no clear evidence of the saturation effects were found at the small x HERA data. The HT terms in the SFs $F_{2,\text{T}}$ obtained in this variant of the fit are given in Fig.1. Surprisingly, we observe big positive contribution of the twist-6 term to F_T at $x \sim 0.15$. At the same time this contribution is compensated by the negative twist-4 contribution. Because the twist-4 and twist-6 coefficients are similar in magnitude and opposite in sign, the sum of these terms demonstrate weak dependence on Q. This leads us to the conclusion that in fact the twist-6 term in F_T absorbs some non-power-like effects. Indeed, in the variant of fit with no twist-6 terms included magnitude of the pulls is maximal not at the smallest Q, but at $Q^2 \sim 7$ GeV^2, in the region of overlapping of the SLAC and BCDMS data (see Fig.2). These two data sets demonstrate certain discrepancy, which goes into the fake twist-6 contribution, if this term is fitted too. The values of inelasticity y are big for the SLAC data at largest Q and small for the BCDMS data at lowest Q. For this reason the discrepancy affects mostly the HT terms in F_T, which is more sensitive to y than F_2. At the same time the SLAC/BCDMS data discrepancy at $Q^2 \sim 7$ GeV^2 is not crucial for determination of the twist-4 terms. If we rescale the errors in data at this region to bring the pulls to the level of 1σ the corresponding increase of the HTs errors is insignificant. Evidently, this terms are driven by the data at lowest Q used and in principle the SLAC/BCDMS data around $Q^2 \sim 7$ GeV^2 can be even dropped without the loss of statistical sensitivity of the total data sample. Preliminary data by the experiment JLAB-E-118 [7] are in agreement to the SLAC data at low Q, this is in favor of reliability of the latter at $Q \sim 1$ GeV, despite their possible defects in the region of overlapping with the BCDMS data.

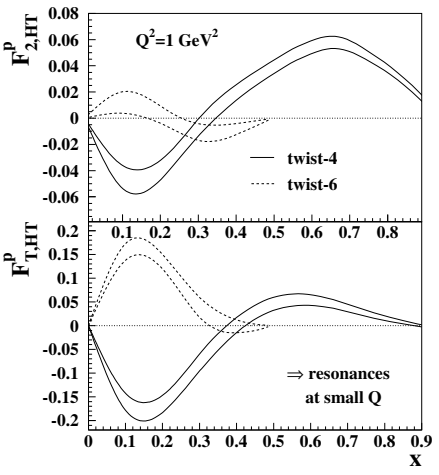

Figure 1: The 1σ error bands for the twist-4 (solid lines) and twist-6 (dashes) terms in the proton F_2 (upper panel) and F_T (lower panel). The arrow indicates region of x with the limited potential for determination of the twist-6 terms due to the cut on W.

[a]Details of the theoretical ansatz can be found in Ref.[4].

Coming to the conclusion that the twist-6 terms observed are just due to certain discrepancy in the data we drop these terms in the final version of the fit. The value of χ^2/NDP for this variant of fit is 3815/3076=1.25, bigger than 1 particularly due to certain discrepancies in data discussed above. Nonetheless the inconsistent data points are spread more or less randomly over kinematics and do not bias results of the fit; rescaling of the errors in the data points with the biggest pulls, which brings the overall value of χ^2/NDP to 1 leads to increase of errors in the PDFs and HTs within 20% only. The twist-4 terms obtained in final version of our fit are given in Fig.3. The HT terms in F_T are remarkably similar to ones in F_2, despite these two terms were fitted independently. As a result the HT term in F_L defined as $H_{\rm L} = H_2 - H_{\rm T}$ is well comparable to 0 within the errors. The HT contribution to the structure function $R = \sigma_{\rm L}/\sigma_{\rm T}$ is also small in the whole range of x considered. This result is different from the conclusion of Ref.[8] about big HT contribution to R. We explain this difference by the fact that the low-Q part of the SLAC data was not considered in Ref.[8], extrapolation of those results to the lower Q must be in disagreement to the data. The total contribution of the HT terms into the DIS cross section is small as compared to the leading-twist (LT) part. For the realistic DIS kinematics the ratio of the HT and LT terms is $\lesssim 10\%$ that justifies the use of twist expansion in our analysis.

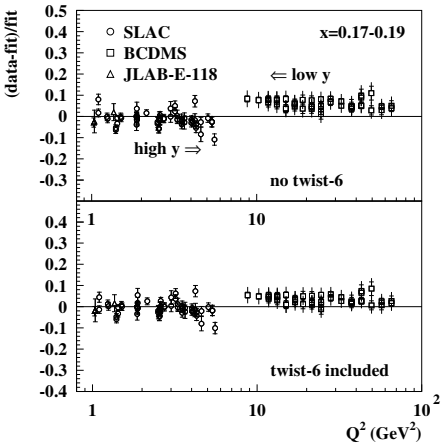

Figure 2: The pulls for the variants of the fit with and without twist-6 terms taken into account. The arrows in the upper panel indicate the high-y and low-y regions for the SLAC and BCDMS data. The data points for JLAB-E-118 experiment at $Q \sim 1$ GeV were not used in the fit.

The value of $\alpha_{\rm s}$ is similar to one obtained in Ref.[4] with the cut $Q^2 > 2.5$ GeV^2 and is in good agreement to the result of the non-singlet DIS data analysis [9]. The PDFs obtained in the fit with the low-Q DIS data included are also not very different from ones of Ref.[4]. This manifests good separation of the LT and HT terms in the fit, correlation coefficients for the LT and HT terms do not exceed 0.3 for the whole range of x. The most significant change is in the gluon distribution at $x \sim 0.3$, which goes up in the low-Q fit (see Fig.4). This is because of significant twist-4 term in R appearing in a fit with the cut $Q^2 > 2.5$ GeV^2, similarly to the analysis of Ref.[8], the LT in R is suppressed, correspondingly. Since the LT in R

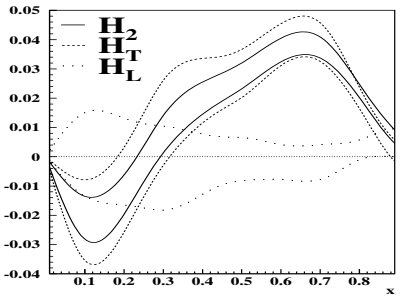

Figure 3: The 1σ error bands for the high-twist terms in the isospin-symmetric combinations of different structure functions (solid lines: F_2, dashes: $F_{\rm T}$, dots: $F_{\rm L}$).

is proportional to the value of gluon distribution the latter is suppressed too, as a result.

The errors in PDFs are improved as compared to the fit of Ref.[4], in particular the d-quark distribution is now determined with the precision of several per cent at $x \sim 0.2$, comparable to precision of the u-quark distribution. This improvement has important phenomenological impact on extraction of the Weinberg angle from the neutrino data. For the analysis by NuTeV collaboration [10] based on the Paschos–Wolfenstein relation a good knowledge of the valence distributions in this region is required to guarantee accurate estimation of the correction for the target non-isoscalarity [11]. This correction is proportional to the ratio x_1/x_0, where x_1 and x_0 are the integrals over x of the iso-vector and iso-scalar combinations of the valence quarks, respectively. For the PDFs obtained in our fit we get $x_1/x_0 = 0.424(6)$ that provides uncertainty in the target non-isoscalarity correction comparable to the experimental errors in the NuTeV data.

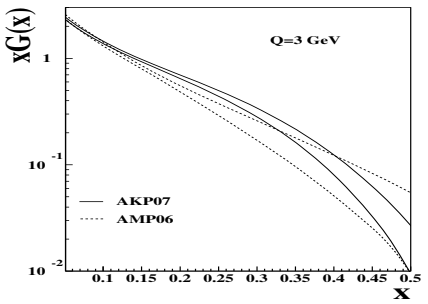

Figure 4: The 1σ error bands for the gluon distribution obtained in our fit (solid lines) compared to one of Ref.[4](dashes).

In summary, we conclude that existing DIS data can be well described down to $Q \sim 1$ GeV within the NNLO QCD approximation combined with the phenomenological high-twist corrections. The twist-4 terms in $F_{2,T}$ extracted from the global QCD fit to the DIS data supplemented by the fixed-target Drell-Yan data are found to be within 10% of the LT terms for the kinematics considered, while the HT contribution to F_L is found to be comparable to 0 within the errors at $x \gtrsim 0.1$. Obtained PDFs set with improved precision and tuned to the low-Q DIS data can be used for modeling the low-Q lepton-nucleon scattering.

References

[1] Slides:
`http://indico.cern.ch/contributionDisplay.py?contribId=29&sessionId=8&confId=9499`

[2] S. Moch, J. A. M. Vermaseren and A. Vogt, Nucl. Phys. B **688** (2004) 101; A. Vogt, S. Moch and J. A. M. Vermaseren, Nucl. Phys. B **691** (2004) 129; J. A. M. Vermaseren, A. Vogt and S. Moch, Nucl. Phys. B **724** (2005) 3; S. Moch and M. Rogal, arXiv:0704.1740 [hep-ph].

[3] O. Nachtmann, Nucl. Phys. B **63** (1973) 237; H. Georgi and H. D. Politzer, Phys. Rev. D **14** (1976) 1829.

[4] S. Alekhin, K. Melnikov and F. Petriello, Phys. Rev. D **74** (2006) 054033.

[5] M. R. Adams *et al.* [E665 Collaboration], Phys. Rev. D **54** (1996) 3006.

[6] S. A. Kulagin and R. Petti, Nucl. Phys. A **765**, 126 (2006).

[7] C. Keppel, private communication.

[8] J. L. Miramontes, M. A. Miramontes and J. Sanchez Guillen, Phys. Rev. D **40** (1989) 2184.

[9] J. Blümlein, H. Bottcher and A. Guffanti, Nucl. Phys. B **774** (2007) 182.

[10] G. P. Zeller *et al.* [NuTeV Collaboration], Phys. Rev. Lett. **88** (2002) 091802 [Erratum-ibid. **90** (2003) 239902].

[11] S. A. Kulagin, Phys. Rev. D **67** (2003) 091301.

Three- and Four Jet Production in Deep Inelastic Scattering and Low-x Parton Dynamics at HERA

Grażyna Nowak[1]
for the H1 Collaboration

Henryk Niewodniczański Institute of Nuclear Physics PAN
ul. Radzikowskiego 152, 31-342 Krakow, Poland
E-mail: Grazyna.Nowakifj.edu.pl

Parton dynamics characterized by initial state gluon radiation has been studied in deep inelastic e-p processes at low x and Q^2 at HERA using events with three- and four jets in final state both in the full kinematical range and for restrictive topologies with forward (close to the proton direction) jets. The measurement of three jet cross sections are compared to order α_s^2 and α_s^3 of fixed order QCD predictions and to leading order MC programs. Results indicate the presence of large contribution from gluon emission not ordered in transverse momentum at low x and forward rapidities.

1 Introduction

The study of parton dynamics at low x at HERA allows to test the predictions of the DGLAP evolution equations in this kinematic region. In leading order (LO) these approximations neglect terms $\propto \alpha_s \cdot \ln(1/x)$ which become large at small x. Inclusion of these terms may lead to an enhancement of gluon radiation not ordered in transverse momentum $k_\perp$ with respect to the DGLAP expectations. The enhancement should be the largest for high $p_\perp$ forward jets (near to the proton direction). Earlier measurements [2] have shown that the rate of forward jets at low x is much higher compared to QCD predictions with $k_\perp$ -ordered initial state parton showers.

The present analysis [3] includes the measurements of three- and four jet cross sections which require at least one or two gluons, respectively, radiated away from the hard scattering subprocess ($\gamma^\star g \to q\bar{q}$). The data are compared to fixed order QCD predictions at parton level calculated using NLOjet++ program [4] which is able to predict three jet parton cross sections in leading (LO,(α_s^2)) and next to leading (NLO,(α_s^3)) order and four jet cross sections in (LO,(α_s^3)). In addition two LO Monte Carlo (MC) generators which were able to describe forward jet and dijet production at low x are tested: RAPGAP [5] with initial state parton radiation ordered in $k_\perp$ including resolved photon component and DJANGO [6] which uses the color dipole model (CDM) to produce additional gluon radiation.

2 Event and Jet Selection

The data used in this analysis were taken in the 1999 and 2000 running periods, in which HERA collided 920 GeV protons with 27.5 GeV positrons, corresponding to an integrated luminosity of 44.2 pb^{-1}. The kinematic range is defined by: 5 GeV^2 $< Q^2 <$ 80 GeV^2, 0.1 $< y <$ 0.7, $10^{-4} < x < 10^{-2}$.

Jets are found using the inclusive $k_\perp$ cluster algorithm in the $\gamma^\star p$ rest frame. At least 3 jets are required with transverse momenta $p_\perp^\star > 4$ GeV and within the pseudorapidity range: -1$< \eta_{jet}^{lab} <$2.5, with $p_{\perp 1}^\star + p_{\perp 2}^\star > 9$ GeV for the the sum of leading and subleading jets and one jet in the central part of the detector in the range -1 $< \eta_{jet}^{lab} <$ 1.3. After all

cuts 38400 events are selected with at least 3 jets of which 6000 events have more than 3 jets.

3 Results

The differential cross sections are measured as a function of the number of jets (N_{Jet}), the Bjorken variable x, the pseudorapidities of the jets and transverse momenta of the jets. Figure 1 shows the differential cross sections for the N_{Jet}, x and pesudorapidity η of the leading jet compared to fixed order QCD predictions in LO and NLO. For the jet multiplicity distribution which extends up to $N_{Jet} = 7$ also the prediction of the two LO MC programs are shown. The color dipole model (DJANGO(CDM)) gives a very good description of this distribution while RAPGAP is below data for all N_{Jet}. The NLO prediction agrees for $N_{Jet} = 3$, misses a fraction of four jet events and produces no events with more than 4 jets, resulting in a total deficit of 18% of events with four or more jets.

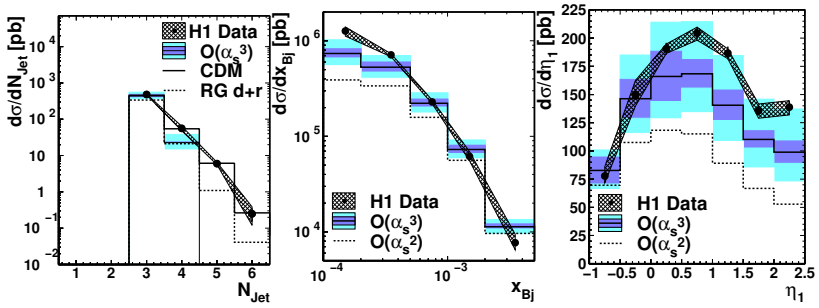

Figure 1: Differential cross sections as a function of jet multiplicity N_{Jet}, the Bjorken variable x_{Bj} and the pseudorapidity of the leading $p^{\star}_{\perp}$ jet η_1. The inner error bars represent the statistical error of the data, the total error bars correspond to the statistical and uncorrelated systematic srrors added in quadrature. The hatched error bands show the estimate of the correlated systematic uncertainties. The dark shaded (inner) error band shows the NLO (α_s^3) prediction including the uncertainties of the hadronization corrections, the light shaded (outer) band shows the scale uncertainty of the NLO calculations added in quadrature to the hadronization uncertainty, the dashed line represents the LO (α_s^2) prediction. The latter is not shown in the N_{Jet} distribution which is also compared to the two LO MC programs RAPGAP (dotted line) and DJANGO(CDM) (solid line).

The kinematic distributions are not described by the LO QCD predictions neither in shape nor in magnitude. Main discrepancies are observed at low x and large η (forward region) where predictions are too low. The NLO calculation shows a clear improvement in all regions where the discrepancies are observed leading to the conclusion that events with more than 3 jets are missing mainly at low x and large η. This is exactly the kinematic region where an excess of jets due to unordered gluon emission is expected.

3.1 Forward Jet Selection

The yield of events with three jets is underestimated by the predictions at low x and large η (in the forward direction). This discrepancy is further investigated using a forward jet selection. A forward jet is defined by Θ_{jet} <20° and $x_{jet} = E_{jet}/E_{p,beam}$ >0.035. Two subsamples are studied: one sample with two central jets ($-1 < \eta_{jet} < 1$) and one forward

jet and the second one with one central jet and two forward jets (one of them with $\eta_{jet} > 1$). Results compared to QCD calculation are shown in Fig. 2 for the variables x and η_1. Going from LO to NLO improves the agreement at low x and large η significantly for both samples but still a large discrepancy remains at low x and large rapidities for the sample with two forward jets.

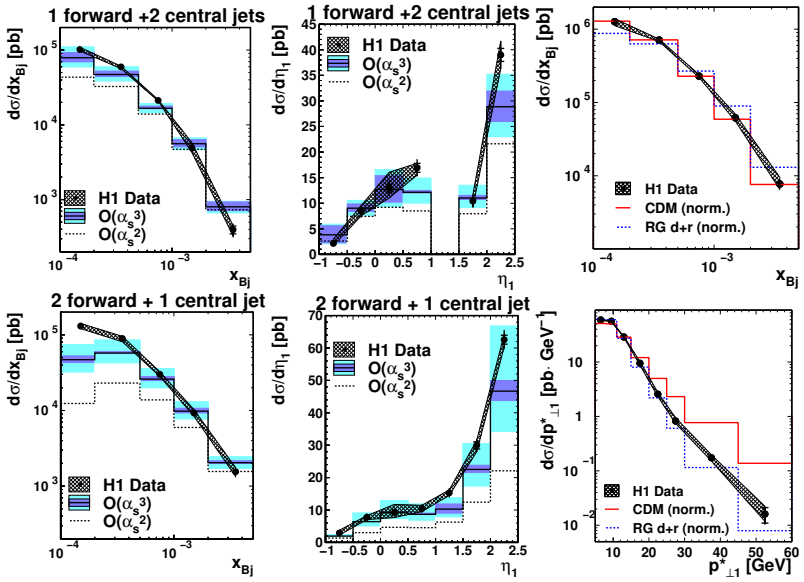

Figure 2: Differential cross sections as a function of the Bjorken variable x_{Bj} (left) and the pseudorapidity of the leading $p^\star_\perp$ jet η_1 (mid) for forward jet selection. Other details are as in the caption to Fig. 1. The two plots (right) are differential three jet cross sections in the Bjorken variable x_{Bj} and the transverse momentum of the leading jet $p^\star_{\perp 1}$. The inner error bars represent the statistical error of the data, the total error bars correspond to the statistical and uncorrelated systematic srrors added in quadrature. The hatched error bands show the estimate of the correlated systematic uncertainties. The data are compared to the two LO MC programs RAPGAP (dashed line) and DJANGO(CDM) (solid line) scaled to the data by factors 1.05 (CDM) resp. 1.51 (RAPGAP).

3.2 Comparison of Three Jet Cross Sections to the LO Monte Carlo Programs

The measured cross sections are compared to the two LO MC programs RAPGAP and DJANGO. The latter describes well the data as shown in Fig. 2 (right) for the Bjorken variable x_{Bj} but does not describe $p^\star_\perp$ distribution. It predicts too many jets with $p^\star_{\perp 1}$ >15 GeV. The RAPGAP prediction fails to describe data with the exception of the momentum and energy distributions.

3.3 Four Jet Cross Section

Cross sections for events with at least four jets can be compared to the fixed order QCD predictions in LO (α_s^3). As already shown in Fig. 1 these predictions are below the data by a factor of 1.8. According to a study using the DJANGO (CDM) program in the four

jet sample there are too few events with three gluon emissions to give new insight into the QCD dynamics compared to the three jet analysis. The four jet cross sections as a function of $p^\star_{\perp 1}$ and $\eta_1 - \eta_4$ as shown in Fig. 3 are therefore only compared to the LO MC generators RAPGAP and DJANGO (CDM). The CDM figure agrees well with data with again the exception of the jet momentum $p^\star_\perp$ distribution. This distribution is again correctly described by the RAPGAP prediction which fails to describe other distributions.

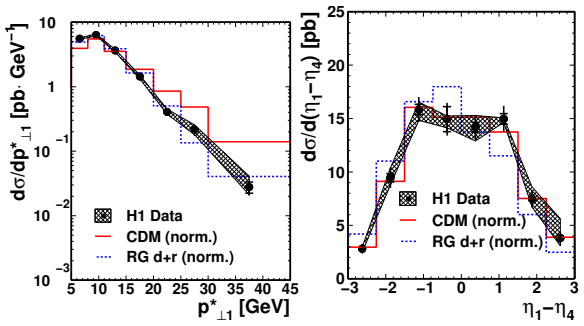

Figure 3: Differential four jet cross sections as a function of the transverse momentum of the leading jet $p^\star_{\perp 1}$ and the pseudorapidity difference of the leading $p^\star_\perp$ jet and the fourth jet $\eta_1 - \eta_4$ (with $p^\star_{\perp 1} > p^\star_{\perp 2} > p^\star_{\perp 3} > p^\star_{\perp 4}$). The inner error bars represent the statistical error of the data, the total error bars correspond to the statistical and uncorrelated systematic errors added in quadrature. The correlated systematic errors are shown by hatched error band. The data are compared to the two LO MC generators RAPGAP (dashed line) and DJANGO (CDM) (solid line). Both MC cross sections are normalized to the data cross sections by factors of 1.01 (CDM) resp. and 2.82 (RAPGAP).

4 Summary

The three- and four jet events at low x are remarkably well described by color dipole model (CDM) with additional gluon radiation not ordered in $k_\perp$ for moderate transverse momenta of the gluons. The remaining discrepancies at higher momenta require further studies. Compared to order α_s^2 predictions, the NLO(α_s^3) QCD calculations show a significant improvement in the data description. Remaining discrepancies are found at low x and large rapidities for the sample with two forward and one central jet. This is the kinematic region where unordered gluon radiation is expected to give a large contribution. We conclude therefore that unordered in $k_\perp$ gluon emission at low x plays an important role.

References

[1] Slides:
`http://indico.cern.ch/contributionDisplay.py?contribId=43&sessionId=8&confId=9499`

[2] A. Aktas *et al.* [H1 Collaboration], Eur. Phys. J. **C46** (2006) 27,
S.Chekanov *et al.* [ZEUS Collaboration], arXiv:hep-ex/0502029.

[3] C. Werner, Ph. D. Thesis, DESY-Thesis-2006-002.

[4] Z. Nagy, Z. Trocsanyi, Phys. Rev. Lett. **87** (2001), 082001;

[5] H. Jung, Comput. Phys. Commun. **86** (1995), 147.

[6] K. Charchula *et al.*, Comput. Phys. Commun. **81**

Forward Jet Production in DIS

L.Khein (on behalf of the ZEUS collaboration)

Skobeltsyn Institute of Nuclear Physics, Moscow State University
MSU, GSP-2, Len.Gory, Moscow 119992, Russia

Forward jet cross sections have been measured in neutral current deep inelastic scattering at low Bjorken-x with the ZEUS detector at HERA using an integrated luminosity of 81.8 pb^{-1}. Measurements are presented for inclusive forward jet as well as for forward jet accompanied by a dijet system. The explored phase space with jet pseudorapidity up to 4.3 is expected to be particularly sensitive to the dynamics of QCD parton evolution at low x. The measurements are compared to fixed order QCD calculations and to leading-order parton-shower Monte Carlo models.

1 Introduction

Forward jets in DIS, i.e. jets at rapidity close to the initial proton, measured at small x_{Bj}, are expected to be a valuable means for discerning the BFKL dynamics of the perturbative QCD. The BFKL evolution proceeds over x and a large space for evolution over x between the corresponding parton in the beginning of the evolution and the parton interacting with the photon appears. An additional condition that the transverse momentum of the forward jet be of the order of the virtuality of the photon diminishes the space for the DGLAP evolution over virtuality. Consequently, BFKL should provide larger cross sections for the forward jet production than DGLAP. Even further discriminative power could be achieved by studying a dijet supplementing the forward jet.

Inclusion in the analysis of the data from the forward plug calorimeter (FPC) of ZEUS allowed an essential increase in the pseudorapidity of forward jets to be attained. Here, results are presented on the study of the forward jet and dijet+forward jet production up to the pseudorapidity $\eta = 4.3$.

2 Theoretical approaches

NLO calculations and Monte Carlo simulations are compared with data. NLO code DISENT is used for inclusive forward jets (shown in [1]) and NLOJET++ for forward jet+dijets, both with the factorisation and renormalisation scales $\mu_{\mathrm{R}} = \mu_{\mathrm{F}} = Q$. Three MC programs are used, representing different approaches to the QCD evolution. The LEPTO MC represents the DGLAP approach. The CASCADE MC represents the CCFM approach and is used with two sets of unintegrated parton (gluon) density function (uPDF), J2003 set-1 and set-2. The ARIADNE MC is an implementation of the Colour Dipole Model (CDM), which provides non-ordered in transverse momentum parton cascade, i.e. BFKL-like evolution. Results with two tunings of ARIADNE are presented, the default tuning and the new tuning as introduced in [2].

3 Results

The analysis is based on the data collected with the ZEUS detector in 1998-2000 years, corresponding to an integrated luminosity of $81.8 \pm 1.5\,\mathrm{pb}^{-1}$. A description of the ZEUS

detector and of the FPC can be found elsewhere [3, 4]. Electrons or positrons with energy of $E_e = 27.5$ GeV collided with protons of energy $E_p = 920$ GeV. The neutral current DIS events were selected with the energy of the scattered electron $E_e^{'} > 10$ GeV, inelasticity $0.04 < y < 0.7$ and $20 < Q^2 < 100$ GeV^2. Only small $x_{\rm Bj}$ events were analysed, $0.0004 < x_{\rm Bj} < 0.005$. Jets were reconstructed with inclusive k_T-algorithm in the Breit frame and thereafter boosted to the laboratory frame. Forward jets within the pseudorapidity range $2 < \eta^{\rm jet} < 4.3$ were selected with the transverse energy in the laboratory frame $E_T^{\rm jet} > 5$ GeV. Two additional requirements were imposed to enhance the BFKL evolution and to suppress the DGLAP evolution: the jet should have a large fraction of the proton momentum $x^{\rm jet} = p_Z^{\rm jet}/p > 0.036$ and the transverse energy of the order of the virtuality of the photon $0.5 < (E_T^{\rm jet})^2/Q^2 < 2$. For the "forward jet+dijet" study, the events were required to have one forward jet, satisfying above conditions except the $(E_T^{\rm jet})^2/Q^2$ cut, and at least two additional jets with $E_T^{\rm jet} > 5$ GeV in the pseudorapidity range $-1.5 < \eta^{\rm jet} < 4.3$. From these additional jets, the two with the highest transverse energy were chosen. The three selected jets were ordered in pseudorapidity such that $\eta^{\rm jet_1} < \eta^{\rm jet_2} < \eta^{\rm fjet}$.

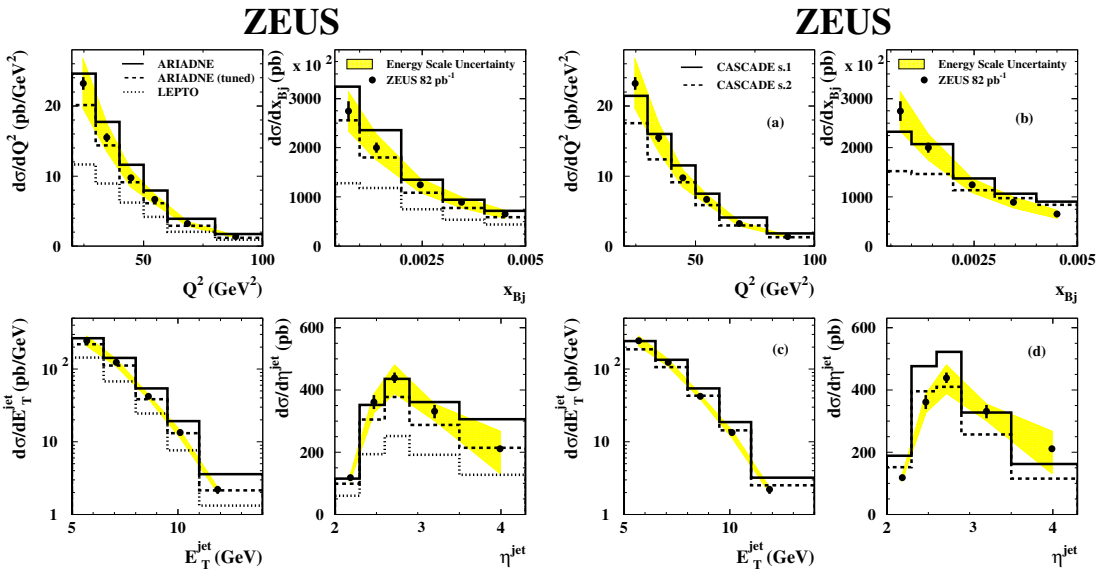

Figure 1: Inclusive forward jet cross sections. Data are compared with LEPTO, default ARIADNE and newly tuned ARIADNE. The shaded area shows the cumulative uncertainty of the CAL and FPC energy scales.

Figure 2: Inclusive forward jet cross sections. Data are compared with CASCADE with two sets of uPDF.

The measured differential forward jet cross sections are compared with the ARIADNE and LEPTO MC in Figure 1. ARIADNE default is in fair agreement with the data with the exception of high $E_T^{\rm jet}$ and high $\eta^{\rm jet}$. The newly tuned ARIADNE yields lower cross section,

in particular at high $E_T^{\rm jet}$ and high $\eta^{\rm jet}$, and provides a better description of the data. The predictions of the LEPTO MC are in agreement with data in shape for all distributions, however the absolute normalisation is below the measurements by about a factor of two.

In Figure 2, data are compared with CASCADE. Set-2 results in lower cross sections than set-1. Neither of two uPDF sets provides overall satisfactory agreement with the measurements.

Forward jet+dijet study was performed through measuring cross sections as functions of two pseudorapidity separation $\Delta\eta_1 = \eta^{\rm jet_2} - \eta^{\rm jet_1}$ and $\Delta\eta_2 = \eta^{\rm fjet} - \eta^{\rm jet_2}$. Additionally, the cross section as a function of $\Delta\eta_2$ was plotted for two intervals of $\Delta\eta_1$, $\Delta\eta_1 < 1$ and $\Delta\eta_1 > 1$.

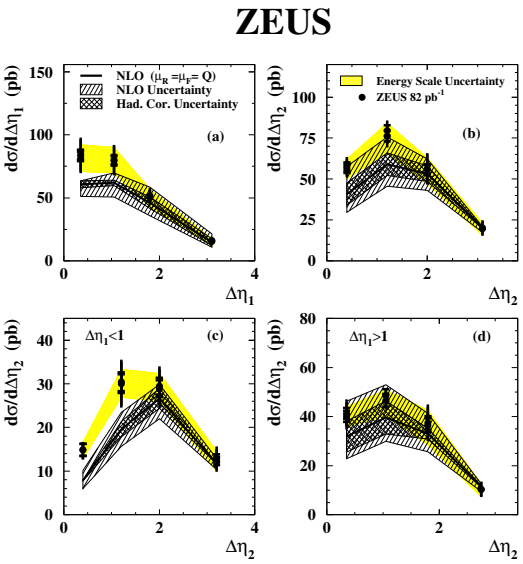

Figure 3: The forward jet+dijet cross sections. Data are compared with the NLO QCD calculations (solid line). The hatched area shows the theoretical uncertainities. The shaded area shows the uncertainty after varying the CAL and FPC energy scales.

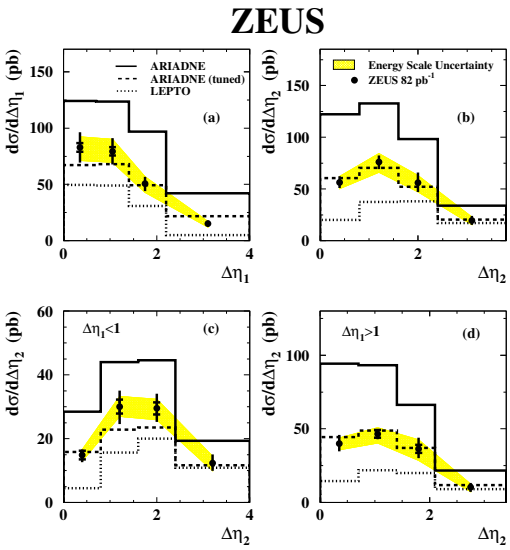

Figure 4: The forward jet+dijet cross sections. Data are compared with LEPTO, default ARIADNE and newly tuned ARIADNE.

Figure 3 shows the comparison of the data with the calculations of NLOJET++. The NLO calculations agree with data at large $\Delta\eta_2$, while does not describe the data at small $\Delta\eta_2$, especially when $\Delta\eta_1$ is small. The large $\Delta\eta_2$ kinematics at low $x_{\rm Bj}$ favours dijets originating from the photon-gluon fusion, with an additional gluon responsible for the forward jet. This case is well treated by NLOJET++. The small $\Delta\eta_1$ and $\Delta\eta_2$ region corresponds to the event configuration in which all the three jets tend to go forward, away from the hard interaction. This configuration favours multigluon emission, which lacks in NLOJET++. Figure 4 shows the comparison of the data with LEPTO and ARIADNE. As before, the LEPTO predictions

are generally significantly below the data. ARIADNE with default tuning overestimates the cross sections, which implies that energetic multiple jets are too often produced. The new tuning of the ARIADNE parameters brings this model into very good agreement with data for all distributions.

4 Conclusions

Forward jets study is performed both by measuring inclusive forward jet cross sections and forward jet+dijet cross sections. Good overall description of the inclusive forward jet cross sections is obtained by the newly tuned ARIADNE MC, representing CDM, i.e. non-ordered in the transverse momentum evolution. The LEPTO MC, representing the DGLAP approach, i.e. strongly ordered in the transverse momentum evolution, significantly underestimates the cross sections. The CASCADE MC, representing the CCFM approach, with J2003 set-1 and J2003 set-2 for unintegrated gluon density, fails to satisfactorily describe the data. These measurements can be used for further adjusting the uPDF.

For the forward jet+dijet cross sections, NLO calculations describe the data at large $\Delta\eta_2$ but underestimate the cross sections at small $\Delta\eta_2$, especially for small values of $\Delta\eta_1$, where in the case of small x_{Bj} the contribution of multiple gluon emission is expected to be large. The predictions of LEPTO, like in the inclusive case, are significantly below the data. ARIADNE with default parameters significantly overestimates the cross sections whereas the new tuning provides good description of the data.

References

[1] Slides:
`http://indico.cern.ch/contributionDisplay.py?contribId=44&sessionId=8&confId=9499`

[2] H1 Coll., A. Aktas et al.,Eur. Phys. J. **C 6**, 239 (2006)

[3] ZEUS Coll, U. Holm (ed.), *The ZEUS Detector*. Status Report (unpublished) DESY 1993, available on http://www-zeus.desy.de/bluebook/bluebook.html.

[4] A. Bamberger et al., Nucl. Inst. Meth. **A 450**, 235, (2000).

BFKL NLL Phenomenology of Forward Jets at HERA and Mueller Navelet Jets at the Tevatron and the LHC

Christophe Royon

DAPNIA/Service de physique des particules,
CEA/Saclay, 91191 Gif-sur-Yvette cedex, France

We perform a BFKL-NLL analysis of forward jet production at HERA which leads to a good description of data over the full kinematical domain. We also predict the azimuthal angle dependence of Mueller-Navelet jet production at the Tevatron and the LHC using the BFKL NLL formalism.

1 Forward jets at HERA

Following the successful BFKL [2] parametrisation of the forward-jet cross-section $d\sigma/dx$ at Leading Order (LO) at HERA [3, 4], it is possible to perform a similar study using Next-to-leading (NLL) resummed BFKL kernels. This method can be used for forward jet production at HERA in particular, provided one takes into account the proper symmetric *two-scale* feature of the forward-jet problem, whose scales are in this case Q^2, for the lepton vertex and k_T^2, for the jet vertex. In this short report, we will only discuss the phenomelogical aspects and all detailed calculations can be found in Ref. [5] for forward jets at HERA and in Ref. [6] for Mueller Navelet jets at the Tevatron and the LHC.

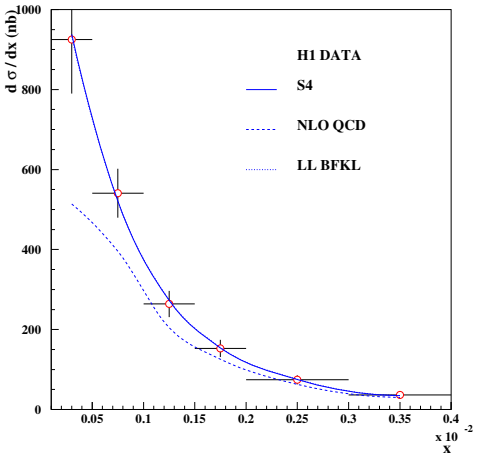

Figure 1: Comparison between the H1 $d\sigma/dx$ measurement with predictions for BFKL-LL, BFKL-NLL (S4) and DGLAP NLO calculations (see text). S4 and LL BFKL cannot be distinguished on that figure.

1.1 BFKL NLL formalism

We perform a saddle point approximation of the BFKL NLL formalism and compare it with the H1 forward jet cross section measurements [a]. The BFKL NLL [7] formalism reads:

$$\frac{d\sigma}{dx} = N \left(\frac{Q^2}{k_T^2}\right)^{\gamma} \alpha_S(k_T^2)\alpha_S(Q^2)\ \sqrt{A}\ \exp\left(\alpha_S(k_T Q)\frac{N_C}{\pi}\chi_{eff}(\gamma_C)\log(\frac{x_J}{x})\right) \exp\left(-A\alpha_S(k_T Q)\log^2(\sqrt{\frac{Q}{k_T}})\right)$$

[a] We are in the process of checking that implementing the full BFKL NLL kernel instead of performing a saddle point approximation does not change the results of this paper and the quality of the fits.

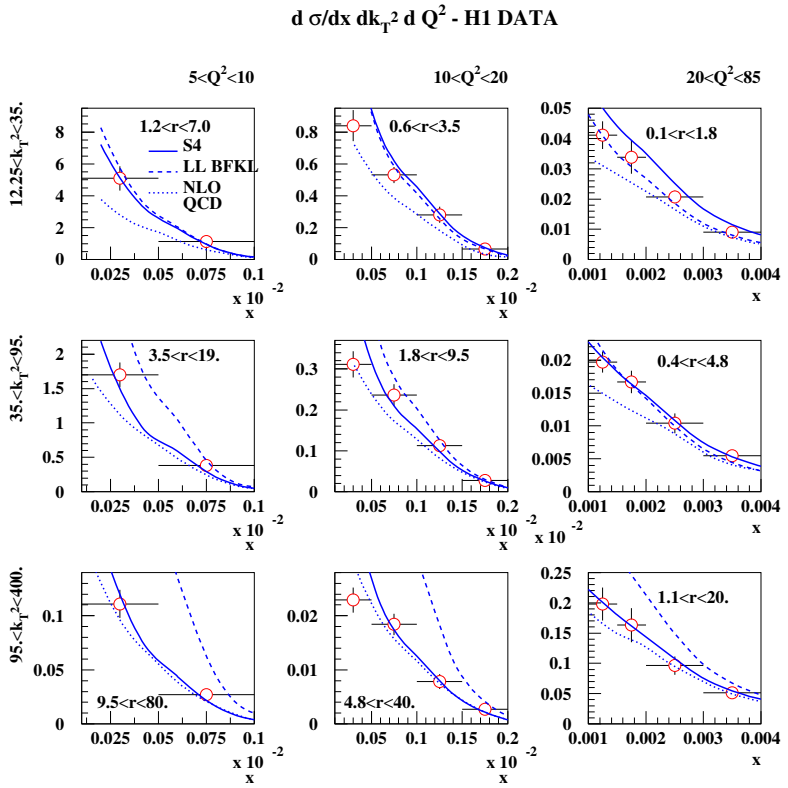

Figure 2: Comparison between the H1 measurement of the triple differential cross section with predictions for BFKL-LL, BFKL-NLL (S4) and DGLAP NLO calculations (see text).

with

$$A^{-1} = \frac{3\alpha_S(k_T Q)}{4\pi} \log \frac{x_J}{x} \chi''_{eff}(\gamma_C)$$
$$\gamma = \gamma_C + \frac{\alpha_S(k_T Q)\chi_{eff}(\gamma_C)}{2}$$

where the saddle point equation is $\chi'_{eff}(\gamma_c) = 0$. The effective kernels $\chi_{eff}(p, \gamma, \bar{\alpha})$ are obtained from the NLL kernel by solving the implicit equation:

$$\chi_{eff} = \chi_{NLL}(p, \gamma, \bar{\alpha}\chi_{eff}).$$

The values of χ are taken at NLL [7] using different resummation schemes to remove spurious singularities defined as CCS, S3 and S4 [8]. Contrary to LL BFKL, it is worth noticing that the coupling constant α_S is taken using the renormalisation group equations, the only free parameter in the fit being the normalisation.

One difficulty arises while fitting H1 $d\sigma/dx$ data [9] : we need to integrate the differential cross section on the bin size in Q^2, x_J (the momentum fraction of the proton carried by the forward jet), k_T (the jet transverse momentum), while taking into account the experimental

cuts. To avoid numerical difficulties, we choose to perform the integration on the bin using the variables where the cross section does not change rapidly, namely k_T^2/Q^2, $\log 1/x_J$, and $1/Q^2$. Experimental cuts are treated directly at the integral level (the cut on $0.5 < k_T^2/Q^2 < 5$ for instance) or using a toy Monte Carlo. More detail can be found about the fitting procedure in Appendix A of Ref. [4].

The NLL fits [5] can nicely describe the H1 data [9] for the S4 scheme ($\chi^2 = 5.6/5$ per degree of freedom with statistical errors only) whereas the S3 and CCS schemes show higher χ^2. ($\chi^2 = 45.9/5$ and $\chi^2 = 20.4/5$ respectively with statistical errors only) The fit χ^2 are good for all schemes if one considers statistical and systematics errors added in quadrature [3, 4]. The DGLAP NLO calculation fails to describe the H1 data at lowest x (see Fig. 1).

The H1 collaboration also measured the forward jet triple differential cross section [9] and the results are given in Fig. 2. The BFKL LL formalism leads to a good description of the data when $r = k_T^2/Q^2$ is close to 1 and deviates from the data when r is further away from 1. This effect is expected since DGLAP radiation effects are supposed to occur when the ratio between the jet k_T and the virtual photon Q^2 are further away from 1. The BFKL NLL calculation including the Q^2 evolution via the renormalisation group equation leads to a good description of the H1 data on the full range. We note that the higher order corrections are small when $r \sim 1$, when the BFKL effects are supposed to dominate. By contrast, they are significant as expected when r is different from one, ie when DGLAP evolution becomes relevant. We notice that the DGLAP NLO calculation fails to describe the data when $r \sim 1$, or in the region where BFKL resummation effects are expected to appear.

2 Mueller Navelet jets at the Tevatron and the LHC

Mueller Navelet jets are ideal processes to study BFKL resummation effects [10]. Two jets with a large interval in rapidity and with similar tranverse momenta are considered. A typical observable to look for BFKL effects is the measurement of the azimuthal correlations between both jets. The DGLAP prediction is that this distribution should peak towards π - ie jets are back-to-bacl- whereas multi-gluon emission via the BFKL mechanism leads to a smoother distribution. The relevant variables to look for azimuthal correlations are the following:

$$\begin{aligned} \Delta\eta &= y_1 - y_2 \\ y &= (y_1 + y_2)/2 \\ Q &= \sqrt{k_1 k_2} \\ R &= k_2/k_1 \end{aligned}$$

The azimuthal correlation for BFKL reads:

$$2\pi \frac{d\sigma}{d\Delta\eta dR d\Delta\Phi} \Big/ \frac{d\sigma}{d\Delta\eta dR} = 1 + \frac{2}{\sigma_0(\Delta\eta, R)} \sum_{p=1}^{\infty} \sigma_p(\Delta\eta, R) \cos(p\Delta\Phi)$$

where in the NLL BFKL framework,

$$\sigma_p = \int_{E_T}^{\infty} \frac{dQ}{Q^3} \alpha_s(Q^2/R)\alpha_s(Q^2 R) \left(\int_{y_<}^{y_>} dy x_1 f_{eff}(x_1, Q^2/R) x_2 f_{eff}(x_2, Q^2 R) \right) \int_{1/2-\infty}^{1/2+\infty} \frac{d\gamma}{2i\pi} R^{-2\gamma}\ e^{\bar{\alpha}(Q^2)\chi_{eff}(p,\gamma,\bar{\alpha})\Delta\eta}$$

and χ_{eff} is the effective resummed kernel. resummation schemes S3 and S4 allowed us to compute the azimuthal correlations at NLL. As expected, the $\Delta\Phi$ dependence is less flat than for BFKL LL and is closer to the DGLAP behaviour [6]. To illustrate this result, we give in Fig. 3 the azimuthal correlation in the CDF acceptance. The CDF collaboration installed the mini-Plugs calorimeters aiming for rapidity gap selections in the very forward regions and these detectors can be used to tag very forward jets. A measurement of jet p_T with these detectors would not be possible but their azimuthal segmentation allows a ϕ measurement. In Fig. 3, we display the jet azimuthal correlations for jets with a $p_T > 5$ GeV and $\Delta\eta$ =6, 8, 10 and 11. For $\Delta\eta$ =11, we notice that the distribution is quite flat, which would be a clear test of the BFKL prediction. Similar measurements are possible at the LHC and predictions can be found in Ref. [6].

Computing the different σ_p at NLL for the

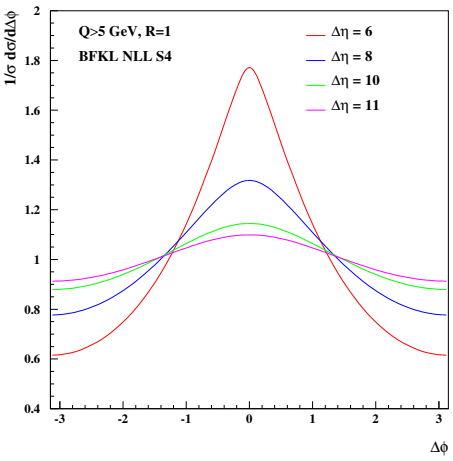

Figure 3: Azimuthal correlations between jets with $\Delta\eta$ =6, 8, 10 and 11 and $p_T > 5$ GeV in the CDF acceptance. This measurement will represent a clear test of the BFKL regime.

References

[1] Slides: `http://indico.cern.ch/contributionDisplay.py?contribId=47&sessionId=8&confId=9499`

[2] L. N. Lipatov, *Sov. J. Nucl. Phys.* **23** (1976) 338; E. A. Kuraev, L. N. Lipatov and V. S. Fadin, *Sov. Phys. JETP* **45** (1977) 199; I. I. Balitsky and L. N. Lipatov, *Sov. J. Nucl. Phys.* **28** (1978) 822.

[3] J.G. Contreras, R. Peschanski and C. Royon, *Phys. Rev.* **D62** (2000) 034006; C. Marquet, R. Peschanski and C. Royon, *Phys. Lett.* **B599** (2004) 236.

[4] C. Marquet and C. Royon, *Nucl. Phys.* **B739** (2006) 131.

[5] O. Kepka, C. Marquet, R. Peschanski and C. Royon, preprints hep-ph/0609299, hep-ph/0612261; A. Sabio Vera and F. Schwennsen, hep-ph/0702158.

[6] C. Marquet, C. Royon, preprint arXiv:0704.3409

[7] V.S. Fadin and L.N. Lipatov, *Phys. Lett.* **B429** (1998) 127; M. Ciafaloni, *Phys. Lett.* **B429** (1998) 363; M. Ciafaloni and G. Camici, *Phys. Lett.* **B430** (1998) 349.

[8] G.P. Salam, *JHEP* **9807** (1998) 019; M. Ciafaloni, D. Colferai and G.P. Salam, *Phys. Rev.* **D60** (1999) 114036; *JHEP* **9910** (1999) 017.

[9] A. Aktas *et al* [H1 Collaboration], *Eur. Phys. J.* **C46** (2006) 27.

[10] A.H. Mueller and H. Navelet, *Nucl. Phys.* **B282** (1987) 727.

Multijet Production at Low x_{Bj} in Deep Inelastic Scattering at HERA

Thomas Erik Danielson*

University of Wisconsin - Dept of Physics
1150 University Avenue Madison, WI 53706 - USA

Inclusive dijet and trijet production in deep inelastic ep scattering has been measured at ZEUS with an integrated luminosity of 82 pb^{-1} for $10 < Q^2 < 100$ GeV^2 and low Bjorken x, $10^{-4} < x_{\mathrm{Bj}} < 10^{-2}$. Measurements of dijet and trijet differential cross sections are presented as functions of Q^2, x_{Bj}, jet transverse energy, and jet pseudorapidity. Also presented are correlations in transverse momenta, azimuthal angles, and pseudorapidity. Calculations at $\mathcal{O}(\alpha_s^3)$ generally describe the trijet data well and improve the description of the dijet data compared to the calculation at $\mathcal{O}(\alpha_s^2)$.

1 Introduction

Multijet production in DIS is an ideal environment for investigating different approaches to parton dynamics at low Bjorken-x, x_{Bj}. An understanding of this regime is of particular relevance in view of the startup of the LHC, where many of the Standard Model processes such as the production of electroweak gauge bosons or the Higgs particle involve the collision of partons with a low fraction of the proton momentum.

In the usual collinear QCD factorisation approach, the cross sections are obtained as the convolution of perturbative matrix elements and parton densities evolved according to the DGLAP evolution equations. In these equations, all orders proportional to $\alpha_s \ln Q^2$ and the double logarithms $\ln Q^2 \cdot \ln 1/x$, where x is the fraction of the proton momentum carried by a parton, which is equal to x_{Bj} in the quark-parton model, are resummed. In the DGLAP approach, the parton participating in the hard scattering is the result of a partonic cascade ordered in transverse momentum, p_T. The partonic cascade starts from a low-p_T and high-x parton from the incoming proton and ends up, after consecutive branching, in the high-p_T and low-x parton entering in the hard scattering. At low x_{Bj}, where the phase space for parton emissions increases, terms proportional to $\alpha_s \ln 1/x$ may become large and spoil the accuracy of the DGLAP approach. In this region the transverse momenta and angular correlations between partons produced in the hard scatter may be sensitive to effects beyond DGLAP dynamics. The information about cross sections, transverse energy, E_T, and angular correlations between the two leading jets in multijet production therefore provides an important testing ground for studying the parton dynamics in the region of small x_{Bj}.

In the ZEUS analysis presented, correlations for both azimuthal angles and pseudorapidity, and correlations in jet transverse energy and momenta for dijet and trijet production in the hadronic ($\gamma^* p$) centre-of-mass (HCM) frame are measured with high statistical precision in the kinematic region restricted to $10 < Q^2 < 100$ GeV^2 and $10^{-4} < x_{\mathrm{Bj}} < 10^{-2}$ [2]. The results are compared with DGLAP-based pQCD calculations from the NLOJET [3] program at next-to-leading order (NLO).

*On behalf of the ZEUS collaboration

2 Single-differential cross sections $d\sigma/dQ^2$, $d\sigma/dx_{\rm Bj}$, $d\sigma/d|\Delta\eta^{\rm jet1,2}_{\rm HCM}$ and trijet to dijet cross section ratios

The single-differential cross-sections $d\sigma/dx_{\rm Bj}$ for dijet and trijet production and the ratio $\sigma_{\rm trijet}/\sigma_{\rm dijet}$ of the trijet cross section to the dijet cross section, as a function $x_{\rm Bj}$ are presented in Fig. 1. The ratio $\sigma_{\rm trijet}/\sigma_{\rm dijet}$ falls steeply with increasing $x_{\rm Bj}$, as shown in Fig. 1. In the cross-section ratios, the experimental and theoretical uncertainties partially cancel, providing a possibility to test the pQCD calculations more precisely than can be done with the individual cross sections. Both the cross sections and the cross-section ratios are well described by the NLOJET calculations, especially at low $x_{\rm Bj}$. The correlations in jet pseudorapidity were examined by measuring $d\sigma/d|\Delta\eta^{\rm jet1,2}_{\rm HCM}|$, where $|\Delta\eta^{\rm jet1,2}_{\rm HCM}|$ is the absolute difference in pseudorapidity of the two jets with highest $E^{\rm jet}_{T,\rm HCM}$. The NLOJET predictions describe the measurements well.

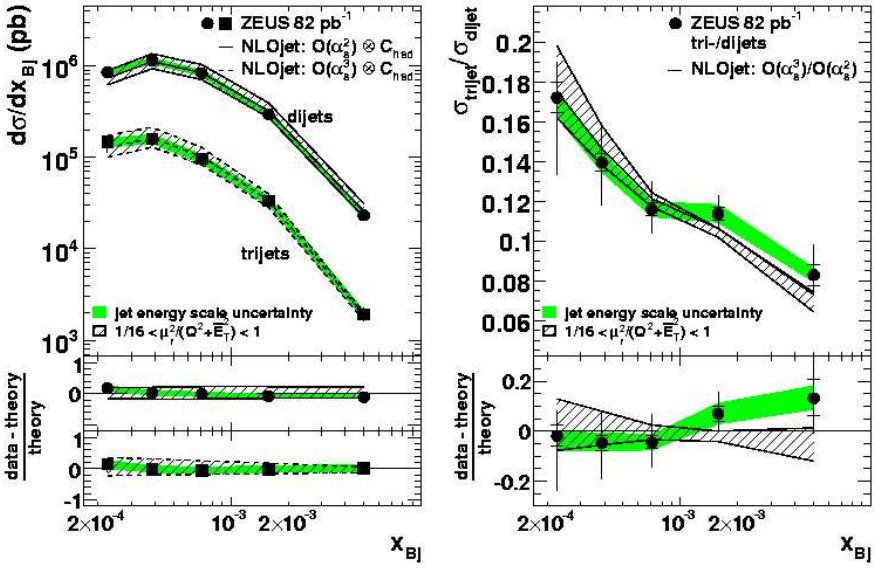

Figure 1: Dijet and trijet cross sections, and the ratio $\sigma_{trijet}/\sigma_{dijet}$, as a function of $x_{\rm Bj}$ compared to predictions from NLOJET.

3 Jet momentum correlations

In addition to correlations in jet pseudorapidity ($|\Delta\eta^{\rm jet1,2}_{\rm HCM}|$), correlations of the jet tranverse momenta have also been investigated. The correlations in jet transverse momenta were examined by measuring two sets of double-differential cross sections: $d^2\sigma/dx_{\rm Bj}d|\Sigma\vec{p}^{\,\rm jet1,2}_{T,\rm HCM}|$ and $d^2\sigma/dx_{\rm Bj}d(|\Delta\vec{p}^{\,\rm jet1,2}_{T,\rm HCM}|/(2E^{\rm jet1}_{T,\rm HCM}))$. The variable $|\Sigma\vec{p}^{\,\rm jet1,2}_{T,\rm HCM}|$ is the transverse component of the vector sum of the jet momenta of the two jets with the highest $E^{\rm jet}_{T,\rm HCM}$. For events

with only two jets $|\Sigma\vec{p}_{T,\mathrm{HCM}}^{\,\mathrm{jet1,2}}| = 0$, and additional QCD radiation increases this value. The variable $|\Delta\vec{p}_{T,\mathrm{HCM}}^{\,\mathrm{jet1,2}}|/(2E_{T,\mathrm{HCM}}^{\mathrm{jet1}})$ is the magnitude of the vector difference of the transverse momenta of the two jets with the highest $E_{T,\mathrm{HCM}}^{\mathrm{jet}}$ scaled by twice the transverse energy of the hardest jet. For events with only two jets $|\Delta\vec{p}_{T,\mathrm{HCM}}^{\,\mathrm{jet1,2}}|/(2E_{T,\mathrm{HCM}}^{\mathrm{jet1}}) = 1$, and additional QCD radiation decreases this value. Figure 2 shows the cross-sections $d^2\sigma/dx_{\mathrm{Bj}}d|\Sigma\vec{p}_{T,\mathrm{HCM}}^{\,\mathrm{jet1,2}}|$ in bins of x_{Bj} for the dijet sample.

At low x_{Bj}, the NLOJET calculations at $\mathcal{O}(\alpha_s^2)$ underestimate the dijet cross sections at high values of $|\Sigma\vec{p}_{T,\mathrm{HCM}}^{\,\mathrm{jet1,2}}|$ and low values of $|\Delta\vec{p}_{T,\mathrm{HCM}}^{\,\mathrm{jet1,2}}|/(2E_{T,\mathrm{HCM}}^{\mathrm{jet1}})$. The description of the data by the NLOJET calculations at $\mathcal{O}(\alpha_s^2)$ improves at higher values of x_{Bj}. A higher-order calculation with NLOJET at $\mathcal{O}(\alpha_s^3)$ for the dijet sample has been obtained for the region $|\Sigma\vec{p}_{T,\mathrm{HCM}}^{\,\mathrm{jet1,2}}| > 4$ GeV, which is compared to the data in Fig. 2; and for the region $|\Delta\vec{p}_{T,\mathrm{HCM}}^{\,\mathrm{jet1,2}}|/(2E_{T,\mathrm{HCM}}^{\mathrm{jet1}}) < 0.85$. With the inclusion of the next term in the perturbative series in α_s, the NLOJET calculations describe the data well. The NLOJET calculations at $\mathcal{O}(\alpha_s^3)$ for trijet production are consistent with the measurements.

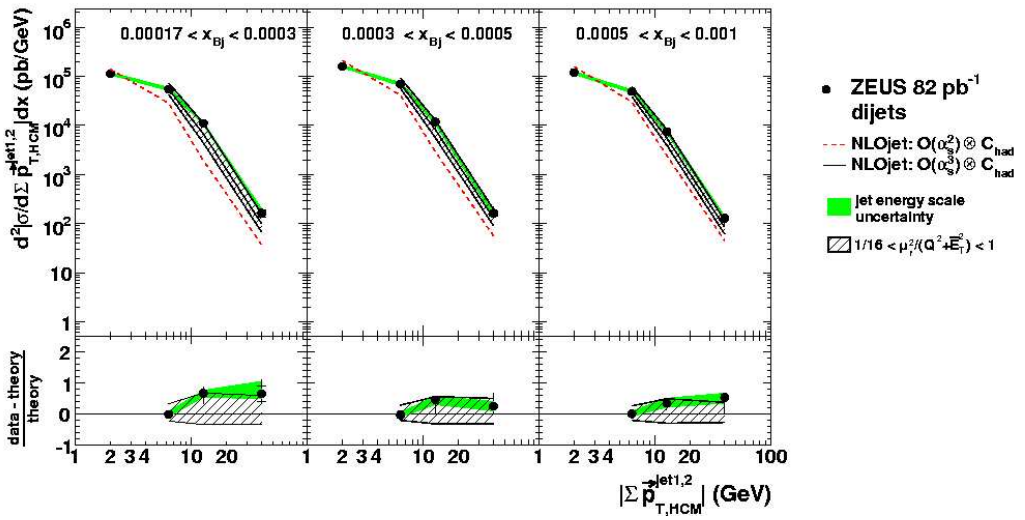

Figure 2: Dijet cross sections as a function of $|\Sigma p_{T,\mathrm{HCM}}^{\mathrm{jet1,2}}|$ compared to predictions from NLOJET at $\mathcal{O}(\alpha_s)^2$ and $\mathcal{O}(\alpha_s)^3$.

4 Azimuthal distributions of the jets

Measurements of the double-differential cross-section $d^2\sigma/dx_{\mathrm{Bj}}d|\Delta\phi_{\mathrm{HCM}}^{\mathrm{jet1,2}}|$, where $|\Delta\phi_{\mathrm{HCM}}^{\mathrm{jet1,2}}|$ is the azimuthal separation of the two jets with the largest $E_{T,\mathrm{HCM}}^{\mathrm{jet}}$, were measured for dijet and trijet production in all bins of x_{Bj}. For both dijet and trijet production the cross section falls with $|\Delta\phi_{\mathrm{HCM}}^{\mathrm{jet1,2}}|$. The NLOJET calculations at $\mathcal{O}(\alpha_S^2)$ for dijet production decrease more rapidly with $|\Delta\phi_{\mathrm{HCM}}^{\mathrm{jet1,2}}|$ than the data and the calculations disagree with the data at low $|\Delta\phi_{\mathrm{HCM}}^{\mathrm{jet1,2}}|$. A higher-order NLOJET calculation at $\mathcal{O}(\alpha_S^3)$ for the dijet sample has been

obtained for the region $|\Delta\phi^{\rm jet1,2}_{\rm HCM}| < 3\pi/4$ and describes the data well. The measurements for trijet production are reasonably well described by the NLOJET calculations at $\mathcal{O}(\alpha_S^3)$, with the description improving somewhat at higher $x_{\rm Bj}$.

A further investigation into the azimuthal correlations has been performed by measuring the cross-section $d^2\sigma/dQ^2dx_{\rm Bj}$ for dijet (trijet) events with $|\Delta\phi^{\rm jet1,2}_{\rm HCM}| < 2\pi/3$ as a function of $x_{\rm Bj}$. For the two-jet final states, the presence of two leading jets with $|\Delta\phi^{\rm jet1,2}_{\rm HCM}| < 2\pi/3$ can indicate another high-E_T jet or set of high-E_T jets outside the measured η range. One of these measured cross sections is presented in Fig. 3. The NLOJET calculations at $\mathcal{O}(\alpha_S^2)$ for dijet production underestimate the data, the difference increasing towards low $x_{\rm Bj}$. The NLOJET calculations at $\mathcal{O}(\alpha_S^3)$ are up to about one order of magnitude larger than the $\mathcal{O}(\alpha_S^2)$ calculations and are consistent with the data, demonstrating the importance of the higher-order terms in the description of the data especially at low $x_{\rm Bj}$. The NLOJET calculations at $\mathcal{O}(\alpha_S^3)$ describe the trijet data within the renormalisation-scale uncertainties.

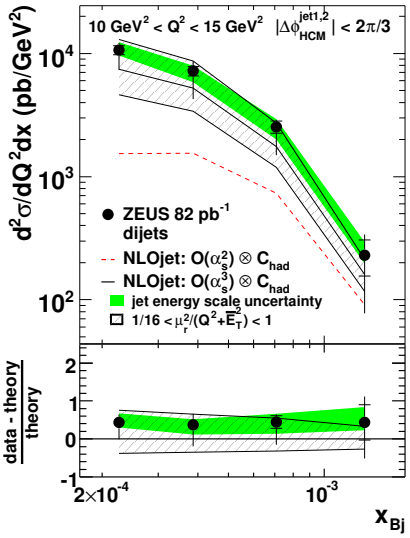

Figure 3: Dijet cross sections in $x_{\rm Bj}$ and Q^2 as a function of $x_{\rm Bj}$ with $\Delta\phi^{\rm jet1,2}_{HCM} < 120^\circ$

5 Summary

Multijet production in deep inelastic ep scattering has been measured in the phase space region $10 < Q^2 < 100$ GeV^2 and $10^{-4} < x_{\rm Bj} < 10^{-2}$ using an integrated luminosity of 82 pb^{-1} collected by the ZEUS experiment. The high statistics have made possible detailed studies of multijet production at low $x_{\rm Bj}$. The dependence of dijet and trijet production on the kinematic variables Q^2 and $x_{\rm Bj}$ and on the jet variables $E^{\rm jet}_{T,\rm HCM}$ and $\eta^{\rm jet}_{\rm LAB}$ is well described by perturbative QCD calculations which include NLO corrections. At low $x_{\rm Bj}$, measurements of dijet production with low azimuthal separation are reproduced by the perturbative QCD calculations provided that higher-order terms ($\mathcal{O}(\alpha_s^3)$) are accounted for. Such terms increase the predictions of pQCD calculations by up to one order of magnitude when the two jets with the highest $E^{\rm jet1,2}_{T,\rm HCM}$ are not balanced in transverse momentum. This demonstrates the importance of higher-order corrections in the low-$x_{\rm Bj}$ region.

References

[1] Slides:
`http://indico.cern.ch/contributionDisplay.py?contribId=45&sessionId=8&confId=9499`

[2] ZEUS Coll., S. Chekanov *et al.* [ZEUS Collaboration], accepted by Nucl. Phys. B (2007), arXiv:0705.1931 [hep-ex].

[3] Z. Nagy and Z. Trocsanyi, Phys. Rev. Lett. **87** (2001) 082001 [arXiv:hep-ph/0104315].

DGLAP and BFKL equations in $N = 4$ SUSY

L. N. Lipatov *

Petersburg Nuclear Physics Institute
Gatchina, 188300, St. Petersburg - Russia

The properties of the BFKL kernel in the next-to-leading approximation in QCD and in supersymmetric models are discussed. The maximal transcendality of anomalous dimensions in $N = 4$ SUSY is formulated. The explicit expressions for the anomalous dimensions up to four loops are given. Their asymptotic behavior at $j \to \infty$ and in the singular points $j = 1, 0, -1, ...$ is compared with predictions.

1 Introduction

The QCD scattering amplitude in the leading logarithmic approximation (LLA) has the Regge-type asymptotics with the gluon trajectory in one loop given below

$$\omega(-|q|^2) = -\frac{\alpha_c}{4\pi^2} N_c \int d^2k \frac{|q|^2}{|k|^2|q-k|^2} \approx -\frac{\alpha_c}{2\pi} \ln \frac{|q^2|}{\lambda^2} . \quad (1)$$

In the coordinate representation the Balitsky-Fadin-Kuraev-Lipatov (BFKL) equation for the Pomeron wave function can be written as follows [2]

$$E\,\Psi(\vec{\rho}_1, \vec{\rho}_2) = H_{12}\,\Psi(\vec{\rho}_1, \vec{\rho}_2)\ ,\ \Delta = -\frac{\alpha_s N_c}{2\pi} \min E\,, \quad (2)$$

where Δ is the Pomeron intercept. The BFKL Hamiltonian in the operator form is simple [3]

$$H_{12} = \ln |p_1 p_2|^2 + \frac{1}{p_1 p_2^*} \ln |\rho_{12}|^2 p_1 p_2^* + \frac{1}{p_1^* p_2} \ln |\rho_{12}|^2 p_1^* p_2 - 4\psi(1)\,, \quad (3)$$

where $\rho_{12} = \rho_1 - \rho_2$. It is invariant under the Möbius transformation [4] and has the property of the holomorphic separability [3]. The quantum numbers of the Möbius group are the anomalous dimension $\gamma = \frac{1}{2} + i\nu$ and the conformal spins n.

The Bartels-Kwiecinskii-Praszalowicz (BKP) equation [5] for the n-gluon composite states in the large-N_c limit has the duality symmetry [6], is integrable [3, 7] and equivalent to a Scgrödinger equation for the Heisenberg spin model [8]. To restore the s-channel unitarity one can use the effective field theory for Reggeized gluons [9]-[11].

2 DGLAP and BFKL dynamics in $N = 4$ SUSY

In the next-to-leading approximation the eigenvalue of the BFKL kernel is written below

$$\omega = \omega_0(n, \gamma) + 4\,\hat{a}^2\,\Delta(n, \gamma)\,,\ \hat{a} = g^2 N_c/(16\pi^2)\,. \quad (4)$$

In QCD $\Delta(n, \gamma)$ is a non-analytic function of the conformal spin $|n|$ [12, 13], but in $N = 4$ SUSY the Kroniker symbols are cancelled [13]. In this model we obtain for $\Delta(n, \gamma)$ the result

$$\Delta(n, \gamma) = \phi(M) + \phi(M^*) - \frac{\rho(M) + \rho(M^*)}{2\hat{a}/\omega}\,,\ M = \gamma + \frac{|n|}{2}\,, \quad (5)$$

*Marie Curie Excellence Chair

$$\rho(M) = \beta'(M) + \frac{1}{2}\zeta(2)\,,\ \beta'(z) = \frac{1}{4}\left[\Psi'\Big(\frac{z+1}{2}\Big) - \Psi'\Big(\frac{z}{2}\Big)\right], \tag{6}$$

where all special functions have the maximal trancedentality property [13]

$$\phi(M) = 3\zeta(3) + \Psi^{''}(M) - 2\Phi(M) + 2\beta^{'}(M)\Big(\Psi(1) - \Psi(M)\Big) \tag{7}$$

and

$$\Phi(M) = \sum_{k=0}^{\infty}\frac{\beta'(k+1)}{k+M} + \sum_{k=0}^{\infty}\frac{(-1)^k}{k+M}\left(\Psi'(k+1)\ -\ \frac{\Psi(k+1)-\Psi(1)}{k+M}\right). \tag{8}$$

For one loop anomalous dimension matrix in the case $N = 4$ the calculations were performed in Ref. [14]. In this model all twist-2 operators belong to the same supermultiplet and have the following anomalous dimension

$$\gamma^{(0)}_{uni}(j) = -4S_1(j-2)\,,\ S_r(j) = \sum_{i=1}^{j}\frac{1}{i^r}\,. \tag{9}$$

Note, that this function has the maximal transcedentality. It leads to an integrability of evolution equations for matrix elements of quasi-partonic operators in $N = 4$ SUSY [14].

3 Two and three loop results

Using maximal transcedentality hypothesis [13] and QCD results [15], one can calculate also the anomalous dimensions in two and three loops [16, 17]

$$\gamma_{uni}(j) = \hat{a}\gamma^{(0)}_{uni}(j) + \hat{a}^2\gamma^{(1)}_{uni}(j) + \hat{a}^3\gamma^{(2)}_{uni}(j) + ...\,, \tag{10}$$

where

$$\frac{1}{8}\,\gamma^{(1)}_{uni}(j+2) = 2S_1(j)\,\big(S_2(j) + S_{-2}(j)\big) - 2S_{-2,1}(j) + S_3(j) + S_{-3}(j)\,, \tag{11}$$

and

$$\begin{aligned}\frac{1}{32}\,\gamma^{(2)}_{uni}(j+2) &= 24\,S_{-2,1,1,1} - 12\,\left(S_{-3,1,1} + S_{-2,1,2} + S_{-2,2,1}\right) + 6\,\left(S_{-4,1} + S_{-3,2} + S_{-2,3}\right)\\ &-3\,S_{-5} - 2\,S_3\,S_{-2} - S_5 - 2\,S_1^2\,(3\,S_{-3} + S_3 - 2\,S_{-2,1}) - S_2\,(S_{-3} + S_3 - 2\,S_{-2,1})\\ &-S_1\left(8\bar{S}_{-4} + \bar{S}^2_{-2} + 4S_2\bar{S}_{-2} + 2S_2^2\right) - S_1\left(3S_4 - 12\bar{S}_{-3,1} - 10\bar{S}_{-2,2} + 16\bar{S}_{-2,1,1}\right)\,.\end{aligned} \tag{12}$$

Here the corresponding harmonic sums are defined below

$$S_a(j) = \sum_{m=1}^{j}\frac{1}{m^a}\,,\ S_{a,b,c,\cdots}(j) = \sum_{m=1}^{j}\frac{1}{m^a}\,S_{b,c,\cdots}(m)\,, \tag{13}$$

$$S_{-a}(j) = \sum_{m=1}^{j}\frac{(-1)^m}{m^a},\ S_{-a,b,\cdots}(j) = \sum_{m=1}^{j}\frac{(-1)^m}{m^a}\,S_{b,\cdots}(m)\,. \tag{14}$$

4 Weak and strong coupling regimes

The above results are in an agreement with the BFKL prediction [13] for the singularities at $j \to 1$

$$\gamma_{uni}^{N=4}(j) = \hat{a}\frac{4}{\omega} - 32\zeta_3\,\hat{a}^2 + 32\zeta_3\,\hat{a}^3\frac{1}{\omega} - \frac{16\hat{a}^4}{\omega^4}\left(32\zeta_3 + \frac{\pi^4}{9}\omega\right) . \tag{15}$$

Note, that recently the four-loop result $\gamma_{uni}^{(3)}(j)$ was calculated with the use of the asymptotic Bethe ansatz [18]. It turned out, that the obtained expression has the singularity in $j = 1$ incompatible with the BFKL prediction. A simple modification of the four loop result taking into account the wrapping effect gives an agreement with the BFKL equation and the following non-linear equation for $j + 2r = \omega \to 0$ $(r = 0, 1, 2, ...)$

$$\omega\gamma_{uni} = \gamma_{uni}^2 + 16\hat{a}^2(S_2 + \zeta_2 - S_1^2) + 4\,\hat{a}\left(1 - \omega S_1 - \omega^2(S_2 + \zeta_2) + \gamma^2(S_2 + S_{-2})\right) ,$$

generalizing the resummation of the double logarithmic terms $\sim \alpha/\omega^2$ (cf. [19]).

Further, the universal anomalous dimension at large j

$$\gamma_{uni}^{N=4} = a(z)\,\ln j\,,\ z = \frac{\alpha N_c}{\pi} = 4\hat{a} \tag{16}$$

can be found from our results up to three loops

$$a(z) = -z + \frac{\pi^2}{12}\,z^2 - \frac{11}{720}\pi^4 z^3 + ... \tag{17}$$

It is remarkable, that using the AdS/CFT correspondence [20] between the superstring model on the anti-de-Sitter space and the $N = 4$ supersymmetric Yang-Mills theory A. Polyakov with collaborators calculated the coefficient $a(z)$ in the strong coupling limit [21]

$$\lim_{z\to\infty} a(z) = -z^{1/2} + \frac{3\ln 2}{4\pi} + ... \tag{18}$$

In Ref. [16] the resummation of the perturbative expansion of $a(z)$ was suggested, which reproduces approximately the three-loop result and the strong coupling limit.

The perturbative calculations of the anomalous dimension at large j are in agreement with the recent papers [22, 23], where integral equations was derived from the integrability of the model. One can rewrite the Eden-Staudacher integral equation [22] as a set of linear equations [24]

$$a_{n,\epsilon} = \sum_{n'=1}^{\infty} K_{n,n'}(\epsilon)\,(\delta_{n',1} - a_{n',\epsilon})\ ,\ K_{n,n'}(\epsilon) =$$

$$2n\sum_{R=0}^{\infty}(-1)^R\,\frac{2^{-2R-n-n'}}{\epsilon^{2R+n+n'}}\zeta(2R+n+n')\,\frac{(2R+n+n'-1)!\,(2R+n+n')!}{R!\,(R+n)!\,(R+n')!\,(R+n+n')!}\,, \tag{19}$$

where the function $a(z)$ is expressed in terms of $a_{1,\epsilon}$

$$a(z) = \frac{2(1-a_{1,\epsilon})}{\epsilon^2}\,,\ \epsilon = \frac{1}{g\sqrt{2}}\,. \tag{20}$$

We can easiliy prove, that the maximal transcedentality property for $a(z)$ is valid in all orders of the perturbation theory and the coefficients in front of the products of the corresponding ζ-functions are integer numbers [24]. It is possibly to show [24], that the asymptotic behaviour of $a(z)$ in the case of the Beisert-Eden-Staudacher equation [22] in the agreement with the AdS/CFT prediction [21].

$$\lim_{g\to\infty} \gamma_{sing} = \frac{2}{\epsilon}\,\frac{I_1(2\epsilon^{-1})}{I_0(2\epsilon^{-1})} \approx 2\sqrt{2}\,g\,-\,\frac{1}{2} \tag{21}$$

Note, that the intercept of the BFKL Pomeron in the strong coupling limit was calculated in Refs. [17] and [25]

References

[1] Slides:
`http://indico.cern.ch/contributionDisplay.py?contribId=188&sessionId=8&confId=9499`

[2] V.S. Fadin, E.A. Kuraev, L.N. Lipatov, Phys. Lett. **B60** 50 (1975);
Ya.Ya. Balitsky, L.N. Lipatov, Yad. Fiz. **28** 1597 (1978).

[3] L.N. Lipatov, Phys.Lett. **B309** 394 (1993).

[4] L.N. Lipatov, JETP **90** 1536 (1986).

[5] J. Bartels, Nucl.Phys. **B175** 365 (1980);
J. Kwiecinski, M. Praszalowicz, *Phys.Lett.*B **B94** 413 (1980).

[6] L.N. Lipatov, Nucl.Phys. **B548** 328 (1999).

[7] L.N. Lipatov *High energy asymptotics of multi-colour QCD and exactly solvable lattice models*, Padova preprint DFPD/93/TH/70, hep-th/9311037, unpublished.

[8] L.N. Lipatov, JETP Lett. **59** 596 (1994);
L.D. Faddeev, G.P. Korchemsky, Phys. Lett. **B342** 311 (1995).

[9] L.N. Lipatov, Nucl.Phys. **B365** 614 (1991).

[10] L.N. Lipatov, Nucl.Phys. **B452** 369 (1995).

[11] E. Antonov, I. Cherednikov, E. Kuraev, L. Lipatov, Nucl.Phys. **B721** 111 (2005).

[12] V. Fadin, L. Lipatov, Phys. Lett. **B429** 127 (1998);
M. Ciafaloni, G. Camici, Phys. Lett. **B430** 349 (1998).

[13] A. Kotikov, L. Lipatov, Nucl.Phys. **B582** 19 (2000), Nucl.Phys. **B661** 19 (2003).

[14] L. Lipatov, talk at "Perspectives in Hadronic Physics", Proc. of Conf. ICTP. Triest, Italy, May 1997.

[15] S. Moch, J.A.M. Vermaseren, A. Vogt, Nucl.Phys. **B688** 101 (2004).

[16] A. Kotikov, L. Lipatov, V. Velizhanin, Phys. Lett. **B557** 114 (2003).

[17] A. Kotikov, L. Lipatov, A. Onishchenko, V. Velizhanin, Phys. Lett. **B595** 521 (2004);
Phys. Lett. **B632** 754 (2006).

[18] A.V. Kotikov, L.N. Lipatov, A. Rej, M. Staudacher, V.N. Velizhanion, arXiv:hep-th/0704.3586v.

[19] R. Kirschner, L.N. Lipatov, Phys.Rev. **D26** 1202 (1982.)

[20] J.M. Maldacena, Adv. Theor. Math. Phys. **2** 231 (1998).

[21] S.S. Gubser, I.R. Klebanov, A.M. Polyakov, Nucl.Phys. **B636** 99 (2002).

[22] B. Eden, M. Staudacher, J. Stat. Mech. **0611** P014 (2006).

[23] N. Beisert, B. Eden, M. Staudacher, J. Stat. Mech. **0701** P021 (2007).

[24] A.V. Kotikov, L.N. Lipatov, Nucl. Phys. **B769** 217 (2007).

[25] R.C. Brower, J. Polchinski, M.J. Strassler, C-I Tan, preprint hep-th/0603115.

Anomalous Dimensions of Twist-Two Operators with High Lorentz Spin

B. Basso *

Laboratoire de Physique Théorique - Université de Paris XI
91405 ORSAY CEDEX - FRANCE

Twist-two anomalous dimensions depend on their Lorentz spin and admit an asymptotic expansion for large values of this quantum number. Recent multi-loop QCD calculations of twist-two anomalous dimensions revealed the existence of an intriguing feature : The coefficients parameterizing their large Lorentz spin expansion satisfy an infinite system of equations, and so are not all independent. We argue that these relations follow from the *parity preserving property* of some related function, the *scaling function*.

1 Introduction

Forward matrix elements of twist-two Wilson operators, $\langle O_N^{(a)}(0)\rangle$, provide the dominant contribution to the structure functions of deeply inelastic scattering in the limit of large momentum transfer. They carry Lorentz spin N and some additional quantum numbers (a). The twist-two operators with the same Lorentz spin mix under a change of the renormalization scale μ and satisfy the Callan-Symanzik equation

$$\left[\mu\frac{\partial}{\partial\mu}+\beta(\alpha_s)\frac{\partial}{\partial\alpha_s}\right]\langle O_N^{(a)}(0)\rangle=-\gamma^{ab}(N,\alpha_s)\langle O_N^{(b)}(0)\rangle. \tag{1}$$

The mixing matrix $\gamma(N,\alpha_s)$, entering Eq. (1), depends on the Lorentz spin and admits a perturbative expansion in the strong coupling constant α_s

$$\gamma(N,\alpha_s)\equiv\gamma(N)=\frac{\alpha_s}{2\pi}\gamma_1(N)+\frac{\alpha_s^2}{4\pi^2}\gamma_2(N)+...$$

The size of the mixing matrix does not depend on the Lorentz spin, but on some other quantum numbers of the Wilson operators under consideration. For the sake of clarity, we will consider two particular examples of twist-two mixing matrices : quark non-singlet anomalous dimension and singlet anomalous dimensions matrix

$$\gamma^{ns}(N),\qquad \gamma^{s}(N)=\begin{pmatrix}\gamma^{qq}(N) & \gamma^{qg}(N)\\ \gamma^{gq}(N) & \gamma^{gg}(N)\end{pmatrix},$$

computed in $\overline{MS}$-scheme.

Beyond the leading order, the analytic expressions for $\gamma^{ns}(N)$ and $\gamma^{s}(N)$ are very cumbersome. Their large Lorentz spin expansions are however simpler and exhibit interesting features. In particular, both quark non-singlet and diagonal elements of the singlet mixing matrix are known to scale logarithmically with the Lorentz spin [3]

$$\gamma(N)=A(\alpha_s)\ln N+\mathcal{O}\left(N^0\right),$$

*Based on a work done in collaboration with G. P. Korchemsky [2].

where $A(\alpha_s)/2 = \Gamma_{cusp}(\alpha_s)$ is the universal cusp anomalous dimension. It only depends on the colour charge (quadratic Casimir) of the fundamental field entering the Wilson operator.

Subleading corrections, suppressed by powers of $1/N$, are not universal and depend on additional quantum numbers. For large N, it is convenient to parameterize them as follows

$$\gamma(N) = \frac{1}{2}A(\alpha_s)\ln\left[N(N+1)e^{2\gamma_E}\right] + B(\alpha_s)$$

$$+\frac{1}{2}C(\alpha_s)N^{-1}\ln\left[N(N+1)e^{2\gamma_E}\right] + D(\alpha_s)N^{-1} + \mathcal{O}(N^{-2}\ln^p N).$$

Based on three-loop explicit expressions for anomalous dimensions, Moch, Vermaseren, Vogt [4] and Dokshitzer, Marchesini, Salam [5] observed interesting relations between the expansion coefficients A, B, C, D : Both for $\gamma^{ns}(N)$ and for diagonal elements of $\gamma^s(N)$, they noted that[a]

$$C(\alpha_s) = \frac{1}{2}A^2(\alpha_s), \qquad \text{and that} \qquad D(\alpha_s) = \frac{1}{2}A(\alpha_s)B(\alpha_s) - \frac{1}{2}A(\alpha_s)\frac{\beta(\alpha_s)}{\alpha_s}. \tag{2}$$

Equations (2) state that the expansion coefficients are not all independent. Moreover, the expressions for C and D to order $\mathcal{O}\left(\alpha_s^{n+1}\right)$ are determined by the coefficients A and B to order $\mathcal{O}\left(\alpha_s^n\right)$.[b] In the next section, we shall see that Eqs. (2) belong to an infinite system of equations, relating the expansion coefficients of twist-two anomalous dimensions for large Lorentz spin. We shall argue that these equations follow from the *parity preserving property* of the *scaling function*.

2 Parity preserving property of the scaling function

In an attempt to interpret Eqs. (2), Dokshitzer, Marchesini and Salam [5] proposed to define the *scaling function* f through the relation

$$\gamma(N) = f\left(N + \frac{1}{2}\gamma(N)\right). \tag{3}$$

Then, they observed that, neglecting the beta-function contribution to D, Eqs. (2) are equivalent to the *vanishing of corrections* $\propto N^{-1}$ in the following parameterization of the *scaling function*

$$f(N) = \frac{1}{2}A(\alpha_s)\ln\left[N(N+1)e^{2\gamma_E}\right] + B(\alpha_s) + 0.N^{-1} + \mathcal{O}\left(N^{-2}\ln^p N\right), \tag{4}$$

for large N. In their approach, the parameterization, Eq. (4), and the vanishing of the correction $\propto N^{-1}$ were motivated by some physical arguments. We would like to indicate another point of view with help of an explicit example. As was already mentioned, Eqs. (3) and (4) fail to take into account the beta-function contribution. To circumvent this difficulty we shall below interpret Eq. (3) in the framework of conformal symmetry and modify it in order to account for the non-vanishing beta-function. But first, let us examine the example

[a] To two-loop accuracy, the relation between A and C was first observed by Curci, Furmanski and Petronzio [6] for the quark non-singlet anomalous dimension.

[b] Taking account that $\beta(\alpha_s) = \mathcal{O}(\alpha_s^2)$.

of the quark non-singlet anomalous dimension. To one-loop order, the anomalous dimension is not sensitive to the beta-function contribution and is given by

$$\gamma(N) = \frac{\alpha_s}{2\pi}\gamma_0(N) + \mathcal{O}(\alpha_s^2), \qquad \gamma_0(N) = C_F\left[4\psi(N+1) + 4\gamma_E - 3 - \frac{2}{N(N+1)}\right].$$

To lowest order, Eq. (3) translates into

$$f(N) = \gamma(N) + \mathcal{O}(\alpha_s^2) = \frac{\alpha_s}{2\pi}\gamma_0(N) + \mathcal{O}(\alpha_s^2).$$

Hence

$$f(N) = \frac{\alpha_s}{2\pi}C_F\left[4\psi(N+1) + 4\gamma_E - 3 - \frac{2}{N(N+1)}\right] + \mathcal{O}(\alpha_s^2). \tag{5}$$

The large N expansion of $\psi(N+1)$ only runs in negative integer powers of the parameter $N(N+1)$

$$\psi(N+1) = \frac{1}{2}\ln\left[N(N+1)\right] + \frac{1}{6}\frac{1}{N(N+1)} - \frac{1}{30}\frac{1}{N^2(N+1)^2} + ... + \mathcal{O}\left(N^{-n}(N+1)^{-n}\right),$$

and from Eq. (5) we conclude that the large N expansion of the scaling function has the same property. We would like to stress that it is this property that guarantees the *absence of contributions* $\propto N^{-1}$ in the large N expansion of the scaling function, Eq. (4). To go beyond one-loop, we need to include into consideration the beta-function contribution.

The scaling function, as defined in Eq. (3), is tied to conformal symmetry. Indeed, if QCD were conformally invariant, the quantity $j = N+\gamma(N)/2$ would be *conformal spin* and would be a good quantum number to classify Wilson operators according to representations of the conformal group. In this case, it would be natural to express anomalous dimensions as a function of the conformal spin j, rather than the Lorentz spin N. This immediately leads to Eq. (3) : $\gamma(N) = f(j)$.

However, QCD is not a conformally invariant theory. Nevertheless, working within the $\overline{MS}$-scheme, it is possible to incorporate conformal symmetry breaking corrections and to arrive at the following improved definition of the scaling function [2]

$$\gamma(N) = f\left(N + \frac{1}{2}\gamma(N) - \frac{\beta(\alpha_s)}{2\alpha_s}\right). \tag{6}$$

Starting from this definition of the scaling function, the *absence of contributions* $\propto N^{-1}$ in the large N expansion of the scaling function, Eq. (4), leads to Eqs. (2), including the beta-function contribution.

The one-loop non-singlet anomalous dimension considered above suggests that the scaling function possesses an important property : The large N expansion of the scaling function only runs in negative integer powers of the parameter $J^2 = N(N+1)$

$$f(N) = \frac{1}{2}A(\alpha_s)\ln\left[J^2 e^{2\gamma_E}\right] + B(\alpha_s) + f^{(1)}\left(\ln J^2\right)J^{-2} + f^{(2)}\left(\ln J^2\right)J^{-4} + \mathcal{O}\left(J^{-6}\right). \tag{7}$$

and so is invariant under the *parity* $N \to -N-1$. We refer to this relation as the *parity preserving property.*

We verified [2] that the parity preserving property holds in QCD for[c]

- two-loop longitudinally polarized singlet anomalous dimensions,
- two-loop gluon linearly polarized anomalous dimension,
- two-loop quark transversity anomalous dimension,
- three-loop non-singlet unpolarized anomalous dimension,
- three-loop singlet unpolarized anomalous dimensions.

Replacing the scaling function in Eq. (6) by its expression, Eq. (7), and expanding $\gamma(N)$ in powers of $1/J$, one obtains that the coefficients in front of *odd powers* of $1/J$ can be expressed in terms of the coefficients accompanying *even powers* of $1/J$ to *less number of loops*. The resulting infinite system of equations include in particular Eqs. (2).

3 Conclusion and outlooks

Starting from the observation that twist-two anomalous dimensions fulfill some intriguing relations, we identified them as a manifestation of the parity preserving property of some related function, the scaling function. Using results for the anomalous dimensions available in the literature, we verified that this property holds in QCD and that it leads to an infinite system of equations constraining twist-two anomalous dimensions.

The parity preserving property is a robust phenomenon : it holds in QCD to all loops in the large β_0 limit for both singlet and non-singlet anomalous dimensions. It can also be extended to a subclass of higher twist operators. It would be interesting to test the parity preserving property for these operators. However, the origin of this property still remains to be understood.

4 Acknowledgments

I would like to thank the organizers of DIS 2007 for hospitality. The work was supported in part by the French Agence Nationale de la Recherche under grant ANR-06-BLAN-0142-02.

5 Bibliography

References

[1] Slides:
`http://indico.cern.ch/contributionDisplay.py?contribId=183&sessionId=8&confId=9499`

[2] B. Basso and G. P. Korchemsky, Nucl. Phys. B **775**, 1 (2007).

[3] G. P. Korchemsky, Mod. Phys. Lett. A **4**, 1257 (1989); G. P. Korchemsky and G. Marchesini, Nucl. Phys. B **406**, 225 (1993).

[4] S. Moch, J. A. M. Vermaseren and A. Vogt, Nucl. Phys. B **688**, 101 (2004); A. Vogt, S. Moch and J. A. M. Vermaseren, Nucl. Phys. B **691**, 129 (2004).

[5] Yu. L. Dokshitzer, G. Marchesini and G. P. Salam, Phys. Lett. B **634**, 504 (2006).

[6] G. Curci, W. Furmanski and R. Petronzio, Nucl. Phys. B **175**, 27 (1980).

[c]Note that the parity preserving relation only holds for eigenvalues of the mixing matrix and not for each element independently. Note also that the explicit expression for the scaling function depends on the particular anomalous dimension we consider.

Recent Developments in Small-x Physics

Arif I. Shoshi[1] *

1-Fakultät für Physik, Universität Bielefeld, D-33501 Bielefeld, Germany

Recent theoretical progress in understanding high-energy scattering beyond the mean field approximation is reviewed. The role of Lorentz invariance and pomeron loops in the evolution, the relation between high-energy QCD and statistical physics and results for the saturation momentum and the scattering amplitude are discussed.

1 Introduction

The high-energy scattering of a dipole off a nucleus/hadron in the *mean field approximation* is decribed by the BK-equation [2]. The main results following from the BK-equation are the geometric scaling behaviour of the scattering amplitude and the roughly powerlike energy dependence of the saturation scale which are both nicely supported by the HERA data.

The recent progress consists in understanding small-x dynamics (near the unitarity limit) *beyond the mean field approximation*, i.e., beyond the BK-equation. A first step beyond the mean field approximation was done in [3] where the BFKL evolution in the scattering process was enforced to satisfy natural requirements as unitarity limits and Lorentz invariance. The result was a correction to the saturation scale and the breaking of the geometric scaling at high energies. Afterwards a relation between high-energy QCD and statistical physics was found [4] which has clarified the physical picture of, and the way to deal with, the dynamics beyond the BK-equation. It has been understood that *gluon number fluctuations* from one scattering event to another and the *discreteness* of gluon numbers, both ignored in the BK evolution and also in the Balitsky-JIMWLK equations [5], lead to the breaking of the geometric scaling and to the correction to the saturation scale, respectivelly. New evolution equations [6, 7, 8], which describe Pomeron loops, have been proposed to account for the above effects. Very recently possible effects of Pomeron loops on various observables [9, 10, 11] have been studied in case they become important in the range of collider energies.

In the following sections I will show the recent developments in some detail by considering equations and results in and beyond the mean field approximation.

2 Mean field approximation

Consider the high-energy scattering of a dipole of transverse size r off a target (hadron, nucleus) at rapidity $Y = \ln(1/x)$. The rapidity dependence of the T-matrix in the mean field approximation is given by the BK-equation which has the schematic structure (transverse dimensions are suppressed)

$$\partial_Y T = \alpha_s \left[T - T\ T\right] \ . \tag{1}$$

The linear part of the BK equation, i.e., the BFKL equation, gives the growth of T with rapidity Y whereas the non-linear term TT tames the growth of T in such a way that the unitarity limit $T \leq 1$ is satisfied.

*The author acknowledges financial support by the DFG under contract 92/2-1.

One of the main results following from the BK-equation is the *geometric scaling* behaviour of the T-matrix [12]

$$T(r, Y) = T(r^2\, Q_s^2(Y)) \ , \tag{2}$$

where $Q_s(Y)$ is the so-called *saturation momentum* defined such that $T(r \simeq 1/Q_s, Y)$ be of $\mathcal{O}(1)$. Eq. (2) means that the T-matrix scales with a single quantity $r^2\, Q_s^2(Y)$ rather than depending on r and Y separatelly. This behaviour implies a similar scaling for the DIS cross section, $\sigma^{\gamma^* p}(Y, Q^2) = \sigma^{\gamma^* p}(Q^2/Q_s^2(Y))$, which is supported by the HERA data.

Another important result that can be extracted from the BK-equation is the rapidity dependence of the saturation momentum (leading-Y contribution)[13],

$$Q_s^2(Y) = Q_0^2\ \mathrm{Exp}\left[\frac{2\alpha_s N_c}{\pi}\frac{\chi(\lambda_0)}{1-\lambda_0}Y\right] \ , \tag{3}$$

where $\chi(\lambda)$ is the BFKL kernel and $\lambda_0 = 0.372$.

The shape of the T-matrix resulting from the BK-equation is preserved in the transition region from weak to strong scattering, $0 < T < 1$, with rising Y (front of the travelling wave): The saturation region at $r \gg 1/Q_s(Y)$ where $T \simeq 1$ however widens up, including smaller and smaller dipoles, due to the growth of the saturation momentum. The situation changes, as we will, once gluon number fluctuations are taken into account.

3 Beyond the mean field approximation

3.0.1 Lorentz invariance plus Unitarity

Let's start with an elementary dipole of size r_1 at rapidity $y = 0$ and evolve it using the BFKL evolution up to $y = Y$. The number density of dipoles of size r_2 at Y in this dipole, $n(r_1, r_2, Y)$, obeys a completeness relation

$$n(r_1, r_2, Y) = \int \frac{d^2 r}{2\pi r^2}\ n(r_1, r, Y/2)\ n(r, r_2, Y/2) \tag{4}$$

where on the right hand side the rapidity evolution is separated in two successive steps, $y = 0 \to y = Y/2 \to y = Y$. With

$$T(r_1, r_2, Y) \simeq c\ \alpha_s^2\ r_2^2\ n(r_1, r_2, Y) \tag{5}$$

eq.(4) can be approximately rewritten in terms of the T-matrix as

$$\left(\frac{1}{r_2^2}\ T(r_1, r_2, Y)\right) \simeq\ \frac{1}{2c\alpha_s^2}\ \int d\rho\ \ \left(\frac{1}{r^2}\ T(r_1, r, Y/2)\right)\ \left(\frac{1}{r_2^2}\ T(r, r_2, Y/2)\right) \tag{6}$$

where $\rho = \ln(r_0^2/r^2)$. In Ref. [3] it was realized that the above completeness relations, or, equivalently, the Lorentz invariance, is satisfied by the BK evolution only by violating unitarity limits. This can be illustrated as follows: Suppose that r_2 is close to the saturation line, $r_2 \simeq 1/Q_s(Y/2)$, so that the left hand side of Eq.(6) is large. On the right hand side of Eq.(6) it turns out that $T(r_1, r, Y/2)/r^2$ is typically very small in the region of ρ which dominates the integral. This means that $T(r, r_2, Y/2)/r_2^2$ must be typically very large and must violate unitarity, $T(r, r_2, Y/2) \gg 1$, in order to satisfy (6).

The simple procedure used in Ref. [3] to solve the above problem was to limit the region of the ρ-integration in Eq.(6) by a boundary $\rho_2(Y/2)$ so that $T(r, r_2, Y/2)/r_2^2$ would never violate unitarity, or $T(r_1, r, Y/2)/r^2$ would always be larger than α_s^2. The main consequence of this procedure, i.e., BK evolution plus boundary correcting it in the weak scattering region, is the following scaling behaviour of the T-matrix near the unitarity limit

$$T(r, Y) = T\left(\frac{\ln(r^2 Q_s^2(Y))}{\alpha_s Y/(\Delta\rho)^3}\right) \tag{7}$$

and the following energy dependence of the saturation momentum

$$Q_s^2(Y) = Q_0^2\ \mathrm{Exp}\left[\frac{2\alpha_s N_c}{\pi}\frac{\chi(\lambda_0)}{1-\lambda_0}Y\left(1 - \frac{\pi^2\chi''(\lambda_0)}{2(\Delta\rho)^2\chi(\lambda_0)}\right)\right] \tag{8}$$

with

$$\Delta\rho = \frac{1}{1-\lambda_0}\ln\frac{1}{\alpha_s^2} + \frac{3}{1-\lambda_0}\ln\ln\frac{1}{\alpha_s^2} + \text{const.}\ . \tag{9}$$

Eq.(7) shows a breaking of the geometric scaling which was the hallmark of the BK equation (cf. Eq.(2)) and Eq.(8) shows the correction to the saturation momentum due to the evolution beyond the mean field approximation (cf. Eq.(3)).

3.0.2 Statistical physics - high density QCD correspondence

The high energy evolution can be viewed also in another way which is inspired by dynamics of reaction-diffusion processes in statistical physics [4]. To show it, let's consider an elementary target dipole of size r_1 which evolves from $y = 0$ up to $y = Y$ and is then probed by an elementary dipole of size r_2, giving the amplitude $\bar{T}(r_1, r_2, Y)$. It has become clear that the evolution of the target dipole is *stochastic* leading to random dipole number realizations inside the target dipole at Y, corresponding to different events in an experiment. The physical amplitude, $\bar{T}(r_1, r_2, Y)$, is then given by averaging over all possible dipole number realizations/events, $\bar{T}(r_1, r_2, Y) = \langle T(r_1, r_2, Y)\rangle$, where $T(r_1, r_2, Y)$ is the amplitude for dipole r_2 scattering off a particular realization of the evolved target dipole at Y.

The mean field descripton breaks down at low target dipole occupancy due to the *discreteness and the fluctuations of dipole numbers*. Because of discreteness the dipole occupancy can not be less than one for any dipole size. Taking this fact into account by using the BK equation with a cutoff when T becomes of order α_s^2 [4], or the occupancy of order one (see Eq.(5)), leads exactly to the same correction for the saturation momentum as given in Eq.(3). The latter cutoff is essentially the same as, and gives a natural explanation of, the boundary used in Ref.[3] and briefly explained in the previous section.

The dipole number fluctuations in the low dipole occupancy region result in fluctuations of the saturation momentum from event to event, with the strength

$$\sigma^2 = \langle\rho_s^2\rangle - \langle\rho_s\rangle^2 = \text{const.}\ \frac{\alpha_s Y}{(\Delta\rho)^3} \tag{10}$$

extracted from numerical simulations of statistical models. The averaging over all events with random saturation momenta, in order to get the physical amplitude, causes the breaking of the geometric scaling and replaces it by the scaling law

$$\langle T(r, Y)\rangle = T\left(\frac{\ln(r^2 Q_s^2(Y))}{\sqrt{\alpha_s Y/(\Delta\rho)^3}}\right)\ . \tag{11}$$

This equation differs from Eq.(7) since Eq.(7) misses dipole number fluctuations.

3.0.3 Pomeron loop equations

It was always clear that the BK equation does not include fluctuations. However, it took some time to realize that also the Balitsky-JIMWLK equations do miss them. As soon as this became clear (first Ref. in [7]), the so-called Pomeron loop equations [6, 7] have been constructed, aiming at a description of fluctuations. They can be written (schematic way, transverse dimensions ignored) as a stochastic equation of Langevin-type,

$$\partial_Y T = \alpha_s \left[T - TT + \alpha_s \sqrt{T}\, \nu \right] \tag{12}$$

or as a hierarchy of coupled equations of averaged amplitudes, the first two of them reading

$$\begin{aligned} \partial_Y \langle T \rangle &= \alpha_s \left[\langle T \rangle - \langle TT \rangle \right] \\ \partial_Y \langle TT \rangle &= \alpha_s \left[\langle TT \rangle - \langle T\, T\, T \rangle + \alpha_s^2 \langle T \rangle \right] \ . \end{aligned} \tag{13}$$

The last term in Eq.(12), containing a non-Gaussian noise ν, is new as compared with the BK equation and accounts for the fluctuations in the dipole number. Eq.(13) reduces to the BK equation in the mean field approximation, $\langle T\, T \rangle = \langle T \rangle \langle T \rangle$. The hierarchy in Eq.(13), as compared with the Balitsky-JIMWLK hierarchy, involves in addition to linear BFKL evolution and pomeron mergings, also pomeron splittings, and therefore *pomeron loops*. The three pieces of evolution are represented by the three terms in the second equation in Eq.(13), respectivelly, in the case where two dipoles scatter off a target.

It isn't yet clear at which energy fluctuation effects start becoming important. The results shown in the previous sections, Eq.(8) and Eq.(11), are valid at asymptotic energies. A solution to the evolution equations, which is not yet available because of their complexity, would have helped to better understand the subasymptotics. However, using the methods outlined in the previous subsections, phenomenological consequences of fluctuations in the fixed coupling case have been studied, for example for DIS and diffractive cross sections [10], forward gluon production in hadron-hadron collisions [11] and for the nuclear modification factor R_pA [9], in case fluctuations become important in the range of LHC energies.

References

[1] Slides: `http://indico.cern.ch/contributionDisplay.py?contribId=46&sessionId=8&confId=9499`

[2] I. Balitsky, Nucl. Phys. B **463** (1996) 99; Y. V. Kovchegov, Phys. Rev. D **60** (1999) 034008.

[3] A. H. Mueller and A. I. Shoshi, Nucl. Phys. B **692** (2004) 175.

[4] E. Iancu, A. H. Mueller and S. Munier, Phys. Lett. B **606** (2005) 342.

[5] For recent reviews and references see e.g. E. Iancu and R. Venugopalan, arXiv:hep-ph/0303204; H. Weigert, Prog. Part. Nucl. Phys. **55** (2005) 461.

[6] A. H. Mueller, A. I. Shoshi and S. M. H. Wong, Nucl. Phys. B **715** (2005) 440.

[7] E. Iancu and D. N. Triantafyllopoulos, Nucl. Phys. A **756** (2005) 419; Phys. Lett. B **610** (2005) 253.

[8] A. Kovner and M. Lublinsky, Phys. Rev. D **71** (2005) 085004.

[9] M. Kozlov, A. I. Shoshi and B. W. Xiao, "Total gluon shadowing due to fluctuation effects, arXiv:hep-ph/0612053.

[10] Y. Hatta, E. Iancu, C. Marquet, G. Soyez and D. N. Triantafyllopoulos, Nucl. Phys. A **773**, 95 (2006).

[11] E. Iancu, C. Marquet and G. Soyez, Nucl. Phys. A **780** (2006) 52.

[12] A. M. Stasto, K. Golec-Biernat and J. Kwiecinski, Phys. Rev. Lett. **86** (2001) 596.

[13] A. H. Mueller and D. N. Triantafyllopoulos, Nucl. Phys. B **640** (2002) 331; S. Munier and R. Peschanski, Phys. Rev. Lett. **91** (2003) 232001.

Multi-Gluon Production at High Energies

Michael Lublinsky

State University of New York - Department of Physics and Astronomy
Stony Brook NY 11794-3800, USA

A systematic approach towards description of semi-inclusive processes at low x and with multiple rescatterings taken into account is highlighted. We solve the problem of inclusive multi-gluon production for arbitrary number of gluons, thus extending previously known results for one and two gluons produced.

This talk is based on Refs. [1].

Within the BFKL approximation the problem of multi-gluon production is solved (Fig. 1) in terms of the BFKL Green function G^{BFKL} and the effective vertex for gluon emission $L(k)$ with k being a momentum of emitted gluon. A schematic expression for the cross section of n-gluon production emitted at different rapidities Y_1 ... Y_n and having momenta k_1 ... k_n reads (with $\Phi^{P,T}$ standing for projectile/target impact factor)

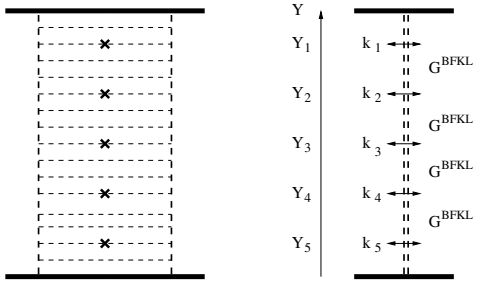

Figure 1: Multi-gluon production within BFKL

$$\frac{d\sigma}{dY_1\, dk_1^2\, \ldots\, dY_n\, dk_n^2} \sim \Phi^T \;\; G^{BFKL}_{Y_n - Y_0}\; L(k_n) \;\; \ldots \;\; G^{BFKL}_{Y_1 - Y_2}\; L(k_1)\; G^{BFKL}_{Y - Y_1} \;\; \Phi^P$$

The question we ask is how to generalize this expression when one of the colliding particles, the target, is large and dense. We then have to take into account the physics of gluon saturation, and associated non-linear evolution equations like BK-JIMWLK. The projectile's gluon scattering of a dense target has the eikonal propagator given by the Wilson line

$$S(x) \;=\; \mathcal{P}\, \exp\left\{ i \int dx^-\, T^a\, \mathbf{A}_t^a(x, x^-) \right\} .$$

with A_t characterizing the target external field. We find it convenient to introduce two targets - one for the amplitude S and another one for its conjugate $\bar{S}$. In the end of our computation we set $S = \bar{S}$. The answer to our posed question has the following form

$$\frac{d\sigma}{dY_1\, dk_1^2 \ldots dY_n\, dk_n^2} \sim \int DSD\bar{S}\, W^T[S]\, \delta(S - \bar{S})\, U_{Y_n - Y_0} \mathcal{O}_g^{k_n} \ldots U_{Y_1 - Y_2} \mathcal{O}_g^{k_1} U_{Y - Y_1} \Sigma^P[S, \bar{S}]$$

with the evolution operator

$$U(Y_1 \,-\, Y_2) \;=\; Exp\,[-\, H_3\,(Y_1 \,-\, Y_2)]$$

Below we will present the Hamiltonian H_3 and the gluon emission vertex $\mathcal{O}_g$. W^T and Σ^P are generalized impact factors, which often appear in the color glass formalism.

We first introduce the gluon production (and scattering) amplitude

$$Q_i^a(z) \;=\; g \int_x \frac{(x-z)_i}{(x-z)^2}\,\left[J_L^a(x) \;-\; S^{ab}(z)\; J_R^b(x)\right]$$

The generators of the left/right color rotations are Lie derivatives

$$J_R^a(x) \;=\; -\,\mathrm{tr}\left\{S(x)\;T^a\;\frac{\delta}{\delta S^\dagger(x)}\right\}, \qquad\qquad J_L^a(x) \;=\; -\,\mathrm{tr}\left\{T^a\;S(x)\;\frac{\delta}{\delta S^\dagger(x)}\right\}$$

In terms of Q the gluon emission operator which is found in Ref. [1] is

$$\mathcal{O}_g^k[S,\bar S] \;=\; \int \frac{d^2z}{2\,\pi}\,\frac{d^2\bar z}{2\,\pi}\;e^{i\,k\,(z\,-\,\bar z)}\;Q_i^a(z,[S])\,Q_i^a(\bar z,[\bar S])$$

This operator is visualized in Fig. 2 The same operator Q enters the expression for the Hamiltonian H_3 first introduced in Ref.[2]

$$H_3[S,\bar S] \;\equiv\; \int_z \left[Q_i^a(z,[S]) \;+\; Q_i^a(z,[\bar S])\right]^2$$

As a first application of the above formalism we consider a single inclusive gluon production (Fig. 3).

Using our general formalism we write the cross section

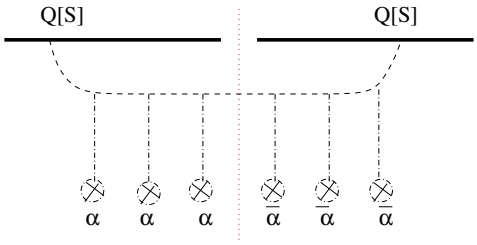

Figure 2: The operator $\mathcal{O}_g$

$$\frac{d\sigma}{dY_1\,dk^2} \;=\; \int DS\,D\bar S\,W^T[S]\,\delta(\bar S\;-\;S)\;U_{Y_1}\;\mathcal{O}_g^k\;U_{Y-Y_1}\;\Sigma_Y^P$$

This can be brought [1] to the following form [3]

$$\frac{d\sigma}{dY_1\,dk^2} \;=\; \frac{\alpha_s}{\pi}\int_{z,\bar z} e^{i\,k(z\,-\,\bar z)}\int_{x,y}\frac{(z-x)_i}{(z-x)^2}\,\frac{(\bar z-y)_i}{(\bar z-y)^2}\,G^{BFKL}(x,y;Y-Y_1)\;\times$$

$$\times\;\left[\langle T_{z,y}\rangle_{Y_1} \;+\; \langle T_{x,\bar z}\rangle_{Y_1} \;-\; \langle T_{z,\bar z}\rangle_{Y_1} \;-\; \langle T_{x,y}\rangle_{Y_1}\right]$$

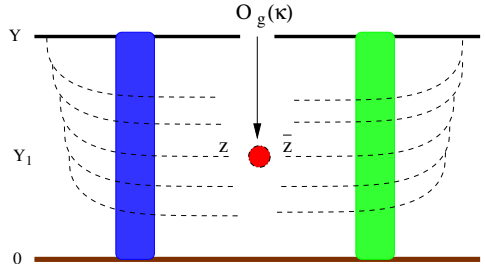

Figure 3: Single gluon production

with $\langle T \rangle$ denoting the S-matrix of a gluonic dipole:

$$\langle T_{x,y} \rangle_{Y_1} \equiv \int DS\, W^T_{Y_1}[S]\, \mathrm{tr}[S^\dagger_x\, S_y]$$

which can be deduced from solutions of the BK-JIMWLK equations. Our solution for the multi-gluon production problem is given in terms of Feynman-like diagrammatic technique. Fig. 4 is an example of a diagram for the one gluon case.

We were not able to proceed with the general formalism beyond the one gluon case. Instead we had to rely on the dipole approximation. In practice we introduce new degrees of freedom and re-express both the Hamiltonian H_3 and the vertex $\mathcal{O}_g$ in the new degrees. The dipole creation operator reads (similarly $\bar{s}$)

$$s_{x,y} = \frac{1}{N}\, tr[S_F(x)\, S^\dagger_F(y)]$$

We also find it necessary to introduce the quadrupole operator

$$q_{x,y,u,v} = \frac{1}{N}\, tr[S_F(x)\, S^\dagger_F(y)\, S_F(u)\, S^\dagger_F(v)].$$

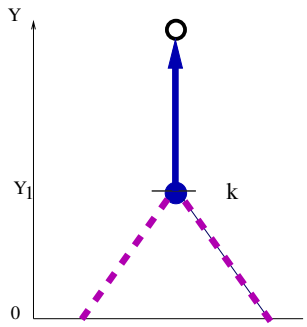

Figure 4: Single gluon production: Diagrammatic representation

It is important to stress that no other higher multiplet operators is needed if the projectile at rest is made only out of dipoles. Furthermore, the quadrupoles of the mixed type arise

$$q^{s\bar{s}}_{x,y,v,u} = \frac{1}{N}\, tr[S_F(x)\, S^\dagger_F(y)\, \bar{S}_F(u)\, \bar{S}^\dagger_F(v)] = q_{x,y,v,u} + t_{x,y,v,u}$$

Note that we have to set $\bar{S} = S$ at the end of our computation $t = 0$. That leads us to a perturbation theory in t.

Re-express the Hamiltonian H_3 in new degrees of freedom we find four terms:

$$H_3 = H_s + H_q + H_t + V_{t\to tt}$$

H_s is the dipole Hamiltonian which generates the BK eq. for the dipole s:

$$\partial_y\, s(x,y) = K^{BFKL} \otimes (s - s\, s)$$

H_q generates a linear evolution of q (similar to BKP) which is also coupled to the external field s:

$$\partial_y\, q(x,y,u,v) = K_1 \otimes q + K_2 \otimes q\, s + K_3 \otimes s\, s$$

The explicit expressions for the kernels K can be found in [1]. H_t generates a linear evolution of t which is also coupled to s:

$$\partial_y\, t(x,y,u,v) = G^{-1}[s] \otimes t + \lambda \otimes t\, t$$

Here G is a propagator in the external *Pomeron* field s.When $x = v$ and $y = u$, the two-point function G coincides with G^{BFKL}. The propagator G and triple t vertex λ are in the basic of our perturbation theory. They define the relevant Feynman rules (Fig. 5).

Finally we have to re-express the insertion operator $\mathcal{Q}_g$ in terms of the new degrees of freedom. We find that $\mathcal{O}_g$ splits into three groups of vertecies (Fig. 6):

Figure 5: The propagator and vertex

$$\mathcal{O}_g(k) \;=\; A_{-1}(k) \;+\; A_0(k) \;+\; A_1(k)$$

The first group reduces the number of t's by one; the second group leaves the number unchanged, the last group increases the number of t's by one. Remember that t is set to zero at the end. So any diagram which has an external line propagating t is zero. Fig. 7 presents an example of our diagram technique as applied to double gluon emission. Our expressions reproduce the result of Ref. [4].

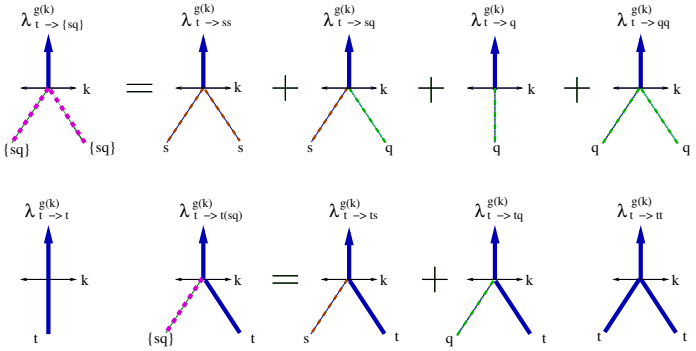

Figure 6: The gluon emission vertices in the dipole approximation

Acknowledgments

Everything which is reported above has been done in collaboration with Alex Kovner. Many thanks to Alex for making hard work into a joy.

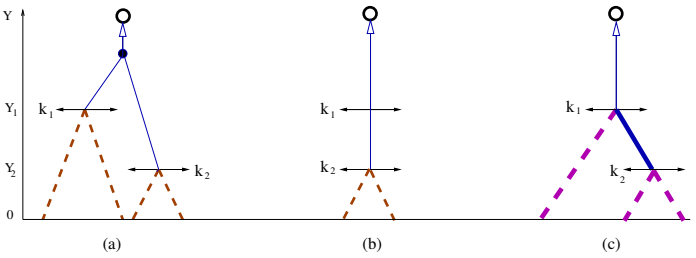

Figure 7: Double-gluon production

References

[1] A. Kovner and M. Lublinsky, JHEP **0611** 083 (2006); A. Kovner, M. Lublinsky and H. Weigert, Phys. Rev. **D74** 114023 (2006).

[2] M. Hentschinski, H. Weigert and A. Schafer, Phys. Rev. **D73** 051501 (2006).

[3] Y. V. Kovchegov and K. Tuchin, Phys. Rev. **D65** 074026 (2002).

[4] J. Jalilian-Marian and Y. V. Kovchegov, Phys. Rev. **D70** 114017 (2004).

[5] Slides: `http://indico.cern.ch/contributionDisplay.py?contribId=51&sessionId=8&confId=9499`

Critical Tests of Unintegrated Gluon Distributions

H. Jung[1], A.V. Kotikov[2], A.V. Lipatov[3] and N.P. Zotov[3]

1- DESY, Hamburg, Germany

2- BLTHPH - JINR, Dubna, Russia

3- SINP - MSU, Moscow, Russia

We use the unintegrated Parton Density Functions of the gluon obtained from a fit to measurements of the structure functions $F_2(x,Q^2)$ and $F_2^c(x,Q^2)$ at HERA to describe the experimental data for $F_2^b(x,Q^2), F_L(x,Q^2)$ and F_L at fixed W.

1 Introduction

The purpose of the present investigation is to study the longitudinal structure function (SF) $F_L(x,Q^2)$ as well as the charm and beauty contributions to the proton SF $F_2(x,Q^2)$ using the k_T-factorization approach of QCD [2]. The SF $F_L(x,Q^2)$ is directly connected to the gluon density in the proton. Only in the naive quark-parton-model $F_L(x,Q^2)=0$, and becomes non-zero in pQCD. However the pQCD leads to controversal results still. It was shown recently [3], that the F_L experimental data from HERA seem to be inconsistent with some of the NLO predictions (in particular the MRST one) at small x. BFKL effects significantly improve the description of the low x data when compared to a standard NLO $\overline{MS}$-scheme global fit. The NNLO global fit becomes better when taking into account higher order terms involving powers of $\ln(1/x)$. It means, that we need a resummation procedure.

On the other hand it is known, that the BFKL effects are taken into account from the very beginning in the k_T-factorization approach [2], which is based on the BFKL [4] or CCFM [5] evolution equations summing up the large logarithmic terms proportional to $\ln(1/x)$ or $\ln(1/(1-x))$ in the LLA. Some applications of the k_T-factorization approach were shown in Refs. [6]. In the framework of k_T-factorization the study of the longitudinal SF F_L began already ten years ago [7], where the small x asymptotics of F_L has been evaluated, using the BFKL results. Since we want to analyze the SF data in a broader range at small x we use a more phenomenological approach in our analyses of F_2 and F_L data [8, 9]. Using the k_T-factorization approach for the description of different SF at small x we hope to obtain additional information (or restrictions), in particular, about one of the main ingradient of k_T-factorization approach - the unintegrated gluon distribution (UGD)

In the k_T-factorization the SF $F_{2,L}(x,Q^2)$ are driven at small x primarily by gluons and are related in the following way to the UGD $x\mathcal{A}(x,\mathbf{k}_T^2,\mu^2)$

$$F_{2,L}(x,Q^2) \;=\; \int_x^1 \frac{dz}{z}\int^{Q^2} dk_T^2 \sum_{i=u,d,s,c} e_i^2 \hat{C}_{2,L}^g(x/z,Q^2,m_i^2,k_T^2) x\mathcal{A}(x,\mathbf{k}_T^2,\mu^2). \qquad (1)$$

The functions $\hat{C}_{2,L}^g(x,Q^2,m_i^2,k_T^2)$ can be regarded as SF of the off-shell gluons with virtuality k_T^2 (hereafter we call them *hard structure functions*). They are described by the sum of the quark box (and crossed box) diagram contribution to the photon-gluon interaction.

To apply Eq.(1) for SF at low Q^2 we change the low Q^2 asymptotics of the QCD coupling constant within hard structure functions. We have used the so called "freezing" procedure

in the "soft" form, when the argument of the strong coupling constant is shifted from Q^2 to $Q^2 + M^2$ [10]. Then $\alpha_s = \alpha_s(Q^2 + M^2)$. For massless quarks $M = m_\rho$ and for massive ones with mass m_Q, $M = 2m_Q$.

To calculate the SF $F_2^{c,b}$ and $F_L(x, Q^2)$ we used the hard SF $\hat{C}_{2,L}^g(x, Q^2, m^2, k_T^2)$ from Ref. [9, 11][a] and two UGD $\mathcal{A}(x, \mathbf{k}_T^2, \mu^2)$ obtained in our previous paper [13]. These UGD are determined by a convolution of the non-perturbative starting distribution $\mathcal{A}_0(x)$ and CCFM evolution denoted by $\bar{\mathcal{A}}(x, \mathbf{k}_T^2, \mu^2)$:

$$x\mathcal{A}(x, \mathbf{k}_T^2, \mu^2) \;=\; \int dz \mathcal{A}_0(z) \frac{x}{z} \bar{\mathcal{A}}(\frac{x}{z}, \mathbf{k}_T^2, \mu^2), \tag{2}$$

where

$$x\mathcal{A}_0(x) \;=\; N x^{-B_g}(1-x)^{C_g}(1-D_g x). \tag{3}$$

The parameters N, B_g, C_g, D_g of $\mathcal{A}_0$ were determined in the fits to F_2 and F_2^c data [14, 15] independently (see [13]) Fig. 1 shows the two different UGD. The small x behaviour of these UGD is very different[b].

To calculate the SF $F_2^b(x, Q^2)$ and $F_L(x, Q^2)$ we took $m_c = 1.4$ GeV and $m_b = 4.75$ GeV and used the $m^2 = 0$ limit of the above Eq. 1 to evaluate the corresponding lightquark contributions to the F_L. Fig. 2 shows the F_2^b as a function of x at fixed Q^2. Fig.3 shows the F_L as a function of x at fixed Q^2. Fig. 4 shows the SF $F_L(Q^2)$ at fixed W compared to the H1 data [18]. It is interesting to observe, that the measured F_2^b seems to prefer the UGD obtained from the fit to F_2 and is inconsitent with the one obtained from F_2^c. Also the measured F_L is better described with the UGD from the F_2 fit. In summary the k_T- factorization approach with the CCFM-evolved UGD obtained from the fits to the $F_2(x, Q^2)$ data reproduces the H1 data for SF $F_2^b(x, Q^2)$, $F_L(x, Q^2)$ and F_L at fixed W (see [13]). The UGD obtained from the fit to F_2^c seems to overshoot the measured F_2^b and F_L at small x. New experimental data for $F_L(x, Q^2)$ but also more precise measurements of the heavy quark structure functions are very important for a precise determination of the UGD.

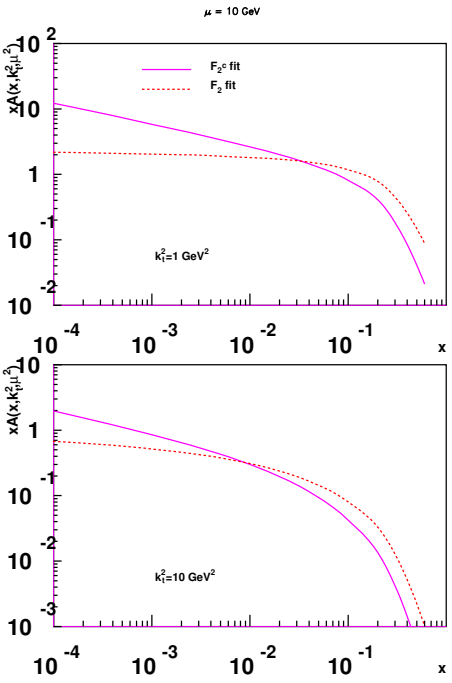

Figure 1: *UGD obtained in the fits to F_2^c (solid curve) and F_2 (dotted curve)*

[a] There is full agreement of our results with the formulae for the photoproduction of heavy quarks from Ref. [12].

[b] See also Ref. [16].

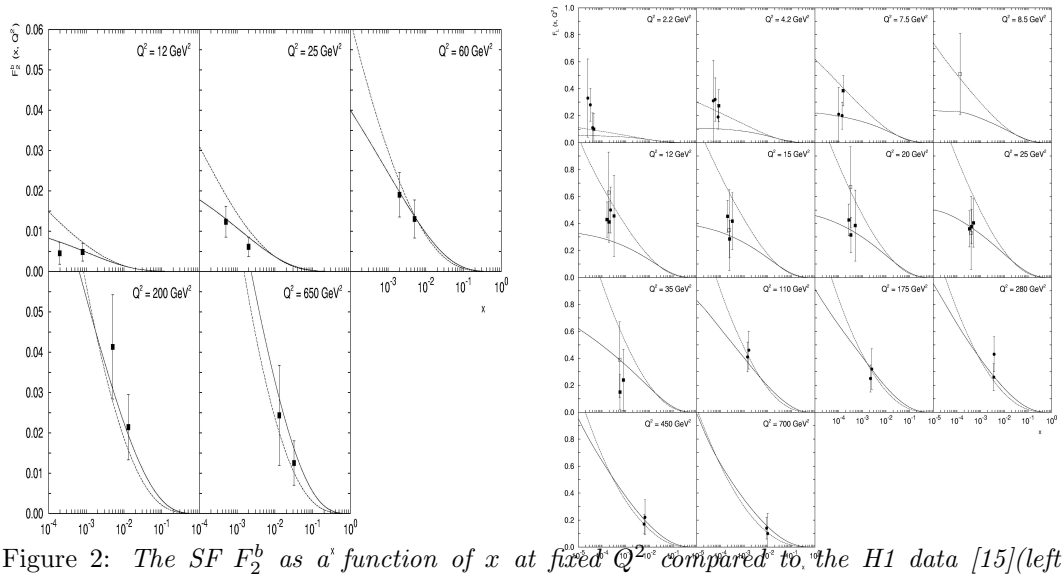

Figure 2: *The SF F_2^b as a function of x at fixed Q^2 compared to the H1 data [15](left panel) The solid and dotted lines are from CCFM-evolved UGD obtained from the fits to $F_2(x, Q^2)$ and $F_2^c(x, Q^2)$. The SF F_L as a function of x at fixed Q^2 compared to the H1 data [14, 17](right panel) The solid and dotted lines are from CCFM-evolved UGD obtained from the fits to $F_2(x, Q^2)$ and $F_2^c(x, Q^2)$.*

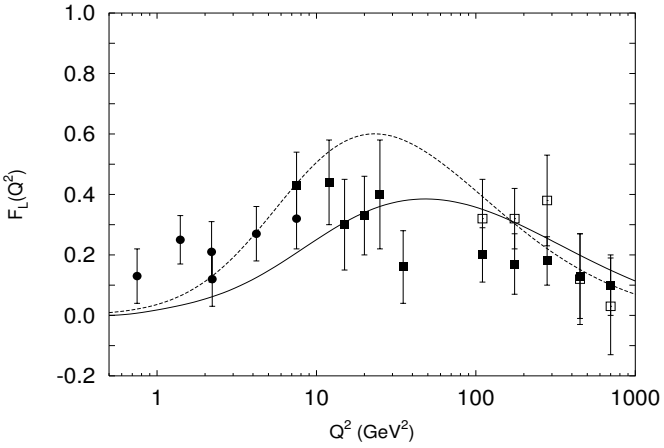

Figure 3: *The Q^2 dependence of SF $F_L(Q^2)$ at fixed $W = 276$ GeV compared to the H1 data [18] The solid and dotted lines are from CCFM-evolved UGD obtained from the fits to $F_2(x, Q^2)$ and $F_2^c(x, Q^2)$.*

References

[1] Slides:
http://indico.cern.ch/contributionDisplay.py?contribId=55&sessionId=8&confId=9499

[2] S. Catani, M. Ciafaloni and F. Hautmann, Nucl. Phys. **B366** 135 (1991);
J.C. Collins and R.K. Ellis, Nucl. Phys. **B360** 3 (1991);
E. Levin, M. Ryskin, Yu. Shabelski and A. Shuvaev Sov. J. Nucl. Phys. **53** 657 (1991).

[3] R.S. Thorne, arXiv:hep-ph/0511351;
C.D. White and R.S. Thorne, Phys. Rev. **D74** 014002 (2006); **D75** 034005 (2007).

[4] L.N. Lipatov, Sov. J. Nucl. Phys. **23** 338 (1976);
E.A. Kuraev, L.N. Lipatov and V.S. Fadin, Sov. Phys. JETP **44** 443 (1976); **45** 199 (1977);
Ya.Ya. Balitzki and L.N. Lipatov, Sov. J. Nucl. Phys. **28** 822 (1978);
L.N. Lipatov, Sov. Phys. JETP **63** 904 (1986).

[5] M. Ciafaloni, Nucl. Phys. **B296** 49 (1988);
S. Catani, F. Fiorani and G. Marchesini, Nucl. Phys. **B336** 18 (1995);
G. Marchesini, Nucl. Phys. **B445** 49 (1995).

[6] Bo Andersson et al. (Small x Collaboration), Eur. Phys. J. **C25** 77 (2002);
J. Andersen et al. (Small x Collaboration), Eur. Phys. J. **C25** 67(2002); **C35** 67 (2004)

[7] S. Catani and F. Hautmann, Nucl. Phys. **B427** 475 (1994);
S. Catani, arXiv:hep-ph/9608310.

[8] B.Badelek, J.Kwiecinski and A. Stasto, Z. Phys. **C74** 297 (1997).

[9] A.V. Kotikov, A.V. Lipatov and N.P. Zotov, Eur. Phys. J. **C26** 51 (2002).

[10] N. Nikolaev and B.M. Zakharov, Z. Phys. **C49** 607 (1991); **C53** 331 (1992).

[11] A.V. Kotikov, A.V. Lipatov and N.P. Zotov, Eur. Phys. J. **C27** 219 (2003).

[12] S. Catani, M. Ciafaloni and F. Hautmann, *Proceedings of the Workshop on Physics at HERA, Hamburg, Germany (1991), v. 2, p. 690.*

[13] H. Jung, A.V. Kotikov, A.V. Lipatov and N.P. Zotov, arXiv: hep-ph/0611093.

[14] H1 Collab., A. Adloff et al., Eur. Phys. J. **C21** 33 (2001).

[15] H1 Collab., A. Adloff et al., Phys. Lett. **B528** 199 (2002); A. Aktas et al., Eur. Phys. J. **C40** 349 (2005); **C45** 23 (2006).

[16] H. Jung, talk in HFS working group on DIS'07.

[17] H1 Collab., A. Aid et al., Phys. Lett. **B393** 452 (1997); N. Gogitidze, J. Phys. **G28** 751 (2002).

[18] E.M. Lobodzinska, *Proceedings of the DIS 2003, Gatchina, St. Petersburg, Russia, p. 93.*

Prompt Photon Production in p–A Collisions at LHC and the Extraction of Gluon Shadowing

François Arleo[1*] and Thierry Gousset[2]

1- CERN, PH Department, TH Division
1211 Geneva 23, Switzerland

2- SubaTech, Université de Nantes, Ecole des Mines de Nantes, IN2P3/CNRS
4 rue Kastler, 44307 Nantes, France

A report is given on the study of using prompt photon production at the LHC to probe the gluon nuclear density, and more specifically the shadowing ratio G_A/G_p that one could access in foreseen p–A runs.

1 Motivations

In the framework of collinear factorization in QCD, shadowing corrections show up as leading-twist modifications of per-nucleon parton densities

$$u_p(x,Q^2) \to u_A(x,Q^2),\ G_p(x,Q^2) \to G_A(x,Q^2),\ldots$$

that can also be described as deviations from 1 of ratios such as

$$R_G^{(A)}(x,Q^2) = G_A(x,Q^2)/G_p(x,Q^2).$$

These deviations are worth knowing in the shadowing region, i.e. $x < 10^{-1}$ for at least two reasons. First, collinear factorization is used to estimate cross sections for hard processes in A–A that are used as baselines from which observed deviations may signal genuine medium effects. Second, it is also interesting in itself for the understanding of the high-parton density regime in QCD.
Nuclear parton densities are extracted from deep inelastic scattering and Drell-Yan data [2]. Several global fits, including DGLAP evolution, exist (EKS [3], HKM [4], nDS [5]) as well as model calculations [6]. The recent *NLO* analysis from de Florian and Sassot [5] is used in the following. One important point which motivates the present analysis is the practically unconstrained amount of glue in a nucleus.

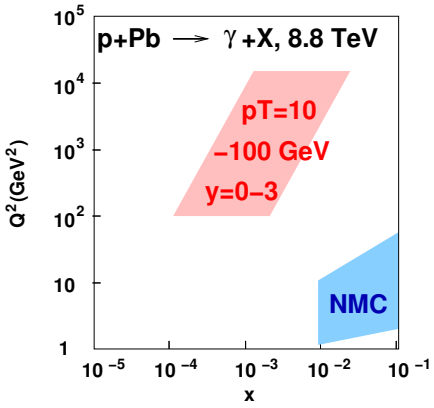

Figure 1: x, Q^2 regions of both NMC and prompt photons at LHC.

*On leave from Laboratoire d'Annecy-le-Vieux de Physique Théorique (LAPTH), UMR 5108 du CNRS ass ociée à l'Université de Savoie, B.P. 110, 74941 Annecy-le-Vieux Cedex, France

2 Inclusive photons

Prompt photons are produced at the parton level and do not result from the decay of a produced hadron such as a π^0. Prompt photon production at large p_T has a cross section

$$\begin{aligned} d\sigma(p+p\to\gamma+X) \overset{\text{LO}}{=}\ & u_1 * \bar{u}_2 * d\hat{\sigma}(u+\bar{u}\to\gamma+g) + \\ & u_1 * G_2 * d\hat{\sigma}(u+g\to\gamma+u) + \cdots + \\ & u_1 * G_2 * D_u^{\gamma} * d\hat{\sigma}(u+g\to u+g) + \cdots \end{aligned}$$

On the right-hand side, the first two lines are examples of *direct* production, whereas the third line shows a *fragmentation* channel. In the kinematical region discussed below, direct production and fragmentation are of comparable importance. For direct production, the Compton channel (second line) is one order of magnitude stronger than the annihilation one (first line).

The cross section

$$\frac{d^3\sigma}{dyd^2p_T}(p+p\to\gamma+X)$$

can be studied as a function of s, p_T, and y. It has been measured at several energies, with various projectiles, giving a rather rich phenomenology. Collider data are fairly well described by pQCD at NLO [7].

The ratio

$$R_{pA} = \frac{d\sigma(p+A\to\gamma+X)}{A\,d\sigma(p+p\to\gamma+X)}$$

is studied at $\sqrt{s} = 8.8$ TeV as a function of $x_T = p_T/(\sqrt{s}/2)$ and y with INCNLO [8], assuming either proton or nuclear parton densities. The result is shown in Fig. 2.

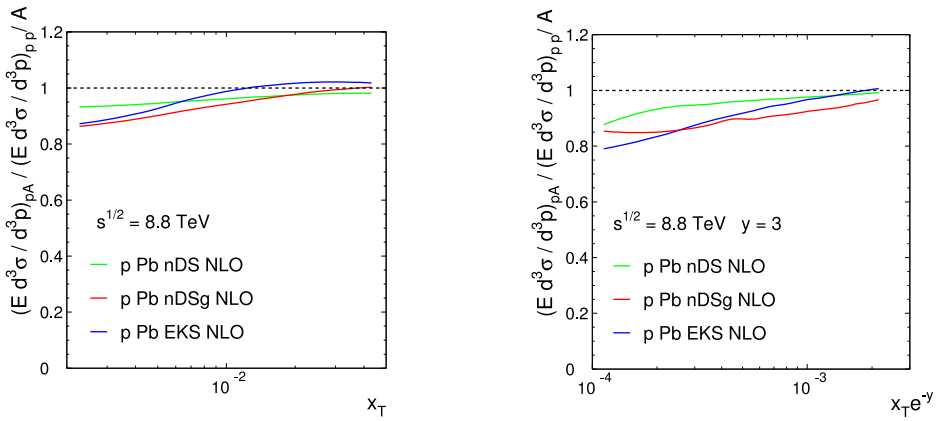

Figure 2: Ratio of inclusive photons at $y = 0$ and $y = 3$ in p–Pb over p–p collisions at $\sqrt{s} = 8.8$ TeV.

The shadowing ratio, R_{pA} is plotted vs $x_T e^{-y}$ that is indicative of the x_2 region probed in the target. The process is sensitive to modifications of parton densities and to the change of isospin composition.

3 Isolated photons

In order to cut out the π^0 background, it is often useful to select prompt photon candidates by way of an isolation criterion. This also eliminates to a large extent the fragmentation component. As a consequence, a direct extraction of shadowing ratios can be devised.

For the direct channel the cross section writes $d\sigma = f_1 * f_2 * d\hat{\sigma}$. The x region probed is selected by the behavior of the parton densities. Ratios such as $R_G = G_A/G_p$ show much less variation. Therefore an approximate expression of $d\sigma_{pA}$ can be obtained by factorizing the parton density ratio out of the convolution. At which x this factorization takes place? To answer this, a closer look to the convolution is necessary.

At leading order, the Compton cross section is

$$\frac{d^3\sigma}{dyd^2p_T} \propto \int dv \quad F^{(1)}\left(\frac{x_T e^y}{2v}\right) G^{(2)}\left(\frac{x_T e^{-y}}{2(1-v)}\right)\left(1-v+\frac{1}{1-v}\right) + G^{(1)}\left(\frac{x_T e^y}{2v}\right) F^{(2)}\left(\frac{x_T e^{-y}}{2(1-v)}\right)\left(v+\frac{1}{v}\right), \tag{1}$$

where $F^{(1)}(x)$ ($F^{(2)}(x)$) stands for the projectile (target) structure function $F_2(x)$ divided by x. At small x_T (and not-too-large $|y|$), $F(x) \sim Ax^{-a}$ and $G(x) \sim Bx^{-b}$ which translates into $F \times G \propto v^a(1-v)^b$. Since a and b are positive and close to each other the change $R \to R(x_T e^{-y})$ is suggested. At $y = 0$, both terms in Eq. (1) contributes the same amount in p–p and the nuclear production ratio is $\approx 0.5\,(R_G + R_{F_2})$. At $y = 3$, the second term in Eq. (1) is suppressed relative to the first and the nuclear production ratio is $\approx R_G$.

The nuclear ratio for isolated photons was computed with JETPHOX [7], using an isolation criterion: $E_T^{\rm had}/p_T^\gamma \leq 0.1$ in a cone of radius $R = 0.4$ around the photon. The result is shown in Fig. 3 (open circles) and compared with $0.5\,(R_G + R_{F_2})$ (dash-dotted line).

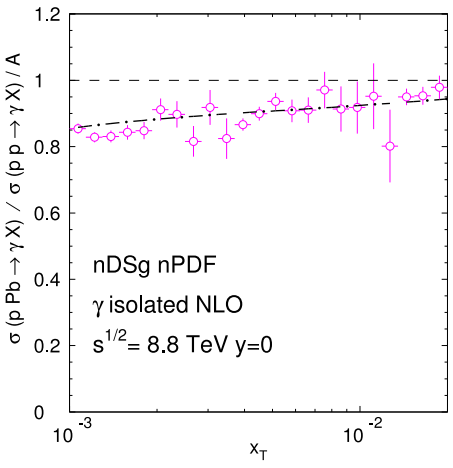

Figure 3: Ratio of isolated photons produced at $y = 0$ in p–Pb over p–p collisions at $\sqrt{s} = 8.8$ TeV.

4 Outlook

Nuclear modifications up to 20% are expected from the extrapolation of the fits made to NMC data and used here to predict nuclear production ratios in prompt photon production at the LHC. This represents challenging measurements, especially because of systematic uncertainties that should be further investigated. It also requires the same energy for p–p and p–A or some extrapolation.

References

[1] Slides:
`http://indico.cern.ch/contributionDisplay.py?contribId=50&sessionId=8&confId=9499`

[2] M. Arneodo, Phys. Rep. **240** 301 (1994).

[3] K. Eskola, V. Kolhinen and C. Salgado, Eur. Phys. J. **9** 61 (1999).

[4] M. Hirai, S. Kumano and M. Miyama, Phys. Rev. **D64** 034003 (2001).

[5] D. de Florian and R. Sassot, Phys. Rev. **D69** 074028 (2004).

[6] N. Armesto, J. Phys. G **32** R367 (2006).

[7] P. Aurenche *et al*, Phys. Rev. **D73** 094007 (2006).

[8] P. Aurenche *et al*, Eur. Phys. J. **9** 107 (1999).

A Unified Approach to $e/\nu - N$ Deep Inelastic Scattering Cross Sections at all Q^2

Arie Bodek[1] and Un-ki Yang[2] *

1. Department of Physics and Astronomy, University of Rochester
Rochester, New York 14618, USA

2 School of Physics and Astronomy, The University of Manchester
Oxford Road, Manchester, M13 9PL U.K.

We present the results of a new scaling variable, ξ_w in modelling neutrino- and electron-nucleon scattering cross sections using effective leading order PDFs. Our model desribes all deep inelastic scattering charged lepton-nucleon scattering data including resonance data (HERA/NMC/BCDMS/SLAC/JLab) from very high Q^2 to very low Q^2 (down to photo-productin region), as well as CCFR neutrino data. Non-perturbative QCD effects at low Q^2 region turn out to be well described by this new scaling variable. Our model is currently used for neutrino oscillation experiments at few GeV region.

The field of neutrino oscillation physics has progressed from the discovery of neutrino oscillation [2] to the era of precision measurements of mass splitting and mixing angles. Currently, cross sections for neutrino interactions in the few GeV region have not been measured well. This results in large systematic uncertainties in the extraction of mass splitting and mixing parameters (e.g. by the MINOS, NOνA , K2K and T2K experiments). Therefore, reliable modeling of neutrino cross sections at low energies is essential for precise neutrino oscillations experiments. In the few GeV region, there are three types of neutrino interactions: quasi-elastic, resonance, and inelastic scattering. It is very challenging to disentangle each contribution separately, especially, resonance production versus deep inelastic scattering (DIS) contributions. There are large non-perturbative QCD corrections to the DIS contributions in this region.

Our approach is to relate neutrino interaction processes using a quark-parton model to precise charged-lepton scattering data. In a previous communication [3], we showed that our effective leading order model using an improved scaling variable ξ_w describes all deep inelastic scattering charged lepton-nucleon scattering data including resonance data (SLAC/BCDMS/NMC/HERA/Jlab) [4, 5] from very high Q^2 to very low Q^2 (down to photo-production region), as well as high energy CCFR neutrino data [6].

The proposed scaling variable, ξ_w is derived using energy momentum conservation, assuming massless initial state quarks bound in a proton of mass M.

$$\xi_w \;=\; \frac{2x(Q^2 + {M_f}^2 + B)}{Q^2[1 + \sqrt{1 + (2Mx)^2/Q^2}] + 2Ax}, \tag{1}$$

here, M_f is the final quark mass (zero except for charm-production in neutrino processes). The parameter A accounts for the higher order (dynamic higher twist) QCD terms in the form of an enhanced target mass term (the effects of the proton target mass are already taken into account using the exact form in the denominator of ξ_w). The parameter B accounts for the initial state quark transverse momentum and final state quark effective $\Delta {M_f}^2$ (originating from multi-gluon emission by quarks). This parameter also allows us to describe the data also in the photoproduction limit (all the way down to $Q^2 = 0$).

*Contact: ukyang@hep.man.ac.uk

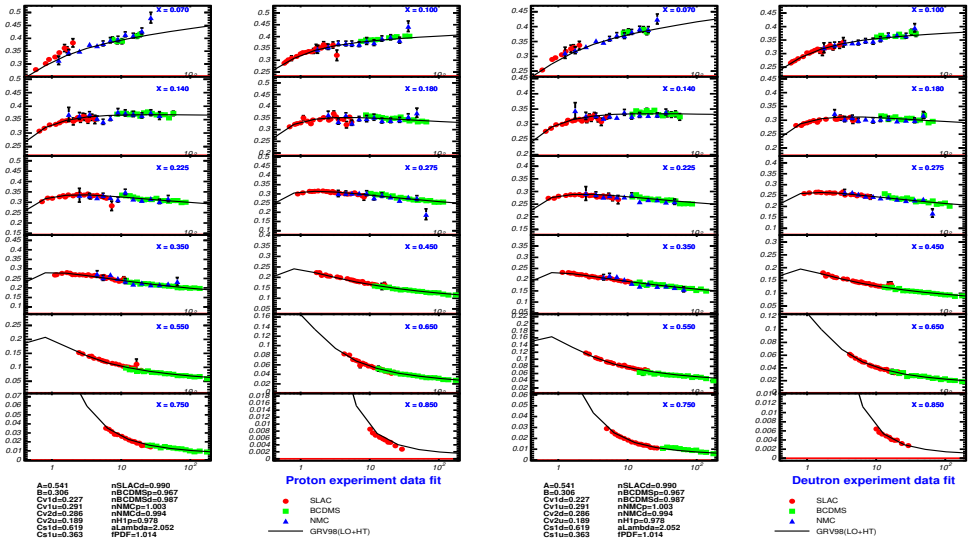

Figure 1: Comparisons of the predictions of our model to DIS F_2 proton data [left], deuteron data [right].

A brief summary of our effective leading order (LO) model is given as follows;

- The GRV98 LO PDFs [7] are used to describe the F_2 data at high Q^2 region.
- The scaling variable x is replaced with the improved scaling variable ξ_w (Eq. 1).
- All PDFs are modified by K factors to describe low Q^2 data in the photoproduction limit.

$$K_{sea}(Q^2) = \frac{Q^2}{Q^2 + C_s}, \qquad K_{valence}(Q^2) = [1 - G_D^2(Q^2)] \left(\frac{Q^2 + C_{v2}}{Q^2 + C_{v1}} \right), \tag{2}$$

  where $G_D = 1/(1+Q^2/0.71)^2$ is the proton elastic form factor. At low Q^2, $[1-G_D^2(Q^2)]$ is approximately $Q^2/(Q^2+0.178)$. Different values of the K factor are obtained for u and d quarks
- The evolution of the GRV98 PDFs is frozen at a value of $Q^2 = 0.80$. Thus, $F_2(x, Q^2 < 0.8) = K(Q^2) \times F_2(\xi, Q^2 = 0.8)$.
- Finally, we fit to all inelastic charged lepton scattering data (SLAC/BCDMS/NMC/H1) and photoproduction data on hydrogen and deuterium. We obtain excellent fits with; A=0.538, B=0.305, C_{v1}^d=0.202, C_{v1}^u=0.291, C_{v2}^d=0.255, C_{v2}^u=0.189, C_{s1}^d=0.621, C_{s1}^u=0.363, and χ^2/DOF =1874/1574. Because of the K factors to the PDFs, we find that the GRV98 PDFs need to be multiplied by a factor of 1.015.

The measured structure functions data are corrected for the relative normalizations and for nuclear binding effects [8] in the deuterium data. A separate charm pair production contribution using the photon-gluon fusion model is added to describe the HERA F_2 and photoproduction data. Our effective LO model describes various DIS and photo-production

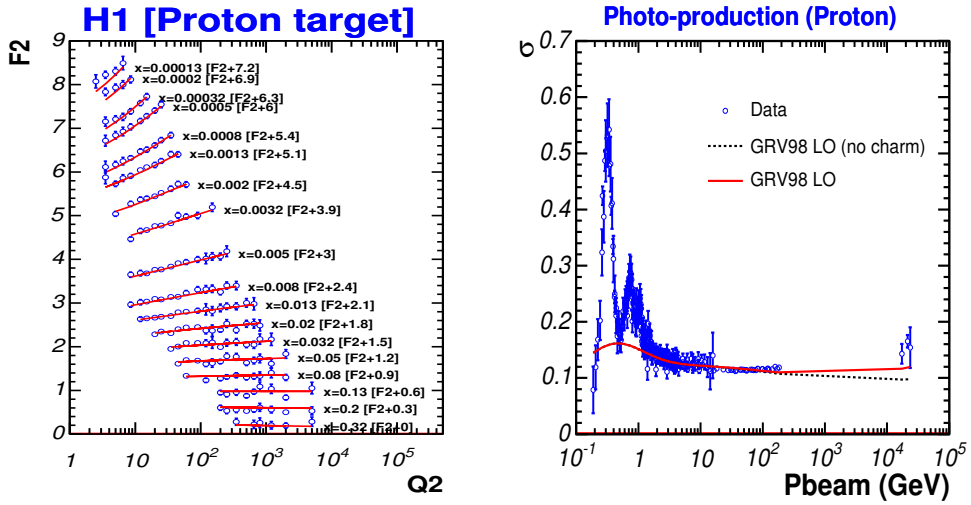

Figure 2: Comparisons of the predictions of our model to F_2 HERA [left], and photo-production data [right].

data down to the $Q^2 = 0$ limit, as shown in Fig. 1 and Fig. 2. We also find a good agreement with the most recent F_L data and F_2 data in the resonance region from the E94-110, and the JUPITER experiments [9] at Jlab, as shown in Fig. 3. Our predictions for F_L are obtained using our F_2 model and R_{1998} [10].

In neutrino scattering, there is an additional axial vector contribution, which is not zero at the $Q^2 = 0$ limit. At high Q^2, both axial and vector contributions are expected to be same. Thus, it is important to understand the axial-vector contribution at low Q^2 by comparing to future low energy neutrino data (e.g. MINERνA [11]). As a preliminary step, we compare the CCFR and CDHSW [12] high energy neutrino data with our model, assuming that the vector contribution is the same as the axial vector contribution. We find that the CCFR/CDHSW neutrino data are well described by our model.

We are currently working on constraining the low Q^2 axial vector contribution using low energy CDHSW and CHORUS [13] data. The form of the fits we plan to use is motivated by the Adler sum rule [14] for the axial vector contribution as follows:

$$K_{sea-ax}(Q^2) = \frac{Q^2 + C_{2s-ax}}{Q^2 + C_{1s-ax}}, \qquad K_{valence}(Q^2) = [1 - F_A^2(Q^2)] \left(\frac{Q^2 + C_{2v-ax}}{Q^2 + C_{1v-ax}} \right), \qquad (3)$$

where $F_A(Q^2) = -1.267/(1+Q^2/1.00)^2$. Nuclear effects for heavy target are also important and may be different for the vector and axial vector structure functions. Future measurements on the axial vector contribution from the MINERνA experiment will be important in constraining this model.

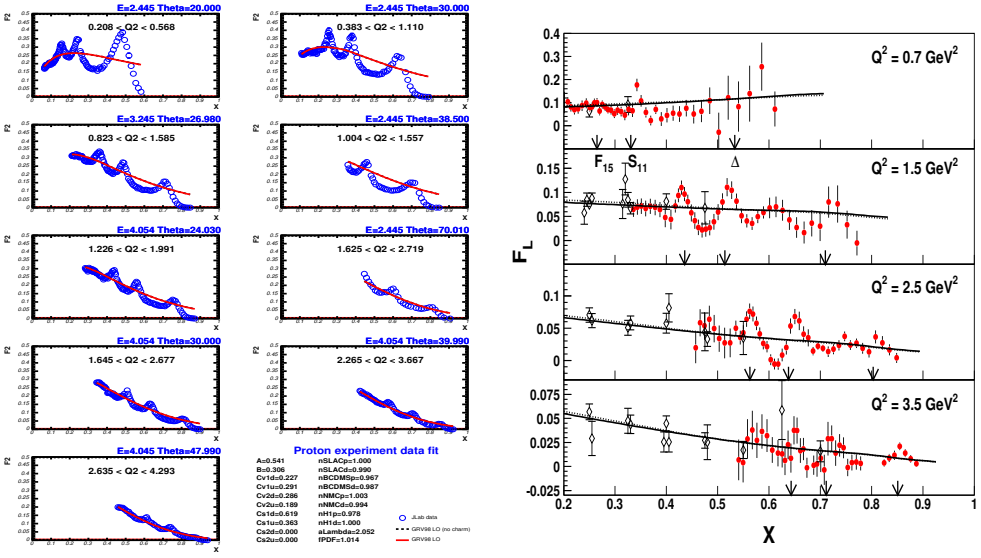

Figure 3: Comparisons of the predictions of our model to F_2 proton resonance data [left], and F_L proton data [right].

References

[1] Slides:
`http://indico.cern.ch/contributionDisplay.py?contribId=56&sessionId=8&confId=9499`

[2] S. Fukuda *et al.*, Phys. Rev. Lett. **85**, 3999 (2000); T. Toshito, hep-ex/0105023.

[3] A. Bodek and U. K. Yang, hep-ex/0308007.

[4] L. W. Whitlow *et al.* (SLAC-MIT), Phys. Lett. B **282**, 433 (1995); A. C. Benvenuti *et al.* (BCDMS), Phys. Lett. B**237**, 592 (1990); M. Arneodo *et al.* (NMC), Nucl. Phys. B**483**, 3 (1997).

[5] C. Keppel, Proc. of the Workshop on Exclusive Processes at High P_T, Newport News, VA, May (2002).]

[6] U. K. Yang, Ph.D. thesis, Univ. of Rochester, UR-1583 (2001).

[7] M. Gluck, E. Reya, A. Vogt, Eur. Phys. J **C5**, 461 (1998).

[8] U. K. Yang and A. Bodek, Phys. Rev. Lett. **82**, 2467 (1999), Eur. Phys. J. C**13**, 241 (2000).

[9] Y. Liang *et al.*, nucl-ex/0410027.

[10] K. Abe *et al.*, *Phys. Lett.* **B452**, 194 (1999).

[11] MINERνA Proposal, D. Drakoulakos *et al.*, hep-ex/0405002

[12] P. Berge *et al.* (CDHSW), Zeit. Phys. **C49**, 607 (1991).

[13] R. Oldeman, Proc. of 30th International Conference on High-Energy Physics (ICHEP 2000), Osaka, Japan, 2000.

[14] S. Adler, Phys. Rev. **143**, 1144 (1966); F. Gillman, Phys. Rev. **167**, 1365 (1968).

A Global Fit to Scattering Data with NLL BFKL Resummations

Chris White[1] * and Robert Thorne[2] †

1- NIKHEF, Kruislaan 409, Amsterdam 1098SJ - The Netherlands
2- Department of Physics and Astronomy, University College London, WC1E 6BT, UK

We perform a global parton fit to DIS and related data, including next-to-leading logarithmic (NLL) BFKL resummations in both the massless and massive sectors. The resummed fit improves over a standard next-to-leading order (NLO) DGLAP fit, with a positive definite gluon at the input scale as opposed to the negative gluon seen at NLO. Furthermore, the predicted longitudinal structure function is free of perturbative instability at small x, and the reduced cross-section shows a turnover at high y (absent in the NLO fit) consistent with the HERA data.

1 Small x Resummation

1.1 Motivation

Current and forthcoming particle collider experiments involve very high energies, such that the momentum fractions x of initial state partons are extremely small. The splitting functions that govern the evolution of parton densities $f_i(x, Q^2)$ with momentum scale Q^2, together with the coefficients that relate these partons to proton structure functions, are unstable at low Bjorken x values due to terms behaving like $x^{-1}\alpha_S^n \log^m(1/x)$ where $n \geq m+1$. Although the standard DGLAP theory (where the splitting and coefficient functions are considered at a fixed order in α_S) works well in parton fits, there is some evidence that a resummation of small x logarithms is necessary. Previous work has shown that a LL analysis fails to describe data well. One resums small x logarithms in the gluon density by solving the *BFKL equation* [2], an integral equation for the unintegrated gluon 4-point function. One then relates this gluon to structure functions using the k_T factorisation formalism [3, 4] to obtain the resummed splitting and coefficient functions.

1.2 Solution of the BFKL equation

Introducing the double Mellin transformed unintegrated gluon density:

$$f(\gamma, N) = \int_0^\infty (k^2)^{-\gamma-1} \int_0^1 dx x^N f(x, k^2), \tag{1}$$

the NLL BFKL equation in (N, γ) space is a double differential equation in γ:

$$\frac{d^2 f(\gamma, N)}{d\gamma^2} = \frac{d^2 f_I(\gamma, Q_0^2)}{d\gamma^2} - \frac{1}{\bar{\beta}_0 N}\frac{d(\chi_0(\gamma) f(\gamma, N))}{d\gamma} + \frac{\pi}{3\bar{\beta}_0^2 N}\chi_1(\gamma) f(\gamma, N),$$

*Supported by the Dutch Foundation for Fundamental Research on Matter (FOM).
†Royal Society University Research Fellow

with $\bar{\beta}_0 = 3/(\pi\beta_0)$. The derivatives in γ arise from the use of the LO running coupling $\alpha_S(k^2) = 1/(\beta_0 \log k^2/\Lambda^2)$ in momentum space, and $\chi_n(\gamma)$ is the Mellin transform of the n^{th}-order BFKL kernel. One may solve this to give:

$$f(N,\gamma) = \exp\left(-\frac{X_1(\gamma)}{\bar{\beta}_0 N}\right) \int_\gamma^\infty A(\tilde{\gamma}) \exp\left(\frac{X_1(\tilde{\gamma})}{\bar{\beta}_0 N}\right) d\tilde{\gamma} \tag{2}$$

for some $A(\tilde{\gamma})$ and $X_1(\tilde{\gamma})$. One would ideally like to factorise the perturbative from the non-perturbative physics to make contact with the collinear factorisation framework. This can be achieved (up to power-suppressed corrections) by shifting the lower limit of the integral in equation (2) from $\gamma \to 0$. Then one finds for the integrated gluon:

$$\mathcal{G}(N,t) = \mathcal{G}_E(N,t)\mathcal{G}_I(Q_0^2,N), \tag{3}$$

where the perturbative piece is:

$$\mathcal{G}_E^1(N,t) = \frac{1}{2\pi\imath} \int_{1/2-\imath\infty}^{1/2+\imath\infty} \frac{f^{\beta_0}}{\gamma} \exp\left[\gamma t - X_1(\gamma,N)/(\bar{\beta}_0 N)\right] d\gamma, \tag{4}$$

where X_1 can be derived from $\chi_0(\gamma)$ and $\chi_1(\gamma)$, and f^{β_0} is a known function of γ. Structure functions have a similar form:

$$\mathcal{F}_E^1(N,t) = \frac{1}{2\pi\imath} \int_{1/2-\imath\infty}^{1/2+\imath\infty} \frac{h(\gamma,N) f^{\beta_0}}{\gamma} \exp\left[\gamma t - X_1(\gamma,N)/(\bar{\beta}_0 N)\right] d\gamma, \tag{5}$$

where $h(\gamma,N)$ is a NLL order impact factor coupling the virtual photon with the BFKL gluon. If all impact factors are known, one can derive all necessary splitting and coefficient functions in double Mellin space (within a particular factorisation scheme) by taking ratios of the above quantities. The non-perturbative dependence then cancels, and one obtains results in momentum and x space by performing the inverse Mellin integrals either numerically or analytically. The exact NLL impact factors are not in fact known, but the LL results supplemented with the correct kinematic behaviour of the gluon have been calculated [5, 6]. We have shown that one expects them to approximate well the missing NLL information in the true impact factors [7].

Consistent implementation of small x resummations in the massive sector requires the definition of a variable flavour number scheme that allows the massive impact factors to be disentangled in terms of heavy coefficient functions and matrix elements. We have devised such a scheme, the DIS(χ) scheme [8]. With resummations in both the massive and massless sectors, one has everything necessary to carry out a global fit to DIS and related data. First, the resummed splitting and coefficient functions are combined with the NLO DGLAP results using the prescription:

$$P^{tot.} = P^{NLL} + P^{NLO} - \left[P^{NLL(0)} + P^{NLL(1)}\right],$$

where the subtractions remove the double counted terms, namely the LO and NLO (in α_S) parts of the resummed results. Then the resulting improved splitting and coefficient functions interpolate between the resummed results at low x, and the conventional DGLAP results at high x.

2 Results

The resummed splitting functions P_+ ($\simeq P_{gg} + 4/9P_{qg}$ at small x) and P_{qg} are shown in figure 1. One sees that the LL BFKL results are much more divergent than the standard NLO results, which are known to describe data well. The addition of the running coupling to the LL BFKL equation suppresses this divergence, but it is still unacceptable. Inclusion of the NLL BFKL kernel, however, leads to a significant dip of the splitting functions below the NLO results. This dip is also observed in other resummation approaches [9, 10] and has an important consequence in the global fit in that it resolves the tension between the Tevatron jet data (which favour a larger high x gluon) and the H1 and ZEUS data (which prefer a higher low x gluon). By momentum conservation, one cannot increase the gluon at both low and high x in a standard NLO DGLAP fit. This is possible in the resummed approach, due to the dip in the splitting functions.

Indeed, the gluon distribution at the parton input scale of $Q_0^2 = 1\text{GeV}^2$ is positive definite over the entire x range. This is in contrast to a NLO fit, where the gluon distribution is negative at small x for low Q^2 values. Whilst a negative gluon is not disallowed, it can lead to negative structure functions which are unphysical. The resummed gluon, however, leads to a prediction for the longitudinal structure function that is positive and growing at small x and Q^2, in contrast to fixed order results which show a significant perturbative instability.

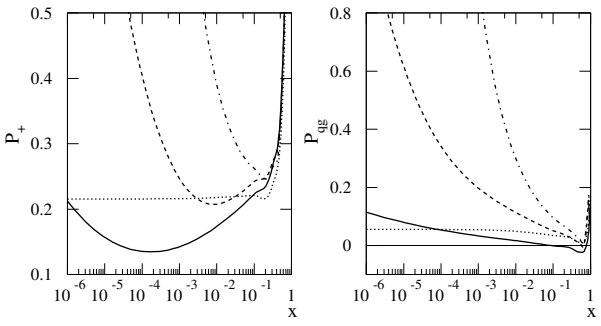

Figure 1: Splitting functions in the DIS scheme for $n_f = 4$, $t = \log(Q^2/\Lambda^2) = 6$: NLL+NLO (solid); LL with running coupling + LO (dashed); LL + LO (dot-dashed); NLO (dotted).

A consequence of a more sensible description for F_L is that a turnover is observed in the reduced cross-section $\tilde{\sigma} = F_2 - y^2/[1+(1-y)^2]\,F_L$ at high y. As seen in figure 2, this is required by the HERA data. Furthermore, this feature is missing in NLO fits (but present at NNLO). Thus the resummations lead to qualitatively different behaviour, consistent with known consequences of higher orders in the fixed order expansion. Overall, we find very compelling evidence of the need for BFKL effects in describing proton structure [11].

References

[1] Slides:
http://indico.cern.ch/contributionDisplay.py?contribId=250&sessionId=8&confId=9499

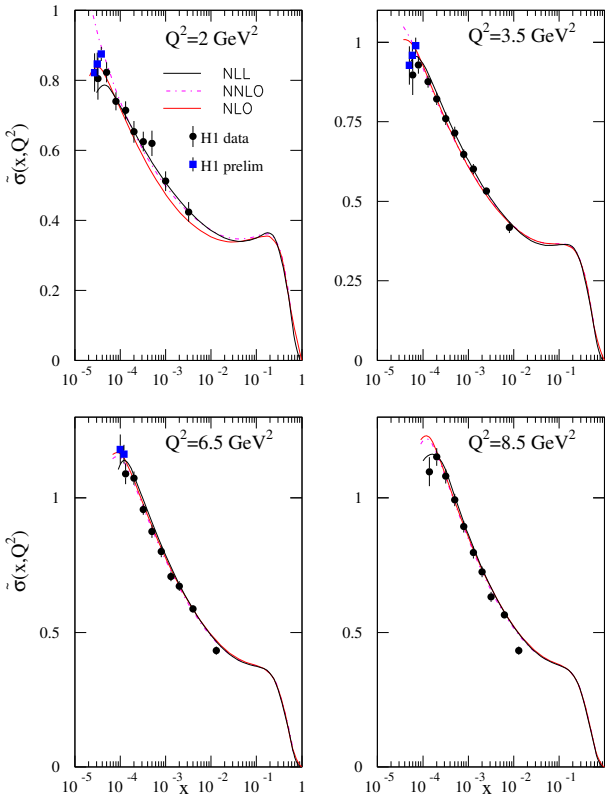

Figure 2: Reduced cross-section data, compared with both resummed and fixed order predictions.

[2] L.N. Lipatov, *Sov. J. Nucl. Phys.*, **23** (1976) 338;
E.A. Kuraev, L.N. Lipatov and V.S. Fadin, *Sov. Phys. JETP*, **45** (1977) 199;
Ya.Ya. Balitsky and L.N. Lipatov, *Sov. J. Nucl. Phys.* **28** (1978) 822.

[3] J. C. Collins and R. K. Ellis *Nucl. Phys. Proc. Suppl.* **18C** (1991) 80–85.

[4] S. Catani, M. Ciafaloni, and F. Hautmann *Phys. Lett.* **B242** (1990) 97.

[5] A. Bialas, H. Navelet, and R. Peschanski. *Nucl. Phys.*, B593:438–450, 2001.

[6] C. D. White, R. Peschanski, and R. S. Thorne. *Phys. Lett.*, B639:652–660, 2006.

[7] C. D. White and R. S. Thorne. *Eur. Phys. J.*, C45:179–192, 2006.

[8] C. D. White and R. S. Thorne. *Phys. Rev.*, D74:014002, 2006.

[9] Guido Altarelli, Richard D. Ball, and Stefano Forte. *Nucl. Phys.*, B742:1–40, 2006.

[10] M. Ciafaloni, D. Colferai, G. P. Salam, and A. M. Stasto. *Phys. Rev.*, D68:114003, 2003.

[11] C. D. White and R. S. Thorne. *Phys. Rev.*, D75:034005, 2007.

BFKL Effects in Azimuthal Angle Correlations of Forward Jets

Agustín Sabio Vera[1] and Florian Schwennsen[2] *

1- Physics Department - Theory Division CERN
CH–1211 Geneva 23 - Switzerland

2- II. Institut für Theoretische Physik - Universität Hamburg
Luruper Chaussee 149 D–22761 Hamburg - Germany

The azimuthal angle correlation of Mueller–Navelet jets at hadron colliders is studied in the NLO BFKL formalism. We highlight the need of collinear improvements in the kernel to obtain good convergence properties and we obtain better fits for the Tevatron data than at LO accuracy. We also estimate these correlations for larger rapidity differences available at the LHC.

1 BFKL cross sections

In [2] we continue the study initiated in [3] of azimuthal correlations in Mueller–Navelet jets [4] using the Balitsky–Fadin–Kuraev–Lipatov (BFKL) equation in the next–to–leading (NLO) approximation [5]. We investigate normalized differential cross sections which are quite insensitive to parton distribution functions and read

$$\frac{d\hat{\sigma}}{d^2\vec{q}_1 d^2\vec{q}_2} = \frac{\pi^2\bar{\alpha}_s^2}{2}\frac{1}{q_1^2 q_2^2}\int\frac{d\omega}{2\pi i}e^{\omega \mathrm{Y}} f_\omega\left(\vec{q}_1,\vec{q}_2\right),$$

where $\bar{\alpha}_s = \alpha_s N_c/\pi$, $\vec{q}_{1,2}$ are the transverse momenta of the tagged jets, and Y their relative rapidity. The Green's function carries the Y–dependence and follows the NLO equation, $\left(\omega - \bar{\alpha}_s\hat{K}_0 - \bar{\alpha}_s^2\hat{K}_1\right)\hat{f}_\omega = \hat{1}$, which acts on the basis including the azimuthal angle, $\langle\vec{q}|\,\nu,n\rangle = \frac{1}{\pi\sqrt{2}}\left(q^2\right)^{i\nu-\frac{1}{2}}e^{in\theta}$. As Y increases the azimuthal dependence is driven by the kernel. This is why we use the LO jet vertices which are simpler than at NLO. The differential cross section in the azimuthal angle $\phi = \theta_1 - \theta_2 - \pi$, with θ_i being the angles of the two tagged jets, is

$$\begin{aligned}
\frac{d\hat{\sigma}\left(\alpha_s,\mathrm{Y},p_{1,2}^2\right)}{d\phi} &= \frac{\pi^2\bar{\alpha}_s^2}{4\sqrt{p_1^2 p_2^2}}\sum_{n=-\infty}^{\infty}e^{in\phi}\,\mathcal{C}_n\left(\mathrm{Y}\right), \\
\mathcal{C}_n\left(\mathrm{Y}\right) &= \frac{1}{2\pi}\int_{-\infty}^{\infty}\frac{d\nu}{\left(\frac{1}{4}+\nu^2\right)}\left(\frac{p_1^2}{p_2^2}\right)^{i\nu}e^{\chi\left(|n|,\frac{1}{2}+i\nu,\bar{\alpha}_s(p_1p_2)\right)\mathrm{Y}}, \\
\chi\left(n,\gamma,\bar{\alpha}_s\right) &= \bar{\alpha}_s\chi_0\left(n,\gamma\right)+\bar{\alpha}_s^2\left(\chi_1\left(n,\gamma\right)-\frac{\beta_0}{8N_c}\frac{\chi_0\left(n,\gamma\right)}{\gamma\left(1-\gamma\right)}\right).
\end{aligned}$$

The eigenvalue of the LO kernel is $\chi_0\left(n,\gamma\right) = 2\psi\left(1\right) - \psi\left(\gamma+\frac{n}{2}\right) - \psi\left(1-\gamma+\frac{n}{2}\right)$, with ψ the logarithmic derivative of the Euler function. The action of $\hat{K}_1$, in $\overline{\mathrm{MS}}$ scheme, can be found

*Supported by the Graduiertenkolleg "Zukünftige Entwicklungen in der Teilchenphysik"

in [6]. The full cross section only depends on the $n = 0$ component, $\hat{\sigma} = \frac{\pi^3 \bar{\alpha}_s^2}{2\sqrt{p_1^2 p_2^2}} \mathcal{C}_0(\mathrm{Y})$. The average of the cosine of the azimuthal angle times an integer projects out the contribution from each of these angular components:

$$\frac{\langle \cos(m\phi) \rangle}{\langle \cos(n\phi) \rangle} = \frac{\mathcal{C}_m(\mathrm{Y})}{\mathcal{C}_n(\mathrm{Y})} \tag{1}$$

The normalized differential cross section is

$$\frac{1}{\hat{\sigma}} \frac{d\hat{\sigma}}{d\phi} = \frac{1}{2\pi} \sum_{n=-\infty}^{\infty} e^{in\phi} \frac{\mathcal{C}_n(\mathrm{Y})}{\mathcal{C}_0(\mathrm{Y})} = \frac{1}{2\pi} \left\{ 1 + 2 \sum_{n=1}^{\infty} \cos(n\phi) \langle \cos(n\phi) \rangle \right\}. \tag{2}$$

The BFKL resummation is not stable at NLO [7, 8]. In the gluon–bremsstrahlung scheme our distributions become unphysical. To improve the convergence we impose compatibility with renormalization group evolution in the DIS limit [9] for all angular components. A good scheme is the angular extension of that discussed in [8], first proposed in [7]:

$$\begin{aligned} \omega = {} & \bar{\alpha}_s (1 + \mathcal{A}_n \bar{\alpha}_s) \left\{ 2\psi(1) - \psi\left(\gamma + \frac{|n|}{2} + \frac{\omega}{2} + \mathcal{B}_n \bar{\alpha}_s\right) \right. \\ & \left. - \psi\left(1 - \gamma + \frac{|n|}{2} + \frac{\omega}{2} + \mathcal{B}_n \bar{\alpha}_s\right) \right\} + \bar{\alpha}_s^2 \left\{ \chi_1(|n|, \gamma) - \frac{\beta_0}{8 N_c} \frac{\chi_0(n, \gamma)}{\gamma(1-\gamma)} \right. \\ & \left. - \mathcal{A}_n \chi_0(|n|, \gamma) \right) + \left(\psi'\left(\gamma + \frac{|n|}{2}\right) + \psi'\left(1 - \gamma + \frac{|n|}{2}\right) \right) \left(\frac{\chi_0(|n|, \gamma)}{2} + \mathcal{B}_n \right) \Bigg\}, \end{aligned} \tag{3}$$

where $\mathcal{A}_n$ and $\mathcal{B}_n$ are collinear coefficients. After this collinear resummation our observables have a good physical behavior and are independent of the renormalization scheme.

2 Phenomenology

The DØ [11] collaboration analyzed data for Mueller–Navelet jets at $\sqrt{s} = 630$ and 1800 GeV. For the angular correlation LO BFKL predictions were first obtained in [12, 13] and failed to describe the data estimating too much decorrelation. An exact fixed NLO analysis using JETRAD underestimated the decorrelation, while HERWIG was in agreement with the data.

In Fig. 2 we compare the Tevatron data for $\langle \cos\phi \rangle = \mathcal{C}_1/\mathcal{C}_0$ with our LO, NLO and resummed predictions. For Tevatron's cuts, where the transverse momentum for one jet is 20 GeV and for the other 50 GeV, the NLO calculation is instable under renormalization scheme changes. The convergence of our observables is poor whenever the coefficient associated to zero conformal spin, $\mathcal{C}_0$, is involved. If we eliminate this coefficient by calculating the ratios defined in Eq. (1) then the predictions are very stable, see Fig. 2. The full angular dependence studied at the Tevatron by the DØ collaboration was published in [11]. In Fig. 1 we compare this measurement with the predictions obtained in our approach. For the differential cross section we also make predictions for the LHC at larger Y in Fig. 3. Our calculation is not exact and we estimated several uncertainties, which are represented by gray bands.

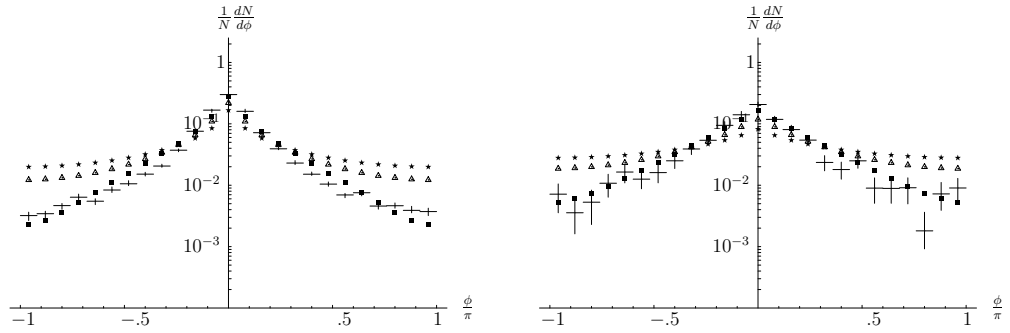

Figure 1: $\frac{1}{N}\frac{dN}{d\phi}$ in a $p\bar{p}$ collider at $\sqrt{s}$=1.8 TeV using a LO (stars), NLO (squares) and resummed (triangles) BFKL kernel. Plots are shown for Y = 3 (left) and Y = 5 (right).

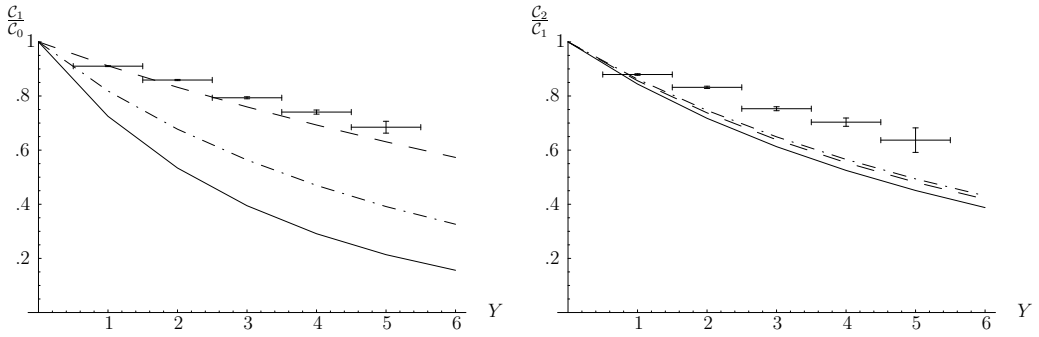

Figure 2: Left: $\langle\cos\phi\rangle = \mathcal{C}_1/\mathcal{C}_0$ and Right: $\frac{<\cos 2\phi>}{<\cos\phi>} = \frac{\mathcal{C}_2}{\mathcal{C}_1}$, at a $p\bar{p}$ collider with $\sqrt{s} = 1.8$ TeV for BFKL at LO (solid) and NLO (dashed). The results from the resummation presented in the text are shown as well (dash–dotted).

3 Conclusions

We have presented an analytic study of NLO BFKL corrections in azimuthal angle decorrelations for Mueller–Navelet jets at hadron colliders. We found that the intercepts for non–zero conformal spins have good convergence. The zero conformal spin component needs of a collinear improvement to get stable results. Uncertainties in our study can be reduced using Monte Carlo techniques. We compared to the data extracted at the Tevatron many years ago. Our results improve with respect to the LO BFKL predictions but show too much azimuthal angle decorrelation. The LHC at CERN will have larger rapidity differences and will be a very useful tool to investigate the importance of BFKL effects in multijet production [15].

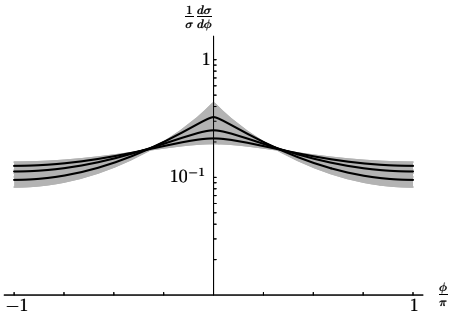

Figure 3: $\frac{1}{\sigma}\frac{d\sigma}{d\phi}$ in our resummation scheme for rapidities Y = 7, 9, 11 from top to bottom. The gray band reflects the uncertainty in s_0 and in the renormalization scale μ.

References

[1] Slides:
`http://indico.cern.ch/contributionDisplay.py?contribId=281&sessionId=8&confId=9499`

[2] A. Sabio Vera, F. Schwennsen, Nucl. Phys. B **776** (2007) 170.

[3] A. Sabio Vera, Nucl. Phys. B **746** (2006) 1.

[4] A. H. Mueller, H. Navelet, Nucl. Phys. B **282** (1987) 727.

[5] V.S. Fadin, L.N. Lipatov, Phys. Lett. B **429**, 127 (1998);
G. Camici, M. Ciafaloni, Phys. Lett. B **430**, 349 (1998).

[6] A. V. Kotikov, L. N. Lipatov, Nucl. Phys. B **582** (2000) 19.

[7] G. P. Salam, JHEP **9807**, 019 (1998).

[8] A. Sabio Vera, Nucl. Phys. B **722** (2005) 65.

[9] M. Ciafaloni, D. Colferai, G. P. Salam, A. M. Stasto, Phys. Rev. D **68** (2003) 114003.

[10] B. Abbott *et al.*, Phys. Rev. Lett. **84** (2000) 5722.

[11] S. Abachi *et al.*, Phys. Rev. Lett. **77** (1996) 595.

[12] V. Del Duca, C. R. Schmidt, Phys. Rev. D **49** (1994) 4510.

[13] W. J. Stirling, Nucl. Phys. B **423** (1994) 56.

[14] C. L. Kim, FERMILAB-THESIS-1996-30.

[15] J. Bartels, A. Sabio Vera, F. Schwennsen, JHEP **0611** (2006) 051.

Parton Distributions for LO Calculations

R.S. Thorne[1]*, A. Sherstnev[2] and C. Gwenlan[1]

1- Department of Physics and Astronomy, University College London, WC1E 6BT, UK

2- Cavendish Laboratory, University of Cambridge, Cambridge, CB3 0HE, UK

We present a study of the results obtained combining LO partonic matrix elements with different orders of partons distributions. These are compared to the *best* prediction using NLO for both matrix elements and parton distributions. The aim is to determine which parton distributions are most appropriate to use in those cases where only LO matrix elements are available, e.g. as in many Monte Carlo generators. Both LO and NLO parton distributions have faults so a modified *optimal* LO set is suggested.

The combination of the order of the parton distribution function (pdf) and the accompanying matrix element is an important issue [1]. It has long been known that LO pdfs in some regions of x and Q^2 are qualitatively different to NLO (and NNLO) pdfs (see [2]) due to important missing corrections in splitting functions or coefficient functions for structure functions which are used to determine the pdfs. Nevertheless, LO pdfs are usually thought to be the best choice for use with LO matrix elements, such as those available in many LO Monte Carlo programs, though all such results should be treated with care. Recently it has been suggested that NLO pdfs may be more appropriate [3], since NLO cross-section corrections are often small. There has already been an investigation of the use of NLO pdfs for the underlying event [4]. There is a big difference in the results when using CTEQ6L and CTEQ6.1M pdfs [5] due to the changes in the gluon, though agreement can be reached by significant retuning. This will affect predictions for other quantities.

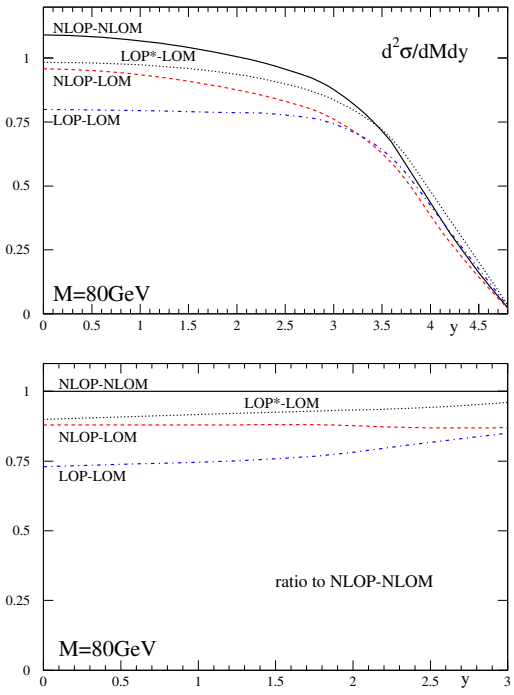

Figure 1: Drell-Yan distribution at the LHC.

In this article we address the differences in predictions obtained for a variety of physical quantities combining different pdfs with LO matrix elements. In each case NLO pdfs combined with NLO matrix elements represent the best prediction – the *truth*. We interpret the features of the results and investigate how a best set of pdfs for use with LO matrix elements may be obtained.

First, let us recall how LO pdfs tend to differ from NLO pdfs. The most marked differences are for light quarks at high x and the gluon distribution at low x. The coefficient functions for structure functions have $\ln(1-x)$ enhancements at higher perturbative order. This means the high-x quarks are smaller as the order increases. The quark-gluon splitting function P_{qg} develops a small-x divergence at NLO (with further $\ln(1/x)$ enhancements at

*Royal Society University Research Fellow

higher orders), so the small x gluon needs to be bigger at LO in order to fit structure function evolution. Indeed, for $Q^2 \sim 1-2$ GeV^2 the NLO gluon is flat or valence-like at small x while at LO it grows much more quickly. These features show up in cross-sections.

Let us start with the simple example of Drell-Yan production of vector-bosons from quark-antiquark annihilation as a function of rapidity at fixed invariant mass = 80GeV, i.e. appropriate for W, Z production, at the LHC. The NLO correction [6] for Drell-Yan production is quite significant, being positive for all rapidity and roughly 12% in this case. The absolute predictions and the ratios of LO matrix element results to the *truth* are show in Fig. 1. We see that indeed we are nearer to the *truth* with LO matrix elements and NLO pdfs [7] than LO matrix elements and LO pdfs [8]. Both LO ME results are too small, but NLO pdfs are closer and a better shape. LO pdfs and the LO matrix elements have the wrong shape being low at central rapidity but increasing at high rapidity where the high-x quark is enhanced at LO. Hence, NLO pdfs seem more appropriate here.

However, there is a small x counter-example. Consider the production of charm in low Q^2 DIS at HERA energies. The NLO matrix elements [9] contain a divergence at small x which is not present at LO. Using NLO pdfs the LO matrix element result is well below the *truth* at low scales and the shape is totally wrong, as seen in Fig. 2. The LO gluon is very large at small x since it has been extracted with missing P_{qg} enhancement at small x, and this compensates the missing small x divergence in the matrix element – LO pdfs and LO matrix elements are more sensible with a compensation between failings in both. Using LO pdfs and NLO matrix elements the result is extremely large since there is a double counting of the small x divergence.

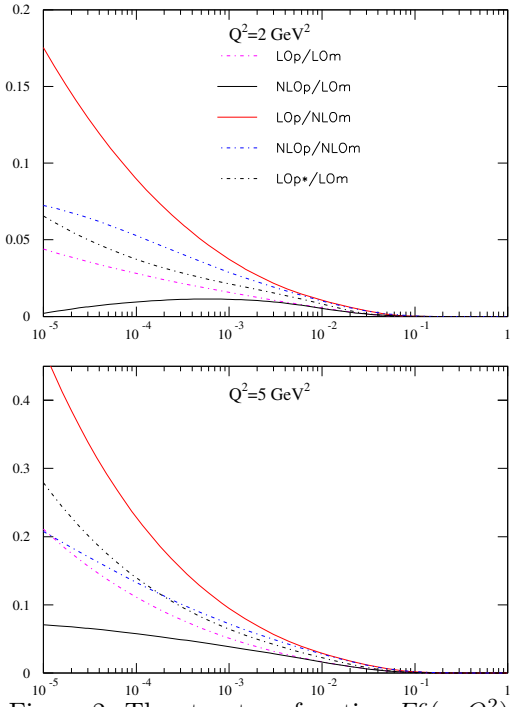

Figure 2: The structure function $F_2^c(x, Q^2)$.

From these two examples we can conclude that sometimes NLO pdfs are better to use if only the LO matrix elements are known, and we can get significant problems with the size and shape if LO pdfs are used. However, we can be completely wrong, particularly at small x, if we use NLO pdfs due to *zero*-counting of small-x terms. Can we find some optimal definition of pdfs which have most desirable features? In order to make progress we need to better understand the difference between LO and NLO pdfs. The missing higher order terms in $\ln(1-x)$, $1/x$ and $\ln(1/x)$ in coefficient functions and/or evolution leads to pdfs at LO which are bigger at $x \to 1$ and at $x \to 0$ in order to compensate. However, from the momentum sum rule there are then not enough partons to go around, and enhancements in some regions lead to depletion in other regions, particularly quarks at $0.001 \leq x \leq 0.1$. This leads to a bad global fit at LO [8] – partially compensated by the LO extraction of $\alpha_S(M_Z^2)$ being ~ 0.130 to help speed evolution, and explains the underestimate of the Drell-Yan production at the LHC at more central rapidities.

This obvious source of problems has lead to a suggestion [10] that relaxing the momentum

sum rule could make LO pdfs rather more like NLO pdfs in the regions where they are normally too small. The resulting pdfs would still be bigger than NLO where necessary, i.e. the high-x quarks and low-x gluon, but would not be depleted elsewhere. It is also useful to use the NLO definition of α_S. Because of quicker running at NLO, the LO and NLO couplings with the same value of $\alpha_S(M_Z^2)$ are very different at lower scales where DIS data used in global fits exists. Near $Q^2 = 1$ GeV^2 the NLO coupling with $\alpha_S(M_Z^2) = 0.120$ is similar to the LO coupling with $\alpha_S(M_Z^2) = 0.130$. Hence, the use of the NLO coupling helps alleviate the discrepancy between pdfs at different orders. Indeed, the NLO coupling already used in some CTEQ LO pdfs [5] and in LO Monte Carlo generators. Relaxing momentum conservation for input pdfs and using the NLO definition of α_S does dramatically improve the quality of the LO global fit, $\chi^2 = 3066/2235$ for the standard LO fit becoming $\chi^2 = 2691/2235$, with a big improvement in the comparison to HERA data. The momentum carried by the input pdfs goes up to 113%. Using the NLO definition the value of $\alpha_S(M_Z^2) = 0.121$.

The modified pdfs, which we denote by LO*, become much more similar to NLO pdfs, in particular at small x the LO* quark distributions evolve as quickly as at NLO and are similar for for $x \sim 0.001 - 0.01$. Similarly $g(x, Q^2)$ is significantly bigger at LO* than at LO, and much bigger than NLO at small x. This will help when used with LO matrix elements for gluon-gluon initiated processes (e.g. Higgs production) where K-factors are often much greater than unity. We now look at the LO* pdfs in our first two examples, see Figs. 1 and 2. For Drell-Yan production at the LHC the LO* pdfs lead to shape of comparable quality as the NLO pdfs and the normalization is better. For the charm structure function comparing all possibilities the LO* pdfs and LO matrix elements are indeed closest to the *truth*.

parton	matrix element	σ (mb)
NLO	NLO	41.5
LO	LO	24.8
LO*	LO	34.8
NLO	LO	16.8

Table 1: $\sigma(b\bar{b})$ totals.

There is a similar conclusion for hadro-production of b quarks at LHC which probes low $x \sim 0.001$. We consider $\sigma(b\bar{b})$ where the initial b quark has $p_T > 10$ GeV and $|\eta| \leq 5$ using a NLO event generator [11] and LO calculations [12]. The total cross-sections are shown in Table. 1. The NLO pdfs and LO matrix element are clearly worst. We also illustrate final state p_T and rapidity distributions in Fig. 3 with $p_T > 18$ GeV for the b quark after showering. Again the best absolute predictions with LO matrix elements uses LO* pdfs and the worst NLO pdfs. However, in this case there is always a problem with the shape as function of p_T. The NLO matrix element has a large positive effect at high p_T and very high η. It is impossible for any parton shape to account for all NLO corrections.

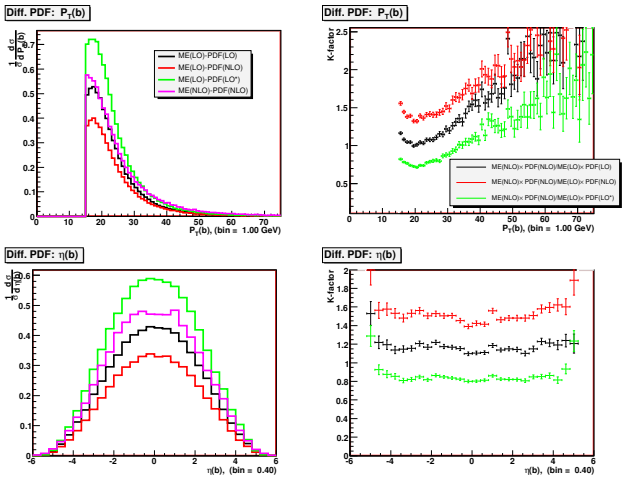

Figure 3: The b cross section at the LHC.

We also look at very high-E_T jet production [13] at the LHC in Fig. 4. Ignoring the lowest E_T, where hadronization and underlying event and possibly small x physics are an issue,

the LO and LO* pdfs with the LO matrix elements are of comparable quality to NLO pdfs. LO and NLO pdfs when combined with LO matrix elements produce results which deviate in opposite directions at high E_T. Also shown is the prediction from LO** pdfs, which have an additional constraint for a harder high-x gluon (this being small at LO even with momentum conservation relaxed). This changes the results little compared to the use of the LO* pdfs.

Hence, we can conclude that a fixed prescription of either LO or NLO pdfs with LO matrix elements or LO Monte Carlo generators will lead each to incorrect results in some cases. To try to improve this situation we have suggested an optimal set of pdfs for LO calculations, the LO* pdfs, which are essentially LO but with various modifications to make their features more NLO-like. These seem to work reasonably well and happen to achieve some of the features obtained by modifying pdfs in a process dependent fashion for use in Monte Carlo generators/resummations discussed in e.g. [14]. More study is underway. However, sometimes NLO matrix element corrections qualitatively change the features of the predictions for a physical process, regardless of how careful one is with pdfs, since new types of partonic process open up. This must always be borne in mind, and accounted for if possible.

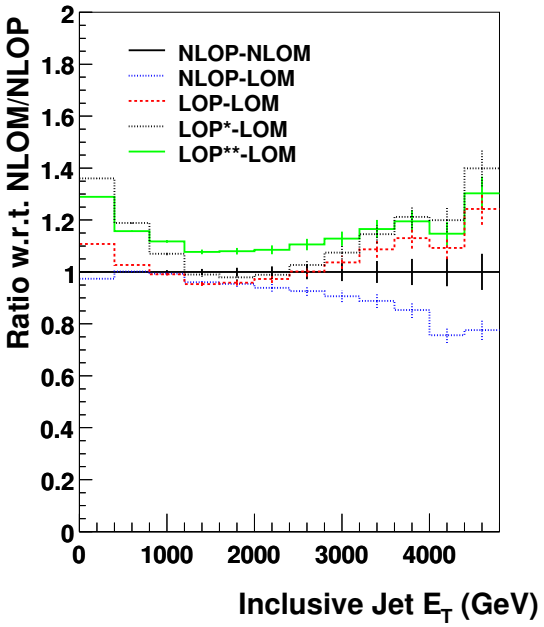

Figure 4: The dijet cross-section at the LHC.

References

[1] Slides: http://indico.cern.ch/contributionDisplay.py?contribId=252&sessionId=8&confId=9499

[2] R. S. Thorne, plenary talk at *DIS06, Tsukuba, Japan, 20-24 Apr 2006*, pp.35, hep-ph/0606307.

[3] J. M. Campbell, J. W. Huston and W. J. Stirling, Rept. Prog. Phys. **70** (2007) 89.

[4] Section by R. Field in M. G. Albrow *et al.* [TeV4LHC QCD Working Group], "Tevatron-for-LHC report of the QCD working group," hep-ph/0610012.

[5] J. Pumplin, D. R. Stump, J. Huston, H. L. Lai, P. Nadolsky and W. K. Tung, JHEP **0207** (2002) 012.

[6] J. Kubar, M. Le Bellac, J. L. Meunier and G. Plaut, Nucl. Phys. B **175** (1980) 251.

[7] A.D. Martin, R.G. Roberts, W.J. Stirling and R.S. Thorne, Phys. Lett. **B604** 61 (2004).

[8] A. D. Martin, R.G. Roberts, W.J. Stirling and R.S. Thorne, Phys. Lett. B **531** (2002) 216.

[9] E. Laenen *et al.*, Nucl. Phys. **B392** (1993) 162; B.W. Harris and J. Smith, Nucl. Phys. **B452** (1995) 109.

[10] T. Sjöstrand, private comments.

[11] S. Frixione and B.R. Webber, JHEP **0206** (2002) 029; S. Frixione *et al.*, JHEP **0308** (2003) 007.

[12] E.Boos *et al.* [CompHEP Collaboration], Nucl. Instrum. Meth. **A534** (2004) 250; A.S. Belyaev *et al.*, hep-ph/0101232; T. Sjöstrand, S. Mrenna and P. Skands, JHEP **0605** (2006) 026.

[13] W.T. Giele, E.W.N. Glover and D.A. Kosower, Nucl.Phys. **B403** (1993) 633.

[14] S. Mrenna, hep-ph/9902471.

New Global Fit to the Total Photon-Proton Cross-Section σ_{L+T} and to the Structure Function F_2

Dominik Gabbert[1] and Lara De Nardo[1,2]

1- DESY, 22603 Hamburg, Germany
2-TRIUMF, Vancouver, British Columbia V6T 2A3, Canada

A fit to world data on the photon-proton cross section σ_{L+T} and the unpolarised structure function F_2 is presented. The 23-parameter ALLM model based on Reggeon and Pomeron exchange is used. Cross section data were reconstructed to avoid inconsistencies with respect to R of the published F_2 data base. Parameter uncertainties and correlations are obtained.

1 Introduction

Deep-inelastic scattering on protons has been studied precisely in the last decades at various energies covering a large kinematic region provided by collider and fixed target experiments, thus providing us with our modern understanding of the proton structure.

The inclusive DIS cross section in the one-photon-exchange approximation is related to the unpolarized structure function $F_2(x, Q^2)$ and the ratio $R(x, Q^2)$ of longitudinal and transverse photo-absoption cross section:

$$\frac{d^2\sigma}{dx\ dQ^2} = \frac{4\pi\alpha_{em}^2}{Q^4}\frac{F_2(x,Q^2)}{x}\left\{1 - y - \frac{Q^2}{4E^2} + \left(1 - \frac{2m^2}{Q^2}\right)\frac{y^2 + Q^2/E^2}{2[1 + R(x,Q^2)]}\right\} . \qquad (1)$$

Here, Q^2 is the square of the photon 4-momentum and $x = Q^2/2M\nu$ with the proton mass M and the photon energy ν in the proton rest frame.

From Eq. (1) it follows that a measurement of the cross section alone is not sufficient to extract both, F_2 and R, and that only a variation of the beam energy E in the proton rest frame for fixed kinematic conditions can give access to both quantities. Alternatively, F_2 can be extracted using parameterizations of world data on R: two common examples are R_{1990} [1] and R_{1998}[2], whose differences reflect the states of world knowledge at the time they were obtained. The sensitivity of the cross section to R increases with y as it can be seen in Eq. (1). The discrepancy in the extracted values of F_2 using the two parameterizations can exceed 4% in the regions of maximum y.

The structure function F_2 is related to the photon-proton cross section σ_{L+T} by the expression:

$$\sigma_{L+T} = \frac{4\pi^2\alpha_{em}}{Q^4}\frac{Q^2 + 4M^2x^2}{1 - x}F_2 . \qquad (2)$$

For virtual photons this relation employs the Hand convention for the virtual photon flux. It was used for technical convenience of consistency between real and virtual photon processes.

This paper reports on a new fit of the photon-proton cross section σ_{L+T} which reflects the recent world knowlege on the cross section and is self-consistent with respect to the use of R, since the cross sections were reconstructed in each case using the value of R that had been used to extract the published values of F_2. A result of the fit is a facility to calculate values of F_2 based on a single parameterization of $R = R_{1998}$.

2 The fit

The fit includes 2740 data points: 574 from the SLAC experiments E49a, E49b, E61, E87, E89a, E89b [3]; 292 from NMC [4]; 787 from H1 [5]; 570 from ZEUS [6]; 91 from E665 [7]; 229 points from BCDMS [8]. Real photon data comprise 196 points from Ref. [9] and 1 from ZEUS [10].

The ALLM functional form is a 23-parameter model of σ_{L+T} where F_2 is described by Reggeon and Pomeron exchange, valid for $W^2 > 4\,\mathrm{GeV}^2$, i.e., above the resonance region, and any Q^2 including the real γ process. Here, W^2 is the invariant squared mass of the photon-proton system. For details on the parameterization we refer to the original papers [11, 12]. The new fit was performed by minimizing the χ^2 defined in Eq. (3) where $D_{i,k} \pm \sigma_{i,k}^{stat} \pm \sigma_{i,k}^{syst}$ are the values of σ_{L+T} for data point i within the data set k, δ_k is the normalization uncertainty in data set k quoted by the experiment, ν_k is a parameter for the normalization of each data set in units of the normalization uncertainty, $T(\mathbf{p}, W^2, Q^2)$ is the functional form of the 23-parameter ALLM parameterization.

The χ^2 takes into account uncorrelated point-by-point statistical and systematic uncertainties and overall normalization uncertainties. The normalization parameters ν_k determine the size of the shifts in units of the normalization uncertainties δ_k.

Parameter	ALLM97	this fit	uncertainty
$m_0^2(\mathrm{GeV}^2)$	0.31985	0.454	0.137
$m_{\mathcal{P}}^2(\mathrm{GeV}^2)$	49.457	30.7	13.4
$m_{\mathcal{R}}^2(\mathrm{GeV}^2)$	0.15052	0.118	0.224
$Q_0^2(\mathrm{GeV}^2)$	0.52544	1.13	1.47
$\Lambda_0^2(\mathrm{GeV}^2)$	0.06527	0.06527	-
$a_{\mathcal{P}1}$	-0.0808	-0.105	0.024
$a_{\mathcal{P}2}$	0.44812	-0.496	0.154
$a_{\mathcal{P}3}$	1.1709	1.31	1.04
$b_{\mathcal{P}4}$	0.36292	-1.43	2.31
$b_{\mathcal{P}5}$	1.8917	4.50	2.46
$b_{\mathcal{P}6}$	1.8439	0.554	0.531
$c_{\mathcal{P}7}$	0.28067	0.339	0.093
$c_{\mathcal{P}8}$	0.22291	0.128	0.104
$c_{\mathcal{P}9}$	2.1979	1.17	1.14
$a_{\mathcal{R}1}$	0.584	0.373	0.150
$a_{\mathcal{R}2}$	0.37888	0.994	0.443
$a_{\mathcal{R}3}$	2.6063	0.781	0.524
$b_{\mathcal{R}4}$	0.01147	2.70	1.84
$b_{\mathcal{R}5}$	3.7582	1.83	2.39
$b_{\mathcal{R}6}$	0.49338	1.26	1.33
$c_{\mathcal{R}7}$	0.80107	0.837	0.500
$c_{\mathcal{R}8}$	0.97307	2.34	2.34
$c_{\mathcal{R}9}$	3.4942	1.79	0.93

Table 1: Parameters of the functional form used in the ALLM parameterization [11]. Results of the ALLM97 fit [12] without uncertainties in comparison to the results discussed in this paper with uncertainties. These uncertainties correspond only to the diagonal elements of the full covariance matrix which must be used to calculate uncertainties in F_2 or cross sections. The parameter Λ_0^2 has no uncertainty as it was fixed in the fit.

$$\chi^2(\mathbf{p}, \boldsymbol{\nu}) = \sum_{i,k} \frac{[D_{i,k}(W^2,Q^2)\cdot(1+\delta_k\nu_k) - T(\mathbf{p},W^2,Q^2)]^2}{({\sigma_{i,k}^{stat}}^2 + {\sigma_{i,k}^{syst}}^2)\cdot(1+\delta_k\nu_k)^2} + \sum_k \nu_k^2$$
$$\approx \sum_{i,k} \frac{[D_{i,k}(W^2,Q^2) - T(\mathbf{p},W^2,Q^2)\cdot(1-\delta_k\nu_k)]^2}{{\sigma_{i,k}^{stat}}^2 + {\sigma_{i,k}^{syst}}^2} + \sum_k \nu_k^2 \,, \qquad (3)$$

In order to keep the number of free parameters as small as possible, the normalization

parameters are determined analytically in each minimization step using the relation

$$\nu_k = \frac{\sum_i \delta_k T_{i,k}(T_{i,k} - D_{i,k})/\sigma_{i,k}^2}{\sum_i T_{i,k}^2 \delta_k^2/\sigma_{i,k}^2 + 1}, \tag{4}$$

obtained by requiring $\partial\chi^2/\partial\nu_k = 0$ in the context of the approximation for χ^2 in the second line of Eq. (3); here $\sigma_{i,k}^2 = {\sigma_{i,k}^{stat}}^2 + {\sigma_{i,k}^{syst}}^2$. This separate extraction is possible since the normalization parameters are not correlated and depend only on the involved data points and the functional parameters. The resulting fit has a reduced χ^2 equal to 0.94; the contributions from each data set, together with the normalization parameters can be found in Ref. [13]. Table 1 shows the final parameters from this fit with the corresponding uncertainties and, for comparison, the parameters from the ALLM97 fit. Figure 1 shows the new fit in comparison with world data and with the ALLM97 fit. A full comparison between the two fits is not possible as in the ALLM97 fit parameter uncertainties were not provided. Presumely, these uncertainties are larger than the those of the new fit, since the size of the current data set is nearly twice as large. The uncertainties in the cross sections calculated from the fit as represented by the error bands in the figure are much smaller than individual error bars on the original data points because of the smoothness constraint inherent in the fitted model. The fit evaluated at any kinematic point is effectively an average of a number of data points.

In conclusion, a new fit of world data on σ_{L+T} and F_2 is presented. Such a fit is consistent in the choice of the R parameterization R_{1998}. Also, for the first time, parameter and fit uncertainties are calculated. A subroutine that allows the calculation of σ_{L+T} and F_2 with their fit uncertainties is available upon request from the authors.

3 Acknowledgments

The authors would like to thank E.C. Aschenauer, A. Miller and W.-D. Nowak for valuable discussions.

References

[1] L.W. Whitlow *et al.*, Phys. Lett. **B250** 193 (1990).
[2] K. Abe *et al.*, Phys. Lett. **B452** 194 (1999).
[3] L.W. Whitlow *et al.*, PhD thesis, Stanford University, SLAC Report 357 (1990).
[4] M. Arneodo *et al.*, Nucl. Phys. **B83** 3 (1997).
[5] A. Aid *et al.*, Nucl. Phys. **B470** 3 (1996); C. Adloff *et al.*, Nucl. Phys. **B497** 3 (1997); C. Adloff *et al.*, Eur. Phys. J. **C13** 609 (2000); C. Adloff *et al.*, Eur. Phys. J. **C19** 269 (2001); C. Adloff *et al.*, Eur. Phys. J. **C21** 33 (2001); C. Adloff *et al.*, Eur. Phys. J. **C30** 1 (2003).
[6] M. Derrick *et al.*, Z. Phys. **C72** 399 (1996); M. Derrick *et al.*, Z. Phys. **C69** 607 (1996); J. Breitweg *et al.*, Phys. Lett. **B407** 432 (1997); J. Breitweg *et al.*, Phys. Lett. **B487** 53 (2000); S. Chekanov *et al.*, Eur. Phys. J. **C21** 443 (2001).
[7] M.R. Adams *et al.*, Phys. Rev. **D54** 3006 (1996).
[8] A.C. Benvenuti *et al.*, Phys. Lett. **B223** 485 (1989).
[9] W.-M. Yao *et al.*, J. of Phys. **G33** 1 (2006).
[10] M. Derrick *et al.*, Z. Phys. **C63** 391 (1994).
[11] H. Abramowicz *et al.*, Phys. Lett. **B269** 465 (1991).
[12] H. Abramowicz and A. Levy, hep-ph/9712415.
[13] Slides:
`http://indico.cern.ch/contributionDisplay.py?contribId=52&sessionId=8&confId=9499`

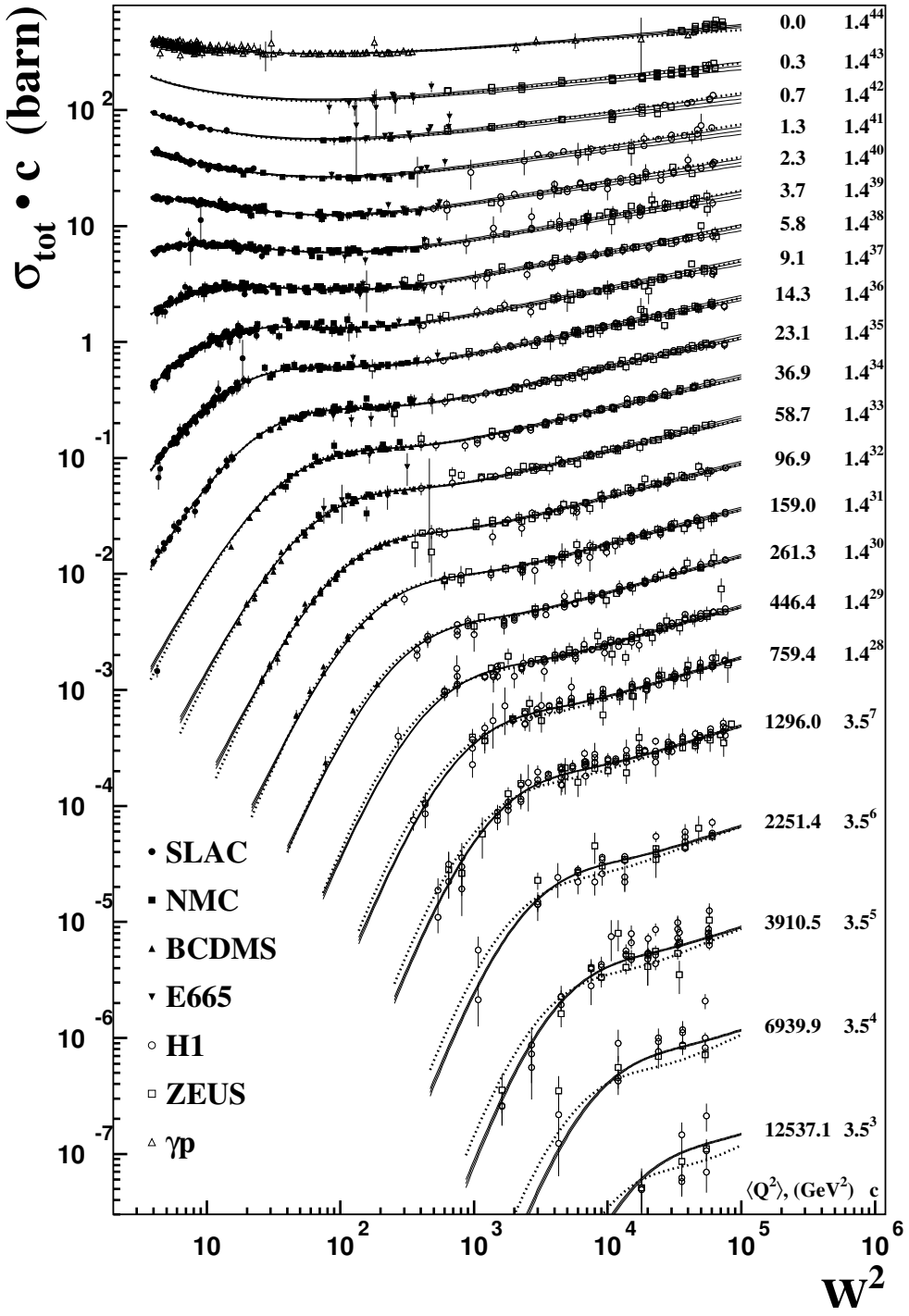

Figure 1: The new fit for σ_{L+T} (continuous curves, with upper and lower uncertainty bands) compared with the ALLM97 fit (dashed curves) and overlapped with data, as a function of W^2 in bins of Q^2.

Progress on Neural Parton Distributions

J. Rojo[1], R. D. Ball[2], L. Del Debbio[2], S. Forte[3], A. Guffanti[2],
J. I. Latorre[4], A. Piccione[5] and M. Ubiali[2] (The NNPDF Collaboration)

1.- LPTHE, CNRS UMR 7589, Universités Paris VI-Paris VII, F-75252, Paris Cedex 05, France

2.- School of Physics, University of Edinburgh, Edinburgh EH9 3JZ, Scotland

3.- Dipartimento di Fisica, Università di Milano,
and INFN, Sezione di Milano, Via Celoria 16, I-20133 Milano, Italy

4.- Departament d'Estructura i Constituents de la Matèria,
Universitat de Barcelona, Diagonal 647, E-08028 Barcelona, Spain

5.- INFN, Sezione di Genova, via Dodecaneso 33, I-16146 Genova, Italy

We give a status report on the determination of a set of parton distributions based on neural networks. In particular, we summarize the determination of the nonsinglet quark distribution up to NNLO, we compare it with results obtained using other approaches, and we discuss its use for a determination of α_s.

1 Introduction

The LHC will require an approach to the search for new physics based on the precision techniques which are customary at lepton machines [2, 3]. This has recently led to significant progress in the determination of parton distribution functions (PDFs) of the nucleon. The main recent development has been the availability of sets of PDFs with an estimate of the associated uncertainty [4, 5, 6]. However, the standard approach to the determination of the uncertainty on parton distributions has several weaknesses, such as the lack of control on the bias due choice of a parametrization and, more in general, the difficulty in giving a consistent statistical interpretation to the quoted uncertainties.

These problems have stimulated various new approaches to the determination of PDFs [8], in particular the neural network approach, first proposed in Ref. [7]. The basic idea is to combine a Monte Carlo sampling of the probability measure on the space of functions that one is trying to determine [8] with the use of neural networks as universal unbiased interpolating functions. In Refs. [7, 9] this strategy was successfully applied to a somewhat simpler problem, namely, the construction of a parametrization of existing data on the DIS structure function $F_2(x, Q^2)$ of the proton and neutron. The method was proven to be fast and robust, to be amenable to detailed statistical studies, and to be in many respects superior to conventional parametrizations of structure functions based on a fixed functional form.

The determination of a parton set involves the significant complication of having to go from one or more physical observables to a set of parton distributions. Recently [10] most of the technical complications required for the construction of a neural parton set have been tackled and solved in the process of constructing a determination of the quark isotriplet parton distribution. This work will be reviewed here. Also, based on this work, we will present preliminary results on the determination of α_s and a determination of the variation in χ^2 which corresponds to a one-sigma variation of the underlying parton distributions. Work to apply the techniques of [10] to the singlet sector is at an advanced stage [11].

2 Determination of the nonsinglet quark distribution

The first application of the neural network approach to parton distributions, a determination of the NS parton distribution $q_{\rm NS}(x,Q_0^2) = (u+\bar{u}-d+\bar{d})(x,Q_0^2)$ from the DIS structure function data of the NMC and BCDMS collaborations, was presented in Ref. [10]. Results for this PDF were obtained at LO, NLO, NNLO for different values of $\alpha_s(M_Z^2)$.

In Ref. [10] we have implemented a new fast and efficient method for solving the evolution equations up to NNLO. This method combines the advantages of $x-$space and $N-$space evolution codes: an x dependent Green function (evolution factor) is determined by inverse Mellin transformation of the exact N-space expression and stored. Evolution of PDFs is then performed by convoluting this Green function with any given boundary condition. The accuracy of this method has been benchmarked up to NNLO with the help of the tables of Refs. [2, 3].

Also, we have implemented a criterion to determine the convergence of the fitting procedure in a way which is free of bias related to the choice of parametrization. To this purpose, the dataset is randomly divided into two sets, of which only one is used in the fit. Convergence is achieved when the quality of the fit to data which are *not* used for minimiztion stops improving.

An important feature of our approach is that it is possible to check quantitatively the statistical features of results using suitable estimators. For example, one can check that the results do not depend on choices made during the fitting procedure, such as the choice of architecture of neural networks, which is analogous to the choice of parton parametrization in conventional fits. Namely, we repeat the fit with a different choice, and compute the distance

$$d[q] = \sqrt{\left\langle \frac{\left(q_i^{(1)} - q_i^{(2)}\right)^2}{(\sigma_i^{(1)})^2 + (\sigma_i^{(2)})^2} \right\rangle_{\rm dat}}\,, \tag{1}$$

where $q_i^{(1)}$, $q_i^{(2)}$ are the predictions for the i-th data point in the two fits, and $\sigma_i^{(1)}$, $\sigma_i^{(2)}$ the predictions for the corresponding statistical uncertainties, and the average is performed over all data. The results of the first and second fit are the same if $d[q] = 1$ on average. This also checks that the statistical uncertainties are correctly estimated. One can similarly check stability of the uncertainty estimate. In Ref. [10] this comparison has been performed succesfully.

In Fig. 1 we compare our results for the NS structure function $F_2^{\rm NS}$ to other published determinations. These results are available through the webpage of the NNPDF Collaboration: `http://sophia.ecm.ub.es/nnpdf`. The large uncertainty that we find is a genuine feature of the determination of the nonsinglet quark distribution from the data included in our fit, and, especially at small x, it appears to reflect the current knowledge of the nonsinglet quark distribution. Indeed, for $x \leq 0.05$ the only data which constrain the $q_{\rm NS}$ combination in global fits are the data used in the determination of Ref. [10]. Hence, our results suggest that standard fits might be underestimating PDF uncertainties.

In recent work on PDF uncertainties [5, 6] it has been suggested that, mostly because of inconsistencies between data, the variation of the total χ^2 which corresponds to a one–sigma variation of the underlying PDFs is of order of $\Delta\chi^2 \sim 50$ for the global fits presented in those references instead of $\Delta\chi^2 = 1$ of a statistically consistent fit [4]. In our approach, this quantity can be computed. We get $\Delta\chi^2 \approx 1.7$ (preliminary). This implies that the NMC

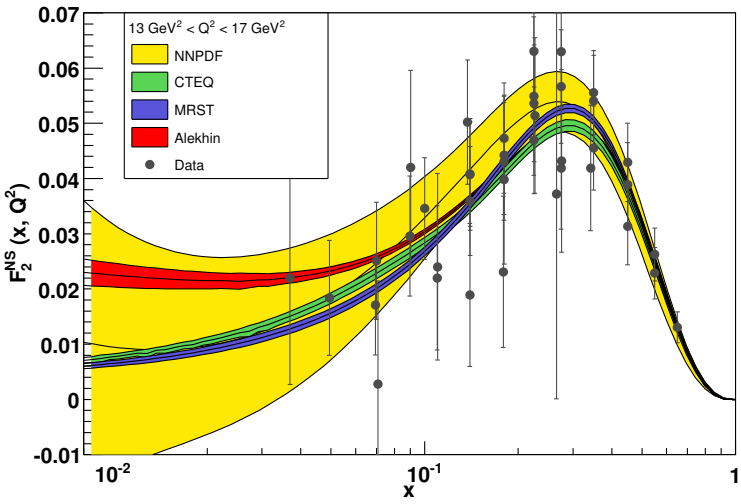

Figure 1:
The nonsinglet structure function $F_2^{\rm NS}$ as determined by the NNPDF collaboration [10] from 229 NMC and 254 BCDMS data points, compared to data and various other determinations.

and BCDMS data are mostly consistent, though some inconsistent data are present [7, 9]. An extensive discussion of the way the published [10] and forthcoming [11] fits based on the neural network approach can be used for the determination of physical parameters (such as α_s) and statistical properties of the data (such as $\Delta\chi^2$) will be presented in a forthcoming publication.

In [10] the strong coupling $\alpha_s(M_Z^2)$ was fixed, but we could also extract it from the fit. The results of a preliminary analysis, shown in Fig. 2, suggest that nonsinglet data determine $\alpha_s(M_Z^2)$ with an uncertainty which is rather larger than that ($\Delta\alpha_s(M_Z^2) \sim 0.002$) obtained in comparable determinations (see e.g. Ref. [12]). This preliminary result is consistent with that obtained using the same data in Ref. [13], with a method which eliminates the need to choose a parton parametrization. This strengthens the conclusion that uncertainties in available PDF fits might be underestimated.

3 Towards a full parton set

The extension of the results described in Ref. [10] to a full global PDF fit has benefited from the increased manpower of the NNPDF Collaboration, and is at a rather advanced stage [11]. In particular, the evolution formalism of Ref. [10] has been extended to the computation of a full set of neutral-current and charged-current structure functions and fully benchmarked. A first full neural parton fit is in is in preparation. It will at first be based on DIS data only, including all available F_2^p and F_2^d fixed target data and the full NC and CC HERA reduced cross sections.

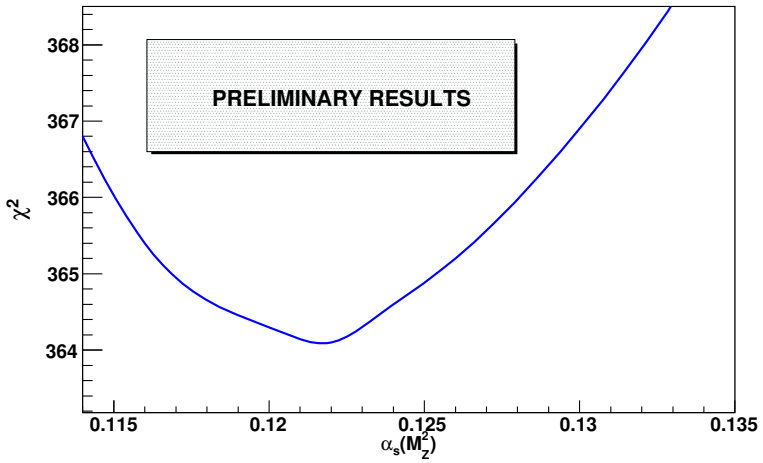

Figure 2:
The χ^2 profile for a preliminary NNLO determination of $\alpha_s(M_Z^2)$ from NS data. The number of data points included in the fit is $N_{\rm dat} = 483$.

References

[1] Slides:
`http://indico.cern.ch/contributionDisplay.py?contribId=32&sessionId=8&confId=9499`

[2] W. Giele et al. The QCD/SM working group: Summary report. `hep-ph/0204316.`

[3] M. Dittmar et al. Parton distributions: Summary report. `hep-ph/0511119.`

[4] Sergey Alekhin. Parton distributions from deep-inelastic scattering data. *Phys. Rev.*, D68:014002, 2003.

[5] J. Pumplin et al. New generation of parton distributions with uncertainties from global QCD analysis. *JHEP*, 07:012, 2002.

[6] A. D. Martin, R. G. Roberts, W. J. Stirling, and R. S. Thorne. Uncertainties of predictions from parton distributions. I: Experimental errors. *Eur. Phys. J.*, C28:455–473, 2003.

[7] Stefano Forte, Lluis Garrido, Jose I. Latorre, and Andrea Piccione. Neural network parametrization of deep-inelastic structure functions. *JHEP*, 05:062, 2002.

[8] W. T. Giele, S. A. Keller and D. A. Kosower. Parton distribution function uncertainties. `hep-ph/0104052.`

[9] Luigi Del Debbio, Stefano Forte, Jose I. Latorre, Andrea Piccione, and Joan Rojo. Unbiased determination of the proton structure function F_2^p with faithful uncertainty estimation. *JHEP*, 03:080, 2005.

[10] Luigi Del Debbio, Stefano Forte, Jose I. Latorre, Andrea Piccione, and Juan Rojo. Neural network determination of parton distributions: The nonsinglet case. *JHEP*, 03:039, 2007.

[11] Richard D. Ball, Luigi Del Debbio, Stefano Forte, Alberto Guffanti, Jose I. Latorre, Andrea Piccione, Juan Rojo, and Maria Ubiali. Neural network determination of parton distributions: The singlet case. *In preparation*, 2007.

[12] J. Blumlein, H. Bottcher and A. Guffanti. Non-singlet QCD analysis of deep inelastic world data at O(alpha(s)**3). Nucl. Phys. B **774** (2007) 182

[13] Stefano Forte, Jose I. Latorre, Lorenzo Magnea, and Andrea Piccione. Determination of α_s from scaling violations of truncated moments of structure functions. *Nucl. Phys.*, B643:477–500, 2002.

The Curvature of $F_2^p(x,Q^2)$ as a Probe of Perturbative QCD Evolutions in the small–x Region

Cristian Pisano

Department of Physics and Astronomy, Vrije Universiteit Amsterdam,
De Boelelaan 1081, 1081 HV Amsterdam - The Netherlands

Perturbative NLO and NNLO QCD evolutions of parton distributions are studied, in particular in the (very) small-x region, where they are in very good agreement with all recent precision measurements of $F_2^p(x,Q^2)$. These predictions turn out to be also rather insensitive to the specific choice of the factorization scheme ($\overline{\rm MS}$ or DIS). A characteristic feature of perturbative QCD evolutions is a *positive* curvature of F_2^p which increases as x decreases. This perturbatively stable prediction provides a sensitive test of the range of validity of perturbative QCD.

The curvature of DIS structure functions like $F_2^p(x,Q^2)$, i.e., its second derivative with respect to the photon's virtuality Q^2 at fixed values of x, plays a decisive role in probing the range of validity of perturbative QCD evolutions of parton distributions in the small-x region. This has been observed recently [1, 2, 3, 4] and it was demonstrated that NLO($\overline{\rm MS}$) evolutions imply a *positive* curvature which increases as x decreases. Such rather unique predictions provide a check of the range of validity of perturbative QCD evolutions. However, the curvature is a rather subtle mathematical quantity which a priori may sensitively depend on the theoretical (non)perturbative assumptions made for calculating it. Our main purpose is to study the dependence and stability of the predicted curvature with respect to a different choice of the factorization scheme (DIS versus $\overline{\rm MS}$) and to the perturbative order of the evolutions by extending the common NLO (2-loop) evolution [3] to the next-to-next-to-leading 3-loop order (NNLO) [4].

The valence $q_v = u_v, d_v$ and sea $w = \bar{q}, g$ distributions underlying $F_2^p(x,Q^2)$ are parametrized at an input scale $Q_0^2 = 1.5$ GeV^2 as follows:

$$x\,q_v(x,Q_0^2) = N_{q_v} x^{a_{q_v}} (1-x)^{b_{q_v}} (1 + c_{q_v}\sqrt{x} + d_{q_v} x + e_{q_v} x^{1.5}) \quad (1)$$

$$x\,w(x,Q_0^2) = N_w x^{a_w} (1-x)^{b_w} (1 + c_w\sqrt{x} + d_w x) \quad (2)$$

and without loss of generality the strange sea is taken to be $s = \bar{s} = 0.5\,\bar{q}$. Notice that we do not consider sea breaking effects ($\bar{u} \neq \bar{d}$, $s \neq \bar{s}$) since the data used, and thus our analysis, are not sensitive to such corrections. The normalizations N_{u_v} and N_{d_v} are fixed by $\int_0^1 u_v dx = 2$ and $\int_0^1 d_v dx = 1$, respectively, and N_g is fixed via $\int_0^1 x(\Sigma + g)dx = 1$. We have performed all Q^2-evolutions in Mellin n-moment space and used the QCD-PEGASUS program [5] for the NNLO evolutions. For definiteness we work in the fixed flavor factorization scheme, rather than in the variable (massless quark) scheme since the results for F_2^p and its curvature remain essentially unchanged [3].

We have somewhat extended the set of DIS data used in [3] in order to determine the remaining parameters at larger values of x and of the valence distributions. The following data sets have been used: the small-x [6] and large-x [7] H1 F_2^p data; the fixed target BCDMS data [8] for F_2^p and F_2^n using $Q^2 \geq 20$ GeV^2 and $W^2 = Q^2(\frac{1}{x} - 1) + m_p^2 \geq 10$ GeV^2 cuts, and the proton and deuteron NMC data [9] for $Q^2 \geq 4$ GeV^2 and $W^2 \geq 10$ GeV^2. This amounts to a total of 740 data points. The required overall normalization factors of

	NNLO($\overline{\rm MS}$)				NLO($\overline{\rm MS}$)			
	u_v	d_v	$\bar{q}$	g	u_v	d_v	$\bar{q}$	g
N	0.2503	3.6204	0.1196	2.1961	0.4302	0.3959	0.0546	2.3780
a	0.2518	0.9249	-0.1490	-0.0121	0.2859	0.5375	-0.2178	-0.0121
b	3.6287	6.7111	3.7281	6.5144	3.5503	5.7967	3.3107	5.6392
c	4.7636	6.7231	0.6210	2.0917	1.1120	22.495	5.3095	0.8792
d	24.180	-24.238	-1.1350	-3.0894	15.611	-52.702	-5.9049	-1.7714
e	9.0492	30.106	—	—	4.2409	69.763	—	—
χ^2/dof	0.989				0.993			
$\alpha_s(M_Z^2)$	0.112				0.114			

Table 1: Parameter values of the NLO and NNLO QCD fits with the parameters of the input distributions referring to (1) and (2).

the data are 0.98 for BCDMS and 1.0 for NMC. The resulting parameters of the NLO($\overline{\rm MS}$) and NNLO($\overline{\rm MS}$) fits are summarized in Table 1.

The quantitative difference between the NLO($\overline{\rm MS}$) and NLO(DIS) results turns out to be rather small [4]. Therefore we do not consider any further the DIS scheme in NNLO. The present more detailed NLO($\overline{\rm MS}$) analysis corresponds to χ^2/dof = 715.3/720 and the results are comparable to our previous ones [3]. Our new NLO(DIS) and NNLO(3-loop) fits are also very similar, corresponding to χ^2/dof = 714.2/720 and 712.0/720, respectively. It should be emphasized that the perturbatively stable QCD predictions are in perfect agreement with all recent high-statistics measurements of the Q^2-dependence of $F_2^p(x,Q^2)$ in the (very) small-x region. Therefore additional model assumptions concerning further resummations of subleading small-x logarithms (see, for example, [10]) are not required [11, 12].

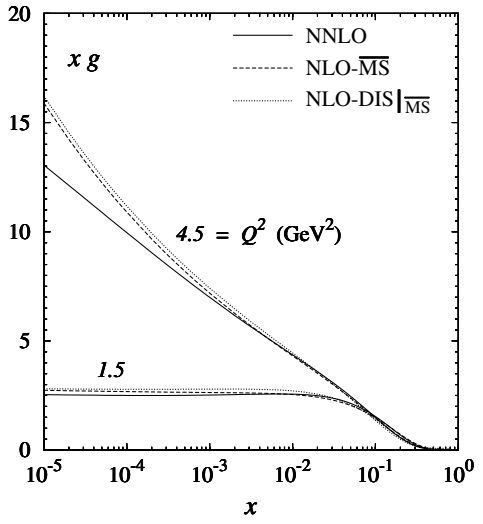

Figure 1: The gluon distributions at the input scale $Q_0^2 = 1.5$ GeV^2 and at $Q^2 = 4.5$ GeV^2.

Figure 1 shows our gluon input distributions in (1) and Table 1 as obtained in our three different fits, as well as their evolved shapes at $Q^2 = 4.5$ GeV^2 in particular in the small-x region. In order to allow for a consistent comparison in the $\overline{\rm MS}$ scheme, our NLO(DIS) results have been transformed to the $\overline{\rm MS}$ factorization scheme. Note, however, that the gluon distribution in the DIS scheme is very similar to the one obtained in NLO($\overline{\rm MS}$) shown in Fig. 1 which holds in particular in the small-x region. This agreement becomes even better for increasing values of Q^2. This agreement is similar for the sea distributions in the

small-x region. Only for $x \gtrsim 0.1$ the NLO(DIS) sea density becomes sizeably smaller than the NLO($\overline{\rm MS}$) one. The NLO results are rather similar but distinctively different from the NNLO ones in the very small-x region at $Q^2 > Q_0^2$. In particular the strong increase of the gluon distribution $xg(x,Q^2)$ as $x \to 0$ at NLO is somewhat tamed by NNLO 3-loop effects.

Turning now to the curvature of F_2^p we first present in Fig. 2 our results for $F_2^p(x,Q^2)$ at $x = 10^{-4}$, together with a global fit MRST01 NLO result [13], as a function of [2]

$$q = \log_{10}\left(1 + \frac{Q^2}{0.5\ \text{GeV}^2}\right)\ . \tag{3}$$

This variable has the advantage that most measurements lie along a straight line [2] as indicated by the dotted line in Fig. 2. All our three NLO and NNLO fits give almost the same results which are also very similar [3] to the global CTEQ6M NLO fit [14]. In contrast to all other fits shown in Fig. 2, only the MRST01 parametrization results in a sizeable curvature for F_2^p. More explicitly the curvature can be directly extracted from

$$F_2^p(x,Q^2) = a_0(x) + a_1(x)q + a_2(x)q^2\ . \tag{4}$$

The curvature $a_2(x) = \frac{1}{2}\,\partial_q^2\, F_2^p(x,Q^2)$ is evaluated by fitting this expression to the predictions for $F_2^p(x,Q^2)$ at fixed values of x to a (kinematically) given interval of q. In Figure 3 we present $a_2(x)$ which results from experimentally selected q-intervals [2, 3, 4]:

$$\begin{aligned} &0.7 \le q \le 1.4 \qquad \text{for} \qquad 2\times 10^{-4} < x < 10^{-2} \\ &0.7 \le q \le 1.2 \qquad \text{for} \qquad 5\times 10^{-5} < x \le 2\times 10^{-4}\,. \end{aligned} \tag{5}$$

It should be noticed that the average value of q decreases with decreasing x due to the kinematically more restricted Q^2 range accessible experimentally. (We deliberately do not show the results at the smallest available $x = 5\times 10^{-5}$ where the q-interval is too small, $0.6 \le q \le 0.8$, for fixing $a_2(x)$ in (4) uniquely and where moreover present measurements are not yet sufficiently accurate). Apart from the rather large values of $a_2(x)$ specific [3, 4] for the MRST01 fit, our NLO and NNLO results agree well with the experimental curvatures as calculated and presented in [2] using the H1 data [6]. Our predictions do *not* sensitively depend on the factorization scheme chosen ($\overline{\rm MS}$ or DIS) and are, moreover, perturbative *stable* with the NNLO 3-loop results lying typically below the NLO ones, i.e. closer to present data [4]. It should be emphasized that the perturbative stable evolutions always result in a *positive* curvature which *increases* as x decreases.

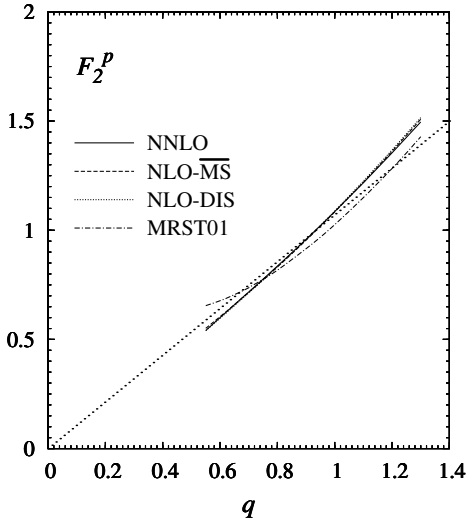

Figure 2: Predictions for $F_2^p(x,Q^2)$ at $x = 10^{-4}$ plotted versus q defined in (3).

Such unique predictions provide a sensitive

test of the range of validity of perturbative QCD! This feature is supported by the data shown in Fig. 3. Future analyses of present precision measurements in this very small-x region (typically $10^{-5} \lesssim x \lesssim 10^{-3}$) should provide additional tests of the theoretical predictions concerning the range of validity of perturbative QCD evolutions.

To conclude, perturbative NLO and NNLO QCD evolutions of parton distributions in the (very) small-x region are fully compatible with all recent high-statistics measurements of the Q^2-dependence of $F_2^p(x, Q^2)$ in that region. The results are perturbatively stable and, furthermore, are rather insensitive to the factorization scheme chosen ($\overline{\rm MS}$ or DIS). Therefore additional model assumptions concerning further resummations of subleading small-x logarithms are not required. A characteristic feature of perturbative QCD evolutions is a *positive* curvature $a_2(x)$ which *increases* as x decreases (cf. Fig. 3). This rather unique and perturbatively stable prediction plays a decisive role in probing the range of validity of perturbative QCD evolutions. Although present data are indicative for such a behavior, they are statistically insignificant for $x < 10^{-4}$. Future analyses of present precision measurements in the very small-x region should provide a sensitive test of the range of validity of perturbative QCD and further information concerning the detailed shapes of the gluon and sea distributions as well.

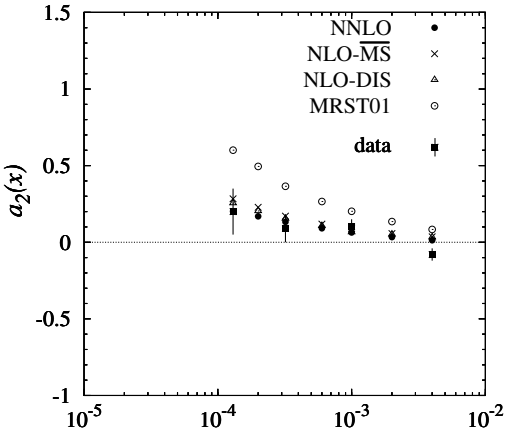

Figure 3: The curvature $a_2(x)$ as defined in (4) for the variable q-intervals in (5).

References

[1] Slides:
`http://indico.cern.ch/contributionDisplay.py?contribId=48&sessionId=8&confId=9499`

[2] D. Haidt, Eur. Phys. J. **C35**, 519 (2004).

[3] M. Gluck, C. Pisano and E. Reya, Eur. Phys. J. **C40**, 515 (2005).

[4] M. Gluck, C. Pisano and E. Reya, Eur. Phys. J. **C50**, 29 (2007).

[5] A. Vogt, Comp. Phys. Comm. **170**, 65 (2005).

[6] C. Adloff et al., H1 Collab., Eur. Phys. J. **C21**, 33 (2001).

[7] C. Adloff et al., H1 Collab., Eur. Phys. J. **C30**, 1 (2003).

[8] A.C. Benvenuti et al., BCDMS Collab., Phys. Lett. **B223**, 485 (1989); **B237**, 599 (1990).

[9] M. Arneodo et al., NMC Collab., Nucl. Phys. **B483**, 3 (1997); **B487**, 3 (1997).

[10] S. Forte, G. Altarelli, R.D. Ball, talk presented at **DIS 2006**, Tsukuba, Japan (April 2006), and references therein (arXiv:hep-ph/0606323).

[11] S. Moch, J.A.M. Vermaseren, A. Vogt, Nucl. Phys. **B688**, 101 (2004).

[12] A. Vogt, S. Moch, J.A.M. Vermaseren, Nucl. Phys. **B691**, 129 (2004).

[13] A.D. Martin, R.G. Roberts, W.J. Stirling, R.S. Thorne, Eur. Phys. J. **C23**, 73 (2002).

[14] J. Pumplin et al., JHEP **7**, 12 (2002).

Structure Functions and Low-x

Electroweak Measurements (Including Top) and Beyond the Standard Model

Electroweak and QCD Combined Fit of HERA-II Data

Gang LI

On behalf of the H1 collaboration,
Laboratoire de l'Accélérateur Linéaire, Université Paris-Sud 11,
IN2P3/CNRS, BP34, 91898 Orsay, France

We report a new Electroweak and QCD combined fit based on H1 measurements. Due to the polarizations of electron and positron beams at HERA-II, the precision of the Electroweak couplings of the light quarks to Z^0 has been improved significantly.

1 Introduction

The deep inelastic scattering (DIS) of leptons off nucleons has played an important role in revealing the structure of matter, in the discovery of weak neutral current interactions and in the foundation of the Standard Model (SM) as the theory of strong and Electroweak (EW) interactions. At HERA, the first lepton-proton collider ever built, the study of DIS has been pursued since 1992 over a wide kinematic range. In terms of Q^2, the negative four-momentum transfer squared, the kinematic coverage includes the region where the electromagnetic and weak interactions become of comparable strength. Both charged current (CC) and neutral current (NC) interactions occur in ep collisions and are studied by the two collider experiments H1 and ZEUS. Many QCD analyses of HERA data have been performed to determine the strong interaction coupling constant α_s [2, 3, 4] and parton distribution functions (PDFs) [3, 5, 6]. In EW analyses, the W boson mass value has been determined from the charged current data at high Q^2 [5, 7, 8, 9, 10, 11, 12], and from combined fit in [13].

Based solely on the precise data recently published by H1 [2, 5, 6, 9] and new data of HERA-II, a combined QCD and EW analysis is performed here and parameters of the Electroweak theory are determined. The published data have been taken by the H1 experiment in the first phase of operation of HERA (HERA-I) with unpolarised e^+ and e^- beams and correspond to an integrated luminosity of 100.8 pb^{-1} for e^+p and 16.4 pb^{-1} for e^-p, respectively. The new data were taken in the second phase of operation (HERA-II, including 2003—2005) with polarized e^+ and e^- beams and correspond to an integrated luminosity of 47.6 pb^{-1} for e^+p and 98.2 pb^{-1} for e^-p respectively.

At HERA, the NC interactions at high Q^2 receive contributions from γZ interference and Z^0 exchange. Thus the NC data can be used to extract the weak couplings of up- and down-type quarks to the Z^0 boson. At high Q^2 and high x, where the NC $e^\pm p$ cross sections are sensitive to these couplings, the up- and down-type quark distributions are dominated by the light u and d quarks. Therefore, this measurement can be considered to determine the light quark couplings. The CC cross section data help to disentangle the up and down quark distributions. At HERA-II, the $e^\pm$ beams are polarized. For neutral current, the cross section can be expressed as:

$$\begin{aligned} \frac{d^2\sigma^\pm_{NC}}{dxdQ^2} &= \frac{2\pi\alpha^2}{xQ^4}\phi^\pm_{NC} \ , \\ \phi^\pm_{NC} &= Y_+\tilde{F}_2 \mp Y_- x\tilde{F}_3 - y^2\tilde{F}_L \ . \end{aligned}$$

Here we neglect the contribution of $\tilde{F}_L$, the other two structure functions are:

$$\begin{aligned} \tilde{F}_2^{\pm} &\simeq F_2^{\gamma} - (\pm P_e a_e)\chi_Z F_2^{\gamma Z} \ , \\ x\tilde{F}_3^{\pm} &\simeq \quad - (a_e)\chi_Z x F_3^{\gamma Z} \ , \end{aligned} \tag{1}$$

where the χ_Z is the propagator of the Z boson. Since $\chi_Z \gg \chi_Z^2$ and $v_e \simeq 0.05$, the pure Z^0 terms and the corresponding terms of v_e have been neglected here.

In the quark parton model, the γZ interference terms can be expressed as :

$$\begin{aligned} F_2^{\gamma Z} &= \sum 2e_i v_i (xq_i + x\bar{q}_i) \ , \\ xF_3^{\gamma Z} &= \sum 2e_i a_i (xq_i - x\bar{q}_i) \ . \end{aligned} \tag{2}$$

According to the formulae 1 and 2, we can see that the polarizations of $e^{\pm}$ put more constraints to the Electroweak couplings. So we can expect high sensitivity of the couplings from the polarized data of HERA-II.

2 Data sets and fit strategies

The QCDFit [14] package has been used in this work. The combined EW-QCD analysis follows the same fit procedure as used in [6, 13]. The QCD analysis is performed using the DGLAP evolution equations [15] at NLO [16] in the MS renormalisation scheme. The contributions of the heavy quarks are taken into account, including the top quark. All quarks are taken to be massless when Q^2 is above their mass thresholds.

Fits are performed to the measured cross sections by fixing the strong coupling constant to be equal to $\alpha_s(M_Z^2) = 0.1185$. The analysis uses an x-space program developed within the H1 Collaboration [17]. In the fit procedure, a χ^2 function which is defined in [2] is minimized. The minimization takes into account correlations between data points caused by systematic uncertainties [6].

In the fits, five PDFs — gluon, xU, xD, $x\bar{U}$ and $x\bar{D}$ are defined by 10 free parameters as in [6, 13]. For all fits, the PDFs obtained here are consistent with those from the H1 PDF 2000 fit [6].

The analysis performed here uses not only HERA-I data sets as in [6], but also the data sets obtained by HERA-II(including 2003−2005 data) which has polarized electron and positron beams. These data cover a Bjorken x range from 3×10^{-5} to 0.65 depending on Q^2. The fit using a toy Monte Carlo data shows that the polarization will improve the Electroweak couplings significantly, especially for the up quark (See figure 1).

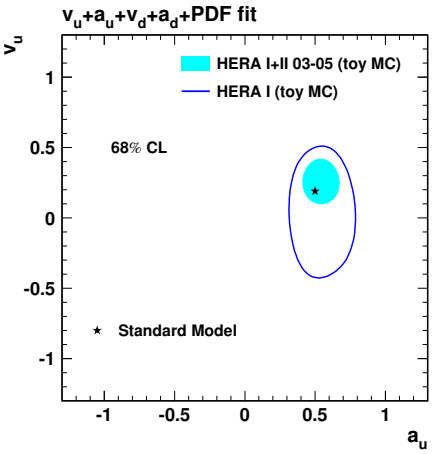

Figure 1: Comparison of fits using a toy Monte Carlo, 94-00 data and 94-05 data.

3 Fit results

In this analysis "fit $v_u - a_u - v_d - a_d$−PDF", the vector and axial-vector dressed couplings of u and d quarks together with PDF are treated as free parameters. The effect of the u and d correlation is studied by fixing either u or d quark couplings to their SM values fits "$v_u - a_u$−PDF" and "$v_d - a_d$−PDF".

The results from this analysis are compared in figure 2 with the previous results of HERA-I [13]. We can see that the precision of u quark couplings are improved significantly as expected, which is due to the contribution of polarized $e^{\pm}$ beams.

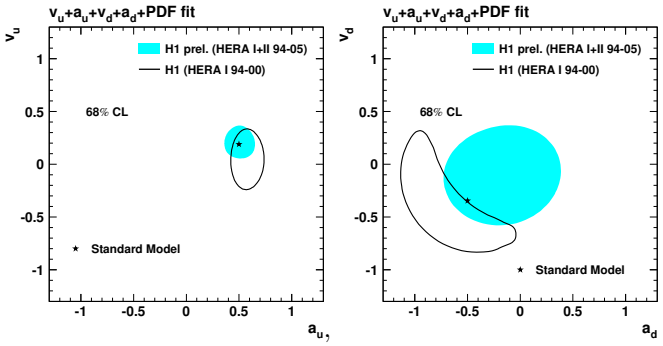

Figure 2: Fit results: contours of vector- and axial-couplings of u and d quark, compared with HERA-I.

The precision is better for the u quark as expected. The superior precision for a_u comes from the γZ interference contribution xF_3. And the improvement of v_u comes from the γZ interference term $F_2^{\gamma Z}$ due to non zero polarization of $e^{\pm}$. Similarly the d-quark couplings v_d and a_d are also constrained by these terms but the smaller electrical charge decreases the effect of these constraints.

The results from this analysis are also compared in figure 3 with similar results obtained previously by the CDF experiment [18]. The HERA determination of the u quark couplings has better precision than that from the Tevatron. These determinations are sensitive to u and d quarks separately, contrary to other measurements of the light quark-Z^0 couplings in νN scattering [19] and atomic parity violation [20] on heavy nuclei. They also resolve any sign ambiguity and the ambiguities between v_u and a_u of the determinations based on observables measured at the Z^0 resonance [21] at LEP.

4 Summary

The vector and axial-vector weak neutral current couplings of u and d quarks to the Z^0 boson have been determined at HERA. The precision of u quark couplings has been improved significantly with respect to the HERA-I results. Also better precision of the u quark couplings was achieved compared with the CDF results [18], and it has no sign ambiguities such as those of LEP [21]. All results are consistent with the Elec-

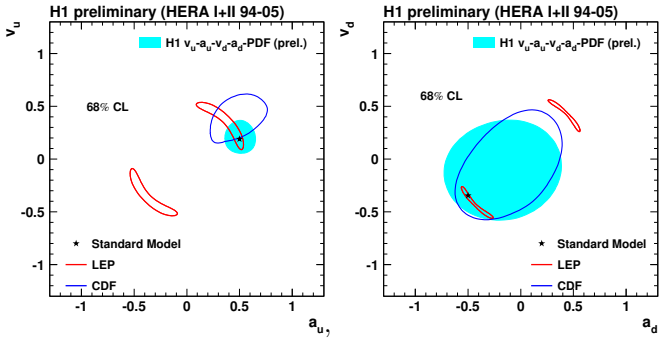

Figure 3: Fit results: contours of vector- and axial-couplings of u and d quark, compared with those of LEP and CDF.

troweak Standard Model.

Further improvement in presision is expected as more HERA-II data will be analysed and included in the combined fit.

References

[1] Slides:
http://indico.cern.ch/contributionDisplay.py?contribId=38&sessionId=14&confId=9499

[2] C. Adloff *et al.* [H1 Collaboration], Eur. Phys. J. **C21** 33 (2001).

[3] S. Chekanov *et al.* [ZEUS Collaboration], Phys. Rev. **D67** 012007 (2003).

[4] S. Chekanov *et al.* [ZEUS Collaboration], Eur. Phys. J. **C42** 1 (2005).

[5] C. Adloff *et al.* [H1 Collaboration], Eur. Phys. J. **C13** 609 (2000).

[6] C. Adloff *et al.* [H1 Collaboration], Eur. Phys. J. **C30** 1 (2003).

[7] T. Ahmed *et al.* [H1 Collaboration], Phys. Lett. **B324** 241 (1994).

[8] S. Aid *et al.* [H1 Collaboration], Phys. Lett. **B379** (1996) 319

[9] C. Adloff *et al.* [H1 Collaboration], Eur. Phys. J. **C19** (2001) 269

[10] J. Breitweg *et al.* [ZEUS Collaboration], Eur. Phys. J. **C12** 411 (2000); [Erratum ibid. **B27** 305 (2003)].

[11] S. Chekanov *et al.* [ZEUS Collaboration], Phys. Lett. **B539** 197 (2002); [Erratum ibid. **B552** (2003) 308].

[12] S. Chekanov *et al.* [ZEUS Collaboration], Eur. Phys. J. **C32** 1 (2003).

[13] A. Aktas *et al.* [H1 Collaboration], Phys. Lett. **B632** 35 (2006).

[14] Manual:
http://h1.web.lal.in2p3.fr/divers/psfiles/notice.ps

[15] Y.L. Dokshitzer, Zh. Eksp. Teor. Fiz. **73** (1977) 1216; V.N. Gribov and L.N. Lipatov, Yad. Fiz. **15** 1218 (1972) ; V.N. Gribov and L.N. Lipatov, Yad. Fiz. **15** 781 (1972); G. Altarelli and G. Parisi, Nucl. Phys. **B126** 298 (1977) .

[16] W. Furmanski and R. Petronzio, Phys. Lett. **B97** 437 (1980).

[17] C. Pascaud and F. Zomer, LAL preprint, **LAL 95-05** (1995); C. Pascaud and F. Zomer, "A fast and precise method to solve the Altarelli-Parisi equations in x space" [hep-ph/0104013].

[18] D. Acosta *et al.* [CDF Collaboration], Phys. Rev. **D71** 052002 (2005)

[19] G.P. Zeller *et al.* [NuTeV Collaboration], Phys. Rev. Lett. **88** 091802 (2002) [Erratum-ibid. **90** 239902 (2003)].

[20] S.C. Bennett and C.E. Wieman, Phys. Rev. Lett.**82** 2484 (1999).

[21] LEP and SLD Electroweak working groups, "Combination of Preliminary Electroweak Measurements and Constraints on the Standard Model"; http://lepewwg.web.cern.ch/LEPEWWG/plots/summer2004/.

Higher Mellin Moments for Charged Current DIS

M. Rogal and S. Moch

Deutsches Elektronensynchrotron DESY
Platanenallee 6, D–15738 Zeuthen - Germany

We report on our recent results for deep-inelastic neutrino(ν)-proton(P) scattering. We have computed the perturbative QCD corrections to three loops for the charged current structure functions F_2, F_L and F_3 for the combination $\nu P - \bar{\nu} P$. In leading twist approximation we have calculated the first six odd-integer Mellin moments in the case of F_2 and F_L and the first six even-integer moments in the case of F_3. As a new result we have obtained the coefficient functions to $\mathcal{O}(\alpha_s^3)$ and we have found the corresponding anomalous dimensions to agree with known results in the literature.

1 Introduction

In our recent research [1], we extended the program of calculating higher order perturbative QCD corrections to the structure functions of charged current deep-inelastic scattering (DIS). Our studies are motivated by the increasingly accurate measurements of neutral and charged current cross sections at HERA with a polarized beam of electrons and positrons [2–4]. At the same time we are also able to quantitatively improve predictions for physics at the front-end of a neutrino-factory, see e.g. Ref. [5]. To be specific, we consider neutrino(ν)-proton(P) scattering in the combination $\nu P - \bar{\nu} P$, which corresponds to charged lepton-proton DIS as far as QCD corrections are concerned. Following Refs. [6–10] we compute the perturbative QCD (pQCD) predictions to three-loop accuracy for a number of fixed Mellin moments of the structure functions F_2, F_L and F_3.

Within the framework of the operator product expansion (OPE), and working in Mellin space, $F_2^{\nu P - \bar{\nu} P}$ and $F_L^{\nu P - \bar{\nu} P}$ are functions of odd Mellin moments only, while only even moments contribute to $F_3^{\nu P - \bar{\nu} P}$. This is opposite to the case of the neutral current structure functions where only even Mellin moments contribute, and to the charged current case for $\nu P + \bar{\nu} P$ scattering [11], which is defined through the OPE for odd Mellin moments only. In the latter results for $F_2^{\nu P + \bar{\nu} P}$ and $F_L^{\nu P + \bar{\nu} P}$ to three-loops can also be directly checked in electromagnetic DIS [12,13] while parameterizations for $F_3^{\nu P + \bar{\nu} P}$ to three-loop accuracy are given in Ref. [14].

2 General formalism

We consider unpolarized inclusive deep-inelastic lepton-nucleon scattering,

$$l(k) \; + \; \mathrm{nucl}(p) \;\; \rightarrow \;\; l'(k') \; + \; X \, , \tag{1}$$

where $l(k)$, $l'(k')$ are leptons of momenta k and k', nucl(p) denotes a nucleon of momentum p and X stands for all hadronic states allowed by quantum number conservation. In our research we are concentrating on charged current neutrino(ν)-proton(P) scattering, i.e. νP, $\bar{\nu} P$ via $W^{\pm}$ boson exchange. As is well known, the differential cross section for the reaction (1) can be written as a product of leptonic $L_{\mu\nu}$ and hadronic $W_{\mu\nu}$ tensors

$$d\sigma \propto L^{\mu\nu} W_{\mu\nu} \, , \tag{2}$$

with $L^{\mu\nu}$ for electroweak or pure electromagnetic gauge boson exchange given in the literature, see e.g. Ref. [15]. The hadronic tensor $W^{\mu\nu}$ in Eq. (2) can be written in terms of so called structure functions F_i, $i = 2, 3, L$.

We are interested in the Mellin moments of structure functions, defined as

$$F_i(n, Q^2) \quad = \quad \int_0^1 dx\, x^{n-2} F_i(x, Q^2)\,, \quad i = 2, L \tag{3}$$

and for $F_3(n, Q^2)$ one has similar relation with n replaced by $n+1$ on the r.h.s. of Eq. (3). Here $Q^2 = -q^2 > 0$, $q = k - k'$ and x is the Bjorken scaling variable defined as $x = Q^2/(2p{\cdot}q)$ with $0 < x \leq 1$.

With the help of the optical theorem and Cauchy's theorem from complex analysis one can relate the Mellin moments of structure functions to the parameters of the OPE for the nucleon forward Compton amplitude $T_{\mu\nu}$:

$$F_i(n, Q^2) \quad = \quad C_{i,\mathrm{ns}}\left(n, \frac{Q^2}{\mu^2}, \alpha_s\right) A^{\mathrm{ns}}_{\mathrm{nucl}}\left(n, \mu^2\right)\,, \qquad i = 2, 3, L \tag{4}$$

and the OPE for $T_{\mu\nu}$ reads as

$$\begin{aligned} T_{\mu\nu} \quad = \quad & 2\sum_n \omega^n \Bigg[e_{\mu\nu}\, C_{L,\mathrm{ns}}\left(n, \frac{Q^2}{\mu^2}, \alpha_s\right) + d_{\mu\nu}\, C_{2,\mathrm{ns}}\left(n, \frac{Q^2}{\mu^2}, \alpha_s\right) \\ & + \mathrm{i}\epsilon_{\mu\nu\alpha\beta} \frac{p^\alpha q^\beta}{p{\cdot}q} C_{3,\mathrm{ns}}\left(n, \frac{Q^2}{\mu^2}, \alpha_s\right) \Bigg] A^{\mathrm{ns}}_{\mathrm{nucl}}\left(n, \mu^2\right) + \text{higher twists}\,, \end{aligned} \tag{5}$$

where higher twist contributions are omitted. $C_{i,\mathrm{ns}}$ denote the Wilson coefficients which are calculable in pQCD and $A^{\mathrm{ns}}_{\mathrm{nucl}}$ are matrix elements of quark non-singlet operators. The latter are not calculable in pQCD, rather they have to be extracted from experimental data. We restrict ourselves to quark non-singlet (ns) operators only since only these give nonvanishing contributions in the combination $\nu P - \nu N$ (see Ref. [11] for details).

Eq. (4) provides the basis to obtain Mellin moments of DIS structure functions in our approach by means of the OPE and the optical theorem. Furthermore, from the careful examination of the symmetry properties of the forward Compton amplitude $T_{\mu\nu}$ and, related, the underlying Feynman diagrams, one can convince oneself that for the charged current $\nu P - \nu N$ DIS, one encounters functions of only odd n for F_2 and F_L and, functions of only even n for F_3, respectively [11].

The pQCD calculation of Wilson coefficients $C_{i,\mathrm{ns}}$ proceeds through the following steps. From the first principles we calculate the partonic forward Compton amplitude $t_{\mu\nu}$. The partonic equivalent of the OPE Eq. (5) for $t_{\mu\nu}$ contains the *same* coefficients $C_{i,\mathrm{ns}}$ as in Eq. (5) and quark matrix elements $A^{\mathrm{ns}}_{\mathrm{q}}$. Projection on the n'th Mellin moment of OPE and on the i'th parton invariant ($i = 2, 3, L$) with the help of the operator $\mathcal{P}^{\mu\nu}_{n,i}$ we get

$$t_{i,\mathrm{ns}}\left(n, \frac{Q^2}{\mu^2}, \alpha_s, \epsilon\right) \equiv \mathcal{P}^{\mu\nu}_{n,i}\, t_{\mu\nu} = C_{i,\mathrm{ns}}\left(n, \frac{Q^2}{\mu^2}, \alpha_s, \epsilon\right) Z_{\mathrm{ns}}\left(\alpha_s, \frac{1}{\epsilon}\right) A^{\mathrm{ns,tree}}_{\mathrm{q}}(n, \epsilon)\,. \tag{6}$$

Both sides of Eq. (6) are renormalized. In particular the renormalization of the local quark operator matrix element $A^{\mathrm{ns}}_{\mathrm{q}}$ gives rise to the factor Z_{ns} on the r.h.s. of Eq. (6). This

equation is our starting point for an iterative determination of the coefficient functions $C_{i,\rm ns}$ and the anomalous dimension $\gamma_{\rm ns}$. The latter appears in a series expansion of $Z_{\rm ns}$ in powers of the strong coupling α_s and negative powers of the parameter ϵ of dimensional regularization, $D = 4 - 2\epsilon$. The $C_{i,\rm ns}$ on the other hand are expanded in α_s and in positive powers of ϵ. Thus the l.h.s. of Eq. (6) leads to a well defined determination of $C_{i,\rm ns}$ and $Z_{\rm ns}$ in pQCD.

3 Calculation and checks

In the previous section, we have briefly explained the method to obtain Mellin moments of the DIS charged current structure functions $F_2^{\nu P-\bar\nu P}$, $F_3^{\nu P-\bar\nu P}$ and $F_L^{\nu P-\bar\nu P}$ together with their respective coefficient functions and anomalous dimensions. To that end we have calculated the Lorentz invariants of the parton Compton amplitude $t_{i,\rm ns}$, $i = 2, 3, L$, as given in the l.h.s. of Eq. (6). Due to the large number of diagrams involved in the calculations up to order α_s^3 sufficient automatization is necessary. First of all, we have generated 3633 diagrams up to three loops with the program QGRAF [16]. For all further calculations we have relied on the latest version of the symbolic manipulation program FORM [17, 18].

For the treatment of QGRAF output, such as analysis of the topologies, the explicit implementation of Feynman rules etc. we have adapted a dedicated FORM procedure *conv.prc* from previous work, e.g. Ref. [13]. Most importantly, this procedure tries to exploit as many symmetry properties of the original Feynman diagrams as possible in order to reduce their total number.

For the calculation of the color factors for each Feynman diagram we have used the FORM package *color.h* [19]. The actual calculation of the Mellin moments of the Feynman integrals has made use of the FORM version of MINCER [20]. Finally, on top of MINCER and MINOS [7] some shell scripts managed the automatic runs of both programs for different parts of the calculation.

We have performed various checks on our computation. Most prominently, we have kept all powers of the gauge parameter ξ throughout the entire calculation for Mellin moments $n \leq 10$ to check that any ξ-dependence vanishes in our final results. The Mellin moments with $n > 10$ were calculated without gauge parameter to facilitate the computations which become increasingly more complicated for higher Mellin n values. For these moments we also used TFORM [21], the multi-threaded version of FORM. On machines with multi-core processors this leads to a significant speed up of our calculations, e.g. a speed-up of $\simeq 5$ on a two-core four processor machine.

We agree with the literature as far as the two-loop coefficient functions [22–26] and the three-loop anomalous dimensions [27] are concerned. In addition, for the first Mellin moment of the coefficient function $C_{2,\rm ns}$ we have obtained exactly $C_{2,\rm ns} = 1$ to all orders in α_s which is in agreement with the Adler sum rule for DIS structure functions,

$$\int\limits_0^1 \frac{dx}{x}\left(F_2^{\nu P}(x,Q^2) - F_2^{\nu N}(x,Q^2)\right) = 2\,. \tag{7}$$

The Adler sum rule measures the isospin of the nucleon in the quark-parton model and does not receive any perturbative or non-perturbative corrections in QCD, see e.g. Ref. [28]. Therefore, this result is another important check of the correctness of our results.

4 Conclusions

We have reported on new results for Mellin moments of the charged current DIS structure functions $F_2^{\nu P-\bar{\nu}P}$, $F_L^{\nu P-\bar{\nu}P}$ and $F_3^{\nu P-\bar{\nu}P}$ including the perturbative QCD corrections to three loops. In the former case (F_2, F_L) we have computed the first six odd-integer Mellin moments while in the latter case (F_3), the first six even-integer moments have been obtained. The results for $F_{2,L}^{\nu P-\bar{\nu}P}$ $n = 1, 3, 5, 7, 9$ and for $F_3^{\nu P-\bar{\nu}P}$ $n = 2, 4, 6, 8, 10$ are available in Ref. [11]. Results for $n = 11$ in the former case and for $n = 12$ in the latter will be published elsewhere. Finally, the discussion of phenomenological consequences of our Mellin space results along with approximate parameterizations the coefficient functions in x are deferred to Ref. [29].

References

[1] Slides: `http://indico.cern.ch/contributionDisplay.py?contribId=24&sessionId=14&confId=9499`.
[2] S. Chekanov et al. *Eur. Phys. J.*, C32:1–16, 2003.
[3] C. Adloff et al. *Eur. Phys. J.*, C30:1–32, 2003.
[4] A. Aktas et al. *Phys. Lett.*, B634:173–179, 2006.
[5] M. L. Mangano et al. hep-ph/0105155, 2001.
[6] S. A. Larin, T. van Ritbergen, and J. A. M. Vermaseren. *Nucl. Phys.*, B427:41–52, 1994.
[7] S. A. Larin, P. Nogueira, T. van Ritbergen, and J. A. M. Vermaseren. *Nucl. Phys.*, B492:338–378, 1997.
[8] A. Retey and J. A. M. Vermaseren. *Nucl. Phys.*, B604:281–311, 2001.
[9] S. Moch, J. A. M. Vermaseren, and A. Vogt. *Nucl. Phys.*, B621:413–458, 2002.
[10] J. Blümlein and J. A. M. Vermaseren. *Phys. Lett.*, B606:130–138, 2005.
[11] S. Moch and M. Rogal. arXiv:0704.1740 [hep-ph], 2007.
[12] S. Moch, J. A. M. Vermaseren, and A. Vogt. *Phys. Lett.*, B606:123–129, 2005.
[13] J. A. M. Vermaseren, A. Vogt, and S. Moch. *Nucl. Phys.*, B724:3–182, 2005.
[14] A. Vogt, S. Moch, and J. Vermaseren. *Nucl. Phys. Proc. Suppl.*, 160:44–50, 2006.
[15] W. M. Yao et al. *J. Phys.*, G33:1–1232, 2006.
[16] P. Nogueira. *J. Comput. Phys.*, 105:279–289, 1993.
[17] J. A. M. Vermaseren. *Nucl. Phys. Proc. Suppl.*, 116:343–347, 2003.
[18] J. A. M. Vermaseren and M. Tentyukov. *Nucl. Phys. Proc. Suppl.*, 160:38–43, 2006.
[19] T. van Ritbergen, A. N. Schellekens, and J. A. M. Vermaseren. *Int. J. Mod. Phys.*, A14:41–96, 1999.
[20] S. A. Larin, F. V. Tkachov, and J. A. M. Vermaseren. NIKHEF-H-91-18.
[21] M. Tentyukov and J. A. M. Vermaseren. hep-ph/0702279, 2007.
[22] W. L. van Neerven and E. B. Zijlstra. *Phys. Lett.*, B272:127–133, 1991.
[23] E. B. Zijlstra and W. L. van Neerven. *Phys. Lett.*, B273:476–482, 1991.
[24] E. B. Zijlstra and W. L. van Neerven. *Phys. Lett.*, B297:377–384, 1992.
[25] E. B. Zijlstra and W. L. van Neerven. *Nucl. Phys.*, B383:525–574, 1992.
[26] S. Moch and J. A. M. Vermaseren. *Nucl. Phys.*, B573:853–907, 2000.
[27] S. Moch, J. A. M. Vermaseren, and A. Vogt. *Nucl. Phys.*, B688:101–134, 2004.
[28] Y. L. Dokshitzer, G. Marchesini, and B. R. Webber. *Nucl. Phys.*, B469:93–142, 1996.
[29] S. Moch, M. Rogal, and A. Vogt. DESY 07-048 , 2007.

New Results from NuTeV

V. Radescu[1] for the NuTeV Collaboration

1- DESY, Notkestrasse 85, Hamburg D-22607 - Germany

The NuTeV experiment has collected high statistics, high energy samples of ν and $\overline{\nu}$ charged-current interactions during 1996-1997 using the sign-selected Fermilab neutrino beam. NuTeV has extracted final ν and $\overline{\nu}$ differential cross sections for DIS single-muon production at $x > 0.015$ and average $Q^2 \sim 15$ GeV^2. Also presented here is the first measurement of Λ_{QCD} from Next-to-Leading Order QCD fits using a theoretical model that fully accounts for heavy quark production.

1 Introduction

The purely weak nature of neutrino interactions makes them a unique probe of the nucleon structure. In charged-current (CC) neutrino DIS the $\nu(\overline{\nu})$ scatters off a quark in the nucleon via exchange of a virtual W-boson. The cross section can be expressed in terms of the structure functions $2xF_1(x,Q^2)$, $F_2(x,Q^2)$, and $xF_3(x,Q^2)$:

$$\frac{d^2\sigma^{\nu(\overline{\nu})}}{dxdy}=\frac{G_F^2 M E_\nu}{\pi}\left[\left(1-y\left(1+\frac{Mx}{2E_\nu}\right)+\frac{y^2}{2}\frac{1+(\frac{2Mx}{Q})^2}{1+R_L}\right)F_2(x,Q^2)\pm\left(y-\frac{y^2}{2}\right)xF_3(x,Q^2)\right], \quad (1)$$

where G_F is the Fermi weak coupling constant, M is the proton mass, E_ν is the incident neutrino energy in the lab frame, and y, the inelasticity, is the fraction of energy transferred to the hadronic system. $R_L(x,Q^2)$ is the ratio of the cross sections for scattering of longitudinally and transversely polarized W-bosons. It relates $F_2(x,Q^2)$ and $2xF_1(x,Q^2)$. Relativistic invariant kinematic variables, x, y, and Q^2, can be evaluated in the lab frame using the experimentally measured quantities: E_μ, the energy of the outgoing primary charged-lepton, E_{had}, the energy deposited at the hadronic vertex, and θ_μ, the scattering angle of the primary muon.

NuTeV is a fixed target deep inelastic neutrino-scattering experiment which took data during 1996-1997 at Fermilab. It combines two important features: the use of a sign selected beam to produce separate ν and $\overline{\nu}$ beams, and the use of a continuous calibration beam running concurrently with the data-taking, which enables the NuTeV experiment to considerably improve its knowledge of the energy scale for hadrons and muons to a precision of 0.43% and 0.7%, respectively [2].

2 Measurement of the Differential Cross Section

The differential cross section per nucleon on iron at a given neutrino energy as function of x, y and E_ν is determined from the differential number of events and the flux, $\Phi(E_\nu)$,

$$\frac{d^2\sigma_{ijk}^{\nu(\overline{\nu})}}{dxdy} \propto \frac{1}{\Phi(E_{\nu i})}\frac{\Delta N_{ijk}^{\nu(\overline{\nu})}}{\Delta x_j \Delta y_k}. \quad (2)$$

Events used in this analysis were triggered by the presence of a muon track. The data selection criteria for the cross section sample requires a good muon track, event containment,

and minimum energies thresholds: $E_{had} > 10$ GeV, $E_\mu > 15$ GeV, and $E_\nu > 30$ GeV. To minimize the effects of the non-perturbative contributions, kinematic cuts of $Q^2 > 1\text{GeV}^2$ and $x < 0.70$ are required.

The neutrino relative flux in energy bins is determined from a nearly independent sample at low hadronic energy ($E_{had} < 20$ GeV). The absolute flux is obtained by normalizing the cross section to the world average value [3]. A detector simulation is used to account for acceptance and resolution effects. This simulation is based on a leading order QCD inspired cross section model [4] which is iteratively fit to the data. The final sample contains 8.6×10^5 neutrino (ν_μ) and 2.4×10^5 anti-neutrino ($\overline{\nu}_\mu$) events.

The following sources of experimental systematic uncertainties on the cross section measurement are considered: muon and hadron energy scales (which dominate) and smearing models, flux uncertainties, and the cross section model which is used to perform the acceptance corrections. The overall normalization uncertainty of the experiment is taken to be 2.1% from the normalization to the world average neutrino cross-section. The NuTeV data is presented together with a full point-to-point covariance matrix that provides the correlation coefficient between any two cross section data points [5].

3 Comparison to other Neutrino Experiments

The NuTeV differential cross section data are compared with measurements from other high statistics neautrino experiments, CCFR [6] and CDHSW [7] (comparison plots are published in [5] and presented in [1]). The three data sets are in reasonable agreement in both level and shape at $0.045 < x < 0.4$.

At $x > 0.40$ CCFR's measurement for both ν and $\overline{\nu}$ cross sections are consistently below the NuTeV result over the entire energy range. Figure 1 shows the ratio of the CCFR and NuTeV differential cross sections as a function of x. The difference in the neutrino cross sections are $4 \pm 1\%$ at $x = 0.45$, $9 \pm 2\%$ at $x = 0.55$, and increases with x up to $18 \pm 2\%$ at $x = 0.65$ (similarly for antineutrinos).

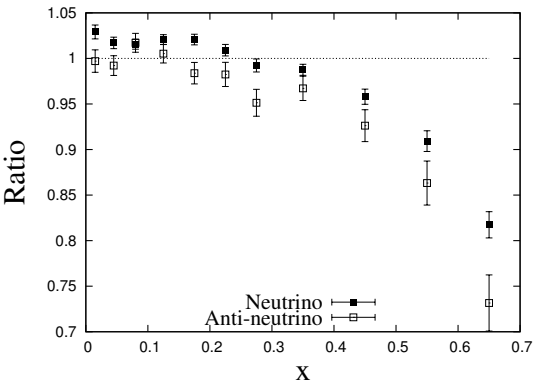

Figure 1: Ratio of CCFR to NuTeV cross sections as function of x over all E and y for neutrinos (filled squares) and anti-neutrinos (open squares).

The largest single contribution to the discrepancy is due to an improved calibration of the magnetic field map of the toroid in NuTeV versus CCFR. NuTeV performed thorough calibrations of muon and hadron responses in the detector including mapping the response over the detector active area and measuring the energy scale over a wide range of energies [2]. This allowed for a precise determination of the the radial dependence of the magnetic field in the toroid. Employing the CCFR model the result is shifted to within 1.6 sigma agreement with CCFR at $x = 0.65$. This accounts for 6% of the 18% difference at $x = 0.65$. The field model differences can also be translated into an effective 0.8% difference in the muon energy scales by integrating the difference in the field models over the toroid.

The cross section model contributes an additional ∼3% to the discrepancy seen at x=0.65. Both experiments determine acceptance corrections using an iterated fit to the cross section data, this necessarily requires that the respective cross section models reflect the data differences.

Other smaller sources for the difference come from muon and hadron energy smearing models which results in a difference of $\sim 2\%$ at $x = 0.65$. All together these three contributions bring the two measurements within 1.2 sigma agreement in the high-x region.

4 Measurement of Λ_{QCD} from NLO QCD fits

The Λ_{QCD} parameter is determined from NLO QCD fits to the structure functions: $xF_3(x,Q^2)$ only (*non-singlet* fit), and to both $F_2(x,Q^2)$ and $xF_3(x,Q^2)$ (*combined* fit). The *non-singlet* fit is independent of the gluon distribution. $xF_3(x,Q^2)$ is extracted from the 1-parameter fit to the y dependence of the difference of ν and $\overline{\nu}$ differential cross sections (Eq. 1). The *combined* fit has an improved statistical precision for Λ_{QCD}. $F_2(x,Q^2)$ and $xF_3(x,Q^2)$ are simultaneously extracted from the 2-parameter fits to the $\nu(\overline{\nu})$ cross sections. For this case input models for ΔxF_3 (a NLO QCD model [10]) and R_L (a fit to the world's measurements [11]) are needed.

Fixed-target DIS experiments are not sensitive to bottom quark excitation, therefore a Λ_{QCD} for the four active flavors is quoted. In order to minimize the non-perturbative QCD effects, only data points with $Q^2 > 5$ GeV^2 and $W^2 > 10$ GeV^2 are used in the NLO QCD fits. The evolution of parton densities starts at $Q_0^2 = 5$ GeV^2, where Λ_{QCD} enters as a free parameter via integro-differential Dokshitzer-Gribov-Lipatov-Altarelli-Parisi (DGLAP) evolution equations [12].

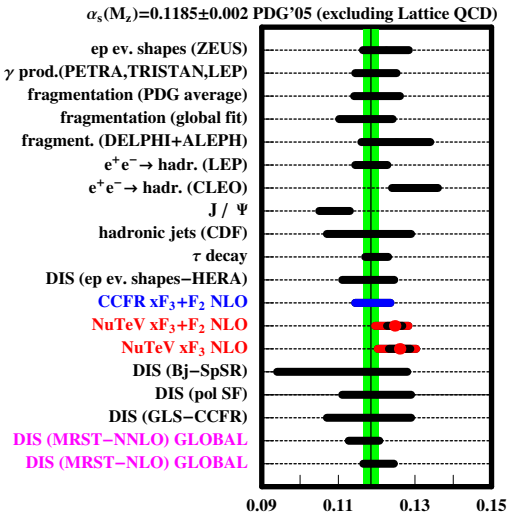

Figure 2: NuTeV $\alpha_S(M_{Z^0})$ in red compared to other experimental measurements [8]. The errors include both experimental and theoretical uncertainties.

Neutrino Scattering is sensitive to heavy quark production, therefore the QCD fits are performed using Aivazis-Collins-Olness-Tung (*ACOT*) model [13] that takes into account heavy quark production [14]. The following results for $\Lambda_{QCD}^{n_f=4}$ with its corresponding $\alpha_S(M_Z)$ are obtained from *non-singlet* and *combined* fits, respectively:

$$\Lambda_{ACOT}^{NLO,(n=4)} = 488 \pm 59(sta+sys)^{+74}_{-113}(th); \quad \alpha_S(M_Z) = 0.1260 \pm 0.0028^{+0.0034}_{-0.0050}; \quad (3)$$

$$\Lambda_{ACOT}^{NLO,(n=4)} = 458 \pm 41(sta+sys)^{+61}_{-87}(th); \quad \alpha_S(M_Z) = 0.1247 \pm 0.0020^{+0.0030}_{-0.0047}. \quad (4)$$

The first error corresponds to total experimental uncertainties (statistical and systematic). The second error is the estimated theoretical uncertainty from the factorization scale dependence (dominant uncertainty). The systematic uncertainties associated with quark masses are found to be small [15]. The experimental systematic uncertainties are propagated from

the extracted differential cross section described in Section 2. The fits are performed using the full covariance error matrix. The largest experimental systematic errors are due to the energy scales and the smearing models, which are of the order of statistical precision.

Figure 2 shows the comparison of the NuTeV measurements of $\alpha_S(M_Z)$ to those of other experiments [8]. The band denotes the world weighted average, as quoted by [8]. The NuTeV results situate above the world average, but agree within errors.

5 Conclusions

The most precise measurement to date of neutrino and anti-neutrino iron differential cross section in the energy range $E_\nu > 30$ GeV, published in [5], has been presented [1]. The systematic uncertainty from the energy scale has been reduced over previous neutrino measurements by about a factor of two. For the first time a full covariance matrix is provided. This data can be used in global fits to constrain the parton distribution functions which are essential to the collider community in calculating cross-sections for particle production and constraining new physics.

A new measurement of Λ_{QCD} from Next-to-Leading Order QCD fits to the Q^2 dependence of neutrino-iron structure functions has been summarized [1] (more details are found in [15]). This is the first measurement of Λ_{QCD} employing a NLO theoretical model which fully accounts for heavy quark production. The NuTeV measurements of Λ_{QCD} from *non-singlet* and *combined* NLO QCD fits, translated into $\alpha_S(M_Z) = 0.1247 \pm 0.0020^{+0.0030}_{-0.0047}$ and $\alpha_S(M_Z) = 0.1260 \pm 0.0028^{+0.0034}_{-0.0050}$, respectively, agree within errors with the world average value. This measurement is one of the most precise determination of α_S to date.

6 Bibliography

References

[1] Slides:
`http://indico.cern.ch/contributionDisplay.py?contribId=282&sessionId=14&confId=9499`

[2] D. A. Harris *et al.*, Nucl. Instrum. Methods **A 447** (2000) 377.

[3] W. Seligman, Ph. D. Thesis, Columbia University, Nevis 292 (1997).

[4] A. J. Buras and K. L. F. Gaemers, Nucl. Phys. **B 132** (1978) 2109.

[5] M. Tzanov *et al.* (NuTeV Collaboration),*Phys. Rev.* **D74** 012008 (2006);

[6] U. K. Yang , Ph. D. Thesis, University of Rochester, (2001).

[7] P. Berge *et al.*, Z. Phys.**C** (1991) 187.

[8] Particle Data Group Listing (2005).

[9] Bardin, D. Y. and Dokuchaeva, JINR-E2-86-260 (1986).

[10] R. S. Thorne and R. G. Roberts, Phys. Lett. **B 421** (1998) 303;
A. D. Martin *et al.* Eur. Phys. J. **C 18** (2000) 117.

[11] L. W. Whitlow *et al.*, Phys. Lett. **B 250** (1990) 193.

[12] Yu. L. Dokshitzer, *Sov.Phys.JETP***46** (1977);

[13] M. A. G. Aivazis, J. C. Collins, F. I. Olness and W. K. Tung Phys. Rev. **D 50**, (1994) 3102.

[14] F. I. Olness, J. F. Owens, private communication.

[15] V. Radescu, Ph. D. Thesis, University of Pittsburgh, (2006).

Structure Functions and Low-x

Diffraction and Vector Mesons

Saturation Model for Exclusive Diffractive Processes, DVCS and F_2 at HERA

Henri Kowalski

DESY
Notkestrasse 85, 22607 Hamburg, Germany

In this talk we present a simultaneous analysis, within an impact parameter dependent saturated dipole model, of exclusive diffractive vector meson (J/ψ, ϕ and ρ) production, deeply virtual Compton scattering and the total $\gamma^* p$ cross section data measured at HERA. Various cross sections measured as a function of the kinematic variables Q^2, W and t are well described, with little sensitivity to the details of the vector meson wave functions. We discuss the determination of the properties of the gluon density in both longitudinal and transverse dimensions, including the impact parameter dependent saturation scale. The overall success of the description indicates universality of the emerging gluon distribution and proton shape. The talk is based on the recent paper written together with Leszek Motyka and Graeme Watt.

Exclusive diffractive processes at HERA, such as exclusive vector meson production or deeply virtual Compton scattering (DVCS), are excellent probes of the proton shape in the perturbative regime. Several investigations have already shown that these processes can be well described within a QCD dipole approach with the vector meson wave functions determined by educated guesses and the photon wave function computed within QED. For an overview and the complete set of references see [2].

The vector meson and DVCS processes are measured at HERA in the small-x regime where the behaviour of the inclusive deep-inelastic scattering (DIS) cross section, or the structure function F_2, is driven by the gluon density. The dipole model allows these processes to be calculated, through the optical theorem, from the gluon density determined by a fit to the total inclusive DIS cross sections. Usually, it is assumed that the evolution of the gluon density is independent of the proton shape in the transverse plane. The investigations of Kowalski and Teaney [3] and Kowalski, Motyka and Watt [2] has shown that the Gaussian form of the proton shape, implied by the data, has implications on the emerging pattern of QCD evolution and saturation effects. The interplay of saturation and evolution effects was first investigated by Bartels, Golec-Biernat and Kowalski [4], where it was found that the total inclusive DIS cross sections, or F_2, can be described either by strong saturation and weak evolution or by strong evolution and weak saturation effects. The investigation of Ref. [3, 2], which took into account also the proton shape in the transverse plane, concluded that saturation effects are substantial in the proton centre, but that the Gaussian form implies that a large contribution to the cross section has to come from the outskirts of the proton, where the gluon density is diluted. Hence the evolution effects have to be strong and play an important role.

The t-distributions determine the area size of the interaction region, B_D. The parameter B_D is obtained by making a fit to the t-distributions of the form $\mathrm{d}\sigma/\mathrm{d}t \propto \exp(-B_D|t|)$. For scattering of very small dipoles B_D is connected to the proton radius R_p via $B_D = R_p^2/3$. However, for larger dipoles the size of the interaction area depends not only on the proton radius but also on the size of the produced vector meson or real photon, which we take into account following the work of Bartels, Golec-Biernat and Peters (BGBP) [5]. This allows

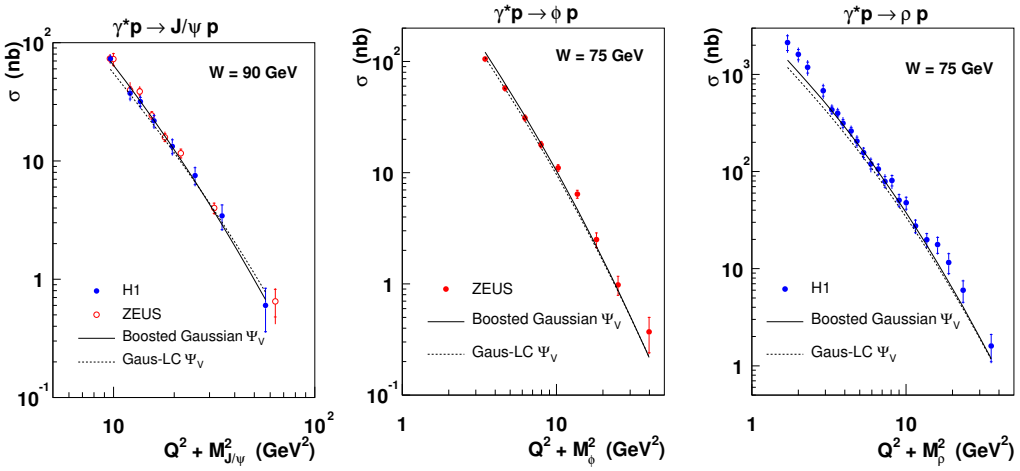

Figure 1: Total vector meson cross section σ vs. $(Q^2 + M_V^2)$ compared to predictions from the model using two different vector meson wave functions.

the data for all vector mesons and DVCS to be described using a unique Gaussian proton shape, independent of the produced final state.

An important finding of this investigation is that, although the vector meson wave functions are not fully known, one obtains a good description of the measured data. The model parameters, which were fixed by the fit to the total inclusive DIS cross section and the vector meson t-distributions, describe the measured Q^2 and W dependence of vector meson production and DVCS very well, together with the absolute normalisation, see Figures 1 and 2. The measured DVCS t-distribution agrees with the model expectation within the measurement error.

The b-Sat model, which gives the best description of data, uses the Glauber–Mueller dipole cross section with DGLAP evolution of the gluon density. Although the overall description of exclusive processes is very good, this approach has some limitations, seen most clearly in the lack of W dependence of B_D in J/ψ photoproduction, see Ref. [2] for more details. Although this is a delicate effect, the measurement precision is sufficient to show that there is a coupling between the transverse and longitudinal evolution variables, that is, $\alpha'_{I\!P} \neq 0$. We therefore introduced impact parameter dependence into the CGC model, the "b-CGC" model, which leads to a considerably poorer fit to F_2 than the b-Sat model and a worse overall description of exclusive processes, but a better description of the $\alpha'_{I\!P}$ parameter. The saturation scale Q_S^2 evaluated in this investigation does not depend sizably on the adopted evolution scheme and is consistent with the results of Ref. [3].

An important finding of this investigation is that the t-dependences of all three vector mesons and the DVCS process can be simultaneously described with one universal shape of the proton, see Figure 3. The parameter characterising the size of the proton, $B_G = 4$ GeV^{-2}, determined in this investigation, corresponds to the proton radius of $R_p = \sqrt{3B_G} = 0.67$ fm. This is rather smaller than the proton charge radius of 0.870 ± 0.008 fm [6]. This leads to a rather surprising result that gluons are more concentrated in the centre of the proton than quarks.

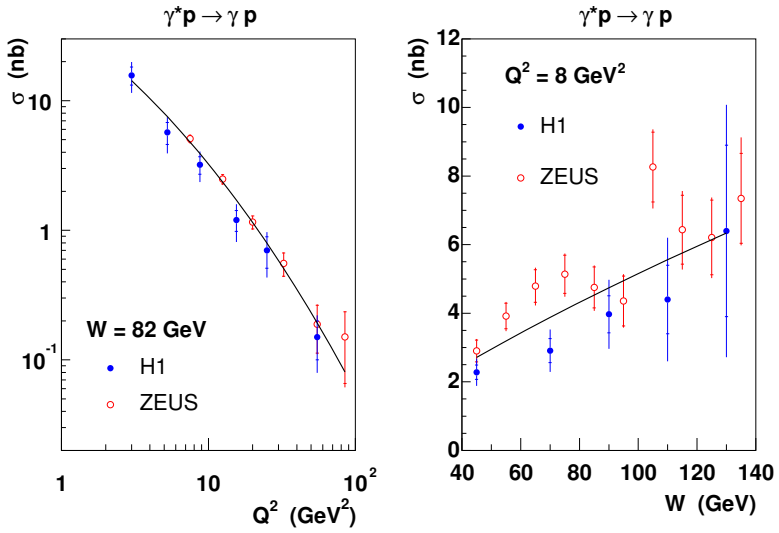

Figure 2: Total DVCS cross sections σ vs. Q^2 (left) and σ vs. W (right) compared to predictions from the b-Sat model.

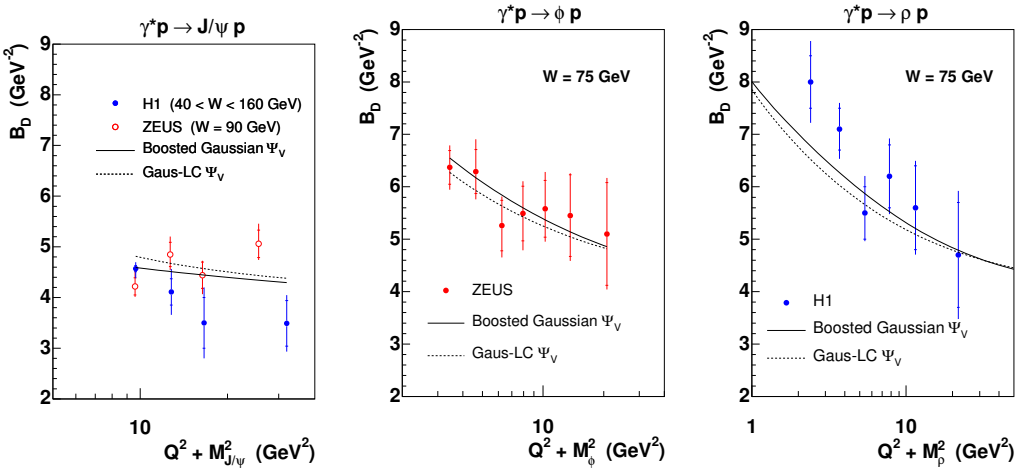

Figure 3: The t-slope parameter B_D vs. $(Q^2 + M_V^2)$, where B_D is defined by fitting $\mathrm{d}\sigma/\mathrm{d}t \propto \exp(-B_D|t|)$, compared to predictions from the b-Sat model using two different vector meson wave functions.

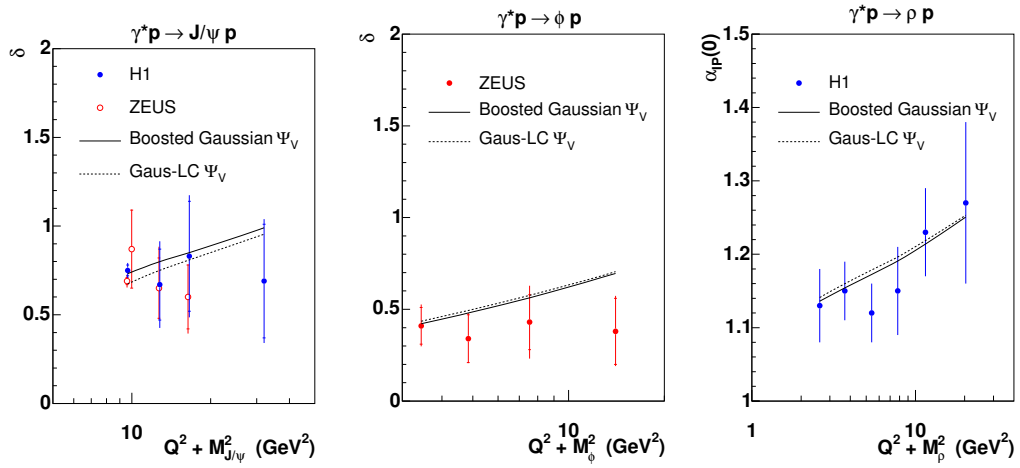

Figure 4: The power δ vs. $(Q^2 + M_V^2)$, where δ is defined by fitting $\sigma \propto W^\delta$, compared to predictions from the b-Sat model using two different vector meson wave functions.

The investigation presented here demonstrates that a wide class of high-energy scattering processes measured at HERA may be understood within a simple and unified framework. The key ingredient is the gluon density which is probed in the longitudinal and transverse directions. The success of the description indicates the universality of the emerging gluon distribution.

Let us finish with a general remark that vector meson and DVCS processes may be used to probe the properties of nuclear matter in a new way. In measurements with polarised beams it is possible to achieve precision which would allow a tomographic picture of protons and nuclei to be obtained. Such a measurement could be performed at the recently proposed *ep* and *eI* collider, EIC, with roughly a half of the HERA centre-of-mass energy and a luminosity of factor 100 to 1000 higher than HERA. The high luminosity should allow to improve substantially the measurement precision for low-x and diffractive processes. This would allow to reduce the errors on the measurement of the rate of rise of the exclusive diffractive process, shown in Fig. 4, and in turn determine precisely the gluon density evolution and saturation effects in the non-forward region, $t \neq 0$.

References

[1] Slides:
`http://indico.cern.ch/contributionDisplay.py?contribId=72&sessionId=15&confId=9499`

[2] H. Kowalski, L. Motyka and G. Watt, Phys. Rev. D **74** (2006) 074016.

[3] H. Kowalski and D. Teaney, Phys. Rev. D **68** (2003) 114005.

[4] J. Bartels, K. Golec-Biernat and H. Kowalski, Phys. Rev. D **66** (2002) 014001.

[5] J. Bartels, K. Golec-Biernat and K. Peters, Acta Phys. Polon. B **34** (2003) 3051.

[6] S. Eidelman *et al.* [Particle Data Group], Phys. Lett. B **592** (2004) 1.

Target Mass Corrections in Diffractive Scattering

J. Blümlein[1], B. Geyer[2] and D. Robaschik[3] *

1- Deutsches Elektronen-Synchrotron, DESY
Platanenallee 6, D-15738 Zeuthen, Germany

2- Center for Theoretical Studies and Institute of Theoretical Physics Leipzig University,
Augustusplatz 10, D-04109 Leipzig, Germany

3- Brandenburgische Technische Universität Cottbus, Fakultät 1,
PF 101344, D–03013 Cottbus, Germany

We describe the twist-2 contributions to inclusive unpolarized and polarized deep-inelastic diffractive scattering in an operator approach. The representation refers to the observed large rapidity gap but does not require reference to a pomeron picture. We discuss both the case of vanishing target mass M and momentum transfer t as well as the effects at finite t and M, which lead to modifications at large β and low values of Q^2.

1 Introduction

Deep-inelastic diffractive scattering is one of the important scattering processes in high-energy ep scattering at HERA. In the small-x domain $\sim 1/8$ of the events are due to this process. It is characterized by inclusive hadron-production with a large rapidity gap between the outgoing proton and all the remainder hadrons. In Refs. [1] two of the present authors developed a description for this process based on the Compton operator and using techniques known in non-forward scattering, cf. [2], for the case that the momentum transfer t between the incoming and the outgoing proton and target masses can be neglected. In the region of smaller values of Q^2 and large values of $\beta = x/x_P$ one expects both finite t and M^2 effects which were worked out in [3] based on related investigations for the non-forward case [4], see also [5]. In this paper we summarize the main findings of these analyzes, cf. also [6].

2 General Structure

The hadronic tensor of the process is determined by three vectors p_1, p_2, q, the incoming and outgoing proton momentum and the momentum transfer in the unpolarized case supplemented by the spin vector of the initial proton S in the polarized case. The following invariants are formed

$$Q^2 = -q^2, \quad W := (p_1+q)^2, \quad x := \frac{Q^2}{Q^+W^2 - M^2}, \quad t := (p_2-p_1)^2, \quad x_P := -\frac{2\eta}{2-\eta} \geq x.$$

The hadronic tensors in case of the unpolarized and polarized cases are of the following form, [1]

$$W_{\mu\nu}^{unp} = \left(-g_{\mu\nu} + \frac{q_\mu q_\nu}{q^2}\right) W_1 + \hat{p}_{1\mu}\hat{p}_{1\nu}\frac{W_3}{M^2} + \hat{p}_{2\mu}\hat{p}_{2\nu}\frac{W_4}{M^2} + (\hat{p}_{1\mu}\hat{p}_{2\nu} + \hat{p}_{2\mu}\hat{p}_{1\nu})\frac{W_5}{M^2}$$

*This paper was supported in part by SFB-TR-9: Computergestütze Theoretische Teilchenphysik.

$$
\begin{aligned}
W_{\mu\nu}^{pol} = \; & i\left[\hat{p}_{1\mu}\hat{p}_{2\nu} - \hat{p}_{1\nu}\hat{p}_{2\mu}\right]\varepsilon_{p_1,p_2,q,S}\frac{\hat{W}_1}{M^6} \; + \quad i\left[\hat{p}_{1\mu}\varepsilon_{\nu S p_1 q} - \hat{p}_{1\nu}\varepsilon_{\mu S p_1 q}\right]\frac{\hat{W}_2}{M^4} \\
+ \quad & i\left[\hat{p}_{2\mu}\varepsilon_{\nu S p_1 q} - \hat{p}_{2\nu}\varepsilon_{\mu S p_1 q}\right]\frac{\hat{W}_3}{M^4} \; + \quad i\left[\hat{p}_{1\mu}\varepsilon_{\nu S p_2 q} - \hat{p}_{1\nu}\varepsilon_{\mu S p_2 q}\right]\frac{\hat{W}_4}{M^4} \\
+ \quad & i\left[\hat{p}_{2\mu}\varepsilon_{\nu S p_2 q} - \hat{p}_{2\nu}\varepsilon_{\mu S p_2 q}\right]\frac{\hat{W}_5}{M^4} \; + \; i\left[\hat{p}_{1\mu}\hat{\varepsilon}_{\nu p_1 p_2 S} - \hat{p}_{1\nu}\hat{\varepsilon}_{\mu p_1 p_2 S}\right]\frac{\hat{W}_6}{M^4} \\
+ \quad & i\left[\hat{p}_{2\mu}\hat{\varepsilon}_{\nu p_1 p_2 S} - \hat{p}_{2\nu}\hat{\varepsilon}_{\mu p_1 p_2 S}\right]\frac{\hat{W}_7}{M^4} \; + \qquad i\varepsilon_{\mu\nu q S}\frac{\hat{W}_8}{M^2} \; .
\end{aligned}
$$

with $\hat{p}_{2\mu}, \hat{\varepsilon}_{\nu p_1 p_2 S}$, etc. the corresponding gauge-invariant completions. In general there are 4 unpolarized and 8 polarized structure functions in case of pure photon exchange.

The twist–2 contributions can be described applying the factorization theorem. Moreover, A. Mueller's generalized optical theorem allows to turn the isolated final state proton into an initial state anti-proton, being separated from the proton by t. In this way the *diffractive state* is formed, from which the hadronic tensor is obtained taking the forward expectation value of the Compton-tensor. Evaluating the process further using the above kinematic variables we are led to a description of the diffractive scattering cross section which does not require any reference to a pomeron picture, but is solely based on the presence of a large rapidity gap.

3 The Case $t = M^2 = O$

In this approximation the number of structure functions reduces to two unpolarized and two polarized ones, because of the collinearity of p_1 and p_2, [1]. Due to this the diffractive state simplifies and leads to a Lorentz structure with lower complexity. For pure photon exchange only the structure functions $F_{1,2}$ resp. $g_{1,2}$ contribute, which in the twist-2 approximation obey a modified Callan–Gross relation

$$F_2(\beta, \eta, Q^2) = 2xF_1(\beta, \eta, Q^2)$$

and the Wandzura-Wilczek, respectively. As shown in [1], the evolution equations, changing $x \to \beta$ are the same as for inclusive deep–inelastic scattering. To derive the diffractive evolution equations one considers the evolution equations for non–forward scattering Ref. [2b]

$$\mu^2 \frac{d}{d\mu^2} O^A(\kappa_+\tilde{x}, \kappa_-\tilde{x}; \mu^2) = \int D\kappa' \gamma^{AB}(\kappa_+, \kappa_-, \kappa'_+, \kappa'_-; \mu^2) O^B(\kappa'_+\tilde{x}, \kappa'_-\tilde{x}; \mu^2)$$

which turn into

$$\mu^2 \frac{d}{d\mu^2} f^A(\vartheta, \eta; \mu^2) = \int_{\vartheta}^{-\mathrm{sign}(\vartheta)/\eta} \frac{d\vartheta'}{\vartheta'} P^{AB}\left(\frac{\vartheta}{\vartheta'}, \mu^2\right) f_B(\vartheta', \eta; \mu^2)$$

in the case $t, M^2 \to 0$. The value of ϑ is determined by the absorptive condition as $\vartheta = 2\beta$.

4 Target Mass Corrections

At low values of Q^2 and large values of β both target mass and finite t–effects become important. As shown in Ref. [3], following [4], these effects have to be dealt with together. The method is a generalization of the treatment of target mass effects in [7] to the non–forward case. The now more complicated diffractive states $\langle p_1, -p_2, t|$ imply that the pre-parton densities emerging in this case depend on two light–cone variables $z_\pm$, non of which can be integrated out. For further treatment we define the variables

$$\vartheta = z_- + \frac{z_+}{\eta}, \qquad \zeta = \frac{z_-}{\vartheta}.$$

The presence of the variable ζ implies that the full Lorentz structure outlined above contributes, assuming azimuthal angular integrals are not carried out. Four unpolarized and eight polarized structure functions contribute. The partonic description being possible in the case $t, M^2 \to 0$ at the level of observables does not hold anymore in this case, since p_1 and p_2 are no longer collinear. Instead, one has to perform definite integrals (the ζ-integrals in [3]) over pre-partonic two-particle correlation functions, which cannot be determined by experiment directly. The absorptive condition in the present case is given by

$$\vartheta = -\frac{2\beta}{\kappa} \quad \frac{1}{1+\sqrt{1+4\beta^2\mathcal{P}^2(\eta,\zeta,t)/Q^2}} \; .$$

Here $|\mathcal{P}(\eta,\zeta)|$ takes the role of the nucleon mass in the case of forward scattering. It holds $\mathcal{P}^2 = t(1-\zeta/\eta) + (4M^2 - t)\zeta^2 \geq 0$. As an example, we present the M^2 and t corrections for the un-integrated unpolarized structure functions $F^a_{1,2}$ [3] :

$$\begin{aligned}
F_1^a(\vartheta,\zeta) &\equiv \Phi_a^{(0)}(\vartheta,\zeta) + \frac{\kappa\mathcal{P}^2}{[(q\mathcal{P})^2 - q^2\mathcal{P}^2]^{1/2}}\Phi_a^{(1)}(\vartheta,\zeta) + \frac{\kappa^2[\mathcal{P}^2]^2}{(q\mathcal{P})^2 - q^2\mathcal{P}^2}\Phi_a^{(2)}(\vartheta,\zeta) \\
F_2^a(\vartheta,\zeta) &\equiv \Phi_a^{(0)}(\vartheta,\zeta) + \frac{3\kappa\mathcal{P}^2}{[(q\mathcal{P})^2 - q^2\mathcal{P}^2]^{1/2}}\Phi_a^{(1)}(\vartheta,\zeta) + \frac{3\kappa^2[\mathcal{P}^2]^2}{(q\mathcal{P})^2 - q^2\mathcal{P}^2}\Phi_a^{(2)}(\vartheta,\zeta)
\end{aligned}$$

Here the $\zeta-$dependent distribution functions $\Phi_a^{(k)}(\vartheta,\zeta)$ are iterated integrals of the correlation function $\Phi_a^{(0)}(\vartheta,\zeta) = f_a(\vartheta,\zeta)$, cf. [3]. a denotes the respective kinematic invariant, implying kinematic dependences in general.

Although no partonic description is obtained one still may study, whether twist–2 relations between structure functions exist. In case of the Callan–Gross relation this is not expected, since it is absent also for forward scattering [7]. However, the Wandzura–Wilczek relation between the twist–2 contributions of the polarized structure functions g_1 and g_2 holds also in the diffractive case for finite values M^2, t, as in many other cases [8–10]. Here the $\zeta-$integral can be carried out.[a] This is not the case for other structure functions. Below this integral, however, all the different structure functions can be represented by a *single* $\zeta-$dependent two–particle distribution function in the unpolarized and polarized case, respectively. The different $\zeta-$dependence of the respective pre-factors and the fact that the $\zeta-$integral is definite prevents to access the corresponding pre–parton distribution functions.

[a] It would be interesting to see, whether the generalization of integral relations derived for the forward polarized case for the twist–2 and twist–3 contributions [8, 9] can be generalized to diffractive scattering for electro-weak boson exchange.

At the twist–2 level diffractive parton distributions exist whenever the $M^2, t \to 0$ approximation holds. For large values of β and small values of Q^2 this is not the case. This is also the kinematic region in which one expects higher twist operators to contribute in the light cone expansion.[b]

The twist–2 scaling violations of the diffractive structure functions in case of M^2, t being finite are different from those in the limit $M^2, t \to 0$. Unlike the case there, the non–forward evolution equations do not simplify in the same way and the $\zeta-$dependence will remain here too.

5 Conclusions

Deep-inelastic diffractive scattering can be described taking the expectation value of the Compton Operator between the diffractive states $\langle p_1, p_2; t|$ obtained by applying A. Mueller's generalized optical theorem. In the limit $M^2, t \to 0$, two polarized and two unpolarized structure functions contribute to the scattering cross section at twist $\tau = 2$. They are related by a modified Callan-Gross relation (in lowest order), resp. the Wandzura-Wilzcek relation in all orders. Target mass corrections accounting for all M^2, t-effects are required in the region of large values of β and low values of Q^2. The set of genuine diffractive structure functions becomes larger due to these effects: four unpolarized structure functions and eight polarized structure functions (with one relation) contribute. These structure functions can be decomposed into generally different diffractive parton densities due to the ζ–integral. In the case of $M^2, t \to 0$ the scaling violations of the twist $\tau = 2$ contribution to the diffractive structure functions are described by the evolution equations for forward scattering replacing $x \to \beta$. The present approach results into a thorough description demanding a rapidity gap without any need to invoke a "pomeron".

References

[1] J. Blümlein and D. Robaschik, Phys. Lett. B **517** (2001) 222. Phys. Rev. D **65** (2002) 096002.

[2] D. Müller, D. Robaschik, B. Geyer, F. M. Dittes and J. Horejsi, Fortsch. Phys. **42** (1994) 101. J. Blümlein, B. Geyer and D. Robaschik, Nucl. Phys. B **560** (1999) 283 ; A. V. Belitsky and A. V. Radyushkin, Phys. Rept. **418** (2005) 1.

[3] J. Blümlein, B. Geyer and D. Robaschik, Nucl. Phys. B **755** (2006) 112.

[4] B. Geyer, D. Robaschik and J. Eilers, Nucl. Phys. B **704** (2005) 279.

[5] A. V. Belitsky and D. Müller, Phys. Lett. B **507** (2001) 173.

[6] Slides: `http://indico.cern.ch/contributionDisplay.py?contribId=133&sessionId=4&confId=9499`

[7] H. Georgi and H. D. Politzer, Phys. Rev. D **14** (1976) 1829.

[8] J. Blümlein and N. Kochelev, Phys. Lett. B **381** (1996) 296; Nucl. Phys. B **498** (1997) 285.

[9] J. Blümlein and A. Tkabladze, Nucl. Phys. B **553** (1999) 427.

[10] J. D. Jackson, G. G. Ross and R. G. Roberts, Phys. Lett. B **226** (1989) 159; A. Piccione and G. Ridolfi, Nucl. Phys. B **513** (1998) 301; J. Blümlein and D. Robaschik, Nucl. Phys. B **581** (2000) 449; B. Geyer and M. Lazar, Phys. Rev. D **63** (2001) 094003; J. Blümlein, V. Ravindran and W. L. van Neerven, Phys. Rev. D **68** (2003) 114004; B. Geyer and D. Robaschik, Phys. Rev. D **71** (2005) 054018.

[11] K. Golec-Biernat and A. Luszczak, arXiv:0704.1608 [hep-ph].

[b] For a phenomenological higher-twist approach see [11].

Small x Gluon From Exclusive J/ψ Production

T. Teubner[1], A.D. Martin[2], C.J. Nockles[1] and M. Ryskin[3,2]

1- Dept of Mathematical Sciences
University of Liverpool - Liverpool L69 3BX, U.K.

2- Dept of Physics and Institute for Particle Physics Phenomenology
University of Durham - Durham DH1 3LE, U.K.

3- Petersburg Nuclear Physics Institute
Gatchina - St. Petersburg, 188300, Russia

HERA data for exclusive J/ψ production is used to determine the gluon distribution of the proton in the region $10^{-4} \lesssim x \lesssim 10^{-2}$ and $2 \lesssim \mu^2 \lesssim 10$ GeV^2, where the uncertainty on the gluon extracted from global parton analyses is large.

1 Introduction

Global fits of parton distribution functions currently do not reliably determine the gluon at small x and small to medium scales. This is due to both the lack of precise structure function data for $x \lesssim 10^{-4}$ and due to the limited sensitivity of the inclusive F_2 data to the gluon, which is determined only by the evolution. However, data for the exclusive $\gamma^* p \to J/\psi\, p$ process offer an attractive opportunity to determine the low x gluon density, since here the gluon couples *directly* to the charm quark and the cross section is proportional to the gluon density *squared* [2]. The mass of the $c\bar{c}$ vector meson, $M_{J/\psi}$, introduces a relatively hard scale, allowing for a description within perturbative QCD, even for J/ψ photoproduction. In leading order (LO) the diffractive scattering is described by (colourless) two-gluon exchange, see Fig. 1. To leading logarithmic accuracy, the amplitude is directly proportional to the gluon density, and the cross section is given by

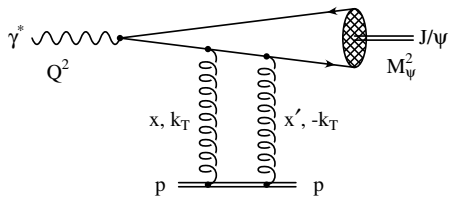

Figure 1: Leading order diagram for diffractive production of J/ψ.

$$\frac{\mathrm{d}\sigma}{\mathrm{d}t}\left(\gamma^* p \to J/\psi\; p\right)\Big|_{t=0} = \frac{\Gamma_{ee} M_{J/\psi}^3 \pi^3}{48\alpha} \frac{\alpha_s(\bar{Q}^2)^2}{\bar{Q}^8} \left[x g(x,\bar{Q}^2)\right]^2 \left(1 + \frac{Q^2}{M_{J/\psi}^2}\right), \qquad (1)$$

where Γ_{ee} is the electronic width of the J/ψ. As usual $x = (Q^2 + M_{J/\psi}^2)/(W^2 + M_{J/\psi}^2)$, with Q^2 the photon virtuality and W the $\gamma^* p$ c.m. energy, and the effective scale $\bar{Q}^2 = (Q^2 + M_{J/\psi}^2)/4$. To obtain the total cross section from forward scattering, $t = 0$, we assume an exponential behaviour and divide by the experimentally measured slope parameter $b = 4.5$ GeV^2. Equation (1) assumes $x = x'$ and is only correct to leading $\ln 1/x$ in the high energy limit. For a realistic description of elastic vector meson production at HERA energies, effects from skewing ($x \neq x'$) and from the real part of the amplitudes have to be taken into account. The effect of skewing is calculable at small x. If we assume a gluon behaviour $x g(x,\mu^2) \sim x^{-\lambda}$, then the correction factor to $O(x)$ accuracy is [3] $R_g = \left(2^{2\lambda+3}/\sqrt{\pi}\right)\, \Gamma(\lambda+\frac{5}{2})/\Gamma(\lambda+4)$.

Contributions from the real part of the amplitudes are taken into account by dispersion relation methods, see e.g. [4], and can be approximated by $\mathrm{Re}\mathcal{A} = \pi\lambda\,\mathrm{Im}\mathcal{A}/2$.

2 Next-to-leading order corrections

At higher order a variety of corrections arise. Relativistic corrections from the J/ψ wave function have to be considered together with higher-order Fock components $c\bar{c}g$ of J/ψ. As shown in [5], when using the experimentally measured Γ_{ee}, these corrections are small and of $\mathcal{O}(4\%)$. We will hence neglect them in the following. However, going beyond the leading logarithmic approximation and performing the integral over the gluon transverse momentum k_T leads to large corrections [4, 6, 7]. This is done by employing k_T factorization and using the unintegrated gluon, thus replacing the leading order amplitude

$$\mathcal{A}^{\mathrm{LLA}} \;\sim\; \frac{\alpha_s(\bar{Q}^2)}{\bar{Q}^4}\int^{\bar{Q}^2}\frac{\mathrm{d}k_T^2}{k_T^2}\,f(x,k_T^2) \;=\; \frac{\alpha_s(\bar{Q}^2)}{\bar{Q}^4}\,xg(x,\bar{Q}^2) \tag{2}$$

by an integral over the unintegrated gluon distribution,

$$\mathcal{A}^{\mathrm{NLO}} \;\sim\; \frac{\alpha_s(Q_0^2)\,xg(x,Q_0^2)}{\bar{Q}^4} \;+\; \frac{\alpha_s(\bar{Q}^2)}{\bar{Q}^2}\int_{Q_0^2}^{Q^2_{\max}}\frac{\mathrm{d}k_T^2}{\bar{Q}^2+k_T^2}\,\frac{\partial xg(x,k_T^2)}{\partial k_T^2}\,. \tag{3}$$

Here a transition parameter Q_0^2 has been introduced to take into account contributions from the infrared regime in which the unintegrated gluon distribution is ill-defined. We note that varying Q_0^2 leads only to very modest modifications of the results discussed below, for more details see [8]. Also, in the naive definition of the unintegrated gluon in Eq. (3) we have neglected the Sudakov suppression factor. For the kinematical regime studied here these additional corrections are small.

In addition to these corrections there are higher-order α_s corrections to the photon impact factor, i.e. to the $c\bar{c}gg$ vertex. They have not yet been calculated within the k_T factorization scheme, but are part of the next-to-leading order (NLO) corrections studied in [9] within the collinear factorization scheme. Part of these corrections generates the running of α_s, while a part is similar to the gluon Reggeization in the BFKL approach. However, large corrections of this sort are absorbed by the choice of the factorization scale. It is therefore expected that the k_T factorization approach accounts for the major part of the NLO corrections, and that the resulting 'NLO' gluon may be compared to that of NLO global parton fits.[a] For a more detailed discussion of these issues see [8].

3 Results

Equation (1), supplemented by skewing and real part corrections, is used to determine the leading order gluon distribution from a fit to HERA data for exclusive J/ψ production [10, 11]. Having tried different ansätze for the gluon distribution, it has turned out that the

[a] The global partons are defined in the $\overline{\mathrm{MS}}$ regularization scheme. The NLO partons obtained in the following should also be considered to be in the $\overline{\mathrm{MS}}$ scheme, since the $\overline{\mathrm{MS}}$ definition of α_s is used, and moreover the factorization scale which provides the cancellation of the $\alpha_s \ln 1/x$ correction also is specified in the $\overline{\mathrm{MS}}$ scheme.

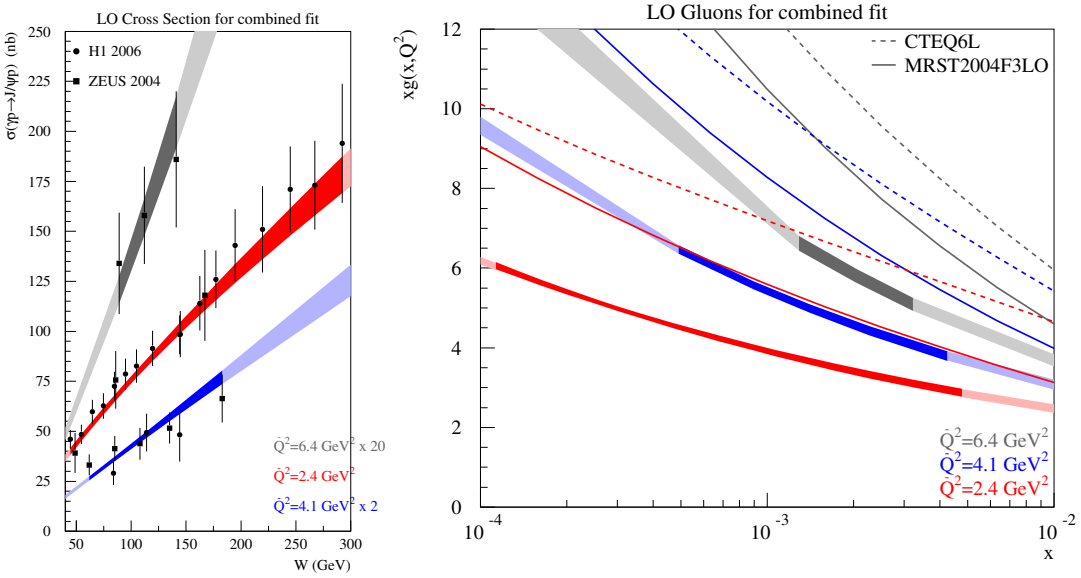

Figure 2: Left panel: Fit of the LO formula Eq. (1), including skewing and real part corrections and using a gluon with form (4), to diffractive J/ψ data, shown for selected Q^2 values. Right panel: Corresponding gluon distribution of the LO fit compared to global fits.

simple ansatz[b]

$$xg(x,\mu^2) = N \cdot x^{a-b\ln(\mu^2/0.45\,\mathrm{GeV}^2)} \tag{4}$$

gives a good fit to the J/ψ data, with a $\chi^2_{\mathrm{min}}/(d.o.f. = 48) = 0.86$. The results of the LO fit for the cross section and the resulting gluon are shown in Figs. 2 for a choice of Q^2 values. The width of the bands indicates the uncertainties and stronger shading the range of the available data. On the right panel, gluon global fits from the MRST [13] and CTEQ [14] collaborations are shown for comparison. Our fitted gluon shows a slightly milder growth with decreasing x and is smaller in normalization. Employing our 'NLO' description using k_T factorization and the integral over the unintegrated gluon as described above, a fit with similar quality, $\chi^2_{\mathrm{min}}/(d.o.f. = 48) = 1.1$, is obtained. However, as demonstrated in the left panel of Fig. 3, the fit slightly undershoots the data at higher Q^2, which has lower weight. The corresponding gluon is shown in the right panel of Fig. 3, again together with curves for two different examples of gluons from recent global fits. The gluons determined in this fit are in good agreement with the MRST gluon at very low scales and in the upper x range, but show much less evolution at larger scales. This is a consequence of the sizeable contributions to the k_T integral from larger scales k_T due to the rising anomalous dimension of the gluon. In contrast, in standard DGLAP fits based on collinear factorization with strong k_T ordering no such large scale contributions exist, but similar corrections are captured order-by-order through the coefficient functions. In this context it is interesting to note that NNLO gluons

[b]Such a form has already successfully been used in [12] for the analysis of inclusive diffractive DIS data.

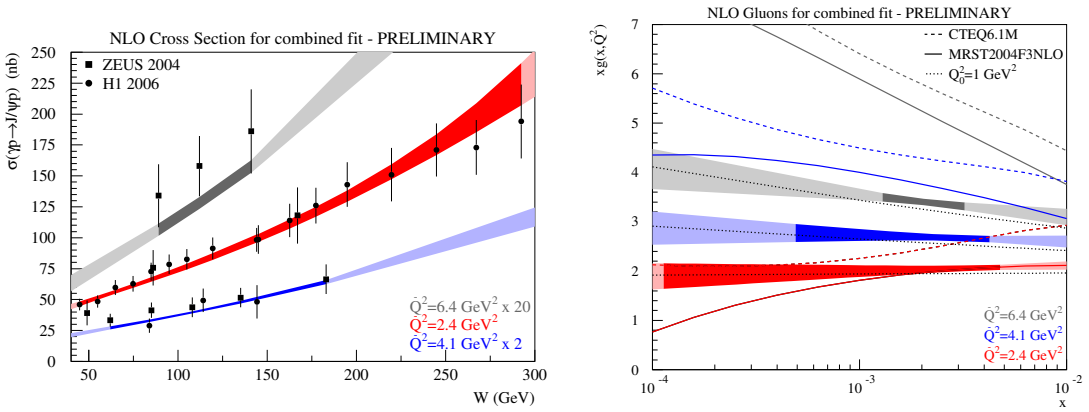

Figure 3: NLO fit as desribed in the text, obtained with $Q_0^2 = 2$ GeV^2. Left panel: Cross section for selected Q^2 values. Right panel: Corresponding gluon compared to NLO gluons from global fits. (The dotted lines are obtained with $Q_0^2 = 1$ GeV^2.)

are much flatter (and even start to decrease at smaller x) compared to NLO fits. In light of this the behaviour of the 'NLO' gluon fits presented here may be viewed as more physical and could be used directly in predictions of different processes based on k_T factorization. Further work to scrutinize the connection between the different schemes is ongoing with the goal to better constrain the gluon at small x.

4 Acknowledgments

TT thanks the UK Particle Physics and Astronomy Research Council for an Advanced Fellowship.

References

[1] Slides: `http://indico.cern.ch/contributionDisplay.py?contribId=73&sessionId=15&confId=9499`
[2] M.G. Ryskin, Z. Phys. **C37** (1993) 89.
[3] A.G. Shuvaev, K.J. Golec-Biernat, A.D. Martin and M.G. Ryskin, Phys. Rev. **D60** (1999) 014015.
[4] M.G. Ryskin, R.G. Roberts, A.D. Martin and E.M. Levin, Z. Phys. **C76** (1997) 231.
[5] P. Hoodbhoy, Phys. Rev. **D56** (1997) 388.
[6] E.M. Levin, A.D. Martin, M.G. Ryskin and T. Teubner, Z. Phys. **C74** (1997) 671.
[7] A.D. Martin, M.G. Ryskin and T. Teubner, Phys. Rev. **D62** (2000) 014022.
[8] A.D. Martin, C.J. Nockles, M.G. Ryskin and T. Teubner, in preparation.
[9] D. Yu. Ivanov, A. Schäfer, L. Szymanowski and G. Krasnikov, Eur. Phys. J. **C34** (2004) 297.
[10] H1 Collaboration, A. Aktas *et al.*, Eur. Phys. J. **C46** (2006) 585.
[11] ZEUS Collaboration, J. Breitweg *et al.*, Z. Phys. **C75** (1997) 215; Eur. Phys. J. **C6** (1999) 603; ZEUS Collaboration, S. Chekanov *et al.*, Nucl. Phys. **B695** (2004) 3.
[12] A.D. Martin, M.G. Ryskin and G. Watt, Eur. Phys. J. **C37** (2004) 285.
[13] A.D. Martin, W.J. Stirling, R.S. Thorne, Phys. Lett. **B636** (2006) 259.
[14] CTEQ Collaboration, J. Pumplin *et al.*, JHEP **0207** (2002) 012; D. Stump *et al.*, JHEP **0310** (2003) 046; W.K. Tung *et al.*, JHEP **0702** (2007) 053.

x-Evolution of Phenomenological Dipole Cross Sections

Daniël Boer, Andre Utermann* and Erik Wessels

Department of Physics and Astronomy,
Vrije Universiteit Amsterdam,
De Boelelaan 1081, 1081 HV Amsterdam, The Netherlands

Deep inelastic scattering at small x can be described very effectively using saturation inspired dipole models. We investigate whether such models are compatible with the numerical solutions of the Balitsky-Kovchegov (BK) equation which is expected to describe the nonlinear evolution in x of the dipole cross section. We find that the BK equation yields results that are qualitatively different from those of phenomenological studies. Geometric scaling is recovered only towards asymptotic rapidities. In this limit the value of the anomalous dimension $\gamma(r, x)$ at the saturation scale approaches approximately 0.44, in contrast to the value 0.63 commonly used in the models.

At small x, deep inelastic scattering (DIS) can be described as the scattering of a color dipole, which the photon fluctuates into, off the proton [2]. The linear BFKL equation, which describes the dipole-proton interaction in terms of gluon ladders, predicts an exponential growth of the corresponding cross section as $\log 1/x$ increases, potentially violating unitarity. Hence, interactions between BFKL gluon ladders may become important, which leads to a nonlinear evolution approximately described by the Balitsky-Kovchegov (BK) equation [3]. As a consequence of the nonlinearity, the dipole cross section saturates with decreasing x, thereby offering a resolution to the unitarity problem. The inclusive HERA data at low x ($x \lesssim 0.01$) could be described well by a dipole cross section of the form $\sigma = \sigma_0 N_{\rm GBW}(r, x)$, where the scattering amplitude $N_{\rm GBW}$ is given by [4]

$$N_{\rm GBW}(r, x) = 1 - \exp\left[-\tfrac{1}{4} r^2 Q_s^2(x)\right], \tag{1}$$

r denotes the transverse size of the dipole, $\sigma_0 \simeq 23$ mb and the x-dependence of the saturation scale is given by $Q_s(x) = 1\,\text{GeV}\,(x_0/x)^{\lambda/2}$, where $x_0 \simeq 3 \times 10^{-4}$ and $\lambda \simeq 0.3$. The scattering amplitude depends on x and r through the combination $r^2 Q_s^2(x)$ only, which is known as geometric scaling and leads to the prediction that the structure function F_2 is a function of $Q^2/Q_s^2(x)$ only. This prediction was checked in a model independent way [5] and holds widely even though the GBW model (1) is not applicable at large Q^2. It should be mentioned that the leading order BK equation leads to a faster evolution in x [6] ($Q_s^2(x) \sim 1/x^\lambda$ where $\lambda \simeq 0.9$) than the experimental data seem to favor ($\lambda \simeq 0.3$). This discrepancy can be reduced by introducing a running coupling constant.

Hadron production in *d-Au* collisions can also be described by saturation inspired dipole models [7–9]. However, these data seem to require geometric scaling violation. The dipole scattering amplitude modified in this respect is given by [7–9]

$$N(r, x) = 1 - \exp\left[-\tfrac{1}{4}(r^2 Q_s^2(x))^{\gamma(r,x)}\right]. \tag{2}$$

The exponent γ is usually referred to as the "anomalous dimension", although the connection of N with the gluon distribution may not be clear for all cases considered below. Following partly [7, 10], in [8, 9] a few requirements were used to determine a parameterization of γ.

*Talk [1] presented by Andre Utermann

Firstly, one assumes that $\gamma(r,x)$ approaches 1 in the limit $r \to 0$. Therefore the "DGLAP" limit $N \sim r^2$ is recovered for all x. Secondly, at the saturation scale, $r = 1/Q_s$, γ should be constant to ensure geometric scaling in this region. This constant γ_s is chosen to be $\simeq 0.628$. The value of γ_s is motivated by a saddle point analysis of a solution of the BFKL equation with saturation boundary conditions [6] and also shows up in the traveling wave approach [11]. Thirdly, if one writes $\gamma = \gamma_s + \Delta\gamma$, then $\Delta\gamma$ should decrease as $1/y$ for $y \to \infty$ at fixed $r^2 Q_s^2$. This ensures that geometric scaling is asymptotically recovered. Furthermore, the parameters were adjusted in such a way that geometric scaling holds approximately for finite y in a growing region between $Q_s(y)$ and roughly $Q_s^2(y)/\Lambda_{\mathrm{QCD}}$. Note that the parameterization in [9] is intended to describe $N(r,x)$ in this so-called extended geometric scaling region only. To simplify the procedure of the required Fourier transformation of N (2), $\gamma(r,x)$ was replaced in [7–9] by $\gamma(1/k,x)$ where k is the transverse momentum of the scattered parton that will fragment into the final state hadron.

We want to check whether these requirements for $\gamma(r,x)$ are compatible with the non-linear evolution of the dipole scattering amplitude N. The BK equation for N reads [3]

$$\frac{\partial N\left(r=|\vec{x}_t-\vec{y}_t|,x\right)}{\partial y} = \frac{\bar{\alpha}_s}{2\pi}\int d^2 z_t \frac{(\vec{x}_t-\vec{y}_t)^2}{(\vec{x}_t-\vec{z}_t)^2(\vec{y}_t-\vec{z}_t)^2}\Big[N\left(|\vec{x}_t-\vec{z}_t|,x\right)+N\left(|\vec{z}_t-\vec{y}_t|,x\right) - N\left(|\vec{x}_t-\vec{y}_t|,x\right)-N\left(|\vec{x}_t-\vec{z}_t|,x\right)N\left(|\vec{z}_t-\vec{y}_t|,x\right)\Big]. \tag{3}$$

Here $\bar{\alpha}_s = \alpha_s N_c/\pi$. We will not consider the impact parameter dependence of N.

The BKsolver program [12] provides a numerical solution of the amplitude $\mathcal{N}(k,x)$ in momentum space. In order to use this solution of the BK equation (3) to constrain $\gamma(r,x)$, one first has to find $N(r,x)$ by Fourier transforming to coordinate space:

$$N(r,x) \equiv r^2 \int \frac{d^2 k_t}{2\pi}\, e^{-i\vec{k}_t\cdot\vec{r}_t}\,\mathcal{N}(k,x) = r^2 \int_0^\infty dk\, k\, J_0(kr)\,\mathcal{N}(k,x)\,. \tag{4}$$

Using the Ansatz (2) one can extract $\gamma(r,x)$ from the resulting $N(r,x)$,

$$\gamma(r,x) = \log[\log[(1-N(r,x))^{-4}]]/\log[r^2\, Q_s^2(x)]\,. \tag{5}$$

This equation requires as a separate input the value of $Q_s(x)$, which can be found by equating the right hand sides of Eqs. (2) and (4) for $r = 1/Q_s$. Combining the resulting values of Q_s with Eq. (5), we obtain a numerical result for $\gamma(r,x)$, which is shown in Fig. 1a.

The resulting $\gamma(r,x)$ has the following features:

1. For $r \to 0$, $\gamma(r,x)$ asymptotically approaches 1.
2. At the saturation scale, $\gamma(r,x)$ is not a constant.
3. For decreasing x, $\gamma(r,x)$ approaches a limiting curve, $\gamma_\infty(rQ_s(x))$, indicated in Fig. 1 by $y = \infty$. Hence, after a longer evolution one indeed recovers geometric scaling.

The fact that for small distances γ asymptotically approaches 1 is understandable from the BK equation, since in this limit it reduces to the BFKL equation. In the limit of small distances, the solution to the BFKL equation is dominated by either the saddle point or the initial condition, both leading to $\gamma \to 1$, since here we use the MV model as the initial condition, see [13] for details.

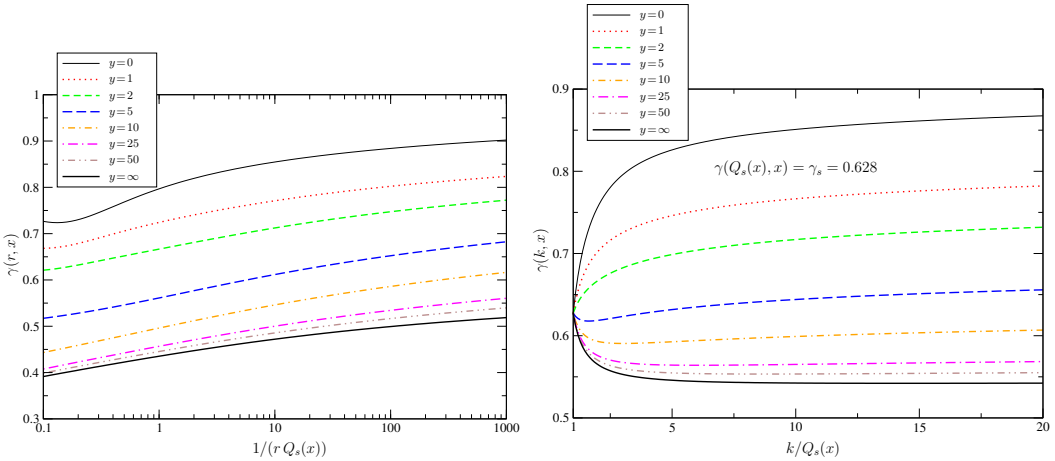

Figure 1: a) $\gamma(r,x)$ resulting from the relations (4) and (5) as a function of $1/(rQ_s(x))$ and $y = \log x_0/x$. b) $\gamma(k,x)$ as a function of $k/Q_s(x)$ for various rapidities $y = \log x_0/x$.

It turns out that γ is clearly not constant, not even at $r = 1/Q_s$, unlike in [7–9]. However, asymptotically geometric scaling is recovered as γ approaches γ_∞. Writing

$$\gamma(r,x) = \gamma_\infty(rQ_s(x)) + \Delta\gamma(r,x)\,, \tag{6}$$

it turns out that, similar to the parameterizations used in [7–9], $\Delta\gamma(r,x)$ decreases as $1/y$ for $y \to \infty$ and fixed $rQ_s(x)$. At the saturation scale γ is given in the small-x limit by

$$\lim_{x\to 0} \gamma(r = 1/Q_s(x), x) = \gamma_\infty(1) \approx 0.44\,, \tag{7}$$

which is significantly below $\gamma_s = 0.628$. This is not in disagreement with theoretical expectations [6, 11]. Rather it indicates that requiring γ in Eq. (2) to be constant at Q_s does not follow from the BK equation.

In [7–9], $N(r,x)$ (2) was considered with $\gamma(r,x)$ replaced by $\gamma(1/k,x)$. This approximation scheme we will discuss next. The procedure of extracting γ becomes quite different when γ depends on k, since the dipole cross section N then depends on both r and k, so that it is not related to $\mathcal{N}(k,x)$ by a straightforward inverse Fourier transform (4) anymore:

$$\mathcal{N}(k,x) \equiv \int_0^\infty \frac{dr}{r}\, J_0(kr)\, \left(1 - \exp\left[-\tfrac{1}{4}(r^2 Q_s^2(x))^{\gamma(k,x)}\right]\right)\,. \tag{8}$$

Instead of by using the inverse Fourier transform, we will extract γ by numerically solving Eq. (8), imposing the following condition. In order to test the Ansatz in [8, 9], we will fix $\gamma(k,x)$ in such a way that it equals the constant $\gamma_s \approx 0.628$ at the saturation scale. The x-dependence of Q_s is determined by explicitly solving Eq. (8) for $k = Q_s$ and $\gamma(Q_s,x) = 0.628$. Now we can extract γ from relation (8) for any given value of x and k. Fig. 1 shows the results for $\gamma(k,x)$ as a function of k/Q_s above Q_s, for a broad range of rapidities. For small rapidities the resulting γ looks very similar to the one in [9] (cf. Fig. 4 of Ref. [9]). As one can see, for larger y the resulting γ is not compatible with the parameterization in [9] anymore; it first decreases before it rises towards 1 asymptotically.

For a discussion of additional important issues like the dependence on initial conditions, the x-dependence of Q_s in our approach and the running coupling case we refer to [13].

Discussion & Conclusions

The numerical solutions of the BK equation do not display exact geometric scaling, although they approach a solution showing such scaling at asymptotic y. Assuming the solutions to be of the form (2), where scaling violations are encoded in the "anomalous dimension" γ, therefore leads to the conclusion that $\gamma(r, x)$ is not a function of $rQ_s(x)$ exclusively. In particular, it is never simply a constant, not even at the saturation scale ($r = 1/Q_s$). At asymptotically large rapidities, γ reaches a limiting function $\gamma_\infty(rQ_s(x))$. This function is universal for a large range of initial conditions [13]. At the saturation scale, γ_∞ equals approximately 0.44, which is considerably smaller than the corresponding values in the phenomenological models [7, 9, 10]. For small values of rQ_s the limiting function seems to reach γ_s [13], in accordance with the traveling wave results of Refs. [11].

Performing the replacement of $\gamma(r, x) \to \gamma(1/k, x)$ does allow one to find a solution for which $\gamma(k = Q_s, x)$ is kept fixed. The behavior of $\gamma(1/k, x)$ is then for small rapidities qualitatively similar to the parameterization in [9]. However, the usually considered choice $\gamma(k = Q_s, x) = \gamma_s = 0.628$ yields some unwanted features, i.e. $\Delta\gamma$ being negative in a region above the saturation scale and the absence of solutions below the saturation scale, although the Ansatz was not intended for that region. Keeping $\gamma(k = Q_s, x)$ fixed at a smaller value, e.g. at $\gamma_\infty(rQ_s = 1) \approx 0.44$, seems more suitable [13], but it remains to be investigated whether such a choice allows for a good fit of all relevant DIS, *d-Au* and *p-p* data.

It would be interesting to consider modifications of phenomenological models for the dipole scattering amplitude that are compatible with both the BK equation and the data. Given the fact that the BK evolution does not respect geometric scaling around Q_s, phenomenological parameterizations that reflect this feature would seem a natural choice. Fortunately, the LHC and a possible future electron-ion collider will provide data over a larger range of momenta and rapidities, so that one can expect to test the evolution properties of the models more accurately.

References

[1] Slides:
`http://indico.cern.ch/contributionDisplay.py?contribId=69&sessionId=15&confId=9499`

[2] A. H. Mueller, Nucl. Phys. B **335**, 115 (1990).

[3] I. Balitsky, Nucl. Phys. B **463**, 99 (1996); Y. V. Kovchegov, Phys. Rev. D **60**, 034008 (1999).

[4] K. Golec-Biernat and M. Wüsthoff, Phys. Rev. D **59**, 014017 (1999).

[5] A. M. Stasto, K. Golec-Biernat and J. Kwiecinski, Phys. Rev. Lett. **86**, 596 (2001).

[6] A. H. Mueller and D. N. Triantafyllopoulos, Nucl. Phys. B **640**, 331 (2002).

[7] D. Kharzeev, Y.V. Kovchegov and K. Tuchin, Phys. Lett. B **599**, 23 (2004).

[8] A. Dumitru, A. Hayashigaki and J. Jalilian-Marian, Nucl. Phys. A **765**, 464 (2006).

[9] A. Dumitru, A. Hayashigaki and J. Jalilian-Marian, Nucl. Phys. A **770**, 57 (2006).

[10] E. Iancu, K. Itakura and S. Munier, Phys. Lett. B **590**, 199 (2004).

[11] S. Munier and R. Peschanski, Phys. Rev. Lett. **91**, 232001 (2003); Phys. Rev. D **69**, 034008 (2004).

[12] R. Enberg, "BKsolver: numerical solution of the Balitsky-Kovchegov nonlinear integro-differential equation", available at URL: http://www.isv.uu.se/∼enberg/BK/.

[13] D. Boer, A. Utermann and E. Wessels, Phys. Rev. D **75**, 094022 (2007).

Universality of QCD Traveling Waves with Running Coupling

Guillaume Beuf[1], Robi Peschanski[1] and Sebastian Sapeta[2,3]

1- Service de Physique Théorique, Orme des Merisiers, CEA/Saclay 91191 Gif-sur-Yvette Cedex, FRANCE

2- Jagiellonian University, Institute of Physics, Ul. Reymonta 4 PL-30-059 Cracow, POLAND.

3- Department of Physics, CERN, Theory Division, CH-1211, Geneva 23, Switzerland.

"Geometric scaling", *i.e.* the dependence of DIS cross-sections on the ratio Q/Q_S, where $Q_S(Y)$ is the rapidity-dependent *saturation* scale, can be theoretically obtained from universal "traveling wave" solutions of the nonlinear Balitsky-Kovchegov (BK) QCD evolution equation at fixed coupling. We examine the similar mean-field predictions beyond leading-logarithmic order, including running QCD coupling.

1 Motivation

"Geometric scaling" (GS) is a striking empirical scaling property first observed in deep-inelastic (DIS) cross-sections . It consists in the dependence of $\gamma^* p$ cross-sections on the ratio $Q/Q_S(Y)$, where $\log Q_S \propto Y$ is the rapidity-dependent *saturation* scale. On a theoretical ground, GS can be found as a consequence of saturation effects in QCD, when the density of gluons become large enough to impose unitarity constraints on the scattering amplitude. It has been shown [2] that the QCD evolution with a nonlinear term describing unitarity damping, the Balitsky-Kovchegov (BK) equation, leads to asymptotic "traveling wave" solutions exhibiting the GS property [2]. They are "universal" since they do not depend neither on the initial conditions nor on the precise form of the nonlinear damping terms.

These results were mainly obtained at leading logarithmic order. In the present contribution, we describe how higher orders, in particular incorporating running QCD coupling, influence these predictions. Potential effects may be due to, *e.g.*, next-to-leading (NLL) contributions to the evolution kernel, higher-order resummations schemes, observable dependence, infra-red regularization, position *vs.* momentum formulation. These aspects and the restauration of universality at high enough rapidity Y has been discussed in Refs.[3], whose results are here briefly described. The main difference with the fixed coupling prediction is a new kind of geometrical scaling with $\log Q_S \propto \sqrt{Y}$, which appears to be as well verified by data [4] as the original GS property.

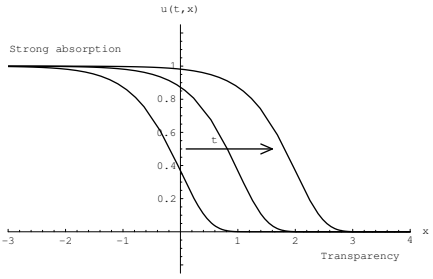

Figure 1: Traveling waves

2 The Balitsky-Kovchegov equation with running coupling

Before entering the discussion, let us introduce the traveling wave method in the case [2] where the running coupling has been introduced *de facto* in momentum space. One writes

$$\left[bLog\left(k^2/\Lambda^2\right)\right]\,\partial_Y \mathcal{T} = \left\{\chi_{LL}\left(-\partial_{Logk^2}\right)\right\}\mathcal{T} - \mathcal{T}^2\ , \tag{1}$$

where $\mathcal{T}(k,Y)$ is the dipole-target amplitude in momentum space, χ_{LL} the leading-log QCD kernel and $\left[bLog\left(k^2/\Lambda^2\right)\right]^{-1} \equiv \alpha(k^2)$, the one-loop QCD running coupling. The asymptotic solutions of the BK equation can be obtained by recognizing the same structure [2] than the traveling wave equation $u(t,x) \to u(t-vx)$

$$[x]\ \partial_t u(t,x) = \left\{\partial_x^2 + 1\right\} u(t,x) - u^2(t,x)\ ,$$

where the traveling-wave/BK "dictionnary" is the following:
$Time = t \sim \sqrt{Y}$; $Space = x \sim \log k^2$; $Traveling\ wave\ u(t,x) = u(x - v_c t) \sim \mathcal{T}$.
Using the dictionnary, one thus recognizes the GS property $u(x - v_c t) \sim \mathcal{T}(k^2/e^{v_c\sqrt{Y}})$, with a saturation scale $Q_S(Y) \sim e^{v_c\sqrt{Y}}$, where v_c is the critical wave velocity determined [2] from the linear kernel χ_{LL}.

3 Traveling waves beyond leading QCD logs

Let us introduce the general traveling-wave method for the extension beyond QCD leading logarithms. It consists in the following steps:

- Solve the evolution equation restricted to linear terms in terms of a dispersion relation: $u(t,x) \sim \int d\gamma\ e^{\gamma[x - v(\gamma)t]}$
- Find the critical (minimal) velocity $v_c = \min v(\gamma) = v(\gamma_c)$ which is selected by the nonlinear damping *independently* of its precise form.
- Verify sharp enough initial conditions $\gamma_0 > \gamma_c$, in order for the critical wave form to be selected.

The mathematical properties of such obtained solutions ensure that the corresponding asymptotic solutions are "universal" that is independent from initial conditions, the nonlinear damping terms and from details of the linear kernel away from the critical values. Hence the traveling-wave method defines *universality classes* from which different equations admit the same asymptotic solutions. One caution is that the range of asymptotics may depend on the singularity structure of the kernel. This may have a phenomenological impact on the possibility of using these solutions in the available experimental range of rapidities. The saddle-point behaves as $\omega_s \sim Y^{-1/2}$ *except* near singularities in γ of the kernel.

In order to illustrate the method, let us consider the general form of the NLL-extended BK equation, replacing in equation (1), $\chi_{LL}\left(-\partial_L\right) \to \chi_{NLL}\left(-\partial_L, \partial_Y\right)$, where $L = \log k^2$. Introducing the function

$$X(\gamma,\omega) = \int_{\gamma_0}^{\gamma} d\gamma'\, \chi_{NLL}(\gamma',\omega)\ ,$$

the linear solution reads

$$\mathcal{T}(L,Y) = \int \frac{d\gamma}{2\pi i}\mathcal{T}_0(\gamma)\ \exp\left[-\gamma L + \frac{1}{b\omega_s}\left(2X(\gamma,\omega_s) - \omega_s \dot{X}(\gamma,\omega_s)\right)\right]\ ,$$

where a dot means ∂_ω and ω_s is given by the saddle-point equation

$$Yb\omega_s^2 - X(\gamma,\omega_s) + \omega_s \dot{X}(\gamma,\omega_s) = 0\ . \tag{2}$$

From the solutions of the saddle-point equation, one can infer [3]:

- *For generic kernels beyond leading logs*: The kernels may contain singularities up to triple poles due to the NLL contribution. By integration, new single and double-pole singularities appear in X at next leading order. The universality class is still the same but subasymptotics corrections may be large, and thus the critical wave solutions delayed to very large energies.
- *For Renormalization-Group improved kernels [5]*: The behaviour of the kernels χ_{NLL} near the singularities are simple poles. This leads only to mild logarithmic singularities in the function $X(\gamma,\omega)$. The net result [3] is that one finds the same universality class as the equation (1), since the ω dependence in X can be neglected and thus $\chi_{NLL} \to \chi_{LL}$.

The same approach has been followed for recent QCD formulations of the Balitsky-Kovchegov equation with running coupling constant obtained from quark-loop calculation [6]. It leads to the same conclusion (with the same warning about eventual kernel singularities): the universality class for the BK equations with running coupling is the one defined by Eq.(1).

4 Geometric Scaling in $\sqrt{Y}$.

On a phenomenological ground, the main property of solutions corresponding to the universality class of Eq.(1) is the traveling-wave form $u(x,t) \sim u(x - v_c t) = u(k^2/e^{v_c\sqrt{Y}})$ in the asymptotic regime. Assuming a simple relation between that amplitude and the $\gamma^* p$ cross-section, one is led to look for geometric scaling of the form $\sigma^{\gamma^* p} \sim (Q^2/e^{v_c\sqrt{Y}})$, with $v_c = cst$. In Fig.2, one displays the corresponding data plot [4]. The validity of the scaling property has been quantified using the 'Quality Factor" QF method, which allows to determine the adequacy of a given scaling hypothesis with data independently of the form of the scaling curve [4].

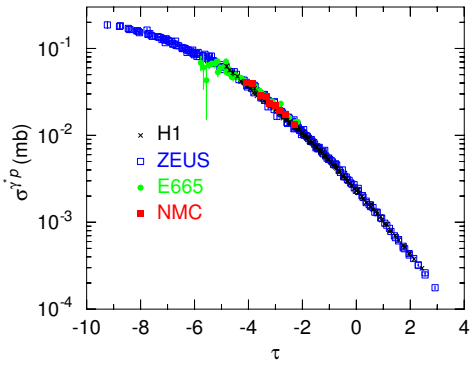

Figure 2: Geometric Scaling in $\sqrt{Y}$ [4]

One may also use the QF method to evaluate the scheme dependence of the subasymptotic, nonuniversal terms in the theoretical formulae. In this case, the geometric scaling prediction is considered in a "strong" version, namely, with the critical parameters (such as v_c) fixed apriori by the theory. In Fig.3 one displays the QF for geometric scaling for different NLL schemes. The top QF is larger than .1 which ensures a good GS property (similar than fig.2). Depending on the resummation scheme (S_3, S_4, CCS, see [5]), $|Y_0|$ gives the typical strength of the non-universal terms. The S4 scheme seems to reach GS sooner (at smaller $|Y_0|$).

5 Conclusions

Let us give the main results of our analysis:

• *Mean-field saturation beyond leading-logs:* The modified Balitsky-Kovchegov equations including running coupling and higher-order QCD corrections to the linear kernel asymptotically converge to the same traveling-wave solution.

• *Characterisation of the universality class:* The universality class of these solutions is the BK equation with the leading logarithmic BFKL kernel supplemented by a factorized running coupling whose scale is given by the gluon transverse momentum. Higher order contributions to the kernel will affect the subasymptotic behaviour.

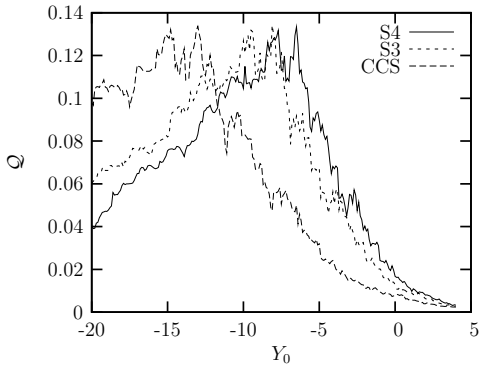

Figure 3: NLL Quality Factors [4]

• *Higher-order effects in the kernel:* The renormalization-group improved kernels are expected to improve the convergence towards the universal behaviour, spurious singularities being canceled.

• *Geometric Scaling:* Geometric scaling in $\sqrt{Y}$ is a generic prediction of the universality class of the BK equation with running coupling. It is well borne out by actual data, using the "Quality Factor" method [4] to quantify the validity of the scaling hypothesis without assuming the scaling curve a priori.

• *Nonuniversal terms:* When using the theoretical "critical" parameters geometrical scaling is verified but requires the introduction of scheme-dependent subasymptotic

Prospects of the present studies are interesting. On the theoretical side, it would be fruitful to investigate the universality properties of QCD equations beyond the mean-field approximation. On the phenomenological side, the problem is still not settled to know whether there is a slow drift towards the universal solutions or whether it exists subasymptotic traveling wave structures, as mathematically [7] or numerically [8] motivated.

References

[1] Slides: `http://indico.cern.ch/contributionDisplay.py?contribId=70&sessionId=15&confId=9499`

[2] S. Munier and R. Peschanski, Phys. Rev. D **69**, 034008 (2004).

[3] R. Peschanski and S. Sapeta, Phys. Rev. D **74**, 114021 (2006);
G. Beuf and R. Peschanski, Phys. Rev. D **75**, 114001 (2007).

[4] F. Gelis, R. Peschanski, G. Soyez and L. Schoeffel, Phys. Lett. B **647**, 376 (2007).

[5] G. P. Salam, JHEP **07**, 019 (1998);
M. Ciafaloni, D. Colferai, and G. P. Salam, Phys. Rev. **D60**, 114036 (1999).

[6] I. Balitsky, Phys. Rev. D **75**, 014001 (2007).
Y. V. Kovchegov and H. Weigert, Nucl. Phys. A **784**, 188 (2007).

[7] C. Marquet, R. Peschanski and G. Soyez, Phys. Lett. B **628**, 239 (2005)

[8] J. L. Albacete and Y. V. Kovchegov, arXiv:0704.0612 [hep-ph].

Electroweak Measurements (Including Top) and Beyond the Standard Model

Convenors:
Martin Wessels,
James Ferrando,
Thomas Nunnemann,
Michael Spira

W Mass and Width Measurements at the Tevatron

Sarah Malik

University College London - Department of Physics and Astronomy
Gower Street, London, WC1E 6BT, U.K.

A measurement of the W boson mass (M_W) and width (Γ_W) using 200 and 350 pb^{-1} of CDF Run II data respectively is presented. The measurements were performed in both the electron and muon channels. The W mass is obtained by fitting the peak of the W transverse mass distribution, whereas the width is extracted by fitting the tail of the distribution. We measure $M_W = 80413 \pm 48$ MeV and $\Gamma_W = 2032 \pm 71$ MeV both of which represent the single most precise measurements of these quantities to date.

1 Introduction

The mass of the W boson receives radiative corrections from loops of virtual particles. The most dominant contributions are from the Higgs boson loop and the top-bottom loop where the Higgs boson contribution is proportional to the logarithm of its mass (M_H). A precision measurement of the W mass therefore allows us to place an indirect constraint on M_H. The width of the W boson is predicted with high precision within the Standard Model (SM), its measurement provides a valuable test of the SM prediction.

W bosons are produced in proton-antiproton collisions at the Tevatron, predominantly via valence quark anti-quark annihilation. Events are selected where the W boson decays leptonically to $e\nu$ or $\mu\nu$ as these decay modes provide relatively clean signatures for detection. The invariant mass of the W is difficult to reconstruct, since a large fraction of longitudinal information is lost as fragments of the $q\bar{q}$ collision escape down the beam pipe. Transverse quantities are therefore used for the measurements, in particular the transverse mass, M_T, which is defined as:

$$M_T = \sqrt{2p_T^l p_T^\nu (1 - cos\phi_{l\nu})}\,, \tag{1}$$

where p_T^l is the transverse momentum of the charged lepton, p_T^ν is the transverse momentum of the neutrino and $\phi_{l\nu}$ is the azimuthal angle between the charged lepton and the neutrino. The W mass is extracted by fitting the peak of the M_T distribution, the region 65-90 GeV. The width is obtained by fitting the tail of the distribution (90-200 GeV) and exploiting the slower fall-off of the Breit-Wigner lineshape compared to the detector resolution.

A dedicated, fast Monte Carlo simulation is used to generate the M_T distribution used in the fits. Parton Distribution Functions (PDFs) are provided by the CTEQ6M [6] set. The W is produced with a non-zero transverse momentum, and the shape of the p_T spectrum is taken from RESBOS [3]. All final state QED radiation is simulated with the Berends and Kleiss [4] program for the width and WGRAD [5] for the mass.

2 Lepton Momentum Scale and Resolution

One of the key aspects of the measurement is an accurate determination of the lepton momentum. The momentum of the lepton is measured in the Central Outer Tracker(COT), a cylindrical drift chamber placed in a magnetic field of 1.4 T. Charged particles ionise

atoms of the gas in the chamber producing a track where the momentum of the lepton can be inferred from the curvature of the track. The momentum scale and resolution of the COT is calibrated using the control samples, $J/\psi \to \mu\mu$, $\Upsilon(1S) \to \mu\mu$ and $Z \to \mu\mu$. The invariant mass of the dimuon pair is measured and compared to the world average mass of the reconstructed particle, in order to calibrate the detector.

3 Lepton Energy Scale and Resolution

The energy of the lepton is measured in the Central Electromagnetic Calorimeter (CEM). The CEM is calibrated by using E/p, the ratio of the energy measured in the calorimeter to the momentum measured in the COT. By using this quantity, the already well calibrated momentum measurement can be used to calibrate the calorimeter. The energy scale obtained from this method is then cross-checked by using the resonance peak of the $Z \to ee$ sample. The invariant mass of the dielectron pair as measured in the calorimeter is compared to the world average mass of the Z boson.

4 Hadronic Recoil Calibration

The neutrino is not detected in the CDF detector, its transverse momentum can be inferred from the missing transverse energy ($\not\!\!E_T$) in the detector. This is obtained by summing the energy of all calorimeter towers excluding those containing or neighbouring the electron. This is what is referred to as the recoil, and it is denoted by $\vec{U}$. The $\not\!\!E_T$ can then be defined in terms of the recoil as $-(\vec{U} + \vec{p_T^l})$.

The recoil receives contributions from three main sources. When the W boson is produced, it recoils against initial state gluon radiation from the incoming quarks giving it a net non-zero transverse momentum. Gluon radiation forms hadronic jets that end up in the calorimeter. Other processes coinciding with W boson production(underlying event) also contribute to the recoil as well as final state photon radiation from the charged lepton which is not emitted collinear with the lepton.

The recoil can be resolved into two components, U_1 which is parallel to the direction of the p_T of the Z and U_2 which is perpendicular to it. U_1 is largely boson p_T dependent and U_2 is mostly underlying event dependent. This enables a parametrisation of the recoil in terms of these components. Parameters of the model are determined by fitting to $Z \to ll$ data and minimum-bias data.

5 Backgrounds

The W event sample is contaminated by backgrounds arising from several sources. These can be divided into two types, electroweak and non-electroweak backgrounds.

Electroweak backgrounds consist of $Z \to ll$ events which can fake a W event if one of the leptons is not reconstructed and $W \to \tau\nu$ where the τ decays to an electron or muon. Non-electroweak backgrounds consist of multi-jet events and in the muon channel, kaons and pions decaying in the COT.

W bosons decaying to hadrons can fake $W \to l\nu$, if one of the jets fakes a lepton and the other is mis-measured producing a false $\not\!\!E_T$. In the muon channel, kaons and pions that decay in the drift chamber can produce a track that contains a kink and this can be

ΔM_W [MeV]	e	μ	C
Lepton Scale	30	17	17
Lepton Resolution	9	3	0
Recoil Scale	9	9	9
Recoil Resolution	7	7	7
Lepton ID	3	1	0
Lepton Removal	8	5	5
Backgrounds	8	9	0
$p_T(W)$	3	3	3
PDF	11	11	11
QED	11	12	11
Total Systematic	39	27	26
Statistical	48	54	0
Total	62	60	26

$\Delta\Gamma_W$ [MeV]	e	μ	C
Lepton Scale	21	17	12
Lepton Resolution	31	26	0
Simulation	13	0	0
Recoil	54	49	0
Lepton ID	10	7	0
Backgrounds	32	33	0
$p_T(W)$	7	7	7
PDF	16	17	16
QED	8	1	1
M_W	9	9	9
Total Systematic	78	70	23
Statistical	60	67	0
Total	98	97	23

Table 1: Systematic and statistical uncertainties for the W mass (left) and width (right). The last column denotes the uncertainties that are common between the electron and the muon channels.

falsely reconstructed as a track with a high p_T. The amount and shape of background contamination in the signal sample is estimated using data for non-electroweak background and Pythia [2] Monte Carlo for electroweak background. Backgrounds are added to the Monte Carlo templates.

6 Results

The systematic and statistical uncertainties for M_W and Γ_W are summarised in Table1. M_W was obtained by fitting the three kinematic distributions m_T, p_T^l and p_T^ν. The combined fitted value obtained is $M_W = 80413 \pm 48$ MeV, which is the world's most precise single measurement of this quantity. The result increases the world average central value by 6 MeV and reduces the uncertainty by 15%. Figure 1 shows the M_T fits for M_W in the electron and muon channels.

Figure 2 shows the M_T fits for Γ_W in the electron and muon decay channels. The combined fitted value obtained is $\Gamma_W = 2032 \pm 71$ MeV, also the world's most precise single direct measurement of this quantity. This result reduces the world average central value by 44 MeV and the uncertainty by 22% and is in good agreement with the Standard Model prediction.

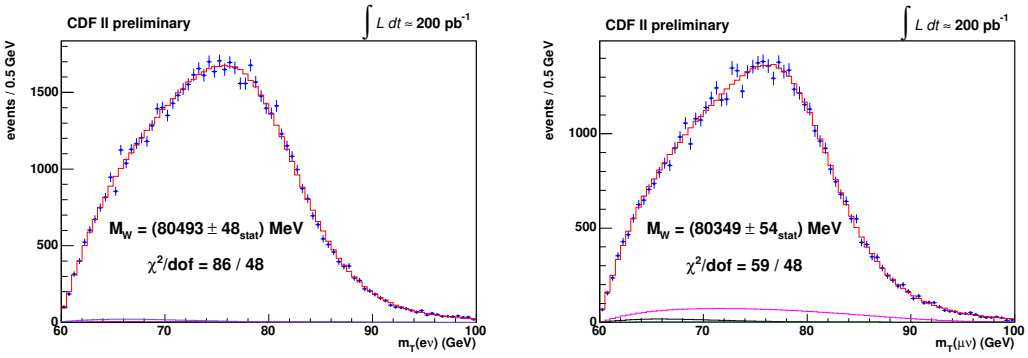

Figure 1: Transverse mass fits for M_W in $W \to e\nu$ (left) and $W \to \mu\nu$ (right)

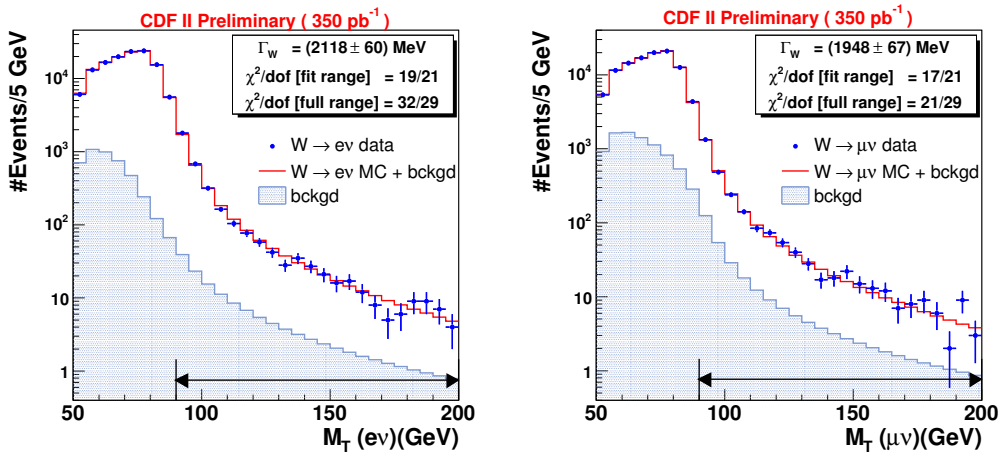

Figure 2: Transverse mass fits for Γ_W in $W \to e\nu$ (left) and $W \to \mu\nu$ (right)

References

[1] Slides:
`http://indico.cern.ch/contributionDisplay.py?contribId=105&sessionId=9&confId=9499`

[2] T. Sjostrand, P. Eden, C. Friberg, L. Lonnblad, G. Miu, S. Mrenna and E. Norrbin, Comput. Phys. Commun. **135** (2001) 238.

[3] C. Balazs, C. P. Yuan, Phys. Rev. D **56**, (1997) 5558.

[4] F. A. Berends, R. Kleiss, J. P. Revol and J. P. Vialle, Z. Phys. C **27** (1985) 155; F. A. Berends and R. Kleiss, Z. Phys. C **27** (1985) 365.

[5] U. Baur, S. Keller and D. Wackeroth, Phys. Rev. D **59**, (1998) 013002.

[6] J. Pumplin, D. R. Stump, J. Huston, H. L. Lai, P. Nadolsky and W. K. Tung, JHEP **0207** (2002) 012.

Top Quark Production and Properties

Cecilia E. Gerber

University of Illinois at Chicago - Department of Physics
845 W. Taylor St. M/C 273, Chicago IL 60607-7059, USA

I present recent results on top quark production and properties in $p\overline{p}$ collisions at a center of mass energy of 1.96 TeV. The measurements were performed by the CDF and D0 collaborations using approximately 1 fb^{-1} of data taken during Run II at the Tevatron.

1 Introduction

The top quark was discovered at the Fermilab Tevatron Collider in 1995 [2, 3] and completes the quark sector of the three-generation structure of the standard model (SM). It is the heaviest known elementary particle with a mass approximately 40 times larger than that of the next heaviest quark, the bottom quark. It differs from the other quarks not only by its much larger mass, but also by its lifetime which is too short to build hadronic bound states. The top quark is one of the least-studied components of the SM, and the Tevatron, with a center of mass energy of $\sqrt{s} = 1.96$ TeV, is at present the only accelerator where it can be produced. The top quark plays an important role in the discovery of new particles, as the Higgs boson coupling to the top quark is stronger than to all other fermions. Understanding the production properties of top quark pairs is in itself a test of perturbative Quantum Chromo Dynamics (pQCD); in addition, it is a crucial ingredient in the discovery of new physics beyond the SM.

In the following sections I will present results for the measurement of the $t\overline{t}$ pair production cross section, studies of $t\overline{t}$ pair production mechanisms, and measurements of the top quark charge.

2 Studies of $t\overline{t}$ pair production mechanisms

At Tevatron energies, top quarks are produced predominantly in pairs. Within the SM, the top quark decays almost exclusively into a W boson and a b quark, resulting in two W bosons and 2 b jets in each $t\overline{t}$ pair event. The W boson itself decays into one lepton and its associated neutrino, or hadronically. We have classified the $t\overline{t}$ pair decay channels as follows: the dilepton channels where both W bosons decay leptonically into an electron or a muon (ee, $\mu\mu$, $e\mu$), the lepton + jets channels where one of the W bosons decays leptonically and the other hadronically (e+jets, μ+jets), and the all-jets channel where both W bosons decay hadronically. Production cross sections have been measured in all decay channels. The lepton + jets channels have less statistics than the all-jets channel, but the background level is significantly smaller, making it the channel of choice for the measurement of top quark properties.

2.1 Measurement of the $t\overline{t}$ pair production cross section

The total top quark pair production cross section for a hard scattering process initiated by a $p\overline{p}$ collision at $\sqrt{s}$ is a function of the top quark mass m_t. For a top quark mass

of 175 GeV, the predicted SM $t\bar{t}$ production cross section is $6.7^{+0.7}_{-0.9}$ pb [4]. Deviations of the measured cross section from the theoretical prediction could indicate effects beyond QCD perturbation theory. Explanations might include substantial non-perturbative effects, new production mechanisms, or additional top quark decay modes beyond the SM. Previous measurements [5, 6] show good agreement with the theoretical expectation within the experimental precision.

Recent new results became available from both CDF and D0 based on approximately 1 fb^{-1} of data. They are summarized in Fig. 1, together with the theoretical predictions. As can be seen in the plots, the uncertainties on the latest experimental results are reaching the theoretical uncertainty of $\approx$ 12%, with 10% uncertainty expected once the 2 fb^{-1} of data already on tape are analyzed.

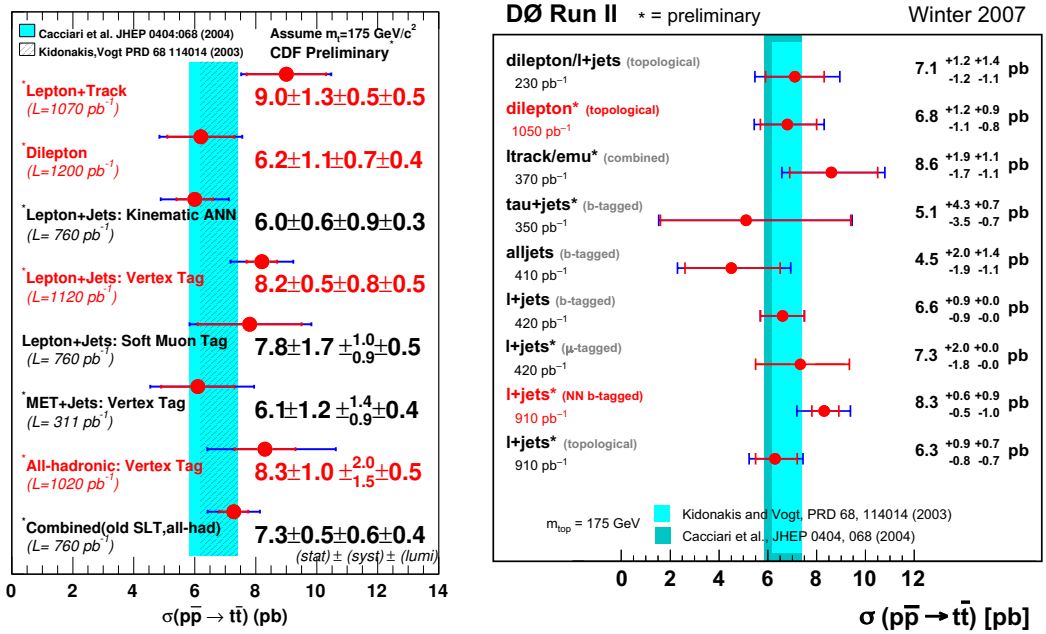

Figure 1: Summary of $t\bar{t}$ pair production cross section measurements at $\sqrt{s} = 1.96$ TeV from CDF (left), and D0 (right). Theoretical predictions are shown as vertical bands. The newest experimental results have total uncertainties (excluding luminosity) of $\approx$ 15%, close to the theoretical uncertainty of 12%.

2.2 Measurement of $\frac{\sigma(gg\to t\bar{t})}{\sigma(q\bar{q}\to t\bar{t})}$

At leading order, $t\bar{t}$ production proceeds through the $q\bar{q} \to t\bar{t}$ and $gg \to t\bar{t}$ processes, with the $q\bar{q}$ process contributing 85% to the production cross section, and the gg process contributing only 15%. NLO theoretical predictions are available [4], but suffer from large uncertainties. Measuring the relative fraction of $t\bar{t}$ events produced via a particular production mechanism provides a direct test of pQCD and may reveal the existence of $t\bar{t}$ production and decay mechanisms beyond the ones predicted by the SM [7].

CDF has studied the relative fraction of $t\bar{t}$ events produced via gluon-fusion: $\frac{\sigma(gg\to t\bar{t})}{\sigma(q\bar{q}\to t\bar{t})}$. Two methods were used for this analysis. The first one takes advantage of the fact that the top quark decays before hadronizing, allowing the different production processes to retain their kinematic characteristics in the final state. A neural network was built using two production and six decay variables and was used to maximize the discrimination between gg and $q\bar{q}$ produced events. Using 695 pb^{-1} of data, a 95% C.L. limit on the relative fraction of $t\bar{t}$ events produced by the gg process is found to be less than 51%.

The second method uses the clear correlation observed between the average number of gluons and the average number of low p_T charged particles present in a given sample to extract the fraction of $t\bar{t}$ events that originate from the gg process. Using 1 fb^{-1} of data, CDF measures for the first time $\frac{\sigma(gg\to t\bar{t})}{\sigma(q\bar{q}\to t\bar{t})} = 0.01 \pm 0.16(stat) \pm 0.07(syst)$, in agreement with SM expectations.

2.3 Search for $t\bar{t}$ Resonances

Several beyond the SM theories [8] predict the resonant production of $t\bar{t}$ pairs. Using 955 pb^{-1} of data, CDF has studied the $t\bar{t}$ invariant mass spectrum in lepton + jets events containing at least 4 jets, with at least one jet being identified as originating from a b quark. The sample contains 347 events, with 73 ± 9 events expected to originate from background processes. The observed spectrum is consistent with SM expectations, showing no evidence for additional resonant production mechanisms. This agreement is used to set various model-dependent limits on resonant $t\bar{t}$ production [9].

3 Measurement of the top quark charge

The electric charge, one of the fundamental properties of particles, has not been determined yet for the top quark. Within the SM, the top quark has charge $q = +2e/3$ and decays into a W^+ boson and a bottom quark ($q = -1e/3$). An alternative scenario [10] has been proposed, in which the top quark observed at the Tevatron would actually be an exotic quark of charge $q = -4e/3$, that decays into a W^- boson and a bottom quark. Within this exotic model (XM), the SM top quark would be more massive, and not observed yet. The first method to discriminate between the two hypotheses was developed by the D0 collaboration. Using 370 pb^{-1} of integrated luminosity, D0 found that their data agreed much better with the SM than with the XM hypothesis [11].

A new analysis [12] recently became available by the CDF collaboration based on 695 pb^{-1} of lepton + jets events with at least 2 jets identified as b-jets, and 955 pb^{-1} of dilepton events with at least 1 b-jet. The charge of the top quark is determined from the charge of the decay products. The charge of the W boson is directly taken from the charge of the lepton. The charge of the jets identified as b-jets is determined by combining the p_T and charge of the tracks associated to the jet. This procedure assigns the correct charge to the jet in approximately 60% of the cases. The last step is the association of the lepton and the b-jet originating from the same top decay branch. The association is estimated from MC to be correct in 86% of the cases for the lepton + jets events, and in 96% of the cases for the dilepton events. The result is extracted using the technique of hypothesis testing. CDF uses the SM as the null hypothesis, and selects, a-priori, the probability of incorrectly rejecting the SM to be 1%. If the XM is true, 81% of all p-values will fall below 0.01. The measured p-value from data under the SM hypothesis is 0.35. This value is greater than 1%, meaning

that the XM hypothesis is excluded at the 81% C.L. CDF also computes the Bayes Factor and concludes that the data strongly favor the SM over the XM hypothesis.

4 Conclusions

The Tevatron has entered a new era of top quark precision measurements. The experimental precision on the top quark pair production cross section results is approaching the theoretical uncertainty, making comparisons between different channels and methods interesting. In addition, a series of new measurements of top quark properties are becoming available based on the larger statistics samples collected in 1 fb^{-1} of collider data. All measurements are in agreement with SM expectations.

CDF and D0 have already written to tape more than twice the amount of data used for these results. The lepton + jets sample with two identified b-jets is completely dominated by $t\bar{t}$ events. With larger data sets, as the ones that will be available at the Tevatron in the near future, this sample will allow for precise measurements of top quark properties for the first time.

Acknowledgments

I would like to thank my collaborators from the CDF and D0 collaborations for their help in preparing this document. I also thank the staffs at Fermilab and collaborating institutions, and acknowledge support from the National Science Foundation (USA).

References

[1] Slides:
http://indico.cern.ch/contributionDisplay.py?contribId=106&sessionId=9&confId=9499

[2] F. Abe *et al.*, CDF Collaboration, Phys. Rev. Lett. **74** 2626 (1995).

[3] S. Abachi *et al.*, D0 Collaboration, Phys. Rev. Lett. **74** 2632 (1995).

[4] N. Kidonakis and R. Vogt, Phys. Rev. D **68**, 114014 (2003). M. Cacciari, S. Frixione, M. L. Mangano, P. Nason, and G. Ridolfi, JHEP **0404**, 68 (2004).

[5] D. Acosta *et al.*, CDF Collaboration, Phys. Rev. Lett. **93**, 142001 (2004); Phys. Rev. D **71**, 052003 (2005); Phys. Rev. D **71**, 072005 (2005); Phys. Rev. D **72**, 032008 (2005); Phys. Rev. D **74**, 072005 (2006); Phys. Rev. Lett. **96**, 202002 (2006); Phys. Rev. Lett. **97**, 082004 (2006).

[6] V. M. Abazov *et al.*, D0 Collaboration, Phys. Lett. B **626**, 35 (2005); Phys. Lett. B **626**, 45 (2005); Phys. Lett. B **626**, 55 (2005); Phys. Rev. D **74**, 112004 (2006).

[7] G.L. Kane and S. Mrenna, Phys. Rev. Lett. **77**, 3502-3505 (1996).

[8] A. Leike, Phys. Rep. 317, 143 (1999); J. Rosner, CERN-TH/96-169 (1996); T. Rizzo, Phys. Rev. D **61**, 055005 (2000); L. Sehgal, M. Wanninger, Phys. Lett. B **200**, 211 (1988); C. Hill, S. Park, Phys. Rev. D **49**, 4454 (1994).

[9] CDF Collaboration public result:
http://www-cdf.fnal.gov/physics/new/top/2006/mass/mttb/mttb_pub.pdf

[10] D. Chang, W. Chang, and E. Ma, Phys. Rev. D **59**, 091503 (1999); **61**, 037301 (2000); D. Choudhury, T.M. Tait, and C. E. Wagner, Phys. Rev. D **65**, 053002 (2002).

[11] V. M. Abazov *et al.*, D0 Collaboration, Phys. Rev. Lett. **98**, 041801 (2007).

[12] CDF Collaboration public result:
http://www-cdf.fnal.gov/physics/new/top/2007/topProp/top_charge/publicTQpage.html

Top Mass and Decay Properties

Jeannine Wagner
on behalf of the CDF and DØ Collaborations

Universität Karlsruhe - Institut für Experimentelle Kernphysik
Wolfgang-Gaede-Str. 1, 76131 Karlsruhe - Germany

A summary of the most precise top mass measurements of the DØ and CDF collaborations is presented. The measurements utilize top anti-top candidates in three different decay channels. In addition this article shows most recent measurements of the W helicity in top decay. The integrated luminosity used for all measurements presented in this article ranges between $0.9\,\mathrm{fb}^{-1}$ and $1.0\,\mathrm{fb}^{-1}$.

1 Introduction

In 1995 the top quark was discovered at the Tevatron proton-antiproton collider at Fermilab by the CDF and DØ collaborations [2, 3]. It is the most massive known elementary particle and the Tevatron collider is so far the only place to study the top quark.

At the Tevatron collider, with a center-of-mass energy of $\sqrt{s} = 1.96$ TeV, most top quarks are pair-produced via the strong interaction. In the standard model the top quark decays predominantly into a W boson and a b quark, with a branching ratio close to 100%. Different decay channels are distinguished according to the decay mode of the W-boson. Because of the difficult identification of τ-leptons all analyses presented in this article make no use of τ-leptons.

2 Top Mass Measurements

A precisely measured top mass m_t allows together with the W boson mass for predictions of the Higgs mass. Loops including a top quark lead to a correction of the W mass which is proportional to m_t^2, while loops including the Higgs lead to a logarithmic correction factor for the W mass. Thus a measurement of the top and W mass leads together with these loop calculations to a constraint on the Higgs mass.

At the Tevatron two analysis techniques are used to measure the top mass. One method is called template method. Here one observable strongly correlated to the true top mass is calculated for each event and the true top mass is then extracted by comparing simulated distributions for signal and background to the data distribution. In the second technique a probability as a function of the true top mass M_t and the reconstructed quantities x is calculated for each event separately for $t\bar{t}$ signal and background. Because in the computation of these probabilities enter the leading order matrix element of either signal or background processes this technique is called matrix element method. The total probability $P_{evt}(x|M_t)$ for an event is then obtained by $P_{evt}(x;M_t) = f_{top} \cdot P_{sig}(x;M_t) + (1 - f_{top}) \cdot P_{bg}(x)$, where the fraction f_{top} of signal events enters. Then the likelihoods for each event are multiplied and from the sample likelihood the most likely top mass m_t is determined.

Much effort has already been put into the measurement of the top mass and meanwhile the uncertainties of the top mass are dominated by systematic uncertainties. The dominating systematic uncertainty is the uncertainty on the jet energy scale. The jet energy scale is a factor applied to the calorimeter jets to get parton level jets. New sophisticated analysis

strategies had to be developed to make significant progress in the reduction of the top mass uncertainty.

The challenges of the three decay channels and the most precise top mass measurements in each decay channel are presented in the following.

2.1 Top Mass in the Lepton+Jets Channel

In the Lepton+Jets decay channel, one top quark decays semileptonically and the second top quark decays hadronically, leading to a signature of one charged lepton, missing transverse energy resulting from the undetected neutrino, and four jets. Out of these four jets both collaborations require at least one jet to be tagged as b-jet. The amount of background is at medium level and is composed of mainly W-boson events with associated jets and a smaller fraction of QCD multi-jet events. A bonus of this decay channel is the possibility of an in-situ calibration of light quark jets from the hadronically decaying W boson. This in-situ technique is crucial for the current top mass precision.

The most precise top mass measurements of CDF and DØ both make use of the in-situ technique, leading to a strong reduction of the dominant systematic uncertainty, the jet energy scale. Both measurements use matrix element methods. The CDF measurement [4] yields $m_t = 170.8 \pm 2.2(\text{stat.}) \pm 1.4(\text{syst.})$ GeV/c^2 and the DØ measurement [5] yields $m_t = 170.5 \pm 2.4(\text{stat.}) \pm 1.2(\text{syst.})$ GeV/c^2. Both measurements are well consistent with each other and very competitive. In case of the CDF measurement the largest uncertainty comes now from the initial and final state radiation, the second largest uncertainty is due to the b-jet energy scale uncertainty, while in case of the DØ measurement the largest uncertainty is due to the b-jet energy scale uncertainty.

2.2 Top Mass in the Dilepton Channel

In the Dilepton decay channel, both top quarks decay semileptonically, leading to a signature of two charged leptons, large missing transverse energy resulting from the two undetected neutrinos, and two jets. The amount of background events is at low level, where mainly di-boson events and events with a real W- or Z-boson and associated jets contribute. The challenge of this decay channel is the under-constrained system due to the presence of two neutrinos.

The most precise CDF measurement [6] is a matrix element method. In order to deal with the under-constrained system the event probabilities P_{evt} are integrated over both unmeasured neutrino energies. The measurement yields $m_t = 164.5 \pm 3.9(\text{stat.}) \pm 3.9(\text{syst.})$ GeV/c^2.

The most precise measurement of DØ [7] is a template method. In order to deal with the under-constrained system, the pseudorapidities of the two neutrinos are assumed for a hypothetical top mass. For each hypothesis an expected missing transverse momentum is calculated and a weight according to the agreement between the calculated and the observed missing transverse energy is then assigned to this hypothesis. For each event the mean and root mean square (rms) values of the distribution: weights versus hypothetical top mass, are determined and used to fit the top mass. The result of this measurement is $m_t = 172.5 \pm 5.8(\text{stat.}) \pm 5.5(\text{syst.})$ GeV/c^2.

2.3 Top Mass in the All Hadronic Channel

In the All Hadronic decay channel, both top quarks decay hadronically, leading to a signature of six jets. Out of these six jets at least one jet is required to be tagged as b-jet. The amount of background events is huge and consists mainly of multi-jet events. The actual challenge of this channel is the reduction of the huge background. That is the reason why a further selection on the event topology is necessary, for example with a neural net. A bonus of this channel is again the possibility of an in-situ calibration of light quark jets using the mass of the hadronically decaying W bosons.

So far, only CDF has performed measurements in this decay channel. The most precise measurement [8] applies a matrix element assisted 2D template method. It uses for the first time the in-situ technique. The signal templates are determined from matrix element calculations, while the background templates are determined from a data-driven model. The top mass is then determined from a fit of the signal and background templates to the data. This analysis yields a top mass of $m_t = 171.1 \pm 3.7(\text{stat.}) \pm 2.1(\text{syst.})$ GeV/c^2.

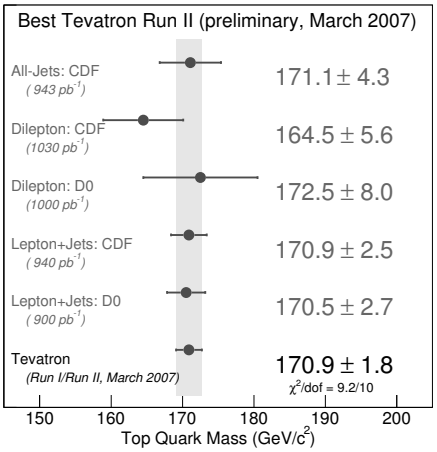

Figure 1: Most precise top mass measurements and Tevatron top mass combination.

2.4 Tevatron Top Mass Combination

A summary of the most precise top mass measurements is presented in Figure 1. The Tevatron top mass combination [9] including all these new very precise top mass measurement yields $m_t = 170.9 \pm 1.8(\text{stat.+syst.})$ GeV/c^2, corresponding to a relative uncertainty of the top mass below 1.1%.

3 Top Decay Properties

Although the top mass is now measured with a relative uncertainty at the 1% level the question remains whether the standard model successfully predicts the properties of the top quark. This article addresses one interesting aspect of top quark decay properties, namely the W helicity in top decays.

In general the W boson can either be longitudinally, left-handed or right-handed polarized. In the standard model a fraction F_0 of longitudinally polarized W bosons of 70% is predicted, the fraction F_- of left-handed W bosons is predicted to be 30% while the fraction F_+ of right-handed W boson is in the SM strongly V-A suppressed and is predicted to be zero. Deviations from these SM values would indicate new physics. A possible V+A coupling would lead to an altered $F+$ value. An altered F_0 value would be an indication for an non-SM electroweak symmetry breaking mechanism.

All measurements look at the leptonic decay of the W boson from the top quark. In the most recent measurements $\cos\theta^*$ is used as observable, with θ^* being the angle between the charged lepton and the negative direction of the top quark in the rest frame of the W-boson.

The two most recent W helicity results are performed by CDF [10] and they both utilize the Lepton+Jets channel. Performing a fit to the distribution of the reconstructed $\cos\theta^*$, the fit yields $F+ = -0.03 \pm 0.07$ when F_0 is fixed to its Standard Model value of 0.7, while the fit yields $F_0 = 0.59^{+0.14}_{-0.13}$ if F_+ is fixed to the Standard Model value of 0. Figure 2 shows the unfolded differential $\cos\theta^*$ distribution. In a second analysis a simultaneous fit of F_0 and F_+ has been performed for the first time, yielding: $F_+ = -0.06 \pm 0.10$ and $F_0 = 0.74 \pm 0.26$. However, the uncertainties are still large for the simultaneous fit and even in the constrained fit the result is still statistically limited. The F_+ measurement from CDF using the invariant mass of the charged lepton and the b-jet [11] and the F_+ measurement from DØ [12] give consistent results. In summary, all DØ and CDF measurements are consistent with the Standard Model prediction.

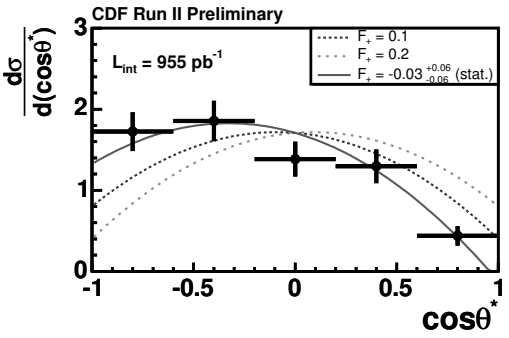

Figure 2: Unfolded differential $\cos\theta^*$ distribution.

4 Summary

In this article recent measurements of the top mass and of top decay properties have been presented. By now the top mass measurements are systematically limited. The new Tevatron top mass combination yields $m_t = 170.9 \pm 1.8$ GeV/c^2 leading to a relative uncertainty at the 1% level. Concerning the top decay properties, all measurements are still statistically limited and so far no deviation compared to the Standard Model prediction is observed.

References

[1] Slides:
`http://indico.cern.ch/contributionDisplay.py?contribId=107&sessionId=9&confId=9499`

[2] F. Abe *et al.*, Phys. Rev. Lett. **74** 2626 (1995).

[3] S. Abachi *et al.*, Phys. Rev. Lett. **74** 2632 (1995).

[4] A. Abulencia *et al.*, FERMILAB-PUB-07-070-E, submitted to Phys. Rev. Lett..

[5] DØ conference note 5362 (2007).

[6] A. Abulencia *et al.*, Phys. Rev. **D75**, 031105(R) (2007).

[7] DØ conference note 5347 (2007).

[8] A. Abulencia *et al.*, Phys. Rev. Lett. **98**, 142002 (2007).

[9] Tevatron Electroweak Working Group, arXiv:hep-ex/0703034 (2007).

[10] CDF conference note 8380 (2006);
CDF conference note 8368 (2006).

[11] A. Abulencia *et al.*, Phys. Rev. Lett. **98**, 072001 (2007).

[12] V. M. Abazov *et al.*, Phys. Rev. **D75**, 031102(R) (2007).

Single Top Quark Production at the Tevatron

Shabnam Jabeen

Boston University - Dept of Physics
590 Commonwealth Ave Boston, MA 02215

The Run II of the Tevatron has started in 2001 and the D0 and CDF experiments have collected more than 2 fb^{-1} data since then. We present the results of a search for electroweak production of single top quarks in $p\bar{p}$ collisions at $\sqrt{s} = 1.96$ TeV at the Fermilab Tevatron collider, using a dataset with integrated luminosity of nearly 1 fb^{-1}.

1 Introduction

First observed in 1995 [1], the top quark is one of a pair of third-generation quarks in the standard model of particle physics. It has charge $+2/3e$ [2] and a mass of 171.4 ± 2.1 GeV [3], about 40 times heavier than its isospin partner, the bottom quark. We present the results of a search for top quarks produced singly via the electroweak interaction from the decay of an off-shell W boson or fusion of a virtual W boson with a b quark [4, 5, 6]. All previously measured top quarks have come from the decay of a highly energetic gluon, which produces top quark - top antiquark ($t\bar{t}$) pairs. The standard model prediction for the cross section for $p\bar{p} \to t\bar{t}$ is 6.7 pb [7, 8], for the s-channel single top quark process $p\bar{p} \to tb$ it is 0.9 ± 0.1 pb, and for the t-channel process it is 2.0 ± 0.3 pb [5]. For brevity, we use the notation "tb" to mean the sum of $t\bar{b}$ and $\bar{t}b$, and "tqb" to mean the sum of $tq\bar{b}$ and $\bar{t}\bar{q}b$. The main tree-level Feynman diagrams for single top quark processes are shown in Fig. 1.

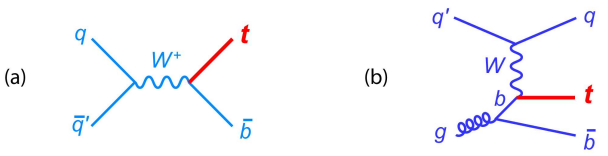

Figure 1: Leading order Feynman diagrams for (a) s-channel single top quark production and (b) t-channel production.

Top quarks are interesting particles to study since their very high mass implies a Yukawa coupling to the Higgs boson with a value near unity, unlike any other known particle. They also decay before they hadronize, allowing the properties of a naked quark such as spin to be transferred into its decay products and thus be measured and compared to standard model predictions. Events with single top quarks can also be used to study the Wtb coupling, and to measure directly the absolute value of the CKM matrix element $|V_{tb}|$ without assuming three generations of quarks. A value not close to one would imply the existence of a fourth quark family.

The rsults presented here are part of a series performed by the CDF and D0 experiments. Both CDF and D0 published papers [9, 10, 11, 12] using Run I and Run II data but none of these searches was sensitive enough to observe single top quark production.

2 Search Strategy and Event Selection

The search focuses on the final state consisting of one high transverse momentum (p_T) isolated electron or muon and missing transverse energy ($\not\!\!E_T$) together with a b-quark jet from the decay of the top quark ($t \to Wb \to \ell\nu b$), and an additional b antiquark in the case of s-channel production, or an additional light-quark jet and a b-antiquark jet for t-channel production. The b-antiquark jet produced in the t-channel is rarely reconstructed since it is produced in the forward direction with low transverse momentum. The main backgrounds in this analysis share the same lepton+jets final state; they are W-boson production in association with jets (W+jets), top quark pair production ($t\bar{t}$) in the lepton+jets and dilepton final states if a jet or a lepton is not reconstructed, and multijet production, where a jet is misreconstructed as an electron, or a heavy-flavor quark decays to a muon that is misidentified as isolated from the jet.

D0 selects 1,398 lepton+jets data events, which is expected to contain 62 ± 13 single top quark events. The analysis is split into twelve orthogonal channels based on the lepton flavor (e or μ), jet multiplicity (2, 3, or 4), and number of identified b jets (1 or 2), to increase the search sensitivity since the expected signal acceptance and signal to background ratio differ significantly from channel to channel.

CDF selects 644 candidate events for this analysis by requiring a W + 2 jet event topology only, which is expected to contain 38 ± 6 single top quark events. One or both of the two jets should be identified as a b-jet using the secondary vertex tag requirement. CDF further requires the missing transverse energy and the jets not to be collinear for low values of missing transverse energy. This requirement removes a large fraction of the non-W background while retaining most of the signal.

Since we expect the single top quark signal events to constitute only a small fraction of the selected event samples, a counting experiment will not have sufficient sensitivity to verify their presence. Both CDF and D0 use sophisticated analysis techniques (listed below) to discriminate signal from backgrounds. The resulting discriminant distributions are used to set limits or measure the production cross-section.

- Boosted Decision Trees - used by D0
- Matrix Elements - used by D0 and CDF
- Likelihood Discriminants - used by CDF
- Bayesian Neural Networks - used by D0 and CDF

3 Results

In case of CDF, the Likelihood method and Neural Networks set a limit of $\sigma_{s+t} < 2.7$ pb at 95%C.L. and $\sigma_{s+t} < 2.6$ pb at 95%C.L. respectivley. The Matrix Elements method measures a cross section of $\sigma_{s+t} = 2.7^{+1.5}_{-1.3}$ pb with a p-value = 1.0% corresponding to a significance of 2.3σ. Using pseudo experiments, the correlation between these three analyses is detremined to be 60-70% with a 1.2% probabaility that one could get a combination of results given above.

The three methods used by D0, Decision Trees, Matrix Elements, Bayesian Neural Networks measure a production cross section of $\sigma_{s+t} = 4.9 \pm 1.4$ pb, $\sigma_{s+t} = 4.6^{+1.8}_{-1.5}$ pb, $\sigma_{s+t} = 5.0 \pm 1.9$ pb respectively, with respective p-values corresponding to a significanse of 3.4σ, 2.9σ and 2.3σ. It should be noted here that CDF and D0 use slightly different

methods to measure p-values and thus the two values are not directly comparable. The correlation between these three analysis methods is measured using the ensemble of pseudo-datasets. The Boosted Decision Tree analysis is 39% correlated with the matrix element analysis and 57% correlated with the Bayesian Neural Networks analysis.

D0 uses the Best Linear Unbiased Estimate (BLUE) method [13] to obtain the combined measurement.

$$\sigma\left(p\bar{p} \to tb + X,\ tqb + X\right) \quad = 4.7 \pm 1.3 \text{ pb} \quad (\text{DT} + \text{ME} + \text{BNN combined}),$$

The p-value for the combination corresponds to a significanse of 3.5σ, thus providing the first evidence for single top production. Fig. 2 summarizes the measurements from the individual analyses as well as the combination.

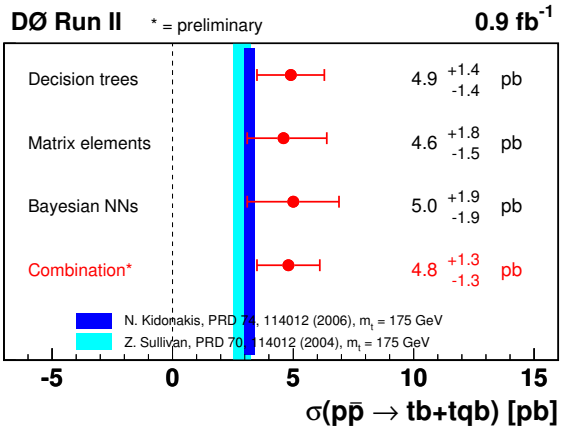

Figure 2: The single top cross section measurements using real data, from the individual analyses and the combination.

D0 also sets a lower limit of $|V_{tb}| > 0.68$ on the absolute value of the CKM matrix element $|V_{tb}|$ based on the single top quark analysis. These result by D0 has already been published [14] .

4 Bibliography

For more information on results from both experiments please visit the following public web pages:

D0: `http://www-d0.fnal.gov/Run2Physics/top/public/fall06/singletop/`
CDF: `http://www-cdf.fnal.gov/physics/new/top/top.html`

4.1 Link to slides

`http://indico.cern.ch/contributionDisplay.py?contribId=109&sessionId=9&confId=9499`

References

[1] F. Abe *et al.* (CDF Collaboration), Phys. Rev. Lett. **74**, 2626 (1995); S. Abachi *et al.* (D0 Collaboration), Phys. Rev. Lett. **74**, 2632 (1995).

[2] V.M. Abazov *et al.* (D0 Collaboration), submitted to Phys. Rev. Lett., hep-ex/0608044.

[3] The Tevatron Electroweak Working Group for the CDF and D0 Collaborations, hep-ex/0608032.

[4] S.S.D. Willenbrock and D.A. Dicus, Phys. Rev. D **34**, 155 (1986); S. Dawson and S.S.D. Willenbrock, Nucl. Phys. **B 284**, 449 (1987); C.-P. Yuan, Phys. Rev. D **41**, 42 (1990); S. Cortese and R. Petronzio, Phys. Lett. **B 253**, 494 (1991); R.K. Ellis and S.J. Parke, Phys. Rev. D **46**, 3785 (1992); D.O. Carlson and C.-P. Yuan, Phys. Lett. **B 306**, 386 (1993); G. Bordes and B. van Eijk, Nucl. Phys. **B 435**, 23 (1995); T. Stelzer and S. Willenbrock, Phys. Lett. **B357**, 125 (1995); M.C. Smith and S. Willenbrock, Phys. Rev. D **54**, 6696 (1996); A.P. Heinson, A.S. Belyaev, and E.E. Boos, Phys. Rev. D **56**, 3114 (1997); T. Stelzer, Z. Sullivan and S. Willenbrock, Phys. Rev. D **56**, 5919 (1997); T. Stelzer, Z. Sullivan and S. Willenbrock, Phys. Rev. D **58**, 094021 (1997); B.W. Harris *et al.*, Phys. Rev. D **66**, 054024 (2002); Q.-H. Cao *et al.*, Phys. Rev. D **72**, 094027 (2005); N. Kidonakis, hep-ph/0609287.

[5] Z. Sullivan, Phys. Rev. D **70**, 114012 (2004).

[6] Q.-H. Cao, R. Schwienhorst, and C.-P. Yuan, Phys. Rev. D **71**, 054023 (2005).

[7] N. Kidonakis and R. Vogt, Phys. Rev. D **68**, 114014 (2003).

[8] M. Cacciari *et al.*, J. High Energy Phys. **0404**, 068 (2004).

[9] D. Acosta *et al.* (CDF Collaboration), Phys. Rev. D **65**, 091102 (2002); D. Acosta *et al.* (CDF Collaboration), Phys. Rev. D **69**, 053003 (2004).

[10] B. Abbott *et al.* (D0 Collaboration), Phys. Rev. D **63**, 031101 (2001); V.M. Abazov *et al.* (D0 Collaboration), Phys. Lett. **B 517**, 282 (2001).

[11] D. Acosta *et al.* (CDF Collaboration), Phys. Rev. D **71**, 012005 (2005).

[12] V.M. Abazov *et al.* (D0 Collaboration), Phys. Lett. **B 622**, 265 (2005); V.M. Abazov *et al.* (D0 Collaboration), submitted to Phys. Rev. D, hep-ex/0604020.

[13] L. Lyons, D. Gibaut, and P. Clifford, Nucl. Instrum. Methods **A 270**, 110 (1988); R. J. Barlow, *Statistics: A Guide To The Use Of Statistical Methods In The Physical Sciences*, The Manchester Physics Series, John Wiley and Sons, New York (1989); G. Cowan, *Statistical Data Analysis*, Oxford (1998).

[14] D0 Collaboration, Search for single top production PLB 622, 265 (2005)

Single Top Studies with MCFM *

Francesco Tramontano

Università di Napoli "Federico II" - Dipartimento di Scienze Fisiche
and INFN sezione di Napoli, Via Cintia, I-80125 - Napoli, Italy

We report about next to leading order calculations for single top production at hadron colliders. These calculations have been implemented into the general purpose next to leading order Montecarlo program MCFM. They describe the production of single top to all the three possible channels foreseen in the Standard Model and the leptonic decay of the top quark with full spin correlation.

1 Introduction

In the Standard Model (SM) single top events may occurr only through weak interaction so that the evidence for single top production at the Tevatron [2] makes new tests of the SM possible. In particular we can test the Wtb weak vertex and in principle we could get information on its prefactor, the CKM matrix element V_{tb}.

Another strong motivation to calculate accurate predictions for single top event rates and distributions is the fact that such events give a significant contribution as background to Higgs boson discovery both at the Tevatron and the LHC. For a complete review on the subject see ref. [3]. The three ways to produce single top at the hadron colliders are the s-channel, the t-channel and the t-W associated production, the last two being sensitive to the b-pdf, nowadays still based on calculation rather then on measurements. In Figure 1 the leading order (LO) Feynman graphs for the three machanisms are painted. Calculations at LO are affected by large theoretical errors. The first serious approximation in QCD is obtained by including $O(\alpha_S)$ radiative corrections. Only at next to leading order (NLO) we obtain accurate predictions of event rates sensitive to the structure of jets in the final state. Furthermore, only at NLO we get important informations about the choice of factorization and renormalization scales. In Figure 2, we show the renormalization and factorization scale dependence of LO and NLO total rates for Wt production normalized to the LO rate for a fixed scales choice [4]. Previous NLO calculations [5] did not include the decays of the top quark (and the

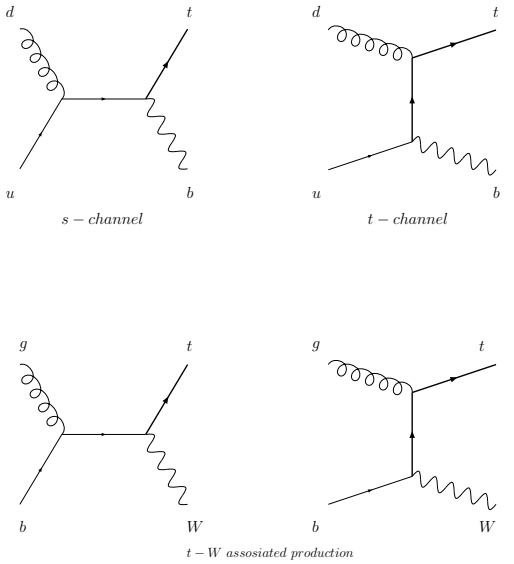

Figure 1: Leading order graphs representing the three possible mechanisms to produce single top (bold).

*The slides of this contribution can be found at the URL in ref. [1]

process	$p\bar{p}$ $\sqrt{s} = 1.96TeV$	$p\bar{p}$ $\sqrt{s} = 14TeV$
s-channel	0.872 pb	10.4 pb
t-channel	1.92 pb	245 pb
t-W	0.143 pb	68.7 pb

Table 1: Next to leading order cross sections for each channel of single top quark production at the Tevatron and LHC.

W boson in the case of the associated production). We added the leptonic decay of the top quark with full spin correlation, and included the effects of gluon radiation in the decay. The calculations were implemented in the next to leading order Montecarlo program MCFM [6]

2 Calculation

The NLO predictions for the total cross sections of the three single top channels are reported in Table 1 both for the Tevatron and the LHC. In refs. [7] and [4] the interested reader can find all the details of the calculations as well as a discussion of all the approximations. We work in the on shell approximation for the top quark. This is motivated by the fact that diagrams without an on shell top quark are suppressed by Γ_t/m_t. Furthermore, we neglect the interference of radiation emitted in the production and the decay stages. This simplifing approximation is possible due to the large difference in the time scale for the production $(1/m_t)$ and the decay $(1/\Gamma_t)$ of the top quark. The error introduced by this approximation is expected to be $O(\alpha_S \Gamma_t/m_t)$ [8]. We also assume $m_b = 0$ through all the calculations and inlcude no showering and hadronization. The cancellation of the singularities between the real and virtual contributions is performed with the subtraction method with massive quarks [9]. We extend this method by introducing a tunable parameter that controls the size of the subtractions. In this way we perform quicker calculations because the subtractions are evaluated only in the phase space region surrounding the singularities. Furthermore, the independence on this parameter is a valuable check of the implementation. The inclusion of the radiation in the decay of the top quark has been done through the implementation of a specific subraction counterterm mapping the singularities of the real matrix element [7]. This procedure can be useful to study the $t\bar{t}$ associated production with the decay of the top quarks. The comparison of this calculation with the forthcoming measurements for $t\bar{t}$ asso-

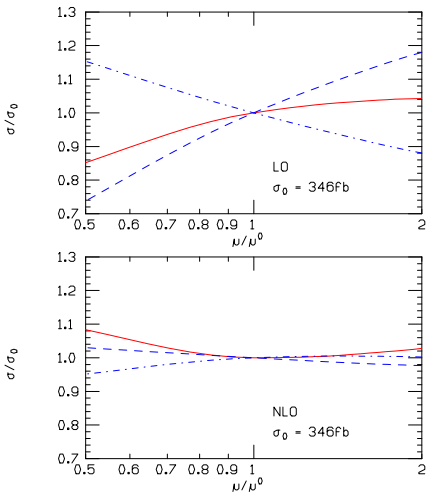

Figure 2: Factorization and renormalization scale dependence for W-t associate production cross section at leading order (top) and next to leading order (bottom). Solid curves represent the variation of both scales.

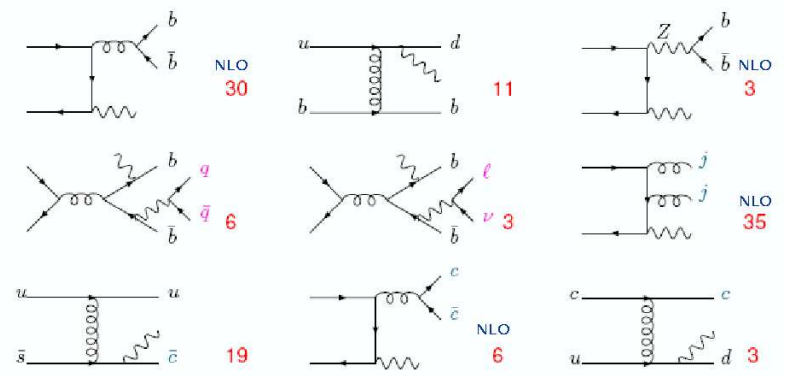

Figure 3: Main background processes for single top search at the Tevatron and their rate with the cuts contained in Table 2.

ciated production at Tevatron could improve the estimation of the top mass in the standard model.

3 Results

In ref. [7] we performed a signal and background analysis of the single top events at Tevatron, where only s and t channels can lead to an evidence for single top. Many background processes can be calculated at NLO within MCFM. With the cuts given in Table 2 we consider the contribution of the background events represented in Figure 3. Their estimated rates are also reported in the figure, together with the specification if they are evaluated at NLO. Furthermore, in Figure 4 we plot the distribution of the Ht variable, the sum of the lepton p_T, missing transverse energy and jet transverse momenta for the signal and the sum of the backgrounds. At the LHC the rate for the Wt channel is larger than the s-channel. It represents a large sourse of background for the Higgs boson searches through the discovery channel $H \to WW^*$. In Figure 5 we plot the distribution of the opening angle in the transverse plane beetwen the two charged leptons from the two W's both for signal and top backgrounds [4]. For the Wt channel the NLO corrections introduce important modifications to the simple LO prediction.

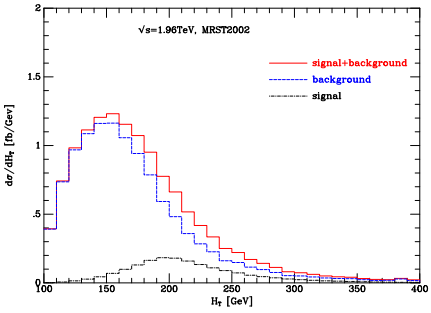

Figure 4: The Ht distributions of signal, background and signal plus background for s- and t-channel single top production at the Tevatron.

References

[1] Slides:
http://indico.cern.ch/contributionDisplay.py?contribId=110&sessionId=9&confId=9499

$p_T^e > 20\ GeV,$	$\lvert\eta^e\rvert < 1.1,$	$\not{E}_T > 20\ GeV,$
$p_T^{jet} > 15\ GeV,$	$\lvert\eta^{jet}\rvert < 2.8,$	$\Delta_R > 1,$

Table 2: Set of cuts used to study single top events at the Tevatron [7].

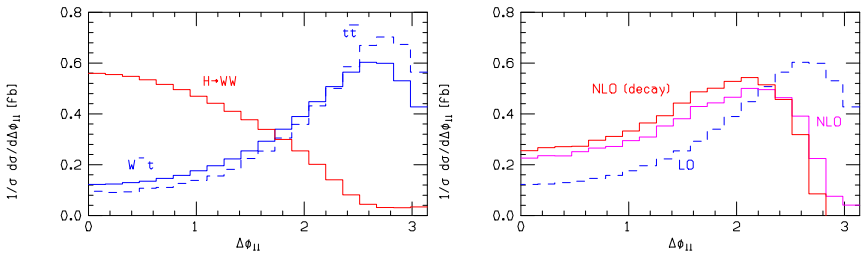

Figure 5: The opening angle between the leptons in the $H \to WW$ and $t\bar{t}$ associated production (left panel) and for the W-t associated production (right panel). Cross sections are normalized to unity, after suitable search cuts have been applied for an Higgs boson with mass 155 GeV.

[2] B. Stelzer [for the CDF Collaboration], arXiv:0706.0282 [hep-ex];
A. Garcia-Bellido [for the D0 collaboration], arXiv:0706.0037 [hep-ex].

[3] C. E. Gerber *et al.* [THe TeV4LHC-Top and Electroweak Working Group], arXiv:0705.3251.

[4] J. Campbell and F. Tramontano, Nucl. Phys. B **726**, 109 (2005) [arXiv:hep-ph/0408158].

[5] M. C. Smith and S. Willenbrock, Phys. Rev. D **54**, 6696 (1996) [arXiv:hep-ph/9604223];
G. Bordes and B. van Eijk, Nucl. Phys. B **435**, 23 (1995).
T. Stelzer, Z. Sullivan and S. Willenbrock, Phys. Rev. D **56**, 5919 (1997) [arXiv:hep-ph/9705398].
B. W. Harris, E. Laenen, L. Phaf, Z. Sullivan and S. Weinzierl, Phys. Rev. D **66**, 054024 (2002) [arXiv:hep-ph/0207055].
Z. Sullivan, arXiv:hep-ph/0408049;
S. Zhu, Phys. Lett. B **524**, 283 (2002) [Erratum-ibid. B **537**, 351 (2002)].

[6] J. M. Campbell and R. K. Ellis, Phys. Rev. D **60**, 113006 (1999) [arXiv:hep-ph/9905386];
J. M. Campbell and R. K. Ellis, Phys. Rev. D **62**, 114012 (2000) [arXiv:hep-ph/0006304];
J. Campbell and R. K. Ellis, Phys. Rev. D **65**, 113007 (2002) [arXiv:hep-ph/0202176].

[7] J. Campbell, R. K. Ellis and F. Tramontano, Phys. Rev. D **70**, 094012 (2004) [arXiv:hep-ph/0408158].

[8] V. S. Fadin, V. A. Khoze and A. D. Martin, Phys. Lett. B **320**, 141 (1994) [arXiv:hep-ph/9309234];
V. S. Fadin, V. A. Khoze and A. D. Martin, Phys. Rev. D **49**, 2247 (1994); K. Melnikov and O. I. Yakovlev, Phys. Lett. B **324**, 217 (1994) [arXiv:hep-ph/9302311];
R. Pittau, Phys. Lett. B **386**, 397 (1996) [arXiv:hep-ph/9603265];
C. Macesanu, Phys. Rev. D **65**, 074036 (2002) [arXiv:hep-ph/0112142].

[9] S. Catani and M. H. Seymour, Phys. Lett. B **378** (1996) 287 [hep-ph/9602277];
S. Catani and M. H. Seymour, Nucl. Phys. B **485** (1997) 291 [Erratum-ibid. B **510** (1997) 291] [hep-ph/9605323];
S. Catani, S. Dittmaier, M. H. Seymour and Z. Trocsanyi, Nucl. Phys. B **627**, 189 (2002) [arXiv:hep-ph/0201036].

Higher-Order Threshold Corrections for Single Top Quark Production

Nikolaos Kidonakis *

Kennesaw State University, Physics #1202
1000 Chastain Rd., Kennesaw, GA 30144-5591, USA

I discuss single top quark production at the Tevatron and the LHC. The cross section, including soft-gluon threshold corrections through NNNLO, is presented for each partonic channel. The higher-order corrections provide significant contributions to the single top cross sections at both colliders.

1 Introduction

Single top quark production at hadron colliders can proceed through three distinct partonic processes: the t channel ($qb \to q't$ and $\bar{q}b \to \bar{q}'t$) which involves the exchange of a spacelike W boson, the s channel ($q\bar{q}' \to \bar{b}t$) which proceeds via a timelike W boson, and associated tW production ($bg \to tW^-$) [1]. The t channel processes are numerically the largest at both the Tevatron and the LHC. At the Tevatron the s channel is second in magnitude and tW production has the smallest cross section. At the LHC, tW production has a much bigger cross section than the s channel.

The cross sections for all these processes receive contributions from soft-gluon emission which can be dominant near threshold [2, 3]. Threshold resummation organizes these contributions and can be used to compute higher-order corrections for many processes [4, 5, 6]. For the partonic process with momenta $p_1+p_2 \to p_3+p_4$ we define $s=(p_1+p_2)^2$, $t=(p_1-p_3)^2$, $u=(p_2-p_3)^2$ and $s_4 = s+t+u-m_3^2-m_4^2$. Near threshold, s_4 approaches zero and the soft-gluon corrections take the form $[\ln^l(s_4/m_t^2)/s_4]_+$, where m_t is the top quark mass and $l \leq 2n-1$ for the n-th order corrections. We calculate these corrections through next-to-next-to-next-to-leading order (NNNLO) in the strong coupling α_s at next-to-leading logarithmic (NLL) accuracy at the Tevatron [2] and the LHC [3]. This requires one-loop calculations in the eikonal approximation.

The NLO soft-gluon corrections can be written in the form

$$\frac{d^2\hat{\sigma}^{(1)}}{dt\,du} = F^B \frac{\alpha_s(\mu_R^2)}{\pi} \left\{ c_3 \left[\frac{\ln(s_4/m_t^2)}{s_4} \right]_+ + c_2 \left[\frac{1}{s_4} \right]_+ + c_1^\mu \, \delta(s_4) \right\}$$

where F^B is the Born term for each channel and μ_R is the renormalization scale. For the t and s channels the leading logarithm coefficient is $c_3^{t,s} = 3C_F$ while for the tW channel it is $c_3^{tW} = 2(C_F + C_A)$, where $C_F = (N_c^2-1)/(2N_c)$ and $C_A = N_c$ with $N_c = 3$ the number of colors. The NLL coefficient is $c_2^s = -\frac{7}{4}C_F + 2C_F \ln\left(\frac{s(s-m_t^2)}{(t-m_t^2)(u-m_t^2)}\right) - 2C_F \ln\left(\frac{\mu_F^2}{m_t^2}\right)$ for the s channel, where μ_F is the factorization scale, and similar expressions can be given for the other channels. The complete virtual corrections ($\delta(s_4)$ terms) cannot be derived from threshold resummation but one can derive the factorization and renormalization scale terms denoted by c_1^μ in the above equation [2].

*This work has been supported by the National Science Foundation under Grant No. PHY 0555372.

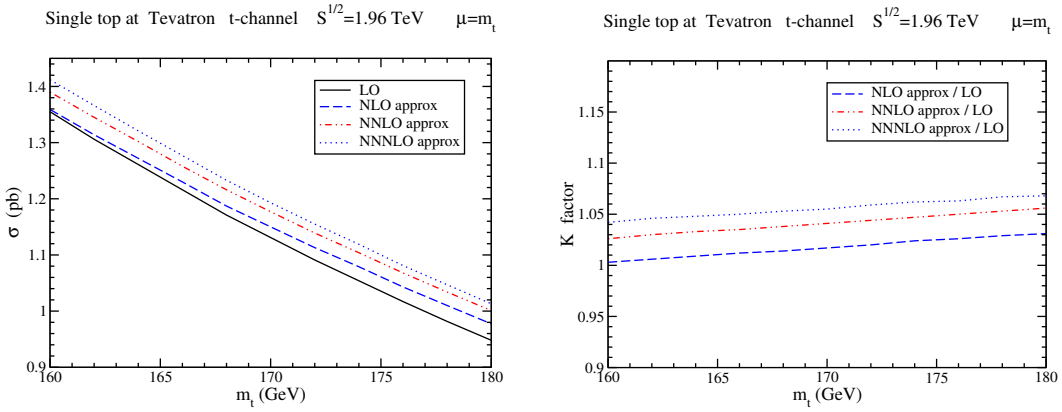

Figure 1: t-channel single top quark cross section at the Tevatron.

The NNLO soft-gluon corrections for the t and s channels are

$$\frac{d^2\hat{\sigma}^{(2)}_{t,s}}{dt\,du} = F^B \frac{\alpha_s^2(\mu_R^2)}{\pi^2} \left\{ \frac{1}{2} c_3^2 \left[\frac{\ln^3(s_4/m_t^2)}{s_4} \right]_+ + \left[\frac{3}{2} c_3\, c_2 - \frac{\beta_0}{4} c_3 + C_F \frac{\beta_0}{8} \right] \left[\frac{\ln^2(s_4/m_t^2)}{s_4} \right]_+ \right\}$$

plus subleading terms [2], where the appropriate expression for F_B and c_3, c_2 for each channel must be used, and where $\beta_0 = (11C_A - 2n_f)/3$ is the lowest-order β function, with n_f the number of light quark flavors. A similar expression holds for the tW channel (by deleting $C_F\beta_0/8$ above). Since this is a NLL calculation, only the leading and NLL terms shown above are complete. However we can also calculate exactly terms involving μ_F and μ_R as well as terms with ζ constants in the subleading logarithms. Complete expressions and further details are provided in Ref. [2].

The NNNLO soft-gluon corrections for each channel can be written as

$$\frac{d^2\hat{\sigma}^{(3)}}{dt\,du} = F^B \frac{\alpha_s^3(\mu_R^2)}{\pi^3} \left\{ \frac{1}{8} c_3^3 \left[\frac{\ln^5(s_4/m_t^2)}{s_4} \right]_+ + \left[\frac{5}{8} c_3^2 c_2 - \frac{5}{48} \beta_0 c_3 (2c_3 - C_F) \right] \left[\frac{\ln^4(s_4/m_t^2)}{s_4} \right]_+ \right\}$$

plus subleading terms [2], again with the appropriate expression for F_B and c_3, c_2.

2 Single top quark production at the Tevatron

We now calculate the contribution of these corrections to the single top cross section at the Fermilab Tevatron. The MRST 2004 NNLO parton densities [7] are used for the numerical results. We find that the threshold corrections are dominant in all partonic channels.

Figure 1 shows the results for the cross section in the t channel. In the left-hand plot we show the leading-order (LO) cross section as well as the cross sections with the NLO, NNLO, and NNNLO soft-gluon corrections included versus the top quark mass m_t, with the factorization and renormalization scales set equal to m_t. On the right-hand plot we show the K factors, which are the ratios of the higher-order cross sections to LO. We see that the corrections in this channel are relatively small. Our best estimate for the cross

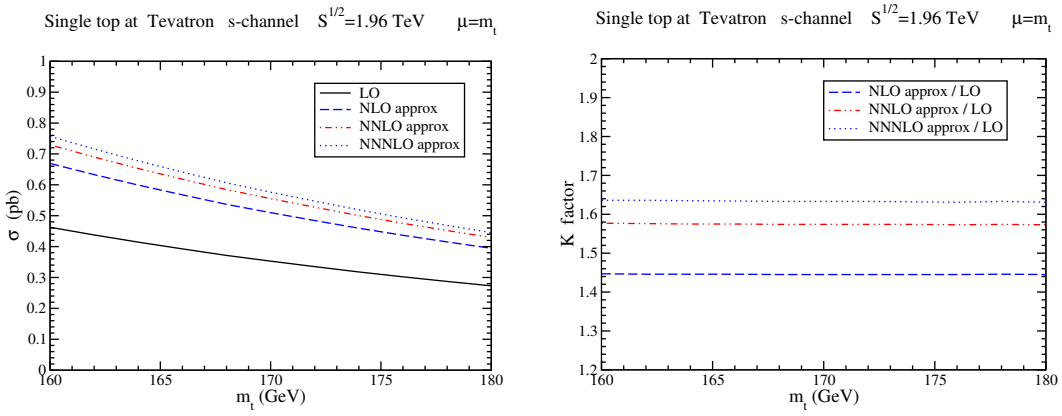

Figure 2: s-channel single top quark cross section at the Tevatron.

section is calculated after matching to the exact NLO cross section [8], i.e. by adding the soft-gluon corrections through NNNLO to the exact NLO cross section. Below we give results for two choices of the top quark mass, $m_t = 170$ GeV and $m_t = 175$ GeV. We find $\sigma^{t-\text{channel}}(m_t = 170\,\text{GeV}) = 1.17 \pm 0.06$ pb and $\sigma^{t-\text{channel}}(m_t = 175\,\text{GeV}) = 1.08 \pm 0.06$ pb. The uncertainty indicated includes the scale dependence and the pdf uncertainties.

Figure 2 shows the results for the cross section and K factors in the s channel. In this channel the corrections are large, providing up to 65% enhancement of the leading-order cross section. After matching, we find $\sigma^{s-\text{channel}}(m_t = 170\,\text{GeV}) = 0.56 \pm 0.03$ pb and $\sigma^{s-\text{channel}}(m_t = 175\,\text{GeV}) = 0.49 \pm 0.02$ pb.

The single top cross section at the Tevatron in the tW channel is rather small, even though the K factors are large (up to 85% enhancement). Our estimate for the cross section is $\sigma^{tW}(m_t = 170\,\text{GeV}) = 0.15 \pm 0.03$ pb and $\sigma^{tW}(m_t = 175\,\text{GeV}) = 0.13 \pm 0.03$ pb.

For all three channels at the Tevatron the cross section for single anti-top production is identical to that shown above for single top production.

Finally, we note that there has been recent evidence for single top quark production at the Tevatron [9] with a cross section consistent with the above results.

3 Single top quark production at the LHC

Next we calculate the threshold corrections for the single top cross section at the CERN LHC. It turns out that in the t channel the threshold corrections are not a good approximation of full QCD corrections, hence we only update the exact NLO result [8], while in the s and tW channels the threshold approximation holds and we provide results including the NNNLO soft-gluon corrections. Also at the LHC the cross section for single top is different from that for single antitop production in the t and s channels.

The exact NLO cross section for single top production in the t channel at the LHC is $\sigma_{\text{top}}^{t-\text{channel}}(m_t = 170\,\text{GeV}) = 152 \pm 6$ pb and $\sigma_{\text{top}}^{t-\text{channel}}(m_t = 175\,\text{GeV}) = 146 \pm 5$ pb. For single antitop production in the t channel the exact NLO cross section is $\sigma_{\text{antitop}}^{t-\text{channel}}(m_t = 170\,\text{GeV}) = 93 \pm 4$ pb and $\sigma_{\text{antitop}}^{t-\text{channel}}(m_t = 175\,\text{GeV}) = 89 \pm 4$ pb.

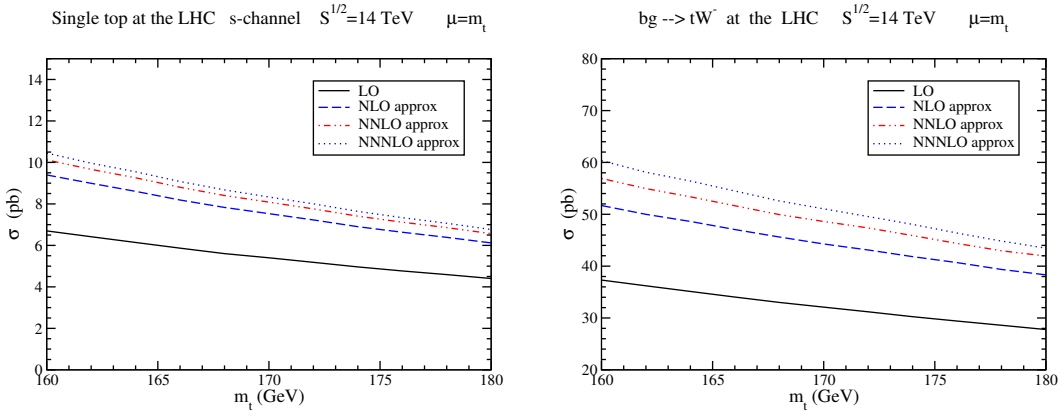

Figure 3: s-channel single top (left) and tW (right) cross sections at the LHC.

Figure 3 (left) shows results for single top production in the s channel at the LHC. The contribution from soft gluons is significant (up to 55% enhancement). After matching to the exact NLO cross section [8], we find $\sigma_{\rm top}^{s-{\rm channel}}(m_t = 170\,{\rm GeV}) = 8.0^{+0.6}_{-0.5}$ pb and $\sigma_{\rm top}^{s-{\rm channel}}(m_t = 175\,{\rm GeV}) = 7.2^{+0.6}_{-0.5}$ pb.

The corresponding results for single antitop production at the LHC in the s channel are $\sigma_{\rm antitop}^{s-{\rm channel}}(m_t = 170\,{\rm GeV}) = 4.5 \pm 0.2$ pb and $\sigma_{\rm antitop}^{s-{\rm channel}}(m_t = 175\,{\rm GeV}) = 4.0 \pm 0.2$ pb. Here the soft-gluon corrections are somewhat smaller (less than 20%).

Figure 3 (right) shows results for single top production at the LHC in the tW channel. This channel has a significant cross section at the LHC. Also the soft-gluon corrections are quite large, providing around 60% enhancement. After matching to the exact NLO cross section [10], we find $\sigma^{tW}(m_t = 170\,{\rm GeV}) = 44 \pm 5$ pb and $\sigma^{tW}(m_t = 175\,{\rm GeV}) = 41 \pm 4$ pb. The cross section for associated antitop production is identical to that for a top quark.

References

[1] Slides:
`http://indico.cern.ch/contributionDisplay.py?contribId=111&sessionId=9&confId=9499`

[2] N. Kidonakis, Phys. Rev. **D74** 114012 (2006).

[3] N. Kidonakis, Phys. Rev. **D75** 071501(R) (2007).

[4] N. Kidonakis, Int. J. Mod. Phys. **A19** 1793 (2004); Mod. Phys. Lett. **A19** 405 (2004).

[5] N. Kidonakis, Phys. Rev. **D73** 034001 (2006); PoS HEP2005 055 (2006); DIS 2006 463 (2007).

[6] N. Kidonakis and A. Belyaev, JHEP **12** 004 (2003); N. Kidonakis and A. Sabio Vera, JHEP **02** 027 (2004); R.J. Gonsalves, N. Kidonakis and A. Sabio Vera, Phys. Rev. Lett. **95** 222001 (2005); N. Kidonakis, R.J. Gonsalves, and A. Sabio Vera, DIS 2006 337 (2007).

[7] A.D. Martin, R.G. Roberts, W.J. Stirling and R.S. Thorne, Phys. Lett. **B604** 61 (2004).

[8] B.W. Harris, E. Laenen, L. Phaf, Z. Sullivan and S. Weinzierl, Phys. Rev. **D66** 054024 (2002).

[9] D0 Collaboration, Phys. Rev. Lett. **98** 181802 (2007).

[10] S.H. Zhu, Phys. Lett. **B524** 283 (2002); (E) **B537** 351 (2002).

Early Electroweak and Top Quark Physics with CMS

Frank-Peter Schilling *

University of Karlsruhe - Institut für Experimentelle Kernphysik
D-76128 Karlsruhe - Germany

The Large Hadron Collider is an ideal place for precision measurements of the properties of the electroweak gauge bosons $W^{\pm}, Z^0$, as well as of the top quark. In this article, a few highlights of the prospects for performing such measurements with the CMS detector are summarized, with an emphasis on the first few 1/fb of data.

1 Introduction

At the Large Hadron Collider (LHC), $W^{\pm}$ and Z^0 bosons as well as top quarks will be produced copiously, due to the large center-of-mass energy of 14 TeV (which leads to increased production cross sections with respect to e.g. the TEVATRON) as well as the high luminosity of up to 10^{34} cm^{-2}s^{-1}. These samples can be used not only for precision measurements of standard model parameters such as m_W and m_t, but also for detector commissioning, alignment and calibration. Furthermore, standard model processes involving $W^{\pm}, Z^0$ bosons and top quarks constitute the primary sources of background in many Higgs boson and new physics searches.

This article [1] summarizes a few highlights of recent studies [2] of the potential of the CMS experiment regarding top quark and electroweak physics, in particular in view of the first few 1/fb of data. They have been performed with a full detector simulation, are based on the reconstruction software and calibration procedures demonstrated in [3], and include estimates of the main systematic uncertainties.

2 Electroweak Physics

The reactions $pp \to W + X$ and $pp \to Z + X$, with subsequent leptonic decays of the $W^{\pm}$ and Z^0 bosons, have a large cross section and are theoretically well understood. Cross sections above 10 nb (1 nb) are expected at the LHC for the $W \to l + \nu$ ($Z \to l^+ + l^-$) channel in the fiducial region of the CMS detector. Thousands of leptonic $W^{\pm}$ and Z^0 decays will be recorded for luminosities as low as 1 pb^{-1}. Hence, they are useful for many purposes, including a precise luminosity monitor, a high-statistics detector calibration and alignment tool and to demonstrate the performance of the CMS experiment. These reactions will be among the first to be measured at the LHC.

The measurement of the inclusive production of $W^{\pm}$ and Z^0 bosons with CMS has been studied in [4] and [5] for the muon and electron decay channel, respectively. The emphasis has been put on a start-up oriented event selection with high purity. Already for an integrated luminosity of 1 fb^{-1}, the uncertainty in the measured cross section will be dominated by systematics. In case of the muon channel,

$$\Delta\sigma/\sigma(pp \to Z + X \to \mu\mu + X) = 0.13\ (\text{stat.}) \pm 2.3\ (\text{syst.})\ \%$$
$$\Delta\sigma/\sigma(pp \to W + X \to \mu\nu + X) = 0.04\ (\text{stat.}) \pm\ 3.3\ (\text{syst.})\ \%\ ,$$

*on behalf of the CMS Collaboration

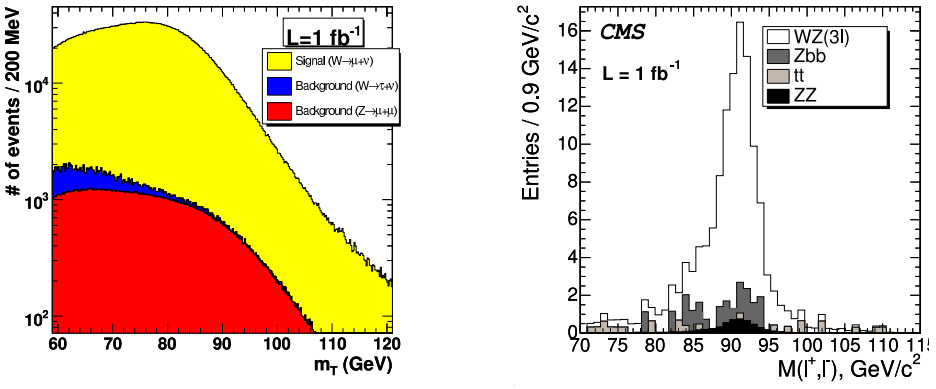

Figure 1: (left) Transverse mass distribution in the $W \to \mu\nu$ channel for 1 fb^{-1}. (right) Dilepton invariant mass distribution in the $WZ \to 3l$ channel for 1 fb^{-1}.

where the systematic error is dominated by a 2% uncertainty originating from the modeling of the boson p_T dependence, which enters in the acceptance determination. Another important source of theoretical uncertainty is the imperfect knowledge of the parton density functions (PDFs), which affects the absolute normalization by $5-7\%$ [4]. Unless more precise PDF sets become available, this will be a limiting factor in comparisons between experiment and theory and in luminosity measurements via W, Z counting. But the argument can also be turned around: These processes can yield important PDF constraints, even without very precise knowledge of the luminosity, in particular by measuring the shapes of differential lepton distributions [6].

The $W^{\pm}$ boson mass is an important Standard Model (SM) parameter. CMS has investigated the use of methods involving W/Z ratios in the mass measurement, which have the advantage that many experimental and theoretical uncertainties cancel [7]. Figure 1(left) shows the simulated transverse mass distribution for 1 fb^{-1} in the muon channel [8]. For both electron and muon channel, the statistical error on m_W is estimated as 40 (15) MeV for 1 (10) fb^{-1}. The total experimental uncertainty is estimated as 40 (20) and 64 (30) MeV for the electron and muon channel, respectively. Apart from the PDF uncertainty, the dominating theoretical uncertainty originates from the modeling of the lepton p_T distribution (estimated as 30 MeV), which may be improved with higher-order calculations. Combining electron and muon channel, the uncertainty on m_W may be reduced to 10 (stat.) $\pm$ 20 (syst.) for 10 fb^{-1}.

The production of diboson pairs can be used to probe triple gauge boson couplings and thus the non-abelian gauge symmetry of electroweak interactions. Such processes are also sensitive to new physics. At the LHC the production cross sections for WZ and ZZ pairs are large (50 and 20 pb respectively). CMS has studied the production of WZ (e or μ channels) as well as of ZZ ($4e$ channel) pairs [9]. For 1 fb^{-1}, 97 events are expected in the WZ channel (Fig. 1(right)), and a 5σ discovery is possible with just 150 pb^{-1} of data. In the $ZZ \to 4e$ channel, 71 events are expected for 10 fb^{-1}. The large signal over background (S/B) ratio makes these measurements very useful to assess the background in the search for the Higgs boson.

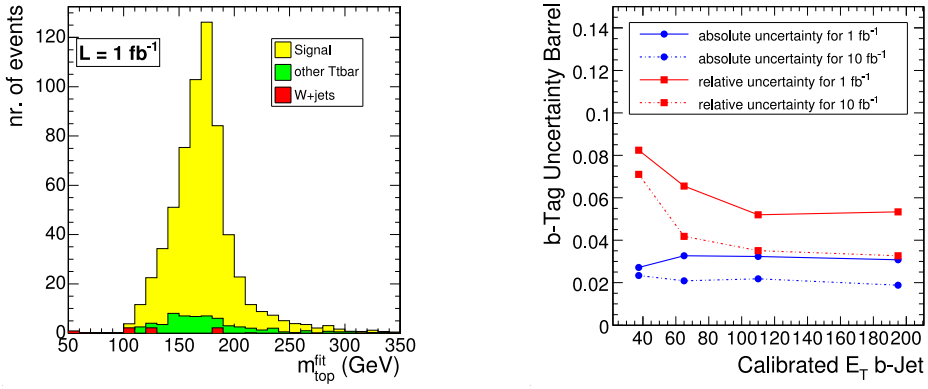

Figure 2: (left) Reconstructed m_t distribution in the semileptonic channel for 1 fb^{-1}. (right) b-tagging uncertainty in the barrel detector as a function of jet p_T, determined from $t\bar{t}$ events.

3 Top Quark Physics

The $t\bar{t}$ production cross section at the LHC is ~ 830 pb (e.g. [10]), which is more than two orders of magnitude higher than at the TEVATRON. At a luminosity of $2 * 10^{33}$ cm^{-2}s^{-1}, about 1 $t\bar{t}$ pair will be produced per second, predominantly gluon-induced. Also the cross section of the electroweak production of single top quarks is large, ~ 245 pb in the t-channel. In 1 fb^{-1} of data, around 800K $t\bar{t}$ pairs and 350K single top quarks will be produced, which makes the LHC experiments ideal laboratories to precisely measure top quark properties. In addition, since large samples of $t\bar{t}$ events will be available already with the first year's data, they can also be used as a detector commissioning tool, e.g. to study lepton identification and isolation, jet and missing E_T energy scales and b-tagging performance. The initial goal will be to measure the $t\bar{t}$ cross section, followed by the mass measurement and studies of single top production, polarization or search for flavor-changing neutral currents (FCNC).

The measurement of the $t\bar{t}$ cross section has been studied in all three decay modes [11, 12]. In the semileptonic channel (Fig. 2(left)), the cross section can be determined from event counting due to the high $S/B \sim 27$. For 1 (10) fb^{-1}, the statistical and systematic uncertainties are estimated as 1.2 (0.4) and 9.2% respectively, where the systematic uncertainty is dominated by the knowledge of the b-tagging efficiency, which is conservatively estimated as 7%. If it could be reduced to 2%, the total error on $\sigma(t\bar{t})$ could be reduced to 7% at 10 fb^{-1}, which would already constrain m_t indirectly to $\Delta m_t \sim 2-3$ GeV, comparable to the precision of the direct measurements at the TEVATRON. For the dilepton and fully hadronic channels, the statistical (systematic) uncertainties are estimated as 0.9 (11)% and 3 (20)% respectively at 10 fb^{-1}.

The top quark mass m_t is related to the Higgs mass via loop corrections. Also the measurement of m_t has been studied in all decay modes. In the semileptonic channel [13], a simple gaussian fit is compared with the more sophisticated *ideogram* method. For 10 fb^{-1}, a precision of $\Delta m_t = 0.21$ (stat.) ± 1.13 (syst.) GeV is estimated for this method. Thus, a 1 GeV uncertainty on m_t looks achievable, but requires a very good detector understanding. The other decay modes [12] have been investigated as well. In the dilepton channel an uncertainty of $\Delta m_t = 1.5$ (0.5) (stat.) $\pm$ 2.9 (1.1) (syst.) GeV is estimated for 1(10) fb^{-1},

where the systematic error is dominated by the jet energy scale uncertainty. In the fully hadronic channel, where a jet pairing likelihood is applied to improve the S/B from 1/9 to 1/3 at constant efficiency, the estimate is $\Delta m_t = 0.6$ (stat.) $\pm$ 4.2 (syst.) GeV for 1 fb^{-1}.

Due to the large cross section $t\bar{t}$ events are useful as a tool to commission and calibrate the detector. For instance, a study has shown that the light quark jet energy scale can be constrained to the level of 3% by applying a m_W constraint in $t\bar{t}$ events [14]. Furthermore, a high purity selection of dilepton $t\bar{t}$ events can be used to constrain the relative b-tagging efficiency (Fig. 2(right)) to 6 (4)% with 1 (10) fb^{-1} of data, as demonstrated in [15].

The electroweak production of single top quarks has been studied in [16, 17]. Single top production is a process is sensitive to new physics (e.g. heavy W' bosons, FCNC or charged Higgs bosons), but also provides a direct handle on the $|V_{tb}|$ CKM matrix element. In the t-channel, which has the biggest cross section, 2400 events are selected with an optimized selection (S/B $\sim$ 1.3), which allows the cross section to be determined with an accuracy of $\Delta\sigma/\sigma \sim 2.7$ (stat.) $\pm$ 8.1(syst.) % for 10 fb^{-1} of data. The s- and tW-channels have been investigated as well. There, the estimated uncertainties are larger.

4 Conclusions

Due to the large cross sections, the CMS experiment will be able to make important measurements of $W^{\pm}, Z^0$ boson and top quark production already with the first LHC data. These measurements not only constrain standard model parameters and determine backgrounds to many new physics signals, but are also very useful as detector commissioning tools and calibration candles.

References

[1] Slides:
`http://indico.cern.ch/contributionDisplay.py?contribId=113&sessionId=9&confId=9499`

[2] CMS Collaboration, "Physics Technical Design Report, Vol. II: Physics Performance", J. Phys. G: Nucl. Part. Phys. **34** (2007) 995-1579.

[3] CMS Collaboration, "Physics Technical Design Report, Vol. I: Detector Performance and Software", CERN/LHCC **2006-001** (2006).

[4] J. Alcaraz, CMS Note **2006/082** (2006).

[5] G. Dissertori *et al.*, CMS Note **2006/124** (2006).

[6] A. Tricoli, A. Cooper-Sarkar and C. Gwenlan, "Uncertainties on W and Z production at the LHC", in proceedings of HERA-LHC workshop, CERN **2005-014** (2005). [hep-ex/0509002]

[7] W. Giele and S. Keller, Phys. Rev. **D57** 4433 (1998). [hep-ph/9704419]

[8] V. Buge *et al.*, CMS Note **2006/061** (2006).

[9] V. Brigljevic *et al.*, CMS Note **2006/108** (2006).

[10] N. Kidonakis and R. Vogt., Phys. Rev. **D68** 114014 (2003).

[11] J. D'Hondt, J. Heyninck and S. Lowette, CMS Note **2006/064** (2006).

[12] M. Davids *et al.*, CMS Note **2006/077** (2006).

[13] J. D'Hondt, J. Heyninck and S. Lowette, CMS Note **2006/066** (2006).

[14] J. D'Hondt *et al.*, CMS Note **2006/025** (2006).

[15] S. Lowette *et al.*, CMS Note **2006/013** (2006).

[16] V. Abramov *et al.*, CMS Note **2006/084** (2006).

[17] P. Yeh *et al.*, CMS Note **2006/086** (2006).

Measurements of the CKM Sides at the B Factories

Isamu Nakamura

KEK, 1-1 Oho Tsukuba Ibaraki, 305-0801, Japan

Recent results of the measurements of the CKM sides at B factories are summarised. In this talk, both inclusive and exclusive measurements of the CKM matrix elements $V_{\rm ub}$ and $V_{\rm cb}$, carried out by two experiments BaBar and Belle, are presented.

1 Introduction

After the discovery of CP violation in B decay, the theory of CKM has been tested extensively in B factories. So far all measurements are consistent with the theory of CKM. To go further one has to improve the accuracy of the measurements in the angles and sides of the CKM triangle. Among these measurements the angle β (or ϕ_1) is most precisely determined and its error is a mere one degree. Since the side $|V_{\rm ub}/V_{\rm cb}|$ is opposite to the angle β, and is less accurately measured compared to β, improvement of the measurement of the side $|V_{\rm ub}/V_{\rm cb}|$ is very important to verify further the theory of CKM. Figure 1 shows the allowed region of the CKM triangle determined by measurements of angles(left) and sides(right) only.

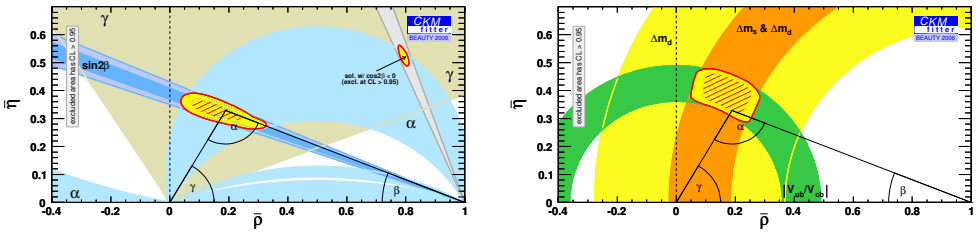

Figure 1: Allowed region of the CKM triagnle.

The CKM element $V_{\rm xb}$ can be determined using semileptonic decays given by the formula,

$$\Gamma(\mathrm{b} \to \mathrm{x}\ell^-\bar{\nu}) = \frac{G_F^2}{192\pi^2} |V_{\rm xb}|^2 \, m_{\rm b}^5 \left(1 + \mathrm{C.F.}\right), \qquad (1)$$

where x is either c or u. So basically $V_{\rm xb}$ can be determined by counting the number of b→x$\ell\nu$ events. However for the precise measurement, determination of the correction term, C.F., is necessary, and is known to be difficult. In the inclusive measurement the term is determined with the help of Heavy Quark Effective theory (HQET), while in the exclusive measurement it is determined in terms of form factor by Lattice QCD.

All averaged results are taken from the Heavy Flavour Averaging Group [2]

2 Measurement of $V_{\rm cb}$

2.1 $V_{\rm cb}$ from inclusive semileptonic decays

For the inclusive decay b→c$\ell\nu$, the C.F. in Equation 1 is described as

$$\mathrm{C.F.} = (1 + A_{\rm ew}) A_{\rm nonpert} A_{\rm pert} = f_{\rm OPE}(m_{\rm b}, m_{\rm c}, a_i),$$

where m_b, m_c are the masses of the b and c quark and a_i are additional parameters depending on the scheme. There are two separate calculations available for the function f_{OPE}, in the kinetic scheme [3] and the 1S scheme [3]. In these calculations, distributions of experimental observables, lepton momentum and invariant mass of the hadronic part of the decay, are predicted. By fitting these distributions, f_{OPE}, and hence V_{cb} can be determined.

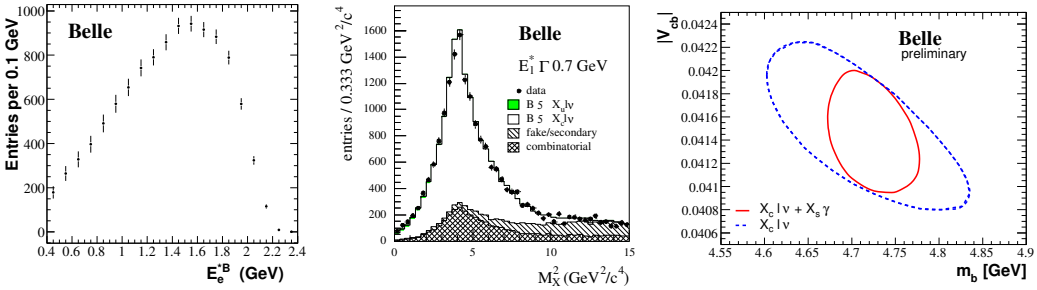

Figure 2: Lepton momentum (left), Hadronic mass (center), and V_{cb}–m_b contour (right)

Figure 2 shows the lepton momentum (left) and hadronic mass distribution (center) measured by Belle [4] as well as the fitted V_{cb}–m_b contour (right) in the kinetic scheme. V_{cb} is determined as $(41.93 \pm 0.91) \times 10^{-3}$ and $(41.49 \pm 0.56) \times 10^{-3}$ for the kinetic and 1S scheme, respectively [2].

2.2 V_{cb} from exclusive semileptonic decays

The CKM parameter V_{cb} is also measured by utilizing an exclusive decay $B \to D^* \ell\nu$ with the following formula,

$$\frac{d\Gamma(B \to D^* \ell\nu)}{dw\, d\cos\theta_\ell\, d\cos\theta_V\, d\chi} = \frac{G_F^2}{48\pi^3} \mathcal{G}(w) |V_{cb}|^2 \mathcal{F}(w; \cos\theta_\ell, \cos\theta_V, \chi, f_j),$$

where w is the boost of the D^* in the B restframe, $\theta_\ell, \theta_V, \chi$ are angles of the decay products defined in Figure 3 and f_j are the form factors. BaBar measured three angular distributions to fit simultaneously the form factor f_j and w distributions using data corresponding to 79 fb^{-1} [5]. Figure 3 shows also the distribution of w. By averaging the result with the

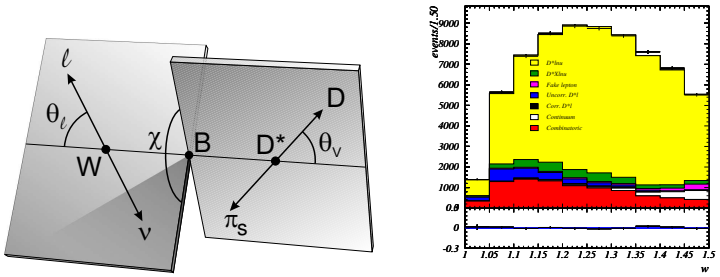

Figure 3: Definition of angles (left), w distribution (right)

other measurements, $\mathcal{F}(1)|V_{cb}|$ is determined as $(35.8 \pm 0.6) \times 10^{-3}$. Using the lattice QCD calculation of $\mathcal{F}(1) = 0.919^{+0.030}_{-0.035}$ [6], a V_{cb} value of $(39.0 \pm 0.7^{+1.3}_{-1.5}) \times 10^{-3}$ is obtained.

3 Measurement of V_{ub}

3.1 V_{ub} from inclusive semileptonic decays

The CKM element V_{ub} can be determined by measuring the inclusive branching fraction $B(B \to X_u \ell\nu)$ using equation 1. Since the b→u branching fraction is about 50 times smaller than that of b→c, one has to utilize some kinematic variables, such as the lepton momentum, the leptonic invariant mass, q^2, or the hadronic mass, M_X, to enhance b→u decay against b→c. Hence, what is actually measured is the partial branching fraction. From the partial branching fraction, V_{ub} can be determined by the formula,

$$|V_{ub}| = \sqrt{\frac{\Delta B(b \to u \ell^- \bar{\nu})}{\mathcal{R}(\Delta\phi)}},$$

where the factor $\mathcal{R}(\Delta\phi)$ is the partial rate in the kinematic phase space predicted by theory. There are several calculations available for this factor $\mathcal{R}$. Figure 4 shows the q^2 distribution

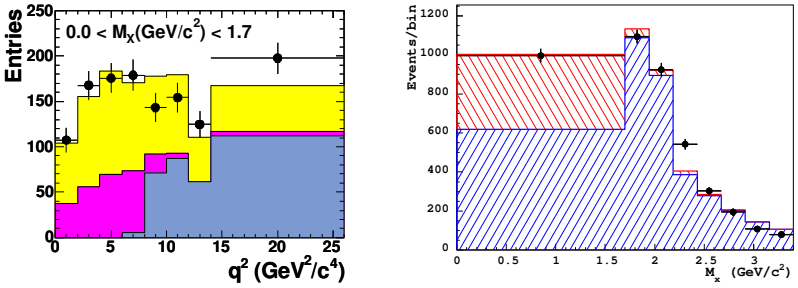

Figure 4: q^2 distribution (left) and hadronic mass distribution (right)

(left) measured by BaBar [7] and the distribution of hadronic mass (right) measured by Belle [7]. Fitting these distributions with the expected b→u and b→c shape, the number of b→u events, hence the partial branching fractions are obtained. The measured branching fractions with various kinematic selections are averaged and turned into a V_{ub} value using $\mathcal{R}$ predicted by theory. For the BLNP calculation [8] $|V_{ub}| = (4.52 \pm 0.19_{exp} \pm 0.27_{th}) \times 10^{-3}$ and for the DGE calculation [8] $|V_{ub}| = (4.46 \pm 0.20_{exp} \pm 0.20_{th}) \times 10^{-3}$.

3.2 V_{ub} from exclusive semileptonic decays

The CKM element V_{ub} can be measured in the exclusive decay $B \to \pi\ell\nu$ using the differential rate, given by

$$\frac{d\Gamma(B \to \pi\ell\nu)}{dq^2} = \frac{G_F^2 |V_{ub}|^2}{192\pi^2 m_b^3} \lambda(q^2)^{\frac{3}{2}} \left|f(q^2)\right|^2, \qquad q^2 = (p_\ell + p_\nu)^2.$$

The form factor $\left|f(q^2)\right|$ is calculated by theories, such as Light Cone Sum Rules [9] or Lattice QCD [9]. Experimentally, there are three different analyses for three different tagging methods. The analysis without requirement on the other side of the B has an advantage in the event statistics, while it suffers from large number of background events. On the

other hand the tagged analysis has smallest efficiency with purest signal, which is shown in Figure 5 (Left) [10], where the signal can be clearly separated from the background. Also shown in the Figure is the q^2 distribution obtained in BaBar's untagged analysis as well as the fitted distribution predicted by various theories [10]. By averaging the results of the measurements, $|V_{\rm ub}|$ is calculated as $(3.41 \pm 0.12_{\rm exp}\ ^{+0.56}_{-0.38\ \rm th}) \times 10^{-3}$ using the form factor calculated by LCSR [9] and $(3.97 \pm 0.22_{\rm exp}\ ^{+0.59}_{-0.41\ \rm th}) \times 10^{-3}$ using unquenched lattice QCD calculation [9].

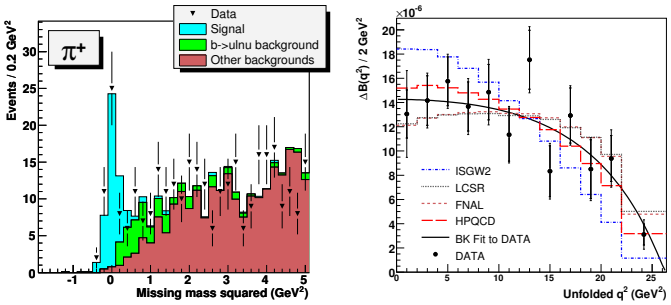

Figure 5: Reconstructed neutrino mass (left) and q^2 (right) distribution

4 Summary

The CKM elements $V_{\rm cb}$ and $V_{\rm ub}$ are measured using both inclusive and exclusive decays. The results are summarised in Table 1. Although these results are obtained by different experimental techniques and using different theoretical treatments, the results are very consistent with each other. Some measurements are limited experimentally and some are by the theory uncertainty. To get the precision of 5%, both experimental and theoretical effort are necessary.

	$\lvert V_{\rm cb}\rvert$ (10^{-3})	$\lvert V_{\rm ub}\rvert$ (10^{-3})
Exclusive	39.4 ± 1.6	4.0 ± 0.6
Inclusive	41.5 ± 0.6	4.5 ± 0.3

Table 1: Measured values of $V_{\rm cb}$ and $V_{\rm ub}$

References

[1] Slides:
`http://indico.cern.ch/contributionDisplay.py?contribId=114&sessionId=9&confId=9499`

[2] HFAG Summer2006, E. Barberio *et al.*, arXiv:0704.3575

[3] 1S: C. Bauer, *et al.*, Rhys. Rev. **D70** 094017; Kinetic: P. Gambino, *et al.*, Eur. Phys. J **C34** 181

[4] C. Schwanda, *et al.*, Rhys. Rev. **D75** 32005(2007); P. Urquijo, *et al.* Rhys. Rev. **D75** 32001(2007)

[5] BaBar Collaboration, hep-ex/0607076.

[6] S. Hashimoto, *et al.*, Phys. Rev. **D66** 014503(2002)

[7] BaBar Collaboration, hep-ex/0507017; Belle Collaboration, I. Bizjak *et al.*, Rhys. Rev. Lett **95** 241801 2005

[8] BLNP: S.W. Bosch, *et al.*, Phys. Rev. **D72** 073006(2005);
DGE: J.R. Anderson, *et al.*, JHEP, 061:097(2006)

[9] LCSR: P. Ball, *et al.*, Phys. Rev. **D71** 014029(2005); LQCD: E. Dalgic,*et al.*,Phys. Rev. **D73** 074502(2006)

[10] BaBar Collaboration, hep-ex/0612020; Belle Collaboration, hep-ex/0610054

Measurement of the CKM Angles at BaBar and Belle.

Nick Barlow

University of Manchester - School of Physics and Astronomy
Oxford Road, Manchester - United Kingdom

The primary goal of the BaBar and Belle experiments is to overconstrain the CKM Unitarity Triangle. Measurements of the angles of this triangle, known as β, α, and γ (or ϕ_1, ϕ_2, and ϕ_3) give insight into the Standard Model description of CP violation in the quark sector. BaBar and Belle have recorded almost 1 ab^{-1} combined, and have measured β to high precision. Measurements of α and γ are less precise at present, but both experiments are rapidly accumulating data and developing new analysis techniques, and measurements of these angles will continue to provide useful constraints on the Standard Model description of CP violation in the years to come.

1 Introduction

The BaBar and Belle experiments are both based at asymmetric-energy e^+e^- colliders operating at the $\Upsilon(4S)$ resonance. Pairs of B mesons are produced in a coherent state, so that if one B decays into a flavour eigenstate at time $t = 0$, the other B must be the opposite flavour at that time. The asymmetric beam energies result in the B mesons being boosted with respect to the laboratory frame, such that the decay distance (and hence the time difference Δt) between the two B decays is measurable. If a B decays into a final state f_{CP} that is accessible from both B^0 and $\overline{B^0}$, interference between the situation where this B decays directly into f_{CP} and where it mixed into the opposite flavour before decaying can give rise to time-dependent CP violation. By fully reconstructing the B decay into f_{CP}, "tagging" the flavour of the other B, and measuring the time difference Δt between their decays, we measure the time-dependend asymmetry $a_{f_{CP}}(\Delta t)$, which can be expressed as a sum of sine and cosine terms:

$$\begin{aligned} a_{f_{CP}}(\Delta t) &= \frac{\Gamma(B^0(\Delta t) \to f_{CP}) - \Gamma(\overline{B^0}(\Delta t) \to f_{CP})}{\Gamma(B^0(\Delta t) \to f_{CP}) + \Gamma(\overline{B^0}(\Delta t) \to f_{CP})} \\ &= S_{CP}\sin(\Delta m_B \Delta t) + C_{CP}\cos(\Delta m_B \Delta t), \end{aligned} \quad (1)$$

where Δm_B is the mass difference between the two mass eigenstates of the neutral B system. For decays with no direct CP violation (i.e. $\Gamma(B \to f) = \Gamma(\overline{B} \to f)$), the coefficient C_{CP} of the cosine term is expected to be zero, and the asymmetry will oscillate sinusoidally with an amplitude S_{CP} that can often be directly related to one of the angles of the Unitarity Triangle.

2 Measuring the angle β (ϕ_1)

2.1 $b \to c\bar{c}s$ decays

The "golden channel" for measuring β at the B factories is $B \to J/\psi K^0_S$. No direct CP violation is expected in this decay channel, as the tree diagram and the leading penguin diagram have the same weak phase. This means that the coefficient C_{CP} of the cosine term in Eq. 1 is expected to be zero, while $S_{CP} = \sin(2\beta)$. In addition, the branching

fraction is relatively large ($\mathcal{O}(10^{-3})$), and the decay of a J/ψ into two leptons gives a clear experimental signature. New results in this decay channel were announced in summer 2006 by both BaBar, based on 384M $B\overline{B}$ events [2], and Belle, based on 535M $B\overline{B}$ events [3]. BaBar also include the decay channels $\psi(2S)K^0_S$, $\eta_c K^0_S$ and $\chi_{c1}K^0_S$ that have CP eigenvalue -1, but Belle omits these in order to obtain a higher purity sample. Both experiments also use the decay channel $B \to J/\psi K^0_L$, which has the opposite CP eigenvalue. This sample is much less pure due to the difficulty of reconstructing the K^0_L, but is nonetheless useful in reducing the statistical error on $\sin(2\beta)$. BaBar measure $\sin(2\beta) = 0.714 \pm 0.032 \pm 0.018$, while Belle obtain $\sin(2\beta) = 0.642 \pm 0.031 \pm 0.017$.

2.2 Penguin-dominated decays

It is also possible to measure $\sin(2\beta)$ using decays with $b \to q\overline{q}s$ transitions, where q is a down-type quark (s or d). These involve flavour-changing-neutral currents, which are only possible at loop level in the Standard Model, and in some cases such as $B \to \phi K^0$, the decay is expected to be completely penguin-dominated, resulting in negligible direct CP violation (which might otherwise arise through the interference between tree and penguin amplitudes). It is interesting to compare the value of $\sin(2\beta)$ obtained with these channels with that obtained from $b \to c\overline{c}s$, as any deviation could be due to New Physics particles contributing to the loop. Recently, both BaBar and Belle observed statistically significant CP violation in the decay channel $B \to \eta' K^0$. With a dataset containing 384M $B\overline{B}$ events, BaBar [6] measure $S_{CP} = 0.58 \pm 0.10 \pm 0.03$, $C_{CP} = -0.16 \pm 0.07 \pm 0.03$. Belle [3] measure $S_{CP} = 0.64 \pm 0.10 \pm 0.04$, $C_{CP} = 0.01 \pm 0.07 \pm 0.05$ using 535M $B\overline{B}$ events. Figure 1 is a plot from the Heavy Flavor Averaging Group (HFAG) [7], showing a comparison of S_{CP} measurements in penguin-dominated decays with the value measured in B decays to charmonium. It can be seen that all the penguin modes tend to give lower values, and while this is not yet statistically significant, it will be extremely interesting to see if this discrepancy persists as BaBar and Belle accumulate more data.

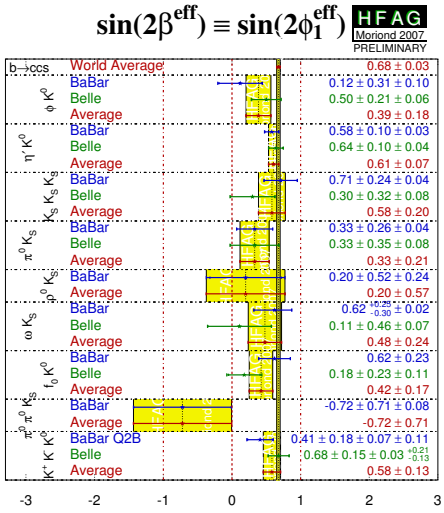

Figure 1: Values of S_{CP} measurements from penguin-dominated modes, compared with the average obtained from $b \to c\overline{c}s$ decays.

3 Measuring the angle α (ϕ_2)

The angle α can be measured using $b \to u\overline{u}d$ decays, such as $B \to \pi^+\pi^-$, $B \to \rho^+\rho^-$ and $B \to \rho^+\pi^-$. However, for all these decay channels, it is expected that both tree and penguin diagrams will contribute, leading to possible direct CP violation, such that the amplitude S_{CP} of the time-dependent asymmetry oscillation is $\sin(2\alpha_{eff})$ rather than $\sin(2\alpha)$. Gronau and London [8] have outlined a technique for separating out the tree and

penguin contributions using an isospin analysis based on the relative branching fractions for $B \to \pi^+\pi^-$, $B \to \pi^\pm\pi^0$, and $B \to \pi^0\pi^0$ (this is also applicable to $\rho^\pm$ and ρ^0). However, some of these decay channels have small branching fractions and are experimentally hard to measure, so the uncertainty on the measured value of α is still largely due to the uncertainty on $(\alpha - \alpha_{eff})$.

For the decay channel $B \to \pi^+\pi^-$, Belle measure $S_{CP} = -0.61 \pm 0.10 \pm 0.04$ and $C_{CP} = -0.55 \pm 0.08 \pm 0.05$ [9], using 535M $B\overline{B}$ events. BaBar measure $S_{CP} = -0.6 \pm 0.11 \pm 0.03$ and $C_{CP} = -0.21 \pm 0.09 \pm 0.02$ [10]. There is still some discrepancy between the BaBar and Belle results for C_{CP}, though this is smaller than in previous publications from both collaborations.

The decay channel $B \to \rho^+\rho^-$ has the additional complication that it is a pseudoscalar-to-vector-vector decay, and so the final state could potentially be a mixture of CP-odd and CP-even eigenstates. However, it turns out that the decay is almost 100% longitudinally polarized. In addition, the measured ratio of branching fractions for $B \to \rho^0\rho^0$ and $B \to \rho^\pm\rho^0$ [11] indicates that the fractional contribution to the decay amplitude from penguin diagrams is smaller than for $B \to \pi^+\pi^-$. This makes $\rho^+\rho^-$ the best single channel for measuring α. With a dataset containing 535M $B\overline{B}$ events, Belle measures $S_{CP} = 0.19 \pm 0.30 \pm 0.08$ [12], while BaBar measure $S_{CP} = -0.17 \pm 0.20^{+0.05}_{-0.06}$ [13] using 384M $B\overline{B}$ pairs.

It is worth noting that all these measurements of $\sin(2\alpha_{eff})$ give multiple possible solutions for the value of α. The CKMFitter [14] and UTFit[15] collaborations have averaged the measurements from both experiments, for all decay channels, using frequentist and Bayesian techniques respectively. Both groups find one of the solutions is compatible with the Standard Model: CKMFitter obtain $\alpha = (93^{+11}_{-9})^o$ and UTFit find α to be between 81^o and 105^o at the 95% C.L.

4 Measuring the angle γ (ϕ_3)

The angle γ is the phase of the CKM matrix element V_{ub}, and is experimentally the hardest to reach at the B factories. It can be measured in $B^\pm \to DK^\pm$ decays where the D decays into a final state accessible to both D^0 and $\overline{D^0}$. Interference between the colour-allowed decay $B^+ \to \overline{D^0}K^+$ and the colour suppressed decay $B^+ \to D^0K^+$ (and likewise for B^-) gives rise to CP violation, but unfortunately the ratio of colour-suppressed to colour-allowed branching fractions is small, and therefore the interference is hard to measure. Three techniques are used at the B factories: the *GLW* method [16] where the D decays into a CP eigenstate; the *ADS* method [17], where the D decays into $K\pi$; and the *GGSZ* method [18], using the Dalitz plot of the D decay into $K^0_S\pi^+\pi^-$. With the GGSZ technique, BaBar measures $\gamma = (92 \pm 42 \pm 10 \pm 13)^o$ [19] with 347M $B\overline{B}$ events. Belle uses a sample of 386M $B\overline{B}$ events to obtain $\gamma = (53^{+15}_{-18} \pm 13 \pm 9)^o$ [20]. In both cases, the third error is due to the uncertainty in the Dalitz model.

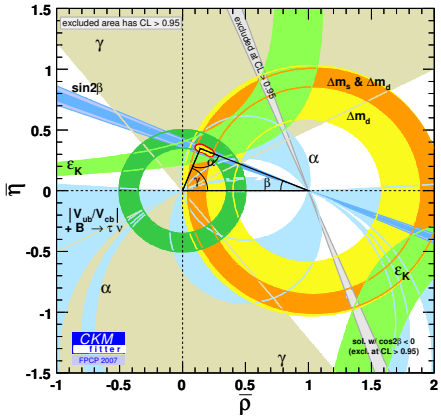

Figure 2: Constraints on the position of the apex of the Unitarity Triangle from all measurements.

5 Conclusions

Figure 2 shows a fit from the CKMFitter collaboration [14] illustrating the current constraints on the position of the apex of the CKM Unitarity Triangle from measurements of its sides and angles. At present, all measurements are compatible with each other and with the Standard Model, and the measurement of β provides one of the strongest constraints. The uncertainties on the angles β, α, and γ are approximately 1^o, 10^o and 35^o respectively. In the coming years, as BaBar and Belle accumulate more data, the uncertainties on γ and in particular on α will reduce substantially, and will provide an excellent test of the Standard Model description of CP violation.

6 Bibliography

References

[1] Slides:
`http://indico.cern.ch/contributionDisplay.py?contribId=115&sessionId=9&confId=9499`

[2] B. Aubert *et al.*, arXiv:hep-ex/0703021, submitted to Phys. Rev. Lett.

[3] K. F. Chen *et al.*, Phys. Rev. Lett. **98** 031892 (2007).

[4] S. Fratina *et al.*, Phys. Rev. Lett. **98** 221802 (2007).

[5] B. Aubert *et al.*, arXiv:0705.1190, submitted to Phys. Rev. Lett.

[6] B. Aubert *et al.*, Phys. Rev. Lett. **98** 031801 (2007).

[7] `http://www.slac.stanford.edu/xorg/hfag`

[8] M. Gronau and D. London, Phys. Rev. Lett. **65** 3381 (1990).

[9] H. Ishino *et al.*, Phys. Rev. Lett **98** 211801 (2007).

[10] B. Aubert *et al.*, Phys. Rev. Lett. **99** 021603 (2007).

[11] B. Aubert *et al.*, Phys. Rev. Lett. **97** 261801 (2006).
B. Aubert *et al.*, Phys. Rev. Lett. **98** 111801 (2007).

[12] K. Abe *et al.*, Phys. Rev. **D76** 011104 (2007).

[13] B. Aubert *et al.*, arXiv:0705.2157, submitted to Phys. Rev. D.

[14] `http://ckmfitter.in2p3.fr/`

[15] `http://utfit.roma1.infn.it/`

[16] M. Gronau and D. London, Phys. Lett. **B253** 483 (1991).
M. Gronau and D. Wyler, Phys. Lett. **B265** 172 (1991).

[17] D. Atwood, I. Dunietz and A. Soni, Phys. Rev. **D63** 036005 (2001).

[18] A. Giri, Y. Grossman, A. Soffer and J. Zupan, Phys. Rev. **D68** 054018 (2003).

[19] B. Aubert *et at.*, arXiv:hep-ex/0707104.

[20] A. Poluektov *et al.*, Phys. Rev. **D73** 112009 (2006).

How to Kill a Penguin

Ulrich Haisch

Universität Zürich - Institut für Theoretische Physik
CH-8057 Zürich - Switzerland

Within constrained minimal-flavor-violation the large destructive flavor-changing Z-penguin managed to survive eradication so far. We give a incisive description of how to kill it using the precision measurements of the $Z \to b\bar{b}$ pseudo observables. The derived stringent range for the non-standard contribution to the universal Inami-Lim function C leads to tight two-sided limits for the branching ratios of all Z-penguin dominated flavor-changing K- and B-decays.

1 Introduction

The effects of new heavy particles appearing in extensions of the standard model (SM) can be accounted for at low energies in terms of effective operators. The unprecedented accuracy reached by the electroweak (EW) precision measurements performed at the high-energy colliders LEP and SLC impose stringent constraints on the coefficients of the operators entering the EW sector. Other severe constraints came in recent years from the BaBar, Belle, CDF, and DØ experiments and concern extra sources of flavor and *CP* violation that represent a generic problem in many scenarios of new physics (NP). The most pessimistic but experimentally well supported solution to the flavor puzzle is to assume that all flavor and *CP* violation is governed by the known structure of the SM Yukawa interactions. In these minimal-flavor-violating (MFV) [2, 3, 4] models correlations between certain flavor diagonal high-energy and flavor off-diagonal low-energy observables exist since, by construction, NP couples dominantly to the third generation. In order to simplify matters, we restrict ourselves in the following to the class of constrained MFV (CMFV) [5] models, i.e., scenarios that involve only SM operators, and thus consider just left-handed currents.

2 General considerations

That new interactions unique to the third generation can lead to an intimate relation between the non-universal $Zb_L\bar{b}_L$ and the flavor non-diagonal $Zd_L^j\bar{d}_L^i$ vertices has been shown recently in [6]. Whereas the former structure is probed by the ratio of the Z-boson decay width into bottom quarks and the total hadronic width, R_b^0, the bottom quark asymmetry parameter, $\mathcal{A}_b$, and the forward-backward asymmetry for bottom quarks, $A_{\rm FB}^{0,b}$, the latter ones appear in many K- and B-decays.

In the effective field theory framework of MFV [4], one can easily see how the $Zb_L\bar{b}_L$ and $Zd_L^j\bar{d}_L^i$ operators are linked together. The only relevant dimension-six contributions compatible with the flavor group of MFV stem from the $SU(2) \times U(1)$ invariant operators

$$\begin{aligned} \mathcal{O}_1 &= i\left(\bar{Q}_L Y_U Y_U^\dagger \gamma_\mu Q_L\right) \phi^\dagger D^\mu \phi\,, \\ \mathcal{O}_2 &= i\left(\bar{Q}_L Y_U Y_U^\dagger \tau^a \gamma_\mu Q_L\right) \phi^\dagger \tau^a D^\mu \phi\,, \end{aligned} \tag{1}$$

that are built out of the quark doublets Q_L, the Higgs field ϕ, the up-type Yukawa matrices Y_U, and the $SU(2)$ generators τ^a. After EW symmetry breaking, $\mathcal{O}_{1,2}$ are responsible for

both the effective $Zb_L\bar{b}_L$ and $Zd_L^j\bar{d}_L^i$ vertex. Since all up-type quark Yukawa couplings except the one of the top, y_t, are small, one has $(Y_U Y_U^\dagger)_{ji} \sim y_t^2 V_{tj}^* V_{ti}$ and only this contribution matters in Eq. (1).

Within the SM the Feynman diagrams responsible for the enhanced top correction to the $Zb_L\bar{b}_L$ coupling also generate the $Zd_L^j\bar{d}_L^i$ operators. In fact, in the limit of infinite top quark mass the corresponding amplitudes are up to Cabibbo-Kobayashi-Maskawa (CKM) factors identical. Yet there is a important difference between them. While for the physical $Z \to b\bar{b}$ decay the diagrams are evaluated on-shell, in the case of the low-energy $Z \to d^j\bar{d}^i$ transitions the amplitudes are Taylor-expanded up to zeroth order in the external momenta. As far as the momentum of the Z-boson is concerned the two cases correspond to $q^2 = M_Z^2$ and $q^2 = 0$.

The general features of the small momentum expansion of the one-loop $Z \to b\bar{b}$ vertex can be nicely illustrated with the following simple but educated example. Consider the scalar integral

$$C_0 = \frac{m_3^2}{i\pi^2} \int \frac{d^4l}{D_1 D_2 D_3}\,, \qquad (2)$$

with $D_i = (l + p_i)^2 - m_i^2$ and $p_3 = 0$. Note that we have set the space-time dimension to four since the integral is finite and assumed without loss of generality $m_3 \neq 0$.

In the limit of vanishing bottom quark mass one has for the corresponding momenta $p_1^2 = p_2^2 = 0$. The small momentum expansion of the scalar integral C_0 then takes the form

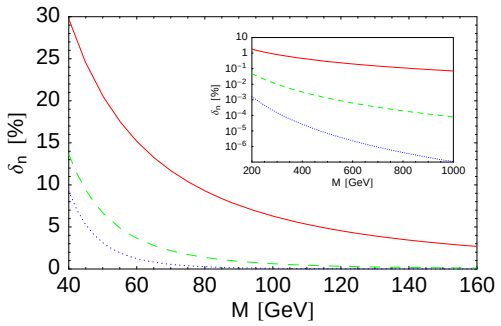

Figure 1: Relative deviations δ_n as a function of M. The solid, dashed, and dotted curve correspond to $n = 1, 2$, and 3, respectively. See text for details.

$$C_0 = \sum_{n=0}^{\infty} a_n \left(\frac{q^2}{m_3^2}\right)^n\,, \qquad (3)$$

with $q^2 = (p_1 - p_2)^2 = -2p_1 \cdot p_2$. The expansion coefficients a_n are given by [7]

$$a_n = \frac{(-1)^n}{(n+1)!} \sum_{l=0}^{n} \binom{n}{l} \frac{x_1^l}{l!} \frac{\partial^l}{\partial x_1^l} \frac{\partial^n}{\partial x_2^n} g(x_1, x_2)\,, \qquad (4)$$

where

$$g(x_1, x_2) = \frac{1}{x_1 - x_2} \left(\frac{x_1 \ln x_1}{1 - x_1} - \frac{x_2 \ln x_2}{1 - x_2}\right)\,, \qquad (5)$$

and $x_i = m_i^2/m_3^2$. Notice that in order to properly generate the expansion coefficients a_n one has to keep x_1 and x_2 different even in the zero or equal mass case. The corresponding limits can only be taken at the end.

To illustrate the convergence behavior of the small momentum expansion of the scalar integral in Eq. (3) for on-shell kinematics, we confine ourselves to the simplified case $m_1 = m_2 = M$ and $m_3 = m_t$. We define

$$\delta_n = a_n \left(\frac{M_Z^2}{m_t^2}\right)^n \left(\sum_{l=0}^{n-1} a_l \left(\frac{M_Z^2}{m_t^2}\right)^l\right)^{-1}\,, \qquad (6)$$

for $n = 1, 2, \ldots$. The M-dependence of the relative deviations δ_n is displayed in Fig. 1. We see that while for $M \lesssim 50\,\text{GeV}$ higher order terms in the small momentum expansion have to be included in order to approximate the exact on-shell result accurately, in the case of $M \gtrsim 150\,\text{GeV}$ the first correction is small and higher order terms are negligible. For the two reference scales $M = \{80, 250\}\,\text{GeV}$ one finds for the first three relative deviations δ_n numerically +9.3%, +1.4%, and +0.3%, and +1.1%, +0.02%, +0.00004%, respectively.

3 Model calculations

The above considerations can be corroborated in another, yet model-dependent way by calculating explicitly the difference between the value of the $Zd^j_L\bar{d}^i_L$ vertex form factor evaluated on-shell and at zero external momenta. In [6] this has been done in four of the most popular, consistent, and phenomenologically viable scenarios of CMFV, i.e., the two-Higgs-doublet model (THDM) type I and II, the minimal-supersymmetric SM (MSSM) with MFV [3], all for small $\tan\beta$, the minimal universal extra dimension (mUED) model [8], and the littlest Higgs model [9] with T-parity (LHT) [10] and degenerate mirror fermions [11]. In the following we will briefly summarize the most important findings of [6].

In the limit of vanishing bottom quark mass, possible non-universal NP contributions to the renormalized off-shell $Zd^j_L\bar{d}^i_L$ vertex can be written as

$$\Gamma^{\text{NP}}_{ji} = \frac{G_F}{\sqrt{2}}\frac{e}{\pi^2}M_z^2\frac{c_W}{s_W}V^*_{tj}V_{ti}C_{\text{NP}}(q^2)\bar{d}^j{}_L\gamma_\mu d^i{}_L Z^\mu\,, \tag{7}$$

where $i = j = b$ and $i \neq j$ in the flavor diagonal and off-diagonal case. G_F, e, s_W, and c_W denote the Fermi constant, the electromagnetic coupling constant, the sine and cosine of the weak mixing angle, respectively, while V_{ij} are the corresponding CKM matrix elements.

As a measure of the relative difference between the complex valued form factor $C_{\text{NP}}(q^2)$ evaluated on-shell and at zero momentum we introduce

$$\delta C_{\text{NP}} = 1 - \frac{\text{Re}\,C_{\text{NP}}(q^2 = 0)}{\text{Re}\,C_{\text{NP}}(q^2 = M_z^2)}\,. \tag{8}$$

The dependence of δC_{NP} on the charged Higgs mass $M_H^\pm$, the lighter chargino mass $M_{\tilde{\chi}_1}^\pm$, the compactification scale $1/R$, and x_L which parameterizes the mass of the heavy top T_+ is illustrated in Fig. 2. The allowed parameter regions after applying experimental and theoretical constraints are indicated by the colored (grayish) bands and points.

In the THDMs, the mUED, and the CMFV version of the LHT model the maximal allowed suppressions of $\text{Re}\,C_{\text{NP}}(q^2 = M_z^2)$ with respect to $\text{Re}\,C_{\text{NP}}(q^2 = 0)$ amounts to less than 2%, 5%, and 4%, respectively. This feature confirms the general argument presented in the last section. The situation is less favorable in the case of the CMFV MSSM, since δC_{MSSM} frequently turns out to be larger than one would expected on the basis of the model-independent considerations if the masses of the lighter chargino and stop both lie in the hundred GeV range. However, the large deviation δC_{MSSM} are ultimately no cause of concern, because $|\text{Re}\,C_{\text{MSSM}}(q^2 = 0)/\text{Re}\,C_{\text{SM}}(q^2 = 0)|$ itself is always below 10%. In consequence, the model-independent bounds on the NP contribution to the universal Z-penguin function that will be derived in the next section do hold in the case of the CMFV MSSM. More details on the phenomenological analysis of δC_{NP} in the THDMs, the CMFV MSSM, the mUED, and the LHT model including the analytic expressions for the form factors $C_{\text{NP}}(q^2)$ can be found in the recent article [6].

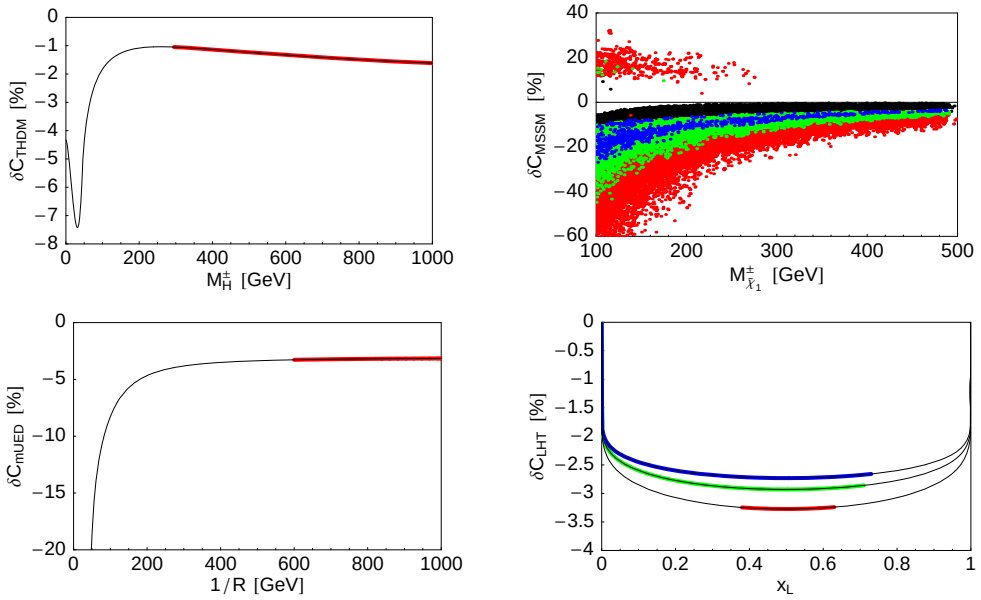

Figure 2: Relative difference $\delta C_{\rm NP}$ in the THDMs, the MSSM, the mUED, and the LHT model as a function of $M_H^\pm$, $M_{\tilde\chi_1}^\pm$, $1/R$, and x_L. Regions in the $M_{\tilde\chi_1}^\pm - \delta C_{\rm MSSM}$ plane where $|\mathrm{Re}\, C_{\rm MSSM}(q^2=0)|$ amounts to at least 2%, 4%, and 6% of $|\mathrm{Re}\, C_{\rm SM}(q^2=0)|$ are indicated by the red (gray), green (light gray), and blue (dark gray) points, respectively. In the case of the LHT model the shown curves correspond, from bottom to top, to the values $f = 1, 1.5$, and 2 TeV of the symmetry breaking scale. See text for details.

4 Numerical analysis

Using the technique of epsilon parameters a model-independent numerical analysis of $\Delta C = \mathrm{Re}\, C(q^2=0) - \mathrm{Re}\, C_{\rm SM}(q^2=0)$ is a back-on-the-envelope calculation. The variation $\epsilon_b^{\rm NP} = \epsilon_b - \epsilon_b^{\rm SM}$ arising from NP contributions to $Zb_L\bar b_L$ can be defined through the inclusive partial width of $Z \to b\bar b$ as follows [12]

$$\Gamma_{bb}^{\rm NP} = (\sqrt{2} G_F M_Z^2)^{\frac{1}{2}} \left(g_V^b (\bar b \gamma_\mu b) - g_A^b (\bar b \gamma_\mu \gamma_5 b) \right) Z^\mu \,, \tag{9}$$

where

$$\frac{g_V^b}{g_A^b} = \left(1 + \frac{4 s_W^2}{3} + \epsilon_b^{\rm NP} \right) \frac{g_A^d}{g_A^b} \,, \quad g_A^b = (1 + \epsilon_b^{\rm NP})\, g_A^d \,. \tag{10}$$

From Eqs. (7), (8), and (9) one obtains

$$\Delta C = - \frac{\pi^2}{\sqrt{2} G_F M_Z^2 c_W^2} (1 + \delta C_{\rm NP})\, \epsilon_b^{\rm NP} \,. \tag{11}$$

By combining experimental [13] and theoretical uncertainties [15] in ϵ_b and $\epsilon_b^{\rm SM}$ linearly one finds

$$\epsilon_b^{\rm NP} = (0.4 \pm 2.5) \times 10^{-3}\,. \qquad (12)$$

Assuming $\delta C_{\rm NP} = \pm 0.1$ one then arrives at

$$\Delta C = -0.04 \pm 0.26\,, \qquad (13)$$

which implies that large negative contributions that would reverse the sign of the SM Z-penguin amplitude are highly disfavored in CMFV scenarios due to the strong constraint from R_b^0 [6]. Interestingly, such a conclusion cannot be drawn by considering only flavor constraints [14], since a combination of $\mathcal{B}(\bar{B} \to X_s\gamma)$, $\mathcal{B}(\bar{B} \to X_s l^+ l^-)$, and $\mathcal{B}(K^+ \to \pi^+ \nu\bar{\nu})$ does not allow to distinguish the SM solution $\Delta C = 0$ from the wrong-sign case $\Delta C \approx -2$ at present.

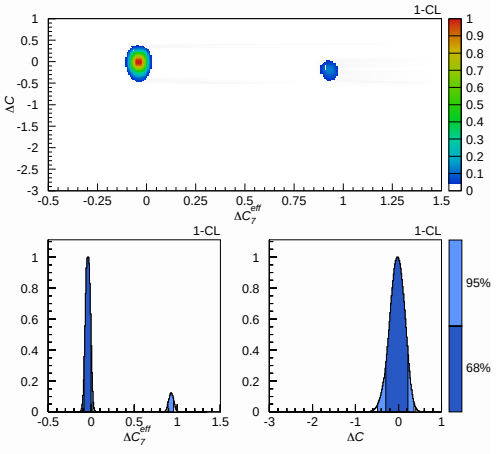

Figure 3: Constraints on $\Delta C_7^{\rm eff}$ and ΔC within CMFV that follow from a combination of the $Z \to b\bar{b}$ POs with the measurements of $\bar{B} \to X_s\gamma$ and $\bar{B} \to X_s l^+ l^-$. The colors encode the frequentist $1 - {\rm CL}$ level and the corresponding 68% and 95% probability regions as indicated by the bars on the right side of the panels. See text for details.

The result in Eq. (13) agrees amazingly well with the numbers of a thorough global fit to the POs R_b^0, $\mathcal{A}_b$, and $A_{\rm FB}^{0,b}$ [13] and the measured $\bar{B} \to X_s\gamma$ [17] and $\bar{B} \to X_s l^+ l^-$ [18] BRs obtained by employing customized versions of the `ZFITTER` [15] and the CKMfitter package [19]. Neglecting contributions from EW boxes these bounds read [6]

$$\begin{aligned} \Delta C &= -0.026 \pm 0.264 \quad (68\%\,{\rm CL})\,, \\ \Delta C &= [-0.483, 0.368] \quad (95\%\,{\rm CL})\,. \end{aligned} \qquad (14)$$

The constraint on ΔC within CMFV following from the simultaneous use of R_b^0, $\mathcal{A}_b$, $A_{\rm FB}^{0,b}$, $\mathcal{B}(\bar{B} \to X_s\gamma)$, and $\mathcal{B}(\bar{B} \to X_s l^+ l^-)$ can be seen in Fig. 3.

One can also infer from this figure that two regions, resembling the two possible signs of the amplitude $\mathcal{A}(b \to s\gamma) \propto C_7^{\rm eff}(m_b)$, satisfy all existing experimental bounds. The best fit value for $\Delta C_7^{\rm eff} = C_7^{\rm eff}(m_b) - C_{7\,{\rm SM}}^{\rm eff}(m_b)$ is very close to the SM point residing in the origin, while the wrong-sign solution located on the right is highly disfavored, as it corresponds to a $\mathcal{B}(\bar{B} \to X_s l^+ l^-)$ value considerably higher than the measurements [20]. The corresponding limits are [6]

$$\begin{aligned} \Delta C_7^{\rm eff} &= -0.039 \pm 0.043 \quad (68\%\,{\rm CL})\,, \\ \Delta C_7^{\rm eff} &= [-0.104, 0.026] \cup [0.890, 0.968] \quad (95\%\,{\rm CL})\,. \end{aligned} \qquad (15)$$

Similar bounds have been presented previously in [14]. Notice that since the SM prediction of $\mathcal{B}(\bar{B} \to X_s\gamma)$ [16] is now lower than the experimental world average by $1.2\,\sigma$, extensions of the SM that predict a suppression of the $b \to s\gamma$ amplitude are strongly constrained. In particular, even the SM point $\Delta C_7^{\rm eff} = 0$ is almost disfavored at 68% CL by the global fit.

The stringent bound on the NP contribution ΔC given in Eq. (14) translates into tight two-sided limits for the BRs of all Z-penguin dominated flavor-changing K- and B-decays as

Observable	CMFV	SM	Experiment
$\mathcal{B}(K^+ \to \pi^+ \nu\bar{\nu}) \times 10^{11}$	$[4.29, 10.72]$	$[5.40, 9.11]$	$\left(14.7^{+13.0}_{-8.9}\right)$ [21]
$\mathcal{B}(K_L \to \pi^0 \nu\bar{\nu}) \times 10^{11}$	$[1.55, 4.38]$	$[2.21, 3.45]$	$< 2.1 \times 10^4$ (90% CL) [22]
$\mathcal{B}(K_L \to \mu^+\mu^-)_{\rm SD} \times 10^9$	$[0.30, 1.22]$	$[0.54, 0.88]$	–
$\mathcal{B}(\bar{B} \to X_d \nu\bar{\nu}) \times 10^6$	$[0.77, 2.00]$	$[1.24, 1.45]$	–
$\mathcal{B}(\bar{B} \to X_s \nu\bar{\nu}) \times 10^5$	$[1.88, 4.86]$	$[3.06, 3.48]$	< 64 (90% CL) [23]
$\mathcal{B}(B_d \to \mu^+\mu^-) \times 10^{10}$	$[0.36, 2.03]$	$[0.87, 1.27]$	$< 3.0 \times 10^2$ (95% CL) [24]
$\mathcal{B}(B_s \to \mu^+\mu^-) \times 10^9$	$[1.17, 6.67]$	$[2.92, 4.13]$	$< 9.3 \times 10^1$ (95% CL) [25]

Table 1: Bounds for various rare decays in CMFV and the SM at 95% CL. The available experimental information is also shown. See text for details.

shown in Tab. 4. A strong violation of any of the bounds by future measurements will imply a failure of the CMFV assumption, signaling either the presence of new effective operators and/or new flavor and CP violation. A way to evade the given limits is the presence of sizable corrections $\delta C_{\rm NP}$ and/or box contributions. While these possibilities cannot be fully excluded, general arguments and explicit calculations indicate that they are both difficult to realize in the CMFV framework.

5 Conclusions

R.I.P. large destructive CMFV Z-penguin!

6 Post scriptum

Assuming the correctness of the SM, the $1.2\,\sigma$ deviation between the most recent SM prediction [16] and the measured value of $\bar{B} \to X_s\gamma$ can be accommodated by a value of the strong coupling constant that is higher than the world average of $\alpha_s(M_Z)$ [26]. Using the same input as in [16], the next-to-next-to-leading order SM estimate and the measurements of $\bar{B} \to X_s\gamma$ would agree within errors for the nominal value

$$\alpha_s(M_Z) = 0.129 \pm 0.006_{\rm expt} \pm 0.005_{\rm theo}\,. \tag{16}$$

Of course, trying to explain the slight tension in $\bar{B} \to X_s\gamma$ by a shift in $\alpha_s(M_Z)$ should be considered a purely academic exercise. Nothing more, nothing less.

Acknowledgments

I am grateful to A. Weiler for fruitful collaboration, valuable comments on the manuscript, and technical support. A big thank you to A. Banfi for encouraging me to extract a value for $\alpha_s(M_Z)$ from $\bar{B} \to X_s\gamma$. This work has been supported by the Schweizer Nationalfonds.

References

[1] Slides:
`http://indico.cern.ch/contributionDisplay.py?contribId=117&sessionId=9&confId=9499`

[2] R. S. Chivukula and H. Georgi, Phys. Lett. B **188**, 99 (1987).

[3] E. Gabrielli and G. F. Giudice, Nucl. Phys. B **433**, 3 (1995) [Erratum-ibid. B **507**, 549 (1997)]; A. Ali and D. London, Eur. Phys. J. C **9**, 687 (1999); A. J. Buras *et al.*, Phys. Lett. B **500**, 161 (2001).

[4] G. D'Ambrosio *et al.*, Nucl. Phys. B **645**, 155 (2002).

[5] M. Blanke *et al.*, JHEP **0610**, 003 (2006) and references therein.

[6] U. Haisch and A. Weiler, 0706.2054 [hep-ph].

[7] J. Fleischer and O. V. Tarasov, Z. Phys. C **64**, 413 (1994).

[8] T. Appelquist, H. C. Cheng and B. A. Dobrescu, Phys. Rev. D **64**, 035002 (2001).

[9] N. Arkani-Hamed *et al.*, JHEP **0207**, 034 (2002).

[10] H. C. Cheng and I. Low, JHEP **0309**, 051 (2003) and **0408**, 061 (2004).

[11] I. Low, JHEP **0410**, 067 (2004).

[12] G. Altarelli, R. Barbieri and F. Caravaglios, Nucl. Phys. B **405**, 3 (1993) and Phys. Lett. B **314**, 357 (1993).

[13] S. Schael *et al.*, Phys. Rept. **427**, 257 (2006).

[14] C. Bobeth *et al.*, Nucl. Phys. B **726**, 252 (2005).

[15] D. Y. Bardin *et al.*, Comput. Phys. Commun. **133**, 229 (2001); A. B. Arbuzov *et al.*, Comput. Phys. Commun. **174**, 728 (2006) and `http://www-zeuthen.desy.de/theory/research/zfitter/index.html`

[16] M. Misiak *et al.*, Phys. Rev. Lett. **98**, 022002 (2007); M. Misiak and M. Steinhauser, Nucl. Phys. B **764**, 62 (2007).

[17] S. Chen *et al.* [CLEO Collaboration], Phys. Rev. Lett. **87**, 251807 (2001); P. Koppenburg *et al.* [Belle Collaboration], Phys. Rev. Lett. **93**, 061803 (2004); B. Aubert *et al.* [BaBar Collaboration], Phys. Rev. Lett. **97**, 171803 (2006).

[18] B. Aubert *et al.* [BaBar Collaboration], Phys. Rev. Lett. **93**, 081802 (2004); K. Abe *et al.* [Belle Collaboration], hep-ex/0408119.

[19] J. Charles *et al.* [CKMfitter Group], Eur. Phys. J. C **41**, 1 (2005) and `http://ckmfitter.in2p3.fr/`

[20] P. Gambino, U. Haisch and M. Misiak, Phys. Rev. Lett. **94**, 061803 (2005).

[21] S. C. Adler *et al.* [E787 Collaboration], Phys. Rev. Lett. **79**, 2204 (1997), **84**, 3768 (2000), **88**, 041803 (2002) and Phys. Rev. D **70**, 037102 (2004); V. V. Anisimovsky *et al.* [E949 Collaboration], Phys. Rev. Lett. **93**, 031801 (2004).

[22] J. K. Ahn *et al.* [E391a Collaboration], Phys. Rev. D **74**, 051105 (2006) [Erratum-ibid. **74**, 079901 (2006)].

[23] R. Barate *et al.* [ALEPH Collaboration], Eur. Phys. J. C **19**, 213 (2001).

[24] R. P. Bernhard, hep-ex/0605065.

[25] A. Sanchez-Hernandez, talk given at Rencontres de Moriond "Electroweak interactions and Unified theories", La Thuile, Italy, March 10-17, 2007, `http://moriond.in2p3.fr/`

[26] W. M. Yao *et al.* [Particle Data Group], J. Phys. G **33**, 1 (2006); S. Bethke, Prog. Part. Nucl. Phys. **58**, 351 (2007).

Searches for Standard Model Higgs at the Tevatron

Rocío Vilar Cortabitarte for D0 and CDF collaborations

Instituto de Física de Cantabria - Universidad de Cantabria - CSIC
Avda. Los Castros s/n, 39005 Santander, Spain

A summary of the latest results of Standard Model Higgs boson searches from CDF and D0 presented at the DIS 2007 conference is reported in this paper. All analyses presented use 1 fb^{-1} of Tevatron data. The strategy of the different analyses is determined by the Higgs production mechanism and decay channel.

1 Introduction

The Higgs boson is the only Standard Model (SM) particle which remains unobserved. It is introduced in the spontaneous electroweak symmetry breaking mechanism, through which SM particles acquire mass. The Higgs mass is not predicted by the theory, however it can be constrained due to its predicted couplings to other particles. Global fits to precision electroweak data, which includes the latest mass measurements for W ($m_W = 80.398 \pm 0.025$ GeV [2] and top ($m_t = 170.9 \pm 1.8$ GeV [3]), favors a light Higgs with mass below 144 GeV [2]. Direct Higgs searches performed at LEP set a lower mass limit of 114 GeV. If this limit is included in the previous calculation, the upper mass limit increases to 182 GeV.

Both Tevatron experiments, D0 and CDF, have established the search for the SM Higgs as one of their highest priorities. Higgs sensitivity workshops at the Tevatron [4] show that the required luminosity to exclude a 115 GeV Higgs starts at around 2 fb$^-$1 per experiment. Both experiments have recorded approximately 1.7 fb^{-1} of data, although the analyses presented in this paper use 1 fb^{-1} of Tevatron data.

Higgs boson production cross sections in the SM are small at Tevatron energies, of the order or 1-0.1 pb depending on the production mechanism. Gluon fusion, $gg \rightarrow H$, is the dominant production mechanism. In the low mass region ($m_H < 135$ GeV) the highest branching ratio decay channel corresponds to $H \rightarrow b\bar{b}$, and the gluon fusion channel has an overwhelming QCD background. The most relevant production mechanism is therefore the associated production to a vector boson (W or Z). The main backgrounds are $t\bar{t}$, $Wb\bar{b}$, $Zb\bar{b}$ and dibosons. In the intermediate mass range ($135 < m_H < 200$ GeV), where the predominant decay channel is $H \rightarrow WW$, gluon fusion production has manageable backgrounds, the most relevant being dibosons, Drell-Yan, $t\bar{t}$ and single top.

Since the Higgs signal is 2 to 3 orders of magnitude below the backgrounds, optimal detector performance and analysis techniques are crucial. For discovery/exclusion one needs: better signal acceptances by improving the triggers and b-tagging efficiency; reduced backgrounds by improving the di-jet resolution and b-tagging algorithms; extraction of the signal from the enormous background by using sophisticated analysis techniques, such as multivariate techniques, Neural Networks (NN) or Matrix Element. No single improvement by itself will reach the sensitivity needed. All channels studied by both experiments must be combined, and as much data as possible must be analyzed.

2 Low Higgs mass region, $m_H < 135$ GeV

Here the strategy is to look for associated production of Higgs with a vector boson, with the Higgs decaying to $b\bar{b}$.

2.1 $WH \to l\nu b\bar{b}$

This channel is the golden channel at the Tevatron. The signature is a high transverse momentum, p_T, isolated lepton (e or μ), missing transverse energy ($\not\!\!E_T$) from the neutrino, and two or more high p_T jets with one or two jets identified as a b-jets. The main background is W+jets production, which is estimated from a combination of data and MC. Both experiments use very similar selection criteria. D0 [5] has significantly improved the sensitivity by increasing the muon trigger acceptances using a full coverage of the detector, and by dividing the sample into two categories of events, with one or two jets identified as a b (tagged jet). CDF has improved the b-jet identification by using an additional Neural Network to further reduce the c and light-quark content of tagged jets. Using ≈ 1 fb^{-1} of data, no excess is observed in the invariant mass distribution of the two tagged jets (see Fig 1), so upper cross section limits at 95% C.L. are set. For $m_H = 115$ GeV, D0 sets a limit of 1.3 pb (1.1 pb expected), and CDF sets a limit of 3.4 pb (2.2 pb expected).

D0 [7] also uses a Matrix Element approach to extract the signal from the background in this channel. This technique uses the LO Matrix Element to compute event probability densities for signal and background, creating a discriminant for each event, see Fig 2. This discriminant is a likelihood ratio constructed for each event by dividing the signal probabilities by the sum of the signal plus background probabilities. No excess is found and an upper limit of 1.7 pb (1.2 pb expected) is set for $m_H = 115$ GeV.

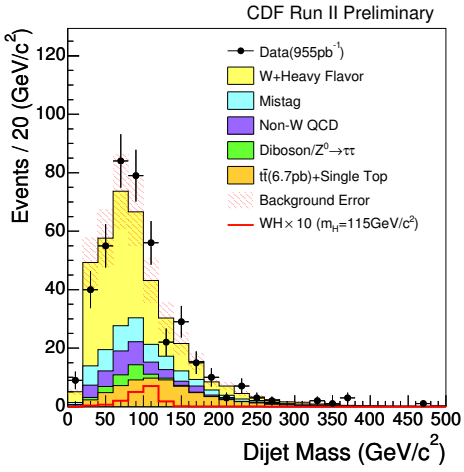

Figure 1: CDF invariant mass distribution of the two tagged jets for the WH analysis.

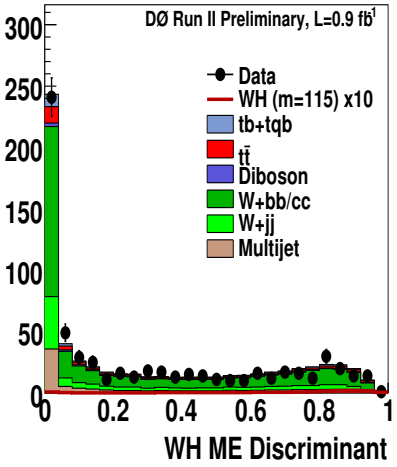

Figure 2: D0 discriminant distribution for the Matrix Element WH analysis.

2.2 $ZH \to l^+l^-b\bar{b}$

The signature for this channel is two high p_T isolated leptons and two high E_T jets that could be identified as b jets. The main backgrounds come from Z+jets, $Zb\bar{b}$, Drell-Yan, dibosons and top. Although this channel has the smallest yield of events, the requirement of two identified leptons to reconstruct the Z mass results in the cleanest sample. D0 [8] uses the invariant mass of the two jets to discriminate signal from background. CDF use a two dimensional Neural Network discriminant based on eight variables to maximize signal over background. CDF [9] also improves the sensitivity further by using two different categories of events depending on the number of b-jets identified, and improving the energy resolution of the jets by applying an additional correction to the jet energy according to its projection onto the $\not\!\!E_{\rm T}$ direction. This correction improves the di-jet mass resolution from 14% to 9% for the two identified b-jets category, see Fig 3. No excess is observed, so CDF sets a 95% C.L. cross section upper limit of 1.3 pb (1.3 pb expected) and D0 sets a limit of 1.9 pb (1.81 pb expected) for $m_H = 115$ GeV.

2.3 $ZH \to \nu\nu b\bar{b}$

The signature is two high E_T jets that could be tagged, and high $\not\!\!E_{\rm T}$ due to the two neutrinos. The two jets must recoil against the $\not\!\!E_{\rm T}$. The main backgrounds are Z+jets, $Zb\bar{b}/c\bar{c}$, dibosons and QCD, which are very challenging because of the heavy flavor modeling and jet mis-reconstructions. This channel has the advantage that it gains some acceptance from the WH when the lepton is lost. Both experiments use the special kinematics of this signature and b-identification to reduce the backgrounds. Checks are made to verify the modeling of the QCD and W/Z+jets backgrounds in control regions sensitive to them. A fit to the invariant mass distribution of the two jets, figures 4 and 5, shows that there is no excess, and upper limits are set 14 times over the SM cross-section prediction (10 times expected) for D0 [10] and 16 times for CDF [11] (15.4 expected).

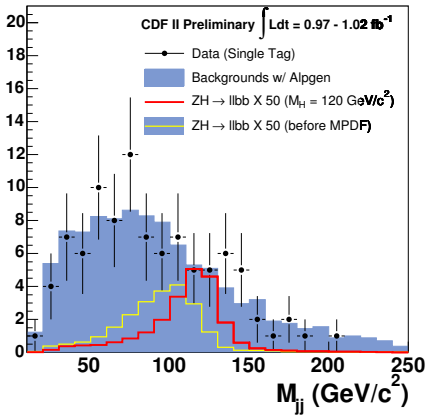

Figure 3: CDF invariant mass distribution of the two tagged jets for the ZH analysis. The red (yellow) histogram is the invariant mass distribution for the Higgs signal after (before) applying further jet energy corrections.

3 Intermediate Higgs mass region, $m_H > 135$ GeV

At higher Higgs masses, the decay mode to vector bosons is kinetically possible, allowing to use the gluon fusion production mode. This gives the biggest event yields. The $H \to WW^*$ decays with the subsequent electronic and/or muonic decays of the W's provide a promising search channels with manageable backgrounds.

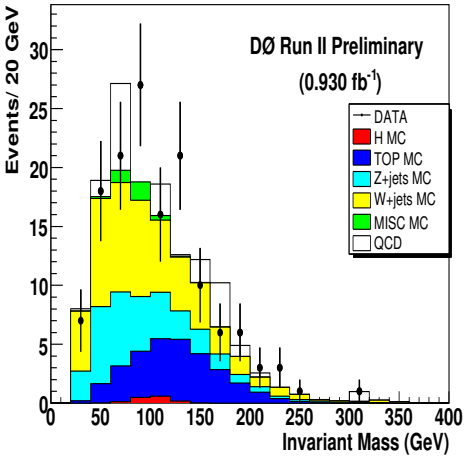

Figure 4: D0 invariant mass distribution of the two tagged jets for the ZH analysis.

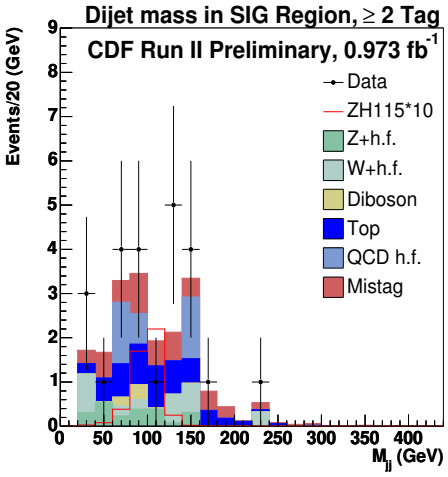

Figure 5: CDF invariant mass distribution of the two tagged jets for the ZH analysis.

3.1 $H \to WW^*$

The signature for this channel is two high p_T, isolated leptons with opposite charge and high $\not\!\!E_{\rm T}$ due to the neutrinos. The main backgrounds are dibosons, $t\bar{t}$ and Drell-Yan. The Higgs mass cannot be directly reconstructed due to the neutrinos. The spin correlations between the decay products of the Higgs boson are used to suppress the backgrounds. The leptons from the Higgs tend to have small angles, while the leptons from other backgrounds are expected to be back-to-back. Both experiments have performed an analysis using this distribution to search for the Higgs boson [12], setting cross section upper limits. Using the same selection criteria CDF has used a Neural Network analysis based on two subsequent NN's, one to reduce the Drell-Yan background and one to separate signal from background. Using the NN the limit improves by a factor of 1.6. CDF [14] increases the geometric lepton acceptance by defining new lepton type categories, including regions of the detector without complete instrumentation. These leptons were used in CDF's observation of WZ production [13]. Using all the lepton categories, the expected sensitivity increases from 2.5 to 4 compared to the cut-based analysis. In addition, a Matrix Element technique is used to separate signal from background, similar to the one explained for the $WH \to l\nu b\bar{b}$ analysis, see Fig 6. The likelihood ratios are constructed for different signal hypothesis to validate the background modeling. No significant excess is observed, and an upper cross section limit of 3.5 times the SM prediction is set (5 times expected) for $m_H = 160$ GeV.

4 Combined Limits

Last summer, the first Tevatron Run II SM Higgs production cross section upper limits using 290-950 fb^{-1} were set [15]. The 95% C.L. upper limits were a factor of 10.4 (3.8) higher than the expected cross sections for m_H=115 (160) GeV/. These results have already been reached by the individual channels shown above, namely CDF's $ZH \rightarrow l^+l^-b\bar{b}$ and $H \rightarrow WW$ and D0's $WH \rightarrow l\nu b\bar{b}$. D0 has set cross section upper limits on Higgs production [16] for Higgs masses ranging from 100 to 200 GeV combining all the channels (WH, ZH and $H \rightarrow WW$) with approximately 1 fb^{-1} of data, see Fig 7.

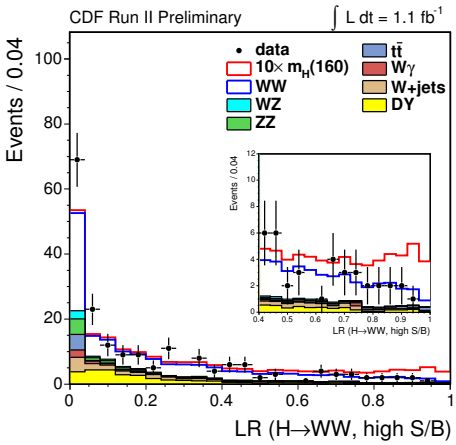

Figure 6: Likelihood ratio for the $H \rightarrow WW^*$ channel, using the Matrix Element technique and improved lepton acceptance.

5 Conclusions

New preliminary results have been presented at this conference, with very encouraging outcomes. Cross section limits are scaling much better than by just a luminosity factor. Both experiments, CDF and D0, have shown that improving analyses by increasing acceptances, improving jet energy resolution, b-tagging, and using advanced analysis techniques such as Matrix Element, Neural Networks, or Boosted Decision Trees can gain a sensitivity factor of ≈ 1.3 without adding data. The prospects for Higgs at the Tevatron depend also on a large integrated luminosity, but Tevatron is performing well and is on its way to deliver 8 fb^{-1} of data by 2009.

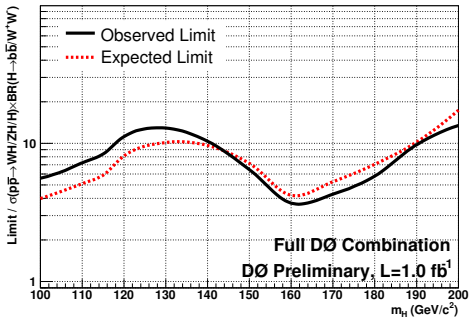

Figure 7: D0 SM Higgs production cross section upper limits from the combination of all different channels using 1 fb^{-1} of data.

6 Acknowledgments

I would like to thank the members of the CDF and D0 collaborations for their work and effort in achieving the results presented in this report.

References

[1] Slides:
http://indico.cern.ch/contributionDisplay.py?contribId=118&sessionId=9&confId=9499

[2] LEPElectroweak Working Group, http://lepewwg.web.cern.ch/LEPEWWG/, March 2007 results.

[3] E. Brubaker *et al.* [Tevatron Electroweak Working Group], "Combination of CDF and D0 Results on the Mass of the Top Quark," arXiv:hep-ex/0608032.

[4] M. Carena *et al.* [Higgs Working Group Collaboration], "Report of the Tevatron Higgs working group," arXiv:hep-ph/0010338;

L. Babukhadia *et al.* [CDF and D0 Working Group Members], "Results of the Tevatron Higgs sensitivity study," FERMILAB-PUB-03-320-E, 2003.

[5] D0 Collab., " Search for the WH Production at $sqrts = 1.96$ TeV with 1 fb^{-1} of Data.", D0 Note 5357-CONF, 2007.

[6] CDF Collb., " Search for Standard Model Higgs Boson Production in Association with $W^{\pm}$ Boson at CDF with 1 fb^{-1}". CDF Note 8390, 2006.

[7] D0 Collab., " Search for the WH Production Using The Matrix Element Analysis Technique in 900 pb^{-1} of Data Collected with the D0 detector ", D0 Note 5365-CONF, 2007.

[8] D0 Collab., " Search for the ZH ($ZH \to l^+l^-b\bar{b}$ Production with the D0 detector in $p\bar{p}$ Collisions at $sqrts = 1.96$ TeV", D0 Note 5275-CONF, 2006.

[9] CDF Collab., " Search for $ZH \to l^+l^-b\bar{b}$ in 1 fb^{-1} of CDF Run2 Data", CDF Note 8742, 2007.

[10] D0 Collab., " Search for the Standard Model Higgs Boson in the Channel $ZH \to \nu\nu b\bar{b}$ at $sqrts = 1.96$ TeV", D0 Note 5353-CONF, 2007.

[11] CDF Collab., "Search for The Standard Model Higgs bosons in $\not\!\!E_{\rm T}$ and B-jets Signature in $p\bar{p}$ Collisions at $sqrts = 1.96$ TeV", CDF Note 8442, 2006.

[12] A. Abulencia *et al.* [CDF Collaboration], "Search for a neutral Higgs boson decaying to a W boson pair in p anti$p$ collisions at $\sqrt{s} = 1.96$-TeV," Phys. Rev. Lett. **97**, 081802 (2006) [arXiv:hep-ex/0605124];
D0 collab., " Search for the Higgs boson in $H \to WW^* \to ll'$ ($l, l' = e, \mu$) decays with 950 pb^{-1} at D0 in Run II", D0 Note 5063-CONF.

[13] A. Abulencia *et al.* [CDF Collaboration], "Observation of WZ Production," Phys. Rev. Lett. **98**, 161801 (2007) [arXiv:hep-ex/0702027].

[14] CDF Collab., "Search for $H \to WW^*$ Production ith Matrix Element Methods in $p\bar{p}$ collisions at at $sqrts = 1.96$ TeV", CDF Note 8774, 2007.

[15] D0 and CDF collab. "Combined D0 and CDF Upper Limits on Standard-Model Higgs-Boson Production", CDF Note 8384 and D0 Note 5227, 2006.

[16] D0 Collab., "Combined Upper Limits on Standard-Model Higgs-Boson Production from the D0 Experiment", D0 Note 5380-CONF.

SUSY and non-SM Higgs Searches at the Tevatron

Raimund Ströhmer[1] On behalf of the D0 and CDF Collaboration. *

1- Ludwig-Maximilians-Universität München - Department für Physik
Am Coulombwall 1, 85748 Garching - Germany

We report on recent results on searches for non-standard model Higgs bosons and for supersymmetric partners of the standard-model particles. The Higgs searches are performed in the channels $\phi b(\bar{b}) \rightarrow b\bar{b}b(\bar{b})$ and $\phi \rightarrow \tau\tau$. Di- and trilepton final sates are studied in the context of gaugino searches. Squark and gluino searches are performed in final states containing at least two jets and a large missing transverse energy. Long-lived neutralinos are searched for by studying the timing of photons in the CDF electromagnetic calorimeter.

1 Non-standard model Higgs

The minimal supersymmetric extension of the standard model (MSSM) contains two Higgs doublets leading to 5 observable Higgs-bosons (h^0, H^0, A^0, $H^{\pm}$). For large values of the ratio of the vacuum expectation values of the two Higgs doublets $\tan\beta = v_u/v_d$ the production cross sections for neutral Higgs bosons are significantly increased. In addition the A-boson is nearly mass-degenerate with either the h-boson or the H-boson. Searches therefore take the contributions from all three neutral Higgs-bosons which will be denoted generically as ϕ in to consideration. The main decays in the relevant parameter range are $\phi \rightarrow \tau\tau$ (10%) and $\phi \rightarrow b\bar{b}$ (90%). For the latter decay only the associated production with one or two additional b quarks is considered in order to reduce backgrounds sufficiently. D0 studied in a 900 pb^{-1} the invariant dijet mass for events with 3 tagged b jets. The background shape was estimated from events with two tagged b jets and normalized outside the signal region. Depending on the $\tilde{t}$ *mix parameter* values of $\tan\beta < 50-60$ could be excluded for a 120 GeV Higgs boson. The decay $\phi \rightarrow \tau\tau$ was studied in the channels $e\mu$, $e\tau$, and $\mu\tau$ by CDF and the channel $\mu\tau$ by D0 (e and μ denote the leptonic τ-decays while τ denotes the hadronic decay). The visible mass was reconstructed as $m_{vis} = P_{\tau_1}^{vis} + P_{\tau_2}^{vis} + P_t^{miss}$ (see Fig. 1).

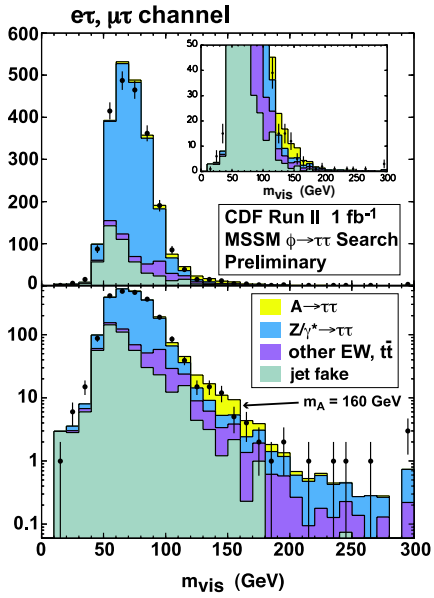

Figure 1: Visible mass for the CDF $\phi \rightarrow \tau\tau$ search

D0 did not see any excess while CDF observed a less than two sigma excess in the region expected from an 160 GeV Higgs in the $e\tau$ and $\mu\tau$ channels. The exclusion region as function of $\tan\beta$ and the Higgs mass have only a minimal dependence on the

*This research was supported by the DFG cluster of excellence Origin and Structure of the Universe (www.universe-cluster.de)

model parameters ($\tilde{t}$ mixing and *sign* μ). They are shown for the m_h^{max} scenario in which the $\tilde{t}$ mixing is chosen to maximize the Higgs mass and for $\mu > 0$ in Fig. 2.

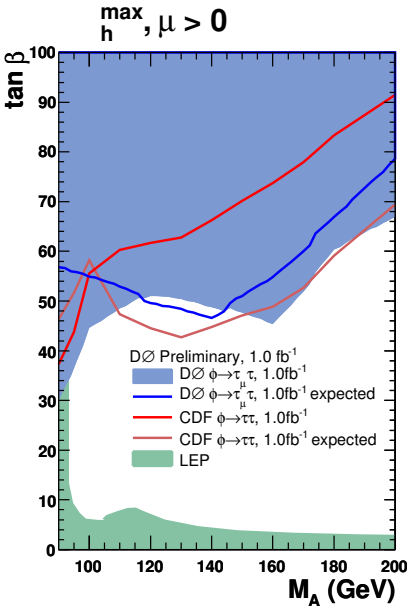

Figure 2: Exclusion region of the $\phi \rightarrow \tau\tau$ search

2 Search for Supersymmetric Particles

In the search for supersymmetry the lightest supersymmetric particle (LSP) plays an important role. Heavier supersymmetric particles will decay via decay chains into it. In the minimal supersymmetric model (replacing fields by superfields without introducing additional couplings) the LSP is stable because no decay in only non supersymmetric particle is allowed since replacing only one particle with its supersymmetric partner in Feynman diagrams included in the standard-model would violate angular momentum conservation by $\frac{1}{2}\hbar$. Cosmological constrains require the LSP to be neutral leading to signatures with large missing transverse energy due to the unobserved (only weakly interacting) LSP. In scenarios with a gravitino as LSP and a neutralino as next to lighted supersymmetric particle one would expect isolated photons and missing energy in the final state. If the LSP only weakly couples to other SUSY particles one would expect long lived particles.

Since the SUSY particles are pair produced and have cascade decays one can expect signals with multiple jets and/or leptons. Up to now no SUSY particles have been observed. Therefore they have to be heavy which might result in decay products with high transverse momentum, as long as the mass difference between the heavier SUSY particle and the LSP is not too small and the momentum is not shared by too many particles in the decay chain.

2.1 Trilepton Final States

Figure 3 shows one of the diagrams Feynman diagram of a chargino neutralino pair decaying into a final state of three leptons and missing transverse energy. The signal is in principal very clean however requiring both the chargino and the neutralino to decay leptonically leads to small branching ratios. In addition in the relevant parameter space the mass difference of the neutralino and the chargino to the LSP is only of about 50 GeV leading to low transverse momenta of the lowest p_t lepton. Fig. 4 shows a scenario ($m_0 = 72$ GeV,$m_{1/2} = 175$ GeV, $tan\beta = 3$, $A_0 = 0$ GeV and $\mu > 0$ with a slepton mass of $m_{\tilde{l}_R} = 104.4$ Gev slightly below the neutralino mass $m_{\tilde{\chi}_0^2} = 112.4$ GeV leading to a very low p_t lepton.

The selection efficiency has been significantly increased by only requiring 2 identified leptons. In order to reduce the background sufficiently two approaches have been followed. Either both leptons were required to have same signed electric charges or an additional isolated track without explicit lepton identification was required. In order to cover the

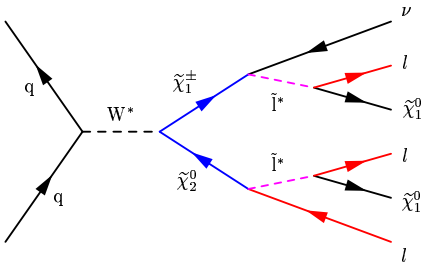

Figure 3: Feynman diagram of a trilepton final state

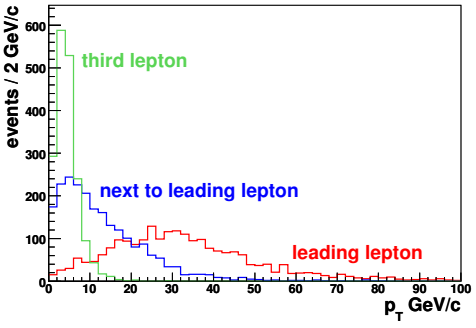

Figure 4: Transverse momentum of the three leptons at generator level

different combinations of final state leptons and different lepton trigger requirements CDF performed a total of 14 different analysis while D0 performed 6 analysis.

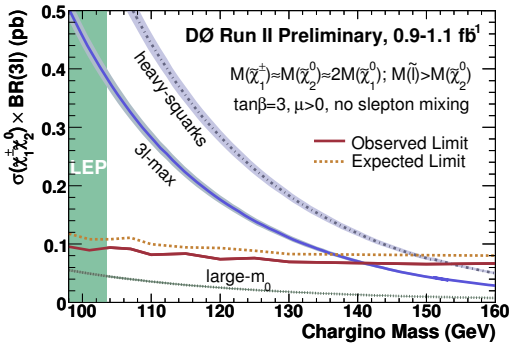

Figure 5: Limits and model predictions for $\sigma \times Br(3l)$

Limits on the cross section times branching ratio $\sigma \times Br(3l)$ have been compared with different mSUGRA inspired scenarios (see Fig.5). For a chargino mass of 140 GeV the observed 95 % CL limit of D0 on $\sigma \times Br(3l)$ is 0.07 pb^{-1} while the expected limit is 0.08 pb^{-1}. For CDF, using different model assumptions, the observed and expected limits are 0.2 pb^{-1} and 0.1 pb^{-1} respectively. In the *large-m_0* scenario with large $\tilde{l}$ and $\tilde{q}$ the branching ratio into leptons is too small to exclude any chargino masses. On the other hand in the *3l-max* scenario with $M(\tilde{l}) \simeq M(\tilde{\chi}_1^{\pm})$ the D0 experiment can exclude chargino masses below 140 GeV.

2.2 Search for Squarks and Gluinos

Scalar quarks and gluinos can be pair produced via the strong interaction. The decays $\tilde{q} \to q\tilde{\chi}_0^1$ and $\tilde{g} \to gq\tilde{\chi}_0^1$ lead to final states with large missing transverse energy and 2, 3, or 4 jets from the decays of $\tilde{q}\tilde{q}$, $\tilde{q}\tilde{g}$, or $\tilde{g}\tilde{g}$ respectively. The background can be reduced by cuts on the missing transverse energy, the sum of the transverse energies of the jets (e.g. $E_t^{mis} > 150$ GeV and $H_T = \Sigma E_T < 400$ GeV for the 3 jet analysis as shown in Fig.6), and the requirement that the missing energy does not point in the directions of the leading jets. Limits can be either given as functions of the squark and gluino mass or as function of the mSUGRA parameters as shown in Fig.7. For mSUGRA scenarios with $\tan\beta = 0$, $A_0 = 0$ and $\mu < 0$ squark masses below 375 GeV and gluon masses below 289 GeV can be excluded with 95 % CL.

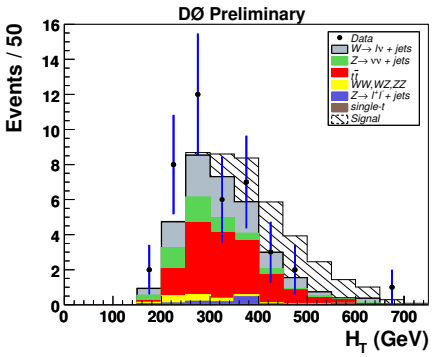

Figure 6: Sum of the transverse energies of the jets ($H_T = \Sigma_{jet} E_T$) for the 3 jet gluino and squark search.

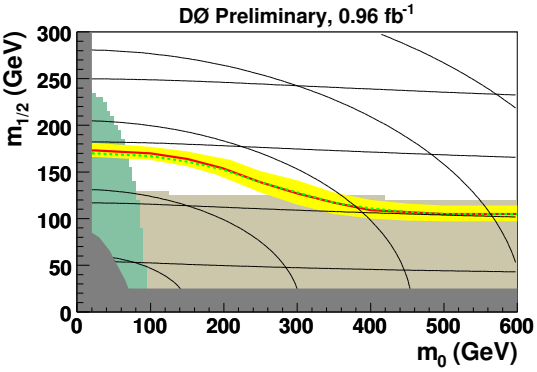

Figure 7: Limits on mSUGRA parameters. Values below the red line are excluded by the D0 squark and gluino search. The green and brown regions are excluded by LEP searches for sleptons and charginos respectively.

2.3 Long-lived Neutralinos

For neutralinos with lifetimes of order 5 ns the arrival time of the photons in the CDF calorimeter can be used to search for $\tilde{\chi}_1^0 \to \gamma \tilde{G}$. For a gauge mediated SUSY braking model (GMSB) with $M_{mess} = 2\Lambda$, $\tan\beta = 15$ $N_{mess} = 1$, $\mu > 0$, $m_{\tilde{\chi}_1^0} = 100$ GeV and $\tau_{\tilde{\chi}_1^0} = 5$ ns cross sections below 0.128 pb have been excluded by the CDF experiment with 95 % CL.

3 Conclusions

Due to the increased Higgs production cross section at large $\tan\beta$ searches for SUSY Higgs in $b\bar{b}$ and $\tau\tau$ final states have a large potential if SUSY at large $\tan\beta$ is realized.

SUSY searches in the trilepton final states for squarks and gluino decays and for long lived neutralinos have been discussed. In addition to these CDF and D0 performed many other searches like searches for GMSB signals with isolated photons and missing transverse energy, long lived charged particles, stopped gluinos, stop and sbottom quarks, R-parity violation SUSY signatures, and rare B decays. Current analysis are based on an integrated luminosity of about $1 fb^{-1}$. One can therefore expect either significant improvements of the limits or evidence for physics beyond the standard-model with increased statistics.

References

[1] Slides:
http://indico.cern.ch/contributionDisplay.py?contribId=119&sessionId=9&confId=9499

[2] further details:
http://www-cdf.fnal.gov/physics/physics.html
http://www-d0.fnal.gov/Run2Physics/WWW/results.htm

Prospects for Higgs and BSM Searches at LHC

Daniela Rebuzzi[1] *

1- Pavia University and INFN, Sezione di Pavia
Via A. Bassi, 6 - 27100 Pavia, Italy

The Large Hadron Collider is undergoing its final installation at CERN. The first *pp* collisions at 14 TeV in the center of mass are foreseen by summer 2008. ATLAS and CMS commissioning is well underway, the two experiment installations are concluding. Despite the initial phase will be devoted to the understanding and the calibration of the detectors and to the *re-discovery* of the Standard Model, discoveries in the Higgs and beyond the Standard Model physics can be achieved in the first years.

The present paper presents, with increasing integrated luminosity order, the ATLAS and CMS discovery reaches of the LHC first data taking period.

1 Introduction

The Standard Model (SM) has been proved by the LEP experiments with precisions up to 0.1%. Nevertheless there are issues connected with it which are still open. The most crucial is related to how fermions and vector bosons acquire their mass after the Electroweak Symmetry breaking (EWSB). The SM cannot exist without a neutral scalar particle, the Higgs boson. If an Higgs particle exists, the problem of the quadratically divergent corrections to its mass has to find a solution.

In the SM, a fine tuning cares of them, but a more elegant solution would be preferred, like the ones predicted by several Beyond the Standard Model (BSM) models. If no Higgs particles is found, alternative solutions should be invoked to explain the EWSB, like Technicolor or Compositeness.

The Large Hadron Collider (LHC), currently in its final installation stage at CERN, has the unique possibility to explore the TeV energy scale and to search for new physics and new particles with mass up to 5 TeV. The first *pp* collision, foreseen by the end of 2007, will have a center of mass energy of 900 GeV ($\mathcal{L} = 10^{29}$ cm^{-2} s^{-1}). The first interactions at 14 TeV are scheduled for summer 2008, then one can estimate to collect (per experiment) up to 1 fb^{-1} by the end of 2008 ($\mathcal{L} < 10^{33}$ cm^{-2} s^{-1}) and up to 10 fb^{-1} by the end of 2009 ($\mathcal{L} = 10^{33}$ cm^{-2} s^{-1}).

The present paper discusses how the discovery possibilities of ATLAS and CMS, the two general purpose experiments which will take data at the LHC, could evolve together with the collected integrated luminosity L and progressive knowledge of the detector performance. The achievements on Higgs and BSM physics will be discussed, starting from 100 pb^{-1} to 5 fb^{-1}, with focus on processes with large cross section and small SM backgrounds and possibly with clear kinematic signatures (peak, edge) and leptonic final states.

2 High mass di-lepton resonances (100 pb^{-1})

Resonances in lepton-lepton invariant mass distributions are predicted by several BSM models. The di-lepton channel offers a prominent and clear signature, with two electrons or two

*email address: daniela.rebuzzi@pv.infn.it

muons in the finale state, and can be considered a benchmark for the theory and the detectors.

The background is dominated by the Drell-Yan production; other backgrounds (ZZ, ZW, WW, $t\bar{t}$) are smaller and easily reducible thorough kinematic selections. The main selection cut requires a pair of high p_T isolated opposite-sign leptons. The favorite discovery channel is the di-electron, since the calorimeters have an good resolution (lower that 1%) in the TeV region. $Z' \to \mu\mu$ is anyway possible, also with the imperfect knowledge of the muon systems that ATLAS and CMS will have at the early stage of data taking.

A 1 TeV-reach is achievable for all the models, already with 100 pb^{-1}. A signal can be reach very early, within the first weeks of data taking at 14 TeV energy.

3 Micro Black Holes (100 pb^{-1})

An integrated luminosity of 100 pb^{-1} would be enough to provide a first evidence of high-p_T objects as the micro black holes (BH), foreseen in large Extra-Dimension theories. Microscopic black holes can be produced when $E_{cm} > M_{Pl}$ (which is at TeV scale in these models) and two colliding partons have impact parameter smaller that the radius of a BH.

The partonic cross section estimation at LHC is motivated by (semi)classical geometric arguments and is of the order of 100 pb, potentially large. At high luminosity more than one BH with mass larger than 5 TeV can be created per second at LHC. The BHs behave roughly as black bodies and *evaporate* in a short time (10^{-27} s) via Hawking radiation, giving rise to a large multiplicity of SM particles in the final state (including gauge bosons and Higgs bosons), isotropically distributed. The separation from the background, which mostly consists of QCD jets, can occur by means of the event shape variables.

The 5σ discovery contours shows that the first collected 100 pb^{-1} would allow to explore the BH mass region up to 4 TeV, for $n < 7$.

4 SUSY early searches (1 fb^{-1})

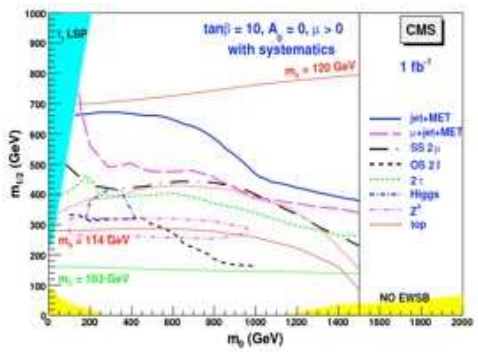

Figure 1: CMS 5σ discovery reaches with $L = 1$ fb^{-1} for different SUSY signatures.

Supersymmetry (SUSY) is the most popular template for the exploration of new physics at the LHC. In SUSY for each fermionic state there is a bosonic partner with the same mass and the same couplings, therefore SUSY is a broken symmetry. There are several mechanisms to mediate SUSY breaking, the main being the gravity mediation (mSUGRA), the gauge mediation, the anomaly mediation.

The classical SUSY signatures are based on the so-called Minimal Supersymmetry Model (MSSM), which has only soft SUSY breaking terms and a minimal particle content. The additional R-parity conservation, which is imposed, has two consequences which crucially affect the phenomenology: the superparticles are produced in pairs and the lightest supersymmetric particle (LSP) is stable. Therefore, sparticles decay in lighter sparticles or in SM particles, and the decay chain eventually ends up in the LSP.

A typical signature for a SUSY event at the LHC consists of jets + leptons + large missing E_T, from the LSP which escapes the detection.

LHC can cover a wide range of parameters of the MSSM, providing a crucial test for the MSSM and low-energy SUSY. Figure 1 shows the 5σ discovery reaches for CMS, for different signatures, in the mSUGRA parameter space (m_0 = universal scalar mass, $m_{1/2}$= universal gaugino mass) and for a given choice of the model parameters.

The cross sections are high (1-100 pb for squark/gluino masses $\sim$ 0.5-1.0 TeV), therefore the statistic will not be a limit to the SUSY discovery at LHC: 100 pb^{-1} will allow to explore the mass range up to 1.3 TeV, 1 fb^{-1} will increase this limit up to 1.8 TeV and 10 fb^{-1} up to 2.2 TeV. The discovery is bound by the time needed to understand the detector performance (E_T miss tails, lepton identification, etc.) and to collect sufficient statistics of SM control samples. Indeed, SUSY will manifest itself as an excess over the SM background, for instance in the *effective mass* ($M_{eff} = \sum_{i=1}^{4} |p_T(jet_i)| + E_T^{miss}$) distribution. More time will be needed to understand the backgrounds (SM and instrumental) and therefore before convincing than a SUSY excess can be claimed.

5 SM Higgs Discovery Potential

As outlined above, if the Higgs mechanism describes the EWSB, a neutral scalar particle, the Higgs boson, must exist. One of the main goals of LHC is to explore the existence of an Higgs particle with mass below 1 TeV. The current limits on the Higgs mass come from the LEP direct search ($M_H > 114.4$ GeV at 95% CL) and from the fit to the EW data ($M_H <$ 144 GeV at 95% CL, January 2007). If one wants to investigate on an early discovery or evidence of a SM Higgs boson, channels with an high branching ratio and not overwhelmed by SM backgrounds should be considered. Good candidates for a first observation are the $H \to WW^{(*)}$ and the $H \to ZZ^{(*)}$ channels (with the Higgs produced both via ggF and VBF), due to the high production rate, the branching ratio above 90%, the good trigger possibility and the signal/background ratio.

5.1 $H \to WW^{(*)} \to ll\nu\nu$ (1 - 3 fb^{-1})

This channel has two leptons and two neutrinos in the final state. Due to the neutrinos, which escape the detection, the Higgs mass peak cannot be reconstructed. The main backgrounds are due to $t\bar{t}$ and the continuum WW production. The analysis selection requires two oppositely charged isolated and high-p_T leptons and large E_T^{miss} (from neutrinos). Contrary to the background, the leptons from the signal are spin correlated, and the request of a small opening angle is the most effective for the background reduction. A reduction of the top background can be obtained also by vetoing events with jet activity.

A 5 σ Higgs evidence of a SM Higgs is possible already with 1fb^{-1} if the particle is in the 160-168 GeV mass range, which increase to 155-175 GeV with 3 fb^{-1}. Therefore a 5σ Higgs signal might be observable in the first year at LHC. Actually, being $H \to WW^{(*)}$ a counting channel (no mass peak), confirmation from other channels will be needed before claiming the discovery. As for SUSY, the understanding of the SM background from data is of crucial importance.

5.2 $H \to ZZ^{(*)} \to 4l$ (3 - 4 fb^{-1})

The combination of a narrow reconstructed mass peak and relatively low backgrounds makes this channel the *golden* one for the SM Higgs discovery, above 180 GeV when the cross section for two Z on-mass-shell opens. The main backgrounds are $Zb\bar{b}$ and $t\bar{t}$ (reducible) and the irreducible ZZ continuum production.

The analysis selection requires isolated high-p_T leptons (muons, electrons) from the interaction vertex. The significance can be improved by applying Z mass constraint and by cutting events out of a window around the Higgs mass peak. Crucial for this channel are the efficiency and the resolution on the lepton reconstruction and a good impact parameter resolution to suppress $Zb\bar{b}$ and $t\bar{t}$ backgrounds.

The region around $M_H \sim 200$ GeV can be investigated with 3 fb^{-1}, while 5 fb^{-1} will allow for a 5σ discovery on the large mass range, from 200 to 450 GeV.

6 Dynamical EWSB: Technicolor (5 fb^{-1})

Technicolor provides an alternative to the Higgs mechanism. It introduces a new strong interaction providing a dynamical nature for EWSB. The new QCD-like force acts on particles named technifermions at a scale $\Lambda_{TC} \sim \nu_{weak} = 246GeV$. In this picture there is no need for Higgs boson(s) and the fine tuning problem is automatically removed.

A good candidate for an early discovery is the $\rho_{TC} \to WZ$ channel, which has the advantages of a clean leptonic final state with isolated leptons and the possibility to apply W and Z the kinematic constraint. The background is dominated by the SM processes WZ, ZZ, $Zb\bar{b}$ and $t\bar{t}$. The 5σ discovery contours in the [$M(\rho_{TC})$,$M(\pi_{TC})$] parameter space shows a signal sensitivity starting from 3 fb^{-1}.

7 Conclusions

The first LHC physics run at 14 TeV are foreseen in summer 2008. The initial emphasis will be focused on understanding the detector performance and SM processes but both ATLAS and CMS will have the possibility to achieve important discoveries in the SM Higgs sector and for the BSM physics.

8 Acknowledgments

I would like to express my gratitude to: G. Polesello, F. Gianotti, M. Schumacher, V. Vercesi, L. Fayard, S. Eno, A. Nikitenko, A. Nisati, S. Rosati.

References

[1] Slides:
`http://indico.cern.ch/contributionDisplay.py?contribId=121&;sessionId=9&;confId=9499`
[2] CMS Physics TDR, Volume II, CERN-LHCC-2006-021.
[3] ATLAS TDR, Volume II, CERN/LHCC/99-15.

Physics Prospects at the International Linear e^+e^- Collider

Alexei Raspereza

Max-Planck-Institute for Physics
Foehringer Ring 6, 80830 Munich

The International Linear Collider (ILC) will have an extremely rich physics program and it will be an ideal experimental tool to explore the structure of the Electroweak Symmetry Breaking. If the Higgs mechanism is realised in Nature, the ILC will allow for a precise determination of the Higgs boson profile. Furthermore, alternative models of Electroweak Symmetry Breaking and theories beyond the Standard Model will be probed. In this paper the features of the machine are outlined, the detector performance goals are discussed and the physics potential of the linear collider is reviewed. The note is based on the talk given at the DIS-2007 Conference [1].

1 Introduction

Over the last few decades a consensus has emerged within the particle physics communities worldwide that the next big experimental facility after the Large Hadron Collider (LHC) at CERN should be an electron-positron linear collider, the International Linear Collider (ILC), operating at energies between a few hundred GeV and approximately one TeV. Owing to its striking features, such as tunable center-of-mass energy and polarisation of beams, the high energy reach, well defined initial state, clean environment and low backgrounds, the ILC has a high potential for the detailed exploration of the Electroweak Symmetry Breaking (EWSB) mechanism and theories beyond the Standard Model and will significantly complement the data which will be collected at the LHC.

2 Machine and Detector Performance Goals

In 2004 the cold superconducting technology had been recommended for the ILC [2]. Since then much effort has been invested by accelerator physicists worldwide to optimise the machine design against its cost. These efforts resulted in the Baseline Configuration Document published in the fall of 2006 [3]. It is planned that in the first phase, the ILC will be operated at center-of-mass energy of a few hundred GeV, thus covering the scale of electroweak symmetry breaking. The machine can then be upgraded to an energy of approximately 1 TeV in order to extend its discovery potential. With the design luminosity of $2 \cdot 10^{34}\mathrm{s}^{-1}\mathrm{cm}^{-2}$, one expects to collect about 500 fb^{-1} of data during a sub-TeV energy run of the ILC. A large part of these data will be collected with polarised electron (up to 80%) and positron (up to 50%) beams.

The ambitious physics program sets stringent requirements on the ILC detector performance. The overall tracking system must provide excellent momentum resolution for charged particles ($\delta(1/p_t) \leq 5 \cdot 10^{-5} \cdot p_t$) to facilitate e.g. precise reconstruction of the dilepton recoil mass in the channel $ZH \to \ell^+\ell^- X$ or accurate determination of the kinematics in the lepton energy spectrum from final states, involving leptons and lightest stable Supersymmetric particle. Efficient reconstruction of multi-jet final states, resulting e.g. from

double Higgs-strahlung processes, requires an excellent jet energy resolution. The benchmark goal for the ILC detector is $\delta E_{jet}/E_{jet} = 30\%/\sqrt{E_{jet}}$. Finally, a micro-vertex detector has to ensure an impact parameter resolution $\delta(IP) = 5\mu m \oplus 10\mu m/p \cdot \sin^{3/2}\theta$ to enable measurements of tauonic and hadronic branching fractions of the Higgs boson at the percent level. A number of detector concepts have emerged over the recent years offering a variety of technological ways to reach the detector performance dictated by the ILC physics program. The description of these concepts and possible technological solutions can be found in the corresponding detector outline documents [4].

3 Physics Program

In this section, the potential of the ILC is illustrated with two topics, chosen for reference, namely the study of the Higgs mechanism and exploration of supersymmetric models.

3.1 Higgs Physics

A detailed investigation of the Higgs mechanism implies the precise determination of the Higgs boson profile. The ILC is capable of detecting Higgs particle independently of its decay mode. This is done by exploiting the Higgs-strahlung process, $e^+e^- \to ZH$, with subsequent decay of the Z boson to electron or muon pairs. The signal manifests itself as a peak in the di-lepton recoil mass spectrum as illustrated in Fig. 1. Using this channel the Higgs-strahlung cross section and therefore the Higgs coupling to the Z boson can be determined in a model independent way with a relative accuracy of a few percent [5]. The mass of the Higgs boson is best measured with fully reconstructible final states, such as $ZH \to q\bar{q}b\bar{b}$, $ZH \to \ell^+\ell^- b\bar{b}$, $ZH \to q\bar{q}W^+W^- \to 6jets$, $ZH \to \ell^+\ell^- W^+W^- \to 2\ell + 4jets$. In these channels the kinematic fits, imposing 4-momentum conservation and constraining mass of the decay products of the Z boson to its nominal mass can be applied, improving the resolution on the Higgs boson mass m_H. Dedicated studies showed that m_H can be measured with an accuracy ranging from 40 to 70 MeV for m_H between 120 and 180 GeV [6].

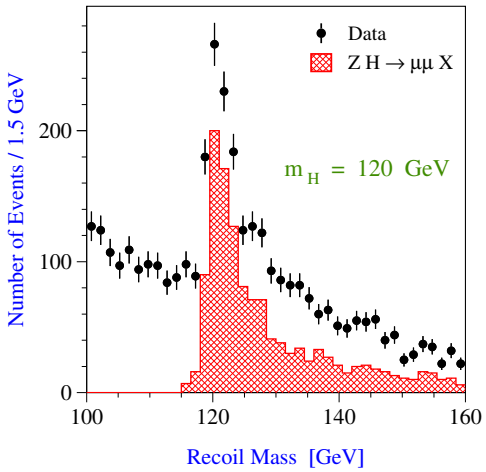

Figure 1: Di-muon recoil mass spectrum in the $ZH \to \mu^+\mu^- X$ channel.

If a signal is detected in the recoil mass spectrum, the measurement of the spin of the observed particle is crucial for its identification as the Higgs boson. It can be performed by analysing the energy dependence of the Higgs-strahlung cross section just above the kinematic threshold [7]. For a spin zero particle the rise of the cross section is expected to be $\sim \beta$, where β is the velocity of the boson in the center-of-mass system. For a spin one particle the rise is $\sim \beta^3$ and for spin two like $\sim \beta^5$. With a very small luminosity of about ten fb^{-1} per energy point the scalar nature of the Higgs boson can be established and

other spin hypotheses are strongly disfavoured, as shown in Figure 2. There are particular scenarios for s=1 and 2, which show a threshold behaviour similar in shape to the s=0 one. This can be disentangled using angular information in addition.

Being responsible for the mass generation, the Higgs boson prefers to couple stronger to heavier particles. Hence, establishment of the mass-coupling relation will be a crucial test of the Higgs mechanism. The couplings of the SM particles to the Higgs boson can be accessed through the measurements of the Higgs decay branching ratios. For a light Higgs boson (m_H = 120 GeV), the attainable precision on the branching ratios ranges from 1% for $H \to b\bar{b}$ [8] to about 20% for the $H \to \gamma\gamma$ decay [9].

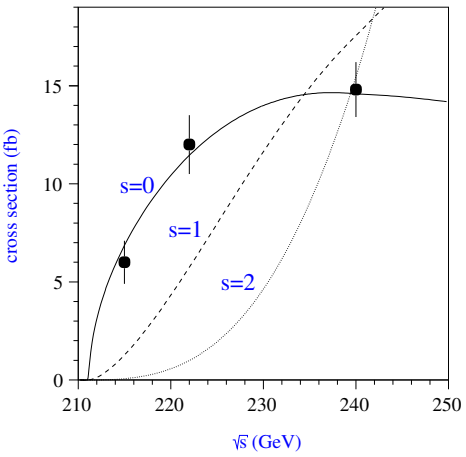

Figure 2: The threshold behaviour of the Higgs-strahlung cross section. The dots represent simulated data and the curves indicate theoretical predictions for various spin hypotheses.

A determination of the Higgs self-coupling along with the Higgs boson mass would allow for the reconstruction of the Higgs potential, thus providing a consistency check of the Higgs mechanism of EWSB. For a light Higgs boson the highest statistics channel to study the Higgs self-coupling is provided by the six-jet final states, resulting from the double Higgs-strahlung process, $e^+e^- \to ZHH$. Efficient reconstruction of these final states requires excellent jet energy resolution. Sensitivity can be further improved by utilising the $e^+e^- \to HH\nu\bar{\nu}$ channel. A dedicated studies [10] showed that for a jet energy resolution of $40\%/\sqrt{E_{jet}}$, a relative accuracy of 14(18)% on the Higgs self-coupling can be achieved with 2 ab^{-1} of data collected at center-of-mass energy of 500(1000) GeV. An improvement of the resolution to $30\%/\sqrt{E_{jet}}$ will reduce the amount of luminosity, needed to reach the same level of precision, by a factor of 2.2.

3.2 Supersymmetry

Supersymmetry (SUSY) is an attractive concept, which allows to overcome a number of inconsistencies with the SM. SUSY stabilises the hierarchy between electroweak and Planck scales, provides a clear path to Grand Unified Theories and introduces gravity in a natural way as a quantum field theory. In the minimal supersymmetric extension of the SM (MSSM) each conventional particle acquires a superpartner differing in spin by $\frac{1}{2}$. The LHC and ILC machines will explore SUSY in different and complementary ways. Heavy strongly interacting SUSY particles − scalar quarks and gluinos − will be produced with high rates in proton-proton collisions at the LHC. The ILC, on the other hand, will be an instrument for precise spectroscopy of electroweakly interacting SUSY particles. The corresponding sfermion sector comprises left- and right-handed superpartners of the SM leptons, while the non-strongly interacting gauginos mix with the higgsinos to form the corresponding mass eigenstates: two pairs of charginos $\tilde{\chi}_i^{\pm}$ (i = 1,2) and four neutralinos $\tilde{\chi}_i^0$ (i = 1..4). In

the MSSM the multiplicative quantum number R-parity is conserved, $R_p = +1$ for SM particles and R_p = -1 for their supersymmetric partners. This implies the existence of a lightest supersymmetric particle (LSP), which is stable and to which all supersymmetric particles eventually decay. In most of the models the lightest neutralino $\tilde{\chi}_1^0$ is assumed to be the LSP. Scalar leptons are produced in e^+e^- collisions in pairs, $e^+e^- \to \tilde{\ell}_i^+\tilde{\ell}_j^-, \tilde{\nu}\bar{\tilde{\nu}}$ via s-channel Z/γ exchange or t-channel $\tilde{\chi}$ exchange for the first generation. The left-handed and right-handed states can be disentangled using the beam polarisation, e.g. $\tilde{\ell}_R\tilde{\ell}_R$ production has much larger cross section for right-handed electrons than for left-handed ones. Positron polarisation further enhances the effect. The isotropic two-body decays, $\tilde{\ell}^- \to \ell^-\tilde{\chi}_i^0$ and $\tilde{\nu}_\ell \to \ell^-\tilde{\chi}_i^+$, lead to an essentially flat lepton energy spectrum with a minimum and maximum energy ("endpoints"). From the kinematic "endpoints" the masses of the primary slepton and the secondary chargino or neutralino can be measured. Figure 3 shows an example of the reconstructed muon energy in the process $e_L^+e_R^- \to \tilde{\mu}_R^+\tilde{\mu}_R^- \to \mu^+\tilde{\chi}_1^0\mu^-\tilde{\chi}_1^0$. [11]. Alternatively, the mass information can be accessed via measurements of the slepton pair production cross section in the vicinity of the kinematic threshold [12]. Charginos and neutralinos are produced in pairs, $e^+e^- \to \tilde{\chi}_i^+\tilde{\chi}_j^-$, $e^+e^- \to \tilde{\chi}_i^0\tilde{\chi}_j^0$ via s-channel Z/γ exchange and t-channel $\tilde{e}$ and $\tilde{\nu}_e$ exchange and decay into lighter partners and gauge bosons or sfermion-fermion pairs $\tilde{\chi}_i \to Z/W\tilde{\chi}_j$, $\tilde{\chi}_1^\pm \to \tilde{\tau}^\pm\nu_\tau \to \tau^\pm\nu_\tau\tilde{\chi}_1^0$, $\tilde{\chi}_2^0 \to \tilde{\ell}\ell \to \ell\ell\tilde{\chi}_1^0$. The most promising method to measure the lightest chargino and the next to the lightest neutralino masses is the threshold scan. Dedicated studies showed that the masses can be measured with a statistical precision of 0.55 GeV [12]. The mass of the next heavier neutralino, $\tilde{\chi}_2^0$, can be measured by threshold scan of $e_R^+e_L^- \to \tilde{\chi}_2^0\tilde{\chi}_2^0 \to 4\tau + 2\tilde{\chi}_1^0$. With an integrated luminosity of 100 fb^{-1}, distributed over five scan points, a precision on the mass of 1.2 GeV can be achieved. The heavy charginos and neutralinos can be detected via their associated production with the lighter ones, followed by the decays $\tilde{\chi}_j \to W/Z\tilde{\chi}_i$. The expected accuracy of the mass measurement of a few GeV is feasible [13].

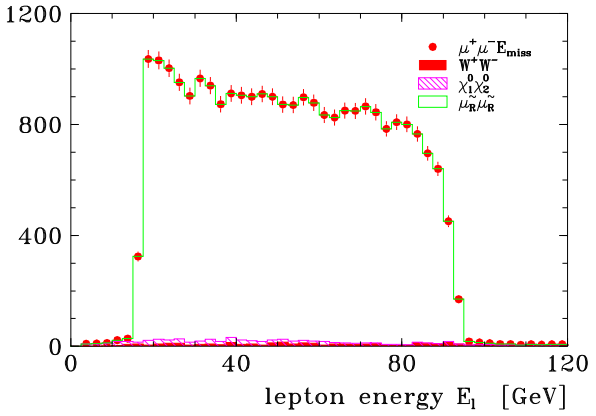

Figure 3: The spectrum of muon energy in the reaction $e_L^+e_R^- \to \tilde{\mu}_R^+\tilde{\mu}_R^- \to \mu^+\tilde{\chi}_1^0\mu^-\tilde{\chi}_1^0$. Center-of-mass energy is 400 GeV. Integrated luminosity is 200 fb^{-1}.

Charginos are the mixture of Winos and Higgsinos. The Wino component is accessible via chargino pair production through t-channel exchange, which couples only to left-handed electrons. Hence, the mixing parameters in the chargino sector can be measured by varying the beam polarisation [14]. By measuring mixing in the chargino sector one gets access to the fundamental supersymmetric parameters, namely the gaugino mass parameter M_2, the Higgs mixing parameter μ and the ratio of the vacuum expectation values of the two Higgs doublets, $\tan\beta$. In a similar way the properties of the neutralino system, which is mixture of Bino, Wino and two Higgsinos, can be determined. By measuring the dependence of

neutralino pair production on the beam polarisation, in addition to the parameters M_2, μ and $\tan\beta$, the gaugino mass parameter M_1 can be extracted [12]. All these parameters are of utmost importance for the reconstruction of the low energy SUSY Lagrangian and for probing the underlying fundamental physics at higher scales.

4 Conclusion

The ILC physics potential is not limited to the study of the Higgs mechanism and the exploration of the SUSY. The ILC will have a high sensitivity to a wide spectrum of signatures predicted by other theoretical models, e.g. postulating extra spatial dimensions, extended gauge sector and additional heavy fermion fields. Alternative scenarios of EWSB, such as strongly interacting gauge fields or compositeness, will also be probed. Finally, precise measurements of the electroweak observables will allow to probe the physics via virtual effects. A comprehensive description of the physics program at the ILC can be found elsewhere [12]. A successful realization of this program requires universality of the detector from the hardware side and universality of thinking from the human side. Both are needed to embrace not only anticipated scenarios but also unexpected physics signatures, which Nature may provide us with.

References

[1] Slides:
`http://indico.cern.ch/contributionDisplay.py?contribId=122&sessionId=9&confId=9499`

[2] International Technology Recommendation Panel. Executive Summary.
`http://www.interactions.org/pdf/ITRPexec.pdf`

[3] Global Design Effort. Baseline Configuration Document.
available at `http://www.linearcollider.org`

[4] GLD, LDC, SiD and 4-th Outline Documents.
`http://physics.uoregon.edu/~lc/wwstudy/concepts/`

[5] P. Garcia-Abia, W. Lohmann, EPJdirect **C2** (2000) 1

[6] P. Garcia-Abia, W. Lohmann, A. Raspereza, Eur. Phys. J. **C44** (2005) 481

[7] M.T. Dova, P. Garcia-Abia, W. Lohmann, LC-PHSM-2001-055, hep-ph/0302113

[8] T. Kuhl, K. Desch, LC-PHSM-2007-001

[9] J.C. Brient, LC-PHSM-2002-003; M. Battaglia, hep-ph/9910271

[10] P. Gay, Ph. Gris, *"Higgs Self Coupling at* e^+e^- *Linear Collider"*, talk given at LCWS06 Workshop in Bangalore, 8-13 March 2006

[11] H.U. Martyn, LC-PHSM-2003-071.

[12] F. Richard, J.R. Schneider, D. Trines and A. Wagner, *"TESLA : Technical Design Report"*, DESY 2001-01, ECFA 2001-209, TESLA Report 2001-023, TESLA-FEL 2001-05 (2001).

[13] U. Nauenberg, talk at ECFA/DESY LC Workshop Prague, November 2002,
http://www-hep2.fzu.cz/ecfadesy/Talks/SUSY.

[14] S. Choi *et al.*, Eur.Phys.J. **C14** (2000) 535;
G. Moortgat-Pick, A. Bartl, H. Fraas, W. Majerotto, LC-TH-2000-033.

Events with an Isolated Lepton and Missing Transverse Momentum at ZEUS

Katherine Korcsak-Gorzo (on behalf of the ZEUS Collaboration)

University of Oxford - Department of Physics
Denys Wilkinson Building, Keble Road, OX1 3RH Oxford, United Kingdom

A search for events with isolated high transverse energy leptons and large missing transverse momentum has been performed with the ZEUS detector at HERA using data samples with a total integrated luminosity of 432 pb^{-1} taken during the 1996-2006 running period. The results are compared to the Standard Model predictions.

1 Introduction

These proceedings report on the results of an investigation of the production of isolated leptons in events with a topology matching the electron[a] or muon decay channel of singly produced W bosons in electron-proton collisions at centre of mass energies of 300 and 318 GeV. Single W production is a rare Standard Model (SM) process and an important source of background to searches for physics beyond the Standard Model. Investigations of the process $ep \to eWX, W \to l\nu$, where $l = \mu, e, \tau$, have been performed at HERA by both the H1 [3] and ZEUS [2] collaborations. The H1 collaboration observed an excess of events with isolated muons or electrons, high missing transverse momentum and large values of hadronic transverse momentum over the SM prediction. The search presented here uses ZEUS data collected over a ten year period from 1996 to 2006 for both electron and muon channels and does not confirm this excess.

The study was performed by selecting events containing isolated electrons or muons with high transverse momentum, in events with large missing transverse momentum. The data set comprises the 1996-97, 1999-2000, 2003-04, 2006 e^+p and the 1998-99, 2004-06 e^-p running periods, with total integrated luminosities of 228 and 204 pb^{-1}, respectively. The centre of mass energy ($\sqrt{s}$) was 318 GeV in all running periods apart from 1996-1997 when it was 300 GeV.

2 Monte Carlo simulation of the signal $e^\pm p \to e^\pm WX$ and of the background

The leading order (LO) cross section for $e^\pm p \to e^\pm WX$ has been calculated using the EPVEC generator[4]. EPVEC calculates the cross section in two regions, corresponding to photoproduction and deep inelastic scattering. The photon and proton structure functions used in the calculation are GRV-G(LO) and CTEQ5D, respectively. The final state simulation does not include hard gluon radiation. Such calculations yield a total cross section of 0.9 pb for $\sqrt{s} = 300$ GeV and 1.1 pb for $\sqrt{s} = 318$ GeV. The uncertainties on these values are approximately 5% for the choice of boundary between the two regions (set at 25 GeV [2]), 5% for the choice of proton structure function, 10% for the choice of photon structure function and 10% from the choice of Q^2 scale used in EPVEC. Next-to-leading order corrections have been calculated to be of the order of 10%, but they were not used in this analysis.

[a] In this paper "electron" refers both to electrons and positrons unless specified.

The most important background to W production in the electron decay-channel arises from high Q^2 charged and neutral current deep inelastic scattering (DIS) events. These DIS events have been simulated using the DJANGO6 interface to the Monte Carlo (MC) programs HERACLES 4.5 and LEPTO 6.5. Leading order electroweak radiative corrections were included and higher order QCD effects were simulated using the colour-dipole model (CDM) of ARIADNE or parton showers based on a leading-logarithm approximation (MEPS). The hadronisation of the partonic final state was performed by JETSET. The process $\gamma\gamma \to l^+l^-$, which is a minor contribution to the background in the electron decay channel of W boson, is the most important background in the muon channel was simulated using the GRAPE dilepton generator. Direct and resolved photoproduction processes were simulated using the HERWIG 6.1 event generator but they are found not to contribute after the event pre-selection.

The generated events were passed through the GEANT-based ZEUS detector and trigger simulation programs. They were reconstructed and analysed by the same program chain as the data.

3 Event Reconstruction and Data Preselection

The missing transverse momentum is defined as: $P_T = \sqrt{\left(\sum_i p_{X,i}\right)^2 + \left(\sum_i p_{Y,i}\right)^2}$, where $p_{X,i} = E_i \sin\theta_i \cos\phi_i$ and $p_{Y,i} = E_i \sin\theta_i \sin\phi_i$ are calculated from individual energy deposits in clusters of calorimeter cells corrected for energy loss in inactive material. The angles θ_i and ϕ_i are estimated from the geometric cell centres and the event vertex. In $W \to e\nu$ events, P_T as defined above is an estimate of the missing transverse momentum carried by the neutrino. In $W \to \mu\nu$ events the muon as a minimum ionising particle deposits very little energy in the calorimeter and therefore a better estimate of the transverse momentum carried by the neutrino can be obtained if the momentum of the muon is calculated from the muon track measured in the central tracking detector. Events that passed the trigger requirements were further required to have P_T greater than 12 GeV. The transverse momentum calculated excluding the inner ring of calorimeter cells around the forward beam pipe hole, also had to be greater than 9 GeV. Hadron transverse momentum P_T^X is defined as the sum over those calorimeter cells that are not assigned to lepton candidate clusters and for the muon-channel it was required that $P_T^X > 9$ GeV. The transverse momentum of the leptons had to be $P_T^e > 5$ GeV and $P_T^\mu > 10$ GeV, respectively. Longitudinal momentum conservation ensures that $E - p_Z$ (δ), defined as: $\delta \equiv \sum_i E_i(1 - \cos\theta_i)$ with the sum over all energy deposits, peaks at twice the electron beam energy $E_e = 27.5$ GeV for fully contained events. Only events with $5 < \delta < 60$ GeV for the electron channel and with $\delta < 70$ GeV for the muon channel were chosen in the preselection. The transverse mass is defined as: $M_T = \sqrt{2P_T^l P_T^\nu (1 - \cos\phi^{l\nu})}$, where P_T^l is the lepton transverse momentum, P_T^ν is the magnitude of P_T and $\phi^{l\nu}$ is the azimuthal separation of the lepton and the missing P_T vectors. For electrons the preselection required $M_T > 10$ GeV, whereas, for muons the cut was at $M_T > 5$ GeV. The polar angle of the lepton track had to be less than 2 rad to reduce the contribution from neutral current processes which rise significantly beyond that point. In addition, since most fake leptons are misidentified hadrons close to jets, the background was further reduced by requiring that the lepton track be separated by at least 0.5 units in $\{\eta, \phi\}$ space from other tracks associated with the event vertex with momentum larger than

0.2 GeV, where ϕ is the azimuthal angle and $\eta = -\log(\tan(\theta/2))$ is the pseudo-rapidity, a measure of the polar angle. This track isolation cut was augmented by a similar cut on isolation of the lepton's energy deposit in the calorimeter which required that the energy not associated with the lepton had to be less than 4 GeV in a cone with radius 0.8 units in $\{\eta, \phi\}$ space around the lepton cluster. Other pre-selection cuts were applied to ensure that the track associated with the lepton was well reconstructed and to avoid contamination from non ep interaction backgrounds.

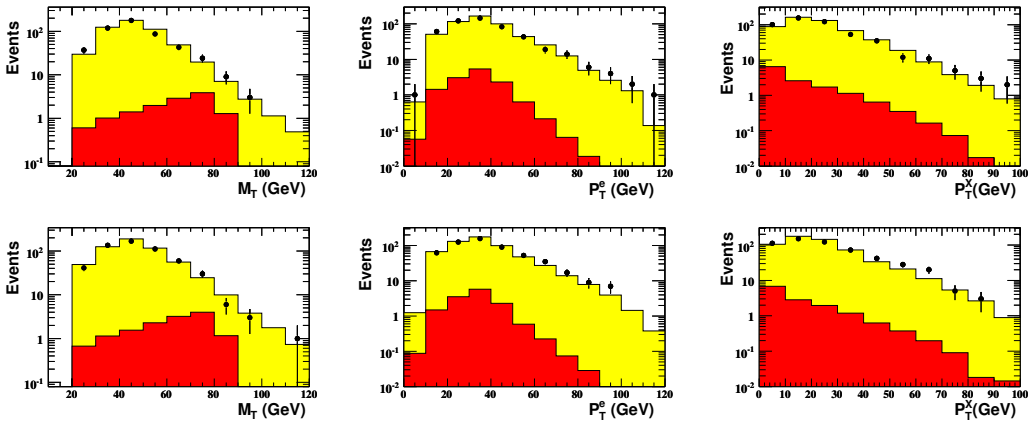

Figure 1: Electron-channel preselection 96-06 e^+p (top row) and 98-06 e^-p (bottom row). The SM expectation is show in yellow (light grey), the contribution of the signal in red (dark grey).

Figures 1 and 2, show the level of agreement, for the electron and muon channels respectively, between the measured quantities and the SM expectation, after the above preselection is applied. The plots demonstrate that the backgrounds are well understood. Further cuts are now applied to select events matching the topology of single W production. In the electron-channel the selection is refined by increasing the cut on the electron's transverse momentum to $P_T^e > 10$ GeV, reducing δ to below 50 GeV and requiring a lower cut on the acoplanarity angle $\phi_{\rm ACOP} > 0.3$ which is applied for events with $P_T^X > 4$ GeV. The acoplanarity angle is the azimuthal separation of the outgoing lepton and the vector in the $\{X, Y\}$ plane that balances the P_T^X vector. For well measured neutral current events, the acoplanarity angle is close to zero, while large acoplanarity angles indicate large missing energies. The missing transverse momentum is increased to $P_T > 25$ GeV unless $\xi_e^2 > 5000$ GeV^2, where the quantity ξ_e^2 is defined as $\xi_e^2 = 2E_eE'_e(1 + \cos\theta_e)$, where E_e is the electron beam energy and E'_e, θ_e are the energy and the angle of th eisolated elecron as measured in the calorimeter. For neutral current events with the scattered beam electron identified as the isolated lepton ξ_e^2 is Q^2. Neutral current events will generally have low values of ξ_e^2 whilst electrons from W decay will generally have high values of ξ_e^2. The muon-channel was required to satisfy three cuts after the preselection: $\phi_{\rm ACOP} > 0.2$, $P_T^X > 12$ GeV and $P_T > 12$ GeV.

The numbers of data events and the Standard Model expectations after these final sets of cuts are summarised in Tab. 1 for the e^-p and e^+p data separately. The first two columns show the electron and muon-channel separately and the third column is the sum of these

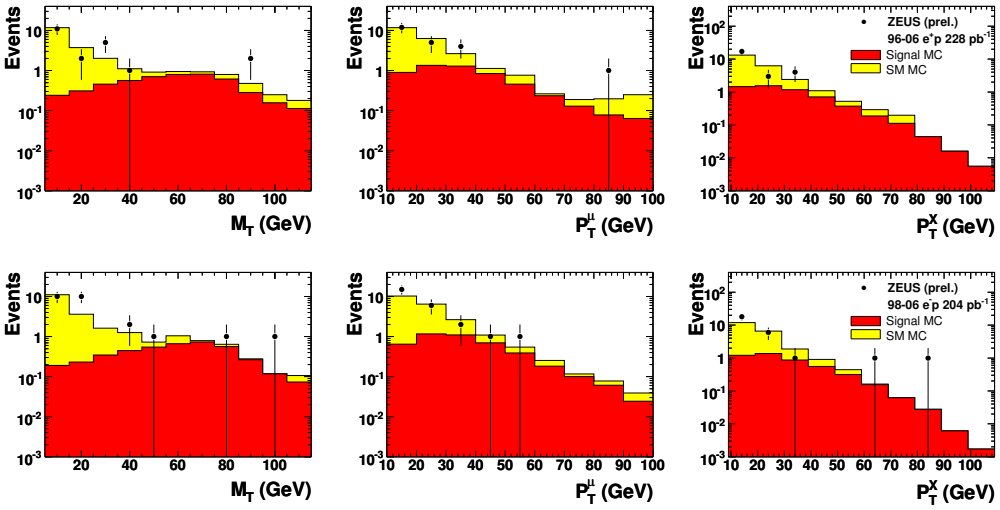

Figure 2: Muon-channel preselection 96-06 e^+p (top row) and 98-06 e^-p (bottom row). The SM expectation is show in yellow (light grey), the contribution of the signal in red (dark grey).

ZEUS $P_T^X > 25$ GeV	e channel obs./exp. (signal)	μ channel obs./exp. (signal)	e and μ obs./exp. (signal)
e^-p 204 pb^{-1}	$5/3.8 \pm 0.6$ (55%)	$2/2.2 \pm 0.3$ (68%)	$7/6.0 \pm 0.7$ (60%)
e^+p 228 pb^{-1}	$1/3.2 \pm 0.4$ (75%)	$3/3.1 \pm 0.5$ (80%)	$4/6.3 \pm 0.6$ (77%)

Table 1: Final numbers of electron and muon events against the SM expectations with the number in brackets giving the fraction of the W signal contribution to the latter.

two. In every case, the agreement between the obseved data events and the Standard Model expectation is good and the excess observed by H1 cannot be confirmed.

The errors take into account statistical and systematic uncertainties. However, theoretical uncertainities on the W production cross section were not included in the errors on the SM prediction.

References

[1] Slides:
`http://indico.cern.ch/contributionDisplay.py?contribId=123&sessionId=9&confId=9499`

[2] ZEUS Coll., S. Chekanov et al., Phys. Lett. **B 559**, 153 (2003).

[3] H1 Coll., V. Andreev et. al., Phys. Lett. **B 561**, 241 (2003).

[4] U. Baur, J.A.M. Vermaseren and D. Zeppenfeld, Electroweak Vector Boson Production in High-Energy ep Collisions, Nucl. Phys. **B 375**, 3 (1992).

[5] K-P. Diener, C. Schwanenberger and M. Spira, Eur. Phys. J. **C 25**, 405 (2002).

Search for Events with Isolated High P_T Leptons and Large $P_T^{\rm miss}$ using the H1 Detector at HERA

Ytsen de Boer*

Institute of Experimental and Theoretical Physics (ITEP)
Bolshaya Chermushkinskaya 25
117218 Moscow, Russian Federation

A search for events with energetic isolated leptons and large transverse momentum imbalance produced at HERA using the H1 detector is presented [1]. The full H1 data set of $e^{\pm}p$ data collected in the period 1994 - 2007 at center of mass energies $\sqrt{s}$ of 300 to 320 GeV is employed, corresponding to a total integrated luminosity of 478 pb^{-1}. In the electron and muon channel, a good overall agreement with the Standard Model (SM) is found with 59 events observed where 58.9 $\pm$ 8.2 are expected. In the e^+p data at large hadronic transverse momentum P_T^X >25 GeV, 21 events are observed where only 8.9 $\pm$ 1.5 are expected. This corresponds to an excess of 3.0σ. In the tau channel 20 events are observed where 19.5 $\pm$ 3.2 are expected, in good agreement with the SM.

1 Introduction

The H1 and ZEUS experiments have previously reported [2, 3, 4, 5, 6] searches for events with an isolated lepton and large missing transverse momentum ($P_T^{\rm miss}$). In the electron (e) and muon (μ) channel, H1 has reported [4] a 3σ excess of data events over the SM expectation in the region of hadronic transverse momentum $P_T^X > 25$ GeV in HERA I data. The ZEUS Collaboration performed a similar analysis but could not confirm the excess [3].

H1 has updated [1, 7] its analysis which now includes the full HERA I+II data set at high energy[a]. The data corresponds to an integrated luminosity of 478 pb^{-1}, collected in the period 1994 - 2007: 184 pb^{-1} of e^-p and 294 pb^{-1} of e^+p data.

The search for isolated tau (τ) leptons has also been updated [1, 8] to include the full high energy data set. In addition the selection procedure has been improved.

2 The Search for Isolated Electrons and Muons

The signal topology in this channel consists of at least one isolated electron or muon with large transverse momentum (P_T) in the final state together with genuine large $P_T^{\rm miss}$. The main SM contribution to this topology is single W production where the W decays into an electron or muon and a neutrino, $e^{\pm}p \to eW\,(\to e/\mu+\nu)\,X$, where the hadronic system X typically has low P_T. The production via charged currents $e^{\pm}p \to \nu W\,(\to e/\mu+\nu)\,X$ is also considered. Both leptons from the W decay have a Jacobian peak around 40 GeV, corresponding to half the W mass. The neutrino of the W boson escapes undetected and accounts for the missing transverse momentum in the event. In the electron channel, the

*For the H1 Collaboration

[a]The term 'high energy' refers to the period where the center of mass energy $\sqrt{s}$ was 300-320 GeV. HERA is currently running at lower energies for which the expected yield is considerably smaller.

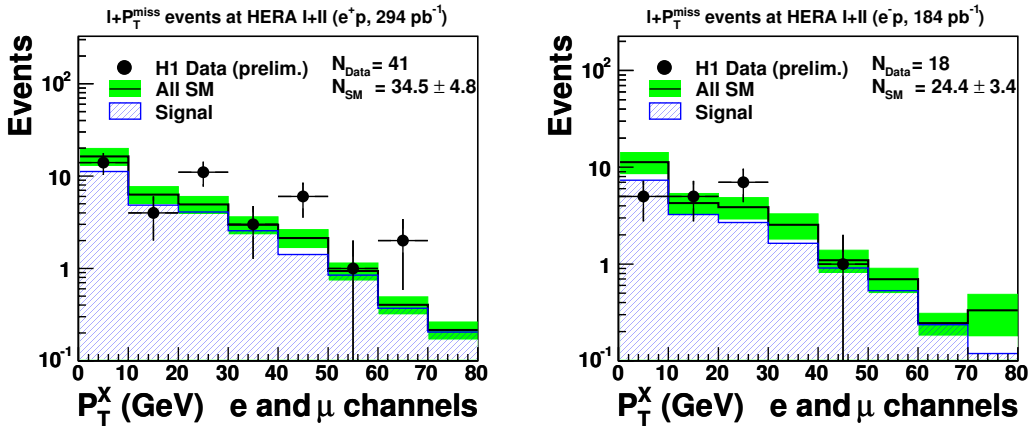

Figure 1: Distribution of the hadronic transverse momentum P_T^X in the electron and muon channel for HERA I+II data.

smaller contribution to the signal from Z^0 production, $ep \to eZ^0 (\to \nu\bar{\nu}) X$, is also taken into account.

The event selection is the same as used in the HERA I analysis [4]. The isolated lepton should have $P_T > 10$ GeV and polar angle $5^o < \theta < 140^o$. It should be isolated from jets and other tracks. The events are requiered to have a transverse momentum imbalance, measured in the calorimeter, of at least 12 GeV. Further cuts are applied to reduce the remaining SM background, whilst preserving a large signal purity.

The final sample contains 59 data events for 58.9 ± 8.2 expected from the SM. The SM signal purity is typically $\sim$ 70%. The P_T^X spectra for the e^-p and e^+p data are shown in Figure 1. The e^-p sample is in agreement with the SM with 18 events observed where 24.4 ± 3.4 are expected. In the e^+p data, 41 events are observed for 34.5 ± 4.8 expected, also in agreement with the SM. In the region $P_T^X > 25$ GeV, which is atypical for the SM signal processes, 21 events are observed where only 8.9 ± 1.5 are expected. This corresponds to an excess of 3.0σ. It should be noted that the excess is observed in both lepton channels.

The ZEUS Collaboration updated their analysis and reports [9] good agreement with the SM in all regions of phase space and cannot confirm the excess. A comparison between the H1 and ZEUS acceptances is shown in Figure 2. Both experiments observe events at high P_T^X. The H1 acceptance in P_T^X is larger due to the larger coverage in θ but it should be noted that most (not all) H1 events at high P_T^X are in the common phase space, visible for both H1 and ZEUS.

3 The Search for Isolated Tau Leptons

Events with isolated τ leptons and $P_T^{\rm miss}$ are searched for in the full data sample collected by H1 at HERA corresponding to an integrated luminosity of 471 pb^{-1} [1, 8].

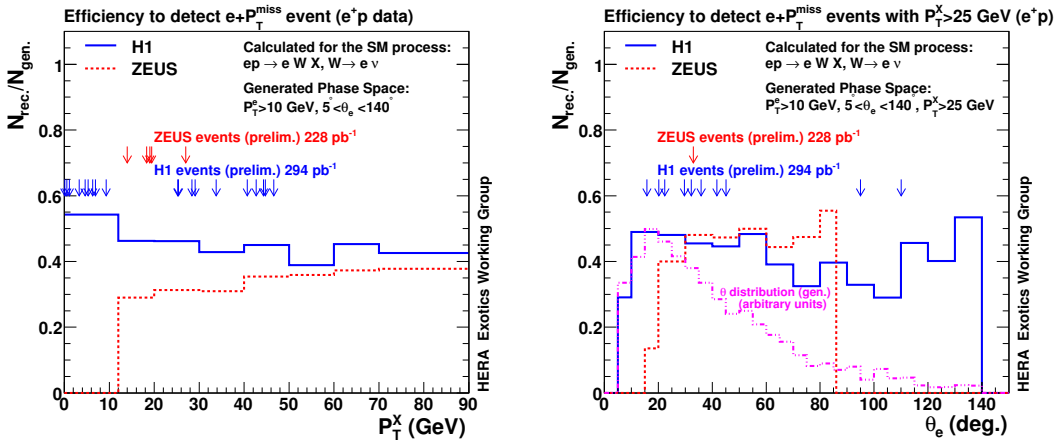

Figure 2: Comparison of the efficiencies of the H1 and ZEUS analyses to select events containing isolated electrons or muons and missing transverse momentum in the HERA e^+p data. Left: the efficiency, defined as N_{rec} / N_{gen}, as function of hadronic transverse momentum P_T^X in the electron channel. Right: the efficiency in the electron channel at large $P_T^X > 25$ GeV as a function of the electron polar angle θ. In both figures, the H1 (ZEUS) efficiency is given by the solid (dashed) line. The data events observed by each experiment are indicated by the arrows.

The only SM contribution to the signal topology originates from single W production followed by W decay into a τ and a ν_τ. The τ decay channel used for this analysis is the '1-prong' hadronic decay channel for which the branching ratio is 43%. The typical topology of this process consists of a pencil-like narrow jet with exactly one track and large $P_T^{\rm miss}$.

The event selection used in this preliminary analysis is based on the published HERA I analysis [6]. The τ lepton decay products are identified as narrow jets with a radius $R < 0.12$, in a data sample with $P_T^{\rm miss} > 12$ GeV. Cone radii and distances between tracks are in $\eta - \phi$ space. The track segment from the inner tracker chambers attributed to the jet should be inside a cone of radius 0.3 around the jet center.

A total of 20 events are observed for 19.5 ± 3.2 expected from the SM. Figure 3 shows the P_T^X spectra of the τ data sample, for the e^-p and e^+p data separately. In the e^-p sample 10 events are observed where 8.6 ± 1.5 are expected. In the e^+p sample 10 events are observed where 10.8 ± 1.8 are expected. At high P_T^X one event is observed where 0.99 ± 0.13 are expected. The contribution from SM single W production is below 10%, hence the sample is largely dominated by (Charged Current) background. All results in this channel are in good agreement with the SM.

4 Summary

A preliminary search for events with isolated high P_T leptons and large $P_T^{\rm miss}$ produced at HERA using the H1 detector is presented [1]. The full H1 data set of $e^\pm p$ data collected in the period 1994 - 2007 at center of mass energies $\sqrt{s}$ of 300 to 320 GeV is used corresponding to a total integrated luminosity of 478 pb^{-1}. In the electron and muon channels, 59 events

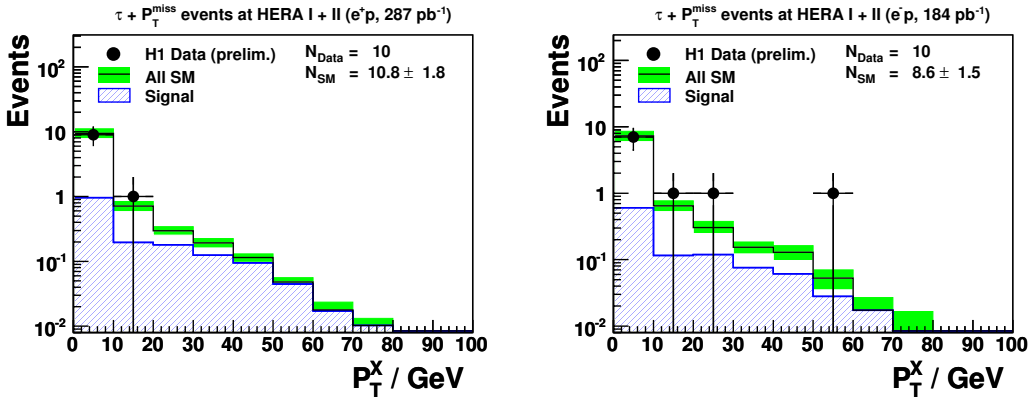

Figure 3: Distribution of the hadronic transverse momentum P_T^X of τ+$P_T^{\rm miss}$ events in HERA I+II data. The data are represented by the dots. The open histogram is the contribution from SM single W production and is given by the hatched histogram. N_{data} is the total number of events observed, N_{SM} is the total SM expectation. The total error on the SM expectation is given by the shaded band.

are observed for 58.9 ± 8.2 expected from the SM, dominated at 70% by single W production. However, in the e^+p data sample for the region $P_T^X > 25$ GeV, 21 events are observed where only 8.9 ± 1.5 are expected. Therefore, the 3σ fluctuation, previously observed using HERA I data, persists in the e^+p data after an increase of the luminosity by a factor of 3. In the isolated tau channel, 20 events are observed, in good agreement with the SM expectation of 19.5 ± 3.2. The separate e^-p and e^+p data sets display good agreement with the SM.

5 Bibliography

References

[1] Slides:
http://indico.cern.ch/contributionDisplay.py?contribId=124&sessionId=9&confId=9499

[2] C. Adloff *et al.* [H1 Collaboration], Eur. Phys. J. C **5**, 575 (1998) [hep-ex/9806009].

[3] J. Breitweg *et al.* [ZEUS Collaboration], Phys. Lett. B **471**, 411 (2000) [hep-ex/9907023].

[4] V. Andreev *et al.* [H1 Collaboration], Phys. Lett. B **561**, 241 (2003) [hep-ex/0301030].

[5] S. Chekanov *et al.* [ZEUS Collaboration], Phys. Lett. B **583**, 41 (2004) [hep-ex/0311028].

[6] A. Aktas *et al.* [H1 Collaboration], Eur. Phys. J. C **48**, 699 (2006) [arXiv:hep-ex/0604022].

[7] Preliminary Isolated Electrons and Muons: H1prelim-07-063
https://www-h1.desy.de/h1/www/publications/htmlsplit/H1prelim-07-063.long.html

[8] Preliminary Isolated Tau: H1prelim-07-064
https://www-h1.desy.de/h1/www/publications/htmlsplit/H1prelim-07-064.long.html

[9] Slides:
http://indico.cern.ch/contributionDisplay.py?contribId=123&sessionId=9&confId=9499

Multi-Lepton Production in ep Collisions at H1

Gerhard Brandt *

Universität Heidelberg - Physikalisches Institut
Philosophenweg 12, 69120 Heidelberg - Germany

A search for multi-lepton (electron or muon) events at high transverse momenta in the data sample of $e^{\pm}p$ collisions collected with the H1 detector at HERA in the years 1994-2007 is presented [1]. The data sample corresponds to an integrated luminosity of 459 pb^{-1}. Yields of di-lepton and tri-lepton events are measured and a general good agreement is found with Standard Model (SM) predictions. Combining all channels, four events are observed with a scalar sum of lepton transverse momenta ($\sum P_T$) greater than 100 GeV, compared to a SM expectation of 1.9 ± 0.4.

1 Introduction

Multi-lepton events at high transverse momenta are of special interest as these signatures might reveal new physics beyond the SM. Events with two or more leptons with high transverse momentum P_T are measured in electron-proton collisions at HERA using the full HERA I+II high-energy data sample at centre-of-mass energies up to $\sqrt{s} = 320$ GeV. The data were collected in the years 1994-2007 and correspond to an integrated luminosity of 459 pb^{-1}. This comprises of 286 pb^{-1} of e^+p collisions and 173 pb^{-1} of e^-p collisions.

Within the SM the production of multi-lepton events in ep collisions mainly proceeds via photon-photon interactions [2]. Precise cross-section measurements of both electron (e) and muon (μ) pair production at high P_T have already been performed by the H1 collaboration using HERA I data [3, 4].

2 Selection

Electron candidates are identified as compact clusters in the calorimeters with energies above 5 GeV and in the polar angular range $5^\circ < \theta < 175^\circ$. They are required to be isolated from other leptons or jets. In the central region $20^\circ < \theta < 150^\circ$ the electron identification is complemented by tracking conditions, requiring a tight geometrical and P_T match between track and cluster.

Muon candidates are identified with $P_T > 2$ GeV in the range $20^\circ < \theta < 160^\circ$ by associating a track in the inner tracking systems with a track segment or an energy deposit in the outer muon chambers. Calorimetric energy depositions in the vicinity of the track are required to be typical for minimally ionising particles, such as muons. In di-muon events, cosmic background radiation is reduced by the requirement that the opening angle between the two muons is smaller than 160°.

The final multi-lepton selection requires that there be at least two lepton candidates (electron or muon) identified in the central region, of which one must have $P_T > 10$ GeV and the other $P_T > 5$ GeV. Additional identified lepton candidates are accepted without extra requirements. Leptons are counted and the events are classified into di-lepton ee, $\mu\mu$ and $e\mu$ samples, and tri-lepton eee and $e\mu\mu$ samples.

*for the H1 Collaboration.

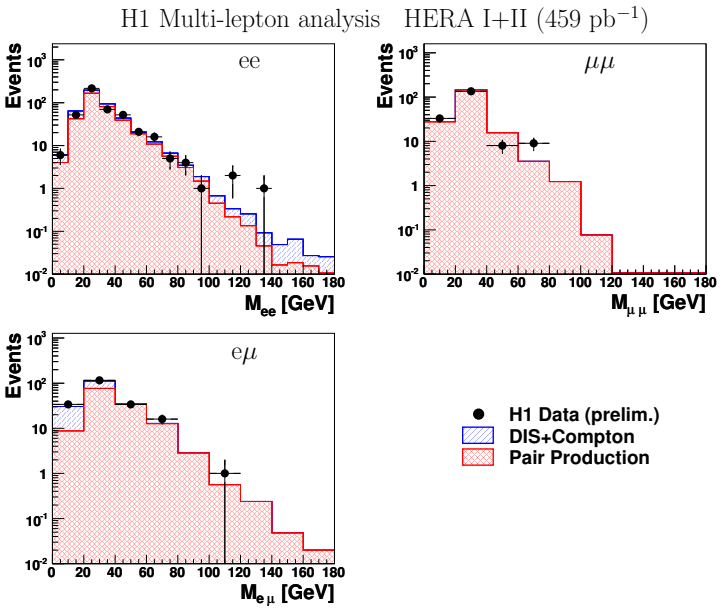

Figure 1: Invariant masses $M_{\ell\ell'}$ of the leptons for events selected in the di-lepton (ee, $\mu\mu$ and $e\mu$) classes compared to the SM expectation.

3 Results

The invariant mass $M_{\ell\ell'}$ distributions for the two leptons in the di-lepton classes are shown in Fig. 1. The invariant mass distributions of the two highest P_T leptons in the eee class M_{12}, and for the $ee\mu$ class the highest P_T muon with the electron $M_{e\mu}$ and the second muon $M_{\mu\mu}$ are shown in Fig. 2. The observed event yields are in good agreement with the SM expectation which is dominated by pair production.

The event yields for all classes in the region $M_{\ell\ell'} > 100$ GeV are shown in Tab. 1, also for collisions with a positron or electron beam separately. The interesting events seen at high invariant masses in the ee and eee classes were observed in HERA I e^+p data and previously reported [3]. Two e$\mu\mu$ events are observed in the new HERA II data, one of which has a high $\mu - \mu$ and the other a high $e - \mu$ invariant mass.

The event yields for events with $\sum P_T > 100$ GeV are shown in Tab. 2. Four events are observed in all channels combined while 1.9 ± 0.4 are expected in the SM. These four data events correspond to the three ee events observed in HERA I data [3] and one new e$\mu\mu$ event observed in HERA II data. The four events with $\sum P_T > 100$ GeV are all observed in e^+p collisions only, where the SM expectation is 1.2 ± 0.2 events.

4 Conclusions

Multi-lepton events with electrons and muons were studied using the full HERA I+II data set. The measurement extends previous analyses by including HERA II data. The event yields in the di-lepton (ee, $\mu\mu$ and $e\mu$) and tri-lepton (eee and $e\mu\mu$) sub-samples are in

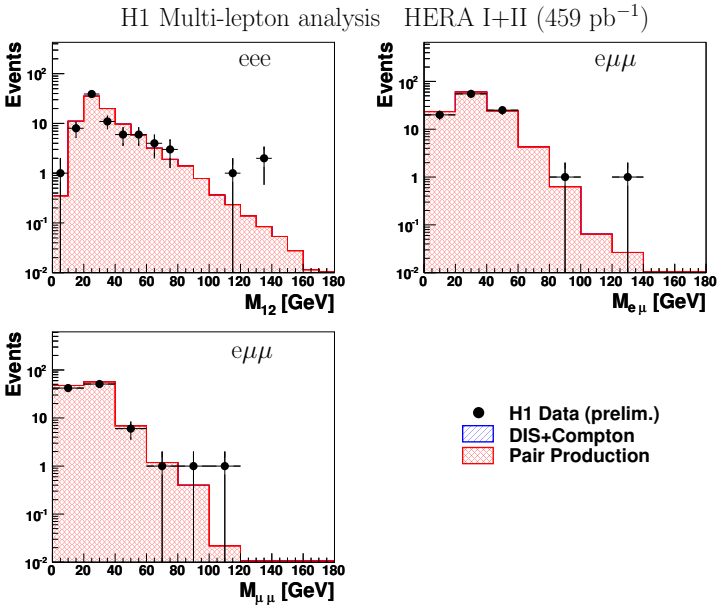

Figure 2: Distribution of the invariant mass M_{12} of the two highest P_T electrons for the *eee* sample (top left). For the e$\mu\mu$ sample, invariant mass combinations of the electron with the higest P_T muon ($M_{e\mu}$, top right) and of both muons ($M_{\mu\mu}$, bottom left) are presented.

H1 Multi-lepton analysis HERA I+II (preliminary)

Selection	Data	SM	Pair Production	NC-DIS + Compton
e^+p collisions (286 pb^{-1})				
ee M_{12} >100 GeV	3	1.0 ± 0.2	0.6 ± 0.2	0.4 ± 0.1
$\mu\mu$ $M_{\mu\mu}$ >100 GeV	0	0.06 ± 0.03	0.06 ± 0.03	—
eμ $M_{e\mu}$ >100 GeV	1	0.53 ± 0.05	0.53 ± 0.05	—
eee M_{12} >100 GeV	3	0.6 ± 0.1	0.6 ± 0.1	—
e$\mu\mu$ $M_{e\mu}$ >100 GeV	1	0.04 ± 0.02	0.04 ± 0.02	—
e$\mu\mu$ $M_{\mu\mu}$ >100 GeV	1	0.007 ± 0.005	0.007 ± 0.005	—
e^-p collisions (173 pb^{-1})				
ee M_{12} >100 GeV	0	0.55 ± 0.1	0.3 ± 0.1	0.25 ± 0.07
$\mu\mu$ $M_{\mu\mu}$ >100 GeV	0	0.03 ± 0.02	0.03 ± 0.02	—
eμ $M_{e\mu}$ >100 GeV	0	0.3 ± 0.05	0.3 ± 0.05	—
eee M_{12} >100 GeV	0	0.32 ± 0.06	0.32 ± 0.06	—
e$\mu\mu$ $M_{e\mu}$ >100 GeV	0	0.04 ± 0.01	0.04 ± 0.01	—
e$\mu\mu$ $M_{\mu\mu}$ >100 GeV	0	0.006 ± 0.004	0.006 ± 0.004	—
All data (459 pb^{-1})				
ee M_{12} >100 GeV	3	1.5 ± 0.3	0.9 ± 0.2	0.6 ± 0.2
$\mu\mu$ $M_{\mu\mu}$ >100 GeV	0	0.09 ± 0.05	0.09 ± 0.05	—
eμ $M_{e\mu}$ >100 GeV	1	0.9 ± 0.1	0.9 ± 0.1	—
eee M_{12} >100 GeV	3	0.9 ± 0.2	0.9 ± 0.2	—
e$\mu\mu$ $M_{e\mu}$ >100 GeV	1	0.1 ± 0.04	0.1 ± 0.04	—
e$\mu\mu$ $M_{\mu\mu}$ >100 GeV	1	0.03 ± 0.02	0.03 ± 0.02	—

Table 1: Yields for high di-lepton masses, $M > 100$ GeV in all analysed samples. For the *eee* sample, the mass of the two highest P_T electrons is shown. The errors on the prediction include model uncertainties and experimental systematic errors added in quadrature.

H1 Multi-lepton analysis HERA I+II (459 pb^{-1}, preliminary)

ΣE_T >100 GeV				
Data sample	Data	SM	Pair Production	NC-DIS + Compton
e^+p (286 pb^{-1})	4	1.2 ± 0.2	1.0 ± 0.2	0.2 ± 0.1
e^-p (173 pb^{-1})	0	0.8 ± 0.2	0.6 ± 0.2	0.2 ± 0.1
All (459 pb^{-1})	4	1.9 ± 0.4	1.5 ± 0.3	0.4 ± 0.1

Table 2: Yields of events with $\sum P_T > 100$ GeV for the combination of di- and tri-leptons. The errors on the prediction include model uncertainties and experimental systematic errors added in quadrature.

good agreement with the SM prediction. The distribution of the scalar sum of transverse momenta of the leptons is studied for the combination of all di- and tri-lepton sub-samples. The overall agreement with the SM is good, but four interesting events with a large scalar sum of transverse momenta are observed in e^+p collisions only, in a region where the SM expectation is 1.2 ± 0.2.

References

[1] Slides:
`http://indico.cern.ch/contributionDisplay.py?contribId=126&sessionId=9&confId=9499`
H1prelim-07-062:
`http://www-h1.desy.de/h1/www/publications/htmlsplit/H1prelim-07-062.long.html`.

[2] J. A. M. Vermaseren, Nucl. Phys. B **229** (1983) 347.

[3] A. Aktas *et al.* [H1 Collaboration], Eur. Phys. J. C **31** (2003) 17 [hep-ex/0307015].

[4] A. Aktas *et al.* [H1 Collaboration], Phys. Lett. B **583** (2004) 28 [hep-ex/0311015].

Multi-Lepton Production in ep Collisions at ZEUS

Osamu Ota *

Tokyo Metropolitan University
1-1 Minamioosawa, Hachioji Tokyo, Japan
ota@hakone.phys.metro-u.ac.jp

Multi-electron and di-tau production at high transverse momentum have been studied in ep collisions using the ZEUS detector at HERA. The data collected during the years 1996-2006 were used in the analysis, corresponding to an integrated luminosity of approximately 450 pb^{-1}. The results are compared with the Standard Model prediction.

1 Introduction

At HERA, multi-lepton production with high transverse momentum can be explored up to invariant masses of the order of 100 GeV. The dominant process is the two-photon process, $\gamma\gamma \rightarrow l^+l^-$, well understood in the Standard Model (SM) [2]. Therefore any excess over the SM prediction, especially in the high mass region, would be a sign of new phenomena. The H1 Collaboration has reported the observation of an excess in both di-electron ("ee") and tri-electron ("eee") samples in the high mass region for an integrated luminosity of $\mathcal{L}$=115 pb^{-1} [3]. The present analysis was performed with the ZEUS detector using a higher interated luminosity, combining the HERA-I data ($\mathcal{L}$=121 pb^{-1}) with the new HERA-II data ($\mathcal{L}$=325 pb^{-1}), collected during the years 2003-2006.

2 Event Selection

2.1 Multi-electron

Electron candidates were reconstructed as electromagnetic (EM) clusters in the Uranium-Scintillator Calorimeter (CAL). Depending on the angle θ_e, the electron candidates were classified into three regions; central ($20^\circ < \theta_e < 150^\circ$), forward ($5^\circ < \theta_e < 20^\circ$) and backward ($150^\circ < \theta_e < 175^\circ$). The electrons in the central region were required to be matched to a track from the central tracking detector (CTD). The following energy thresholds were required : E_e>10 GeV for electrons in the forward and the central regions, and E_e>5 GeV for those in the backward region. The events were required to have at least two electrons in the central region, one with transverse momentum calculated from the CAL P_T>10 GeV, and the other with P_T>5 GeV.

2.2 Di-tau

We looked for a topology in which a di-tau decays into an electron and the other into a muon. The selection criteria for electrons and muons were as follows :

- Electron identification - Similar to the multi-electron analysis, EM clusters were required to have energy greater than 4 GeV, and if found in the range $17^\circ < \theta_e < 150^\circ$, they were required to be matched to a track from the CTD;

*on behalf of the ZEUS collaboration

- Muon identification - the tracks from the CTD were required to be matched to a minimum ionizing particle (MIP) cluster in the CAL or to tracks from the muon chamber. The transverse momentum of the muon candidate ($P_{T,\mu}$) was required to be greater than 2 GeV.

The final selection was designed to further suppress the di-muon background. The quantity $E - P_z$ which was defined as $(E - P_z)_{CAL} + (E - P_z)_{\mu,track}$ was required to be below 45 GeV [a] and events which had an additional calorimeter deposit consistent with a MIP but not found by the muon algorithm were rejected. Additionally, events with a measured electron charge equal to -1 were required to have $\theta_e <$ 1 rad.

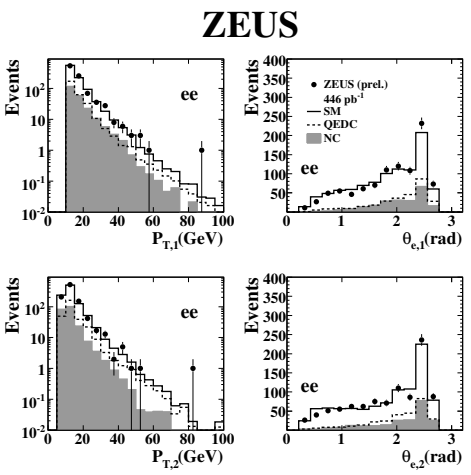

Figure 1: Comparison of the transverse momentum and polar angle distributions of the two highest P_T electrons with the SM expectations in the di-electron ("ee") sample.

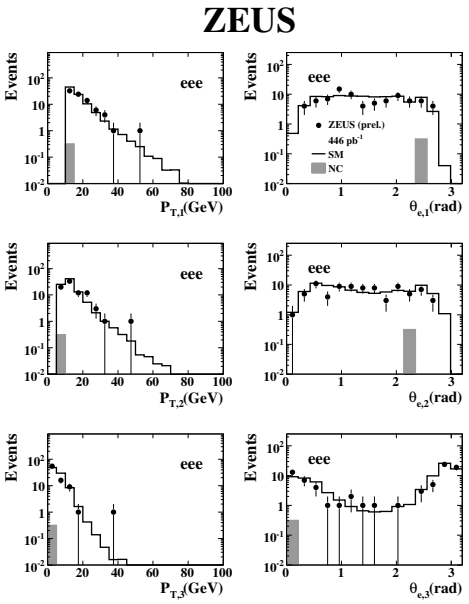

Figure 2: Comparison of the transverse momentum and polar angle distributions of the three highest P_T electrons with the SM expactations in the tri-electron ("eee") sample.

3 Results

The distributions of the transverse momentum, $P_{T,i}$, and polar angle, $\theta_{e,i}$, of the i^{th} highest-P_T electron in the final state of the di-electron ("ee") and of the tri-electron ("eee") events are shown in Fig.1 and Fig.2, respectively.

The event yield observed in the di-electron and tri-electron samples, with the SM predictions are summarised in Table.1. The data yields are in good agreement with the SM

[a] E and P_z are the energy and the longitudinal momentum, respectively. $(E-P_z)_{CAL}$ means the quantity $E - P_z$ measured by the CAL and $(E - P_z)_{\mu,track}$ is the one measured by the CTD for muons.

Topology	DATA	SM	GRAPE	QEDC	NC
ee M_{12}>80GeV	15	14.0±1.1	5.7±0.6	6.0±0.6	2.2±0.4
eee M_{12}>80GeV	3	$3.4^{+0.5}_{-0.1}$	3.4±0.3	<0.2	<0.5
ee M_{12}>100GeV	5	4.3±1.1	1.1±0.2	2.3±1.1	0.9±0.2
eee M_{12}>100GeV	1	$1.1^{+0.5}_{-0.1}$	1.1±0.1	<0.02	<0.5

Table 1: The observed and predicted multi-electron event yield for the ee and eee samples. The quoted uncertainties include MC statistics, luminosity measurement and electron enegy scale. Upper limit of 68% CL are given in case no MC event was remained after selection cuts.

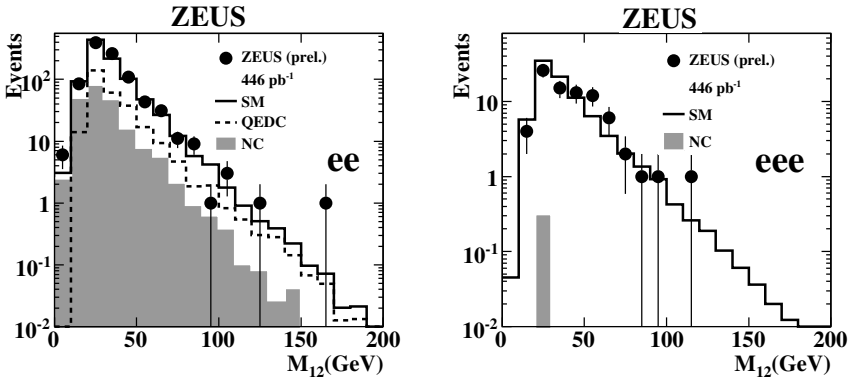

Figure 3: Distribution of the invariant mass M_{12} of the two highest P_T electrons compared with the SM expectations.

expectations, where the uncertainties on the SM expectation include the MC statistics, luminosity measurement and the electron energy scale uncertainty. If no MC event remained after the event selection, the upper limit of 68% CL is given.
The distributions of the invariant mass M_{12} of the di-electron samples and of the two highest P_T electrons from the tri-electron samples are presented in Fig.3.

In the di-tau search, three events remained after selection cuts compared with 2.0 ± 0.8 expected from the SM di-tau process. The expected number of events from di-muon background was found to be less than 0.2. The distributions of the polar angle and of the transverse momentum of the electron and muon coming from the decays of the tau candidates are shown in Fig.4.

4 Conclusions

A search for multi-electrons production with high transverse momentum was performed with HERA-I and HERA-II data, corresponding to a total integrated luminosity of 446 pb^{-1}.

The measured event yields in di-electron and tri-electron production in the final state

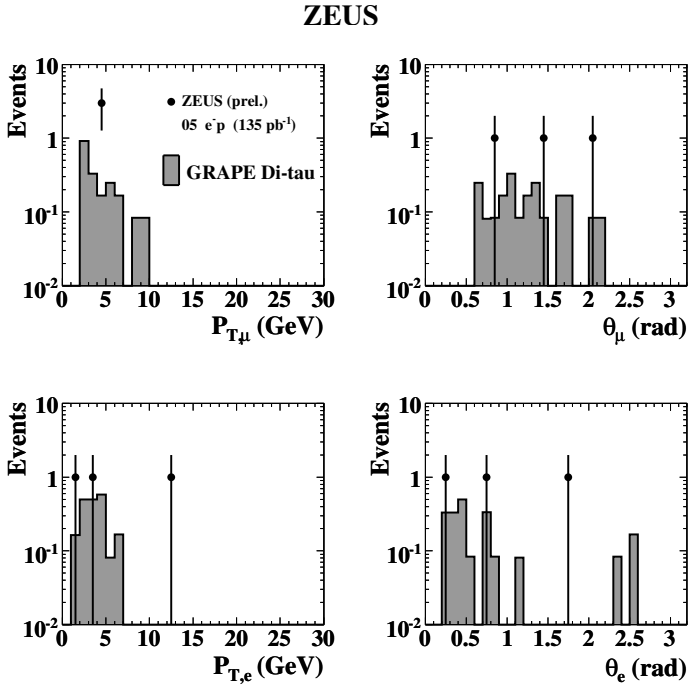

Figure 4: Comparison of the measured distribution of polar angles θ_μ and θ_e and transverse momenta $P_{T,\mu}$ and $P_{T,e}$ of the final state electron and muon with the SM expectations.

were found to be in good areement with the SM predictions and in particuler no excess was found in the high invariant mass region.

As for the di-tau search, the leptonic decay modes were analyzed with the 2005 data, corresponding to 135 pb^{-1}, yielding results compatible with the SM expectations. Three events were found in the final sample where no background is expected.

References

[1] Slides:
`http://indico.cern.ch/contributionDisplay.py?contribId=125&sessionId=9&confId=9499`

[2] J.A.M Vermaseren, Nucl. Phys. **B229**, 347 (1983).

[3] H1 Collaboration, *Multi-Electron Production at High Transverse Momenta in ep Collisions at HERA*, Eur. Phys. J. **C31**, 17-29 (2003).

A General Search for New Phenomena at HERA

E. Sauvan
On behalf of the H1 Collaboration

CPPM, IN2P3-CNRS et Université de la Méditerranée
163 Avenue de Luminy F-13288 Marseille, France

A model-independent search for deviations from the Standard Model prediction is performed in e^+p and e^-p collisions at HERA II using all high energy data recorded by the H1 experiment. This corresponds to a total integrated luminosity of 337 pb^{-1}. All event topologies involving isolated electrons, photons, muons, neutrinos and jets with high transverse momenta are investigated in a single analysis. Events are assigned to exclusive classes according to their final state. A statistical algorithm is used to search for deviations from the Standard Model in distributions of the scalar sum of transverse momenta or invariant mass of final state particles and to quantify their significance. A good agreement with the Standard Model prediction is observed in most of the event classes. The most siginificant deviation is found in the μ-j-ν channel in e^+p collisions.

1 Introduction

At HERA electrons[a] and protons collide at a centre-of-mass energy of up to 319 GeV. These high-energy electron-proton interactions provide a testing ground for the Standard Model (SM) complementary to e^+e^- and $p\overline{p}$ scattering. The approach presented here consists of a comprehensive and generic search for deviations from the SM prediction at large transverse momenta. The present analysis follows closely the strategy of the previous publication from the H1 experiment [2]. All high P_T final state configurations involving electrons (e), muons (μ), jets (j), photons (γ) or neutrinos (ν) are systematically investigated. The complete HERA II data sample (2003–2007) is used, corresponding to a total integrated luminosity of 337 pb^{-1} shared between e^+p (178 pb^{-1}) and e^-p (159 pb^{-1}) collisions.

2 Data Analysis and Results

All final states containing at least two objects (e, μ, j, γ, ν) with $P_T > 20$ GeV in the polar angle range $10^\circ < \theta < 140^\circ$ are investigated. All selected events are classified into exclusive event classes according to the number and types of objects detected in the final state (e.g. e-j, μ-j-ν, j-j-j-j). The criteria used in the identification of each type of particle are chosen to ensure an unambiguous identification, while retaining high efficiencies [2]. All experimentally accessible combinations of objects have been studied and data events are found in 23 event classes.

A precise and reliable estimate of all relevant processes present at high transverse momentum in ep interactions is needed to ensure an unbiased comparison to the SM. Hence several Monte Carlo generators are used to generate a large number of events in all event classes, carefully avoiding double-counting of processes. The simulation contains the order α_S matrix elements for QCD processes, while second order α matrix elements are used to calculate QED processes. Additional jets are modelled using leading logarithmic parton showers as a representation of higher order QCD radiation.

[a] In this paper "electrons" refers to both electrons and positrons, unless otherwise stated.

The event yields observed in each event class are presented and compared to the SM expectation in figures 1(a) and (b) for e^+p and e^-p collisions, respectively. In each class, a good description of the number of observed data events by the SM prediction is seen. This demonstrates the good understanding of the detector response and of the SM processes in the considered phase space. Distributions of the scalar sum of transverse momenta $\sum P_T$ of all objects are presented in figure 2 for e^+p data.

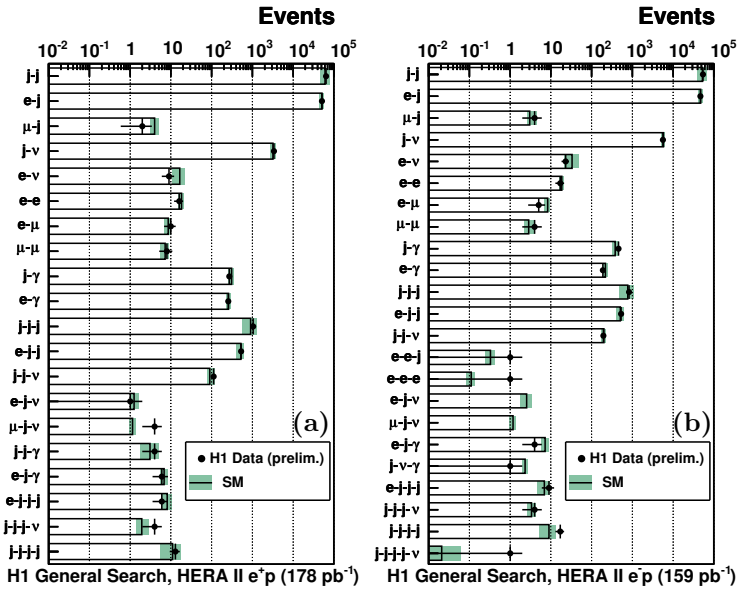

Figure 1: The data and the SM expectation for all event classes with observed data events or a SM expectation greater than one event. The results are presented separately for e^+p (a) and e^-p (b) collisions.

3 Search for deviations

In order to quantify the level of agreement between the data and the SM expectation and to identify regions of possible deviations, the same search algorithm as developed in [2] is used. All possible regions in the histograms of $\sum P_T$ and M_{all} distributions are considered. The number of data events (N_{obs}), the SM expectation (N_{SM}) and its total systematic uncertainty (δN_{SM}) are calculated for each region. A statistical estimator p is defined to judge which region is of most interest. This estimator is derived from the convolution of the Poisson probability density function (pdf) to account for statistical errors with a Gaussian pdf, $G(b; N_{SM}, \delta N_{SM})$, with mean N_{SM} and width δN_{SM}, to include the effect of non negligible systematic uncertainties [2]. The value of p gives an estimate of the probability of a fluctuation of the SM expectation upwards (downwards) to at least (at most) the observed number of data events in the region considered. The region of greatest interest (of greatest deviation) is the region having the smallest p-value, $p_{\min}$.

The possibility that a fluctuation with a value $p_{\min}$ occurs anywhere in the distribution

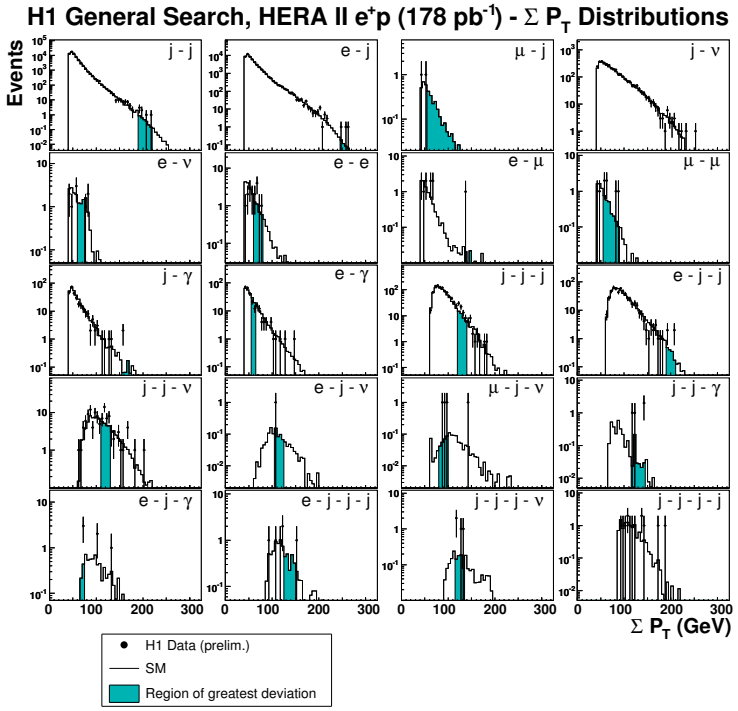

Figure 2: Distributions of $\sum P_T$ for classes with at least one data event, for e^+p data. The shaded areas show the regions of greatest deviation chosen by the search algorithm.

is estimated. This is achieved by creating hypothetical data histograms following the pdfs of the SM expectation. The algorithm is then run on those hypothetical histograms to find the region of greatest deviation and the corresponding $p_{\min}^{SM}$ is calculated. The probability $\hat{P}$ is then defined as the fraction of hypothetical data histograms with a $p_{\min}^{SM}$ equal to or smaller than the $p_{\min}$ value obtained from the real data. $\hat{P}$ is a measure of the statistical significance of the deviation observed in the data. The event class of most interest for a search is thus the one with the smallest $\hat{P}$ value. Depending on the final state, a $p_{\min}$-value of $5.7 \cdot 10^{-7}$ ("5σ") corresponds to a value of $-\log_{10} \hat{P}$, the negative decade logarithm of $\hat{P}$, between 5 and 6. The overall degree of agreement with the SM can further be quantified by taking into account the large number of event classes studied in this analysis. Among all studied classes there is some chance that small $\hat{P}$ values occur. This probability can be calculated with MC experiments. A MC experiment is defined as a set of hypothetical data histograms following the SM expectation with an integrated luminosity equal to the amount of data recorded. The complete search algorithm and statistical analysis are applied to the MC experiments analgously as to the data. This procedure is repeated many times. The expectation for the $\hat{P}$ values observed in the data is then given by the distribution of $\hat{P}^{SM}$ values obtained from all MC experiments. The probability to find in the MC experiments a $\hat{P}$ value smaller than in the data can be calculated and gives us the global significance of the observed deviation.

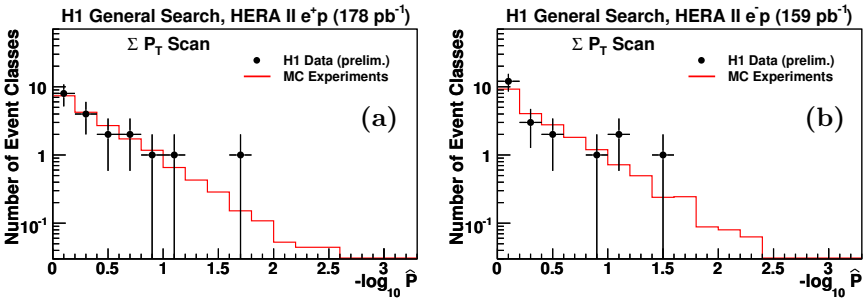

Figure 3: The $-\log_{10}\hat{P}$ values for the data event classes and the expected distribution from MC experiments as derived by investigating the $\sum P_T$ distributions in e^+p (a) and e^-p (b) data.

The $\hat{P}$ values observed in the real data in all event classes[b] are compared in figure 3 to the distribution of $\hat{P}^{SM}$ obtained from the large set of MC experiments, normalised to one experiment. The comparison is presented for the scans of the $\sum P_T$ distributions. All $\hat{P}$ values range from 0.01 to 0.99, corresponding to event classes where no significant discrepancy between data and the SM expectation is observed. These results are in agreement with the expectation from MC experiments. The most significant deviation from SM predictions is observed in the μ-j-ν event class and in e^+p collisions with a value of $-\log_{10}\hat{P}$ equal to 1.7. In the previous H1 analysis [2] based on HERA I data and dominated by e^+p collisions, the largest deviation was also found in this event class, with $-\log_{10}\hat{P} = 3$.

4 Conclusions

All the data collected with the H1 experiment during HERA II running period (2003–2007) have been investigated for deviations from the SM prediction at high transverse momentum. All event topologies involving isolated electrons, photons, muons, neutrinos and jets are investigated in a single analysis. A good agreement between data and SM expectation is found in most event classes. In each event, class the invariant mass and sum of transverse momenta distributions of particles have been systematically searched for deviations using a statistical algorithm. No significant deviation is observed in the phase-space and in the event topologies covered by this analysis. The largest deviation from SM expectation is observed in the μ-j-ν event class in e^+p collisions.

References

[1] Slides: `http://indico.cern.ch/contributionDisplay.py?contribId=127&sessionId=9&confId=9499`

[2] A. Aktas *et al.* [H1 Collaboration], Phys. Lett. B **602** (2004) 14 [hep-ex/0408044].

[b] Due to the uncertainties of the SM prediction in the j-j-j and j-j-j-ν event classes at highest M_{all} and $\sum P_T$ (see [2]), where data events are observed, no reliable $\hat{P}$ values can be calculated for these classes. These event classes are not considered to search for deviations from the SM in this extreme kinematic domain.

An Interface to High p_t HERA Data: Quaero@H1

Sascha Caron[1] and Bruce Knuteson[2] *

1- Physikalisches Institut, Universität Freiburg, Germany;
e-mail: scaron@physik.uni-freiburg.de

2- Massachusetts Institute of Technology;
e-mail: knuteson@mit.edu

Distributions from high-p_T HERA event data analyzed in a general search for new physics at H1 have been incorporated into QUAERO, an algorithm designed to automate tests of specific hypotheses with high energy collider data. This article introduces the framework and shows examples to illustrate the algorithm's performance.

1 Introduction

On 30$^{\text{th}}$ June 2007, data taking ended at the HERA accelerator. Data analysis will still continue for a few years. In the years after HERA new theoretical scenarios will be constructed, and HERA data may yet prove to be useful in their testing. HERA data may even prove to be important in constraining theoretical interpretations of findings made at the Large Hadron Collider. Unfortunately, re-interpretation of previous data typically requires a re-analysis with expert collaboration-specific knowledge. The QUAERO framework [3] allows quick testing of any specific hypothesis against collider event data, with the analysis performed by an algorithm that encapsulates the expert knowledge of the experiment. QUAERO@H1 incorporates distributions published by the H1 Collaboration in a general search for new physics into this QUAERO framework [2]. Within this system new theoretical scenarios can be tested with HERA data and exclusion contours (or discovery regions) can be produced on demand. The system is available to users via a web interface [6].

2 Available data and the H1 General Search

The H1 General Search has been published in Ref. [4]. This search investigates events with high-p_T objects (electrons, muons, jets, photons, and the presence of missing transverse energy) produced in ep collisions at HERA. The histograms published by H1 (the invariant masses and the sums of the transverse momenta for high-p_T events) are used as input to the QUAERO algorithm in the studies described in this paper.

The H1 data available within QUAERO correspond to

- 36.4 pb^{-1} of 27.5 GeV positrons on 820 GeV protons, at a center of mass energy of 301 GeV;
- 13.8 pb^{-1} of 27.5 GeV electrons on 920 GeV protons, at a center of mass energy of 319 GeV; and
- 66.4 pb^{-1} of 27.5 GeV positrons on 920 GeV protons, at a center of mass energy of 319 GeV.

Standard object identification criteria are used to define electrons (e), muons (μ), photons (γ), and jets (j) [4]. All identified objects are required to have $p_T > 20$ GeV and

*The authors thank the H1 collaboration for supporting Quaero@H1.

$10^\circ < \theta < 140^\circ$. A neutrino object ($\not{p}$) is defined for missing transverse momentum above 20 GeV. The experimental sources of systematic error affecting the modeling of these data are identical to those considered in Ref. [4] and are included into QUAERO. Several Monte Carlo event generators are combined to estimate dominant Standard Model processes [4]. These generated events serve as the reference model to which hypotheses presented to QUAERO are compared.

3 Turbosim for H1 and the QUAERO algorithm

To keep QUAERO fast and standalone, a fast detector simulation algorithm (TURBOSIM@H1) is built in accordance with the H1 detector simulation. It is based on a large lookup table of one half million lines mapping particle-level objects to objects reconstructed in the detector. Validation of TURBOSIM@H1 has been performed by running an independent sample of one million events through both the H1 full simulation and TURBOSIM@H1. The event classification and the kinematic distributions of the events from the two simulation chains are compared using a Kolmogorov-Smirnov (KS) test. TURBOSIM@H1 has been found in agreement with the full simulation of H1.

QUAERO provides a convenient interface to the understanding represented by high energy collider data, backgrounds, and detector response. This interface is designed to facilitate the test of any specific hypothesis against such data. A physicist wishing to test her hypothesis against H1 data will provide her hypothesis in the form of commands to one of the built-in event generators. QUAERO uses the specified event generator to generate signal events corresponding to e^+p collisions at 301 GeV, e^-p collisions at 319 GeV, and e^+p collisions at 319 GeV. The response of the H1 detector to these events is simulated using TURBOSIM@H1. Three distinct samples of events exist at this point: the data $\mathcal{D}$; the Standard Model prediction SM; and the hypothesis $\mathcal{H}$, which is the sum of included Standard Model processes and the physicist's signal. Each sample of events is partitioned into exclusive final states, categorized by reconstructed objects with $p_T > 20$ GeV. In each exclusive final state, a pre-defined list of two variables — the summed scalar transverse momentum ($\sum p_T$) and the invariant mass of all objects (m_{all}) — are ranked according to the difference between the Standard Model prediction and the physicist's hypothesis $\mathcal{H}$. The variable showing the most difference is used and densities are estimated from the Monte Carlo events predicted by SM and $\mathcal{H}$. These densities are used to define a discriminant, which is binned to distinguish SM from $\mathcal{H}$. The likelihood ratio $\mathcal{L} = p(\mathcal{D}|\mathcal{H})/p(\mathcal{D}|\text{SM})$ is determined using this binning, and systematic errors are integrated numerically. The result returned by QUAERO is the decimal logarithm of this likelihood ratio. The measurement of model parameters using QUAERO is easily accomplished by graphing $\log_{10}\mathcal{L}$ as a function of varied parameter values, with multiple QUAERO submissions. This information, in addition to plots showing data, Standard Model prediction, and the physicist's hypothesis, are returned in an email.

A rough useful comparison of the sensitivity of QUAERO's results (which take the form of the decimal logarithm of a likelihood ratio) with previous analyses (which typically take the form of 95% confidence level exclusion limits) can be made by comparing $\log_{10}\mathcal{L} = -1$ with the 95% confidence level exclusion limit.

4 One example: Leptoquarks

QUAERO@H1 has been used to search for leptoquarks, particles possessing both lepton

and baryon quantum numbers that arise naturally in Grand Unified Theories. Attention is restricted to a scalar leptoquark coupling to a positron and an up quark. The coupling λ of the LQ-e-u vertex and the leptoquark mass m_{LQ} are allowed to vary. The interaction Lagrangian is assumed to be of the form

$$\begin{aligned} \mathcal{L} &= \lambda \,\mathrm{LQ}\, \bar{u}_R \, e_L + \mathrm{h.c.} \\ &\quad + i g_s G^*_\mu (\mathrm{LQ}^* \overleftrightarrow{\partial}^\mu \mathrm{LQ}), \end{aligned} \tag{1}$$

where LQ is a scalar leptoquark field; $\bar{u}_R$ and e_L represent a right-handed anti-up quark and left-handed electron; G_μ is the gluon field; and $g_s = \sqrt{4\pi\alpha_s} \approx 1.2$. MadEvent [5] is used to generate events corresponding to these Lagrangian terms within Quaero .

The subset of D0 Run I data made available in the first implementation of Quaero [3] has been incorporated into the current version of Quaero. Plots of Quaero's result in the parameter plane of λ and m_{LQ} using the H1 and D0 data separately are shown in Fig. 1. Quaero's result using H1 and D0 data combined is shown in Fig. 1. Quaero is able to make use of the Tevatron's λ-independent exclusion of leptoquarks with low mass and HERA's λ-dependent exclusion at higher masses to rule out more of the parameter space than either collider is able to on its own.

The use of Quaero@H1 to search for R-parity violating supersymmetry and excited quarks can be found in Ref. [2].

5 Summary

The histograms of the invariant masses and the sum of transverse momenta from the high-p_T events selected in a general search for new physics at H1 have been incorporated into Quaero, a framework for automating tests of hypotheses against data. The resulting interface (Quaero@H1) will allow future users to quickly compare new theoretical scenarios to HERA data.

6 Bibliography

References

[1] slides:
`http://indico.cern.ch/contributionDisplay.py?contribId=128&sessionId=9&confId=9499`

[2] S. Caron and B. Knuteson, arXiv:hep-ph/0612201.

[3] V. M. Abazov *et al.* [D0 Collaboration], Phys. Rev. Lett. **87** (2001) 231801 [arXiv:hep-ex/0106039].

[4] A. Aktas *et al.* [H1 Collaboration], Phys. Lett. B **602** (2004) 14 [arXiv:hep-ex/0408044].

[5] F. Maltoni and T. Stelzer, JHEP **0302** (2003) 027 [arXiv:hep-ph/0208156].

[6] Quaero: `http://mit.fnal.gov/Quaero`

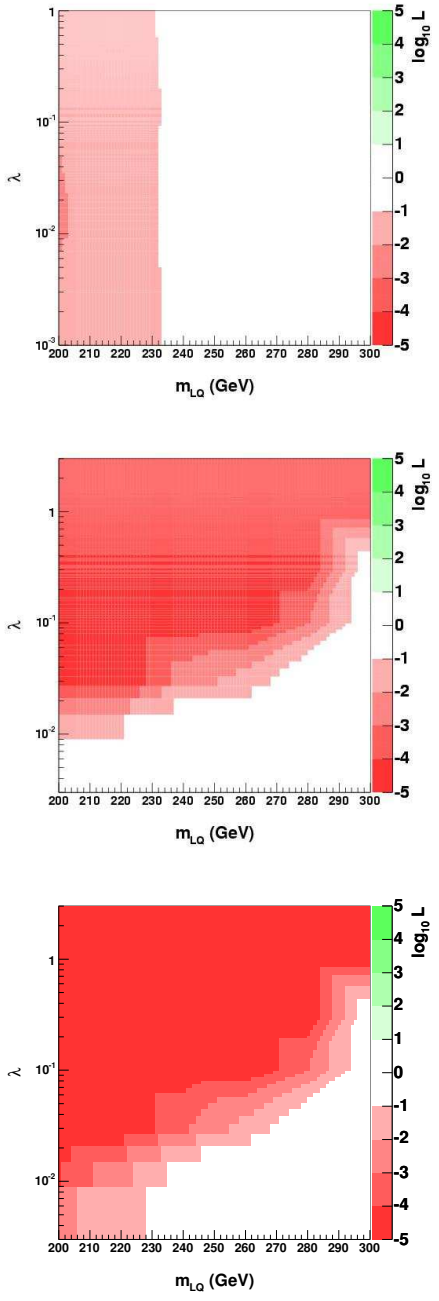

Figure 1: QUAERO's log likelihood ratio as a function of the coupling λ and leptoquark mass m_{LQ} for the Leptoquark example. Shown separately are results from QUAERO using data from DØ Tevatron Run I (upper plot) and using data from H1 HERA Run I (middle plot) and using data from both experiments.

Search for Leptoquarks and Lepton Flavour Violation with the H1 Experiment at HERA

Ana Dubak[1,2]

1- University of Montenegro, Faculty of Science
Cetinjski put bb, Podgorica, Montenegro

2- Max-Planck-Institute for Physics
Föhringer Ring 6, Munich, Germany

Recent results of searches for leptoquarks with the H1 experiment at HERA are presented. A search for first generation leptoquarks is performed using e^-p data with longitudinally polarised electrons collected in the second phase of HERA running. A search for lepton flavour violating processes $ep \to \mu X$ and $ep \to \tau X$ is performed using e^+p and e^-p data from the first phase of HERA running collected from 1998 to 2000. No evidence for direct or indirect production of leptoquarks has been found. The results are interpreted in terms of limits on the Yukawa coupling of leptoquarks and lepton flavour violating processes.

1 Introduction

Leptoquarks (LQs) are colour triplet bosons which appear in various unifying theories beyond the Standard Model (SM). At HERA, leptoquarks could be singly produced by the fusion of the initial state electron[a] of energy 27.6 GeV with a quark from the incoming proton of energy 920 GeV. The phenomenology of LQs is discussed in detail in [2]. This note presents a search for LQs coupling to first generation fermions in scattering of longitudinally polarised electrons on protons at a centre-of-mass energy of $\sqrt{s} \approx 320$ GeV. For the lefthanded running phase with an average polarisation of -27%, the integrated luminosity amounts to 60 pb^{-1}, whereas for righthanded running phase with an average polarisation of 34%, 32 pb-1 of data are analysed.

The LQ concept can also be used to search for lepton flavour violation (LFV) processes in electron-proton collisions. In ep collisions at HERA, LFV processes $ep \to \mu X$ and $ep \to \tau X$ lead to final states with a muon or a tau and a hadronic system X. The search for LFV phenomena is performed in ep collision data with unpolarised electrons recorded during the years 1998-2000 by the H1 experiment, corresponding to an integrated luminosity of 66.5 pb^{-1} for e^+p collisions and 13.7 pb^{-1} for e^-p collisions at a centre-of-mass energy $\sqrt{s} = 319$ GeV.

2 Search for Leptoquarks

Due to the more favourable quark-densities of quarks with respect to anti-quarks at high x, the e^-p data sets are mostly sensitive to LQs with fermion number $F = |L + 3B| = 2$. The search reported here considers the decays LQ $\to eq$ and LQ$\to \nu q$ where q represents both quarks and anti-quarks. These LQ decays lead to final states similar to those of deep-inelastic scattering (DIS) neutral current (NC) and charged current (CC) interactions at

[a] In this note "electron" refers generically to both electrons and positrons. Where distinction is required the symbols e^+ and e^- are used.

very high Q^2, the negative four-momentum transfer squared. If the final state is of type eq, the LQ mass is reconstructed from the measured kinematics of the scattered electron. If the final state is of type νq, the LQ mass is reconstructed from the hadronic final state [2].

This search is based on inclusive NC and CC DIS data in the kinematic domain $Q^2 > 500$ GeV^2 and $0.1 < y < 0.9$, where the inelasticity variable y is defined as $y = Q^2/M^2$. The cuts on y remove regions of poor reconstruction, poor resolution, large QED radiative effects and background from photoproduction processes. The selection of NC-like events requires an identified electron with transverse momentum above 11 GeV. The selection of CC-like events follows closely that presented in [2, 3]. The missing transverse momentum is required to be greather than 12 GeV.

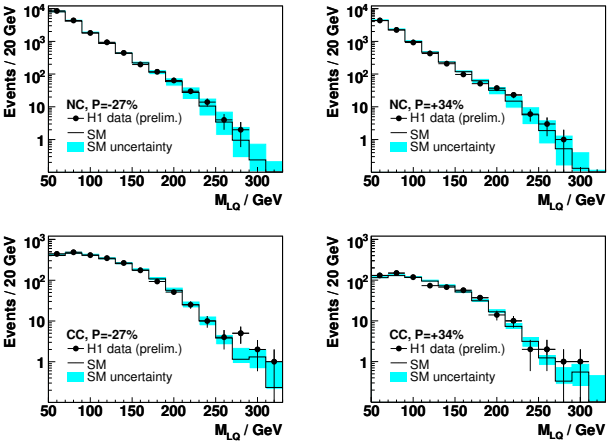

Figure 1: Mass spectra for the neutral current (up) and the charged current events (down).

The mass spectra measured for NC-like and CC-like events in the left- and righthanded data sets, shown in figure 1, are compared with the SM predictions, obtained using a Monte-Carlo calculation [4] and the CTEQ5D parametrisation [5] for the parton densities. In all cases the data are well described by the SM prediction.

Since no evidence for LQ production is observed in either the NC or CC data samples, the data are used to set constraints on LQs which couple to first generation fermions.

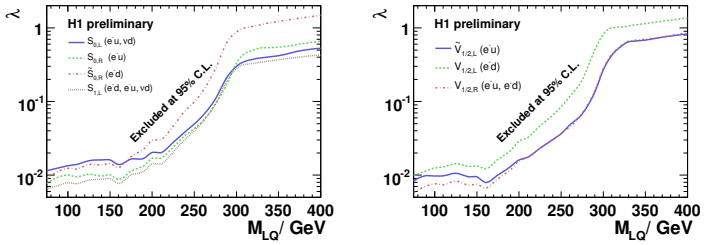

Figure 2: Exclusion limits for the 7 LQs with $F = 2$. The limits are expressed at 95% CL on the coupling λ as a function of the leptoquark mass. Domains above the curves are excluded.

The resulting constraints for the four scalar and the three vector LQs with $F = 2$ are shown in figure 2. The areas above the curves are excluded at 95% CL. The strongest constraints on the coupling λ can be set for LQ masses below the kinematic limit of the s-channel. At higher masses the production is no longer resonant, but rather contact interaction like and the cross section scales approximately with $(\lambda/M_{LQ})^4$. For a coupling of electromagnetic strength ($\lambda = \sqrt{4\pi\alpha_{em}} = 0.3$) this analysis rules out LQ masses below 276 to 304 GeV, depending on the LQ type.

3 Search for Lepton Flavour Violation

This analysis presents a search for LFV mediated by LQs with $F = 0$ and $F = 2$. For convenience only one LFV transition is considered: either between the first and the second generations $ep \to LQ \to \mu X$ or between the first and the third generations $ep \to LQ \to \tau X$.

To determine the signal detection efficiencies, events with LQs are generated using the LEGO [6] event generator with the CTEQ5L parametrisation of the parton distribution functions (PDF) of the proton [7]. The LQ signal expectation is a function of the LQ type, mass, coupling constant and branching ratio β_{LFV}. The contributions from SM background processes which may mimic the signal include NC and CC DIS, photoproduction, lepton pair production and real W boson production.

LQs with couplings to the first and second generation leptons can be produced in ep collisions and may decay to a muon and a quark. The signature is an isolated high P_T muon back-to-back to the hadronic system in the transverse plane. In general, a muon deposits a very small fraction of its energy in the LAr calorimeter. The signal is therefore expected to exhibit large P_T^{calo}, which is the net transverse momentum reconstructed from all clusters recorded in the LAr calorimeter alone. A detailed description of selection criteria is presented in [8].

Leptoquarks with couplings to the first and the third lepton generation can be produced in ep collisions and may decay to a tau and a quark. Tau leptons are identified using the electronic, muonic and hadronic decays of the tau. The final state resulting from the electronic tau decay, $\tau \to e\nu_e\nu_\tau$, leads to an event topology that is very similar to that of high Q^2 NC DIS events. The preselection follows that presented in [2]. Muonic tau decays $\tau \to \mu\nu_\mu\nu_\tau$ result in similar final states as the high P_T muon signatures of muonic LQ decay. Therefore the same selection cuts are applied here. The hadronic decays of the high P_T tau lead to a typical signature of a high high P_T "pencil-like" jet. The signal topology is a di-jet event with no leptons. The final selection criteria for all three tau decay channels are given in [8].

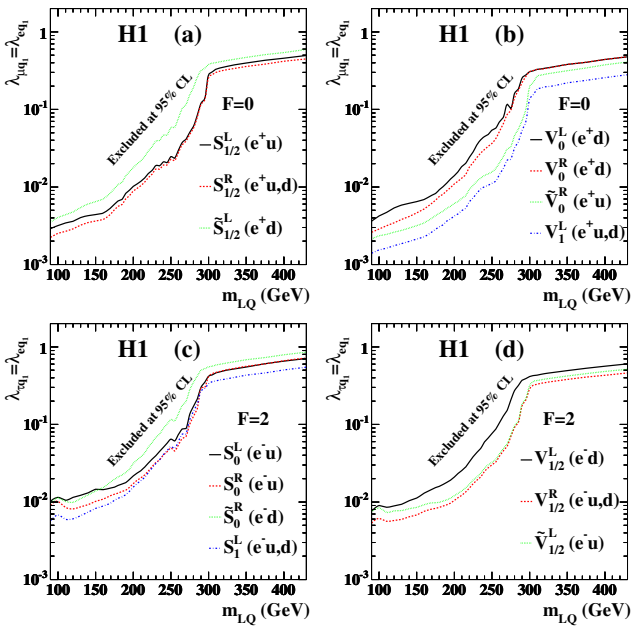

Figure 3: Comparison of limits at 95% CL on the coupling constants λ_{lq} assuming $\lambda_{\mu q} = \lambda_{eq}$ (a,b) and $\lambda_{\tau q} = \lambda_{eq}$ (c,d) as a function of the LQ mass m_{LQ}. The areas above the lines represent the excluded regions.

No candidate is found in the final data sample of the muon channel nor in the electronic and muonic tau decay channel. One event is selected in hadronic tau decay channel which is in agreement with the SM expectation.

The results of the search are interpreted in terms of exclusion limits on the mass and the coupling of LQs that may mediate LFV. In order to cover the full LQ decay width and to generalise the results of LFV searches in ep collisions to an arbitrary weight between the lepton flavour conservation (LFC) and LFV decay channels, the searches for LFC decays presented in [9] are combined with each of the LFV search channels μX or τX of the present analysis.

Upper limits on the coupling $\lambda_{\mu q}$ and $\lambda_{\tau q}$ of all 14 LQ types to a muon-quark pair and a tau-quark pair, respectively, are determined as a function of the LQ mass. Assuming lepton universality the couplings $\lambda_{\mu q}$ and $\lambda_{\tau q}$ are taken to be equal to λ_{eq}. Examples of such a limits are shown in figure 3.

Figure 4 shows an example of excluded regions for one LQ type in the λ_{lq_1}-λ_{eq_1} plane for the case of an arbitrary decay rate between the LFC and LFV decay channels, β_{LFV}. For $\beta \gg 0.05$ ($\lambda_{lq} \gg \lambda_{eq}$) the present analysis extends significantly the published limits on λ_{eq} to lower values.

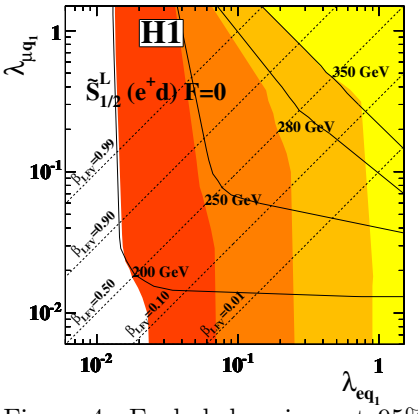

Figure 4: Excluded regions at 95% CL (filled) in λ_{lq_1}-λ_{eq_1} plane for four different leptoquark masses. The bounds deduced without the combination with first generation LQs are shown as black curves corresponding to the different LQ masses.

4 Conclusion

A search for LQs with fermion number F = 2 has been performed using the polarised $e^- p$ data recorded by H1 in 2005. No signal has been observed and constraints on leptoquarks have been set, which for F = 2 LQs extend beyond the domains excluded previously by H1. For a coupling of electromagnetic strength, LQ masses below 276 - 304 GeV can be ruled out, depending on the LQ type.

No signal for the LFV processes $ep \to \mu X$ or $ep \to \tau X$ is found. Constraints on LFV LQ couplings are set combining the LFV search with the search for first generation LQs. Assuming a coupling of electromagnetic strength, leptoquarks mediating lepton flavour violating processes $e \to \mu$ and $e \to \tau$ can be ruled out up to masses of 459 GeV and 379 GeV, respectively.

References

[1] Slides: `http://indico.cern.ch/contributionDisplay.py?contribId=129&sessionId=9&confId=9499`

[2] C. Adloff *et al.*, Eur. Phys. J. **C11** 447 (1999) [Erratum-ibid. **C14** 553 (1999)], [hep-ex/9907002].

[3] C. Adloff *et al.*, Eur. Phys. J. **C19** 269 (2001), [hep-ex/0012052].

[4] DJANGO 6.2; G.A. Schuler and H. Spiesberger, Proc. of the Workshop Physics at HERA, W. Buchmüller and G. Ingelman (Editors), (October 1991, DESY-Hamburg) Vol. 3 p. 1419.

[5] H. L. Lai *et al.*, Eur. Phys. J. **C12** 375 (2000), [hep-ph/9903282].

[6] K. Rosenbauer, dissertation RWTH Aachen (in German), PITHA 95/16, July 1995.

[7] J. Pumplin *et al.*, JHEP 0207 012 (2002), [hep-ph/0201195]

[8] A. Aktas *et al.*, submitted to Eur. Phys. J. **C**, [hep-ex/0703004]

[9] A. Aktas *et al.*, Phys. Lett. **B629** 9 (2005), [hep-ex/0506044].

Search for Excited Leptons at HERA

TRINH Thi Nguyet
On behalf of the H1 Collaboration

Centre de Physique des Particules de Marseille
163 Avenue de Luminy, F-13288 Marseille Cedex 9, France

Searches for excited electrons and neutrinos have been performed using the complete HERA I and II data samples collected by the H1 detector at $\sqrt{s} = 320$ GeV corresponding to an integrated luminosity of up to 435 pb^{-1}. In absence of a signal, the limits on the ratio of the coupling to the compositeness scale derived extend the excluded region to higher masses than has been possible in previous searches.

1 Introduction

Compositeness models [2] attempt to explain the hierarchy of masses in the Standard Model (SM) by the existence of a substructure within the fermions. Several of these models predict excited states of the known leptons. Excited leptons (F^*) are assumed to have the same electroweak SU(2) and U(1) gauge couplings, g and g', to the vector bosons, but are expected to be grouped into both left- and right-handed weak isodoublets with vector couplings. The existence of the right-handed doublets is required to protect the ordinary light leptons from radiatively acquiring a large anomalous magnetic moment via the F^*FV interaction (where V is a γ, Z, or W). Considering only the electroweak interaction, the phenomenological model describes this interaction by the Lagrangian density:

$$L_{F^*F} = \frac{1}{2\Lambda}\bar{F^*_R}\sigma^{\mu\nu}[gf\frac{\vec{\tau}}{2}\partial_\mu\vec{W}_\nu + g'f'\frac{Y}{2}\partial_\mu B_\nu]F_L + h.c.$$

where the new weights f and f' multiply the standard coupling constants g and g' corresponding to the weak SU(2) and the electromagnetic U(1) sectors respectively. The matrix $\sigma^{\mu\nu}$ is the covariant bilinear tensor, τ are the Pauli matrices, $W_{\mu\nu}$ and $B_{\mu\nu}$ represent the fully gauge invariant field tensors, and Y is the weak hypercharge. The parameter Λ has units of energy and can be regarded as the compositeness scale. The relative values of f and f' affect the size of the single-production cross section, their detection efficiencies and also the branching ratios of excited leptons.

Excited electrons and neutrinos may be produced in electron(positron)-proton collisions at HERA via t-channel $\gamma(Z)$ or $W^\pm$ gauge boson exchange. In the case of excited neutrinos, the cross section is much larger in e^-p collsions than in e^+p collsions due to the favourable valence u-quark and the helicity enhancement, specific to CC-like processes. Therefore the search for excited neutrinos uses only e^-p sample data with an integrated luminosity of 184 pb^{-1}. In the case of excited electrons, both e^-p and e^+p collision modes are used, corresponding to total integrated luminosity of 435 pb^{-1}.

2 Data analysis and results

Excited leptons ($l = e, \nu$) are searched for in the following decay channels: $l^* \to l\gamma$, $l^* \to lZ$, $l^* \to lW$. The final states resulting from the Z or W hadronic decays are taken into account

Search for e*, ν^* HERA I+II ($\sqrt{s} = 320$ GeV, preliminary)

Selection	Data	SM	Efficiency × BR
$e^* \to \nu W_{\hookrightarrow qq}$	172	175 ± 39	$\sim$ 40 %
$e^* \to e Z_{\hookrightarrow qq}$	351	318 ± 64	$\sim$ 45 %
$e^* \to e\gamma$	112	125 ± 19	60–70 %
$\nu^* \to \nu\gamma$	9	15 ± 4	50 %
$\nu^* \to e W_{\hookrightarrow qq}$	198	189 ± 33	30–40 %
$\nu^* \to \nu Z_{\hookrightarrow qq}$	111	102 ± 24	40 %
$\nu^* \to e W_{\hookrightarrow \nu\mu}$	0	0.54 ± 0.04	3–4.5 %
$\nu^* \to e W_{\hookrightarrow \nu e}$	0	0.6 ± 0.3	4–6 %
$\nu^* \to \nu Z_{\hookrightarrow ee}$	0	0.12 ± 0.04	2 %

Table 1: Observed and predicted event yields for the event classes of e^* and ν^* searches. The selection efficiency for the signal multiplied by the branching ratio (BR) in each decay channel is also presented.

for both excited electrons and neutrinos and the Z or W leptonic decays are taken into account only for excited neutrinos. In the following, the selection criteria are described for the decay channels.

The $\nu^* \to \nu\gamma$ channel

Candidate events are selected by requiring missing transverse momentum $P_T^{miss} > 15$ GeV, where the photon is identified as an isolated electromagnetic (e.m.) cluster in the LAr calorimeter within a polar angle of 5° to 120°. The photon candidates measured within the acceptance of the central tracker ($\theta^\gamma > 20°$) are required to have no associated tracks. The neutral current (NC) and charged current (CC) backgrounds are reduced by imposing the longitudinal momentum balance $E - P_Z > 45$ GeV for events with photon candidates at lower transverse momentum $P_T^\gamma < 40$ GeV and by requiring the virtuality (Q^2_γ) to satisfy $\log(Q^2_\gamma) > 3.5$ GeV^2. The background is further suppressed by rejecting events with a transverse momentum of the final hadronic in the calorimeter $P_T^h < 5$ GeV.

The $e^* \to e\gamma$ channel

Candidate events are selected with two isolated e.m. clusters in the LAr calorimeter of transverse energy greater than 20 GeV and 15 GeV, respectively, and with a polar angle between 5° and 130°. The sum of the energies of the two clusters has to be greater than 100 GeV. The background from NC is further suppressed by rejecting events with a total transverse energy of the two isolated e.m. clusters lower than 75 GeV.

The $e^* \to eZ, \nu W$ and $\nu^* \to eW, \nu Z$ channels with $Z, W \to qq'$

These channels use subsample of events with at least two jets with high transverse momentum $P_T^{j1(j2)} > 20(15)$ GeV reconstructed within $5° < \theta^{j1(j2)} < 130°$. The dijet invariant mass must be compatible with the relevant boson mass and should be closest to them.

Events with two high P_T jets and one electron: The channels $e^* \to eZ_{\to qq}$ and $\nu^* \to eW_{\to qq}$ are characterised by at least two high P_T jets and an energetic isolated e.m. cluster $P_T^e > 10$ GeV ($P_T^e > 20$ GeV for $e^* \to eZ_{\to qq}$) in the polar angle $5° < \theta^e < 130°$. The

polar angle of the highest P_T jet resulting from W boson should be lower than 80°. The dijet invariant mass has to be greater than 60 GeV. If P_T^e <65 GeV, the dijet invariant mass must be greater than 75 GeV. In the case of the $\nu^* \to eW_{\to qq}$ channel, to reduce the NC background, the polar angle of e.m. cluster must be lower than 90°. Furthermore, the background is reduced by requiring the virtuality computed from the e.m. cluster kinematics Q^2 >2500 GeV^2 if P_T^e <25 GeV and by requiring a third jet with P_T >5 GeV to be present in the event if P_T^e >50 GeV.

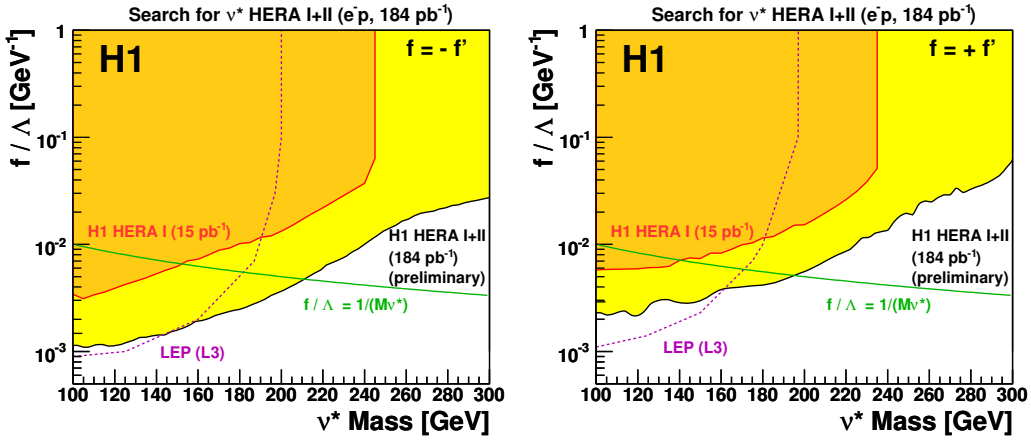

Figure 1: The 95% C.L. limits obtained for coupling constants (f/Λ) as a function of the excited neutrino mass within two assumptions: $f = -f'$ (left) and $f = +f'$ (right). The observed limits from this annalysis using all H1 e^-p data is presented by the yellow area. Values of the couplings above the curves are excluded. The orange-dark area corresponds to the exclusion domain published by the H1 experiment using 98/99 data and the dashed line to the exclusion limit from the L3 experiment at LEP [4].

Events with two high P_T jets and P_T^{miss}: The channels $e^* \to \nu W_{\to qq}$ and $\nu^* \to \nu Z_{\to qq}$ are characterised by at least two high jets and P_T^{miss} >12 GeV. In the case of $e^* \to \nu W_{\to qq}$ channel, the ratio V_{ap}/V_p of transverse energy flow anti-parallel and parallel to the hadronic final state [3] is required to be lower than 0.3 to reject the photoproduction (γp) background. The dijet invariant mass is required to be greater than 50 GeV. Furthermore, if P_T^{miss} <65 GeV the dijet is required to have an invariant mass above 65 GeV. In the case of the $\nu^* \to \nu Z_{\to qq}$ channel, a dijet invariant mass greater than 60 GeV is required. In order to reduce CC background, the total hadronic system is required to have a polar angle above 20° and a third jet with P_T >5 GeV has to be present in the event if P_T^{miss} <65 GeV. The longitudinal balance $E - P_Z$ >25 GeV is imposed if P_T^{miss} <50 GeV. In addition, events with P_T^{miss} <30 GeV are only accepted if the topological variable V_{ap}/V_p >0.1.

The $\nu^* \to eW, \nu Z$ channels with $Z \to ee$,$W \to \nu e(\mu)$

Events with two electron and P_T^{miss}: These channels use a subsample of events with two high P_T isolated e.m. clusters $P_T^{e1(e2)} > 20(15)$ GeV and a polar angle $5° < \theta^{e1(e1)} < 100°(120°)$ and P_T^{miss} >12 GeV. The clusters are required to have associated tracks if they are measured within the acceptance of the central tracker.

Events with one muon and an electron: Candidate events containing an islolated muon plus an isolated electron, both having a high transverse momentum $P_T^{e(\mu)} > 20(10)$ GeV and a polar angle $5° < \theta^{e(\mu)} < 100°(160°)$ are selected. A cut P_T^{miss} >12 GeV is applied. The backgrounds are reduced by requiring the virtuality (Q_e^2) to satisfy $\log(Q_e^2)$>3 GeV^2.

The observed number of events are compared to the expected SM background in table 1 for each search channel. A good overall agreement is found for all channels. No significant deviation is observed in the data. The selection efficiency for each decay channel for the both e^* and ν^* search is presented also in the table 1.

3 Interpretation and Conclusions

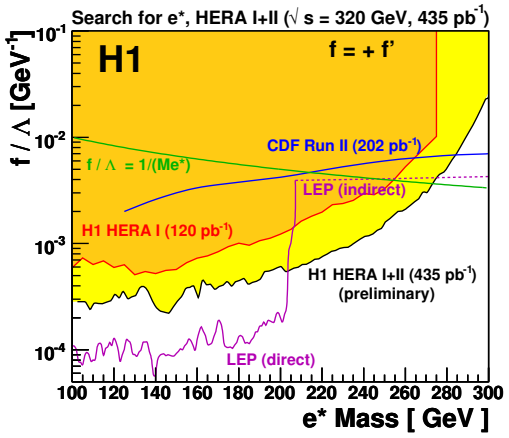

Figure 2: The 95% C.L. limits obtained for coupling constants (f/Λ) as a function of the excited electron mass within assumption: $f = +f'$. The observed limit from this analysis using 435 pb^{-1} of H1 data is presented by the yellow area. The orange-dark area corresponds to the exclusion domain published by the H1 experiment using HERA I data. The combined exclusion limit from LEP experiments is presented by the violet line. The result of the CDF [5] experiment at the Tevatron is also shown.

In absence of a signal for both excited electron and neutrino production, upper limits on the coupling f/Λ have been derived at 95% Confidence Level (C.L.) as a function of excited electron and neutrino masses. In case of excited neutrinos production, the obtained limits are displayed for the two assumptions $f = -f'$ and $f = +f'$ (figure 1). For $f = -f'$ (maximal $\gamma\nu{*}\nu$ coupling) and assuming $f/\Lambda = 1/M_{\nu*}$, excited neutrinos with masses below 211 GeV are excluded at 95% C.L. The limits on the ratio f/Λ also are given for the excited electron for the hypothesis $f = +f'$ (figure 2). We do not consider the case $f = -f'$, because the $\gamma e^* e$ coupling constant would be equal to zero and the production cross section of the excited electron is very small. For this hypothesis and assuming $f/\Lambda = 1/M_{e^*}$, excited electrons with masses below 273 GeV are excluded at 95% C.L.

References

[1] Slides `http://indico.cern.ch/contributionDisplay.py?contribId=131&sessionId=3&confId=9499`

[2] U. Baur, M. Spira and P. M. Zerwas, Phys. Rev. **D 42** (1990) 815.

[3] C. Adloff *et al.* [H1 Collaboration], Phys. Lett. **B 525** (2002) 9, [hep-ex/0110037].

[4] M. Acciarri *et al.* [L3 Collaboration], Phys. Lett. **B 502** (2001) 37, [hep-ex/0011068].

[5] D. Acosta *et al.* [CDF Collaboration], Phys. Rev. Lett. **94** (2005) 101802, [hep-ex/0410013].

Tevatron Searches for Physics Beyond the SM and the MSSM

David Stuart

University of California, Santa Barbara
Dept. of Physics, Santa Barbara, CA. U.S.A

A survey is given of recent results from searches at the Tevatron for physics beyond the standard model concentrating specifically on searches beyond the traditional super-symmetry signatures.

1 Introduction

The Tevatron experiments, CDF and D0, have many new results [1] on direct searches for evidence of non-Standard Model phenomena with Run 2 data. Most of these results are obtained from approximately 1 fb^{-1} of integrated luminosity.

Searches can either be structured to have optimal sensitivity to specific models, or they can be optimized for broader sensitivity by looking for deviations in specific final states. Searches that focus on the minimal super-symmetric standard model are examples of the former; the results of those searches are given elsewhere [2] in these proceedings. In this talk I cover non-SUSY searches and separate them into model specific and signature specific searches.

The slides [3] contain plots of the data and results. Reproducing those plots here is not efficient. Instead, I concentrate on discussion of the results.

2 Model specific searches

Perhaps the most familiar non-SUSY search modes are for new massive gauge bosons, which appear in many unification models. A new neutral gauge boson, a Z', would manifest as a narrow di-lepton mass bump. The most recent such search from CDF uses di-electrons. The main background is high mass Drell-Yan production. Instrumental backgrounds, such as di-jets faking electrons, are quite small by comparison. The mass region above 150 GeV/c^2 is scanned for resonances; there are some bins that fluctuate, as is expected with many trials, but none are significant. Cross-section limits of about 10 fb are derived for Z' masses above the highest mass events observed, which are at about 500 GeV/c^2. This corresponds to a mass limit of 920 GeV/c^2 assuming SM like couplings.

Similarly, D0 has completed a recent search for a new charged boson, a W' in the $e\nu$ channel. A W' would produce a broad excess at large transverse mass, where the dominant background is the high mass tail of $W \to e\nu$. Instrumental backgrounds are again negligible. The data is well described by the background prediction, with the highest transverse mass event having 620 GeV/c^2. Cross-section limits of about 20 fb are obtained, which correspond to a mass limit of 965 GeV/c^2 assuming SM like couplings.

Searches for extra-dimension models have produced recent results in both RS [4] and ADD [5] models. CDF has searched for resonant $G \to \gamma\gamma$ production, which they combine with $G \to ee$ results derived from the di-electron search described above. D0 directly combines the ee and $\gamma\gamma$ modes at the analysis stage by not requiring a track match for their

electron candidates. Both experiments present mass limits on RS gravitons as a function of the coupling, $k/M_{\rm pl}$, that range from about 300 GeV/c^2 at $k/M_{\rm pl} = 0.01$ to 860 GeV/c^2 for $k/M_{\rm pl} = 0.1$.

Another RS mode is $G \to ZZ$, which CDF searched using the four electron final state. The background is very small for this mode; the SM ZZ contribution at high mass is negligible, and the Z plus jet-fakes contribution is small. However, the expected signal is also quite small. The graviton branching ratio to ZZ is higher than to ee or $\gamma\gamma$, but the $Z \to ee$ branching ratio penalty is large and comes in squared. So, they used very loose electron selection and a χ^2 measure of the Z mass consistency. They observe no high mass events, but do find one low mass event that is consistent with the 0.5 events expected from SM ZZ.

The searches for RS models involve resonant graviton production. A difference class of models, the ADD models with large extra dimensions, involve production of a Kaluza-Klein tower of gravitons that radiate into the bulk and cause missing energy. Final state graviton radiation, i.e., $gg \to g \to gG$, would produce a monojet plus missing transverse energy (MET). CDF has searched for that signature, in fact allowing one or two jets for better sensitivity. There are backgrounds from QCD with fake MET, W's, and $Z \to \nu\nu$+jet. The jet E_T spectrum from a graviton signal does not differ substantially in shape from $Z \to \nu\nu$+jet. It is just a tower of many closely spaced gravitons that would produce a falling E_T spectrum similar to the QCD radiation in Z+jet. As such, the search amounts to checking the normalization, not the shape. Monte Carlo predictions are not sufficiently reliable for that, so data is used to estimate all the backgrounds, e.g., $Z \to ee$+jet is used to predict $Z \to \nu\nu$+jet with $\approx 10\%$ uncertainty. With careful selection, the QCD background becomes negligible and the irreducible Z background dominates. The missing energy spectrum in data is consistent with the background estimate, and limits are derived corresponding to effective planck masses of about 1 TeV, with some variation depending on the number of large extra dimensions.

D0 has recently completed a search for an excited electron, which would be evidence for compositeness. The production could occur through a contact interaction, and the signature is a narrow resonance in the $e\gamma$ spectrum, with the normalization dependent on the compositeness scale. As in the previously discussed searches, the QCD background is negligible compared to the irreducible background, in this case from Drell-Yan+γ production. D0's data is in good agreement with the expected background, and they derive limits on the compositeness scale ranging from 1 TeV for $m_{e*} = 800$ GeV up to 6 TeV for a low mass excited electron. Similar analyses have been done searching for excited muons [6].

D0 has a recent result from a search for a second generation leptoquark. Leptoquarks are bosons that carry both color and lepton number and arise in models attempting to unify the lepton and quark families. In the case that one of the, pair-produced, LQs decays to a muon and the other to a neutrino, the signature is a muon, 2 jets, and MET. The backgrounds from W+jets and top are large, but LQs give a characteristic kinematic signature in that the muon and one of the jets would reconstruct to a peak at the LQ mass. D0's data is consistent with the expected background, and cross section limits of about 100 fb are obtained that correspond to masses of about 210 GeV.

CDF has completed a search for a 4th generation quark, a b prime, decaying to a Z. Since a 4th generation quark is constrained to have small couplings to the 1st three generations, the direct decay to W plus charm is suppressed and it could decay via a loop diagram to a Z and a b. They select events with a dilepton Z plus at least 3 jets and then look for large total jet energy that would come from a massive object. The dominant background is SM

Z+jets, which they predict using the data because this is a regime that is not expected to be well-modeled by LO or NLO MCs. That data-based prediction is made by fitting the jet E_T spectrum below the 30 GeV jet threshold and integrating the projection above the threshold to obtain the total number of events with 3 or more jets. Then they fold the predicted jet E_T spectra into a sum of jet energy and find the data to be consistent. As an interesting validation check, they use the top sample to check that they can similarly predict the W+multi-jet background solely from low E_T data. The data's W+3 jet excess over that prediction matches the expected top contribution.

3 Signature specific searches

The previously described b' search did not use a b-tag even though the $b' \to bZ$ model would have two b jets. Requiring a b-tag would likely have improved the sensitivity to that particular model, but it would make the search insensitive to models without b quarks. That is an example of the trade-off between optimizing for sensitivity to a specific model or to a broader range of new phenomena, and that search was indeed intended to be sensitive to more than just a b'. I'll now describe several other Tevatron searches that aim to be model-independent, that is, they trade model-specific sensitivity for breadth of sensitivity.

In addition to the $Z+ \geq 3$ jet search, CDF has carried out a general search for high p_T Z's. Any massive particle that decays to a Z would give it high p_T, mostly independent of the details in the model. The Z p_T spectrum in data is observed to be consistent with background expectations from Monte Carlo, but the background is large. To expand sensitivity, they search for other objects in addition to the Z; additional leptons, photons, MET, or large total energy (H_T). These modes encompass several SM background sources, such as WZ, $Z\gamma$, and ZZ. The goal is sensitivity to a breadth of new physics, but it is also sensitive to how well one understands many different SM processes. There is fair agreement. For example, 14 events are found in both the $ee\gamma$ and $\mu\mu\gamma$ category, with expected backgrounds of 12.4 ± 1.5 and 15.0 ± 1.8 events, respectively. The $ee + H_T$ and $\mu\mu + H_T$ categories contain 45 and 53 events with expected backgrounds of $36.4^{+4.9}_{-5.8}$ and $41.3^{+5.0}_{-5.2}$ events, respectively. The ee+MET and $\mu\mu$+MET categories contain 97 and 74 events with expected backgrounds of 85.4 ± 12.3 and $55.9^{+9.7}_{-5.8}$ events, respectively.

This approach has been generalized from Z specific dileptons to all dileptons, which expands the range of SM background sources to include WW and top. They again search for additional objects in the event adding high E_T and b-tagged jets to the list given above. This search finds one $e\mu$ event with a total energy of over 850 GeV with a b-tag and 3 jets, which looks top-like upon close inspection.

A similar CDF search examines di-photon events looking for other objects: leptons, MET, or another photon. There was, of course, one event in Run 1 with two photons, two electron candidates and missing energy that would fall with this search. They find no anomalies in the $\gamma\gamma$+lepton category with 3 events observed and 7.6 ± 0.8 expected. Four events are observed with three photons compared to an expected background of 2.2 ± 0.7. One di-photon event with MET> 75 GeV is found with 0.24 ± 0.22 expected.

The final result presented is a search for a stable, charged, massive particle. The search is designed to be model independent, although example model motivations come from a stau or stop as the next to lightest susy particle with long lifetime due to suppressed couplings in gauge mediated susy breaking scenarios. A long-lived gluino in split-susy is another, more recently popular, scenario. Any such heavy charged particle would penetrate the calorimeters

like a muon because there is insufficient energy in the center of mass for showering to occur when the calorimeter's nuclei collide with the particle. But, it would be slow; a slow muon. D0 previously carried out a search looking for late hits in the muon chamber scintillators. CDF has recently completed a search using its time of flight counters, which have resolution of order 100 ps. Given the speed, β, obtained from the timing, and the momentum, the particle's mass is calculated. They use electrons from W's as a control sample for the timing resolution and obtain a background prediction from lower p_T muons. No excess is found in the high p_T and high mass muon sample. Model independent limits are calculated, without unfolding acceptance, of about 10 fb for weakly interacting particles. The limit for strongly interacting particles is about 5 times larger due to fragmentation effects.

4 Summary

There are several general things to note about this broad survey of results. In most of the analyses, instrumental backgrounds such as QCD jets faking leptons are negligible. This was not the case in early Tevatron results; it is apparent that the experiments have gained a mature understanding of their data and methods. Several of the analyses use data-based background prediction methods to probe regions beyond the normal purview of LO or NLO Monte Carlo calculations.

No significant excesses were observed in these analyses. Several $\approx 2\sigma$ fluctuations are present, as there should be after examining many different modes and a large number of kinematic bins. Those deviations that are merely statistical fluctuations will disappear in the six to eight fold larger final Tevatron sample (and be replaced by other fluctuations). Deviations that are real, but not yet significant, would grow, which makes the future of Tevatron search results interesting.

References

[1] All CDF and D0 results are available at `http://www-cdf.fnal.gov` and `http://www-d0.fnal.gov`

[2] R. Strohmer, these proceedings.

[3] Slides:
`http://indico.cern.ch/contributionDisplay.py?contribId=132&sessionId=9&confId=9499`

[4] L. Randall and R. Sundrum, Phys. Rev. Lett. **83** 3370 (1999); Ibid 4690.

[5] N. Arkani-Hamed, S. Dimopoulos, G. Dvali, Phys. Lett. **B429** 263 (1998).

[6] A. Abulencia et al., The CDF Collaboration, Phys. Rev. Lett. **97** 191802 (2006); V.M. Abazov et al., The D0 Collaboration, Phys. Rev. **D 73** 111102 (2006)

Spin Physics

Convenors:
Delia Hasch,
Gerhard Mallot,
Daniel Boer

The Status of the Polarized Parton Densities

Johannes Blümlein *

Deutsches Elektronen-Synchrotron, DESY, Platanenallee 6, D-15738 Zeuthen, Germany

A survey is given on the present knowledge of the polarized parton distribution functions. We give an outlook on further developments desired both on the theoretical as well on the experimental side to complete the understanding of the spin–structure of nucleons in the future.

1 Introduction

Deeply inelastic scattering provides a clean way to extract the parton densities of nucleons. After the initial observation that the nucleon spin is not formed by the quarks dominantly [2], detailed measurements of the polarized structure functions followed during the last 20 years. The central question concerns now the parton distribution functions and their scale evolution rather than just their first moment. Since the nucleon spin receives also contributions from the angular momentum of the quarks and gluons, these degrees of freedom have also to be studied. This requires the analysis of non–forward scattering cross sections. In inclusive deep–inelastic scattering the sensitivity to resolve the different sea–quark contributions is rather limited. One way to extract this information consists in measuring semi–inclusive processes [3]. A central question concerns the polarized gluon distribution, which can be determined from the scaling violations of $g_1(x,Q^2)$, deep–inelastic heavy flavor production, and hard processes measured at hadron colliders. The inclusive and semi–inclusive hard processes in polarized scattering provide an important laboratory to test QCD. More than exploring the level of twist–2, which has been investigated in some detail already, one may probe the twist–3 contributions in various transverse spin processes. In the following we survey the theoretical status of inclusive polarized deeply inelastic scattering and the status of polarized parton densities, cf. also [4]. We close with an outlook on investigations required in the future.

2 Theoretical Aspects

In the deep–inelastic domain the polarized nucleon structure functions receive contributions of leading and higher twist, depending on the region in Q^2 and W^2 probed. The leading twist contributions are those of twist $\tau = 2$ for $g_1(x,Q^2)$ [a] and $\tau = 2,3$ for $g_2(x,Q^2)$. At the level of twist–2 one may extract the polarized parton densities from the data on the structure function $g_1(x,Q^2)$ performing an analysis in the framework of perturbative QCD. During the past decades higher orders have been approached steadily. The running of $\alpha_s(\mu^2)$ is known to $O(\alpha_s^4)$ [6], both the polarized anomalous dimensions [7] [b] and massless Wilson coefficients [9] were calculated to $O(\alpha_s^2)$ and the first non-singlet moment, the polarized Bjorken sum-rule, to $O(\alpha_s^3)$ [10]. The heavy flavor Wilson coefficients, in the whole kinematic region, are only known to $O(\alpha_s)$ [11]. For $Q^2 \gg m^2$, i.e. in the region $Q^2/m^2 \gtrapprox 10$, the

*This paper was supported in part by SFB-TR-9: Computergestütze Theoretische Teilchenphysik.

[a] Note that $g_1(x,Q^2)$ contains twist $\tau = 3$ contributions due to target mass corrections, [5].

[b] Due to the Ward identity $P_{\rm NS}^{qq} = \Delta P_{\rm NS}^{qq}$ this splitting function is also known to $O(\alpha_s^3)$, [8].

Wilson coefficients were calculated in $O(\alpha_s^2)$, [12]. An interesting property is exhibited by the gluonic heavy flavor Wilson coefficient, the first moment of which vanishes in leading and next-to-leading order [11, 12]. Given a positive polarized gluon density, this implies a negative correction to $g_1(x, Q^2)$ in the region $x \lessapprox 10^{-2}$ and a positive contribution above. Conversely, the Wandzura–Wilczek relation implies a positive correction for the twist–2 part of $g_2(x, Q^2)$ for $x \lessapprox 2 \cdot 10^{-2}$, but a negative correction for larger x–values, cf. [13]. The anomalous dimensions for the evolution of the transversity distribution are known to $O(\alpha_s^2)$ in general [14] and for a series of moments to $O(\alpha_s^3)$ [15]. At present only next-to-leading order QCD analyzes can be performed to extract the polarized parton distributions.

At the level of the twist–3 contributions to the polarized structure functions several sum–rules and integral relations were derived, cf. [5,16]. The twist–2 contributions to the structure function $g_2(x, Q^2)$ is given by the Wandzura–Wilczek relation [17] for the quarkonic, gluonic, heavy flavor contributions, target mass corrections, and even diffractive scattering, cf. [5, 13, 18]. The twist–3 contributions to the structure function $g_2(x, Q^2)$ were calculated to one–loop order. The $O(\alpha_s)$ non-singlet and singlet anomalous dimension matrices, respectively their corresponding expressions in momentum fraction space, were derived in Refs. [19] using different techniques. The $O(\alpha_s)$ Wilson coefficients were calculated in [20]. Although the precision on $g_2(x, Q^2)$ improved during the last years [21] and some difference between the data and the Wandzura–Wilczek approximation is seen, still more precise data are required to test the QCD–predictions. First non-singlet moments of the twist–3 operator expectation values were determined in lattice simulations [22, 23].

Also in case of the polarized structure functions small-x resummations are discussed, which can be described on the basis of infrared evolution equations [24] and emerge both for the non-singlet [25] and singlet structure functions [26, 27]. These resummations apply to the leading pole $O((\alpha_s/N^3)^k)$-terms only, with N the Mellin-variable. Performing the resummation one obtains a branch–cut instead of the perturbative pole-terms, which yields a milder singularity. The resummation is consistently accounted for by the Callan-Symanzik equations for the evolution of parton densities. As detailed numerical studies, which were performed in Refs. [25, 27], show [c], one has to take into account not only the leading pole terms, but also the resummed sub-leading terms, see also [29], which are not yet calculated completely. They are known, however, for the first two orders in α_s (and partly to $O(\alpha_s^3)$) for all sub-leading terms, which suggest the general form. The comparison of the leading and sub-leading terms shows, that at least three sub-leading terms are required to match the exact results. Ignorance of these contributions, as unfortunately still partly present in the contemporary literature, results into misleading quantitative analyzes. Sometimes also "DGLAP" evolution is opposed to "infrared evolution equations", etc. Here again a clarifying word is in order. In practice both concepts address twist–2 parton distributions. Their scale evolution results from the factorization of the collinear singularities and is ruled by the anomalous dimensions $P_{ij}(N, a_s) = \sum_{k=1}^{\infty} a_s^k P_{ij}^{(k-1)}(N)$. The corresponding Callan-Symanzik equations have to be solved for high enough orders in the coupling constant in the range of Bjorken-x, demanded by the experimental data. These equations cover the small-x and the less singular terms which are equally important in quantitative analyzes.

[c] For the unpolarized case see [28].

3 Parton Distributions

The polarized parton distribution functions may be determined by a QCD–analysis of the structure function $g_1(x, Q^2)$. The data analysis requires a detailed description of the denominator of the polarization asymmetry, which has to include empiric parameterizations both for $F_2(x, Q^2)$ and $F_L(x, Q^2)$ including potential higher twist contributions, since the region of Q^2 and W^2, which is analyzed, covers rather low values, unlike the case in unpolarized analyzes [30]. Usually one would like to limit the data analysis to the region $Q^2 \gtrapprox 4\,\mathrm{GeV}^2$, which will be possible in future measurements at a facility like EIC [31]. The present data sets only allow a cut $Q^2 \gtrapprox 1\,\mathrm{GeV}^2$. In the analysis the correlation of the different parameters of the parton distribution functions at Q_0^2 and the QCD–scale Λ_{QCD} are rather essential. Measuring the gluon distribution function $\Delta G(x, Q^2)$, and to some extent also the sea–quark distributions, the slope effects of $\partial g_1(x, Q^2)/\partial \ln(Q^2)$ are important. In case of ΔG there one observes a very strong correlation with $\alpha_s(Q^2)$ due to the evolution equations. Special assumptions on Λ_{QCD}, as fixing this value to other measurements, may introduce severe biases. In the inclusive analysis not all the parameters chosen to model the parton distributions can be measured. For the data sets currently available this applies in particular to those parameters which describe the range of medium values of x. Their error may be-

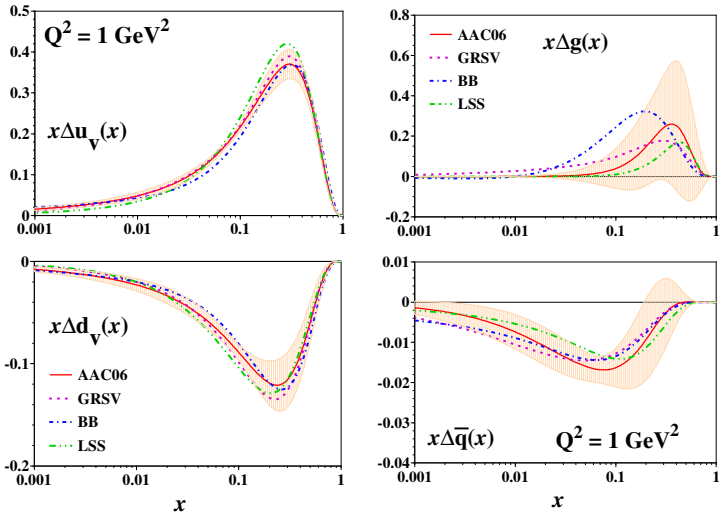

Figure 1: The polarized parton distributions from different analyzes at the scale $Q^2 = 1\,\mathrm{GeV}^2$, [33]. AAC06 : [33]; GRSV : [34]; BB : [32]; LSS : [35].

come rather large compared to their value. These parameters can be fixed after a first minimization and form a certain model. Their value has to be re–fitted after the global minimum was found, but will usually not change significantly, cf. [32]. The relative normalization of the different data sets is fitted within the allowed margins quoted by the experiments, to account for global systematic effects. In Figure 1 recent parton distribution functions [32–35] are compared. Further parameterizations were given in [36–39]. Within the present errors there is good agreement between all analyzes. The valence quark distribution functions are determined best, with a positive polarized up-quark and and a negative down-quark distribution. The sea–quark distribution is found to be mainly negative, but with a larger error. To resolve the different flavors of the sea-quark contributions semi-inclusive data were analyzed [3], yet

with rather large errors. Under certain assumptions the error on the strange-quark density becomes rather low [36]. Alternatively to the standard QCD fits neural-network techniques were used to determine the polarized parton densities in [38]. In this analysis a larger error than found using the conventional methods is obtained in the small x region, were data are sparse. If compared to earlier analyzes [32] the polarized gluon distribution comes out at lower values including more recent data [33, 35, 40]. The polarized gluon distribution function, although being obtained with positive central values in unconstrained fits, is still compatible with zero within the errors. In some analyzes [35, 39, 41] one demands, as second option, also a negative normalization of the gluon distribution in a constrained fit. The corresponding distribution is slightly negative and allowed by the data under the constraint used. The ratio $\Delta G/G$ was also measured in open charm photo–production [42]. Here the experimental errors are still large and the result is compatible with zero. Using the fit results of the polarized parton distributions one may form moments, cf. [32], to be compared with lattice simulations, in particular for the valence-quark distributions. Here the crucial point is to control the systematic effects and to approach realistic values of the pion mass. Currently values in the range $m_\pi \sim 270\,\mathrm{MeV}$ can be reached in dynamical quark simulations. In this way new non-perturbative quantitative test of QCD will be possible soon [22, 23, 43].

4 Future Avenues

The current picture of the polarized nucleon is still in a move and more efforts in theory and experiment are needed to complete it. In the forthcoming years the data-analysis from HERMES and COMPASS will lead to still better parton distribution functions. It would be important to measure the structure function $F_2(x, Q^2)$ at HERMES, which would yield an improved systematic understanding of the data. Yet the experimental precision of the structure function $g_1(x, Q^2)$ is limited and high–luminosity measurements at a future facility as EIC [31] is highly desirable to provide detailed QCD–tests for $\Lambda_{\rm QCD}$, the parton distributions and their moments to be compared with lattice simulations. The experiments at RHIC will improve our knowledge on the polarized sea–quark and gluon distributions. Important information on the large-x behaviour of all distribution functions, can be gained in the experiments at JLAB running at an increased beam energy. The HERA experiments, COMPASS and the JLAB experiments will finalize their measurements on deeply-virtual Compton scattering (DVCS) [44] during the forthcoming years and we may hope to get constraints on the quark angular momentum [45] using Ji's sum-rule [46].

As shown in [47] the theory error of the polarized gluon distribution at NLO is still large. The calculation of the 3–loop anomalous dimensions are therefore required to diminish this uncertainty. Very high statistics measurements have to be performed in the long–term future for DVSC to extract constraints on the angular momentum of the gluon from the scaling violations of the non–forward scattering cross sections. As is well–known, the scaling violations of the transversity distribution function $h_1(x, Q^2)$ are larger than those of the non–singlet part of $g_1(x, Q^2)$. Detailed high statistics measurements of this quantity are desirable to establish this prediction of QCD experimentally. Very little is known about the higher twist contributions to polarized deeply–inelastic scattering. Here we may hope for results from the experiments at JLAB. For the general kinematic region again high–luminosity experiments as planned for EIC would provide an excellent opportunity. Dedicated studies of the twist–3 contributions to several processes should be carried out and measurements

shall be performed to isolate the twist–4 contributions. An interesting open issue is formed by twist–3 effects [5, 16] in deep–inelastic scattering in electro–weak interactions, which can be studied at future neutrino factories [48]. The present status of our knowledge on polarized parton densities is not yet sufficient and calling for refined measurements in various places which are crucial for the final understanding of the spin–structure of the nucleons. This will require extensive experimentation at a high–luminosity facility such as the future Electron–Ion–Collider.

References

[1] Slides:
`http://indico.cern.ch/contributionDisplay.py?contribId=71&sessionId=15&confId=9499`

[2] M. J. Alguard *et al.* (SLAC), Phys. Rev. Lett. **37** (1976) 1261; **41** (1978) 70.

[3] A. Airapetian *et al.* [HERMES Collaboration], Phys. Rev. D **71** (2005) 012003.

[4] J. Blümlein, arXiv:hep-ph/0510212.

[5] J. Blümlein and A. Tkabladze, Nucl. Phys. B **553** (1999) 427.

[6] T. van Ritbergen, J. A. M. Vermaseren and S. A. Larin, Phys. Lett. B **400** (1997) 379;
M. Czakon, Nucl. Phys. B **710** (2005) 485.

[7] R. Mertig and W. L. van Neerven, Z. Phys. C **70** (1996) 637;
W. Vogelsang, Nucl. Phys. B **475** (1996) 47; Phys. Rev. D **54** (1996) 2023.

[8] S. Moch, J. A. M. Vermaseren and A. Vogt, Nucl. Phys. B **688** (2004) 101.

[9] E. B. Zijlstra and W. L. van Neerven, Nucl. Phys. B **417** (1994) 61 [Erratum-ibid. B **426** (1994) 245; **773** (2007) 105].

[10] S. A. Larin and J. A. M. Vermaseren, Phys. Lett. B **259** (1991) 345.

[11] A. D. Watson, Z. Phys. C **12** (1982) 123.

[12] M. Buza, Y. Matiounine, J. Smith and W. L. van Neerven, Nucl. Phys. B **485** (1997) 420;
J. Blümlein and S. Klein, DESY 07–027;
I. Bierenbaum, J. Blümlein and S. Klein, arXiv:0706.2738 [hep-ph].

[13] J. Blümlein, V. Ravindran and W. L. van Neerven, Phys. Rev. D **68** (2003) 114004.

[14] S. Kumano and M. Miyama, Phys. Rev. D **56** (1997) 2504;
A. Hayashigaki, Y. Kanazawa and Y. Koike, Phys. Rev. D **56** (1997) 7350;
W. Vogelsang, Phys. Rev. D **57** (1998) 1886.

[15] J. A. Gracey, Phys. Lett. B **643** (2006) 374; JHEP **0610** (2006) 040.

[16] J. Blümlein and N. Kochelev, Nucl. Phys. B **498** (1997) 285;

[17] S. Wandzura and F. Wilczek, Phys. Lett. B **72** (1977) 195.

[18] J. D. Jackson, G. G. Ross and R. G. Roberts, Phys. Lett. B **226** (1989) 159;
J. Blümlein and N. Kochelev, Phys. Lett. B **381** (1996) 296;
A. Piccione and G. Ridolfi, Nucl. Phys. B **513** (1998) 301;
J. Blümlein and D. Robaschik, Phys. Rev. D **65** (2002) 096002;
J. Blümlein, B. Geyer and D. Robaschik, Nucl. Phys. B **755** (2006) 112; arXiv:0706.2478 [hep-ph].

[19] E. V. Shuryak and A. I. Vainshtein, Nucl. Phys. B **201** (1982) 141;
A. P. Bukhvostov, E. A. Kuraev and L. N. Lipatov, JETP Lett. **37** (1983) 482 [Pisma Zh. Eksp. Teor. Fiz. **37** (1983 SPHJA,60,22-32.1984 ZETFA,87,37-55.1984) 406];
A. P. Bukhvostov, G. V. Frolov, L. N. Lipatov and E. A. Kuraev, Nucl. Phys. B **258** (1985) 601;
P. G. Ratcliffe, Nucl. Phys. B **264** (1986) 493;
I. I. Balitsky and V. M. Braun, Nucl. Phys. B **311** (1989) 541;
X. D. Ji and C. h. Chou, Phys. Rev. D **42** (1990) 3637;
A. Ali, V. M. Braun and G. Hiller, Phys. Lett. B **266** (1991) 117;
J. Kodaira, Y. Yasui and T. Uematsu, Phys. Lett. B **344** (1995) 348;
J. Kodaira, Y. Yasui, K. Tanaka and T. Uematsu, Phys. Lett. B **387** (1996) 855;
J. Kodaira, T. Nasuno, H. Tochimura, K. Tanaka and Y. Yasui, Prog. Theor. Phys. **99** (1998) 315;
B. Geyer, D. Müller and D. Robaschik, Nucl. Phys. Proc. Suppl. **51C** (1996) 106;
D. Müller, Phys. Lett. B **407** (1997) 314;
V. M. Braun, G. P. Korchemsky and A. N. Manashov, Phys. Lett. B **476** (2000) 455; Nucl. Phys. B **597** (2001) 370; B **603** (2001) 69.

[20] X. D. Ji, W. Lu, J. Osborne and X. T. Song, Phys. Rev. D **62** (2000) 094016;
A. V. Belitsky, X. D. Ji, W. Lu and J. Osborne, Phys. Rev. D **63** (2001) 094012.

[21] X. Zheng *et al.* [Jefferson Lab Hall A Collaboration], Phys. Rev. C **70** (2004) 065207.

[22] M. Göckeler *et al.*, [QCDSF collaboration], Phys. Rev. D **72** (2005) 054507;
H. W. Lin, arXiv:0707.3844 [hep-lat].

[23] D. Dolgov *et al.* [LHPC collaboration], Phys. Rev. D **66** (2002) 034506.

[24] R. Kirschner and L. N. Lipatov, Nucl. Phys. B **213** (1983) 122.

[25] J. Blümlein and A. Vogt, Phys. Lett. B **370** (1996) 149;
J. Blümlein, S. Riemersma and A. Vogt, Nucl. Phys. Proc. Suppl. **51C** (1996) 30.

[26] J. Bartels, B. I. Ermolaev and M. G. Ryskin, Z. Phys. C **72** (1996) 627.

[27] J. Blümlein and A. Vogt, Phys. Lett. B **386** (1996) 350.

[28] J. Blümlein, V. Ravindran, W. L. van Neerven and A. Vogt, arXiv:hep-ph/9806368;
J. Blümlein and A. Vogt, Phys. Rev. D **58** (1998) 014020; D **57** (1998) 1.

[29] J. Blümlein and W. L. van Neerven, Phys. Lett. B **450** (1999) 412.

[30] A. D. Martin, R. G. Roberts, W. J. Stirling and R. S. Thorne, Eur. Phys. J. C **35** (2004) 325;
J. Pumplin, A. Belyaev, J. Huston, D. Stump and W. K. Tung, JHEP **0602** (2006) 032;
S. Alekhin, K. Melnikov and F. Petriello, Phys. Rev. D **74** (2006) 054033;
J. Blümlein, H. Böttcher and A. Guffanti, Nucl. Phys. B **774** (2007) 182;
J. Blümlein, arXiv:0706.2430 [hep-ph].

[31] C. Aidala et al. [EIC Working Group], A White Paper Prepared for the NSAC LPR 2007, A High Luminosity, High Enery Electron-Ion-Collider.

[32] J. Blümlein and H. Böttcher, Nucl. Phys. B **636** (2002) 225.

[33] M. Hirai, S. Kumano and N. Saito, Phys. Rev. D **74** (2006) 014015.

[34] M. Glück, E. Reya, M. Stratmann and W. Vogelsang, Phys. Rev. D **63** (2001) 094005.

[35] E. Leader, A. V. Sidorov and D. B. Stamenov, Phys. Rev. D **73** (2006) 034023.

[36] D. de Florian, G. A. Navarro and R. Sassot, Phys. Rev. D **71** (2005) 094018.

[37] S. Atashbar Tehrani and A. N. Khorramian, JHEP **0707** (2007) 048.

[38] A. Guffanti, talk at SPIN06, Kyoto, 2006;
J. Rojo *et al.* [NNPDF Collaboration], arXiv:0706.2130 [hep-ph];
L. Del Debbio, S. Forte, J. I. Latorre, A. Piccione and J. Rojo [NNPDF Collaboration], JHEP **0703** (2007) 039.

[39] V. Y. Alexakhin *et al.* [COMPASS Collaboration], Phys. Lett. B **647** (2007) 8.

[40] J. Blümlein and H. Böttcher, in preparation.

[41] K. Kurek, these proceedings.

[42] K. Kurek, arXiv:hep-ex/0607061;
G. K. Mallot, arXiv:hep-ex/0612055;
S. Koblitz [COMPASS Collaboration], arXiv:0707.0175 [hep-ex].

[43] Ph. Hägler *et al.* [LHPC Collaborations], arXiv:0705.4295 [hep-lat];
W. Schroers, Eur. Phys. J. A **31** (2007) 784;
R. G. Edwards *et al.* [LHPC Collaboration], Phys. Rev. Lett. **96** (2006) 052001;
A. A. Khan *et al.*, Phys. Rev. D **74** (2006) 094508;
K. Jansen et al., in preparation.

[44] A. V. Belitsky and A. V. Radyushkin, Phys. Rept. **418** (2005) 1 and references therein.

[45] F. Ellinghaus, W. D. Nowak, A. V. Vinnikov and Z. Ye, Eur. Phys. J. C **46** (2006) 729.

[46] X. D. Ji, Phys. Rev. Lett. **78** (1997) 610.

[47] J. Blümlein and H. Böttcher, Nucl. Phys. A **721** (2003) 333.

[48] M. L. Mangano *et al.*, arXiv:hep-ph/0105155.

The Deuteron Spin-Dependent Structure Function g_1^d

Krzysztof Kurek *
On behalf of COMPASS Collaboration.

Andrzej Soltan Institute for Nuclear Studies, Hoza 69, 00-681 Warsaw, Poland.

Results on the deuteron longitudinal inclusive spin-dependent asymmetry A_1^d and the spin-dependent structure function g_1^d are presented. The data have been collected by the COMPASS experiment at CERN during the years 2002-2004 using the 160 GeV/c polarised muon beam scattered off a polarised ^{6}LiD target. The values obtained for Γ_1^d, the first moment of $g_1^d(x)$, and the flavor-singlet axial current matrix element, a_0, are also shown. The results of QCD fits in the NLO approximation on all g_1 deep inelastic data are presented.

1 Introduction

The EMC spin asymmetry measurement [2, 3] and the naive interpretation of the results following from the Ellis-Jaffe sum rule [4] have introduced the so-called "spin crisis": quarks carry a very small fraction of the nucleon's helicity. The next experiments at CERN, DESY and SLAC confirmed that quarks are only responsible for roughly 1/3 of the nucleon's helicity. The quark helicity distributions $\Delta q_i(x, Q^2)$ are related to a vector-axial quark current which is not conserved due to the Adler-Bell-Jackiw anomaly. This fact allows to explain the spin crisis by changing the interpretation of the measurement: instead of quark spin contents $\Delta\Sigma = \int_0^1 \sum_{i=1}^{n_f} \Delta q_i(x, Q^2)dx$ the combination $\Delta\Sigma - (3\alpha_s)/(2\pi)\Delta G$ is measured, where ΔG is a gluon polarization inside the nucleon. This interpretation was a "driving force" in preparation a series of new polarized DIS type experiments related to direct measurements of ΔG: HERMES in DESY, SMC and COMPASS at CERN, STAR and PHENIX at RHIC.
To complete the picture, beside the quark's helicity $\Delta\Sigma$, and the gluon polarization ΔG also an orbital angular momentum of quarks and gluons can build the nucleon spin structure. In this paper I will present new results of the longitudinal inclusive asymmetry A_1^d and the spin-dependent structure function g_1^d obtained by COMPASS collaboration after analyzing the data sets collected in years 2002-2004. The experiment is using a 160 GeV/c polarized muon beam from the SPS at CERN scattered off a polarized ^{6}LiD target (for more details see [5]). The paper is organized as follows. In Section 2 the longitudinal inclusive asymmetry A_1^d and the g_1^d structure function for small x and small Q^2 domain are presented. The A_1^d asymmetry and the g_1^d structure function results for the DIS region ($Q^2 > 1$ (GeV/c)^2) and the results of the perturbative QCD analysis of the world data as well as estimation of the first moment of g_1^d structure function are presented in Section 3. Conclusions are presented in Section 4.

*This work was partially supported by SPUB 621/E-78/SPB CERN/P-03.

2 The longitudinal helicity asymmetry A_1^d and g_1^d structure function for the small x and small Q^2 domain.

The cross-section longitudinal helicity asymmetry:

$$A_{LL}^d = \frac{\sigma^{\leftrightarrows} - \sigma^{\rightrightarrows}}{\sigma^{\leftrightarrows} + \sigma^{\rightrightarrows}}$$

can be decomposed into the virtual photon-deuteron asymmetries A_1^d and A_2^d: $A_{LL}^d = D(A_1^d + \eta A_2^d) \simeq DA_1^d$, where the photon depolarization factor D (as well as η), depends on the event kinematics. Arrows correspond to relative orientation of the incoming muon and the target deuteron helicities and all factors which contain A_2^d have been neglected since they are very small. The spin-dependent structure function g_1^d is related to the asymmetry A_1^d as follows:

$$g_1^d \simeq \frac{F_2^d}{2x(1+R)} A_1^d$$

where F_2^d and R are unpolarized (spin independent) structure functions. The asymmetry and the g_1 structure function have been calculated for events with small Q^2 ($Q^2 < 1$ (GeV/c)^2) and small x ($0.00004 < x < 0.02$). The presented data come from the years 2002 and 2003. The final sample used in the analysis contains 300 million events. The values of F_2 for $x > 0.0009$ and $Q^2 > 0.2$ (GeV/c)^2 have been taken from [6] and from [7] in the rest of the phase space. R comes from [8] for $Q^2 > 0.5$ (GeV/c)^2. For lower Q^2 R is proportional to Q^2 at the photoproduction limit.

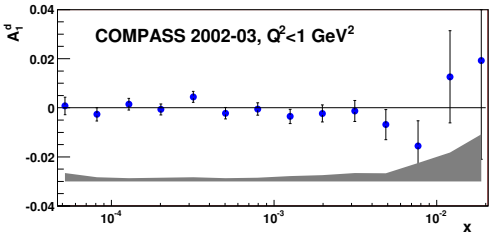

Figure 1: The COMPASS results of the A_1^d in the low x and low Q^2 region.

The results for the asymmetry A_1^d as a function of x are presented in Figure 1.

Figure 2 shows the results on the g_1^d structure function. The shadowed bands indicate the systematics errors and the error bars with the data points mark statistical ones. Systematic errors are mainly due to false asymmetries. The results are consistent with zero in the considered x range.

The statistical precision of A_1^d and g_1^d in the COMPASS is ten times higher than in the SMC ones [9]. The SMC and the COMPASS results are consistent in the overlap region. Details of the analysis can be found in [10].

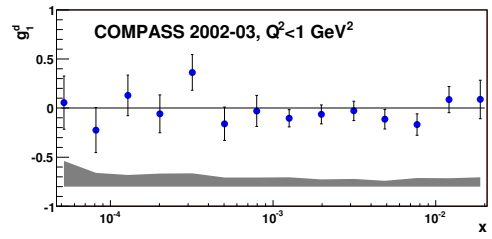

Figure 2: The COMPASS results of the g_1^d in the low x and low Q^2 region.

3 The A_1^d asymmetry and the g_1^d structure function for high Q^2. QCD analysis and the first moment of g_1^d.

Figure 3 shows the results on the A_1^d asymmetry for $Q^2 > 1$ (GeV/c)^2 (DIS domain) as a function of x as measured in COMPASS and superposed to results of previous experiments at CERN [6], DESY [11] and SLAC [12, 15]. Again, small terms related to A_2^d have been neglected. The data were collected during the years 2002-2004. The resulting sample consists of 89 million events. The asymmetry results from 2002-2003 data have been published in [13] while the full data sample results are recently published in [14].

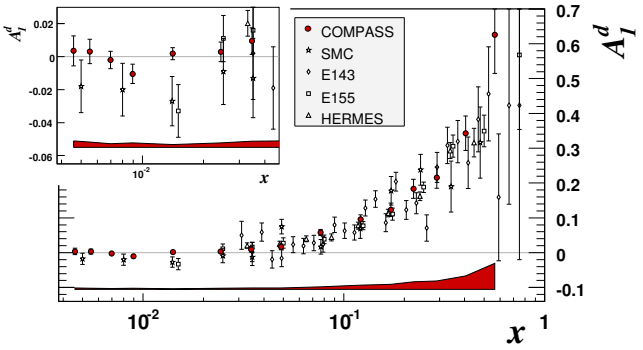

Figure 3: The asymmetry $A_1^d(x)$ for $Q^2 > 1$ (GeV/c)^2. Only statistical errors are shown with a data points. The COMPASS systematic errors are marked by shadowed areas.

The asymmetry is consistent with zero for $x < 0.03$. The spin-dependent structure function g_1^d has been calculated with F_2^d parametrization of [6] and the R parametrization taken from [8].
A new NLO QCD fit of all g_1 data at $Q^2 > 1$ (GeV/c)^2 from deuteron [6, 11, 12, 15] (including the new COMPASS data), proton [3, 6, 11, 12, 16] and ^{3}He [17] targets has been performed. In total 230 data points have been used. The NLO fits have been performed in $\overline{MS}$ scheme with input parametrization at $Q^2 = 3$ (GeV/c)^2 of the quark singlet spin distribution $\Delta\Sigma(x)$, the non-singlet distributions $\Delta q_3(x)$ and $\Delta q_8(x)$ and the gluon distribution function $\Delta G(x)$ in the form: $\Delta F_k \sim \eta_k x^{\alpha_k}(1-x)^{\beta_k}(1+\gamma_k x)$. The distributions have been evolved according to the DGLAP equations. The moments η_k for the non-singlet distributions $\Delta q_3(x)$ and $\Delta q_8(x)$ have been fixed by the baryon decay constants $(F+D)$ and $(3F-D)$ respectively [18], assuming $SU(3)_f$ symmetry. The linear term γx has been used only for singlet distribution. β_G has been fixed because it is poorly constrained by the data. Finally 10 parameters in the input distributions have been fitted. In order to keep the parameters in the physical range, the polarized strange sea and gluon distributions have been required to satisfy the so-called positivity condition: $|\Delta s(x)| \leq s(x)$ and $|\Delta G(x)| \leq G(x)$ at all Q^2 values.

The unpolarized distributions in this test have been taken from the MRST parametrization [19]. The fit has been performed with two different programs [20] which give consistent values of the fitted parameters and similar χ^2-probabilities. Each program yields two solutions, one with ΔG positive, the other with ΔG negative. The g_1^d structure function results evolved to $Q^2 = 3$ (GeV/c)^2 and the results of the fit are shown in Figure 4.

Previous fits of the g_1 structure function, not including the COMPASS data, found positive ΔG and the fitted $g_1^d(x)$ getting negative for $x \leq 0.025$ at $Q^2 = 3$ (GeV/c)^2. The new COMPASS data do not show any evidence for a decrease of the structure function at small x.

More details concerning the NLO QCD COMPASS fits can be found in [14].

Using the experimental values measured by the COMPASS experiment the first moment of $g_1^d(x)$,Γ_1^d, has been calculated at $Q^2 = 3(\mathrm{GeV/c})^2$. Taking into account the contribution from the fits in the unmeasured regions of $x < 0.003$ and $x > 0.7$ the following value of the Γ_1^d has been obtained:

$$\Gamma_1^d(Q^2 = 3(GeV/c)^2) = 0.050 \pm 0.003(stat) \pm 0.003(evol.) \pm 0.005(syst.)$$

The second error is related to the differences in the QCD evolution between the two fits. The flavor-singlet axial current matrix element, a_0 has been found to be: $a_0 = 0.35 \pm 0.03(stat.) \pm 0.05(syst.)$. Here the value of $a_8 = 0.585 \pm 0.025$ from [18] has been used.

4 Conclusions.

The new results of the longitudinal inclusive helicity asymmetry A_1^d measured in the range 0.002 $(\mathrm{GeV/c})^2 < Q^2 < 100$ $(\mathrm{GeV/c})^2$ have been presented. The asymmetry for small Q^2 domain corresponds to very small x: $0.00004 < x < 0.03$ and is consistent with zero. The DIS events ($Q^2 > 1$ $(\mathrm{GeV/c})^2$) cover x region from 0.004 up to 0.7. The COMPASS results are in agreement with those from previous experiments and improve considerably the statistical accuracy in the small x region. For DIS events the results of new NLO QCD fits have been presented. Two solutions for ΔG positive and negative have been found to describe data equally well. The first moment of the $g_1^d(x)$ structure function has been estimated using COMPASS data and the flavor-singlet axial current matrix element, a_0 has been found.

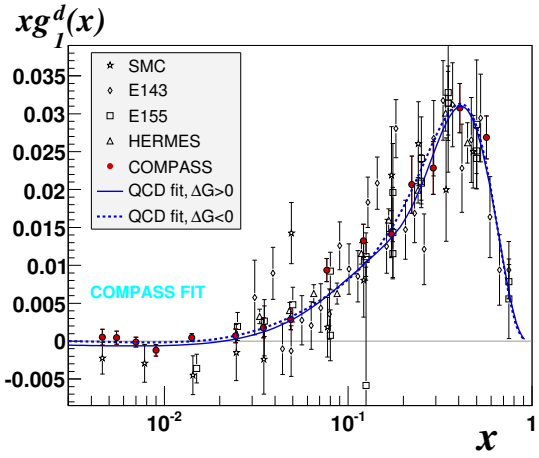

Figure 4: Measured values of $xg_1^d(x)$ evolved to $Q^2 = 3$ $(\mathrm{GeV/c})^2$. Only statistical errors are shown with data points. The curves show the results of QCD fits (first program from [20]) with $\Delta G > 0$ and $\Delta G < 0$.

References

[1] Slides:
`http://indico.cern.ch/contributionDisplay.py?contribId=134&sessionId=4&confId=9499`

[2] EMC, J. Ashman *et al.*, Phys. Lett. **B206** 364 (1988).

[3] EMC, J. Ashman *et al.*, Nucl. Phys. **B328** 1 (1989).

[4] J. Ellis and R. L. Jaffe, Phys. Rev. **D9** 1444 (1974), Phys. Rev. **D10** 1669 (1974).

[5] COMPASS, P. Abbon *et al.*,CERN-PH-EP/2007-001, hep-ex/0703049, to be published in*Nucl. Ins. and Meth.*.

[6] SMC, B. Adeva *et al.*, Phys. Rev. **D58** 112001 (1998); Erratum *ibid.* **D62** 079902.

[7] B. Badełek and J. Kwieciński, Phys. Lett. **B295** 263 (1992).

[8] E143, K. Abe *et al.*, Phys. Lett. **B452** 194 (1999).

[9] SMC, B. Adeva *et al.*, Phys. Rev. **D60** 072004 (1999).
[10] COMPASS, V. Yu. Alexakhin *et al.*, Phys. Lett. **B647** 330 (2007).
[11] HERMES, A. Airapetian *et al.*, Phys. Rev. **D75** 012003 (2005).
[12] E143, K. Abe *et al.*, Phys. Rev. **D58** 112003 (1998).
[13] COMPASS, E. S. Ageev *et al.*, Phys. Lett. **B612** 154 (2005).
[14] COMPASS, E. V. Yu. Alexakhin *et al.*, Phys. Lett. **B647** 8 (2007).
[15] E155, P. L. Anthony *et al.*, Phys. Lett. **B463** 339 (1999).
[16] E155, P. L. Anthony *et al.*, Phys. Lett. **B493** 19 (2000).
[17] E142, P. L. Anthony *et al.*, Phys. Rev. **D54** 6620 (1996);
E154, K. Abe *et al.*, Phys. Rev. Lett. **79** 26 (1997);
JLAB/Hall A, A .X. Zheng *et al.*, Phys. Rev. Lett. **92** 012004 (2004);
HERMES, K. Ackerstaff *et al.*, Phys. Lett. **B404** 383 (1997).
[18] Y. Goto *et al.*, Phys. Rev. **D62** 034017 (2000).
[19] A. D. Martin *et al.*, Eur. Phys. J. **C4** 463 (1998).
[20] SMC, B. Adeva *et al.*, Phys. Rev. **D58** 112002 (1998) ;
A. N. Sissakian, O. Yu. Shevchenko and O. K. Ivanov, Phys. Rev. **D70** 074032 (2004).

Final Results on the Measurement of the Structure Functions g_1^p and g_1^d at HERMES

Lara De Nardo[1,2]
on behalf of the HERMES Collaboration

1- DESY, 22603 Hamburg, Germany
2-TRIUMF, Vancouver, British Columbia V6T 2A3, Canada

Final results on precise measurements of the spin structure functions of the proton $g_1^p(x,Q^2)$ and deuteron $g_1^d(x,Q^2)$ are presented over the kinematic range $0.0041 \leq x \leq 0.9$ and $0.18\ \mathrm{GeV}^2 \leq Q^2 \leq 20\ \mathrm{GeV}^2$. The data were collected at the HERMES experiment at DESY, in deep-inelastic scattering of 27.6 GeV longitudinally polarized positrons off longitudinally polarized hydrogen and deuterium gas targets internal to the HERA storage ring.

1 Introduction

The structure functions $g_1^{p,d}$ can be extracted from the measurement of double-spin asymmetries $A_{||}^{p,d}$ of cross sections in inclusive deep-inelastic scattering $\ell + N \rightarrow \ell + X$ of longitudinally polarized charged leptons off longitudinally polarized protons and deuterons:

$$g_1^{p,d}(x,Q^2) = \frac{1}{1-\frac{y}{2}-\frac{y^2}{4}\gamma^2}\left[\frac{Q^4}{8\pi\alpha^2 y}\frac{\partial^2\sigma_{UU}^{p,d}(x,Q^2)}{\partial x \partial Q^2}A_{||}^{p,d}(x,Q^2) + \frac{y}{2}\gamma^2\, g_2^{p,d}(x,Q^2)\right], \quad (1)$$

when a model is used for the unpolarized cross section $\partial^2\sigma_{UU}^{p,d}(x,Q^2)/\partial x\partial Q^2$ and the structure function $g_2^{p,d}$ In Eq. (1) x is the fraction of the nucleon's light-cone momentum carried by the struck quark, $-Q^2$ is the squared four-momentum transferred by the virtual photon, and y and γ are kinematic factors.

At any order in $\alpha_s(Q^2)$ and in a leading-twist approximation, the proton and neutron structure functions $g_1^{p,n}$ are a convolution of singlet ($\Delta\Sigma(x,Q^2)$), non-singlet ($\Delta q_{NS}^{p,n}(x,Q^2)$) and gluon helicity distributions ($\Delta g(x,Q^2)$) [2] with the corresponding Wilson coefficient functions $\Delta C(x,\alpha_s(Q^2))$ [3]:

$$g_1^{p,n}(x,Q^2) = \frac{1}{2}\langle e^2\rangle\left[\Delta C_\Sigma \otimes \Delta\Sigma + 2N_q\Delta C_g \otimes \Delta g + \Delta C_{NS}^{p,n} \otimes \Delta q_{NS}^{p,n}\right]. \quad (2)$$

The deuteron structure function g_1^d is related to g_1^p and g_1^n by the relation:

$$g_1^d = \frac{1}{2}(g_1^p + g_1^n)\left(1 - \frac{3}{2}\omega_D\right), \quad (3)$$

where $\omega_D = 0.05 \pm 0.01$ takes into account the D-state admixture to the deuteron wave function. The last expression allows for the extraction of the neutron structure function g_1^n from the combined measurements of g_1^p and g_1^d at the same values of x and Q^2.

These proceedings report on the final results on the HERMES measurement of the structure functions g_1^p and g_1^d, with the consequent extraction of g_1^n. Details can be found in Ref. [4].

2 Data

Proton data were collected in 1996 and 1997 (the latter have been previously published in [5]), while the deuteron data were collected in the year 2000. While the accuracy of the HERMES proton data is comparable to that of earlier measurements, the HERMES deuteron data are more precise than all published data.

Kinematic and geometric cuts were imposed to make sure that the event was a DIS event and that the lepton tracks were fully contained within the spectrometer aperture, which limits the acceptance to scattering angles $0.04 \leq \theta \leq 0.22$ mrad. The constraint $y > 0.1$ excludes regions of low momentum resolution [6], $y \leq 0.91$ discards the low momentum region where the trigger efficiencies have not yet reached a momentum plateau. The requirement $W^2 > 3.24$ GeV^2 suppresses the region of baryon resonances. The resulting (x, Q^2) region, defined by $0.0041 \leq x \leq 0.9$ and 0.18 GeV$^2 \leq Q^2 \leq 20$ GeV^2, was divided into 19 bins in x and into up to 3 bins in Q^2, guided by the available statistics. The positron and electron identification was achieved with a probability analysis based on the responses of the Transition Radiation Detector, the Pre-Shower Detector, the Calorimeter, and the Čerenkov Detector (for proton data) or the RICH Detector (for deuteron data). A correction for charge symmetric background from meson Dalitz decays or photon conversions into e^+e^- pairs was applied in each kinematic bin by subtracting the number of leptons with the charge opposite to that of the beam particle. Such a correction reaches up to 25% and is concentrated in the high-y bins.

3 Extraction

The measured asymmetry $A_{||}^m$ was obtained from the number of events obtained when the polarization of the lepton beam and that of the target nucleons were parallel ($N^{\vec{\Rightarrow}}$) and anti-parallel ($N^{\vec{\Leftarrow}}$) as:

$$A_{||}^m(x,Q^2) = \frac{1}{P_T P_B} \frac{N^{\vec{\Leftarrow}}(x,Q^2)\ \mathcal{L}^{\vec{\Rightarrow}} - N^{\vec{\Rightarrow}}(x,Q^2)\ \mathcal{L}^{\vec{\Leftarrow}}}{N^{\vec{\Leftarrow}}(x,Q^2)\ \mathcal{L}^{\vec{\Rightarrow}} + N^{\vec{\Rightarrow}}(x,Q^2)\ \mathcal{L}^{\vec{\Leftarrow}}} \tag{4}$$

where $\mathcal{L}^{\vec{\Rightarrow}}$ and $\mathcal{L}^{\vec{\Leftarrow}}$ are the deadtime-weighted luminosities, while P_B ($P_B = 0.53 \pm 0.018$ for proton and $P_B = 0.53 \pm 0.010$ for deuteron data) and P_T ($P_T = 0.85 \pm 0.032$ for proton and $P_T = 0.84 \pm 0.03$ for deuteron data) are the beam and target average polarizations. After data selection as discussed above, the events available for asymmetry analyses on proton and deuteron were 3.5M for the proton and 10.2M for the deuteron.

The asymmetry $A_{||}$ was evaluated separately for the top and bottom halves, thus allowing polarization-independent systematic effects present in each detector half to cancel independently, and the final asymmetry was obtained as the weighted average of the two. In the case of the deuteron the measured asymmetry was corrected for the small contribution coming from the tensor structure function b_1^d, previously measured at HERMES [7]. Corrections for radiative and detector smearing effects, as well as for the background coming from elastic and quasi-elastic scattering were achieved with the application of an unfolding algorithm. After unfolding, the data points are statistically correlated but systematic correlations due to kinematic smearing have been removed, resulting in a resolution of a single-bin width.

The structure function g_1^p and g_1^d were then extracted from the Born asymmetry using the parameterizations [8], [9] and [10] to model the unpolarized cross section, while g_2 was

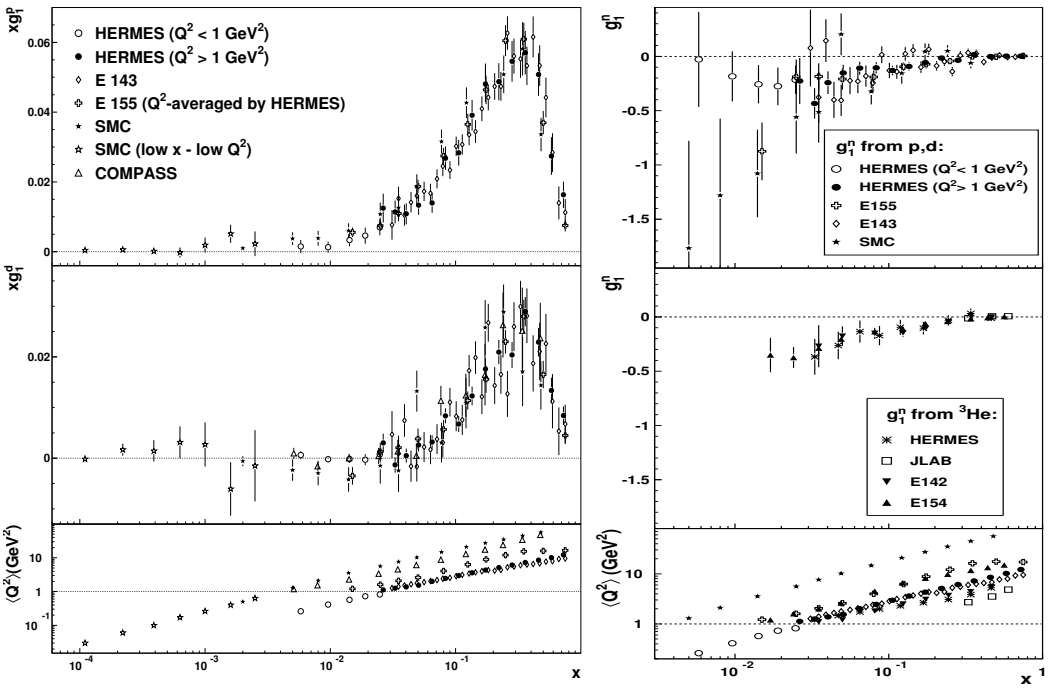

Figure 1: Left panel: HERMES results on xg_1^p and xg_1^d vs x, shown on separate panels, compared to data from SMC [11], E143 [12], E155 [13], and COMPASS [14]. The HERMES data points are statistically correlated by unfolding QED radiative and detector smearing effects. Right panel, top plot: the structure function g_1^n obtained from g_1^p and g_1^d, compared with similar data from SMC [11], E143 [12], and E155 [13] in the HERMES x-range. Right panel, second plot from the top: g_1^n as obtained from an ^{3}He target [21]. The bottom panels show the $\langle Q^2 \rangle$ of each data point in the top two panels. In all plots the error bars represent total uncertainties.

computed from a parameterization of all available proton and deuteron data [15, 16, 17, 18, 19]. The values of g_1 at the average Q^2 in each x bin were obtained from the evolution of the g_1 values in each Q^2 bin to the average Q^2 in each x bin by using an NLO QCD fit to all available g_1 data based on the 'BB' code [20], The systematic uncertainties originate from the experiment (beam and target polarizations, particle identification, misalignment of the detector) and the parameterizations (g_2, F_2, R, A_{zz}^d, ω_D), with the largest contributions coming from the beam and target polarization uncertainties.

The results are shown in Fig.1 (left), in comparison with those from other experiments. In the case of the proton, the central values of the SMC data points are larger than those of HERMES, in the low-x region. This reflects the difference in $\langle Q^2 \rangle$ values between the two experiments, and is expected from the Q^2 evolution of g_1. In the case of the deuteron, the HERMES data are compatible with zero for $x < 0.04$. In this region the SMC data favor negative values for g_1^d while the COMPASS results [14], at a similar Q^2 of SMC, are also consistent with zero.

The neutron structure function g_1^n was extracted from g_1^p and g_1^d using Eq. (3) and is

shown in the right panel of Fig. 1. Compared to previous data, $g_1^n(x)$ is now very well restricted by the HERMES measurement. The structure function g_1^n is slightly positive in the very high x region, and negative everywhere else. The new results suggest that g_1^n gradually approaches zero from below and, while it is based on data with $Q^2 \leq 1$ GeV^2, it does not support the earlier conjecture of a strong decrease of $g_1^n(x)$ for $x \to 0$ based on the E154 and SMC data.

The first moments of g_1 provide important information on the spin structure of the nucleon, in particular when results on proton, deuteron and neutron are combined. The precision of the integrals is less affected by the unfolding procedure since all inter-bin correlations from the unfolding procedure are taken into account. For $x < 0.04$, $g_1^d(x)$ becomes compatible with zero and its measured integral shows saturation. Under this assumption, and assuming of the validity of SU(3) flavor symmetry in hyperon β-decays, the values $\Delta s + \Delta\bar{s} = -0.085 \pm 0.013(\text{theo.}) \pm 0.008(\text{exp.}) \pm 0.009(\text{evol.})$ (negative and different from zero by about 4.7 σ), $\Delta u + \Delta\bar{u} = 0.842 \pm 0.004(\text{theo.}) \pm 0.008(\text{exp.}) \pm 0.009(\text{evol.})$ and $\Delta d + \Delta\bar{d} = -0.427 \pm 0.004(\text{theo.}) \pm 0.008(\text{exp.}) \pm 0.009(\text{evol.})$ are obtained for the quark distributions, using HERMES deuteron data alone, in the $\overline{MS}$ scheme at order $\mathcal{O}(\alpha_s^2)$, at $Q^2 = 5$ GeV^2. Additionally, the total quark contribution to the nucleon's spin is obtained as $\Delta\Sigma = 0.330 \pm 0.011(\text{theo.}) \pm 0.025(\text{exp.}) \pm 0.028(\text{evol.})$. This result suggests that the nucleon helicity gets a substantial contribution from quark helicities, even though there is still need for contributions from gluon helicities and angular momentum.

References

[1] Slides:
`http://indico.cern.ch/contributionDisplay.py?contribId=135&sessionId=4&confId=9499`

[2] G. Altarelli *et al.*, Nucl. Phys. **B496** 337 (1997).

[3] R. Mertig and W.L. van Neerven, Z. Phys. **C70** 637 (1996).

[4] A. Airapetian *et al.*, Phys. Rev. **D75** 0122007 (2007).

[5] A. Airapetian*et al.*, Phys. Lett. **B442** 484 (1998).

[6] K. Ackerstaff *et al.*, Nucl. Instrum. Meth. **417** 230 (1998).

[7] A. Airapetian *et al.*, Phys. Rev. Lett. **95** 242001 (2005).

[8] H. Abramowicz and A. Levy, arXiv:hep-ph/9712415 (1997).

[9] P. Amaudruz *et al.*, Nucl. Phys. **B371** 3 (1992).

[10] L.W. Whitlow *et al.*, Phys. Lett. **BB250** 193 (1990).

[11] B. Adeva *et al.*, Phys. Rev. **D58** 112001 (1998); B. Adeva *et al.*, Phys. Rev. **D60** 072004 (1999); B. Adeva *et al.*, Phys. Rev. **D62** 079902 (2000).

[12] K. Abe *et al.*, Phys. Rev. **D58** 112003 (1998).

[13] P.L. Anthony *et al.*, Phys. Lett. **B493** 19 (2000); P.L. Anthony *et al.*, Phys. Lett. **B463** 339 (1999).

[14] E.S. Ageev *et al.*, Phys. Lett. **B612** 154 (2005).

[15] P.L. Anthony *et al.*, Phys. Lett. **B458** 529 (1999).

[16] K. Abe *et al.*, Phys. Rev. Lett. **76** 587 (1996).

[17] P.L. Anthony *et al.*, Phys. Lett. **B553** 18 (2003).

[18] D. Adams *et al.*, Phys. Lett. **B336** 125 (1994).

[19] D. Adams *et al.*, Phys. Lett. **B396** 338 (1997).

[20] J. Blümlein and H. Böttcher, Nucl. Phys. **B 636** 225 (2002).

[21] X. Zheng *et al.*, Phys. Rev. **C70** 065207 (2004); K. Ackerstaff *et al.*, Phys. Lett. **B404** 383 (1997); P.L. Anthony *et al.*, Phys. Rev. **D54** 6620 (1996); K. Abe *et al.*, Phys. Rev. Lett. **79** 26 (1997).

Polarized Parton Densities and Higher Twist in the Light of the Recent CLAS and COMPASS data

E. Leader[1], A. V. Sidorov[2] and D. B. Stamenov[3] *

1- Imperial College, Prince Consort Road, London SW7 2BW, England

2- Bogoliubov Theoretical Laboratory, Joint Institute for Nuclear Research, 141980 Dubna, Russia

3- Institute for Nuclear Research and Nuclear Energy, Bulgarian Academy of Sciences
Blvd. Tsarigradsko Chaussee 72, Sofia 1784, Bulgaria

The impact of the recent very precise CLAS and COMPASS g_1/F_1 data on polarized parton densities and higher twist effects is discussed. We demonstrate that the low Q^2 CLAS data improve essentially our knowledge of higher twist corrections to the spin structure function g_1, while the large Q^2 COMPASS data influence mainly the strange quark and gluon polarizations which slightly decrease. We find also that the present inclusive DIS data cannot rule out a negative polarized and changing in sign gluon densities.

1 Introduction

One of the features of polarized DIS is that a lot of the present data are in the preasymptotic region ($Q^2 \sim 1-5$ GeV^2, 4 GeV^2 < W^2 < 10 GeV^2). This is especially the case for the experiments performed at the Jefferson Laboratory. As was shown in [2], to confront correctly the QCD predictions to the experimental data including the preasymptotic region, the *non-perturbative* higher twist (powers in $1/Q^2$) corrections to the nucleon spin structure functions have to be taken into account too.

In this talk we discuss the impact of the recent very precise CLAS [3] and COMPASS [4] inclusive polarized DIS data on the determination of both the longitudinal polarized parton densities (PDFs) in the nucleon and the higher twist (HT) effects. These experiments give important information about the nucleon structure in quite different kinematic regions. While the CLAS data entirely belong to the preasymptotic region and as one can expect they should mainly influence the higher twist effects, the COMPASS data on the spin asymmetry A_1^d are large Q^2 data and they should affect mainly the polarized parton densities. In addition, due to COMPASS measurements we have for the first time accurate data at small x ($0.004 < x < 0.015$), where the behaviour of the spin structure function g_1^d should be more sensitive to the sign of the gluon polarization.

2 Results of analysis

The method used to extract simultaneously the polarized parton densities and higher twist corrections to g_1 is described in [2]. According to this method, the g_1/F_1 and $A_1(\approx g_1/F_1)$ data have been fitted using the experimental data for the unpolarized structure function

*This work was supported by a UK Royal Society Joint International Project Grant and RFBR Grants (No 05-01-00992, 06-02-16215, 07-02-01046).

$F_1(x,Q^2)$

$$\left[\frac{g_1(x,Q^2)}{F_1(x,Q^2)}\right]_{exp} \Leftrightarrow \frac{g_1(x,Q^2)_{\rm LT}+h(x)/Q^2}{F_1(x,Q^2)_{exp}}\ . \qquad (1)$$

As usual, F_1 is replaced by its expression in terms of the usually extracted from unpolarized DIS experiments F_2 and R and the phenomenological parametrizations of the experimental data for $F_2(x,Q^2)$ [5] and the ratio $R(x,Q^2)$ of the longitudinal to transverse γN cross-sections [6] are used. Note that such a procedure is equivalent to a fit to $(g_1)_{exp}$, but it is more precise than the fit to the g_1 data themselves actually presented by the experimental groups because here the g_1 data are extracted in the same way for all of the data sets. In Eq. (1) "LT" denotes the leading twist contribution to g_1 (logarithmic in Q^2 NLO pQCD expression where the target mass corrections are taken into account), while $h(x)/Q^2$ corresponds to the first term in the $(\Lambda^2_{\rm QCD}/Q^2)^n$ expansion of higher twist effects.

Let us discuss now how inclusion of the CLAS EG1 proton and deuteron g_1/F_1 data [3] and the *new* COMPASS data on A_1^d [4] influence our previous results [7] on polarized PDFs and higher twist obtained from the NLO QCD fit to the world data (*see* the references in [7]), before the CLAS and the latest COMPASS data were available.

2.1 Impact of CLAS data

As the CLAS data are mainly low Q^2 data where the role of HT becomes important, they should help to fix better the higher twist effects. Indeed, due to the CLAS data, the determination of HT corrections to the proton and neutron spin structure functions, $h^p(x)$ and $h^n(x)$, is significantly improved in the CLAS x region, compared to the values of HT obtained from our LSS'05 analysis [7] in which a NLO($\overline{\rm MS}$) QCD approximation for $g_1(x,Q^2)_{\rm LT}$ was used. This effect is illustrated in Fig. 1. One can conclude now that the HT corrections

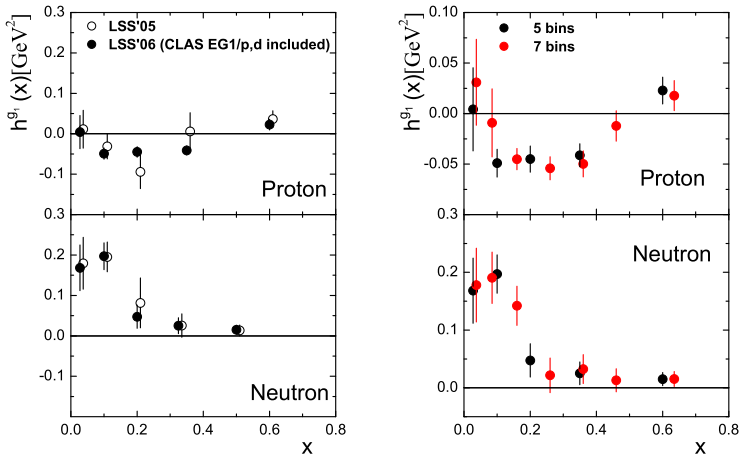

Figure 1: Effect of CLAS data on the higher twist values (left). Comparison between the HT values corresponding to 5 and 7 bins (right).

for the proton target are definitely different from zero and negative in the x region: 0.1-0.4.

Also, including the CLAS data in the analysis, the HT corrections for the neutron target are better determined in the x region: 0.2-0.4. Note that $h^n(x)$ at $x \sim 0.5$ was already fixed very precisely from the JLab Hall A data on the ratio $g_1^{(n)}/F_1^{(n)}$. As expected, the central values of the polarized PDFs are practically *not* affected by the CLAS data. This is a consequence of the fact that at low Q^2 the deviation from logarithmic in Q^2 pQCD behaviour of g_1 is accounted for by the higher twist term in g_1. However, the accuracy of the determination of polarized PD is essentially improved. This improvement (see [1, 8]) is a consequence of the much better determination of higher twist contributions to the spin structure function g_1, as discussed above. Because of the good accuracy of the CLAS data, one can split the measured x region of the world+CLAS data set into 7 bins instead of 5, as used up to now, and therefore, can determine more precisely the x-dependence of the HT corrections to g_1. As seen in Fig. 1, the more detailed x-space behaviour of the HT contribution, obtained when using 7 x-bins, suggests a smoother function dependence in x and will help us to calculate more precisely their first moments in the experimental x region and to compare them with the predictions given by different theoretical models.

The main message from this analysis is: It is impossible to describe the very precise CLAS data if the HT corrections are NOT taken into account. Note that if the low Q^2 data are not too accurate, it would be possible to describe them using only the leading twist term (logarithmic in Q^2) in g_1, *i.e.* to mimic the power in Q^2 dependence of g_1 with a logarithmic one (using different forms for the input PDFs and/or more free parameters associated with them) which was done in the analyses of another groups before the CLAS data have appeared.

2.2 Impact of new COMPASS data

In contrast to the CLAS data, the COMPASS data are mainly at large Q^2 and the only precise data at small x : $0.004 < x < 0.02$. The new data are based on 2.5 times larger statistics than those of COMPASS'05 and give more precise and detailed information about A_1^d at small x (see Fig. 2a). The QCD theoretical curves for A_1^d corresponding to the

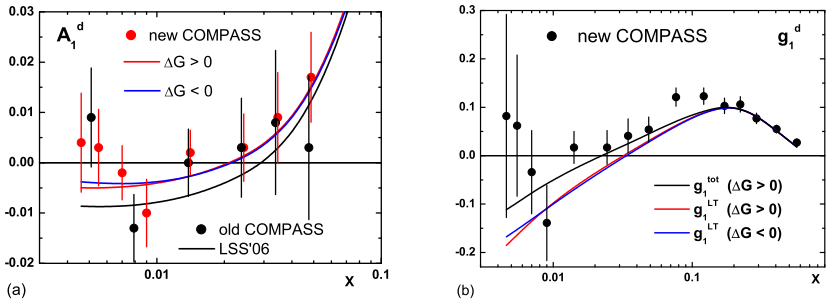

Figure 2: Comparison of our NLO($\overline{\rm MS}$) results for A_1^d (a) and g_1^d (b) corresponding to $\Delta G > 0$ and $\Delta G < 0$ with the new COMPASS data at measured x and Q^2 values.

best fits with positive and negative ΔG lie above the old one at $x < 0.1$. As a result, the COMPASS'06 data do not influence $(\Delta u + \Delta\bar{u})$ and $(\Delta d + \Delta\bar{d})$ parton densities, while

the magnitudes of both the polarized gluon and strange quark sea densities and their first moments slightly decrease (see Refs. [1, 8]). As a consequence, $\Delta\Sigma(Q^2 = 1\ \mathrm{GeV}^2)$ increases from (0.165 ± 0.044) to (0.207 ± 0.040) for $\Delta G > 0$ and (0.243 ± 0.065) for $\Delta G < 0$. As expected, the values of HT are practically not affected by COMPASS data excepting the small x where Q^2 are also small. We have found that the HT effects at small x are large, up to 40% of the magnitude of $(g_1^d)_{\mathrm{LT}}$ (see Fig. 2b) and therefore, in the presence of HT, g_1^d, as well as A_1^d (Fig. 1a), are not too sensitive to the sign of the gluon polarization at small x. These results are in contrast to those obtained in the COMPASS analysis [4] where the higher twist corrections are not taken into account (for details see [1, 8]).

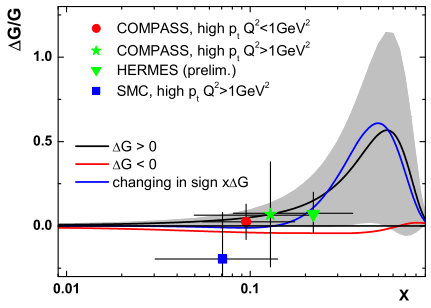

Figure 3: Comparison between the experimental data and NLO($\overline{\mathrm{MS}}$) curves for the gluon polarization $\Delta G(x)/G(x)$ at $Q^2 = 3\ \mathrm{GeV}^2$ corresponding to $\Delta G > 0$, $\Delta G < 0$ and an oscillating-in-sign $x\Delta G$. Error bars represent the total (statistical and systematic) errors.

We have observed that the present inclusive DIS data cannot rule out the solutions with negative and changing in sign gluon polarizations. The shape of the negative gluon density differs from that of positive one. In all the cases the magnitude of ΔG is small: $|\Delta G| = 0.2$ and the corresponding polarized quark densities are very close to each other. In Fig. 3 the ratio $\Delta G(x)/G(x)$ calculated for the different $\Delta G(x)$ obtained in our analysis and using $G(x)_{\mathrm{MRST'02}}$ for the unpolarized gluon density, is compared to the existing direct measurements of $\Delta G/G$. The most precise value for $\Delta G/G$, the COMPASS one, is well consistent with any of the polarized gluon densities determined in our analysis.

In conclusion, it was demonstrated that the inclusion of the low Q^2 CLAS data in the NLO QCD analysis of the world DIS data improves essentially our knowledge of HT corrections to g_1 and does not affect the central values of PDFs, while the large Q^2 COMPASS data influence mainly the strange quark and gluon polarizations, but practically do not change the HT corrections. These results strongly support the QCD framework, in which the leading twist pQCD contribution is supplemented by higher twist terms of $\mathcal{O}(\Lambda^2_{\mathrm{QCD}}/Q^2)$.

References

[1] Slides:
`http://indico.cern.ch/contributionDisplay.py?contribId=136&sessionId=4&confId=9499`

[2] E. Leader, A.V. Sidorov and D.B. Stamenov, Phys. Rev. **D67** 074017 (2003).

[3] K.V. Dharmwardane *et al.* (CLAS Collaboration), Phys. Lett. **B641** 11 (2006).

[4] V.Yu. Alexakhin *et al.* (COMPASS Collaboration), Phys. Lett. **B647** 8 (2007).

[5] M. Arneodo *et al.* (NMC Collaboration), Phys. Lett. **B364** 107 (1995).

[6] K. Abe *et al.* (SLAC E143 Collaboration), Phys. Lett. **B452** 194 (1999).

[7] E. Leader, A.V. Sidorov and D.B. Stamenov, Phys. Rev. **D73** 034023 (2006).

[8] E. Leader, A.V. Sidorov and D.B. Stamenov, Phys. Rev. **D75** 074027 (2007).

Photoproduction of Hadron Pairs at Fixed-Target Experiments

Christof Hendlmeier[1], Marco Stratmann[2] and Andreas Schäfer[1]

1- Universität Regensburg - Institut für Theoretische Physik, D-93040 Regensburg - Germany
2- Radiation Laboratory - RIKEN, Wako, Saitama 351-0198 - Japan

We consider the photoproduction of two hadrons in polarized lepton-nucleon collisions in the framework of perturbative QCD at the next-to-leading order accuracy [1]. After illustrating how to obtain the experimentally relevant observables, a phenomenological study of the photoproduction of hadron pairs at high transverse momenta is presented. We show theoretical predictions for the relevant cross sections at COMPASS and HERMES kinematics as well as theoretical uncertainties.

1 Motivation

After more than 25 years of studying polarized deep-inelastic lepton-nucleon scattering (DIS) the prime question is still how the proton spin-$\frac{1}{2}$ is composed of the spins and orbital angular momenta of its constituents, quarks and gluons. The single most important result is the finding that quarks spins contribute only little - about 25% - to the proton spin [2]. The measurement of $\Delta g(x,\mu)$, the polarized gluon distribution of the proton, is the next logical step to clarify the spin puzzle, since it turns out that in the light cone gauge the first moment of $\Delta g(x,\mu)$ has the interpretation of the total contribution of the gluons spin to the proton's spin-$\frac{1}{2}$. The extraction of Δg in polarized DIS is, however, very difficult as it contributes only via scaling violations and at higher orders in the strong coupling constant α_s. Therefore the prime goal of all current experiments with polarized beams is to determine Δg directly.

In particular at the Relativistic Heavy Ion Collider (RHIC) at Brookhaven National Laboratory (BNL), many different processes can be studied where Δg enters dominantly already at the lowest order (LO) approximation of perturbative QCD (pQCD): for example prompt photon and heavy flavor production, jet and single-inclusive hadron production as well as di-hadron production [3]. First results from the PHENIX and STAR collaboration at RHIC indicate that a large and positive gluon distribution is strongly disfavored in the probed region of momentum fractions x, $0.03 \lesssim x \lesssim 0.2$ [4].

In addition to RHIC, further information on the spin structure of nucleons can be obtained by fixed-target experiments like COMPASS [5] at CERN or HERMES [6] at DESY. One promising process for the determination of Δg at the low energies available at fixed-target experiments turned out to be the production of hadron pairs at high transverse momenta p_T [7]. Some experimental results are already available [8].

2 Technical framework

We consider the spin-dependent inclusive photoproduction process

$$\vec{l}(p_l) + \vec{N}(p_N) \to l'(p_{l'}) H_c(p_c) H_d(p_d) X, \tag{1}$$

where a longitudinally polarized lepton $\vec{l}$ with four momentum p_l scatters off a longitudinally polarized nucleon $\vec{N}$ with four-momentum p_N producing two hadrons H_c and H_d with

four momenta p_c and p_d, respectively. The two produced hadrons are assumed to have high transverse momenta $p_{T,c/d}$. Making use of the factorization theorem, the polarized cross section can be written as a convolution of non-perturbative parton distribution and fragmentation functions and hard, short-distance partonic cross sections:

$$d\Delta\sigma \equiv \frac{1}{2}[d\sigma_{++} - d\sigma_{+-}] = \sum_{abcd} \int dx_a dx_b dz_c dz_d \Delta f^l(x_a, \mu_f) \Delta f^N(x_b, \mu_f) \times$$
$$d\Delta\hat{\sigma}^{ab\to cdX'}(S, x_a, x_b, p_c/z_c, p_d/z_d, \mu_f, \mu'_f, \mu_r) D_c^{H_c}(z_c, \mu'_f) D_d^{H_d}(z_d, \mu'_f). \quad (2)$$

The sum runs over all possible partonic channels $ab \to cd$ with $d\Delta\hat{\sigma}^{ab\to cdX'}$ the relevant, perturbatively calculable hard partonic cross sections at next-to-leading order (NLO) accuracy. The subscripts $(++)$ and $(+-)$ denote the helicities of the lepton beam and the nucleon target at rest. S is the total center-of-mass system (c.m.s.) energy, i.e. $S = (p_l + p_N)^2$. The $\Delta f^N(x_b, \mu_f)$ are the usual spin-dependent parton densities for parton b in a nucleon at a momentum fraction x_b and scale μ_f. $D_{c/d}^{H_{c/d}}(z_{c/d}, \mu'_f)$ describe the fragmentation of a parton c/d into a hadron $H_{c/d}$ at a momentum fraction $z_{c/d}$ and scale μ'_f. $\Delta f^l(x_a, \mu_f)$ represents the spin-dependent Weizsäcker-Williams equivalent photon spectrum [9] describing the collinear radiation of a photon with momentum fraction x_a and virtuality lower than some upper value $Q^2_{\max}$. All phenomenological studies have been done for the so-called *direct* case, where the photon interacts directly with a parton of the nucleon. No *resolved* photon contributions are included so far. For a proper treatment of the collinear, infrared and ultraviolet divergencies appearing in NLO calculations of the hard partonic cross sections we introduced a variable z defined by

$$z \equiv -\frac{\vec{p}_{T,c} \cdot \vec{p}_{T,d}}{p^2_{T,c}} \quad (3)$$

in a system in which the incoming beam defines the longitudinal axis. For a covariant definition of the variable z and some technical details we refer to a work by Aurenche et al. [10]. To guarantee that the two hadrons are in opposite hemispheres, we restrict ourselves to the range $z > 0$. Needless to say, the required spin-averaged cross section $d\sigma$ is straightforwardly obtained by replacing all polarized quantities in Eq. (2) by their appropriate unpolarized counterparts.

3 Phenomenological results

In our phenomenological studies we concentrate on the production of charged hadrons made of light quark flavors. We sum over pions, kaons, and (anti-)protons and use fragmentation functions of KKP [11]. For parton distributions we employ the unpolarized CTEQ6M [12] and polarized GRSV standard sets [13] as well as the sets of DNS [14]. If it is not stated otherwise, the factorization/renormalization scales in Eq. (2) are all set equal $\mu \equiv \mu_f = \mu'_f = \mu_r = p_{T,c} + p_{T,d}$. All NLO results presented in this paper are preliminary.

3.1 Two-hadron production at COMPASS

At the COMPASS experiment at CERN polarized muons are scattered with a beam energy of $E_\mu = 160$ GeV off the deuterons in a polarized ^{6}LiD solid-state target corresponding to a c.m.s. energy of $\sqrt{S} \simeq 18$ GeV. For the calculations we demand that hadron H_c has a

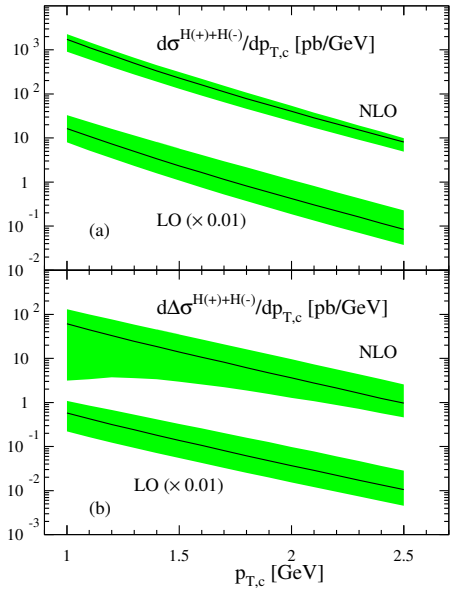

Figure 1: Scale dependence at COMPASS kinematics.

scattering angle less than $\theta_{\max} = 70$ mrad, since it was pointed out in an earlier work [15] that resolved photon contributions become more dominant for the full acceptance of COMPASS, $\theta_{\max} = 180$ mrad. No acceptance cut can be implemented for the other hadron H_d due to the variable z defined in Eq. (3). The fraction x_a of the lepton's momentum taken by the photon is restricted to be in the range $0.1 < x_a < 0.9$, whereas the maximal virtuality $Q^2_{\max}$ in the Weizsäcker-Williams spectrum is $Q^2_{\max} = 0.5$ GeV^2. The fractions of the parton's momenta carried by the produced hadrons are restricted to the range $z_c, z_d \geq 0.1$.

Figure 1 shows the scale dependence of the unpolarized (a) and polarized (b) cross section for COMPASS kinematics at LO and NLO accuracy with a cut $z > 0.6$ on the partonic level. For the polarized parton distributions we employed DNS Set1. The shaded bands indicate the resulting scale uncertainty of the cross sections when varying the scales in the range $1/2(p_{T,c}+p_{T,d}) \leq \mu \leq 2(p_{T,c}+p_{T,d})$. At NLO the scale dependence is reduced in the unpolarized cross section. This might indicate that we are in a regime where perturbative QCD is applicable. However *no* improvement is observed in the polarized case and in both the unpolarized and polarized case for lower z-cuts ($z > 0.2, 0.4$). As a consequence the applicability of the perturbative approach can not be taken for granted. An important benchmark for testing the pQCD framework would be, for instance, to check if the unpolarized data fall within the uncertainty band, where the parton distributions are already known very well.

Once the applicability of pQCD is established, the double spin asymmetry turns out to be very sensitive to the gluon polarization assumed in the calculation. Varying from maximal positive to maximal negative sets of GRSV the asymmetry is in the range $-0.1 \lesssim A_{LL} \lesssim 0.4$ which would allow at least a determination of the sign of Δg.

3.2 Two-hadron production at HERMES

At the HERMES experiment at DESY a longitudinally polarized electron (positron) beam with $E_e \simeq 27.5$ GeV is scattered off a proton or deuterium gas target. We concentrate on results for a deuterium target as this has the better statistics. The corresponding c.m.s. energy is $\sqrt{S} \simeq 7.25$ GeV. We choose a maximal photon virtuality of $Q^2_{\max} = 0.1$ GeV^2 and restrict the momentum fraction x_a of the lepton carried by the produced photon to $0.2 \leq x_a \leq 0.9$. For hadron H_c we use an acceptance cut of 40 mrad $< \theta_{\rm lab} <$ 220 mrad. The fraction of the parton's momenta carried by the produced hadrons are restricted to the range $z_c, z_d \geq 0.1$.

Figure 2 shows the scale dependence of the unpolarized (a) and polarized (b) cross sections as a function of the transverse momentum of one hadron $p_{T,c}$ when varying the scales in the range $1/2(p_{T,c} + p_{T,d}) \leq \mu \leq 2(p_{T,c} + p_{T,d})$. Due to the smaller c.m.s. energy there is no noticeable reduction of the scale dependence when going to NLO accuracy. We observed the same for other z-cuts both for unpolarized and polarized case. We emphasize that all comments about applicability of pQCD also apply here. Again, as it is for COMPASS kinematics, the double spin asymmetry A_{LL} is very sensitive to the chosen Δg polarization: $-0.1 \lesssim A_{LL} \lesssim 0.5$ when varying between $\Delta g = g$ and $\Delta g = -g$ at the input scale with g the unpolarized gluon distribution in the nucleon.

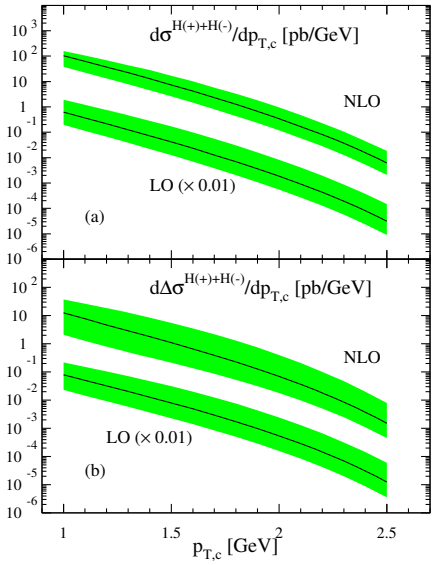

Figure 2: Scale dependence at HERMES kinematics.

Acknowledgments

C.H. was supported by a grant of the "Bayerische Eliteförderung". This work was supported in part by the "Deutsche Forschungsgesellschaft (DFG)".

References

[1] Slides: `http://indico.cern.ch/contributionDisplay.py?contribId=138&sessionId=4&confId=9499`

[2] See, for example: K. Rith, in Proceedings of the 12th International Workshop on Deep Inelastic Scattering (DIS 2004), Strbske Pleso, Slovakia, D. Bruncko *et al.* (eds.), p. 138, (2004).

[3] See, for example: G. Bunce, N. Saito, J. Soffer and W. Vogelsang, Ann. Rev. Nucl. Part. Sci. **50** 525 (2000); C. Aidala *et al.*, Research Plan for Spin Physics at RHIC, BNL report BNL-73798-2005, (2005).

[4] PHENIX Collaboration, S.S. Adler *et al.*, Phys. Rev. Lett. **93** 202002 (2004); Phys. Rev. **D73** 091102 (2006); K. Boyle, AIP Conf. Proc. **842** 351 (2006); STAR Collaboration, B.I. Abelev *et al.*, Phys. Rev. Lett. **97** 252001 (2006).

[5] COMPASS Collaboration, G. Baum *et al.*, CERN/SPSLC 96-14 (1996).

[6] HERMES Collaboration, The HERMES Physics Program & Plans for 2001-2006, DESY-PRC, 2000.

[7] A. Bravar, D. von Harrach and A. Kotzinian, Phys. Lett. **B421** 349 (1998).

[8] HERMES Collaboration, A. Airapetian *et al.*, Phys. Rev. Lett. **84** 2584 (2000); Spin Muon Collaboration (SMC), B. Adeva *et al.*, Phys. Rev. **D70** 012002 (2004); COMPASS Collaboration, E.S. Ageev *et al.* Phys. Lett. **B633** 25 (2006).

[9] D. de Florian and S. Frixione, Phys. Lett. **B457** 236 (1999).

[10] P. Aurenche *et al.*, Z. Phys. **C24** 309 (1984); Z. Phys. **C29** 459 (1985).

[11] B.A. Kniehl *et al.*, Nucl. Phys. **B582** 541 (2000).

[12] CTEQ Collaboration, J. Pumplin *et al.*, JHEP **0207** 012 (2002).

[13] M. Glück, E. Reya, M. Stratmann and W. Vogelsang, Phys. Rev. **D63** 094005 (2001).

[14] D. de Florian, G.A. Navarro and R. Sassot, Phys. Rev. **D71** 094018 (2005).

[15] C. Hendlmeier, M. Stratmann and A. Schäfer, Eur. Phys. J. **C48** 135 (2006).

Determination of $\Delta g/g$ from HERMES Data on High-p_T Inclusive Charged Hadrons

Patricia Liebing on behalf of the Hermes Collaboration

RIKEN-BNL Research Center
Brookhaven National Laboratory, Upton, NY 11973, USA

Hermes has used a high statistics data sample of charged inclusive hadrons to measure double spin asymmetries as a function of p_T. From these asymmetries $\Delta g/g$ has been extracted in the region of $1 < p_T < 2$ GeV, corresponding to $x \approx 0.2 - 0.3$. The information on the background asymmetry and the subprocess kinematics has been obtained from a Leading Order Monte Carlo model and existing parametrizations of the spin dependent quark distributions. Values for $\Delta g/g$ have been calculated both as a function of the measured p_T and x. The results will be presented together with comparisons of the Monte Carlo and data and a study on the effects of varying the model's parameters.

1 Further Information

More information on the data analysis, the underlying physics of the Pythia Monte Carlo program [2] and the tuning of the Monte Carlo can be found in Ref. [3], with an update on the results and the extraction methods in Ref. [4]. A Hermes publication is in preparation.

2 Bibliography

References

[1] Slides:
`http://indico.cern.ch/contributionDisplay.py?contribId=139&sessionId=4&confId=9499`

[2] T. Sjöstrand *et al.*, Comput. Phys. Commun. **135** (2001) 238 [arXiv:hep-ph/0010017].

[3] P. Liebing, Ph.D. Thesis, Universität Hamburg, DESY-THESIS-2004-036 (2004).

[4] P. Liebing, "Extraction of Delta g/g from Hermes Data on Inclusive Charged Hadrons," AIP Conf. Proc. **915** (2007) 331 [arXiv:0707.3617 [hep-ex]].

Determination of $\Delta G\,/\,G$ from Open Charm Events at COMPASS

S. Koblitz *

Universität Mainz - Institut für Kernphysik
Becherweg 45, 55099 Mainz - Germany

One of the main goals of the COMPASS experiment at CERN is the determination of the gluon polarisation in the nucleon, $\Delta G\,/\,G$. It is determined from spin asymmetries in the scattering of 160 GeV/c polarised muons on a polarised LiD target. The gluon polarisation is accessed by the selection of photon-gluon fusion (PGF) events. A very clean selection of PGF events can be obtained with charmed mesons in the final state. Their detection is based on the reconstruction of $D^\star$ and D^0 mesons in the COMPASS spectrometer. The analysis method for the first measurement of $\Delta G/G$ from the open charm channel is described. The result from COMPASS for the 2002-2004 data taking period is shown.

1 Introduction

In the framework of QCD, the spin of the nucleon is composed of the contributions from the quark spin, $\Delta\Sigma$, and the gluon spin, ΔG, as well as the orbital angular momenta of quarks, L_q, and gluons, L_g: $S_N = \frac{1}{2} = \frac{1}{2}\Delta\Sigma + \Delta G + L_q + L_g$. The discovery, that the quark contribution $\Delta\Sigma$ is small [2], led to a series of measurements to determine the other spin contributions. Since QCD fits only give weak constraints on ΔG, it has to be measured directly. First investigations were performed by the HERMES [3] and the SMC[4] collaborations using high p_t hadron pairs in the final state. The primary goal of the COMPASS experiment is to perform a precise measurement of $\frac{\Delta G}{G}$ also with a new approach. Therefore charmed meson production is studied, since the selection of charmed mesons in the final state provides an event sample of photon-gluon fusion (PGF) events with no background from other physical processes.

2 D-Meson reconstruction

The PGF process is the main reaction for the production of charm quarks in DIS. Due to the high charm mass, the charm content of the nucleon can be neglected as well as the production of charm quarks during fragmentation. In the independent fragmentation of a $c\bar{c}$ pair most frequently D mesons are produced. On average 1.2 D^0 mesons are produced per each $c\bar{c}$ pair [5].
The D^0 mesons are reconstructed from their $K\,\pi$ decay which has a branching ratio of 3.8 %. The reconstruction is done using tracks reconstructed in the COMPASS spectrometer. A detailed description of the spectrometer can be found in [6]. The thick nucleon target of the COMPASS experiment does not allow a separation of production and decay vertex of the charmed meson. Thus, the reconstruction of D mesons is done on a combinatorial basis. For each oppositely charged track pair in a given event the invariant mass is calculated using

*supported by BMBF.

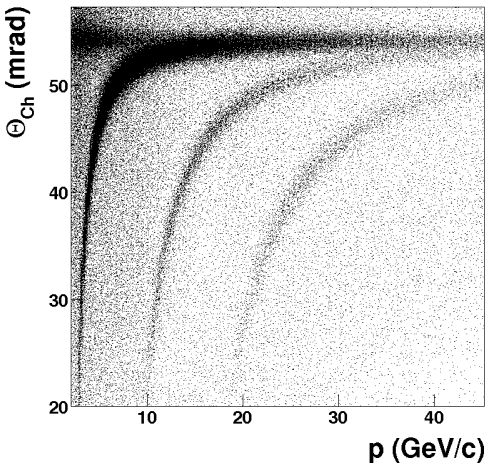

Figure 1: Cherenkov angles measured with RICH-1 vs. particle momenta. The histogram content in the kaon region is multiplied by a factor 30, in the proton region by a factor 150.

the kaon mass hypothesis for one of the tracks.

To suppress the high combinatorial background several cuts are applied on the track pair. The most important requirement is the particle identification for the kaon candidate from the Ring Imaging CHerenkov detector. The RICH allows to separate π, K and p in a momentum range from the particle's Cherenkov threshold to about 50 GeV. Figure 1 shows the RICH response for these three particle types as a function of their momenta. As can be seen, kaons can be identified starting from the kaon threshold around 9 GeV.

Due to the large charm mass the fraction of energy from the virtual photon that is carried by the meson, z, is expected to be higher for a real charmed meson than for combinatorial background. Therefore a cut of $z > 0.25$ is applied on the D^0 candidates. A third cut to reduce the combinatorial background is applied on the angle between the D^0 flight direction and the K momentum vector in the D^0 rest frame, $|\cos\theta^\star_K| < 0.5$.

With these cuts the ratio of open charm events to combinatorial background is still in the order of 1 : 10 (cf. Fig. 2). Therefore, a second more exclusive channel is also studied: $D^\star \rightarrow D^0\pi \rightarrow K\pi\pi$. Due to the small mass difference between $D^\star$ and D^0, combinatorial background can be very much suppressed by a cut on the mass difference: $3.1\,\text{MeV} < M_{K\pi\pi} - M_{K\pi} - M_\pi < 9.1\,\text{MeV}$. Here, $M_{K\pi\pi}$ denotes the mass of the $D^\star$ candidate and $M_{K\pi}$ the mass of the D^0 candidate. Since this so-called $D^\star$ tag is very effective in the reduction of combinatorial background, the z and the $\cos\theta^\star$ cuts can be relaxed. With $z > 0.2$ and $|\cos\theta^\star| < 0.85$ for $D^\star$ tagged D^0 mesons a signal to background ratio of 1:1 can be obtained (cf. Fig. 2).

3 Analysing Power

The ΔG measurement at COMPASS is based on the Photon Gluon Fusion (PGF) process. In this process the photon emitted by the incoming muon interacts with a gluon embedded in the nucleon. The interaction occurs via the exchange of a virtual quark resulting in a $q\bar{q}$ pair in the final state. Studying the scattering of a polarised muon beam off a polarised target gives access to experimental muon-nucleon asymmetries of the tagged PGF process. To access the gluon polarisation ΔG information about the hard subprocess is needed, which is combined in the analysing power a_{LL}. It contains the information about the partonic asymmetries from the muon-gluon scattering process. To determine a_{LL} the kinematic variables of the hard subprocess are needed.

Since only one of the two mesons is reconstructed, the full kinematics of the PGF process is not known for each single event. Thus, a parametrisation based on measured quantities was introduced, providing an estimation of a_{LL} for each open charm event. The parametrisation was obtained by training a neural network with an event sample generated with the

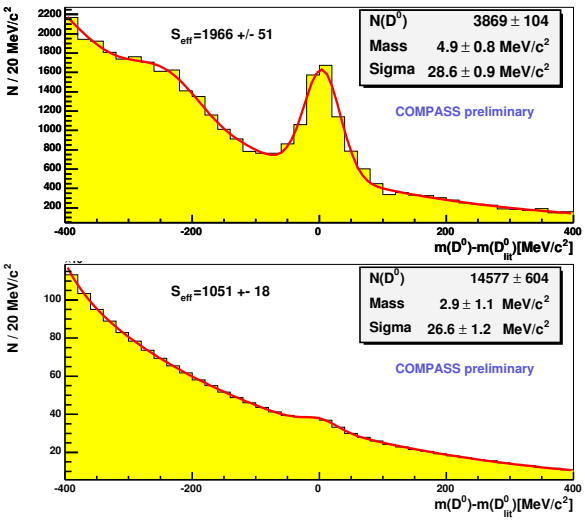

Figure 2: Kπ mass spectra for $D^\star$ tagged events (upper plot) and the sample without $D^\star$ tag ($S_{eff} = S^2/(B+S)$ is the effective signal)

AROMA generator in leading order QCD. For these events the full PGF kinematics were available as well as the reconstructed observables from the D^0 mesons. The correlation between the a_{LL} values coming directly from the generated quantities and the reconstructed a_{LL} from the parametrisation is about 82%. This procedure allows an evaluation of the analysing power for every event entering the $\Delta G/G$ determination.

4 Analysis Method

The data analysis leading to $\Delta G/G$ is based on event rates for scattering from a polarised muon beam off a polarised target. Since a separation between the remaining background events and the signal events in the final event sample is not possible, the signal purity of the event sample, $\sigma_{PGF}/\sigma_{PGF}+\sigma_B$, has to be introduced. It is determined from a fit to the final mass spectra. To optimise the description of the signal purity, this fit is done separately for events from the two target cells and for different bins of a_{LL}.

The observed event counting rates $N_{u,d}$ in the two oppositely polarised target cells of the COMPASS target are related to $\Delta G/G$ by

$$N_{u,d} = a\,\Phi\,n\,(\sigma_{PGF}+\sigma_B)(1+P_{\rm T}\,P_{\rm B}\,f(a_{LL}\,\frac{\sigma_{PGF}}{\sigma_{PGF}+\sigma_B}\,\frac{\Delta G}{G}+a_{LL}^B\,\frac{\sigma_B}{\sigma_{PGF}+\sigma_B}\,A_B))\ ,$$

where $P_{\rm B}$ ($P_{\rm T}$) denotes the beam (target) polarisation and n the number of nuclei in the target. The dilution factor f describes the fraction of polarisable material in the target. For ^6LiD this dilution factor is about 50%. The beam particle is required to cross both target cells providing a cancellation of the beam flux Φ. To cancel out the acceptance difference for the two cells, the target spin orientation is reversed every eight hours, leading to a total of 4 counting rates. From their double ratio

$$\delta = \frac{N_u \cdot N_d'}{N_u' \cdot N_d}$$

$\Delta G/G$ can be determined assuming a negligible background asymmetry A_B and a stable detector performance leading to a cancellation of the acceptance factors,

$$\frac{a_u \cdot a_d'}{a_d \cdot a_u'} = 1\ .$$

This method is applied to the events from every data taking period as well as for the two channels separately. To improve the statistical significance of the result, event weighting is used. The final result is then calculated as the weighted mean of the results for each channel and data taking period.

5 Results

With the 2002-2004 data the preliminary result for the COMPASS open charm analysis of

$$< \frac{\Delta G}{G} >= -0.57 \pm 0.41(\text{stat}) \pm 0.17$$

was obtained. For the measured sample the average x_g is 0.15 with RMS 0.08 and the hard scale at which this result was obtained is $13\,\text{GeV}^2$.

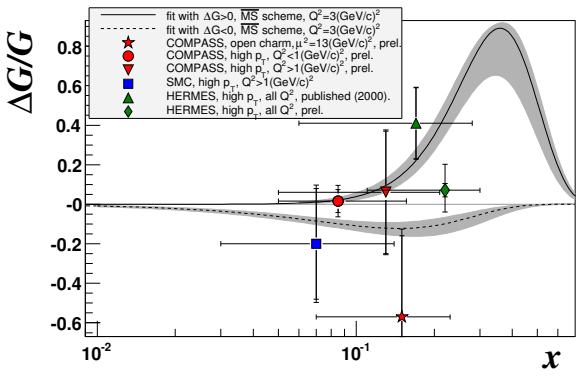

Figure 3: Comparison of the $\frac{\Delta G}{G}$ measurements from COMPASS, SMC [4] and HERMES [3]. The curves show the parametrisations at $3\,\text{GeV}^2$ in the $\overline{\text{MS}}$ scheme from [7] Note that the open charm point was obtained at a much higher scale.

The largest contributions to the systematic uncertainty of this result are possible false asymmetries (0.10), the choice of the fit function for the signal purity (0.09) and possible background asymmetries (0.07). There was no observation of any background asymmetry or false asymmetry from detector instabilities, so the actual values of these contributions are dominated by the statistical precision of the study. The influence of the choice for the fit function to describe the signal purity was estimated using different fit functions in the determination of $\Delta G/G$.
Further contributions to the systematic uncertainty are coming from the choice of Monte Carlo parameters (0.05), the number of bins for the signal-purity fit (0.04) and the uncertainties of the dilution factor (0.03) and the polarisation measurements (both 0.03).

6 Summary

The result for the first $\frac{\Delta G}{G}$ measurement from the open charm channel is presented. This is the most direct measurement of $\frac{\Delta G}{G}$ since it is only weakly dependent on Monte Carlo simulation. A comparison of the COMPASS results and other existing results is given in figure 3. The measurements are compared with the parton parametrisations from [7]. The data points give an indication that curves corresponding to small values of ΔG are favored. The analysis of the data taken in 2006 is in progress.

References

[1] Slides:
`http://indico.cern.ch/contributionDisplay.py?contribId=140&sessionId=4&confId=9499`

[2] EMC, J. Ashman et al., *Phys. Lett.* **B206**, 364 (1988).

[3] HERMES, A.Airapetian et al., *Phys. Rev. Lett.* **84**(2000) 2584.

[4] SMC, B. Adeva et al., *Phys. Rev.* **D70** (2004)012002

[5] COMPASS proposal, G. Baum et al., CERN/SPSLC 96-14.

[6] COMPASS, P. Abbon et al., CERN-PH-EP/2007-001, hep-ex/0703049, to be published in *Nucl. Inst. and Meth.*.

[7] COMPASS, E.V.Yu. Alexakhin et al., *Phys. Lett* **B647** 8 (2007).

Study of Proton Helicity Structure in Polarized $p + p$ Collisions at PHENIX

Kensuke Okada[1] for the PHENIX collaboration

1- RIKEN-BNL Research Center
BNL Bldg.510A Upton NY,11973

In this report, we describe a study of proton helicity structure in polarized p+p collisions at PHENIX. Up until now, we have focused on π^0 measurements. The asymmetry measurement rejects the maximum gluon polarization scenario. With higher integrated luminosity, various probes will provide complementary results.

1 Introduction

Polarized lepton-nucleon deep inelastic scattering (DIS) experiments revealed that only $\sim$ 25% of proton spin is carried by quarks and anti-quarks. A principal goal of the spin program at RHIC [2] is to determine the gluon spin contribution to the proton spin, using longitudinally polarized proton collisions where the gluon in the polarized proton interacts in leading order process. The evidence of gluon polarization should appear in the double helicity production asymmetries (A_{LL}) shown in Eq.1, where P is polarization of proton beam, and $\sigma_{++(+-)}$ is the production rate in beam polarization direction of ++(+-).

$$A_{LL} \equiv \frac{1}{P^2} \cdot \frac{\sigma_{++} - \sigma_{+-}}{\sigma_{++} + \sigma_{+-}} \tag{1}$$

2 PHENIX experiment

The PHENIX detector is composed of central arms ($|\eta| < 0.35$, ϕ:2*0.5π) and muon arms ($1.2 < |\eta| < 2.4$, ϕ:2π). In 2006, a forward electromagnetic calorimeter was newly installed. The collision information is provided by the beam-beam counter (BBC) and the zero degree counter (ZDC). Those are also used as luminosity monitors. The detailed description of the PHENIX detector can be seen elsewhere [3]. The longitudinal spin program was started in 2003. In 2006, PHENIX recorded collision data at the energy of $\sqrt{s} = 200$ GeV for the total integrated luminosity of 7.5 pb^{-1} with the polarization of $\sim$60%.

3 Cross section measurements of single particles

Before extracting the asymmetry (Eq.1), it is important to confirm the applicability of our theoretical baseline with the cross section measurement. We published several cross section measurements of single particle production[4]. The integrated luminosity was calculated from the BBC counts. The conversion factor is obtained via the van der Meer scan technique [5].
For example, neutral pion, direct photon, and single electron (a representative of charm/bottom hadrons) are interesting probes for the gluon measurement. Factorized perturbative QCD calculations describe our measurements well.

4 Spin asymmetry measurement at RHIC

At RHIC, the key feature to reduce the systematic uncertainty is in our bunch structure of the proton beams. They consist of 120 bunches and the revolution time is only 1.2 micro seconds. Each bunch has different polarization direction. By using the rapidly changing combinations of polarization direction, we can reduce the systematics of detector instability in the asymmetry measurement. However the characteristics of each bunch crossing are not identical. One obvious factor is luminosity. To normalize the luminosity difference, the BBC is used again. Since the BBC detects the same hard scattering interaction, it is important to confirm if there is no asymmetry in the BBC measurement itself. For this purpose, we checked a relative difference to ZDC counts. Currently the statistics of ZDC counts determines the uncertainty of relative luminosity measurement. One way to check the uncertainty related to bunch characteristics is to confirm null asymmetry by assigning random polarization direction patterns.

4.1 Asymmetry measurement in π^0 production

The neutral pion (π^0) is a suitable probe of gluons in the proton for PHENIX, for the following reasons.
- In the low p_T region, the dominant process is gluon-quark scattering.
- It is the most common particle in the hadron final state.
- PHENIX has a finely granulated central electromagnetic calorimeter with a triggering feature.

Figure 1 shows our preliminary π^0 asymmetry result as a function of $p_T^{\pi^0}$. The points are from the data with integrated luminosity of 1.8 pb^{-1} in Run5 (2005) and 7.5 pb^{-1} in Run6 (2006). Only high p_T points are included from Run6 fast track analysis. The theory curves in the figure are GRSV curves [6]. Figure 2 shows the χ^2 values as a function of ΔG (at $Q^2 = 1$ GeV^2) in the theory. The maximum ΔG scenario is rejected. It should be noted that there is no uncertainty for the model assumption included.

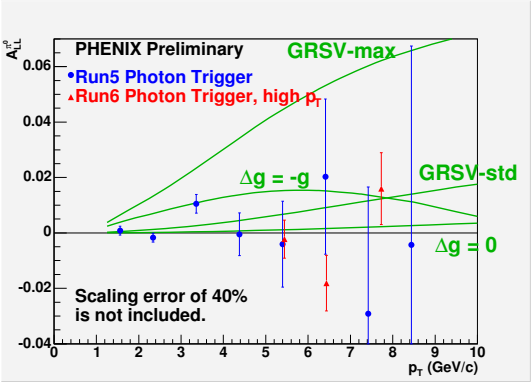

Figure 1: $A_{LL}^{\pi^0}$.Run6 data includes only p_T higher than 5GeV/c

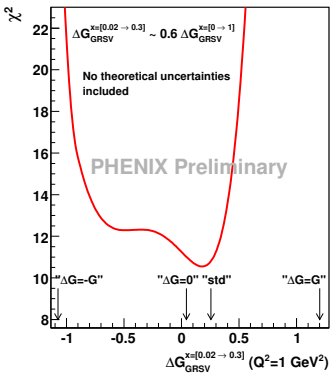

Figure 2: Data-Theory comparison (χ^2) plot.

With a different collision energy, a different kinematic region can be investigated. For example, in $\sqrt{s} = 62$ GeV, the production cross section is about a hundred times larger than in $\sqrt{s} = 200$ GeV in terms of $x_T (\equiv 2p_T/\sqrt{s})$, while the theory predicts A_{LL} to be almost scaled. Although the luminosity is down by an order due to the larger emittance, it still wins at the higher x_T region. Figure 3 shows the measurement from Run6 $\sqrt{s} = 62$ GeV data ($\int L = 0.06\text{pb}^{-1}$). The applicability of pQCD calculation is to be checked with cross section measurement.

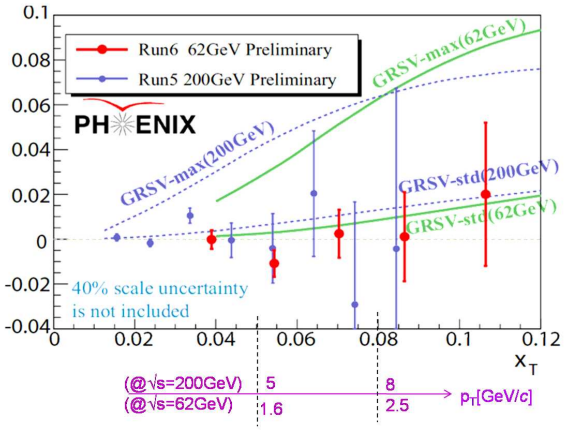

Figure 3: $\pi^0 A_{LL}$ at $\sqrt{s} = 62$ GeV as a function of $x_T (\equiv 2p_T/\sqrt{s})$.

4.2 Asymmetry measurement in various channels

As the integrated luminosity is increased, channels other than π^0 come into view.

4.2.1 The central arm

Figure 4 gives a rough idea of yields of several channels in the PHENIX central arm, and shows a statistical uncertainties of asymmetry measurement in two different conditions.

$\pi^{\pm}$: In the p_T range where gluon-quark scattering is dominant, the charge difference of this probe is thought to be sensitive to the sign of gluon polarization through the struck quark's favored/disfavored fragmentation function. Though the production probability is the same to π^0, the current PHENIX setup has a little disadvantage in the trigger and the tracking system.

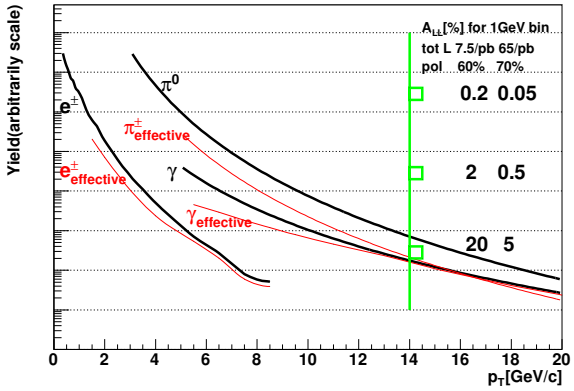

Figure 4: A rough estimation of single particle yields in the central arm. Statistical uncertainties in the double spin asymmetry measurement are shown.

Direct γ: In the theoretical point of view, this is a golden channel for gluons through the

gluon Compton scattering process. However in addition to its small production probability, there are background photons from hadronic decay (mostly π^0's), which dilute the signal.

$e^{\pm}$: The electron is a representative of charm or bottom particles. Since those heavy particles are produced through the gluon fusion process, it could be a good probe for gluon. The experimental disadvantage to π^0 is the limitation of data acquisition rate in the low p_T region ($p_T <\sim 1.5$ GeV/c) and contamination of conversion electrons.

PHENIX has also asymmetry results of η and "jet" production.

4.2.2 The muon arm

In the muon arm, the asymmetry of J/ψ production with di-muon decay mode has been measured. It is starving for statistics. On the other hand, the detector is sensitive to hadron production with decay muons and punch-through hadrons.

4.2.3 The forward electromagnetic calorimeter (MPC)

It has a clear signal of π^0. It will provide information of π^0 production asymmetry in the large rapidity region.

4.2.4 A different double spin asymmetry measurement

One of ongoing analyses is to measure the spin dependence of dijet k_T using two particle correlations(π^0 - $h^{\pm}$). It has been proposed to have a sensitivity to the angular momentum component from an analogy of classical spinning disks [7]. It requires theoretical supports.

5 Summary

For the longitudinal spin program, the PHENIX experiment accumulated about 7.5 pb^{-1} of data at $\sqrt{s} = 200$ GeV with roughly 60% proton beam polarization and 0.1 pb^{-1} of data at $\sqrt{s} = 62$ GeV with 50% polarization. Up until now, we have performed spin asymmetry measurement focusing on π^0 production with the central electromagnetic calorimeters. Despite low integrated luminosity, it was shown that the $\sqrt{s} = 62$ GeV data have comparable sensitivity to the gluon polarization for the high $x_T (\equiv 2p_T/\sqrt{s})$ region.

The longitudinal polarization program at $\sqrt{s} = 200$ GeV will be accomplished with about $70pb^{-1}$ and 70% polarization in 2008. With higher statistics, various probes other than π^0 will be analyzed, which will provide complementary results.

References

[1] Slides:
`http://indico.cern.ch/contributionDisplay.py?contribId=141&sessionId=4&confId=9499`

[2] Research plan for spin physics at RHIC, BNL-73798-2005 (2005)

[3] K.Adcox *et al.*: Nucl. Inst. Meth. A**499**, 469 (2003)

[4] A. Adare *et al.*: Phys. Rev. Lett. **97**, 252002 (2006); S. S. Adler *et al.*: Phys. Rev. Lett. **91**, 241803 (2003); S. S. Adler *et al.*: Phys. Rev. Lett. **98**, 012002 (2007)

[5] K. A. Dress and Z. Xu, "Proceedings of the PAC2001 Conference",3120 (2001)

[6] B. Jäger *et al.*: Phys. Rev. **D67**, 054005 (2003); M. Glück *et al.*: Phys. Rev. **D63**, 094005 (2001).

[7] T.-c. Meng, J.-c. Pan, Q.-b. Xie, and W. Zhu: Phys. Rev. **D40**, 769 (1989).

Extracting the Gluon Piece of the Spin Puzzle New Inclusive Jet Results from STAR

Renee Fatemi for the STAR Collaboration

Massachusetts Institute of Technology
Laboratory of Nuclear Science
77 Massachusetts Ave. Cambridge, MA 02139 USA

This contribution presents the most recent mid-rapidity inclusive jet results from 3 pb^{-1} of data collected from longitudinally polarized proton collisions at $\sqrt{s} = 200$ GeV during the 2005 RHIC run. The inclusive jet asymmetry, A_{LL}, with it's increased transverse momentum range and precision, provides strong constraints on the gluon helicity distribution when compared with existing next-to-leading order perturbative QCD evaluations.

Measurements of the partonic helicity distribution functions in the proton are essential for a complete understanding of the long range, non-perturbative properties of Quantum Chromodynamics (QCD). Three decades of polarized lepton-nucleon deep-inelastic-scattering (DIS) experiments [2] have shown that the probability for a quark spin to be aligned with the spin of the parent proton is $\sim 25\%$. Conservation of angular momentum requires the quark (ΔQ) and gluon (ΔG) total spin and orbital angular momentum ($L_Q + L_G$) within the proton to sum to $\frac{\hbar}{2}$, motivating investigations into the size of the remaining components of the sum rule. Traditional fixed-target DIS experiments couple to the gluon distributions only at next-to-leading order (NLO), providing limited constraints on ΔG[3][4]. As a result, several programs designed to directly access ΔG have been established and have produced initial results [5][6][7][8][9]. Measurements of higher statistical precision and broader Q^2 reach continue to be recorded and released [10]. During the 2005 RHIC run STAR sampled 3 pb^{-1} of proton collisions with an average longitudinal beam polarization of 50% and $\sqrt{s} = 200$ GeV. As a result, the inclusive jet asymmetry measurement, spanning a transverse momentum (p_T) range of $5-32$ GeV, represents the most precise measurement over the largest p_T range to date.

The Solenoidal Tracker at RHIC (STAR) Collaboration utilizes the polarized proton beam provided by the Relativistic Heavy Ion Collider (RHIC) to study final state interactions resulting from quark-quark (qq), quark-gluon (qg) and gluon-gluon (gg) scattering. STAR's large acceptance facilitates jet reconstruction, allowing for a nearly fragmentation independent reconstruction of the partonic characteristics inside the proton. The inclusive jet double spin asymmetry A_{LL},

$$A_{LL} = \frac{1}{P_Y P_B}\frac{N^{++} - N^{+-}}{N^{++} + N^{+-}} = \frac{\sum_{AB\to CX} \Delta f_A \Delta f_B \Delta\sigma_{AB\to CX}}{\sum_{AB\to CX} f_A f_B \sigma_{AB\to CX}} \quad (1)$$

is constructed from a ratio of the helicity aligned (N^{++}) and anti-aligned (N^{+-}) luminosity normalized jet yields and is related at leading order to the product of the initial polarized (Δf) and unpolarized (f) parton distribution functions and partonic polarized ($\Delta\sigma_{AB\to CX}$) and unpolarized ($\sigma_{AB\to CX}$) cross-sections. The agreement between data and NLO perturbative QCD (pQCD) predictions for the inclusive jet cross-section[9] motivate the ultimate extraction of the gluon helicity distribution from these asymmetry measurements.

The STAR detector systems [11] relevant for jet reconstruction are the Time Projection Chamber (TPC) and the Barrel (BEMC) and Endcap (EEMC) Electromagnetic Calorimeters. The TPC provides momentum information on charged particles scattered in the pseudorapidity region $|\eta| < 1.4$. The BEMC and EEMC measure the neutral energy deposited per event in the range spanning $-1 < \eta < 2$. The minimum bias trigger (MINB) was defined by a coincidence signal between East and West Beam Beam Counters (BBC) [12], which are segmented scintillator detectors located on either side of the interaction region at $3.3 < |\eta| < 5.0$. Enhancement of jet reconstruction at high transverse momentum (p_T) was achieved by requiring a MINB plus High Tower (HT) or Jet Patch (JP) trigger to be fullfilled. The HT trigger required a single BEMC tower ($\Delta\phi = \Delta\eta = 0.05$) to exceed a low/high threshold of 2.6/3.5 GeV. The JP trigger, included for the first time in this analysis, required that a cluster of towers ($\Delta\phi = \Delta\eta = 1.0$) exceed the low/high threshold of 4.5/6.5 GeV. Finally the BBC also serves as the STAR luminosity monitor, providing the spin dependent luminosity normalization for the asymmetry analysis.

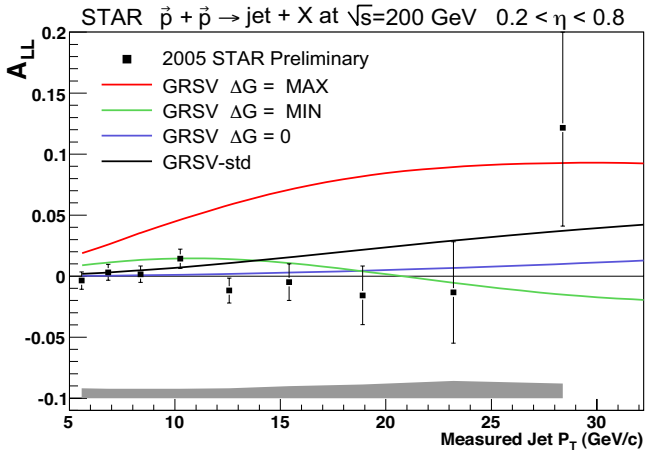

Figure 1: The 2005 STAR mid-rapidity inclusive jet asymmetry calculated from from 3 pb^{-1} of sampled data. The error bars are statistical only with systematic errors represented by the gray shaded band as the bottom. The curves are NLO pQCD calculations[14] depicting the inclusive jet asymmetry for various input ΔG distributions.

The STAR jetfinder is based on the mid-point cone algorithm [13], which clusters TPC tracks and BEMC tower energies greater than 0.2 GeV into jets of radius $R = \sqrt{\Delta\phi^2 + \Delta\eta^2} = 0.4$, requiring a split/merge fraction of 0.5 and seed energy of 0.5 GeV. Jet reconstruction is limited to the region of the BEMC which was fully implemented and incorporated into the trigger during the 2005 run, resulting in the requirement that the jet axis lies at least 0.2 units in pseudorapidity from the detector edge ($0.2 < \eta_{jet} < 0.8$). Beam background, not associated with the hard scattering, results in an excess of neutral energy from the calorimeters to be clustered into the reconstructed jet. The sub-sample of jets dominated by this beam background are removed by requiring the neutral energy fraction of the jet be less than 0.8. Additionally, the jets were required to originate from a vertex of $\sim \pm 60$ cm along the beamline.

Figure 1 shows the 2005 STAR inclusive jet A_{LL} as a function of the measured jet p_T. Although the HT and JP trigger rates were matched in bandwidth, the high threshold JP trigger jet reconstruction efficiency was on average 50% greater than the HT, resulting in half of the final jet sample originating from the higher threshold JP trigger. In order to maintain a uniform trigger bias, each jet was required offline to contain a trigger tower (HT) or patch (JP). The grey shaded band represents the systematic error, excluding the 25% uncertainty on the beam polarization values. The leading contributions to the systematic error result from an estimate of the bias introduced to the asymmetries from the trigger and jet reconstruction requirements and a conservative upper limit on possible false asymmetries in the measurement. Additional, less significant, systematic contributions arise from non-longitudinal beam components and the effect of beam background on the asymmetry and relative luminosity measurements. No significant bunch or fill dependent systematics were observed. The 2005 jet asymmetries are in good agreement with previous STAR inclusive jet measurements [9] in the region of kinematic overlap.

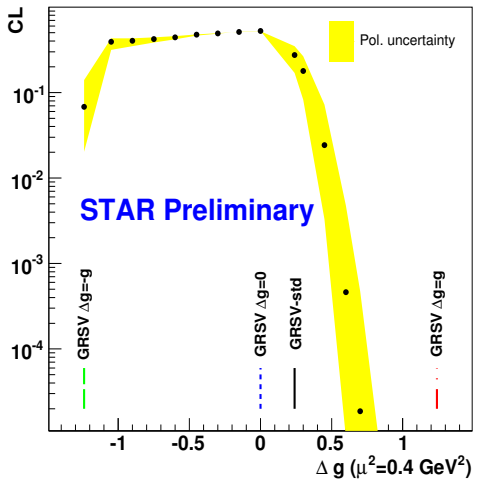

Figure 2: Confidence level comparisons between the 2005 STAR inclusive jet asymmetry measurement and NLO pQCD calculations for various gluon distributions within the GRSV framework[15][14]. The yellow shaded band represent the systematic error due to the beam polarization uncertainty.

The curves in Fig.1 are NLO pQCD calculations of inclusive jet asymmetries[14] for several variations of ΔG at the input scale. The black curve (standard) incorporates the ΔG which gives a best fit to the DIS data within the GRSV formulation[15]. The red (green) curves indicate scenarios where the gluons are completely (anti-)aligned with the proton spin. The blue curve shows $\Delta G = 0$ and therefore all non-zero values derive from the quark spins only. The jet asymmetries are clearly not consistent with the maximal polarization case, but are also not yet precise enough to distinguish between the minimal, standard and zero scenarios. The precision of the measurement does allow, within the GRSV framework, for the exclusion of several ΔG values between the standard and maximal case. Figure 2

quantifies this comparison by showing the confidence level at which this measurement rules out various input gluon distributions. The 2005 results rule out $\Delta G > 0.5$ at $\sim 95\%$ level. In comparison, the $\chi^2 = \pm 1$ range for the GRSV standard gluon fit spanned $\Delta G = -0.45$ to 0.7. Systematic errors and their correlations across p_T bins are accounted for in the confidence level calculations, with the yellow shaded band representing the possible systematic shift due to the beam polarization uncertainty. The p_T reach of this measurement translates into a sampling of $\sim 50\%$ of the total integral ($x_{Bjorken} = 0.03 - 0.3$) of the gluon helicity distribution.

The STAR 2005 inclusive jet results provide a significant contribution to the global understanding of ΔG. Although the measurements presented here clearly place stronger constraints on the gluon distribution than the fixed target DIS data, only their inclusion within a global analysis of world data will allow for a definitive extraction of ΔG.

Acknowledgements

The authors would like to thank the organizers of the conference for the opportunity to present these results. We would also like to thank for W. Vogelsang and M. Stratmann for providing additional curves of the inclusive jet asymmetries with varying input gluon polarization values.

References

[1] Slides:
`http://indico.cern.ch/contributionDisplay.py?contribId=142&sessionId=4&confId=9499`
[2] EMC, J. Ashman *et al.*, Nucl. Phys. **B328**,1 (1989);
B.W. Filippone and X.D. Ji, Adv. Nucl. Phys. **26**, 1 (2000) and references therein.
[3] SMC, B. Adeva *et. al*, Phys. Rev. **D58**, 112002 (1998).
[4] E155, P.L. Anthony *et al.*, Phys. Lett. **B493**, 19 (2000).
[5] HERMES, A. Airapetian *et al.* Phys. Rev. Lett. **84** 2584-2588, (2000).
[6] SMC, B Adeva *et al.* , Phys. Rev. **D70** 012002, (2004).
[7] PHENIX, S.S. Adler *et al.* Phys. Rev. Lett. **93** 202002, (2004).
[8] COMPASS, E.S. Ageev *et al.* Phys. Lett. **B633** 25-32, (2006).
[9] STAR, B.I. Abelev *et al.*, Phys. Rev. Lett **97** 252001, (2006).
[10] PHENIX, S.S. Adler *et al.* Phys. Rev. **D73** 091101, (2006).
[11] Special Issue: RHIC and Its Detectors, Nucl. Instrum. Meth. **A499**, 2003.
[12] J.Kiryluk *et al.*, hep-ex/0501072, published in Spin 2004 Conference Proceedings, Trieste, Italy.
[13] G.C. Blazey *et al.* arXiv:hep-ex/0005012
[14] B. Jager, M. Stratmann, W. Vogelsang, Phys. Rev. **D70** 034010, 2004.
[15] M. Glück, E. Reya, M. Stratmann and W. Vogelsang, Phys. Rev. **D69** 094005, 2001.

Longitudinal Spin Measurements with Inclusive Hadrons in Polarized p+p Collisions at 200 GeV

Frank Simon (for the STAR Collaboration)

Massachusetts Institute of Technology
77 Massachusetts Ave, Cambridge, MA 02139, USA

We present measurements of the double longitudinal spin asymmetries for inclusive π^0 and $\pi^{+(-)}$ production in polarized p+p collisions at $\sqrt{s} = 200$ GeV at mid-rapidity with the STAR detector from the 2005 RHIC run. These measurements are used to access $\Delta G/G$, the gluon polarization in the proton. The observed unpolarized inclusive cross sections show good agreement with NLO pQCD calculations. The double longitudinal spin asymmetries are compared to NLO pQCD calculations based on different assumptions for the gluon polarization in the nucleon to provide constraints on $\Delta G/G$. At the present level of statistics the measured asymmetries disfavor a large positive gluon polarization, but cannot yet distinguish between other scenarios.

1 Introduction

A primary goal of the polarized p+p program at the Relativistic Heavy Ion Collider (RHIC) is the determination of the gluon polarization ΔG in the proton via spin asymmetry measurements in a variety of processes [2]. Inclusive processes such as neutral pion, charged pion, and jet production provide sensitivity to gluons through the dominant subprocesses $gg \to gg$ and $qg \to qg$ at low and intermediate p_T. Because of the difference in the sign of the polarization for up and down valence quarks, the difference of the measured asymmetries in the π^+ channel and the π^- channel is sensitive to the sign of the gluon polarization in the p_T range where $qg \to qg$ contributions are sizable. These inclusive probes have only modest luminosity requirements and are natural first steps in longitudinal spin program. The unpolarized cross sections provide constraints on fragmentation functions and important validation of the NLO pQCD calculations used to interpret the measured spin asymmetries. The STAR experiment, with its large acceptance tracking and calorimetry, is uniquely capable of full jet reconstruction at RHIC, allowing a direct study of fragmentation through the association of a detected π^0 with its parent jet.

2 Analysis and Results

STAR detects neutral pions near mid-rapidity with its barrel electromagnetic calorimeter (BEMC) via reconstruction of the invariant mass of photon pairs; charged pions at high transverse momentum are identified in the time projection chamber (TPC) via their specific energy loss, dE/dx [3]. For both these measurements, a trigger on the electromagnetic energy deposited in the calorimeter is crucial to select events with a hard initial scattering. For the present analyses two types of calorimeter triggers were used. The high tower (HT) trigger selects events with high energy deposition in one calorimeter tower ($\Delta\eta \times \Delta\varphi = 0.05 \times 0.05$), making this a good π^0 and photon trigger. The jet patch (JP) trigger selects events with significant energy deposited in a trigger patch of the calorimeter ($\Delta\eta \times \Delta\varphi = 1 \times 1$). This is used to trigger on the electromagnetic energy in a jet. Each of these triggers is used with two different energy thresholds, referred to as HT1, HT2, JP1 and JP2. To achieve high

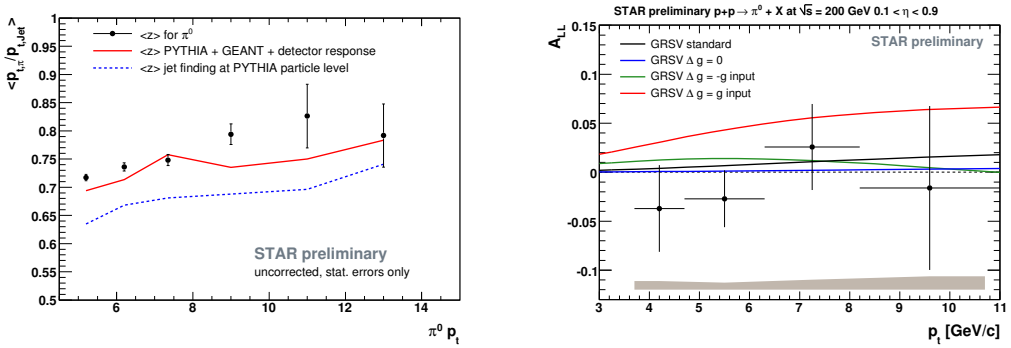

Figure 1: **Left**: Mean momentum fraction of HT1 triggered π^0 in their associated jet as a function of p_T. The data points are plotted at the bin center in p_T and not corrected for acceptance or trigger effects. Only statistical errors are shown. The solid red and the dashed blue line show the π^0 $\langle z \rangle$ for PYTHIA simulations with a full GEANT detector simulation and with jet finding on the PYTHIA particle level, respectively, indicating the size of resolution and reconstruction effects.
Right: Double longitudinal spin asymmetry for inclusive π^0 production together with NLO pQCD predictions based on different assumptions for ΔG. The systematic error shown by the gray band does not include a 9.4% normalization uncertainty due to the polarization measurement.

detector live-time for the highest energy triggers, the minimum bias (MB), the HT1, and the JP1 triggers are prescaled during data taking. For the 2005 run period, only half of the BEMC was fully installed and commissioned, giving a coverage of $0 < \eta < 1$ for all azimuthal angles φ. This limits the acceptance for calorimeter triggers and for neutral pion reconstruction in this run.

The unpolarized cross sections for both neutral and charged pions have been discussed in more detail in [3, 4]. Good agreement with NLO pQCD calculations [5] over several orders of magnitude in the cross section has been observed for both particle species. These measurements consistently favor the KKP fragmentation functions [6] over other sets.

To investigate the momentum fraction carried by high p_T π^0's in their parent jet, identified neutral pions were associated with jets found [7] in the same event. An association was made if the pion was within the jet cone of 0.4 in η and φ. To avoid edge effects, the analysis is restricted to $0.4 < \eta_{jet} < 0.6$. Because other analyses have shown that calorimeter-only jets without any charged tracks are often associated with beam background, a maximum ratio of the neutral to total energy of 0.95 is imposed. The left side of figure 1 shows the mean momentum fraction $\langle z \rangle$ of neutral pions associated with jets for HT1 triggers as a function of the pion's p_T. The momentum fraction is not corrected for acceptance, efficiency or resolution of the jet reconstruction. The mean momentum fraction of π^0 in electromagnetically triggered jets is approximately 0.75, and rises slightly with p_T, consistent with measurements of leading charged hadrons in jets in fixed-target experiments [8]. Also shown in this figure is the mean momentum fraction of neutral pions in jets in PYTHIA [9] simulations, both with jet finding on the PYTHIA particle level, and with a full detector simulation in

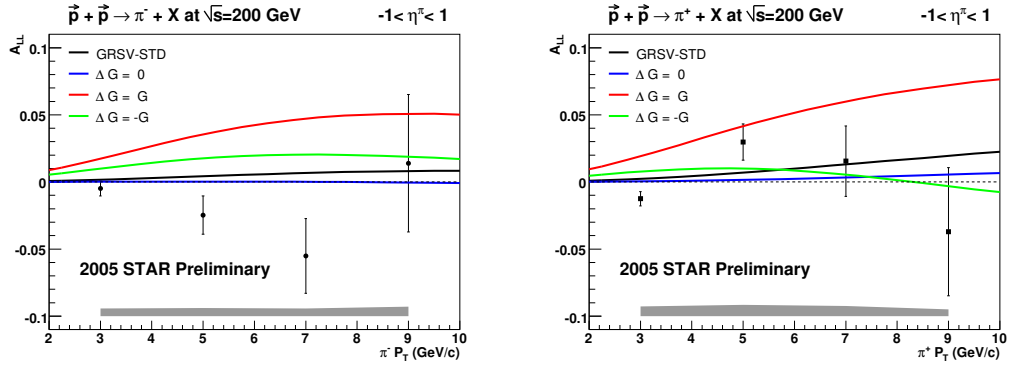

Figure 2: Double longitudinal spin asymmetries for inclusive charged pion production. $A_{LL}(\pi^-)$ is displayed in the left panel and $A_{LL}(\pi^+)$ is on the right. The asymmetries are compared to theoretical predictions of A_{LL} incorporating various scenarios for the gluon polarization. The error bars are statistical; point-to-point systematic uncertainties are added in quadrature and shown as the gray band at the bottom of each figure. A scale uncertainty of 9.4% from the uncertainty on the beam polarization measurements is not included.

GEANT. The difference between these two gives an impression of the size of the detector and reconstruction effects on the mean momentum fraction. These effects are dominated by the jet reconstruction, since the momentum determination for neutral pions in the electromagnetic calorimeter is very precise. The simulation results suggest that resolution and reconstruction effects increase the observed $\langle z \rangle$ by about 10%.

The longitudinal double spin asymmetry is given by

$$A_{LL} = \frac{1}{P_1 P_2} \frac{(N^{++} - RN^{+-})}{(N^{++} + RN^{+-})}, \tag{1}$$

where $P_{1,2}$ are the mean measured beam polarizations and R is the ratio of integrated luminosities for equal and opposite beam helicities. N^{++} and N^{+-} are the particle yields in equal and opposite beam helicity configurations, respectively. The polarizations are obtained with the RHIC polarimeters [10]. Typical polarization values during the run period were $\sim$ 50%. The relative luminosities are monitored in STAR with the BBCs. Typical R values were around 1.1. The integrated luminosity for the asymmetries for both neutral and charged pion production is ~ 1.6 pb^{-1} from the 2005 RHIC longitudinally polarized proton run.

The right side of figure 1 shows the measured double spin asymmetry for inclusive π^0 production, together with theoretical predictions assuming different gluon polarization scenarios [11]. The systematic errors shown in the figure include contributions from π^0 yield extraction and background subtraction, remaining background, possible non-longitudinal spin contributions and relative luminosity uncertainties. An overall normalization uncertainty of 9.4%, due to errors on the polarization values obtained with the RHIC polarimeters, is not included. Studies of parity-violating single spin asymmetries and randomized spin patterns show no evidence for bunch to bunch or fill to fill systematics. The GRSV standard curve is based on the best fit to DIS data; the other curves show scenarios of extreme positive, negative and vanishing gluon polarizations. The data are consistent with three of these evaluations and tend to disfavor the scenario with a large positive gluon polarization.

Figure 2 shows the double longitudinal spin asymmetries for inclusive charged pions [12]. The same theoretical predictions as for the π^0 case are also shown here. To obtain a flavor-separated result the KKP fragmentation functions [6] used for the calculations are modified by multiplying favored fragmentation functions by $(1 + z)$ and unfavored ones by $(1 - z)$. The leading systematic error in this analysis is the trigger bias, because the events are triggered on electromagnetic energy deposition, while charged hadrons are analyzed. This is different from the π^0 case, where the trigger is directly sensitive to neutral pions. As in the case of the π^0 asymmetry, the results are least consistent with the maximal positive gluon polarization scenario, but discerning among the other scenarios is limited by statistics. The double longitudinal asymmetry of $(\pi^+ + \pi^-)$ has been found to be consistent with the asymmetry of π^0.

3 Conclusion

The STAR experiment at the Relativistic Heavy Ion Collider has obtained preliminary results on the cross section and the double longitudinal spin asymmetry of inclusive neutral and charged pion production in polarized p+p collisions at $\sqrt{s} = 200$ GeV. The measured cross sections are found to be in good agreement with NLO pQCD predictions. The longitudinal asymmetries disfavor the maximal positive gluon polarization scenario, but currently have no resolving power among other scenarios due to limited statistics. With the large increase in sampled luminosity and polarization in the 2006 run, a significant improvement of the statistical power of these analyses is expected in the near future.

References

[1] Slides:
`http://indico.cern.ch/contributionDisplay.py?contribId=143&sessionId=4&confId=9499`

[2] G. Bunce, N. Saito, J. Soffer and W. Vogelsang, Ann. Rev. Nucl. Part. Sci. **50**, 525 (2000).

[3] F. Simon [STAR Collaboration], AIP Conf. Proc. **870**, 428 (2006) [arXiv:hep-ex/0608050].

[4] J. Adams *et al.* [STAR Collaboration], Phys. Lett. B **637**, 161 (2006).

[5] B. Jager, A. Schafer, M. Stratmann and W. Vogelsang, Phys. Rev. D **67**, 054005 (2003).

[6] B. A. Kniehl, G. Kramer and B. Potter, Nucl. Phys. B **597**, 337 (2001).

[7] B. I. Abelev *et al.* [STAR Collaboration], Phys. Rev. Lett. **97**, 252001 (2006).

[8] G. Boca *et al.*, Z. Phys. C **49**, 543 (1991).

[9] T. Sjostrand *et al.*, Comput. Phys. Commun. **135**, 238 (2001).

[10] H. Okada *et al.*, arXiv:hep-ex/0601001.

[11] B. Jager, M. Stratmann and W. Vogelsang, Phys. Rev. D **70**, 034010 (2004).

[12] A. Kocoloski, arXiv:hep-ex/0612005.

Valence Quarks Polarization from COMPASS

A.Korzenev,* for the COMPASS collaboration

Mainz University, Institute of Nuclear Physics, D-55099, Mainz, Germany

A first evaluation of the polarized valence quark distribution $\Delta u_v(x) + \Delta d_v(x)$ from the COMPASS experiment (CERN/SPS) is presented. The data were collected by COMPASS in the years 2002–2004 using a 160 GeV polarized muon beam scattered off a large polarized ^{6}LiD target and cover the range $1 < Q^2 < 100$ GeV^2 and $0.006 < x < 0.7$. The analysis is based on the difference asymmetry, $A^{h^+-h^-}$, for hadrons of opposite charges, which gives a direct access to the polarization of valence quarks.

1 Introduction

Nowadays, there is growing of interest in semi-inclusive deep inelastic scattering experiments (SIDIS) with longitudinally polarized beams and targets as they provide an additional information on the spin structure of the nucleon compared to the inclusive DIS measurements. The SIDIS data allow to separate the valence and sea contributions to the nucleon spin.

Previous measurements of the valence quark helicity distributions were done by the SMC [2, 3] and the HERMES [4] collaborations. The SMC data cover a similar kinematic range as the COMPASS data, but with statistics which is an order of magnitude lower. HERMES has a high statistics data set and PID, thus it can disentangle all five quark helicity distributions. However the x-range is quite limited: $0.023 < x < 0.6$.

In the present analysis we use the so called difference asymmetry which is determined from the difference of cross sections of positive and negative hadrons h^+ and h^-:

$$A^{h^+-h^-} = \frac{(\sigma^{h+}_{\uparrow\downarrow} - \sigma^{h-}_{\uparrow\downarrow}) - (\sigma^{h+}_{\uparrow\uparrow} - \sigma^{h-}_{\uparrow\uparrow})}{(\sigma^{h+}_{\uparrow\downarrow} - \sigma^{h-}_{\uparrow\downarrow}) + (\sigma^{h+}_{\uparrow\uparrow} - \sigma^{h-}_{\uparrow\uparrow})}. \tag{1}$$

Here arrows indicate the relative direction of the beam and target polarizations. The difference asymmetry approach was developed and used in SMC [5, 2]. Results obtained with this approach, as compared to the traditional single hadron approach [3, 4], are "cleaner" from the theoretical point of view because of the very weak sensitivity of $A^{h^+-h^-}$ to uncertainties coming from fragmentation functions (FF). As it is shown in [5] FFs cancel out from $A^{h^+-h^-}$ in LO QCD. For the deuteron target the asymmetry is:

$$A_d^{h^+-h^-} \equiv A_d^{\pi^+-\pi^-} = A_d^{K^+-K^-} = \frac{\Delta u_v + \Delta d_v}{u_v + d_v}, \quad \text{where} \quad \Delta q_v \equiv \Delta q - \Delta \bar{q}. \tag{2}$$

The fact that kaons contribute to the asymmetry exactly like pions allows to avoid statistical losses due to hadron identification. Starting from NLO QCD the difference asymmetry depends also on FFs. However their effect is small [6].

The single hadron asymmetries A^{h+} and A^{h-} can be used to obtain $A^{h^+-h^-}$:

$$A^{h^+-h^-} = \frac{1}{1-r}(A^{h+} - rA^{h-}), \quad \text{with} \quad r = \frac{\sigma^{h-}_{\uparrow\downarrow} + \sigma^{h-}_{\uparrow\uparrow}}{\sigma^{h+}_{\uparrow\downarrow} + \sigma^{h+}_{\uparrow\uparrow}} = \frac{N^-}{N^+} \cdot \frac{a^+}{a^-}. \tag{3}$$

*Supported by the BMBF. On leave from JINR, Dubna, Russia. E-mail: korzenev@mail.cern.ch

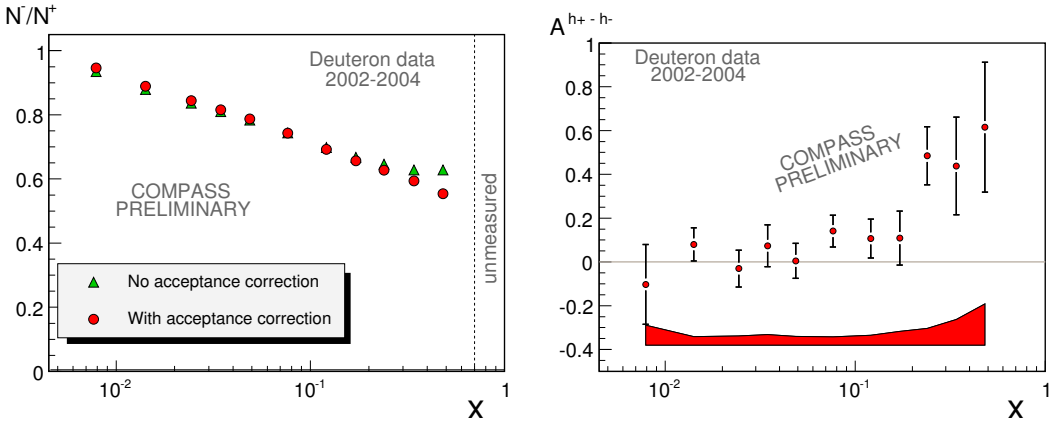

Figure 1: Left: The hadron number ratio N^-/N^+ and the same ratio corrected for the acceptance which represents $\sigma^{h^-}/\sigma^{h^+}$. Right: Difference asymmetry $A^{h^+-h^-}$.

The ratio of cross sections for negative and positive hadrons, r, depends on the event kinematics and could, in principle, be measured in unpolarized experiments. In practice, it will be obtained from the hadron number ratio N^-/N^+ corrected by the ratio of their acceptances a^-/a^+.

Since the deuteron is an isoscalar target we can not distinguish between up and down quarks. Nevertheless having measured the first moment of $\Delta u_v(x)+\Delta d_v(x)$ and combining its value with axial charges a_0 and a_8 the information about the symmetry of sea quark distributions can be extracted. Since $\Delta s + \Delta\bar{s} = \frac{1}{3}(a_0 - a_8)$ one can show that

$$\Delta\bar{u} + \Delta\bar{d} = (\Delta s + \Delta\bar{s}) + \frac{1}{2}(a_8 - \Gamma_v), \quad \text{where} \quad \Gamma_v = \int_0^1 (\Delta u_v(x) + \Delta d_v(x))dx. \tag{4}$$

The $SU(3)_f$ symmetric sea ($\Delta\bar{u} = \Delta\bar{d} = \Delta s = \Delta\bar{s}$) will obviously lead to Γ_v=a_8. In contrast, if measurements give $\Gamma_v = a_8 + 2(\Delta s + \Delta\bar{s})$ it will point to a strong asymmetry for the first moments of light sea quarks $\Delta\bar{u} = -\Delta\bar{d}$.

2 Extraction of the asymmetry

In the analysis data collected during the years 2002–2004 have been used. We require for all events to have a reconstructed primary interaction vertex defined by the incoming and the scattered muons. The energy of the beam muon is constrained to be in the interval $140 < E_\mu < 180$ GeV. To equalize fluxes through the two target cells it is required for the trajectory of the incoming muon to cross both cells. The kinematic region is defined by cuts on the photon virtuality Q^2 and the fractional energy y transfered from the beam muon to the virtual photon. The requirement $Q^2 > 1\,\mathrm{GeV}^2$ selects the region of DIS. The cut $y > 0.1$ removes events which are problematic from reconstruction point of view due to a small energy transfer. The region which is the most affected by radiative corrections is eliminated with the cut $y < 0.9$. At low x (high W), where cross-sections of positive and negative hadrons are approximately equal, the statistical error of $A^{h^+-h^-}$ increases drastically. Due to this

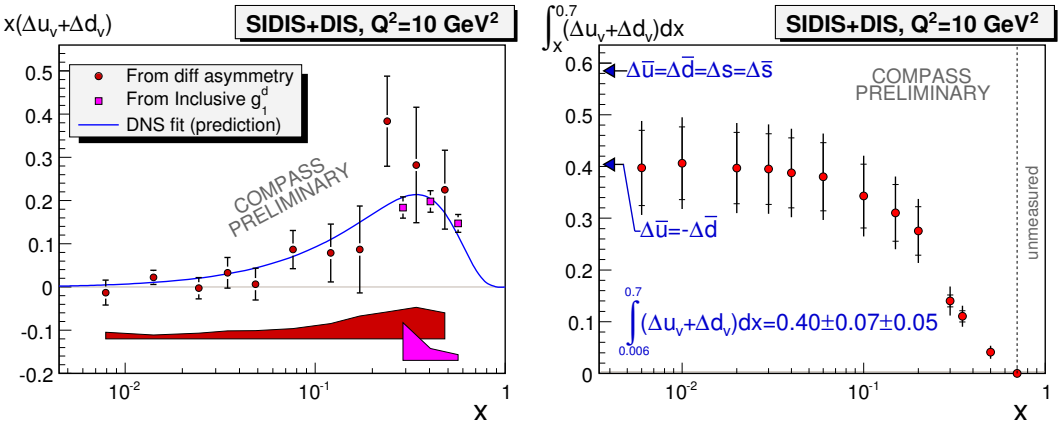

Figure 2: Left: Polarized valence quark distribution $x(\Delta u_v{+}\Delta d_v)$ evolved to $Q^2 = 10\,\mathrm{GeV}^2$ according to the DNS fit at LO [8]. The line shows the prediction from the fit. Right: Corresponding integral of $\Delta u_v(x){+}\Delta d_v(x)$ as the function of the low x limit of integration.

reason we consider only $x > 0.006$. For hadron tracks coming from the primary vertex the cut $z > 0.2$ is applied to select the current fragmentation region. Hadron identification is not used. The resulting sample contains 30 and 25 millions of positive and negative hadrons, respectively.

The contributions to the systematic error from the target and beam polarizations, the dilution and depolarization factors amount to 8% of the asymmetry value when added in quadrature. The upper limit of the false asymmetry which could be generated by instabilities of the spectrometer components was evaluated as a fraction of statistical error: $\sigma_{false} < 0.5\sigma_{stat}$. The asymmetry $A^{h^+-h^-}$ with its statistical and systematic errors is shown in Fig. 1.

3 Extraction of $\Delta u_v{+}\Delta d_v$ and its first moment

The values of $\Delta u_v{+}\Delta d_v$ are obtained by multiplying $A^{h^+-h^-}$ by the unpolarized valence distribution of MRST 2004 at LO [7]. Corrections for the deuteron D-state contribution and for the fact that the unpolarized parton distributions originates from F_2, in which $R = \sigma_L/\sigma_T$ was different from zero, are applied

$$\Delta u_v + \Delta d_v = \frac{u_v + d_v}{(1 + R(x, Q^2))(1 - 1.5\omega_D)} A^{h^+-h^-}. \qquad (5)$$

The evaluation of the first moment, Γ_v, requires the evolution of all $\Delta u_v(x){+}\Delta d_v(x)$ points to a common Q^2. This is done by using the DNS parametrization in LO [8] which is based on the global QCD analysis of all DIS g_1 data prior to COMPASS as well as the SIDIS data from SMC and HERMES. The parametrization corresponding to KKP fragmentation functions was used. The resulting distribution at $Q^2{=}10\,\mathrm{GeV}^2$ is shown in Fig. 2. A good agreement of the curve with the COMPASS points illustrates the consistency between the three experiments.

For $x > 0.3$ the unpolarized sea contribution to F_2 practically vanishes. Due to positivity conditions $|\Delta q| < q$ the polarized sea contribution to the spin of the nucleon also can be

	x-range	Q^2 GeV^2	$\Delta u_v + \Delta d_v$		$\Delta\bar{u} + \Delta d$	
			Value of the exper.	DNS	Value of the exper.	DNS
SMC 98	0.003–0.7	10	$0.26 \pm 0.21 \pm 0.11$	0.386	$0.02 \pm 0.08 \pm 0.06$	-0.009
HERMES 05	0.023–0.6	2.5	$0.43 \pm 0.07 \pm 0.06$	0.363	$-0.06 \pm 0.04 \pm 0.03$	-0.005
COMPASS	0.006–0.7	10	$0.40 \pm 0.07 \pm 0.05$	0.385	$0.0 \pm 0.04 \pm 0.03$	-0.007

Table 1: Estimates of the first moments $\Delta u_v + \Delta d_v$ and $\Delta\bar{u} + \Delta\bar{d}$ from the SMC [3], HERMES [4], COMPASS data and also from the DNS fit at LO [8].

neglected. It allows to replace at LO Eq. (5) by

$$\Delta u_v + \Delta d_v \;=\; \frac{36}{5}\frac{g_1^d(x,Q^2)}{(1-1.5\omega_D)} - \Big(2(\Delta\bar{u} + \Delta\bar{d}) + \frac{2}{5}(\Delta s + \Delta\bar{s})\Big) \tag{6}$$

which gives a much more precise evaluation of $\Delta u_v + \Delta d_v$ at high x. In the calculation we omit the second term of the right side of this equation. However it is used to evaluate the systematic error. The values of g_1^d from [9] were used. In total, we obtain

$$\Gamma_v(0.006 < x < 0.7)\Big|_{\mathrm{Q^2=10\ GeV^2}} = 0.40 \pm 0.07(\mathrm{stat.}) \pm 0.05(\mathrm{syst.}), \tag{7}$$

which is 2σ below the value corresponding to a flavor symmetric sea and very close to the value expected for $\Delta\overline{u} = -\Delta\overline{d}$ (see Eq. (4) where $\Delta s + \Delta\bar{s}$ is taken from [9]). The comparison with first moments obtained with results of SMC and HERMES can be found in Tab. 1.

As one can judge from Fig. 2 the integral is practically constant at low x. Thus the low x contribution to Γ_v is expected to be negligible. The contribution to Γ_v for $x > 0.7$ estimated with the LO DNS parametrization is 0.004.

4 Conclusion

A first LO evaluation of the polarized valence quark distribution $\Delta u_v(x) + \Delta d_v(x)$ from the COMPASS deuteron data is presented. The data were collected by COMPASS in the years 2002–2004 and cover the range $1 < Q^2 < 100$ GeV^2 and $0.006 < x < 0.7$. The analysis was based on the difference asymmetry approach. It leads to the first moment of $\Delta u_v + \Delta d_v$: $0.40 \pm 0.07(\mathrm{stat.}) \pm 0.05(\mathrm{syst.})$ which favors the "asymmetric" light sea scenario $\Delta\overline{u} = -\Delta\overline{d}$ as compared to the "symmetric" one $\Delta\overline{u} = \Delta\overline{d} = \Delta s = \Delta\bar{s}$.

References

[1] Slides:
`http://indico.cern.ch/contributionDisplay.py?contribId=144&sessionId=4&confId=9499`
[2] (SMC) B. Adeva *et al.,* Phys. Lett. **B369** 93 (1996).
[3] (SMC) B. Adeva *et al.,* Phys. Lett. **B420** 180 (1998).
[4] (HERMES) A.Airapetian *et al.,* Phys. Rev. **D71** 012003 (2005).
[5] L.L. Frankfurt *et al.,* Phys. Lett. **B230** 141 (1989).
[6] A.N. Sissakian, O.Yu. Shevchenko and O.N. Ivanov, Phys. Rev. **D73** 094026 (2006).
[7] A.D.Martin, W.J.Stirling and R.S.Thorne, Phys. Lett. **B636** 259 (2006).
[8] D. de Florian, G.A.Navarro and R.Sassot, Phys. Rev. **D71** 094018 (2005).
[9] (COMPASS) V.Yu.Alexakhin *et al.*, Phys. Lett. **B647** 8 (2007).

Spin Structure Function g_1 at Small x and Arbitrary Q^2

B.I. Ermolaev[1] *, M. Greco[2] and S.I. Troyan[3]

1- Ioffe Physico-Technical Institute - Laboratory of Astrophysics and Cosmic rays
194021 St.Petersburg - Russia

2- University Rome III - Department of Physics and INFN
Rome - Italy

3- St.Petersburg Institute of Nuclear Physics - Department of Theoretical Physics
188300 Gatchina - Russia

The Standard Approach (SA) for the description of the structure function g_1 combines the DGLAP evolution equations with the standard fits for the initial parton densities. The DGLAP equations describe the region of large Q^2 and large x, so there are no theoretical grounds to exploit them at small x. In practice, extrapolation of DGLAP into the region of small x is done by complementing DGLAP with ad hoc, singular ($\sim x^{-a}$) phenomenological fits for the initial parton densities. The factors x^{-a} are wrongly believed to be of non-perturbative origin. Actually, they mimic the summation of logs of x and should not be included in the fits when the summation is accounted for. Contrary to SA, the summation of logarithms of x is a straightforward and natural way to describe g_1 in the small-x region. This approach can be used both at large and small Q^2 where DGLAP cannot be used by definition. Confronting this approach and SA shows that the singular initial parton densities and the power Q^2-corrections (or at least a sizable part of them) do not describe real physical phenomena but they are just artifacts caused by extrapolating DGLAP into the small-x region.

1 Introduction

The *Standard Approach* (**SA**) for description of the structure function g_1 involves the DGLAP evolution equations[2] and standard fits[3] for the initial parton densities δq and δg. The fits are defined from phenomenological considerations at $x \sim 1$ and $Q^2 = \mu^2 \sim 1$ GeV^2. The DGLAP equations are one-dimensional, and describe the Q^2 -evolution only, converting δq and δg into the evolved distributions Δq and Δg. They represent g_1 at the region **A**:

$$\mathbf{A:} \quad Q^2 \gg \mu^2 \ , \qquad x \lesssim 1 \ . \tag{1}$$

The x -evolution is supposed to come by convoluting Δq and Δg with the coefficient functions C_{DGLAP}. However, in the leading order $C^{LO}_{DGLAP} = 1$ and the NLO corrections account for one- or two- loop contributions and neglect higher loops. It is the correct approximation in the region **A** but becomes false in the region **B:**

$$\mathbf{B:} \quad Q^2 \gg \mu^2 \ , \qquad x \ll 1 \tag{2}$$

where contributions $\sim \ln^k(1/x)$ are large and should be accounted for to all orders in α_s. C_{DGLAP} do no include the *total summation of leading logarithms of* x (**LL**), so there are no theoretical grounds to exploit DGLAP at small x. However, **SA** extrapolates DGLAP

*B.I. Ermolaev is grateful to the Organizing Committee of the workshop DIS2007 for financial support of his participation in the workshop.

into the region **B**, invoking special fits for δq and δg. The general structure of such fits (see Refs. [3]) is as follows:

$$\delta q = N x^{-a} \varphi(x) \tag{3}$$

where N is a normalization constant; $a > 0$, so x^{-a} is singular when $x \to 0$, and $\varphi(x)$ is regular in x at $x \to 0$. As we showed in Ref. [4], the factor x^{-a} in Eq. (3) just mimics the result of **LL** performed in Refs [5, 6]. Similarly to **LL**, the factor x^{-a} provides the steep rise to g_1 at small x and sets the Regge asymptotics for g_1 at $x \to 0$, with the exponent a being the intercept. The presence of this factor is very important for extrapolating DGLAP into the region **B:** When the factor x^{-a} is dropped from Eq. (3), DGLAP stops to work at $x \lesssim 0.05$ (see Ref. [4] for detail). Accounting for **LL** is beyond the DGLAP framework because **LL** come from the phase space region not included in the DGLAP ordering. Indeed the DGLAP -ordering is

$$\mu^2 < k_{1\perp}^2 < k_{2\perp}^2 < ... < Q^2 \tag{4}$$

for the ladder partons. **LL** can be accounted only when the ordering Eq. (4) is lifted and all $k_{i\perp}$ obey

$$\mu^2 < k_{i\perp}^2 < (p+q)^2 \approx (1-x)2(pq) \approx 2(pq) \tag{5}$$

at small x. Replacing Eq. (4) by Eq. (5) leads inevitably to the change of the DGLAP parametrization

$$\alpha_s^{DGLAP} = \alpha_s(Q^2) \tag{6}$$

by the alternative parametrization of α_s obtained in Ref. [7] and used in Refs. [5, 6] in order to find explicit expressions accounting for **LL** for g_1 in the region **B**. Obviously, those expressions require fits for the initial parton densities without singular factors x^{-a}. Let us note that the replacement of Eq. (4) by Eq. (5) brings a more involved μ -dependence to g_1. Indeed, Eq. (4) makes the contributions of gluon ladder rungs to be infrared (IR) stable, with μ acting as a IR cut-off for the lowest rung and $k_{i\perp}$ playing the role of the IR cut-off for the $i+1$-rung. In contrast, Eq. (5) implies that μ acts as the IR cut-off for every rung.

Besides the regions **A** and **B**, it is also necessary to know g_1 in the region **C**:

$$\textbf{C:} \quad Q^2 < \mu^2 \ , \qquad x \ll 1 \ . \tag{7}$$

This region is studied experimentally by the COMPASS collaboration. Obviously, DGLAP cannot be exploited here. Alternatively, in Refs. [8, 9] we obtained expressions for g_1 in the region **C**. In particular, in Ref. [8] we showed that g_1 practically does not depend on x at small x, even at $x \ll 1$. Instead, it depends on the total invariant energy $2(pq)$. Experimental investigation of this dependence is extremely interesting because according to our results g_1, being positive at small $2(pq)$, can turn negative at greater values of this variable. The position of the turning point is sensitive to the ratio between the initial quark and gluon densities, so its experimental detection would enable to estimate this ratio. In Ref. [9] we have analyzed the power contributions $\sim 1/(Q^2)^k$ to g_1 usually attributed to higher twists. We have proved that a great amount of those corrections have a simple perturbative origin and have summed them. Therefore, the genuine impact of higher twists can be estimated only after accounting for the perturbative Q^2 -corrections.

2 Description of g_1 in the regions B and C

The total sum of the double-logarithms (DL) and single-logarithms of x in the region **B** was done in Refs. [5, 6]. In particular, the non-singlet component, g_1^{NS} of g_1 is

$$g_1^{NS}(x,Q^2) = (e_q^2/2)\int_{-\imath\infty}^{\imath\infty}\frac{d\omega}{2\pi\imath}(1/x)^\omega C_{NS}(\omega)\delta q(\omega)\exp\left(H_{NS}(\omega)\ln(Q^2/\mu^2)\right)\,, \qquad (8)$$

with the new coefficient function C_{NS} and new anomalous dimension H_{NS}. H_S and C_{NS} account for DL and SL contributions to all orders in α_s and depend on the IR cut-off μ. As is shown in Refs. [5, 6], there exists an optimal scale for fixing μ: $\mu \approx 1$ Gev for g_1^{NS} and $\mu \approx 5$ GeV for g_1^S. The arguments in favor of existence of the optimal scale were given in Ref. [9]. Eq. (8) predicts that g_1 has the power behavior in x and Q^2 when $x \to 0$:

$$g_1^{NS} \sim \left(Q^2/x^2\right)^{\Delta_{NS}/2}\,, \qquad g_1^S \sim \left(Q^2/x^2\right)^{\Delta_S/2} \qquad (9)$$

where the non-singlet and singlet intercepts are $\Delta_{NS} = 0.42$ and $\Delta_S = 0.86$ respectively. The asymptotic expressions (9) should be used with great care: According to Ref. [4], Eq. (9) should not be used at $x \gtrsim 10^{-6}$. So, Eq. (8) should be used instead of Eq. (9) in the region of small x so far available. Expressions accounting **LL** for the singlet g_1 in the region **B** were obtained in Ref. [6]. They are more complicated because involve two coefficient functions and four anomalous dimensions.

Region **C** is defined in Eq. (7). It includes small Q^2, so there are not large contributions $\ln^k(Q^2/\mu^2)$ in this region. In other words, the DGLAP ordering of Eq. (4) does not make sense in the region **C** , which makes impossible exploiting DGLAP here. In contrast, Eq. (4) is not sensitive to the value of Q^2 and therefore **LL** does make sense in the region **C**. In Ref. [8] we suggested that the shift

$$Q^2 \to Q^2 + \mu^2 \qquad (10)$$

allows to extrapolate our previous results obtained in the region **B** to the region **C**. Then in Ref. [9] we proved this suggestion. Therefore, applying Eq. (10) to g_1^{NS} leads to the following expression for g_1^{NS} valid simultaneously in the regions **B** and **C**:

$$g_1^{NS}(x+z,Q^2) = (e_q^2/2)\int_{-\imath\infty}^{\imath\infty}\frac{d\omega}{2\pi\imath}\Big(\frac{1}{x+z}\Big)^\omega C_{NS}(\omega)\delta q(\omega)\exp\left(H_{NS}(\omega)\ln\left((Q^2+\mu^2)/\mu^2\right)\right)\,, \qquad (11)$$

where $z = \mu^2/2(pq)$. Obviously, Eq. (11) reproduces Eq. (8) in the region **B**. Expression for g_1^S looks similarly but more complicated, see Refs. [8, 9] for detail.

3 Prediction for the COMPASS experiments

The COMPASS collaboration now measures the singlet g_1^S at $x \sim 10^{-3}$ and $Q^2 \lesssim 1$ GeV^2, i.e. in the kinematic region beyond the reach of DGLAP. However, our formulae for g_1^{NS} and g_1^S obtained in Refs. [8, 9] cover this region. Although expressions for singlet and non-singlet g_1 are different, with formulae for the singlet being much more complicated, we can explain the essence of our approach, using Eq. (11) as an illustration. According to results of [6],

$\mu \approx 5$ GeV for g_1^S, so in the COMPASS experiment $Q^2 \ll \mu^2$. It means, $\ln^k(Q^2+\mu^2)$ can be expanded into series in Q^2/μ^2, with the first term independent of Q^2:

$$g_1^S(x+z,Q^2,\mu^2) = g_1^S(z,\mu^2) + \sum_{k=1}(Q^2/\mu^2)^k E_k(z) \tag{12}$$

where $E_k(z)$ account for **LL** in z and

$$g_1^S(z,\mu^2) = (< e_q^2/2 >) \int_{-\imath\infty}^{\imath\infty} \frac{d\omega}{2\pi\imath} (1/z)^\omega \left[C_S^q(\omega)\delta q(\omega) + C_S^g(\omega)\delta g(\omega)\right] , \tag{13}$$

so that $\delta q(\omega)$ and $\delta g(\omega)$ are the initial quark and gluon densities respectively and $C_S^{q,g}$ are the singlet coefficient functions. Explicit expressions for $C_S^{q,g}$ are given in Refs. [6, 8]. The initial parton densities can be approximated by constants: $\delta q \approx N_q$ and $\delta g \approx N_g$, so

$$g_1(Q^2 \ll \mu^2) \approx (< e_q^2 > /2) N_q G_1(z) , \qquad G_1 = \int_{-\imath\infty}^{\imath\infty} \frac{d\omega}{2\pi\imath} (1/z)^\omega \left[C_S^q + (N_g/N_q C_S^g)\right] . \tag{14}$$

The results for G_1 for different values of the ratio $r = N_g/N_q$ are shown in Fig. 1.

References

[1] Slides:
http://indico.cern.ch/contributionDisplay.py?contribId=148&sessionId=4&confId=9499

[2] G. Altarelli and G. Parisi, Nucl. Phys. **B126** 297 (1977);
V.N. Gribov and L.N. Lipatov, Sov. J. Nucl. Phys. **15** 438 (1972);
L.N.Lipatov, Sov. J. Nucl. Phys. **20** 95 (1972);
Yu.L. Dokshitzer, Sov. Phys. JETP **46** 641 (1977).

[3] G. Altarelli, R.D. Ball, S. Forte and G. Ridolfi, Nucl. Phys. **B496** 337 (1997);
Acta Phys. Polon. **B29** 1145 (1998);
E. Leader, A.V. Sidorov and D.B. Stamenov, Phys. Rev. **D73** 034023 (2006);
J. Blumlein, H. Botcher, Nucl. Phys. **B636** 225 (2002);
M. Hirai at al. Phys. Rev. **D69** 054021 (2004).

[4] B.I. Ermolaev, M. Greco and S.I. Troyan, Phys. Lett. **B622** 93 (2005).

[5] B.I. Ermolaev, M. Greco and S.I. Troyan, Nucl.Phys. **B594** 71 (2001); **B571** 137 (2000).

[6] B.I. Ermolaev, M. Greco and S.I. Troyan, Phys.Lett. **B579** 2004 (321).

[7] B.I. Ermolaev, M. Greco and S.I. Troyan, Phys.Lett. **B 522** 57 (2001).

[8] B.I. Ermolaev, M. Greco and S.I. Troyan, Eur.Phys.J **C50** 823 (2007);
arXiv: hep-ph/0605133 (2006).

[9] B.I. Ermolaev, M. Greco and S.I. Troyan, arXiv: hep-ph/0607024 (2006).

[10] B.I. Ermolaev, M. Greco and S.I. Troyan, arXiv: hep-ph/0704.0341 (2007).

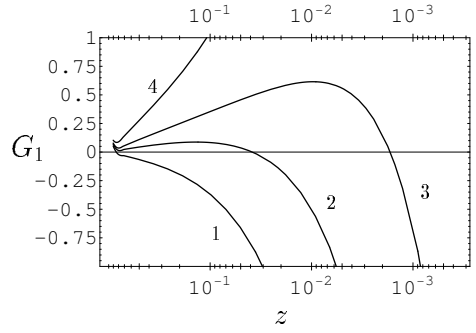

Figure 1: G_1 evolution with decreasing $z = \mu^2/2(pq)$ for different values of ratio $r = \delta g/\delta q$: curve 1 - for $r = 0$, curve 2 - for $r = -5$, curve 3 -for $r = -8$ and curve 4 -for $r = -15$.

Fragmentation Function Measurements at Belle

Akio Ogawa[1], Matthias Grosse Perdekamp[2] and Ralf Seidl[1,2]

1- RIKEN Brookhave Research Center
Upton, NY 11973-5000, USA

2- University of Illinois at Urbana-Champaign
1110 W Green Street, Urbana, IL 61801, USA

In order to measure the quark transverse spin distribution of the nucleon one has to combine it with another chiral-odd object. This can for example be the Collins fragmentation function or the Interference fragmentation function. At the KEKB e^+e^- collider the Belle experiment has published the first measurement of the Collins fragmentation function with a data sample of 29 fb^{-1}. In an updated analysis a data sample of 547 fb^{-1} has been analyzed reducing the statistical errors significantly.

Introduction

At leading twist 3 quark distribution functions (DF) in the nucleon are present; the experimentally well known unpolarized quark DF, the experimentally less known quark helicity DF and the so far undetermined transversity DF. The latter cannot be measured in inclusive DIS due to its chiral-odd nature, since all possible interactions are chiral-even for nearly massless quarks. Therefore one needs an additional chiral-odd function in the cross section to access transversity. This can be achieved either by an anti quark transversity DF in double transversely polarized Drell-Yan processes or, alternatively, one can have a chiral-odd fragmentation function in semi-inclusive deep inelastic scattering (SIDIS) or hadroproduction. The most prominent chiral-odd fragmentation function is the Collinsfunction [2], which measures the azimuthal distribution of an unpolarized hadron around the axis of the transversely polarized quark's momentum. A second chiral-odd fragmentation function is the Interference fragmentation function [3], where one meeasures the azimuthal distribution of a hadron pair around the quark axis. In SIDIS nonzero Collins asymmetries have been measured [4], but in order to extract transversity one has to obtain the fragmentation function separately. This can be acchieved in a e^+e^- collider.

1 The Belle experiment

The Belle [5] experiment at the asymmetric e^+e^- collider KEKB at Tsukuba, Japan, is mainly dedicated to the study of CP violation in B meson decays. Its center of mass energy is tuned to the $\Upsilon(4S)$ resonance at $\sqrt{s} = 10.58$ GeV. Part of the data was also recorded 60 MeV below the resonance. Originally only these off-resonance events were studied in order to measure spin dependent fragmentation functions (FF). Since one selects only two-jet-like events requiring a thrust value larger than 0.8 only less than 2% of the B events remain in the on-resonance data sample. Therefore, it is possible to include also that data sample in the analsys. In total an integrated luminosity of 547 fb^{-1} has been analyzed. The aerogel Čerenkov counter, time-of-flight detector and the central drift chamber enable a good particle identification and tracking, which is crucial for these measurements. Using the information from the silicon vertex detector, one selects tracks originating from the interaction region and

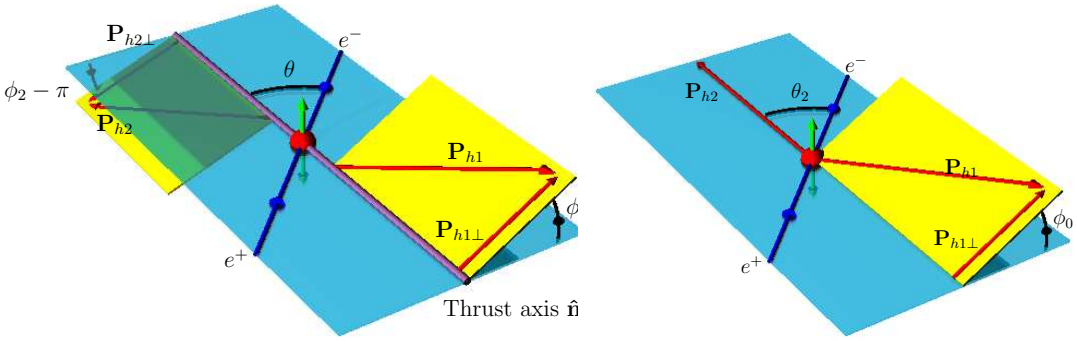

Figure 1: Description of the azimuthal angles ϕ_0, ϕ_1 and ϕ_2 relative to the scattering plane defined by the lepton axis and either the thrust axis $\hat{n}$ or the momentum of the 2^{nd} hadron P_{h2}.

thus reducing the contribution of hadrons from heavy meson decays. To reduce the amount of hard gluon radiative events, a thrust value larger of 0.8 and a virtual photon momentum in the two-hadron center-of-mass system below 3.5 GeV is required. In such a 2-jet topology the thrust axis can be used as an approximation of the original quark direction. We also require that the fractional energy $z \stackrel{CMS}{=} 2E_h/Q > 0.2$ in order to significantly reduce the contribution of pions arising from the vector meson decays or of those assigned to a wrong hemisphere.

Collins FF

The Collins effect occurs in the fragmentation of a transversely polarized quark with polarization S_q and 3-momentum k into an unpolarized hadron of transverse momentum $P_{h\perp}$ with respect to the original quark direction. According to the Trento convention [6] the number density for finding an unpolarized hadron h produced from a transversely polarized quark q is defined as:

$$D_{hq^\uparrow}(z, P_{h\perp}) = D_1^q(z, P_{h\perp}^2) + H_1^{\perp q}(z, P_{h\perp}^2)\frac{(\hat{\mathbf{k}} \times \mathbf{P}_{h\perp}) \cdot \mathbf{S}_q}{zM_h}, \tag{1}$$

where the first term describes the unpolarized FF $D_1^q(z, P_{h\perp})$, with $z \stackrel{CMS}{=} \frac{2E_h}{Q}$ being the fractional energy the hadron carries relative to half of the center of mass system (CMS) energy Q. The second term, containing the Collins function $H_1^{q\perp}(z, P_{h\perp}^2)$, depends on the spin of the quark and thus leads to an asymmetry as it changes sign under flipping the quark spin. The vector product can accordingly be described by a $\sin(\phi)$ modulation, where ϕ is the azimuthal angle spanned by the transverse momentum and the plane defined by the quark spin and its momentum. In e^+e^- hadron production the Collins effect can be observed by a combined measurement of a quark and an anti quark fragmentation. Combining two hadrons from different hemispheres in jetlike events, with azimuthal angles ϕ_1 and ϕ_2 as defined in Fig. 1, would result in a $\cos(\phi_1 + \phi_2)$ modulation.

In the CMS these azimuthal angles are defined between the transverse component of the hadron momenta with regard to the thrust axis $\hat{n}$ and the plane spanned by the lepton momenta and $\hat{n}$. The comparison of the thrust axis calculations using reconstructed and generated tracks in the MC sample shows an average angular separation between the two of 75 mrad with a a root mean square of 74 mrad. Due to that small biases in one of the reconstruction methods used could arise and were studied as discussed later. Following reference [7] one either computes the azimuthal angles of each pion relative to the thrust axis which results in a $\cos(\phi_1 + \phi_2)$ modulation or one calculates the azimuthal angle relative to the axis defined by the 2^{nd} pion which results in a $\cos(2\phi_0)$ modulation. While the first method directly accesses moments of the Collins functions, the second method contains a convolution integral of the Collins FF over possible transverse momenta of the hadrons.

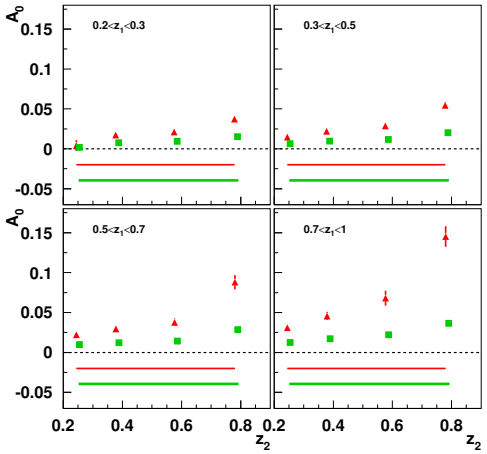

Figure 2: Light quark (uds) A_0 asymmetries as a function of z_2 for the 4 z_1 bins. The UL data is described by the triangles, its systematic error being the top error band while the UC data is described by the squares and its systematics by the lower error band.

1.1 Measured asymmetries

We measure the azimuthal asymmetries $N(2\phi)/\langle N_0 \rangle$, where $N(2\phi)$ denotes the number of hadron pairs in bins of either $2\phi_0$ or $\phi_1 + \phi_2$ and $\langle N_0 \rangle$ is the average number of hadron pairs in that particular bin. The main backgrounds, producing similar azimuthal asymmetries as the Collins effect, are the radiation of soft gluons and acceptance effects. The gluonic contribution is proportional to the unpolarized FF and is independent of the charge of the hadrons. Consequently taking the ratio of the normalized distributions for unlike-sign over like-sign pairs the gluonic distributions cancel in the leading order:

$$\begin{aligned} \frac{R_\alpha^U}{R_\alpha^L} &:= \frac{\frac{N(2\phi)}{\langle N_0 \rangle}|_{Unlikesign}}{\frac{N(2\phi)}{\langle N_0 \rangle}|_{Likesign}} \\ &\approx 1 + \frac{\sin^2\theta}{1 + cos^2\theta} \left(F\left(\frac{H_1^{\perp,fav}}{D_1^{fav}}, \frac{H_1^{\perp,dis}}{D_1^{dis}} \right) + \mathcal{O}f(Q_T, \alpha_S)^2 \right) cos(2\phi) \quad , \end{aligned} \tag{2}$$

where θ is either the angle between the colliding leptons and the produced hadron or the thrust axis for methods $\alpha = 0, 12$, respectively. Favored and disfavored FF (fav,dis) describe the fragmentation of a light quark into a pion of same or opposite charge sign. Obviously also acceptance effects cancel in the double ratios. The latter are fit by the sum of a constant term and a cosine modulation, $B_\alpha + A_\alpha \cos(2\phi)$. The double ratios of unlike sign over like sign pairs showed the existence of the Collins effect and gave a hint about the overall

magnitude [8]. As suggested in [9], measuring also double ratios containing any combination of charged pion pairs reveals additional information on the ratio of the favored and disfavored Collins functions. The A_0 results with the updated statistics are shown as function of the fractional energies z_1 and z_2 in Fig.2. The A_{12} results are similar and all are consistent with the previously published data. The data has been corrected for the contribution of charmed hadron decays. A nonzero asymmetry is visible for both double ratios, and the U/C are about 40% of the U/L results. The data shows a rising behavior with rising fractional energy z for both results. Several systematic cross-checks of the analysis method were performed and the differences in the results are quoted as systematic uncertainties: Instead of double ratios we used the subtraction method for the unlike from the like sign or charged pion asymmetries; the constant fit to the double ratios obtained in MC (without a Collins contribution) together with its statistical error and a similar fit to double ratios of positively charged over negatively charged pion pair data were assigned as systematic error. The differences to the results when fitting the double ratios also with higher order azimuthal modulations were added to the systematic errors. All contributions to the systematic errors were added in quadrature. The presented measurement represents a substantial update of the data sample used to obtain the first evidence of the Collins effect and will help to disentangle the favored to disfavored Collins function ratio.

References

[1] Slides:
`http://indico.cern.ch/contributionDisplay.py?contribId=149&sessionId=4&confId=9499`

[2] J. C. Collins: Nucl. Phys **B396**(1993):161.

[3] R. L. Jaffe, X. m. Jin and J. a. Tang: Phys. Rev. **D57**(1998):5920

[4] A. Airapetian et al.(Hermes) Phys. Rev. Lett.**94**(2005)012002.

[5] A. Abashian et al.(Belle): Nucl. Instrum. Meth.**A479**(2002)117.

[6] A. Bacchetta, U. D'Alesio, M. Diehl, A. Miller: Phys. Rev. **D70**(2004):117504.

[7] D. Boer, R. Jakob, P. J. Mulders: Phys. Let. **B 424**(1998):143.

[8] R. Seidl, et al.(Belle): Phys. Rev. Lett. **96**(2006):232002.

[9] A. Efremov, K. Goeke and P. Schweitzer: [arXiv:hep-ph/0603054].

HERMES Measurements of Collins and Sivers Asymmetries from a Transversely Polarised Hydrogen Target

Markus Diefenthaler (on behalf of the HERMES collaboration)

Friedrich-Alexander-Universität Erlangen-Nürnberg - Physikalisches Institut II
Erwin-Rommel-Straße 1, 91058 Erlangen - Germany

Azimuthal single-spin asymmetries (SSA) in semi-inclusive electroproduction of π-mesons and charged K-mesons in deep-inelastic scattering of positrons and electrons on a transversely polarised hydrogen target were observed. Significant SSA amplitudes for both the Collins and the Sivers mechanism are presented for the full data set recorded with transverse target polarisation at the HERMES experiment.

1 Contribution

In 2005 the HERMES collaboration published first evidence for azimuthal single-spin asymmetries (SSA) in the semi-inclusive production of charged pions on a transversely polarised hydrogen target [2]. Significant signals for both the Collins [3] and Sivers mechanisms [4] were observed in data recorded during the 2002–2003 running period of the HERMES experiment. Below we present a preliminary analysis of these data combined with additional data taken in the years 2003–2005; i.e. an preliminary analysis of the full data set with transverse target polarisation [1]. All data were recorded at a beam energy of 27.6 GeV using a transversely nuclear-polarised hydrogen-target internal to the HERA storage ring at DESY. The HERMES dual-radiator ring-imaging Čerenkov counter allows full $\pi^{\pm}$, $K^{\pm}$, p separation for all particle momenta within the range $2\,\mathrm{GeV} < \boldsymbol{P}_{\mathrm{h}} < 15\,\mathrm{GeV}$. Therefore, a preliminary analysis of SSA in the electroproduction of charged kaons on a transversely polarised target is also presented. In addition the measurement is accompanied by an preliminary analysis of reconstructed neutral-pion events.

At leading twist, the longitudinal momentum and spin of the quarks inside the nucleon are described by three parton distribution functions: the well-known momentum distribution $q\left(x,Q^2\right)$, the known helicity distribution $\Delta q\left(x,Q^2\right)$ [5] and the (experimentally) unknown transversity distribution $\delta q\left(x,Q^2\right)$ [6, 7, 8, 9]. In the helicity basis, transversity is related to a quark-nucleon forward scattering amplitude involving helicity flip of both nucleon and quark ($N^{\Rightarrow}q^{\leftarrow} \longrightarrow N^{\Leftarrow}q^{\rightarrow}$). As it is chiral-odd, transversity cannot be probed in inclusive deep-inelastic scattering (DIS). At HERMES transversity in conjunction with the chiral-odd Collins fragmentation function [3] is accessible in SSA in semi-inclusive DIS on a transversely polarised target (*Collins mechanism*). The Collins fragmentation function describes the correlation between the transverse polarisation of the struck quark and the transverse momentum $\boldsymbol{P}_{\mathrm{h}\perp}$ of the hadron produced. As it is also odd under naive time reversal (T-odd) it can produce a SSA, i.e. a left-right asymmetry in the momentum distribution of the produced hadrons in the plane transverse to the virtual photon direction.

The *Sivers mechanism* can also cause a SSA: The T-odd Sivers distribution function [4] describes the correlation between the transverse polarisation of the nucleon and the transverse momentum $\boldsymbol{p}_{\perp}$ of the quarks within. A non-zero Sivers mechanism provides

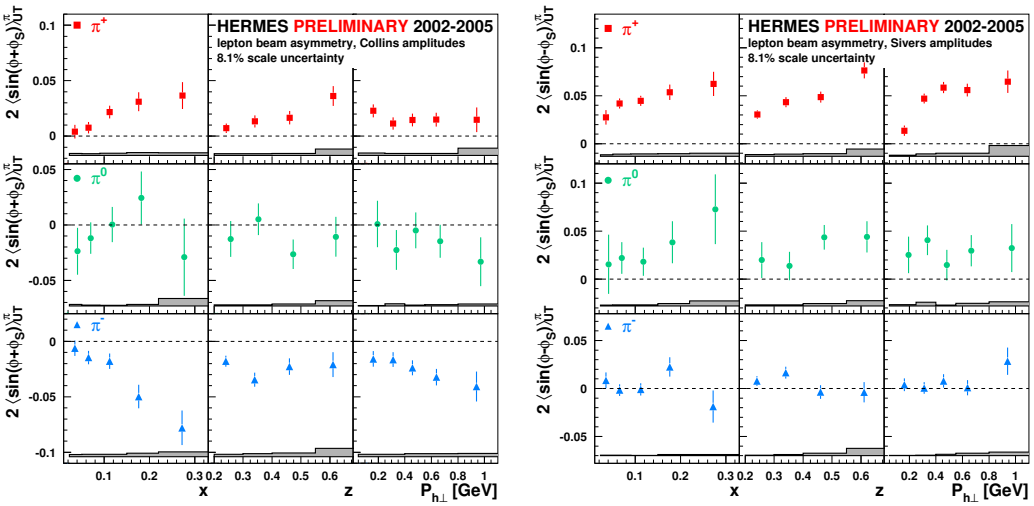

Figure 1: Collins amplitudes (left column) and Sivers amplitudes (right column) for π-mesons (as labelled) as function of x, z and $\boldsymbol{P}_{\mathrm{h}\perp}$. The error bands represent the maximal systematic uncertainty; the common overall 8.1% scaling uncertainty is due to the target polarisation uncertainty.

a non-zero Compton amplitude involving nucleon helicity flip without quark helicity flip ($N^{\Rightarrow}q^{\leftarrow} \longrightarrow N^{\Leftarrow}q^{\leftarrow}$), which must therefore involve orbital angular momentum of the quark inside the nucleon [10, 11].

With a transversely polarised target, the azimuthal angle ϕ_{S} of the target spin direction in the "$\Uparrow$" state is observable in addition to the azimuthal angle ϕ of the detected hadron. Both azimuthal angles are defined about the virtual-photon direction with respect to the lepton scattering plane. The additional degree of freedom ϕ_{S}, not available with a longitudinally polarised target, results in distinctive signatures: $\sin(\phi+\phi_{\mathrm{S}})$ for the Collins mechanisms and $\sin(\phi-\phi_{\mathrm{S}})$ for the Sivers mechanism [12].

The corresponding azimuthal amplitudes azimuthal amplitudes are extracted using maximum likelihood fits. The Collins amplitudes $\langle\sin(\phi+\phi_{\mathrm{S}})\rangle^{\mathrm{h}}_{\mathrm{UT}}$ and the Sivers mechanism $\langle\sin(\phi-\phi_{\mathrm{S}})\rangle^{\mathrm{h}}_{\mathrm{UT}}$ were extracted simultaneously to avoid cross-contamination. To allow for contribution from all theoretically possible Fourier modulations the terms for $\sin\phi_{\mathrm{S}}$, $\sin(2\phi-\phi_{\mathrm{S}})$ and $\sin(3\phi-\phi_{\mathrm{S}})$ have to be added in the probability density function F:

$$
\begin{aligned}
\mathrm{F}\left(2\langle\sin(\phi\pm\phi_S)\rangle^{\mathrm{h}}_{\mathrm{UT}},\ldots,\phi,\phi_S\right) = \frac{1}{2}\Big(1+P^z_\alpha\big(\;& 2\langle\sin(\phi+\phi_S)\rangle^{\mathrm{h}}_{\mathrm{UT}}\cdot\sin(\phi+\phi_S)+\\
& 2\langle\sin(\phi-\phi_S)\rangle^{\mathrm{h}}_{\mathrm{UT}}\cdot\sin(\phi-\phi_S)+\\
& 2\langle\sin(3\phi-\phi_S)\rangle^{\mathrm{h}}_{\mathrm{UT}}\cdot\sin(3\phi-\phi_S)+\\
& 2\langle\sin(2\phi-\phi_S)\rangle^{\mathrm{h}}_{\mathrm{UT}}\cdot\sin(2\phi-\phi_S)+\\
& 2\langle\sin\phi_S\rangle^{\mathrm{h}}_{\mathrm{UT}}\cdot\sin\phi_S\big)\Big)
\end{aligned}
$$

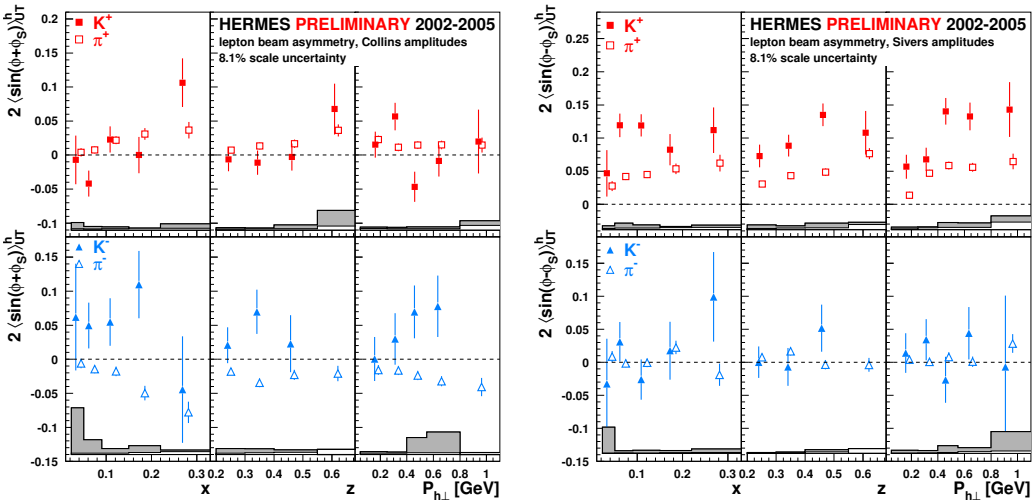

Figure 2: Collins amplitudes (left column) and Sivers amplitudes (right column) for charged kaons (closed symbols, as labelled) and charged pions (open symbols, as labelled) as function of x, z and $\boldsymbol{P}_{\mathrm{h}\perp}$. The error bands represent the maximal systematic uncertainty; the common overall 8.1% scaling uncertainty is due to the target polarisation uncertainty.

Here P_α^z denotes the degree of the target polarisation.

In Figures 1 and 2 the lepton-beam Collins and Sivers amplitudes as a function of x, z and $\boldsymbol{P}_{\mathrm{h}\perp}$ are shown. Semi-inclusive DIS events were selected subject to the kinematic requirements $Q^2 > 1\,\mathtt{GeV}^2$, $y < 0.95$, $W^2 > 10\,\mathtt{GeV}^2$, $2\,\mathtt{GeV} < \boldsymbol{P}_{\mathrm{h}} < 15\,\mathtt{GeV}$, $0.2 < z < 0.7$ and $\theta_{\gamma^*\mathrm{h}} > 0.02\,\mathtt{rad}$, where $\theta_{\gamma^*\mathrm{h}}$ is the angle between the direction of the virtual photon and the hadron. The selected ranges in x and $\boldsymbol{P}_{\mathrm{h}\perp}$ are $0.023 < x < 0.4$ and $0.05\mathtt{GeV} < \boldsymbol{P}_{\mathrm{h}\perp} < 2\mathtt{GeV}$. These preliminary results are based on ten times more statistics than that in the publication [2] and are consistent with the published result.

The Collins amplitude is positive for π^+, compatible with zero for π^0 and negative for π^-. Also, the magnitude of the π^- amplitude appears to be comparable or larger than the one for π^+. This leads to the conclusion that the disfavoured Collins fragmentation function has a substantial magnitude with an opposite sign compared to the favoured Collins fragmentation function. For charged kaons no statistically significant non-zero Collins amplitudes are found. However, the Collins amplitudes for K^+ are within statistical accuracy consistent to the π^+ amplitudes.

The significantly positive average Sivers amplitudes observed for π^+, π^0 and K^+ imply a non-vanishing orbital angular momentum of the quarks inside the nucleon. As the magnitude of the K^+ amplitude is the larger than the one for π^+, the sea quark contribution to the Sivers mechanism appears to be important. Thus the orbital angular momentum of anti-quarks could be significant and highly flavour dependent. For π^- and K^- the Sivers amplitudes are consistent with zero.

Isospin symmetry of π-mesons is fulfilled for the extracted Collins and Sivers amplitudes.

Although formally, the contribution to the SSA of π-mesons and K-mesons from the decay of exclusively produced vector mesons is a part of the semi-inclusive DIS cross section,

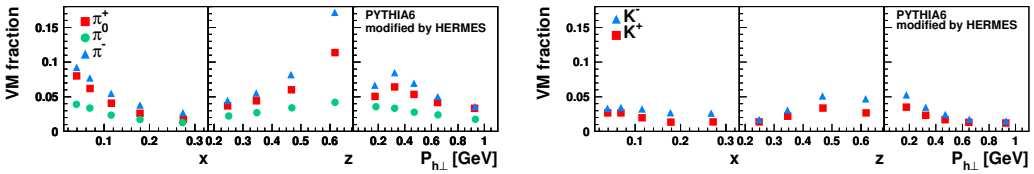

Figure 3: Simulated fraction of π-mesons (left column) and charged K-mesons originating from diffractive vector meson production and decay.

a too large contribution might contradict the assumptions of factorisation, i.e. summation over a larger number of contributing channels. As an indication, the simulated fraction of π-mesons and charged K-mesons originating from diffractive vector meson production and decay is shown in Figure 3

2 Acknowledgements

This work has been supported by the German Bundesministerium für Bildung und Forschung (BMBF) (contract nr. 06 ER 125I and 06 ER 143) and the European Community-Research Infrastructure Activity under the FP6 "Structuring the European Research Area" program (HadronPhysics I3, contract nr. RII3-CT-2004-506078).

3 Bibliography

References

[1] Slides: `http://indico.cern.ch/contributionDisplay.py?contribId=150&sessionId=4&confId=9499`.

[2] A. Airapetian et al. Single-spin asymmetries in semi-inclusive deep-inelastic scattering on a transversely polarized hydrogen target. *Physical Review Letters*, 94:012002, 2005.

[3] John C. Collins. Fragmentation of transversely polarized quarks probed in transverse momentum distributions. *Nuclear Physics*, B396:161–182, 1993.

[4] Dennis W. Sivers. Single spin production asymmetries from the hard scatterung of point- like constituents. *Physical Review*, D41:83, 1990.

[5] A. Airapetian et al. Quark helicity distributions in the nucleon for up, down, and strange quarks from semi-inclusive deep-inelastic scattering. *Physical Review*, D71:012003, 2005.

[6] John P. Ralston and Davison E. Soper. Production of dimuons from high-energy polarized proton proton collisions. *Nuclear Physics*, B152:109, 1979.

[7] Xavier Artru and Mustapha Mekhfi. Transversely polarized parton densities, their evolution and their measurement. *Z. Phys.*, C45:669, 1990.

[8] Rober L. Jaffe and Xiang-Dong Ji. Chiral odd parton distributions and polarized drell-yan. *Physical Review Letters*, 67:552–555, 1991.

[9] J. L. Cortes, B. Pire, and J. P. Ralston. Measuring the transverse polarization of quarks in the proton. *Z. Phys.*, C55:409–416, 1992.

[10] Matthias Burkardt. Quark correlations and single spin asymmetries. *Physical Review*, D69:057501, 2004.

[11] Stanley J. Brodsky, Dae Sung Hwang, and Ivan Schmidt. Final-state interactions and single-spin asymmetries in semi-inclusive deep inelastic scattering. *Physical Letters*, B530:99–107, 2002.

[12] Daniel Boer and P. J. Mulders. Time-reversal odd distribution functions in leptoproduction. *Physical Review*, D57:5780–5786, 1998.

Collins and Sivers Asymmetries from COMPASS

Andrea Bressan*
(on behalf of the COMPASS collaboration)

CERN, 1217 Geneve 23, Switzerland
E-mail: Andrea.Bressan@cern.ch

In the years 2002-2004 the COMPASS experiment has collected data with a polarized ^{6}LiD target and a 160 GeV muon beam. About 20% of the running time has been devoted to measure transverse spin effects in semi inclusive deep inelastic scattering, one of the main objectives of the COMPASS spin program. The results for the Collins and the Sivers asymmetries, both for unidentified and identified hadrons, are presented here. The measured asymmetries on the ^{6}LiD target are small and compatible with zero within the few percent statistical errors, an important result which can be interpreted as cancellation between u and d quark contribution in the deuteron and which allows to better constrain the parton distribution functions.

1 The Collins and Sivers mechanism

At twist-two level, three independent quark distribution functions are needed to describe the quark spin content of the nucleon; the momentum distribution $q(x)$, the helicity distribution $\Delta q(x)$ and the transversity distribution $\Delta_T q(x)$. At variance with q and Δq, $\Delta_T q$ is chiral-odd and cannot be measured in inclusive deep inelastic scattering (DIS), which is the main source of information on the nucleon partonic structure [2]. However, it can be measured in semi-inclusive DIS (SIDIS) in combination with chiral-odd fragmentation functions, such as the the Collins fragmentation function ΔD_a^h for hadron production, and the interference fragmentation function $H_1^{\sphericalangle}$ for hadron pair production [3], giving rise to an azimuthal single spin asymmetry (SSA) in the final state hadrons [4].

The Collins mechanism is not the only way to create SSA for single hadrons distributions; a different mechanism, where SSA arises from correlation between the nucleon spin and the quark intrinsic transverse momentum k_T was proposed by Sivers [5] and is described by the so called Sivers distribution function, $\Delta_0^T q(x, k_T)$. The Collins and Sivers effects can be easily disentangled in SIDIS since they are related to asymmetries in two independent azimuthal angles. The general expression for the single hadron production cross sections contains six more transverse target polarization dependent azimuthal asymmetries, which also have been extracted in COMPASS; for a review of the results see [6].

The Collins mechanism leads to a modulation in the azimuthal distribution of the inclusively produced hadrons given by:

$$N(\Phi_C) = \alpha(\Phi_C) \cdot N_0 \left(1 + A_{\mathrm{Col}} \cdot P_T \cdot f \cdot D_{NN} \sin \Phi_C\right),$$

where the function α contains the apparatus efficiency and acceptance, P_T is the target polarization ($\sim 50\%$), $D_{NN} = (1-y)/(1-y+y^2/2)$ is the spin transfer coefficient and f is the target dilution factor, i. e. the fraction of polarizable nuclei in the target ($\sim 40\%$); $\Phi_C = \phi_h - \phi_{S'} = \phi_h + \phi_S - \pi$ is the Collins angle, with ϕ_h the hadron azimuthal angle and

*on leave of absence from Università degli Studi di Trieste and INFN - Sezione di Trieste

$\phi_{S'}$ the final azimuthal angle of the quark spin and ϕ_S the azimuthal angle of the nucleon spin in the $\gamma - N$ system. Finally

$$A_{\mathrm{Col}} = \frac{\sum_q e_q^2 \cdot \Delta_T q(x) \cdot \Delta D_q^0(z, p_T^h)}{\sum_q e_q^2 \cdot q(x) \cdot D_q^h(z, p_T^h)}$$

is the Collins asymmetry, arising from the product of the transversity distribution $\Delta_T q$ and the Collins fragmentation function ΔD_q^0 (the quantities in the denominator are the known momentum distribution q and the unpolarized fragmentation function D_q^h).

The azimuthal modulation arising from the Sivers mechanism can be written as:

$$N(\Phi_S) = \alpha(\Phi_S) \cdot N_0 \left(1 + A_{\mathrm{Siv}} \cdot P_T \cdot f \sin \Phi_S\right),$$

with a modulation expressed in terms of the Sivers angle $\Phi_S = \phi_h - \phi_S$, where again ϕ_h the hadron azimuthal angle and ϕ_S the azimuthal angle of the nucleon spin. The Siver asymmetry is defined as:

$$A_{\mathrm{Siv}} = \frac{\sum_q e_q^2 \cdot \Delta_0^T q(x, p_T^h) \cdot D_q^h(z)}{\sum_q e_q^2 \cdot q(x) \cdot D_q^h(z)}$$

Since in this case the unpolarized fragmentation functions are known, the measurement of the Siver asymmetry for both positive and negative produced hadrons allows directly to extract the Siver functions, if the measured asymmetry are different from zero, while a zero result for an isoscalar target like the one used in COMPASS can come both from a vanishing Sivers function or from a cancellation between u and d quark contributions.

2 Results

The event selection requires standard DIS cuts, i.e. $Q^2 > 1$ $((GeV)/c)^2$, mass of the final hadronic state $W > 5$ GeV/c^2, $0.1 < y < 0.9$, and the detection of at least one hadron in the final state. For the detected hadrons it is also required that:

- the fraction of the virtual photon energy carried is $z(= E_h/E_\gamma) > 0.2$ to select hadron from the current fragmentation region (for the leading hadrons, i.e. the hadron with the largest z in the event, the cuts selection is more strict: $z > 0.25$ and, in case that the missing $z_{\mathrm{miss}} = 1 - \sum_h z_h > z_{\mathrm{leading}}$, no neutral blob in the calorimeters with an energy larger than that of the leading hadron);
- $p_T > 0.1$ GeV/c (where p_T is the hadron transverse momentum with respect to the virtual photon direction) for a better determination of the azimuthal angle ϕ_h.

The resulting Collins and Sivers asymmetries from the whole deuteron data for all hadrons of the event fulfilling the described criteria are shown in figure 1 [7], with the error bars accounting only for the statistical uncertainty. The asymmetries are measured as a function of x_{Bj}, z and p_T^h. Different sources of systematic effects have been checked, showing that systematic errors are much smaller than the statistical uncertainty. Both the Collins and Sivers asymmetries turned out to be small and compatible with zero; the same behavior is observed when only leading hadrons are considered [7].

Even if there were theoretical predictions for small asymmetries (given an opposite contribution for the u and d quark, resulting in a large cancellation for isoscalar targets like the

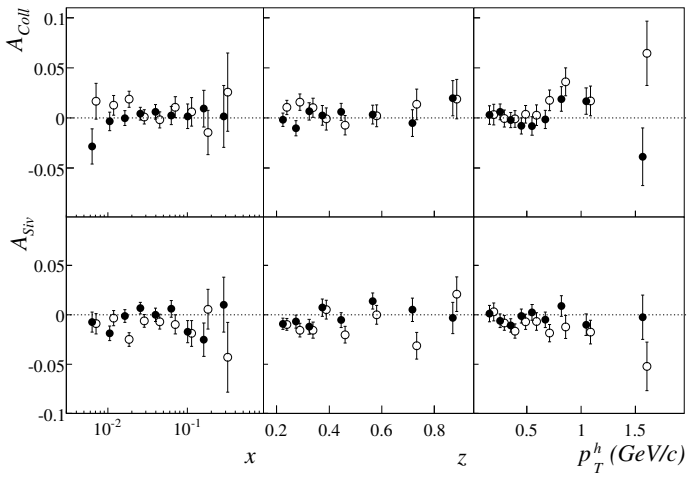

Figure 1: Collins and Sivers asymmetry for positive (full points) and negative (open points) hadrons as a function of $x_{\rm Bj}$, z and p_T^h.

deuteron), it was not obvious that the measured asymmetries have been so small. For what concerns the Collins mechanism, HERMES have measured (on the u-dominated proton) a non-zero Collins asymmetry, providing a convincing evidence that both the transversity distribution $\Delta_T u(x)$ and the Collins fragmentation function $\Delta_T^0 D_u^h(z)$ are different from zero. An independent evidence that the Collins mechanism is a sizable effect came by the recent analysis of the Belle collaboration, which is measuring the azimuthal distribution in the $e^+e^- \to h^+h^-X$ reaction [8].

Recently, a global analysis of the HERMES, COMPASS and Belle data has allowed a first extraction of the transverity distributions [9], while for a global analysis of COMPASS and HERMES results for the Sivers asymmetry see [10].

The sizable Sivers asymmetry measured by the HERMES collaboration in the case of positive pions produced on protons, is indicating that the Sivers mechanism is also at work. The zero result of COMPASS for the Sivers asymmetries of both positive and negative hadrons suggest that $\Delta_0^T d \sim -\Delta_0^T u$.

The same analysis done for the charged hadrons has been repeated to extract the Collins and Sivers asymmetries for $\pi^\pm$ and $\mathrm{K}^\pm$, using the information of the RICH detector to identify the hadrons. The COMPASS RICH1 detector uses C_4F_{10} as radiator gas, with a refractive index of ~ 1.0015 for 7 eV Cerenkov photons, that gives a 2 (9) GeV threshold for pions (kaons), and allows to separate pions from kaons up to 45-50 GeV. More than 80% of the hadrons in this energy interval identified by the RICH are pions and the rest are kaons. The measured asymmetries for pions are similar to those shown in fig. 1; the Collins and Sivers asymmetries for kaons are shown in figure 2. Also in this case the measured asymmetries are small, and compatible with zero; the only indication for a signal, both positive and negative kaons, is visible in the Collins asymmetries as a function of x in the $x \sim 0.1$ region. Since it is only one point at two-three standard deviations from zero, this observation needs to be confirmed by more precise measurements.

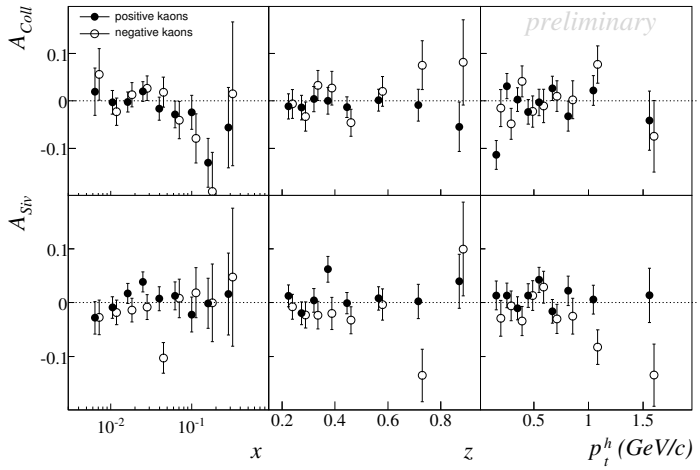

Figure 2: Collins and Sivers asymmetry for positive (full points) and negative (open points) kaons as a function of $x_{\rm Bj}$, z and p_T^h.

The COMPASS 2007 run will be devoted to the data taking with a polarized proton (NH_3) target, and the data will allow to measure the Collins and Sivers asymmetries at the same energy of the deuteron results presented here.

References

[1] Slides:
`http://indico.cern.ch/contributionDisplay.py?contribId=151&sessionId=4&confId=9499`

[2] see, f.i., V. Barone, A. Drago and P. G. Ratcliffe, Phys. Rept. **359** (2002) 1.

[3] C. Schill, "Transversity signals in two-hadron production at COMPASS", these proceedings.

[4] J. C. Collins, Nucl. Phys. B **396** (1993) 161.

[5] D. W. Sivers, Phys. Rev. D **41** (1990) 83.

[6] A. Kotzinian, "Beyond Collins and Sivers: further measurements of target transverse spin-dependent azimuthal asymmetries in semi-inclusive DIS from COMPASS", these proceedings.

[7] The COMPASS Collaboration, E.S. Ageev *et. al*, Nucl. Phys. **B 765** (2007) 31

[8] The Belle Collaboration, K. Abe *et al.*, Phys. Rev. Lett. 96 (2006) 232002.

[9] M. Anselmino *et al.*, Phys. Rev. D **75**, 054032 (2007) and [arXiv:hep-ph/0701006v1].

[10] M. Anselmino *et al.*, Phys. Rev. D **72**, 094007 (2005)

Transversity and Collins Functions: from $e^+e^- \to h_1h_2X$ to SIDIS Processes

M. Anselmino[1], M. Boglione[1], U. D'Alesio[2], A. Kotzinian[1,3], F. Murgia[2], A. Prokudin[1] and C. Türk[1]

1- Dipartimento di Fisica Teorica, Università di Torino and INFN, Sezione di Torino
Via P. Giuria 1, I-10125 Torino, Italy

2- Dipartimento di Fisica, Università di Cagliari and INFN, Sezione di Cagliari,
C.P. 170, I-09042 Monserrato (CA), Italy

3- Yerevan Physics Institute, 375036 Yerevan, Armenia,
JINR, 141980 Dubna, Russia

We present [1] the first simultaneous extraction of the transversity distribution and the Collins fragmentation function, obtained through a combined analysis of experimental data on azimuthal asymmetries in semi-inclusive deep inelastic scattering (SIDIS), from the HERMES and COMPASS Collaborations, and in $e^+e^- \to h_1h_2X$ processes, from the Belle Collaboration.

Among the three leading twist parton distributions, that contain basic information on the internal structure of nucleons, the transversity distribution is the most difficult to access. Due to its chiral-odd nature it can only appear in physical processes which require a quark helicity flip. At present the most accessible channel is the SIDIS process with a polarized target, where the corresponding azimuthal asymmetry, $A_{UT}^{\sin(\phi_S+\phi_h)}$, involves the transversity distribution coupled to the Collins fragmentation function [2], also unknown. Indeed it has received a lot of attention in the ongoing experimental programs of HERMES [3], COMPASS [4], and JLab Collaborations.

A crucial breakthrough in this strategy has recently been achieved with the independent measurement of the Collins function via the azimuthal correlation observed in the two-pion production in e^+e^- annihilation by the Belle Collaboration at KEK [5].

Let us start with the $e^+e^- \to h_1h_2X$ process. We choose the reference frame so that the elementary $e^+e^- \to q\bar{q}$ scattering occurs in the $\hat{xz}$ plane, with the back-to-back quark and antiquark moving along the $\hat{z}$-axis identified as the jet thrust axis. The cross section corresponding to this process can be expressed as (see Ref. [6]):

$$\frac{d\sigma^{e^+e^-\to h_1h_2X}}{dz_1\,dz_2\,d^2\boldsymbol{p}_{\perp 1}\,d^2\boldsymbol{p}_{\perp 2}\,d\cos\theta} = \frac{3\pi\alpha^2}{2s}\sum_q e_q^2\Big\{(1+\cos^2\theta)\,D_{h_1/q}(z_1,p_{\perp 1})\,D_{h_2/\bar{q}}(z_2,p_{\perp 2}) + \frac{1}{4}\sin^2\theta\;\Delta^N D_{h_1/q^\uparrow}(z_1,p_{\perp 1})\,\Delta^N D_{h_2/\bar{q}^\uparrow}(z_2,p_{\perp 2})\,\cos(\varphi_1+\varphi_2)\Big\}, \quad (1)$$

where φ_i are the azimuthal angles identifying the direction of the observed hadron h_i in the helicity frame of the fragmenting quark q, z_i and $\boldsymbol{p}_{\perp i}$ are the hadron light-cone momentum fractions and transverse momenta, and θ is the scattering angle in the $e^+e^- \to q\bar{q}$ process. $\Delta^N D_{h/q^\uparrow}(z,p_\perp)$ is the Collins function, also known as $H_1^\perp$ (see Ref. [7]). To compare with data we have to *i*) perform a change of angular variables from (φ_1,φ_2) to $(\varphi_1,\varphi_1+\varphi_2)$ and integrate over $p_{\perp 1}$, $p_{\perp 2}$, and over φ_1; *ii*) normalize the result to the azimuthal averaged cross section; *iii*) take the ratio R of unlike-sign to like-sign pion-pair production:

$$R \simeq 1+\cos(\varphi_1+\varphi_2)\,A_{12}(z_1,z_2)\,, \quad \text{where} \quad A_{12}(z_1,z_2) = \frac{1}{4}\,\frac{\langle\sin^2\theta\rangle}{\langle 1+\cos^2\theta\rangle}\,(P_U-P_L)\,, \quad (2)$$

the angle θ is averaged over a range of values given by the detector acceptance,

$$P_{U(L)} = \frac{\sum_q e_q^2\, \Delta^N D_{\pi^+/q^\uparrow}(z_1)\, \Delta^N D_{\pi^{-(+)}/\bar{q}^\uparrow}(z_2)}{\sum_q e_q^2 D_{\pi^+/q}(z_1)\, D_{\pi^{-(+)}/\bar{q}}(z_2)}\,, \quad \text{and} \tag{3}$$

$$\Delta^N D_{h/q^\uparrow}(z) = \int d^2\boldsymbol{p}_\perp \Delta^N D_{h/q^\uparrow}(z, p_\perp) = \int d^2\boldsymbol{p}_\perp \frac{2p_\perp}{z m_h}\, H_1^{\perp q}(z, p_\perp) = 4\, H_1^{\perp (1/2)q}(z)\,. \tag{4}$$

For fitting purposes, it is convenient to re-express P_U and P_L in terms of favoured and unfavoured fragmentation functions (and similarly for the $\Delta^N D$),

$$D_{\pi^+/u,\bar{d}} = D_{\pi^-/d,\bar{u}} \equiv D_{\rm fav}\,; \quad D_{\pi^+/d,\bar{u}} = D_{\pi^-/u,\bar{d}} = D_{\pi^\pm/s,\bar{s}} \equiv D_{\rm unf}\,. \tag{5}$$

In addition, the Belle Collaboration presents the same set of data, analysed in a different reference frame: following Ref. [7], one can fix the $\hat{z}$-axis as given by the direction of the observed hadron h_2 and the $\hat{xz}$ plane as determined by the lepton and the h_2 directions. An azimuthal dependence of the other hadron h_1 with respect to this plane has been measured. In this configuration the corresponding ratio becomes

$$R \simeq 1 + \cos(2\,\phi_1) A_0(z_1, z_2)\,, \quad A_0(z_1, z_2) = \frac{1}{\pi}\, \frac{z_1\, z_2}{z_1^2 + z_2^2}\, \frac{\langle \sin^2\theta_2 \rangle}{\langle 1 + \cos^2\theta_2 \rangle}\, (P_U - P_L)\,. \tag{6}$$

Let us now consider the SIDIS process $\ell\, p \to \ell\, h\, X$. We take, in the $\gamma^* - p$ c.m. frame, the virtual photon and the proton colliding along the $\hat{z}$-axis with momenta $\boldsymbol{q}$ and $\boldsymbol{P}$ respectively, and the leptonic plane to coincide with the $\hat{xz}$ plane.

To single out the spin dependent part of the fragmentation of a transversely polarized quark we consider the $\sin(\phi_S + \phi_h)$ weighted asymmetry (at $\mathcal{O}(k_\perp/Q)$):

$$\begin{aligned} A_{UT}^{\sin(\phi_S+\phi_h)} &= 2\, \frac{\int d\phi_S\, d\phi_h\, [d\sigma^\uparrow - d\sigma^\downarrow]\, \sin(\phi_S + \phi_h)}{\int d\phi_S\, d\phi_h\, [d\sigma^\uparrow + d\sigma^\downarrow]} \\ &= \frac{\displaystyle\sum_q e_q^2 \int d\phi_S d\phi_h d^2\boldsymbol{k}_\perp \Delta_T q(x, k_\perp) \frac{d(\Delta\hat{\sigma})}{dy} \Delta^N D_{h/q^\uparrow}(z, p_\perp) \sin(\phi_S + \varphi + \phi_q^h) \sin(\phi_S + \phi_h)}{\displaystyle\sum_q e_q^2 \int d\phi_S d\phi_h\, d^2\boldsymbol{k}_\perp f_{q/p}(x, k_\perp) \frac{d\hat{\sigma}}{dy} D_{h/q}(z, p_\perp)}\,. \end{aligned} \tag{7}$$

In the above equation $\Delta_T q(x, k_\perp)$ is the unintegrated transversity distribution, $d\hat{\sigma}/dy$ is the planar unpolarized elementary cross section and $\frac{d(\Delta\hat{\sigma})}{dy} = \frac{4\pi\alpha^2}{sxy^2}\,(1 - y)$. The $\sin(\phi_S + \varphi + \phi_q^h)$ azimuthal dependence in Eq. (7) arises from the combination of the phase factors in the transversity distribution function, in the non-planar $\ell\, q \to \ell\, q$ elementary scattering amplitudes, and in the Collins fragmentation function (see Ref. [6] and [8]). We assume

$$f_{q/p}(x, k_\perp) = f_{q/p}(x)\, \frac{e^{-k_\perp^2/\langle k_\perp^2 \rangle}}{\pi \langle k_\perp^2 \rangle}\,, \qquad D_{h/q}(z, p_\perp) = D_{h/q}(z)\, \frac{e^{-p_\perp^2/\langle p_\perp^2 \rangle}}{\pi \langle p_\perp^2 \rangle}\,, \tag{8}$$

where $f_{q/p}(x)$ and $D_{h/q}(z)$ are the usual integrated parton distribution and fragmentation functions and the average values of $k_\perp^2$ and $p_\perp^2$ are taken from Ref. [9]: $\langle k_\perp^2 \rangle = 0.25\,\text{GeV}^2$, $\langle p_\perp^2 \rangle = 0.20\,\text{GeV}^2$. For the transversity and the Collins functions we choose

$$\Delta_T q(x, k_\perp) = \frac{1}{2} \mathcal{N}_q^T(x)\, \left[f_{q/p}(x) + \Delta q(x) \right]\, \frac{e^{-k_\perp^2/\langle k_\perp^2 \rangle}}{\pi \langle k_\perp^2 \rangle}\,, \tag{9}$$

$$\Delta^N D_{h/q^\uparrow}(z,p_\perp) = 2\,\mathcal{N}_q^C(z)\; D_{h/q}(z,p_\perp)\,\sqrt{2e}\,\frac{p_\perp}{M}\,e^{-p_\perp^2/M^2}\,, \tag{10}$$

$$\mathcal{N}_q^T(x) = N_q^T\,x^\alpha(1-x)^\beta\,\frac{(\alpha+\beta)^{(\alpha+\beta)}}{\alpha^\alpha\beta^\beta}\,,\;\; \mathcal{N}_q^C(z) = N_q^C\,z^\gamma(1-z)^\delta\,\frac{(\gamma+\delta)^{(\gamma+\delta)}}{\gamma^\gamma\delta^\delta}\,, \tag{11}$$

with $|N_q^T|$, $|N_q^C| \leq 1$ and where Δq is the helicity distribution.

Notice that our parameterizations are devised in such a way that the transversity distribution function and the Collins function automatically obey their proper bounds.

By insertion of the above expressions into Eq. (7), we obtain

$$A_{UT}^{\sin(\phi_S+\phi_h)} = \frac{\dfrac{P_T}{M}\dfrac{1-y}{sxy^2}\sqrt{2e}\dfrac{\langle p_\perp^2\rangle_C^2}{\langle p_\perp^2\rangle}\dfrac{e^{-P_T^2/\langle P_T^2\rangle_C}}{\langle P_T^2\rangle_C^2}\displaystyle\sum_q e_q^2\mathcal{N}_q^T(x)\left[f_{q/p}(x)+\Delta q(x)\right]\mathcal{N}_q^C(z)D_{h/q}(z)}{\dfrac{e^{-P_T^2/\langle P_T^2\rangle}}{\langle P_T^2\rangle}\dfrac{[1+(1-y)^2]}{sxy^2}\displaystyle\sum_q e_q^2\,f_{q/p}(x)\;D_{h/q}(z)}\,, \tag{12}$$

$$\text{with }\;\langle p_\perp^2\rangle_C = \frac{M^2\langle p_\perp^2\rangle}{M^2+\langle p_\perp^2\rangle}\,,\qquad \langle P_T^2\rangle = \langle p_\perp^2\rangle + z^2\langle k_\perp^2\rangle\,,\qquad \langle P_T^2\rangle_C = \langle p_\perp^2\rangle_C + z^2\langle k_\perp^2\rangle\,. \tag{13}$$

Using the above expressions for $\Delta_T q$ and $\Delta^N D_{\pi/q^\uparrow}$ both in $A_{UT}^{\sin(\phi_S+\phi_h)}$, Eq. (12), and in A_{12}, Eq. (2), we can fix all free parameters by performing a best fit of the HERMES, COMPASS and Belle data. We checked that using A_0 instead of A_{12} leads to a consistent extraction (see Ref. [6] for details).

Our results are collected in Figs. 1, 2 where we present a comparison of our curves with the data. Figure 3 shows our extracted transversity distributions and Collins functions.

Summarizing, our global analysis of present data on azimuthal asymmetries measured in SIDIS and $e^+e^- \to \pi\pi X$ allows to get quantitative estimates of both the transversity and the Collins function. In particular, we find: *i*) $|\Delta_T u| > |\Delta_T d|$, and both smaller than the corresponding Soffer bound; *ii*) $\Delta_T u$ tightly constrained by HERMES data alone, whereas COMPASS data help in constraining the transversity for d quarks; *iii*) unfavoured Collins functions larger in size (and opposite in sign) than the favoured ones.

References

[1] Slides: `http://indico.cern.ch/contributionDisplay.py?contribId=152&sessionId=4&confId=9499`

[2] J. C. Collins, Nucl. Phys. **B396**, 161 (1993).

[3] HERMES Collaboration, A. Airapetian *et al.*, Phys. Rev. Lett. **94**, 012002 (2005).

[4] COMPASS Collaboration, E. S. Ageev *et al.*, Nucl. Phys. **B765**, 31 (2007), hep-ex/0610068.

[5] Belle Collaboration, R. Seidl *et al.*, Phys. Rev. Lett. **96**, 232002 (2006).

[6] M. Anselmino *et al.*, Phys. Rev. **D75**, 054032 (2007), hep-ph/0701006.

[7] D. Boer, R. Jakob, and P. J. Mulders, Nucl. Phys. **B504**, 345 (1997).

[8] M. Anselmino *et al.*, Phys. Rev. **D73**, 014020 (2006), hep-ph/0509035.

[9] M. Anselmino *et al.*, Phys. Rev. **D71**, 074006 (2005), hep-ph/0501196.

[10] A. V. Efremov, K. Goeke, and P. Schweitzer, Phys. Rev. **D73**, 094025 (2006).

[11] W. Vogelsang and F. Yuan, Phys. Rev. **D72**, 054028 (2005).

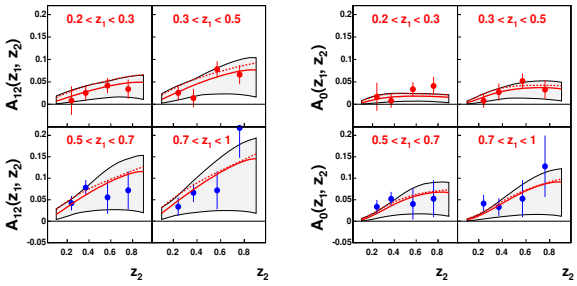

Figure 1: Data on two different azimuthal correlations in unpolarized $e^+e^- \to h_1 h_2 X$ processes, as measured by Belle Collaboration [5], compared to the curves obtained from our fit. The solid (dashed) lines correspond to the global fit obtained including the $A_{12}(A_0)$ asymmetry; the shaded area corresponds to the theoretical uncertainty on the parameters.

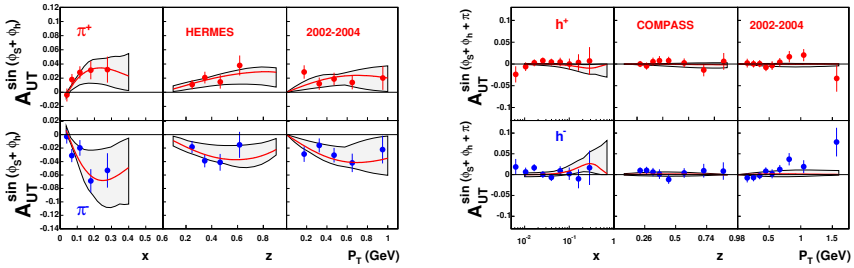

Figure 2: Our results compared with HERMES data [3] on $A_{UT}^{\sin(\phi_S+\phi_h)}$ for $\pi^\pm$ production (left panel) and COMPASS data on $A_{UT}^{\sin(\phi_S+\phi_h)}$, for the production of positively and negatively charged hadrons off a deuterium target [4] (right panel).

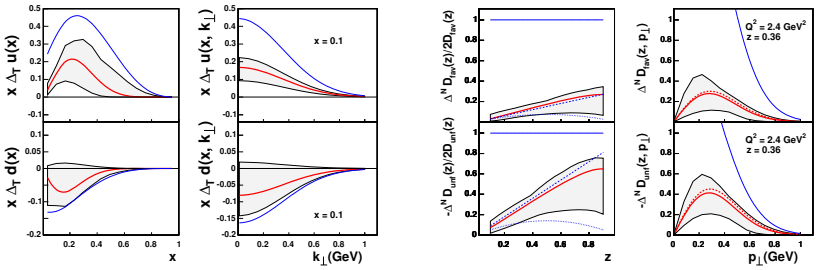

Figure 3: First panel: $x\,\Delta_T u(x)$ (upper plot) and $x\,\Delta_T d(x)$ (lower plot), vs. x at $Q^2 = 2.4$ GeV^2. The Soffer bound is also shown for comparison (bold blue line). Second panel: $x\,\Delta_T u(x, k_\perp)$ (upper plot) and $x\,\Delta_T d(x, k_\perp)$ (lower plot), vs. $k_\perp$ at a fixed value of x. Third panel: the z dependence of the moment of the Collins functions, Eq. (4), normalized to twice the unpolarized fragmentation functions; also shown the results of Refs. [10] (dashed line) and [11] (dotted line). Fourth panel: the $p_\perp$ dependence of the Collins functions.

Flavor Dependence of T-odd PDFs

Leonard P. Gamberg[1], Gary R. Goldstein[2], and Marc Schlegel[3]

1- Penn State University-Berks -Department of Physics and Astronomy
Reading, PA 19610 - USA

2- Tufts University - Department of Physics and Astronomy
Medford, MA 02155 - USA

3- Thomas Jefferson National Accelerator Facility - Theory Division
Newport News, VA 23608- USA

The flavor dependence of the naive time reversal odd ("T-odd") parton distributions for u- and d-quarks are explored in the spectator model. The flavor dependence of $h_1^\perp$ is of significance for the analysis of the azimuthal $\cos(2\phi)$ asymmetries in unpolarized SIDIS and DY-processes, as well as for the overall physical understanding of the distribution of transversely polarized quarks in unpolarized nucleons. As a by-product of the formalism, we calculate the chiral-odd but "T-even" function $h_{1L}^\perp$ which enables us to present a prediction for the single spin asymmetry $A_{UL}^{\sin(2\phi)}$ for a longitudinally polarized target in SIDIS.

Naive time reversal-odd ("T-odd") transverse momentum dependent (TMD) parton distributions (PDFs) have gained considerable attention in recent years. Theoretically they can account for non-trivial transverse spin and momentum correlations such as single spin asymmetries (SSA) in hard scattering processes when transverse momentum scales are on the order of that of quarks in hadrons, namely $P_T \sim k_\perp \ll \sqrt{Q^2}$. A prominent example is the Sivers function $f_{1T}^\perp$ [2] which explains the observed SSA in semi-inclusive deep inelastic scattering (SIDIS) for a transversely polarized proton target by the HERMES collaboration [3]. It describes correlations of the intrinsic quark transverse momentum and the transverse nucleon spin. The corresponding SSA on a deuteron target measured by COMPASS [4] vanishes, indicating a flavor dependence of the Sivers function. Another leading twist "T-odd" parton distribution, the chiral-odd Boer-Mulders function $h_1^\perp$ [5] correlates the transverse spin of a quark with its transverse momentum within the nucleon. We focus on the flavor dependence of these "T-odd" functions where for example $h_1^\perp$ is important for the analysis of the azimuthal $\cos(2\phi)$ asymmetry in unpolarized SIDIS and Drell-Yan [6, 7]. We also consider the flavor dependence of the "T-even" function $h_{1L}^\perp$, which is of interest in the transverse momentum and quark spin correlations in a longitudinally polarized target [8].

Considerable understanding of TMDs and fragmentation functions (FF) have been gained from model calculations using the spectator framework [9, 10, 6, 7, 11, 12].

In this formalism we start (cf. [13]) from the definition of the unintegrated color gauge invariant quark-quark correlator which contains the gauge link indicated by the Wilson line, $\mathcal{W}[a\,|\,b]$, and work in Feynman gauge in which the transverse Wilson line vanishes [14]. In the diquark model the sum over the complete set of intermediate on-shell states in the definition of the correlator is represented by a single one-particle diquark state $|\,dq;\,p_{dq},\lambda\rangle$, where p_{dq} is the diquark momentum and λ its polarization. The diquark is "built" from two valence quarks which can be scalar-spin 0 or axial vector-spin 1. The unintegrated correlator is then

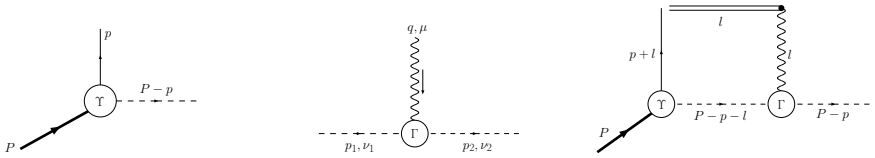

(a) Nucleon-Diquark-Quark vertex

(b) Diquark-gluon vertex

(c) Box-graph hermitian conjugated

Figure 1: Different vertices for the axial-vector diquark and contribution of the gauge link in the one-gluon approximation.

given by

$$\Phi_{ij}(p;P,S) = \sum_{\lambda} \frac{\delta((P-p)^2 - m_s^2)\Theta(P^0-p^0)}{(2\pi)^3} \langle P,S|\,\bar{\psi}_j(0)\,\mathcal{W}[0\,|\,\infty,0,\vec{0}_T]\,|\,dq;\,P-p,\lambda\rangle \times \langle\, dq;\,P-p,\lambda|\,\mathcal{W}[\infty,0,\vec{0}_T\,|\,0]\,\psi_i(0)\,|P,S\rangle. \quad (1)$$

The essence of the diquark spectator model is to calculate the matrix elements in Eq. (1) by the introduction of effective The nucleon-diquark-quark vertices $\Upsilon_s(N)$ and $\Upsilon^{\mu}_{ax}(N)$ are represented in Fig. 1 (a). For example, the matrix element for the axial vector diquark is

$$\langle adq;\,P-p;\lambda|\,\psi_i(0)\,|P,S\rangle = i\frac{g_{ax}(p^2)}{\sqrt{3}}\varepsilon^*_{\mu}(P-p;\lambda)\frac{\left[(\not{p}+m_q)\gamma_5\left[\gamma^{\mu}-R_g\frac{P^{\mu}}{M}\right]u(P,S)\right]_i}{p^2-m_q^2+i0}, \quad (2)$$

where the polarization vector of the axial-vector diquark is ε_{μ}, $u(P,S)$ denotes the nucleon spinor and M and m_q are nucleon and quark masses, respectively. The unpolarized TMD f_1 is obtained by inserting these expressions into Eq. (1) and projecting from the quark-quark correlator

$$f_1(x,\vec{p}_T^{\,2}) = \frac{1}{4}\int dp^-\,\left(\mathrm{Tr}\left[\gamma^+\Phi(p;P,S)\right] + \mathrm{Tr}\left[\gamma^+\Phi(p;P,-S)\right]\right)\Big|_{p^+=xP^+}, \quad (3)$$

We have also calculated the distribution of transversely polarized quarks in a longitudinally polarized target, $h_{1L}^{\perp}$ by replacing Γ^+ with $\Gamma^+\Gamma^i\Gamma_5$ and S by S_L, the spin 4-vector in longitudinal direction. Their analytic expressions in the scalar and axial vector diquark sectors are given in [15].

In the spectator framework the "T-odd" TMDs [9] are generated by the gauge link [10, 6, 7]. The leading contribution, arising from the interference between tree- and box graph which contains an imaginary part necessary for "T-odds", is represented in Fig. 1 (c) in which the double line is an eikonal, and l is the loop momentum. For an axial-vector diquark we model the composite nature of the diquark through an anomalous magnetic moment κ [16]. In the notation of Fig. 1 (b) the gluon-diquark axial diquark vertex is

$$\Gamma^{\mu\nu_1\nu_2}_{ax} = -ie_{dq}\left[g^{\nu_1\nu_2}(p_1+p_2)^{\mu} + (1+\kappa)\left(g^{\mu\nu_2}(p_2+q)^{\nu_1} + g^{\mu\nu_1}(p_1-q)^{\nu_2}\right)\right]. \quad (4)$$

For $\kappa = -2$ the vertex Γ_{ax} reduces to the standard γWW-vertex. We express the matrix elements including the gauge link, $\langle dq;\,P-p|\,\mathcal{W}[\infty,0,\vec{0}_T\,|\,0]\,\psi_i(0)\,|P,S\rangle$ in the one gluon

approximation [15]. Projecting the Boer-Mulders function,

$$\epsilon_T^{ij} p_T^j h_1^\perp(x,\vec{p}_T^{\,2}) = \frac{M}{4}\int dp^- \left(\mathrm{Tr}\left[\Phi_{\mathrm{unpol}}(p,S) i\sigma^{i+}\gamma_5\right] + \mathrm{Tr}\left[\Phi_{\mathrm{unpol}}(p,-S) i\sigma^{i+}\gamma_5\right]\right), \quad (5)$$

where $\epsilon_T^{ij} \equiv \epsilon^{-+ij}$ the axial-vector diquark contribution is given by the expression,

$$\begin{aligned}
\epsilon_T^{ij} p_T^j h_1^{\perp,ax}(x,\vec{p}_T^{\,2}) &= -\frac{e_q e_{dq}}{8(2\pi)^3}\frac{1}{\vec{p}_T^{\,2}+\tilde{m}^2}\frac{M}{P^+}\int\frac{d^4l}{(2\pi)^4}\left\{\frac{1}{3}g_{ax}\left((l+p)^2\right)g_{ax}^*\left(p^2\right)\times\right. \\
&\mathcal{D}_{\rho\eta}(P-p-l)\left(\sum_\lambda \varepsilon_\sigma^*(P-p;\lambda)\varepsilon_\mu(P-p;\lambda)\right)\times \\
&\frac{\left[g^{\sigma\rho}\, v\cdot(2P-2p-l)+(1+\kappa)\left(v^\sigma\left(P-p+l\right)^\rho + v^\rho\left(P-p-2l\right)^\sigma\right)\right]}{\left[l\cdot v+i0\right]\left[l^2-\lambda^2+i0\right]\left[(l+p)^2-m_q^2+i0\right]}\times \\
&\left.\mathrm{Tr}\Big[\left(\not{P}+M\right)\left(\gamma^\mu - R_g\frac{P^\mu}{M}\right)\left(\not{p}-m_q\right)\gamma^+\gamma^i\left(\not{l}+\not{p}+m_q\right)\left(\gamma^\eta + R_g\frac{P^\eta}{M}\right)\gamma_5\Big]\right\} + \text{ h.c.}\,. \quad (6)
\end{aligned}$$

$\mathcal{D}(P-p-l)$ denotes the propagator of the axial-vector diquark. Since the numerator in Eq. (6) contains at most the loop momentum to the fourth power we can write it in the following manner, $\sum_{i=1}^4 N^{(i)}_{\alpha_1\ldots\alpha_i} l^{\alpha_1}\ldots l^{\alpha_i} + N^{(0)}$. The (real) coefficients (tensors) $N^{(i)}_{\alpha_1\ldots\alpha_i}$ depend only on external momenta and can be computed in a straight-forward manner. The integration over the light cone components, l^+ and l^-, are easily performed; however, calculating the l^+-integral results in an integral that is potentially ill-defined. This happens when $g(p^2)$ is a holomorphic function in p^2 and at least one of the Minkowski indices is light-like in the minus direction, e.g. $\alpha_1 = -$, $\alpha_2,\ldots,\alpha_i \in \{+,\perp\}$ resulting in an integral of the form $\int dl^+\,\delta(l^+)\Theta(-l^+)$, implying that $l^+ = 0$ and $l^- = \infty$. This signals the existence of a light cone divergence in Ref. [12].

One can handle the light cone divergences by introducing phenomenological form factors with additional poles [15],

$$g_{ax}(p^2) = \frac{(p^2-m_q^2)f(p^2)}{\left[p^2-\Lambda^2+i0\right]^n}. \quad (7)$$

For $n \geq 3$ there are enough powers of l^+ to eliminate this divergence. $f(p^2)$ is a covariant Gaussian [15] which cuts off the p_T integrations and Λ is an arbitrary mass scale fixed by fitting f_1 to data. Similarly, the Sivers-function is projected from the trace of the quark-quark correlator (1) (see e.g. [17]),

$$2S_T^i\epsilon_T^{ij}p_T^j f_{1T}^\perp(x,\vec{p}_T^{\,2}) = \frac{M}{2}\int dp^-\left(\mathrm{Tr}\left[\gamma^+\Phi(p;P,S_T)\right] - \mathrm{Tr}\left[\gamma^+\Phi(p;P,-S_T)\right]\right)\Big|_{p^+=xP^+}. \quad (8)$$

It is well-known [6] that in the scalar diquark approximation the $h_1^\perp$ and $f_{1T}^\perp$ coincide. By contrast the different Dirac structure for the chiral even $f_{1T}^\perp$ and chiral odd $h_1^\perp$ in the axial-vector diquark sector, Eq. (5) and (8) respectively, lead to different coefficients in the decomposition $N^{(i)}_{\alpha_1\ldots\alpha_i}$ [15]. We fix most of the model parameters such as masses and normalizations by comparing the model result for the unpolarized f_1 for u and d quarks to the low-scale ($\mu^2 = 0.34\mathrm{GeV}$) data parameterization of GRV [18] see Fig. 2. Note that PDFs for u and d quarks are given by linear combinations of PDFs for an axial vector and

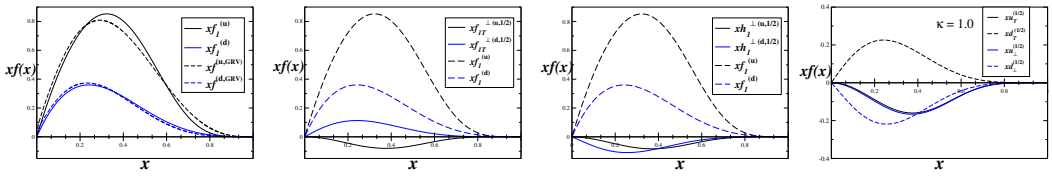

Figure 2: The unpolarized up and down quark distributions functions (left) versus x compared to the low scale parameterization of GRV [18]. The half moment of the Sivers function (center-left) and Boer-Mulders function (center-right) and the unpolarized up and down quark distributions ($\kappa = 1.0$). The half-moment (left) and first moments (right) of the Boer-Mulders and Sivers functions versus x fitted to extractions from data were presented in Ref. [19]

scalar diquark, $u = \frac{3}{2}f^{sc} + \frac{1}{2}f^{ax}$ and $d = f^{ax}$ [13, 11]. For "T-odd" PDFs we fix the sign and the strength of the final state interactions, the product of the charges of the diquark and quark, by comparing $f_{1T}^{\perp}$ for u and d quarks in the diquark model with the existing data parameterizations (see Ref. [19]). The "one-half" moments $q_T^{(1/2)}$ (where $q = u, d$) of the Sivers and Boer-Mulders functions

$$\frac{1}{2}q_T^{(1/2)}(x) = f_{1T}^{\perp(q,1/2)}(x) = \int d^2p_T \, \frac{|\vec{p}_T|}{2M} \, f_{1T}^{\perp(q)}(x, \vec{p}_T^{\,2}),$$

are displayed along with the unpolarized u and d quark distributions in Fig. 2. The "one-half" and first moments [15] of the up and down quark Sivers functions are negative and positive respectively while the up and down quark Boer-Mulders functions are *both negative* over the full range in Bjorken-x. We also note that the u-quark Sivers function and Boer-Mulders function are nearly equal, even with the inclusion of the axial vector spectator diquark.

Having explored the flavor dependence of the $h_1^{\perp}$ we are now in a position to extend early phenomenological work on "T-odd" contributions to azimuthal asymmetries in SIDIS[7]. We consider the spin independent double "T-odd" $\cos 2\phi$ asymmetry for π^+ and π^- production. We focus on the important contributions to the cross section for unpolarized SIDIS [17]

$$\frac{d\sigma}{dx\, dy\; dz\, d\phi_h\, dP_{h\perp}^2} \approx \frac{2\pi\alpha^2}{xyQ^2}\left[\left(1 - y + \frac{1}{2}y^2\right) F_{UU,T} \;+\; (1-y)\cos(2\phi_h)\, F_{UU}^{\cos 2\phi_h}\right],$$

where the structure function $F_{UU}^{\cos 2\phi_h}$ involves a convolution of the Boer-Mulders and Collins fragmentation function

$$F_{UU}^{\cos 2\phi_h} = \mathcal{C}\left[-\frac{2\hat{\boldsymbol{h}}\cdot\boldsymbol{k}_T\hat{\boldsymbol{h}}\cdot\boldsymbol{p}_T - \boldsymbol{k}_T\cdot\boldsymbol{p}_T}{MM_h} h_1^{\perp} H_1^{\perp}\right], \tag{9}$$

$\mathcal{C}$ is the convolution integral. Our input for the Collins functions is based on recent work in [20] where the Collins function was calculated in the spectator framework. It was assumed that $H_1^{\perp(dis-fav)} \approx -H_1^{\perp(fav)}$ in the pion sector, thereby satisfying the Schaefer-Teryaev sum rule [21] locally. We estimate the azimuthal asymmetry $A_{UU}^{\cos 2\phi}$ (cf. Eq. (9)), where $A_{UU}^{\cos 2\phi} \equiv \int \cos 2\phi \, d\sigma / \int d\sigma$. In Fig. 3 we display the $A_{UU}^{\cos 2\phi}(P_T)$ in the range of HERMES [3] and future JLAB kinematics [22] as well as x dependence in the range $0.5 < P_T < 1.5$ GeV/c.

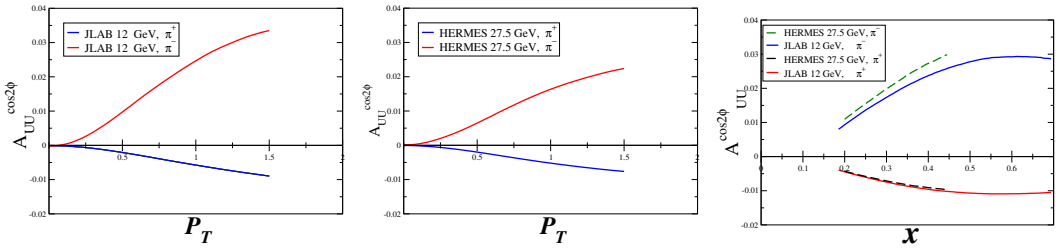

Figure 3: The $\cos 2\phi$ asymmetry for and $\pi^{\pm}$ as a function of P_T at JLAB 12GeV and HERMES (center) kinematics. Right: $\cos 2\phi$ asymmetry for $\pi^{\pm}$ as a function of x at JLAB 12GeV and HERMES kinematics.

Having calculated the chiral-odd but "T-even" parton distribution $h_{1L}^{\perp}$ we use this result together with the result of Ref. [20] for the Collins function to give a prediction for the $\sin(2\phi)$ single spin asymmetry A_{UL} for a longitudinally polarized target. A decomposition into structure functions of the cross section of semi-inclusive DIS for a longitudinally polarized target reads (see e.g. [17])

$$\frac{d\sigma_{UL}}{dx\,dy\,dz\,d\phi_h\,dP_{h\perp}^2} \approx \frac{2\pi\alpha^2}{xyQ^2}\,S_{\parallel}\left[(1-y)\sin(2\phi_h)\,F_{UL}^{\sin(2\phi)} + (2-y)\sqrt{1-y}\sin(\phi_h)\,F_{UL}^{\sin\phi}\right], \tag{10}$$

$S_{\parallel}$ is the projection of the spin vector on the direction of the virtual photon. In a partonic picture the structure function $F_{UL}^{\sin(2\phi)}$ is a leading twist object (while $F_{UL}^{\sin\phi}$ is sub-leading) and given by a convolution of the TMD $h_{1L}^{\perp}$ and the Collins function (cf. [17])

$$F_{UL}^{\sin(2\phi)} = \mathcal{C}\left[-\frac{2\hat{\boldsymbol{h}}\cdot\boldsymbol{k}_T\,\hat{\boldsymbol{h}}\cdot\boldsymbol{p}_T - \boldsymbol{k}_T\cdot\boldsymbol{p}_T}{MM_h}\,h_{1L}^{\perp}H_1^{\perp}\right]. \tag{11}$$

We display the results for the single spin asymmetry $A_{UL}^{\sin(2\phi)}$ in Fig. 4 using the kinematics of the upcoming JLab 12 GeV upgrade. We note that the π^- asymmetry is large and positive due to the model assumption $H_1^{\perp(dis-fav)} \approx -H_1^{\perp(fav)}$. This asymmetry has been measured at HERMES for longitudinally polarized protons [23] and deuterons [24]. The data show that for the proton target at HERMES 27.5 GeV kinematics both π^+ and π^- asymmetries are consistent with 0 down to a sensitivity of about 0.01. These asymmetries could be non-zero, but with magnitudes less than 0.01 or 0.02. These results are considerably smaller than our predictions for the JLab upgrade. For the deuteron target the results are consistent with 0 for π^+ and π^-. This SIDIS data for polarized deuterons could reflect the near cancellation of u- and d-quark $h_{1L}^{\perp}$ functions and/or the large unfavored Collins function contributions. There is also CLAS preliminary data [25] at 5.7 GeV that shows slightly negative asymmetries for π^+ and π^- and leads to the extraction of a negative $xh_{1L}^{\perp(u)}$. This suggests that the unfavored Collins function (for $d \to \pi^+$) is not contributing much. Data from the upgrade should help resolve these phenomenological questions.

We have performed calculations of transverse momentum dependent parton distributions, including the Boer-Mulders function $h_1^{\perp}$, the Sivers function $f_{1T}^{\perp}$ along with $h_{1L}^{\perp}$ in the

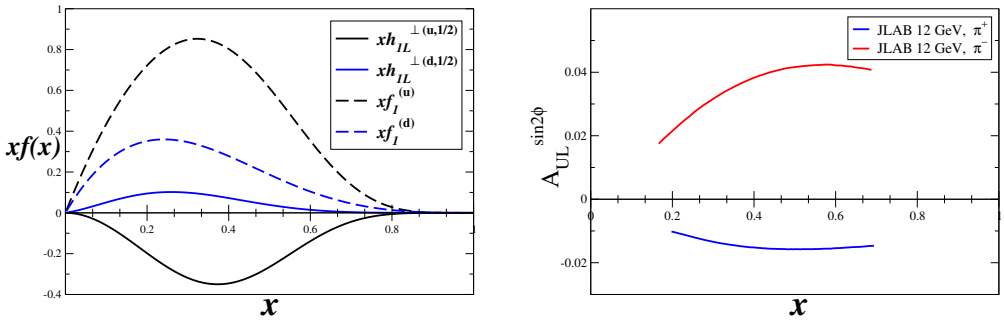

Figure 4: Left Panel: The half-moment of $xh_{1L}^{\perp(1/2)}$ versus x compared to the unpolarized up and down quark distribution functions. Right Panel: The $\sin 2\phi$ asymmetry for π^+ and π^- as a function of x at JLAB 12GeV kinematics.

framework of an axial-vector and a scalar diquark spectator model. The calculation of these functions in both sectors allowed us to explore their flavor dependence, i.e. to compute $h_1^\perp$, $f_{1T}^\perp$ and $h_{1L}^\perp$ for a u-quark and a d-quark. We used these results along with the Collins fragmentation function $H_1^\perp$. to estimate the azimuthal asymmetries $A_{UU}^{(\cos(2\phi))}$ and $A_{UL}^{(\sin(2\phi))}$ in SIDIS. In summary, a refined diquark spectator model, including axial vector di-quarks leads to both u- and d-quark "T-odd" TMDs and provides the ingredients for predicting a range of asymmetries for future experiments.

Acknowledgments

This work is supported in part by the U.S. Department of Energy under contracts, DE-FG02-07ER41460 (LG), and DE-FG02-92ER40702 (GRG).

References

[1] Slides:
`http://indico.cern.ch/contributionDisplay.py?contribId=154&sessionId=4&confId=9499`
[2] D. W. Sivers, Phys. Rev. **D41**, 83 (1990).
[3] HERMES, A. Airapetian *et al.*, Phys. Rev. Lett. **94**, 012002 (2005), hep-ex/0408013.
[4] COMPASS, V. Y. Alexakhin *et al.*, Phys. Rev. Lett. **94**, 202002 (2005), hep-ex/0503002.
[5] D. Boer and P. J. Mulders, Phys. Rev. **D57**, 5780 (1998), hep-ph/9711485.
[6] G. R. Goldstein and L. Gamberg, (2002), hep-ph/0209085.
[7] L. P. Gamberg, G. R. Goldstein, and K. A. Oganessyan, Phys. Rev. **D67**, 071504 (2003), hep-ph/0301018.
[8] A. M. Kotzinian and P. J. Mulders, Phys. Lett. **B406**, 373 (1997), hep-ph/9701330.
[9] S. J. Brodsky, D. S. Hwang, and I. Schmidt, Phys. Lett. **B530**, 99 (2002), hep-ph/0201296.
[10] X.-d. Ji and F. Yuan, Phys. Lett. **B543**, 66 (2002), hep-ph/0206057.
[11] A. Bacchetta, A. Schaefer, and J.-J. Yang, Phys. Lett. **B578**, 109 (2004), hep-ph/0309246.
[12] L. P. Gamberg, D. S. Hwang, A. Metz, and M. Schlegel, Phys. Lett. **B639**, 508 (2006), hep-ph/0604022.
[13] R. Jakob, P. J. Mulders, and J. Rodrigues, Nucl. Phys. **A626**, 937 (1997), hep-ph/9704335.
[14] A. V. Belitsky, X. Ji, and F. Yuan, Nucl. Phys. **B656**, 165 (2003), hep-ph/0208038.
[15] L. P. Gamberg, G. R. Goldstein, and M. Schlegel, (2007), arXiv:0708.0324 [hep-ph].
[16] G. R. Goldstein and J. Maharana, Nuovo Cim. **A59**, 393 (1980).
[17] A. Bacchetta *et al.*, JHEP **02**, 093 (2007), hep-ph/0611265.
[18] M. Gluck, E. Reya, and A. Vogt, Eur. Phys. J. **C5**, 461 (1998), hep-ph/9806404.

[19] M. Anselmino *et al.*, (2005), hep-ph/0511017.
[20] A. Bacchetta, L. Gamberg, G. Goldstein, and A. Mukherjee, hep-ph/0707:3372.
[21] A. Schafer and O. V. Teryaev, Phys. Rev. **D61**, 077903 (2000), hep-ph/9908412.
[22] H. Avakian *et al.*, approved JLab proposal PR 12-06-112. (2006).
[23] HERMES, A. Airapetian *et al.*, Phys. Rev. Lett. **84**, 4047 (2000), hep-ex/9910062.
[24] HERMES, A. Airapetian *et al.*, Phys. Lett. **B562**, 182 (2003), hep-ex/0212039.
[25] CLAS, H. Avakian, P. E. Bosted, V. Burkert, and L. Elouadrhiri, AIP Conf. Proc. **792**, 945 (2005), nucl-ex/0509032.

Measurement of Transverse Lambda Polarization in Quasi-Real Photoproduction at HERMES

Yu. Naryshkin

Petersburg Nuclear Physics Institute,
St. Petersburg, Gatchina, 188350 Russia

Transverse Λ and $\bar{\Lambda}$ polarization produced inclusively in quasi-real photon-nucleon scattering have been studied by the HERMES experiment using a 27.57 GeV positron beam incident on hydrogen and deuterium gas targets. The average transverse polarizations were found to be $P_n^{\Lambda} = 0.078 \pm 0.006\,(\text{stat}) \pm 0.012\,(\text{syst})$ and $P_n^{\bar{\Lambda}} = -0.025 \pm 0.015\,(\text{stat}) \pm 0.018\,(\text{syst})$ for Λ and $\bar{\Lambda}$ respectively. The dependences of P_n^{Λ} on the transverse and longitudinal momenta of the Λ hyperon were also studied.

1 Introduction

The polarization of Λ particles has been observed and investigated in many high-energy scattering experiments, with a wide variety of hadron beams and kinematic settings [2, 3, 4]. It is almost always found to be negative. A rather consistent kinematic behavior of the polarization has also been observed: its magnitude increases almost linearly with the transverse momentum p_{T} of the Λ hyperon up to $p_{\mathrm{T}} \approx 4$ GeV, where a plateau is reached. In photoproduction, the existing data are not conclusive because of lack of statistics. Here we report on the first statistically significant observation of non-zero transverse Λ polarization in high energy (non-exclusive) photon scattering.

The Λ hyperon is a uniquely useful particle in spin physics: the parity-violating nature of its weak decay $\Lambda \rightarrow p\pi^-$ results in an angular distribution where the protons are preferentially emitted along the spin direction of their parent Λ. The angular distribution of the Λ decay products may thus be used to measure its polarization, providing a rare opportunity to explore spin degrees of freedom in the fragmentation process. In the rest frame of the Λ it has the form

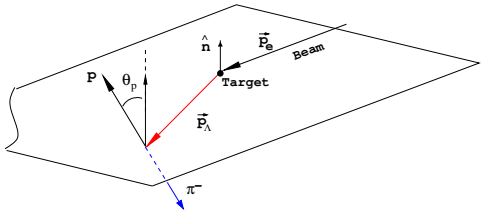

Figure 1: Schematic diagram of inclusive Λ production and decay. The angle θ_p of the decay proton with respect to the normal $\hat{n}$ to the scattering plane is defined in the Λ rest frame.

$$\frac{dN}{d\Omega_p} = \frac{dN_0}{d\Omega_p}(1 + \alpha P^{\Lambda} \cdot cos\theta_p). \qquad (1)$$

Here, θ_p is the angle between proton momentum and Λ polarization direction in the Λ rest frame (Fig.1), P^{Λ} is the polarization of the Λ, and $\alpha = 0.642 \pm 0.013$ is the analyzing power of the parity-violating weak decay. The symbols $dN/d\Omega_p$ and $dN_0/d\Omega_p$ denote the distributions for the decay of polarized and unpolarized Λ samples respectively. Because of the parity-conserving nature of the strong interaction, any final-state hadron polarization in a reaction with unpolarized beam and target must point along a pseudo-vector direction. In the case of inclusive hyperon production,

the only available direction of this type is the normal $\hat{n}$ to the scattering plane formed by the cross-product of the vectors along the laboratory-frame momenta of the positron beam ($\vec{p}_e$) and the Λ ($\vec{p}_\Lambda$):

$$\hat{n} = \frac{\vec{p}_e \times \vec{p}_\Lambda}{|\vec{p}_e \times \vec{p}_\Lambda|}. \tag{2}$$

2 The HERMES experiment and data analysis

The Λ photoproduction data were accumulated by the HERMES experiment at DESY. In this experiment, the 27.6 GeV positron beam of the HERA *e-p* collider passes through an open-ended tubular storage cell into which polarized or unpolarized target atoms in undiluted gaseous form are continuously injected. The HERMES detector is described in detail in Ref. [5].

This analysis combines the data collected at HERMES in the years 1996 – 2000. The sample includes data taken with both longitudinally polarized and unpolarized targets (the latter being of much higher density than the former), while the positron beam was always longitudinally polarized. As the target spin direction was reversed every 90 seconds, the average target polarization was negligibly small. The target species included hydrogen, deuterium, and a variety of heavier gases.

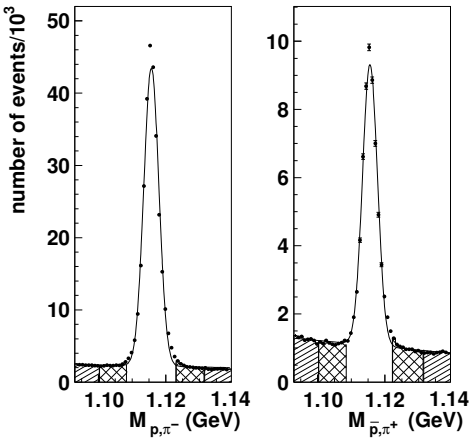

Figure 2: Invariant mass distributions for Λ and $\bar{\Lambda}$ events. For the polarization analysis, Λ and $\bar{\Lambda}$ events within a $\pm 3.3\,\sigma$ invariant mass window around the mean value of the fitted peak were chosen, and a background-subtraction procedure was applied.

The Λ hyperons were identified in the analysis through their $p\pi^-$ decay channel. Events were selected by requiring the presence of at least two hadron candidates of opposite charge. The kinematics of the Λ ($\bar{\Lambda}$) decay products detected by the HERMES spectrometer is such that the proton (antiproton) momentum is always much higher than that of the pion. Two spatial vertices were reconstructed for each event. First the secondary (decay) vertex was determined from the intersection (i.e., point of closest approach) of the proton (antiproton) and pion tracks. Then the intersection of the reconstructed hyperon track with the nominal beam axis was used to determined the primary (production) vertex. In both cases, the distance of closest approach was required to be less than 1.5 cm. In addition the transverse distance between the decay vertex and the nominal beam axis was required to be larger than 1 cm. If more than one positive or negative hadron was found in one event, all possible combinations of positive and negative hadrons were used.

All tracks were also required to satisfy a series of fiducial-volume cuts designed to avoid the inactive edges of the detector. Furthermore the two hadron tracks were required to be reconstructed in one spectrometer half to avoid effects caused by any possible misalignment of the two spectrometer halves relative to each other. For tracks fulfilling these requirements

the invariant mass of the hadron pair was evaluated. The resulting spectra are shown in Fig.2.

The extraction of the Λ polarization from the data was accomplished using a moment method which exploits the top/bottom symmetry of the detector and is described in Refs. [6, 7]. In order to study possible effects of detector misalignment and inefficiency detailed Monte-Carlo simulations were performed. The small contribution from the background under the Λ invariant mass peak to the extracted polarizations was corrected for using a side-band subtraction method.

3 Results

Averaged over the experimental kinematics, the net Λ polarization is found to be signficantly positive while the net $\bar{\Lambda}$ polarization is consistent with zero: $P_\Lambda = 0.078 \pm 0.006(\text{stat}) \pm 0.012(\text{syst})$. and $P_{\text{n}}^{\bar{\Lambda}} = -0.025 \pm 0.015(\text{stat}) \pm 0.018(\text{syst})$ [7].

In order to estimate the systematic uncertainty of the measurement an identical analysis was carried out for reconstructed h^+h^- hadron pairs, both with leading protons (Λ-like case) and with leading antiprotons ($\bar{\Lambda}$-like case). Events within two mass windows above and below the Λ ($\bar{\Lambda}$) mass window (1.093 GeV $< M_{h^+h^-} <$ 1.108 GeV, and 1.124 GeV $< M_{h^+h^-} <$ 1.139 GeV) were selected with the hadrons' point of closest approach required to be inside the target region. False polarization values of 0.012 ± 0.002 and 0.018 ± 0.002 were found in the Λ-like and $\bar{\Lambda}$-like cases respectively. These values were used as estimates of the systematic error on the Λ and $\bar{\Lambda}$ polarization. As an additional check on a possible false polarization, the decay $K_s^0 \to \pi^+\pi^-$ was studied. The false polarization of the K_s^0 sample was found to be 0.012 ± 0.004 and 0.002 ± 0.004 in the Λ-like and $\bar{\Lambda}$-like cases respectively.

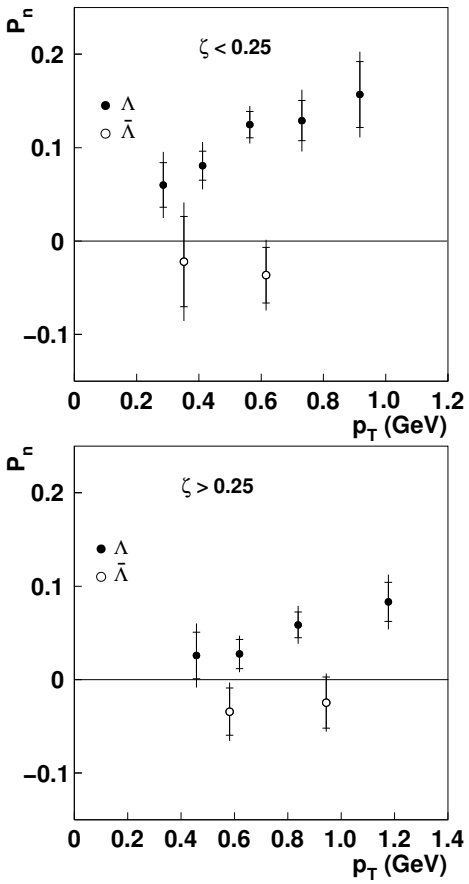

Figure 3: Transverse polarizations P_Λ and $P_{\bar{\Lambda}}$ as a function of p_{T} for hyperons from the regions $\zeta < 0.25$ (upper panel) and $\zeta > 0.25$ (lower panel). The inner error bars represent the statistical uncertainties; the outer error bars represent the statistical and systematic uncertainties added in quadrature.

As information on the virtual photon kinematics was not available in this inclusive measurement, the kinematic dependence of the polarization could only be studied as a function of variables derived from the eN system. The selected variables were p_T and

$\zeta \equiv (E_\Lambda + p_{z\Lambda})/(E_e + p_e)$, where p_T is the transverse momentum with respect to the (lepton) beam, E_Λ and $p_{z\Lambda}$ are the energy and z-component of the Λ momentum (where the z-axis is defined as the lepton beam direction), and E_e, p_e are the energy and momentum of the positron beam.

The variable ζ provides an approximate measure of whether a hyperon was produced in the forward or backward region in the center-of-mass frame of the $\gamma^* N$ reaction. The natural variable to use to separate these kinematic regimes would be $x_{\rm F} = p_\parallel^\Lambda / p_{\rm max}^\Lambda$, evaluated in the $\gamma^* N$ system, but this variable is not available in an inclusive measurement. Nevertheless, a simulation of the reaction using the PYTHIA program reveals a reasonable correlation between ζ and $x_{\rm F}$ variables. In particular, all events at $\zeta \geq 0.25$ are produced in the kinematic region $x_{\rm F} > 0$, while for $\zeta < 0.25$ there is a mixture of events originating from the kinematic regions $x_{\rm F} > 0$ and $x_{\rm F} < 0$. In Fig. 3, the transverse Λ and $\bar{\Lambda}$ polarizations are shown versus $p_{\rm T}$ for the two intervals $\zeta < 0.25$ and $\zeta > 0.25$. In both regimes the Λ polarization rises linearly with $p_{\rm T}$. The Λ and $\bar{\Lambda}$ polarizations as functions of ζ are shown in Fig. 4. The Λ polarization appears to increase in the low-ζ region while the $\bar{\Lambda}$ polarization shows no visible dependence on either ζ or $p_{\rm T}$.

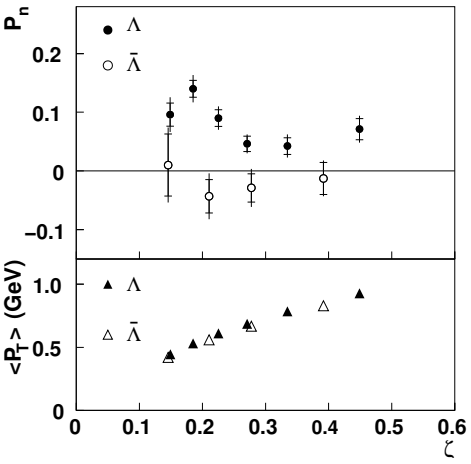

Figure 4: Transverse polarizations P_Λ and $P_{\bar{\Lambda}}$ (upper panel) and mean $\langle p_{\rm T} \rangle$ (lower panel) as functions of $\zeta = (E_\Lambda + p_{z\Lambda})/(E_e + p_e)$.

4 Acknowledgments

We gratefully acknowledge the DESY staff and the staffs of the collaborating institutions. This work was supported by the Russian Academy of Science and the Russian Federal Agency for Science and Innovations.

References

[1] Slides:
`http://indico.cern.ch/contributionDisplay.py?contribId=155&sessionId=4&confId=9499`

[2] K. Heller, in "Proceedings of the 12$^{\rm th}$ International Symposium on High-Energy Spin Physics (SPIN 96)", edited by C.W. de Jager, T.J. Ketel, P.J. Mulders, J.E.J. Oberski, M. Oskam-Tamboezer (World Scientific, Singapore, 1997), p.23.

[3] J. Lach, Nucl. Phys. (Proc. Suppl.) **50** 216 (1996)

[4] WA89 Collaboration, M.I. Adamovich , Eur. Phys. J. **C32** 221 (2004)

[5] HERMES Collaboration, K. Ackerstaff *et al.*, Nucl. Instrum. Methods **A417** 230 (1998).

[6] S. Belostotski DESY-HERMES-06-57.
Prepared for 58th Scottish Universities Summer School in Physics (SUSSP58): A NATO Advanced Study Institute and EU Hadron Physics 13 Summer Institute, St. Andrews, Scotland, 22-29 Aug 2004.

[7] A, Airapetian *et al.*, arXiv:hep-ex/07043133 (2007).

Summary of PHENIX Transverse Spin Physics Results

K.Oleg Eyser on behalf of the PHENIX collaboration

University of California,
Riverside, CA 92521, USA

The PHENIX experiment at the Relativistic Heavy Ion Collider (RHIC) has accumulated a substantial data set of transversely polarized protons over the last few years. Measurements include inclusive single spin asymmetries at mid-rapidities at $\sqrt{s} = 200$ GeV. In 2006, new data sets of 2.7 pb^{-1} at $\sqrt{s} = 200$ GeV and 20 nb^{-1} at $\sqrt{s} = 62.4$ GeV have been taken. Along with a new calorimeter at forward rapidities, a variety of asymmetries and probes has been proposed, which may help to disentangle the contributions from the theoreatical model calculations. We present the status of the PHENIX measurements, and how they can help lead to a deeper understanding of the transverse proton spin structure.

1 Introduction

Large single-spin asymmetries have been observed in different high energy $p + p$ collisions in the past [2], although they were expected to vanish in perturbative QCD calculations at large transverse momenta p_T. The spin structure of the nucleon includes a term called transversity distribution δq, which is different from the longitudinal quark distribution Δq because relativistic boosts and rotations do not commute. Transversity therefore probes the relativistic nature of the nucleon and can be determined from transversely polarized scattering processes

$$A_{TT} \propto (\delta q)^2, \qquad A_N \propto \delta q.$$

The analyzing power A_N poses a direct measure of transversity in combination with another chiral odd function. Proposed models include spin dependent fragmentation functions (Collins effect, [3]), asymmetries in the intrinsic transverse momentum distributions of partons (Sivers effect, [4]), and quark gluon field interference in higher twist calculations [5]. The latter might have a major impact in the investigated energy regime, especially at lower p_T.

2 The PHENIX Experiment

The PHENIX experiment uses a multi-purpose detector with a high bandwidth data acquisition system and multiple triggers. The central arms cover -0.3 to 0.3 in pseudo-rapidity η and two times $\pi/2$ in azimuthal angle. Charged particles are tracked in a drift chamber (DC) outside of a central axial magnetic field and followed by several layers of pad chambers (PC1 through PC3). A ring imaging Cerenkov detector (RICH) allows particle separation of pions and electrons below the threshold momentum of 4.9 GeV/c. Additionally, the particle energies are measured in PbSc and PbGl electro-magnetic calorimeters (EMCAL).

The two muon arms cover the full azimuth at $1.2 < |\eta| < 2.4$. Each arm consists of three tracker stations (MuTr) followed by muon identification detectors (MuID) sandwiched between steel absorbers.

Also, there are two sets of global detectors, the beam-beam-counters (BBC) and the zero degree calorimeter (ZDC), which mainly serve trigger and monitoring purposes. In 2006, a

new $PbWO_4$ calorimeter was commissioned in the south hemisphere of the experiment in forward direction ($3.2 < \eta < 3.8$) with full azimuthal coverage.

3 Asymmetries

Transverse single spin asymmetries are described by:

$$\epsilon = A_N \cdot P \cdot < \cos\varphi >= \frac{N^+ - N^-}{N^+ + N^-},$$

where the combination of the polarization P and the analyzing power A_N can lead to an azimuthal modulation of the differential cross section. Since this asymmetry is maximum perpendicular to the polarization vector and vanishes in its direction, for extended detectors, the cosine-modulation has to be taken into account. The yields N^+ and N^- refer to two different polarization states, which in this case point in the direction of $\varphi = 0.5 \cdot \pi$ and $\varphi = 1.5 \cdot \pi$.

Asymmetries between the left and right side hemispheres of the detectors are considered to be simple asymmetries, as are pure polarization asymmetries in one detector, i.e. asymmetries between two polarization states $P^\uparrow = +P$ and $P^\downarrow = -P$. These asymmetries are susceptible to acceptance, efficiency, and luminosity differences of the respective yields. Therefore, it is usually better to use geometric means of the yields and thereby removing those effects in first order:

$$A_N = \frac{1}{P} \cdot \frac{\sqrt{N^\uparrow_{left} \cdot N^\downarrow_{right}} - \sqrt{N^\downarrow_{left} \cdot N^\uparrow_{right}}}{\sqrt{N^\uparrow_{left} \cdot N^\downarrow_{right}} + \sqrt{N^\downarrow_{left} \cdot N^\uparrow_{right}}}.$$

4 Results

PHENIX has measured inclusive neutral pion and charged hadron cross sections and single spin asymmetries in the central region previously [6]. Cross sections have been shown to be in good agreement with perturbative QCD calculations. Asymmetries are consistent with zero and have been utilized to constrain the gluon Sivers function [7].

Forward neutron asymmetries have been measured in the ZDC in forward and backward hemispheres. These asymmetries vanish at negative x_F and rise to about 8% at positive x_F as expected from RHIC-IP12 [8]. From the azimuthal distributions, one can determine the alignment of the polarization vector. Forward neutron asymmetries are, therefore, utilized as a monitoring tool for the spin rotator commissioning.

Recent measurements from 2006 include a first glimpse into heavy flavour production. Since heavy quarks are expected to be predominantly produced by gluon fusion and gluons do not exhibit transversity, the Collins mechanism should be minimized. Measured single spin asymmetries could then be more easily connected to gluon (or less prominently quark) Sivers function. The J/Ψ di-muon decay is detected in the muon arms, see figure 1. Several checks of background asymmetries have been carried out, including same-sign di-muon spectra and sidebands around the J/Ψ-peak. So far, the asymmetries are consistent with zero.

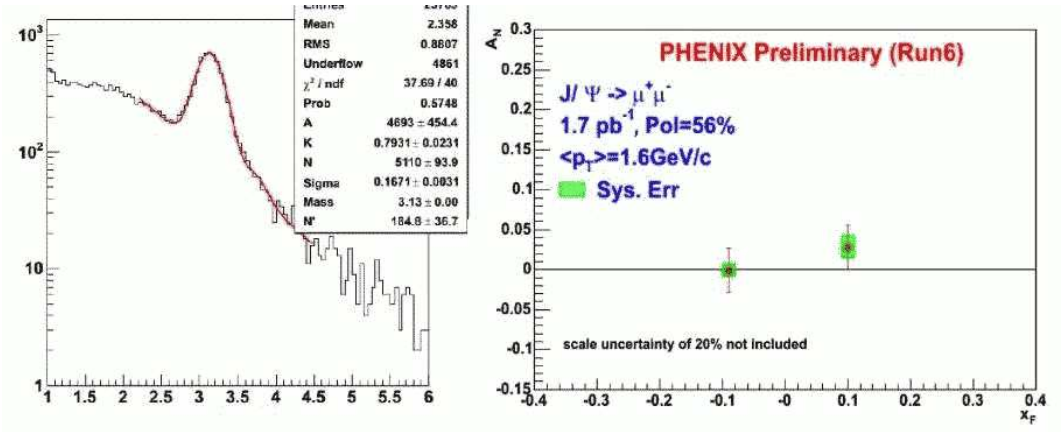

Figure 1: $J/\Psi \to \mu\mu$: mass spectrum with di-muon peak at 3 GeV. Single spin asymmetry from forward and backward directions (positive and negative x_F).

5 Outlook

A new electro-magnetic calorimeter has been installed in the south detector arm prior to the 2006 RHIC run. After commissioning, a data set of 20 nb^{-1} could be recorded at $\sqrt{s} = 62.4$ GeV. While the analysis is still on-going, the detector calibration was finished in early 2007 and first pion asymmetries of a few percent have been seen and seem to follow the general behaviour of those seen by BRAHMS and STAR. These asymmetries can additionally be used for the monitoring of the polarization vector, see figure 2. The figure is exemplary and contains only part of the data set. The beam polarization is not yet considered in the asymmetries.

Another proposed way to directly access the Sivers function is to look for asymmetries in two-jet back-to-back correlations [9]. In this correlation, the Collins effect should average out and not contribute to any asymmetry. For PHENIX, the jet prediction has been smeared out in order to transfer it to two-hadron correlations. A first proof-of-principle analysis has been done with 2005 data with only a residual transverse component in the longitudinal polarization.

Transversity on the other hand might be directly probed via interference fragmentation functions. A Sivers function would not contribute to a correlation asymmetry between two hadrons, this time coming from the same fragmentation process. Such an analysis depends on the knowledge of the interference fragmentation functions, which have to be extracted from other experiments, e.g. Belle.

6 Summary

PHENIX has measured transverse single spin asymmetries of inclusive neutral pions and charged hadrons at mid-rapidities in the past. Forward neutron asymmetries are seen and utilized for monitoring of the polarization vector in the interaction region. New analyses include heavy flavours via J/Ψ production with its di-muon decay. First neutral pion asymmetries have been seen at large rapidities, which generally show the same behaviour of the

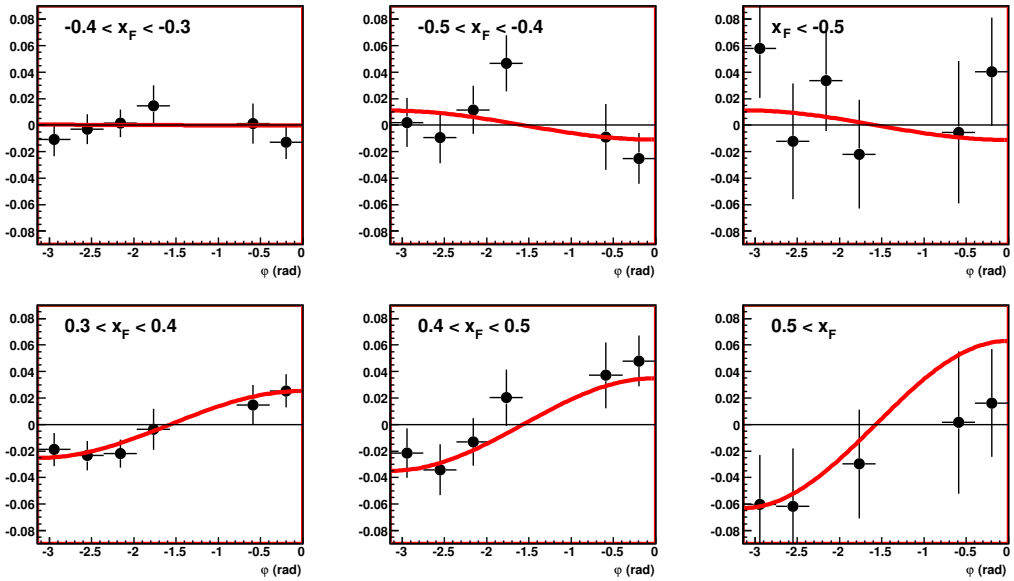

Figure 2: Raw neutral pion single spin asymmetries at large rapidities ($3.2 < \eta < 3.8$). The asymmetries are calculated with geometric means of yields, see above, and fitted with a cosine function. The polarization has not yet been included.

pion asymmetries seen in BRAHMS and STAR. Future analyses will include two-hadron correlations to probe the Sivers function and directly access transversity.

References

[1] Slides:
`http://indico.cern.ch/contributionDisplay.py?contribId=156&sessionId=4&confId=9499`

[2] D.L. Adams *et al.*, Phys. Lett. **B264** 462 (1991);
J. Adams *et al.*, Phys. Rev. Lett. **92** 171801 (2004).

[3] J. Collins, Nucl. Phys. **B396** 161 (1993).

[4] D. Sivers, Phys. Rev. D **43** 261 (1991).

[5] Y. Koike, "Single transverse-spin asymmetry in p p(pol.) –¿ pi X and e p(pol.) –¿ pi [arXiv:hep-ph/0210396].

[6] S. Adler *et al.*, Phys. Rev. Lett. **95** 202001 (2005).

[7] M. Anselmino *et al.*, Phys. Rev. D **74** 094011 (2006).

[8] A. Bazilevsky *et al.*, Phys. Lett. B **650** (2007) 325 [arXiv:hep-ex/0610030].

[9] C.J. Bomhof *et al.*, Phys. Rev. D **75** (2007) 074019 [arXiv:hep-ph/0701277]; D. Boer and W. Vogelsang, Phys. Rev. D **69**, 094025 (2004) [arXiv:hep-ph/0312320].

Measurement of Transverse Spin Effects with the Forward Pion Detector at STAR in Polarized p+p Collisions at 200GeV

Steven Heppelmann for the STAR collaboration.

Penn State University
University Park, Pa. 16802, USA

The STAR collaboration presents preliminary measurements of A_N, the transverse single spin asymmetries in $p + p \rightarrow \pi^0 + X$ interactions at $\sqrt{s} = 200GeV/c$ with rapidity in the range from 3.3 to 3.7. The data were collected with the STAR FPD and FPD++ detectors during RHIC Run 6. With this much larger data set than that of earlier RHIC runs, a determination of the transverse momentum (p_T) dependence of A_N for narrow bins of the Feynman X_F out to $p_T > 3GeV/c$ is presented. While all the current theories predict that the asymmetry at fixed X_F should fall with p_T, this experimental measurement shows no reduction in asymmetry as a function of p_T. These asymmetries correspond to production in a regime where NLO PQCD calculations can successfully describe the spin summed cross sections.

1 Background

In this paper we present preliminary results from STAR for data taken during RHIC Run 6 on the transverse single spin asymmetries in the reaction

$$p + p \rightarrow \pi^0 + X.$$

Data were collected using the FPD [2] and FPD++ [3] detectors at STAR, which are located in the far forward regions relative to the two polarized proton beams.

The STAR results are part of broader effort involving electron or proton scattering from polarized nucleons for the study of spin observables associated with so called **T odd** processes. The calculations of single transverse asymmetries must provide non-vanishing amplitudes for helicity flip and non-flip. The T odd asymmetries require the interference between these amplitudes. One interfering amplitude must be out of phase from the other by 90^o for non-vanishing single transverse spin asymmetries to be possible. Neither a helicity flip nor the required phase difference is present in the lowest twist term of the perturbative calculation.

Such processes present a challenge for theory as they occur in regimes where the spin averaged cross sections can be calculated in leading twist PQCD but the transverse spin dependence of these cross sections vanishes in this leading twist, collinear factorization picture. The calculations of these transverse asymmetries then pushes theoretical calculations toward the more non-trivial questions in QCD.

The additional methods required to enable the calculation of non-zero transverse single spin asymmetries have been of three main types. In the **Sivers Effect** [4] a spin dependent transverse momentum is explicitly added to the more common longitudinal momentum dependence of the parton distribution functions. In the **Collins Effect** [5] a similar transverse spin dependence is associated with the transverse momentum dependence of fragmentation

functions. Each of these methods generates a fixed p_T bias that is dependent upon transverse spin but should be independent of the hard scattering process. If factorization between the hard scattering process and parton distribution is valid, and this is not proven for these formulations, it is very difficult to avoid the conclusion that the asymmetry should fall with p_T. In particular, for a cross section that falls in proportion to a power of p_T, these arguments suggest that asymmetry would be expected to fall as $1/p_T$. Recent calculations of Collins and Sivers effects bear out this general observation [6].

The third alternative involves higher twist effects and these too, almost by definition, require the calculated asymmetry to fall at least as the inverse power of p_T [7]. So in the current view of how these transverse asymmetries can come about, the requirement that the single spin asymmetry should falls with p_T is quite universal.

2 The Measurement

The forward electromagnetic calorimetry in STAR has evolved through several stages as the spin program at RHIC has progressed. The first **pre-FPD** detector consisted of prototype lead/scintillator and lead glass modules placed about 7 meters from the interaction point in STAR both left and right of the beam. It was with this apparatus that the first published transverse single spin asymmetry π^0 data from RHIC were obtained [8].

In subsequent RHIC polarized proton runs, FPD modules were installed North and South of the beam (left and right), both east and west of the interaction region. Each of the left and right FPD detectors consisted of a 7x7 array of lead glass scintillators, each cell with transverse dimensions 3.8 cm x 3.8 cm. The central part of the FPD++ detector, used in this analysis, has the same fiducial transverse size as the FPD. Smaller arrays were placed above and below the beam line where, with vertically polarized beam, no up/down asymmetry is expected.

For this result, single π^0's are reconstructed in FPD modules east of the interaction region or in FPD++ modules west of the interaction region. The calibration of calorimeter cells was determined to an accuracy of about 2% by fitting with the π^0 mass distribution. Run 6 was by far the most successful run for transverse spin in STAR as is summarized in Table 1. The figure of merit for statistical significance of single spin measurements based on polarization and luminosity is about 50 times greater for Run 6 than for the previous runs combined.

Because of parity and rotational invariance, the transverse single spin asymmetry, defined by

$$A_N = \frac{\sigma_+ - \sigma_-}{\sigma_+ + \sigma_-}$$

can be measured either with a single detector location by changing the transverse beam polarization or with a single polarization and symmetrical measurement in a left detector vs right detector. The first method requires a careful measurement of the ratio of spin up to spin down luminosity. The second method requires a careful measurement of the left vs. right acceptance of the detectors.

With both the FPD or FPD++, we have symmetrical acceptance left and right of the beam. With the spin transverse quantization direction vertical, a superior method for calculating the asymmetry is called the cross ratio method. We define, for example, N_R+ as the observed number of events involving the right(R) detector with transverse spin (+). With

this convention and taking the beam polarization to be P_{bm}, we calculate the cross ratio for asymmetry, which is defined as

$$A_N \equiv \frac{1}{P_{bm}} \frac{\sqrt{N_{L+}}\sqrt{N_{R-}} - \sqrt{N_{R+}}\sqrt{N_{L-}}}{\sqrt{N_{L+}}\sqrt{N_{R-}} + \sqrt{N_{R+}}\sqrt{N_{L-}}}.$$

	Run2	Run3	Run5	Run6
Det	pre FPD	FPD 6 mods	FPD 8 mods	East FPD West FPD++
P_{bm}	15%	30%	45%	60%
$\int Ldt$ pb^{-1}	0.15	0.25	0.1	6.8
$<\eta>$	3.8	± 3.3 ± 4.0	± 3.7 ± 4.0	-3.7 $+3.3$

Table 1: Transverse spin runs at STAR with forward calorimetry: 2001-2006.

The cross ratio method for calculating A_N is insensitive to both the ratio of luminosities for the two spin states and to the ratio of left to right acceptance.

The data presented here involves two detector settings with nominal acceptance around rapidities of $\eta = 3.3$ and $\eta = 3.7$. For previous measurements of A_N, a narrow range of acceptance in rapidity, implies a high degree of correlation between Feynman X_F and transverse momentum p_T. With good statistics over this range of rapidities, we are able to study the p_T dependence for fixed bins in X_F.

3 Results

The A_N values determined from Run 6 data are shown in Figure 1. It is seen that the transverse single spin asymmetry for π^0 production grows at large and positive X_F, where positive X_F corresponds to the forward direction for the polarized proton.

As expected, the asymmetry for forward production is large but for backward production, it is small or zero. As discussed above, current theories predict that the asymmetry should fall with increasing transverse momentum at fixed X_F. These predictions imply that smaller rapidity should be associated with smaller asymmetry when X_F is fixed. From the figure, these data indicate the opposite trend.

In Figure 2, the data have been divided into five X_F bins. Within each X_F bin, the dependence of A_N upon p_T is shown. While we observe that the asymmetry may be rising for p_T in the lower part of the p_T range shown, there is no evidence of the fall off with p_T that current theory predicts.

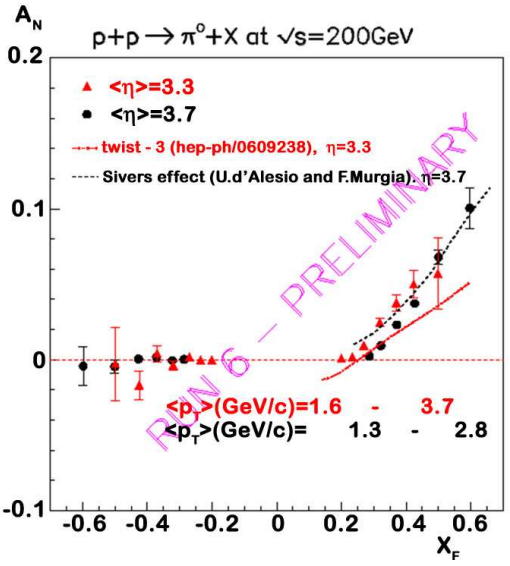

Figure 1: Single Transverse Spin π^0 Asymmetry.

4 Summary

These data are of higher p_T and X_F than the $0.04 < x_{\rm Bjorken} < 0.3$ and $0.1 < p_{T,\pi} < 1$ GeV/c range associated with the semi-inclusive deep inelastic scattering (SIDIS) data recently used to determine Sivers moments.

Integrated over p_T, the X_F dependence of these SSA results can be explained by models of the Sivers type [6] or with collinear twist-3 calculations [7]. Both approaches, however, predict the falloff of asymmetry with p_T at fixed X_F by about one inverse power of p_T. Because we have verified that the corresponding spin averaged cross sections are in accordance with NLO PQCD calculations [2] and fall very nearly as power of p_T, a large class of models will predict a p_T^{-1} dependence of the asymmetry.

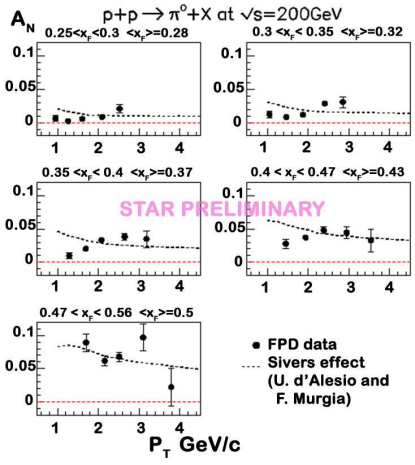

Figure 2: A_N vs p_T for bins in X_F.

These new results pose exciting challenges to present day theory. Both naïve considerations of Sivers or Collins contributions to SSA from a spin dependent δk_T and detailed calculations predict an asymmetry that should fall with p_T in the regime of these data. It seems likely that more exotic implementations of these approaches may be required to fit this experimental result. Recently, interesting questions have been raised about the application of factorization theorems in processes related to this measurement [9]. The data presented here, in conjunction with recent transverse single spin asymmetry measurements from SIDIS experiments, should greatly constrain future PQCD related models.

References

[1] Slides: `http://indico.cern.ch/contributionDisplay.py?contribId=245&sessionId=4&confId=9499`

[2] John Adams et al. Forward neutral pion production in p+p and d+au collisions at s(nn)**(1/2) = 200-gev. *Phys. Rev. Lett.*, 97:152302, 2006.

[3] L. C. Bland et al. Future of low-x forward physics at rhic. *Eur. Phys. J.*, C43:427–435, 2005.

[4] Dennis W. Sivers. Hard scattering scaling laws for single spin production asymmetries. *Phys. Rev.*, D43:261–263, 1991.

[5] John C. Collins, Steve F. Heppelmann, and Glenn A. Ladinsky. Measuring transversity densities in singly polarized hadron hadron and lepton - hadron collisions. *Nucl. Phys.*, B420:565–582, 1994.

[6] Umberto D'Alesio and Francesco Murgia. Parton intrinsic motion in inclusive particle production: Unpolarized cross sections, single spin asymmetries and the sivers effect. *Phys. Rev.*, D70:074009, 2004.

[7] Chris Kouvaris, Jian-Wei Qiu, Werner Vogelsang, and Feng Yuan. Single transverse-spin asymmetry in high transverse momentum pion production in p p collisions. *Phys. Rev.*, D74:114013, 2006.

[8] John Adams et al. Cross sections and transverse single-spin asymmetries in forward neutral pion production from proton collisions at s**(1/2) = 200-gev. *Phys. Rev. Lett.*, 92:171801, 2004.

[9] John Collins and Jian-Wei Qiu. Factorization is violated in production of high-transverse- momentum particles in hadron hadron collisions. 2007.

Single Spin Asymmetries of Identified Hadrons in $p^{\uparrow}+p$ at $\sqrt{s} = 62.4$ and 200 GeV

J.H. Lee and F. Videbæk (for the BRAHMS Collaboration)

Physics Department, Brookhaven National Laboratory
Upton, NY 11973, USA

Measurements of x_F-dependent single spin asymmetries (SSA) of identified charged hadrons, $\pi^{\pm}$, $K^{\pm}$, p, and $\bar{p}$, from transversely polarized proton collisions at $\sqrt{s} = 200$ and 62.4 GeV at RHIC are presented. The energy and flavor dependent asymmetry measurements bring new insight into the fundamental mechanisms of transverse spin asymmetries and the description of hadronic structure by Quantum Chromodynamics (QCD).

1 Introduction

Transverse spin dependence of hadron cross-setions in $p^{\uparrow}p$ ($\bar{p}^{\uparrow}p$) reactions at the energy regime where perturbative QCD (pQCD) is applicable are expected to be negligibly small in the lowest-order QCD approximation, whereas experimentally large asymmetries have been observed for large Feynman-x, $x_F = 2p_L/\sqrt{s}$. The main theoretical focus in accounting for the observed SSAs in the framework of QCD has been on the role of transverse momentum dependent (TMD) partonic effects in the structure of the initial transversely polarized nucleon [5] and on the fragmentation process of a polarized quark into hadrons [6]. Higher twist effects ("twist-3") arising from quark-gluon correlation effects beyond the conventional twist-2 distribution have been also considered as a possible origin of SSAs [7, 8]. Recently, new measurements of SSAs have been available from semi-inclusive deep-inelastic scattering (SIDIS) [9, 10] and $p^{\uparrow}+p$ at RHIC, providing more insight into the fundamental mechanisms of SSA as well as the relevant hadron structure [11, 12].

We present measurements of SSAs for $\pi^{\pm}$, $K^{\pm}$, p, and $\bar{p}$ at forward rapidities covering high-x_F at $\sqrt{s} = 62.4$ GeV and also at $\sqrt{s} = 200$ GeV. A simultaneous description of SSAs and the unpolarized cross-sections [13] in a wide kinematic range will be a crucial test for a partonic pQCD description. In particular, flavor dependent SSA measurements allow more complete and stringent tests of theoretical models due to the flavor dependence of parton distribution functions and fragmentation processes.

2 SSA Measurements at high-x_F

The SSA is defined as a "left-right" asymmetry of produced particles from the hadronic scattering of transversely polarized protons off unpolarized protons. Experimentally the asymmetry can be obtained by flipping the spins of polarized protons, and is customaryly defined as the analyzing power A_N:

$$A_N = \frac{1}{\mathcal{P}} \frac{(N^+ - \mathcal{L}N^-)}{(N^+ + \mathcal{L}N^-)}, \tag{1}$$

where $\mathcal{P}$ is the polarization of the beam, $\mathcal{L}$ is the spin dependent relative luminosity ($\mathcal{L} = \mathcal{L}_+/\mathcal{L}_-$) and $N^{+(-)}$ is the number of detected particles with beam spin vector oriented up (down).

The average polarization of the beam $\mathcal{P}$ as determined from the on-line CNI measurements is about 50% for RHIC Run-5 (200 GeV) and about 60% for Run-6 (62.4 GeV). The systematic error on the A_N measurements is estimated to be 20% including uncertainties from the beam polarization (∼18%). The systematic error represents mainly scaling uncertainties on the values of A_N. The data presented here were collected with the BRAHMS detector system [14] in polarized $p+p$ collisions from Run-5 with a recorded integrated luminosity corresponding to 2.4 pb^{-1} at $\sqrt{s}$ = 200 GeV and from Run-6 with a recorded integrated luminosity of 0.21 pb^{-1} at $\sqrt{s}$ = 62.4 GeV. The kinematic coverage of the data taken with BRAHMS-FS at 2.3° and 4° for $\sqrt{s}$ = 200 GeV and at 2.3° and 3° for $\sqrt{s}$ = 62.4 GeV as a function of p_T and x_F are shown in Fig. 1.

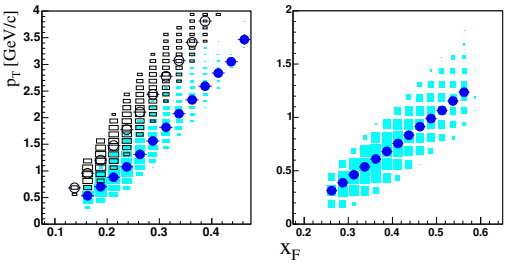

Figure 1: p_T vs. x_F for the data used in the SSA analysis at $\sqrt{s}$ = 200 GeV (left Panel). The open symbols are for FS at 4° and closed boxes are at 2.3° at full field setting. At $\sqrt{s}$ = 62.4 GeV (right panel), data from FS at 2.3° and 3° are combined. Mean values of p_T at a given x_F value are displayed as circles.

3 Results

The analyzing power A_N for charged pions, $A_N(\pi^+)$ and $A_N(\pi^-)$ at $\sqrt{s}$ = 200 GeV as a function of x_F are shown in Fig. 2 for the two FS angle settings with p_T coverages shown in Fig. 1. The A_N values are positive for π^+ and negative for π^- decreasing with p_T. The asymmetries and their x_F-dependence are qualitatively in agreement with the measure-

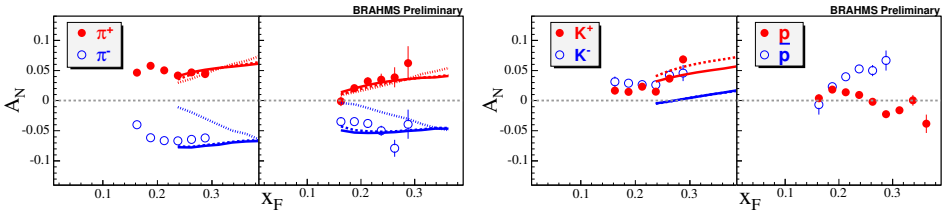

(a) A_N vs. x_F for $\pi^\pm$

(b) A_N vs. x_F for $K^\pm$, p and $\bar{p}$

Figure 2: A_N vs. x_F for pions (a) and for $K^\pm$, p and $\bar{p}$ (b) at $\sqrt{s}$ = 200 GeV. Pions are measured using the FS at 2.3° (left panel) and 4° (right panel), and kaons and protons are measured at 2.3°. The curves are from the twist-3 calculations with (line) and without (broken) sea- and anti-quark contributions. The predictions from the Sivers effect are shown as dotted lines. Errors are statistical only.

ments from E704/FNAL [3] and also the $A_N(\pi^0)$ measurements at RHIC [11]. The $1/p_T$ dependence might indicate that A_N is in accordance with the expected power-suppressed nature of A_N [15]. Figure 2 compares $A_N(\pi)$ with a pQCD calculation in the range of

$p_T > 1$ GeV/c using "extended" twist-3 parton distributions [7] including "non-derivative" contributions [15, 16]. In this framework, two calculations are compared with the data: two valence densities (u_v,d_v) in the ansatz with and without sea- and anti-quark contribution in the model fit. The calculations describe the data within the uncertainties. The dominant contribution to SSAs are from valence quarks and sea- and anti-quark contributions are small that the current measurements are not able to quantitatively constrain the contribution. The data are also compared with the Sivers mechanism, which successfully describes FNAL/E704 A_N data. The calculations compared with the data use valence-like Sivers functions [17, 18] for u and d quarks with opposite sign. The fragmentation functions used are from the KKP parameterization [19], but the Kretzer fragmentation functions [20] gives similar results. The calculations shown with dotted lines in the figure underestimate A_N for both p_T ranges, which indicates that TMD parton distributions are not sufficient to describe the SSA data at this energy. In valence-like models (no Sivers effect from sea-quarks and/or gluons), non-zero positive $A_N(K^-)$ implies large non-leading fragmentation functions ($D_u^{K^-}$, $D_d^{K^-}$) and insignificant contribution from strange quarks. Twist-3 calculations also undershoot $A_N(K^-)$ due to the small contribution of sea and strange-quark contributions to A_N in the model. In Fig. 2, protons show no significant asymmetries compared to anti-protons, but require more understanding of their production mechanism to theoretically describe their behavior, because a significant fraction of the protons might still be related to the polarized beam fragments under the constraint of baryon conservation at this kinematic range.

The analyzing power A_N for charged pions in $p^\uparrow + p$ collisions at $\sqrt{s} = 62.4$ GeV as a function of x_F is shown in Fig. 3 with p_T coverages as shown in Fig. 1. For positive x_F the measured A_N values show strong dependence on x_F reaching large asymmetries up to $\approx 40\%$ at $x_F \approx 0.6$. In $p^\uparrow + p$ collisions, SSAs at $x_F < 0$ probe the kinematics of the sea (gluon) region of $p^\uparrow$ at small-x and the valence region of p. The measured insignificant A_N for $x_F < 0$, where $\hat{u} \to 0$, indicates that A_N is dominated by processes where $\hat{t}$ is small, and it shows no significant contribution to A_N from processes where gq scattering is enhanced. Compared with twist-3 calculations for $p_T > 1$ GeV/c, A_N for π^+ and π^- are in agreement qualitatively, while predictions based on the Sivers effect especially undershoot the π^- data. Similarly as for the 200 GeV data, strangeness asymmetries at 62.4 GeV, $A_N(K^-)$, need an extra or a different mechanism to account for positively non-zero $A_N(K^-)$ at a similar level of $A_N(K^+)$ as shown in Fig. 3.

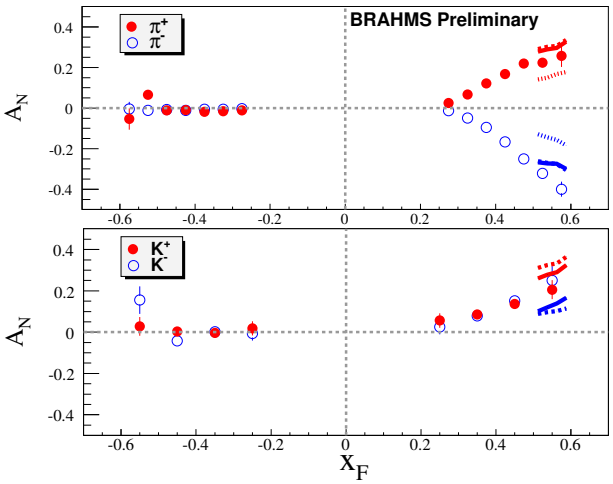

Figure 3: A_N vs. x_F for $\pi^\pm$ and $K^\pm$ at $\sqrt{s} = 62.4$ GeV for positive and negative x_F. See Fig.2 for descriptions of the curves shown.

4 Summary

In summary, BRAHMS has measured SSAs for inclusive identified charged hadron production at forward rapidities in $p^{\uparrow}+p$ at $\sqrt{s} = 200$ GeV and 62.4 GeV. A twist-3 pQCD model of A_N describes the x_F dependence of $A_N(\pi)$ and the energy dependence for $p_T > 1$ GeV/c where the calculations are applicable. However, it is a challenge for pQCD models to consistently describe spin-averaged cross sections at lower energies. Measurements of A_N for kaons and protons suggest the manifestation of non-pQCD phenomena and/or call for more theoretical modeling with good understanding of the fragmentation processes. The energy and flavor dependent SSA measurements of identified hadrons allow more complete and stringent tests of theoretical models of partonic dynamics in the RHIC energy regime.

Acknowledgments

We thank Feng Yuan and Umberto D'Alesio for providing us with their calculations shown in this contribution. This work was supported by Brookhaven Science Associates, LLC under Contract No. DE-AC02-98CH10886 with the U.S. Department of Energy and by a sponsored research grant from Renaissance Technologies Corporation.

References

[1] Slides:
`http://indico.cern.ch/contributionDisplay.py?contribId=157&sessionId=4&confId=9499`
[2] G.L. Kane, J. Pumplin and W. Repko, Phys. Rev. Lett. **41** 1689 (1978).
[3] D.L. Adams *et al.* (E704 Collaboration), Phys. Lett. **B264** 462 (1991).
[4] A. Bravar *et al.* (E704 Collaboration), Phys. Rev. Lett. **77** 2626 (1996).
[5] D. Sivers, Phys. Rev. **D41** 83 (1990).
[6] J.C. Collins, Nucl. Phys. **B396** 161 (1993).
[7] J. Qiu and G. Sterman, Phys. Rev. **D59** 014004 (1999).
[8] For a review, see J. Kodaira and K. Tanaka, Prog. Theor. Phys. **101** 191 (1999).
[9] A. Airapetian *et al.* (HERMES Collaboration), Phys. Rev. Lett. **94** 012002 (2005).
[10] V.Y. Alexakhin *et al.* (COMPASS Collaboration), Phys. Rev. Lett. **94** 202002 (2005).
[11] J. Adams *et al.* (STAR Collaboration), Phys. Rev. Lett. **92** 171801 (2004).
[12] J.H. Lee (BRAHMS Collaboration), in Proceedings of XIV International Workshop on Deep Inelastic Scattering (DIS06), Tsukuba, Japan (2006).
[13] D. Boer, D. Hasch and G. Mallot, these proceedings;
I. Arsene *et al.* (BRAHMS Collaboration), Phys. Rev. Lett. **98** 252001 (2007).
[14] M. Adamczyk *et al.* (BRAHMS Collaboration), Nucl. Instr. Meth. **A499** 437 (2003).
[15] C. Kouvaris *et al.*, Phys. Rev. **D74** 1104013 (2006).
[16] The calculations were provided by F. Yuan.
[17] U. D'Alesio and F. Murgia, Phys. Rev. **D70** 074009 (2004).
[18] The calculations were provided by U. D'Alesio.
[19] B.A. Kniehl *et al.*, Nucl. Phys. **B597** 337 (2001).
[20] B.A. Kretzer, Phys. Rev. **D62** 054001 (2000).

Soft Gluon Resummation and a Novel Asymptotic Formula for Double-Spin Asymmetries in Dilepton Production at Small Transverse Momentum

Hiroyuki Kawamura[1], Jiro Kodaira[2*] and Kazuhiro Tanaka[3]

1- Radiation Laboratory, RIKEN, Wako 351-0198, Japan

2- Theory Devision, KEK, Tsukuba 305-0801, Japan

3- Department of Physics, Juntendo University, Inba, Chiba 270-1695, Japan

We discuss the double-spin asymmetries $\mathcal{A}_{TT}(Q_T)$ in transversely polarized Drell-Yan process at small transverse momentum Q_T of the produced dilepton. Soft gluon radiations relevant for small Q_T are resummed to all orders in α_s, up to the next-to-leading logarithmic accuracy. We show that the soft gluon contributions to polarized and unpolarized cross sections mostly cancel in the asymmetries, but significant corrections still remain. We propose a novel asymptotic formula for $\mathcal{A}_{TT}(Q_T)$ at small Q_T, which provides a new approach to extract the transversity $\delta q(x)$ from the experimental data.

Transversly polarized Drell-Yan (tDY) process, $p^\uparrow p^\uparrow \to l^+ l^- X$, is one of the processes where we can measure the chiral-odd transversity distributions, $\delta q(x)$. The NLO cross sections of tDY, with the transverse momentum Q_T of the final dilepton unobserved (integrated), has been studied at RHIC kinematics in [2], and it turned out that the corresponding double transverse-spin asymmetries A_{TT} are small because, at RHIC, the sea-quark distributions are probed at small partonic momentum fraction x. Here, we consider the double-spin asymmetries $\mathcal{A}_{TT}(Q_T)$ for the Q_T-observed case, especially at small Q_T, where the bulk of dileptons is produced. For Q_T smaller than the invariant mass Q of the dilepton, soft gluon emissions contributing as $\alpha_s^n \log^m(Q^2/Q_T^2)/Q_T^2$ ($m \le 2n-1$) bring dominant corrections in each order in α_s. We perform all-order resummation of them at the next-to-leading logarithmic (NLL) accuracy, i.e., of the LL ($m = 2n-1$) and NLL ($m = 2n-2, 2n-3$) terms. The parton distributions at the low scale Q_T can participate in $\mathcal{A}_{TT}(Q_T)$, while A_{TT} in [2] is determined solely by the distributions at the scale Q; $\mathcal{A}_{TT}(Q_T)$ may be larger than A_{TT}.

The spin-dependent part of the Q_T-differential cross section can be expressed as [3, 4]

$$\frac{\Delta_T d\sigma}{dQ^2 dQ_T^2 dy d\phi} = \cos(2\phi)\frac{\alpha^2}{3\,N_c\,S\,Q^2}\left[\Delta_T\tilde{X}^{\rm NLL}(Q_T^2,Q^2,y) + \Delta_T\tilde{Y}(Q_T^2,Q^2,y)\right], \tag{1}$$

where $\sqrt{S}$ and y denote the energy of the the incoming protons and rapidity of dilepton in the proton-proton CM system, and ϕ is the azimuthal angle of one of the outgoing leptons with respect to the proton's spin axis. The first term $\Delta_T\tilde{X}^{\rm NLL}$ denotes the NLL resummed cross section which is given by the integral over the impact parameter b, according to the general formalism of Collins-Soper-Sterman [5] combined with varous kinds of elaboration [3, 4, 6]:

$$\Delta_T\tilde{X}^{\rm NLL}(Q_T^2,Q^2,y) = \int_{\mathcal{C}} db\frac{b}{2}J_0(bQ_T)e^{S(b,Q)-g_{NP}b^2}\left[\,\delta H\left(x_1^0,x_2^0;\frac{b_0^2}{b^2}\right)\right. \tag{2}$$
$$\left. + \frac{\alpha_s(Q^2)}{2\pi}\left\{\int_{x_1^0}^1\frac{dz}{z}\Delta_T C_{qq}^{(1)}(z)\delta H\left(\frac{x_1^0}{z},x_2^0;\frac{b_0^2}{b^2}\right) + \int_{x_2^0}^1\frac{dz}{z}\Delta_T C_{qq}^{(1)}(z)\delta H\left(x_1^0,\frac{x_2^0}{z};\frac{b_0^2}{b^2}\right)\right\}\right],$$

*Deceased.

where $x^0_{1,2} = \sqrt{Q^2/S}e^{\pm y}$ is the Drell-Yan scaling variables, $J_0(bQ_T)$ is a Bessel function, $b_0 = 2e^{-\gamma_E}$ with the Euler's constant γ_E, and

$$\delta H(x_1, x_2; \mu^2) = \sum_q e_q^2 \left[\delta q(x_1, \mu^2)\delta\bar{q}(x_2, \mu^2) + \delta\bar{q}(x_1, \mu^2)\delta q(x_2, \mu^2)\right]. \quad (3)$$

Using $\lambda = \beta_0\alpha_s(Q^2)\log(Q^2b^2/b_0^2+1) \equiv \beta_0\alpha_s(Q^2)\tilde{L}$ with $\beta_0 = (11N_c - 2N_f)/(12\pi)$, the large logarithmic corrections are resummed into the Sudakov factor $e^{S(b,Q)} = e^{h^{(0)}(\lambda)/\alpha_s(Q^2)+h^{(1)}(\lambda)}$, where $h^{(0)}(\lambda) = (A_q^{(1)}/2\pi\beta_0^2)[\lambda + \log(1-\lambda)]$ with $A_q^{(1)} = 2C_F = (N_c^2-1)/N_c$ collects the LL contributions, and $h^{(1)}(\lambda)$ corresponds to the NLL contributions; the explicit form of $h^{(1)}(\lambda)$, as well as another perturbatively calculable function $\Delta_T C_{qq}^{(1)}(z)$, is found in [3, 4]. $\tilde{L}$ plays a role of the large logarithmic expansion parameter in the b space, as $b \sim 1/Q_T$. We have introduced the Gaussian smearing factor $e^{-g_{NP}b^2}$ in (2), with a nonperturbative parameter g_{NP} [5], to take care of the long-distance behavior in the extremely large $|b|$ region. For the detail of elaboration of (2) beyond CSS, including the choice of the b-integration contour $\mathcal{C}$, see [3, 4]. The second term in (1), $\Delta_T\tilde{Y}$, is of $\mathcal{O}(\alpha_s)$, and does not contain the singular terms to be resummed, such as $\sim \log(Q^2/Q_T^2)/Q_T^2$ and $1/Q_T^2$; $\Delta_T\tilde{Y}$ is determined [3] such that the expansion of (1) to $\mathcal{O}(\alpha_s)$ reproduces the LO cross section for finite Q_T, which is of $\mathcal{O}(\alpha_s)$. Accordingly, we refer to (1) as the "NLL+LO" cross section. The NLL+LO cross section for unpolarized DY process is obtained similarly as (1), with $\tilde{X}^{\rm NLL}$ and $\tilde{Y}$ as the counterparts of $\Delta_T\tilde{X}^{\rm NLL}$ and $\Delta_T\tilde{Y}$, so that the NLL+LO asymmetry reads [4]

$$\mathcal{A}_{TT}(Q_T) = \frac{\cos(2\phi)}{2}\frac{\Delta_T\tilde{X}^{\rm NLL}(Q_T^2, Q^2, y) + \Delta_T\tilde{Y}(Q_T^2, Q^2, y)}{\tilde{X}^{\rm NLL}(Q_T^2, Q^2, y) + \tilde{Y}(Q_T^2, Q^2, y)}. \quad (4)$$

In the following Figs. 1 and 2, we show the asymmetries $\mathcal{A}_{TT}(Q_T)$ for $\phi = 0$, using a model of the NLO transversity distributions constructed as in [2], and $g_{NP} = 0.5$ GeV^2 for the nonperturbative parameter of (2). Figure 1 shows [4] the asymmetries at RHIC kinematics, $\sqrt{S} = 200$ GeV, $Q = 5$ GeV, and $y = 2$. The solid line shows the NLL+LO result (4), the dot-dashed line shows the NLL result $\mathcal{A}_{TT}^{\rm NLL}(Q_T)$, obtained by omitting $\Delta_T\tilde{Y}$ and $\tilde{Y}$ in (4), and the two-dot-dashed line shows the LL result $\mathcal{A}_{TT}^{\rm LL}(Q_T)$, which is obtained by retaining only the LL terms in $\mathcal{A}_{TT}^{\rm NLL}(Q_T)$:

$$\mathcal{A}_{TT}^{\rm LL}(Q_T) = \frac{\cos(2\phi)}{2}\frac{\delta H(x_1^0, x_2^0; Q^2)}{H(x_1^0, x_2^0; Q^2)}, \quad (5)$$

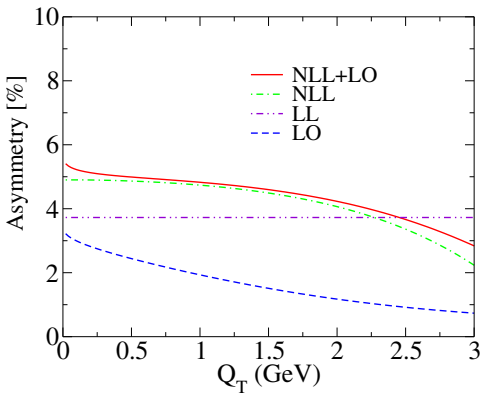

Figure 1: The asymmetries at RHIC, using $\sqrt{S} = 200$ GeV, $Q = 5$ GeV, $y = 2$ and $\phi = 0$.

where H is obtained from δH of (3) by replacing $\delta q(x, \mu^2)$ with the density distributions $q(x, \mu^2)$, and (5) is independent of Q_T [4]. The dashed line shows the LO asymmetry as the ratio of the LO cross sections. The NLL+LO result is flat and close to $\mathcal{A}_{TT}^{\rm NLL}(Q_T)$ in the small Q_T region around $Q_T \simeq 1$ GeV: in this region, the NLL+LO cross section (1) and the corresponding unpolarized one are dominated by the resummed contributions $\Delta_T\tilde{X}^{\rm NLL}$ and

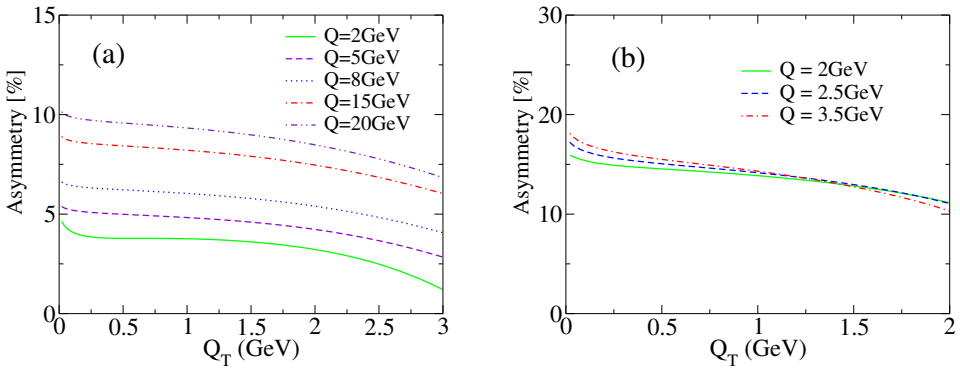

Figure 2: The NLL+LO asymmetries (4) for $\phi = 0$ at (a) RHIC kinematics with $\sqrt{S} = 200$ GeV and $y = 2$, and (b) J-PARC kinematics with $\sqrt{S} = 10$ GeV and $y = 0$.

$\tilde{X}^{\rm NLL}$, and form a well-developed peak [3, 4]; moreover, the Sudakov factor $e^{S(b,Q)}$ of (2) due to soft gluon resummation is universal up to the NLL level, so the dominant contributions cancel between $\Delta_T\tilde{X}^{\rm NLL}$ and $\tilde{X}^{\rm NLL}$ in $\mathcal{A}_{TT}^{\rm NLL}(Q_T)$. However, remarkably, some effects at the NLL level survive the cancellation, and raise $\mathcal{A}_{TT}^{\rm NLL}(Q_T)$ at small Q_T significantly compared with $\mathcal{A}_{TT}^{\rm LL}(Q_T)$ that coincides with the conventional asymmetry A_{TT} [2] using Q_T-integrated cross sections, up to the NLO ($\mathcal{O}(\alpha_s)$) corrections. On the other hand, the LO result is much smaller than the other asymmetries and decreases as Q_T increases, indicating that the soft gluon resummation is crucial for the prediction of the asymmetries.

The NLL+LO asymmetries $\mathcal{A}_{TT}(Q_T)$ of (4) at RHIC kinematics, $\sqrt{S} = 200$ GeV, $y = 2$, and various values of Q, are presented in Fig. 2 (a), which shows that $\mathcal{A}_{TT}(Q_T)$ increases for increasing Q. This Q dependence is a result of the small-x behavior of the relevant parton distributions, in particular, the steep rise of the unpolarized sea-distributions for small $x_{1,2}^0 = \sqrt{Q^2/S}e^{\pm y}$, which enhances the denominator of (4) for small Q. Figure 2 (b) is same as Fig. 2 (a), but for possible polarized pp experiment at J-PARC, $\sqrt{S} = 10$ GeV, $y = 0$, and $Q = 2, 2.5, 3.5$ GeV, where the distributions at moderate x are probed and $\mathcal{A}_{TT}(Q_T)$ at the flat region are around 15%, irrespective of the value of Q. We find [4] that all cases of Figs. 2 (a) and (b) in fact obey the similar mechanism as shown in Fig. 1, resulting in the values of $\mathcal{A}_{TT}(Q_T)$ larger by 20-30% than the corresponding NLO A_{TT}.

The NLL+LO asymmetry (4) in the flat region as in Figs. 1, 2 can be generically approximated, to good accuracy, as $\mathcal{A}_{TT}(Q_T) \approx \mathcal{A}_{TT}^{\rm NLL}(Q_T = 0)$, which is completely expressed by $\Delta_T\tilde{X}^{\rm NLL}$ and $\tilde{X}^{\rm NLL}$ at $Q_T = 0$. The b-integration in those quantities can be evaluated analytically by the saddle-point method: for (2) at $Q_T = 0$, we get [4]

$$\Delta_T\tilde{X}^{\rm NLL}(0, Q^2, y) = \left(\frac{b_0^2}{4Q^2\beta_0\alpha_s(Q^2)}\sqrt{\frac{2\pi}{\zeta''(\lambda_{SP})}}e^{-\zeta(\lambda_{SP})+h^{(1)}(\lambda_{SP})}\right)\delta H\left(x_1^0, x_2^0;\ b_0^2/b_{SP}^2\right), \tag{6}$$

where $\zeta(\lambda) = -\lambda/(\beta_0\alpha_s(Q^2)) - h^{(0)}(\lambda)/\alpha_s(Q^2) + (g_{NP}b_0^2/Q^2)e^{\lambda/(\beta_0\alpha_s(Q^2))}$, and $b_{SP} = (b_0/Q)e^{\lambda_{SP}/(2\beta_0\alpha_s(Q^2))}$, with λ_{SP} satisfying $\zeta'(\lambda_{SP}) = 0$, i.e.,

$$1 - \frac{A_q^{(1)}}{2\pi\beta_0}\frac{\lambda_{SP}}{1-\lambda_{SP}} = \frac{g_{NP}b_0^2}{Q^2}e^{\frac{\lambda_{SP}}{\beta_0\alpha_s(Q^2)}}. \tag{7}$$

	$\sqrt{S} = 200$ GeV, $y = 2$					$\sqrt{S} = 10$ GeV, $y = 0$		
Q	2GeV	5GeV	8GeV	15GeV	20GeV	2GeV	2.5GeV	3.5GeV
SP-I	4.3%	5.4%	6.6%	8.7%	9.8%	14.1%	14.5%	14.8%
SP-II	7.3%	8.7%	9.8%	11.8%	12.7%	14.7%	14.8%	14.2%

Table 1: $\mathcal{A}_{TT}^{\rm NLL}(Q_T = 0)$ for $\phi = 0$ using the saddle-point formula (8).

Here (6) gives the saddle-point formula in the NLL accuracy, and corresponds to extension of that in the LL level in the literature [5]: the solution of (7) formally determines the saddle point at the LL level combined with the contribution due to the Gaussian factor $e^{-g_{NP}b^2}$ in (2), but we find [4] that the "shift" of the saddle point at the NLL level from λ_{SP} yields only the NNLL corrections to (6); note that the NNLL contributions are of $\mathcal{O}(\alpha_s)$, according to the counting of the relevant logarithms in the region $Q_T \approx 0$ (see also [5]). The saddle-point formula for $\tilde{X}^{\rm NLL}(0, Q^2, y)$ can be obtained similarly, and the result is given by the above result (6) with the replacement $\delta H(x_1^0, x_2^0;\ b_0^2/b_{SP}^2) \to H(x_1^0, x_2^0;\ b_0^2/b_{SP}^2)$. The common factor, in the parentheses of (6), involves "very large perturbative effects" due to the universal Sudakov factor, but this factor cancels out for the asymmetry. We get [4]

$$\mathcal{A}_{TT}^{\rm NLL}(Q_T = 0) = \frac{\cos(2\phi)}{2} \frac{\delta H\left(x_1^0, x_2^0;\ b_0^2/b_{SP}^2\right)}{H\left(x_1^0, x_2^0;\ b_0^2/b_{SP}^2\right)} \ , \tag{8}$$

which is exact up to the NNLL ($\mathcal{O}(\alpha_s)$) corrections for $Q_T \approx 0$. This clarifies the mechanism discussed in Fig. 1: the contributions surviving the cancellation in (8) are entirely absorbed into the unconventional scale b_0/b_{SP} for the relevant distribution functions. Compared with (5), participation of the new scale b_0/b_{SP} is the effect at the NLL level, and, remarkably, b_0/b_{SP} using (7) depends weakly on Q, as $b_0/b_{SP} \simeq 1$ GeV for all cases in Figs. 1 and 2 [4]. This explains why $\mathcal{A}_{TT}(Q_T)$ at small Q_T is always larger than (5), or the NLO A_{TT} in [2]. Also $\mathcal{A}_{TT}^{\rm NLL}(Q_T)$ does not approach to $\mathcal{A}_{TT}^{\rm LL}(Q_T)$ even in the $Q \to \infty$ limit.

In Table 1, both "SP-I" and "SP-II" show $\mathcal{A}_{TT}^{\rm NLL}(Q_T = 0)$ using (8) with (7), but these two cases differ by the contributions at the NNLL level, reflecting mismatch to classify the terms between NLL and NLO (for the detail of SP-I, II, see [4]). SP-I reproduces $\mathcal{A}_{TT}(Q_T = 0)$ in the flat region in Fig. 2 to the 10% accuracy, i.e., to the canonical size of $\mathcal{O}(\alpha_s)$ corrections associated with the NLL accuracy. However, SP-II overestimates for RHIC, demonstrating that certain NNLL corrections would grow at the small-x region, the edge region of the phase space, beyond the canonical size. To this accuracy, our simple formula (8) is applicable in order to extract the NLO transversity distributions directly from the data.

This work was supported by the Grant-in-Aid for Scientific Research No. B-19340063.

References

[1] Slides:
`http://indico.cern.ch/contributionDisplay.py?contribId=159&sessionId=4&confId=9499`
[2] O. Martin et al., Phys. Rev. **D57** 3084 (1998); ibid. **D60** 117502 (1999).
[3] H. Kawamura, J. Kodaira, H. Shimizu and K. Tanaka, Prog. Theor. Phys. **115**, 667 (2006).
[4] H. Kawamura, J. Kodaira and K. Tanaka, arXiv:hep-ph/0703079, to appear in Nucl. Phys. **B** (2007).
[5] J. C. Collins, D. Soper and G. Sterman, Nucl. Phys. **B250** 199 (1985).
[6] G. Bozzi et al., Phys. Lett. **B564** 65 (2003); Nucl. Phys. **B737** 573 (2006); arXiv:0705.3887 [hep-ph].

Factorization and Gauge Invariance of Twist-3 Cross Section for Single Spin Asymmetry

Yuji Koike[1] and Kazuhiro Tanaka[2]

1- Department of Physics, Niigata University, Ikarashi, Niigata 950-2181, Japan

2- Department of Physics, Juntendo University, Inba-gun, Chiba 270-1695, Japan

We prove factorization and gauge invariance of the twist-3 single-spin-dependent cross section in the leading order perturbative QCD, which was missing in the previous literature. We emphasize that the consistency relation from the Ward identities for color gauge invariance is crucial to guarantee the cancelation among the various gauge-noninvariant contributions in the cross section. This relation also proves the absence of the "derivative" terms in the cross section corresponding to the hard-pole and soft-fermion-pole contributions. Applying the formalism to SIDIS, $ep^\uparrow \to e\pi X$, we have derived the complete cross section associated with the twist-3 distribution for the transversely polarized nucleon.

In the framework of the collinear factorization for hard inclusive processes, single spin asymmetry (SSA) in semi-inclusive reactions is a twist-3 observable and can be described by using certain quark-gluon correlation functions on the lightcone. In our recent paper [2], we have establised the twist-3 formalism for SSA, providing a proof for factorization property and gauge invariance of the single spin-dependent cross section in the leading order perturbative QCD, which was missing in the previous literature [3]-[10]. We also applied the method to derive the formula for SSA in semi-inclusive deep inelastic scattering (SIDIS), $ep^\uparrow \to e\pi X$. Here we shall state what had to be clarified for the twist-3 calculation in the previous literature, refering the readers to [2] for the details.

There are two independent twist-3 distribution functions for the transversely polarized nuleon. They can be defined in terms of the gluon's field strength $F^{\alpha\beta}$ as

$$\begin{aligned} &M_F^\alpha(x_1,x_2)_{ij} \\ &\quad= \int\frac{d\lambda}{2\pi}\int\frac{d\mu}{2\pi}e^{i\lambda x_1}e^{i\mu(x_2-x_1)}\langle p\ S_\perp|\bar\psi_j(0)[0,\mu n]gF^{\alpha\beta}(\mu n)n_\beta[\mu n,\lambda n]\psi_i(\lambda n)|p\ S_\perp\rangle \\ &\quad= \frac{M_N}{4}\,(\not p)_{ij}\,\epsilon^{\alpha pnS_\perp}G_F(x_1,x_2)+i\frac{M_N}{4}\,(\gamma_5\not p)_{ij}\,S_\perp^\alpha\widetilde G_F(x_1,x_2)+\cdots\,, \end{aligned} \tag{1}$$

where ψ is the quark field, p and $S_\perp$ are, respectively, momentum and spin vectors of the nucleon. p can be regarded as light-like ($p^2=0$) in the twist-3 accuracy, n^μ is the light-like vector ($n^2=0$) with $p\cdot n=1$, and the spin vector satisfies $S_\perp^2=-1$, $S_\perp\cdot p=S_\perp\cdot n=0$. $[\mu n,\lambda n]$ is the gauge-link operator. The twist-3 distributions can also be defined in terms of the transverse component of the covariant dervative $D_\perp^\alpha=\partial_\perp^\alpha-igA_\perp^\alpha$ as

$$\begin{aligned} &\int\frac{d\lambda}{2\pi}\int\frac{d\mu}{2\pi}e^{i\lambda x_1}e^{i\mu(x_2-x_1)}\langle p\ S_\perp|\bar\psi_j(0)[0,\mu n]D_\perp^\alpha(\mu n)[\mu n,\lambda n]\psi_i(\lambda n)|p\ S_\perp\rangle \\ &\quad= \frac{M_N}{4}\,(\not p)_{ij}\,\epsilon^{\alpha pnS_\perp}G_D(x_1,x_2)+i\frac{M_N}{4}\,(\gamma_5\not p)_{ij}\,S_\perp^\alpha\widetilde G_D(x_1,x_2)+\cdots\,. \end{aligned} \tag{2}$$

By introducing the nucleon mass M_N, the four functions G_F, $\widetilde G_F$, G_D and $\widetilde G_D$ are defined as dimensionless. The "F-type" functions $\{G_F,\widetilde G_F\}$ and the "D-type" functions $\{G_D,\widetilde G_D\}$

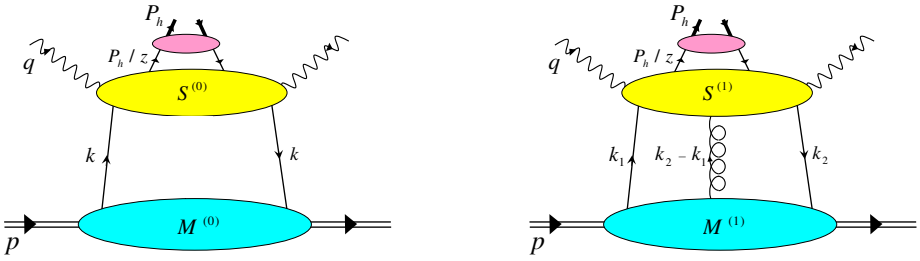

Figure 1: Generic diagrams for the hadronic tensor of $ep^\uparrow \to e\pi X$ which contribute in the twist-3 accuracy.

are not independent. They are related as [7]

$$G_D(x_1,x_2) = P\frac{1}{x_1-x_2}G_F(x_1,x_2), \tag{3}$$

$$\widetilde{G}_D(x_1,x_2) = \delta(x_1-x_2)\widetilde{g}(x_1) + P\frac{1}{x_1-x_2}\widetilde{G}_F(x_1,x_2), \tag{4}$$

where $\widetilde{g}(x)$ is a function expressed in terms of $\{G_F, \widetilde{G}_F\}$ and the twist-2 quark helicity distribution $\Delta q(x)$ [7] . The relations (3) and (4) indicate that one cannot find the partonic hard cross sections for the F-type and D-type functions independently. We use the "less singular" F-type functions as a complete set for the twist-3 distributions.

To present our formalism we focus on the single-spin-dependent cross section in SIDIS, $e(\ell) + p^\uparrow(p,S_\perp) \to e(\ell') + \pi(P_h) + X$, and consider the contribution associated with the twist-3 distribution in the transversely polarized nucleon. Here the twist-2 fragmentation function for the final pion is immediately factorized from the hadronic tensor $W_{\mu\nu}(p,q,P_h)$ ($q = \ell - \ell'$ is the momentum of the virtual photon) as

$$W_{\mu\nu}(p,q,P_h) = \sum_{j=q,g}\int \frac{dz}{z^2} D_j(z) w^j_{\mu\nu}(p,q,\frac{P_h}{z}) \ , \tag{5}$$

where $D_j(z)$ is the quark and gluon fragmentation functions for the pion. To extract the twist-3 effect in $w^j_{\mu\nu}$, one has to analyze the diagrams shown in Fig. 1, where the momenta for the parton lines are assigned. The lower blobs in the figure represent the nucleon matrix elements. They are the Fourier transforms of the correlation functions which are schmatically written as $M^{(0)}(k) \sim \langle\bar\psi\psi\rangle$ and $M^{(1)\alpha}(k_1,k_2) \sim \langle\bar\psi A^\alpha\psi\rangle$, where $\langle\cdots\rangle \equiv \langle pS_\perp|\cdots|pS_\perp\rangle$. The middle blobs, $S^{(0)}(k,q,P_h/z)$ and $S^{(1)}_\alpha(k_1,k_2,q,P_h/z)$, are the partonic hard scattering parts, and the upper blobs represent the fragmentation function for the pion. To analyze these diagrams, we work in the Feynman gauge. A standard procedure to extract the twist-3 effect is the collinear expansion in terms of the parton momenta k and $k_{1,2}$ around the component pararell to the parent nucleon's momentum p. Since $M^{(1)\alpha=\perp}$ is suppressed by $1/p^+$ compared with $M^{(1)\alpha=+}$, one needs the collinear expansion only for the component $S^{(1)}_+ = S^{(1)}_\rho p^\rho/p^+$ for the right diagram of Fig. 1.

In the approach by Qiu and Sterman [4] using Feynman gauge, $\partial^\perp A^+$ appearing in the collinear expansion is identified as a part of the gluon's field strength $F^{\perp+} = \partial^\perp A^+ - \partial^+ A^\perp -$

$ig[A^\perp, A^+]$, and thus $\partial S_\rho^{(1)}(k_1, k_2, q, P_h/z)p^\rho/\partial k_{2\perp}^\alpha\Big|_{k_i=x_ip}$, appearing as the coefficient of $\langle\bar\psi(\partial^\perp A^+)\psi\rangle$, was identified as the hard part for the F-type functions. In order to justify this procedure, it is necessary to show that "$-\partial^+A^\perp$" also appears with exactly the same coefficient as that for $\partial^\perp A^+$. Note that, in the Feynman gauge, the matrix element of the type $\langle\bar\psi\partial^\perp A^+\psi\rangle$ is equally important as $\langle\bar\psi\partial^+A^\perp\psi\rangle$, and both matrix elements have to be treated as the same order in the collinear expansion. This is because, even though $\langle\bar\psi A^+\psi\rangle \gg \langle\bar\psi A^\perp\psi\rangle$ in the Feynman gauge in a frame with $p^+ \gg p^-, p^\perp$, action of $\partial^\perp$ to the gluon field in $\langle\bar\psi A^+\psi\rangle$ brings relative suppression compared with ∂^+.

On the other hand, $A^\perp$ was identified as a part of $D^\perp = \partial^\perp - igA^\perp$ in [4], and $S_\perp^{(1)}(x_1p, x_2p, q, P_h/z)$, appearing as the coefficient of $\langle\bar\psi A^\perp\psi\rangle$, was treated as the hard part for the D-type functions, independently from the F-type functions. However, if one identifies "$-\partial^+A^\perp$" part in $F^{\perp+}$, it also affects the coefficients of $\langle\bar\psi A^\perp\psi\rangle$.

In this way, the twist-3 formalism presented by [4] was not complete, in particular, the gauge invariance and uniqueness of factorization formula was not shown explicitly.

Above consideration forces us to reorganize the collinear expansion. Since F-type and D-type functions are related as in (3) and (4), we take the approach of expressing the cross section in terms of F-type functions only. Detailed analysis of the diagrams shown in Fig. 1 shows that the single-spin-dependent cross section in the leading order perturbation theory arises solely from the right diagram in Fig.1. Taking into account the $-\partial^+A^\perp$ term in $F^{\perp+}$, we eventually arrive at the following result for $w_{\mu\nu}^j$ in (5):

$$w_{\mu\nu}^j = \int dx_1 \int dx_2 \mathrm{Tr}\left[i\omega^\alpha{}_\beta M_F^\beta(x_1, x_2)\, \frac{\partial S_\rho^{(1)}(k_1, k_2, q, P_h/z)p^\rho}{\partial k_2^\alpha}\bigg|_{k_i=x_ip}\right], \quad (6)$$

with the consistency conditions

$$(x_2 - x_1)\, \frac{\partial S_\rho^{(1)}(k_1, k_2, q, P_h/z)p^\rho}{\partial k_2^\alpha}\bigg|_{k_i=x_ip} + S_\alpha^{(1)}(x_1p, x_2p, q, P_h/z) = 0, \quad (7)$$

$$\frac{\partial S_\rho^{(1)}(k_1, k_2, q, P_h/z)p^\rho}{\partial k_1^\alpha}\bigg|_{k_i=x_ip} + \frac{\partial S_\rho^{(1)}(k_1, k_2, q, P_h/z)p^\rho}{\partial k_2^\alpha}\bigg|_{k_i=x_ip} = 0, \quad (8)$$

for $\alpha = \perp$, where $M_F^\beta(x_1, x_2)$ is given in (1), $\omega^{\alpha\beta} = g^{\alpha\beta} - p^\alpha n^\beta$ and $\mathrm{Tr}[\cdots]$ indicates the Dirac trace, while color trace is implicit. In (6), the real quantity $w_{\mu\nu}^j$ is given as the pole contributions [3, 4] from internal propagators of the hard part $\partial S_\rho^{(1)}(k_1, k_2, q, P_h/z)p^\rho/\partial k_2^\alpha\Big|_{k_i=x_ip}$, which are classified as hard-pole (HP), soft-fermion-pole (SFP) and soft-gluon-pole (SGP) contributions. Since these three kinds of poles occur at different points in phase space, one can prove that each pole contribution satisfies the two conditions (7) and (8) separately, and the whole hadronic tensor $w_{\mu\nu}^j$ can be written in terms of the F-type functions only, including all the HP, SFP and SGP contributions. We emphasize the crucial role of the two conditions (7) and (8): Using these conditions for each pole contribution, the various terms associated with the gauge-noninvariant matrix elements, arising in the collinear expansion of $w_{\mu\nu}^j$, cancel out and only the term shown in (6) remains, which guarantees the factorization of the cross section and the gauge invariance of the formula. In particular, the first condition (7) can be proved using the Ward identities for color gauge invariance (see [2] for the detail).

Pragmatically, the authors of [4] reached the same formula (6), but only for the SGP contribution. We emphasize, however, that our argument leading to (6) is totally different from [4], in particular, (6) is the principal formula for all HP, SFP and SGP contributions.

For the HP and SFP contributions in which $x_1 \neq x_2$, (7) can be rewritten as

$$\left.\frac{\partial S_\rho^{(1)}(k_1,k_2,q,P_h/z)p^\rho}{\partial k_2^\alpha}\right|_{k_i=x_ip} = \frac{1}{x_1-x_2} S_\alpha^{(1)}(x_1p,x_2p,q,P_h/z). \tag{9}$$

Owing to this relation, one can obtain the relevant hard cross section in (6) also through $S_\perp^{(1)}(x_1p,x_2p,q,P_h/z)$, which is much simpler to calculate than the derivative of the amplitude, $\left.\partial S_\rho^{(1)}(k_1,k_2,q,P_h/z)p^\rho/\partial k_2^\alpha\right|_{k_i=x_ip}$. Since $S_\perp^{(1)}(x_1p,x_2p,q,P_h/z)$ does not contain any derivative, the HP and SFP contributions do not appear as the derivative terms, such as those $\propto dG_F(x_{bj},x)/dx$ or $d\widetilde{G}_F(x_{bj},x)/dx$ etc. For the SGP contribution, one has to calculate the derivative $\left.\partial S_\rho^{(1)}(k_1,k_2,q,P_h/z)p^\rho/\partial k_2^\alpha\right|_{k_i=x_ip}$, because of the lack of the relation (9) for $x_1 = x_2$, and it gives rise to the derivative terms with $dG_F(x,x)/dx$. For the HP and SFP contributions, one can also rewrite the cross section in terms of D-type functions by using the relations (3) and (4) for $x_1 \neq x_2$, without any subtlety.

We have applied the above formalism to SIDIS and derived [2] the complete single-spin-dependent cross section for $ep^\uparrow \to e\pi X$ associated with the twist-3 distributions for the transversely polarized nucleon, including all three kinds (HP, SFP and SGP) of pole contributions for $G_F(x_1,x_2)$ and $\widetilde{G}_F(x_1,x_2)$.

Our twist-3 formalism can be easily extended to other processes, such as Drell-Yan and direct photon productions, $p^\uparrow p \to \gamma^{(*)}X$, and the pion production in pp collision, $p^\uparrow p \to \pi X$, which gives solid theoretical basis to the previously obtained cross section formula [4]-[10].

The work of K.T. was supported by the Grant-in-Aid for Scientific Research No. B-19340063.

References

[1] Slides:
`http://indico.cern.ch/contributionDisplay.py?contribId=158&sessionId=4&confId=9499`

[2] H. Eguchi, Y. Koike and K. Tanaka, Nucl. Phys. **B763** 198 (2007).

[3] A. V. Efremov and O. V. Teryaev, Sov. J. Nucl. Phys. **36** 140 (1982) [Yad. Phiz. **36** 242 (1982)]; Phys. Lett. **B150** 383 (1985).

[4] J. Qiu and G. Sterman, Nucl. Phys. **B378** 52 (1992).

[5] J. Qiu and G. Sterman, Phys. Rev. **D59** 014004 (1999).

[6] Y. Kanazawa and Y. Koike, Phys. Lett. **B478** 121 (2000); Phys. Lett. **B490** (2000) 99; Phys. Rev. **D64** 034019 (2001).

[7] H. Eguchi, Y. Koike and K. Tanaka, Nucl. Phys. **B752** 1 (2006).

[8] X. D. Ji, J. W. Qiu, W. Vogelsang and F. Yuan, Phys. Rev. Lett. **97** 082002 (2006); Phys. Rev. **D73** 094017 (2006).

[9] X. D. Ji, J. W. Qiu, W. Vogelsang and F. Yuan, Phys. Lett. **B638** 178 (2006).

[10] C. Kouvaris, J. W. Qiu, W. Vogelsang, F. Yuan, Phys. Rev. **D74** 114013 (2006).

Novel Master Formula for Twist-3 Soft-Gluon-Pole Mechanism to Single Transverse-Spin Asymmetry

Yuji Koike[1] and Kazuhiro Tanaka[2] *

1- Department of Physics, Niigata University, Ikarashi, Niigata 950-2181, Japan

2- Department of Physics, Juntendo University, Inba-gun, Chiba 270-1695, Japan

We prove that twist-3 soft-gluon-pole (SGP) cross section for single spin asymmetries is determined by a certain "primordial" twist-2 cross section up to kinematic and color factors in the leading order perturbative QCD. This unveils universal structure behind the SGP cross sections in a variety of hard processes, and also the special role of the scale invariance in the corresponding primordial cross section, which leads to remarkable simplification of the SGP cross sections for the production of massless particle, such as those for pion production $p^\uparrow p \to \pi X$ and direct-photon production $p^\uparrow p \to \gamma X$.

The single transverse-spin asymmetry (SSA) is observed as "T-odd" effect proportional to $\vec{S}_\perp \cdot (\vec{p} \times \vec{q})$ in the cross section for the scattering of transversely polarized proton with momentum p and spin $S_\perp$, off unpolarized particle with momentum p', producing a particle with momentum q which is observed in the final state. Famous examples [2] are $p^\uparrow p \to \pi X$ with the large asymmetry $A_N \sim 0.3$ observed in the forward direction, and semi-inclusive deep inelastic scattering (SIDIS), $ep^\uparrow \to e\pi X$, by HERMES and COMPASS Collaborations. The Drell-Yan (DY) process, $p^\uparrow p \to \ell^+\ell^- X$, and the direct γ production, $p^\uparrow p \to \gamma X$, at RHIC, J-PARC, etc. are also expected to play important roles for the study of SSA.

The SSA requires, (i) nonzero $q_\perp$ originating from transverse motion of quark or gluon; (ii) proton helicity flip; and (iii) interaction beyond Born level to produce the interfering phase for the cross section. For processes with $q_\perp \sim \Lambda_{\rm QCD}$, all (i)-(iii) may be generated nonperturbatively from the T-odd, transverse-momentum-dependent parton distribution/fragmentation functions [3]. For large $q_\perp \gg \Lambda_{\rm QCD}$, (i) should come from perturbative mechanism, while the nonperturbative effects can participate in the other two, (ii) and (iii), allowing us to obtain large SSA. This is realized as the twist-3 mechanism in QCD for the SSA. Recently we have thoroughly discussed the collinear-factorization property and gauge invariance in the twist-3 mechanism in the context of the SSA in SIDIS [4]. We have also revealed universal structure behind the twist-3 mechanism [5, 6], which we discuss here.

As an example, consider the DY production of the dilepton with $q_\perp \gg \Lambda_{\rm QCD}$: The large $q_\perp$ of (i) is provided by hard interaction as the recoil from a hard final-state parton, as illustrated in Fig. 1. Proton helicity flip (ii) is provided by the participation of the coherent, nonperturbative gluon from the transversely polarized proton, the lower blob in Fig. 1, associated with the twist-3 quark-gluon correlation functions such as $G_F(x_1, x_2)$ with x_1 (x_2) the lightcone momentum fraction of the quark leaving from

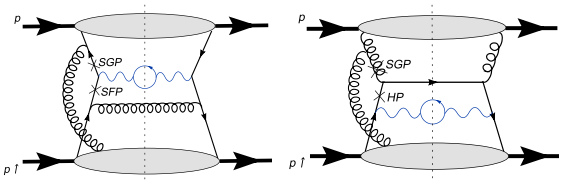

Figure 1: Typical diagrams for DY process with $q_\perp \gg \Lambda_{\rm QCD}$. The cross $\times$ denotes the pole contribution of the parton propagator.

*Supported by the Grant-in-Aid for Scientific Research No. B-19340063.

(entering into) the proton [4]. Due to the coupling of this coherent gluon, some parton propagators in the partonic subprocess can be on-shell, and this produces the imaginary phase of (iii) as the pole contribution using $1/(k^2+i\varepsilon) = P(1/k^2) - i\pi\delta(k^2)$. Depending on the value of the coherent-gluon's momentum k_g at the corresponding poles, these are soft-gluon pole (SGP) for $k_g = 0$, and soft-fermion pole (SFP) and hard pole (HP) for $k_g \neq 0$.

Among these three-types of poles, the SGP deserves special attention; indeed, the SGP is considered to give dominant twist-3 mechanism in many phenomenological applications (see e.g. [4, 5]). We have derived the *master formula* for the SGP cross section, which embodies the remarkable structure that the SGP contributions from many Feynman diagrams of the type of Fig. 1 are united into a derivative of the 2-to-2 partonic Born diagrams without the coherent-gluon line: The SSA for the DY process can be expressed as [5]

$$\frac{d\sigma^{\rm DY}_{\text{tw-3,SGP}}}{[d\omega]} = \frac{\pi M_N}{2C_F}\epsilon^{\sigma pnS_\perp}\sum_{j=\bar{q},g}\mathcal{B}_j\int\frac{dx'}{x'}\int\frac{dx}{x}f_j(x')\frac{\partial H_{jq}(x',x)}{\partial(x'p'^\sigma)}G_F^q(x,x), \tag{1}$$

where $j=\bar{q}$ and g represent the "$q\bar{q}$-annihilation" and "qg-scattering" channels, respectively, corresponding to the left and right diagrams in Fig. 1. $f_j(x')$ denotes the twist-2 parton distribution functions for the unpolarized proton, and M_N is the nucleon mass representing nonperturbative scale associated with the twist-3 correlation function $G_F^q(x,x)$ for the flavor q. The sum over quark and antiquark flavors is implicit for the index q as $q = u, \bar{u}, d, \bar{d}, \cdots$. $[d\omega] = dQ^2dyd^2q_\perp$ denotes the relevant differential elements with $Q^2 = q^2$ and y the rapidity of the virtual photon. The color factors are introduced as $\mathcal{B}_q = 1/(2N_c)$ and $-1/(2N_c)$ for quark and antiquark flavors, respectively, $\mathcal{B}_g = N_c/2$, and $C_F = (N_c^2-1)/(2N_c)$. The derivative with respect to p' is taken under $p'^2 = 0$, and $H_{jq}(x',x)$ denote the partonic hard-scattering functions which participate in the unpolarized twist-2 cross section for DY process as

$$\frac{d\sigma^{\rm unpol,DY}_{\text{tw-2}}}{[d\omega]} = \sum_{j=\bar{q},g}\int\frac{dx'}{x'}\int\frac{dx}{x}f_j(x')H_{jq}(x',x)f_q(x). \tag{2}$$

Namely, in order to obtain the explicit formula for the twist-3 SGP contributions to the SSA, knowledge of the twist-2 unpolarized cross section is sufficient.

A proof of (1) is described in detail in [5]: Only the *initial-state interaction* (ISI) diagrams like Fig. 1, where the coherent gluon couples to an "external parton" associated with an initial-state hadron, survive as the SGP contributions for DY process, while the SGPs from the other diagrams cancel out combined with the corresponding "mirror" diagrams [7]. For such ISI diagrams, the coherent-gluon insertion and the associated SGP structure can be disentangled from the partonic subprocess, keeping the remaining factors mostly intact. For the *scalar-polarized* coherent-gluon, this is performed using Ward identity; moreover, also for the transversely-polarized coherent-gluons that are relevant at the twist-3 level, this can be performed exactly through the logic different from the scalar-polarized case [5]. Using the background field gauge, the three-gluon coupling relevant to the qg-scattering channel can be disentangled similarly as the quark-gluon coupling case. After disentangling ISI with the coherent gluons, the collinear expansion in terms of the parton transverse momenta gives the twist-3 cross section (1) at the SGP, as the response of 2-to-2 partonic subprocess to the change of the transverse momentum carried by the external parton, to which the coherent gluon had coupled. Note that $\mathcal{B}_{\bar{q}}$ and $\mathcal{B}_g$ in (1) come from the insertion of the color matrix t^a in the fundamental and adjoint representations, respectively, into the 2-to-2 subprocess, as the remnant of the coherent-gluon insertion via the quark-gluon and three-gluon vertices.

The hard-scattering functions in the twist-2 factorization formula (2) are expressed as $H_{jq}(x',x) = (\alpha_{em}^2\alpha_s e_q^2/3\pi N_c s Q^2)\widehat{\sigma}_{jq}(\hat{s},\hat{t},\hat{u})\delta\left(\hat{s}+\hat{t}+\hat{u}-Q^2\right)$, where $s = (p+p')^2$, and explicit form of $\widehat{\sigma}_{jq}(\hat{s},\hat{t},\hat{u})$ in terms of the partonic Mandelstam variables $\hat{s},\hat{t}$ and $\hat{u}$ can be found in Eq. (28) in [5]. The derivative in (1) can be performed through that for the $\hat{u}$, and this may act on either $\widehat{\sigma}_{jq}$ or the delta function in $H_{jq}(x',x)$, where the latter case produces the derivative of the twist-3 correlation function, $dG_F^q(x,x)/dx$, as well as the non-derivative term $\propto G_F^q(x,x)$, by partial integration with respect to x. Our master formula (1) yields [5]

$$\frac{d\sigma^{\rm DY}_{\text{tw-3,SGP}}}{dQ^2dyd^2q_\perp} = \frac{\alpha_{em}^2\alpha_s e_q^2}{3\pi N_c s Q^2}\frac{\pi M_N}{C_F}\epsilon^{pnS_\perp q_\perp}\sum_{j=\bar{q},g}\mathcal{B}_j\int\frac{dx'}{x'}\int\frac{dx}{x}\delta\left(\hat{s}+\hat{t}+\hat{u}-Q^2\right)f_j(x')$$
$$\times\left\{\begin{matrix}\widehat{\sigma}_{jq}\\ -\hat{u}\end{matrix}x\frac{dG_F^q(x,x)}{dx}+\left[\frac{\widehat{\sigma}_{jq}}{\hat{u}}-\frac{\partial\widehat{\sigma}_{jq}}{\partial\hat{u}}-\frac{\hat{s}}{\hat{u}}\frac{\partial\widehat{\sigma}_{jq}}{\partial\hat{s}}-\frac{\hat{t}-Q^2}{\hat{u}}\frac{\partial\widehat{\sigma}_{jq}}{\partial\hat{t}}\right]G_F^q(x,x)\right\}. \quad (3)$$

This novel expression not only reproduces the known pattern [7] that the partonic hard scattering functions associated with the derivative term are directly proportional to those participating in the twist-2 unpolarized process, $\widehat{\sigma}_{jq}$, but also reveals the structure that was hidden in the corresponding formula in the literature [7]: the partonic hard-scattering functions associated with the non-derivative term are also completely determined by $\widehat{\sigma}_{jq}$.

We obtain the SSA for the direct γ production in the real-photon limit, $Q^2 \to 0$; here only the massless particles participate in the 2-to-2 Born subprocess, so that the corresponding partonic cross sections $\widehat{\sigma}_{jq}$ are scale-invariant as $(\hat{u}\partial/\partial\hat{u}+\hat{s}\partial/\partial\hat{s}+\hat{t}\partial/\partial\hat{t})\widehat{\sigma}_{jq}=0$. Consequently, (3) reduces to the compact structure where $-\widehat{\sigma}_{jq}/\hat{u}$ appears both for derivative and non-derivative terms, as the coefficient for the combination, $xdG_F^q(x,x)/dx - G_F^q(x,x)$ [5].

The DY process can be formally transformed into SIDIS, $ep^\uparrow \to e\pi X$, *crossing* the initial unpolarized proton into the final-state pion with momentum P_h, and the virtual photon into the initial-state one. The proof of (1) discussed above is unaffected by the analytic continuation corresponding to this "crossing transformation": $p' \to -P_h$, $x' \to 1/z$, $f_{\bar{q}}(x') \to D_q(z)$, $f_g(x') \to D_g(z)$, and $q^\mu \to -q^\mu$, where $D_j(z)$ denote the twist-2 parton fragmentation functions for the final-state pion, and the new q^μ gives $Q^2 = -q^2$. Our master formula (1) now gives the SGP contribution to the SSA in SIDIS, which is actually associated with the corresponding *final-state interaction* (FSI) diagrams, as ($\mathcal{C}_q \equiv \mathcal{B}_{\bar{q}}, \mathcal{C}_g \equiv \mathcal{B}_g$) [5]

$$\frac{d\sigma^{\rm SIDIS}_{\text{tw-3,SGP}}}{[d\omega]} = \frac{\pi M_N}{C_F z_f^2}\epsilon^{pnS_\perp P_{h\perp}}\frac{\partial}{\partial q_T^2}\frac{d\sigma^{\rm unpol,SIDIS}_{\text{tw-2}}}{[d\omega]}\bigg|_{f_q(x)\to G_F^q(x,x),\ D_j(z)\to\mathcal{C}_j z D_j(z)}, \quad (4)$$

in a frame where the 3-momenta $\vec{q}$ and $\vec{p}$ of the virtual photon and the transversely polarized nucleon are collinear along the z axis. $[d\omega] = dx_{bj}dQ^2dz_f dq_T^2 d\phi$, where, as usual, $x_{bj} = Q^2/(2p\cdot q)$, $z_f = p\cdot P_h/p\cdot q$, $q_T = P_{h\perp}/z_f$, and ϕ is the azimuthal angle between the lepton and hadron planes. The twist-2 unpolarized cross section in the RHS of (4) is known to have several terms with different ϕ-dependence, proportional to $1, \cos\phi$, and $\cos 2\phi$, respectively (see [4]). Performing the derivative in (4) explicitly, the result obeys the similar pattern as (3) with derivative and non-derivative terms, for each azimuthal dependence, and unveils the structure behind the complicated formula obtained by direct evaluation of the diagrams [4].

Our master formula can be extended to "QCD-induced" pp collisions, like $p^\uparrow p \to \pi X$ [6]. For example, the $qq \to qq$ scattering subprocess induce the twist-2 unpolarized cross section,

$$E_h\frac{d^3\sigma^{pp\to\pi X}_{\text{tw-2}}}{d^3P_h} = \frac{\alpha_s^2}{s}\int\frac{dz}{z^2}\frac{dx'}{x'}\frac{dx}{x}\delta(\hat{s}+\hat{t}+\hat{u})D_q(z)f_q(x')f_q(x)\widehat{\sigma}_U(\hat{s},\hat{t},\hat{u}), \quad (5)$$

for $p(p)+p(p')\to\pi(P_h)+X$, where $E_h\equiv P_h^0$, and $\widehat{\sigma}_U(\hat{s},\hat{t},\hat{u})=(C_F/N_c)(\hat{s}^2+\hat{u}^2)/\hat{t}^2+(C_F/N_c)(\hat{s}^2+\hat{t}^2)/\hat{u}^2+(-2C_F/N_c^2)\hat{s}^2/(\hat{t}\hat{u})$ is the $qq\to qq$ unpolarized cross section [8]. The SGP contribution from the interference between $qqg\to qq$ and $qq\to qq$ is generated by FSI and ISI with the coherent gluon as in Fig. 2 (a) and (b), which can be treated similarly as the SIDIS and DY cases, respectively, and yields [6] the twist-3 cross section for $p^\uparrow p\to\pi X$:

$$E_h\frac{d^3\sigma^{pp\to\pi X}_{\text{tw-3,SGP}}}{d^3P_h}=\frac{\pi M_N\alpha_s^2}{s}\int\frac{dz}{z^2}\frac{dx'}{x'}\frac{dx}{x}\delta(\hat{s}+\hat{t}+\hat{u})D_q(z)f_q(x')\left[x\frac{dG_F^q(x,x)}{dx}-G_F^q(x,x)\right]$$
$$\times\left[\frac{1}{z}\epsilon^{S_\perp P_h pn}+\frac{x'\hat{t}}{\hat{s}}\epsilon^{S_\perp p' pn}\right]\left(\frac{\hat{s}\,\widehat{\sigma}_F(\hat{s},\hat{t},\hat{u})}{\hat{t}\hat{u}}-\frac{\widehat{\sigma}_I(\hat{s},\hat{t},\hat{u})}{\hat{u}}\right),\qquad(6)$$

where the hard cross sections from the FSI and ISI diagrams, $\widehat{\sigma}_W=A_{W,1}(\hat{s}^2+\hat{u}^2)/\hat{t}^2+A_{W,2}(\hat{s}^2+\hat{t}^2)/\hat{u}^2+A_{W,3}\hat{s}^2/(\hat{t}\hat{u})$ for $W=F$ and I, are the same as the above $\widehat{\sigma}_U$, except for the associated color factors $A_{W,i}$ that come from the *color insertion* of t^a, similarly as $\mathcal{B}_j$ of (1). Note that the combination, $xdG_F^q(x,x)/dx-G_F^q(x,x)$, in (6) is a consequence of the scale invariance, $\widehat{\sigma}_U(\hat{s},\hat{t},\hat{u})=\widehat{\sigma}_U(\lambda\hat{s},\lambda\hat{t},\lambda\hat{u})$, similarly as in $p^\uparrow p\to\gamma X$ discussed below (3). These remarkable structures arise universally for all the other relevant channels associated with the "primordial" 2-to-2 partonic subprocesses, $q\bar{q}\to q\bar{q}$, $q\bar{q}\to gg$, $qg\to qg$, etc. (see also [8]).

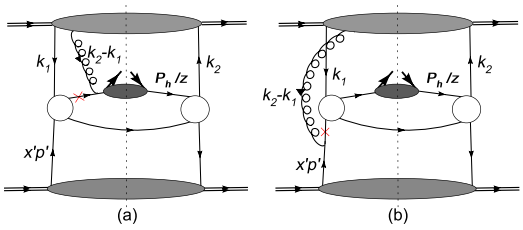

Figure 2: (a) and (b) as FSI and ISI diagrams for SGP mechanism, respectively. White circles denote hard scattering between quarks.

We have derived the novel master formula which gives the twist-3 SGP contributions to the SSA entirely in terms of the knowledge of the "primordial" twist-2 cross section. This is based on the new approach, which allows us to disentangle ISI as well as FSI with the soft coherent-gluon, irrespective of the details of the corresponding partonic subprocess. Thus our single master formula is applicable universally to all processes relevant to SSA, including QED-induced processes like DY process, direct γ production, SIDIS, etc., and also QCD-induced processes like $p^\uparrow p\to\pi X$, $p^\uparrow p\to$ 2jets X, $pp\to\Lambda^\uparrow X$, etc. For SSA associated with the chiral-even twist-3 function $G_F^q(x,x)$, the primordial twist-2 process is unpolarized as discussed above, while for SSA associated with the chiral-odd functions, the primordial process is the polarized one [6]. The primordial twist-2 structure behind the SGP mechanism manifests gauge invariance of the results, and unveil the remarkable role of scale invariance.

References

[1] Slides:
`http://indico.cern.ch/contributionDisplay.py?contribId=160&sessionId=4&confId=9499`

[2] See the articles on the data at RHIC, and those from HERMES, COMPASS, etc. in these proceedings.

[3] D. Boer, Phys. Rev. **D60** 014012 (1999).

[4] H. Eguchi, Y. Koike and K. Tanaka, Nucl. Phys. **B752** 1 (2006); ibid. **B763** 198 (2007).

[5] Y. Koike and K. Tanaka, Phys. Lett. **B646** 232 (2007).

[6] Y. Koike and K. Tanaka, arXiv:hep-ph/0703169, Phys. Rev. **D** in press (2007).

[7] X.D. Ji, J.W. Qiu, W. Vogelsang and F. Yuan, Phys. Rev. **D73** 094017 (2006).

[8] C. Kouvaris, J.W. Qiu, W. Vogelsang and F. Yuan, Phys. Rev. **D74** 114013 (2006).

The Role of Gauge Invariance in Single-Spin Asymmetries

C.J. Bomhof and P.J. Mulders

Vrije Universiteit Amsterdam - Department of Physics and Astronomy
NL-1081 HV Amsterdam - the Netherlands

We argue that, through the Wilson lines, gauge invariance has as an effect that the hard functions in weighted spin-asymmetries in hadronic scattering processes are given by gluonic pole cross sections, rather than the usual partonic cross sections.

1 Introduction

The interest in the transverse polarization properties of hadrons has been increasing considerably over the last decades after the observation of large single transverse spin asymmetries A_N in processes such as $pp{\to}\Lambda^{0\uparrow}X$, $p^\uparrow p{\to}\pi X$ and $p^\uparrow\bar{p}{\to}\pi X$, see *e.g.* [2]. Typically, single-spin asymmetries (SSA) are defined as the difference of the scattering cross sections with opposite spin orientations divided by the spin averaged cross section. As such, the spin asymmetries are pre-eminent observables for the spin dependent parton distribution functions, such as the quark transversity function $h_1(x)$, which cannot be probed in inclusive DIS.

A mechanism to generate single-spin asymmetries through soft gluon interactions between the target remnants and the initial and final state partons was first proposed in the context of collinear factorization [3, 4]. Hence, this collinear factorization formalism involves, apart from the usual twist-two collinear distribution functions, also twist-three collinear quark-gluon matrix elements. Since they contain a gauge field operator corresponding to a soft gluon, they are referred to as *gluonic pole matrix elements*. An important example is the Qiu-Sterman matrix element $T_F(x,x)$ [3]. Several other mechanisms for generating SSA's through the effects of the intrinsic transverse momenta of the partons have also been proposed. For instance, in the Sivers effect the asymmetry arises in the initial state due to a correlation between the intrinsic transverse motion of an unpolarized quark and the transverse spin of its parent hadron [5]. The effect is described by a transverse momentum dependent (TMD) function $f_{1T}^\perp(x,p_T^2)$. However, based on time-reversal arguments it was expected to vanish [6]. It will, therefore, be understood that it came as a surprise when Brodsky, Hwang and Schmidt in 2002 showed that leading twist spin asymmetries can anyway be generated in a spectator diquark model where the scattered quark undergoes an additional gluonic interaction with the target remnants [7]. It was soon realized that the time-reversal arguments that were used to predict a vanishing Sivers effect were flawed as they neglected the presence of the Wilson lines. The *Wilson lines* or *gauge links* $\mathcal{U}=\mathcal{P}\exp[-ig\int dz{\cdot}A(z)]$ are path-ordered exponentials that are required to obtain gauge-invariant definitions of parton distribution and fragmentation functions. Taking the Wilson lines properly into account it was found instead that time-reversal leads to the important conclusion that the Sivers functions in SIDIS and Drell-Yan scattering have opposite signs

$$f_{1T}^\perp(x,p_T^2)\,\big\rfloor_{\text{Drell-Yan}} = -f_{1T}^\perp(x,p_T^2)\,\big\rfloor_{\text{SIDIS}}\ , \tag{1}$$

and that finite Sivers contributions are possible after all [8]. Single-spin effects due to the Sivers mechanism in SIDIS have now been observed by several collaborations [9].

The discussion above exemplifies the important role that the Wilson lines have come to play. Today it is recognized that they are not just mere operators to obtain gauge invariant definitions of parton distribution functions but also that they, through the Sivers (and Boer-Mulders [10]) effect, can themselves be regarded as sources for single-spin asymmetries. The Wilson lines are also crucial ingredients in the derivation of the relation $2Mf_{1T}^{\perp(1)}(x) = -gT_F(x,x)$ found in [11], demonstrating that the first transverse moment of the Sivers function is a gluonic pole matrix element (the same is true for the Boer-Mulders function). The remarkable 'universality' property of the TMD Sivers functions in Eq. (1) is a prediction intrinsic to QCD which follows from the presence of the Wilson lines or, stated differently, from the gluonic initial and final-state interactions. Experimental verification of this prediction would be profound support for our understanding of the physics underlying the generation of spin asymmetries. It could be tested by comparing the signs of the single transverse-spin asymmetries in SIDIS and Drell-Yan scattering. As stated in the previous paragraph, SSA due to the Sivers mechanism in SIDIS have now been observed by several collaborations. However, measurements of the single-spin asymmetry in Drell-Yan scattering are lacking behind. The reason is that the lepton-antilepton pair is a relatively rare final state in hadron-hadron scattering compared to purely hadronic or hadron-photon final states. Also in those processes the gluonic initial and final-state interactions (the Wilson lines) leave their fingerprints, though the effects are more intricate since the hard functions are more complicated. However, until precise measurements for the single-spin asymmetries in the 'gold-plated' Drell-Yan process become available, they may also be used to test the formalism describing single-spin asymmetries. The role of gauge invariance in these more complicated scattering processes is the topic of the next section.

2 Dijet and Photon-Jet Production in Hadron-Hadron Scattering

In the basic hadronic processes, SIDIS, Drell-Yan scattering and e^+e^--annihilation, the hard functions are just simple electromagnetic vertices (at tree-level). Depending on the particular process only initial or final-state gluonic interactions contribute and, correspondingly, only future and past pointing Wilson lines occur. However, when going to hadronic processes that involve hard functions with more colored external legs, such as in hadronic dijet or photon-jet production, there can be both initial and final state gluonic interactions. As a result, the Wilson lines will also be more complicated than just the simple future and past pointing Wilson lines [12]. In fact, the final-state interactions will give rise to future pointing Wilson lines at each of the outgoing partons (where the representations of the color-matrices will depend on the particular type of parton) as is the case in SIDIS. Similarly, the initial-state interactions will lead to past pointing Wilson lines at the incoming partons as in Drell-Yan scattering. The Wilson lines distributed over the different external partons of the hard function can subsequently be joined together by making a color-flow decomposition of the hard function, such that they can be connected along the color-flow lines. In particular this means that the full gauge link will have a different substructure for each of the color-flow diagrams. More importantly, it implies that each of the Feynman diagrams that contribute to the hard function might have a different gauge link structure [12]. For the TMD distribution functions this seems to complicate things considerably. However, for the collinear distribution functions remarkable simplifications occur. In fact, for the collinear T-even parton distribution functions all process dependence of the Wilson lines disappears. For the T-odd distribution functions the effect of the jungle of Wilson lines is to relate their

first transverse moments for different processes by simple color factors:

$$f_{1T}^{\perp(1)}(x)\,\big\rfloor_{D(ab\to cd)} = C_G^{[D(ab\to cd)]}\, f_{1T}^{\perp(1)}(x)\,\big\rfloor_{\rm SIDIS}\ , \tag{2}$$

and similarly for the transverse moments of the Boer-Mulders functions. The color factors C_G are determined by the gauge links and, hence, depend on the scattering process $ab\to cd$. Moreover, they depend on the particular Feynman diagram D that contributes to this process [12, 13]. For that reason they are in a natural way associated to the hard functions in which they can, then, be absorbed. Consequently, the resulting hard functions will have the generic structure $d\hat{\sigma}_{[a]b\to cd} = \sum_D C_G^{[D]} d\hat{\sigma}^{[D]}_{ab\to cd}$, which will be referred to as *gluonic pole cross sections* and which should be contrasted to the usual partonic cross sections $d\hat{\sigma}_{ab\to cd} = \sum_D d\hat{\sigma}^{[D]}_{ab\to cd}$. The summations run over all Feynman diagrams D that contribute to the scattering process $ab\to cd$ and the $d\hat{\sigma}^{[D]}$ are their pQCD expressions. The gluonic pole cross section has a bracketed subscript indicating which parton is associated with the gluonic pole matrix element. They appear as the hard functions whenever gluonic pole matrix elements contribute, such as the first moments of the Sivers or Boer-Mulders functions. This is typically the case in weighted azimuthal spin asymmetries. Hence, the effect of the gauge links (or, equivalently, of the initial and final state interactions) for weighted SSA's is that the hard functions of these observables will be given by the (manifestly gauge invariant) gluonic pole cross sections [13], rather than the usual partonic cross sections as might be expected in a 'generalized parton model approach'. Several other recent theoretical studies of single-spin asymmetries seem to point in a similar direction [14, 15], though more research is required to convey the exact connection between the different formalisms.

The effects of the gluonic initial and final-state interactions for the fully TMD treatment of these processes is not so clear-cut. In ref. [15] a TMD factorization formula was proposed for the quark-Sivers contribution to the SSA in dijet production in proton-proton scattering. This formula involves the gluonic pole cross sections found in refs. [12, 13] as hard functions, but folded with the TMD distribution functions as measured in SIDIS (*i.e.* with a future pointing Wilson line). The work of [12, 13] and [15] could be related by extending the relation in Eq. (2) between the first moments of the Sivers functions to the full TMD functions, in analogy to the relation between the Sivers functions in SIDIS and Drell-Yan scattering as given in Eq. (1). On the other hand, the jungle of Wilson lines found in refs. [12, 13] in conjunction with a model calculation led the authors of ref. [16] to conclude that TMD factorization is violated in hadron-hadron scattering with hadronic final states. Future studies will have to clarify what the relation is between the work in refs. [12, 13, 15, 16].

Using the azimuthal imbalance of the outgoing jet pair ($p^\uparrow p\to jjX$) or photon-jet pair ($p^\uparrow p\to\gamma jX$) weighted single-spin asymmetries have been constructed that involve the gluonic pole cross sections at leading twist [13, 17, 18]. Predictions for the quark-Sivers contribution to these spin-asymmetries in dijet production have been presented [1, 17], making use of recently obtained parametrizations [19] for the quark-Sivers first-moments (Qiu-Sterman matrix elements) obtained by fitting to A_N data taken at E704, BRAHMS and STAR, and for the quark-Sivers half-moments obtained by fitting to SSA's measured at HERMES. First experimental measurements for this process have been performed at RHIC in 2006 [20]. The results seem to indicate that the full QCD treatment, which makes use of gluonic pole cross sections to account for the competing effects of the gluonic initial and final-state interactions, is consistent with the preliminary data, while the 'generalized parton model approach', which only uses partonic cross sections, overestimates the measurements [20].

However, the experimental results are at the same time consistent with vanishing SSA's in dijet production and more measurements to increase statistics in concurrence with more elaborate theoretical studies would therefore be welcome.

Predictions for the single-spin asymmetry in the similar photon-jet production process have been made in kinematical regions accessible at RHIC. For these predictions use was made of parametrizations [21] for the quark-Sivers function obtained by fitting to HERMES and COMPASS data. The main result is that the effect of the gluonic initial and final-state interactions is to flip the sign of the spin-asymmetry in the full QCD treatment compared to the generalized parton model result [1, 18]. This can be understood intuitively by observing that the dominant partonic channel is $qg \to \gamma q$ scattering, where in the large-N limit the color flows from the initial quark and through the gluon back into the initial state. There the initial-state interactions lead to the sign flip of the spin asymmetry, as is also the case in Drell-Yan scattering. However, in the $qg \to \gamma q$ process the initial-state interactions are gluon self-couplings and, hence, the experimental measurement of the sign flip would test the very non-abelian nature of QCD. It is also shown that the Boer-Mulders and gluon-Sivers effects are too small to affect this conclusion. Therefore, by measuring the sign of the asymmetry one has a test of the QCD formalism to describe the generation of single-spin asymmetries that is equally legitimate as the measurement of the SSA in Drell-Yan scattering.

References

[1] Slides: `http://indico.cern.ch/contributionDisplay.py?contribId=161&sessionId=4&confId=9499`

[2] G. Bunce *et al.*, Phys. Rev. Lett. **36** 1113 (1976); D.L. Adams *et al.*, Phys. Lett. **B261** 201 (1991), Phys. Lett. **B264** 462 (1991), Z. Phys. **C56** 181 (1992).

[3] J.W. Qiu and G. Sterman, Phys. Rev. Lett. **67** 2264 (1991), Nucl. Phys. **B378** 52 (1992), Phys. Rev. **D59** 014004 (1999).

[4] A.V. Efremov and O.V. Teryaev, Sov. J. Nucl. Phys. **36** 140 (1982), Phys. Lett. **B150** 383 (1985); Y. Kanazawa and Y. Koike, Phys. Lett. **B478** 121 (2000); H. Eguchi *et al.*, Nucl. Phys. **B763** 198 (2007); Y. Koike and K. Tanaka, Phys. Lett. **B646** 232 (2007).

[5] D. Sivers, Phys. Rev. **D41** 83 (1990); Phys. Rev. **D43** 261 (1991).

[6] J.C. Collins, Nucl. Phys. **B396** 161 (1993).

[7] S.J. Brodsky *et al.*, Phys. Lett. **B530** 99 (2002).

[8] J.C. Collins, Phys. Lett. **B536** 43 (2002).

[9] A. Airapetian *et al.*, Phys. Rev. Lett. **94** 012002 (2005); M. Diefenthaler, AIP Conf. Proc. **792** 933 (2005); V.Y. Alexakhin *et al.*, Phys. Rev. Lett. **94** 202002 (2005); E.S. Ageev *et al.*, Nucl. Phys. **B765** 31 (2007).

[10] D. Boer and P.J. Mulders, Phys. Rev. **D57** 5780 (1998).

[11] D. Boer *et al.*, Nucl. Phys. **B667** 201 (2003).

[12] C.J. Bomhof *et al.*, Phys. Lett. **B596** 277 (2004), Eur. Phys. J. **C47** 147 (2006).

[13] A. Bacchetta *et al.*, Phys. Rev. **D72** 034030 (2005); C.J. Bomhof and P.J. Mulders, JHEP **02** 029 (2007).

[14] Y. Koike and K. Tanaka, arXiv:hep-ph/0703169 (2007); P.G. Ratcliffe and O.V. Teryaev, arXiv:hep-ph/0703293 (2007).

[15] J.W. Qiu *et al.*, arXiv:0704.1153, arXiv:0706.1196 [hep-ph] (2007).

[16] J.C. Collins and J.W. Qiu, arXiv:0705.2141 [hep-ph].

[17] C.J. Bomhof *et al.*, Phys. Rev. **D75** 074019 (2007).

[18] A. Bacchetta *et al.*, arXiv:hep-ph/0703153 (2007).

[19] C. Kouvaris *et al.*, Phys. Rev. **D74** 114013 (2006); F. Yuan, AIP Conf. Proc. **842** 383 (2006).

[20] J. Balewski, arXiv:hep-ex/0612036 (2006); J. Balewski, talk presented at the 15th International Workshop on Deep-Inelastic Scattering (DIS2007), April 16-20, 2007, Munich, Germany.

[21] M. Anselmino *et al.*, Phys. Rev. **D72** 094007 (2005).

Measurement of Sivers Asymmetry for Di-jets at STAR in Polarized p+p Collisions at 200GeV

J. Balewski for the STAR Collaboration

Indiana University Cyclotron Facility
2401 Milo B. Sampson Lane, Bloomington, IN, 474081, USA

STAR Collaboration is reporting measurement of transverse single spin asymmetry (TSSA) for di-jet produced in collisions of transversely polarized protons at RHIC at $\sqrt{s} = 200$ GeV. The measurement probes (Sivers) correlations between the transverse spin orientation of a proton and the transverse momentum directions of its partons. Measured TSSA are consistent with zero. It agrees with recent calculations basedon on non-zero HERMES results from DIS folded with contrabalancing ISI and FSI required to restore time reversal invariance, violated by postulated Sivers mechanism in p+p. With both beams polarized, the wide pseudorapidity ($-1 \leq \eta \leq +2$) coverage for jets permits separation of Sivers functions for the quark and gluon dominated kinematic regime.

1 Introduction

The decomposition of the proton's intrinsic spin among helicity preferences and orbital angular momentum of its quark and gluon constituents is a topic of intense interest [2] and ongoing experiments [3, 4, 5]. Parton orbital contributions are particularly difficult to measure, with one possible manifestation being the so-called Sivers effect [6]: a correlation of parton transverse momentum ($\vec{k}_T$) with the proton's spin ($\vec{s}_{\rm p}$) and momentum ($\vec{p}_{\rm p}$) directions, yielding $\langle \vec{s}_{\rm p} \cdot (\vec{p}_{\rm p} \times \vec{k}_T) \rangle \neq 0$. Such a three-vector correlation is allowed, without violating time reversal invariance, if orbital components of the proton's light-cone wave function combine with initial (ISI) and/or final-state interaction (FSI) contributions to the process of interest [7, 8].

For colliding proton beams moving along the $\pm\hat{z}$-axis and vertically polarized along $\pm\hat{y}$, the Sivers effect gives a preferential sideways (along $\pm\hat{x}$) kinematic boost to jet momenta (see Fig.1), causing [9] a spin-dependent average deviation ($\delta\phi$) from 180° azimuthal jet opening angle. For colliding partons with different x_B values, there is

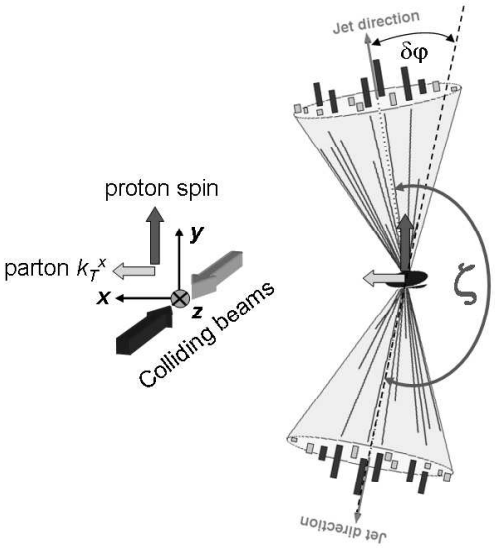

Figure 1: Sivers effect gives a spin dependent sideways kinematic boost to jet momenta. The spin dependent opening angle ζ is defined as $\pi + \delta\phi$ or $\pi - \delta\phi$ for spin direction up or down, respectively.

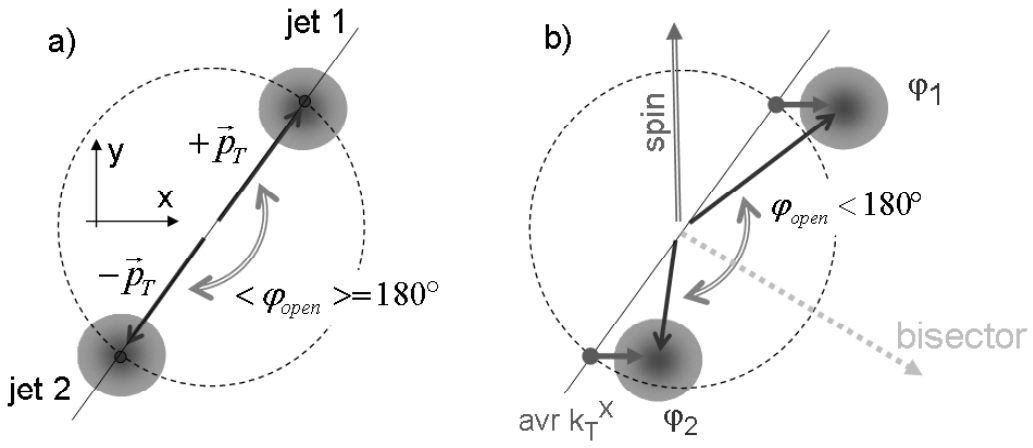

Figure 2: Simple M-C model of Sivers TSSA results with correlation of direction of di-jet bisector vector with the direction of proton spin. a) Random initial state $\vec{k}_T$ of scattered partons yields back-to-back configuration. b)A non-zero average transverse k_T^x of parton correlated with transverse polarization of initial proton leads to experimentaly measurable side boost of both jets.

an additional longitudinal boost of the jets that we exploit to separate high-x_B parton from low-x_B gluon Sivers functions.

2 Experimental results

We report measurements made in 2006 at RHIC with an integrated pp luminosity of 1.1 pb^{-1} sampled by the STAR detector [10]. The detector subsystems most critical to the present measurements are the barrel (BEMC) and endcap (EEMC) electromagnetic calorimeters [10], which provide full azimuthal (ϕ) coverage spanning pseudorapidities $|\eta| \leq 0.98$ and $1.08 \leq \eta \leq 2.0$, respectively. The EMC's are subdivided into towers that subtend small regions in $\Delta\eta$ and $\Delta\phi$. Digitized signals from the towers are summed in STAR trigger hardware over $\Delta\eta \times \Delta\phi \approx 1.0 \times 1.0$ "jet patches". The hardware (level 0) trigger used for the present measurements required a transverse energy (E_T) sum exceeding 4.0 GeV for at least one BEMC or EEMC jet patch, plus a summed (over the full EMC) $E_T^{tot} > 14$ GeV. The trigger further required coincident signals indicating a valid collision from forward ($3.3 \leq |\eta| \leq 5.0$) beam-beam counters (BBC) located at each end of the STAR detector [11]. These conditions were supplemented by a software (level 2) trigger that passed events that had at least two localized (to $\Delta\eta \times \Delta\phi = 0.6 \times 0.6$) EMC energy depositions, one with E_T exceeding 3.6 GeV and the other 3.3 GeV, with an azimuthal separation $\geq 60°$.

In order to validate the off-line event analysis algorithm a simple M-C model generating events with non-zero Sivers TSSA has been constructed, as illustrated in Fig. 2. Two-parton scattering events were generated randomly with a uniform distribution in $\hat{\phi}_1$ (and initially with $|\hat{\phi}_2 - \hat{\phi}_1| = 180°$) and a p_T distribution reproducing the p_T spectrum of experimentaly reconstructed di-jets. Each colliding parton was given a random initial-state transverse

momentum drawn from a model $\vec{k}_T$ distribution centered at zero for the y-component, but with non-zero $\pm\langle k_T^x \rangle$ for the x-component (Fig. 2b), with the sign correlated with $\vec{s}_{\rm p} \times \vec{p}_{\rm p}$ to simulate the Sivers effect. The resulting vector sum $\vec{k}_T^{+z} + \vec{k}_T^{-z}$ was added to the initially thrown outgoing parton momenta $\vec{p}_{T,1}$ and $\vec{p}_{T,2}$ to deduce boosted azimuthal angles $\phi_{1,2}$. The magnitude of $\vec{K}_T$ smearing was adjusted to reproduce experimental width of di-jet opening angle ζ. These could then be further smeared with a resolution Gaussian of width $\sigma(\phi) = 6.3°$, deduced by comparing EMC-only jet reconstruction to the parent parton directions in a simulation utilizing the PYTHIA 6.205 event generator [12] and GEANT [13] modeling of the STAR detector response.

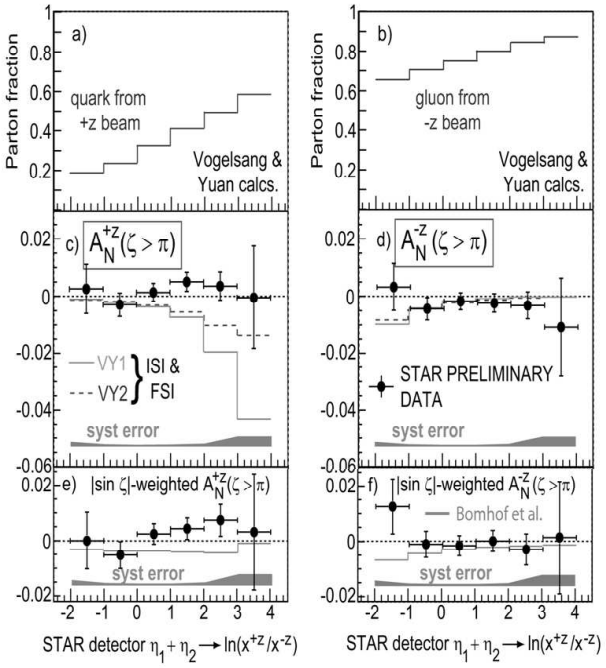

Figure 3: Measured and calculated asymmetries vs. di-jet pseudorapidity sum for $+\hat{z}$ (left) and $-\hat{z}$ (right) beams. (a,b): Fraction of the calculated di-jet cross section with a quark (gluon) from the $+\hat{z}$ ($-\hat{z}$) beam. (c,d): Unweighted asymmetries compared with pQCD calculations [14] (histograms). (e,f): Asymmetries for $|\sin\zeta|$-weighted yields, compared with calculations [14, 16] based on twist-3 quark-gluon correlations. We have reversed the sign of the calculated A_N to apply the Madison convention. Vertical (horizontal) bars on the data indicate statistical uncertainties (bin widths). The systematic error bands combine in quadrature the f uncertainty and the effect of multi-jet contributions to the ζ distribution. The systematic error bands exclude a $\pm 20\%$ beam polarization normalization uncertainty.

The measure of Sivers TSSA, A_N, is defined as:

$$A_N \overline{P} f = \frac{N_L - N_R}{N_L + N_R}$$

where N_L (N_R) is the di-jet yield for the bisector vector (see Fig. 2b) pointing to the

left (right) with respect to direction of polarization of the proton. $\overline{P}$ is projection of beam polarization magnitude on the axis perpendicular to bisector axis. The factor $f = 0.85 \pm 0.07$ corrects for dilution of a parton-level asymmetry by the trigger-level ϕ resolution smearing. It was defined from simple M-C simulation described above.

In this paper we axtracted A_N using the cross ratio method to exploit azimuthal symmetry of the STAR detector and alternating polarization pattern of both colliding beams at RHIC.

The measured asymmetries, shown in Fig. 3c-e as a function of $\eta_1 + \eta_2$, are compared to calculations [14] for two models of quark Sivers functions fitted to SIDIS results [15]. Figure 3(e-f) compares measured and calculated [14] A_N with yields weighted by $|\sin\zeta|$ [16], as needed to connect to a more robustly interpretable gauge link structure [17], given the apparent breakdown of factorization for back-to-back dijets [18].

3 Conclusions

We report first measurement of Sivers TSSA for di-jets produced in proton-proton collisions. Integrated over the STAR EMC η acceptance and $|\zeta - 180°| \leq 68°$, the full analyzed sample yields 2.6×10^6 di-jets with average $A_N^{\pm z}$ values consistent with zero for both beams, within statistical uncertainties $\approx \pm 0.002$. From simple M-C model, these results probe Sivers $\langle k_T^x \rangle$ preferences as small as $\sim \pm 3$ MeV/c, or $\pm 0.2\%$ of the inferred rms width of the $k_T^{x,y}$ distributions. Appearent discrepancy with non-zero Sivers TSSA observed in DIS by HERMES has been attributed [14] to cancelation between ISI vs. FSI and u- and d-quark Sivers functions required in calculation of di-jet production in p+p.

References

[1] Slides: `http://indico.cern.ch/contributionDisplay.py?contribId=246&sessionId=4&confId=9499`

[2] B.W. Filippone and X.D. Ji, Adv. Nucl. Phys. **26**, 1 (2001) and references therein.

[3] S.S. Adler *et al.* [PHENIX Collaboration], Phys. Rev. Lett. **93**, 202002 (2004) and Phys. Rev. **D 73**, 091102(R) (2006).

[4] B.I. Abelev *et al.* [STAR Collaboration],*hep-ex/0608030.*

[5] E.S. Ageev *et al.* [COMPAS Collaboration],Phys. Lett. **B 633**, 25 (2006).

[6] D.W. Sivers, Phys. Rev. **D 41**, 83 (1990) and Phys. Rev. **D 43**, 261 (1991).

[7] S.J. Brodsky, D.S. Hwang and I. Schmidt, Phys. Lett. **B 530**, 99 (2002) and Nucl. Phys. **B 642**, 344 (2002).

[8] J.C. Collins, Phys. Lett. **B 536**, 43 (2002).

[9] D. Boer and W. Vogelsang, Phys. Rev. **D 69**, 094025 (2004).

[10] K.H. Ackermann, *et al.* [STAR Collaboration], Nucl. Instrum. Meth. **A 499**, 624 (2003); M. Beddo *et al.*, *ibid.* 725; C.E. Allgower *et al.*, *ibid.* 740.

[11] J. Kiryluk [STAR Collaboration], *hep-ex*/0501072, published in Spin 2004 Conf. Proc., Trieste, Italy.

[12] T. Sjostrand *et al.*, Comput. Phys. Commun. **135**, 238 (2001).

[13] GEANT 3.21, CERN program library.

[14] C.J. Bomhof, P.J. Mulders, W. Vogelsang and F. Yuan, *hep-ph*/0701277 and private communication.

[15] A. Airapetian *et al.* [HERMES Collaboration], Phys. Rev. Lett. **94**, 012002 (2005).

[16] The $|\sin\zeta|$-weighted asymmetries from [14] are divided by the measured $\langle|\sin\zeta|\rangle = 0.33$ in Fig. 3(e,f). This rescaling corrects for a failure to weight the calculated unpolarized cross section, as needed to compare to measured analyzing powers with unit maximum magnitude.

[17] A. Bacchetta, C.J. Bomhof, P.J. Mulders and F. Pijlman, Phys. Rev. **D 72**, 034030 (2005).

[18] J. Collins and J.-W. Qiu, *hep-ph*/0705.2141.

Transverse Momentum in Semi-Inclusive DIS

Alessandro Bacchetta

Theory Group, DESY, 22603 Hamburg, Germany

The cross section for semi-inclusive deep inelastic scattering can be decomposed in terms of 18 structure functions. At low transverse momentum of the detected hadron, the structure functions can be expressed in terms of transverse-momentum-dependent parton distribution and fragmentation functions. Here, a few selected examples are illustrated and discussed.

I present a selection of results from a recent work [2], where semi-inclusive deep inelastic scattering, $\ell(l)+N(P) \to \ell(l-q)+h(P_h)+X$, was analyzed in the regime of low transverse momentum of the detected hadron, with the goal of completing the existing literature on the subject. In the following, the standard variables Q^2, x, y, z are used. M and M_h denote the respective masses of the nucleon and of the hadron h. Azimuthal angles are defined in accordance to the Trento conventions [3]. $P_{h\perp}$ denotes the component of P_h perpendicular to q, in, e.g., the proton-photon Breit frame.

Assuming single photon exchange, the lepton-hadron cross section can be computed as the contraction of the hadronic and the leptonic tensor and expressed by a set of structure functions. For unpolarized beam and target, the cross section contains only four structure functions. Neglecting corrections of order $1/Q^2$, it can be written as

$$\begin{aligned}\frac{d\sigma}{d\Gamma} = \frac{2\pi\,\alpha^2\,y}{8zQ^4}\,2MW^{\mu\nu}\,L_{\mu\nu} = \frac{2\pi\alpha^2}{xyQ^2}\Big\{\big(1-y+y^2/2\big)\;F_{UU,T} + (1-y)\;F_{UU,L} \\ + (2-y)\,\sqrt{1-y}\,\cos\phi_h\;F_{UU}^{\cos\phi_h} + (1-y)\,\cos(2\phi_h)\;F_{UU}^{\cos 2\phi_h}\Big\},\end{aligned} \tag{1}$$

where $d\Gamma = dx\,dy\,dz\,d\phi_h\,dP_{h\perp}^2$. The structure functions depend on x, Q^2, z and $P_{h\perp}^2$. There is no established notation for the structure functions. Here as in [2], the superscript indicates the azimuthal modulation generated in the cross section. The first and second subscript indicate the respective polarization of beam and target. When needed, the third subscript specifies the polarization of the virtual photon.

In the kinematical limit where Q^2 becomes large while x, z and $P_{h\perp}^2$ remain fixed, it has been proven [4] that the cross section up to leading order in $1/Q$ can be factorized into a hard photon-quark scattering process and *transverse momentum dependent distribution and fragmentation functions* (for the regime $M^2 \ll P_{h\perp}^2 \ll Q^2$, see e.g. [5]). Here, it is assumed that factorization applies up to subleading order in the $1/Q$ expansion, and only graphs with the hard scattering at tree level are considered. Loops can then only occur as shown, e.g., in Fig. 1 b, c. It is convenient to introduce the shorthand notations

$$\hat{\mathbf{h}} = \mathbf{P}_{h\perp}/|\mathbf{P}_{h\perp}| \quad \text{and} \quad \mathcal{C}\big[\ldots\big] = x\sum_a e_a^2 \int d^2\mathbf{p}_T\,d^2\mathbf{k}_T\,\delta^{(2)}\big(\mathbf{p}_T - \mathbf{k}_T - \mathbf{P}_{h\perp}/z\big)\ldots, \tag{2}$$

where the sum runs over the quark and antiquark flavors a, and e_a denotes their fractional

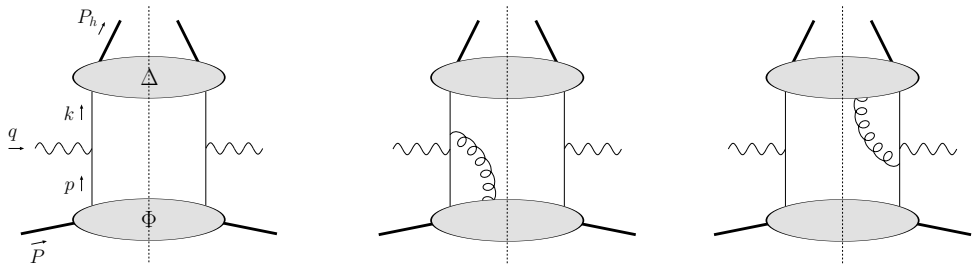

Figure 1: Examples of graphs contributing to semi-inclusive DIS at low transverse momentum of the produced hadron.

charge. The corresponding expression of the hadronic tensor is [6]

$$2MW^{\mu\nu} = \frac{2z}{x}\mathcal{C}\Big\{\mathrm{Tr}\Big[\Phi^a(x,p_T)\gamma^\mu\Delta^a(z,k_T)\gamma^\nu\Big] - \frac{1}{Q\sqrt{2}}\,\mathrm{Tr}\Big[\gamma^\alpha\gamma^-\gamma^\nu\tilde{\Phi}^a_{A\,\alpha}(x,p_T) \times \gamma^\mu\Delta^a(z,k_T) + \gamma^\alpha\gamma^+\gamma^\mu\tilde{\Delta}^a_{A\,\alpha}(z,k_T)\gamma^\nu\Phi^a(x,p_T) + \mathrm{h.c.}\Big]\Big\} + \mathcal{O}(1/Q^2). \tag{3}$$

The quark-quark correlators Φ and Δ can be decomposed up to order $1/Q$ in a general way in terms of transverse-momentum-dependent distribution functions. The quark-gluon-quark correlators $\tilde{\Phi}_A$ and $\tilde{\Delta}_A$ can be related to the quark-quark correlators by means of the QCD equations of motion. Eventually, this allows the computation of the hadronic tensor and of the structure functions appearing in the cross section.

The full calculation leads to the following results [2]

$$F_{UU,T} = \mathcal{C}\big[f_1 D_1\big], \qquad F_{UU,L} = 0, \tag{4}$$

$$F_{UU}^{\cos\phi_h} = \frac{2M}{Q}\,\mathcal{C}\left[-\frac{\hat{\mathbf{h}}\cdot\mathbf{k}_T}{M_h}\left(x h\, H_1^\perp + \frac{M_h}{M}\, f_1\frac{\tilde{D}^\perp}{z}\right) - \frac{\hat{\mathbf{h}}\cdot\mathbf{p}_T}{M}\left(x f^\perp D_1 + \frac{M_h}{M}\, h_1^\perp\frac{\tilde{H}}{z}\right)\right], \tag{5}$$

$$F_{UU}^{\cos 2\phi_h} = \mathcal{C}\left[-\frac{2\,(\hat{\mathbf{h}}\cdot\mathbf{k}_T)\,(\hat{\mathbf{h}}\cdot\mathbf{p}_T) - \mathbf{k}_T\cdot\mathbf{p}_T}{M M_h}\, h_1^\perp H_1^\perp\right]. \tag{6}$$

The distribution (fragmentation) functions f_1 (D_1), $f^\perp$ ($\tilde{D}^\perp$), h ($\tilde{H}$), and $h_1^\perp$ ($H_1^\perp$) depend on x (z) and p_T^2 (k_T^2) and should carry a flavor index a.

To order $1/Q$, the function $F_{UU,L}$ vanishes. The structure function $F_{UU}^{\cos\phi_h}$ is subleading-twist, i.e. $1/Q$-suppressed compared to the other two nonvanishing ones. Measurements of $F_{UU}^{\cos\phi_h}$ have been reported in Refs. [7, 8]. This structure function is associated with the so-called Cahn effect. If one neglects the contribution from interaction-dependent functions and T-odd functions Eq. (5) becomes

$$F_{UU}^{\cos\phi_h} \approx \frac{2M}{Q}\,\mathcal{C}\left[-\frac{\hat{\mathbf{h}}\cdot\mathbf{p}_T}{M}\, f_1 D_1\right]. \tag{7}$$

This coincides with the $\cos\phi_h$ term calculated to order $1/Q$ in the parton model with intrinsic transverse momentum included in distribution and fragmentation functions, see e.g. Eqs. (32) and (33) in Ref. [9].

The structure function $F_{UU}^{\cos 2\phi_h}$ contains the functions $h_1^\perp$ (Boer-Mulders function) and $H_1^\perp$ (Collins function). Measurements have been reported in Refs. [8].

Upon integration over the transverse momentum of the outgoing hadron, the integrated semi-inclusive DIS result is recovered, i.e.,

$$F_{UU,T}(x,z,Q^2) = x \sum_a e_a^2 \, f_1^a(x) \, D_1^a(z), \qquad F_{UU,L}(x,z,Q^2) = 0, \tag{8}$$

where $$f_1^a(x) = \int d^2\mathbf{p}_T \; f_1^a(x,p_T^2), \qquad D_1^a(z) = z^2 \int d^2\mathbf{k}_T \, D_1^a(z,k_T^2). \tag{9}$$

Finally, the standard inclusive DIS structure function is obtained by

$$F_T(x,Q^2) = \int dz \; z \, F_{UU,T}(x,z,Q^2) = x \sum_a e_a^2 \; f_1^a(x). \tag{10}$$

The analysis of the cross section and of the structure functions for polarized beams and targets can be carried out in an analogous way. There are in total 18 structure functions, eight are $\mathcal{O}(1/Q^0)$, eight are $\mathcal{O}(1/Q)$, and two are of higher order. One subleading-twist structure function, $F_{LU}^{\sin\phi_h}$, appears if the beam is longitudinally polarized and the target unpolarized. The only available measurement is by the CLAS collaboration [10]. Two structure functions, $F_{UL}^{\sin\phi_h}$ and $F_{UL}^{\sin 2\phi_h}$, appear if the beam is unpolarized and the target longitudinally polarized. They have been measured only by the HERMES collaboration [11]. Two structure functions, F_{LL} and $F_{LL}^{\cos\phi_h}$, require longitudinal polarization of both beam and target. The first one has already been measured in the past, but little is known about its transverse-momentum dependence, which could yield interesting information on orbital angular momentum.

The structure functions with transversely polarized targets are nine in total. $F_{UT,T}^{\sin(\phi_h-\phi_S)}$ and $F_{UT}^{\sin(\phi_h+\phi_S)}$ received a lot of attention from the theoretical and experimental side in the last years. They contain the Sivers and transversity distribution functions, respectively [12]. The COMPASS collaboration has recently completed the task of measuring eight of these structure functions for a deuteron target; preliminary data were presented during this conference [13]. I highlight here two illustrative examples that deserve particular attention. The first one is

$$F_{LT}^{\cos(\phi_h-\phi_S)} = \mathcal{C}\left[\frac{\hat{\mathbf{h}}\cdot\mathbf{p}_T}{M} g_{1T} D_1\right], \tag{11}$$

requiring both longitudinally polarized beam and transversely polarized target. Through the measurement of this asymmetry and with the knowledge of the unpolarized fragmentation functions, it is possible to measure the parton distribution function g_{1T}^q, which is the only chiral-even, T-even, leading-twist function in addition to the well-known unpolarized distribution function, f_1^q, and helicity distribution function, g_1^q.

Another interesting structure function is

$$\begin{aligned} F_{UT}^{\sin\phi_S} = \frac{2M}{Q}\,\mathcal{C}\Bigg\{ & \left(x f_T D_1 - \frac{M_h}{M}\, h_1 \frac{\tilde{H}}{z} \right) \\ & - \frac{\mathbf{k}_T\cdot\mathbf{p}_T}{2MM_h} \left[\left(x h_T H_1^\perp + \frac{M_h}{M} g_{1T} \frac{\tilde{G}^\perp}{z} \right) - \left(x h_T^\perp H_1^\perp - \frac{M_h}{M} f_{1T}^\perp \frac{\tilde{D}^\perp}{z} \right) \right] \Bigg\}, \end{aligned} \tag{12}$$

generating a $\sin\phi_S$ modulation in single-spin asymmetries with a transversely polarized target. Upon integration over the transverse momentum of the outgoing hadron, only one term survives, namely

$$F_{UT}^{\sin\phi_S}(x,z,Q^2) = -x \sum_a e_a^2 \frac{2M_h}{Q} h_1^a(x) \frac{\tilde{H}^a(z)}{z}, \tag{13}$$

where the transversity distribution function appears, multiplied by a subleading-twist fragmentation function. It could therefore be a good observable for transversity studies.

Another interesting limit of Eq. (12) is that of semi-inclusive jet production, $\ell(l) + N(P) \to \ell(l-q) + \mathrm{jet}(P_j) + X$. The structure function for this process can be obtained from Eq. (12) by replacing $D_1(z,k_T^2)$ with $\delta(1-z)\delta^{(2)}(\mathbf{k}_T)$, setting all other fragmentation functions to zero and integrating over z. This gives

$$F_{UT}^{\sin\phi_S}(x,P_{j\perp}^2,Q^2) = x \sum_a e_a^2 \frac{2M}{Q} x f_T^a(x,P_{j\perp}^2), \tag{14}$$

In totally inclusive DIS this structure function has to vanish due to time-reversal invariance. Starting from Eq. (13) or Eq. (14) and performing the required integrations, the following two relations can be derived

$$\sum_h \int dz\ \tilde{H}^a(z) = 0, \qquad\qquad \int d^2\mathbf{p}_T\ f_T(x,p_T^2) = 0. \tag{15}$$

The second relation can also be used to establish a connection between the Sivers function and the Qiu-Sterman effect (see, e.g., [14]).

In conclusion, I presented a selection of the results obtained in [2], where the cross section for semi inclusive deep inelastic scattering off a polarized nucleon for low transverse momentum of the detected hadron was analyzed, completing the existing literature. I pointed out that there are in general 18 structure functions, nine of which have been already measured in some experiments. More measurements will hopefully come in the future from HERMES, COMPASS, and JLab.

References

[1] Slides:
`http://indico.cern.ch/contributionDisplay.py?contribId=163&sessionId=4&confId=9499`
[2] A. Bacchetta *et al.*, JHEP **02**, 093 (2007).
[3] A. Bacchetta, U. D'Alesio, M. Diehl and C. A. Miller, Phys. Rev. **D70**, 117504 (2004).
[4] X. Ji, J.-P. Ma and F. Yuan, Phys. Rev. **D71**, 034005 (2005).
[5] Y. Koike and K. Tanaka, these proceedings, arXiv:0706.2545 [hep-ph], arXiv:0706.2117 [hep-ph].
[6] D. Boer, P. J. Mulders and F. Pijlman, Nucl. Phys. **B667**, 201 (2003).
[7] EMC, M. Arneodo *et al.*, Z. Phys. **C34**, 277 (1987). M. R. Adams, *et al.*, Phys. Rev. **D48**, 5057 (1993),
[8] ZEUS, J. Breitweg *et al.*, Phys. Lett. **B481**, 199 (2000). S. Chekanov, *et al.*, hep-ex/0608053.
[9] M. Anselmino *et al.*, Phys. Rev. **D71**, 074006 (2005).
[10] CLAS, H. Avakian *et al.*, Phys. Rev. **D69**, 112004 (2004).
[11] HERMES, A. Airapetian *et al.*, Phys. Lett. **B622**, 14 (2005). Phys. Lett. **B562**, 182–192 (2003).
[12] A. Bressan, M. Diefenthaler, these proceedings.
[13] A. Kotzinian, these proceedings, arXiv:0705.2402 [hep-ex].
[14] A. Bacchetta, hep-ph/0511085.

Transversity Signals in Two-Hadron Production at COMPASS

Christian Schill on behalf of the COMPASS collaboration

Physikalisches Institut der Albert-Ludwigs-Universität Freiburg
Hermann-Herder-Str. 3, 79104 Freiburg, Germany.

New results on single spin asymmetries of identified charged pion and kaon pairs produced in deep-inelastic scattering of muons on a transversely polarized ^6LiD target are presented. The data were taken in the years 2003 and 2004 with the COMPASS spectrometer at CERN with a 160 GeV muon beam from the CERN SPS accelerator. The asymmetries can be interpreted in the context of transversity as a convolution of the chiral-odd interference fragmentation function $H_1^\sphericalangle$ with the transverse spin distribution of quarks $\Delta_T q(x)$. The measured azimuthal target spin asymmetries on the deuteron are compatible with zero within a small statistical error of about 1%.

1 Introduction

An important missing piece in our understanding of the spin structure of the nucleon is the transversity distribution function $\Delta_T q(x)$. It is the only one of the three leading-twist quark distribution functions $q(x), \Delta q(x)$ and $\Delta_T q(x)$ that so-far remains unmeasured. The function $\Delta_T q(x)$ describes the distribution of transversely polarized quarks in a transversely polarized nucleon. It is difficult to measure $\Delta_T q(x)$, since it is a chiral-odd function which can only be probed in combination with another chiral-odd function. So far, attempts were made to access transversity in convolution with the Collins fragmentation function in single hadron production [2, 3].

An alternative probe suggested to access transversity is the measurement of two-hadron production in semi-inclusive deep-inelastic scattering on a transversely polarized target. In this case, transversity is accessible via the chiral-odd two-hadron interference fragmentation function $H_1^\sphericalangle(z, M_h^2)$. The properties of interference fragmentation functions are described in detail in Refs. [4, 5, 6, 7, 8, 9]. New COMPASS results for identified pion and kaon pairs are presented in this contribution [1].

2 Two-hadron asymmetry

At leading twist, the fragmentation function of a polarized quark into a pair of hadrons is expected to be of the form

$$D_q^{2h}(z, M_h^2) + H_1^\sphericalangle(z, M_h^2) \sin\theta \sin\phi_{RS},$$

where M_h is the invariant mass of the hadron pair and $z = z_1 + z_2$ is the fraction of available energy carried by the two hadrons. $D_q^{2h}(z, M_h^2)$ is the unpolarized fragmentation function into two hadrons, and the interference fragmentation function $H_1^\sphericalangle(z, M_h^2)$ is the spin dependent T-odd part of the fragmentation function of a transversely polarized quark q into a hadron pair. The angles θ and ϕ_{RS} (see Fig. 1) are defined according to Ref. [10]. $\phi_{RS} = \phi_R + \phi_S - \pi$ is the sum of the azimuthal angle ϕ_R of a plane containing the two hadrons and the azimuthal angle ϕ_S of target spin vector with respect to the lepton scattering plane. In COMPASS ϕ_R is defined as the azimuthal angle of $\vec{R}_T$, the transverse component of the vector

$$\overrightarrow{R} = \frac{z_2 \cdot \overrightarrow{p}_1 - z_1 \overrightarrow{p}_2}{z_1 + z_2}$$

where the indices 1 and 2 refer to the two final state hadrons. θ is the polar angle of the first hadron in the two-hadron center-of-mass frame with respect to the direction of the summed hadron momentum $\overrightarrow{p}_h = \overrightarrow{p}_1 + \overrightarrow{p}_2$. With the applied cuts, θ peaks close to $\pi/2$ with $< \sin\theta > \approx 0.95$. The following results are obtained by integrating over $\sin\theta$. The number of hadron pairs in a bin of the Bjorken variable x, or of z, or of M_h is given by

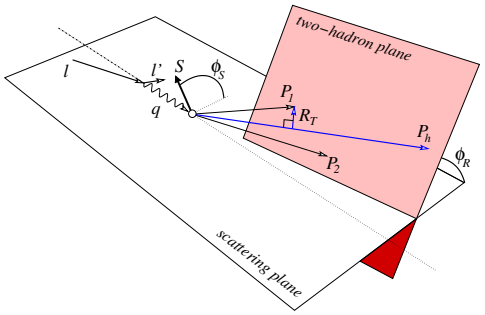

Figure 1: Definition of azimuthal angles ϕ_R and ϕ_S.

$$N^{\pm}(\phi_{RS}) = N_0 \cdot (1 \pm A_{UT}^{\sin\phi_{RS}} \cdot \sin\phi_{RS}),$$

where $\pm$ refers to the transverse target spin orientation and N_0 is the mean number of detected hadron pairs averaged over $\sin\phi_{RS}$. From the angular distribution of the hadron pairs, one can thus measure the asymmetry

$$A_{RS} = \frac{1}{f P_T D} \cdot A_{UT}^{\sin\phi_{RS}},$$

where $f \approx 0.38$ is the target dilution factor, $P_T \approx 0.5$ the target polarization and D the depolarization factor given by $D = (1-y)/(1-y+y^2/2)$, where y is the fractional energy transfer of the lepton.

The measured asymmetry can be factorized into a convolution of the transversity distribution $\Delta_T q(x)$ of the quarks of flavor q and the interference fragmentation $H_1^{\sphericalangle}(z, M_h^2)$ [10]:

$$A_{RS} = \frac{\Sigma_q \, e_q^2 \cdot \Delta_T q(x) \cdot H_1^{\sphericalangle}(z, M_h^2)}{\Sigma_q \, e_q^2 \cdot q(x) \cdot D_q^{2h}(z, M_h^2)},$$

summed over all quark flavors q. Both the interference fragmentation function $H_1^{\sphericalangle}(z, M_h^2)$ and the corresponding spin averaged fragmentation function into two hadrons $D_q^{2h}(z, M_h^2)$ are unknown, and need to be measured in e^+e^- annihilation or to be evaluated using models [6, 7, 8, 9]. They are expected to depend on $z = z_1 + z_2$ and on the invariant mass M_h of the two hadrons.

3 Event selection

The data discussed here have been taken in the years 2003 and 2004 in the COMPASS experiment at CERN [3]. It uses a secondary 160 GeV μ^+ beam from π and K decay in the CERN SPS M2 beamline. The muons are scattered on a transversely polarized solid state ${}^6LiD$ target. The target consists of two 60 cm long target cells with opposite polarization. To minimize systematic effects, the direction of the target polarization is reversed in both cells once a week. The scattered muons and the produced hadrons are detected in a 50 m long large-acceptance forward spectrometer with excellent particle identification capabilities. A large scale Ring Imaging Cherenkov detector (RICH) is used to distinguish pions, kaons and

protons [11]. It allows to separate pions and kaons over a large momentum range from the Cherenkov thresholds of 3 GeV/c respectively 9 GeV/c for pions and kaons up to 43 GeV/c.

The event selection was done in the same way as in the previous analysis of the Collins and Sivers asymmetries [2, 3]. For the selection of the DIS event sample, kinematic cuts of the squared four-momentum transfer $Q^2 > 1$ (GeV/c)^2, the hadronic invariant mass $W >$ 5 GeV/c^2 and the fractional energy transfer of the muon $0.1 < y < 0.9$ were applied. The average x, y and Q^2 in the final data sample is $x = 0.035$, $y = 0.33$ and $Q^2 = 2.4$ (GeV/c)^2. The mean hadron multiplicity is 1.9 hadrons per event.

Hadron pairs originating from the primary vertex are selected, where the first hadron has positive and the second one negative charge. The hadron pairs are separated into $\pi^+\pi^-$, $K^+\pi^-$, π^+K^-, and K^+K^- pairs based on the information of the RICH detector. Selection cuts of $z_1 > 0.1$ and $z_2 > 0.1$ suppress hadrons from the target fragmentation and $z = z_1 + z_2 < 0.9$ reject exclusively produced ρ-mesons. The resulting event sample contains 3.7 million $\pi^+\pi^-$, 0.3 million $K^+\pi^-$, 0.25 million π^+K^- and 0.1 million K^+K^- pairs. By combining data from both target cells as well as from sub-periods with opposite target polarization in a double ratio product described in detail in Ref. [3], the acceptance function of the spectrometer cancels out and the azimuthal asymmetry $A_{RS}(x, z, M_h)$ is extracted by a fit to the data. In various studies, it could be shown that systematic effects of the measurement are considerably smaller than the statistical uncertainty of the data.

4 Results

Figure 2 shows the preliminary results for the target single spin asymmetry $A_{RS}(x, y, M_h)$ for identified hadron pairs. In the first row, the asymmetry for $\pi^+\pi^-$ is displayed, in the second for $K^+\pi^-$ pairs, in the third for π^+K^- and in the last row for K^+K^- pairs. The asymmetries are plotted as a function of x, z and M_h. The measured asymmetries are very small and compatible with zero within the statistical precision of the data points. They do not show a significant dependence on the kinematic variables x and z and on the hadron pair invariant mass M_h.

5 Discussion

In several theoretical models, predictions have been made for the measured asymmetries $A_{RS}(x, z, M_h)$ for pions or unidentified hadrons on a deuteron target [7, 9]. The expected values of the asymmetry are generally small and below 1%. The small signal is attributed in these calculations to a partial cancellation of the asymmetries originating from scattering on *up* and *down* quarks of the proton and neutron in the isoscalar deuteron target. In 2007, COMPASS is taking data with a transversely polarized proton target, where the asymmetries are expected to be larger [9]. Together with the deuteron data presented here, a separation of the asymmetries originating from *up* and *down* quarks shall then be possible.

References

[1] Slides: `http://indico.cern.ch/contributionDisplay.py?contribId=165&sessionId=4&confId=9499`

[2] A. Bressan (COMPASS) and A. Kotzinian (COMPASS), these proceedings.

[3] V.Yu. Alexakhin *et al.* [COMPASS collaboration] Phys. Rev. Lett. **94**, 202002 (2005) and E.S. Ageev *et al.* [COMPASS collaboration] Nucl. Phys. **B765**, 31 (2007).

[4] J.R. Collins, S.F. Heppelmann and G.A. Ladinsky, Nucl. Phys. **B420**, 565 (1994).

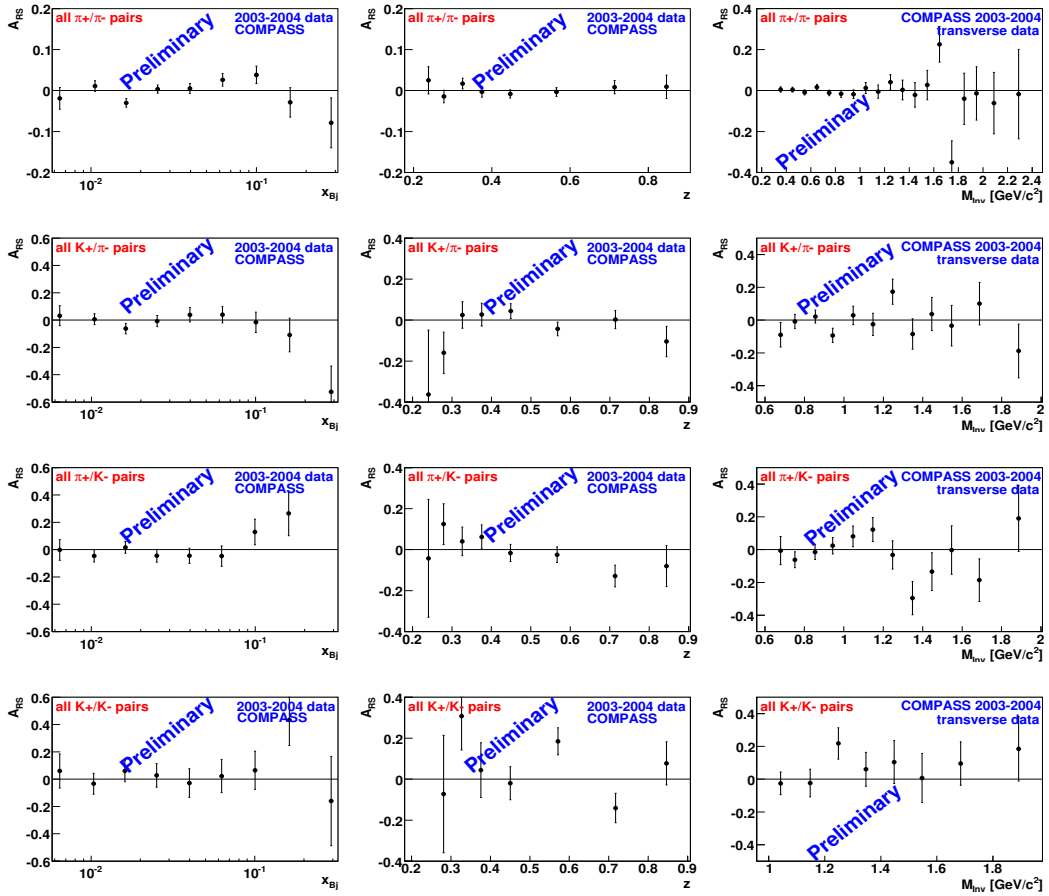

Figure 2: Asymmetries A_{RS} for identified hadron pairs: $\pi^+\pi^-$ (top row), $K^+\pi^-$ (second row), $K^-\pi^+$ (third row) and K^+K^- (last row). The asymmetries are shown as a function of x (left colum), z (middle column) and M_h (right column).

[5] X. Artru and J.C. Collins, Z. Phys. **C69**, 277 (1996).

[6] R.L. Jaffe, X. Ji and J. Tang, Phys. Rev. Lett. **80**, 1166 (1998).

[7] A. Bianconi, S. Boffi, R. Jakob and M. Radici, Phys. Rev. **D62**, 034008 (2000).

[8] M. Radici, R. Jakob and A. Bianconi, Phys. Rev. Lett **D65**, 074031 (2002).

[9] A. Bacchetta and M. Radici, Phys. Rev. **D67**, 094002 (2003), Phys. Rev. **D69**, 074026 (2004) and Phys. Rev. **D74** 114007 (2006).

[10] X. Artru, hep-ph/0207309 (2002).

[11] P. Abbon *et al.* [COMPASS collaboration] hep-ex/0703049, accepted by NIM **A**.

Evolution Equations for Di-hadron Fragmentation Functions

Marco Radici

INFN and Dipartimento di Fisica Nucleare e Teorica - Università di Pavia
via Bassi 6, I27100 Pavia - Italy

Di-hadron Fragmentation Functions describe the probability that a quark hadronizes into two hadrons plus anything else, i.e. the process $q \to h_1\, h_2\, X$. Via a suitable single-spin asymmetry in semi-inclusive deep inelastic scattering (SIDIS), they can be used to extract the quark transversity distribution h_1 in the nucleon, a missing cornerstone of the nucleon partonic spin structure. I will discuss their evolution equations when they are explicitly depending on the invariant mass of the two hadrons. The equations are necessary to connect two-particle-inclusive measurements at different energies.

1 Introduction

Di-hadron Fragmentation Functions (DiFF) have been introduced for the first time in the context of $e^+e^- \to h_1h_2X$ reaction [2], and later have been recognized to be necessary in order to guarantee factorization of all collinear singularities [3]. However, in all these studies DiFF were always considered as functions only of the energy fractions z_1 and z_2 delivered to the two hadrons, while most of the experimental information consists of their invariant mass distribution M_h. Also the twist analysis of the quark-quark correlator for two-hadron inclusive production (see Fig. 1) indicates that the extracted DiFF are in general functions also of the pair relative momentum $R = P_1 - P_2$ [4], whose transverse spatial component $\mathbf{R}_T$ is related to M_h [5]. In this case, I will refer to the socalled extended DiFF (extDiFF).

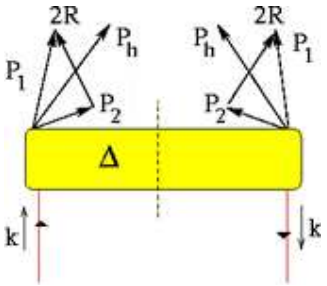

Figure 1: The quark-quark correlator for fragmentation in two hadrons.

ExtDiFF can act as spin analyzers of the fragmenting quark; in particular the transverse polarization $\mathbf{s}_T$ of the latter can be related to the azimuthal orientation of the plane containing $\mathbf{P}_1$ and $\mathbf{P}_2$ via the mixed product $\mathbf{s}_T \cdot \mathbf{P}_1 \times \mathbf{P}_2$ (see Fig. 2). The strength of this effect is described by the extDiFF $H_1^{\sphericalangle}$. In SIDIS on transversely polarized targets, this function appears in combination with the transversity function, a leading-twist partonic distribution yet undetermined. The unknown extDiFF can be extracted from e^+e^- annihilations in two hadron pairs [6].

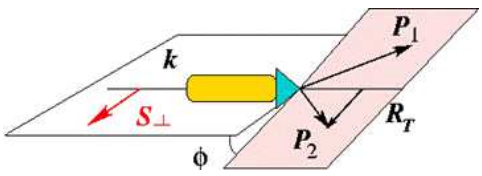

Figure 2: The nonperturbative effect $\mathbf{s}_T \cdot \mathbf{P}_1 \times \mathbf{P}_2$ generating the single-spin asymmetry.

The HERMES and COMPASS collaborations have recently reported preliminary measurements of the asymmetry induced by the $\mathbf{s}_T \cdot \mathbf{P}_1 \times \mathbf{P}_2$ effect at the average scale $\langle Q^2 \rangle = 2.53$

GeV^2 [7, 8]. The BELLE collaboration is planning to extract $H_1^{\sphericalangle}$ in e^+e^- annihilation but at the higher scale $s \approx 100$ GeV^2 [9]. In this talk I will discuss the evolution equations for extDiFF.

2 Evolution equations for DiFF

As already anticipated in Sec. 1, DiFF are necessary to get a finite cross section for the $e^+e^- \to h_1 h_2 X$ process at NLO order [3]. The reason relies in the indistinguishability of the two mechanisms depicted in Fig. 3, which both lead to the observed hadron pair, either through DiFF or through separate single-hadron fragmentations after a partonic branching occurring at an arbitrary scale, intermediate between the hard Q^2 one and the soft Q_0^2 one. The consequence is the appearance of an inhomogenous term in the evolution equations for DiFF [3].

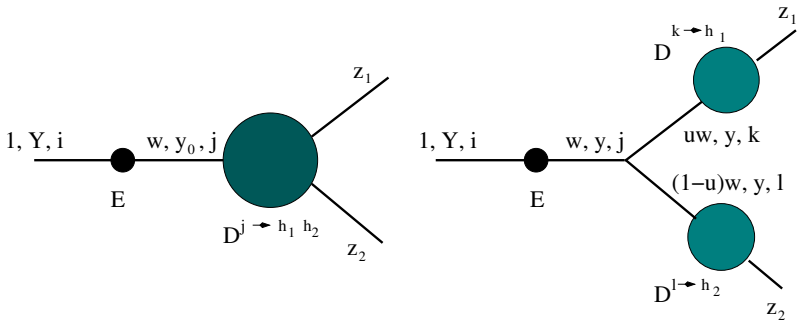

Figure 3: Double- and single-hadron fragmentations; the momentum fractions are indicated along with the scales and the parton indices; the black dots represent the parton evolution function E (see text).

Making use of the techniques of jet calculus [2], the result of Ref. [3] can be easily reproduced when the two hadrons are emitted close in phase space (*i.e.*, inside the same jet) and wide-angle hard partons are neglected. The phase-space structure of collinear singularities singled out in the fixed-order calculation of Ref. [3] can be translated in jet calculus as a degeneracy in all possible competing mechanisms that could realize the desired final state.

It is convenient to introduce the evolution variable

$$y = \frac{1}{2\pi\beta} \ln \left[\frac{\alpha_s(Q_0^2)}{\alpha_s(Q^2)} \right] , \tag{1}$$

between some two arbitrary hard Q^2 and soft Q_0^2 scales. If working at Leading Log Approximation (LLA), α_s and β are the usual strong coupling constant and β function, both at one loop. We can introduce also the parton evolution function $E_j^i(x, y)$, which expresses the probability of finding a parton j at scale Q_0^2 with a momentum fraction x of the parent parton i at scale Q^2. It satisfies standard DGLAP evolution equations [2] and can be shown to resum all collinear leading logarithms of the kind $\alpha_s^n \ln^n(Q^2/Q_0^2)$ [10]. The evolution variable Y corresponding to the initial hard scale Q^2 is not zero, as one could deduce from Eq. 1, but can be defined by replacing Q_0^2 with the renormalization scale μ_R^2 in Eq. 1 itself.

In this picture, the fragmentation process of Fig. 3 is described by

$$\frac{1}{\sigma_{\rm jet}}\frac{d\sigma^{i\to h_1h_2}}{dz_1dz_2dY} = \int_{z_1+z_2}^1 \frac{dw}{w^2}\,E_j^i(w,Y-y_0)\,D^{j\to h_1h_2}\left(\frac{z_1}{w},\frac{z_2}{w},y_0\right) + \int_{y_0}^Y dy\int_{z_1+z_2}^1\frac{dw}{w^2}\int_{\frac{z_1}{w}}^{1-\frac{z_2}{w}}\frac{du}{u(1-u)}\,E_j^i(w,Y-y)\,\hat{P}_{kl}^j(u) \times D^{k\to h_1}\left(\frac{z_1}{wu},y\right)\,D^{l\to h_2}\left(\frac{z_2}{w(1-u)},y\right)\,, \quad (2)$$

where $\hat{P}$ are the usual real Altarelli-Parisi splitting functions, $D^{i\to h}$ are single-hadron fragmentation functions, and $D^{i\to h_1h_2}$ are DiFF. Taking the derivative d/dY of Eq. 2, and further transforming the dependence upon Y back to the one on Q^2, it easy to recover the inhomogeneous evolution equation for $D^{i\to h_1h_2}$ in the jet calculus language [10].

3 Evolution equations for extDiFF

The difference between extDiFF and DiFF is the explicit dependence of the former upon the transverse component of the hadron pair relative momentum, $\mathbf{R}_T$, or, equivalently, upon their invariant mass M_h through the relation [5, 10]

$$R_T^2 = \frac{z_1z_2}{z_1+z_2}\left[\frac{M_h^2}{z_1+z_2}-\frac{M_1^2}{z_1}-\frac{M_2^2}{z_2}\right]\,. \quad (3)$$

Knowledge of the R_T^2 scale makes the scale of the partonic branching no longer arbitrary. In fact, at LLA the virtualities of the involved partons are related by [10]

$$k_j^2 = \frac{k_k^2}{u}+\frac{k_l^2}{1-u}+\frac{r_T^2}{u(1-u)} \approx r_T^2 \approx R_T^2\,, \quad (4)$$

where r_T^2 is the relative momentum of the partons k and l carrying momentum fractions u and $1-u$ of the parent parton j, respectively.

Consequently, the arbitrary intermediate scale y appearing in the second term of Eq. 2 collapses to y_T, defined similarly to Y but with the replacement $Q^2 \leftrightarrow R_T^2$. The analogue of Eq. 2 for extDiFF becomes, therefore,

$$\frac{1}{\sigma_{\rm jet}}\frac{d\sigma^{i\to h_1h_2}}{dz_1dz_2dR_T^2dY} = \int_{z_1+z_2}^1 \frac{dw}{w^2}\,E_j^i(w,Y-y_0)\,D^{j\to h_1h_2}\left(\frac{z_1}{w},\frac{z_2}{w},R_T^2,y_0\right) + \frac{\alpha_s(R_T^2)}{2\pi R_T^2}\int_{z_1+z_2}^1\frac{dw}{w^2}\int_{\frac{z_1}{w}}^{1-\frac{z_2}{w}}\frac{du}{u(1-u)}\,E_j^i(w,Y-y_T)\,\hat{P}_{kl}^j(u) \times D^{k\to h_1}\left(\frac{z_1}{wu},y_T\right)\,D^{l\to h_2}\left(\frac{z_2}{w(1-u)},y_T\right)\,. \quad (5)$$

Taking the derivative d/dY of the previous expression, and further transforming back to the usual Q^2, we finally get [10]

$$\frac{d}{d\ln Q^2}D^{i\to h_1h_2}(z_1,z_2,R_T^2,Q^2) = \frac{\alpha_s(Q^2)}{2\pi}\int_{z_1+z_2}^1\frac{du}{u^2}\,D^{j\to h_1h_2}\left(\frac{z_1}{u},\frac{z_2}{u},R_T^2,Q^2\right)\,P_{ji}(u)\,, \quad (6)$$

where P_{ji} are the complete Altarelli-Parisi splitting functions, including the virtual contributions.

The same result holds also for the polarized fragmentation function $H_1^{\sphericalangle}$, provided that the splitting kernels δP for transversely polarized partons are used [10]. Equation 6 can also be conveniently diagonalized using a double Mellin transformation [10].

On the basis of Eq. 6, we argue that the cross section at NLO order for the inclusive production of two hadrons h_1 and h_2, inside the same jet and with invariant mass M_h, can be expressed in the factorized form

$$\frac{d\sigma^{h_1 h_2}}{dz_1 dz_2 dR_T^2 dQ^2} = \sum_i \sigma^i \otimes D^{i\to h_1 h_2}(R_T^2, Q^2) \,, \tag{7}$$

where σ^i are the same coefficient functions found in the case of single-hadron inclusive production.

4 Acknowledgments

I warmly thank F.A. Ceccopieri and A. Bacchetta, without whom this work would not have been possible.

References

[1] Slides:
`http://indico.cern.ch/contributionDisplay.py?contribId=167&sessionId=4&confId=9499`
[2] K. Konishi, A. Ukawa and G. Veneziano, Phys. Lett. **B78** 243 (1978).
[3] D. de Florian and L. Vanni, Phys. Lett. **B578** 139 (2004).
[4] A. Bianconi *et al.*, Phys. Rev. D**62** 034008 (2000).
[5] A. Bacchetta and M. Radici, Phys. Rev. D**67** 094002 (2003).
[6] D. Boer, R. Jakob and M. Radici, Phys. Rev. D**67** 094003 (2003).
[7] P.B. van der Nat (HERMES), arXiv:hep-ex/0512019 (2005).
[8] A. Martin (COMPASS), arXiv:hep-ex/0702002 (2007).
[9] K. Hasuko *et al.*, AIP Conf. Proc. **675** 454 (2003).
[10] F.A. Ceccopieri, M. Radici and A. Bacchetta, Phys. Lett. **B650** 81 (2007).

Beyond Collins and Sivers: Further Measurements of the Target Transverse Spin-Dependent Azimuthal Asymmetries in Semi-Inclusive DIS from COMPASS

Aram Kotzinian *
on behalf of the COMPASS collaboration

INFN, Sezione di Torino, Via P. Giuria 1, I-10125 Torino, Italy

In semi-inclusive DIS of polarized leptons on a transversely polarized target eight azimuthal modulations appear in the cross-section. Within QCD parton model four azimuthal asymmetries can be interpreted at leading order, two of them being the already measured Collins and Sivers asymmetries. The other two leading twist asymmetries, related to different transverse momentum dependent quark distribution functions, and also additional four asymmetries which can be interpreted as twist-three contributions have been measured for the first time at COMPASS, using a 160 GeV/c longitudinally polarized ($P_{beam} \simeq -0.8$) muon beam and a transversely polarized ^6LiD target. We present here the preliminary results from the 2002-2004 data.

1 Introduction

During last few years many exciting experimental results and theory development are obtained in SIDIS on the transversely polarized target. Up to now only the measurements [2, 3, 4] of Sivers and Collins asymmetries were performed by HERMES and COMPASS collaborations and together with data from BELLE [5] they allow a first extraction the transversity and Sivers transverse momentum dependent (TMD) distribution functions (DFs) and Collins fragmentation function (FF). In addition to these, the general expression of SIDIS cross section [6] contains six more target transverse polarization dependent azimuthal asymmetries. Here we present the preliminary results on these asymmetries for the first time measured by COMPASS from the 2002-2004 data.

1.1 Definition of asymmetries

In the following the notations of Ref. [7] are used. There are eight azimuthal modulations related to the target transverse polarization:

$$\begin{aligned} &w_1(\phi_h,\phi_s)=\sin(\phi_h-\phi_s),\ w_2(\phi_h,\phi_s)=\sin(\phi_h+\phi_s),\ w_3(\phi_h,\phi_s)=\sin(3\phi_h-\phi_s),\\ &w_4(\phi_h,\phi_s)=\sin(\phi_s),\ w_5(\phi_h,\phi_s)=\sin(2\phi_h-\phi_s),\ w_6(\phi_h,\phi_s)=\cos(\phi_h-\phi_s),\\ &w_7(\phi_h,\phi_s)=\cos(\phi_s),\ w_8(\phi_h,\phi_s)=\cos(2\phi_h-\phi_s), \end{aligned} \tag{1}$$

*On leave from Yerevan Physics Institute, 375036 Yerevan, Armenia and JINR, 141980 Dubna, Russia.

where first two correspond to Sivers and Collins effects. The expression for the cross section in interest can be represented as

$$\begin{aligned} d\sigma(\phi_h,\phi_s,...) &\propto (1+|\mathbf{S}_T|\sum_{i=1}^{5} D^{w_i(\phi_h,\phi_s)} A_{UT}^{w_i(\phi_h,\phi_s)} w_i(\phi_h,\phi_s) \\ &+ P_{beam}|\mathbf{S}_T|\sum_{i=6}^{8} D^{w_i(\phi_h,\phi_s)} A_{LT}^{w_i(\phi_h,\phi_s)} w_i(\phi_h,\phi_s)+...\big), \end{aligned} \tag{2}$$

where $\mathbf{S}_T$ is the target transverse polarization. We factored out the explicitly calculable depolarization factors, $D^{w_i(\phi_h,\phi_s)}$, and defined the asymmetries as the ratios of corresponding structure functions to unpolarized one:

$$A_{BT}^{w_i(\phi_h,\phi_s)} \equiv \frac{F_{BT}^{w_i(\phi_h,\phi_s)}}{F_{UU,T}}, \tag{3}$$

where $B = L$ or $B = U$ corresponds to beam polarization dependent or independent part of asymmetry.

The depolarization factors entering in Eq. (2) depend only on y and are given as

$$\begin{aligned} &D^{\sin(\phi_h-\phi_s)}(y) = 1, \;\; D^{\cos(\phi_h-\phi_s)}(y) = \frac{y(2-y)}{1+(1-y)^2}, \\ &D^{\sin(\phi_h+\phi_s)}(y) = D^{\sin(3\phi_h+\phi_s)}(y) = \frac{2(1-y)}{1+(1-y)^2}, \\ &D^{\sin(2\phi_h-\phi_s)}(y) = D^{\sin(\phi_s)}(y) = \frac{2(2-y)\sqrt{1-y}}{1+(1-y)^2}, \\ &D^{\cos(2\phi_h-\phi_s)}(y) = D^{\cos(\phi_s)}(y) = \frac{2y\sqrt{1-y}}{1+(1-y)^2}. \end{aligned} \tag{4}$$

The asymmetries extracted from the data as amplitudes of corresponding azimuthal modulations (raw asymmetries) are then given by

$$A_{UT,\,raw}^{w_i(\phi_h,\phi_s)} = D^{w_i(\phi_h,\phi_s)}(y) f |S_T| A_{UT}^{w_i(\phi_h,\phi_s)}, \;\; (i=1,5), \tag{5}$$

$$A_{LT,\,raw}^{w_i(\phi_h,\phi_s)} = D^{w_i(\phi_h,\phi_s)}(y) f P_{beam} |S_T| A_{LT}^{w_i(\phi_h,\phi_s)}, \;\; (i=6,8), \tag{6}$$

where f is the target polarization dilution factor.

In the QCD parton model the asymmetries $A_{LT}^{\cos(\phi_h-\phi_s)}$ and $A_{UT}^{\sin(3\phi_h-\phi_s)}$ are given by the ratio of convolutions of spin-dependent to spin-independent twist two DFs and FFs, for example

$$A_{UT}^{\sin(3\phi_h-\phi_s)} = \frac{h_{1T}^{\perp q} \otimes H_{1q}^{\perp h}}{f_1^q \otimes D_{1q}^h}, \tag{7}$$

and can be used for extraction of DFs g_{1T}^q and $h_{1T}^{\perp q}$ describing the quark longitudinal and transverse (along quark transverse momentum) polarization in the transversely polarized nucleon. The other asymmetries can be interpreted as Cahn kinematic corrections to spin effects on the transversely polarized nucleon [6], for example:

$$A_{LT}^{\cos(\phi_s)} = \frac{M}{Q}\frac{g_{1T}^q \otimes D_{1q}^h}{f_1^q \otimes D_{1q}^h}. \tag{8}$$

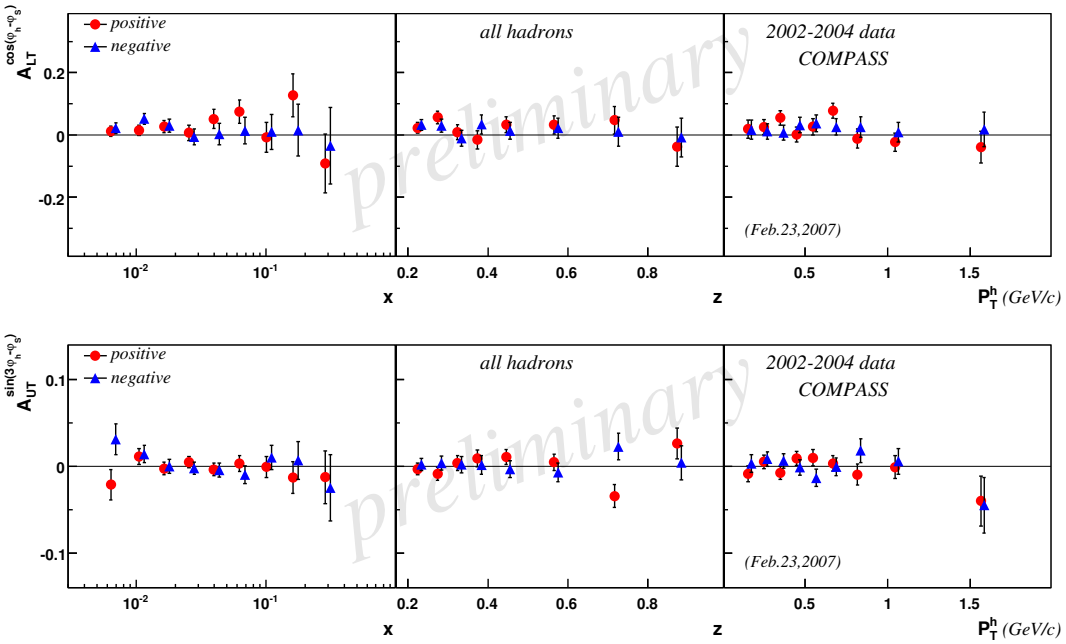

Figure 1: The asymmetries $A_{LT}^{\cos(\phi_h-\phi_s)}$ and $A_{UT}^{\sin(3\phi_h-\phi_s)}$ as a function of x, z and P_T^h.

2 Results

The event selection and asymmetry extraction are done as described in [4]. The following kinematic cuts were imposed: $Q^2 > 1$ (GeV/c)^2, $W > 5$ GeV, $0.1 < y < 0.9$, $P_T^h > 0.1$ GeV/c and $z > 0.2$. In Figs. 1 and 2 for the first time we present six target transverse spin dependent asymmetries extracted from COMPASS 2002–2004 data collected on deuterium target. The estimated systematic errors are smaller than statistical. All six newly measured asymmetries are compatible with zero within statistical errors.

References

[1] Slides:
`http://indico.cern.ch/contributionDisplay.py?contribId=168&sessionId=4&confId=9499`

[2] A. Airapetian *et al.* [HERMES Collaboration], Phys. Rev. Lett. **94**, 012002 (2005)

[3] V. Y. Alexakhin *et al.* [COMPASS Collaboration], Phys. Rev. Lett. **94**, 202002 (2005) [arXiv:hep-ex/0503002].

[4] E. S. Ageev *et al.* [COMPASS Collaboration], Nucl. Phys. B **765**, 31 (2007) [arXiv:hep-ex/0610068];

[5] R. Seidl *et al.* [Belle Collaboration], Phys. Rev. Lett. **96**, 232002 (2006) [arXiv:hep-ex/0507063].

[6] A. Kotzinian, Nucl. Phys. B **441**, 234 (1995) [arXiv:hep-ph/9412283].

[7] A. Bacchetta, M. Diehl, K. Goeke, A. Metz, P. Mulders and M. Schlegel, JHEP **0702**, 093 (2007) [arXiv:hep-ph/0611265].

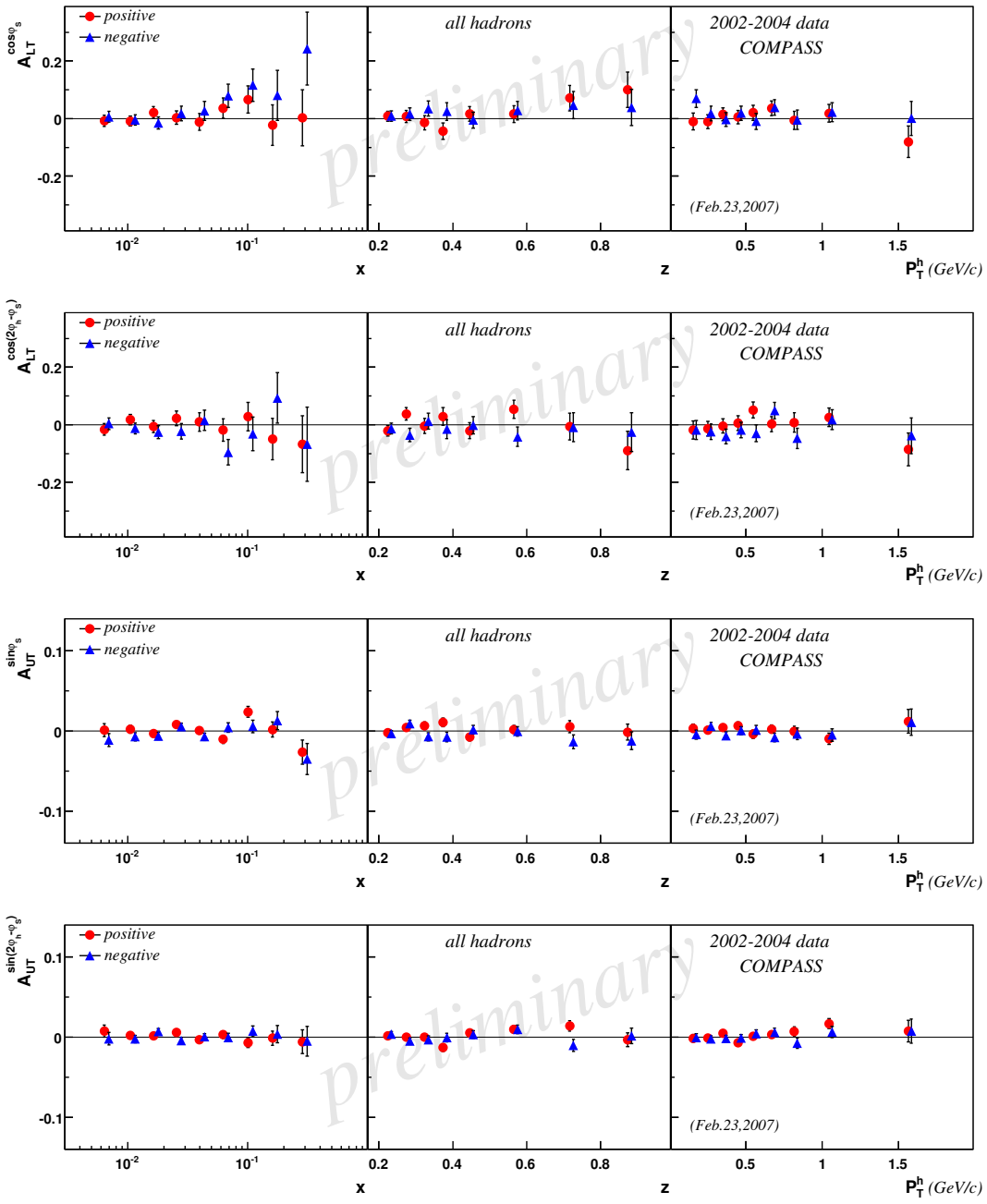

Figure 2: The asymmetries $A_{LT}^{\cos\phi_s}$, $A_{LT}^{\cos(2\phi_h-\phi_s)}$, $A_{UT}^{\sin\phi_s}$ and $A_{UT}^{\sin(2\phi_h-\phi_s)}$ as a function of x, z and P_T^h.